Study of hadronic B meson decays with the LHCb spectrometer (at LHC) and an investigation of detector requirements for the Future Circular Collider (FCC-ee)

Tristan Miralles

▶ **To cite this version:**

Tristan Miralles. Study of hadronic B meson decays with the LHCb spectrometer (at LHC) and an investigation of detector requirements for the Future Circular Collider (FCC-ee). Accelerator Physics [physics.acc-ph]. Université Clermont Auvergne, 2024. English. NNT : 2024UCFA0099 . tel-04959240

HAL Id: tel-04959240

https://theses.hal.science/tel-04959240v1

Submitted on 20 Feb 2025

HAL is a multi-disciplinary open access archive for the deposit and dissemination of scientific research documents, whether they are published or not. The documents may come from teaching and research institutions in France or abroad, or from public or private research centers.

L'archive ouverte pluridisciplinaire **HAL**, est destinée au dépôt et à la diffusion de documents scientifiques de niveau recherche, publiés ou non, émanant des établissements d'enseignement et de recherche français ou étrangers, des laboratoires publics ou privés.

UNIVERSITE CLERMONT AUVERGNE

ECOLE DOCTORALE DES SCIENCES FONDAMENTALES

THESE

présentée pour obtenir le grade de

DOCTEUR D'UNIVERSITE

Spécialité : Constituants élémentaires

Par MIRALLES Tristan

Study of hadronic B meson decays with the LHCb spectrometer (at LHC) and an investigation of detector requirements for the Future Circular Collider (FCC-*ee*)

Soutenue publiquement le 18 octobre 2024 devant le jury :

Mme. Ana TEIXEIRA	Président du jury
M. Fabrizio PALLA	Rapporteur
M. Patrick ROBBE	Rapporteur
M. Thomas LATHAM	Examinateur
M. Stéphane MONTEIL	Directeur de thèse
M. Eric COGNERAS	Encadrant

Remerciements

To begin these acknowledgments, I would like to express my sincere thanks to Ana Teixeira, the president of my jury, for the time and effort she dedicated to overseeing my work. I am also deeply grateful to Fabrizio Palla and Patrick Robbe for serving as my reviewers and for their invaluable feedback. My thanks go as well to Thomas Latham for his commitment in evaluating my work. To all of you, thank you for giving me the opportunity to defend my thesis and, ultimately, for making it possible for me to achieve my goal of becoming a doctor.

Je tiens ensuite à exprimer ma profonde gratitude envers mes encadrants. Stéphane, merci pour tous les moments passés à m'aider sur mon travail de thèse et pour les nombreuses discussions enrichissantes, que ce soit en conférence (à Londres, Marseille, et Annecy), au laboratoire, ou pendant la préparation des travaux pratiques. Tu m'as offert de nombreuses opportunités de présenter mon travail et m'as soutenu dans les moments difficiles, tout en maintenant un enthousiasme constant tout au long de ces trois années. Eric, je te remercie pour ta bienveillance et ton aide précieuse lorsque j'ai rencontré des difficultés avec nos logiciels. Ton engagement sur l'analyse de Dalitz intégrée dans le temps a été crucial pour son inclusion dans ma thèse. Je suis également reconnaissant pour tous les moments agréables partagés pendant nos repas et pour les nombreux conseils que tu m'as prodigués. Merci à vous deux pour votre soutien, tant humain que professionnel ; vous êtes de véritables exemples d'intégrité scientifique. Merci à vous d'avoir toujours été bienveillants avec moi, et de m'avoir soutenu alors même que je partageais avec vous mon choix de quitter la Physique des particules expérimentales après la thèse. Je suis heureux de vous avoir eus comme encadrants et je n'aurais pas pu espérer un meilleur encadrement.

Je souhaiterais également remercier mes collègues. Merci à l'équipe LHCb du laboratoire, notamment Olivier, Régis, Ziad, Vincent, Yingrui, Zehua, et Chandi, pour vos conseils lors des réunions et les bons moments partagés. Merci aux membres de la petite équipe FCC du laboratoire, Romain et Hervé, pour vos conseils. Un grand merci aussi à l'équipe administrative du laboratoire, en particulier à Florence, Géraldine, et Cyril, pour votre aide précieuse dans l'organisation de mes différentes missions. Je suis également reconnaissant envers mes collaborateurs du groupe $K^0_S hh'$ pour leurs feedbacks et le travail conjoint sur nos projets. Merci à Emmanuel Perez pour son aide précieuse sur mon analyse FCC.

Maintenant, je tiens à remercier mes amis, du laboratoire et d'ailleurs. Désolé par avance si j'en oublie. Thanks a lot to my lab friends Lars (my mission buddy), Mike (the best office mate), Jessy, Gaetan, Nicolas, and Laetitia; I wish you all the best for your futures. Merci beaucoup à Zoé, Baptiste, Léane, Antoine, Manon (B.), Joscelin, Thibault, Axel, Romain, Manon (S.), Mathilde, Mag, Alison et Manu. Merci à tous pour votre soutien et pour les bons moments partagés. J'espère que nous continuerons à créer de nombreux souvenirs ensemble !

Il me paraît également important de remercier l'équipe pédagogique de la Préparation aux Études Scientifiques, la formation que j'ai suivie entre mon Bac STAV en aménagement paysager et mon parcours universitaire. Sans cette dernière, je n'aurais pas pu réaliser mon parcours universitaire, et donc en être là aujourd'hui. Je tiens aussi à remercier les équipes pédagogiques de la Licence de Physique et du Master Physique Fondamentale et Applications. Vos enseignements m'ont porté jusqu'en thèse.

Enfin, je veux terminer ces remerciements par ma famille. Merci à ma belle-famille Sandrine, Richard, Valentin et Lisa (même si tu es arrivée un peu plus tard) pour tous les moments ressourçants partagés ensemble, que ce soit dans l'Aveyron, près d'Angers et du Mans, ou dans la plus belle région de France (l'Auvergne!). Un remerciement spécial à nos animaux de compagnie, et en particulier à mon chat Flocon, pour leur capacité à recentrer notre attention sur les choses simples et à nous aider à relativiser nos problèmes. Ces moments partagés avec eux ont été essentiels pour maintenir un équilibre de vie durant ces années intenses. Je tiens aussi à remercier l'ensemble des membres de ma famille directe. J'ai la chance de faire partie d'une famille unie, ce qui m'a assurément aidé pendant ces trois années. Je veux également rendre hommage à mes deux grands-pères qui nous ont quittés plus tôt cette année. Bien sûr, je tiens à remercier mes parents, qui ont toujours cru en moi, m'ont toujours soutenu, surtout lorsque j'ai fait le choix audacieux d'envisager un parcours universitaire, moi qui n'avais jamais excellé à l'école auparavant. Malheureusement, ma mère nous ayant quittés en 2020, je ne pourrai pas partager avec elle la joie de devenir docteur. C'est pourquoi je tiens à lui dédier ce travail et à lui rendre hommage. Je suis devenu l'homme que je suis aujourd'hui grâce à mes parents et aux valeurs qu'ils m'ont transmises. Mes derniers mots sont pour Maëlys, avec qui je partage ma vie depuis bientôt huit ans. Tu es un pilier de ma vie, et je ne te remercierai jamais assez pour tout le soutien que tu m'as apporté pendant la thèse. Tu as été au premier rang dans tous les moments de doute. Même quand j'étais difficile à vivre, tu as toujours été là. Clairement, même si tu ne la comprends pas vraiment, cette thèse te doit beaucoup et c'est aussi un peu la tienne. Nous avons fait nos études ensemble, traversé les pires épreuves, acheté une maison ensemble, et je suis sûr que (plus tard) nous deviendrons de bons parents ensemble. Je suis impatient de partager avec toi la vie qui nous attend. Merci pour tout.

Abstract

The thesis consists of two studies examining the decay of neutral B mesons to test the Standard Model.

The first study investigates charmless three-body hadronic decays of neutral B mesons with a K^0_S in the final state, using the Run I and Run II datasets from the Large Hadron Collider (LHC) recorded by the LHCb spectrometer. This study prominently features the first measurement of the branching fraction for $B^0_s \to K^0_S K^+ K^-$ and updates the measurements for four additional decay modes. The methodology, from data sample selection to branching fraction determination, is thoroughly described. In particular, an innovative method is presented that makes the best use of the available statistics to determine the selection efficiency. Furthermore, the development of L0Hadron trigger corrections, essential for this and other LHCb analyses, is detailed. Preliminary evidence of *CP* violation in $B^0_s \to K^0_S \pi^+ \pi^-$ is suggested through preliminary results of the first $B^0_s \to K^0_S \pi^+ \pi^-$ untagged Dalitz time-integrated analysis, building on previous branching fraction measurements.

The second study explores the potential of future experiments at the Future Circular Collider FCC-*ee* to unravel the quark transition $b \to s\tau^+\tau^-$, which remains unobserved to date. At the meson scale, the decay $B^0 \to K^{*0}\tau^+\tau^-$, with subsequent transitions $K^{*0} \to K^+\pi^-$ and $\tau \to \pi\pi\pi\nu_\tau$, is analysed using a method to explicitly reconstruct the two undetected neutrinos. The detector requirements to study this decay are evaluated; in particular, the vertexing resolution performance is emulated and compared to IDEA, a detector concept used for FCC-*ee* simulations. Simulated signal events and dominant background events are analysed to determine the precision of the $B^0 \to K^{*0}\tau^+\tau^-$ branching fraction measurement as a function of vertexing resolution performance, and therefore establishing vertex detector requirements.

Résumé

La thèse se compose de deux études examinant la désintégration des mésons beaux neutres afin de tester le Modèle Standard.

La première étude examine les désintégrations hadroniques sans charme à trois corps des mésons beaux neutres avec un K_S^0 dans l'état final, en utilisant les données du Run I et du Run II provenant du Large Hadron Collider (LHC) enregistrées par le spectromètre LHCb. Cette étude présente notamment la première mesure du rapport d'embranchement pour $B_s^0 \to K_S^0 K^+ K^-$ et met à jour les mesures de quatre modes de désintégration supplémentaires. La méthodologie, depuis la sélection de l'échantillon de données jusqu'à la détermination des rapports d'embranchements, est décrite en détail. En particulier, une méthode innovante est présentée, utilisant au mieux la statistique disponible pour déterminer l'efficacité de la sélection. De plus, le développement des corrections du trigger L0Hadron, essentielles pour cette analyse et d'autres analyses à LHCb, est détaillé. Des indices de violation *CP* dans $B_s^0 \to K_S^0 \pi^+ \pi^-$ sont suggérés à travers les résultats préliminaires de la première analyse de Dalitz intégrée dans le temps sans tagging de saveur de $B_s^0 \to K_S^0 \pi^+ \pi^-$, s'appuyant sur les mesures de rapport d'embranchement.

La deuxième étude explore le potentiel des futures expériences au Future Circular Collider FCC-*ee* pour découvrir la transition de quark $b \to s\tau^+\tau^-$, qui reste à ce jour non observée. À l'échelle du méson, la désintégration $B^0 \to K^{*0}\tau^+\tau^-$, avec les transitions $K^{*0} \to K^+\pi^-$ et $\tau \to \pi\pi\pi\nu_\tau$, est analysée en utilisant une méthode pour reconstruire explicitement les deux neutrinos non détectés. Les prérequis du détecteur pour étudier cette désintégration sont évalués ; en particulier, la performance de résolution sur la position du vertex est simulée et comparée à IDEA, un concept de détecteur utilisé pour les simulations FCC-*ee*. Les événements de signal simulés et les événements de bruit de fond dominants sont analysés pour déterminer la précision de la mesure du rapport d'embranchement de $B^0 \to K^{*0}\tau^+\tau^-$ en fonction de la performance de résolution sur la position du vertex, établissant ainsi les prérequis du détecteur de vertex.

Summary

Introduction **1**

1 Standard Model and Flavour Physics **3**
1.1 Standard Model of particle physics and Flavours . . . 3
1.1.1 Standard Model in a nutshell . . . 3
1.1.2 How flavours shaped the Standard Model : the fermions history . . . 5
1.1.3 Standard Model limits . . . 6
1.2 The CKM matrix . . . 7
1.2.1 The CKM mixing matrix . . . 7
1.2.2 Representation . . . 7
1.3 *CP* violation in Standard Model . . . 10
1.3.1 The *CP* symmetry . . . 10
1.3.2 *CP* violation manifestation . . . 11
1.3.3 The different types of *CP* violation . . . 12
CP violation in decay . . . 12
CP violation in mixing . . . 12
CP violation in interference (or mixing-induced *CP* violation) . . . 13
1.4 Phenomenology of hadronic B-decays . . . 14
1.4.1 Quark level transitions . . . 14
1.4.2 Hadron level transition . . . 15
1.4.3 Physical observables . . . 16
1.4.4 The $B^0_{(s)} \to K^0_S hh'$ decays study interests . . . 18
1.5 Phenomenology of semileptonic B-decays . . . 19
1.5.1 Quark level transition . . . 19
1.5.2 The hadron-level transition of interest . . . 19
1.5.3 Physical observables . . . 20
1.5.4 Experimental status . . . 21
1.5.5 A comment on B-meson Lepton Flavour Universality . . . 22

2 The instruments **23**
2.1 The Large Hadron Collider . . . 23
2.1.1 Global description . . . 23
2.1.2 Protons acceleration . . . 24
2.1.3 LHC performances . . . 25
2.1.4 The experiments . . . 26
2.2 LHCb detector . . . 27
2.2.1 b-hadron production at LHC . . . 27
2.2.2 General overview of the detector . . . 27
2.2.3 Tracking system . . . 30
Vertex locator (VELO) . . . 30

Tracker Turicencis (TT) . . . 30
Magnet . . . 31
T stations . . . 32
Track categories at LHCb . . . 33
2.2.4 Particle identification system . . . 33
RICH detectors . . . 34
Calorimeter system . . . 34
Muon system . . . 38
PID techniques . . . 38
2.2.5 Trigger . . . 39
L0 trigger . . . 39
High Level Trigger 1 . . . 40
High Level Trigger 2 . . . 40
Trigger decision . . . 40
2.3 LHCb tools . . . 42
2.3.1 LHCb Software . . . 42
2.3.2 $B^0_{d,s} \to K^0_S h^+ h'^-$ datasets and MC samples . . . 42
Data samples . . . 43
MC samples . . . 43
Trigger . . . 44
Stripping . . . 45
Events reconstruction . . . 47
2.4 L0 trigger corrections determination . . . 50
2.4.1 Trigger efficiency determination . . . 50
A data driven method . . . 50
HCAL measurements: real transverse energy . . . 50
L0Hadron candidates . . . 52
Needed observables . . . 52
Effects to consider . . . 53
2015 specificity . . . 55
2.4.2 Underlying energy maps determination . . . 55
Run II . . . 55
Run I . . . 56
2.4.3 $\pi^\pm$ and $K^\pm$ efficiency tables determination . . . 57
Tuples creation . . . 57
Tables determination . . . 58
2.4.4 Calibration maps determination . . . 58
2.4.5 L0Hadron proton efficiency tables determination . . . 61
Run II tuples creation . . . 61
Run II tables determination . . . 61
Run I tables estimates . . . 61
2.4.6 Another maps for users: $b\bar{b}$ underlaying energy maps . . . 63
2.4.7 Conclusion of this work . . . 64
2.5 The FCC-*ee* project . . . 65
2.5.1 Global description . . . 65
2.5.2 *b*-hadron production at FCC-*ee* . . . 65
2.5.3 The IDEA detector . . . 66
2.5.4 FCC-*ee* tools . . . 67

3 Search for the decay $B_s^0 \to K_S^0 K^+ K^-$ **69**
3.1 Selection and backgrounds . . . 70
3.1.1 Preselection . . . 70
3.1.2 Topological MVA . . . 71
Discriminating variables . . . 71
The topological MVA score . . . 72
3.1.3 Multivariate classifier based on Particle identification information . . . 72
PID variables . . . 75
PID selection Tool . . . 75
3.1.4 Vetoes and additional cuts . . . 78
3.1.5 2D optimisation . . . 78
3.1.6 Summary . . . 79
3.2 Mass fit . . . 81
3.2.1 Fit Model . . . 81
General procedure . . . 81
B^0 and B_s^0 signal . . . 82
Crossfeeds backgrounds . . . 84
Partially reconstructed backgrounds . . . 85
Combinatorial background . . . 86
Overview . . . 87
3.2.2 Fit results . . . 87
PrincipalPeak optimisation . . . 87
SecondaryPeak optimisation . . . 90
3.2.3 The *sPlot* method . . . 106
3.3 Efficiency . . . 107
3.3.1 Signal efficiency patterns over the DP . . . 107
Acceptance of the Generator Level Cut . . . 108
Selection efficiency . . . 108
PID efficiency . . . 110
3.3.2 Total efficiency . . . 111
3.3.3 Average efficiency computation . . . 111
3.3.4 Efficiency tables . . . 115
3.4 Systematics . . . 120
3.4.1 About branching fraction determinations . . . 120
3.4.2 Systematics from mass fit . . . 120
3.4.3 Systematics from efficiency determination . . . 122
Tracking . . . 122
Trigger . . . 124
PIDcorr . . . 124
Propagation through average efficiency determination . . . 125
Binning scheme . . . 125
Signal kinematics simulations . . . 126
Relative efficiencies . . . 127
3.4.4 Self consistency check between yield and efficiency determination . . . 130
3.5 Branching fraction measurements . . . 133
3.5.1 Combined relative branching fraction determination . . . 133
Averaging method . . . 133
χ^2 test results . . . 134
3.5.2 Combined relative branching fraction measurements . . . 135
3.5.3 Comparison with the previous analysis . . . 135

3.6 Conclusion of the analysis . . . 137

4 Prototyping of the $B_s^0 \to K_S^0\pi^+\pi^-$ time-integrated Dalitz plot analysis 138
4.1 The Dalitz formalism . . . 138
4.1.1 The Dalitz Plot . . . 138
4.1.2 Helicity angle . . . 139
4.1.3 The Square Dalitz Plot . . . 140
4.1.4 Isobar Model . . . 141
4.1.5 Angular distributions . . . 142
4.1.6 Lineshapes . . . 143
Relativistic Breit Wigner . . . 143
Gounaris-Sakurai . . . 143
EFKLLM . . . 144
4.1.7 Probability density function . . . 144
4.2 $B_s^0 \to K_S^0\pi^+\pi^-$ time-integrated analysis . . . 146
4.2.1 CRAFT overview . . . 146
4.2.2 $B_s^0 \to K_S^0\pi^+\pi^-$ P.D.F. and likelihood function . . . 146
4.2.3 $B_{d,s}^0 \to K_S^0 h^+ h'^-$ branching fraction measurements inputs . . . 147
Data used . . . 147
Combinatorial background distributions . . . 148
Fraction of signal . . . 149
MU-MD combined efficiency maps . . . 151
4.2.4 DP fit . . . 152
4.2.5 Preliminary results . . . 153
4.3 Chapter conclusion . . . 158

5 $B^0 \to K^{*0}\tau^+\tau^-$ at FCC-ee 159
5.1 Topological reconstruction of the decay . . . 160
5.1.1 The topology of $B^0 \to K^{*0}\tau^+\tau^-$ events . . . 160
5.1.2 Neutrinos reconstruction method . . . 160
5.1.3 Selection rule . . . 162
5.2 Signal reconstruction method . . . 164
5.2.1 The $B^0 \to K^{*0}\tau^+\tau^-$ signal candidates . . . 164
5.2.2 Neutrino reconstruction and selection rule . . . 164
MC reconstruction . . . 165
Vertices performance emulation . . . 165
Simulated data reconstruction . . . 166
5.2.3 Expected yields of signal at FCC-ee . . . 167
5.3 Backgrounds and selection . . . 168
5.3.1 Backgrounds . . . 168
Identification . . . 168
Branching fractions estimation . . . 168
Visible BF determination . . . 171
Backgrounds to consider . . . 171
Backgrounds generation . . . 174
5.3.2 Selection . . . 175
Events weighting . . . 175
Selection rule behavior on the backgrounds . . . 175
Calorimeter performance impact . . . 176
XGBoost selection . . . 177

5.4 Precision of the Branching Fraction measurement . . . 184
5.4.1 Method . . . 184
Results and vertexing requirements . . . 185
5.5 Comparison to state-of-the-art vertex detector . . . 188
5.5.1 Actual IDEA vertexing performance on $B^0 \to K^{*0}\tau^+\tau^-$ . . . 188
5.5.2 Vertexing improvement by tuning the tracks performance . . . 189
5.5.3 IDEA emulation . . . 191
5.5.4 IDEA results and vertexing requirements . . . 191
5.5.5 Regular detector improvements . . . 194
5.6 Conclusion of the analysis . . . 197

Conclusion **199**

A Appendix to Chapter 1 **201**
A.1 A demonstration of the neutral meson time dependant decay rates formulae . . . 201
A.1.1 The quantum mechanics of neutral B^0 meson mixing . . . 201
A.1.2 Time evolution of B^0 meson . . . 202

B Appendix to Chapter 2 **204**
B.1 Average occupancy maps . . . 204
B.2 π and K trigger efficiency tables . . . 208
B.3 Calibration maps . . . 213
B.4 π, K and p trigger efficiency tables . . . 217
B.5 Proton Run I efficiency tables estimate method . . . 222
B.6 Comparison of the new and the previous Run I efficiency tables . . . 228
B.7 $b\bar{b}$ average occupancy maps . . . 236

C Appendix to Chapter 3 **238**
C.1 MC fit results . . . 238
C.1.1 Signal . . . 238
Parameters . . . 238
Plots . . . 240
C.1.2 Crossfeed . . . 242
Plots . . . 242
Parameters . . . 244
C.2 Data fit results . . . 245
C.2.1 PrincipalPeak optimisation . . . 245
Plots . . . 245
Background yields tables . . . 259
C.2.2 Background yields tables of the SecondaryPeak optimisation . . . 261
C.3 L0 trigger correction for $B^0_{d,s} \to K^0_S h^+ h'^-$ . . . 263
C.3.1 Context . . . 263
C.3.2 Inputs . . . 263
MC unfiltered sample . . . 263
L0Hadron . . . 263
C.3.3 Application . . . 264
Event selection . . . 264
Corrected L0Hadron MC efficiency computation . . . 264
Projection in sqDP . . . 266
Pure MC efficiency . . . 270
L0Hadron correction determination . . . 273

C.3.4 Comparison with former TOS corrections . . . 275
C.3.5 Another correction determination for systematic study . . . 277
C.4 Detailed efficiency tables before magnet combination . . . 279
C.5 Polarity combined efficiency tables . . . 288
C.6 Mass fit systematics tables . . . 296
C.7 Detailed efficiency tables before magnet combination with systematics . . . 302
C.8 Polarity combined efficiency tables with systematics . . . 310
C.9 Relative efficiency tables . . . 318
C.10 Self concistency test results . . . 326
C.11 Individual relative branching fractions . . . 329
C.11.1 $B^0 \to K^0_S K^\pm \pi^\pm$ . . . 329
C.11.2 $B^0 \to K^0_S K^+ K^-$ . . . 332
C.11.3 $B^0_s \to K^0_S \pi^+ \pi^-$ . . . 333
C.11.4 $B^0_s \to K^0_S K^\pm \pi^\pm$ . . . 334
C.11.5 $B^0_s \to K^0_S K^+ K^-$ . . . 337

D Appendix to Chapter 5 **338**
D.1 Discriminative variables distributions . . . 338
D.2 Precision of the BF measurement extra-plots . . . 350
D.3 IDEA resolution extra plots . . . 358
D.4 IDEA fitted precision extra-plots . . . 363
D.5 Improved detectors extra-plots . . . 365

E Résumé français **370**
E.1 Introduction . . . 370
E.2 Contexte des études . . . 371
E.2.1 Modèle Standard et Physique des saveurs . . . 371
E.2.2 Motivation pour l'étude de $B^0_{d,s} \to K^0_S h^+ h'^-$ . . . 372
E.2.3 Motivation pour l'étude de $B^0 \to K^{*0} \tau^+ \tau^-$ . . . 372
E.3 Les instruments . . . 374
E.3.1 Le LHC . . . 374
E.3.2 Le spéctromètre LHCb . . . 374
E.3.3 Le projet FCC-*ee* . . . 376
E.4 Recherche de $B^0_s \to K^0_S K^+ K^-$ . . . 378
E.4.1 Sélection . . . 378
E.4.2 Nombre d'événements . . . 379
E.4.3 Efficacités . . . 379
E.4.4 Systématiques . . . 383
E.4.5 Résultats . . . 384
E.5 Analyse en amplitude intégrée dans le temps de $B^0_s \to K^0_S \pi^+ \pi^-$ . . . 385
E.5.1 CRAFT . . . 385
E.5.2 Apport de la mesure des rapports d'embranchement . . . 385
E.5.3 DP fit . . . 386
E.6 $B^0 \to K^{*0} \tau^+ \tau^-$ à FCC-*ee* . . . 388
E.6.1 Reconstruction topologique de la désintégration . . . 388
E.6.2 Bruit de fond et sélection . . . 389
E.6.3 Détermination de la précision sur le rapport d'embranchement . . . 391
E.6.4 Résultats . . . 392
E.7 Conclusion . . . 394

Bibliography **395**

Introduction

The Standard Model of Particle Physics (SM) accounts for three of the four elementary forces and successfully describes natural phenomena down to scales of the order 10^{-18} m. As an illustration, the top and the Higgs particles discoveries, at the mass predicted by the LEP (Large Electron Positron collider) [1], at LHC and Tevatron.

Despite these successes, there are theoretical, observational, and experimental reasons to go beyond. Among them, the only source of *CP* violation in the SM arises from the *CP*-violating phase, which emerges from the Cabibbo-Kobayashi-Maskawa (CKM) paradigm [2, 3], but this is not enough to explain the baryonic asymmetry in the Universe [4]. Moreover, SM in its current form cannot explain the origin of neutrino masses [5]. To address SM shortcomings, theorists have put a lot of effort into building various models, or Beyond SM (BSM) models, such as those involving new gauge bosons like the Z' model [6], or those introducing new types of particles like the leptoquark model [7, 8]. In that context, increasingly powerful and complex particle colliders have been built, until today and the LHC [9], to test the SM.

The work reported in this thesis consists mainly of two studies that examine the decay of neutral B mesons. The first study investigates charmless three-body hadronic decays of neutral B mesons with a K^0_S in the final state, these decays are an interesting place to explore *CP* violation processes and to test the SM. This study uses data recorded by the LHCb spectrometer [10] from 2011 to 2018. The main part of the study is dedicated to the measurements of the $B^0_{d,s} \to K^0_S h^+ h'^-$ branching fractions and especially to the search for $B^0_s \to K^0_S K^+ K^-$ unobserved to date. The second study explores the potential of future experiments at the Future Circular Collider FCC-*ee* [11] to unravel the rare heavy-flavoured quark transition $b \to s\tau^+\tau^-$, which remains unobserved to date and which is an interesting place to test SM limits and BSM models. The capabilities of detectors to measure this transition strongly depend on the performance of the vertex detector, which is why this study is used as a benchmark to determine the characteristics of the needed vertex detector.

The first chapter of the thesis presents the global scientific context of these two studies from an introduction to SM until rapid discussions of the phenomenology of hadronic and semileptonic B mesons decay. After that, the second chapter presents the experimental framework of the thesis, from a presentation of the LHC with the LHCb spectrometer to a description of the FCC-*ee* project. In addition, this chapter also presents a technical work done on the LHCb software for the collaboration. The third chapter then details the work done for the main LHCb analysis of this study, namely the measurement of the $B^0_{d,s} \to K^0_S h^+ h'^-$ modes branching fractions and the search for $B^0_s \to K^0_S K^+ K^-$. This work is a complete LHCb analysis with, among other things, the building of an advanced selection of signal decays and the development of an innovative method to determine the signal efficiencies. Hereafter, the $B^0_{d,s} \to K^0_S h^+ h'^-$ decays study at LHCb is closed, in the fourth chapter, by presenting a preliminary amplitude analysis of $B^0_s \to K^0_S \pi^+ \pi^-$ aimed at providing the building blocks of the full analysis and the first hints of potential *CP* violation observation. Finally, the fifth chapter is dedicated to the $b \to s\tau^+\tau^-$ prospective study at FCC-*ee*, using at meson scale the $B^0 \to K^{*0}\tau^+\tau^-$ transition. For this study, a specific reconstruction method has been built to solve fully the kinematics of the decay, allowing to draw perspectives on the observation as function of the vertex detector

performances.

Chapter 1

Standard Model and Flavour Physics

In this chapter, the scientific context of the thesis is reported. The first section presents the Standard Model (SM) of particle physics through the prism of Flavour Physics, establishing the fundamental framework and theoretical bases. The second section explores the Cabibbo-Kobayashi-Maskawa (CKM) matrix, elucidating its role in quark mixing and *CP* violation within the SM. The third section delves into *CP* violation in the SM, a crucial phenomenon that provides insight into the asymmetry between matter and antimatter. The fourth section introduces the phenomenology of hadronic $B-$decays, providing the motivation behind the first study presented in this thesis. Finally, the fifth section briefly encapsulates the phenomenology of semileptonic B-decays, highlighting another aspect of B-meson decays that offers complementary information to hadronic decays and further tests the robustness of the SM.

1.1 Standard Model of particle physics and Flavours

1.1.1 Standard Model in a nutshell

The Standard Model (SM) [12] is the reference theory to describe the Nature at the scale of its elementary components. It accounts for three of the fundamental interactions : the electromagnetic interaction, the weak (nuclear) interaction, and the strong (nuclear) interaction. In its current formulation, the SM describes how the elementary particles and/or antiparticles of matter, the fermions and/or antifermions, including both quarks and leptons, interact through the exchange of gauge bosons. The electromagnetic gauge boson is the massless and neutral photon. The weak interaction gauge bosons are three massive bosons, the two charged $W^{\pm}$ and the neutral Z^0. The strong interaction gauge bosons are eight massless and electrically neutral gluons g.

The SM is a renormalizable quantum field theory constructed under the principle of local gauge invariance under the $SU(3)_C \otimes SU(2)_L \otimes U(1)_Y$ symmetry group transformations. $SU(2)_L \otimes U(1)_Y$ provides a unified description of electromagnetic and weak interactions. $SU(2)_L$ governs the weak interaction, it is a non-abelian group that acts only on left-handed fermions (chirality), and with the weak isospin as the charge of the interaction. As such, the interaction is mediated by three gauge bosons W_i with $i = 1, 2, 3$. The previously introduced intermediate bosons $W^{\pm}$ are a linear combination of W_1 and W_2. The gauge boson W_3 governs the neutral current part of the interaction. The weak hypercharge group $U(1)_Y$ features the interaction quantum number $Y/2 = I_3 + Q$ with I_3 the third weak isospin component and Q the electric charge. A single gauge boson denoted B is therefore introduced once the local gauge invariance is required. Since W_3 and B are neutral bosons, they can mix in quantum mechanics to yield the abovementioned physical fields Z and γ. The group $SU(3)_C$ governs the strong interaction with the colour as the charge of the interaction. The local gauge invariance of the theory under

$SU(2)_L \otimes U(1)_Y$ requires both the gauge bosons and the fermions to be massless. However, the Brout-Englert-Higgs (BEH) mechanism [13, 14] introduces a doublet of complex scalar fields of $SU(2)_L$ that spontaneously breaks the symmetry. Four new degrees of freedom are introduced and three of them can be used to provide mass to $W^{\pm}$ and Z^0, while preserving the photon massless. The last degree of freedom is the BEH scalar boson. The discovery of a particle experimentally compatible with the BEH boson by ATLAS and CMS at the LHC in 2012 [15,16], is one of the biggest SM successes. The Yukawa couplings of the elementary fermions provide a Lagrangian mass term for them. Fermion masses are free parameters of the theory, nothing fixes their values.

Mathematically, all the theory is encapsulated by the SM Lagrangian [17] which can be seen as a sum of four terms, as given in equation 1.1.1:

$$\mathcal{L}_{\text{SM}} = \mathcal{L}_{\text{gauge}} + \mathcal{L}_{\text{fermion}} + \mathcal{L}_{\text{Yukawa}} + \mathcal{L}_{\text{BEH}}. \tag{1.1.1}$$

$\mathcal{L}_{\text{gauge}}$ is the term describing how gauge bosons interact with each other and their kinetic energies:

$$\mathcal{L}_{\text{gauge}} = -\frac{1}{4} F^a_{\mu\nu} F^{\mu\nu a},$$

with $F^a_{\mu\nu}$ corresponding to the field strength tensor for the gauge boson a, a is photon, $W^{\pm}$, Z^0 or gluons.

$\mathcal{L}_{\text{fermion}}$ is the term describing how fermions interact with gauge bosons and their kinetic energies:

$$\mathcal{L}_{\text{fermion}} = i\bar{\psi}_j \gamma^\mu D_\mu \psi_j,$$

with ψ_j the Dirac spinor of the fermion j, γ^μ are the Dirac matrices and D_μ is the covariant derivative featuring the gauge bosons which reads as:

$$D_\mu = \partial_\mu - i\frac{g'}{2} Y B_\mu - i\frac{g}{2} \sigma_j W^j_\mu - i\frac{g_s}{2} \lambda_a G^a_\mu,$$

where ∂_μ is the space-time derivative, Y is the hypercharge, B is the B boson, g' is the coupling Y and B, σ_j are the Pauli matrices (weak isospin), W^j are three gauge bosons (denoted as W_i above), g is the coupling between σ_j and W^j, G^a is the gluon gauge field (eight gluons), λ_a are the eight Gell-Mann matrices, and g_s is the strong interaction coupling constant.

$\mathcal{L}_{\text{Yukawa}}$ is the term describing how fermions interact with the BEH field:

$$\mathcal{L}_{\text{Yukawa}} = \bar{\psi}_i \lambda_{ij} \psi_j \phi + h.c.,$$

with λ_{ij} the Yukawa coupling between the i and j fermions, ϕ is the BEH scalar field and $h.c.$ stands for hermitian conjugate.

$\mathcal{L}_{\text{BEH}}$ is the term containing the mass terms of the gauge boson and their interaction with the BEH field:

$$\mathcal{L}_{\text{BEH}} = |D_\mu \phi|^2 - V(\phi),$$

with $V(\phi)$ the BEH potential (featuring the BEH self-interactions).

The quarks and leptons are divided into three generations, each corresponding to $SU(2)_L$ doublets. The first generation of quarks is made of the up- and down- flavoured quarks, the second generation of the charm- and strange- flavoured quarks, and the third generation of the top- and bottom- flavoured quarks. The first generation of leptons is made of the electron and its associated neutrino, the second of the muon and its associated neutrino, and the third of the tau and its associated neutrino. From the first to the third generations, the corresponding fermions share the same electric charge and spin, but the mass increases. Figure 1.1 summarises the elemental particles embodied by the current SM formulation.

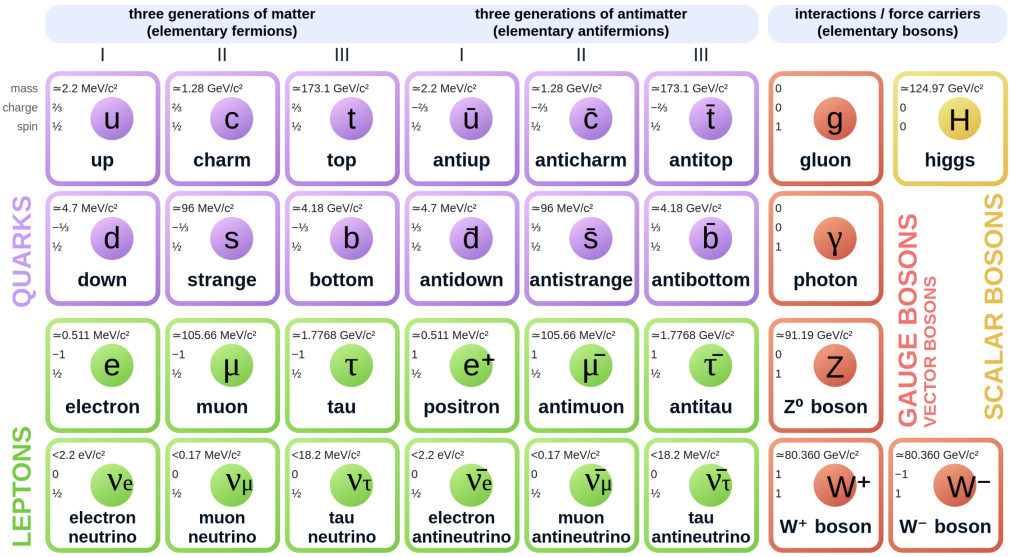

Figure 1.1: Summary of the elementary particles in the SM.

1.1.2 How flavours shaped the Standard Model : the fermions history

The Flavour Physics is a field of particle physics focussing on the study of the fermion generation couplings and the properties attached to each flavour. Some of the flavours are denoted as heavy in the SM, with respect to the masses of the corresponding particles. The heavy flavoured quarks are the charm and the bottom quarks (the top quark is excluded by usage / convention here), where the heavy flavoured lepton is the τ.

Each of the elementary fermions is an important piece of the SM puzzle. Their experimental discoveries were cornerstones of the SM. In the following a review of these discoveries is done per generation.

The electron e^- has been the first fermion, and elementary particle, discovered, in 1897 through cathode rays [18]. The electron neutrino ν_e, the $SU(2)_L$ doublet partner of the electron, was first proposed in 1930 [19] and discovered in 1955 in a nuclear reactor experiment [20]. The quark model was proposed in 1964 [21] and has been confirmed by the discovery of up u and down d quarks in 1968 through electron scatterings experiment on hydrogen and helium targets [22].

The muon μ^- was discovered in cosmic-ray through cloud chamber experiments in 1937 [23,24]. The discovery of the muon neutrino ν_μ was achieved in 1962 [25], providing to the muon its doublet partner. The concept of strangeness, has been introduced in the 1950's through a conserved quantum number in the strong and electromagnetic interaction but not in the weak interaction, to explain the observed lifetime of 10^{-10}s of the K^0 meson compared to the 10^{-23}s expected in the strong interaction decays. When the quark model was proposed, the strangeness required a quark to be associated with, and so the discovery of the quarks in 1968 confirmed, in addition to u and d, the existence of the strange s quark.The necessity for a fourth quark was raised in 1970 to provide a mechanism (known as Glashow-Iliopoulos-Maiani mechanism, GIM) to forbid Flavour Changing Neutral Currents as suggested by the scarcity of the decay $K^0_L \to \mu^+\mu^-$ [26]. The charm c quark was discovered in 1974 with the discovery of $c\bar{c}$ J/ψ meson [27, 28].

The searches for a heavier lepton start in the 1960's [29], but despite these efforts, the τ^- was discovered in 1975 in electron-positron collisions [30, 31]. The τ^- because of its large mass ($1776.86\,\mathrm{MeV/c^2} \simeq 17 m_\mu \simeq 3500 m_e$) is the only lepton that can directly decay to hadrons (particles made of quarks). Since the τ^- discovery, the existence of the ν_τ was implied and it was discovered in 2000 [32]. The beauty b quark was theoretically introduced in 1973 to explain

CP violation in the SM [33], and it was discovered in 1977 in proton nucleon collisions [34]. A sixth quark is required to complete the third doublet introduced with *CP* violation. The top t quark was discovered in 1995 in proton-antiproton collisions [35, 36]. Due to its very large mass compared to other quarks, t is the only one that has a decay time smaller than the hadronisation time, not allowing it to combine with other quarks to form hadrons, but enabling direct observations through its decays. It is worth to note that the top quark mass was known to be large before his discovery due to the smallness of the B^0 mixing oscillation frequency.

The Flavour physics measurements (lifetime of strange particles, suppression of the FCNC, *CP* symmetry breaking etc..) have shaped the SM from its beginning to date. It is likely that Flavour physics will still be useful to question the completeness of the SM.

1.1.3 Standard Model limits

The SM is currently the reference theory that describes three of the four fundamental forces of nature. For the time being, SM has been confirmed by most of the experiments performed, the latter being the measurement of a particle compatible with the BEH boson at LHC [15, 16]. Despite its successful story, the current formulation of the SM does not manage to explain all the observed/known phenomena. In this section, some of the shortcomings of the SM are presented.

The current theory that describes gravity is the General Relativity [37] postulated by Einstein in 1915. The General Relativity explains that the gravity comes from spacetime curvature, which can not be, for the time being, translated in a quantum physics framework.

The SM cannot explain to date what dark matter [38] and dark energy [39], two essential components of the current cosmological model, are. Dark matter is a hypothetical form of matter introduced to explain astrophysical observations such as the motion of galaxies within galaxy clusters. Dark energy is a hypothetical form of energy invoked to explain the accelerating expansion of the universe. In the current cosmological reference model, Λ_{CDM} [40], dark energy contributes to 68% of the density energy of the universe, dark matter to 26% and ordinary matter, the one explained by the SM, only to 5%. It is always difficult to relate unambiguously cosmological observations and the SM as self-contained questions.

The SM assumes that neutrinos are massless, however experiments have found a phenomenon called neutrinos oscillation [41, 42] that requires the neutrinos to be massive. The neutrino oscillation is a process by which the leptonic flavour of a neutrino can change due to the different bases of the flavour and the mass eigenstates.

The SM does not predict that there are three generations of fermions nor their ordering in mass. This is known as one of the Flavour problems.

Though the SM contains all the necessary ingredients [43–45], the SM cannot explain to date the amplitude of the baryon asymmetry (the matter-antimatter asymmetry) [46]. The Big Bang should have produced matter and antimatter, potentially leading to their full annihilation if present in equivalent quantities. However, the observable universe is made almost entirely of matter, pointing toward an asymmetry in the early universe. The SM, featuring *CP* violation processes, predicts an asymmetry between matter and antimatter, but with a magnitude not compatible with the observation.

Beyond the direct exploration of some of the shortcomings mentioned aboveline, one of the goals of the current experimental programs is to find departures of the measurements from their SM predictions. If such a discrepancy is observed, it will serve as a guideline to build the physics principles of the actual model of Nature.

The heavy flavoured decays, corresponding to the framework of this thesis, are especially interesting laboratories for search for new physics (NP) and evaluate the BSM models.

1.2 The CKM matrix

1.2.1 The CKM mixing matrix

The CKM mixing matrix is a unitary matrix that embodies the change of flavour in weak interaction of quarks. The CKM matrix was introduced in 1973 by Kobayashi and Maskawa [3] as a generalisation of the Cabibbo matrix introduced in 1963 [2]. In the SM, the CKM matrix appears *naturally* after the spontaneous symmetry breaking and the diagonalisation of the mass matrices [47].

A first way to write the CKM matrix is:

$$V_{\text{CKM}} = \begin{pmatrix} V_{ud} & V_{us} & V_{ub} \\ V_{cd} & V_{cs} & V_{cb} \\ V_{td} & V_{ts} & V_{tb} \end{pmatrix},$$

where V_{ij} is the CKM matrix term involving the $i \to j$ or $j \to i$ quark flavour transition.

The CKM matrix, as a 3×3 complex unitary matrix, can be parameterised by only four parameters: three mixing angles (rotation angles) and one complex phase [48]. So, the CKM matrix can be rewritten as:

$$V_{\text{CKM}} = \mathcal{R}_{23}(\theta_{23}, 0) \otimes \mathcal{R}_{13}(\theta_{13}, \delta_{13}) \otimes \mathcal{R}_{12}(\theta_{12}, 0),$$

the complex phase δ_{13} is responsible of the *CP* violation in weak interaction allowed by the SM.

The standard CKM matrix parameterisation adopted by the Particle Data Group (PDG) [47] is:

$$V_{\text{CKM}} = \begin{pmatrix} c_{12}c_{13} & s_{12}c_{13} & s_{13}e^{-i\delta_{13}} \\ -s_{12}c_{23} - c_{12}s_{23}s_{13}e^{i\delta_{13}} & c_{12}c_{23} - s_{12}s_{13}s_{23}e^{i\delta_{13}} & s_{23}c_{13} \\ s_{12}s_{23} - c_{12}c_{23}s_{13}e^{i\delta_{13}} & -c_{12}s_{23} - s_{12}c_{23}s_{13}e^{i\delta_{13}} & c_{23}c_{13} \end{pmatrix},$$

where $c_{ij} = \cos\theta_{ij}$ and $s_{ij} = \sin\theta_{ij}$ with $i, j = 1, 2, 3$.

Altomari and Wolfenstein introduced an alternative parameterisation [49, 50]. This parameterisation was motivated by the measured hierarchy between the magnitudes of the matrix elements $s_{13} \ll s_{23} \ll s_{12} \ll 1$. The four corresponding independent real parameters read λ corresponding to the sine of the Cabibbo angle (measured at $\lambda = \sin\theta_{12} = 0.22499 \pm 0.00067$ [47]), A, ρ, and η. The CKM matrix is developed in order of λ power according to:

$$s_{12} = \lambda, s_{23} = A\lambda^2, s_{13}e^{-i\delta_{13}} = A\lambda^3(\rho - i\eta).$$

As an example, the $\mathcal{O}(\lambda^4)$ CKM matrix reads:

$$V_{\text{CKM}} = \begin{pmatrix} 1 - \lambda^2/2 - \lambda^4/8 & \lambda & A\lambda^3(\rho - i\eta) \\ -\lambda & 1 - \lambda^2/2 - \lambda^4/8(1 + 4A^2) & A\lambda^2 \\ A\lambda^3(1 - \rho - i\eta) & -A\lambda^2 + A\lambda^4/2(1 - 2\rho - 2i\eta) & 1 - A^2\lambda^4/2 \end{pmatrix} + \mathcal{O}(\lambda^5).$$

1.2.2 Representation

The unitarity of the CKM matrix ($V_{\text{CKM}}V_{\text{CKM}}^{\dagger} = I$) leads to unitarity relations between matrix elements:

$$\sum_{i=1}^{3} |V_{ij}|^2 = \sum_{j=1}^{3} |V_{ij}|^2 = 1, \tag{1.2.1}$$

$$\sum_{i=1}^{3} V_{ji}V_{ki}^* = \sum_{i=1}^{3} V_{ij}V_{ik}^* = 0 \,\forall\, j \neq k, \tag{1.2.2}$$

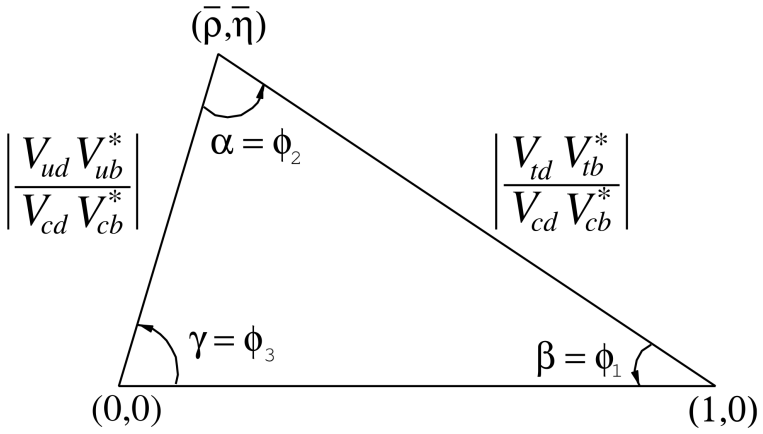

Figure 1.2: The popular non squashed unitarity triangle corresponding to equation 1.2.4 with α, β and γ the associated angles of similar sizes. The coordinates of this frame are defined in the text. The correspondence between the apex coordinates and the ρ and η is define in the text.

were V_{xy} denotes the CKM matrix element of the x type up quark and the y type down quark transition, $x = u, c, t$ and $y = d, s, b$. As a complex 3×3 matrix, the CKM matrix must be described with eighteen real parameters, but the nine unitary relations reduce this to nine (3 real and 6 complex parameters). Moreover, each quark field can be redefined but one reference field phase leading to five additional constraints and finally the CKM matrix can be parameterised with four parameters only.

The unitarity relations defined by equation 1.2.2 can then be normalised as:

$$\frac{\sum_{i=1}^{3} V_{ij} V_{ik}^*}{V_{i'j'} V_{i'k'}^*} = 0, \tag{1.2.3}$$

where i', j', k' correspond to one of the i, j, k combination in numerator. Normalised unitarity relations are generally displayed in the so-called unitarity triangles. For example one can write:

$$\frac{V_{ud}V_{ub}^*}{V_{cd}V_{cb}^*} + \frac{V_{cd}V_{cb}^*}{V_{cd}V_{cb}^*} + \frac{V_{td}V_{tb}^*}{V_{cd}V_{cb}^*} = 0, \tag{1.2.4}$$

and draw the corresponding unitarity triangle, given in Figure 1.2.

This triangle is defined by its angles:

$$\alpha = \arg\left(-\frac{V_{td}V_{tb}^*}{V_{ud}V_{ub}^*}\right), \beta = \arg\left(-\frac{V_{cd}V_{cb}^*}{V_{td}V_{tb}^*}\right), \gamma = \arg\left(-\frac{V_{ud}V_{ub}^*}{V_{cd}V_{cb}^*}\right), \tag{1.2.5}$$

and its lengths:

$$R_u = \left|\frac{V_{ud}V_{ub}^*}{V_{cd}V_{cb}^*}\right|, R_t = \left|\frac{V_{td}V_{tb}^*}{V_{cd}V_{cb}^*}\right|, \left|\frac{V_{cd}V_{cb}^*}{V_{cd}V_{cb}^*}\right| = 1.$$

The apex of this triangle is defined by its coordinates $\bar{\rho} + i\bar{\eta} = -\left(\frac{V_{ud}V_{ub}^*}{V_{cd}V_{cb}^*}\right)$, Taylor series identification leads to [51]:

$$\bar{\rho} + i\bar{\eta} = \frac{\sqrt{1-\lambda^2}(\rho + i\eta)}{\sqrt{1 - A^2\lambda^4 + A^2\lambda^4\sqrt{1-\lambda^2}(\rho + i\eta)}}$$

From which R_u and R_t can be rewritten:

$$R_u = \sqrt{\bar{\rho}^2 + \bar{\eta}^2} \text{ and } R_t = \sqrt{(1-\bar{\rho}^2) + \bar{\eta}^2}$$

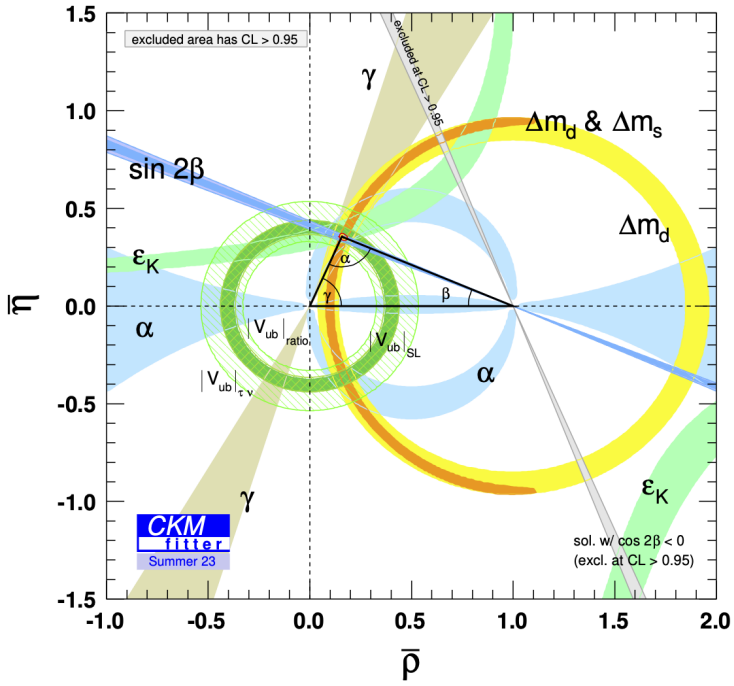

Figure 1.3: Status of the unitarity triangle parameters measurements [51].

The experimental measurement of the non squashed unitarity triangle is of first importance to evaluate the mechanism of *CP* violation in weak interaction in the SM. The triangle parameters are measured through various decay or mixing processes. The figure 1.3 displays the present status of the triangle measurements compiled by the CKMfitter group, *CP* violation in weak interaction is confirmed by the measurement of $\bar{\eta} \neq 0$.

1.3 *CP* violation in Standard Model

1.3.1 The *CP* symmetry

Discrete transformation operators play an important role in quantum mechanics as they provide a mathematical description of discrete symmetry operations in a system. For the work related to LHCb reported in this thesis, the *CP* transformation is of first importance, as its ultimate goal is to perform *CP* violation measurements. The *CP* operator combines the parity operator P with the charge conjugation operator C. Each of those transformations are detailed below.

The parity operator effect is to invert the sign of the space coordinates. For example, on a wave function $\psi(\vec{r},t)$ defined with the space coordinates $\vec{r}=(x,y,z)$ and the time coordinate t, $P(\psi(\vec{r},t)) = \psi(-\vec{r},t)$. It is also possible to define restricted-parity operators, such as P_x applying to the x space coordinate only. From a given ultra-relativistic lepton ℓ^- of right chirality (L for left-handed or R for right-handed), for which helicity[1] is chirality, this operator gives the same lepton with an inverted chirality since the spin is a pseudo-vector (don't change under P transformation):

$$\ell^-_L \xrightarrow{P} \ell^-_R.$$

Until the end of the 1950s, the general thinking was that all particle physics processes featured a parity symmetry, meaning that the physical process must be identical for an object and its P transformation. However, Wu in 1957 [52] and Goldhaber in 1958 [53] have shown a maximal violation of the parity symmetry by the weak interaction with their respective experiments.

The effect of the charge conjugation operator is to transform a particle into its corresponding antiparticle by inverting the sign of their charges. The charges involved can be the electric charge, the colour, and a variety of specific quantum numbers (such as leptonic numbers, strangeness, ...). From the previous lepton taken as an example, this operator gives the corresponding antilepton without changing the chirality:

$$\ell^-_L \xrightarrow{C} \ell^+_L.$$

An experiment in 1968 [54] has shown that charge conjugation symmetry is violated by weak interaction. As a consequence of the observed violations in parity and charge conjugation symmetries in weak interaction, only left-handed particles or right-handed antiparticles are selected by weak interaction.

The *CP* operator effect is to transform a particle into its corresponding antiparticle and to revert its chirality. Keeping the same lepton example, this transformation reads:

$$\ell^-_L \xrightarrow{CP} \ell^+_R.$$

CP transforms matter to antimatter, and if *CP* is an exact symmetry of Nature, *SM* should describe matter and antimatter in the same way. However, the Cronin and Fitch experiment in 1964 [55], in which the decay K^0 to $\pi^+\pi^-$ has been measured at the end of a long beam line, has shown a slight *CP* symmetry violation in weak interaction. The SM handle to justify *CP* violation in weak interaction is the complex phase δ_{13} of the CKM matrix, which allows $V_{ij} \neq V^\dagger_{ij}$.

[1] $h = \frac{1}{2}\frac{\vec{p}}{p}.\vec{\sigma}$, where h is the helicity operator, $\vec{p}$ the momentum of the particle and $\vec{\sigma}/2$ the spin operator for 1/2 spin particle. Helicity is the projection of the spin on the momentum direction. The parity transformation inverts $\vec{p}$ and so the helicity.

1.3.2 *CP* violation manifestation

In the following, the essential pieces of *CP* violation manifestation in neutral mesons, provided by quantum mechanics, are presented. Neutral mesons are from first principles rich laboratories to study *CP* violation. As neutral particles without baryon number, particles and antiparticles can mix to form the weakly decaying physics states. *CP* symmetry breaking can therefore manifest itself both in the decay and in the mixing processes, as well as in the interference between mixing and decay as will be detailed in the following. A B^0 meson is used in the following as illustration to derive the main *CP* violation equations, the two diagrams describing the $B^0 - \bar{B^0}$ mixing in the SM are shown in Figure 1.4.

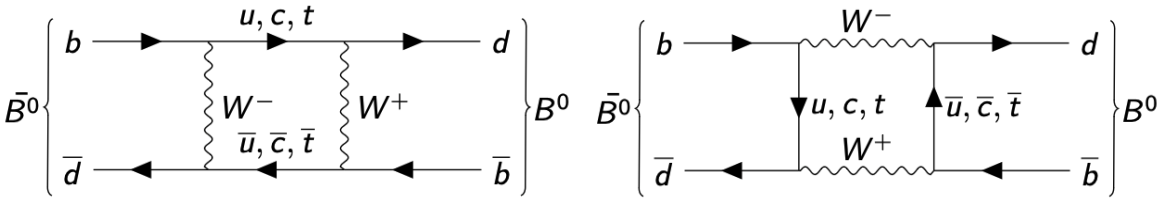

Figure 1.4: The two box diagrams describing the $B^0 - \bar{B^0}$ mixing in the SM.

By writing the quantum mechanics of the $B^0 - \bar{B^0}$ system, and by combining it with the time evolution of B^0 and $\bar{B^0}$ one should write the four possible time-dependent decay rates for the initial $|B^0\rangle$ or $|\bar{B^0}\rangle$ state to go into a f or $\bar{f}$ final state. A typical demonstration of these formulae is given in Appendix A.1. The four possible time-dependent decay rates of the initially produced $|B^0\rangle$ and $|\bar{B^0}\rangle$, can be written:

$$\begin{aligned}
\frac{\mathrm{d}\Gamma_{B^0\to f}(t)}{\mathrm{dt}} &= \frac{e^{-\Gamma t}}{2}|A_f|^2(1+|\lambda_f|^2)[1+C_f\cos(\Delta m t)-S_f\sin(\Delta m t)],\\
\frac{\mathrm{d}\Gamma_{\bar{B^0}\to f}(t)}{\mathrm{dt}} &= \frac{e^{-\Gamma t}}{2}\left|\frac{p}{q}\right|^2|A_f|^2(1+|\lambda_f|^2)[1-C_f\cos(\Delta m t)+S_f\sin(\Delta m t)],\\
\frac{\mathrm{d}\Gamma_{\bar{B^0}\to \bar{f}}(t)}{\mathrm{dt}} &= \frac{e^{-\Gamma t}}{2}|\bar{A}_{\bar{f}}|^2(1+|\bar{\lambda}_{\bar{f}}|^2)[1+\bar{C}_{\bar{f}}\cos(\Delta m t)-\bar{S}_{\bar{f}}\sin(\Delta m t)],\\
\frac{\mathrm{d}\Gamma_{B^0\to \bar{f}}(t)}{\mathrm{dt}} &= \frac{e^{-\Gamma t}}{2}\left|\frac{q}{p}\right|^2|\bar{A}_{\bar{f}}|^2(1+|\bar{\lambda}_{\bar{f}}|^2)[1-\bar{C}_{\bar{f}}\cos(\Delta m t)+\bar{S}_{\bar{f}}\sin(\Delta m t)],
\end{aligned} \tag{1.3.1}$$

where Γ is the B^0 average decay rate, Δm is the mass difference between the two mass eigenstates of $|B^0\rangle - |\bar{B^0}\rangle$, p and q are the complex coefficients associated respectively to $|B^0\rangle$ and $|\bar{B^0}\rangle$ in the $|B^0\rangle - |\bar{B^0}\rangle$ mixing process (involving the B^0 mass eigenstates), A_f and $\bar{A}_{\bar{f}}$ are the decay amplitudes for $|B^0\rangle$ and $|\bar{B^0}\rangle$ to decay in the final state f and $\bar{f}$ respectively, and λ_f and $\bar{\lambda}_{\bar{f}}$ are defined as:

$$\lambda_f = \frac{1}{\bar{\lambda}_f} = \frac{q\bar{A}_f}{pA_f},\ \bar{\lambda}_{\bar{f}} = \frac{1}{\lambda_{\bar{f}}} = \frac{pA_{\bar{f}}}{q\bar{A}_{\bar{f}}}. \tag{1.3.2}$$

The *CP* violation observables $C_f, S_f, \bar{C}_{\bar{f}}$ and $\bar{S}_{\bar{f}}$ introduced in 1.3.1 are:

$$\begin{aligned}
C_f &= \frac{1-|\lambda_f|^2}{1+|\lambda_f|^2},\ S_f = \frac{2\,\mathrm{Im}(\lambda_f)}{1+|\lambda_f|^2},\\
\bar{C}_{\bar{f}} &= \frac{1-|\bar{\lambda}_{\bar{f}}|^2}{1+|\bar{\lambda}_{\bar{f}}|^2},\ \bar{S}_{\bar{f}} = \frac{2\,\mathrm{Im}(\bar{\lambda}_{\bar{f}})}{1+|\bar{\lambda}_{\bar{f}}|^2}.
\end{aligned} \tag{1.3.3}$$

To evaluate the *CP* violation parameters, a comparison between the decay rates $\Gamma_{B^0\to f}$ and $\Gamma_{CP(B^0\to f)}$ is made, here $CP(B^0\to f)$ is the transformation of the $B^0\to f$ process under the

CP operator. With these notations, the general *CP* asymmetry parameter integrated over time reads as:

$$\mathcal{A}_{CP} = \frac{\Gamma_{CP(B^0 \to f)} - \Gamma_{B^0 \to f}}{\Gamma_{CP(B^0 \to f)} + \Gamma_{B^0 \to f}}. \tag{1.3.4}$$

CP symmetry is violated if $\Gamma_{CP(B^0 \to f)} \neq \Gamma_{B^0 \to f}$ leading to $\mathcal{A}_{CP} \neq 0$. In general, to observe *CP* violation, differences between processes and their corresponding *CP*-conjugates are searched. *CP* violation observation is linked to the existence of interferences between different amplitudes that play in these processes. These interferences are represented in SM by the complex phase in the coupling that breaks *CP* invariance. There are three possible types of *CP* violation, the next section describes them.

1.3.3 The different types of *CP* violation

CP violation in decay

A *CP* violation in decay can be measured if the decay amplitude corresponding to a process is different from that of the conjugated process *CP*: this is a direct *CP* violation. The *CP* violation in decay asymmetry parameter can be determined by starting from equation 1.3.4 and by considering the first and the third decay rates of equation 1.3.1. The cross decays corresponding to the others decay rates are not considered in that case, leading to null $A_{\bar{f}}$ and $\bar{A}_f$ and consequently to null λ_f and $\bar{\lambda}_{\bar{f}}$. Finally, all the time dependent parts of the decay rates can be factored out, and the asymmetry parameter is now time independent and reads as:

$$\mathcal{A}_{CP} = \frac{|\bar{A}_{\bar{f}}|^2 - |A_f|^2}{|\bar{A}_{\bar{f}}|^2 + |A_f|^2}. \tag{1.3.5}$$

CP violation in decay appends if $|\bar{A}_{\bar{f}}|^2 \neq |A_f|^2$, this requires to have at least two amplitudes that contribute to the decay. With two contributing amplitudes, the decay amplitudes can be written:

$$\begin{aligned} A_f &= a_1 e^{i(\delta_1 + \phi_1)} + a_2 e^{i(\delta_2 + \phi_2)}, \\ \bar{A}_{\bar{f}} &= a_1 e^{i(\delta_1 - \phi_1)} + a_2 e^{i(\delta_2 - \phi_2)}, \end{aligned} \tag{1.3.6}$$

with 1 and 2 denoting the two contributions, $a_{1,2}$ the associated real magnitudes, $\delta_{1,2}$ the associated strong phase and $\phi_{1,2}$ the associated weak phase. In this case, the asymmetry parameter becomes:

$$\mathcal{A}_{CP} = \frac{2a_1 a_2 \sin(\delta_1 - \delta_2)\sin(\phi_1 - \phi_2)}{a_1^2 + a_2^2 + 2a_1 a_2 \cos(\delta_1 - \delta_2)\cos(\phi_1 - \phi_2)}. \tag{1.3.7}$$

This expression highlights that *CP* violation can occur only if both weak and strong phase between the contributions are different.

Measurement of *CP* violation (all types) requires one to know the flavour (particle or antiparticle) of the initial meson, this is called flavour-tagging information. *CP* violation in decay has been observed at the beginning of the 2000s for K^0 mesons [56, 57], in 2004 for B^0 mesons [58, 59], in 2013 for B_s^0 mesons [60] (in $B_s^0 \to K^-\pi^+$) and in charm meson decays in 2019 [61].

CP violation in mixing

A *CP* violation in mixing occurs, for B^0, if the oscillation $B^0 \to \bar{B}^0$ is different from $\bar{B}^0 \to B^0$, this is an indirect *CP* violation. The asymmetry parameter associated to this type of *CP*

violation reads as:

$$\mathcal{A}_{CP} = \frac{\Gamma_{\bar{B}^0 \to B^0} - \Gamma_{B^0 \to \bar{B}^0}}{\Gamma_{\bar{B}^0 \to B^0} + \Gamma_{B^0 \to \bar{B}^0}}, \tag{1.3.8}$$

where the decay rates can be rewritten with the time evolution of B^0 (see Appendix A.1) $\Gamma_{\bar{B}^0 \to B^0} = |\langle B^0 | \bar{B}^0(t) \rangle|$ and $\Gamma_{B^0 \to \bar{B}^0} = |\langle \bar{B}^0 | B^0(t) \rangle|$. Finally, this A_{CP} is only made-up of p and q ratios:

$$\mathcal{A}_{CP} = \frac{\left|\frac{p}{q}\right| - \left|\frac{q}{p}\right|}{\left|\frac{p}{q}\right| + \left|\frac{q}{p}\right|}. \tag{1.3.9}$$

Therefore, *CP* violation in mixing occurs if $\left|\frac{p}{q}\right| \neq 1$.

The *CP* violation in mixing has only been observed in the $K^0 - \bar{K^0}$ system, first in 1964 [55]. Currently, there is no observation of *CP* violation in mixing for $B^0 - \bar{B^0}$ and $B_s^0 - \bar{B_s^0}$ systems, which is why $|\frac{p}{q}| = 1$ is assumed in the following.

CP violation in interference (or mixing-induced *CP* violation)

A *CP* violation in interference comes from interference between decay and mixing processes, such as $B^0 \to \bar{B^0} \to f_{CP}$ and $B^0 \to f_{CP}$, where f_{CP} denotes a *CP* eigenstate ($f_{CP} = \bar{f_{CP}}$). A *CP* violation in interference is another indirect *CP* violation. This type of *CP* violation required to define a time dependant *CP* asymmetry parameter, which reads as:

$$\mathcal{A}_{CP}(t) = \frac{\frac{\mathrm{d}\Gamma_{\bar{B}^0 \to f_{CP}}(t)}{\mathrm{dt}} - \frac{\mathrm{d}\Gamma_{B^0 \to f_{CP}}(t)}{\mathrm{dt}}}{\frac{\mathrm{d}\Gamma_{\bar{B}^0 \to f_{CP}}(t)}{\mathrm{dt}} + \frac{\mathrm{d}\Gamma_{B^0 \to f_{CP}(t)}}{\mathrm{dt}}}. \tag{1.3.10}$$

Considering $|\frac{p}{q}| = 1$ and injecting the corresponding decay rates from equation 1.3.1, $\mathcal{A}_{CP}$ becomes:

$$\mathcal{A}_{CP}(t) = S_{f_{CP}} \sin(\Delta m t) - C_{f_{CP}} \cos(\Delta m t), \tag{1.3.11}$$

where $S_{f_{CP}}$ and $C_{f_{CP}}$ are the *CP* violation observable of equation 1.3.3 corresponding to f_{CP}. By introducing the *CP*-eigenvalues $\eta_{CP} = \pm 1$, these observables read:

$$S_{f_{CP}} = \eta_{CP} \frac{2\,\mathrm{Im}(\lambda_{f_{CP}})}{1 + |\lambda_{f_{CP}}|^2},\ C_{f_{CP}} = \eta_{CP} \frac{1 - |\lambda_{f_{CP}}|^2}{1 + |\lambda_{f_{CP}}|^2}. \tag{1.3.12}$$

Therefore, *CP* violation in interference if $S_{f_{CP}} \neq 0$ or $C_{f_{CP}} \neq 0$.

CP violation in interference has been observed in the $K^0 - \bar{K^0}$ system in 1999 [62] and in the $B^0 - \bar{B^0}$ system in 2001 [63, 64].

1.4 Phenomenology of hadronic B-decays

1.4.1 Quark level transitions

At quark level, hadronic B meson decays consist of b quark transitions to a fully hadronic final state [65], *e.g.* only made up of quarks. There exist four types of these b-quark transitions in the SM, which are presented below with examples of Feynman diagrams and additional comments ($\bar{b}$ transitions obtained by doing $q \leftrightarrow \bar{q}$ and $W^+ \leftrightarrow W^-$).

The simplest type of these b quark transitions is a b tree transition to a lighter up-type quark q_u. This type of transition proceeds through charge current via W^- involving $V_{q_u b}.V^*_{q_u q_d}$ CKM matrix elements, where q_d denotes a down-type quark. Figure 1.5 shows an example of the $b \to u\bar{u}d$ tree transition, which is CKM suppressed by the V_{ub} vertex.

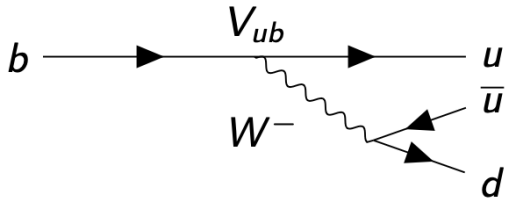

Figure 1.5: Example of an hadronic $b \to u$ quark tree transition. This transition is CKM suppressed by the V_{ub} vertex.

The second type of these transitions is b gluonic penguin transition [47] to a lighter down-type quark q_d. This is a Flavour Changing Neutral Current (FCNC). FCNCs transitions are highly suppressed in the SM because they proceed only via loop diagrams (higher order diagrams than tree *e.g.* penguin and box diagrams). Gluonic penguin transition of a b quark consists first in a $b \to W^- q_u$ transition, where q_u denotes an up-type quark, here most likely a t quark because the $W q_u$ coupling in the loop is proportional to the square of q_u mass, second in a gluon emission by q_u which leads to a quark-antiquark pair, and thirdly to a $W^- q_u \to q_d$ transition (W^- absorption) where q_d denotes a lighter down-type quark. Figure 1.6 shows an example of the $b \to d\bar{d}d$ gluonic penguin transition suppressed by the V^*_{td} vertex.

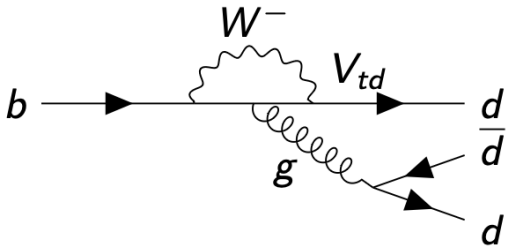

Figure 1.6: Example of an hadronic $b \to d$ quark gluonic penguin transition. This transition is CKM suppressed by the V_{td} vertex and FCNC suppressed.

The third type of these transitions is b electroweak (EW) penguin transition [47] to a lighter down-type quark q_d, another FCNC transition. EW penguin transition of a b quark consists first in a $b \to W^- q_u$ transition, where q_u denotes an up-type quark, most likely a t quark, second in a Z^0 or γ emission by W^- which leads to a quark-antiquark pair, and thirdly to a $W^- q_u \to q_d$ transition (W^- absorption) where q_d denotes a lighter down-type quark. The EW penguin transition is more suppressed than the gluonic penguin transition because the electroweak interaction is weaker than the strong interaction (coupling constants are smaller)

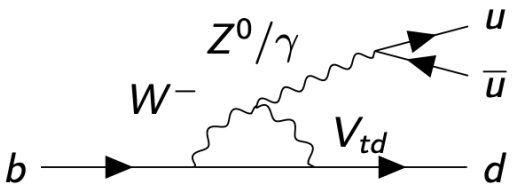

Figure 1.7: Example of an hadronic $b \to d$ quark electroweak penguin transition. This transition is CKM suppressed by the V_{td} vertex and FCNC suppressed.

at the energy scale of a b hadron. Figure 1.7 shows an example of the $b \to d\bar{u}u$ EW penguin transition.

The last type of these transitions is quark annihilation amplitudes. They are tree-level amplitudes but provide a different phenomenology than the one shown in the beginning of this section: the two initial state quarks disappear! This amplitude is mentioned in anticipation of the description at hadron level where the second initial quark can be the companion quark forming the meson. Figure 1.8 shows two examples of the b quark annihilation transitions.

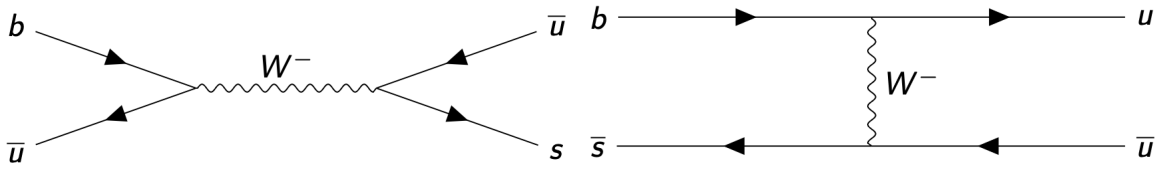

Figure 1.8: Example of quark annihilation diagrams involving a b quark and resulting in a fully hadronic final state.

1.4.2 Hadron level transition

B mesons involve an additional quark, with respect to the decaying b quark (see Section 1.4.1), which remains and acts as a spectator quark, with the exception of the abovementioned annihilation diagrams. The work reported in this thesis is about neutral B-meson decays, including both $B^0 = |\bar{b}d\rangle$ and $B_s^0 = |\bar{b}s\rangle$ initial states. It focuses especially on charmless three-body decays for the LHCb study on hadronic B-decays :

- Charmless B decays are decays without production of a c quark in the final state
- Three-body B decays are decays with three hadrons in the final state.

The three-body charmless $B_{d,s}^0$ decays provide a rich laboratory for searching CP-violation. They are dominated by quasi-two-body decays, meaning first the decay from $B_{d,s}^0$ to a hadron and a intermediate resonance, which decays subsequently to two hadrons through strong interaction. In the following, different types of hadron-level transitions corresponding mainly to $B_s^0 \to K_S^0\pi^+\pi^-$ and some to $B^0 \to K_S^0\pi^+\pi^-$, two modes of interest for this thesis, are presented and discussed.

The first type of hadron-level transition is flavour-specific quasi-two-body decay, which involves a charged resonance. This process allows one to tag the $B_{(s)}^0$ or $\bar{B}_{(s)}^0$ nature of the initial meson by looking at the sign of the resonance, the sign of the additional hadron, or both. In the case where several amplitudes contribute to this process, it is possible to observe CP violation in decays as shown in equation 1.3.7. Figure 1.9 shows two amplitudes that contribute

to the flavour-specific decay[2] $B_s^0 \to K^{*-}(\to K_S^0\pi^-)\pi^+$ in the SM, where K^{*-} denote the wide variety of resonances such as $K^{*-}(892)$, $K_0^{*-}(1430)$, $K_2^{*-}(1430)$, *etc.*; and thus offer several opportunities to observe *CP* violation in decay.

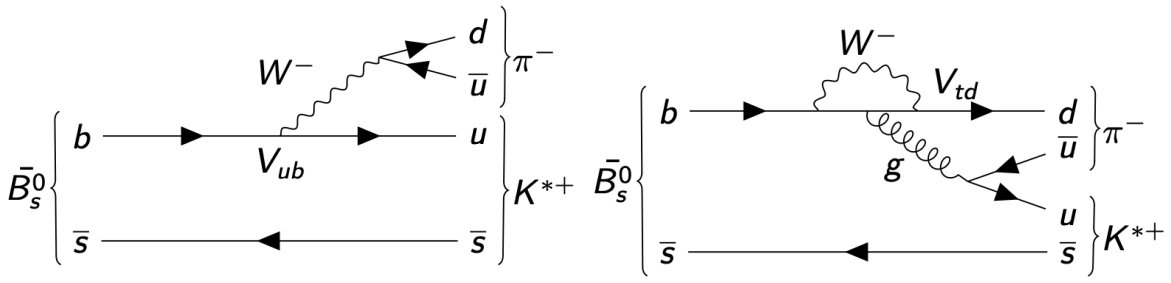

Figure 1.9: $B_s^0 \to K_S^0\pi^+\pi^-$ charge conjugated flavour-specific decays, involving $K^{*+} \to K_S^0\pi^+$, through tree quark transition (left) and gluonic penguin quark transition (right).

The second type of hadron-level transition is *CP* eigenstate quasi-two-body decay[3], which involves neutral resonance. Because of the neutral resonance, this process is not self-tagging the quark flavour in comparison to the previous one, requiring more elaborate techniques. This process allows to potentially access *CP* violation in the interference between mixing and decay. Figure 1.10 shows several amplitudes in the SM that contribute to the *CP* eigenstate decay $B_{(s)}^0 \to K_S^0\rho^0(770)(\to \pi^+\pi^-)$ and $B_{(s)}^0 \to K_S^0 f_0(\to \pi^+\pi^-)$.

The last type of hadron level transition is nonresonant transition, which involves quark-antiquark pair from the vacuum to form the three-body final state. This process causes a flat phase-space contribution to be accounted for in the possible *CP* violation studies allowed by these modes. Figure 1.11 shows two non-resonant amplitudes that contribute to the decay $B_s^0 \to K_S^0\pi^+\pi^-$ in the SM.

Quark annihilation amplitudes in SM can occur as well for the decays of interest in this work. They are not represented here since subdominant.

1.4.3 Physical observables

The study of *CP* violation through $B_{(s)}^0 \to K_S^0\pi^+\pi^-$ channels can allow one to determine physical observables depending on the *CP* violation type targeted. These channels could proceed through penguin quark-level transitions which are more sensitive to NP contributions, making those interesting laboratories to test the SM. In the following, two physical observables for these modes are presented, corresponding to *CP* violation in decay and to *CP* violation in interference between mixing decay. More information on the *CP* violation physical observables can be found in this thesis [66].

One of the next goals of the studies of charmless hadronic-transitions with the LHCb spectrometer, introduced in the thesis (see Chapter 4), is to use $B_s^0 \to K_S^0\pi^+\pi^-$ to study *CP* violation in decay through the flavour-specific transition involving the K^{*+} resonances. Analysis of $B_s^0 \to K_S^0\pi^+\pi^-$ could allow one to perform, uniquely at LHCb, the first asymmetry parameters measurement in $B_s^0 \to K^{*-}(\to K_S^0\pi^-)\pi^+$, with experimental observables defined as:

$$\mathcal{A}_{CP}^{K^{*\pm}} = \frac{N(B_s^0 \to K^{*-}\pi^+) - N(\bar{B}_s^0 \to K^{*+}\pi^-)}{N(B_s^0 \to K^{*-}\pi^+) + N(\bar{B}_s^0 \to K^{*+}\pi^-)}, \tag{1.4.1}$$

[2]Flavour-specific decay means a decay where the charged daughters allow to determine directly the nature of the mother (B_s^0 or $\bar{B}_s^0$ here).

[3]*CP* eigenstate decay means a decay where the electric charges of the daughters do not allow to determine directly the nature of the mother (B_s^0 or $\bar{B}_s^0$ here).

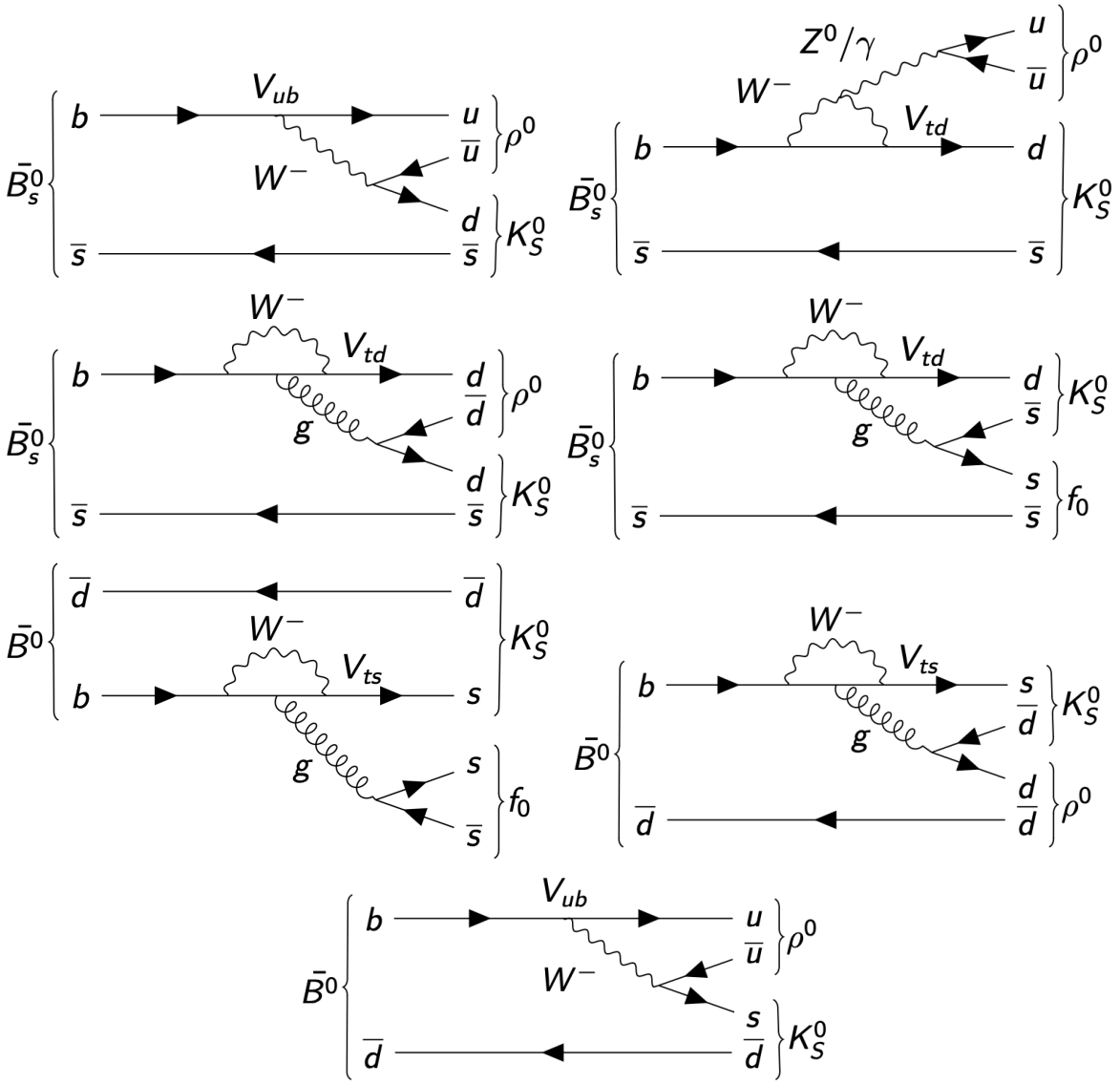

Figure 1.10: $B_s^0 \to K_S^0\pi^+\pi^-$ charge conjugated *CP* eigenstate decays, involving $\rho^0(770) \to \pi^+\pi^-$ or $f_0 \to \pi^+\pi^-$, through tree quark transition (very upper left), EW penguin quark transition (very upper right) and two gluonic penguin quark transitions (upper center). The figure displays as well diagrams corresponding $B^0 \to K_S^0\pi^+\pi^-$ *CP* eigenstate decays through two gluonic penguin quark transitions (bottom center) and tree quark transition (very bottom). The work reported in this thesis is focused on K_S^0 final state, however, $K^0\bar{K^0}$ is implied in the hadronisation notation.

where $K^{*\pm}$ denotes any possible $K^{*\pm}$ resonance, $N(B_s^0 \to y)$ denotes the number of $B_s^0 \to y$ decay measured and $N(\bar{B}_s^0 \to \bar{y})$ denotes the number of $\bar{B}_s^0 \to \bar{y}$. The measurement of these *CP* asymmetry parameters would complete the already significant knowledge of *CP* symmetry breaking in charmless hadronic-decays, unraveling new final states and potentially challenging the SM predictions.

One more ambitious goal related to $B_{(s)}^0 \to K_S^0\pi^+\pi^-$ for LHCb is to study *CP* violation in interference between decay and mixing through *CP*-eigenstate transitions involving neutral resonances. The SM predictions are in this case more precise than for direct *CP* asymmetries. Regarding the fact that this type of *CP* violation study requires to perform time-dependent analysis, it needs experimental samples of high statistics of signal decays. The plan is to study first $B^0 \to K_S^0\pi^+\pi^-$ (which is five times more probable than $B_s^0 \to K_S^0\pi^+\pi^-$, see Section 1.4.4). The main goal of this study will be to access the measurement of $\sin(2\beta)$ of the unitarity triangle

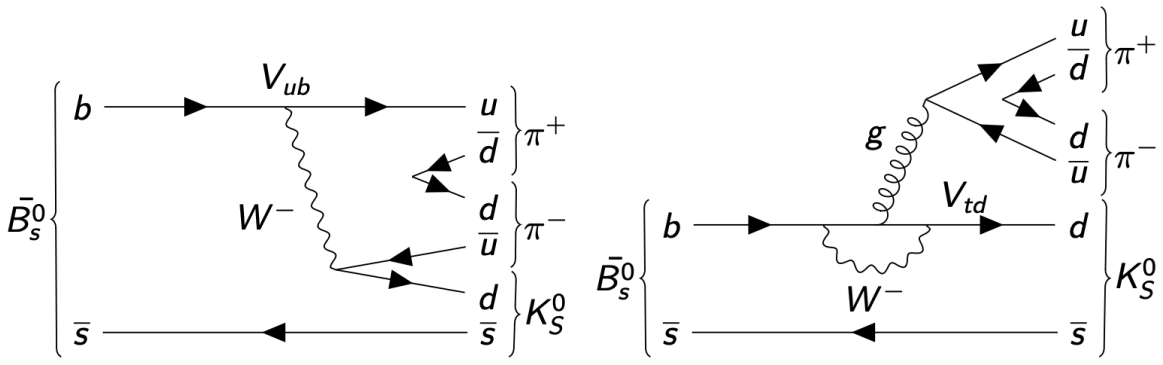

Figure 1.11: $B_s^0 \to K_S^0\pi^+\pi^-$ charge conjugated non-resonant decays, involving quark-antiquark pair from the vacuum, through tree quark-transition (left) and gluonic penguin quark-transition (right).

in a channel different from the one used regularly. The parameter $\sin(2\beta)$ is usually accessed by the so-called charmed golden mode $B^0 \to J/\psi K_S^0$ measurement; the actual average value of $\sin(2\beta)$ given by the Heavy FLavor AVeraging group (HFLAV) is 0.699 ± 0.017 [67]. The comparison of the two different $\sin(2\beta)$ measurements, proceeding from dominant tree and loop amplitudes, respectively, could highlight NP effects in case of departure and is therefore a powerful test of the SM.

1.4.4 The $B^0_{(s)} \to K^0_S hh'$ decays study interests

The LHCb work reported in this thesis is dedicated to the study of $B^0_{(s)} \to K^0_S hh'$ decay modes where $h^{(\prime)}$ can be $\pi^\pm$ or $K^\pm$. Two mid-term long-term goals of this study were presented in Section 1.4.3. The first step towards these objectives is to perform the branching fraction measurements of these modes with the entire LHCb dataset recorded to date.

A previous LHCb analysis done with the available Run I data, has measured the $B^0_{(s)} \to K^0_S hh'$ branching fractions relative to $B^0 \to K^0_S\pi^+\pi^-$ (the more probable mode, in order to factor out detector effects), and the results were [68]:

$$\frac{BF(B^0 \to K^0_S K^+K^-)}{BF(B^0 \to K^0_S\pi^+\pi^-)} = 0.549 \pm 0.018\,(\text{stat.}) \pm 0.033\,(\text{syst.}), \tag{1.4.2}$$

$$\frac{BF(B^0 \to K^0_S K^\pm\pi^\mp)}{BF(B^0 \to K^0_S\pi^+\pi^-)} = 0.123 \pm 0.009\,(\text{stat.}) \pm 0.015\,(\text{syst.}), \tag{1.4.3}$$

$$\frac{BF(B^0_s \to K^0_S\pi^+\pi^-)}{BF(B^0 \to K^0_S\pi^+\pi^-)} = 0.191 \pm 0.027\,(\text{stat.}) \pm 0.031\,(\text{syst.}) \pm 0.011\,(f_s/f_d), \tag{1.4.4}$$

$$\frac{BF(B^0_s \to K^0_S K^\pm\pi^\mp)}{BF(B^0 \to K^0_S\pi^+\pi^-)} = 1.70 \pm 0.07\,(\text{stat.}) \pm 0.11\,(\text{syst.}) \pm 0.10\,(f_s/f_d), \tag{1.4.5}$$

and

$$\frac{BF(B^0_s \to K^0_S K^+K^-)}{BF(B^0 \to K^0_S\pi^+\pi^-)} \in [0.008, 0.051]\text{at } 90\% \text{ confidence level.} \tag{1.4.6}$$

The latter measurement exhibits a hint for this decay with a statistical significance corresponding to about two standard deviations. The goal of the current branching fraction measurement analysis reported in this manuscript is to update these results and aim at unraveling the decay mode $B^0_s \to K^0_S K^+K^-$ with the addition of the Run II LHCb dataset.

The branching fraction analysis will serve as starting point toward *CP* violation study analyses, as the ones reported for $B^0_s \to K^0_S\pi^+\pi^-$ in Section 1.4.3. *CP* violation in decay has been reported in the $B^0 \to K^0_S\pi^+\pi^-$ amplitude analysis [69, 70] with the former LHCb dataset.

1.5 Phenomenology of semileptonic B-decays

1.5.1 Quark level transition

Semileptonic B meson decays consist of b-quark transitions to final states made of quarks and leptons. There exist two types of these transitions in the SM, which are presented in the following with examples of Feynman diagrams and comments ($\bar{b}$ transitions obtained by doing $x \leftrightarrow \bar{x}$, for a given particle x, and $W^+ \leftrightarrow W^-$).

The simplest type of these b quark transitions in the SM is a tree-level transition to a lighter up-type quark q_u and a subsequent decay of the W into a lepton-antineutrino pair $\ell^-\bar{\nu}_\ell$. In this case ℓ denotes e, μ or τ. Due to the $V_{q_u b}$ CKM matrix element involved, the $b \to c\ell^-\bar{\nu}_\ell$ is more probable than $b \to u\ell^-\bar{\nu}_\ell$. Figure 1.12 shows the tree diagram of $b \to c\ell^-\bar{\nu}_\ell$ transitions.

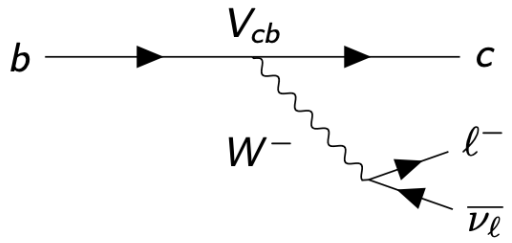

Figure 1.12: Example of the most probable $b \to q_u\ell^-\bar{\nu}_\ell$ transition.

The second type of these b quark transitions involves FCNC in the SM to produce a lighter down-type quark q_d and a lepton-antilepton pair $\ell^+\ell^-$. Due to their FCNC-suppressed nature, $b \to q_d\ell^+\ell^-$ transitions are named rare semileptonic decays. These transitions can proceed through EW penguin or box diagrams and involve $V_{tb}.V^*_{tq_d}$ CKM matrix elements. Figure 1.13 displays the two dominating diagrams in the SM corresponding to the $b \to s\ell^+\ell^-$ transition. The FCC-related work reported in this thesis is focused on the study of the rare b semi-taunic $b \to s\tau^+\tau^-$ transition. The next section focusses in turn on the corresponding decay mode.

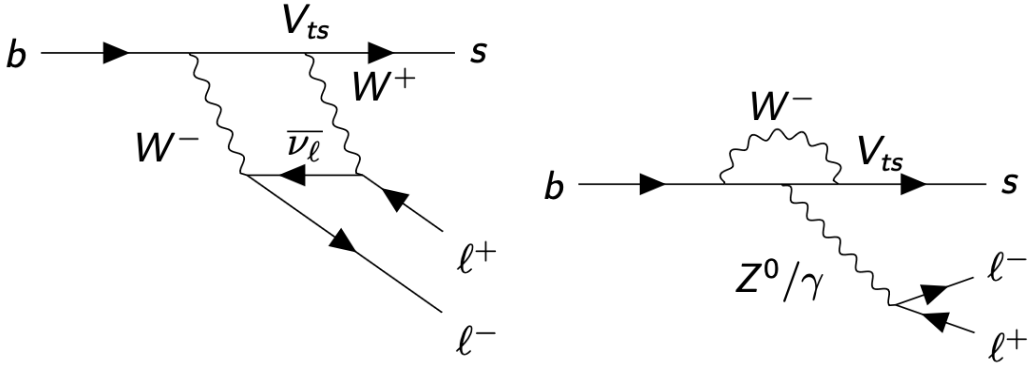

Figure 1.13: The box (left) and EW penguin (right) Feynman diagrams corresponding to $b \to s\ell^-\ell^+$ transitions. The EW penguin diagram can be rewritten with the Z^0/γ line coming from the W^- loop, both representation are valid.

1.5.2 The hadron-level transition of interest

The FCC related work reported in this thesis is dedicated to a rare semi-tauonic neutral B meson decay, similarly to Section 1.4.2. The decay studied is $B^0 \to K^{*0}(892)\tau^+\tau^-$ and the two

corresponding diagrams are shown in Figure 1.14. The K^{*0} is a resonance that goes in $K\pi$ with $K^+\pi^-(\sim 70\%) + K^0_S\pi^0(\sim 30\%)$.

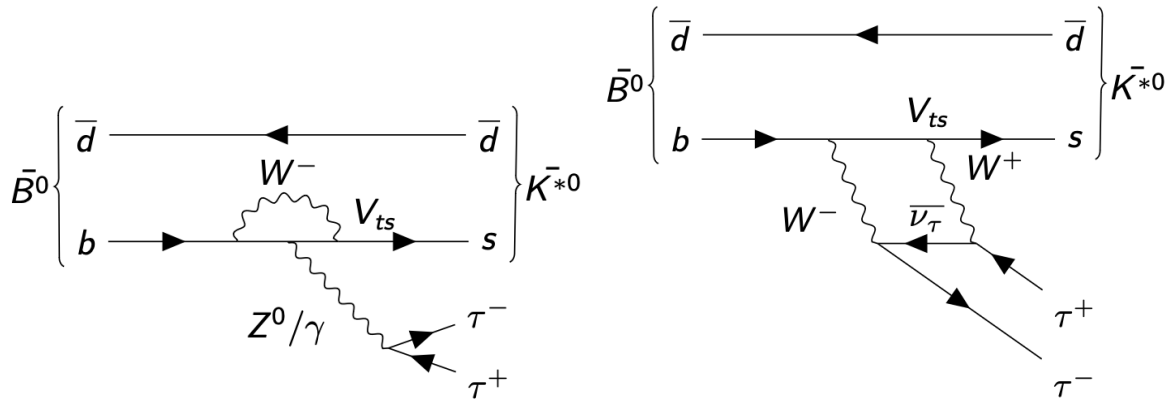

Figure 1.14: EW penguin (left) and box (right) Feynman diagrams of $B^0 \to K^{*0}\tau^+\tau^-$ charge conjugate mode.

In terms of physical interest, fermion couplings among the third-generation are the most demanding to observe experimentally, and consequently the less well-known. Specific models addressing the Flavour problem(s), *e.g.* the mass hierarchy among fermion generations and the minimal flavour violation suggested by the neutral meson mixing phenomenology, are often providing $b \to \tau$ ($m_\tau \sim 20 m_\mu$) enhancement or modification with respect to the SM prediction. It should be noted that the heaviest SM particles (with the notable exception of the BEH boson) are virtually involved in the loops that contribute to the amplitude of the $b \to s\tau^+\tau^-$ process. These amplitudes can *naturally* welcome new heavy degrees of freedom and are therefore sensitive to potential Beyond Standard Model (BSM) amplitudes such as those involving new gauge bosons Z' [6] or new types of particles such as leptoquarks [7, 8] for example.

The main challenge to observe $b \to s\tau^+\tau^-$ quark transition comes from the measurements of neutrinos that occur from τ decays. The mode studied features a $K^{*0}(892) \to K^+\pi^-$ as it provides the secondary vertex of decay that is needed to reconstruct kinematically the decay (see Section 5). By contrast, decay modes featuring final states such as $B^+ \to K^+\tau^+\tau^-$ or $B^0 \to K^0_S\tau^+\tau^-$ are not providing the secondary vertex information.

1.5.3 Physical observables

The study of the $B^0 \to K^{*0}\tau^+\tau^-$ transition can allow to determine physical observables to potentially unravel NP effects. Most of these observables are theoretically already extracted, assuming NP effects or not, from the Effective Field Theory EFT framework. The EFT framework describes physical systems at a specific scale without requiring a detailed understanding of the underlying fundamental theories at smaller scales. The key idea behind EFT is that different physical phenomena can be described using different theories, each valid at its own characteristic scale, with simpler descriptions emerging at larger scales.

The EFT framework allows one to write the effective weak Hamiltonian corresponding to the $b \to s\tau^+\tau^-$ transitions at an energetic scale μ below m_W (compatible with the case of a B^0 decay) in the SM, as:

$$\mathcal{H}^{\text{eff}}_{\text{SM}} = -4\frac{G_F}{\sqrt{2}} V_{tb}V^*_{ts}\Big(\sum_{i=1}^{2} C_i(\mu)O^c_i(\mu) + \sum_{i=3}^{8} C_i(\mu)O_i(\mu) + \sum_{i=9}^{10} C^{\tau\tau}_i(\mu)O_i(\mu)\Big) + \text{h.c.}, \qquad (1.5.1)$$

where G_F is the Fermi coupling constant, the $C^{\tau\tau}_i$'s are the Wilson coefficients of the considered EFT *e.g.* coefficients that encode the effects of high-energy physics on low-energy observable, and

the O_i^c's are the operators describing the dynamics/interactions of the system for the considered EFT. In addition, one should write a corresponding effective weak Hamiltonian assuming NP effects as:

$$\mathcal{H}^{\text{eff}} = \mathcal{H}^{\text{eff}}_{\text{SM}} - 4\frac{G_F}{\sqrt{2}} V_{tb}V_{ts}^*(\sum_{i=9}^{10} \delta C_i^{\tau\tau}(\mu)O_i(\mu) + \sum_{i=9}^{10} C_i^{\tau\tau,\prime}(\mu)O_i'(\mu)) + \text{h.c.}, \tag{1.5.2}$$

where the $\delta C_i(\mu)$s are corrections to the effective Wilson coefficient (an extension of the regular ones), $O_i'(\mu)/C_i'(\mu)$ are variants of the regular operators/coefficients. The new Wilson coefficients and corrections introduced in equation 1.5.2 are one way to introduce NP effects in the theory. The heavy degrees of freedom of the SM ($w^{\pm}$ and t) of the diagrams presented above are integrated out in this framework (as the NP degrees of freedom), making the Wilson coefficients fully calculable in the SM. A more detailed expressions of the Wilson coefficients and operators can be found in Ref. [71].

From the previously defined EFT framework, the impact of NP effects on several possible observables of $B^0 \to K^{*0}\tau^+\tau^-$ has been evaluated [71], promoting their experimental measurement as a good way to test the validity of SM. These observables include the τ polarisation asymmetries that measure the difference in the production rates of τ polarisation (orientation of its spin with respect to its momentum) in the decay, the τ forward-backward asymmetry that measures the production rate asymmetry of τ in the forward and backward direction of the decay, and the branching fraction of the decay. Figure 1.15 shows a comparison between $BF(B^0 \to K^{*0}\tau^+\tau^-)$ predicted by the SM and by an NP scenario derived from the equation 1.5.2, highlighting possible deviations between the SM and the measurement depending on NP effects amplitude $B^0 \to K^{*0}\tau^+\tau^-$. First things first: the $B^0 \to K^{*0}\tau^+\tau^-$ observable of interest for this thesis is the branching fraction.

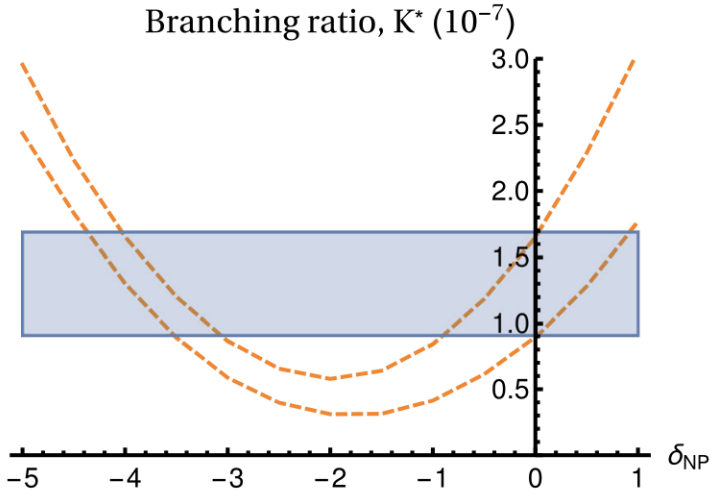

Figure 1.15: $BF(B^0 \to K^{*0}\tau^+\tau^-) \pm 1\sigma$ predicted by the SM (blue rectangle) and the one predicted for a NP scenario with $\delta C_9 = -C_9' = -\delta C_{10} = -C_{10}' = \delta_{\text{NP}}$ with δ_{NP} real (delimited by the orange dashed lines), as function of δ_{NP} [71]. The SM prediction is naturally flat with respect to δ_{NP}.

1.5.4 Experimental status

Very scarce experimental handles do exist on the quark transitions $b \to s\tau\tau$ despite the remarkable possibilities offered by the current Flavour experiments at colliders, LHCb and Belle II. Though the LHCb experiment [10] (see Section 2.1.1) records highly-boosted b-hadrons produced with enormous cross-sections, its geometry (as a spectrometer) in conjunction with

the hadronic environment does not allow to date to constrain the missing energy characteristic of these decays. By contrast, the Belle II experiment [72] benefits from a clean environment and can use the energy-momentum constraint. However, the modest boost experienced by the B-mesons at the $\Upsilon(4S)$ energy threshold makes it difficult to resolve the τ decays. In addition, limits on the branching fractions of the $b \to s\tau^+\tau^-$ modes have been assessed [73], but their values are several orders of magnitude larger than the SM prediction. The simultaneous advantages of the boost at the Z pole and the experimental cleanliness of FCC-ee interactions (see Section 2.5), make it an adequate laboratory to search for $b \to s\tau^+\tau^-$ quark transitions and so $B^0 \to K^{*0}\tau^+\tau^-$.

The work reported in Chapter 5 is a feasibility study of $BF(B^0 \to K^{*0}\tau^+\tau^-)$ measurement at FCC-ee under the SM assumption. The goal is to estimate the FCC-ee capabilities and to determine the detector performance requirements. Being able to reach the SM value with a given machine will allow it to directly validate or reject the SM for this observable. But $BF(B^0 \to K^{*0}\tau^+\tau^-)$ is predicted to be at $\mathcal{O}(10^{-7})$, which is very small and SM could be rejected even without reaching the SM value if, for example, the branching fraction appears to be higher than expected (at an experimentally accessible level).

1.5.5 A comment on B-meson Lepton Flavour Universality

The Lepton Flavour Universality (LFU) is a consequence of the Standard Model fermion representations, that features identical couplings of the three charged leptons with the gauge bosons. Intriguing and appealing tensions with respect to the LFU have been reported by the LHCb experiment, in the ratios of semileptonic $b \to s\ell^+\ell^-$ transitions involving electrons or muons. The case to study final states with τ particles is made naturally in the context of these anomalies. The observables are defined as branching fraction ratios such as $R_{K^{(*)}} = BF(B \to K^{(*)}\mu^+\mu^-)/BF(B \to K^{(*)}e^+e^-)$ [74]. The LHCb collaboration provided recently updated measurements [75] of these ratios. The executive summary of the results is shown in figure 1.16. A fair agreement with the SM predictions is now reported, with precisions at the level of $5-10\%$ dominated by statistical uncertainties. The near future will shed further light on other semileptonic Flavour observables sectors, such as R_{D,D^*} [76, 77] or the $b \to s\ell^+\ell^-$ angular analyses [78, 79]. Though the tensions with the SM predictions are relaxed for some classes of observables, the case to search for LFU violations in the quark transitions involving τ leptons is self-contained and remains vibrant (see Section 1.5.2).

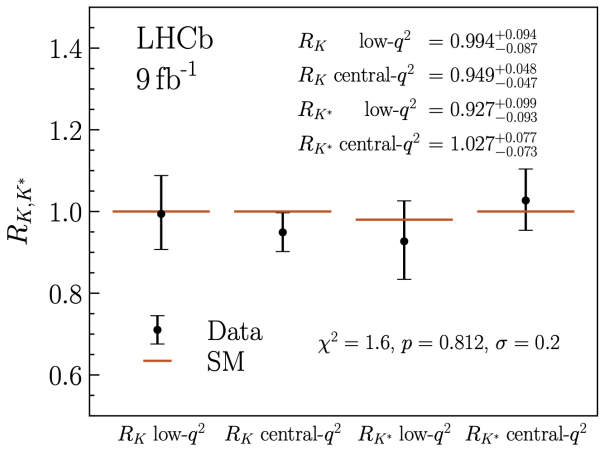

Figure 1.16: Summary of the 2022 R_{K,K^*} measurements performed by LHCb.

Chapter 2

The instruments

The quest for knowledge in Particle Physics as any other experimental science requires experiments but the scope of these experiments (both concerning instruments, collaborations, and physics cases) bring specific challenges. This is the case for the experiments involved in this thesis work. The work reported in this thesis uses data recorded from 2011 to 2018 by the LHCb detector, as well as the corresponding LHCb simulations and the ones generated in the context of the FCC-*ee* project. The simulations in Particle Physics experiments combine experimental measurements with theory-based modellings. They will be used extensively in this work and a section of this chapter is dedicated to their description. The following chapter provides a brief description of the Large Hadron Collider (LHC), the LHCb experiment, the tools used in LHCb, a work realised to build correction to apply to LHCb simulations and the Future Circular Collider (FCC) in its e^+e^- phase FCC-*ee*.

2.1 The Large Hadron Collider

The Large Hadron Collider acceleration facility (LHC) [9], located at the European Laboratory for Particle Physics (CERN) on the French-Swiss border, is currently the world's largest scientific complex in High Energy Physics. The following section provides a quick description of the LHC.

2.1.1 Global description

The LHC consists of a two-ring particle accelerator where protons or ions beams circulate in opposite directions. The work presented in this thesis analyses events from proton beams collision. The LHC is the successor of the previous CERN circular collider, the Large Electron Positron Collider [80] (LEP) and is housed in the same 100 m underground tunnel with a circumference of approximately 27 km. Figure 2.1 displays the LHC location.

The LHC can accelerate proton beams up to an energy of 6.5 TeV, which means up to 13 TeV in the centre-of-mass energy of a two-protons collision. The protons beams are guided in the LHC thanks to thousands of magnets : 1232 dipole magnets are used to bend them, 392 quadrupole magnets are used to focus them, and just before the collisions other magnets are used to squeeze the proton beams in order to increase the probability of collisions. Since the first collisions with LHC protons in September 10^{th} in 2008 at 450 GeV beam energy, the LHC timetable is organised with successive data taking periods named Run, when collisions are produced, and stop period used for maintenance and upgrade. The data used in this work were recorded during Run I (2011 to 2012) and Run II (2015 to 2018) of the LHC. During Run I the centre-of-mass energy was set at 7 TeV (2011) and 8 TeV (2012), compared to 13 TeV throughout Run II.

Figure 2.1: LHC footprint, the four main experiments are also indicated.

The first ion collisions in LHC were recorded on 8^{th} of November 2010, with lead ions, at a centre-of-mass energy of 2.76 TeV per nucleon collision. Almost exactly twelve years after, the 18^{th} of November 2022, the LHC has recorded lead ion collisions at a record centre-of-mass energy of 5.36 TeV per nucleon-nucleon collision.

The use of pp collisions at LHC, compared to e^+e^- collisions at LEP, has been motivated by the possibility of reaching higher energy with protons compared to electrons/positrons. Particles moving along a circular trajectory lose energy due to synchrotron radiation [81], the corresponding radiated power can be written as in Equation 2.1.1:

$$P_r = \frac{2q^2c}{3R^2}\left[\frac{E}{mc^2}\right]^4, \tag{2.1.1}$$

where q is the particle charge, E the particle energy, m the particle mass, R is the trajectory radius of curvature and c is the speed of light. Synchrotron radiations limit the possibility of a circular collider to reach high energy, and the two main possibilities to reduce them are to increase the radius of curvature of the machine (build bigger accelerators) or to use heavier particles. Starting from LEP, the second possibility has been implemented at CERN with LHC. Measurements of inelastic pp cross-section σ_{pp}, representing the probability of two protons to collide and produce an event, have been performed at 7 TeV and 13 TeV giving values around 67 mb[1] [82] and 75 mb [83] respectively.

The main disadvantage of pp collisions compared to e^+e^- collisions comes from the fact that p, in contrast to $e^\pm$, are not elementary particles. A proton is made up of three valence quarks $|u, u, d\rangle$, sea quarks, and gluons. The composite structure of the proton causes pp collisions to be more complicated than e^+e^-, leading to busier events due to a more important number of particles generated. This issue is addressed at LHC by a more complex selection pipeline of events of interest compared to e^+e^- machines.

2.1.2 Protons acceleration

Protons are accelerated through a serie of different systems before being injected into the LHC. Protons are first extracted from the ionisation of hydrogen molecules stored in a hydrogen

[1] 1 b (barn) = 10^{-28}m^2.

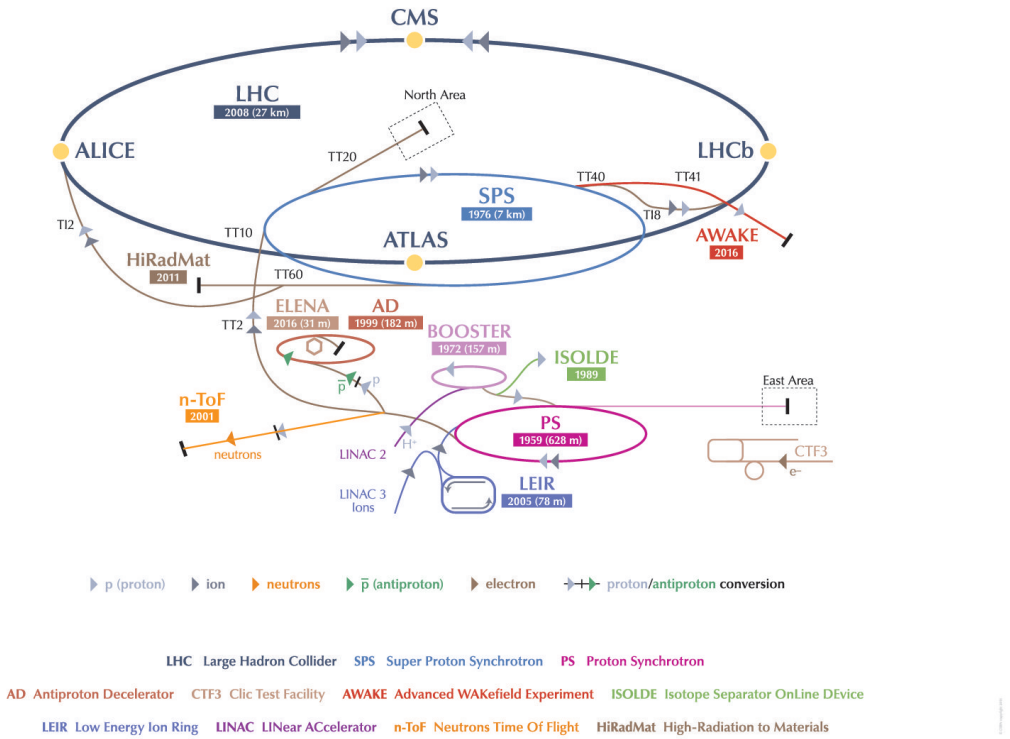

Figure 2.2: Scheme representing the CERN accelerator complex and the four LHC detectors (yellow points).

bottle. Until the end of Run II, the protons are then accelerated by the LINear ACcelerator 2 (LINAC2) at an energy of 50 MeV; however, LINAC2 has been replaced by LINAC4 in 2020 for the next runs. After that, protons are accelerated by the Proton Synchrotron (PS) Booster at an energy of 1.4 GeV (before 2020, changed to 2 GeV after). Subsequently, the protons entered the PS [84], a previous CERN particle accelerator used in the 1960s, and are accelerated to 25 GeV. These protons were used at the $p\bar{p}$ collider (ISR) at the early 1980's yielding the discoveries of the $W^{\pm}$ [85] and Z^0 [86] bosons. Hereafter, the protons go into the Super Proton Synchrotron (SPS), another CERN particle accelerator used from the 1970s to 1980s (before the LEP), and are accelerated to 450 GeV. Finally, protons are injected into the LHC rings. Figure 2.2 displays a scheme of the CERN accelerator complex.

2.1.3 LHC performances

In fact, the LHC does not collide individual protons, but groups of them ($\sim 10^{11}$) named bunches, to maximise the probability of collision. These bunches are characterised by their intensities (the number of protons in them), their spacing in time (or time interval between two bunches), and their numbers.

The two most important parameters for a particle collider are the center-of-mass collision energy and the luminosity $\mathcal{L}$, which is a measure of the number of collisions. The luminosity of a machine at an interaction point is given [87] by Equation 2.1.2:

$$\mathcal{L} = \frac{n_{\mathrm{b}} N_1 N_2 F}{4\pi\varepsilon\beta^*}, \tag{2.1.2}$$

Parameter	Run I	Run II
Collision energy (TeV)	$7 \rightarrow 8$	13
Bunch spacing (ns)	50	25
Number of bunches	1400	2500
Bunch intensity (10^{11} p per bunch)	1.6	1.2
Pile-up (average number of collisions per bunch crossing)	45	60
Emittance (μm)	2.2	2.2
β^* (cm)	80	$30 \rightarrow 25$
Crossing angle (μrad)	-	$300 \rightarrow 260$
Peak luminosity ($10^{-34}\text{cm}^{-2}\text{s}^{-1}$)	0.8	2.0

Table 2.1: Summary of LHC performance parameters [87] used during Run I and Run II.

where $N_{1,2}$ correspond the number of protons in each bunch, n_b is the number of colliding bunches, F is a geometric factor that encapsulate the crossing-angle, ε is the emittance and β^* is the value of the betatron function at the interaction point. The betatron function can read as $\beta(z) = \beta^* + z^2/\beta^*$ where z is the distance along the beam direction from the collision point. Knowing the production cross-section σ of a process, the number of events corresponding to that process in a machine with luminosity $\mathcal{L}$ is given by : $N = \sigma \times \int \mathcal{L}\text{d}t$.

The LHC main parameters are summarised for Run I and Run II in table 2.1.

2.1.4 The experiments

When accelerated, the protons beams collide at four interaction points corresponding to the four particle detectors located on the LHC. Each detector is associated with an experiment, the following will introduce all of them.

The ALICE [88] detector, for "A Large Ion Collider Experiment", is dedicated to heavy-ion physics at the LHC. ALICE has been designed to study the quark-gluon plasma phase of matter by recreating conditions similar to the ones just after the Big Bang. The ALICE collaboration is made up of 2000 scientists from 40 countries (April 2022 number).

The ATLAS [89] detector, for "A Toroidal LHC ApparatuS", is one of the two general purpose detectors of the LHC. ATLAS has, simultaneously with CMS (see below), made the discovery of a particle compatible with the Brout-Englert-Higgs boson in 2012 [15]. The ATLAS collaboration implicates more than 5500 scientists from 42 countries (March 2022 number).

The CMS [90] detector, for "the Compact Muon Solenoid", is the second general purpose detector of the LHC. CMS has, simultaneously with ATLAS, made the discovery of a particle compatible with the Brout-Englert-Higgs boson in 2012 [16]. The CMS collaboration involves 5500 scientists from 54 countries (May 2022 number).

The LHCb [10] detector, for "Large Hadron Collider beauty", is specialised in the study of heavy-flavoured particles including b and c quarks at LHC. LHCb investigates the slight differences between matter and antimatter to find new sources of *CP* violation. The LHCb collaboration includes about 1595 scientists from 20 countries (March 2022 number). As a significant part of the work presented in this thesis has been carried out within the LHCb collaboration, a more detailed description of its detector is given in the following section.

2.2 LHCb detector

As most of the work reported in this thesis has been done within the LHCb collaboration, the following section is dedicated to the description of the LHCb detector including a discussion of the specific characteristics of the physics studied in LHCb.

2.2.1 b-hadron production at LHC

As the work reported in this thesis is focused on the study of b-hadron decays, it is important to explain their productions at LHC.

The production of b-hadrons begins with the production of b quarks, which are dominated by pair creations that result in $b\bar{b}$ pairs. In pp collisions, the contributions to the production of $b\bar{b}$ pairs come from the gluon-gluon interaction $gg \to b\bar{b}$, dominant at LHC, and from quark-antiquark annihilation $q\bar{q} \to b\bar{b}$. Figure 2.3 shows examples of processes that contribute to $b\bar{b}$ production at LHC. Measurements of $b\bar{b}$ production cross-section have been performed at the energies in the centre-of-mass of Run I (7 TeV) and Run II (13 TeV) giving values around 295 µb and 600 µb, respectively [91].

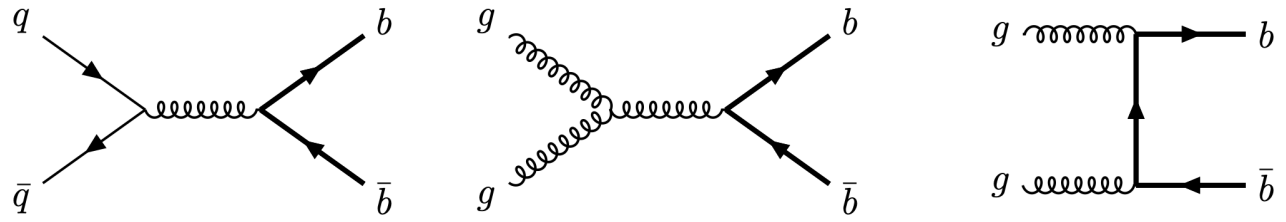

Figure 2.3: Example of interactions producing a $b\bar{b}$ quark pair at LHC [92]. From left to right one quark-antiquark annihilation process and two gluon-gluon interaction processes.

Due to the huge momentum asymmetries between the partons (gluons or quarks) involved in the collision and the fact that the collision energy at LHC is larger than the b mass, the $b\bar{b}$ pair produced at LHC is generally boosted along the forward or backward direction of the beam axis, the beam axis denotes the axis along which proton beams are accelerated. This behaviour allows to build detector with acceptance focused on specific range of polar angle, the angle between the beam and the particle direction, and/or pseudorapidity, a variable that gives the closeness of a particle to the beam axis, in order to study $b\bar{b}$ events. This is developed further in Section 2.2.2.

When a b (anti)quark is created, it must hadronize with one or two other quarks to make a hadron. There are two types of hadrons, the first are the mesons made of the b quark (antiquark respectively) and an additionnal antiquark (quark respectively), like $B_s^0 = |\bar{b}s\rangle$ or $B^- = |b\bar{u}\rangle$. The second type are the baryons made of the b quark (antiquark respectively) and two additionnal quarks (antiquarks respectively),such as $\Lambda_b^0 = udb$. The proportion of the different b-hadron generated is dominated by the hadronization fractions that have been measured in pp collisions by LHCb [93, 94].

2.2.2 General overview of the detector

As a detector focused on the study of heavy quarks, the design of the LHCb detector has been driven by the properties of $b\bar{b}$ production at LHC described in Section 2.2.1. Because the $b\bar{b}$ pairs are produced in the forward or backward direction close to the beam axis, the LHCb detector is designed as a single-arm dipole spectrometer placed forward of the interaction point as in Figure 2.4. Concretely, the LHCb detector takes place 100 m underground, near the town

of Ferney-Voltaire in France, it weighs 5600 t, it is 21 m long, 10 m high, and 13 m wide. The detector layout for Run I and Run II is shown in Figure 2.4.

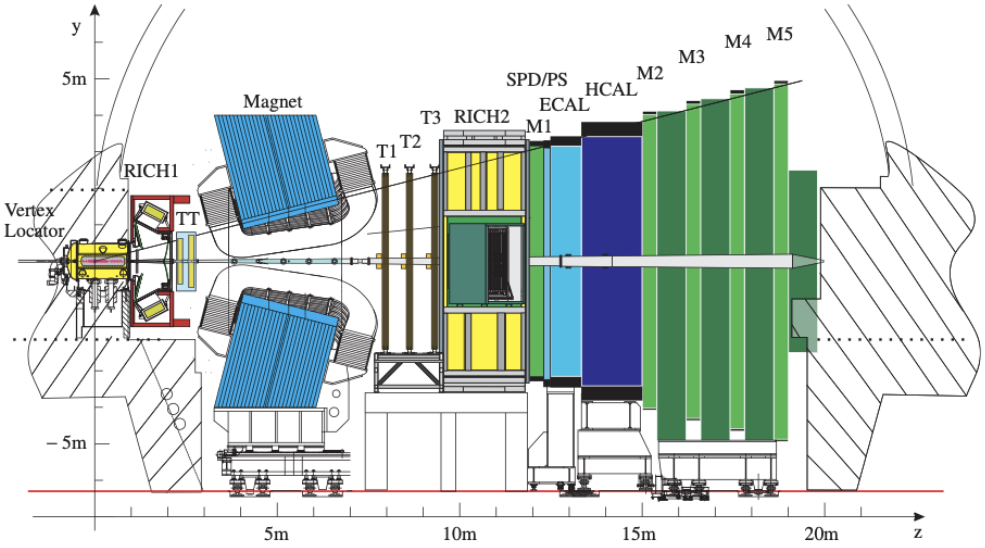

Figure 2.4: LHCb side schematic view [95] as it was during Run I and Run II. The beam axis is denoted by the z.

To describe the dimensions of LHCb, the right-handed Cartesian coordinate system is used. The origin of the coordinate system is set at the pp interaction point, which means inside the VErtex LOcator (VELO).

The LHCb detector covers a specific region in space with acceptance between 10 mrad and 250 mrad on the horizontal plane with respect to the beam axis and from 10 mrad to 300 mrad on the vertical plane, which leads to approximately 4% coverage of the solid angle. The larger horizontal coverage compared to the vertical coverage has been motivated by the fact that the LHCb dipole magnet bends the charge particles in the horizontal plane [96]. In terms of pseudorapidity η, the coverage of LHCb is in the range of 2 to 5. Figure 2.5 displays histograms of the $b\bar{b}$ pairs production at LHC for 14 TeV collisions with representation of LHCb acceptance together with a general purpose detector (like ATLAS or CMS) acceptance. At 14 TeV collisions it has been found that 24% of the $b\bar{b}$ pairs are within the acceptance of LHCb compared to 41% for a general purpose detector, but by covering the most boosted area LHCb is focused on b-hadrons that have flight the most, which is instrumental at analysis level[2].

The LHCb detector is designed to operate at smaller luminosities than those quoted in Sections 2.1.1 and 2.2.1 for LHC. The LHCb pp inelastic cross-section has been determined to be (55.0 ± 2.4) mb [82] and $(62.2 \pm 0.2 \pm 2.5)$ mb [83] at 7 TeV and 13 TeV, respectively. The $b\bar{b}$ pair production cross-section has been determined to be $(72.0 \pm 0.3 \pm 6.8)$ µb and $(154.3 \pm 1.5 \pm 14.3)$ µb at 7 TeV and 13 TeV, respectively [91]. The two to three orders of magnitude difference between σ_{pp} and $\sigma_{b\bar{b}}$ at LHCb leads to deal with an environment overwhelmed by backgrounds, which is a disadvantage compared to other heavy flavour focused experiments like Belle II [99] (B-factories) using e^+e^- collisions.

The collision rate provided for LHCb is significantly lower than what is sent to other LHC experiments because of a reduced beam focus and a luminosity levelling. The LHCb detector has recorded 3 fb^{-1} of data during Run I and 6 fb^{-1} of data during Run II as shown in Figure 2.6.

It is possible to divide the detector components into two categories:

[2]Using the b-hadrons that have more flight lead to more displaced vertices with respect to the primary vertex (pp collision point) which helps against the combinatorial backgrounds.

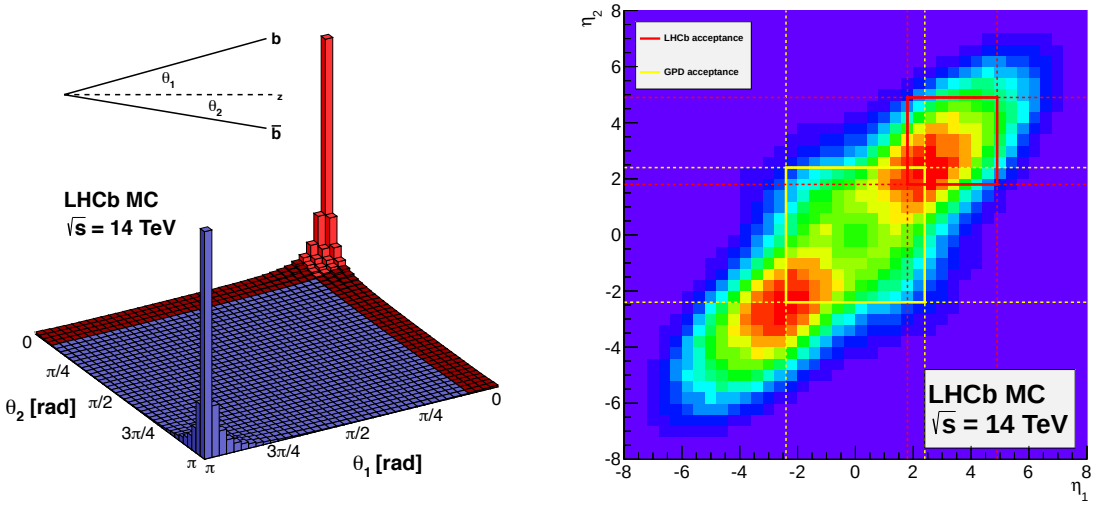

Figure 2.5: $b\bar{b}$ production at 14 TeV in terms of polar angle (left), and in terms of pseudorapidities (right). LHCb covered the red area and a general purpose detector acceptance is represented by the yellow square on the right. These plots [97] have been produced through MC simulations via PYTHIA [98].

1. the tracking system composed by the vertex locator (VELO), the magnet, the Tracker Turicensis (TT) and the T stations, described in Section 2.2.3,

2. the particle identification (PID) system which consists of two Ring-Imaging CHerenkov detectors (RICH), the calorimetry system and the muon chambers, described in Section 2.2.4.

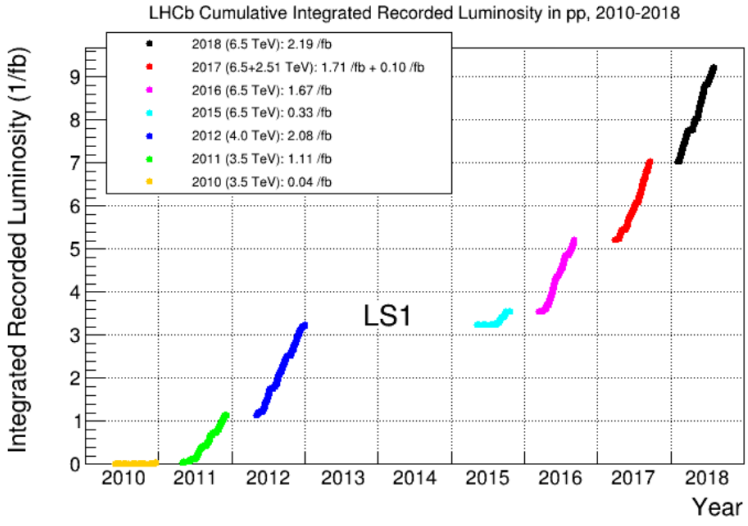

Figure 2.6: LHCb cumulative integrated recorded luminosity [100] from 2010 to 2018. 2010 is not considered in this work. LS1 stands for "Long Shutdown 1", the technical stop period between Run I and Run II when the detectors was upgraded.

2.2.3 Tracking system

In particle physics experiments, the role of the tracking system is to determine the characteristics of the tracks, a track corresponds to the footpath let in the detectors by a final charged particle, including their momenta, their charges, and their emission points or vertices. Accurate determination of the vertices positions and good momentum resolutions are key parameters in most LHCb analyses. This section describes the components of the LHCb tracking system from the closest subpart to the interaction point to the most distant one.

Vertex locator (VELO)

The typical flight distance, between the creation and decay points, corresponding respectively to the pp collision point or primary vertex and to the decay vertex, of a b-hadron at LHC energies is about 1 cm allowing separation of its decay and creation points. VELO [101] is the detector responsible for determining the positions of these vertices. VELO measures the primary tracks, from the charged particle generated at the primary vertex together with the b-hadron, and the displaced tracks from the primary vertex, possibly from the b-hadron decay. A vertexing algorithm uses the measurements to infer the best possible vertices.

Practically, the vertex locator consists of a silicon strip detector that encloses the interaction point. The vertex locator is made up of two halves with 21 stations each placed along the beam axis and composed of two layers of silicon microstrips. Driven by the High Level Trigger (see Section 2.2.5) performances, VELO track measurements are performed using cylindrical coordinates (r, ϕ, z). A track is reconstructed from the hits recorded from ionisation of the detector active materials. Concretely when a charged particle ionises a cell of a station, r and ϕ are determined by the two-layer microstrips[3] of the station, and z is determined by the position of the station. The sensitive area of the stations starts at 8 mm of the beam axis. During ramping and injection of LHC, the VELO halves are open on the LHCb x-axis to protect the detector. Schematic views of the VELO are given in Figure 2.7.

The performances of the VELO have been measured, from 2011 recorded data, to 98 % of track finding efficiency (ability to detect the tracks), a primary vertex resolution of 13 µm in the transverse plane, a primary vertex resolution of 71 µm on the beam axis, and an impact parameter resolution of less than 35 µm for particles with transverse momentum greater than 1 GeV/c [102].

Tracker Turicencis (TT)

The TT [103] detector (formerly known as the Trigger Tracker) is the first Silicon Tracker (ST) of LHCb (the second is described in Section 2.2.3). STs are used to reconstruct tracks close to the beam axis, where the occupancy is the largest. All ST detectors use silicon micro-strip sensors with a strip pitch around 200 µm resulting in a single hit spatial resolution of 50 µm.

The TT detector is located upstream of the LHCb magnet just after the RICH1 and covers the full LHCb acceptance. Technically, the TT detector is made up of two stations (TTa and TTb) for a total of four detection layers (each 150 cm wide and 130 cm high). The four layers are in a $(x - u - v - x)$ arrangement where x means a layer with vertical strips, u means a layer with strips rotated by a stereo angle of $-5°$ and v means a layer with strips rotated by a stereo angle of $+5°$. The first two layers belong to the first TT station and the two others belong to the second station. An illustration of the TT detector layout is shown in Figure 2.8.

The four-layer configuration of the TT allows to reconstruct the track parameters with a high resolution in the bending plane of LHCb and also to reduce the combinatorial background.

[3]Each station layer corresponds to a sensor, R-Sensor or ϕ-Sensor, the disposition of the two layers is inverted from a station to neighbors ones.

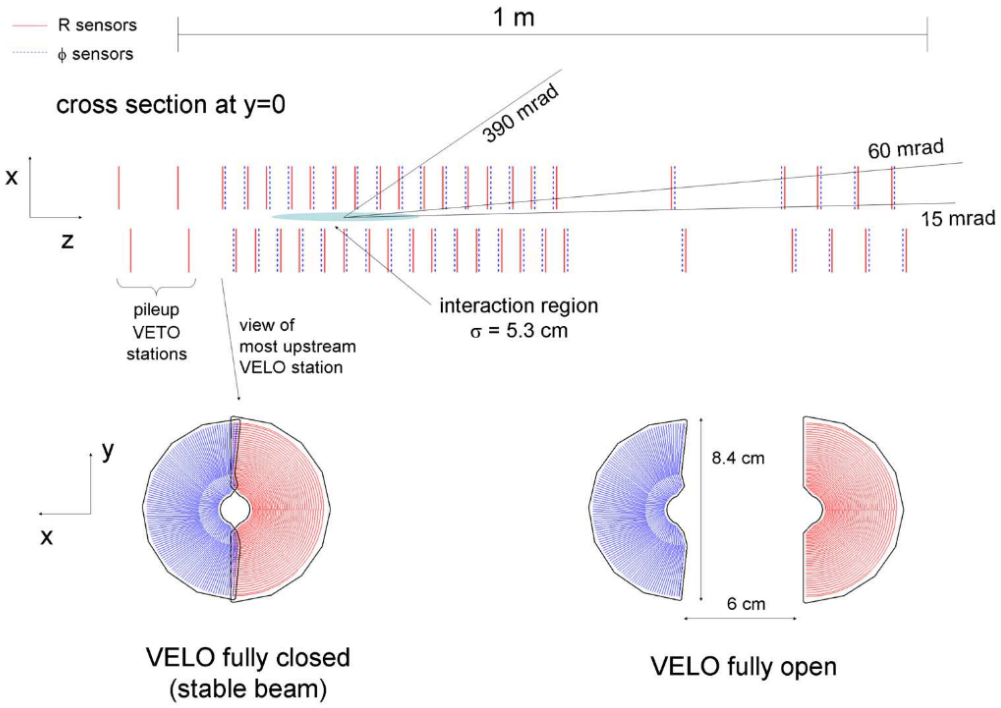

Figure 2.7: Schematic view of the VELO showing xz projection (top) and illustration of the closed and open configurations for two sensors on xy projection (bottom) [10].

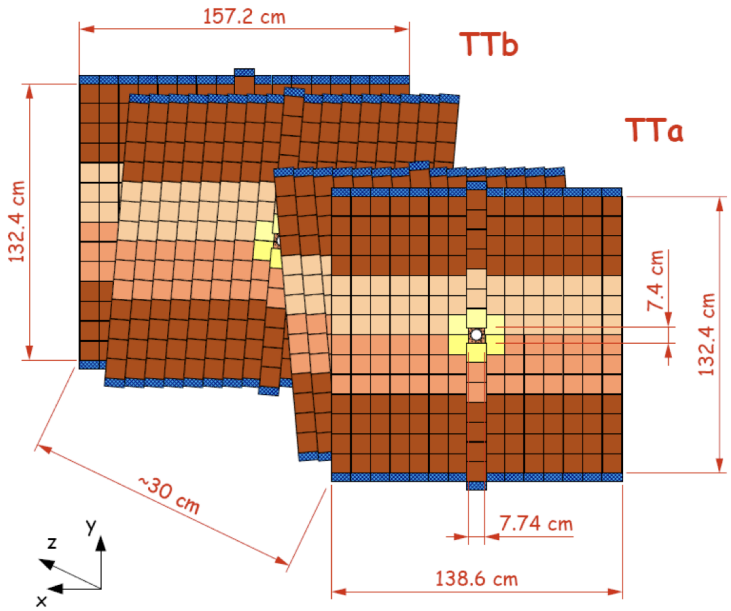

Figure 2.8: The TT detector layout with the four layers grouped in two stations [105].

In the Run II tracking algorithm, the TT, which provides the first hit after VELO, is used to accelerate the tracking process by allowing the algorithm to reduce the track searching window in tracking station [104].

Magnet

The track momentum measurement in a particle physics detector is an indirect measurement. A magnetic field is used to bend the charge particle trajectory whose curvature allows to deduce

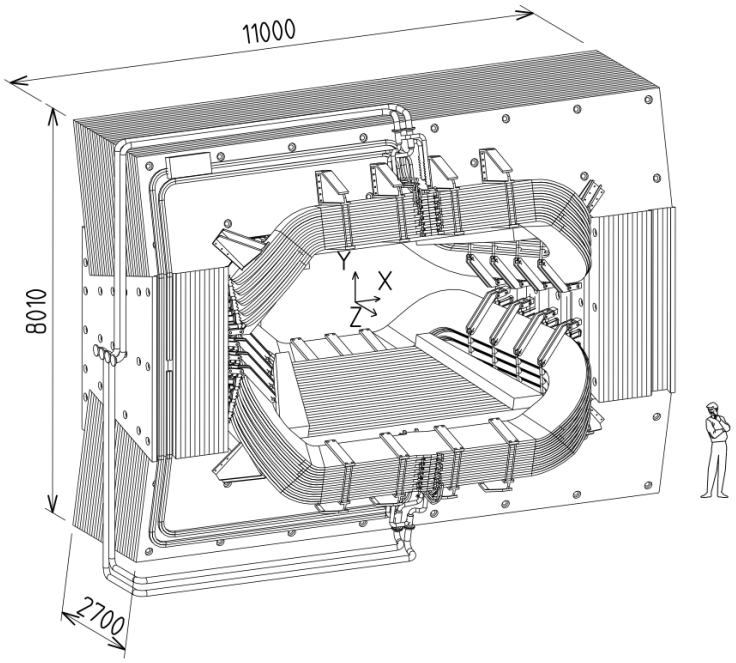

Figure 2.9: Schematic view of the LHCb magnet [106].

the charge and momentum according to the equation 2.2.1:

$$p = \frac{R}{0.3B}, \tag{2.2.1}$$

where p is the particle momentum in GeV, R is the radius of curvature of its trajectory in m and B is the applied magnetic field in T.

LHCb uses a warm dipole magnet [96, 106] or yoke, located 5 m downstream of the pp interaction region to generate its magnetic field. The LHCb yoke is made up of two coils, 25 tons each, and a 1450 tons steel frame for a total weight of 1500 tons. The outer dimensions of the magnet are 11 m horizontally (x), 8 m vertically (y), and 2.6 m in the beam direction (z).

The LHCb magnet generates an integrated magnetic field of $\int B.dl = 4\,\mathrm{T\,m}$ along the y axis of LHCb to bend the tracks in the xz plane. The bending power of the magnet allows LHCb to measure the momentum of a particle that traverses the whole tracking system with a resolution of 0.4% and 0.6% at 2 GeV/c and 100 GeV/c, respectively. An illustration of the LHCb magnet is shown in Figure 2.9.

The LHCb magnet can be swapped between two polarities, MagUp and MagDown. This feature is used to tackle charge detection asymmetries due to detector defects that can mimic the *CP*-violation ones. In order to record the same amount of data for each polarity, a periodic swap is realised.

T stations

The Tracking stations (T stations), at the number of three, are located downstream the LHCb magnet and form the last pieces of the tracking system. The T stations are composed of two parts: the Inner Tracker (IT) in the center of the T stations and the Outer Tracker (OT) surrounding the IT.

The IT, which constitutes the second Silicon Tracker of LHCb, is made up of four detector boxes that reproduce the TT structure located around the beam pipe in each T station. It is limited in acceptance in a compromise budget/performance.

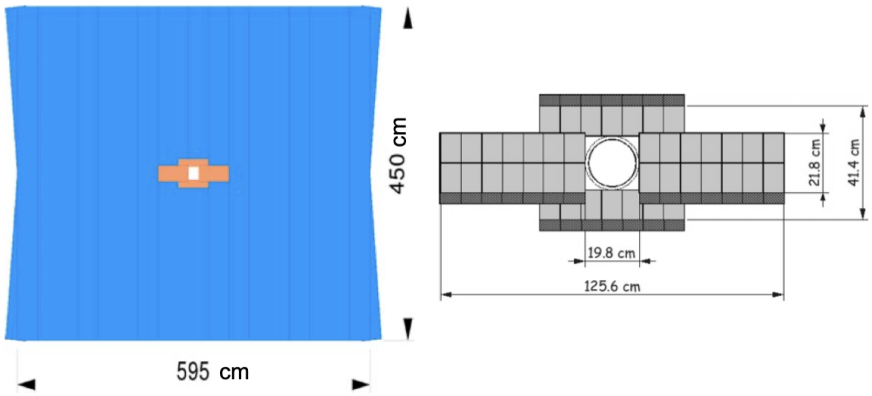

Figure 2.10: Layout of one of the three T station (left) and zoom onto the center part layout (right) [107].

The OT is a drift-time detector used to reconstruct tracks outside of the IT acceptance. The OT structure is made up of four detector layers in each T station, the first two layers are aligned on the LHCb y axis, where the last two are rotated by $\pm 5°$. In opposition to TT and IT, the OT is a gaseous detector with a mixture of argon and carbon dioxide.

Figure 2.10 displays the layout of a T station.

Track categories at LHCb

In a tracking system, the tracks are reconstructed from the hits generated by charged particles that cross the tracking system. Depending on where the hits associated to a track are recorded, five categories of tracks are defined in LHCb:

- **VELO tracks**: tracks reconstructed from hits in the VELO only, they are useful for the primary vertices determination.
- **Upstream tracks**: tracks reconstructed from hits in the VELO and the TT, they correspond to particles with low momenta pushed outside the acceptance of the T station by the magnet.
- **Long tracks**: tracks reconstructed from hits in the whole tracking system (VELO, TT and T stations), consequently, they are reconstructed with the best momentum resolution.
- **Downstream tracks**: tracks reconstructed from hits in the TT and the T stations, they mainly come from the products of long-lived particles, such as K^0_S, which decay outside the VELO.
- **T tracks**: tracks reconstructed from hits in the T station only, they come mainly from secondary interactions.

An illustration of the track categories in LHCb is given in Figure 2.11.

2.2.4 Particle identification system

In particle physics experiments, the role of the Particle IDentification (PID) system is to identify the final state particle species (π, K, p, $e^{\pm}$ and $\mu^{\pm}$), which is of first importance's in many LHCb analyses. This section describes the components of the LHCb PID system from the closest to the most distant of the interaction point.

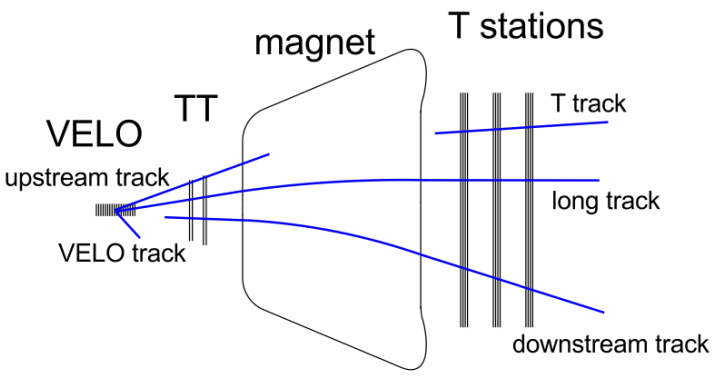

Figure 2.11: Illustration of the different track categories at LHCb with respect to the tracking system layout [108]

.

RICH detectors

When a charged particle passes through a dielectric medium at a speed higher than the light speed in that medium, photons are emitted on a cone around the particle flight direction : this is the Cherenkov effect [109]. LHCb uses two Ring Imager CHerenkov (RICH) detectors to identify particle species from the light emitted by the Cherenkov effect. The RICH layouts are shown in Figure 2.12.

The first detector, RICH1, is placed between VELO and TT. RICH1 covers a momentum range from around 1 GeV/c to 60 GeV/c, covers the full LHCb acceptance from ±25 mrad to ±300 mrad in the bending plane xz and to ±250 mrad in the vertical plane. RICH1 uses aerogel and C_4F_{10} as radiators. With respect to its characteristics, RICH1 is used to identify low-momenta charged particles.

The second detector, RICH2, is placed between the T stations and the first muon station. RICH2 covers a momentum range from around 15 GeV/c to 100 GeV/c, covers a smaller angular region from ±15 mrad to ±120 mrad in the bending plane xz and to ±100 mrad in the vertical plane. RICH2 uses the CF_4 as radiator. With respect to its characteristics, RICH2 is used to identify high-momenta charged particles which are produced close to the beam direction.

Figure 2.13 displays the RICH PID efficiency in 2017 on p and K identification. This illustrates the ability of RICH to correctly identify p and K as function of the particle momentum. The efficiency associated to misidentification *e.g.* when a kaon is wrongly identified to a pion. One can observe that the misidentification of π with K reaches 30% at 100 GeV. The analysis presented in this work relies prominently on a high performance charged hadron identification.

Calorimeter system

In a particle physics detector, the calorimeter system is designed to measure the energy of the particles by degrading it. The (transverse) energy measurement is used at the first trigger level (L0 see Section 2.2.5). Calorimetric information is as well used to provide further particle identification (photons, electrons, muons, charged hadrons).

The LHCb calorimeter system [111], placed between the first and second muon stations, identifies and measures the energy deposited by electrons and photons (electromagnetic) and neutral and charged hadrons (hadronic). The calorimeter is formed out of four subdetectors: the Scintillator Pad Detector (SPD), the PreShower (PS), the Electromagnetic Calorimeter (ECAL), and the Hadronic Calorimeter (HCAL). These LHCb subdetectors are stacked along the collision axis (z axis in the LHCb coordinate system) as shown in Figure 2.14.

SPD and PS are two planes of scintillating pads separated by a 15 mm thick lead converter

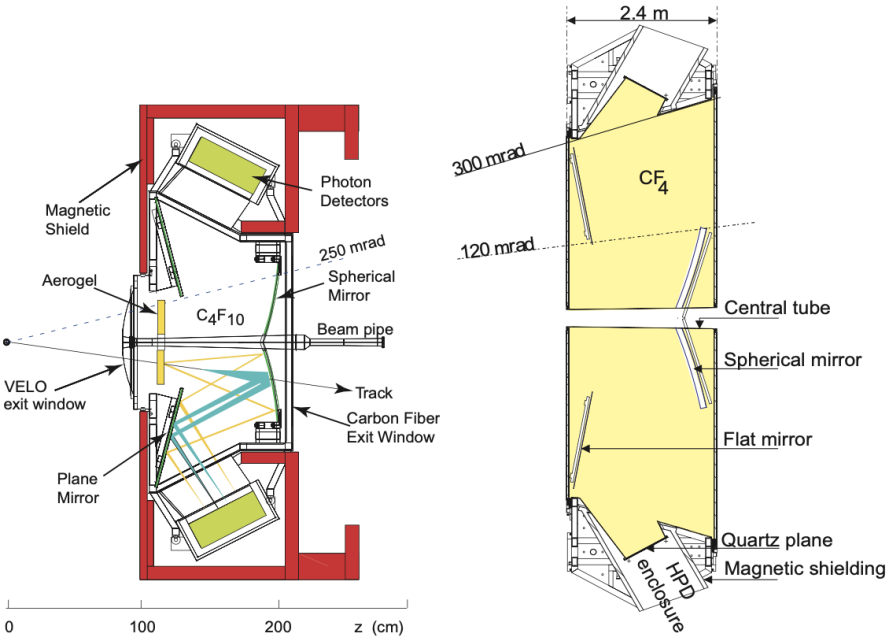

Figure 2.12: Schematic side view of the RICH1 (left) and top view of the RICH2 (right) [10].

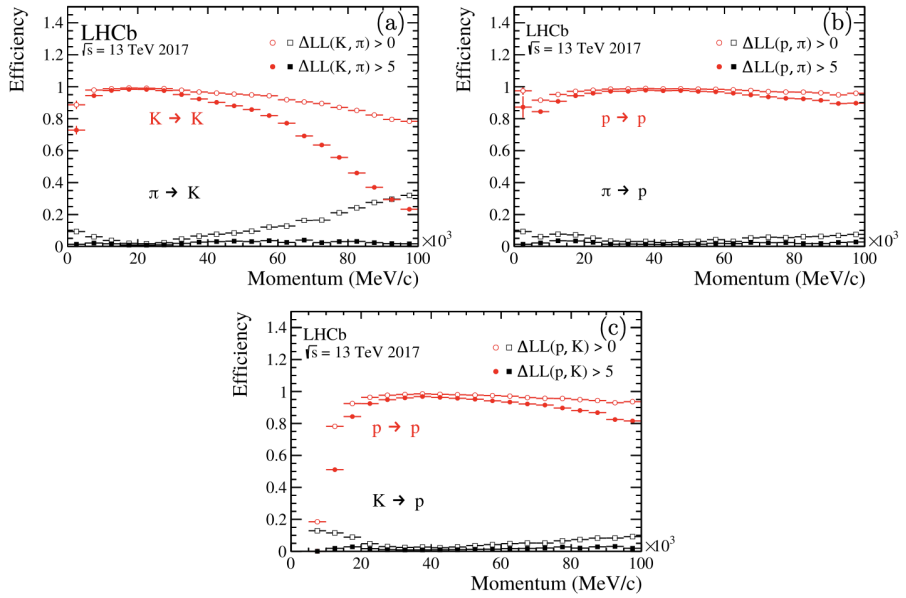

Figure 2.13: The efficiency of selecting kaons (a), protons (b and c), with the associate leakage from misidentifying pions (a and b) and kaons (c) as a function of momentum [110]. Two selections are made, a loose selection (hollow circles) and a tight selection (solid circles).

wall, corresponding to 2.5 X_0 radiation length. SPD identifies charged particles, and PS identifies electromagnetic particles ($e^{\pm}$ and γ). They are followed by a sampling electromagnetic calorimeter (ECAL) and a hadron calorimeter (HCAL). ECAL measures electromagnetic showers, and HCAL measures hadronic showers (typically from π, K, or p).

The longitudinal segmentation into these four components give to LHCb calorimeter the ability to distinguish the different types of particles ($e^{\pm}, \gamma, h$) responsible of the energy deposits at the trigger level, as illustrated in Figure 2.14.

To obtain a good energy and position resolution on individual particles, the calorimeters are segmented in the plane transverse to the beam axis. Because of the higher particle density in

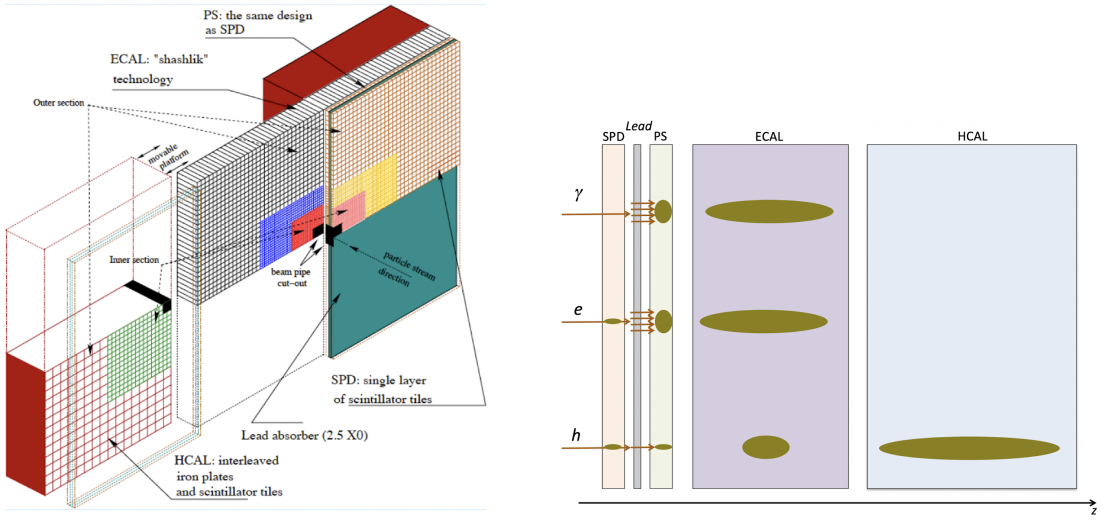

Figure 2.14: Structure of the LHCb calorimeter (left) and particle identification with respect to each of the four subdetectors via deposit location (right) [112]. Hadron could be charged or neutral. The energy measured in the ECAL matching the HCAL cells is added to the HCAL one.

the center, the size of the cells is defined as a function of the distance to the beam axis. Three regions are hence defined for ECAL, PS and SPD:

- Inner area, closest to the beam axis where the cells are the smallest,
- Middle area, where the cells size are intermediate between Inner and Outer areas,
- Outer area, "far" from the beam axis where the cells are the largest.

The HCAL is divided in only two regions (Inner and Outer) on the same principle. Due to the beam pipe, there is an uninstrumented area in the center of each subdetector.

To simplify the combination of the subdetectors information for the L0 trigger, the transverse segmentation of SPD, PS and ECAL is projective (cell boundaries are aligned and cell sizes are adjusted to take into account their different positions on the beam axis). The HCAL cells are accordingly larger than the other ones; the size has been chosen as a multiple of the previous one. Cell characteristics are summarised in Figure 2.15.

All four subdetectors operate on the same principle: the light produced in scintillator tiles by the charged particles contained in the shower developed from the incoming particle is collected by wave-length shifting fibers, then is transported to photo-multiplier tubes (PMT) connected to the read-out front-end electronics, and is then sampled at a rate of 40 MHz equal to the LHC bunch crossing frequency. The absorber medium is lead for the wall separating SPD/PS, same for ECAL, and iron for HCAL. In the following, short technical descriptions of the four subdetectors are provided.

The SPD is a plane of scintillator pads located before the 2.5 X_0 lead converter wall. The sensitive area of SPD is 7.57 m $\times$ 6.17 m in the (x,y) plane. The SPD thickness is 1.5 cm. The photo-multiplier tubes used to read out the detector are Multi Anode Photo-Multiplier Tubes (MAPMT) which can handle 64 channels (cells). The SPD is a binary detector: an energy threshold is configured. If the energy deposit in the cell is larger, a hit is recorded.

The PS is a plane of scintillator pads located after the 2.5 X_0 lead converter wall. The sensitive area of the PS is larger than the one of the SPD because of the projectivity between the subdetectors. The sensitive area of the PS is 7.6 m $\times$ 6.2 m in the (x,y) plane. The PS thickness is 1.5 cm. It uses the same MAPMT than the SPD. The PS measure an energy, it

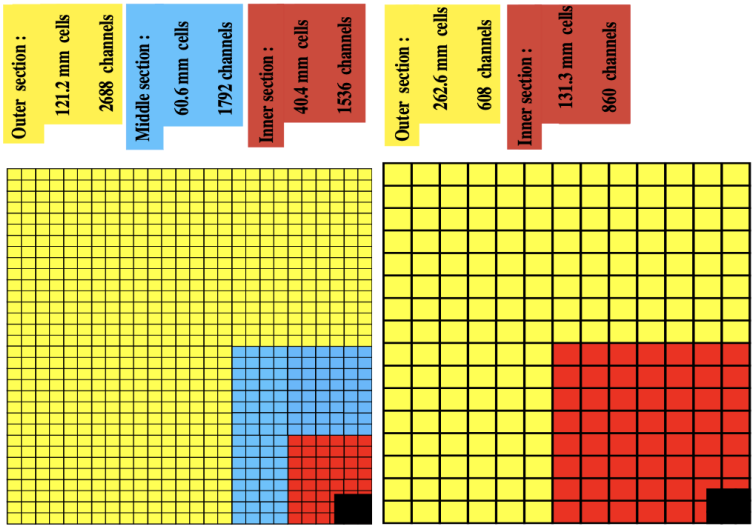

Figure 2.15: Transverse segmentation of the SPD/PS and ECAL with ECAL cell sizes given (left) and the HCAL (right) [10]. Only one quarter of the detector is represented.

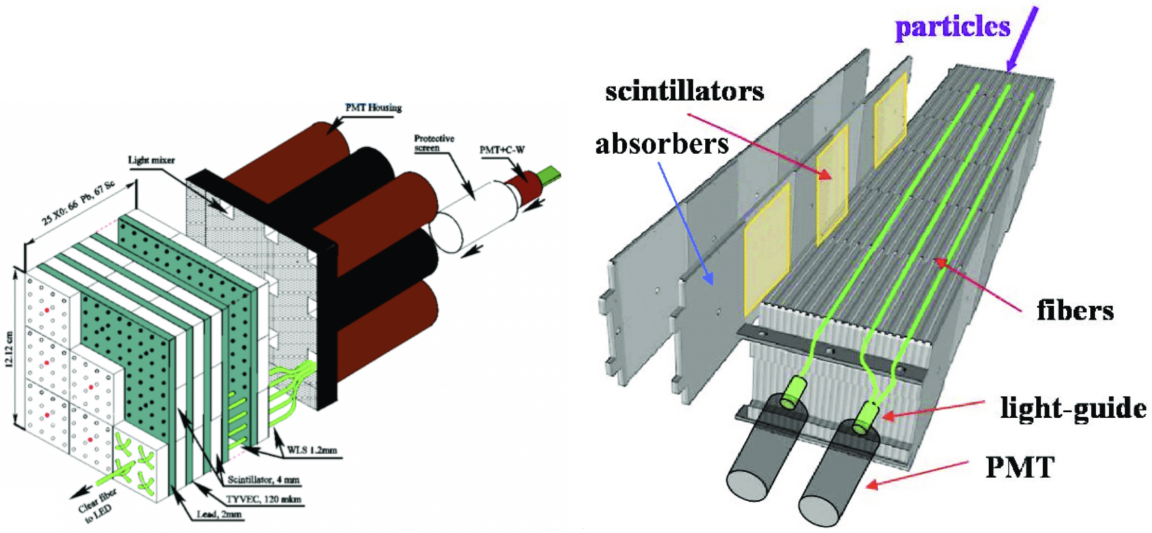

Figure 2.16: Schematic representation of one INNER ECAL module (left) and schematic representation of a HCAL module with the tile assembly (right) [10].

is not a binary detector, but for the trigger, the measurement is converted to a single bit by comparison to a threshold.

The ECAL uses the shashlik technology of sampling calorimeters composed of an alternation of lead plates and scintillators stacked orthogonally to the beam axis. The scheme of an inner module of the ECAL is shown in Figure 2.16. The total depth of the ECAL volume is 83.5 cm, which includes 42 cm of sampling "lead and scintillator plates" components (corresponding to $25X_0$ and $1.1\lambda_I$). The Moliere radius of the ECAL is 3.5 cm and the corresponding energy resolution is given by $\sigma_E = a\sqrt{E} \oplus bE$, where a is 8% to 10% depending on the area (inner, middle, or outer), b is 0. 9% and E the energy in GeV.

The HCAL is another shashlik sampling calorimeter, it consists of scintillator and iron tiles parallel to the z axis. Figure 2.16 shows how the tiles are grouped into large modules. The total depth of the HCAL is 123.3 cm, including 120 cm of sampling volume (5.6 λ_I).

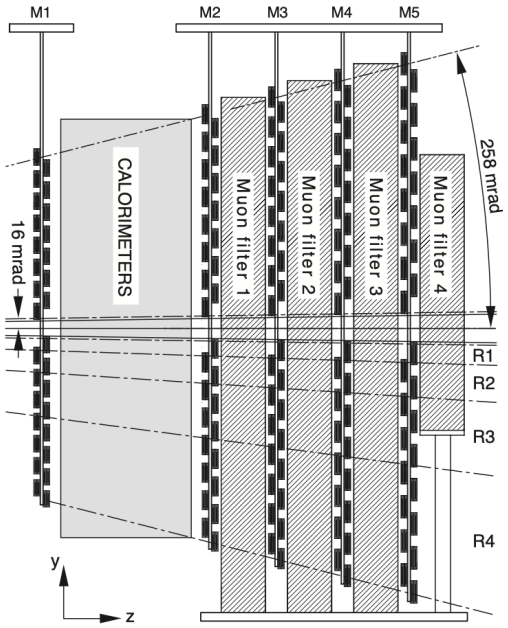

Figure 2.17: Side view of the muon system [10].

Muon system

Since a large number of LHCb studies involve muons in the final state (such as decay channels $B^0 \to K^{*0}\mu^+\mu^-$ [113], $B_s^0 \to \mu^+\mu^-$ [114] or $B_s^0 \to J/\psi(\mu^+\mu^-)\phi$ [115]) a dedicated detector system is used to identify them and measure their momenta at the trigger level.

The muon system [116, 117] is made up of five stations (M1-M5). The first station (M1) is located between RICH2 and calorimeters to avoid multiple scattering effects that may possibly affect the particle trajectories, and is composed of a triple-GEM detector for its innermost part and of Multi Wire Proportional Chambers (MWPC) elsewhere. The other stations (M2-M5), placed alternatively with 80 cm thick iron planes, are located at the end of the LHCb detector and are composed of MWPC. An overview of the muon system is given in Figure 2.17.

The muon system detects 46% of the muons from B-hadrons decays because of its angular acceptance of ± 300 mrad in the horizontal plane and ± 200 mrad in the vertical plane. At the reconstruction level, trajectories from the T stations and hits from the muon system are combined. If correspondences are found for tracks, they are promoted as muon candidates.

PID techniques

The Particle Identification (PID) in LHCb is performed by combining the PID detector information. Charged particles ($e^\pm, \mu^\pm, \pi^\pm, K^\pm, p$ and $\bar{p}$) are identified with the RICH detectors, the calorimeters, and the muon system. Neutral particles (γ and π^0 reconstructed from $\pi^0 \to \gamma\gamma$) are identified only with the calorimeters.

For each particle (corresponding to a track if charged), the recorded PID information are used to build two variable types: log-likelihood difference (DLL) and `ProbNN`. The work reported in this thesis used `ProbNN` variables.

The DLL is defined as the difference between a given PID hypothesis (y) and the pion PID hypothesis, as writen in equation 2.2.2:

$$\mathrm{DLL}_y = \ln \mathcal{L}_y - \ln \mathcal{L}_\pi = \ln \frac{\mathcal{L}_y}{\mathcal{L}_\pi}, \tag{2.2.2}$$

where $\mathcal{L}_i$ ($i = y$ or π) is the likelihood function built on the PID system information.

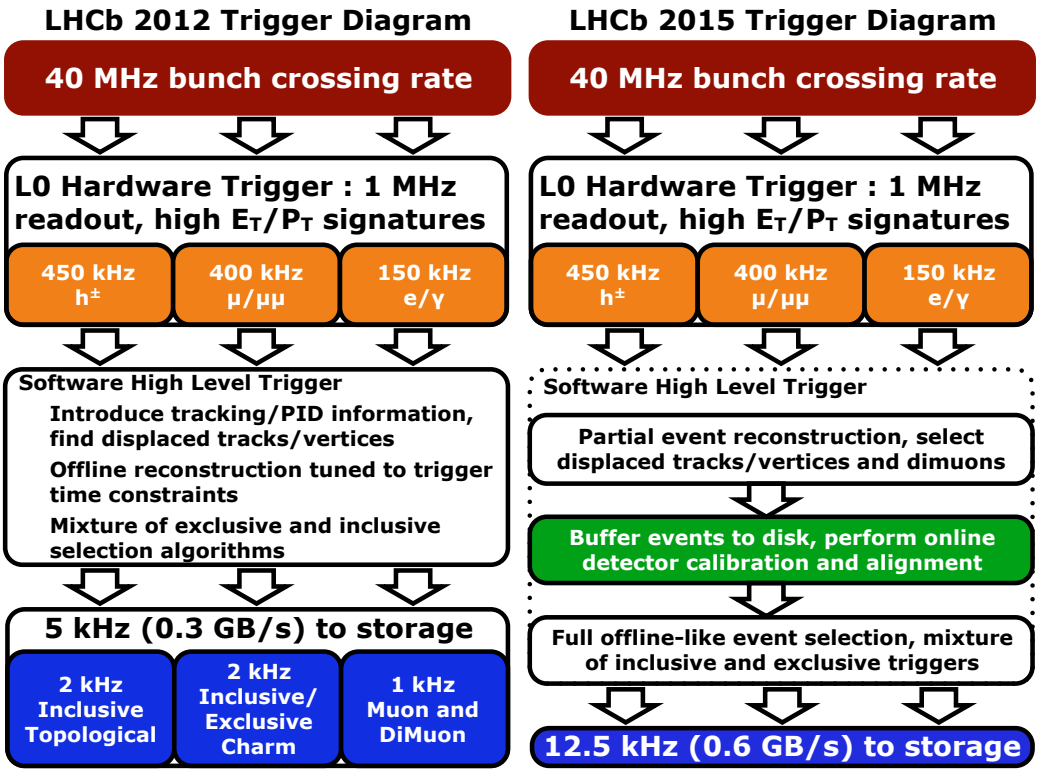

Figure 2.18: Summary of the LHCb trigger in Run I (left) and Run II (right) [121], Software High Levels Trigger means both HLT1 and HLT2.

The `ProbNN` variables are built from the PID system information using a recursive Neural Network (NN) named Hopkins network [118]. Concretely, for each candidate, several PID hypotheses are tested through `ProbNN`y, where y corresponds to a given PID hypothesis ($e^{\pm}, \mu^{\pm}, \pi^{\pm}, K^{\pm}, p$ and $\bar{p}$). `ProbNN`y output is the probability that the candidate considered corresponds to y.

2.2.5 Trigger

From an initial pp bunch crossing frequency of 40 MHz at LHC, collision rates of 15 MHz for Run I and 30 MHz for Run II have been obtained at LHCb [119]. Unfortunately, it is impossible to store all the events recorded at LHCb due to actual technological limitations. But first, with regard to the $b\bar{b}$ production cross section, not all events are $b\bar{b}$ events, and second, among the $b\bar{b}$ events, not all are interesting to study (too high multiplicity or outside acceptance). The LHCb (in its first phase) mitigation is embodied in the hardware trigger system [120].

The role of the LHCb trigger system was to reduce the event rate to storage at 5 kHz for Run I and 12.5 kHz for Run II. The LHCb trigger system is divided into three levels, first the hardware Level 0 trigger (L0 trigger) operating directly on the detector outputs, and then two software level triggers, written in C++, deported in processor farm, the High Level Trigger 1 and 2 (HLT1 and HLT2). Figure 2.18 shows the LHCb trigger system with additional details. The different trigger levels are presented below.

L0 trigger

The L0 trigger is a hardware trigger operating on the collision and aiming at rejecting quickly uninteresting events. It reduces the event rate to 1 MHz. The L0 trigger is divided into three detector-based subsystems: pile-up, L0 calorimeter trigger, and L0 muon trigger.

The pile-up subsystem estimates the number of primary vertices in event from VELO information to build a decision. The L0 muon trigger is fired if a muon track is reconstructed from the muon system, if this track is compatible with the interaction point, and if the measured transverse momentum p_T of the muon is over a threshold (in the case of multiple muon candidates, the decision is based on the one with the highest p_T).

The L0 calorimeter trigger combines information from SPD, PS, ECAL and HCAL to build three decisions, L0Electron, L0Hadron, and L0Photon. Starting from a 2×2 cluster in ECAL, an electron candidate is built if matching hits are found in PS and SPD, a photon candidate is built if matching hits are found in PS only, and a hadron candidate is built if matching hits are found in HCAL. The transverse energies E_T of the candidates are used to fire the corresponding decisions if they are above the set thresholds (specific to the type of candidate and the data-taking period). If several candidates of one type are found, only the one with the highest E_T is used in the decision. Additionally, to reduce computational cost, the SPD number of hits is used to reject too busy events, with limits set to 450 for Run II and 600 for Run I. In this manuscript a work related to L0Hadron trigger corrections is presented in Section 2.4.

Based on previous decisions, the L0 Decision Unit (L0DU) [122], an electronic board, takes the final decision to send or not send an event to the next trigger stage.

High Level Trigger 1

The HLT1 uses a set of inclusive *lines* (trigger requirements) grouped in several classes like technical or muon dedicated lines. HLT1 makes decision based on information coming from the tracking system. It keeps events for which tracks with very good quality are found, e.g. tracks with high p_T and large Impact Parameter (IP which is the distance of closest approach of a track to the primary vertex) with respect to all the primary vertices of the event. HLT1 run lines optimised for different types of final particle in parallel, allowing one to tune the selection for various analyses. Events kept by HLT1 are sent to HLT2.

High Level Trigger 2

The HLT2 performs a reconstruction of the events. During Run I the tracks were combined to reconstruct intermediate particle candidates (such as K^0_S from two π used in this manuscript), during Run II, thanks to processors farm update, a first full reconstruction was performed. The reconstructed information are used to build various decisions corresponding to different analyses. Due to the upgrades (processors farm update and others) done between Run I and Run II, better samples have been built for Run II.

Trigger decision

For each event, all the trigger decisions established are stored in a 32-bit encoded key, the Trigger Configuration Key (TCK), which are used to make a first selection of the interesting samples for analyses. Three non-exclusive categories are used to classified events at each trigger level:

- **Trigger On Signal (TOS) events** corresponding to events for which trigger objects associated to the signal (the decay of interest) are energetic enough (particle beyond L0 threshold) to trigger the events.
- **Trigger Independent of Signal (TIS) events** corresponding to events for which trigger objects not associated to the signal have triggered the events.
- **TIS and TOS events** corresponding to events belonging to the two previous categories.

Section 2.3.2 details, among other information, the triggers used in the LHCb analysis reported in this thesis.

2.3 LHCb tools

In this section, the LHCb computing tools are presented together with a projection of their basic use in the $B^0_{d,s} \to K^0_S h^+ h'^-$ analysis.

2.3.1 LHCb Software

The LHCb software [123, 124] is made up of several packages that are used from Monte Carlo simulations (needed to estimate efficiency) to event reconstruction and at physics analysis level. All packages are built within the object-orientated GAUDI framework [125] which provides a common environment to develop application in HEP experiments such as LHCb and ATLAS. One of the most important task of the software is to allow users to deal with recorded and simulated events. In the following, the most important pieces of software are presented with an emphasis on their applications on data and simulation.

The recorded events (data) that pass the L0 trigger are processed by the MOORE [126] application to apply the HLT lines, before being written on disk storage as raw data. An off-line reconstruction of them is performed taking advantage of the LHC Computing Grid [127], featuring BRUNEL [128] and, since Run II, MOORE applications. After that the DaVinci [129] software performs a new filtering step named *Stripping*, the stripping allows to go one step further towards analysis by applying dedicated physical cuts (by combining tracks or using particle hypotheses). A set of stripping requirements is named a stripping line. Stripping lines exist for almost all analyses at LHCb (some of them are used in several analyses). After this process, DaVinci stored the data as ROOT[4] [130] files, merging all user-defined inputs needed to analyse the data with a specific structure.

The simulated events are made thanks to the GAUSS [131] framework. First, the pp collisions are generated by PYTHIA8 [98, 132] and the decays of the collisions products are simulated by EvtGen [133] and PHOTOS [134]. Second, the interaction of the simulated particles in the LHCb detector is simulated by the GEANT4 [135] software. Third, the simulated behaviour in the detector of the particles is digitised by the BOOLE package to provide data-like detector responses. At the same step, in order to reduce the pressure on the computing resources, simulated events outside the LHCb acceptance are vetoed-out thanks to requirements named Generator Level Cut (GLC). Third, the BRUNEL and MOORE applications are used in a way similar to what is done on the data due to the previous steps. Finally, DaVinci is used to process the simulated events in the same way as the data, in order to provide ROOT files equivalent to the data ones.

For both data and simulation, the PIDCalib package is used to determine the corresponding PID performances and eventually correct the PID variables in the simulation to have a behaviour that matches the data one. All the LHCb softwares presented here and others are kept on the LHCb CERN Gitlab page [136].

Once ROOT files of both simulation and data are provided, the remaining part of the analyses can be performed on CERN computing servers or directly on user machines. At this level, it is usual to use various programming languages, the work presented in this manuscript has mainly been done with ROOT and Python [137] featuring libraries like Uproot [138], Scikit [139], Awkward Array [140], Numpy [141], Pandas [142], and Matplotlib [143].

2.3.2 $B^0_{d,s} \to K^0_S h^+ h'^-$ datasets and MC samples

In the following, a concrete example of the use of the LHCb tools is given through the prism of the analysis $B^0_{d,s} \to K^0_S h^+ h'^-$ (where $h^{(\prime)}$ corresponds to π or K and K^0_S goes to $\pi^+\pi^-$ in the final

[4]ROOT is an object-oriented framework developed to perform data analysis in High Energy Physics (HEP).

state) presented in Chapter 3. The $B^0_{d,s} \to K^0_S h^+ h'^-$ analysis aims to discover $B^0_s \to K^0_S K^+ K^-$ and to update the branching fraction measurement other $B^0_{d,s} \to K^0_S h^+ h'^-$ modes. This section presents both the data samples and the MC samples used in the analysis $B^0_{d,s} \to K^0_S h^+ h'^-$, in addition to the trigger requirements and the stripping selections applied.

Data samples

$B^0_{d,s} \to K^0_S h^+ h'^-$ uses the full LHCb dataset, recorded in 2011 and 2012 (Run I), and from 2015 to 2018 (Run II). Table 2.2 summarises the data-taking conditions and stripping versions used for each year.

Year	c.m. energy	Luminosity	Stripping version
2011	7 TeV	1.11 fb^{-1}	`Stripping20r1`
2012	8 TeV	2.08 fb^{-1}	`Stripping20`
2015	13 TeV	0.33 fb^{-1}	`Stripping24r1`
2016	13 TeV	1.67 fb^{-1}	`Stripping28r1`
2017	13 TeV	1.71 fb^{-1}	`Stripping29r2`
2018	13 TeV	2.19 fb^{-1}	`Stripping34`

Table 2.2: List of the data samples used in this analysis, the data-taking conditions and the corresponding stripping versions.

MC samples

The MC samples are generated with conditions as similar as possible to the data-taking conditions. All samples used here were produced using `Sim09`. For each sample, the events were generated with a uniform distribution in the square Dalitz plane (sqDP).

These are three-body decays, so they have a non-trivial distribution across the phase space, which is conventionally represented as a 2D plane known as a Dalitz plot. There are several equivalent ways of defining the axes, the best-known approach uses the squares of two-body invariant masses, but here one rescaled two-body mass and the cosine of one angle are used. Other studies of multibody BnoC decays have shown that most of the structure and many of the events are concentrated near the edges of the phase space, this is because the masses of charmless resonances (ρ, K^*, etc.) are light compared to the B meson mass. Generating events uniformly in the square Dalitz plot is a common choice when studying charmless B decays because it has two big advantages: first, it generates more events near the edges of the phase space, i.e. the region of physical interest, and roughly mimics what the data are doing, second, it allows one to divide the phase space into rectangular bins which makes efficiency modelling and correction simpler. Note that the phase-space distribution does not have to be perfect when generating MC events, since data-driven corrections are applied later. More details about the Dalitz plane are given in Chapters 3 and 4.

The number of events corresponding to each sample, the magnet polarity and the data taking period are given in Table 2.3 for Run I and Table 2.4 for Run II, while Table 2.5 summarises the simulation conditions.

The trigger configuration (TCK) often changes during the data-taking. Generally, MC samples are simulated using one trigger configuration that best represents the conditions in the corresponding data-taking year. 2012 is a special case: during the technical stop at the end of June 2012, major changes were made to the HLT2 topological lines resulting, among other things, in the inclusion of K^0_S candidates reconstructed with downstream tracks. Due

to this change in the trigger, 2012 cannot be treated as a single homogeneous sample with identical conditions; instead, two distinct MC samples are used, each with a representative TCK corresponding to the period before or after the June technical stop. In the following, they will be referred to as 2012a (before June changes) and 2012b (after June changes).

Some very loose cuts have been applied to signal MC events at the generator level, to reduce the average CPU and disk consumption per useful event. These cuts ensure that the decay products are within the LHCb acceptance and apply some kinematic requirements that are looser than the cuts that will be applied later. The same requirements are applied to all decay modes. A complete list of these cuts can be found in Table 2.6.

Mode	Event type	2011 Sim09f		2012a Sim09f		2012b Sim09f	
		Mag. Down	Mag. Up	Mag. Down	Mag. Up	Mag. Down	Mag. Up
$B^0 \to K^0_S\pi^+\pi^-$	11104127	1,145,934	1,024,558	1,118,117	1,260,028	1,009,270	1,000,177
$B^0 \to K^0_S K^+K^-$	11104117	1,097,056	1,393,779	1,093,774	1,029,548	1,000,748	1,001,588
$B^0 \to K^0_S K^\pm\pi^\mp$	11304165	1,090,089	1,232,656	1,009,452	1,181,179	1,005,393	1,002,828
$B^0_s \to K^0_S\pi^+\pi^-$	13104126	1,381,239	1,086,745	1,107,872	1,025,546	1,035,152	1,029,250
$B^0_s \to K^0_S K^+K^-$	13104136	1,159,799	1,150,884	1,261,310	1,129,587	1,002,846	1,027,273
$B^0_s \to K^0_S K^\pm\pi^\mp$	13304106	1,124,732	1,131,317	1,004,502	1,204,447	1,066,764	1,076,761

Table 2.3: Number of MC events generated for each mode according to the year and the magnet polarity (Run I).

Mode	Event type	2015 Sim09e		2016 Sim09e		2017 Sim09h		2018 Sim09h	
		Mag. Down	Mag. Up	Mag. Down	Mag. Up	Mag. Down	Mag. Up	Mag. Down	Mag. Up
$B^0 \to K^0_S\pi^+\pi^-$	11104127	2,055,032	2,008,492	2,001,287	2,001,205	2,047,030	2,013,872	2,003,225	2,007,150
$B^0 \to K^0_S K^+K^-$	11104117	2,017,345	2,001,073	2,004,882	2,000,835	2,026,293	2,019,889	2,069,974	2,002,150
$B^0 \to K^0_S K^\pm\pi^\mp$	11304165	2,004,600	2,003,133	2,031,373	2,007,537	2,029,900	2,045,425	2,001,631	2,100,602
$B^0_s \to K^0_S\pi^+\pi^-$	13104126	2,042,502	2,006,784	2,011,125	2,023,340	2,287,076	2,039,002	2,163,560	2,045,473
$B^0_s \to K^0_S K^+K^-$	13104136	2,045,297	2,136,559	2,001,293	2,004,224	2,015,320	2,000,437	2,004,205	2,056,433
$B^0_s \to K^0_S K^\pm\pi^\mp$	13304106	2,002,461	2,004,447	2,013,167	2,003,733	2,050,728	2,145,405	2,007,248	2,142,297

Table 2.4: Number of MC events generated for each mode according to the year and the magnet polarity (Run II).

Year	CONDDB	DDDB	pileup factor ν	TCK	Stripping
2011	sim-20160614-1-vc-m{u,d}100	20170721-1	2.0	0x40760037	Stripping20r1
2012a	sim-20160321-2-vc-m{u,d}100	20170721-2	2.5	0x409f0045	Stripping20
2012b	sim-20160321-2-vc-m{u,d}100	20170721-2	2.5	0x4097003d	Stripping20
2015	sim-20161124-vc-m{u,d}100	20170721-3	1.6	0x411400a2	Stripping24r1
2016	sim-20170721-2-vc-m{u,d}100	20170721-3	1.6	0x6139160F	Stripping28r1
2017	sim-20190430-1-vc-m{u,d}100	20170721-3	1.6	0x62661709	Stripping29r2
2018	sim-20190430-vc-m{u,d}100	20170721-3	1.6	0x617d18a4	Stripping34

Table 2.5: MC generation conditions for each year.

Trigger

All events have to pass the full trigger chain (L0-HLT1-HLT2) described below. A summary of the trigger requirements for each year is given in Table 2.7.

Cut	Description
	B **candidate**
$p_{\mathrm{T}}(B) > 1500$ MeV	Transverse momentum of the B candidate
	$h^{(\prime)}$ **candidates**
$0.010 < \theta(h^{(\prime)}) < 0.400$	Charged daughters of the B within detector acceptance.
$1.8 < \eta(h^{(\prime)}) < 5.0$	Pseudo-rapidity of $h^{(\prime)}$ candidates.
3.0GeV < p($h^{(\prime)}$) < 150GeV	Total momentum.
	K^0_{S} **candidate**
$2 < \eta(K^0_{\mathrm{S}}) < 5$	Pseudo-rapidity of K^0_{S} candidate.
`ksTT` = GVEV & (GFAEVX (GVZ , 1.e+10) < 240 * centimeter)	valid K^0_{S} must decay less than 240 cm downstream of interaction point
	K^0_{S} **daughters**
$1.6 < \eta(\pi^{\pm}) < 5.2$	Pseudo-rapidity of K^0_{S} candidate daughters.
2.0GeV < p($\pi^{\pm}$) < 150GeV	Total momentum.
`bothPI` = 2 == GNINTREE (('pi+' == GABSID))	K^0_{S} must decay to two charged pions

Table 2.6: Cuts applied at MC generator level for $B \to K^0_{\mathrm{S}}\, h^+ h'^-$.

At L0, we require that either the B candidate is TOS on L0Hadron (meaning that one or more of the daughter tracks was matched to calorimeter deposits that activated the L0Hadron line) `OR` that the B candidate is TIS on at least one of a list of physics channels[5] (e.g. L0Muon).

At HLT1, TOS on the standard one-track or two-track lines is required. These are well adapted to $B^0_{d,s} \to K^0_{\mathrm{S}} h^+ h'^-$ where two charged hadrons are produced at a displaced vertex and where there is a large energy release in the B decay.

In HLT2, TOS on one of the standard topological channels is required, using the two-, three-, and four-body versions in logical OR since there are four charged tracks in the final state when including the K^0_{S} daughters.

We note that for Run I, the trigger requirements at all levels are very similar to those used in the previous $B^0_{d,s} \to K^0_{\mathrm{S}} h^+ h'^-$ analysis [144]. The only difference is that the previous analysis used L0Global TIS instead of a list of physics TIS channels.

Stripping

K^0_{S} mesons are reconstructed from two tracks of opposite charge, each given the pion mass hypothesis. Because of the long K^0_{S} lifetime and boost, at LHCb a large fraction of K^0_{S} produced will decay after leaving the VELO (or toward the end of the VELO, not leaving enough hits to reconstruct a VELO track segment). As is standard, the use of both long tracks and downstream tracks has been done. In this manuscript, these categories are denoted as LL (the K^0_{S} candidate is reconstructed from two long tracks) and DD (the K^0_{S} candidate is reconstructed from two downstream tracks)[6]. K^0_{S} candidates reconstructed as LL have, on average, better mass, momentum, and vertex resolution than those reconstructed as DD. However, in the sample, there is roughly twice as much signal in the DD category.

The stripping lines used are dedicated to the $B^0_{d,s} \to K^0_{\mathrm{S}} h^+ h'^-$ decay modes study. In order to avoid duplication between different final states, these lines treat all charged hadrons as pions (but without applying any PID requirements), they are refited offline afterwards with the correct mass hypothesis. The lines have a similar structure for Run I and Run II, although the details of the cuts differ between the two Runs. Different stripping lines are used for each K^0_{S} reconstruction category:

- Run I: `StrippingB2KShhDDLine` and `StrippingB2KShhLLLine`

[5] L0Global TIS not use because it is not possible to fully determine its efficiency. This costs essentially nothing in statistics: for example, in MC this represents $< 0.1\%$ in 2015 and $< 0.01\%$ in 2016.

[6] No attempt to use LD combinations. Although it is in principle possible to get a little bit of signal in this category, the small potential gain would not be justified by the extra complexity. Upstream tracks and T tracks have also not been used, as they have a poor momentum resolution.

Year	Trigger requirements	HLT1 trigger requirements	HLT2 trigger requirements
2011	B_L0HadronDecision_TOS	B_Hlt1TrackAllL0Decision_TOS	B_Hlt2Topo2BodyBBDTDecision_TOS
	B_L0DiMuonDecision_TIS		B_Hlt2Topo3BodyBBDTDecision_TOS
	B_L0MuonDecision_TIS		B_Hlt2Topo4BodyBBDTDecision_TOS
	B_L0ElectronDecision_TIS		B_Hlt2Topo2BodySimpleDecision_TOS
	B_L0PhotonDecision_TIS		B_Hlt2Topo3BodySimpleDecision_TOS
	B_L0HadronDecision_TIS		B_Hlt2Topo4BodySimpleDecision_TOS
2012	(same as 2011)	(same as 2011)	B_Hlt2Topo2BodyBBDTDecision_TOS
			B_Hlt2Topo3BodyBBDTDecision_TOS
			B_Hlt2Topo4BodyBBDTDecision_TOS
2015	B_L0HadronDecision_TOS	B_Hlt1TrackMVADecision_TOS	B_Hlt2Topo2BodyDecision_TOS
	B_L0DiMuonDecision_TIS	B_Hlt1TwoTrackMVADecision_TOS	B_Hlt2Topo3BodyDecision_TOS
	B_L0MuonDecision_TIS		B_Hlt2Topo4BodyDecision_TOS
	B_L0ElectronDecision_TIS		
	B_L0PhotonDecision_TIS		
	B_L0HadronDecision_TIS		
	B_L0MuonEWDecision_TIS		
	B_L0MuonNoSPDDecision_TIS		
	B_L0JetElDecision_TIS		
	B_L0JetPhDecision_TIS		
2016	B_L0HadronDecision_TOS	(same as 2015)	(same as 2015)
	B_L0DiMuonDecision_TIS		
	B_L0MuonDecision_TIS		
	B_L0ElectronDecision_TIS		
	B_L0PhotonDecision_TIS		
	B_L0HadronDecision_TIS		
	B_L0MuonEWDecision_TIS		
	B_L0JetElDecision_TIS		
	B_L0JetPhDecision_TIS		
2017,2018	B_L0HadronDecision_TOS	(same as 2015)	(same as 2015)
	B_L0DiMuonDecision_TIS		
	B_L0MuonDecision_TIS		
	B_L0ElectronDecision_TIS		
	B_L0PhotonDecision_TIS		
	B_L0HadronDecision_TIS		
	B_L0MuonEWDecision_TIS		

Table 2.7: List of trigger requirements used for each year. A logical OR is implied between each line and a logical AND is implied between the columns. The trigger criteria are nearly constant throughout Run II, the only changes are that B_L0MuonNoSPDDecision_TIS was not used after 2015, and that B_L0JetElDecision_TIS and B_L0JetPhDecision_TIS were not used after 2016.

- Run II: StrippingB2KShh_DD_Run2_OS_Line and StrippingB2KShh_LL_Run2_OS_Line

The stripping lines are summarized below, links to the stripping pages associated with the lines, where the full details of the reconstruction and selection used in the stripping may be found, are given in Table 2.8.

All of these lines apply global event cuts, selecting events with fewer than 250 Long tracks and at least one primary vertex (PV).

The K^0_S candidates are taken from the StdLooseKsDD and StdLooseKsLL containers. These containers use cuts on pions candidates and two pion candidates combinations to select the K^0_S candidates from $K^0_S \to \pi^+\pi^-$. The B candidates are formed by combining a K^0_S candidate with two oppositely charged tracks, each assigned with a pion mass hypothesis. In Run I, the $h^{(\prime)}$ candidates are taken from StdLoosePions whereas in Run II they are taken from StdAllNoPIDsPions, while neither apply PID cuts. The container used in Run I requires tracks with transverse momentum greater than 250 MeV ($p_{\rm T}(h^{(\prime)}) > 250$ MeV) as well as a minimum impact parameter χ^2 with respect to the PV bigger than four ($\min\chi^2_{\rm IP}$ $(\pi^\pm) > 4$). In contrast,

Year	Version	LL line	DD line
2011	Stripping20r1	StrippingB2KShhLLLine	StrippingB2KShhDDLine
2012	Stripping20	StrippingB2KShhLLLine	StrippingB2KShhDDLine
2015	Stripping24r1	StrippingB2KShh_LL_Run2_OS_Line	StrippingB2KShh_DD_Run2_OS_Line
2016	Stripping28r1	StrippingB2KShh_LL_Run2_OS_Line	StrippingB2KShh_DD_Run2_OS_Line
2017	Stripping29r2	StrippingB2KShh_LL_Run2_OS_Line	StrippingB2KShh_DD_Run2_OS_Line
2018	Stripping34	StrippingB2KShh_LL_Run2_OS_Line	StrippingB2KShh_DD_Run2_OS_Line

Table 2.8: Links to stripping line definitions (working as of March 2023).

these cuts are not included in `StdAllNoPIDsPions`. This change in the stripping was made for the benefit of future amplitude analyses, since the previous cut was removing low-p_{T} candidates located in the corners of the Dalitz plane that are particularly relevant for Dalitz plane analysis. However, for *the* BF measurements analysis, they represent a small fraction of the total signal events and would not make a major difference to the statistical uncertainty. Not applying these cuts also causes a dramatic increase in the background level. These cuts will be added back in the preselection step for Run II, see Section 3.1.6. So in practice, the tracklists are aligned between Runs I and II for the analysis.

As is standard, stripping cuts are applied in three stages DaughterCuts, CombinationCut and MotherCut. The DaughterCut applies requirement on the daughters particle decay, CombinationCut applies requirement on the combinations of daughters made to build the decaying mother particle without any fit (no mother hypothesis considered), and MotherCut applies requirement on the fitted mother candidates. The cuts are chosen to reduce bias to the Dalitz plane distribution and mainly use topological variables such as the χ^2 of the vertex fit (χ^2_{vtx}), the flight distance χ^2 from the related PV (χ^2_{FD}), the minimum impact parameter (IP) χ^2 of a track with respect to the related PV ($\mathrm{min}\chi^2_{\mathrm{IP}}$), the distance of closest approach of two or more particles (DOCA), and the cosine of the direction angle to the related PV (DIRA).

Tables 2.9 and 2.10 summarise the stripping cuts used for Run I and Run II, respectively.

Events reconstruction

The output of the stripping process serves as the input for ntuple-making jobs. For both data and MC, the ntuples are produced with `Bender` [145] version `32r4p3`. As noted above, during the stripping stage the charged tracks produced at the B decay ($h^{(\prime)}$) were assigned the pion identity and mass hypothesis. It has been updated: when filling the ntuples, the mass hypotheses and identities are changed to match the final state ($K^0_{\mathrm{S}}\pi^+\pi^-$, $K^0_{\mathrm{S}}K^+\pi^-$, $K^0_{\mathrm{S}}\pi^+K^-$, $K^0_{\mathrm{S}}K^+K^-$) and the decay tree is refitted using `DecayTreeFitter` (DTF) [146]. This refit updates all relevant variables coherently. As part of the DTF refit, additional constraints may be applied. Two results are saved, first from a refit with no extra constraints, and second from a refit with the K^0_{S} mass constrained to its nominal value and the B candidate constrained to originate at the PV. The latter, with the two constraints applied, is used in the $B^0_{d,s} \to K^0_{\mathrm{S}}h^+h'^-$ analysis.

Cut step	Candidate(s)	StrippingB2KShhDDLine	StrippingB2KShhLLLine
DaughterCuts	K^0_S	$p(K^0_S) > 6000.0$ MeV	-
		$\lvert m_{\pi^+\pi^-} - m^{\rm PDG}_{K^0_S}\rvert < 30.0$ MeV	$\lvert m_{\pi^+\pi^-} - m^{\rm PDG}_{K^0_S}\rvert < 20.0$
		$\chi^2_{\rm vtx}(K^0_S) < 12.0$	idem
		$\chi^2_{\rm FD}(K^0_S) > 50.0$	$\chi^2_{\rm FD}(K^0_S) > 80.0$
	K^0_S daughters	$p(\pi^\pm) > 2.0$ GeV	idem
		$\min\chi^2_{\rm IP}$ $(\pi^\pm)> 4$	$\min\chi^2_{\rm IP}$ $(\pi^\pm)> 9$
		-	$p_{\rm T}(\pi^\pm) > 250$ MeV
		DOCA χ^2 of K^0_S daughters< 25	idem
		-	track χ^2/ndf < 4.0
		-	track ghost probability < 0.5
	$h^\pm$ $(\pi^\pm)$	track χ^2/ndf < 4.0	idem
		track ghost probability < 0.5	idem
		$p_{\rm T}(h^\pm) > 250$ MeV	idem
		$\min\chi^2_{\rm IP}$ $(h^\pm)> 4$	idem
CombinationCut		$p_{\rm T}(B) > 1000.0$ MeV	idem
		$p_{\rm T}(K^0_S) + p_{\rm T}(h^+) + p_{\rm T}(h^-) > 4200.0$ MeV	$p_{\rm T}(K^0_S) + p_{\rm T}(h^+) + p_{\rm T}(h^-) > 3000.0$ MeV
		at least 2 of (h^+, h^-, K^0_S) with $p_{\rm T} > 800$ MeV	idem
		$(4000 < m_{K^0_S h^+ h'^-} < 6200)$ MeV	idem
		`AVAL_MAX(MIPDV(PRIMARY),PT)`¿0.05	idem
		DOCA χ^2 of any pair of $(h^+, h^-, K^0_S)< 5$	idem
MotherCut		$p_{\rm T}(B) > 1500.0$ MeV	idem
		$\chi^2_{\rm vtx}(B) < 12.0$	idem
		DIRA$(B)> 0.999$	DIRA> 0.9999
		$\min\chi^2_{\rm IP}$ $(B)< 6.0$	$\min\chi^2_{\rm IP}$ $(B)< 8.0$
		B flight distance w.r.t. any PV > 1.7 mm	B flight distance > 1.0 mm
		$\chi^2_{\rm FD}(B) > 50$	idem
		$\sum\chi^2_{\rm IP}$ for all charged hadrons in tree > 50	-

Table 2.9: Stripping requirements for Run I. As the stripping is applied in different steps, the same cut can appear multiple times. When this happens, only the last occurrence of the cut, the tightest version, is listed in this table. The charged input lists used for the charged decay products of the B are `StdAllLoosePions`, and the K^0_S candidates are based on `StdLooseKsDD` and `StdLooseKsLL` with additional cuts (below) applied.

Cut step	Candidate(s)	StrippingB2KShh_DD_Run2_OS_Line	StrippingB2KShh_LL_Run2_OS_Line
TriggerCuts	HLT1	Hlt1TrackMVADecision	idem
		Hlt1TwoTrackMVADecision	idem
		Hlt1IncPhiDecision (Hlt1PhiIncPhiDecision)	idem
	HLT2	Hlt2Topo{2,3,4}BodyDecision	idem
		Hlt2IncPhiDecision (Hlt2PhiIncPhiDecision)	idem
DaughterCuts	K^0_S	$p(K^0_S) > 6000.0\,\text{MeV}$	-
		$\lvert m_{\pi^+\pi^-} - m^{\text{PDG}}_{K^0_S}\rvert < 30.0\,\text{MeV}$	$\lvert m_{\pi^+\pi^-} - m^{\text{PDG}}_{K^0_S}\rvert < 20.0\,\text{MeV}$
		$\chi^2_{\text{vtx}}(K^0_S) < 12.0$	idem
		$\chi^2_{\text{FD}}(K^0_S) > 50.0$	$\chi^2_{\text{FD}}(K^0_S) > 80.0$
	K^0_S daughters	$p(\pi^\pm) > 2.0\,\text{GeV}$	idem
		$\min\chi^2_{\text{IP}}\ (\pi^\pm) > 4$	$\min\chi^2_{\text{IP}}\ (\pi^\pm) > 9$
		-	$p_{\text{T}}(\pi^\pm) > 250\,\text{MeV}$
		DOCA χ^2 of K^0_S daughters< 25	idem
		track $\chi^2/\text{ndf} < 4.0$	idem
		-	track ghost probability < 0.5
	$h_{1,2}$	track $\chi^2/\text{ndf} < 4.0$	idem
		track ghost probability < 0.5	idem
CombinationCut		$p_{\text{T}}(B) > 1000.0\,\text{MeV}$	idem
		$p_{\text{T}}(K^0_S) + p_{\text{T}}(h^+) + p_{\text{T}}(h^-) > 4200.0\,\text{MeV}$	$p_{\text{T}}(K^0_S) + p_{\text{T}}(h^+) + p_{\text{T}}(h^-) > 3000.0\,\text{MeV}$
		at least 2 of (h^+, h^-, K^0_S) with $p_{\text{T}} > 800\,\text{MeV}$	idem
		$(4000 < m_{K^0_S h^+ h'^-} < 6200)\,\text{MeV}$	idem
		DOCA χ^2 between (h^+, K^0_S) and between (h^-, K^0_S) both < 25	idem
MotherCut		$p_{\text{T}}(B) > 1500.0\,\text{MeV}$	idem
		$\chi^2_{\text{vtx}}(B) < 12.0$	idem
		$\text{DIRA}(B) > 0.999$	idem
		$\chi^2_{\text{FD}}(B) > 5$	idem
		$Z_{\text{vtx}}(K^0_S) - Z_{\text{vtx}}(B) > 15.0\,\text{mm}$	idem
		$\chi^2_{\text{IP}}\ (\text{B}) < 6.0$	-
		$\sum\chi^2_{\text{IP}}$ for all charged hadrons in tree > 50.0	idem

Table 2.10: Stripping requirements for Run II. As the stripping is applied in different steps, the same cut can appear multiple times. When this happens, only the last occurrence of the cut, the tightest version, is listed in this table. The charged input lists used for the charged decay products of the B are StdAllNoPIDsPions, and the K^0_S candidates are based on StdLooseKsDD and StdLooseKsLL with additional cuts (below) applied.

2.4 L0 trigger corrections determination

The L0Hadron trigger line of LHCb is of first importance for the work presented in this thesis and for a number of LHCb analyses. Unfortunately, the L0Hadron behaviour in LHCb MC samples is known to be not well simulated, and this requires to build L0Hadron corrections from data, to apply on the MC in order to enhance the related efficiency determination.

In the following section, a technical work dedicated to the determination of these corrections for LHCb is summarised. The complete work is reported in an LHCb technical note [147] written in collaboration with Stéphane Monteil and Patrick Robbe. The goal of this section is to explain the method used to build L0Hadron corrections needed to tackle various trigger effects. A first determination of the L0Hadron corrections for Run II was already derived from the method explained below, but this was not the case for the Run I ones. This work provides the L0Hadron corrections for Run I and Run II. This section outlines the method used to determine the corrections, presents quantitatively the experimental inputs necessary to the method and the obtained results.

2.4.1 Trigger efficiency determination

A data driven method

Extensive work has been done to simulate the calorimeter trigger system in LHCb Monte Carlo productions. This is useful to understand trigger behaviour and to monitor trigger performance. But, as exhaustive as it is, this simulation cannot include all the effects that can affect the trigger. Several elements strongly influence the trigger behaviour but are very difficult to predict and model, among them there are ageing, disabled cells, or occupancy.

Therefore, the trigger-related quantities are not reachable via simple Monte Carlo simulation, and a data-driven method has to be used. L0Hadron trigger corrections, needed in physics analysis, can only be performed using real data.

HCAL measurements: real transverse energy

Hadrons (electromagnetic particles, respectively) reach the HCAL (ECAL, respectively) and initiate a shower. This energy deposit is then converted as transverse energy via the reached cells coordinates. Mathematically the transverse energy in the calorimeter is calculated as:

$$E_T = E \times \sin\theta \text{ with} \tag{2.4.1}$$

$$\sin\theta = \sqrt{\frac{x^2+y^2}{x^2+y^2+z^2}} \tag{2.4.2}$$

with E the energy deposit by a particle in the calorimeter cells, θ is the angle between the beam direction and the line defined by the interaction point and the center of the cell. Here $\sin\theta$ is rewritten via the position of the center of the cell reached (x, y, z) in Cartesian coordinates, with by definition the LHCb HCAL $z = 13.33\,\text{m}$ measured from the interaction point. This definition of the transverse energy is natural for neutral particles, but ignores the bending of the trajectory caused by magnets for charged tracks and differs in this case from the track transverse momentum. This is why in the following another quantity is defined for the charged particles.

LHCb measures the energy of particles with its calorimeter system; the tracking system combined with the magnet measures the momentum p and the transverse momentum p_T of the charged particles. Although the total energy is conserved, it is not the case for transverse quantities because of the magnet bending of the particle track. Calorimeter performance has to be studied carefully, because the p_T of a particle is not the same when crossing the tracking

system and at the HCAL level, and this p_T is not directly correlated to the E_T measured by the HCAL.

Depending on their charge and the magnet polarity, the charged particles trajectories are bent in one direction or another, as illustrated by the projection given in Figure 2.19. For a given magnet polarity, tracks of particles with opposite charges are bent in opposite directions. Consequently, in the picture, the purple and green tracks correspond to the same charge, as well as the blue and red ones which are opposite to the previous ones. Figure 2.19 shows that on the left side of the HCAL, the θ angle computed from the HCAL cell coordinates is overestimated for the purple track (negative charge) with respect to the angle given by the tracking system (in grey) where the one corresponding to the blue track (positive charge) is underestimated with respect to the angle given by the tracking system. The conclusions are opposite with respect to the particle charges on the right side of the HCAL (green and red tracks).

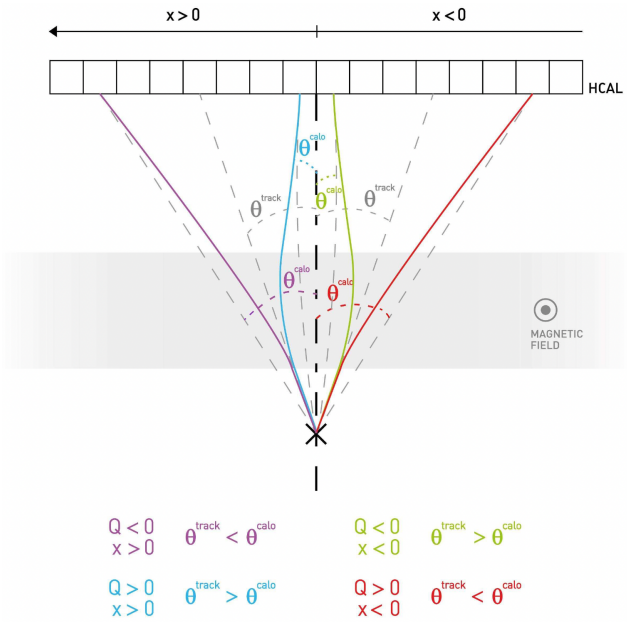

Figure 2.19: Diagram [148] representing tracks coming from the interaction point and impacting the HCAL, seen from the top. The tracks are bent by the magnetic field in one direction or the other depending on their charge Q. The dashed lines show the difference between the θ angle reconstructed by the HCAL and by the tracking system. Because of the E_T definition given by equation 2.4.1 this discrepancy leads to two different transverse energy for the same track. The same effect applies to any other transverse quantity.

To compare the transverse energy of a particle and the associated one measured in the HCAL as shown in equation 2.4.1, a recomputation of the first one is performed using tracking characteristics displaced at the HCAL z position. This new quantity is the real transverse energy, it is written as

$$E_T^{real} = \sin\theta^{track} \times \sqrt{p^2 + m^2} \tag{2.4.3}$$

where $\sin\theta^{track}$ is computed by injecting the coordinates of the projection of the track from the tracking system to the HCAL in 2.4.2, p is the momentum of the particle measured by the tracker and m is its mass.

The L0Hadron trigger efficiencies must vary across the E_T spectrum due to the energy threshold to select interesting events. Consequently, these efficiencies need to be established as a function of energy or, for practical purpose related to the HCAL measurement, as a function of a transverse quantity. To ensure consistency between tracking and HCAL measurements,

the efficiencies should be presented as a function of E_T^{real} extracted at the HCAL level using equation 2.4.3, rather than the directly measured p_T by the tracking system.

L0Hadron candidates

The requirements for the L0Hadron candidates are summarised in Table 2.11. L0Hadron candidates can be issued by three types of charged hadrons: pions, kaons, and protons. In this work, the efficiency tables will be determined for each of these particles and their charge conjugate independently. Calibration decays to study the candidates are as follows:

- $D^{*+} \to D^0(K\pi)\pi^+$ for pions and kaons, where the pions candidates correspond to the ones coming from the D^0 decay in order to reach a wide E_T range, the other pions are soft particles e.g. emitted with less energy,
- $\Lambda^0 \to p\pi$ for protons.

The performance group has written calibration tuples for those decays from the recorded pp collisions. There is a tuple for each hadron candidate (including the charge conjugate version), data-taking period, and magnet polarity of the detector, but 2015 (see Section 2.4.1) and the Run I protons. These tuples contain the needed quantities (presented below) in order to determine the L0Hadron efficiency tables.

Year	L0Hadron E_T	L0Hadron SPD
2011	$E_T > 3.6\,\text{GeV}$	$nSPDhits < 600$
2012	$E_T > 3.5 - 3.74\text{GeV}$	$nSPDhits < 600$
2015	$E_T > 3.1 - 3.6\text{GeV}$	$nSPDhits < 450$
2016	$E_T > 3.22 - 3.89\text{GeV}$	$nSPDhits < 450$
2017	$E_T > 2.98 - 3.89\text{GeV}$	$nSPDhits < 450$
2018	$E_T > 3.79\,\text{GeV}$	$nSPDhits < 450$

Table 2.11: Summary of the L0Hadron trigger thresholds used for Run I and Run II, for several years various TCK's are used and the E_T threshold can change among years, in these cases the ranges of the thresholds are displayed.

Needed observables

To produce the efficiency table as a function of the real transverse energy, which are part of the L0Hadron correction process, for each calibration tuples and HCAL region (Inner or Outer), it is needed to know for each event:

- its TIS or TOS category. In this work, a TIS (Trigger Independent of Signal) event is an event triggered by the L0 Muon component of the L0 trigger (which corresponds to the detection of a muon candidate with enough transverse momentum in the muon chambers). A TOS (Trigger On Signal) event is an event triggered simultaneously by the L0Muon and the L0Hadron components.
- the E_T^{real} attached to the particle of interest,
- the positions of the cluster (x, y) attached to the particle of interest.

Together, these informations allow one to build for each E_T^{real} bin (to be built) the efficiency of the L0Hadron trigger by taking the ratio of the TOS over TIS events.

Effects to consider

As in any experimental quantity, some additional effects appear in the HCAL measurements and have an impact on the measurements. The undesirable effects to correct and the methods used to take them into account are explained in the following.

Background that populates the samples

As the method built to determine the L0Hadron trigger efficiency is data-driven, real data are used. Naturally, these real data of $D^{*+} \to D^0(K\pi)\pi^+$ for pions and kaons or $\Lambda^0 \to p\pi$ for protons contain signal as well as background (events wrongly identified as signal). To build as correct corrections as possible for each sample, it is needed to weight each event with respect to his probability to come from signal or background in order to statistically subtract the background in the samples. The weights are made using the *sPlot* method [149]. The *sPlot* method consists of consecutive fits of each component of the sample (signal and background) on a given quantity in order to determine the yields associated to each of them and build a sWeight (weight of interest).

For the π and K samples, the quantity on which the *sPlot* is performed is the D^0 invariant mass. The model used to fit the signal is a double Gaussian [150] model centered on the D^0 mass given by the PDG [47] and the one use to fit the background component is a first-order Chebychev [151] polynomial. For protons samples, the quantity on which the *sPlot* is performed is the Λ^0 invariant mass. The model used to fit the signal is a double Crystal Ball model [152] centered on the Λ^0 mass given by the PDG and the one used to fit the background component is a first-order Chebychev polynomial [151].

Distances between tracks

Whether concerning the protons samples or the pions/kaons ones, irregularities in the measured efficiency have been observed when the projections on the HCAL of the two tracks originating from the same particle decay (π-K for $D^{*+} \to D^0(K\pi)\pi^+$ and p-π for $\Lambda^0 \to p\pi$) are too close. This is explained by the overlap of the two clusters in the HCAL which increases the energy measured by the trigger. It has been decided to consider only events where the distance between the projection on the HCAL of these tracks is at least equal to 1000 mm.

Distances between signal tracks

It is possible to have an overlap between the cluster of the L0Hadron main candidate and the one due to another track. In this case the energy due to the signal track is modified by the presence of this second track. It is important to consider this effect: for that, the energy profile of the shower in the HCAL is taken from a particle gun simulation [153] and the energy distribution as a function of the distance between the tracks are built, in the Inner and Outer areas of the HCAL. The distributions are fitted by a two Gaussian function and the fraction, of the energy coming from a particle of transverse energy E_T impacting HCAL at (x_0, y_0) overlapping in a

2×2 cluster of cell size c centered on (x, y) is found to be:

$$f_{overlap}(E_T, x, x_0, y, y_0) = \frac{E_T}{4}\alpha \left[\left[\text{erf}\left(\frac{x - x_0 + c}{\sqrt{2}\sigma_1}\right) + \text{erf}\left(\frac{-x + x_0 + c}{\sqrt{2}\sigma_1}\right) \right] \left[\text{erf}\left(\frac{y - y_0 + c}{\sqrt{2}\sigma_1}\right) + \text{erf}\left(\frac{-y + y_0 + c}{\sqrt{2}\sigma_1}\right) \right] \right] + \frac{E_T}{4}(1 - \alpha) \left[\left[\text{erf}\left(\frac{x - x_0 + c}{\sqrt{2}\sigma_2}\right) + \text{erf}\left(\frac{-x + x_0 + c}{\sqrt{2}\sigma_2}\right) \right] \left[\text{erf}\left(\frac{y - y_0 + c}{\sqrt{2}\sigma_2}\right) + \text{erf}\left(\frac{-y + y_0 + c}{\sqrt{2}\sigma_2}\right) \right] \right], \quad (2.4.4)$$

where σ_1 and σ_2 are the widths of the two Gaussian functions, c is the cell size and α is the fraction of the first Gaussian function in the fit, all given by table 2.12.

Parameter	Inner	Outer
c	131 mm	262 mm
α	0.76	0.79
σ_1	64 mm	100 mm
σ_2	202 mm	240 mm

Table 2.12: Fit results to determine the distance between signal tracks corrective fraction.

Fraction of tracks that do not reach the HCAL

In the data, not all tracks reach the HCAL surface; the fraction of signal tracks without energy deposits must be determined. The distribution of these tracks are given in term of E_T, this distribution follow an exponential decreasing law, which one is determined by fitting the distribution in Inner and Outer region with:

$$f_{empty}(E_T) = Ae^{-BE_T}, \quad (2.4.5)$$

where A and B are the parameters of the law. The fit performed in each region gives the results [153] in table 2.13.

Parameter	Inner	Outer
A	0.08	0.23
B	6.5×10^{-4} MeV^{-1}	7.4×10^{-4} MeV^{-1}

Table 2.13: Fit results for fraction of tracks that not reach the HCAL

Occupancy effect

There is an underlying energy generated by the event multiplicity in the HCAL cells. It is needed to subtract it from the E_T of the L0Hadron candidates. The underlying energy maps determination for each HCAL region, data-taking period, and magnet polarity will be explained in the next section. With these maps, the E_T measured for a given L0Hadron candidate in a given cell can be corrected from the underlying energy of the cell multiplied by 4 due to the fact that a 2×2 cluster corresponds to each candidate.

HCAL cells miscalibration

The HCAL could suffer from small miscalibration among cells. To address this effect, a sequential fit of the L0Hadron trigger efficiency as a function of E_T is performed to build HCAL calibration maps. This procedure is presented in Section 2.4.4.

2015 specificity

Before diving into the correction determination, a comment is in order on the 2015 datasets. During the 2015 operation, a threshold was incorrectly applied in the calorimeter electronic. This feature was reproduced in subsequent dedicated simulations, but no valid L0Hadron variables are available from the calibration samples. It has therefore been chosen to apply to 2015 simulation samples the correction tables from 2016 corrections. Consequently, 2015 L0Hadron correction table are not provided in the following.

2.4.2 Underlying energy maps determination

Run II

As explained previously, the average occupancy (mean underlying energy) of the HCAL must be considered. The average occupancy map is therefore derived for each data taking period, magnet polarity and HCAL region (inner or outer).

In order to determine these maps, real data are used. For the Run II, FullTurbo datasets, recorded with a closed VELO are taken from the LHCb bookkeeping for each data taking period and polarity. In LHCb Run II, Turbo means tuples reconstructed via online trigger reconstruction. This method to build calibration tuples was not available in Run I.

The average underlying energy maps are determined on these datasets using D^0 L0Muon TIS events in the HLT2 line Hlt2PIDD02KPiTagTurboCalib [154] which selects $D^0 \to K\pi$ events from $D^{*+} \to D^0\pi^+$ processes. The common way to select $D^{*+} \to D^0\pi^+$ events is to use a narrow window of $m_{D^{*+}} - m_{D^0}$ as the distribution peaks around 145 MeV. Unfortunately, the mass difference $m_{D^{*+}} - m_{D^0}$ was not available in 2016 turbo tuples.

To use the best of the available information for each period, it has been decided to place a $m_{D^{*+}} - m_{D^0}$ cut on 2017 and 2018 and to determine a $m_{D^{*+}}$ cut that yields equivalent purity (and determined on 2017 and 2018) on 2016 data samples. The signal-to-noise ratio S/B is used as a figure of merit to optimise the cuts. The distribution of m_{D^0} is fitted with a two-Gaussian [150] model for the signal and a first-order Chebychev [151] polynomial for the background.

The $m_{D^{*+}} - m_{D^0}$ cut has been set to $(m_{D^{*+}} - m_{D^0} > 143\,\text{MeV})\&(m_{D^{*+}} - m_{D^0} < 147\,\text{MeV})$, leading to $S/B \sim 13$ in the $[1800, 1920]$MeV m_{D^0} window for the 2018 MU, 2018 MD, 2017 MU, and 2017 MD samples. A $m_{D^{*+}}$ cut to $(m_{D^{*+}} > 1985\,\text{MeV})\&(m_{D^{*+}} < 2035\,\text{MeV})$ leads to $S/B \sim 20$, which satisfies the above-line requirements. This cut is therefore used for the 2016 samples.

The cuts applied to select D^0 L0Muon TIS candidates are summarised in table 2.14. The selected events are stored in ROOT [155] files with a TTree that contains energy deposits and their positions recorded by the HCAL. These operations are carried out on the GRID through Ganga [156] jobs. In order to conserve a good balance between statistics and processing time, 100 files of each dataset are used, to determine the average underlying energy maps.

From the output ROOT files, 2D histograms of energy recorded in Inner and Outer HCAL as function of the cell are filled; these histograms correspond therefore to the total occupancy in the HCAL. The average occupancy maps are obtained by normalising the histogram entries to the total number of events. All those distributions are equivalent for all years and polarities

$D^* \to D^0\pi$	Hlt2PIDD02KPiTagTurboCalib
π	$p_T > 100\,\text{MeV/c}$, $p > 1000\,\text{MeV/c}$, $\chi^2_{track}/ndf < 3$
$D^0\pi$	$\lvert m(D^0) - m(D^*) + 82.5\,\text{MeV/c}^2\rvert < 82.5\,\text{MeV/c}^2$
D^*	$\chi^2_{vertex}/ndf < 15$, $\lvert m(D^0) - m(D^*) + 77.5\,\text{MeV/c}^2\rvert < 77.5\,\text{MeV/c}^2$
$D^0 \to K\pi$	Hlt2/Hlt2CharmHadPIDD02KPiMassFilter
K, π	$\chi^2_{IP} > 16$, $p_T > 250\,\text{MeV/c}$, $p > 2000\,\text{MeV/c}$, $\chi^2_{track}/ndf < 3$
$K\pi$	$max(K_{p_T}, \pi_{p_T}) > 1000\,\text{MeV/c}$, $DOCA(K,\pi) < 0.1\,\text{mm}$,$p_T > 1500\,\text{MeV/c}$, $\lvert m - 1865\,\text{MeV/c}^2\rvert < 75\,\text{MeV/c}^2$
D^0	$\chi^2_{IP} < 20$, $\chi^2_{VS} > 49$, $DIRA_{PV} > 0.9999$, $\chi^2_{vertex}/ndf < 10$, $\lvert m - 1865\,\text{MeV/c}^2\rvert < 75\,\text{MeV/c}^2$
Trigger	$L0MuonDecision = True$
17-18 specific	$m_{D^*} - m_{D^0} > 143\,\text{MeV/c}^2$, $m_{D^*} - m_{D^0} < 147\,\text{MeV}$
16 specific	$m_{D^*} > 1985\,\text{MeV/c}^2$, $m_{D^*} < 2035\,\text{MeV/c}^2$

Table 2.14: Summary of the cuts applied to produce the average underlying energy maps.

and only the maps in 2018 are shown. For completeness, the occupancy figures for other years are presented in Appendix B.1.

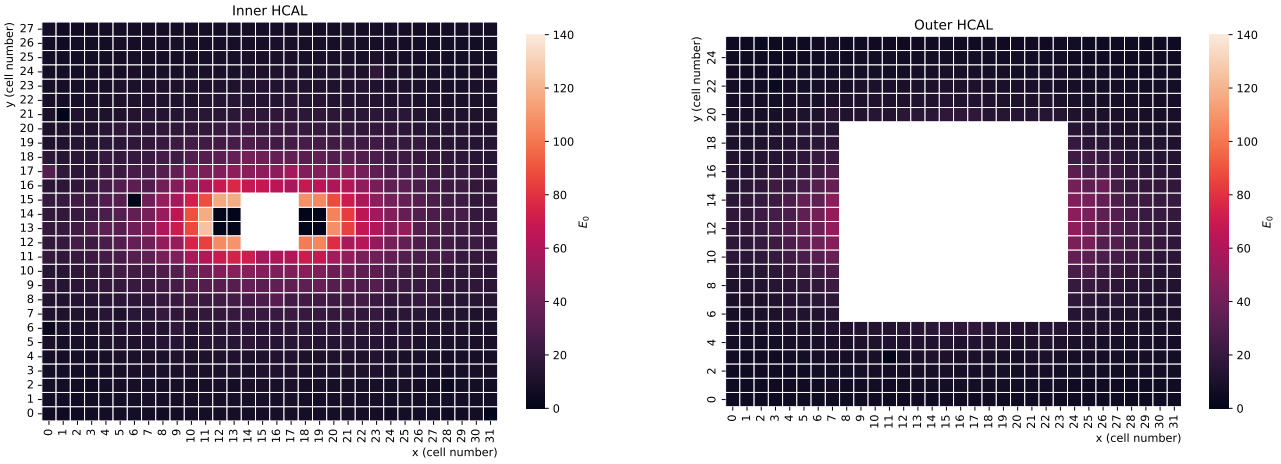

Figure 2.20: Average occupancy maps in MeV/event, for 2018 MD data with a reconstructed $D^* \to D^0\pi$ candidate.

Run I

Run II underlying energy maps are used to derive Run I Underlying Energy maps. From Run I to Run II, several parameters have changed concerning the pp collisions at the LHC including the center of mass energy, the number of interactions per crossing, the size of the bunches, ... To consider them, a good approximation of the HCAL occupancy effect, available in the LHCb analysis, to compare Run I and Run II comes from the average number of SPD hits, nSPDhits.

The goal is to compute a multiplicative factor built onto the aforementioned quantity to scale the Run II underlying energy maps to be used for Run I. A priori, any data samples stripped for an LHCb analysis could be taken as references. The stripped samples produced for the $B^0_{d,s} \to K^0_S h^+ h'^-$ analysis (see Chapter 3). The weight factor is defined as:

$$f = \frac{< \text{nSPDhit} >_{\text{Run I}}}{< \text{nSPDhit} >_{\text{Run II}}}. \tag{2.4.6}$$

The calculations are done individually, for each combinations of Run I/Run II data taking periods, $h^{(\prime)}$ species ($\pi^{\pm}$ or $K^{\pm}$), K^0_S reconstruction type (LL and DD), and polarity (MU and MD). Expectedly, it has been found that the choice of the Run II period, the decay configurations, and the magnet polarity used plays a minor role. In contrast, the choice of the Run I data-taking period has an impact. Beyond the energy increase from 2011 to 2012, the experimental conditions have also changed; in particular, the average μ recorded by LHCb[7] is higher in 2012 than in 2011 (the one for the data recorded during Run II is stable).

Regarding the previous observation, the factors have been built with 2018 as Run II reference and with the $B^0 \to K^0_S\pi^+\pi^-$ decay mode. Finally, the factors to build the Run I underlying energy maps from 2018 ones are found to be:

$$f_{11} = 0.925;\ f_{12} = 0.955; \tag{2.4.7}$$

where the index denotes the year of the Run I. The Underlying Energy maps for the Run I are obtained with the operation

$$E_{0,x,y} = f_y \times E_{0,x,2018}, \tag{2.4.8}$$

where $E_{0,x,y}$ denotes the Underlying Energy maps of HCAL region x and period y, f_y denotes the multiplicative factor determined for the y period to apply on each bin of the 2018 map.

The 2012 MD Underlying Energy maps are given in Figure 2.21, other maps are given in Appendix B.1.

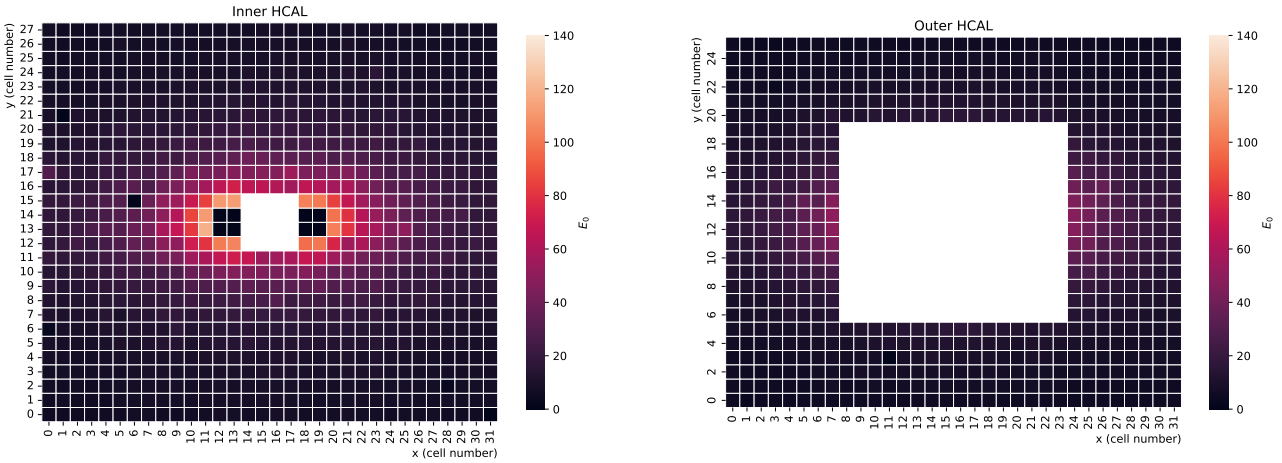

Figure 2.21: Average occupancy maps in MeV/event, build for 2012 MD.

2.4.3 $\pi^{\pm}$ and $K^{\pm}$ efficiency tables determination

Tuples creation

In order to determine the efficiency tables, sWeighted PIDCalibration data samples are used. The decay $D^{*+} \to D^0(K\pi)\pi^+$ is considered to gather pure samples of charged pion and kaon candidates. Tuples have been built by the LHCb physics performance team for each data-taking period and polarity.

The histogram of the number of particles in bins of the HCAL energy deposits is filled, splitted as a function of the HCAL region (inner and outer) and track trigger condition (TIS or TOS). Therefore, four weighted 3D histograms are obtained per particle species. The TIS selection corresponds to the L0Muon decision, less than 450 (600) hits recorded in the SPD for

[7]available at https://lbgroups.cern.ch/online/OperationsPlots/index_files/

Run II (Run I) and a separation at the entrance of the calorimeter higher than 1000 mm with respect to the other particle coming from the considered decay (which means K from D^0 for π, π from D^0 for K). The TOS selection adds a requirement on the L0Hadron decision related to the considered particle. Finally, the energy deposited by the particle is corrected by the average underlying energy previously defined.

To account for the 4-cells size of the HCAL cluster, the transverse energy deposit of the particle is replaced via the equation 2.4.9:

$$E_T = E_T + 4E_0, \tag{2.4.9}$$

where the recorded transverse E_T in the cell and the corresponding average underlying energy E_0 are used to compute the E_T to consider. Each event is then weighted with respect to its sWeight.

Tables determination

From the aforementioned histograms, efficiency tables as a function of the real transverse energy for π and K in both inner and outer HCAL regions are built by integrating the TIS (TOS) histograms over the HCAL cells to obtain 1D histograms of the number of TIS (TOS) events as a function of the transverse energy. The L0Hadron TOS efficiency table per bin of E_T is obtained following:

$$\varepsilon_k = \frac{n_{\mathrm{TOS},k}}{n_{\mathrm{TIS},k}}, \tag{2.4.10}$$

where ε_k denotes the efficiency in an E_T bin, $n_{\mathrm{TOS},k}$ the corresponding number of TOS events in this bin and $n_{\mathrm{TIS},k}$ the corresponding number of TIS events in the same bin.

The statistical error attached to these efficiencies is estimated by taking for each bin the maximum uncertainty given by Clopper-Pearson intervals (lower and upper) based on Beta distribution with a coverage of 1σ as this estimate is conservative and applicable in low statistic bins. In case of a wrong calculation in a bin (for example, if the bin is empty), the uncertainty is set to 100 %, which concerns a small fraction of the bins (mostly very high or low transverse energy bins) .

Since the histograms are weighted with respect to to the sWeight of each event, equation 2.4.10 might lead to a non-physical efficiency (e.g. negative value, empty bin or value above 1). A post-processing is applied to define valid values everywhere. The problematic efficiency is set to 0 or 1 depending on the issue (sign/bin). This post-processing concerns very high or low transverse energy bins, and, more specifically, few percents of the bins in Run II and up to 20% in Run I.

The 2018 and 2012 MD efficiency tables and their attached uncertainties are displayed, for K and π particles, in Figures 2.22 and 2.23. Other tables are provided in Appendix B.2.

2.4.4 Calibration maps determination

Calibration maps are needed to correct the miscalibration between the HCAL cells, what consists in providing a single calibration factor per HCAL cell. The $\pi^{\pm}$ and $K^{\pm}$ efficiency tables determined show that statistical uncertainties become important at very low and high transverse energy. To determine the calibration maps, only the efficiencies corresponding to transverse energies in the [200,6000] MeV range are considered, as it is the range with the largest accuracy. The efficiency is modelled by:

$$\epsilon(E_T) = \left(1 - Ae^{-BE_T}\right)\left[\frac{1}{2} - \frac{1}{2}\,\mathrm{erf}\frac{T/\beta - E_T}{\sigma\sqrt{2E_T}}\right], \tag{2.4.11}$$

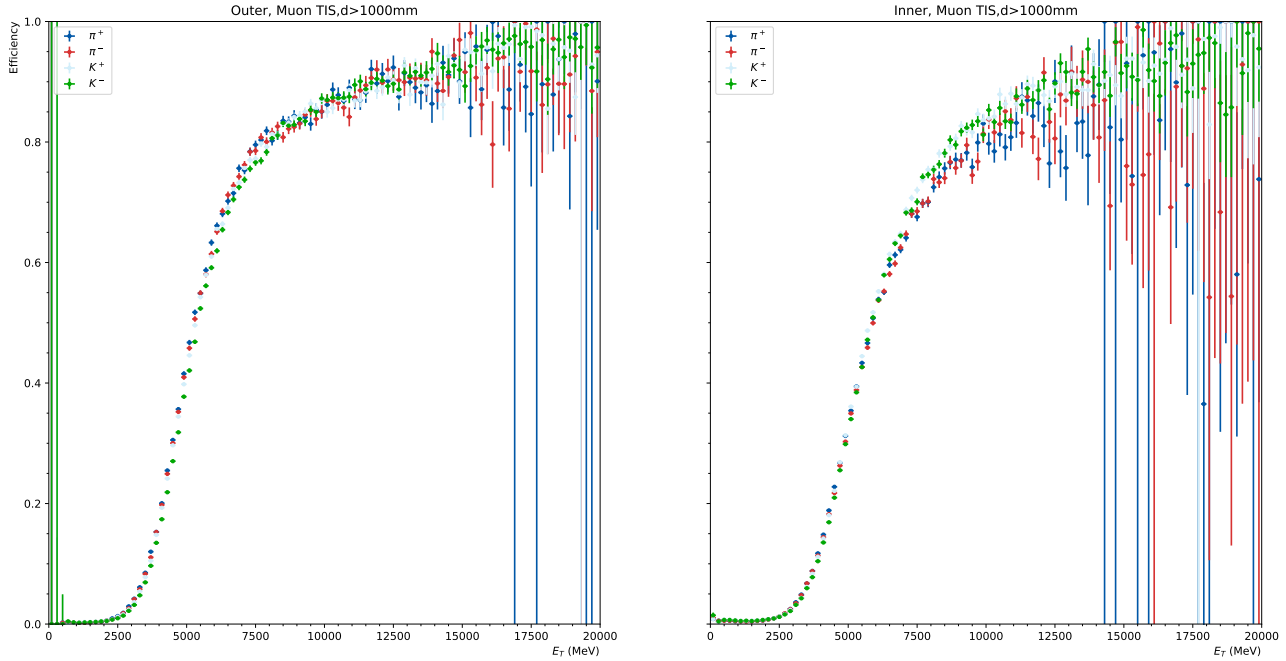

Figure 2.22: Efficiency tables for π and K as obtained with the 2018 MD sample.

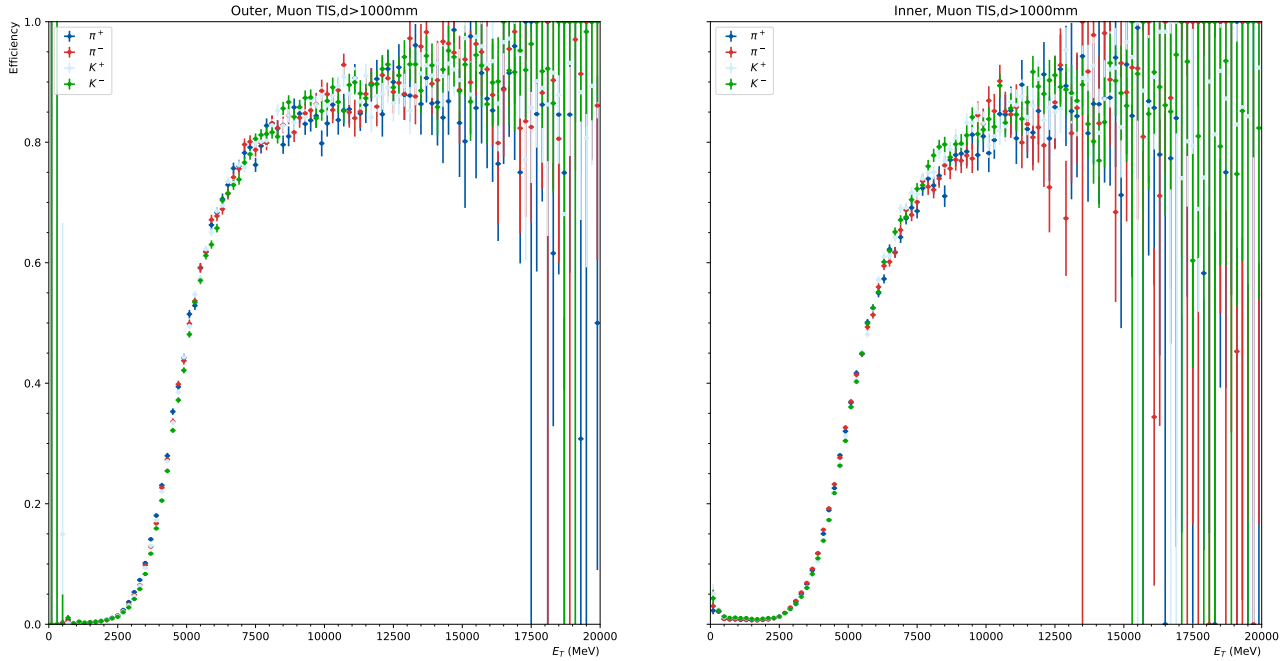

Figure 2.23: Efficiency tables for π and K as obtained with the 2012 MD sample.

where A and B are taken from the fit defined in section 2.4.1 depending on the area of the HCAL considered, T is a threshold in energy fixed at 3850 MeV, E_T is the transverse energy corrected by the occupancy as defined previously, σ is the resolution on the transverse energy. The fitted parameters are β and σ.

A simultaneous (all cells together) fit of the model of equation 2.4.11 to the efficiency template is performed for each year, polarity, and HCAL region. This average efficiency model is then further used as input to the calibration fit per cell.

An updated model for each particle is then established to define a per-cell correction factor

b:

$$\epsilon(E_T) = \left(1 - Ae^{-BE_T}\right)\left[\frac{1}{2} - \frac{1}{2}\,\mathrm{erf}\,\frac{T/(\beta \times b) - E_T}{\sigma\sqrt{2E_T}}\right], \tag{2.4.12}$$

where A, B, T designate the same quantities as in equation 2.4.11, β and σ are taken for each particles from the previous fit and b is the parameter to measure.

The models defined in equation 2.4.12 are used to perform a fit to the efficiency measured in individual HCAL cells to determine for each of them a per-cell corrective factor. This factor is then applied to the previously determined β for each type of particle. Finally, the calibration maps are the maps of the b parameter fitted in each cell (inner and outer region).

It has been noticed that in some cells, the b fit was not converging. This effect is mitigated by taking as the value the average of the fitted b obtained in the converging neighbouring cells. In addition, the low statistics of the Run I samples created areas in which several values were not defined. This effect is mitigated by merging the two magnet polarity samples.

The calibration maps for 2018 and 2012 MD are shown in Figures 2.24 and 2.25. The others are provided in Appendix B.3.

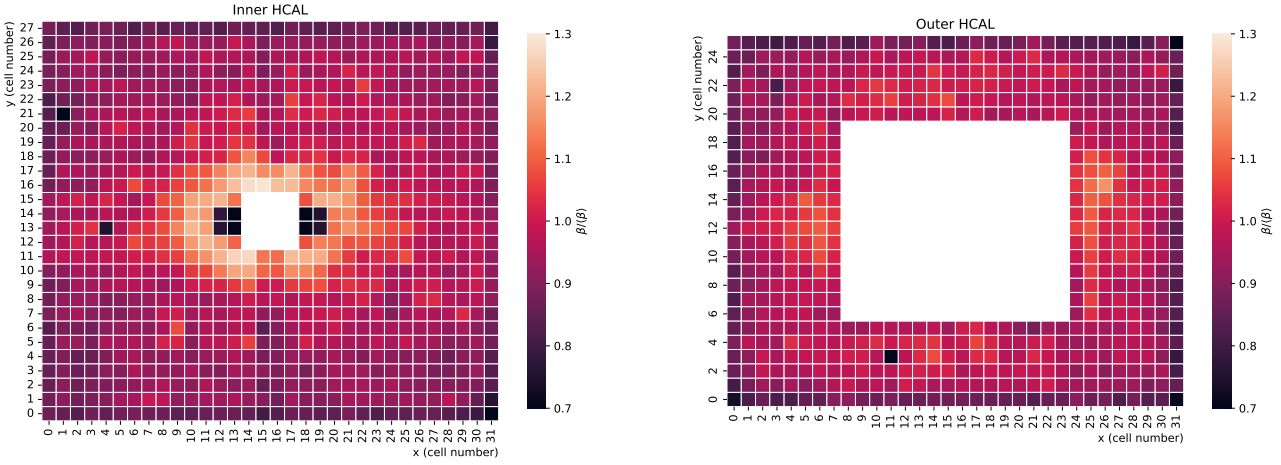

Figure 2.24: HCAL cell-by-cell calibration maps obtained for the 2018 MD sample.

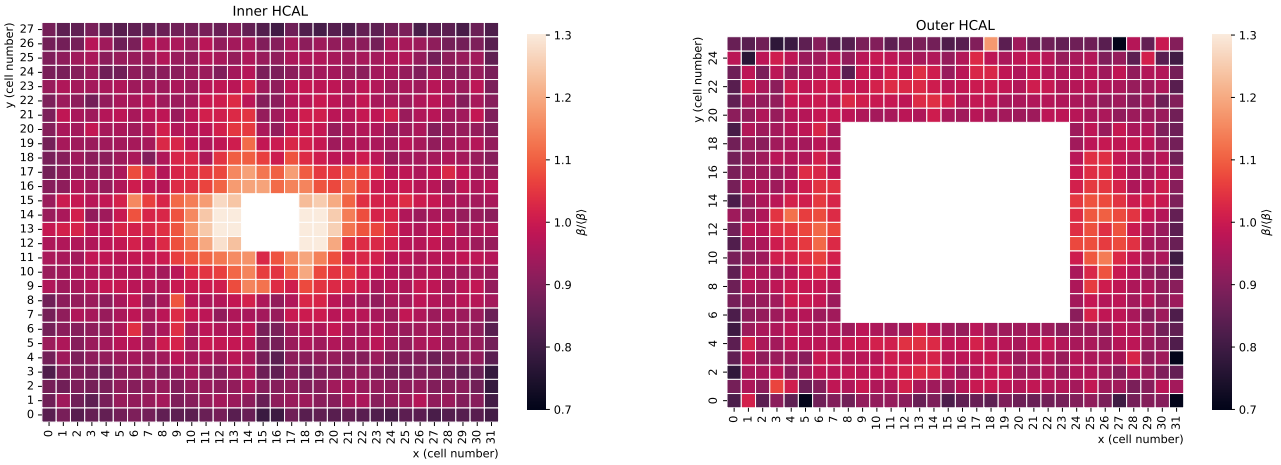

Figure 2.25: HCAL cell-by-cell calibration maps obtained for the 2012 MD sample.

2.4.5 L0Hadron proton efficiency tables determination

Run II tuples creation

In order to determine the L0Hadron proton efficiency tables for the Run II, sWeighted (via $\Lambda^0 \to p\pi$) PID data calibration samples are used. Tuples have been build similarly to what was done for π and K.

The histogram of the number of particles in bins of the HCAL energy deposits is filled, splitted by HCAL region (inner and outer) and track trigger condition (TIS or TOS). Therefore, four weighted 3D histograms are obtained per proton charge (p or $\bar{p}$). The TIS selection corresponds to a fired L0Muon decision, less than 450 hits recorded in the SPD (to avoid large multiplicity events and be consistent with the Global Event Cuts) and a separation greater than 1000 mm with respect to the π coming from Λ^0. The TOS selection adds a fired L0Hadron decision linked to the considered particle. Finally, the energy deposit by the proton is corrected from the miscalibration effects as well as from the average underlying energy effects.

Due to the average size of the cluster in the HCAL of 4 cells and the calibration factor, the energy deposit of the particle is replaced via equation 2.4.13:

$$E_T = b.E_T + 4E_0, \tag{2.4.13}$$

where the recorded transverse E_T in the cell, the corresponding calibration factor b and the corresponding average underlying energy E_0 are used to compute the corrected E_T to consider. Each event is weighted with respect to to its sWeight.

Run II tables determination

From the aforementioned histograms, efficiency tables as function of the real transverse energy for p and $\bar{p}$ in both the inner and outer HCAL regions are computed by integrating the TIS and TOS histograms over the HCAL cells to obtain 1D histograms of the TIS and TOS number of events as function of the transverse energy. The Run II efficiency tables are then built following the very same method as what is done for $\pi^\pm$ and $K^\pm$ (see Section 2.4.3).

The efficiency tables built and the attached uncertainties for protons are displayed together with π and K for 2018 MD in Figures 2.26. Others are provided in Appendix B.4.

Run I tables estimates

There are currently no available proton tuples for Run I, therefore, no efficiency table is derived with the current method for Run I protons. A workaround has been developed.

The idea of the method is to perform an estimate of the Run I protons efficiency tables from the observed hierarchy of the kaons efficiency tables between Run I and Run II, since the development of the calorimetric showers of kaons and anti-kaons ($m_{K^\pm} = 493.7\,\text{MeV}$) follows a similar physics of quark annihilation cross-section as protons and antiprotons($|\bar{u}s\rangle \sim |\bar{u}\bar{u}d\rangle$ and $|u\bar{s}\rangle \sim |uu\bar{d}\rangle$ from quark annihilation point of view). The estimate is made by assuming that a similar Run I/Run II hierarchy is expected between the kaon and the proton efficiency tables. Concretely, the method is based on the determination of corrective factors Run I/Run II from the kaon tables, which are then applied to the Run II proton tables to build the Run I proton tables. The method is used to produce different protons tables for 2011 and 2012, for MU and MD polarities, for p and $\bar{p}$ (using respectively K^+ and K^- following the charge of the particle) and for the inner and outer HCAL regions. The guesstimation method is detailed in Appendix B.5.

The efficiency tables built and the attached uncertainties for protons are displayed together with π and K for 2012 MD in Figures 2.27. Others are provided in Appendix B.4.

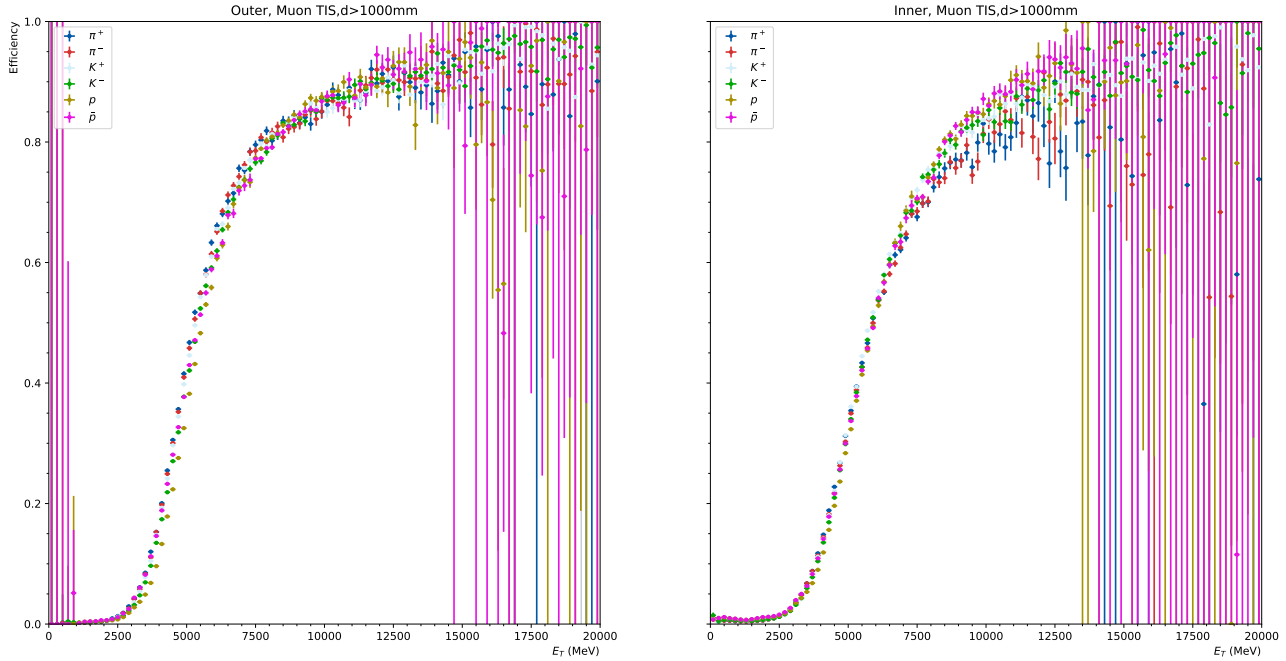

Figure 2.26: Efficiency tables for π,K and p build for 2018 MD.

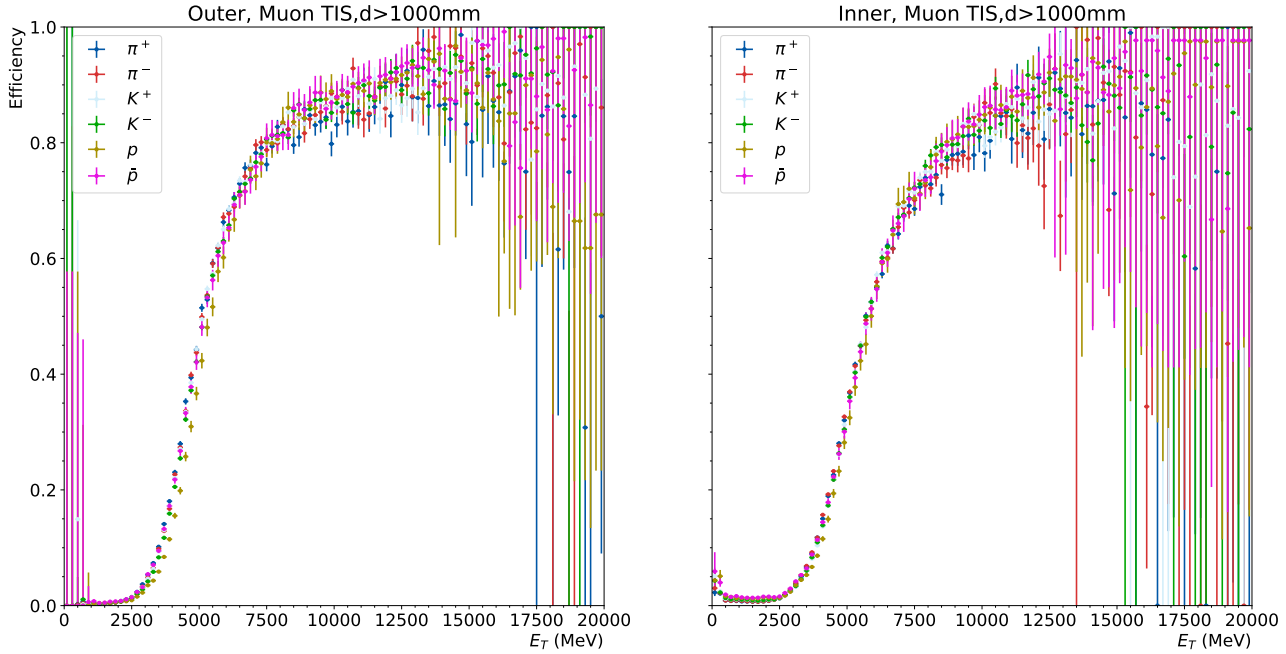

Figure 2.27: Efficiency tables for π,K and p build for 2012 MD.

In addition, a comparison of the new and previous (obtained with a less educated method) Run I efficiency tables has been done and has shown that the tables determined here fixed the majority of the previous tables issues. For example, the rise of the efficiency is better described now, the E_T range of the tables has been increased, and the proton tables behave now reasonably. The details of this comparison are provided in Appendix B.6.

2.4.6 Another maps for users: $b\bar{b}$ underlaying energy maps

At the user level, the average underlying energy maps, as well as the calibration maps and the efficiency tables, will have to be used to correct the L0Hadron effect onto MC samples. The average underlying energy maps constructed in Section 2.4.2 correspond to $c\bar{c}$ events, since charm calibration data were used and are made available. Analysts aiming at b-flavoured events can, however, use advantageously average underlying energy maps determined with $b\bar{b}$ events instead of $c\bar{c}$ events to correct for the average occupancy.

For Run II, to determine these $b\bar{b}$ average underlying energy maps, thedata used are the same as those of Section 2.4.2 but with different Turbo lines and cuts. Practically, $\Lambda_b^0 \to \Lambda_c\pi$ L0Muon TIS events are taken via the HLT2 line Hlt2PIDLb2LcPiTurboCalib [154]. This line is only available for 2016 tuples. The stability of the running conditions allows to use this map for the other data-taking periods. The cuts applied to select $\Lambda_b^0 \to \Lambda_c\pi$ L0Muon TIS events are summarised in Table 2.15.

$\Lambda_b^0 \to \Lambda_c\pi$	Hlt2PIDLb2LcPiTurboCalib
π	$\chi^2_{IP} > 25$, $DLL_{K\pi} < -5$, $p_T > 500\,\text{MeV/c}$, $p > 3000\,\text{MeV/c}$, $\chi^2_{track}/ndf < 3$
$\Lambda_c\pi$	$p_T(\Lambda_c) + p_T(\pi) > 3000\,\text{MeV}$, $\lvert m - 5620\,\text{MeV/c}^2\rvert < 350\,\text{MeV/c}^2$
Λ_b^0	$\chi^2_{IP} < 10$, $\chi^2_{VS} > 100$, $DIRA_{PV} > 0.9999$, $\chi^2_{vertex}/ndf < 25$, $\lvert m - 5620\,\text{MeV/c}^2\rvert < 300\,\text{MeV/c}^2$
$D^0 \to K\pi$	Hlt2/Hlt2PIDLc2KPPiVetoFilter
K	$\chi^2_{IP} > 9$, $DLL_{K\pi} > 5$, $p_T > 400\,\text{MeV/c}$, $p > 1000\,\text{MeV/c}$, $GhostProb < 1$, $\chi^2_{track}/ndf < 3$, $HasRich$
p	$\chi^2_{IP} > 6$, $p_T > 1000\,\text{MeV/c}$, $p > 1000\,\text{MeV/c}$, $GhostProb < 1$, $\chi^2_{track}/ndf < 3$
π	$\chi^2_{IP} > 9$, $DLL_{K\pi} < -5$, $p_T > 400\,\text{MeV/c}$, $p > 1000\,\text{MeV/c}$, $GhostProb < 1$, $\chi^2_{track}/ndf < 3$, $HasRich$
$Kp\pi$	$p_T(K) + p_T(p) + p_T(\pi) > 2000\,\text{MeV/c}$, $NumChildren(\chi^2_{IP} > 12) \geq 2$, $NumChildren(\chi^2_{IP} > 16) \geq 1$, $NumChildren(p_T > 400\,\text{MeV}/c) \geq 1$, $NumChildren(p_T > 400\,\text{MeV}/c) \geq 2$, $\lvert m - 2286.5\,\text{MeV/c}^2\rvert < 85\,\text{MeV/c}^2$
Λ_c	$\chi^2_{VS} > 50$, $\tau > 0.0001\,\text{ns}$, $DIRA_{PV} > 0$, $\chi^2_{vertex}/ndf < 10$, $m(K \to K, p \to \pi, \pi \to \pi) > 1735\,\text{MeV/c}^2$, $\lvert m - 2286.5\,\text{MeV/c}^2\rvert < 75\,\text{MeV/c}^2$, $\lvert m(K \to K, p \to K, \pi \to \pi) - 1968\,\text{MeV/c}^2\rvert > 20\,\text{MeV/c}^2$, $\lvert m(K \to K, p \to \pi, \pi \to \pi) - 1870\,\text{MeV/c}^2\rvert > 20\,\text{MeV/c}^2$
Trigger	$L0MuonDecision = True$
Additional cuts	$m_{\Lambda_b^0} < 5700\,\text{MeV/c}^2, m_{\Lambda_c} > 2265\,\text{MeV/c}^2, m_{\Lambda_c} < 2305\,\text{MeV/c}^2$

Table 2.15: Summary of the cuts applied to produce the $b\bar{b}$ average underlying energy maps.

The Run II $b\bar{b}$ underlaying energy maps are built similarly to what has been done for the $c\bar{c}$ ones in Section 2.4.2. For Run I, the same method as the one described in Section 2.4.2 is used by taking Run II maps corrected by the factors given in equation 2.4.7.

The $b\bar{b}$ average underlying energy maps corresponding to Run II and 2012 MD are shown in Figures 2.28 and 2.29. Other maps are provided in Appendix B.7.

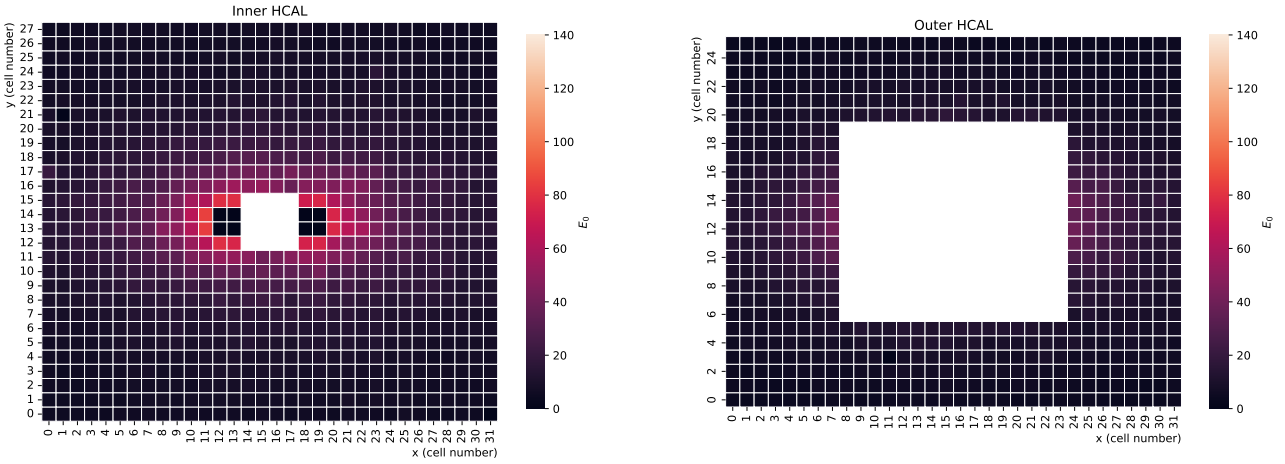

Figure 2.28: Average occupancy maps build for Run II MD from $b\bar{b}$ events.

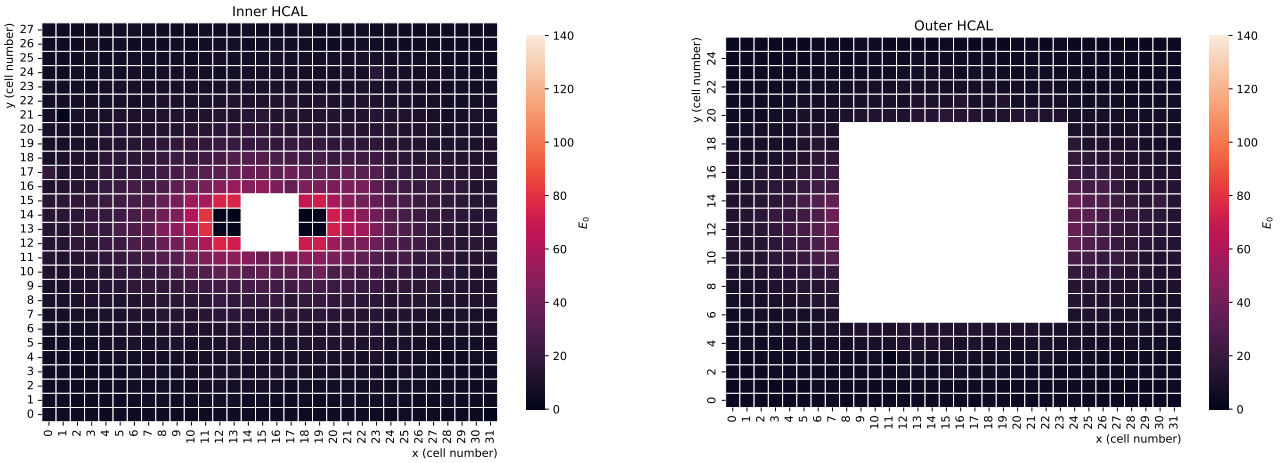

Figure 2.29: Average occupancy maps build for 2012 MD from $b\bar{b}$ events.

2.4.7 Conclusion of this work

The first goal of this work was to provide better Run I L0Hadron trigger corrections compared to what was done before; this has been done by the determination of the average occupancy maps, the calibration maps, and the efficiency tables for the Run I hadrons. The second goal was to update the Run II L0Hadron trigger correction due to slight changes in the method; this has been done.

Comparisons have shown that the new L0Hadron trigger correction behaves better than the previous ones (concerning what is comparable). Currently, the p efficiency tables for Run I are determined from a specific method using the K efficiency table and scaling them with factors computed from Run I and Run II tables, because of the unavailability of the correct p Run I calibration samples. Concerning the issue with 2015 data, the fact that no L0Hadron variables are in the calibration tuples imposes the use of 2016 inputs for the 2015 simulation in order to build the L0Hadron corrections.

Concerning the use of all the L0Hadron correction inputs to determine the L0Hadron correction factors to apply at the analysis level, a vademecum presenting the determination of those relative to the $B^0_{d,s} \to K^0_S h^+ h'^-$ analysis (see Chapter 3) is provided in Appendix C.3.

2.5 The FCC-*ee* project

2.5.1 Global description

The Future Circular Collider (FCC) [11, 157, 158] is a particle collider project, currently in the phase of Feasibility Study, hosted by CERN. This new machine is expected to take over from the High Luminosity LHC[8] [159] (HL-LHC) in the exploration of particle physics at the horizon of 2040. The collider project consists in two phases: an e^+e^- collider, with a center-of-mass energy span from 90 GeV to 360 GeV, crossing all the relevant electroweak thresholds, it shall be followed, using the same civil engineering infrastructure, by a pp collider at an energy in the center-of-mass at or above 100 TeV. The footprint of the machine wiggles between France and Switzerland and the most recent implementation features a ring of around 91 km of circumference (tunnels of 4 m of diameter) placed 300 m underground, as shown in Figure 2.30.

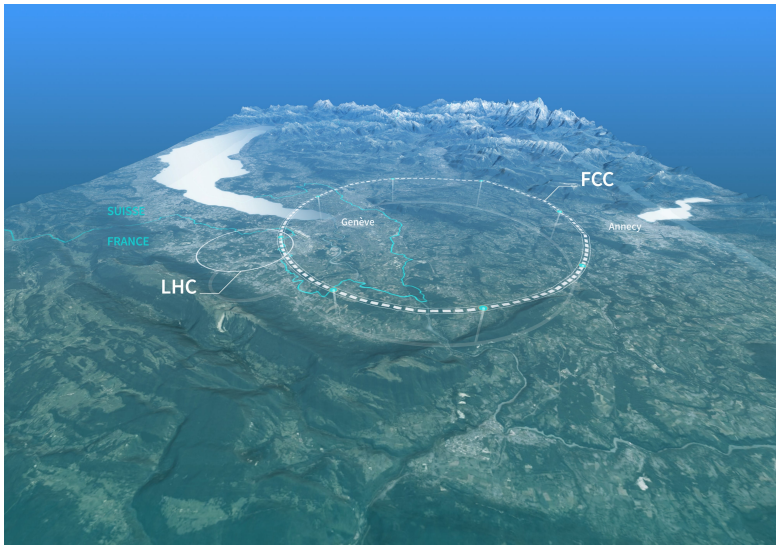

Figure 2.30: FCC footprint, 91km circular collider.

The LHC would serve as an injector for the FCC-pp, allowing to maximally benefit from the current CERN infrastructures. The FCC related work reported in this document focusses on the first phase of the FCC: FCC-*ee*.

The exquisite statistics which can be obtained at FCC-*ee* is displayed in the luminosity plot in Figure 2.31, where several e^+e^- collider projects performance are superimposed. The current baseline of the FCC-*ee* design comprises four interaction points. Figure 2.32 summarises the center-of-mass operation scheme. In particular, the Z pole running, of interest for the work reported in this thesis, will consist in four years of data taking and will gather 6×10^{12} Z (or Z^0) decays.

2.5.2 *b*-hadron production at FCC-*ee*

Compared to the LHC (see Section 2.2.1), the b-hadron production process at FCC-*ee* is simpler due to the use of elementary particle collisions. When running at the Z pole, FCC-*ee* will perform collisions at a center-of-mass energy around $m_Z = 90\,\text{GeV}$ to study Z decays. In that case, the large partial width of the Z boson into $b\bar{b}$ pairs [160], combined with the hadronisation

[8]The High Luminosity LHC (HL-LHC) is an upgrade for the LHC, planned to start for 2029, with five to ten times more luminosity comparing to the present. Specifically, the total amount of data recorded at LHCb with actual LHC and HL-LHC is expected to be around $50\,\text{fb}^{-1}$.

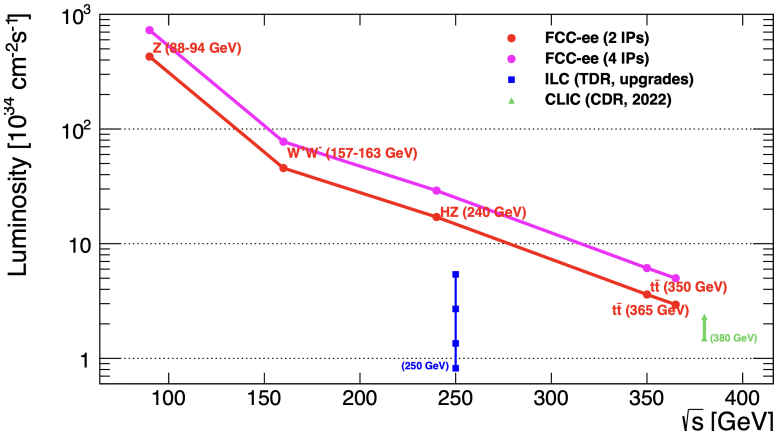

Figure 2.31: Comparison of e^+e^- collider luminosities.

Working point	Z, years 1-2	Z, later	WW, years 1-2	WW, later	ZH	$t\bar{t}$	
$\sqrt{s}$ (GeV)	88, 91, 94		157, 163		240	340–350	365
Lumi/IP (10^{34} cm^{-2}s^{-1})	70	140	10	20	5.0	0.75	1.20
Lumi/year (ab^{-1})	34	68	4.8	9.6	2.4	0.36	0.58
Run time (year)	2	2	2	0	3	1	4
Number of events	6 10^{12} Z		2.4 10^8 WW		1.45 10^6 HZ + 45k WW → H	1.9 10^6 $t\bar{t}$ +330k HZ +80k WW → H	

Figure 2.32: Operation scheme in the current FCC-*ee* baseline.

fraction corresponding to $b \to B^0$ in Z decays [161], provides about 740×10^9 B^0 mesons $(B^0 + \bar{B}^0)$. Figure 2.33 displays the main process at play in $e^+e^- \to b\bar{b}$.

FCC-*ee* combines the virtue of a clean experimental environment, due to e^+e^- collisions, and the presence of boosted b-hadrons, because $m_Z \gg m_b$. It gathers the advantageous attributes of the current flavour physics experiments, Belle II at SUPERKEB [162] and LHCb at CERN. The big cross-section obtained at LHC is to a certain extent mitigated by the exquisite luminosity expected at the Z pole.

2.5.3 The IDEA detector

Among the detector concepts at hand for FCC-*ee*, the IDEA concept [163–165] (Innovative Detector for Electron-positron Accelerators) is used in Chapter 5. This detector project comprises a high-granularity vertex detector with pixel read-out (as developed for the ALICE experiment [166]), an ultralight drift chamber (followed by an ultimate silicon layer), which complements the tracking system and potentially allows for hadron particle identification by ionisation cluster counting. A dual read-out calorimeter with two possible options, a longitudinal

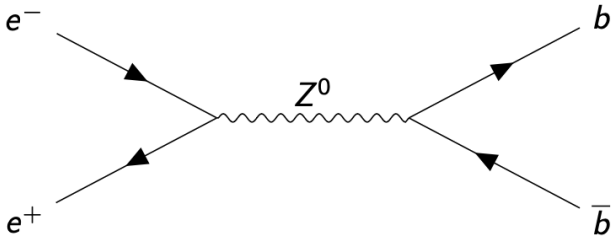

Figure 2.33: Feynman diagram for $b\bar{b}$ quark pair production from e^+e^- annihilation at Z pole.

unsegmented dual-readout fibre calorimeter (combining electromagnetic and hadronic calorimeters) or a dual-readout crystal (electromagnetic calorimeter) + dual-readout fibre calorimeter (hadronic calorimeter), completes the sub-detectors. An artistic view of this detector concept is shown in Figure 2.34.

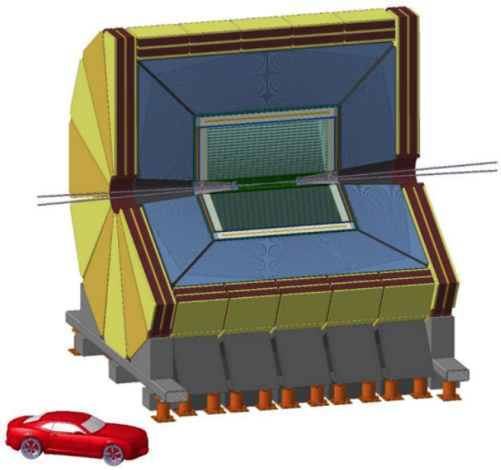

Figure 2.34: IDEA detector

The IDEA version used is limited to the tracking system. The purpose of Chapter 5 is to assess the vertex detector performance necessary to observe $B^0 \to K^{*0}\tau^+\tau^-$ at the SM value (see Section 5). The resolution on the decay vertex measurements will therefore be emulated (several performances are then tested) and compared to the actual IDEA working point (in its current design).

2.5.4 FCC-*ee* tools

The signal events used in the FCC related work done in this thesis are generated with Pythia [98] ($Z \to b\bar{b}$ and hadronisation) and EvtGen [133] (to force the decay of B mesons with adequate models – B2SLL for the B decay and Tauola for the subsequent three-prongs τ decays) through exclusive samples (signal events are $B^0 \to K^{*0}\tau^+\tau^-$ with the specific channel presented in Chapter 5). The reconstruction is performed with the FCCAnalyses software [167] using Delphes [168] simulation (featuring the IDEA detector) and the winter2023 production version. The simulated data use particles reconstructed with the momentum resolution given by the IDEA tracking system, *i.e.* the vertex detector complemented by the drift chamber. The decay files used to simulate the signal samples can be found on the winter2023 branch of the official FCC-config github project following the path FCCee/Generator/EvtGen/Bd2KstarTauTau.dec.

An analyzer (see [167]), which is a Python script based on the use of C++ dedicated classes for FCC-*ee* analyses (running within the FCCAnalyses software) has been run to make the analysis level tuples from high-level quantities build from the Pythia output. The analysis level tuples contain various information:

- MC-Truth kinematics of the particles (momentum, energy, decay vertex position),
- MC-truth PID-PDG index of the particles,
- MC-truth informationconcerning the genealogy of the events,
- MC-truth primary vertex of the events,
- reconstructed simulated kinematics of the final particles,

- association tags between MC-truth and reconstructed simulated particles.

The analysis of these tuples is mainly based on the Python computing language with Uproot [138] and Awkward Array [140] libraries.

Chapter 3

Search for the decay $B^0_s \to K^0_S K^+ K^-$

This chapter is dedicated to the branching fraction measurement of the $B^0_{d,s} \to K^0_S h^+ h'^-$ modes (with $h' = \pi^\pm, K^\pm$) with the Run I + Run II LHCb datasets, whose scientific motivation has been reported in Section 1.4. The goals of this analysis are first to specifically discover the $B^0_s \to K^0_S K^+ K^-$ decay mode and secondly to improve the measurement of the other decay modes. In order to factor out LHCb detector effects, the final observables of the analysis are the branching fractions relative to $B^0 \to K^0_S \pi^+ \pi^-$. All the work performed for this analysis will serve as a starting point toward amplitude analyses (with a preliminary analysis in Chapter 4). The details of the data samples, MC samples, trigger, stripping, and event reconstruction of the analysis have already been presented in Section 2.3.2. This chapter presents the remaining pieces of the analysis.

This branching fraction measurement analysis of the $B^0_{d,s} \to K^0_S h^+ h'^-$ modes is a long-term analysis at LHCb that implies LPCA (Clermont), LPNHE (Paris), and Warwick University (UK), since 2016. Due to this timescale, together with permanent researchers, several generations of Ph.D. students have contributed to this analysis, and the publication is scheduled for the end of 2024. Even if my contribution to this analysis mostly concerns efficiency determination and the related systematics, this chapter presents a summary of the whole analysis. All the details of the analysis are in a dedicated analysis note [169], a CERN internal document.

The key formula for this analysis is the branching fraction of the $B^0_{d,s} \to K^0_S h^+ h'^-$ modes relative to $B^0 \to K^0_S \pi^+ \pi^-$, which reads:

$$\frac{BF(B^0_{d,s} \to K^0_S h^+ h'^-)}{BF(B^0 \to K^0_S \pi^+ \pi^-)} = \frac{N_{B^0_{d,s} \to K^0_S h^+ h'^-}}{N_{B^0 \to K^0_S \pi^+ \pi^-}} \frac{\epsilon_{B^0 \to K^0_S \pi^+ \pi^-}}{\epsilon_{B^0_{d,s} \to K^0_S h^+ h'^-}} \frac{f_d}{f_{d,s}} \tag{3.0.1}$$

where $N_{B^0_{d,s} \to K^0_S h^+ h'^-}$ denotes the yield (number of events in data) of $N_{B^0_{d,s} \to K^0_S h^+ h'^-}$, $N_{B^0 \to K^0_S \pi^+ \pi^-}$ denotes the yield of $B^0 \to K^0_S \pi^+ \pi^-$, $\epsilon_{B^0_{d,s} \to K^0_S h^+ h'^-}$ denotes the efficiency of the selection developed for the analysis on $B^0_{d,s} \to K^0_S h^+ h'^-$, $\epsilon_{B^0 \to K^0_S \pi^+ \pi^-}$ denotes the efficiency of the selection developed for the analysis on $B^0 \to K^0_S \pi^+ \pi^-$ and $f_{d(s)}$ is the hadronisation fraction of $b \to B^0_{(s)}$. The yields are extracted from a mass fit to data, the efficiencies are determined from MC simulated signal samples, and the ratio of hadronisation fraction has to be introduced if the B mesons in numerator and denominator are different.

Starting from all the related material in the previous chapters, the first section presents the selection built for the analysis, the second section describes the efficiency determination, the third section presents the yields determination, the fourth section summarises the considered systematics and the fifth section presents the branching fraction determinations.

3.1 Selection and backgrounds

The trigger and stripping lines, discussed in Section 2.3.2, form the initial part of the selection. Further offline selections have been applied to reject the background events of the analysis. Five different types of background have been identified, the combinatorial background coming from random track combination, the partially reconstructed background for which a photon or pion is not reconstructed (*e.g.* $B^0 \to K^0_S\pi^+\pi^-\pi^0$), the crossfeeds backgrounds coming from misidentification of another $B^0_{d,s} \to K^0_S h^+h'^-$ mode (*e.g.* $B^0 \to K^0_S\pi^+K^-$ in $B^0 \to K^0_S\pi^+\pi^-$), Λ^0_b crossfeeds account for $\Lambda^0_b \to K^0_S ph$ decays where the proton is misidentified as a π or a K, and decays to the same final state $K^0_S h^+_1 h^-_2$ proceeding through an intermediate open-charm hadron or a charmonium state.

The total selection consists of a simple cut-based preselection (Section 3.1.1), followed by two multivariate selectors (named MVAs). The first MVA (Section 3.1.2) is designed to separate signal decays from the combinatorial background and uses kinematic and topological variables. The second MVA (Section 3.1.3) is designed to reject crossfeed backgrounds and uses PID variables. The use of MVAs is motivated by their ability to take advantage of the correlation between the discriminative variables to reject the background comparing to simple rectangular cuts. Finally, certain vetoes / additional cuts are applied to suppress charmed background / Λ^0_b crossfeed (Section 3.1.4).

There is no formal optimisation for the preselection and vetoes. For the two MVAs, a two-dimensional optimisation is performed (Section 3.1.5). It is worth noting here that the optimisation is done separately for each subsample × final state × signal peak. For example, 2018/LL/$K^0_S K^+K^-/B^0$ is optimised separately from 2018/DD/$K^0_S K^+K^-/B^0$ and from 2018/LL/$K^0_S K^+K^-/B^0_s$ (and of course also from 2018/LL/$K^0_S\pi^+\pi^-/B^0$). In most cases, this is obvious, since signal yields and backgrounds can vary greatly from one spectrum to another, but using separate optimisations for the B^0 and B^0_s peaks in a single spectrum is a little less intuitive. The reason for doing it is the same, though: the expected yields of the two peaks differ (as do the sources and amounts of background underneath them), so different working points are optimal; in general, a smaller yield benefits from a tighter selection.

3.1.1 Preselection

A loose selection is applied after the stripping to reduce the amount of combinatorial background before the Multivariate Analysis (MVA). The used preselection cuts are based on the previous analysis choices (summarised in Table 3.1)and further described in the following. The prescription is to avoid cuts on the variables which lead to a non-flat efficiency across the Dalitz plane. The used variables are then :

- A clearly isolated B vertex is required. The isolation variable is computed by comparing the χ^2 of the vertex formed with the signal candidate tracks and the χ^2 of the vertices formed by adding, in turn, each other Long track in the event (`B_STRIP_VTXISOCHI2ONETRACK`).
- Since K^0_S has a long lifetime, it is required that the z position of the K^0_S vertex is at least 30 mm downstream of the B vertex. This removes direct charmless decays that do not proceed via a K^0_S (*e.g.* $B^0 \to \pi^+\pi^-h^+h'^-$) and unphysical combinations in which the K^0_S vertex is upstream of the B vertex.
- Tracks compatible with a muon are removed by requiring `!isMuon`.
- The momentum of the $h^{(\prime)}$ tracks is required to be within the range where the RICH detectors have useful kaon-pion separation ($3 < p < 100\,\text{GeV}/c$).

- As mentioned in section 2.3.2, some of the cuts present in the Run I stripping lines were loosened in the Run II stripping lines. This improved the efficiency in some parts of the Dalitz plane, but greatly increased background. Since the purpose of this analysis is to measure branching fractions and not the Dalitz plane distribution, and because of the previous Run I analysis was not statistically limited and had quite large systematic uncertainties associated with the background description, this is not a great trade-off for the present analysis. The cuts on the transverse momentum of the tracks and on the $\min\chi^2_{\rm IP}$ are therefore reintroduced for this analysis.

Table 3.1: Preselection cuts. Note that for Run I, the cuts on the transverse momenta and the $\min(\chi^2_{\rm IP})$ of the candidates are already included in the stripping line, so they are not applied again here.

Preselection cut	Description
`B_STRIP_VTXISOCHI2ONETRACK` > 4	B vertex isolation variable
`KS_ENDVERTEX_Z` $-$ `B_ENDVERTEX_Z` > 30	$K^0_{\rm S}$ vertex separation w.r.t. the B vertex
`h{1,2}_isMuon == 0`	Reject $h^{(\prime)}$ candidates compatible with the muon hypothesis
$3000 \leq p\ (h^{(\prime)}) \leq 100000$	Fiducial cut
$\min\chi^2_{\rm IP}\ (h^{(\prime)}) > 4$	Minimum IP χ^2 of the charged daughters with respect to the related PV
$p_{\rm T}(h^{(\prime)}) > 250$ MeV	Minimum transverse momentum of the charged daughters.

3.1.2 Topological MVA

A Multi-Variate Analysis (MVA) selector based on boosted decision tree (BDT) has been trained in view to remove especially the combinatorial background thanks to the topological and kinematic variables in events. The training and testing steps require both signal and background samples. The signal samples consist of truth-matched events from signal MC[1], and the background is taken from the upper mass sideband of the data (B candidate mass above 5425 MeV). The trigger, stripping, and preselection requirements described above are applied to these samples before they are used for training. In addition, vetoes against $\Lambda^0_b \to K^0_{\rm S} p\pi$ and $\Lambda^+_c \to pK^0_{\rm S}$ to the background training samples are applied. This is done to optimise this selector specifically against combinatorial background, as opposed to physics backgrounds that have similar or identical topologies and kinematics to the signal and that are likely to end up in the upper mass sideband[2].

To allow for an unbiased test of the training performance, the signal and background samples are each randomly split into two subsamples: one for testing, one for validation. The events are split so that approximately 70% is used for training and 30% for testing.

Since the six $K^0_{\rm S}h^+h'^-$ decay modes have rather similar topological properties, they are all decays of a B meson into a $K^0_{\rm S}$ plus two light-charged hadrons, the same samples of $B^0 \to K^0_{\rm S}\pi^+\pi^-$ decays are used to train the MVA for all six modes. However, the optimal cut point is evaluated separately for each mode. Different training is performed for each $K^0_{\rm S}$ reconstruction category and for each data-taking period.

Discriminating variables

The input variables of the MVA should satisfy some requirements in addition to having good discriminating power. Ideally, they should have limited impact on the phase space distribution

[1]Truth-matching done by requiring that not only a truth-matched (TRUE_ID) initial B^0_s meson but also of all the daughters individually.

[2]The Λ^+_c veto is relevant because its lifetime is quite short so that $\Lambda^0_b \to \Lambda^+_c h^+(X)$ decays with $\Lambda^+_c \to K^0_{\rm S}p$ are topologically difficult to distinguish from $B \to K^0_{\rm S}h^+\pi^-(X)$.

(i.e. should not sculpt the Dalitz plot), and thus should show little correlation with the Dalitz plane variables. Furthermore, in order to not bias the results, they should not be correlated (or show very little correlation) with the mass of the B meson. As in the previous selection steps, topological variables are used mainly here, such as criteria on the separation and quality of the vertices, the direction angle, and the flight distance of the B meson. Variables related to transverse momentum and pseudorapidity of the B meson are also added. The variable lists are mostly shared between the LL and DD K^0_S reconstruction samples, except for a few variables related to the K^0_S flight distance or IPCHI2 that are not so useful for the downstream case (since K^0_S will always be far from PV). Table 3.3 contains a list of all input variables used in the MVA training. The main change since the previous ($3\,\text{fb}^{-1}$) analysis is the addition of cone asymmetry variables. These are defined as the asymmetry between the value of a variable (*e.g.* p_T) for the particle in question and the sum over all the tracks contained in a cone of 1.5 rad in (η, ϕ) around the particle. The choice of these variables for use in the MVA was the subject of an optimisation that is not discussed here; more information is given in Ref. [170]. The individual impact parameters (or χ^2_{IP}) of the decay products of the B meson are not used as input variables because they are correlated with the position in the Dalitz plot[3]; their sum does not have this drawback, but does have useful signal-background discrimination, so we use that instead.

The topological MVA score

Using these variables, a gradient-boosted decision tree selector [171] is trained. Table 3.2 gives the area under the ROC curve for all data-taking periods and K^0_S reconstruction category. It can be seen that the MVA performance is almost systematically better for the LL subsamples compared to DD, but is quite close to the unity, the optimal value, in all cases.

To check for potential over-training, the MVA outputs for test and training samples are compared. Figure 3.2 shows the over training test on signal and background events of the 2018 DD samples, on linear and logarithmic scales. Kolmogorov-Smirnov tests [172] give a p-value of around 90% for the background components and at a level of a few percent for the signal. Although the agreement looks very good on the linear scale plot, the logarithmic scale plot shows that the test and training samples for signal diverge for low BDT scores. This does imply some overtraining. However, the effect is small in terms of the absolute number of events, and it is not in a region where the selection cuts play. More details on topological MVA are given in Ref. [173].

3.1.3 Multivariate classifier based on Particle identification information

One of the most important sources of background to $B^0_{d,s} \to K^0_S h^+ h'^-$ decays is the cross-feed where final state of the signal B-meson decays are misidentified and swapped to another spectrum. Because these decays are all kinematically and topologically similar, the better available tool to suppress the associated source of background is the charged PID information. The variables used here to identify the charged pions, charged kaons and protons as the two charged-hadron daughters of the B are respectively `PROBNNpi`, `PROBNNk`, and `PROBNNp`, globally referred as `PROBNNh` [4] in the following.

[3] In particular, requiring that IPCHI2 is nonzero for a particular decay product removes the part of the phase space in which that particle is at rest in the B rest frame.

[4] The likelihood-based variable `PIDk` was also considered, in a study done several years ago, but the `PROBNN` varaibles were found to give better performance.

Topological MVA area under the ROC curve		
Data-taking period	DD sample result	LL sample result
2011	0.97	0.98
2012a	0.95	0.98
2012b	0.98	0.97
2015	0.97	0.98
2016	0.97	0.99
2017	0.97	0.99
2018	0.97	0.99

Table 3.2: This table contains the area under the ROC curve of the topological BDT for each data-taking period. It holds this information for both DD and LL categories.

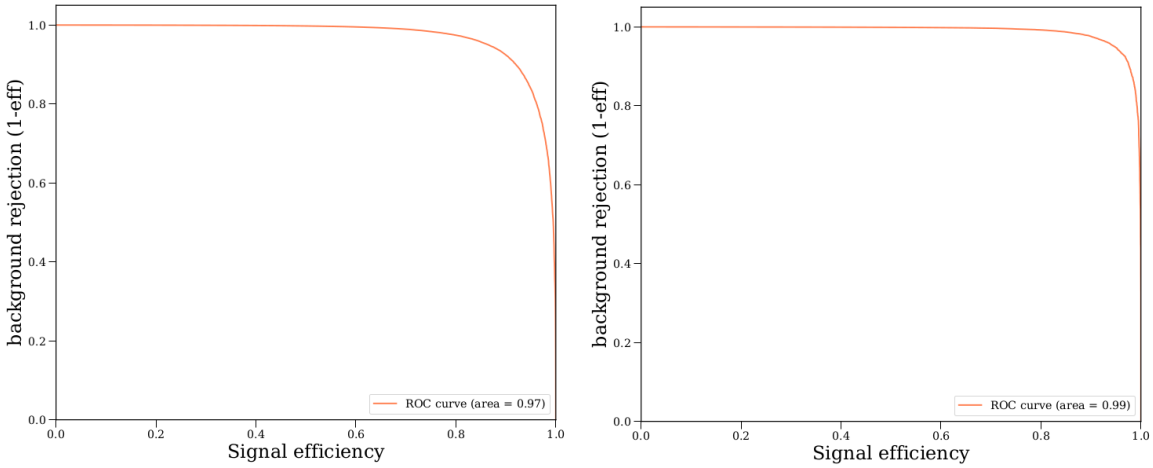

Figure 3.1: ROC curves for the topological multivariate analysis - 2018 DD (LL) on the left (right). We use the area under the ROC curve to estimate how well the algorithm is performing. With an area under the ROC curve equal to or above 0.97 in both cases, we can assume that the classifying tool is performing very well.

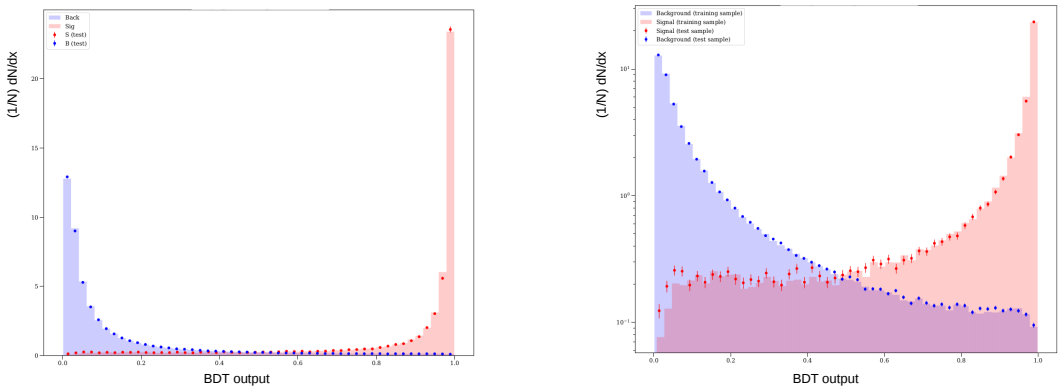

Figure 3.2: Distribution in linear/logarithmic sale (left/right) of the MVA output variable for the signal and background events of the 2018 DD samples, comparing test and training samples. The signal distributions are in red, the backgrounds distributions are in blue, the rectangles denote the train samples and the points denote the test samples.

Table 3.3: This table contains the discriminating variables that are used to train the topological BDT. The name of the variables and a brief definition are given. The samples on which these variables are used as discriminating variables are indicated.

Topological MVA input variables			
Variable	Pseudocode	Description	Sample
$p_T(B)$	B_PT	B transverse momentum	DD and LL
$\eta(B)$	B_ETA	B pseudo-rapidity	DD and LL
$\chi^2_{IP}(B)$	log(B_IPCHI2_OWNPV)	χ^2 significance of the impact parameter of the B	DD and LL
$\chi^2_{FD}(B)$	log(B_VDCHI2_OWNPV)	χ^2 significance of the flight distance of the B	DD and LL
DIRA(B)	log(1.0 - abs(B_DIRA_OWNPV))	cosine of the angle between the B displacement vector and the B momentum vector	DD and LL
$\chi^2_{vtx}(B)$	log(B_ENDVERTEX_CHI2)	Vertex fit quality of the B	DD and LL
$\chi^2_{ISOvtx}(B)$	log(B_STRIP_VTXISODCHI2ONETRACK)	B-meson vertex isolation	DD and LL
$p_T^{asym}(B)$	B_STRIP_CONEPTASYM_1_5	B p_T asymmetry for a cone of radius 1.5 rad around the B-candidate in the $\eta - \phi$ plane	DD and LL
$\chi^2_{IP}(h^+) + \chi^2_{IP}(h^-)$	log(h1_IPCHI2_OWNPV + h2_IPCHI2_OWNPV)	sum of the χ^2_{IP} of the B charged hadron daughters (excluding the K^0_S)	DD
$\chi^2_{IP}(h^+) + \chi^2_{IP}(h^-) + \chi^2_{IP}(K^0_S)$	log(h1_IPCHI2_OWNPV + h2_IPCHI2_OWNPV + KS_IPCHI2_OWNPV)	sum of the χ^2_{IP} of the B daughters (including the K^0_S)	LL
$\chi^2_{FD}(K^0_S)$	KS_VDCHI2_OWNPV	χ^2 of the flight distance of the K^0_S	LL
$p_T^{asym}(K^0_S)$	KS_STRIP_CONEPTASYM_1_5	K^0_S p_T asymmetry for a cone of radius 1.5 rad around the K^0_S-candidate in the $\eta - \phi$ plane	DD and LL
$p^{asym}(B)$	B_STRIP_CONEPASYM_1_5	B p asymmetry for a cone of radius 1.5 rad around the B-candidate in the $\eta - \phi$ plane	DD and LL
$p^{asym}(K^0_S)$	KS_STRIP_CONEPASYM_1_5	K^0_S p asymmetry for a cone of radius 1.5 rad around the K^0_S-candidate in the $\eta - \phi$ plane	DD and LL
$\Delta\eta^{asym}(B)$	B_STRIP_CONEDELTAETA_1_5	cone $\Delta\eta$ asymmetry for the B candidate	DD and LL
$\Delta\eta^{asym}(K^0_S)$	KS_STRIP_CONEDELTAETA_1_5	cone $\Delta\eta$ asymmetry for the K^0_S candidate	DD and LL
$\Delta\phi^{asym}(B)$	B_STRIP_CONEDELTAPHI_1_5	cone $\Delta\phi$ asymmetry for the B candidate	DD and LL
$\Delta\phi^{asym}(K^0_S)$	KS_STRIP_CONEDELTAPHI_1_5	cone $\Delta\phi$ asymmetry for the K^0_S candidate	DD and LL

In this section, the PID variables used are introduced and the MVA construction is presented. In LHCb, the PID variables play an important role for the selection process. However, the MC simulation of the detectors devoted to PID is non-trivial, and the simulations do not reproduce fully the real data behaviour. The `PIDCorr` tool, which is part of the PIDCalib package [174], has been used to improve the data-MC agreement for the simulated PID response. The details of the tool and its usage are not presented in this document, they can be found in Ref. [175] (with also more details on the PID MVA in general). A key advantage of `PIDCorr` is that it preserves the correlations between different PID variables for the same track (which is essential to be used in an MVA).

PID variables

The discriminative variables used as input for the PID MVA are the `PROBNNh` variables. The three types of previously defined variables are used for each of the charged hadron daughters of the B, leading to feed the PID MVA with six inputs `PROBNNh` variables.

Examples of distributions of the `PROBNNh` variables corresponding to 2018 and 2012b $B^0 \to K^0_S\pi^+\pi^-$ are given in Figures 3.3 and 3.4. The two charged hadron daughters are shown separately but, as expected, there is minimal difference between them.

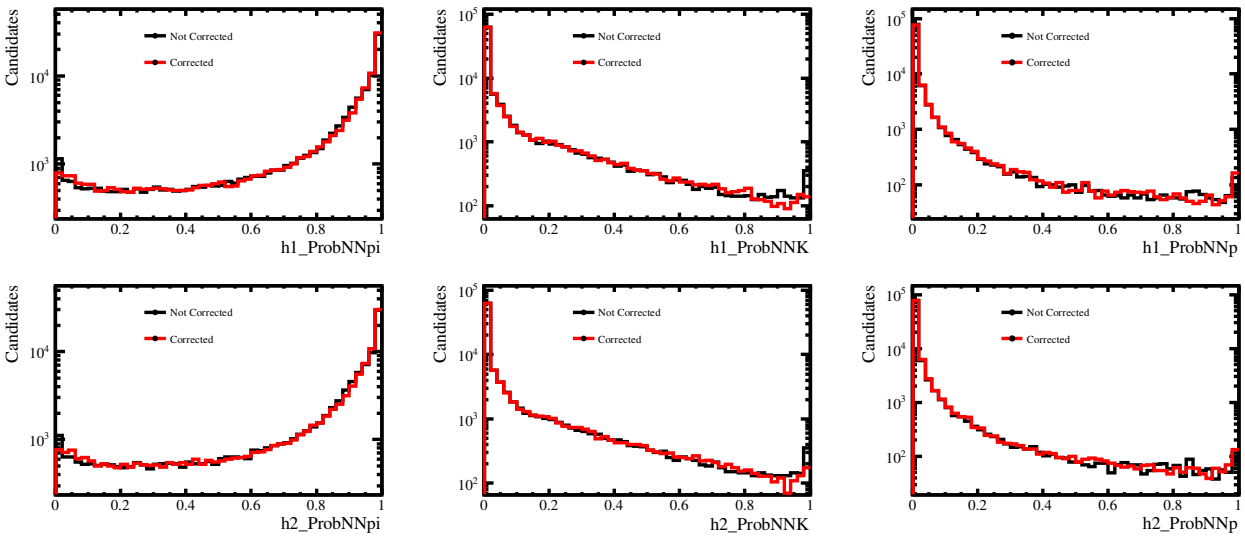

Figure 3.3: Distributions of the `PROBNNh` variables corresponding to $B^0 \to K^0_S\pi^+\pi^-$ 2018 *MagDown* sample for Down-Down K^0_S reconstructions. The black distributions correspond to the out-of-the-box MC variables and red distributions are the one corrected with the `PIDCorr` tool (the ones used in the MVA). The upper row shows the distributions for positively charged hadrons (h1), and the bottom row shows those of negatively charged hadrons (h2). The plots are shown on a logarithmic scale.

PID selection Tool

Among the various MVA technologies, the Scikit-learn Python package [176] has been used, and after comparing the response of different algorithms in this package, the XGBoost [171] (for eXtreme Gradient Boosting) algorithm has been chosen as classifier. The XGBoost algorithm is based on the use of a large number of small decision trees (weak classifier individually) in order to classify a set of entries by using their characteristics and featuring a gradient descent to optimise a loss function.

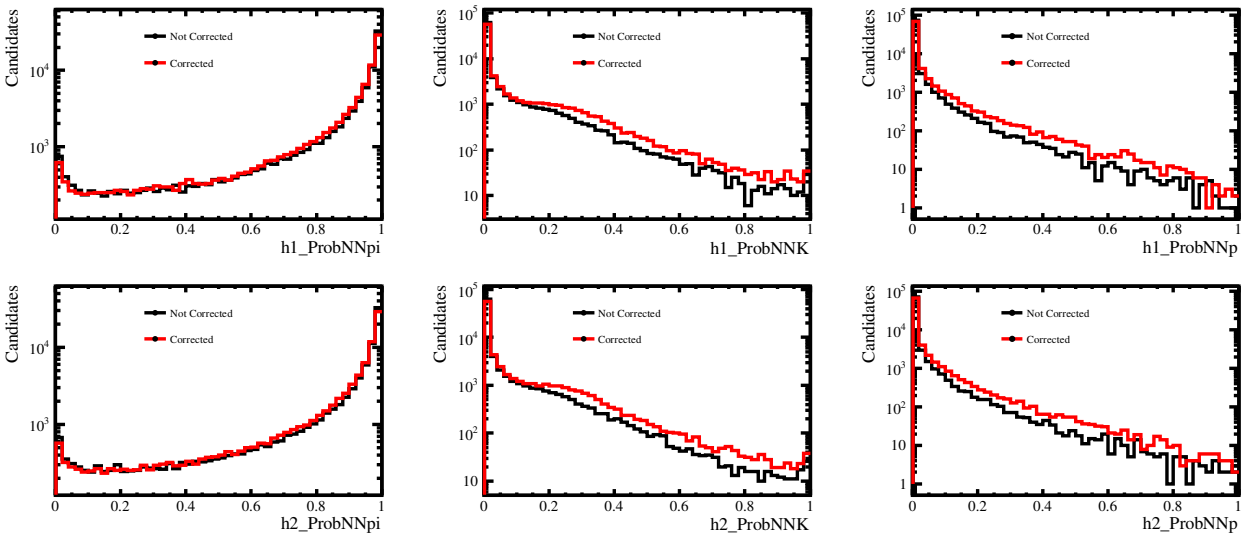

Figure 3.4: Distributions of the `PROBNNh` variables corresponding to $B^0 \to K^0_S\pi^+\pi^-$ 2012b *MagDown* sample for Down-Down K^0_S reconstructions. The black distributions correspond to the out-of-the-box MC variables and red distributions are the one corrected with the `PIDCorr` tool (the ones used in the MVA). The upper row shows the distributions for positively charged hadrons (h1), and the bottom row shows those of negatively charged hadrons (h2). The plots are shown on a logarithmic scale.

An individual classifier is trained for each data subsample (year and K^0_S reconstruction) and specific decay mode. As usual, this training involves signal and background samples, and the signal sample consists of truth-matched signal MC candidates reconstructed under the correct hypothesis. The background sample also uses signal MC with truth requirements[5], but takes candidates reconstructed under the wrong hypothesis (*e.g.* true $B^0 \to K^0_S\pi^+\pi^-$ reconstructed as $B^0 \to K^0_S\pi^+K^-$). Candidates in both training samples are required to pass the same trigger, stripping, and preselection requirements.

One of the most important steps to obtain good performance from an MVA classifier is hyper-parameter tuning. Two of the hyper-parameters of the XGBoost algorithm are considered here: `n_estimator`, which fixes the number of trees, and `max_depth`, which defines the maximum tree depth for base learners. These two parameters have the greatest impact on the results. Table 3.4 shows the final tuned values of these hyper-parameters for each classifier. To tune these parameters, the metric used was the area of the ROC curve[6]. Figure 3.5 shows the ROC curves of the classifiers of the 2012b and 2018 $B^0 \to K^0_S\pi^+\pi^-$ samples for the selected (tuned) hyper-parameters.

The signal and background samples are divided into statistically independent training (70%) and validation (30%) subsamples. To illustrate the MVA's behaviour, histograms of the MVA output for the $B^0 \to K^0_S\pi^+\pi^-$ decay mode are shown in Figure 3.6 for 2012*b* and 2018. While the details of the MVA set-up and training differ between these subsamples (hyper-parameters, input variables, etc), the shapes of the response are broadly similar.

As the last important concern, for each MVA tool, the hyperparameters should be optimised

[5]Note that this is different from the other (topological) MVA, in which the background training sample was taken from data sidebands. This is deliberate: the two MVAs have different, almost orthogonal objectives. The topological MVA is intended to discriminate against combinatorial background, and this PID MVA to discriminate against crossfeed/mis-ID background.

[6]The ROC curve describes how much of the background is rejected at as a function of signal acceptance when varying the cut. For an ideal selector with perfect signal-background discrimination, the area under the ROC curve would be 1.

Table 3.4: The tuned hyper-parameters of the XGBoost classifiers for Run I and Run II.

year	K^0_S	Hyper parameter	$B^0_{d,s} \to K^0_S\pi^+\pi^-$	$B^0_{d,s} \to K^0_S K^+\pi^-$	$B^0_{d,s} \to K^0_S\pi^+K^-$	$B^0_{d,s} \to K^0_S K^+K^-$
Run I	DD	`n_estimator`	350	350	350	350
		max_depth	2	2	2	2
	LL	`n_estimator`	250	250	250	250
		`max_depth`	2	2	2	2
Run II	DD	`n_estimator`	700	700	700	700
		`max_depth`	3	3	3	3
	LL	`n_estimator`	550	500	500	600
		`max_depth`	3	3	3	3

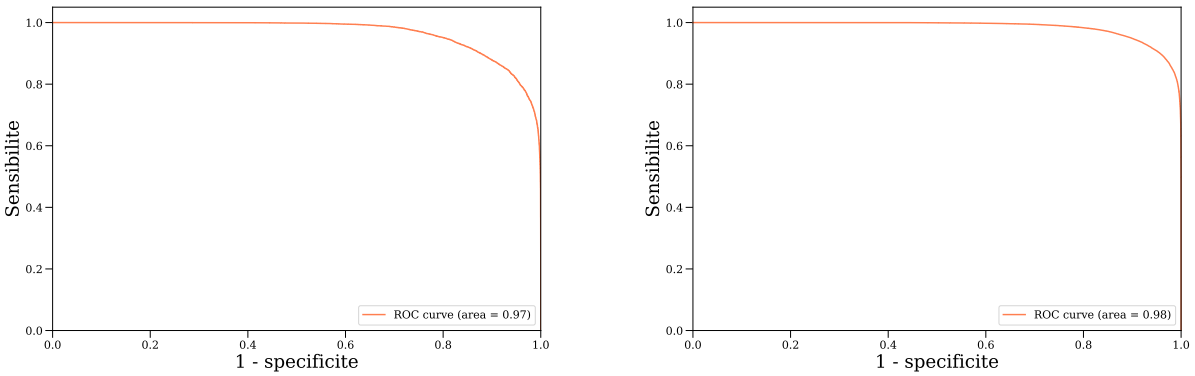

Figure 3.5: The ROC curves of the PID XGBoost selectors of various example $B^0 \to K^0_S\pi^+\pi^-$ samples. The left column shows the 2012b sample, and the right column the 2018 sample for the Down-Down K^0_S reconstruction. The x axis shows one minus the true negative (TN) rate, i.e. the background rejection. The y axis shows the true Positive (TP) rate, i.e. the signal efficiency.

up to the level of overtraining. To be sure about this concern as it can be seen in Fig. 3.6 the outputs of train and test samples are plotted on top of each other, whereas the Kolmogorov-Smirnov (KS) statistics test has been applied on these two samples. No hint of overtraining is spotted.

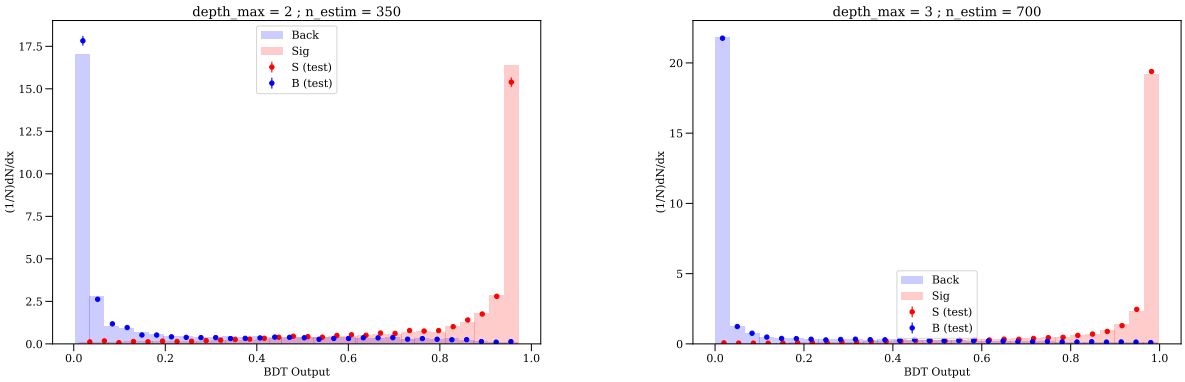

Figure 3.6: Training and validation samples response for the PID XGBoost of 2012b (left) and 2018 (right) discriminant for the $B^0 \to K^0_S\pi^+\pi^-$ Down-DownK^0_S events.

3.1.4 Vetoes and additional cuts

The third type of background sources in the analysis consists of decays with similar or identical final states but proceeding through intermediate charmed or charmonium states such as D^0, D^+, D_s^+, Λ_c^+, or J/ψ. These are removed with vetoes on the invariant masses of various two-body combinations, with a change of mass hypothesis if required. Table 3.5 shows the vetoes that we apply to both the data and the simulated samples.

An additional possible source of misidentification background comes from the K^0_S candidates. In this case, p tracks can be misidentified as π such that $\Lambda \to p\pi^-$ is reconstructed as $K^0_S \to \pi^+\pi^-$. To suppress this background, K^0_S is reconstructed under the $\Lambda \to p\pi^-$ (or conjugate) mass hypothesis and a veto is further applied, which requires $\|M_{p\pi} - 1115.5\| \geq 6.8\,\text{MeV}/c^2$ (determined from a simple Gaussian fit). The efficiency of this veto was checked on signal MC and is found to be high, around 98–99% on all the 2018 and 2012b samples.

The Λ_b^0 crossfeed backgrounds comes from p misidentification to π or K. Those are filtered out by a loose cut on the `PROBNNp` variables associated to the charged hadron daughters of B is applied, requiring `h1_PROBNNp < 0.9 and h2_PROBNNp < 0.9`.

Inv. Mass	Charmed mesons	Charmed Baryons	Charmonia
$K^0_S\pi^+\pi^-$	$D^\pm \to K^0_S\pi^\pm$, $D_s^\pm \to K^0_S\pi^\pm$, $D^\pm \to K^0_S K^\pm$, $D_s^\pm \to K^0_S K^\pm$ $D^0 \to K^\mp\pi^\pm$	Λ_c^+ $(\overline{\Lambda}_c^-) \to K^0_S p$ $(\overline{p})$	$J/\psi \to \pi^+\pi^-$ $\chi_{c0} \to \pi^+\pi^-$
$K^0_S K^\pm\pi^\mp$	$D^\pm \to K^0_S\pi^\pm$, $D^\pm \to K^0_S K^\pm$, $D^0 \to K^\mp\pi^\pm$	Λ_c^+ $(\overline{\Lambda}_c^-) \to K^0_S p$ $(\overline{p})$	
$K^0_S K^+K^-$	$D^\pm \to K^0_S K^\pm$, $D_s^\pm \to K^0_S K^\pm$, $D^0 \to K^\mp\pi^\pm$	Λ_c^+ $(\overline{\Lambda}_c^-) \to K^0_S p$ $(\overline{p})$	$J/\psi \to \pi^+\pi^-$ $\chi_{c0} \to \pi^+\pi^-$

Table 3.5: Summary of vetoes on charmed intermediary states. Vetoes on charmed mesons and baryons are defined as a $\pm 30\,\text{MeV}/c^2$ window around the known value of the resonance mass. Vetoes on charmonia are defined as a $\pm 48\,\text{MeV}/c^2$ window around the known value of the mass. Vetoes that contain a misidentified particle are applied using the corresponding mass hypothesis.

3.1.5 2D optimisation

Two different MVA selectors have been built, aiming to suppress the two main types of background sources (combinatorial, crossfeed/mis-ID) while preserving signal events as much as possible. To find the optimum cut values on their outputs, a 2D optimisation is needed (each dimension is associated to one MVA output). Each subsample (*e.g.* 2012b DD) and final state are optimised separately, and, in addition, two separated optimisations are done for the B^0 and B^0_s peaks.

First, an appropriate figure of merit (FoM) is required. For decay modes that have been observed in previous analyses, the simple signal significance is used:

$$\text{FoM} = \frac{\text{S}}{\sqrt{\text{S} + \text{B}}}\,, \tag{3.1.1}$$

where S and B are the numbers of signal and background events, respectively.

However, for the unobserved mode $B^0_s \to K^0_S K^+K^-$, the expected signal is unknown and an appropriate FoM is the so-called Punzi FoM [177]:

$$\text{FoM}_{\text{Punzi}} = \frac{\epsilon_{\text{sig}}}{\frac{\text{a}}{2} + \sqrt{\text{B}}}\,, \tag{3.1.2}$$

in which ϵ_{sig} is the signal efficiency, which is obtained by counting how many signal MC events pass both MVA cuts and dividing by the number generated[7], and a is a "small number" of standard deviations at which the null hypothesis would be rejected (just for the purposes of this optimisation), a is set to 5 here. The detailed computation of these FoMs are given in Ref. [175]. As a reminder, efficiencies introduced here are not the ones needed for the branching ratios determinations and do not include all corrections (*e.g.* for how events are distributed across the Dalitz plot).

The result of the 2D optimisation is performed mode by mode for each subsample (as usual, splitting into years and K^0_S reconstruction type). Based on the dominant Feynman diagrams, the decay modes of the B meson can be classified as favoured or suppressed, as summarised in Table 3.6. Each final state's spectrum contains two mass peaks (B^0 and B^0_s), one of which is favoured and the other suppressed. In general, the optimum working point for the two peaks is different. Therefore, two optimisations for each final state are performed, one for the favoured peak and the other for the suppressed peak. Sometimes they will be referred as "Loose" and "Tight" cuts (respectively), and sometimes as the "Principal Peak" and "Secondary Peak" optimisations.

Final state	Cabbibo favoured	Cabbibo suppressed
$K^0_S\pi^+\pi^-$	$B^0 \to K^0_S\pi^+\pi^-$	$B^0_s \to K^0_S\pi^+\pi^-$
$K^0_S K^\pm\pi^\mp$	$B^0_s \to K^0_S K^\pm\pi^\mp$	$B^0 \to K^0_S K^\pm\pi^\mp$
$K^0_S K^+K^-$	$B^0 \to K^0_S K^+K^-$	$B^0_s \to K^0_S K^+K^-$

Table 3.6: Categorization of the analysis decay mode in terms of Cabbibo suppressed and Cabbibo favoured modes.

To illustrate how this looks, the optimisation maps of some 2018 DD K^0_S reconstruction decays are presented in Figure 3.7. The optimum working point is simply the point in the 2D plane with the largest value of the FoM. The 2D optimisation provides for each data taking period, K^0_S reconstruction, experimental spectra ($K^0_S\pi^+\pi^-, K^0_S K^+K^-, K^0_S\pi^+K^-, K^0_S K^+\pi^-$), and type of peak (favoured or suppressed); the couple of optimal topological MVA and PID MVA output cuts.

3.1.6 Summary

All the pieces of selections (preselection, MVAs, vetoes, and additional cuts) are finally combined to build the final selections. In the following, the two selections designed for each data taking period, K^0_S reconstruction and experimental spectra ($K^0_S\pi^+\pi^-, K^0_S K^+K^-, K^0_S\pi^+K^-, K^0_S K^+\pi^-$) will be applied to the data and the MC tuples. This means that from each B^0 and B^0_s samples, two selected samples will be determined for each MVA cuts optimisation type.

Even if the selections have been made to discriminate the backgrounds of the analysis, some of them will remain and will have to be considered in the mass fit. This is the case of combinatorial, partially reconstructed, and crossfeeds from other $B^0_{d,s} \to K^0_S h^+ h'^-$ modes backgrounds.

[7]The details of the numerator are not important here, as long as it's the same for all cut values: it is just the FoM optimisation so all that matters is how the numerator changes.

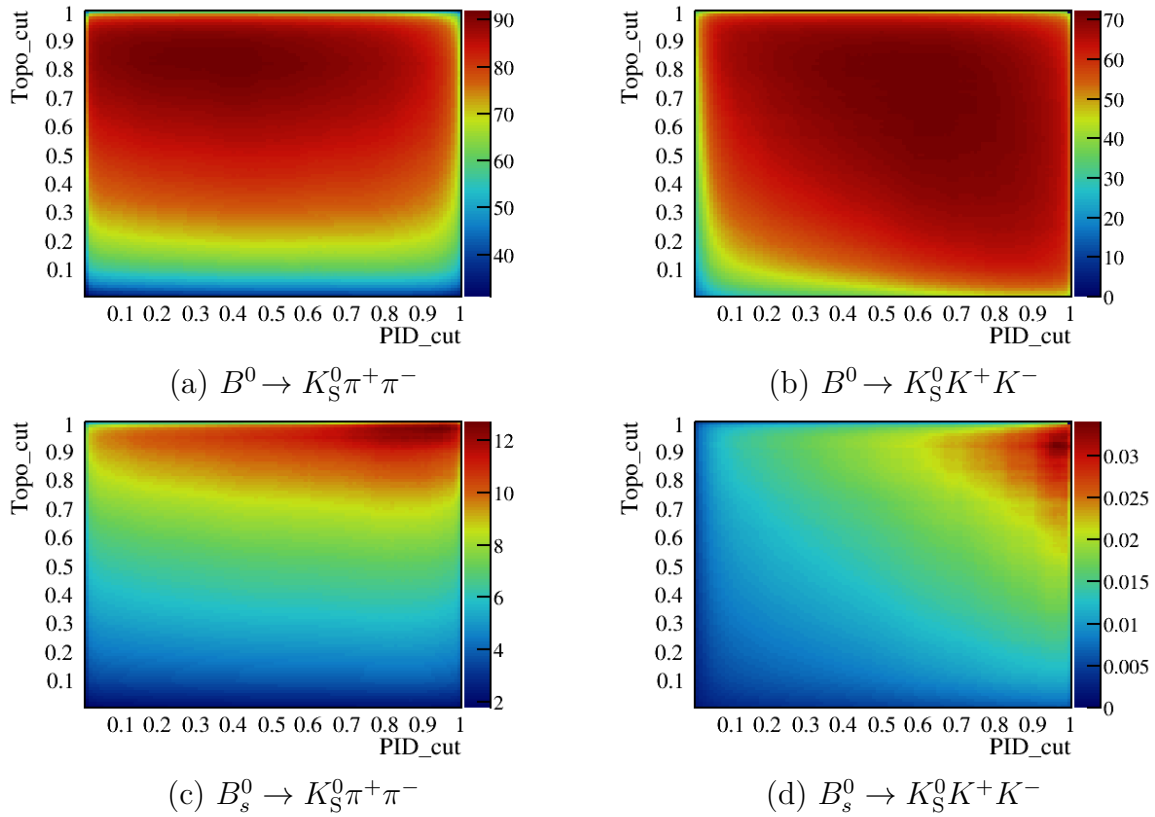

(a) $B^0 \to K^0_S \pi^+ \pi^-$

(b) $B^0 \to K^0_S K^+ K^-$

(c) $B^0_s \to K^0_S \pi^+ \pi^-$

(d) $B^0_s \to K^0_S K^+ K^-$

Figure 3.7: Example of 2D optimisation plots for the 2018 DD K^0_S reconstruction. Decay modes: (a) $B^0 \to K^0_S \pi^+ \pi^-$, (b) $B^0 \to K^0_S K^+ K^-$, (c) $B^0_s \to K^0_S \pi^+ \pi^-$, (d) $B^0_s \to K^0_S K^+ K^-$.

3.2 Mass fit

To determine the branching fractions of the $B^0_{d,s} \to K^0_S h^+ h'^-$ decay modes, it is necessary to measure the number of events, or the yields, of these decay modes in the data after applying the selection built in Section 3.1, as written in equation 3.0.1. The yields of studied decay modes are measured using simultaneous unbinned extended maximum-likelihood fits to the invariant-mass distributions. These fits are named mass fits, and to describe the data as best as possible, they have to take into account all the relevant contributions entering the mass spectrum. Here, the main contribution to consider / model are the signal peaks (B^0 and B^0_S) and all the remaining backgrounds after selection (crossfeeds, partially reconstructed, and combinatorial). Simultaneous fits over the final states studied are realised in order to take into account correlations between them (see section 3.2.1). Figure 3.8 shows an example of a typical mass spectrum to fit where the main area of influence of each fit component is indicated.

A description of the fit model used is first provided in Section 3.2.1, including the general procedure and a description of all the fit components. Secondly, the results of the mass fits are presented in Section 3.2.2, with the extracted yields and corresponding plots. Finally, the method used to bring the phase space information of the decays from the data, extracted from the mass fit, to MC, at the efficiency determination level, is explained in Section 3.2.3.

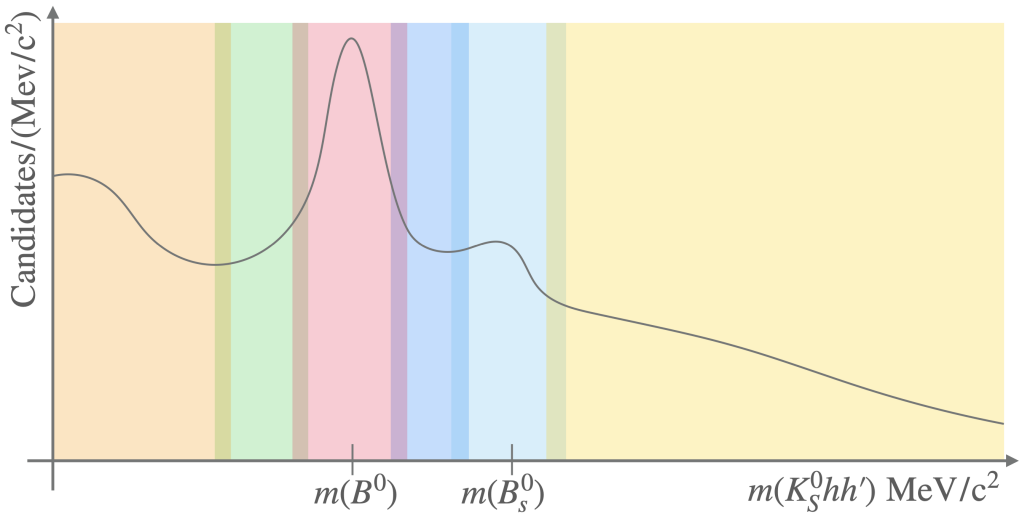

Figure 3.8: Illustration of a typical mass spectrum (B^0 decay favoured like $K^0_S \pi^+ \pi^-$) with the main area of influence of the different components highlighted, with the gray line representing the data trend. The signals peaks are found in the red (B^0) and light blue (B^0_s) areas, the combinarial background is found across the mass range but found alone on the upper region in the yellow area, the crossfeed is mainly found in the tails of the signal peaks in the green and dark blue areas, and finally the partially reconstruction events are grouped in the lower side of the mass spectrum in the orange area.

3.2.1 Fit Model

General procedure

This section presents the mass fit used for the analysis. The general procedure of the fit and the different components of it are presented in dedicated paragraphs.

Fitting scheme The datasets used have passed all selection steps (Triggers-Stripping-PreSelection-Vetoes-MVAsCuts). As mentioned previously, those datasets are separated per data-taking period and per K^0_S reconstruction (LL/DD). Both MVA optimisations are used, the

one for the B^0 decays and the other for the B_s^0 decays. Each optimisation is studied separately. Considering the 4 different final states of interest ($K_S^0K^+K^-$,$K_S^0\pi^+K^-$,$K_S^0K^+\pi^-$,$K_S^0\pi^+\pi^-$), there is a total of 112 spectra to fit. To ensure the overall robustness and stability of the fit, while correctly taking into account the correlations between the spectra, different fitting strategies have been investigated. The chosen baseline strategy is explained below.

All final states and K_S^0 reconstruction (4 final states $\times$ 2 K_S^0 reconstructions) per year and per MVA optimisation are fitted simultaneously (7 years $\times$ 2 MVA optimisations). The fitting is done in 4 consecutive steps. Each step starts using the results from the previous one.

1. Fit the data, only considering the signal peaks (B^0/B_s^0) and the combinatorial background components.
2. Add the descriptions of the partially reconstructed backgrounds to the fit and fit the data.
3. Add the descriptions of the crossfeed backgrounds to the fit and fit the data.
4. If the fit of step 3 did not meet the predefined quality requirements, repeat the fit until the fit quality is sufficient (see table 3.7 for the fit requirements used). The maximum number of iterations is fixed to 10.

Requirement	Description
covQual = 3	Fully accurate covariance matrix (after MIGRAD) [178]
$edm < 0.01$	Expected distance to minimum
fitStatus = 0	Overall variable that characterises the goodness of the fit

Table 3.7: Summary of the fit requirements used in the mass fit.

Mass window The range of the invariant mass studied is limited to 5100-5750 MeV/c^2.

$K^+\pi^-$ and π^+K^- For all modelling purposes, $K_S^0K^+\pi^-$ and $K_S^0\pi^+K^-$ components are taken to be the same, but the yields are extracted separately.

Small yields It happens that the fit estimate yields lower than 1 (most of the time far from 1) for contribution from partially reconstructed background. After step 4, if this is the case, that yield is fixed to 0 and the fit launched again.

$B_s^0 \to K_S^0K^+K^-$ blinding As $B_s^0 \to K_S^0K^+K^-$ was still the only not observed mode in LHCb at the beginning of the analysis, it was first fitted in the $K_S^0K^+K^-$ dataset but the measured yield as well as the corresponding region in the invariant-mass spectra were left blinded to build the analysis without introducing biases (blinding was also applied at the efficiency determination level). But after approval of the collaboration, the blinding has been removed to validate what has been done and proceed to the final modifications.

B^0 and B_s^0 signal

Definition Events that come from the decays of interest.

Model description Each signal peak (B^0 and B_s^0) is modelled with a double Crystal Ball (sum of two Crystal Ball functions, one with a right tail and the other with a left tail). One Crystal Ball (CB) line shape is given by:

$$PDF_{CB,i}(x) = N \begin{cases} \exp(-\frac{t^2}{2}) & \text{if } t > -\alpha_i \\ \frac{1}{(\frac{n_i}{\|\alpha_i\|} - \frac{\alpha_i^2}{\|\alpha_i\|} - t)^{n_i}} \left(\frac{n_i}{\|\alpha_i\|}\right)^{n_i} \exp(-\frac{\alpha_i^2}{2}) & \text{if } t \leq -\alpha_i \end{cases} \quad \text{with } t = \frac{x-\mu}{\sigma}. \tag{3.2.1}$$

With N the normalisation factor. Each CB is implemented using the RooFit `RooCBShape` class [152]. Both CB are taken to have a common mean (μ) and a common width (σ), but the tail parameter (n_i) and the turnover point (α_i) can differ and are given subscripts i; L for the CB with the left-handed tail and R for the CB with the right-handed tail. All of the shape parameters (except for the mean and the width) are taken from fits to MC signal samples and are fixed to those values in the fits to data.

Parameterisation of fits to MC samples For each year and optimisation, 22 shape parameters are fitted for;

- fit for the means $\mu(B^0)$ and $\mu(B_s^0)$, the means are shared between all the finals modes and K_S^0 reconstructions (2 parameters),
- fit for the width $\sigma(B^0)(\pi\pi)(DD)$, this width is expected to be the most defined peak in the studied spectra. The other signal peak widths are defined with respect to this reference width, *e.g.* $\sigma(B_s^0)(K\pi)(LL) = \sigma_r(B_s^0) \times \sigma_r(K\pi) \times \sigma_r(LL) \times \sigma(B^0)(\pi\pi)(DD)$. The σ_r parameters (the three previous ones plus $\sigma_r(KK)$) and $\sigma_r(K\pi)$ are also fitted for (5 parameters),
- fit for the left-handed tail parameters α_L and n_L, shared between the K_S^0 reconstructions and B-mesons (B^0 or B_s^0 decay) (2×3 parameters),
- fit for the right-handed tail parameters α_R and n_R, defined as ratios with respect to the left-handed equivalents (α_R/α_L and n_R/n_L) and are shared between the K_S^0 reconstructions and B-mesons (2×3 parameters),
- fit for the fractions f of the right-handed CB in the double CB (*e.g.* P.D.F.$_{\cdot double\ CB} = f \times$ P.D.F.$_{CB,L} + (1-f) \times$ P.D.F.$_{CB,R}$) are shared between the K_S^0 reconstructions and B-mesons (3 parameters).

The main MC signal fit results (parameters and some plots) are given in Appendix C.1.1.

Parameterisation of the fits to data For each year and optimisation:

- α_i, n_i, σ_r and f are taken from the fit to MC samples and are fixed,
- fit for the means $\mu(B^0)$ and $\mu(B_s^0)$. The mean difference is constrained to the tabulated B_s^0-B^0 mass-difference value: $\Delta m = m_{B_s^0} - m_{B^0} = 5366.92 - 5279.66 = 87.26\,\text{MeV}/c^2$ [179] so only one parameter is left in the fits, this parameters are shared between all the final modes and K_S^0 reconstructions, (1 parameter)
- fit for the width $\sigma(B^0)(\pi\pi)(DD)$, (1 parameter)
- fit for the yields (main measurement in the fits, used in the measurement of the Branching Fraction ratios). All yields are left free to vary. (16 parameters)

Crossfeeds backgrounds

Definition Accounts for events that come from one of the studied decays, where one of the final-state hadrons has been misidentified to form the final-state of another studied decay. These contributions overlap with the signal tails and can affect the extracted signal yields. The crossfeed modes considered per spectrum;

In $K^0_S\pi^+\pi^-$:

- From $B^0 \to K^0_S K^+\pi^-$ and $B^0 \to K^0_S\pi^+K^-$ (on the left of the $B^0 \to K^0_S\pi^+\pi^-$ peak),
- From $B^0_s \to K^0_S K^+\pi^-$ and $B^0_s \to K^0_S\pi^+K^-$ (in between the $B^0 \to K^0_S\pi^+\pi^-$ and $B^0_s \to K^0_S\pi^+\pi^-$ peaks).

In $K^0_S K^+K^-$:

- From $B^0 \to K^0_S K^+\pi^-$ and $B^0 \to K^0_S\pi^+K^-$ (in between the $B^0 \to K^0_S K^+K^-$ and $B^0_s \to K^0_S K^+K^-$ peaks),
- From $B^0_s \to K^0_S K^+\pi^-$ and $B^0_s \to K^0_S\pi^+K^-$ (on the right of the $B^0_s \to K^0_S K^+K^-$ peak).

In $K^0_S K^+\pi^-$ (similarly in $K^0_S\pi^+K^-$):

- From $B^0 \to K^0_S\pi^+\pi^-$ (in between the $B^0 \to K^0_S K^+\pi^-$ and $B^0_s \to K^0_S K^+\pi^-$ peaks),
- From $B^0 \to K^0_S K^+K^-$ (on the left of the $B^0 \to K^0_S K^+\pi^-$ peak).

Only single misidentified decays are taken into account as individual components in the fit in this way; doubly misidentified crossfeeds are neglected.

Model description As for the signal, crossfeeds are modelled with a double Crystal Ball (see equation (3.2.1)). The shape parameters are extracted from fits to simulated samples of crossfeeds that have passed the selections of the spectrum in which they leak into, *e.g.* events from $B^0 \to K^0_S\pi^+\pi^-$ found in the $K^0_S K^+\pi^+$ spectrum which have passed the selection used for the $K^0_S K^+\pi^+$ spectrum.

Parameterisation of fits to MC samples Each crossfeed mode is taken to have the same shape across the years. For each optimisation.

- fit for all the parameters that are needed to characterise a double CB, all 7 parameters are shared across the years and K^0_S reconstruction but are crossfeed-mode dependant. (α_i, n_i, σ_r and f, 7 parameters)

The results of the fit to the MC samples for the crossfeeds are available in Appendix C.1.2.

Parameterisation of fits to data For each year and optimisation.

- All the parameters needed to characterise a double CB are taken from the fits to MC samples.

- Using the misidentification efficiencies and the measurement yield of the source of the crossfeed, it is possible to estimate the yields of the crossfeed contributions,

$$N_{\mathrm{AinB}} = \frac{\epsilon_{(\mathrm{AinB})}}{\epsilon_{\mathrm{A}}} \times N_{\mathrm{A}}, \tag{3.2.2}$$

where N_{AinB} is the crossfeed yield (number of events from decay A that are found in spectrum B), $\epsilon_{(\mathrm{AinB})}$ the ratio of crossfeed events (AinB) that passed B's selection, N_{A} yield of decay A and ϵ_{A} efficiency of A events that pass A's selections. The efficiencies are extracted from studies on MC samples and are given as input in the fit. Since in each spectrum two crossfeed contributions are expected (see above), it is possible to define the yield ratio of the crossfeed contributions per spectrum:

$$\frac{N_{\mathrm{AinB}}}{N_{\mathrm{A'inB}}} = r_{\epsilon(\mathrm{CFinB})} \frac{N_{\mathrm{A}}}{N_{\mathrm{A'}}} = \frac{\epsilon_{\mathrm{AinB}}/\epsilon_{\mathrm{A}}}{\epsilon_{\mathrm{A'inB}}/\epsilon_{\mathrm{A'}}} \times \frac{N_{\mathrm{A}}}{N_{\mathrm{A'}}} \tag{3.2.3}$$

This ratio $r_{\epsilon(\mathrm{CFinB})}$ is fixed in the fit to data, one parameter per spectrum is left floating to measure both crossfeed yields - relatively to the signal yields N_{A} and $N_{\mathrm{A'}}$. In the case of crossfeeds from $K^+\pi^-$ and $K^-\pi^+$, the N_{A} and $N_{\mathrm{A'}}$ are taken as the sum of decays to $K^0_{\mathrm{S}}K^+\pi^-$ and $K^0_{\mathrm{S}}\pi^+K^-$; *e.g.* where $A = B^0 \to K^0_{\mathrm{S}}K\pi$, $N_{\mathrm{A}} = N_{\mathrm{B^0 \to K^0_S K^+\pi^-}} + N_{\mathrm{B^0 \to K^0_S \pi^+ K^-}}$. For spectra with the SecondaryPeak configuration where the number of fitted events is too low to properly define/measure crossfeed yields, the yields of the crossfeeds are fully fixed with equation (3.2.2)[8].

Partially reconstructed backgrounds

Definition Account for decays such as $B^0 \to K^0_{\mathrm{S}}h^+h'^-Y$, where particle Y is not being reconstructed (soft particle or outside of the LHCb acceptance). Partially reconstructed events are expected to come from a variety of channels; different missed particles, different intermediate resonances, and/or different mother particles. Four canonical modes are considered to describe the shape of the partially reconstructed backgrounds in the left-hand part of the analysed mass spectra.

- Partially reconstructed charmed decays such as $B^+ \to D^0\ (K^0_{\mathrm{S}}\pi^+\pi^-)\pi^+$, can originate from B_d or B_s decay processes,
- Partially reconstructed charmless decays such as $B^0 \to K^*\ (K^0_{\mathrm{S}}\pi^0)\rho^0\ (\pi^+\pi^-)$, can originate from B^0 or B^0_s decay processes,
- Partially reconstructed resonant radiative decays such as $B^0 \to \eta'\ (\rho^0\gamma)K^0_{\mathrm{S}}$, only found in the $K^0_{\mathrm{S}}\pi\pi$ spectrum,
- Partially reconstructed non-resonant radiative decays such as $B^0 \to K^0_{\mathrm{S}}\pi^+\pi^-\gamma$, only found in the $K^0_{\mathrm{S}}\pi\pi$ spectrum.

Model description and parameterisation of fits to MC samples These contributions are modelled with an ARGUS function convoluted with a Gaussian distribution (μ, σ). The ARGUS lineshape is given by:

$$\mathrm{P.D.F.}_{ARGUS}(x) = Nm\left[1 - \left(\frac{m}{m_t}\right)^2\right]^p \exp\left[c\left(1 - \left(\frac{m}{m_t}\right)^2\right)\right], \tag{3.2.4}$$

[8] N_A (and $N_{A'}$) are signal yields that are measured in the fit

with N the normalisation factor, p the curvature, c the slope and m_t the threshold. The ARGUS function is implemented using the RooFit `RooArgusBG` class [180], the Gaussian with the RooFit `RooGaussian` class [150] and the convolution is realised with the RooFit `RooFFTConvPdf` class [181]. As for the previously introduced contributions, the shape is taken from fits to simulated samples. Since the goal is only to obtain general shapes for these contributions, the shapes are obtained from fits to simulated partially reconstructed backgrounds in the $K^0_S\pi\pi$ spectra and are shared with the other spectra. Parameter μ is fixed to 0 and parameter m_t is fixed to the expected mass difference between the mother particle and the non-reconstructed particle.
The MC fits are performed simultaneously over the years and the K^0_S reconstructions for each optimisation. The parameters are shared over the spectra, data-taking periods, and K^0_S reconstructions. For 2016 in both SecondaryPeak and PrincipalPeak configurations, the fits to MC do not converge, in those cases the shapes are taken from the fit to 2018 in the corresponding optimisations.

Parameterisation of fits to data For each year and optimisation.

- all the parameters that are needed to characterise the shape are taken from the fits to the MC samples,
- to model for partially reconstructed events from B^0_s decay, the threshold is shifted by $+87.26$ MeV/c^2 (the mass B^0_s-B^0 difference),
- introducing two contributions to account for partially reconstructed events was studied to be enough to correctly model the lower side band of the mass spectrum, only partially reconstructed charmless decays shape's are used,
- the yields of the partially reconstructed charmless decays are left floating,
- the yields of the partially reconstructed radiative decays (resonant and non-resonant) are fixed to the estimate values (see equation (3.2.5)) as the branching fraction of those decays are well known:

$$N_{\text{PartRadDecay}} = \frac{BF_{\text{PartDecay}}}{BF_{B^0\to K^0_S\pi\pi}} \frac{\epsilon_{\text{PartDecay}}}{\epsilon_{B^0\to K^0_S\pi\pi}} \times N_{B^0\to K^0_S\pi\pi}, \tag{3.2.5}$$

  with $N_{\text{PartRadDecay}}$ the yield of the partially reconstructed decays considered, $N_{B^0\to K^0_S\pi\pi}$ the signal-yield of $B^0 \to K^0_S\pi\pi$, ϵ the corresponding efficiencies and BF the corresponding branching fractions. The branching fractions used are taken from the PDG [47]:

  - $BF(B^0 \to K^0\pi^+\pi^-) = (4.97 \pm 0.18)10^{-5}$,
  - $BF(B^0 \to \eta' K^0) \times BF(\eta' \to \rho^0\gamma) \times BF(\rho^0 \to \pi^+\pi^-) = (6.6 \pm 0.4)10^{-5} \times (29.5 \pm 0.4)10^{-2} \times 1 = (1.95 \pm 0.12)10^{-5}$,
  - $BF(B^0 \to K^0\pi^+\pi^-\gamma) = (1.99 \pm 0.18)10^{-5}$.

Combinatorial background

Definition This is the dominant source of background in the studied samples. Combinatorial background originates from random combinations of tracks.

Model description This contribution is modelled with a linear function (first-order Chebychev polynomial), implemented using the RooFit `RooChebychev` class [151].

Parameterisation of fits to data The slope of the combinatorial background is left free to vary in the fits. The $K^0_S K^+\pi^-$ and $K^0_S\pi^+K^-$ spectra are considered to have the same combinatorial slope. This slope is expected to be negative, but it might happen that the slope is found positive in the fit, in those cases the slope is fixed to 0.

Overview

Table 3.8 gives a summary of the different contributions used to modelled data of each final state and the descriptions used for each of them.

Component	Description
B^0 peak (Signal)	Double Crystal Ball
B^0_s peak (Signal)	Double Crystal Ball
Combinatorial	Linear
Crossfeeds (2 components)	Double Crystal Ball
Partially reconstructed backgrounds (2 components)	ARGUS×Gaussian

Table 3.8: Overview of the contributions considered in each final state, with the model used to describe them.

3.2.2 Fit results

PrincipalPeak optimisation

The signal yields and floating parameters from the fits to data using the PrincipalPeak optimisation (optimisation for the favoured decays) are presented in table 3.9 and table 3.10 respectively. The fit results corresponding to 2018 and 2012b DD are shown in Figures 3.10 and 3.9, all the other are given in Appendix C.2.1, together with the yields of the backgrounds.

Logically, the highest yields are obtained for 2018, 2017 and 2016, which are periods with high luminosities and the maximum energy in the collision. One can observe that, for this optimisation, the peak of the unfavoured mode in each spectrum lies below the combinatorial background level. This is not an issue, as the goal of this optimisation is to maximise the statistic of the favoured modes. The distributions associated with the $K^0_S\pi^\pm K^\mp$ spectrum ($K^0_S\pi^+K^-$ and $K^0_S K^+\pi^-$) are as expected very similar.

The $K^0_S K^+K^-$ spectrum fits show the presence of B^0_s signal peaks, leading to yield measurements compatible with a first observation of $B^0_s \to K^0_S K^+K^-$. Because the PrincipalPeak optimisation is looser compared to the SecondaryPeak one, an important amount of background (especially combinatorial) competes with the B^0_s peak. Cleaner $B^0_s \to K^0_S K^+K^-$ peaks / yields are expected with SecondaryPeak optimisation.

Decays	2011	2012a	2012b	2015	2016	2017	2018	Sum
$B^0_d \to K^0_S(\mathrm{LL})\pi^+\pi^-$	$550_{\pm 31}$	$421_{\pm 28}$	$760_{\pm 40}$	$501_{\pm 29}$	$2820_{\pm 70}$	$2900_{\pm 70}$	$3350_{\pm 70}$	$11300_{\pm 140}$
$B^0_d \to K^0_S(\mathrm{DD})\pi^+\pi^-$	$1120_{\pm 50}$	$720_{\pm 40}$	$1990_{\pm 60}$	$990_{\pm 50}$	$6070_{\pm 110}$	$6940_{\pm 120}$	$8550_{\pm 130}$	$26380_{\pm 230}$
$B^0_d \to K^0_S(\mathrm{LL})K^+K^-$	$288_{\pm 21}$	$150_{\pm 14}$	$418_{\pm 23}$	$267_{\pm 19}$	$1550_{\pm 50}$	$1530_{\pm 40}$	$1800_{\pm 50}$	$6010_{\pm 90}$
$B^0_d \to K^0_S(\mathrm{DD})K^+K^-$	$417_{\pm 26}$	$288_{\pm 21}$	$940_{\pm 40}$	$494_{\pm 30}$	$3540_{\pm 80}$	$3510_{\pm 70}$	$4060_{\pm 80}$	$13250_{\pm 150}$
$B^0_d \to K^0_S(\mathrm{LL})K^+\pi^-$	$44_{\pm 13}$	$40_{\pm 10}$	$34_{\pm 14}$	$25_{\pm 13}$	$159_{\pm 25}$	$185_{\pm 27}$	$251_{\pm 27}$	$740_{\pm 50}$
$B^0_d \to K^0_S(\mathrm{DD})K^+\pi^-$	$70_{\pm 19}$	$46_{\pm 14}$	$144_{\pm 28}$	$114_{\pm 18}$	$500_{\pm 50}$	$540_{\pm 50}$	$610_{\pm 50}$	$2020_{\pm 90}$
$B^0_d \to K^0_S(\mathrm{LL})\pi^+K^-$	$69_{\pm 13}$	$14_{\pm 11}$	$69_{\pm 15}$	$38_{\pm 12}$	$239_{\pm 27}$	$202_{\pm 26}$	$229_{\pm 28}$	$860_{\pm 50}$
$B^0_d \to K^0_S(\mathrm{DD})\pi^+K^-$	$97_{\pm 21}$	$26_{\pm 13}$	$130_{\pm 27}$	$87_{\pm 18}$	$500_{\pm 50}$	$590_{\pm 50}$	$610_{\pm 50}$	$2030_{\pm 90}$
$B^0_s \to K^0_S(\mathrm{LL})\pi^+\pi^-$	$37_{\pm 13}$	$30_{\pm 14}$	$62_{\pm 16}$	$49_{\pm 15}$	$204_{\pm 34}$	$166_{\pm 33}$	$280_{\pm 40}$	$830_{\pm 70}$
$B^0_s \to K^0_S(\mathrm{DD})\pi^+\pi^-$	$73_{\pm 23}$	$26_{\pm 17}$	$225_{\pm 35}$	$48_{\pm 25}$	$520_{\pm 60}$	$450_{\pm 60}$	$710_{\pm 70}$	$2050_{\pm 120}$
$B^0_s \to K^0_S(\mathrm{LL})K^+K^-$	$16_{\pm 10}$	$5_{\pm 6}$	$10_{\pm 9}$	$6_{\pm 8}$	$11_{\pm 18}$	$26_{\pm 17}$	$6_{\pm 19}$	$80_{\pm 30}$
$B^0_s \to K^0_S(\mathrm{DD})K^+K^-$	$25_{\pm 13}$	$4_{\pm 9}$	$23_{\pm 16}$	$13_{\pm 14}$	$140_{\pm 40}$	$71_{\pm 29}$	$77_{\pm 32}$	$350_{\pm 60}$
$B^0_s \to K^0_S(\mathrm{LL})K^+\pi^-$	$145_{\pm 16}$	$83_{\pm 12}$	$172_{\pm 18}$	$121_{\pm 16}$	$613_{\pm 34}$	$710_{\pm 40}$	$790_{\pm 40}$	$2640_{\pm 70}$
$B^0_s \to K^0_S(\mathrm{DD})K^+\pi^-$	$264_{\pm 23}$	$150_{\pm 17}$	$527_{\pm 34}$	$238_{\pm 21}$	$1530_{\pm 60}$	$1710_{\pm 60}$	$1940_{\pm 60}$	$6360_{\pm 110}$
$B^0_s \to K^0_S(\mathrm{LL})\pi^+K^-$	$170_{\pm 16}$	$88_{\pm 14}$	$213_{\pm 19}$	$117_{\pm 15}$	$750_{\pm 40}$	$715_{\pm 35}$	$820_{\pm 40}$	$2860_{\pm 70}$
$B^0_s \to K^0_S(\mathrm{DD})\pi^+K^-$	$297_{\pm 24}$	$171_{\pm 18}$	$523_{\pm 33}$	$282_{\pm 24}$	$1590_{\pm 60}$	$1710_{\pm 60}$	$2060_{\pm 60}$	$6640_{\pm 120}$

Table 3.9: Values and statistical uncertainties on the signal yields extracted from the fit to data, in the PrincipalPeak optimisation.

Parameters	2011	2012a	2012b	2015	2016	2017	2018
$\mu(B^0)$	$5284.9_{\pm 0.5}$	$5283.8_{\pm 0.5}$	$5284.38_{\pm 0.34}$	$5280.2_{\pm 0.5}$	$5279.77_{\pm 0.18}$	$5279.54_{\pm 0.17}$	$5280.34_{\pm 0.16}$
$\sigma(\pi\pi)(\mathrm{DD})$	$18.8_{\pm 0.6}$	$17.1_{\pm 0.6}$	$17.7_{\pm 0.4}$	$17.7_{\pm 0.5}$	$17.10_{\pm 0.21}$	$17.05_{\pm 0.19}$	$17.46_{\pm 0.18}$
$c(\pi\pi K^0_S(\mathrm{LL}))$	$-0.59_{\pm 0.13}$	$-0.43_{\pm 0.11}$	$-0.47_{\pm 0.11}$	$-0.61_{\pm 0.10}$	$-0.49_{\pm 0.04}$	$-0.58_{\pm 0.04}$	$-0.42_{\pm 0.05}$
$c(\pi\pi K^0_S(\mathrm{DD}))$	$-0.41_{\pm 0.08}$	$-0.50_{\pm 0.08}$	$-0.34_{\pm 0.05}$	$-0.22_{\pm 0.07}$	$-0.310_{\pm 0.030}$	$-0.297_{\pm 0.030}$	$-0.287_{\pm 0.025}$
$c(KKK^0_S(\mathrm{LL}))$	$-0.09_{\pm 0.23}$	$-0.51_{\pm 0.16}$	$-0.37_{\pm 0.12}$	$-0.31_{\pm 0.12}$	$-0.41_{\pm 0.08}$	$-0.38_{\pm 0.05}$	$-0.48_{\pm 0.04}$
$c(KKK^0_S(\mathrm{DD}))$	$-0.45_{\pm 0.14}$	$-0.38_{\pm 0.18}$	$-0.23_{\pm 0.12}$	$-0.37_{\pm 0.11}$	$-0.21_{\pm 0.05}$	$-0.29_{\pm 0.06}$	$-0.26_{\pm 0.05}$
$c(K\pi K^0_S(\mathrm{LL}))$	$-0.43_{\pm 0.15}$	$-0.48_{\pm 0.12}$	$-0.59_{\pm 0.10}$	$-0.42_{\pm 0.11}$	$-0.52_{\pm 0.05}$	$-0.43_{\pm 0.05}$	$-0.31_{\pm 0.06}$
$c(K\pi K^0_S(\mathrm{DD}))$	$-0.42_{\pm 0.08}$	$-0.52_{\pm 0.09}$	$-0.32_{\pm 0.05}$	$-0.10_{\pm 0.10}$	$-0.308_{\pm 0.026}$	$-0.301_{\pm 0.030}$	$-0.306_{\pm 0.028}$

Table 3.10: Shape parameters extracted from the fit to data using the PrincipalPeak optimisation, with μ the mean of the B^0 peak, σ the width of the $B^0 \to K^0_S$ (DD)$\pi^+\pi^-$ peak and c the slope of the combinatorial background. Fixed parameters are given without uncertainties.

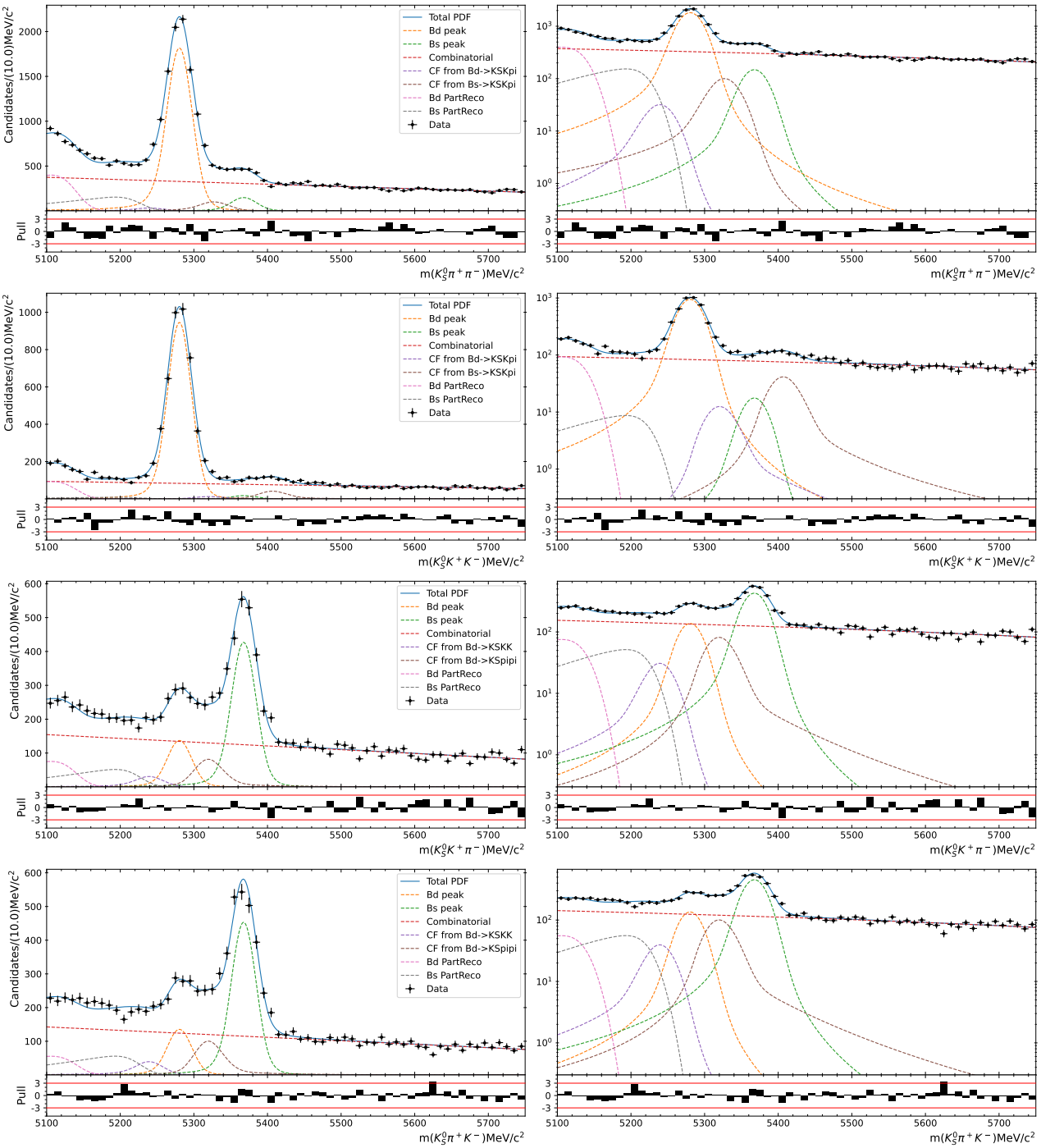

Figure 3.9: Results of the simultaneous fit to data (DD, 2018) with the PrincipalPeak optimisation. The modes $K^0_S\pi^+\pi^-$, $K^0_S K^+K^-$, $K^0_S K^+\pi^-$ and $K^0_S\pi^+K^-$ are shown from top to bottom. The left-hand side plots show the results with a linear scale and the right-hand side with a logarithmic scale.

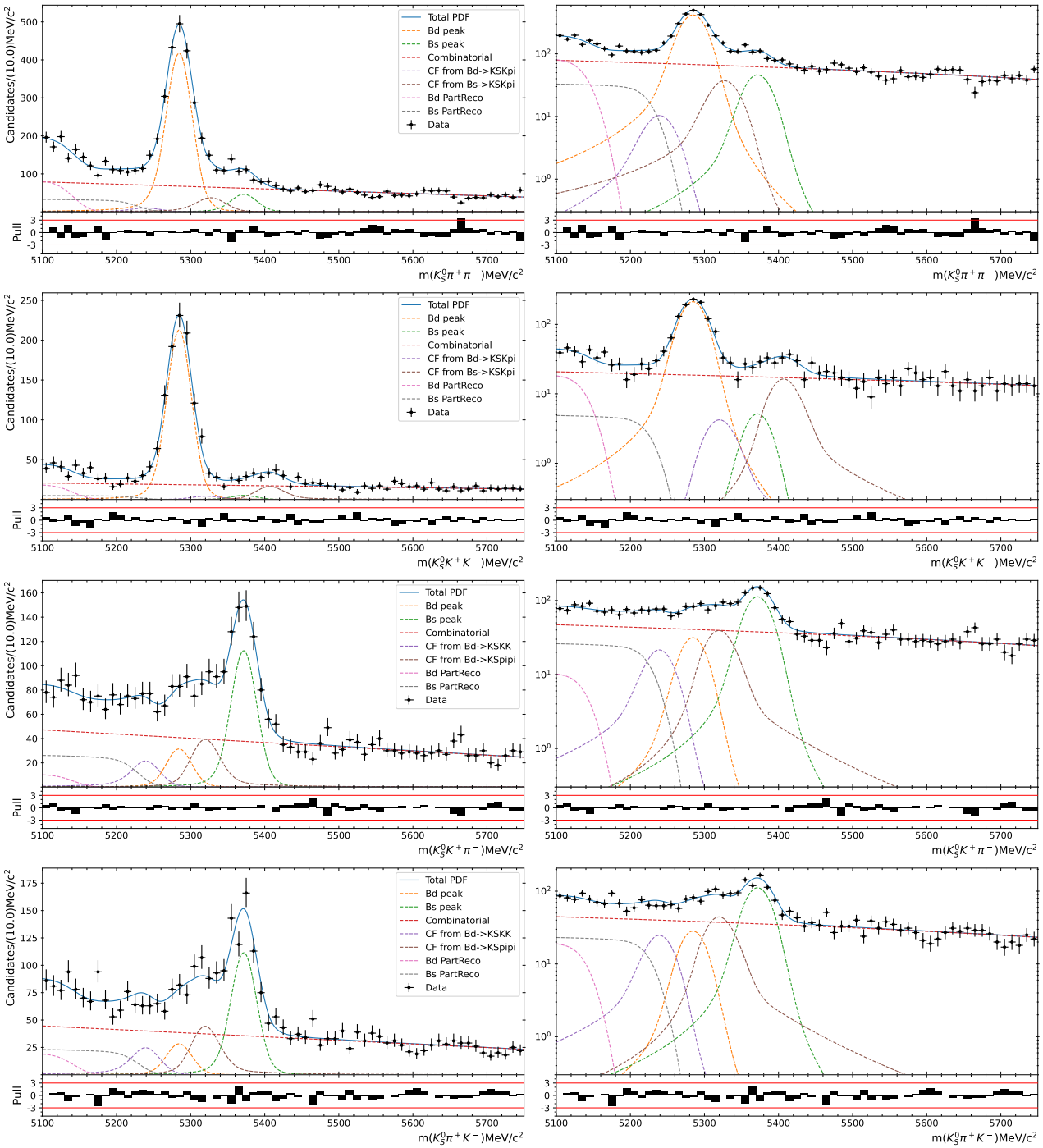

Figure 3.10: Results of the simultaneous fit to data (DD, 2012b) with the PrincipalPeak optimisation. The modes $K^0_S\pi^+\pi^-$, $K^0_SK^+K^-$, $K^0_SK^+\pi^-$ and $K^0_S\pi^+K^-$ are shown from top to bottom. The left-hand side plots show the results with a linear scale and the right-hand side with a logarithmic scale.

SecondaryPeak optimisation

The signal yields and floating parameters from the fits to data using the SecondaryPeak optimisation (optimisation for the suppressed decays) are presented in table 3.11 and table 3.12 respectively. The fit results are shown from Figure 3.11 to 3.24. The background yields are given in Appendix C.2.2.

Compared to the PrincipalPeak optimisation results, smaller yields are obtained, which is expected because the selection used is tighter. This tighter selection allows one to reject more

background, which is instrumental in order to measure the unfavoured mode as indicated by the better backgrounds / unfavoured peaks separations.

As expected, the $K^0_S K^+K^-$ spectrum fits display more clearly the B^0_s signal peaks, compared to the looser optimisation. The $B^0_s \to K^0_S K^+K^-$ signal is unambiguously seen.

Decays	2011	2012a	2012b	2015	2016	2017	2018	Sum
$B^0_d \to K^0_S(\mathrm{LL})\pi^+\pi^-$	$330_{\pm 20}$	$118_{\pm 12}$	$516_{\pm 25}$	$264_{\pm 18}$	$1760_{\pm 50}$	$2040_{\pm 50}$	$2080_{\pm 50}$	$7110_{\pm 90}$
$B^0_d \to K^0_S(\mathrm{DD})\pi^+\pi^-$	$450_{\pm 23}$	$396_{\pm 23}$	$1120_{\pm 40}$	$385_{\pm 22}$	$2990_{\pm 60}$	$3610_{\pm 70}$	$4090_{\pm 70}$	$13040_{\pm 130}$
$B^0_d \to K^0_S(\mathrm{LL})K^+K^-$	$201_{\pm 16}$	$120_{\pm 12}$	$345_{\pm 20}$	$221_{\pm 16}$	$769_{\pm 29}$	$849_{\pm 30}$	$1230_{\pm 40}$	$3730_{\pm 60}$
$B^0_d \to K^0_S(\mathrm{DD})K^+K^-$	$276_{\pm 18}$	$159_{\pm 13}$	$625_{\pm 27}$	$232_{\pm 16}$	$1810_{\pm 40}$	$1640_{\pm 40}$	$2620_{\pm 50}$	$7360_{\pm 90}$
$B^0_d \to K^0_S(\mathrm{LL})K^+\pi^-$	$33_{\pm 7}$	$22_{\pm 6}$	$18_{\pm 6}$	$33_{\pm 9}$	$131_{\pm 18}$	$159_{\pm 19}$	$190_{\pm 20}$	$590_{\pm 40}$
$B^0_d \to K^0_S(\mathrm{DD})K^+\pi^-$	$77_{\pm 14}$	$60_{\pm 11}$	$90_{\pm 14}$	$71_{\pm 12}$	$349_{\pm 30}$	$460_{\pm 40}$	$475_{\pm 33}$	$1580_{\pm 60}$
$B^0_d \to K^0_S(\mathrm{LL})\pi^+K^-$	$47_{\pm 9}$	$31_{\pm 7}$	$42_{\pm 8}$	$23_{\pm 6}$	$196_{\pm 20}$	$180_{\pm 19}$	$214_{\pm 22}$	$730_{\pm 40}$
$B^0_d \to K^0_S(\mathrm{DD})\pi^+K^-$	$99_{\pm 15}$	$24_{\pm 9}$	$99_{\pm 19}$	$46_{\pm 13}$	$369_{\pm 33}$	$416_{\pm 29}$	$472_{\pm 33}$	$1520_{\pm 60}$
$B^0_s \to K^0_S(\mathrm{LL})\pi^+\pi^-$	$18_{\pm 8}$	$13_{\pm 4}$	$40_{\pm 10}$	$22_{\pm 7}$	$128_{\pm 18}$	$106_{\pm 18}$	$165_{\pm 20}$	$490_{\pm 40}$
$B^0_s \to K^0_S(\mathrm{DD})\pi^+\pi^-$	$40_{\pm 9}$	$11_{\pm 8}$	$105_{\pm 15}$	$39_{\pm 9}$	$265_{\pm 26}$	$286_{\pm 26}$	$322_{\pm 28}$	$1070_{\pm 50}$
$B^0_s \to K^0_S(\mathrm{LL})K^+K^-$	$14_{\pm 6}$	$7_{\pm 4}$	$15_{\pm 6}$	$9_{\pm 5}$	$2_{\pm 4}$	$21_{\pm 7}$	$21_{\pm 9}$	$88_{\pm 16}$
$B^0_s \to K^0_S(\mathrm{DD})K^+K^-$	$23_{\pm 7}$	$8_{\pm 4}$	$15_{\pm 7}$	$10_{\pm 5}$	$65_{\pm 12}$	$44_{\pm 10}$	$49_{\pm 14}$	$213_{\pm 24}$
$B^0_s \to K^0_S(\mathrm{LL})K^+\pi^-$	$108_{\pm 12}$	$54_{\pm 9}$	$62_{\pm 9}$	$93_{\pm 12}$	$498_{\pm 26}$	$574_{\pm 28}$	$643_{\pm 30}$	$2030_{\pm 50}$
$B^0_s \to K^0_S(\mathrm{DD})K^+\pi^-$	$214_{\pm 18}$	$129_{\pm 13}$	$342_{\pm 21}$	$155_{\pm 15}$	$1130_{\pm 40}$	$1420_{\pm 50}$	$1500_{\pm 50}$	$4890_{\pm 90}$
$B^0_s \to K^0_S(\mathrm{LL})\pi^+K^-$	$125_{\pm 13}$	$61_{\pm 9}$	$99_{\pm 11}$	$89_{\pm 11}$	$585_{\pm 28}$	$578_{\pm 28}$	$684_{\pm 31}$	$2220_{\pm 50}$
$B^0_s \to K^0_S(\mathrm{DD})\pi^+K^-$	$202_{\pm 17}$	$135_{\pm 15}$	$361_{\pm 25}$	$185_{\pm 18}$	$1230_{\pm 40}$	$1310_{\pm 40}$	$1520_{\pm 50}$	$4930_{\pm 90}$

Table 3.11: Values and statistical uncertainties on the signal yields extracted from the fit to data, in the SecondaryPeak optimisation.

Parameters	2011	2012a	2012b	2015	2016	2017	2018
$\mu(B^0)$	$5284.6_{\pm 0.5}$	$5283.3_{\pm 0.6}$	$5284.4_{\pm 0.4}$	$5280.4_{\pm 0.5}$	$5279.91_{\pm 0.20}$	$5279.73_{\pm 0.19}$	$5280.44_{\pm 0.17}$
$\sigma(\pi\pi)(\mathrm{DD})$	$19.6_{\pm 0.5}$	$17.8_{\pm 0.6}$	$17.24_{\pm 0.33}$	$17.3_{\pm 0.5}$	$17.06_{\pm 0.19}$	$17.37_{\pm 0.18}$	$17.26_{\pm 0.17}$
$c(\pi\pi K^0_S(\mathrm{LL}))$	$-0.88_{\pm 0.12}$	$-0.2_{\pm 0.7}$	$-0.94_{\pm 0.07}$	$-0.73_{\pm 0.18}$	$-0.72_{\pm 0.08}$	$-0.76_{\pm 0.07}$	$-0.52_{\pm 0.09}$
$c(\pi\pi K^0_S(\mathrm{DD}))$	$-0.92_{\pm 0.11}$	$-0.74_{\pm 0.13}$	$-0.48_{\pm 0.13}$	$-0.48_{\pm 0.27}$	$-0.58_{\pm 0.06}$	$-0.56_{\pm 0.07}$	$-0.68_{\pm 0.05}$
$c(KKK^0_S(\mathrm{LL}))$	$-0.08_{\pm 0.33}$	$-0.5_{\pm 0.5}$	$-0.12_{\pm 0.27}$	$-0.69_{\pm 0.27}$	$-0.85_{\pm 0.17}$	$-0.3_{\pm 0.4}$	$-0.51_{\pm 0.13}$
$c(KKK^0_S(\mathrm{DD}))$	$-0.1_{\pm 0.4}$	0	$-0.56_{\pm 0.15}$	$-0.43_{\pm 0.30}$	$-0.66_{\pm 0.10}$	$-0.84_{\pm 0.07}$	$-0.45_{\pm 0.08}$
$c(K\pi K^0_S(\mathrm{LL}))$	$-0.43_{\pm 0.25}$	$-0.32_{\pm 0.30}$	$-0.53_{\pm 0.21}$	$-0.41_{\pm 0.19}$	$-0.67_{\pm 0.06}$	$-0.51_{\pm 0.07}$	$-0.38_{\pm 0.07}$
$c(K\pi K^0_S(\mathrm{DD}))$	$-0.45_{\pm 0.11}$	$-0.47_{\pm 0.13}$	$-0.46_{\pm 0.07}$	$-0.23_{\pm 0.12}$	$-0.36_{\pm 0.04}$	$-0.36_{\pm 0.04}$	$-0.34_{\pm 0.04}$

Table 3.12: Shape parameters extracted from the fit to data using the SecondaryPeak optimisation, with μ the mean of the B^0 peak, σ the width of the $B^0 \to K^0_S$ (DD)$\pi^+\pi^-$ peak and c the slope of the combinatorial background. Fixed parameters are given without uncertainties.

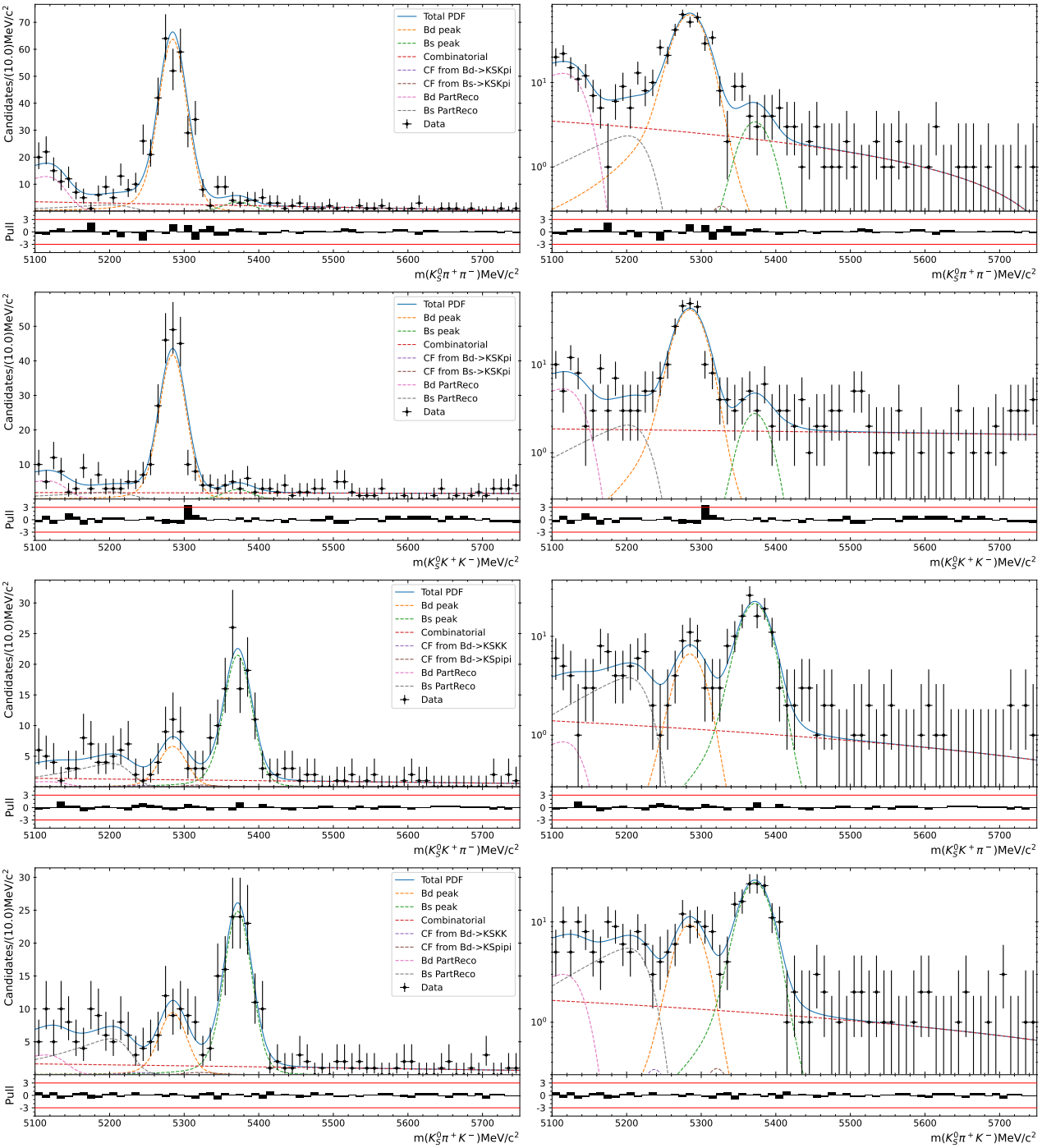

Figure 3.11: Results of the simultaneous fit to data (LL, 2011) with the SecondaryPeak optimisation. The modes $K^0_S\pi^+\pi^-$, $K^0_SK^+K^-$, $K^0_SK^+\pi^-$ and $K^0_S\pi^+K^-$ are shown from top to bottom. The left-hand side plots show the results with a linear scale and the right-hand side with a logarithmic scale.

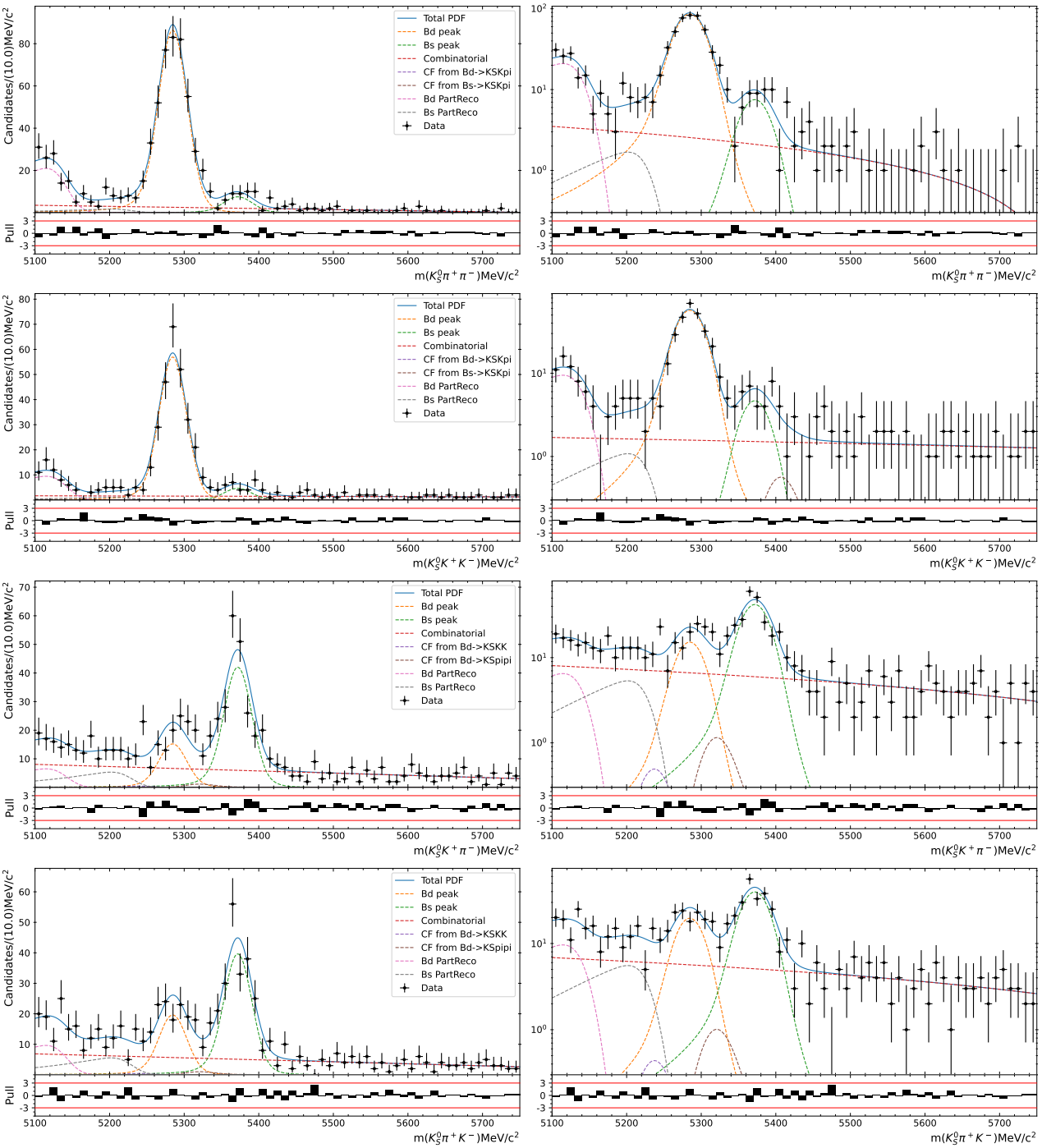

Figure 3.12: Results of the simultaneous fit to data (DD, 2011) with the SecondaryPeak optimisation. The modes $K^0_S\pi^+\pi^-$, $K^0_SK^+K^-$, $K^0_SK^+\pi^-$ and $K^0_S\pi^+K^-$ are shown from top to bottom. The left-hand side plots show the results with a linear scale and the right-hand side with a logarithmic scale.

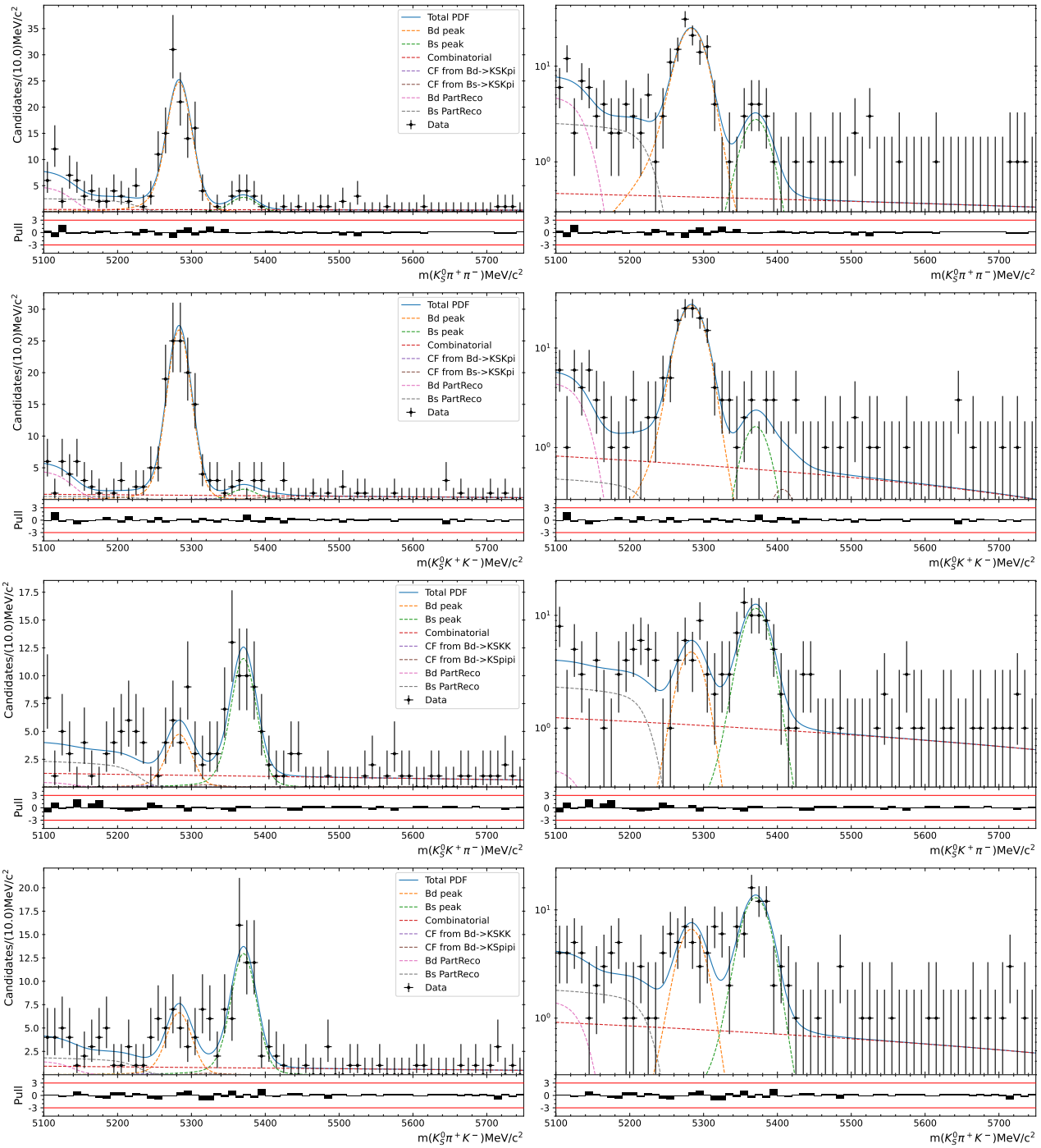

Figure 3.13: Results of the simultaneous fit to data (LL, 2012a) with the SecondaryPeak optimisation. The modes $K^0_S\pi^+\pi^-$, $K^0_SK^+K^-$, $K^0_SK^+\pi^-$ and $K^0_S\pi^+K^-$ are shown from top to bottom. The left-hand side plots show the results with a linear scale and the right-hand side with a logarithmic scale.

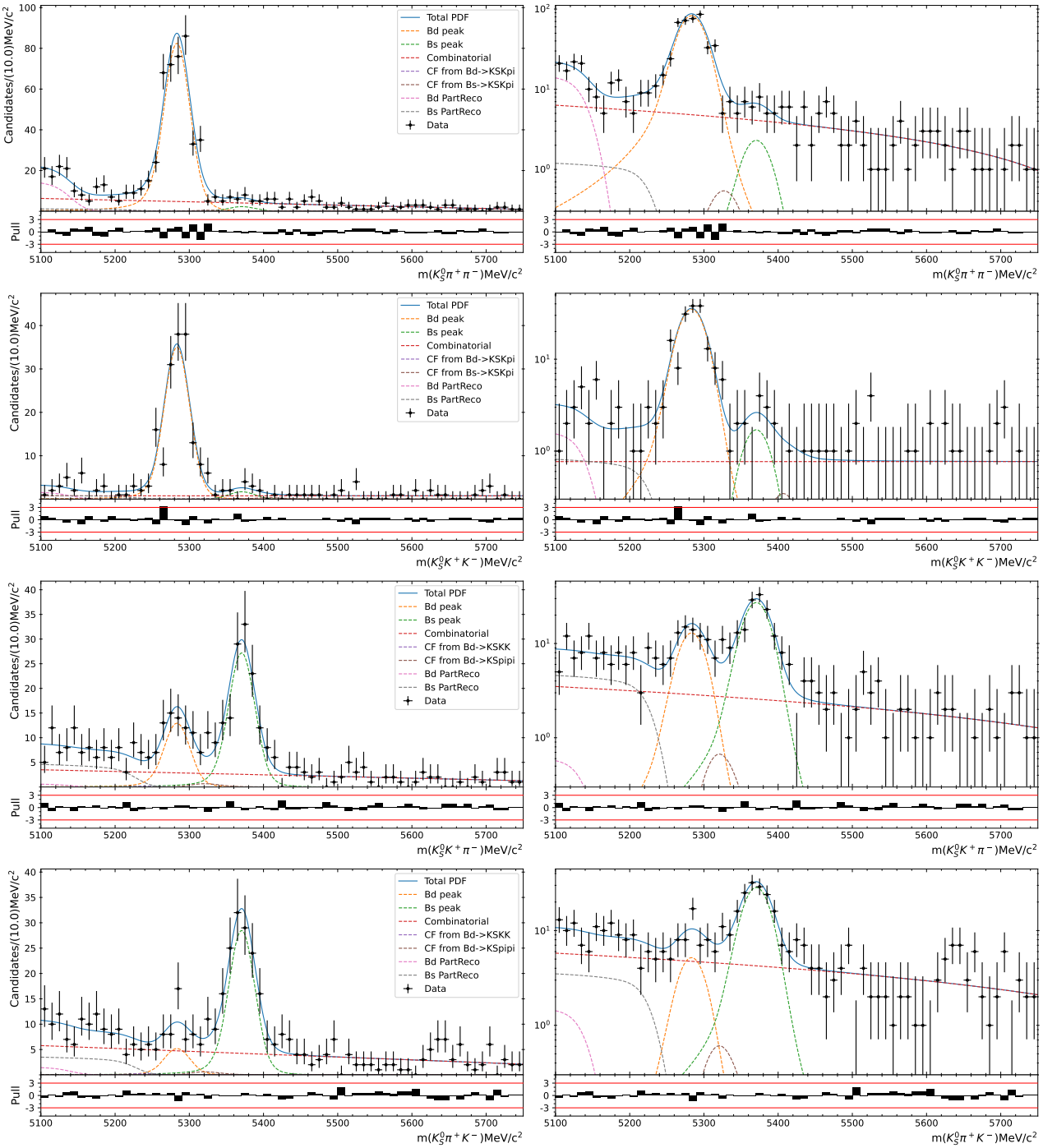

Figure 3.14: Results of the simultaneous fit to data (DD, 2012a) with the SecondaryPeak optimisation. The modes $K^0_S\pi^+\pi^-$, $K^0_SK^+K^-$, $K^0_SK^+\pi^-$ and $K^0_S\pi^+K^-$ are shown from top to bottom. The left-hand side plots show the results with a linear scale and the right-hand side with a logarithmic scale.

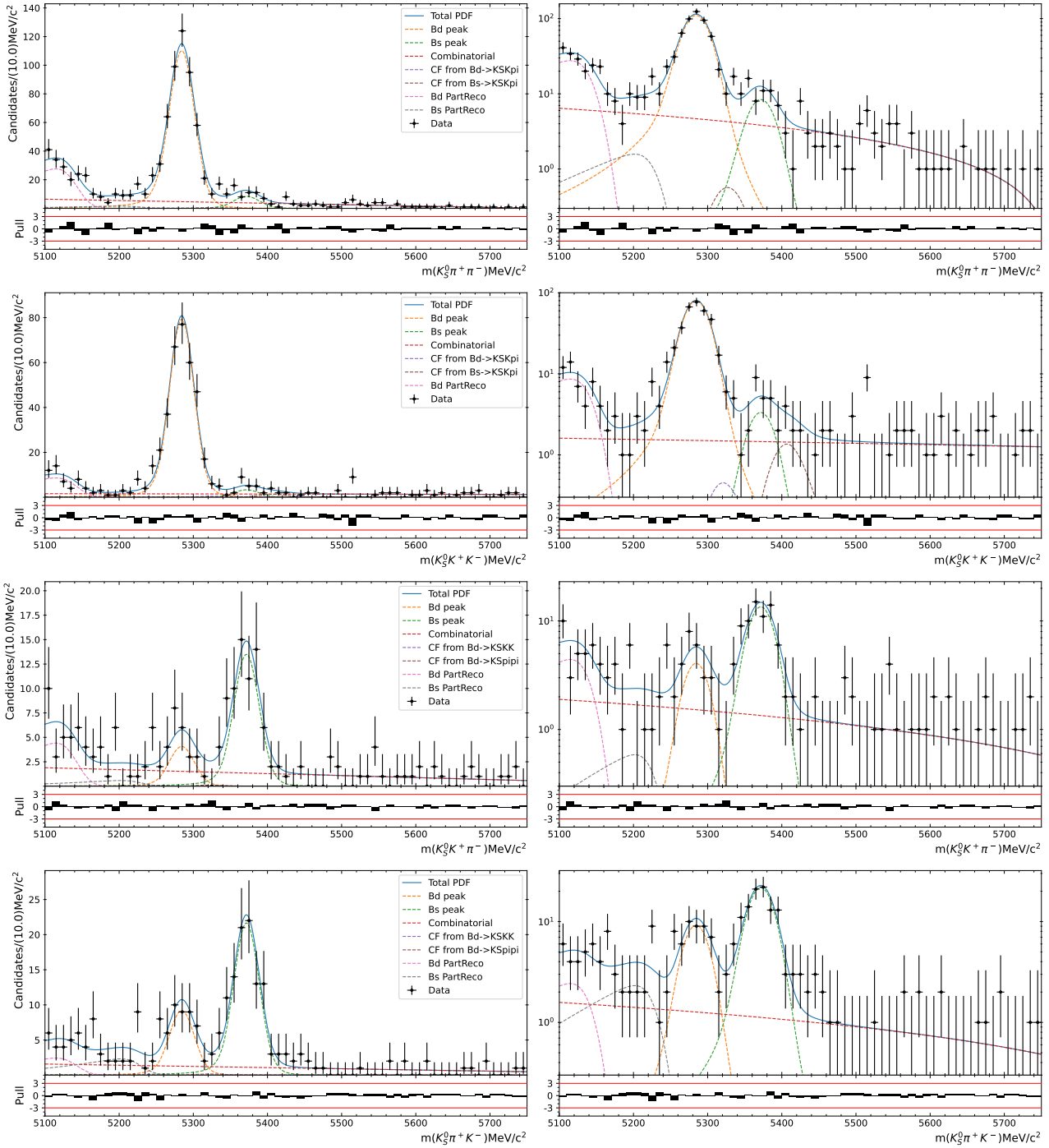

Figure 3.15: Results of the simultaneous fit to data (LL, 2012b) with the SecondaryPeak optimisation. The modes $K^0_S\pi^+\pi^-$, $K^0_SK^+K^-$, $K^0_SK^+\pi^-$ and $K^0_S\pi^+K^-$ are shown from top to bottom. The left-hand side plots show the results with a linear scale and the right-hand side with a logarithmic scale.

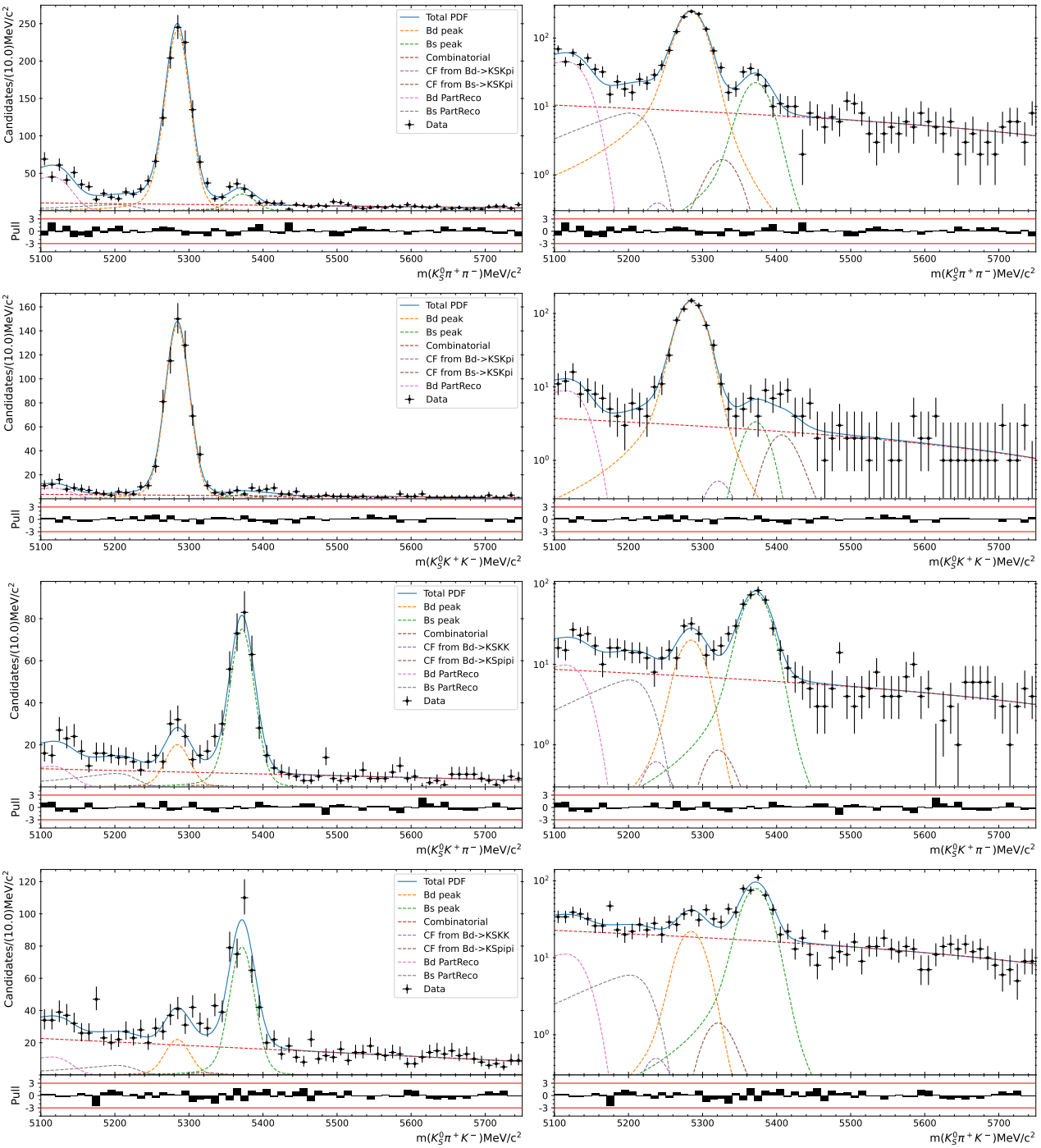

Figure 3.16: Results of the simultaneous fit to data (DD, 2012b) with the SecondaryPeak optimisation. The modes $K^0_S\pi^+\pi^-$, $K^0_SK^+K^-$, $K^0_SK^+\pi^-$ and $K^0_S\pi^+K^-$ are shown from top to bottom. The left-hand side plots show the results with a linear scale and the right-hand side with a logarithmic scale.

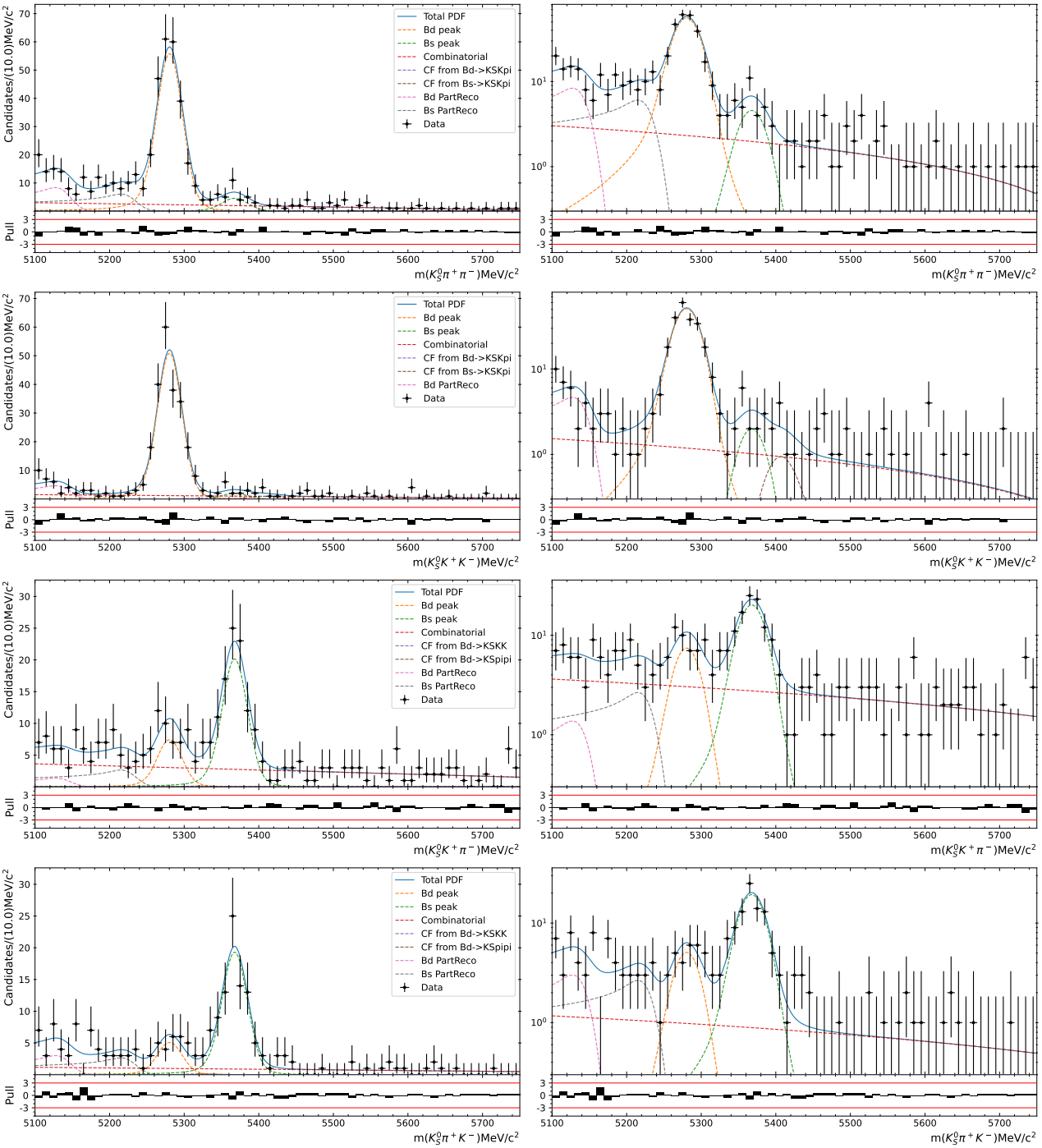

Figure 3.17: Results of the simultaneous fit to data (LL, 2015) with the SecondaryPeak optimisation. The modes $K^0_S\pi^+\pi^-$, $K^0_S K^+ K^-$, $K^0_S K^+\pi^-$ and $K^0_S\pi^+ K^-$ are shown from top to bottom. The left-hand side plots show the results with a linear scale and the right-hand side with a logarithmic scale.

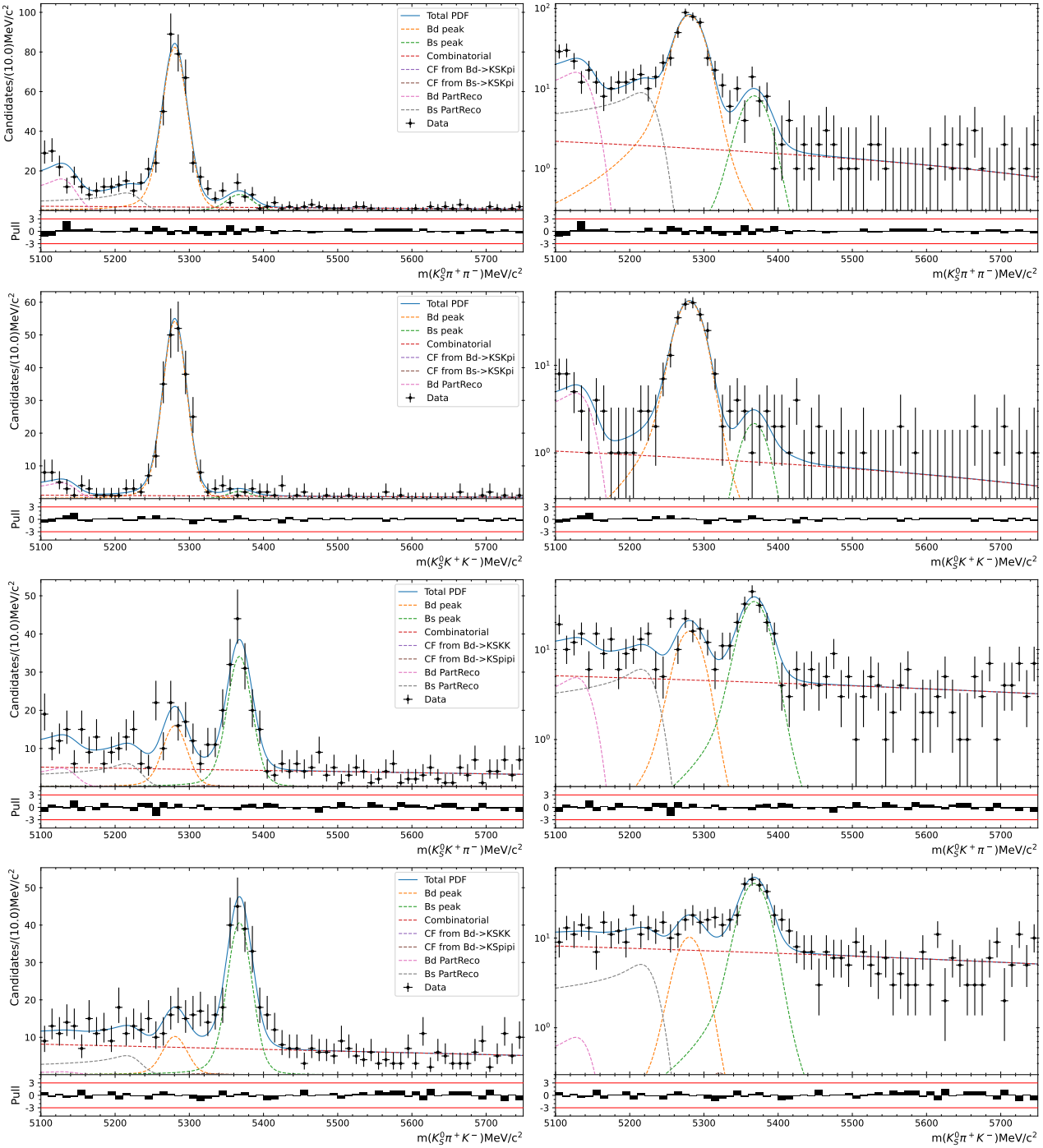

Figure 3.18: Results of the simultaneous fit to data (DD, 2015) with the SecondaryPeak optimisation. The modes $K^0_S\pi^+\pi^-$, $K^0_SK^+K^-$, $K^0_SK^+\pi^-$ and $K^0_S\pi^+K^-$ are shown from top to bottom. The left-hand side plots show the results with a linear scale and the right-hand side with a logarithmic scale.

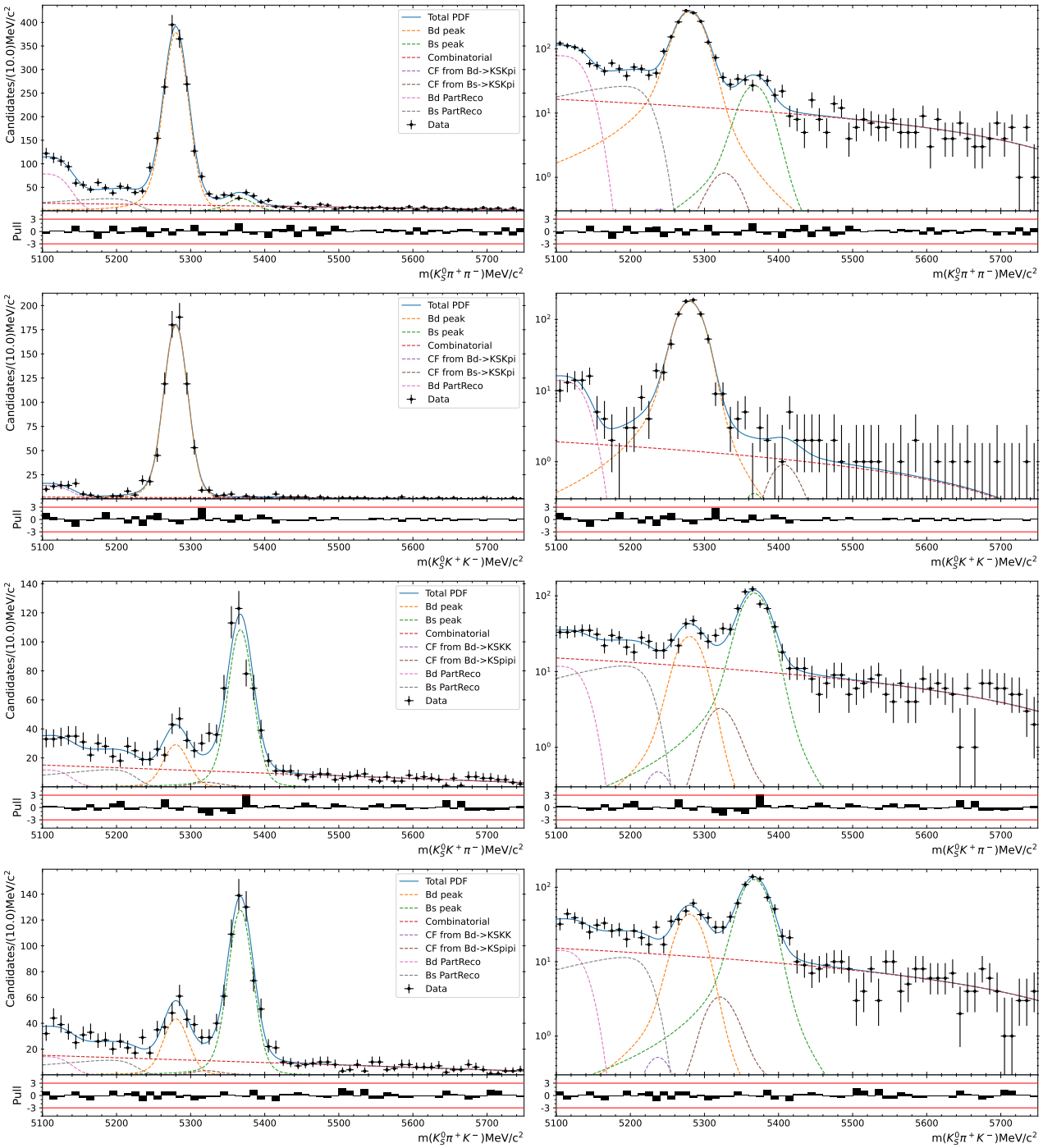

Figure 3.19: Results of the simultaneous fit to data (LL, 2016) with the SecondaryPeak optimisation. The modes $K^0_S\pi^+\pi^-$, $K^0_SK^+K^-$, $K^0_SK^+\pi^-$ and $K^0_S\pi^+K^-$ are shown from top to bottom. The left-hand side plots show the results with a linear scale and the right-hand side with a logarithmic scale.

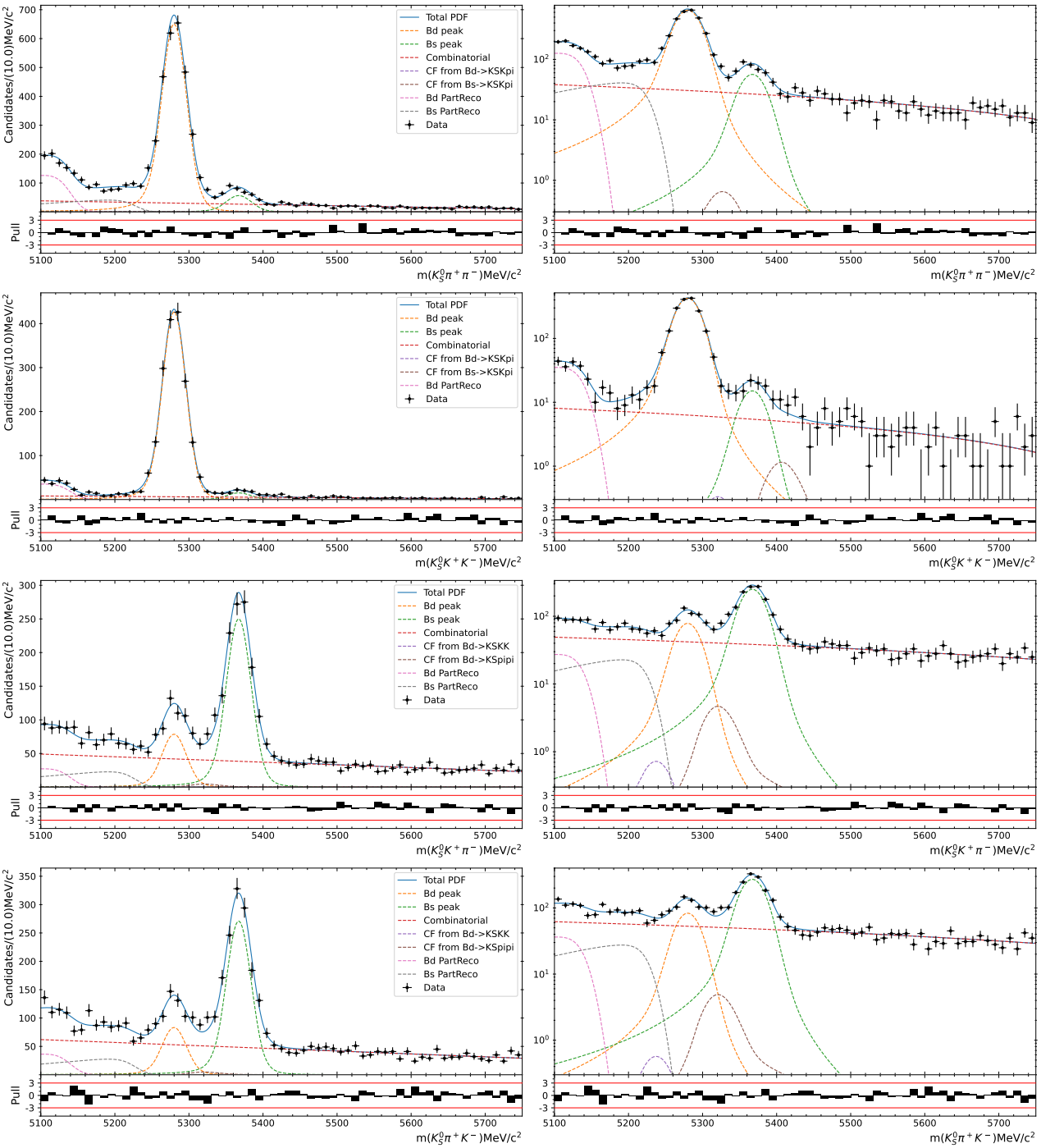

Figure 3.20: Results of the simultaneous fit to data (DD, 2016) with the SecondaryPeak optimisation. The modes $K^0_S\pi^+\pi^-$, $K^0_SK^+K^-$, $K^0_SK^+\pi^-$ and $K^0_S\pi^+K^-$ are shown from top to bottom. The left-hand side plots show the results with a linear scale and the right-hand side with a logarithmic scale. Hint of a missing contribution can bee seen in the $K^0_SK^+K^-$ fit spectrum after the B^0_s crossfeed area, this will be addressed with next update of the analysis.

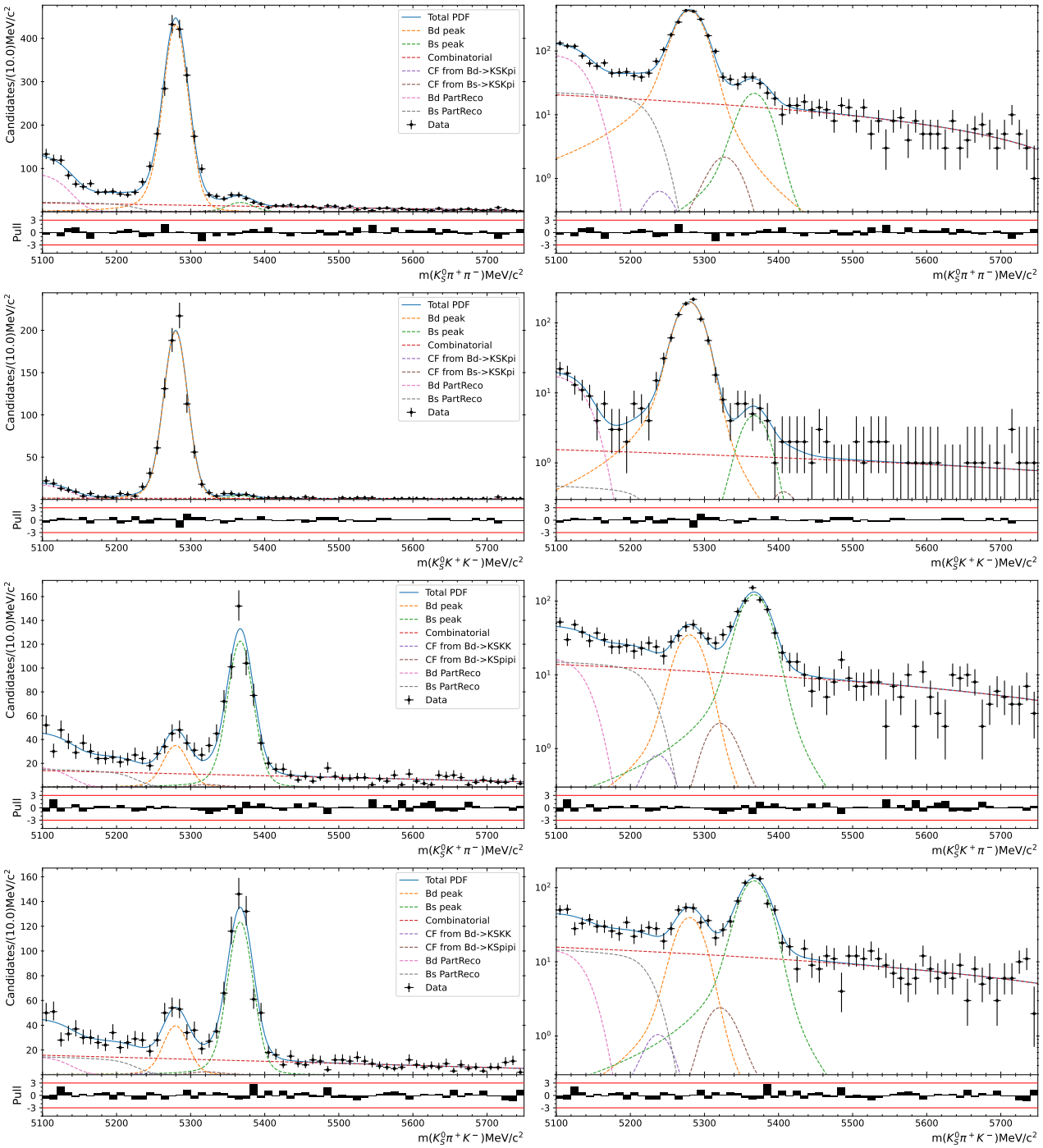

Figure 3.21: Results of the simultaneous fit to data (LL, 2017) with the SecondaryPeak optimisation. The modes $K^0_S\pi^+\pi^-$, $K^0_SK^+K^-$, $K^0_SK^+\pi^-$ and $K^0_S\pi^+K^-$ are shown from top to bottom. The left-hand side plots show the results with a linear scale and the right-hand side with a logarithmic scale.

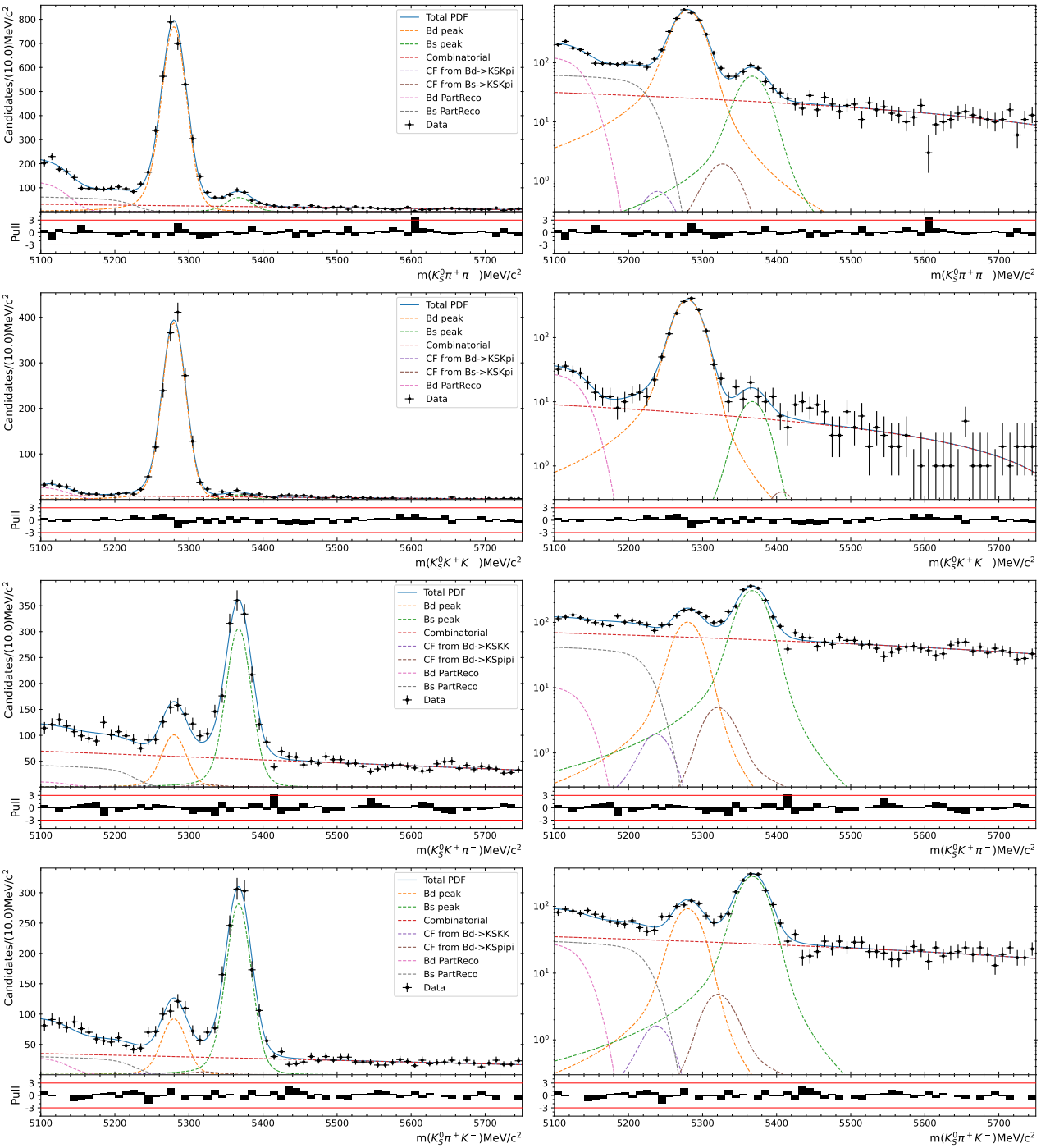

Figure 3.22: Results of the simultaneous fit to data (DD, 2017) with the SecondaryPeak optimisation. The modes $K^0_S\pi^+\pi^-$, $K^0_SK^+K^-$, $K^0_SK^+\pi^-$ and $K^0_S\pi^+K^-$ are shown from top to bottom. The left-hand side plots show the results with a linear scale and the right-hand side with a logarithmic scale. Hint of a missing contribution can bee seen in the $K^0_SK^+K^-$ fit spectrum after the B^0_s crossfeed area, this will be addressed with next update of the analysis.

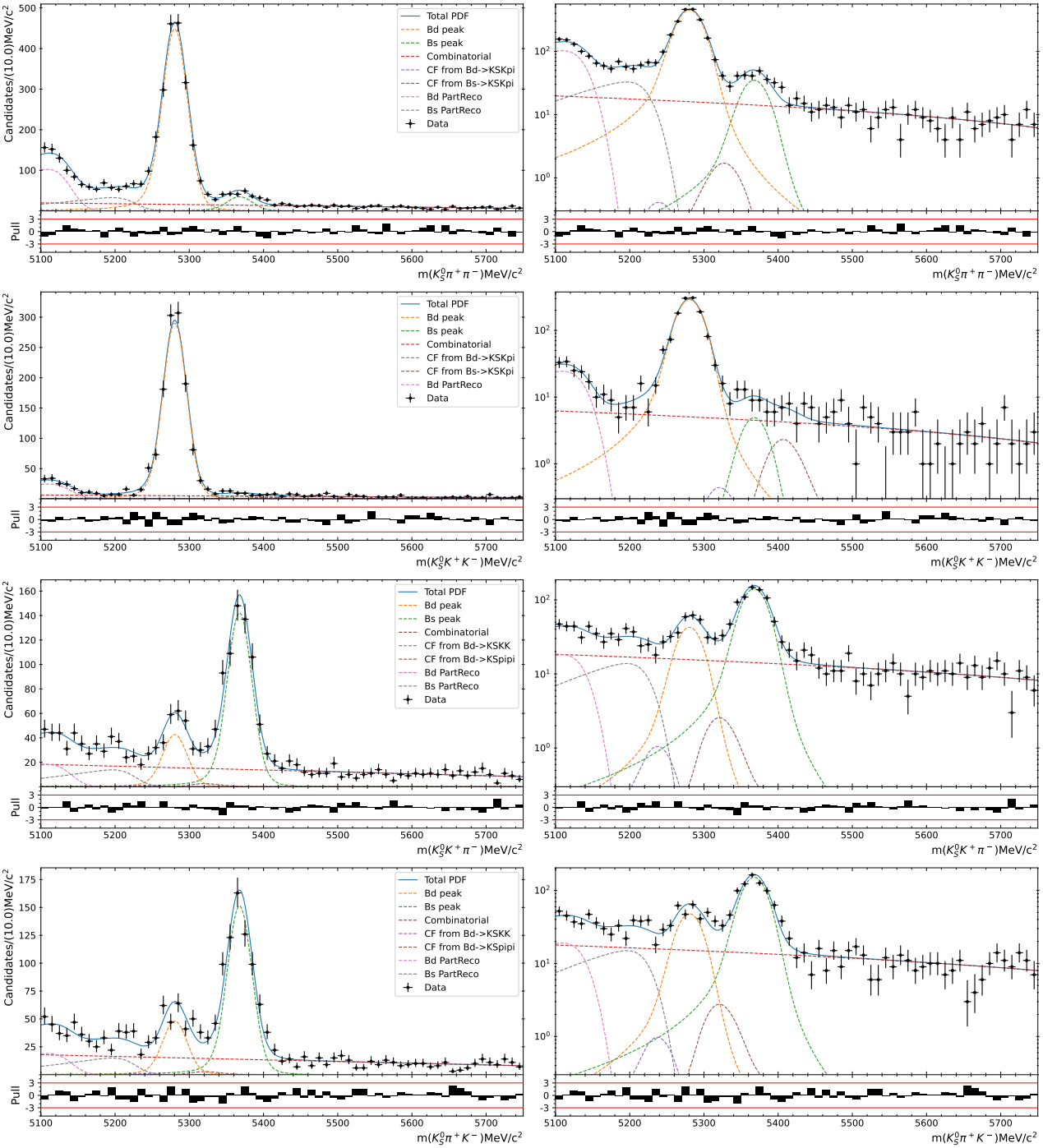

Figure 3.23: Results of the simultaneous fit to data (LL, 2018) with the SecondaryPeak optimisation. The modes $K^0_S\pi^+\pi^-$, $K^0_S K^+K^-$, $K^0_S K^+\pi^-$ and $K^0_S\pi^+K^-$ are shown from top to bottom. The left-hand side plots show the results with a linear scale and the right-hand side with a logarithmic scale.

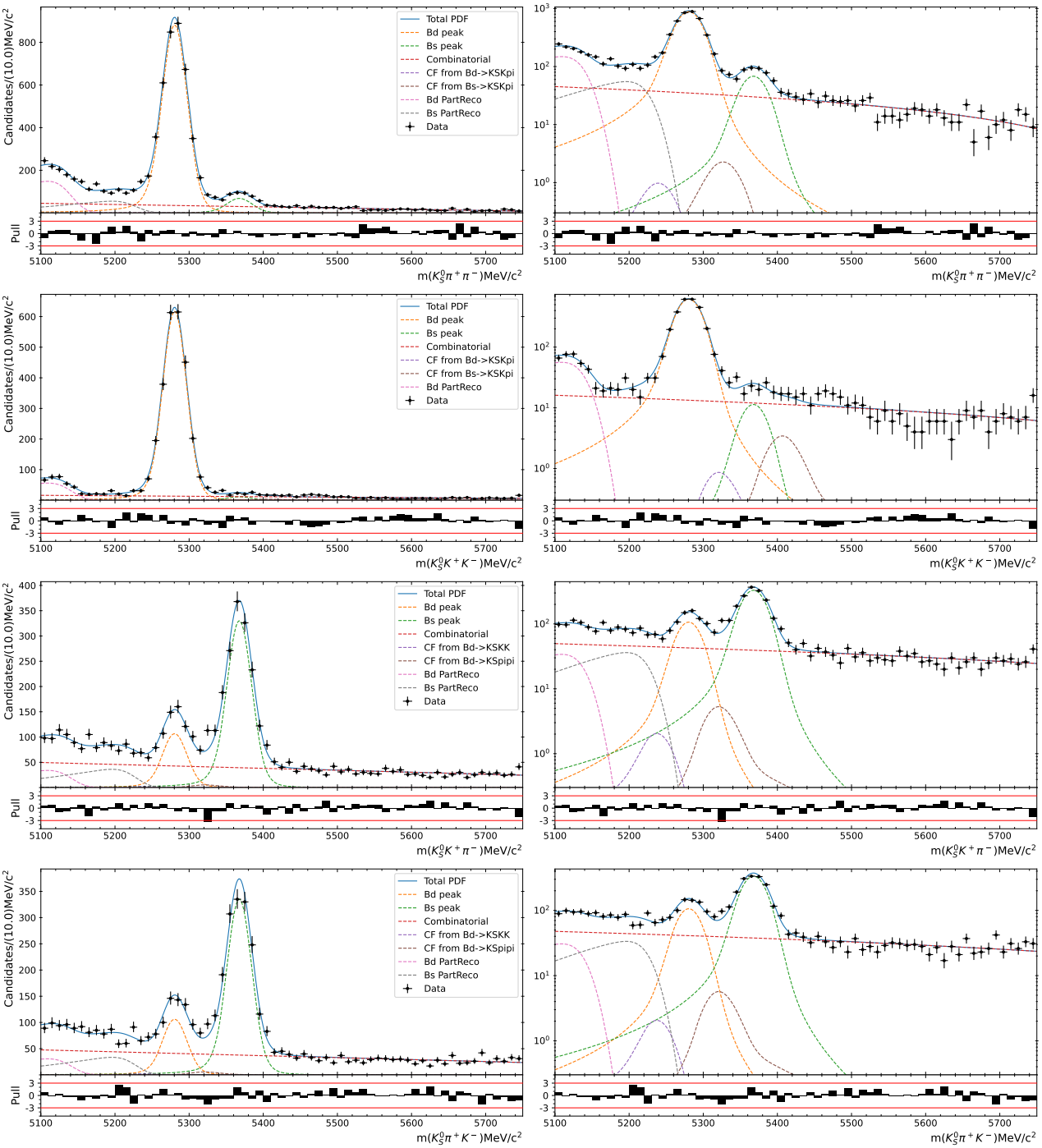

Figure 3.24: Results of the simultaneous fit to data (DD, 2018) with the SecondaryPeak optimisation. The modes $K^0_S\pi^+\pi^-$, $K^0_SK^+K^-$, $K^0_SK^+\pi^-$ and $K^0_S\pi^+K^-$ are shown from top to bottom. The left-hand side plots show the results with a linear scale and the right-hand side with a logarithmic scale. Hint of a missing contribution can bee seen in the $K^0_SK^+K^-$ fit spectrum after the B^0_s crossfeed area, this will be addressed with next update of the analysis.

3.2.3 The *sPlot* method

The events populating each final-state dataset are mixtures of signals and backgrounds, and the phase space of the signal events is not known *a priori*. Information on the signal decays phase space are needed to improve the average efficiency determinations as explained in Section 3.3.

The density estimation technique known as *sPlot* [182] is used on the invariant-mass distributions to predict and reconstruct the distributions of the studied decays in the phase space, here the square Dalitz-plane (see Section 4.1). The parametric descriptions of the signals and the backgrounds obtained from the fits to the mass spectrum are used as input to separate the events into different species. As a result, for each species, a weight denoted as *sWeight* is attributed to each event that quantifies whether this event is part of the considered species.

For each final state, one *sWeight* taking B^0 as the signal (in that case B_s^0 events are considered as background events) and one *sWeight* taking B_s^0 as the signal (in that case B^0 events are considered as background events) are built. The *sWeight* are then applied to the square Dalitz-plane distributions to infer the background-subtracted signal distributions (B^0 or B_s^0) in the Dalitz plane. Figure 3.25 displays the sWeight maps associated to B^0 DD for 2018 and 2012b in the $K_S^0\pi^+\pi^-$ experimental spectrum. The hot bins correspond to the area of sqDP where resonances lie (see Sections 1.4 and 4.1).

This method works here because the invariant mass of the final state (discriminating variable) and the Dalitz plane variables (control variables) are not correlated. For this analysis, the `sweights package` [183] developed from Ref. [184] is used.

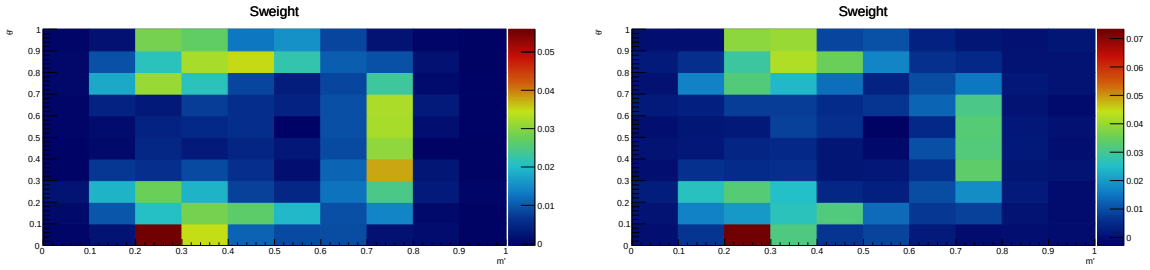

Figure 3.25: B^0 sWeight maps determined on the $K_S^0\pi^+\pi^-$ spectrum with DD K_S^0 reconstruction for 2018 (left) and 2012b (right).

3.3 Efficiency

After the yields, the last pieces needed to determine the branching fraction are the efficiencies. The efficiencies are determined from MC samples on which the selection and reconstruction requirements are applied, by comparing the number of events before and after them. This selection was optimised to provide the best working point for branching fraction studies, while also laying the groundwork for future studies of the Dalitz plot (amplitude analyses, *CP* asymmetry measurements). However, the MC samples do not perfectly reproduce the detector responses and need to be corrected with data calibration samples.

The efficiency of the reconstruction and selection requirements is determined, including how the efficiency varies across the Dalitz plane (in practice the square Dalitz plane denoted as sqDP (see Section 4.1.3)). This variation is not only important for future amplitude analyses but also for the branching fraction measurement: the efficiency corrections require to compute the average efficiency across the sqDP weighted by the distribution of events (see Section 3.2.3), and that distribution is not known a priori (or not well-known in the cases where a knowledge of the amplitude model exists). Thus, to compute the average efficiency, both the event distribution and a description of how the efficiency varies across the sqDP are needed. This is the main goal of this section.

Individual patterns of efficiency components across the sqDP are first introduced in Section 3.3.1. Second, the total efficiency determination in the sqDP is presented in Section 3.3.2. Third, the averaging method used to obtain the individual efficiency number per sample is detailed in Section 3.3.3. And finally, the efficiency tables are given in Section 3.3.4.

3.3.1 Signal efficiency patterns over the DP

Ideally, the efficiency of the signal events would be uniform across Dalitz plane. However, selection cuts, geometrical acceptance, and trigger efficiency decreased the number of events in certain regions of the Dalitz plane more than in other regions. Proper handling of such non-uniformity is crucial at analysis level, because it causes a distortion to the distribution of signal events across the Dalitz plane. The first step is to express the total efficiency ε^{tot} in terms of three distinct components:

$$\varepsilon^{\text{tot}} = \varepsilon^{\text{geom}} \times \varepsilon^{\text{sel|geom}} \times \varepsilon^{\text{PID|sel\&geom}} \tag{3.3.1}$$

where

- $\varepsilon^{\text{geom}}$ is the geometrical and generator level cut efficiency. This efficiency is determined by using MC samples.
- $\varepsilon^{\text{sel|geom}}$ is the selection efficiency which consists of the trigger, stripping and offline selection (except for the PID MVA selector), *given* the geometrical requirements above. This efficiency is also determined from the MC sample. Note that the MC samples will need to be corrected for discrepancies between the data and MC in the tracking and trigger efficiencies.
- $\varepsilon^{\text{PID|sel\&geom}}$ is the efficiency of the particle identification requirements, *given* the selection and geometrical requirements above. This is determined by using the output of the MVA PID selector (see section 3.1.3) on MC samples, corrected via PIDCorr.

The three efficiency components are presented below. Although these individual sources are considered separately, what really counts is the overall efficiency ε^{tot} at each point in the phase space, and that is what will be used in nearly all subsequent calculations.

Acceptance of the Generator Level Cut

To reduce the computational resources used when generating MC samples, a set of cuts is applied at the generation step to reject events for which one or more final-state particles lie outside the detector acceptance. The generator-level cuts used are presented in table 2.6. A key cut applied to the two charged-track decay products of the B is on the angular acceptance, $0.01 < \theta < 0.4\,\text{rad}$, where θ is the angle between the track and the z axis. Geometrical efficiency is measured from MC samples generated in the sqDP by Laura++ [185]. Actually, the events generated by Laura++ were not exactly flat and corrections have been taken into account. The geometrical efficiency of LHCb is determined by applying the LHCb geometry to these samples with Gauss.

Here, it should be considered that it is not necessary to distinguish between triggers or the K^0_S Long-Long and Down-Down categories, because this efficiency is determined solely by the detector geometry and kinematics of the B^0. However, because the B^0 kinematics differ among years of data taking due to the difference in beam energy, it is important to treat each year individually. Figure 3.26 represents the $\varepsilon^{\text{geom}}$ for $B^0 \to K^0_S\pi^+\pi^-$ samples for 2012b and 2018 as an example of Run I and Run II.

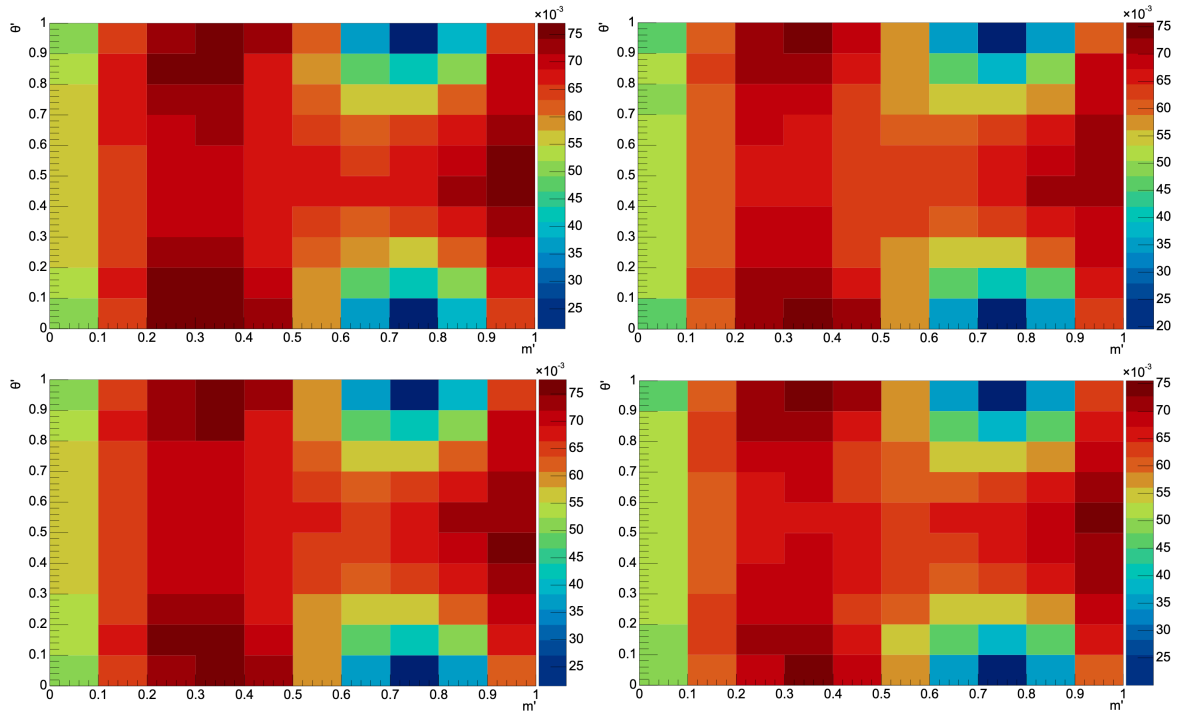

Figure 3.26: Left(Right) $\varepsilon^{\text{geom}}$ across the sqDP for 2018(2012b) $B^0 \to K^0_S\pi^+\pi^-$ samples. Top (Low) row is related to the Up (Down) magnetic separations.

Selection efficiency

To determine selection efficiency, whose requirements consist of trigger, stripping, and topological MVA (derived by 2D optimisation) cuts; the full simulation MC samples are generated with `sqDalitz,TightCut` options (`sqDalitz` means generated flat in the sqDP, `TightCut` stands for the generator level cut displayed in table 2.6) and these selection requirements are applied on it. Since both stripping and multivariate topological selections were defined with the goal of minimal efficiency variation across the Dalitz plane, the most significant contribution to the stiff variation of selection efficiency comes from the trigger selection. There are sources of

discrepancies between MC and data samples related to the tracking and L0 trigger which are discussed in the following.

Data/MC tracking efficiency correction

Following the conventional technique stated in Ref. [186], tracking corrections are made to the selection efficiency to account for the discrepancies in long tracking efficiency for MC and data. The reconstruction efficiency map, for the long tracks, according to the calibration data sample is made by the LHCb Tracking group. This map, also known as the tracking correction table, is made in two bins of pseudorapidity η(1.9-3.2, 3.2-4.9) and five bins of momentum p (5-10, 10–20, 20-40, 40-100, 100-200 GeV/c^2).

To produce the Dalitz plane correction map, first the MC events which the ensemble of cuts of the selection but the PID are selected. The reason to exempt the PID cut is that the PID has many corrections per itself, and since PID depends on the kinematics (and hence tracking reconstruction efficiencies), it is better to factor it out and the tracking efficiency is corrected before getting to the PID. Then, for each event the corresponding p, η, m', and θ' of each B^0-daughter track (except K^0_S daughters) are determined. According to p and η, an efficiency value is selected from the tracking correction table. Then using the corresponding m' and θ' this efficiency is associated to a certain bin of sqDP, and by multiplying the existing values in that bin, a weight is provided that can be used as a correction factor.

In Figure 3.27, the total tracking efficiency correction maps corresponding to the 2018 and 2012b samples, which are calculated by multiplying the corrections for each track event by event is given.

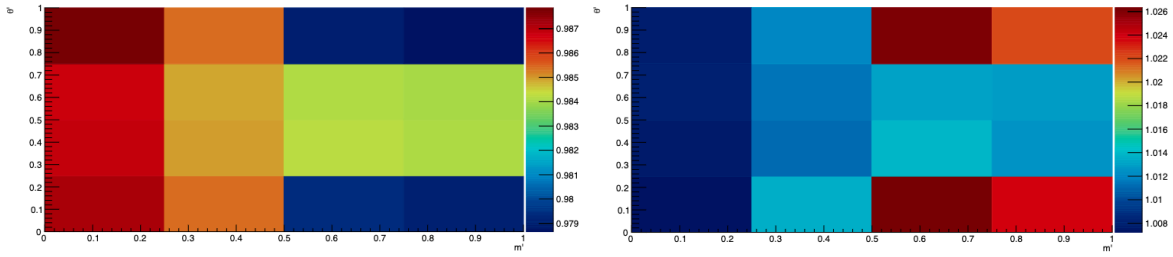

Figure 3.27: Right(Left) tracking efficiency correction C_{tracking} across the sqDP for 2018(2012b) $B^0 \to K^0_S\pi^+\pi^-$ samples.

Data/MC `L0Hadron_TOS` trigger efficiency correction

It is necessary to correct the first-level trigger efficiency in the simulation. Calibration data samples based on reconstructed $D^{(*)}$ candidates with high purity are used to evaluate the `L0Hadron_TOS` track efficiency and provide corrections to MC estimates [187].

Following a data-driven method developed to correct Run II L0Hadron trigger efficiency by taking into account calorimeter effects, such as overlap between the tracks, occupancy and calibration effects, a work has been done to generalise this to the whole LHCb simulations (Run I + Run II) and is presented in Section 2.4. The data calibration samples are D^0 decay candidates issued from a D^* decay, selected with Turbo calibration lines. No a priori trigger L0Hadron trigger requirements are placed. The L0 Hadron trigger efficiency is hence determined as a function of the kinematics of the particles of interest (charged K and π) and includes corrections depending on the calorimeter region, the distance to the closest track, the distance to the beam-pipe and the underlying average energy.

To apply the method to $B^0 \to K^0_S hh'$, simulations without the HLT lines were needed, which was available for the Run1 but not for the Run2 due to the new stripping for these samples. In order to tackle that problem, a set of unfiltered MC samples was used, for which the stripping does not contain the HLT lines. For these unfiltered MC the stripping version is different, however since the stripping was designed to be flat in the sqDP, using these MC samples causes negligible variation with respect to the main ones.

Following the method presented in Appendix C.3 trigger correction maps are provided, built on the sqDP plane, for the $B^0 \to K^0_S hh'$ L0HadronTOS and L0Hadron!TOS&L0TIS events. Corrections are defined as the ratios between the trigger selection efficiencies determined from the data-driven method for the analysis and measured in the MC unfiltered sample. The correction maps are built into sqDP bins. With regard to the physics of interest, it has been decided to use, in order to produce baseline corrections, the underlying energy inputs corresponding to $\bar{b}b$ events. A version with $\bar{c}c$ events can also be used, in all cases the difference between those and the baseline are expected to be low. The $\bar{c}c$ events version will be used to estimate a systematic uncertainty. Figure 3.28 shows the distributions of L0 correction factors for `L0Hadron_TOS` and `L0TIS&!L0Hadron_TOS` for 2018 and 2012b $K^0_S\pi^+\pi^-$ Down-Down downward magnetic direction samples.

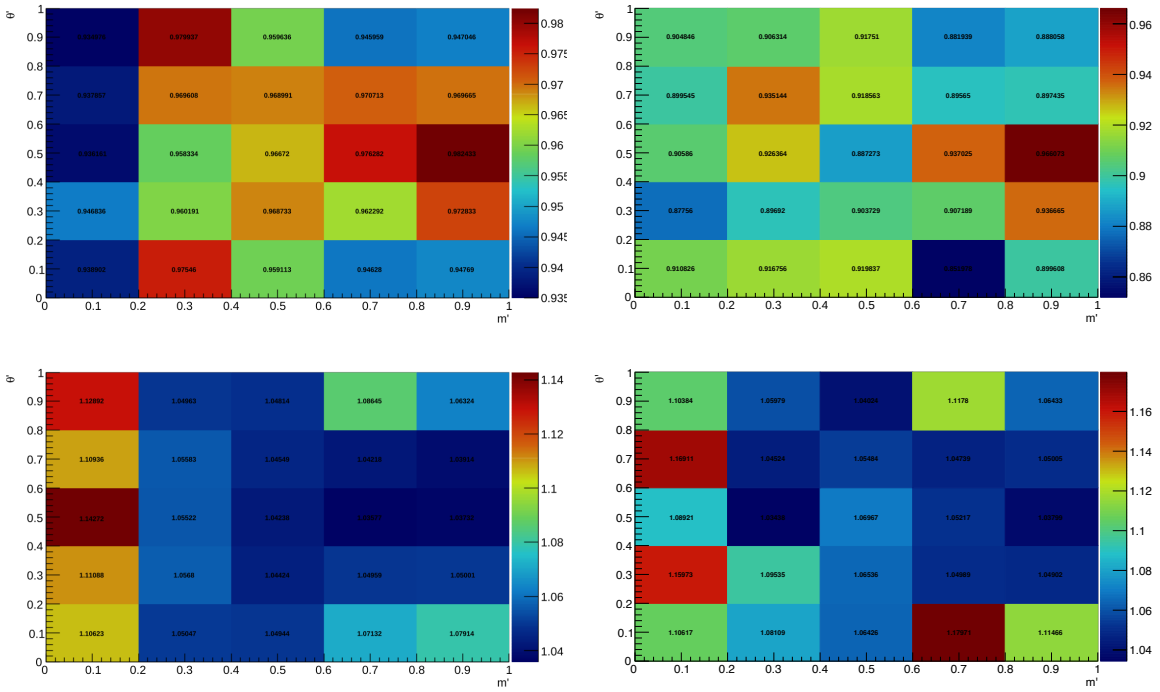

Figure 3.28: Left(right) $C^{\text{TOS}}_{\text{L0corr}} = \varepsilon^{\text{L0TOS}}_{data}/\varepsilon^{\text{L0TOS}}_{MC}$ (top) and $C^{\text{TIS\&!TOS}}_{\text{L0corr}}\varepsilon^{\text{L0TIS\&!L0TOS}}_{data}/\varepsilon^{\text{L0TIS\&!L0TOS}}_{MC}$ (bottom) across the sqDP for 2018(2012b) $B^0 \to K^0_S\pi^+\pi^-$ samples and for the DD K^0_S reconstruction and downward magnetic direction.

PID efficiency

As described in Section 3.1.3, the PID variables of the simulated samples are corrected using `PIDCorr` package prior to the MVA classifier training. The PID efficiency, denoted $\varepsilon^{\text{PID|sel\&geom}}$, is therefore estimated on simulation samples with the corrected version of the individual ProbNN variables. Its estimation receives systematic uncertainties related to the `PIDCorr` use. They are briefly described in Section 3.4, complete details are in the analysis note [169].

3.3.2 Total efficiency

The total selection efficiency can be evaluated by the product of all individual contributions that were discussed above. The formula used to build the corrected efficiency maps is the following:

$$\varepsilon_{\text{tot}}^{\text{corrected}} = \left(\varepsilon_{\text{tot}}^{\text{TOS}} \times C_{\text{L0corr}}^{\text{TOS}} \times \frac{f_{\text{TOS}}^{\text{data}}}{f_{\text{TOS}}^{\text{MC}}} + \varepsilon_{\text{tot}}^{\text{TIS\&!TOS}} \times C_{\text{L0corr}}^{\text{TIS\&!TOS}} \times \frac{f_{\text{TIS\&!TOS}}^{\text{data}}}{f_{\text{TIS\&!TOS}}^{\text{MC}}} \right) \times C_{\text{tracking}} \ , \quad (3.3.2)$$

where $\varepsilon_{\text{tot}}^{\text{TOS}}$ denotes the total selection efficiency for TOS events, $\varepsilon_{\text{tot}}^{\text{TIS\&!TOS}}$ denotes the total selection efficiency for TIS&!TOS events, C_{tracking} denotes the tracking correction, $f_{\text{TOS(TIS\&!TOS)}}^{\text{data(MC)}}$ denotes the fraction of TOS (TIS&!TOS) signal events in data (MC) with $f_{\text{TOS}}^{\text{data}} + f_{\text{TIS\&!TOS}}^{\text{data}} = f_{\text{TOS}}^{\text{MC}} + f_{\text{TIS\&!TOS}}^{\text{MC}} = 1$, $C_{\text{L0}}^{\text{TOS(TIS\&!TOS)}}$ represents the L0Hadron trigger corrections. The ratios $f_{\text{TOS(TIS\&!TOS)}}^{\text{data}} / f_{\text{TOS(TIS\&!TOS)}}^{\text{MC}}$ are needed in order to reweight the trigger corrections applied to the MC with respect to the trigger proportions find in data (a systematic will be dedicated to these ratios). Due to the small statistics of signal events for the unfavoured modes in data, the trigger fractions are always determined with the favoured modes and are then applied to the unfavoured mode (kinematically close).

Figures 3.29 and 3.30 show these maps next to their corresponding statistical uncertainties, which are defined for each bin as the binomial distribution variance corresponding to the efficiency, for 2012b and 2018 $B^0 \to K_S^0 \pi^+ \pi^-$ DD samples, respectively.

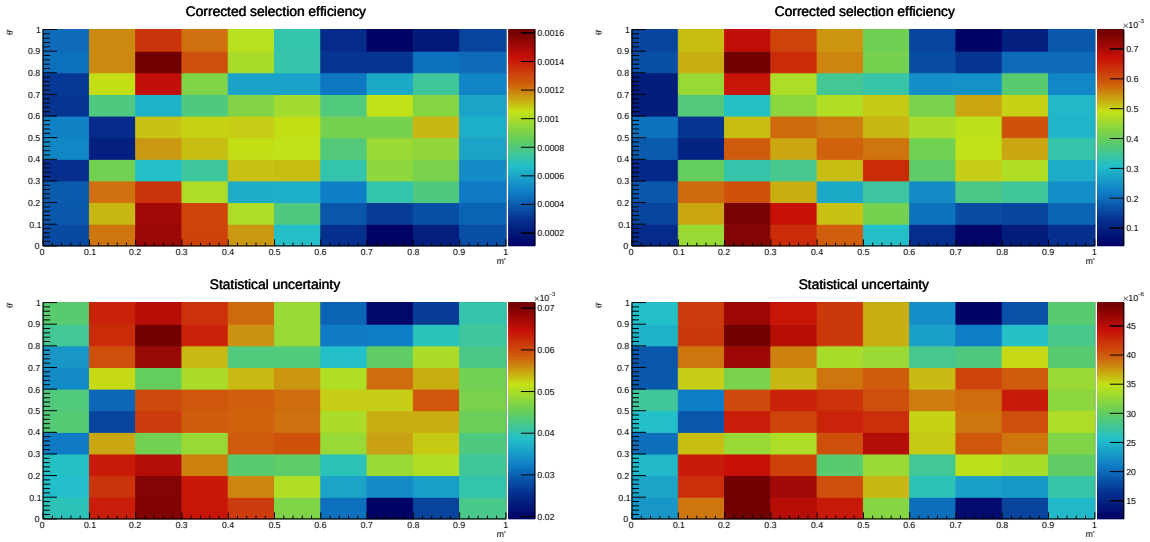

Figure 3.29: Left(Right) column represents $\varepsilon_{\text{tot}}^{\text{corrected}}$ across the Dalitz plane for favoured (unfavoured) mode selection of 2018 $B^0 \to K_S^0 \pi^+ \pi^-$ samples for the DD K_S^0 reconstruction and downward magnetic direction. The first row denote the total efficiency, and the second row denote the statistical uncertainty, respectively.

3.3.3 Average efficiency computation

Efficiency maps have been determined previously for each sample (see Section 3.3.2), *i.e.* one efficiency map per $B-$type (B^0/B_s^0), decay mode, MVA optimisation, K_S^0 reconstruction, data taking period, and magnet polarity (compared to the data, the MC has been split, in addition, with respect to the LHCb magnet polarity).

To calculate the average efficiency for a given sample, the phase space seen as the sqDP is divided into smaller regions (bins) j. Then the average efficiency is given by:

$$\bar{\varepsilon} = \frac{\sum_j S_j}{\sum_j S_j \varepsilon_j^{-1}} = \frac{\sum_j N_j \varepsilon_j}{\sum_j N_j}, \quad (3.3.3)$$

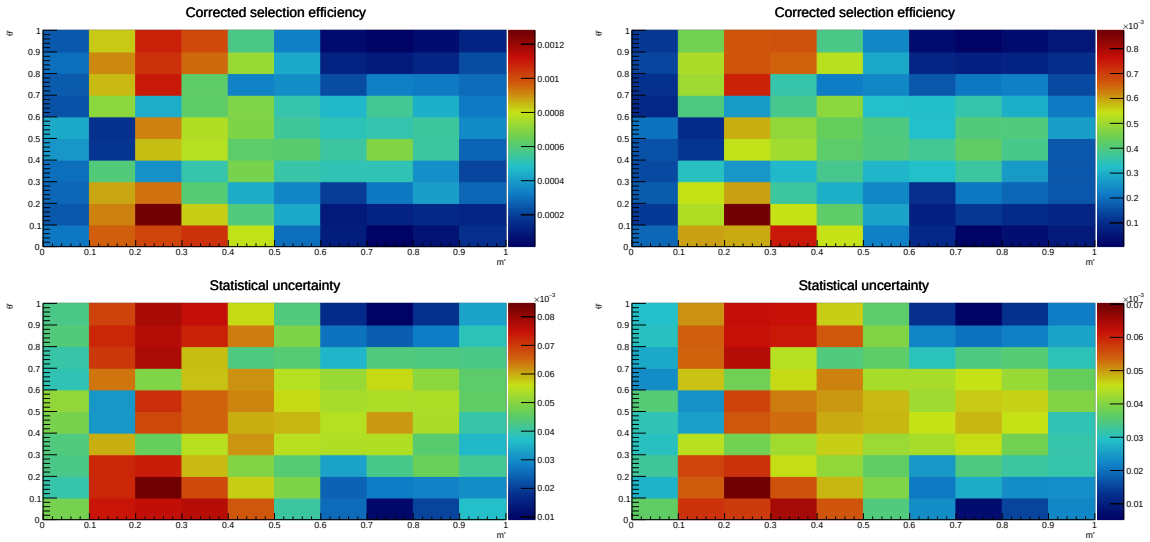

Figure 3.30: Left(Right) column represents $\varepsilon_{\text{tot}}^{\text{corrected}}$ across the Dalitz plane for favoured (unfavoured) mode selection of 2012b $B^0 \to K^0_S \pi^+ \pi^-$ samples for the DD K^0_S reconstruction and downward magnetic direction. The first row denote the total efficiency, and the second row denote the statistical uncertainty, respectively.

where S_j is the expected number of events observed in bin j, ε_j denotes the total corrected efficiency (see equation 3.3.2) in bin j (assumed constant within the bin) and $N_j = S_j \varepsilon_j^{-1}$ is the expected number of events generated in bin j (unknown). The observed numbers of events in bin j is used as an estimator of S_j. Finally, sWeights (see Section 3.2.3) in bin j are taken to model the expected number of events in this bin. This assumption is allowed because empty bins do not contribute in the computation.

By adding a second index k for data-taking periods, we get:

- $\varepsilon_{j,k}$: the total efficiency in bin j for period k for a given subsample ($B-$type, decay mode, magnet polarity, MVA optimisation, K^0_S reconstruction),
- $N_{j,k}$: the expected number of events generated in bin j for period k,
- $S_{j,k}$: the expected number of events observed in bin j for period k, with $S_{j,k} = \varepsilon_{j,k} N_{j,k}$,
- $\bar{\varepsilon}_k$: the weighted-average efficiency for period k.

And the average efficiency of equation 3.3.3 can be rewritten independently for each subsample and data taking period as:

$$\bar{\varepsilon}_k = \frac{\sum_j S_{j,k}}{\sum_j S_{j,k} \varepsilon_{j,k}^{-1}} = \frac{\sum_j N_{j,k} \varepsilon_{j,k}}{\sum_j N_{j,k}}. \tag{3.3.4}$$

However, the expected yields between periods for a given subsample are linked, because the physics (underlying Dalitz plot distribution) are the same. $N_{j,k}$ can read as:

$$N_{j,k} = P_j A_j L_k, \tag{3.3.5}$$

where P_j is the PDF in bin j (assumed constant with the considered bin size), A_j is the phase space of bin j (area for the case of a classical sqDP), and L_k denotes the size of the subsample for the period k. At first order L_k can be seen as the product of the integrated luminosity with the cross section (different from year to year). Using this notation:

$$\frac{N_{j,k}}{L_k} = P_j A_j = cst, \tag{3.3.6}$$

and finally:

$$\frac{N_{j,k}}{L_k} = \frac{N_{j,k'}}{L'_k}, \tag{3.3.7}$$

where k' denotes another period w.r.t. k.

It is now possible to scale the subsample for the period k with another period k':

$$N_{j,k} = N_{j,k'} \frac{L_k}{L'_k}, \tag{3.3.8}$$

and this allows to calculate average efficiency in one subsample period by using another one period as reference. For example, it allows one to use a high statistic period as a reference to compute efficiency of a low statistic period. It is now possible to inject 3.3.8 in 3.3.4, for the general case where a different period is taken as reference for numerator and denominator, the average efficiency becomes:

$$\begin{aligned}
\bar{\varepsilon}_k &= \frac{\sum_j N_{j,k}\varepsilon_{j,k}}{\sum_j N_{j,k}} \\
&= \frac{\sum_j N_{j,k'} \frac{L_k}{L'_k} \varepsilon_{j,k}}{\sum_j N_{j,k''} \frac{L_k}{L''_k}} \\
&= \frac{L''_k}{L'_k} \frac{\sum_j N_{j,k'}\varepsilon_{j,k}}{\sum_j N_{j,k''}} \\
&= \frac{L''_k}{L'_k} \frac{\sum_j S_{j,k'}\varepsilon^{-1}_{j,k'}\varepsilon_{j,k}}{\sum_j S_{j,k''}\varepsilon^{-1}_{j,k''}}.
\end{aligned}$$

By assuming using the same reference in numerator and denominator:

$$\bar{\varepsilon}_k = \frac{\sum_j S_{j,k'}\varepsilon^{-1}_{j,k'}\varepsilon_{j,k}}{\sum_j S_{j,k'}\varepsilon^{-1}_{j,k'}}. \tag{3.3.9}$$

The efficiency ratio introduced in the numerator with respect to equation 3.3.4 converts the computed period from the phase space one to another one. As an example, the indices could be $k' = 2018$ to denote high statistic period and $k = 2012a$ to denote a low statistic period for a given subsample. Then the average efficiencies for 2012a can be computed with 2012a efficiency maps, 2018 sWeights maps, and 2018 efficiency maps.

This allows a more accurate average efficiency determination for the low statistics periods (for which the sWeights can not be accurately determined) as well as for the high statistics periods. It is actually possible to use several phase spaces for each computation and combine the results. Equation 3.3.9 can be rewritten as:

$$\bar{\varepsilon}_{k,k'} = \frac{\sum_j sW_{j,k'}\varepsilon^{-1}_{j,k'}\varepsilon_{j,k}}{\sum_j sW_{j,k'}\varepsilon^{-1}_{j,k'}}, \tag{3.3.10}$$

where $\bar{\varepsilon}_{k,k'}$ is the average efficiency for period k computed with period k' as reference and $S_{j,k'}$ is explicitly replaced by $sW_{j,k'}$. This notation allows to combine information from multiple years by defining the new average efficiency for a given subsample and period k as:

$$\bar{\varepsilon}_k = \frac{\sum_{k'} \bar{\varepsilon}_{k,k'}\omega_{k'}}{\sum_{k'} \omega_{k'}}, \tag{3.3.11}$$

where ω are a set of weights to account for the luminosity of each reference period. Since only the large statistics samples have been used as reference years (2016, 2017 and 2018), a weight

unity is eventually assigned for each reference year, provided that the luminosities are close enough and that other factors (such as optimisation and fit model) should be accounted for. The efficiency finally reads as:

$$\bar{\varepsilon}_k = \frac{\sum_{k'} \bar{\varepsilon}_{k,k'}}{3}. \tag{3.3.12}$$

In the following, the uncertainties directly attached to the formula 3.3.12 are described, and these uncertainties will be part of the efficiency systematics described later in Section 3.4.

The first source of uncertainty comes from the current year k efficiency in each bin, denoting the statistical uncertainty attached to the size of the MC sample of the current year. In each k' computation, this uncertainty map is the same, and the assigned uncertainty is therefore provided by the arithmetic mean over reference years:

$$\sigma_{\bar{\varepsilon}_{1k}} = \frac{\sum_{k'} \sqrt{\sum_j \left(\frac{\partial \bar{\varepsilon}_{k,k'}}{\partial \varepsilon_{j,k}} . \sigma_{\varepsilon_{j,k}} \right)^2}}{3} = \frac{\sum_{k'} \sqrt{\frac{\sum_j (sW_{j,k'} \varepsilon_{j,k'}^{-1} \sigma_{\varepsilon_{j,k}})^2}{(\sum_j sW_{j,k'} \varepsilon_{j,k'}^{-1})^2}}}{3}. \tag{3.3.13}$$

The second source comes from the reference years k' efficiencies in each bin, denoting the statistical uncertainty attached to the size of the MC sample of the reference years. Since the uncertainty map is different and uncorrelated for each reference year, the assigned uncertainty is provided by a weighted average:

$$\frac{1}{\sigma^2_{\bar{\varepsilon}_{2k}}} = \sum_{k'} \frac{1}{\sigma^2_{\bar{\varepsilon}_{2kk'}}}, \tag{3.3.14}$$

where:

$$\begin{aligned}
\sigma^2_{\bar{\varepsilon}_{2kk'}} &= \sum_j \left(\frac{\partial \bar{\varepsilon}_{k,k'}}{\partial \varepsilon_{j,k'}} \sigma_{\varepsilon_{j,k'}} \right)^2 \\
&= \frac{1}{(\sum_{j'} sW_{j',k'} \varepsilon_{j',k'}^{-1})^4} [\sum_j (sW_{j,k'} \varepsilon_{j,k'}^{-2} \sigma_{\varepsilon_{j,k'}})^2 (\sum_{j'} sW_{j',k'} \varepsilon_{j',k'}^{-1} \varepsilon_{j',k})^2 + \\
&\sum_j (sW_{j,k'} \varepsilon_{j,k'}^{-2} \varepsilon_{j,k} \sigma_{\varepsilon_{j,k'}})^2 (\sum_{j'} sW_{j',k'} \varepsilon_{j',k'}^{-1})^2 - \\
&\sum_j 2(sW^2_{j,k'} \varepsilon_{j,k'}^{-4} \varepsilon_{j,k} \sigma^2_{\varepsilon_{j,k'}}) (\sum_{j'} sW_{j',k'} \varepsilon_{j',k'}^{-1} \varepsilon_{j',k}) (\sum_{j'} sW_{j',k'} \varepsilon_{j',k'}^{-1})].
\end{aligned}$$

In addition, a third source of uncertainty has been considered: the variation of the phase space attached to the choice of the reference. The distribution of the difference between the average efficiency $\bar{\varepsilon}_k$ (magnet polarity combined see section 3.3.4) and the average efficiency given by one reference period $\bar{\varepsilon}_{k,k'}$, denoted as Δ, is built per mode (e.g. the different $B^0_{d,s} \to K^0_S h^+ h'^-$ possibilities), K^0_S reconstruction type and MVA optimisation (magnet polarity combination is detailed in section 3.3.4):

$$\Delta = \bar{\varepsilon}_k - \bar{\varepsilon}_{k,k'} \forall k, k'. \tag{3.3.15}$$

The RMS of the distribution is assigned as an uncertainty :

$$\sigma_{\bar{\varepsilon}_{3k}} = \mathrm{RMS}(\Delta_\mathrm{m}), \tag{3.3.16}$$

where m denotes a mode, K^0_S reconstruction type and optimisation type.

The tables of the detailed efficiencies, before the magnet recombination, can be found in Appendix C.4.

The MC samples statistics uncertainty is gathered into $\sigma^{\mathrm{stat}}_{\bar{\varepsilon}_k} = \sqrt{\sigma^2_{\bar{\varepsilon}_{1k}} + \sigma^2_{\bar{\varepsilon}_{2k}}}$ and the third uncertainty is an uncertainty related to the method displayed independently in the following as

$\sigma^{\mathrm{RMS}}_{\bar{\varepsilon}_k}$. At this stage the uncertainty attached to the average efficiency of period k reads:

$$\sigma_{\bar{\varepsilon}_k} = \sqrt{\sigma^{\mathrm{stat}\,2}_{\bar{\varepsilon}_k} + \sigma^{\mathrm{RMS}\,2}_{\bar{\varepsilon}_k}}. \tag{3.3.17}$$

Equation 3.3.12 is used for each year k with $2018, 2017, 2016$ as reference year k' because those are the high statistic periods. The suppressed mode optimisation is taken for each reference as there have phase spaces less populated by backgrounds.

3.3.4 Efficiency tables

The equations 3.3.12 and 3.3.17 are used following the method previously explained in order to determine for each year, decay mode, fit type optimisation, K^0_S reconstruction type, and magnet polarity the average efficiencies and the related uncertainties.

To prepare the use of the average efficiencies together with the yields extracted in section 3.2.2 for which there is no split in polarity, it is necessary to combine for each entry the average efficiencies determined for the two polarities. Among the periods, LHCb has not recorded the same number of events for the two polarities. In order to make an educated averaging of the MagUp and MagDown efficiency, the fraction of events recorded per period for each polarity have been determined following the information given by the LHCb run database from the recorded luminosities. The table 3.13 summarises the results of the MagUp and MagDown fractions to consider per period. The efficiency combination formula is given in equation 3.3.18:

$$\bar{\varepsilon}_i = F_{MD\,y} \times \bar{\varepsilon}_{MD\,i} + F_{MU\,y} \times \bar{\varepsilon}_{MU\,i}. \tag{3.3.18}$$

where i denotes a given sample (year, decay mode, fit type optimisation, K^0_S reconstruction type), $F_{X\,y}$ is the fraction of X polarity to consider for the y period and $\bar{\varepsilon}$ stand for average efficiency.

The related uncertainty is built by taking care of the fact that the σ^{RMS} component of the average efficiencies defined in equation 3.3.16 is by construction identical among the two polarites. The strategy to tackle this rightly is first to combine the σ^{stat} components of the uncertainty defined in equation 3.3.17 following the classic uncertainty propagation formula, as written in equation 3.3.19:

$$\sigma^{\mathrm{stat}}_{\bar{\varepsilon}_i} = \sqrt{(F_{MD\,y} \times \sigma^{\mathrm{stat}}_{\bar{\varepsilon}_{MD\,i}})^2 + (F_{MU\,y} \times \sigma^{\mathrm{stat}}_{\bar{\varepsilon}_{MU\,i}})^2}, \tag{3.3.19}$$

where $\sigma^{\mathrm{stat}}_{\bar{\varepsilon}_{MX\,i}}$ is the statistical uncertainty attached to polarity MX. Secondly the RMS contribution is added quadratically following equation 3.3.20:

$$\sigma_{\bar{\varepsilon}_i} = \sqrt{(\sigma^{\mathrm{stat}}_{\bar{\varepsilon}_i})^2 + (\sigma^{\mathrm{RMS}}_{\bar{\varepsilon}_i})^2}, \tag{3.3.20}$$

where $\sigma^{\mathrm{RMS}}_{\bar{\varepsilon}_i}$ is the second component of the uncertainty defined in equation 3.3.17 (identical among polarities).

The efficiency tables built following the method explained above for $B^0 \to K^0_{\mathrm{S}}\pi^+\pi^-$, $B^0 \to K^0_{\mathrm{S}}K^+K^-$ and $B^0_s \to K^0_{\mathrm{S}}\pi^+\pi^-$ are given in tables 3.14 to 3.19. All other tables are provided in Appendix C.5.

Some comments are in order to discuss the different tables. Since the cuts are different from year to year, it is not expected that identical or even consistent efficiency values are obtained. They are however found in the same ballpark. The two optimisations are very apart, the tighter one provides on average half the one obtained for the favoured optimisation. From year to year, by construction of the method, the uncertainties related to the averaging method (RMS) are identical. By contrast it can be observed that they are varying from mode to mode: the amplitude of the uncertainty reflects the consistency of the three determinations for each year of interest. It is remarkable (though expected) to notice that the largest σ^{RMS} correspond to the signal modes with the largest background contaminations.

Period	MD luminosity (fb^{-1})	MU luminosity (fb^{-1})	F_{MD}	F_{MU}
2011	0.609	0.485	0.550	0.450
2012a	0.328	0.287	0.533	0.467
2012b	0.726	0.741	0.495	0.505
2015	0.193	0.137	0.585	0.415
2016	0.868	0.797	0.521	0.479
2017	0.981	0.835	0.540	0.460
2018	1.046	1.131	0.481	0.519

Table 3.13: Summary table of the recorded luminosity per year per magnet polarity, infered from LHCb run database, and the corresponding polarity fractions.

Year	Mode	K_S^0	$\bar{\varepsilon}$	$\sigma_{\bar{\varepsilon}}^{\text{stat}}$	$\sigma_{\bar{\varepsilon}}^{\text{RMS}}$	$\sigma_{\bar{\varepsilon}}$
2018	$B_d^0 \to K_S^0\pi^+\pi^-$	DD	821.0e-6	6.2e-6	12.2e-6	13.7e-6
2017	$B_d^0 \to K_S^0\pi^+\pi^-$	DD	833.3e-6	6.4e-6	12.2e-6	13.8e-6
2016	$B_d^0 \to K_S^0\pi^+\pi^-$	DD	869.3e-6	6.6e-6	12.2e-6	13.9e-6
2015	$B_d^0 \to K_S^0\pi^+\pi^-$	DD	835.9e-6	6.5e-6	12.2e-6	13.8e-6
2012b	$B_d^0 \to K_S^0\pi^+\pi^-$	DD	519.4e-6	5.8e-6	12.2e-6	13.5e-6
2012a	$B_d^0 \to K_S^0\pi^+\pi^-$	DD	411.6e-6	5.6e-6	12.2e-6	13.4e-6
2011	$B_d^0 \to K_S^0\pi^+\pi^-$	DD	492.0e-6	6.0e-6	12.2e-6	13.6e-6
2018	$B_d^0 \to K_S^0\pi^+\pi^-$	LL	296.9e-6	3.7e-6	6.5e-6	7.5e-6
2017	$B_d^0 \to K_S^0\pi^+\pi^-$	LL	316.9e-6	4.0e-6	6.5e-6	7.6e-6
2016	$B_d^0 \to K_S^0\pi^+\pi^-$	LL	356.3e-6	4.3e-6	6.5e-6	7.8e-6
2015	$B_d^0 \to K_S^0\pi^+\pi^-$	LL	327.5e-6	4.1e-6	6.5e-6	7.7e-6
2012b	$B_d^0 \to K_S^0\pi^+\pi^-$	LL	153.3e-6	3.1e-6	6.5e-6	7.2e-6
2012a	$B_d^0 \to K_S^0\pi^+\pi^-$	LL	176.8e-6	3.7e-6	6.5e-6	7.5e-6
2011	$B_d^0 \to K_S^0\pi^+\pi^-$	LL	187.7e-6	3.8e-6	6.5e-6	7.5e-6

Table 3.14: $B^0 \to K_S^0\pi^+\pi^-$ efficiency tables with the favoured mode optimisation. For each year and K_S^0 reconstruction type, the average efficiency $\bar{\varepsilon}$, the statistical uncertainty $\sigma_{\bar{\varepsilon}}^{\text{stat}}$, the uncertainty linked to the averaging method $\sigma_{\bar{\varepsilon}}^{\text{RMS}}$ and the total uncertainty $\sigma_{\bar{\varepsilon}}$ are given.

Year	Mode	K_S^0	$\bar{\varepsilon}$	$\sigma_{\bar{\varepsilon}}^{\text{stat}}$	$\sigma_{\bar{\varepsilon}}^{\text{RMS}}$	$\sigma_{\bar{\varepsilon}}$
2018	$B_d^0 \to K_S^0\pi^+\pi^-$	DD	413.3e-6	4.1e-6	6.3e-6	7.5e-6
2017	$B_d^0 \to K_S^0\pi^+\pi^-$	DD	442.3e-6	4.4e-6	6.3e-6	7.6e-6
2016	$B_d^0 \to K_S^0\pi^+\pi^-$	DD	438.9e-6	4.3e-6	6.3e-6	7.6e-6
2015	$B_d^0 \to K_S^0\pi^+\pi^-$	DD	346.6e-6	3.8e-6	6.3e-6	7.3e-6
2012b	$B_d^0 \to K_S^0\pi^+\pi^-$	DD	343.8e-6	4.6e-6	6.3e-6	7.8e-6
2012a	$B_d^0 \to K_S^0\pi^+\pi^-$	DD	233.1e-6	4.1e-6	6.3e-6	7.5e-6
2011	$B_d^0 \to K_S^0\pi^+\pi^-$	DD	238.5e-6	4.0e-6	6.3e-6	7.5e-6
2018	$B_d^0 \to K_S^0\pi^+\pi^-$	LL	190.8e-6	2.8e-6	4.4e-6	5.2e-6
2017	$B_d^0 \to K_S^0\pi^+\pi^-$	LL	215.3e-6	3.2e-6	4.4e-6	5.4e-6
2016	$B_d^0 \to K_S^0\pi^+\pi^-$	LL	221.4e-6	3.2e-6	4.4e-6	5.4e-6
2015	$B_d^0 \to K_S^0\pi^+\pi^-$	LL	199.2e-6	3.1e-6	4.4e-6	5.3e-6
2012b	$B_d^0 \to K_S^0\pi^+\pi^-$	LL	108.5e-6	2.6e-6	4.4e-6	5.1e-6
2012a	$B_d^0 \to K_S^0\pi^+\pi^-$	LL	77.8e-6	2.4e-6	4.4e-6	5.0e-6
2011	$B_d^0 \to K_S^0\pi^+\pi^-$	LL	132.9e-6	3.1e-6	4.4e-6	5.4e-6

Table 3.15: $B^0 \to K_S^0\pi^+\pi^-$ efficiency tables with the unfavoured mode optimisation. For each year and K_S^0 reconstruction type, the average efficiency $\bar{\varepsilon}$, the statistical uncertainty $\sigma_{\bar{\varepsilon}}^{\text{stat}}$, the uncertainty linked to the averaging method $\sigma_{\bar{\varepsilon}}^{\text{RMS}}$ and the total uncertainty $\sigma_{\bar{\varepsilon}}$ are given.

Year	Mode	K_S^0	$\bar{\varepsilon}$	$\sigma_{\bar{\varepsilon}}^{\text{stat}}$	$\sigma_{\bar{\varepsilon}}^{\text{RMS}}$	$\sigma_{\bar{\varepsilon}}$
2018	$B_d^0 \to K_S^0 K^+ K^-$	DD	728.2e-6	5.2e-6	3.2e-6	6.1e-6
2017	$B_d^0 \to K_S^0 K^+ K^-$	DD	751.5e-6	5.5e-6	3.2e-6	6.4e-6
2016	$B_d^0 \to K_S^0 K^+ K^-$	DD	893.4e-6	6.0e-6	3.2e-6	6.8e-6
2015	$B_d^0 \to K_S^0 K^+ K^-$	DD	803.7e-6	5.8e-6	3.2e-6	6.6e-6
2012b	$B_d^0 \to K_S^0 K^+ K^-$	DD	449.6e-6	5.5e-6	3.2e-6	6.4e-6
2012a	$B_d^0 \to K_S^0 K^+ K^-$	DD	311.5e-6	4.9e-6	3.2e-6	5.9e-6
2011	$B_d^0 \to K_S^0 K^+ K^-$	DD	360.3e-6	4.8e-6	3.2e-6	5.8e-6
2018	$B_d^0 \to K_S^0 K^+ K^-$	LL	304.8e-6	3.3e-6	2.1e-6	3.9e-6
2017	$B_d^0 \to K_S^0 K^+ K^-$	LL	329.4e-6	3.6e-6	2.1e-6	4.2e-6
2016	$B_d^0 \to K_S^0 K^+ K^-$	LL	370.3e-6	3.8e-6	2.1e-6	4.4e-6
2015	$B_d^0 \to K_S^0 K^+ K^-$	LL	332.8e-6	3.7e-6	2.1e-6	4.3e-6
2012b	$B_d^0 \to K_S^0 K^+ K^-$	LL	147.1e-6	3.2e-6	2.1e-6	3.8e-6
2012a	$B_d^0 \to K_S^0 K^+ K^-$	LL	168.0e-6	3.6e-6	2.1e-6	4.2e-6
2011	$B_d^0 \to K_S^0 K^+ K^-$	LL	190.0e-6	3.6e-6	2.1e-6	4.1e-6

Table 3.16: $B^0 \to K_S^0 K^+ K^-$ efficiency tables with the favoured mode optimisation. For each year and K_S^0 reconstruction type, the average efficiency $\bar{\varepsilon}$, the statistical uncertainty $\sigma_{\bar{\varepsilon}}^{\text{stat}}$, the uncertainty linked to the averaging method $\sigma_{\bar{\varepsilon}}^{\text{RMS}}$ and the total uncertainty $\sigma_{\bar{\varepsilon}}$ are given.

Year	Mode	K_S^0	$\bar{\varepsilon}$	$\sigma_{\bar{\varepsilon}}^{\text{stat}}$	$\sigma_{\bar{\varepsilon}}^{\text{RMS}}$	$\sigma_{\bar{\varepsilon}}$
2018	$B_d^0 \to K_S^0 K^+ K^-$	DD	485.0e-6	4.2e-6	2.0e-6	4.7e-6
2017	$B_d^0 \to K_S^0 K^+ K^-$	DD	374.2e-6	3.9e-6	2.0e-6	4.4e-6
2016	$B_d^0 \to K_S^0 K^+ K^-$	DD	479.3e-6	4.4e-6	2.0e-6	4.8e-6
2015	$B_d^0 \to K_S^0 K^+ K^-$	DD	400.2e-6	4.1e-6	2.0e-6	4.6e-6
2012b	$B_d^0 \to K_S^0 K^+ K^-$	DD	334.3e-6	4.8e-6	2.0e-6	5.2e-6
2012a	$B_d^0 \to K_S^0 K^+ K^-$	DD	210.6e-6	4.1e-6	2.0e-6	4.5e-6
2011	$B_d^0 \to K_S^0 K^+ K^-$	DD	275.2e-6	4.2e-6	2.0e-6	4.7e-6
2018	$B_d^0 \to K_S^0 K^+ K^-$	LL	218.4e-6	2.8e-6	1.5e-6	3.1e-6
2017	$B_d^0 \to K_S^0 K^+ K^-$	LL	183.7e-6	2.7e-6	1.5e-6	3.1e-6
2016	$B_d^0 \to K_S^0 K^+ K^-$	LL	199.7e-6	2.8e-6	1.5e-6	3.2e-6
2015	$B_d^0 \to K_S^0 K^+ K^-$	LL	280.2e-6	3.4e-6	1.5e-6	3.7e-6
2012b	$B_d^0 \to K_S^0 K^+ K^-$	LL	124.0e-6	2.9e-6	1.5e-6	3.3e-6
2012a	$B_d^0 \to K_S^0 K^+ K^-$	LL	141.3e-6	3.3e-6	1.5e-6	3.6e-6
2011	$B_d^0 \to K_S^0 K^+ K^-$	LL	137.9e-6	3.1e-6	1.5e-6	3.4e-6

Table 3.17: $B^0 \to K_S^0 K^+ K^-$ efficiency tables with the unfavoured mode optimisation. For each year and K_S^0 reconstruction type, the average efficiency $\bar{\varepsilon}$, the statistical uncertainty $\sigma_{\bar{\varepsilon}}^{\text{stat}}$, the uncertainty linked to the averaging method $\sigma_{\bar{\varepsilon}}^{\text{RMS}}$ and the total uncertainty $\sigma_{\bar{\varepsilon}}$ are given.

Year	Mode	K_S^0	$\bar{\varepsilon}$	$\sigma_{\bar{\varepsilon}}^{\text{stat}}$	$\sigma_{\bar{\varepsilon}}^{\text{RMS}}$	$\sigma_{\bar{\varepsilon}}$
2018	$B_s^0 \to K_S^0\pi^+\pi^-$	DD	870.9e-6	8.1e-6	35.1e-6	36.0e-6
2017	$B_s^0 \to K_S^0\pi^+\pi^-$	DD	884.3e-6	8.4e-6	35.1e-6	36.1e-6
2016	$B_s^0 \to K_S^0\pi^+\pi^-$	DD	913.6e-6	8.8e-6	35.1e-6	36.2e-6
2015	$B_s^0 \to K_S^0\pi^+\pi^-$	DD	897.2e-6	8.8e-6	35.1e-6	36.2e-6
2012b	$B_s^0 \to K_S^0\pi^+\pi^-$	DD	570.0e-6	8.2e-6	35.1e-6	36.0e-6
2012a	$B_s^0 \to K_S^0\pi^+\pi^-$	DD	458.5e-6	7.6e-6	35.1e-6	35.9e-6
2011	$B_s^0 \to K_S^0\pi^+\pi^-$	DD	548.4e-6	7.8e-6	35.1e-6	35.9e-6
2018	$B_s^0 \to K_S^0\pi^+\pi^-$	LL	329.3e-6	6.2e-6	8.2e-6	10.3e-6
2017	$B_s^0 \to K_S^0\pi^+\pi^-$	LL	357.1e-6	6.5e-6	8.2e-6	10.5e-6
2016	$B_s^0 \to K_S^0\pi^+\pi^-$	LL	397.8e-6	7.2e-6	8.2e-6	10.9e-6
2015	$B_s^0 \to K_S^0\pi^+\pi^-$	LL	360.9e-6	6.8e-6	8.2e-6	10.7e-6
2012b	$B_s^0 \to K_S^0\pi^+\pi^-$	LL	174.8e-6	5.4e-6	8.2e-6	9.9e-6
2012a	$B_s^0 \to K_S^0\pi^+\pi^-$	LL	201.1e-6	6.2e-6	8.2e-6	10.3e-6
2011	$B_s^0 \to K_S^0\pi^+\pi^-$	LL	215.0e-6	6.0e-6	8.2e-6	10.2e-6

Table 3.18: $B_s^0 \to K_S^0\pi^+\pi^-$ efficiency tables with the favoured mode optimisation. For each year and K_S^0 reconstruction type, the average efficiency $\bar{\varepsilon}$, the statistical uncertainty $\sigma_{\bar{\varepsilon}}^{\text{stat}}$, the uncertainty linked to the averaging method $\sigma_{\bar{\varepsilon}}^{\text{RMS}}$ and the total uncertainty $\sigma_{\bar{\varepsilon}}$ are given.

Year	Mode	K_S^0	$\bar{\varepsilon}$	$\sigma_{\bar{\varepsilon}}^{\text{stat}}$	$\sigma_{\bar{\varepsilon}}^{\text{RMS}}$	$\sigma_{\bar{\varepsilon}}$
2018	$B_s^0 \to K_S^0\pi^+\pi^-$	DD	446.5e-6	5.3e-6	20.3e-6	20.9e-6
2017	$B_s^0 \to K_S^0\pi^+\pi^-$	DD	476.0e-6	5.7e-6	20.3e-6	21.0e-6
2016	$B_s^0 \to K_S^0\pi^+\pi^-$	DD	459.2e-6	5.7e-6	20.3e-6	21.0e-6
2015	$B_s^0 \to K_S^0\pi^+\pi^-$	DD	387.4e-6	5.2e-6	20.3e-6	20.9e-6
2012b	$B_s^0 \to K_S^0\pi^+\pi^-$	DD	367.0e-6	6.3e-6	20.3e-6	21.2e-6
2012a	$B_s^0 \to K_S^0\pi^+\pi^-$	DD	266.7e-6	5.5e-6	20.3e-6	21.0e-6
2011	$B_s^0 \to K_S^0\pi^+\pi^-$	DD	270.3e-6	5.1e-6	20.3e-6	20.9e-6
2018	$B_s^0 \to K_S^0\pi^+\pi^-$	LL	215.3e-6	4.7e-6	5.7e-6	7.4e-6
2017	$B_s^0 \to K_S^0\pi^+\pi^-$	LL	248.8e-6	5.1e-6	5.7e-6	7.7e-6
2016	$B_s^0 \to K_S^0\pi^+\pi^-$	LL	253.7e-6	5.4e-6	5.7e-6	7.9e-6
2015	$B_s^0 \to K_S^0\pi^+\pi^-$	LL	220.9e-6	5.0e-6	5.7e-6	7.6e-6
2012b	$B_s^0 \to K_S^0\pi^+\pi^-$	LL	124.6e-6	4.5e-6	5.7e-6	7.2e-6
2012a	$B_s^0 \to K_S^0\pi^+\pi^-$	LL	86.6e-6	3.9e-6	5.7e-6	6.9e-6
2011	$B_s^0 \to K_S^0\pi^+\pi^-$	LL	152.1e-6	4.9e-6	5.7e-6	7.5e-6

Table 3.19: $B_s^0 \to K_S^0\pi^+\pi^-$ efficiency tables with the unfavoured mode optimisation. For each year and K_S^0 reconstruction type, the average efficiency $\bar{\varepsilon}$, the statistical uncertainty $\sigma_{\bar{\varepsilon}}^{\text{stat}}$, the uncertainty linked to the averaging method $\sigma_{\bar{\varepsilon}}^{\text{RMS}}$ and the total uncertainty $\sigma_{\bar{\varepsilon}}$ are given.

3.4 Systematics

The purpose of the analysis reported here is to measure branching fractions and potentially make the first observation of a decay channel. It is needed to consider the uncertainties attached to the measurement: statistical uncertainties coming from the number of events counted in data and systematic uncertainties, which occur from the methods used in the analysis and the inputs taken from the simulated events. The statistical uncertainties, which are attached to the yield determination, have been presented in Section 3.2.2. The first two systematic uncertainties, attached to the MC statistics and the method used to determine the average efficiencies, have been presented in Section 3.3.4. For the completeness and correctness of the analysis, several other systematics are considered. This section is a summary of the systematic part of the analysis note [169].

A reminder about the branching fraction determination is first done as it is needed to understand the level at which several systematics are computed. After that, the systematics coming from the mass fit models are presented. Then, the numerous systematics related to efficiency determination are explained. And finally, a test about yield measurement and efficiency determination self-consistency is described.

3.4.1 About branching fraction determinations

In this analysis, the branching fractions are measured relative to $B^0 \to K^0_S\pi^+\pi^-$ as written in equation 3.0.1, which is recalled here for readability:

$$\frac{BF(B^0_{d,s} \to K^0_S h^+ h'^-)}{BF(B^0 \to K^0_S\pi^+\pi^-)} = \frac{N_{B^0_{d,s}\to K^0_S h^+ h'^-}}{N_{B^0\to K^0_S\pi^+\pi^-}} \frac{\epsilon_{B^0\to K^0_S\pi^+\pi^-}}{\epsilon_{B^0_{d,s}\to K^0_S h^+ h'^-}} \frac{f_d}{f_{d,s}}, \tag{3.4.1}$$

where the N represent the yields measured with the mass fit, the ϵ are the average efficiencies and f are hadronisation fractions (ratio needed if two different B are involved).

In the end, the goal is to provide a unique relative branching fraction measurement for each mode, but in a first instance, relative branching fractions following the splitting of the data/MC samples (data-taking period, K^0_S reconstruction type, and optimisation choice) are determined. The unique banching fractions are obtained by using an averaging method presented in Section 3.5.

Systematics can be computed at several levels of branching fraction determination and propagated, if needed, until the ultimate results. Concerning the systematics related to the mass fit model, they are determined directly at the level of the multiple branching fraction determination. For efficiency related systematics, the goal is to provide all of them at the level of the ratio of efficiencies ($B^0 \to K^0_S\pi^+\pi^-/B^0_{d,s} \to K^0_S h^+ h'^-$), some systematics are directly determined at this level, but others (like those already presented) are determined at the absolute average efficiency level and have to be propagated properly.

3.4.2 Systematics from mass fit

To understand the effects of the different choices (*e.g.* model used, fixed parameters, constraints between contributions, and so on) made in the fitting procedure, a list of sources of systematics uncertainties has been identified. For each of them, the fitting scheme is run again, but in an alternative configuration, changing only one element from the baseline. From the results of the fits in the alternative configuration, the measurement is carried out again and the systematic is taken to be the absolute difference between the baseline and the alternative branching fractions as :

$$\Delta_{syst,conf} = \left| BF_r(X)_{baseline} - BF_r(X)_{conf} \right|, \tag{3.4.2}$$

where $\Delta_{syst,conf}$ is the systematic uncertainty linked to the alternative configuration $conf$, $BF_r(X)_{baseline}$ the branching fraction ratio for channel X measured using results from the Baseline fitting procedure and $BF_r(X)_{conf}$ the branching fraction ratio for channel X measured using results from the alternative fitting procedure.

Thirteen alternative fitting procedures have been built to determine systematics:

1. `GlobalSmallFixed`: in baseline, contributions for which the fit estimates a yield smaller than 1 are fixed to 0 (yield), in this variant, these contributions are fixed to the last estimated value ($\neq 0$ but < 1).

2. `GlobalSmallNotFixed` in this variant, the previous contributions are let free to vary with yield smaller than 1.

3. `GlobalAddRadPart`: in baseline, radiative partially reconstructed contributions (only found in the $K^0_S\pi^+\pi^-$ spectrum) are accounted for in the two lineshapes used for the partially reconstructed events, in this variant, lineshapes to specifically model them are added (one for B^0 and one for B^0_S).

4. `SignalFreeDeltaM`: in baseline, the signal peaks means difference is constrained to the measured mass difference, in this variant, means are letting free.

5. `Signal2Hypatia`: in baseline, signal peaks are modeled with double Crystal Ball, in this variant, double-sided Hypatia [188] are used in place.

6. `CombExp`: in baseline, combinatorial backgrounds are modelled with a linear function, in this variant, an exponential function is used.

7. `CombNoKpipiKBinding`: in baseline, combinatorial slopes are the same for $K^0_SK^+\pi^-$ and $K^0_S\pi^+K^-$ spectra, in this variant, the slopes are independent.

8. `CombNoForcePos`: in baseline, combinatorial slope is fixed to 0 if the fits find it positive, in this variant, the slope can be positive.

9. `CombFit`: in baseline, the combinatorial slope is fitted on all the mass spectrum, in this variant, only the upperside band of the data ($5500\,\mathrm{MeV/c^2} < m < 5750\,\mathrm{MeV/c^2}$) is used.

10. `PartUseCharm`: in baseline, the partially reconstructed backgrounds are modelled out of Charmless MC decays, in this variant, Charmed MC samples are used instead.

11. `PartUseAll`: in this variant, the previous contributions are fitted from both Charm and Charmless MC decays providing two contributions per B type per spectrum.

12. `CFFreeAll`: in baseline, ratios of the crossfeed contributions in the same spectrum are fixed to efficiency ratios, in this variant, they are independant.

13. `CFFreeSmallCF`: in baseline, crossfeed yields are fully contrained by efficiency and yield ratios in SecondaryPeak optimisation for 2011, 2012a, 2012b and 2015, in this variant, they are letting free to vary.

The values of the fit systematics on the relative branching fractions for $B^0 \to K^0_SK^+K^-$ and $B^0_s \to K^0_S\pi^+\pi^-$ are given in tables 3.20 and 3.21. The values for the other modes are given in Appendix C.6. Globally, the biggest systematics occurred from the combinatorial background description.

Year	KS	Selection	*GlobalAddRadPart*	*GlobalSmallFixed*	*GlobalSmallNotFixed*	*SignalFreeDeltaM*	*SignalHypatia2*	*CombExp*	*CombFit*	*CombNoKpipiKBinding*	*CombNoForcePos*	*PartUseCharm*	*PartUseAll*	*CFFreeAll*	*CFFreeSmall*	Total
2011	LL	PP	5.4e-03	0.0e+00	2.0e-05	5.6e-04	2.1e-03	6.9e-03	8.7e-03	7.2e-05	0.0e+00	2.1e-02	4.5e-03	2.9e-02	0.0e+00	6.6e-02
2011	LL	SP	1.3e-02	0.0e+00	6.2e-05	4.6e-04	5.1e-04	1.8e-02	1.8e-02	2.4e-05	0.0e+00	8.7e-03	2.9e-03	6.6e-02	4.3e-02	1.1e-01
2011	DD	PP	6.8e-03	0.0e+00	1.4e-05	3.3e-04	7.1e-04	1.6e-03	5.4e-03	1.4e-04	0.0e+00	7.9e-03	7.1e-03	8.4e-03	0.0e+00	4.6e-02
2011	DD	SP	4.0e-02	0.0e+00	2.5e-05	1.1e-03	1.3e-03	7.8e-03	1.4e-02	4.9e-06	0.0e+00	3.6e-03	2.8e-04	8.3e-03	1.1e-02	7.0e-02
2012a	LL	PP	3.1e-03	1.4e-13	1.1e-05	2.4e-04	5.3e-04	4.8e-03	9.8e-03	4.9e-04	0.0e+00	1.5e-03	1.6e-05	5.4e-03	0.0e+00	5.0e-02
2012a	LL	SP	8.7e-03	0.0e+00	4.3e-06	6.2e-04	1.6e-03	8.6e-03	1.1e-02	2.9e-04	7.9e-05	3.8e-04	8.3e-05	2.8e-03	6.2e-03	9.5e-02
2012a	DD	PP	6.2e-03	1.4e-13	3.7e-06	3.4e-04	8.7e-04	3.4e-04	5.0e-03	5.9e-04	0.0e+00	2.4e-03	6.4e-05	1.4e-02	0.0e+00	5.6e-02
2012a	DD	SP	1.9e-02	0.0e+00	1.6e-05	2.8e-04	3.4e-04	4.0e-03	2.2e-02	2.0e-04	2.2e-03	7.9e-05	1.9e-05	4.8e-03	4.1e-04	5.9e-02
2012b	LL	PP	5.8e-03	7.1e-10	1.0e-05	6.8e-04	1.7e-03	7.0e-03	6.8e-03	5.3e-04	0.0e+00	2.1e-03	8.4e-04	5.2e-03	0.0e+00	5.5e-02
2012b	LL	SP	1.9e-02	6.3e-11	3.5e-05	5.3e-06	8.6e-05	8.1e-03	2.9e-02	2.5e-05	0.0e+00	1.5e-03	7.8e-04	1.4e-02	1.0e-02	7.1e-02
2012b	DD	PP	5.9e-03	1.2e-10	3.7e-05	9.6e-04	1.5e-03	2.9e-03	9.6e-03	1.3e-03	0.0e+00	4.0e-03	2.7e-03	1.7e-02	0.0e+00	4.4e-02
2012b	DD	SP	1.2e-02	3.8e-11	3.8e-05	3.7e-04	1.1e-03	8.5e-03	3.5e-03	2.0e-05	0.0e+00	3.3e-04	4.2e-04	1.5e-02	1.3e-02	5.0e-02
2015	LL	PP	6.3e-03	9.5e-11	3.3e-05	2.1e-04	3.0e-04	1.7e-02	2.8e-03	3.6e-04	0.0e+00	1.9e-03	1.8e-03	5.3e-03	0.0e+00	5.6e-02
2015	LL	SP	6.7e-03	6.9e-10	2.8e-05	5.4e-04	9.3e-04	1.6e-02	1.8e-03	2.1e-04	0.0e+00	4.2e-03	1.7e-03	3.1e-03	9.9e-05	6.9e-02
2015	DD	PP	6.1e-03	5.5e-12	8.0e-06	2.3e-04	3.9e-04	2.2e-04	2.7e-03	6.6e-06	0.0e+00	5.7e-03	4.6e-04	2.2e-03	0.0e+00	4.5e-02
2015	DD	SP	7.1e-03	4.9e-10	1.4e-06	3.4e-04	3.3e-04	7.5e-03	4.2e-03	1.3e-04	0.0e+00	2.8e-03	7.9e-04	1.5e-02	3.0e-02	6.3e-02
2016	LL	PP	6.6e-03	0.0e+00	3.4e-05	1.9e-04	1.5e-03	4.2e-03	4.8e-03	9.3e-07	0.0e+00	2.6e-04	4.8e-04	5.1e-03	0.0e+00	3.1e-02
2016	LL	SP	9.7e-03	1.0e-10	2.6e-05	2.4e-04	1.2e-03	1.1e-02	9.7e-03	3.8e-06	0.0e+00	2.2e-05	3.8e-05	7.2e-03	7.7e-03	3.6e-02
2016	DD	PP	6.1e-03	0.0e+00	1.8e-06	1.3e-04	1.2e-03	4.6e-03	1.4e-02	4.7e-05	0.0e+00	2.0e-03	1.6e-03	2.8e-03	0.0e+00	3.3e-02
2016	DD	SP	1.0e-02	7.1e-11	1.5e-05	6.2e-05	1.3e-03	1.4e-02	1.4e-02	7.0e-06	0.0e+00	1.8e-04	1.9e-04	1.6e-02	1.4e-02	4.3e-02
2017	LL	PP	6.5e-03	2.8e-11	9.3e-06	1.9e-04	2.4e-03	1.3e-02	3.4e-04	8.6e-05	0.0e+00	6.5e-03	6.6e-04	9.6e-04	0.0e+00	3.3e-02
2017	LL	SP	9.7e-03	7.7e-11	6.1e-06	2.8e-04	1.5e-03	1.7e-02	1.2e-02	1.8e-05	0.0e+00	4.0e-04	1.0e-03	1.1e-02	8.5e-03	3.9e-02
2017	DD	PP	6.6e-03	5.8e-11	8.3e-06	2.6e-04	2.8e-03	4.6e-04	4.8e-03	5.9e-05	0.0e+00	1.1e-02	1.7e-03	1.6e-03	0.0e+00	3.0e-02
2017	DD	SP	9.3e-03	4.5e-11	3.4e-06	5.2e-04	1.4e-03	9.2e-03	2.4e-03	3.4e-05	0.0e+00	3.3e-04	1.2e-04	1.3e-02	1.0e-02	3.3e-02
2018	LL	PP	7.1e-03	2.1e-10	7.1e-06	1.3e-04	1.5e-03	5.4e-03	6.1e-03	1.3e-04	0.0e+00	5.2e-03	1.1e-03	4.6e-04	0.0e+00	3.2e-02
2018	LL	SP	8.4e-03	4.3e-13	6.4e-06	4.6e-04	8.5e-04	7.4e-03	5.0e-03	3.7e-06	0.0e+00	2.4e-03	5.3e-04	7.9e-03	3.5e-04	3.5e-02
2018	DD	PP	6.0e-03	1.3e-10	7.6e-06	4.2e-06	2.7e-04	1.1e-03	6.5e-03	9.7e-06	0.0e+00	7.6e-03	5.2e-03	1.1e-03	0.0e+00	2.8e-02
2018	DD	SP	8.8e-03	1.9e-11	1.0e-05	3.8e-04	1.1e-03	1.5e-02	1.1e-02	5.9e-07	0.0e+00	2.8e-03	1.1e-04	2.1e-03	1.3e-03	3.6e-02

Table 3.20: Systematics uncertainties from the fit process for decay $B^0 \to K^0_S K^+ K^-$. PP stands for PrincipalPeak optimisation and SP for SecondaryPeak optimisation.

3.4.3 Systematics from efficiency determination

Several systematics sources related to efficiency determination have been considered. In the following, systematics related to tracking, trigger and the one linked to PIDcorrections are described. Then, depending on their determination method, some of those uncertainties need to be propagated through average efficiency determination, this propagation is described. After that, systematic uncertainties related to the binning scheme on the sqDP and to the signal kinematics simulations are provided. Finally, the determination of the efficiency relative to $B^0 \to K^0_S \pi^+ \pi^-$ with all the previously defined systematic is presented.

Tracking

The LHCb tracking performance group advises to apply a relative systematic uncertainty on the tracking corrections of 0.4% and 0.8% for RunI and RunII, respectively. This systematic source is related to the fraction of hadrons that undergoes hadronic interaction before the T station ($z \simeq 9000$mm) and depends on the nature of the particles of interest. Further details about the `TrackCalib` package and systematic determination are given in [186] and [189].

In order to be used with the efficiency maps determined in section 3.3.2, the systematic corresponding to the hh' tracking corrections are propagated through equation 3.3.2 following

Year	KS	Selection	GlobalAddRadPart	GlobalSmallFixed	GlobalSmallNotFixed	SignalFreeDeltaM	SignalHypatia2	CombExp	CombFit	CombNoKpipiKBinding	CombNoForcePos	PartUseCharm	PartUseAll	CFFreeAll	CFFreeSmall	Total
2011	LL	PP	5.0e-03	0.0e+00	3.0e-05	5.0e-03	4.7e-03	2.1e-02	5.9e-02	2.4e-04	0.0e+00	4.8e-02	4.9e-04	1.6e-03	0.0e+00	1.2e-01
2011	LL	SP	2.8e-02	0.0e+00	1.9e-05	1.0e-03	7.8e-03	2.2e-02	7.5e-02	3.7e-05	0.0e+00	3.4e-02	6.8e-04	1.0e-02	4.4e-02	1.3e-01
2011	DD	PP	8.8e-03	0.0e+00	1.2e-05	1.2e-03	7.4e-03	2.4e-02	9.9e-02	2.9e-04	0.0e+00	1.3e-02	2.5e-03	2.1e-02	0.0e+00	1.3e-01
2011	DD	SP	7.6e-02	0.0e+00	9.2e-08	4.2e-03	2.1e-04	3.5e-04	6.1e-02	1.3e-05	0.0e+00	7.8e-03	2.8e-04	1.3e-02	4.7e-03	1.3e-01
2012a	LL	PP	6.5e-03	8.4e-12	3.8e-05	2.5e-03	6.7e-03	1.8e-02	6.0e-02	3.8e-04	0.0e+00	6.8e-03	4.0e-04	1.7e-04	0.0e+00	1.4e-01
2012a	LL	SP	9.7e-03	0.0e+00	1.9e-06	4.4e-05	3.0e-03	1.6e-03	7.7e-03	1.6e-04	7.4e-05	9.1e-04	7.7e-04	8.1e-03	1.1e-03	1.6e-01
2012a	DD	PP	3.3e-02	3.2e-12	1.9e-05	1.5e-04	9.3e-03	2.4e-02	9.0e-02	3.2e-04	0.0e+00	4.1e-03	1.9e-04	4.1e-03	0.0e+00	1.3e-01
2012a	DD	SP	7.7e-02	0.0e+00	3.3e-05	1.7e-03	5.2e-03	5.0e-03	7.4e-02	4.5e-04	4.4e-05	5.9e-04	1.3e-04	3.0e-03	1.4e-03	1.3e-01
2012b	LL	PP	1.1e-02	3.4e-10	1.0e-04	1.3e-02	3.6e-03	2.5e-02	5.7e-02	2.2e-04	0.0e+00	4.1e-03	4.7e-04	1.8e-02	0.0e+00	1.1e-01
2012b	LL	SP	5.3e-02	1.7e-11	3.5e-05	7.3e-03	9.6e-05	8.6e-03	8.5e-02	5.6e-05	0.0e+00	1.7e-04	6.8e-04	1.1e-02	1.9e-02	1.3e-01
2012b	DD	PP	1.3e-02	2.4e-10	7.2e-05	1.0e-02	9.3e-03	1.3e-02	9.7e-02	1.4e-04	0.0e+00	1.6e-04	1.1e-03	1.3e-02	0.0e+00	1.2e-01
2012b	DD	SP	4.9e-02	4.1e-11	8.5e-05	4.2e-03	5.1e-03	2.0e-02	3.9e-02	5.4e-05	0.0e+00	5.2e-03	1.5e-03	1.3e-02	1.0e-02	9.1e-02
2015	LL	PP	6.2e-03	1.9e-11	8.3e-05	3.2e-03	1.2e-02	3.0e-02	6.8e-02	2.9e-05	0.0e+00	8.9e-04	2.6e-03	1.7e-03	0.0e+00	1.3e-01
2015	LL	SP	5.3e-03	1.1e-11	1.5e-05	2.5e-03	3.1e-03	2.1e-02	3.8e-02	1.4e-04	0.0e+00	7.6e-02	1.8e-03	1.7e-04	3.2e-05	1.3e-01
2015	DD	PP	5.5e-03	6.3e-12	1.9e-05	2.2e-04	9.8e-03	1.1e-02	9.1e-02	1.6e-04	0.0e+00	1.7e-02	1.4e-03	7.3e-03	0.0e+00	1.3e-01
2015	DD	SP	6.3e-03	3.9e-11	5.7e-05	3.1e-03	3.0e-03	2.4e-02	2.8e-02	1.9e-04	0.0e+00	8.6e-02	1.2e-03	4.7e-02	4.2e-02	1.4e-01
2016	LL	PP	1.2e-02	0.0e+00	1.8e-05	9.2e-04	1.1e-02	2.1e-02	8.6e-02	4.2e-05	0.0e+00	3.4e-03	5.7e-04	9.4e-03	0.0e+00	1.0e-01
2016	LL	SP	7.3e-03	1.7e-11	5.1e-06	1.8e-04	4.6e-03	2.2e-02	5.1e-02	3.4e-05	0.0e+00	3.0e-04	3.5e-04	1.5e-02	1.3e-02	7.1e-02
2016	DD	PP	1.4e-02	0.0e+00	5.3e-05	2.9e-04	1.2e-02	1.4e-02	9.6e-02	5.5e-05	0.0e+00	2.7e-03	2.0e-03	5.1e-03	0.0e+00	1.1e-01
2016	DD	SP	1.0e-02	1.2e-10	4.4e-05	6.1e-04	5.0e-03	2.8e-02	6.8e-02	6.8e-05	0.0e+00	3.8e-04	1.7e-04	1.8e-02	2.1e-02	8.8e-02
2017	LL	PP	6.4e-03	4.0e-11	6.4e-06	2.1e-03	1.2e-02	2.4e-02	6.8e-02	9.1e-05	0.0e+00	8.1e-03	2.4e-03	3.1e-03	0.0e+00	8.4e-02
2017	LL	SP	1.3e-02	8.8e-11	6.2e-06	1.5e-03	5.1e-03	3.2e-02	4.3e-02	6.3e-05	0.0e+00	4.4e-03	1.5e-03	1.7e-02	1.8e-02	6.9e-02
2017	DD	PP	7.8e-03	7.0e-12	1.2e-06	4.7e-04	1.5e-02	1.0e-02	6.9e-02	5.0e-05	0.0e+00	3.5e-02	1.8e-04	4.2e-03	0.0e+00	8.7e-02
2017	DD	SP	7.6e-03	1.1e-11	8.1e-08	2.8e-04	5.7e-03	1.9e-02	4.2e-02	7.6e-05	0.0e+00	1.5e-02	1.7e-04	1.3e-02	1.6e-02	6.2e-02
2018	LL	PP	7.8e-03	3.2e-10	1.8e-05	1.7e-03	1.0e-02	9.2e-03	5.5e-02	1.8e-05	0.0e+00	1.4e-02	3.8e-05	3.1e-03	0.0e+00	7.2e-02
2018	LL	SP	7.3e-03	1.9e-12	8.8e-06	1.3e-03	5.2e-03	1.6e-02	3.5e-02	2.6e-06	0.0e+00	4.3e-03	9.7e-04	6.9e-03	1.3e-04	5.6e-02
2018	DD	PP	9.5e-03	5.6e-10	3.4e-05	9.5e-04	9.0e-03	1.3e-02	8.7e-02	7.3e-06	0.0e+00	1.0e-02	3.6e-03	7.6e-03	0.0e+00	9.6e-02
2018	DD	SP	7.2e-03	5.6e-13	1.3e-05	6.1e-04	3.9e-03	2.7e-02	6.5e-02	5.2e-06	0.0e+00	7.3e-03	7.5e-05	3.4e-03	1.9e-03	7.7e-02

Table 3.21: Systematics uncertainties from the fit process for decay $B_s^0 \to K_S^0\pi^+\pi^-$. PP stands for PrincipalPeak optimisation and SP for SecondaryPeak optimisation.

the equation :

$$\sigma_{\text{tracking}} = \left|\frac{\partial\epsilon_{\text{tot}}^{\text{corrected}}}{\partial C_{\text{tracking}}}\right| \times \sigma_{C_{\text{tracking}}} = (\epsilon_{\text{tot}}^{\text{TOS}} \times C_{\text{L0corr}}^{\text{TOS}} \times \frac{f_{\text{TOS}}^{\text{data}}}{f_{\text{TOS}}^{\text{MC}}} + \epsilon_{\text{tot}}^{\text{TIS\&!TOS}} \times C_{\text{L0corr}}^{\text{TIS\&!TOS}} \times \frac{f_{\text{TIS\&!TOS}}^{\text{data}}}{f_{\text{TIS\&!TOS}}^{\text{MC}}}) \times \sigma_{C_{\text{tracking}}}, \tag{3.4.3}$$

where $\sigma_{C_{tracking}}$ corresponds to the absolute uncertainty maps attached to the hh' tracking correction across the DP.

In addition to the hh' tracking systematic, it is needed to introduce another systematic related to the K_S^0 tracking. For this purpose, the differences between MC/data efficiencies in the Downstream/Long tracking and K_S^0 candidate vertexing are examined using the results reported in [190]. These studies are based on partially reconstructed $D^{*+} \to (D^0 \to \phi K_S^0)\pi^+$ decays and provide corrective tables to the MC simulation. A comprehensive study of systematic estimates related to these effects has been conducted for a companion Run I analysis [191], demonstrating a marginal impact on the measurements. The magnitude of the effect has been measured comparable to the tracking correction systematics, which is why for this analysis it has been chosen to set K_S^0 tracking corrections systematic as equivalent to the hh' tracking systematic. This systematic is determined directly on the relative efficiencies and the corresponding values are provided in the related tables.

Trigger

The L0 trigger corrections used in Section 3.3.1 were provided with dedicated uncertainties defined in the sqDP plan as the corrections themselves. In order to be used with the absolute efficiency maps determined in Section 3.3.2, the systematics corresponding to the L0 trigger correction are propagated through equation 3.3.2 following the formula given in equations 3.4.4 and 3.4.5:

$$\sigma_{\text{TOS}} = \left| \frac{\partial \epsilon_{\text{tot}}^{\text{corrected}}}{\partial C_{\text{L0corr}}^{\text{TOS}}} \right| \times \sigma_{C_{\text{L0corr}}^{\text{TOS}}} = \epsilon_{\text{tot}}^{\text{TOS}} \times C_{\text{tracking}} \times \frac{f_{\text{TOS}}^{\text{data}}}{f_{\text{TOS}}^{\text{MC}}} \times \sigma_{C_{\text{L0corr}}^{\text{TOS}}}, \tag{3.4.4}$$

$$\sigma_{\text{TIS\&!TOS}} = \left| \frac{\partial \epsilon_{\text{tot}}^{\text{corrected}}}{\partial C_{\text{L0corr}}^{\text{TIS\&!TOS}}} \right| \times \sigma_{C_{\text{L0corr}}^{\text{TIS\&!TOS}}} = \epsilon_{\text{tot}}^{\text{TIS\&!TOS}} \times C_{\text{tracking}} \times \frac{f_{\text{TIS\&!TOS}}^{\text{data}}}{f_{\text{TIS\&!TOS}}^{\text{MC}}} \times \sigma_{C_{\text{L0corr}}^{\text{TIS\&!TOS}}}, \tag{3.4.5}$$

where $\sigma_{\text{TOS(TIS\&!TOS)}}$ are the absolute efficiency trigger correction systematic maps and $\sigma_{C_{\text{L0corr}}^{\text{TOS(TIS\&!TOS)}}}$ denotes the absolute uncertainty maps attached to the trigger corrections on the sqDP.

Along with the previously defined trigger systematic, two additional sources linked to the trigger correction method are considered. The first is related to the choice of occupancy maps used to determine the trigger corrections. For the analysis maps built with $b\bar{b}$ events are used, but maps made with $c\bar{c}$ events are also provided. The systematic related to this first source is given by the differences between the efficiencies computed with the baseline maps and the others (regarding the fact that the data-taking conditions can be considered close among the Run II, a common systematic is built for those samples). The second source comes from the weighting of the trigger corrections by the $f_{\text{TOS(TIS\&!TOS)}}^{\text{data}}/f_{\text{TOS(TIS\&!TOS)}}^{\text{MC}}$ ratios. The related systematic is assigned from the difference between the efficiencies determined with and without them. Those two trigger-related systematics are determined directly on the relative efficiencies and their values are provided in the corresponding tables.

PIDcorr

The use of the PIDcorr package to correct the PID variables in MC, brings two main categories of effect that can cause bias:

- PID MC sampling: since PIDCorr uses MC samples that are much smaller than the data calibration samples, this finite statistics causes a source of systematic.
- PID control sample parameterisation (PID kernel): since PIDCorr is an unbinned correction method, it uses the Kernel density instead of the histograms. Thus, any variation in this kernel can produce another PID response, and thus it is considered a further source of systematic uncertainties.

The first effect is addressed by using different PID templates, produced by bootstrapped [192] samples, centrally generated by the PID group. An absolute systematic on the PID selection efficiency is assigned by comparing the baseline efficiency to various template efficiencies in bins of sqDP. The second effect is addressed by using a template with a modified kernel definition. A global absolute systematic is therefore assigned to the PID selection efficiency from the difference between the baseline kernel efficiency and various kernel efficiency. The relative systematics related to these two effects are finally propagated in the efficiency determination.

Propagation through average efficiency determination

The systematic related to the hh' tracking correction, the trigger corrections and to the PID MC sampling effect are considered uncorrelated from bin to bin and among the reference periods. They are propagated similarly to what has been done for the statistical uncertainty from equation 3.3.13 to 3.3.14 at the efficiency map averaging level. Systematics related to the TOS and TIS&!TOS trigger corrections are quadratically added to build a global L0 correction systematic uncertainty. The three aforementioned systematics are propagated similarly to what has been done for the statistical uncertainty through reference years combination. The PID kernel relative systematic is added after the averaging on sqDP bins and propagated through reference years combination as in equation 3.3.13.

After propagation of these uncertainties, the four uncertainty numbers on the average efficiency are reported in Appendix C.7 (the total uncertainty per sample is given by the quadratic sum of all the sources).

The propagation of the systematics through the MU-MD average efficiencies recombination is done in two ways:

1. for the systematics that can be considered uncorrelated from one polarity to another, such as the tracking and L0hadron corrections systematics (which are defined with polarities separation), the propagation is done identically to what is done for statistical uncertainty, following equation 3.3.19,

2. for the systematics that are correlated among polarities, such as the one corresponding to the PIDcorr effects (which are defined without polarities separation), the propagation is done following equation 3.4.6:

$$\sigma^X = F_{MD\,y} \times \sigma^X_{MD\,i} + F_{MU\,y} \times \sigma^X_{MU\,i}, \tag{3.4.6}$$

where i denotes a given sample (year, decay mode, fit type optimisation, K^0_S reconstruction type), $F_{P\,y}$ is the fraction of P polarity to consider for the y period and X denotes a given systematic with correlation among polarities.

The per-mode efficiency tables with systematics propagated are given for $B^0 \to K^0_S\pi^+\pi^-$, $B^0 \to K^0_S K^+K^-$ and $B^0_s \to K^0_S\pi^+\pi^-$from tables 3.22 to 3.27. The others are provided in Appendix C.8.

Binning scheme

For the average efficiency determination, the efficiencies are averaged over sqDP, with 10×10 binning as baseline. The choice of the binning used in the sqDP is an additional source of systematic error, and the related uncertainty can be evaluated by varying the binning across each of the θ' and m' axes of sqDP with respect to the baseline binning. Each axis is re-binned from 7 to 13 bins; and the determination of the average efficiencies is done for each and every binning.

The binning systematics are determined by evaluating the spread of the relative efficiencies among binning. To investigate the spread of efficiency ratios, the distributions of the differences between the ratios coming from baseline (10x10) binning configurations and the ratios coming from various binning configurations are built. To have better statistical definitions, the years are combined and the spread is finally evaluated for each mode, K^0_S reconstruction type, and optimisation. The distribution RMS is assigned as binning systematic uncertainty.

Year	Mode	K_S^0	$\bar{\varepsilon}$	$\sigma_{\bar{\varepsilon}}^{\text{stat}}$	$\sigma_{\bar{\varepsilon}}^{\text{tracking}}$	$\sigma_{\bar{\varepsilon}}^{\text{L0corr}}$	$\sigma_{\bar{\varepsilon}}^{\text{PIDMCsampling}}$	$\sigma_{\bar{\varepsilon}}^{\text{PIDkernel}}$	$\sigma_{\bar{\varepsilon}}^{\text{RMS}}$	$\sigma_{\bar{\varepsilon}}$
2018	$B_d^0 \to K_S^0\pi^+\pi^-$	DD	82098.9e-8	619.1e-8	3.5e-8	84.1e-8	42.9e-8	270.8e-8	1219.8e-8	1397.7e-8
2017	$B_d^0 \to K_S^0\pi^+\pi^-$	DD	83328.8e-8	643.4e-8	3.4e-8	85.7e-8	42.4e-8	188.8e-8	1219.8e-8	1395.2e-8
2016	$B_d^0 \to K_S^0\pi^+\pi^-$	DD	86933.3e-8	656.5e-8	3.4e-8	89.7e-8	38.6e-8	229.4e-8	1219.8e-8	1407.5e-8
2015	$B_d^0 \to K_S^0\pi^+\pi^-$	DD	83587.6e-8	651.8e-8	3.4e-8	94.2e-8	70.3e-8	301.2e-8	1219.8e-8	1420.3e-8
2012b	$B_d^0 \to K_S^0\pi^+\pi^-$	DD	51940.4e-8	583.6e-8	1.8e-8	85.8e-8	38.9e-8	711.8e-8	1219.8e-8	1531.0e-8
2012a	$B_d^0 \to K_S^0\pi^+\pi^-$	DD	41160.2e-8	561.6e-8	1.7e-8	77.9e-8	36.0e-8	542.2e-8	1219.8e-8	1450.7e-8
2011	$B_d^0 \to K_S^0\pi^+\pi^-$	DD	49196.5e-8	597.9e-8	1.8e-8	145.4e-8	43.8e-8	666.1e-8	1219.8e-8	1520.6e-8
2018	$B_d^0 \to K_S^0\pi^+\pi^-$	LL	29685.4e-8	368.6e-8	2.0e-8	26.0e-8	20.4e-8	66.1e-8	649.9e-8	750.8e-8
2017	$B_d^0 \to K_S^0\pi^+\pi^-$	LL	31694.3e-8	400.2e-8	2.0e-8	28.7e-8	24.0e-8	67.5e-8	649.9e-8	767.1e-8
2016	$B_d^0 \to K_S^0\pi^+\pi^-$	LL	35629.5e-8	428.7e-8	2.1e-8	32.3e-8	22.7e-8	103.1e-8	649.9e-8	786.3e-8
2015	$B_d^0 \to K_S^0\pi^+\pi^-$	LL	32752.8e-8	409.7e-8	2.0e-8	30.7e-8	26.0e-8	98.8e-8	649.9e-8	775.6e-8
2012b	$B_d^0 \to K_S^0\pi^+\pi^-$	LL	153341.4e-9	3111.4e-9	9.3e-9	225.9e-9	258.1e-9	1796.8e-9	6498.7e-9	7433.8e-9
2012a	$B_d^0 \to K_S^0\pi^+\pi^-$	LL	17684.9e-8	374.5e-8	1.0e-8	23.6e-8	19.3e-8	262.8e-8	649.9e-8	795.3e-8
2011	$B_d^0 \to K_S^0\pi^+\pi^-$	LL	18765.6e-8	376.6e-8	1.0e-8	45.6e-8	20.8e-8	271.4e-8	649.9e-8	800.2e-8

Table 3.22: $B^0 \to K_S^0\pi^+\pi^-$ efficiency table with the favoured mode optimisation. For each year and K_S^0 reconstruction type, the average efficiency $\bar{\varepsilon}$, the statistical uncertainty $\sigma_{\bar{\varepsilon}}^{\text{stat}}$, the uncertainty linked to the tracking correction $\sigma_{\bar{\varepsilon}}^{\text{tracking}}$, the uncertainty linked to the L0Hadron trigger correction $\sigma_{\bar{\varepsilon}}^{\text{L0corr}}$, the uncertainty related to the PID MC sampling effect $\sigma_{\bar{\varepsilon}}^{\text{PIDMCsampling}}$, the uncertainty linked to the PID kernel variation $\sigma_{\bar{\varepsilon}}^{\text{PIDkernel}}$, the uncertainty linked to the averaging method $\sigma_{\bar{\varepsilon}}^{\text{RMS}}$ and the total uncertainty $\sigma_{\bar{\varepsilon}}$ are given.

Year	Mode	K_S^0	$\bar{\varepsilon}$	$\sigma_{\bar{\varepsilon}}^{\text{stat}}$	$\sigma_{\bar{\varepsilon}}^{\text{tracking}}$	$\sigma_{\bar{\varepsilon}}^{\text{L0corr}}$	$\sigma_{\bar{\varepsilon}}^{\text{PIDMCsampling}}$	$\sigma_{\bar{\varepsilon}}^{\text{PIDkernel}}$	$\sigma_{\bar{\varepsilon}}^{\text{RMS}}$	$\sigma_{\bar{\varepsilon}}$
2018	$B_d^0 \to K_S^0\pi^+\pi^-$	DD	41330.5e-8	405.8e-8	1.8e-8	44.3e-8	21.5e-8	136.3e-8	628.5e-8	762.1e-8
2017	$B_d^0 \to K_S^0\pi^+\pi^-$	DD	44229.2e-8	435.6e-8	1.8e-8	46.8e-8	22.5e-8	100.2e-8	628.5e-8	773.0e-8
2016	$B_d^0 \to K_S^0\pi^+\pi^-$	DD	43886.7e-8	431.7e-8	1.8e-8	46.2e-8	19.4e-8	115.8e-8	628.5e-8	772.9e-8
2015	$B_d^0 \to K_S^0\pi^+\pi^-$	DD	34655.9e-8	378.9e-8	1.4e-8	41.1e-8	29.2e-8	124.9e-8	628.5e-8	746.1e-8
2012b	$B_d^0 \to K_S^0\pi^+\pi^-$	DD	34375.0e-8	459.1e-8	1.2e-8	58.8e-8	25.5e-8	471.1e-8	628.5e-8	912.1e-8
2012a	$B_d^0 \to K_S^0\pi^+\pi^-$	DD	23311.6e-8	411.1e-8	1.0e-8	43.2e-8	20.9e-8	307.1e-8	628.5e-8	812.8e-8
2011	$B_d^0 \to K_S^0\pi^+\pi^-$	DD	238455.0e-9	4000.9e-9	9.0e-9	723.7e-9	210.1e-9	3228.8e-9	6285.0e-9	8154.8e-9
2018	$B_d^0 \to K_S^0\pi^+\pi^-$	LL	19084.5e-8	284.1e-8	1.3e-8	16.7e-8	13.2e-8	42.5e-8	437.9e-8	524.2e-8
2017	$B_d^0 \to K_S^0\pi^+\pi^-$	LL	21531.9e-8	317.0e-8	1.4e-8	19.6e-8	16.4e-8	45.8e-8	437.9e-8	543.2e-8
2016	$B_d^0 \to K_S^0\pi^+\pi^-$	LL	22136.8e-8	319.7e-8	1.3e-8	19.9e-8	14.0e-8	64.1e-8	437.9e-8	546.5e-8
2015	$B_d^0 \to K_S^0\pi^+\pi^-$	LL	19921.6e-8	305.7e-8	1.3e-8	18.5e-8	16.0e-8	60.1e-8	437.9e-8	538.0e-8
2012b	$B_d^0 \to K_S^0\pi^+\pi^-$	LL	108457.4e-9	2573.1e-9	6.7e-9	158.8e-9	183.3e-9	1270.9e-9	4379.5e-9	5241.6e-9
2012a	$B_d^0 \to K_S^0\pi^+\pi^-$	LL	77800.5e-9	2441.1e-9	4.7e-9	126.0e-9	90.2e-9	1156.3e-9	4379.5e-9	5147.8e-9
2011	$B_d^0 \to K_S^0\pi^+\pi^-$	LL	132930.2e-9	3120.4e-9	7.3e-9	305.7e-9	149.2e-9	1922.4e-9	4379.5e-9	5720.8e-9

Table 3.23: $B^0 \to K_S^0\pi^+\pi^-$ efficiency table with the unfavoured mode optimisation. For each year and K_S^0 reconstruction type, the average efficiency $\bar{\varepsilon}$, the statistical uncertainty $\sigma_{\bar{\varepsilon}}^{\text{stat}}$, the uncertainty linked to the tracking correction $\sigma_{\bar{\varepsilon}}^{\text{tracking}}$, the uncertainty linked to the L0Hadron trigger correction $\sigma_{\bar{\varepsilon}}^{\text{L0corr}}$, the uncertainty related to the PID MC sampling effect $\sigma_{\bar{\varepsilon}}^{\text{PIDMCsampling}}$, the uncertainty linked to the PID kernel variation $\sigma_{\bar{\varepsilon}}^{\text{PIDkernel}}$, the uncertainty linked to the averaging method $\sigma_{\bar{\varepsilon}}^{\text{RMS}}$ and the total uncertainty $\sigma_{\bar{\varepsilon}}$ are given.

Signal kinematics simulations

Imperfections in the simulation of the kinematics of the signal B-meson candidates might introduce a bias in the efficiency ratios determination. Potential biases induced by the observed discrepancies are evaluated by means of a ML-based method, used to determine event-by-event weight to apply on MC events kinematics to match those in data (reweighted by sWeights). This procedure is applied to the modes with large statistics to obtain a decent sFitted signal distribution, namely $B^0 \to K_S^0\pi^+\pi^-$, $B_s^0 \to K_S^0K^\pm\pi^\mp$ and $B^0 \to K_S^0K^+K^-$ with the so-called PrincipalPeak optimisation.

From these weights, alternative efficiency ratios ($B^0 \to K_S^0\pi^+\pi^-/B_{d,s}^0 \to K_S^0h^+h'^-$) are determined. The distribution of relative differences with the baseline ratios are used to estimate

Year	Mode	K^0_S	$\bar{\varepsilon}$	$\sigma^{\text{stat}}_{\bar{\varepsilon}}$	$\sigma^{\text{tracking}}_{\bar{\varepsilon}}$	$\sigma^{\text{L0corr}}_{\bar{\varepsilon}}$	$\sigma^{\text{PIDMCsampling}}_{\bar{\varepsilon}}$	$\sigma^{\text{PIDkernel}}_{\bar{\varepsilon}}$	$\sigma^{\text{RMS}}_{\bar{\varepsilon}}$	$\sigma_{\bar{\varepsilon}}$
2018	$B^0_d \to K^0_S K^+ K^-$	DD	72816.4e-8	516.3e-8	3.3e-8	56.0e-8	72.8e-8	153.4e-8	322.3e-8	634.4e-8
2017	$B^0_d \to K^0_S K^+ K^-$	DD	75148.9e-8	550.8e-8	3.2e-8	111.7e-8	56.6e-8	173.0e-8	322.3e-8	672.9e-8
2016	$B^0_d \to K^0_S K^+ K^-$	DD	89341.4e-8	599.9e-8	3.6e-8	70.8e-8	62.0e-8	256.8e-8	322.3e-8	733.8e-8
2015	$B^0_d \to K^0_S K^+ K^-$	DD	80372.8e-8	580.0e-8	3.4e-8	67.6e-8	84.9e-8	209.0e-8	322.3e-8	704.1e-8
2012b	$B^0_d \to K^0_S K^+ K^-$	DD	44963.1e-8	550.9e-8	1.7e-8	140.3e-8	326.9e-8	1024.5e-8	322.3e-8	1258.4e-8
2012a	$B^0_d \to K^0_S K^+ K^-$	DD	31146.8e-8	489.8e-8	1.5e-8	118.5e-8	46.5e-8	633.5e-8	322.3e-8	872.5e-8
2011	$B^0_d \to K^0_S K^+ K^-$	DD	36026.4e-8	481.3e-8	1.4e-8	109.4e-8	33.2e-8	298.9e-8	322.3e-8	661.7e-8
2018	$B^0_d \to K^0_S K^+ K^-$	LL	30481.9e-8	326.0e-8	2.1e-8	16.8e-8	45.0e-8	61.1e-8	208.1e-8	394.5e-8
2017	$B^0_d \to K^0_S K^+ K^-$	LL	32939.1e-8	359.8e-8	2.1e-8	35.0e-8	37.2e-8	98.4e-8	208.1e-8	430.2e-8
2016	$B^0_d \to K^0_S K^+ K^-$	LL	37030.8e-8	384.7e-8	2.3e-8	23.1e-8	31.8e-8	90.4e-8	208.1e-8	448.4e-8
2015	$B^0_d \to K^0_S K^+ K^-$	LL	33282.3e-8	372.0e-8	2.1e-8	22.8e-8	74.4e-8	216.4e-8	208.1e-8	484.3e-8
2012b	$B^0_d \to K^0_S K^+ K^-$	LL	14706.1e-8	318.3e-8	1.0e-8	44.9e-8	29.9e-8	207.8e-8	208.1e-8	436.7e-8
2012a	$B^0_d \to K^0_S K^+ K^-$	LL	16797.7e-8	361.4e-8	1.0e-8	34.0e-8	53.6e-8	309.1e-8	208.1e-8	522.9e-8
2011	$B^0_d \to K^0_S K^+ K^-$	LL	189995.0e-9	3586.2e-9	9.8e-9	431.4e-9	436.4e-9	2225.2e-9	2081.1e-9	4745.5e-9

Table 3.24: $B^0 \to K^0_S K^+ K^-$ efficiency table with the favoured mode optimisation. For each year and K^0_S reconstruction type, the average efficiency $\bar{\varepsilon}$, the statistical uncertainty $\sigma^{\text{stat}}_{\bar{\varepsilon}}$, the uncertainty linked to the tracking correction $\sigma^{\text{tracking}}_{\bar{\varepsilon}}$, the uncertainty linked to the L0Hadron trigger correction $\sigma^{\text{L0corr}}_{\bar{\varepsilon}}$, the uncertainty related to the PID MC sampling effect $\sigma^{\text{PIDMCsampling}}_{\bar{\varepsilon}}$, the uncertainty linked to the PID kernel variation $\sigma^{\text{PIDkernel}}_{\bar{\varepsilon}}$, the uncertainty linked to the averaging method $\sigma^{\text{RMS}}_{\bar{\varepsilon}}$ and the total uncertainty $\sigma_{\bar{\varepsilon}}$ are given.

Year	Mode	K^0_S	$\bar{\varepsilon}$	$\sigma^{\text{stat}}_{\bar{\varepsilon}}$	$\sigma^{\text{tracking}}_{\bar{\varepsilon}}$	$\sigma^{\text{L0corr}}_{\bar{\varepsilon}}$	$\sigma^{\text{PIDMCsampling}}_{\bar{\varepsilon}}$	$\sigma^{\text{PIDkernel}}_{\bar{\varepsilon}}$	$\sigma^{\text{RMS}}_{\bar{\varepsilon}}$	$\sigma_{\bar{\varepsilon}}$
2018	$B^0_d \to K^0_S K^+ K^-$	DD	48498.6e-8	421.0e-8	2.2e-8	39.5e-8	48.2e-8	102.2e-8	202.8e-8	482.4e-8
2017	$B^0_d \to K^0_S K^+ K^-$	DD	37423.9e-8	388.9e-8	1.6e-8	58.8e-8	27.5e-8	86.1e-8	202.8e-8	451.6e-8
2016	$B^0_d \to K^0_S K^+ K^-$	DD	47931.7e-8	437.2e-8	1.9e-8	41.8e-8	33.2e-8	137.8e-8	202.8e-8	504.1e-8
2015	$B^0_d \to K^0_S K^+ K^-$	DD	40015.7e-8	409.1e-8	1.7e-8	37.6e-8	40.4e-8	104.0e-8	202.8e-8	471.5e-8
2012b	$B^0_d \to K^0_S K^+ K^-$	DD	33425.2e-8	477.6e-8	1.3e-8	113.1e-8	246.9e-8	761.6e-8	202.8e-8	960.7e-8
2012a	$B^0_d \to K^0_S K^+ K^-$	DD	21059.1e-8	406.4e-8	1.0e-8	76.1e-8	30.7e-8	428.4e-8	202.8e-8	629.7e-8
2011	$B^0_d \to K^0_S K^+ K^-$	DD	27517.3e-8	422.5e-8	1.1e-8	83.4e-8	25.9e-8	228.3e-8	202.8e-8	528.6e-8
2018	$B^0_d \to K^0_S K^+ K^-$	LL	21839.8e-8	277.3e-8	1.5e-8	12.4e-8	31.2e-8	43.8e-8	148.4e-8	319.3e-8
2017	$B^0_d \to K^0_S K^+ K^-$	LL	18371.6e-8	270.2e-8	1.2e-8	20.7e-8	20.0e-8	54.9e-8	148.4e-8	314.5e-8
2016	$B^0_d \to K^0_S K^+ K^-$	LL	19969.2e-8	283.5e-8	1.2e-8	13.5e-8	17.3e-8	48.7e-8	148.4e-8	324.4e-8
2015	$B^0_d \to K^0_S K^+ K^-$	LL	28016.8e-8	339.0e-8	1.8e-8	19.1e-8	62.8e-8	182.1e-8	148.4e-8	417.7e-8
2012b	$B^0_d \to K^0_S K^+ K^-$	LL	123994.6e-9	2933.0e-9	8.5e-9	395.8e-9	249.3e-9	1751.7e-9	1483.6e-9	3753.8e-9
2012a	$B^0_d \to K^0_S K^+ K^-$	LL	141342.3e-9	3322.1e-9	8.5e-9	297.6e-9	447.5e-9	2600.5e-9	1483.6e-9	4504.3e-9
2011	$B^0_d \to K^0_S K^+ K^-$	LL	137859.8e-9	3069.1e-9	7.3e-9	310.4e-9	335.1e-9	1614.6e-9	1483.6e-9	3799.5e-9

Table 3.25: $B^0 \to K^0_S K^+ K^-$ efficiency table with the unfavoured mode optimisation. For each year and K^0_S reconstruction type, the average efficiency $\bar{\varepsilon}$, the statistical uncertainty $\sigma^{\text{stat}}_{\bar{\varepsilon}}$, the uncertainty linked to the tracking correction $\sigma^{\text{tracking}}_{\bar{\varepsilon}}$, the uncertainty linked to the L0Hadron trigger correction $\sigma^{\text{L0corr}}_{\bar{\varepsilon}}$, the uncertainty related to the PID MC sampling effect $\sigma^{\text{PIDMCsampling}}_{\bar{\varepsilon}}$, the uncertainty linked to the PID kernel variation $\sigma^{\text{PIDkernel}}_{\bar{\varepsilon}}$, the uncertainty linked to the averaging method $\sigma^{\text{RMS}}_{\bar{\varepsilon}}$ and the total uncertainty $\sigma_{\bar{\varepsilon}}$ are given.

a unique relative systematic uncertainty for all the ratios. Concretely, a small bias was observed in association with a spread compared to null differences. The sum in quadrature of this observed bias and spread are assigned as systematic.

Relative efficiencies

The determination of the $B^0_{(s)} \to K^0_S h^+ h'^-$ branching fractions relative to $B^0 \to K^0_S \pi^+ \pi^-$, involves $\bar{\varepsilon}_{B^0 \to K^0_S \pi^+ \pi^-} / \bar{\varepsilon}_{B^0_{(s)} \to K^0_S h^+ h'^-}$ ratios of average efficiencies. The average efficiencies relative to $B^0 \to K^0_S \pi^+ \pi^-$ have to be determined together with their uncertainties. The formula corresponding to the propagation of the uncertainties determined on the average efficiencies is

Year	Mode	K_S^0	$\bar{\varepsilon}$	$\sigma_{\bar{\varepsilon}}^{\text{stat}}$	$\sigma_{\bar{\varepsilon}}^{\text{tracking}}$	$\sigma_{\bar{\varepsilon}}^{\text{L0corr}}$	$\sigma_{\bar{\varepsilon}}^{\text{PIDMCsampling}}$	$\sigma_{\bar{\varepsilon}}^{\text{PIDkernel}}$	$\sigma_{\bar{\varepsilon}}^{\text{RMS}}$	$\sigma_{\bar{\varepsilon}}$
2018	$B_s^0 \to K_S^0\pi^+\pi^-$	DD	87089.6e-8	814.6e-8	5.1e-8	115.7e-8	129.1e-8	381.6e-8	3509.2e-8	3626.8e-8
2017	$B_s^0 \to K_S^0\pi^+\pi^-$	DD	88429.5e-8	844.9e-8	4.9e-8	119.6e-8	105.6e-8	370.3e-8	3509.2e-8	3632.0e-8
2016	$B_s^0 \to K_S^0\pi^+\pi^-$	DD	91363.6e-8	877.2e-8	5.0e-8	125.3e-8	122.9e-8	444.7e-8	3509.2e-8	3648.6e-8
2015	$B_s^0 \to K_S^0\pi^+\pi^-$	DD	89719.2e-8	882.6e-8	5.5e-8	132.1e-8	193.8e-8	739.0e-8	3509.2e-8	3700.6e-8
2012b	$B_s^0 \to K_S^0\pi^+\pi^-$	DD	56997.6e-8	817.6e-8	2.9e-8	124.5e-8	156.0e-8	3815.1e-8	3509.2e-8	5251.5e-8
2012a	$B_s^0 \to K_S^0\pi^+\pi^-$	DD	45854.2e-8	758.1e-8	2.5e-8	112.6e-8	119.6e-8	3340.2e-8	3509.2e-8	4906.4e-8
2011	$B_s^0 \to K_S^0\pi^+\pi^-$	DD	54838.5e-8	776.3e-8	2.7e-8	202.5e-8	282.4e-8	5403.1e-8	3509.2e-8	6498.6e-8
2018	$B_s^0 \to K_S^0\pi^+\pi^-$	LL	32931.0e-8	617.8e-8	3.4e-8	44.7e-8	75.1e-8	173.6e-8	824.4e-8	1048.4e-8
2017	$B_s^0 \to K_S^0\pi^+\pi^-$	LL	35705.2e-8	647.4e-8	3.4e-8	48.2e-8	64.3e-8	195.2e-8	824.4e-8	1069.3e-8
2016	$B_s^0 \to K_S^0\pi^+\pi^-$	LL	39780.6e-8	718.4e-8	3.8e-8	55.2e-8	57.4e-8	208.2e-8	824.4e-8	1116.0e-8
2015	$B_s^0 \to K_S^0\pi^+\pi^-$	LL	36085.5e-8	676.1e-8	3.5e-8	53.6e-8	122.4e-8	330.9e-8	824.4e-8	1124.3e-8
2012b	$B_s^0 \to K_S^0\pi^+\pi^-$	LL	17481.2e-8	544.5e-8	1.7e-8	39.8e-8	91.0e-8	1362.7e-8	824.4e-8	1686.1e-8
2012a	$B_s^0 \to K_S^0\pi^+\pi^-$	LL	20106.0e-8	615.6e-8	1.8e-8	40.5e-8	136.7e-8	2093.7e-8	824.4e-8	2337.2e-8
2011	$B_s^0 \to K_S^0\pi^+\pi^-$	LL	21498.8e-8	596.8e-8	1.7e-8	78.4e-8	97.2e-8	1600.6e-8	824.4e-8	1900.9e-8

Table 3.26: $B_s^0 \to K_S^0\pi^+\pi^-$ efficiency table with the favoured mode optimisation. For each year and K_S^0 reconstruction type, the average efficiency $\bar{\varepsilon}$, the statistical uncertainty $\sigma_{\bar{\varepsilon}}^{\text{stat}}$, the uncertainty linked to the tracking correction $\sigma_{\bar{\varepsilon}}^{\text{tracking}}$, the uncertainty linked to the L0Hadron trigger correction $\sigma_{\bar{\varepsilon}}^{\text{L0corr}}$, the uncertainty related to the PID MC sampling effect $\sigma_{\bar{\varepsilon}}^{\text{PIDMCsampling}}$, the uncertainty linked to the PID kernel variation $\sigma_{\bar{\varepsilon}}^{\text{PIDkernel}}$, the uncertainty linked to the averaging method $\sigma_{\bar{\varepsilon}}^{\text{RMS}}$ and the total uncertainty $\sigma_{\bar{\varepsilon}}$ are given.

Year	Mode	K_S^0	$\bar{\varepsilon}$	$\sigma_{\bar{\varepsilon}}^{\text{stat}}$	$\sigma_{\bar{\varepsilon}}^{\text{tracking}}$	$\sigma_{\bar{\varepsilon}}^{\text{L0corr}}$	$\sigma_{\bar{\varepsilon}}^{\text{PIDMCsampling}}$	$\sigma_{\bar{\varepsilon}}^{\text{PIDkernel}}$	$\sigma_{\bar{\varepsilon}}^{\text{RMS}}$	$\sigma_{\bar{\varepsilon}}$
2018	$B_s^0 \to K_S^0\pi^+\pi^-$	DD	44646.8e-8	532.4e-8	2.7e-8	61.4e-8	66.3e-8	195.7e-8	2025.9e-8	2105.8e-8
2017	$B_s^0 \to K_S^0\pi^+\pi^-$	DD	47597.8e-8	567.4e-8	2.7e-8	65.6e-8	56.7e-8	199.3e-8	2025.9e-8	2115.1e-8
2016	$B_s^0 \to K_S^0\pi^+\pi^-$	DD	45916.7e-8	568.9e-8	2.5e-8	64.0e-8	61.7e-8	223.5e-8	2025.9e-8	2118.0e-8
2015	$B_s^0 \to K_S^0\pi^+\pi^-$	DD	38737.5e-8	520.9e-8	2.4e-8	60.6e-8	82.9e-8	319.1e-8	2025.9e-8	2118.5e-8
2012b	$B_s^0 \to K_S^0\pi^+\pi^-$	DD	36699.4e-8	630.5e-8	1.8e-8	82.7e-8	97.5e-8	2456.5e-8	2025.9e-8	3248.5e-8
2012a	$B_s^0 \to K_S^0\pi^+\pi^-$	DD	26668.8e-8	551.3e-8	1.5e-8	63.0e-8	70.1e-8	1942.7e-8	2025.9e-8	2862.0e-8
2011	$B_s^0 \to K_S^0\pi^+\pi^-$	DD	27026.9e-8	514.6e-8	1.3e-8	102.0e-8	134.5e-8	2662.9e-8	2025.9e-8	3389.5e-8
2018	$B_s^0 \to K_S^0\pi^+\pi^-$	LL	21530.5e-8	474.4e-8	2.2e-8	28.8e-8	48.5e-8	113.5e-8	568.6e-8	751.3e-8
2017	$B_s^0 \to K_S^0\pi^+\pi^-$	LL	24880.0e-8	513.1e-8	2.3e-8	33.4e-8	44.1e-8	136.0e-8	568.6e-8	779.9e-8
2016	$B_s^0 \to K_S^0\pi^+\pi^-$	LL	25371.5e-8	541.2e-8	2.4e-8	34.8e-8	36.5e-8	132.8e-8	568.6e-8	797.8e-8
2015	$B_s^0 \to K_S^0\pi^+\pi^-$	LL	22088.6e-8	500.5e-8	2.1e-8	32.0e-8	72.7e-8	202.5e-8	568.6e-8	788.2e-8
2012b	$B_s^0 \to K_S^0\pi^+\pi^-$	LL	12460.5e-8	447.8e-8	1.2e-8	27.3e-8	58.9e-8	971.3e-8	568.6e-8	1213.1e-8
2012a	$B_s^0 \to K_S^0\pi^+\pi^-$	LL	86587.3e-9	3884.1e-9	7.7e-9	194.9e-9	559.8e-9	9016.7e-9	5686.2e-9	11360.9e-9
2011	$B_s^0 \to K_S^0\pi^+\pi^-$	LL	15207.0e-8	489.3e-8	1.2e-8	53.0e-8	67.2e-8	1132.2e-8	568.6e-8	1360.9e-8

Table 3.27: $B_s^0 \to K_S^0\pi^+\pi^-$ efficiency table with the unfavoured mode optimisation. For each year and K_S^0 reconstruction type, the average efficiency $\bar{\varepsilon}$, the statistical uncertainty $\sigma_{\bar{\varepsilon}}^{\text{stat}}$, the uncertainty linked to the tracking correction $\sigma_{\bar{\varepsilon}}^{\text{tracking}}$, the uncertainty linked to the L0Hadron trigger correction $\sigma_{\bar{\varepsilon}}^{\text{L0corr}}$, the uncertainty related to the PID MC sampling effect $\sigma_{\bar{\varepsilon}}^{\text{PIDMCsampling}}$, the uncertainty linked to the PID kernel variation $\sigma_{\bar{\varepsilon}}^{\text{PIDkernel}}$, the uncertainty linked to the averaging method $\sigma_{\bar{\varepsilon}}^{\text{RMS}}$ and the total uncertainty $\sigma_{\bar{\varepsilon}}$ are given.

(the systematics evaluated directly on the ratio level are added in the following):

$$\sigma^{\text{propagated}}_{\frac{\bar{\varepsilon}_{B^0\to K_S^0\pi^+\pi^-}}{\bar{\varepsilon}_{B^0_{(s)}\to K_S^0 h^+h'^-}}} = \frac{\bar{\varepsilon}_{B^0\to K_S^0\pi^+\pi^-}}{\bar{\varepsilon}_{B^0_{(s)}\to K_S^0 h^+h'^-}} \times \sqrt{\left(\frac{\sigma_{\bar{\varepsilon}_{B^0\to K_S^0\pi^+\pi^-}}}{\bar{\varepsilon}_{B^0\to K_S^0\pi^+\pi^-}}\right)^2 + \left(\frac{\sigma_{\bar{\varepsilon}_{B^0_{(s)}\to K_S^0 h^+h'^-}}}{\bar{\varepsilon}_{B^0_{(s)}\to K_S^0 h^+h'^-}}\right)^2}. \tag{3.4.7}$$

The major difficulty for the systematics propagation at this level comes from the fact that the correlations between uncertainties depend on the nature of the h and h' particles considered in the ratio.

In the case where h and h' are both pions, the detector effects based mainly on the final state can be factored out and cancelled in the ratio with $B^0 \to K_S^0\pi^+\pi^-$. This is why for

$\bar{\varepsilon}_{B^0\to K^0_S\pi^+\pi^-}/\bar{\varepsilon}_{B^0_s\to K^0_S\pi^+\pi^-}$ ratios, only σ^{stat} and σ^{RMS} are added quadratically and propagated (uncorrelated propagation in order) in the ratio. In the case where at least h or h' is a kaon, all the uncertainties are propagated on the same principle.

Finally, the uncertainties related to the binning scheme, the L0Hadron underlying energy choice, the weighting of the trigger corrections, the K^0_S tracking and signal kinematics simulations are considered to build the final uncertainty. This is done by adding them quadratically to the uncertainty defined in equation 3.4.7.

Tables 3.28 to 3.31 display the ratios of efficiency measured together with their uncertainties for $B^0\to K^0_S K^+K^-$ and $B^0_s\to K^0_S\pi^+\pi^-$. The other tables are given in Appendix C.9.

It is important to note that the uncertainties linked to the binning scheme and the uncertainties linked to the underlying energy choice for Run II, are by construction identical among years. From all the relative efficiency tables, it appears that globally, the three dominant efficiency related systematics are the one related to the averaging method, the one related to the binning scheme and the one related to the MC statistic (with a variable hierarchy depending on the sample). In addition, the one related to the PID kernel choice can become dominant in some samples. Finally, the one related to the trigger fraction impact becomes dominant for the $K^0_S K^+K^-$ LL 2017 and 2018 samples. On the other hand, the tracking related systematic is several orders of magnitude below the dominant ones, and both L0 corrections, PID MC sampling, and L0 underlying energy choice systematics are at least one order of magnitude below the dominant ones.

The systematics related to the averaging method, the binning scheme and the MC reweighting are by construction maximally correlated among years and/or K^0_S reconstruction type. This is why in the following they will not be used in the branching fraction averaging process.

Year	Mode	K^0_S	$\bar{\varepsilon}_{B\to K^0_S hh'}$	$\bar{\varepsilon}_{B^0_s\to K^0_S\pi^+\pi^-}$	$\frac{\bar{\varepsilon}_{B^0_s\to K^0_S\pi^+\pi^-}}{\bar{\varepsilon}_{B\to K^0_S hh'}}$	$\sigma^{\text{stat}}_{\frac{\bar{\varepsilon}_{B^0_s\to K^0_S\pi^+\pi^-}}{\bar{\varepsilon}_{B\to K^0_S hh'}}}$	$\sigma^{\text{tracking}}_{\frac{\bar{\varepsilon}_{B^0_s\to K^0_S\pi^+\pi^-}}{\bar{\varepsilon}_{B\to K^0_S hh'}}}$	$\sigma^{\text{L0corr}}_{\frac{\bar{\varepsilon}_{B^0_s\to K^0_S\pi^+\pi^-}}{\bar{\varepsilon}_{B\to K^0_S hh'}}}$	$\sigma^{\text{PIDMCsampling}}_{\frac{\bar{\varepsilon}_{B^0_s\to K^0_S\pi^+\pi^-}}{\bar{\varepsilon}_{B\to K^0_S hh'}}}$	$\sigma^{\text{PIDkernel}}_{\frac{\bar{\varepsilon}_{B^0_s\to K^0_S\pi^+\pi^-}}{\bar{\varepsilon}_{B\to K^0_S hh'}}}$	$\sigma^{\text{RMS}}_{\frac{\bar{\varepsilon}_{B^0_s\to K^0_S\pi^+\pi^-}}{\bar{\varepsilon}_{B\to K^0_S hh'}}}$	$\sigma^{\text{binning}}_{\frac{\bar{\varepsilon}_{B^0_s\to K^0_S\pi^+\pi^-}}{\bar{\varepsilon}_{B\to K^0_S hh'}}}$	$\sigma^{\text{L0E2choice}}_{\frac{\bar{\varepsilon}_{B^0_s\to K^0_S\pi^+\pi^-}}{\bar{\varepsilon}_{B\to K^0_S hh'}}}$	$\sigma^{\text{FTrigger}}_{\frac{\bar{\varepsilon}_{B^0_s\to K^0_S\pi^+\pi^-}}{\bar{\varepsilon}_{B\to K^0_S hh'}}}$	$\sigma^{\text{MCreweighting}}_{\frac{\bar{\varepsilon}_{B^0_s\to K^0_S\pi^+\pi^-}}{\bar{\varepsilon}_{B\to K^0_S hh'}}}$	$\sigma^{\text{K}^0_S\text{tracking}}_{\frac{\bar{\varepsilon}_{B^0_s\to K^0_S\pi^+\pi^-}}{\bar{\varepsilon}_{B\to K^0_S hh'}}}$	$\sigma^{\text{tot}}_{\frac{\bar{\varepsilon}_{B^0_s\to K^0_S\pi^+\pi^-}}{\bar{\varepsilon}_{B\to K^0_S hh'}}}$
2018	$B^0_s\to K^0_S K^+K^-$	DD	7.28e-04	8.21e-04	1.12748	0.01167	0.00007	0.00144	0.00127	0.00441	0.01748	0.03701	0.00057	0.00696	0.00749	0.00007	0.04404
2017	$B^0_s\to K^0_S K^+K^-$	DD	7.51e-04	8.33e-04	1.10885	0.01180	0.00007	0.00200	0.00101	0.00358	0.01691	0.03701	0.00057	0.00623	0.00736	0.00007	0.04366
2016	$B^0_s\to K^0_S K^+K^-$	DD	8.93e-04	8.69e-04	0.97305	0.00983	0.00005	0.00127	0.00080	0.00380	0.01410	0.03701	0.00057	0.00431	0.00646	0.00005	0.04174
2015	$B^0_s\to K^0_S K^+K^-$	DD	8.04e-04	8.36e-04	1.04000	0.01105	0.00006	0.00146	0.00140	0.00462	0.01574	0.03701	0.00057	0.00638	0.00691	0.00006	0.04305
2012b	$B^0_s\to K^0_S K^+K^-$	DD	4.50e-04	5.19e-04	1.15518	0.01920	0.00006	0.00408	0.00844	0.03072	0.02836	0.03701	0.00018	0.00392	0.00767	0.00006	0.06040
2012a	$B^0_s\to K^0_S K^+K^-$	DD	3.11e-04	4.12e-04	1.32149	0.02751	0.00008	0.00561	0.00228	0.03202	0.04148	0.03701	0.00028	0.00023	0.00877	0.00008	0.07062
2011	$B^0_s\to K^0_S K^+K^-$	DD	3.60e-04	4.92e-04	1.36557	0.02466	0.00007	0.00579	0.00175	0.02169	0.03599	0.03701	0.00023	0.00050	0.00907	0.00007	0.06215
2018	$B^0_s\to K^0_S K^+K^-$	LL	3.05e-04	2.97e-04	0.97387	0.01596	0.00009	0.00101	0.00159	0.00292	0.02233	0.02898	0.00065	0.01729	0.00647	0.00009	0.04412
2017	$B^0_s\to K^0_S K^+K^-$	LL	3.29e-04	3.17e-04	0.96221	0.01606	0.00009	0.00134	0.00131	0.00353	0.02064	0.02898	0.00065	0.01569	0.00639	0.00009	0.04275
2016	$B^0_s\to K^0_S K^+K^-$	LL	3.70e-04	3.56e-04	0.96216	0.01529	0.00008	0.00106	0.00103	0.00364	0.01836	0.02898	0.00065	0.00670	0.00639	0.00008	0.03889
2015	$B^0_s\to K^0_S K^+K^-$	LL	3.33e-04	3.28e-04	0.98409	0.01651	0.00009	0.00114	0.00233	0.00705	0.02047	0.02898	0.00065	0.00656	0.00653	0.00009	0.04092
2012b	$B^0_s\to K^0_S K^+K^-$	LL	1.47e-04	1.53e-04	1.04271	0.03093	0.00010	0.00353	0.00275	0.01914	0.04659	0.02898	0.00047	0.00326	0.00692	0.00010	0.06643
2012a	$B^0_s\to K^0_S K^+K^-$	LL	1.68e-04	1.77e-04	1.05282	0.03178	0.00009	0.00255	0.00355	0.02490	0.04083	0.02898	0.00030	0.00833	0.00699	0.00009	0.06538
2011	$B^0_s\to K^0_S K^+K^-$	LL	1.90e-04	1.88e-04	0.98769	0.02721	0.00007	0.00328	0.00252	0.01838	0.03587	0.02898	0.00036	0.00345	0.00656	0.00007	0.05725

Table 3.28: $B^0\to K^0_S\pi^+\pi^-$ over $B^0\to K^0_S K^+K^-$ efficiency table for the favoured mode optimisation. For each year and K^0_S reconstruction type, the average efficiency of the considered mode, the average efficiency of $B^0\to K^0_S\pi^+\pi^-$, the ratio of average efficiencies, the related uncertainties split by sources and the final uncertainty are given.

Year	Mode	K^0_S	$\bar{\varepsilon}_{B\to K^0_S hh'}$	$\bar{\varepsilon}_{B^0_s\to K^0_S\pi^+\pi^-}$	$\frac{\bar{\varepsilon}_{B^0_s\to K^0_S\pi^+\pi^-}}{\bar{\varepsilon}_{B\to K^0_S hh'}}$	$\sigma^{\text{stat}}_{\frac{\bar{\varepsilon}_{B^0_s\to K^0_S\pi^+\pi^-}}{\bar{\varepsilon}_{B\to K^0_S hh'}}}$	$\sigma^{\text{tracking}}_{\frac{\bar{\varepsilon}_{B^0_s\to K^0_S\pi^+\pi^-}}{\bar{\varepsilon}_{B\to K^0_S hh'}}}$	$\sigma^{\text{L0corr}}_{\frac{\bar{\varepsilon}_{B^0_s\to K^0_S\pi^+\pi^-}}{\bar{\varepsilon}_{B\to K^0_S hh'}}}$	$\sigma^{\text{PIDMCsampling}}_{\frac{\bar{\varepsilon}_{B^0_s\to K^0_S\pi^+\pi^-}}{\bar{\varepsilon}_{B\to K^0_S hh'}}}$	$\sigma^{\text{PIDkernel}}_{\frac{\bar{\varepsilon}_{B^0_s\to K^0_S\pi^+\pi^-}}{\bar{\varepsilon}_{B\to K^0_S hh'}}}$	$\sigma^{\text{RMS}}_{\frac{\bar{\varepsilon}_{B^0_s\to K^0_S\pi^+\pi^-}}{\bar{\varepsilon}_{B\to K^0_S hh'}}}$	$\sigma^{\text{binning}}_{\frac{\bar{\varepsilon}_{B^0_s\to K^0_S\pi^+\pi^-}}{\bar{\varepsilon}_{B\to K^0_S hh'}}}$	$\sigma^{\text{L0E2choice}}_{\frac{\bar{\varepsilon}_{B^0_s\to K^0_S\pi^+\pi^-}}{\bar{\varepsilon}_{B\to K^0_S hh'}}}$	$\sigma^{\text{FTrigger}}_{\frac{\bar{\varepsilon}_{B^0_s\to K^0_S\pi^+\pi^-}}{\bar{\varepsilon}_{B\to K^0_S hh'}}}$	$\sigma^{\text{MCreweighting}}_{\frac{\bar{\varepsilon}_{B^0_s\to K^0_S\pi^+\pi^-}}{\bar{\varepsilon}_{B\to K^0_S hh'}}}$	$\sigma^{\text{K}^0_S\text{tracking}}_{\frac{\bar{\varepsilon}_{B^0_s\to K^0_S\pi^+\pi^-}}{\bar{\varepsilon}_{B\to K^0_S hh'}}}$	$\sigma^{\text{tot}}_{\frac{\bar{\varepsilon}_{B^0_s\to K^0_S\pi^+\pi^-}}{\bar{\varepsilon}_{B\to K^0_S hh'}}}$
2018	$B^0_d\to K^0_S K^+K^-$	DD	4.85e-04	4.13e-04	0.85220	0.01117	0.00005	0.00115	0.00096	0.00334	0.01344	0.03448	0.00049	0.00293	0.00566	0.00005	0.03935
2017	$B^0_d\to K^0_S K^+K^-$	DD	3.74e-04	4.42e-04	1.18184	0.01692	0.00007	0.00224	0.00106	0.00382	0.01797	0.03448	0.00049	0.00214	0.00785	0.00007	0.04342
2016	$B^0_d\to K^0_S K^+K^-$	DD	4.79e-04	4.39e-04	0.91561	0.01228	0.00005	0.00125	0.00075	0.00357	0.01367	0.03448	0.00049	0.00198	0.00608	0.00005	0.03978
2015	$B^0_d\to K^0_S K^+K^-$	DD	4.00e-04	3.47e-04	0.86606	0.01296	0.00005	0.00131	0.00114	0.00385	0.01631	0.03448	0.00049	0.00181	0.00575	0.00005	0.04095
2012b	$B^0_d\to K^0_S K^+K^-$	DD	3.34e-04	3.44e-04	1.02842	0.02012	0.00005	0.00390	0.00763	0.02735	0.01981	0.03448	0.00016	0.00145	0.00683	0.00005	0.05344
2012a	$B^0_d\to K^0_S K^+K^-$	DD	2.11e-04	2.33e-04	1.10696	0.02894	0.00007	0.00449	0.00190	0.02682	0.03169	0.03448	0.00024	0.00052	0.00735	0.00007	0.06187
2011	$B^0_d\to K^0_S K^+K^-$	DD	2.75e-04	2.38e-04	0.86557	0.01971	0.00005	0.00372	0.00112	0.01376	0.02372	0.03448	0.00013	0.00065	0.00575	0.00005	0.04876
2018	$B^0_d\to K^0_S K^+K^-$	LL	2.18e-04	1.91e-04	0.87384	0.01710	0.00009	0.00091	0.00139	0.00262	0.02091	0.02784	0.00071	0.01573	0.00580	0.00009	0.04238
2017	$B^0_d\to K^0_S K^+K^-$	LL	1.84e-04	2.15e-04	1.17202	0.02439	0.00011	0.00170	0.00156	0.00430	0.02565	0.02784	0.00071	0.01233	0.00778	0.00011	0.04759
2016	$B^0_d\to K^0_S K^+K^-$	LL	2.00e-04	2.21e-04	1.10855	0.02245	0.00010	0.00124	0.00119	0.00420	0.02343	0.02784	0.00071	0.00436	0.00736	0.00010	0.04385
2015	$B^0_d\to K^0_S K^+K^-$	LL	2.80e-04	1.99e-04	0.71106	0.01390	0.00006	0.00082	0.00169	0.00510	0.01608	0.02784	0.00071	0.00752	0.00472	0.00006	0.03655
2012b	$B^0_d\to K^0_S K^+K^-$	LL	1.24e-04	1.08e-04	0.87469	0.02930	0.00008	0.00307	0.00230	0.01605	0.03684	0.02784	0.00039	0.00069	0.00581	0.00008	0.05743
2012a	$B^0_d\to K^0_S K^+K^-$	LL	1.41e-04	7.78e-05	0.55044	0.02158	0.00005	0.00146	0.00186	0.01302	0.03152	0.02784	0.00015	0.00380	0.00365	0.00005	0.04937
2011	$B^0_d\to K^0_S K^+K^-$	LL	1.38e-04	1.33e-04	0.96424	0.03120	0.00007	0.00310	0.00258	0.01794	0.03342	0.02784	0.00033	0.00166	0.00640	0.00007	0.05699

Table 3.29: $B^0\to K^0_S\pi^+\pi^-$ over $B^0\to K^0_S K^+K^-$ efficiency table for the unfavoured mode optimisation. For each year and K^0_S reconstruction type, the average efficiency of the considered mode, the average efficiency of $B^0\to K^0_S\pi^+\pi^-$, the ratio of average efficiencies, the related uncertainties split by sources and the final uncertainty are given.

Year	Mode	K^0_S	$\bar{\varepsilon}_{B\to K^0_S hh'}$	$\bar{\varepsilon}_{B^0_s\to K^0_S\pi^+\pi^-}$	$\frac{\bar{\varepsilon}_{B^0_s\to K^0_S\pi^+\pi^-}}{\bar{\varepsilon}_{B\to K^0_S hh'}}$	$\sigma^{\text{stat}}_{\frac{\bar{\varepsilon}_{B^0_s\to K^0_S\pi^+\pi^-}}{\bar{\varepsilon}_{B\to K^0_S hh'}}}$	$\sigma^{\text{tracking}}_{\frac{\bar{\varepsilon}_{B^0_s\to K^0_S\pi^+\pi^-}}{\bar{\varepsilon}_{B\to K^0_S hh'}}}$	$\sigma^{\text{L0corr}}_{\frac{\bar{\varepsilon}_{B^0_s\to K^0_S\pi^+\pi^-}}{\bar{\varepsilon}_{B\to K^0_S hh'}}}$	$\sigma^{\text{PIDMCsampling}}_{\frac{\bar{\varepsilon}_{B^0_s\to K^0_S\pi^+\pi^-}}{\bar{\varepsilon}_{B\to K^0_S hh'}}}$	$\sigma^{\text{PIDkernel}}_{\frac{\bar{\varepsilon}_{B^0_s\to K^0_S\pi^+\pi^-}}{\bar{\varepsilon}_{B\to K^0_S hh'}}}$	$\sigma^{\text{RMS}}_{\frac{\bar{\varepsilon}_{B^0_s\to K^0_S\pi^+\pi^-}}{\bar{\varepsilon}_{B\to K^0_S hh'}}}$	$\sigma^{\text{binning}}_{\frac{\bar{\varepsilon}_{B^0_s\to K^0_S\pi^+\pi^-}}{\bar{\varepsilon}_{B\to K^0_S hh'}}}$	$\sigma^{\text{L0E0choice}}_{\frac{\bar{\varepsilon}_{B^0_s\to K^0_S\pi^+\pi^-}}{\bar{\varepsilon}_{B\to K^0_S hh'}}}$	$\sigma^{\text{FTrigger}}_{\frac{\bar{\varepsilon}_{B^0_s\to K^0_S\pi^+\pi^-}}{\bar{\varepsilon}_{B\to K^0_S hh'}}}$	$\sigma^{\text{MCreweighting}}_{\frac{\bar{\varepsilon}_{B^0_s\to K^0_S\pi^+\pi^-}}{\bar{\varepsilon}_{B\to K^0_S hh'}}}$	$\sigma^{\text{K}^0_S\text{tracking}}_{\frac{\bar{\varepsilon}_{B^0_s\to K^0_S\pi^+\pi^-}}{\bar{\varepsilon}_{B\to K^0_S hh'}}}$	$\sigma^{\text{tot}}_{\frac{\bar{\varepsilon}_{B^0_s\to K^0_S\pi^+\pi^-}}{\bar{\varepsilon}_{B\to K^0_S hh'}}}$
2018	$B^0_s\to K^0_S\pi^+\pi^-$	DD	8.71e-04	8.21e-04	0.942695	0.011326	N/A	N/A	N/A	N/A	0.040485	0.016535	7.582000e-05	0.001743	0.006259	N/A	0.045640
2017	$B^0_s\to K^0_S\pi^+\pi^-$	DD	8.84e-04	8.33e-04	0.942319	0.011576	N/A	N/A	N/A	N/A	0.039858	0.016535	7.582000e-05	0.002949	0.006257	N/A	0.045210
2016	$B^0_s\to K^0_S\pi^+\pi^-$	DD	9.14e-04	8.69e-04	0.951509	0.011623	N/A	N/A	N/A	N/A	0.038909	0.016535	7.582000e-05	0.000830	0.006318	N/A	0.044306
2015	$B^0_s\to K^0_S\pi^+\pi^-$	DD	8.97e-04	8.36e-04	0.931657	0.011695	N/A	N/A	N/A	N/A	0.038894	0.016535	7.582000e-05	0.001304	0.006186	N/A	0.044304
2012b	$B^0_s\to K^0_S\pi^+\pi^-$	DD	5.70e-04	5.19e-04	0.911273	0.016604	N/A	N/A	N/A	N/A	0.060048	0.016535	6.234000e-05	0.000600	0.006051	N/A	0.064745
2012a	$B^0_s\to K^0_S\pi^+\pi^-$	DD	4.59e-04	4.12e-04	0.897631	0.019241	N/A	N/A	N/A	N/A	0.073666	0.016535	4.188000e-05	0.000531	0.005960	N/A	0.078142
2011	$B^0_s\to K^0_S\pi^+\pi^-$	DD	5.48e-04	4.92e-04	0.897117	0.016738	N/A	N/A	N/A	N/A	0.061567	0.016535	3.000000e-06	0.000433	0.005957	N/A	0.066179
2018	$B^0_s\to K^0_S\pi^+\pi^-$	LL	3.29e-04	2.97e-04	0.901442	0.020282	N/A	N/A	N/A	N/A	0.029979	0.024603	1.839600e-04	0.000167	0.005986	N/A	0.044173
2017	$B^0_s\to K^0_S\pi^+\pi^-$	LL	3.57e-04	3.17e-04	0.887666	0.019614	N/A	N/A	N/A	N/A	0.027411	0.024603	1.839600e-04	0.002213	0.005894	N/A	0.042202
2016	$B^0_s\to K^0_S\pi^+\pi^-$	LL	3.98e-04	3.56e-04	0.895650	0.019435	N/A	N/A	N/A	N/A	0.024727	0.024603	1.839600e-04	0.000887	0.005947	N/A	0.040381
2015	$B^0_s\to K^0_S\pi^+\pi^-$	LL	3.61e-04	3.28e-04	0.907644	0.020448	N/A	N/A	N/A	N/A	0.027465	0.024603	1.839600e-04	0.001385	0.006027	N/A	0.042615
2012b	$B^0_s\to K^0_S\pi^+\pi^-$	LL	1.75e-04	1.53e-04	0.877179	0.032607	N/A	N/A	N/A	N/A	0.055617	0.024603	7.000000e-08	0.001253	0.005824	N/A	0.069263
2012a	$B^0_s\to K^0_S\pi^+\pi^-$	LL	2.01e-04	1.77e-04	0.879581	0.032745	N/A	N/A	N/A	N/A	0.048430	0.024603	1.672300e-04	0.001568	0.005840	N/A	0.063715
2011	$B^0_s\to K^0_S\pi^+\pi^-$	LL	2.15e-04	1.88e-04	0.872869	0.029897	N/A	N/A	N/A	N/A	0.045101	0.024603	1.197300e-04	0.000186	0.005796	N/A	0.059723

Table 3.30: $B^0\to K^0_S\pi^+\pi^-$ over $B^0_s\to K^0_S\pi^+\pi^-$ efficiency table for the favoured mode optimisation. For each year and K^0_S reconstruction type, the average efficiency of the considered mode, the average efficiency of $B^0\to K^0_S\pi^+\pi^-$, the ratio of average efficiencies, the related uncertainties split by sources and the final uncertainty are given. An uncertainty at N/A means maximally correlated (same final state) uncertainty which are cancelled in the ratio.

Year	Mode	K^0_S	$\bar{\varepsilon}_{B\to K^0_S hh'}$	$\bar{\varepsilon}_{B^0_s\to K^0_S\pi^+\pi^-}$	$\frac{\bar{\varepsilon}_{B^0_s\to K^0_S\pi^+\pi^-}}{\bar{\varepsilon}_{B\to K^0_S hh'}}$	$\sigma^{\text{stat}}_{\frac{\bar{\varepsilon}_{B^0_s\to K^0_S\pi^+\pi^-}}{\bar{\varepsilon}_{B\to K^0_S hh'}}}$	$\sigma^{\text{tracking}}_{\frac{\bar{\varepsilon}_{B^0_s\to K^0_S\pi^+\pi^-}}{\bar{\varepsilon}_{B\to K^0_S hh'}}}$	$\sigma^{\text{L0corr}}_{\frac{\bar{\varepsilon}_{B^0_s\to K^0_S\pi^+\pi^-}}{\bar{\varepsilon}_{B\to K^0_S hh'}}}$	$\sigma^{\text{PIDMCsampling}}_{\frac{\bar{\varepsilon}_{B^0_s\to K^0_S\pi^+\pi^-}}{\bar{\varepsilon}_{B\to K^0_S hh'}}}$	$\sigma^{\text{PIDkernel}}_{\frac{\bar{\varepsilon}_{B^0_s\to K^0_S\pi^+\pi^-}}{\bar{\varepsilon}_{B\to K^0_S hh'}}}$	$\sigma^{\text{RMS}}_{\frac{\bar{\varepsilon}_{B^0_s\to K^0_S\pi^+\pi^-}}{\bar{\varepsilon}_{B\to K^0_S hh'}}}$	$\sigma^{\text{binning}}_{\frac{\bar{\varepsilon}_{B^0_s\to K^0_S\pi^+\pi^-}}{\bar{\varepsilon}_{B\to K^0_S hh'}}}$	$\sigma^{\text{L0E0choice}}_{\frac{\bar{\varepsilon}_{B^0_s\to K^0_S\pi^+\pi^-}}{\bar{\varepsilon}_{B\to K^0_S hh'}}}$	$\sigma^{\text{FTrigger}}_{\frac{\bar{\varepsilon}_{B^0_s\to K^0_S\pi^+\pi^-}}{\bar{\varepsilon}_{B\to K^0_S hh'}}}$	$\sigma^{\text{MCreweighting}}_{\frac{\bar{\varepsilon}_{B^0_s\to K^0_S\pi^+\pi^-}}{\bar{\varepsilon}_{B\to K^0_S hh'}}}$	$\sigma^{\text{K}^0_S\text{tracking}}_{\frac{\bar{\varepsilon}_{B^0_s\to K^0_S\pi^+\pi^-}}{\bar{\varepsilon}_{B\to K^0_S hh'}}}$	$\sigma^{\text{tot}}_{\frac{\bar{\varepsilon}_{B^0_s\to K^0_S\pi^+\pi^-}}{\bar{\varepsilon}_{B\to K^0_S hh'}}}$
2018	$B^0_s\to K^0_S\pi^+\pi^-$	DD	4.46e-04	4.13e-04	0.925720	0.014300	N/A	N/A	N/A	N/A	0.044302	0.016149	0.000076	0.000669	0.006147	N/A	0.049661
2017	$B^0_s\to K^0_S\pi^+\pi^-$	DD	4.76e-04	4.42e-04	0.929228	0.014369	N/A	N/A	N/A	N/A	0.041697	0.016149	0.000076	0.002202	0.006170	N/A	0.047422
2016	$B^0_s\to K^0_S\pi^+\pi^-$	DD	4.59e-04	4.39e-04	0.955789	0.015121	N/A	N/A	N/A	N/A	0.044337	0.016149	0.000076	0.000185	0.006346	N/A	0.049955
2015	$B^0_s\to K^0_S\pi^+\pi^-$	DD	3.87e-04	3.47e-04	0.894633	0.015503	N/A	N/A	N/A	N/A	0.049522	0.016149	0.000076	0.000431	0.005940	N/A	0.054672
2012b	$B^0_s\to K^0_S\pi^+\pi^-$	DD	3.67e-04	3.44e-04	0.936666	0.020384	N/A	N/A	N/A	N/A	0.054470	0.016149	0.000065	0.000133	0.006219	N/A	0.060679
2012a	$B^0_s\to K^0_S\pi^+\pi^-$	DD	2.67e-04	2.33e-04	0.874118	0.023751	N/A	N/A	N/A	N/A	0.070462	0.016149	0.000036	0.001025	0.005804	N/A	0.076319
2011	$B^0_s\to K^0_S\pi^+\pi^-$	DD	2.70e-04	2.38e-04	0.882287	0.022390	N/A	N/A	N/A	N/A	0.070105	0.016149	0.000017	0.000898	0.005858	N/A	0.075578
2018	$B^0_s\to K^0_S\pi^+\pi^-$	LL	2.15e-04	1.91e-04	0.886392	0.023571	N/A	N/A	N/A	N/A	0.031012	0.030852	0.000185	0.001815	0.005886	N/A	0.050071
2017	$B^0_s\to K^0_S\pi^+\pi^-$	LL	2.49e-04	2.15e-04	0.865431	0.021931	N/A	N/A	N/A	N/A	0.026477	0.030852	0.000185	0.003341	0.005746	N/A	0.046669
2016	$B^0_s\to K^0_S\pi^+\pi^-$	LL	2.54e-04	2.21e-04	0.872506	0.022477	N/A	N/A	N/A	N/A	0.026083	0.030852	0.000185	0.000833	0.005793	N/A	0.046601
2015	$B^0_s\to K^0_S\pi^+\pi^-$	LL	2.21e-04	1.99e-04	0.901892	0.024684	N/A	N/A	N/A	N/A	0.030531	0.030852	0.000185	0.001302	0.005989	N/A	0.050307
2012b	$B^0_s\to K^0_S\pi^+\pi^-$	LL	1.25e-04	1.08e-04	0.870408	0.037483	N/A	N/A	N/A	N/A	0.053037	0.030852	0.000001	0.002075	0.005780	N/A	0.072163
2012a	$B^0_s\to K^0_S\pi^+\pi^-$	LL	8.66e-05	7.78e-05	0.898522	0.049187	N/A	N/A	N/A	N/A	0.077717	0.030852	0.000179	0.000766	0.005966	N/A	0.097197
2011	$B^0_s\to K^0_S\pi^+\pi^-$	LL	1.52e-04	1.33e-04	0.874139	0.034817	N/A	N/A	N/A	N/A	0.043563	0.030852	0.000101	0.001105	0.005804	N/A	0.064006

Table 3.31: $B^0\to K^0_S\pi^+\pi^-$ over $B^0_s\to K^0_S\pi^+\pi^-$ efficiency table for the unfavoured mode optimisation. For each year and K^0_S reconstruction type, the average efficiency of the considered mode, the average efficiency of $B^0\to K^0_S\pi^+\pi^-$, the ratio of average efficiencies, the related uncertainties split by sources and the final uncertainty are given. An uncertainty at N/A means maximally correlated (same final state) uncertainty which are cancelled in the ratio.

3.4.4 Self consistency check between yield and efficiency determination

The average efficiency determination explained in Section 3.3.3 brings one average efficiency per decay mode, period, optimisation choice, and K^0_S reconstruction type, and the mass fit brings yield measurements for the same samples. A test has been built, in order to check the self-consistency of the results. In order to factor out the BF, the test has to compare a ratio of yields to a ratio of average efficiencies. The chosen projection to build these ratios is to use the two K^0_S reconstruction types. The ratios for a given subsample k are written:

$$R_{\bar{\varepsilon}_k} = \bar{\varepsilon}_{k,DD}/\bar{\varepsilon}_{k,LL}; R_{Y_k} = Y_{k,DD}/Y_{k,LL}, \tag{3.4.8}$$

where $\bar{\varepsilon}$ denotes the average efficiency, Y denotes the number of signal events measured from the mass fit, and DD/LL indicate the K^0_S reconstruction type. In that way, the same physics is addressed by these two numbers.

Since the optimisation of the suppressed mode is less populated by backgrounds, the consistency test is run on it. The ratios for each mode and data-taking periods are built, and their corresponding uncertainties adequately propagated.

The systematics related to efficiencies are propagated through the DD over LL ratios of efficiencies built for the self-consistency test. The detector effects systematics, which depends mainly on the h and h' tracks, such as the PID ones, are considered with maximal DD-LL correlations, leading to their cancellation in the ratios. On the other hand, the tracking correction systematic is expected to be uncorrelated between DD and LL, and the L0trigger corrections systematic is conservatively considered uncorrelated too. The systematics linked to the hh'

tracking and L0trigger corrections are propagated in addition with σ^{stat} and σ^{RMS} through the self consistency test.

Finally, systematics related to the binning scheme, the L0Hadron underlying energy choice, and the trigger fraction impact have been evaluated on the DD/LL efficiency ratios and are added quadratically to the efficiency ratios uncertainties.

The agreement of the two numbers is tested, for each combination, in terms of the statistical significance of the difference between these ratios, denoted as distance in the following. This distance for a given subsample is:

$$\text{distance} = \frac{R_{Y_k} - R_{\bar{\varepsilon}_k}}{\sqrt{\sigma^2_{R_{\bar{\varepsilon}_k}} + \sigma^2_{R_{Y_k}}}}. \tag{3.4.9}$$

For a given entry, the test is passed if the absolute distance is below 2.5σ.

The test results for 2018, 2016, 2012b and 2011 are given in tables 3.32 to 3.35. The other tables are provided in Appendix C.10. For the Run II samples, good consistency is obtained between the efficiency and yield determinations. By contrast, the consistency observed for Run I data is much less satisfactory as far as the high yield samples are concerned, this might indicate absolute reconstruction efficiency differences between long and downstream K^0_S. Finally, a global trend can be observed toward negative distances, which could possibly be linked to the previous explanation. In all cases, the branching fractions are measured with the same K^0_S reconstruction category, and therefore those absolute differences are cancelled out in the relative efficiencies.

Here, it is important to notice that this self consistency test has been useful first to debug both the mass fit and the efficiency determination during the analysis construction. The tables themselves are not expected to be shared in the analysis publication, because a more final check has been performed by building a χ^2 test directly at the branching fraction level. This new test is presented in Section 3.5 and will be reported in the publication.

Mode	$\frac{\bar{\varepsilon}_{\text{DD}}}{\bar{\varepsilon}_{\text{LL}}}$	$\frac{Y_{\text{DD}}}{Y_{\text{LL}}}$	$\sigma_{\frac{\bar{\varepsilon}_{\text{DD}}}{\bar{\varepsilon}_{\text{LL}}}}$	$\sigma_{\frac{Y_{\text{DD}}}{Y_{\text{LL}}}}$	distance
$B^0_d \to K^0_S\pi^+\pi^-$	2.17	1.97	0.08	0.14	-1.23
$B^0_d \to K^0_S K^+\pi^-$	2.56	2.50	0.17	0.64	-0.09
$B^0_d \to K^0_S\pi^+ K^-$	2.42	2.21	0.16	0.60	-0.34
$B^0_d \to K^0_S K^+ K^-$	2.22	2.13	0.04	0.09	-0.90
$B^0_s \to K^0_S\pi^+\pi^-$	2.07	1.95	0.15	0.74	-0.16
$B^0_s \to K^0_S K^+\pi^-$	2.57	2.32	0.14	0.23	-0.90
$B^0_s \to K^0_S\pi^+ K^-$	2.39	2.22	0.13	0.22	-0.65
$B^0_s \to K^0_S K^+ K^-$	2.05	2.31	0.54	1.66	0.15

Table 3.32: 2018 self consistency test table with systematics propagated. For each mode, the ratio of average efficiencies, the ratio of yields, the associated uncertainties and the distance are given.

Mode	$\frac{\varepsilon_{\bar{\mathrm{DD}}}}{\varepsilon_{\bar{\mathrm{LL}}}}$	$\frac{\mathrm{Y_{DD}}}{\mathrm{Y_{LL}}}$	$\sigma_{\frac{\varepsilon_{\bar{\mathrm{DD}}}}{\varepsilon_{\bar{\mathrm{LL}}}}}$	$\sigma_{\frac{\mathrm{Y_{DD}}}{\mathrm{Y_{LL}}}}$	distance
$B^0_d \to K^0_S\pi^+\pi^-$	1.98	1.70	0.07	0.15	-1.70
$B^0_d \to K^0_S K^+\pi^-$	2.41	2.66	0.16	1.07	0.23
$B^0_d \to K^0_S\pi^+K^-$	2.53	1.89	0.15	0.66	-0.95
$B^0_d \to K^0_S K^+K^-$	2.40	2.35	0.05	0.12	-0.40
$B^0_s \to K^0_S\pi^+\pi^-$	1.81	2.07	0.13	0.93	0.28
$B^0_s \to K^0_S K^+\pi^-$	2.36	2.28	0.12	0.30	-0.26
$B^0_s \to K^0_S\pi^+K^-$	2.44	2.10	0.12	0.25	-1.21
$B^0_s \to K^0_S K^+K^-$	2.13	41.59	0.56	141.42	0.28

Table 3.33: 2016 self consistency test table with systematics propagated. For each mode, the ratio of average efficiencies, the ratio of yields, the associated uncertainties and the distance are given. The pathological values for $B^0_s \to K^0_S K^+K^-$ reflects the absence of signal in 2016 data for the Long-Long category. They are kept since the uncertainties do cover as they should.

Mode	$\frac{\varepsilon_{\bar{\mathrm{DD}}}}{\varepsilon_{\bar{\mathrm{LL}}}}$	$\frac{\mathrm{Y_{DD}}}{\mathrm{Y_{LL}}}$	$\sigma_{\frac{\varepsilon_{\bar{\mathrm{DD}}}}{\varepsilon_{\bar{\mathrm{LL}}}}}$	$\sigma_{\frac{\mathrm{Y_{DD}}}{\mathrm{Y_{LL}}}}$	distance
$B^0_d \to K^0_S\pi^+\pi^-$	3.17	2.17	0.17	0.22	-3.58
$B^0_d \to K^0_S K^+\pi^-$	5.40	4.89	0.70	2.25	-0.22
$B^0_d \to K^0_S\pi^+K^-$	5.48	2.37	0.60	1.10	-2.48
$B^0_d \to K^0_S K^+K^-$	2.70	1.81	0.09	0.14	-5.43
$B^0_s \to K^0_S\pi^+\pi^-$	2.95	2.64	0.26	1.42	-0.21
$B^0_s \to K^0_S K^+\pi^-$	4.60	5.52	0.54	0.97	0.82
$B^0_s \to K^0_S\pi^+K^-$	5.05	3.63	0.41	0.61	-1.92
$B^0_s \to K^0_S K^+K^-$	2.75	0.99	0.88	0.80	-1.47

Table 3.34: 2012b self consistency test table with systematics propagated. For each mode, the ratio of average efficiencies, the ratio of yields, the associated uncertainties and the distance are given.

Mode	$\frac{\varepsilon_{\bar{\mathrm{DD}}}}{\varepsilon_{\bar{\mathrm{LL}}}}$	$\frac{\mathrm{Y_{DD}}}{\mathrm{Y_{LL}}}$	$\sigma_{\frac{\varepsilon_{\bar{\mathrm{DD}}}}{\varepsilon_{\bar{\mathrm{LL}}}}}$	$\sigma_{\frac{\mathrm{Y_{DD}}}{\mathrm{Y_{LL}}}}$	distance
$B^0_d \to K^0_S\pi^+\pi^-$	1.79	1.36	0.10	0.25	-1.62
$B^0_d \to K^0_S K^+\pi^-$	3.08	2.32	0.27	1.07	-0.69
$B^0_d \to K^0_S\pi^+K^-$	2.59	2.10	0.20	0.67	-0.71
$B^0_d \to K^0_S K^+K^-$	2.00	1.37	0.06	0.16	-3.68
$B^0_s \to K^0_S\pi^+\pi^-$	1.78	2.20	0.18	1.79	0.24
$B^0_s \to K^0_S K^+\pi^-$	2.56	1.97	0.19	0.35	-1.49
$B^0_s \to K^0_S\pi^+K^-$	2.46	1.61	0.16	0.25	-2.87
$B^0_s \to K^0_S K^+K^-$	2.25	1.69	0.72	1.13	-0.41

Table 3.35: 2011 self consistency test table with systematics propagated. For each mode, the ratio of average efficiencies, the ratio of yields, the associated uncertainties and the distance are given.

3.5 Branching fraction measurements

All the ingredients necessary to measure the five time-integrated ratios of branching fractions to the six physically distinct final states are now at hand. As explained in Section 3.4.1, ratios of branching fractions are built for each subsample individually (splitting by data-taking period, K^0_S reconstruction type, and optimisation), but at the end the goal is to provide one unique branching fraction for each mode. In this section, the method used to build the average ratios of branching fraction is first explained, then the actual results are provided, and finally a comparison with the previous analysis is made.

3.5.1 Combined relative branching fraction determination

First of all, as a reminder, there are two different optimised working points of the MVA selection for each final state. To consider one relative branching fractions for each mode, K^0_S reconstruction type and data-taking period, the most appropriate selection is used, *i.e.* the PrincipalPeak (looser) optimisation is used for most favoured decays such as $B^0 \to K^0_S K^+ K^-$ (but see below for the special case of $B^0 \to K^0_S \pi^+ \pi^-$), and the SecondaryPeak (tighter) optimisation is used for suppressed decays such as $B^0_s \to K^0_S \pi^\pm \pi^\mp$. The formula used to go from the input quantities (yields, efficiencies, etc.) to the observable (ratio of branching fractions BF_r) is:

$$BF_r(B^0_{d,s} \to K^0_S h^+ h'^-) = \frac{BF(B^0_{d,s} \to K^0_S h^+ h'^-)}{BF(B^0 \to K^0_S \pi^+ \pi^-)} = \frac{N_{B^0_{d,s} \to K^0_S h^+ h'^-}}{N_{ref}} \frac{\epsilon_{ref}}{\epsilon_{B^0_{d,s} \to K^0_S h^+ h'^-}} \frac{f_d}{f_{d,s}} \quad (3.5.1)$$

where $BF(X)$ is the branching fraction of decay X, N_X is its fitted yield, ϵ_X is its average efficiency, f_d and f_s are the fragmentation fractions of B^0_d and B^0_s mesons, and N_{ref} and ε_{ref} are the yield and efficiency of the normalisation (reference) channel, $B^0 \to K^0_S \pi^+ \pi^-$. The fragmentation fractions of B^0 and B^0_s mesons are taken from [193]:

$$f_s/f_d(7\,\text{TeV} - 2011) = 0.2390 \pm 0.0076 \quad (3.5.2)$$
$$f_s/f_d(8\,\text{TeV} - 2012) = 0.2385 \pm 0.0075 \quad (3.5.3)$$
$$f_s/f_d(13\,\text{TeV} - \text{Run II}) = 0.2539 \pm 0.0079 \quad (3.5.4)$$

For consistency, the same MVA optimisation choice (PrincipalPeak or SecondaryPeak) is used for both the numerator and denominator decay modes. For example, for the suppressed mode $B^0_s \to K^0_S \pi^+ \pi^-$ the SecondaryPeak optimisation is used, and thus in the corresponding ratio the SecondaryPeak optimisation is also used for the control mode (even though it is a favoured mode).

All individual relative branching fractions determined are given in Appendix C.11.

Averaging method

For each mode X, the average ratio of branching fractions, $BF_r(X)$, is taken as the value that minimises the χ^2:

$$\chi^2(X) = \sum_{ks,y} \left(\frac{BF_r(X) - BF_r(X)_{ks,y}}{(\Delta BF_{ks,y})_{\text{tot}}} \right)^2, \quad (3.5.5)$$

where $(\Delta BF_{ks,y})_{\text{tot}}$ is the total uncertainty on the branching fraction ratio for year y and ks the type of K^0_S reconstruction. This uncertainty should include the statistical uncertainty and the systematic uncertainties uncorrelated among the samples used in the averaging to not

bias the averaged values. However, the results presented here are determined considering all the systematics in the branching fraction averaging. This will be updated in next version of the analysis.

Minimising the χ^2 means finding the $BF_r(X)$ value that sets the χ^2 derivative at zero in:

$$\frac{\mathrm{d}\chi^2(X)}{\mathrm{d}BF_r(X)} = \sum_{ks,y}\left(\frac{2(BF_r(X) - BF_r(X)_{ks,y})}{(\Delta BF_{ks,y})^2_{\mathrm{tot}}}\right) = 0. \tag{3.5.6}$$

The average ratio of branching fraction for mode X can thus be expressed as:

$$BF_r(X) = \frac{1}{\sum_{ks,y} 1/(\Delta BF_{ks,y})^2_{\mathrm{tot}}} \sum_{ks,y} \frac{BF_r(X)_{ks,y}}{(\Delta BF_{ks,y})^2_{\mathrm{tot}}} \tag{3.5.7}$$

Note that for the final results the average is done over all sub-samples (from 2011 to 2018), but it is also possible to average over just some of them. This will be done in Section 3.5.3 for Run I.

χ^2 test results

Using equation 3.5.5 together with the average relative branching fraction allows a χ^2 test to check the compatibility of the individual ratios with the averaged ratios. The χ^2 test is built for each mode using χ^2 by the number of degrees of freedom (χ^2/ndof). This number is determined by computing the χ^2 defined in equation 3.5.5 and dividing it by the number of degrees of freedom *e.g.* the number of individual ratio values minus one, so it is thirteen here. Finally, the p-values associated with each mode are computed from the corresponding χ^2/ndof. It has been defined a priori that the averages won't be examined further if their corresponding p-values are found larger than 5%. Table 3.36 summarises the results of the χ^2 test for the analysis. The output of the test is that no p-values lower than 5% are found but the one attached to $B^0_s \to K^0_{\mathrm{S}}K^+K^-$, which means that most individual ratios are compatible with the averaged ones. The low p-value observed for the decay mode $B^0_s \to K^0_{\mathrm{S}}K^+K^-$ has been tracked down to be due to a subsample of the year 2016 and seems to be a genuine statistical fluctuation.

Decay Mode	χ^2(uncorr)/ndof	$\mathrm{p}-\mathrm{values}$
$B^0 \to K^0_{\mathrm{S}}K^+K^-$	17.7/13	16.93
$B^0 \to K^0_{\mathrm{S}}\pi^+K^-$	11.38/13	57.89
$B^0 \to K^0_{\mathrm{S}}K^+\pi^-$	8.15/13	83.35
$B^0 \to K^0_{\mathrm{S}}K^\pm\pi^\mp$	6.95/13	90.48
$B^0_s \to K^0_{\mathrm{S}}\pi^+\pi^-$	7.6/13	86.87
$B^0_s \to K^0_{\mathrm{S}}K^+K^-$	24.22/13	2.91
$B^0_s \to K^0_{\mathrm{S}}\pi^+K^-$	9.19/13	75.85
$B^0_s \to K^0_{\mathrm{S}}K^+\pi^-$	9.99/13	69.45
$B^0_s \to K^0_{\mathrm{S}}K^\pm\pi^\mp$	9.52/13	73.26

Table 3.36: χ^2 per degree of freedom of the combination for each decay process.

3.5.2 Combined relative branching fraction measurements

The averaged results coming from the method previously defined are:

$$\frac{BF(B^0 \to K^0_S K^+ K^-)}{BF(B^0 \to K^0_S \pi^+ \pi^-)}_{\text{Combined}} = 0.533 \pm 0.006\,(\text{stat.}) \pm 0.006\,(\text{syst.uncorr}) \pm 0.013\,(\text{syst.corr}) = 0.533 \pm 0.015\,(\text{tot.})$$

$$\frac{BF(B^0 \to K^0_S K^\pm \pi^\mp)}{BF(B^0 \to K^0_S \pi^+ \pi^-)}_{\text{Combined}} = 0.1366 \pm 0.0035\,(\text{stat.}) \pm 0.0046\,(\text{syst.uncorr}) \pm 0.0025\,(\text{syst.corr}) = 0.137 \pm 0.006\,(\text{tot.})$$

$$\frac{BF(B^0_s \to K^0_S \pi^+ \pi^-)}{BF(B^0 \to K^0_S \pi^+ \pi^-)}_{\text{Combined}} = 0.276 \pm 0.013\,(\text{stat.}) \pm 0.019\,(\text{syst.uncorr}) \pm 0.010\,(\text{syst.corr}) \pm 0.005\,(f_s/f_d) = 0.276 \pm 0.025\,(\text{tot.})$$

$$\frac{BF(B^0_s \to K^0_S K^+ K^-)}{BF(B^0 \to K^0_S \pi^+ \pi^-)}_{\text{Combined}} = 0.0343 \pm 0.0044\,(\text{stat.}) \pm 0.0031\,(\text{syst.uncorr}) \pm 0.0042\,(\text{syst.corr}) \pm 0.0006\,(f_s/f_d) = 0.034 \pm 0.007\,(\text{tot.})$$

$$\frac{BF(B^0_s \to K^0_S K^\pm \pi^\mp)}{BF(B^0 \to K^0_S \pi^+ \pi^-)}_{\text{Combined}} = 1.782 \pm 0.020\,(\text{stat.}) \pm 0.013\,(\text{syst.uncorr}) \pm 0.020\,(\text{syst.corr}) \pm 0.025\,(f_s/f_d) = 1.78 \pm 0.04\,(\text{tot.})$$

where the systematic uncertainties are presented split into uncorrelated and correlated categories.

As explained in Figures 3.20, 3.22, and 3.24, hint of a missing contribution can be seen in the $K^0_S K^+ K^-$ fit spectra after the B^0_s crossfeed area, and this will be addressed with next update of the analysis. Because of that, the branching fractions provided for both $B^0 \to K^0_S K^+ K^-$ and $B^0_s \to K^0_S K^+ K^-$ in this manuscript are not final and will change. In any case, the discovery of $B^0_s \to K^0_S K^+ K^-$ is already guaranteed from the yields extracted in Section 3.2.2.

3.5.3 Comparison with the previous analysis

As explained in Section 1.4.4, these branching fraction ratios have already been previously measured in LHCb. In particular, a previous analysis [68] measured them with $3\,\text{fb}^{-1}$ of data (Run I dataset only). Table 3.37 compares the results of the previous analysis with this one. The average results of the current analysis are shown from the Run I samples only (for comparison) and from the full Run I + Run II dataset.

Decay Mode	$B^0 \to K^0_S K^+ K^-$	$B^0 \to K^0_S K^\pm \pi^\mp$	$B^0_s \to K^0_S \pi^+ \pi^-$	$B^0_s \to K^0_S K^\pm \pi^\mp$
$BF_r(X)$ published	$0.549 \pm 0.018 \pm 0.033$	$0.123 \pm 0.009 \pm 0.015$	$0.191 \pm 0.027 \pm 0.033$	$1.70 \pm 0.07 \pm 0.15$
$BF_r(X)$ this (only Run I)	$0.509 \pm 0.015 \pm 0.016$	$0.134 \pm 0.010 \pm 0.011$	$0.295 \pm 0.032 \pm 0.040$	$1.88 \pm 0.05 \pm 0.06$
$BF_r(X)$ this	$0.533 \pm 0.006 \pm 0.014$	$0.1366 \pm 0.0035 \pm 0.0052$	$0.276 \pm 0.013 \pm 0.022$	$1.782 \pm 0.020 \pm 0.035$

Table 3.37: Comparison of the measured ratios of branching fractions obtained in three different ways: from this analysis using Run I results only, from this analysis using the full dataset, and from the previous analysis using Run I results only (*published*).

From the statistical uncertainties point of view, as expected, the Run I-only measurements are very similar, and the addition of the Run II reduces them by a factor two or three (roughly in line with, and a little better than, the gain expected from integrated luminosity and cross-section increases). Concerning the systematic uncertainties, the ones of the current analysis are always better (at least when relative uncertainty is considered) than those of the previous analysis. This means that, even for the systematically limited modes, the measurement is improved[9]. Note that because the selection has changed significantly, the statistical uncertainties are not fully correlated with the previous analysis, and the largest systematic uncertainties are changed greatly and probably effectively uncorrelated. With this in mind, it appears that the results

[9]This is not surprising, given that in the previous analysis the dominant systematic uncertainties were associated with the fit model, and in particular with the difficulty of fitting spectra with multiple overlapping crossfeeds. The reduction of crossfeeds is one of the major improvements in this analysis.

for each measured ratio are compatible with the previous LHCb analysis (see also figure 3.31) except for $B_s^0 \to K_S^0\pi^+\pi^-$.

There have been several improvements since the previous analysis, and two, in particular, which make the current results more reliable. First, improvements in the background suppression (particularly crossfeeds, but also partially reconstructed b-hadron decays) allow more accurate measurements. Second, the data samples are much larger, which improves data-driven corrections; this includes the usual items (PID, tracking, trigger) but also the averaging of the efficiency correction itself. The distribution of signal across the phase space is not known *a priori* and must be measured from data; this analysis takes advantage of the large yields in the Run II dataset to control this much better than what was possible previously (and improvements in signal purity help here, also). When reverting to the method employed in the former analysis to determine the selection efficiencies across the phase space, a fair agreement between the selected datasets is observed for all modes.

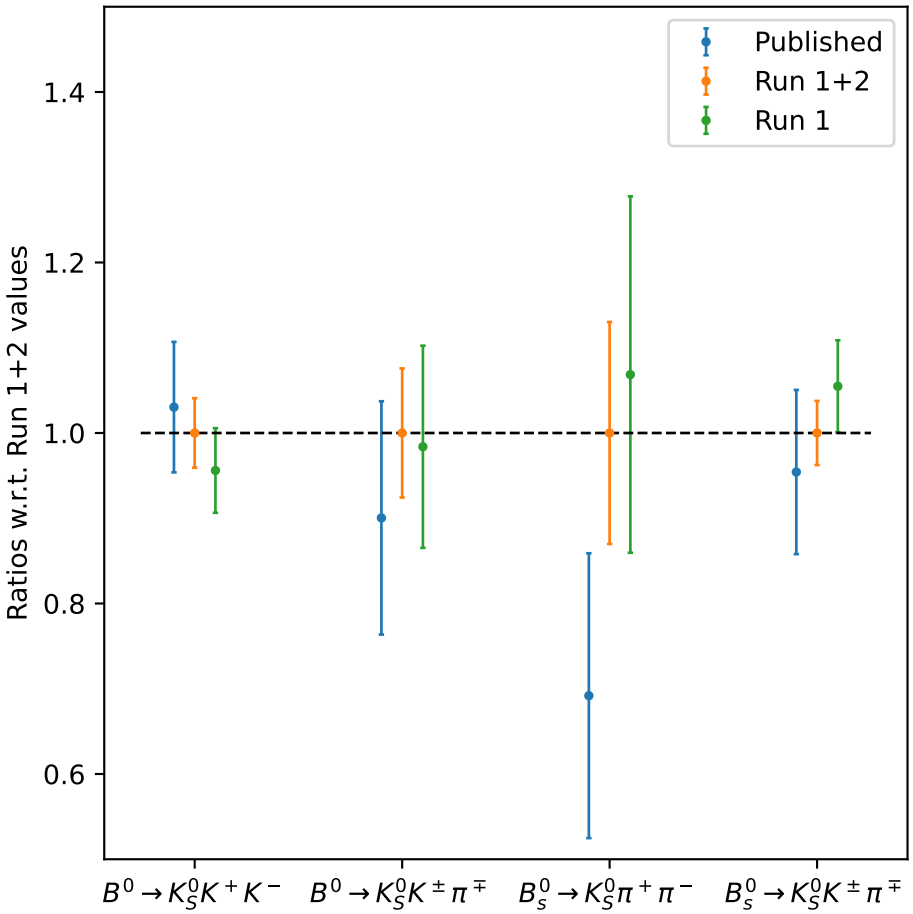

Figure 3.31: Comparison of the measured results (ratios of branching fractions) between this analysis and the previous one. The values are normalised to the results of this analysis (using the full Run I + Run II dataset), which are shown in orange. The green points show the Run I-only averages from this analysis. The blue points show the previous Run I analysis results. The error bars shown include statistical and systematic uncertainties.

3.6 Conclusion of the analysis

The analysis reported in this chapter aimed to measure the branching fractions of the charmless three-body $B-$mesons decays with a K^0_S in the final state, the $B^0_{d,s} \to K^0_S h^+ h'^-$ decays and to observe $B^0_s \to K^0_S K^+ K^-$, with the LHCb data from Run I and Run II. All branching fractions are measured relative to the well-established $B^0 \to K^0_S \pi^+ \pi^-$ mode to factor out detector effects in the measurements.

For these purposes, the full dataset is split into several subsamples. Dedicated selections have been built to prepare the data. The selection features, in particular, two 2D-MVA optimisations, each tuned for the study of the B^0 or the B^0_s decay in a given spectrum. The numbers of decays recorded by LHCb are extracted from simultaneous fits of the mass spectra. Several sources of background are taken into account in the mass fits in order to describe the data as best as possible. The efficiencies are determined from MC simulations weighted with respect to the phase space of the decay found in the data (sWeights) and corrected from various experimental effects (trigger, tracking, PID). The relative branching fraction measurements obtained after recombination of the results associated to each subsample are:

$$\left.\frac{BF(B^0 \to K^0_S K^+ K^-)}{BF(B^0 \to K^0_S \pi^+ \pi^-)}\right|_{\text{Combined}} = 0.533 \pm 0.015\,(\text{tot.})$$

$$\left.\frac{BF(B^0 \to K^0_S K^\pm \pi^\mp)}{BF(B^0 \to K^0_S \pi^+ \pi^-)}\right|_{\text{Combined}} = 0.137 \pm 0.006\,(\text{tot.})$$

$$\left.\frac{BF(B^0_s \to K^0_S \pi^+ \pi^-)}{BF(B^0 \to K^0_S \pi^+ \pi^-)}\right|_{\text{Combined}} = 0.276 \pm 0.025\,(\text{tot.})$$

$$\left.\frac{BF(B^0_s \to K^0_S K^+ K^-)}{BF(B^0 \to K^0_S \pi^+ \pi^-)}\right|_{\text{Combined}} = 0.034 \pm 0.007\,(\text{tot.})$$

$$\left.\frac{BF(B^0_s \to K^0_S K^\pm \pi^\mp)}{BF(B^0 \to K^0_S \pi^+ \pi^-)}\right|_{\text{Combined}} = 1.78 \quad \pm 0.04\,(\text{tot.})$$

Compared to the previous LHCb analysis, this one provides compatible results, except for $B^0_s \to K^0_S \pi^+ \pi^-$, with improved precision. The observed departure on the aforementioned mode comes from the fact that the analysis techniques used are enhanced. The new results are more accurate and educated. Finally, this analysis provides the discovery of $B^0_s \to K^0_S K^+ K^-$.

The analysis is close to its published version but still in the collaboration review process. This means that the results present here can evolve from now to the publication if there is a need for modification. In particular (see Section 3.5.2), the branching fractions provided for both $B^0 \to K^0_S K^+ K^-$ and $B^0_s \to K^0_S K^+ K^-$ are not final. In any case, the discovery of $B^0_s \to K^0_S K^+ K^-$ is guaranteed from the yields extracted.

This branching fraction analysis is the first step towards amplitude analyses that will address the rich phenomenology of the $B^0_{d,s} \to K^0_S h^+ h'^-$ transitions. The Chapter 4 presents a preliminary amplitude analysis of $B^0_s \to K^0_S \pi^+ \pi^-$.

Chapter 4

Prototyping of the $B_s^0 \to K_S^0\pi^+\pi^-$ time-integrated Dalitz plot analysis

This chapter is an outlook about the time-integrated amplitude analysis of $B_s^0 \to K_S^0\pi^+\pi^-$, the next LHCb Clermont analysis of the $B_{(s)}^0 \to K_S^0 h^+ h'^-$ decay modes. The goal of the $B_s^0 \to K_S^0\pi^+\pi^-$ time-integrated amplitude analysis is to search for *CP* violation in decay in quasi-two-body states of $B_s^0 \to K_S^0\pi^+\pi^-$, such as $B_s^0 \to K^{*-}\pi^+$ or $B_s^0 \to K_S^0\rho^0$ (see Section 1.4.2). In order to account for the quasi-two-body decay kinematics specificities, the analysis uses the Dalitz plot formalism [194, 195]. The LHCb Clermont group has already performed a time-integrated analysis of $B^0 \to K_S^0\pi^+\pi^-$ with the LHCb Run I data [70]; the analysis reported in this chapter, with the current LHCb dataset (Run I + Run II); benefits maximally from this work using the previously developed CRAFT software (Clermont Root-based Amplitude Fitter Tool). The CRAFT software [69] was developed by Marouen Baalouch during its thesis. As a user, my contribution to CRAFT mostly concerns the determination of the inputs required from the $B_{(s)}^0 \to K_S^0 h^+ h'^-$ branching fraction analysis.

The work reported in this chapter is only an outlook on the $B_{(s)}^0 \to K_S^0 h^+ h'^-$ branching fraction analysis. The complete analysis would have required more time than what was available in the last part of my Ph.D. program. The goal of this chapter is to briefly present the upcoming analysis with some preliminary plots and results. In this chapter, the formalism of the analysis is first introduced, and then a preliminary analysis, limited to the 2018 data; is presented.

4.1 The Dalitz formalism

In this section, the formalism needed to understand the $B_s^0 \to K_S^0\pi^+\pi^-$ time-integrated analysis is presented. For further details, the reference document is the Marouen Baalouch thesis [69].

4.1.1 The Dalitz Plot

To describe the kinematics of the $B_s^0 \to K_S^0\pi^+\pi^-$ decay, one needs the four 4-vectors energy-momenta of the decay:

$$p_{B_s^0} = (m_{B_s^0}, \vec{p_{B_s^0}}),\ p_{K_S^0} = (E_{K_S^0}, \vec{p_{K_S^0}}),\ p_{\pi^+} = (E_{\pi^+}, \vec{p_{\pi^+}}),\ p_{\pi^-} = (E_{\pi^-}, \vec{p_{\pi^-}}), \tag{4.1.1}$$

here written in the B_s^0 rest frame, with twelve unknowns in the system corresponding to the daughter 4-vector components.

The partial decay rate of $B_s^0 \to K_S^0\pi^+\pi^-$ reads:

$$d\Gamma = \frac{(2\pi)^4}{2m_{B_s^0}} |\mathcal{A}|^2 d\Phi_3(p_{B_s^0}, p_{K_S^0}, p_{\pi^+}, p_{\pi^-}), \tag{4.1.2}$$

where $\mathcal{A}$ corresponds to the decay amplitude of $B_s^0 \to K_S^0\pi^+\pi^-$ and $d\Phi_3$ corresponds to the phase space element of $B_s^0 \to K_S^0\pi^+\pi^-$ defined as

$$d\Phi_3(p_{B_s^0}, p_{K_S^0}, p_{\pi^+}, p_{\pi^-}) = \delta(m_{B_s^0} - E_{K_S^0} - E_{\pi^+} - E_{\pi^-})\frac{dp_{K_S^0}}{E_{K_S^0}}\frac{dp_{\pi^+}}{E_{\pi^+}}\frac{dp_{\pi^-}}{E_{\pi^-}}. \tag{4.1.3}$$

The twelve unknowns in the system can be reduced to only two independent free parameters due to the three-body decay features. Indeed, at first, the knowledge of the three particle daughter masses brings three constraints. Secondly, the energy-momentum conservation in the decay brings four constraints. And third, the spin conservation in the decay brings the last three constraints.

In the end, two of the three two-body invariant masses squared, also named DP variables, are enough to describe the system. The three possible DP variables of the system are:

$$m^2_{K_S^0\pi^+} \equiv s_+ = (p_{K_S^0} + p_{\pi^+})^2, \tag{4.1.4}$$

$$m^2_{K_S^0\pi^-} \equiv s_- = (p_{K_S^0} + p_{\pi^-})^2, \tag{4.1.5}$$

$$m^2_{\pi^-\pi^+} \equiv s_0 = (p_{\pi^-} + p_{\pi^+})^2. \tag{4.1.6}$$

In the analysis s_+ and s_- are chosen to describe the decay kinematics. It is possible to write the remaining DP variable with respect to them via the DP boundary equation:

$$s_0 = m^2_{B_s^0} + m^2_{K_S^0} + m^2_{\pi^+} + m^2_{\pi^-} - s_+ - s_-. \tag{4.1.7}$$

The partial decay rate can then be rewritten with the two DP variables as :

$$d\Gamma = \frac{1}{(2\pi)^3}\frac{|\mathcal{A}|^2}{32m_{B_s^0}}ds_+ds_-. \tag{4.1.8}$$

More details about DP variables and their introduction in the partial decay rate can be found in Appendix A of Ref. [69].

The two chosen DP variables define the $(m^2_{K_S^0\pi^+}, m^2_{K_S^0\pi^-})$ plan, where one can project the $B_s^0 \to K_S^0\pi^+\pi^-$ events. The positions accessible to the events are constrained by the decay kinematic. Figure 4.1 shows the accessible area of the plan for $B_s^0 \to K_S^0\pi^+\pi^-$ and details its limits.

4.1.2 Helicity angle

Consider the indices i, j, and k representing the three daughters of a three-body decay process such as $X \to ijk$. The helicity angle $(\theta_H)_{ij}$ represents the angle between j and k in the ij rest frame. Therefore, $(\theta_H)_{ij}$ is defined as:

$$\cos(\theta_H)_{ij} = \frac{(m^2_{jk})_{\max} + (m^2_{jk})_{\min} - 2m^2_{jk}}{(m^2_{jk})_{\max} - (m^2_{jk})_{\min}}, \tag{4.1.9}$$

where m^2_{jk} is the DP variable built with i and j, $(m^2_{jk})_{\min}$ and $(m^2_{jk})_{\max}$ are the m^2_{jk} limits. For the analysis reported here, $X \to ijk$ is identified as $B_s^0 \to \pi^+\pi^-K_S^0$.

The spin of a quasi-two-body resonance can be identified by its distribution in $\cos(\theta_H)$. For example, a spin 0 or scalar resonance has a uniform distribution in $\cos(\theta_H)$, which is uniform in the DP. A spin 1 or vector resonance populates two regions separated by a depleted node in the DP. A spin 2 or tensor resonance populates three regions separated by two depleted nodes in the DP. Figure 4.2 illustrates the DP distributions corresponding to these three spin values for a resonance of another $B^0_{(s)} \to K_S^0h^+h'^-$ mode. Mathematical details on the angular distribution in the DP can be found in Appendix B of Ref. [69].

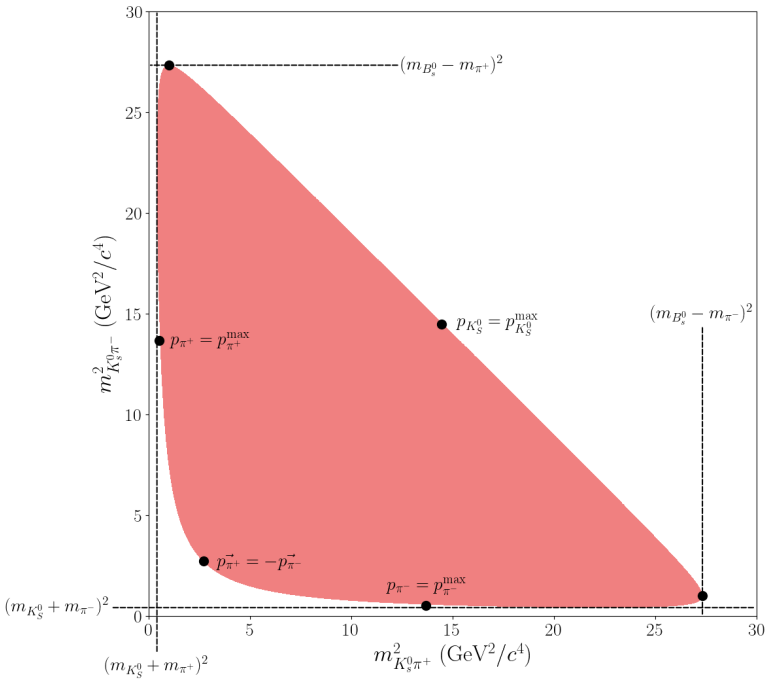

Figure 4.1: Accessible area in the $(m^2_{K^0_S\pi^+}, m^2_{K^0_S\pi^-})$ DP of the $B^0_s \to K^0_S\pi^+\pi^-$ decay, represented in red. The limits of the DP are represented by the dashed lines. The points display special points of the DP in term of daughter four-momenta.

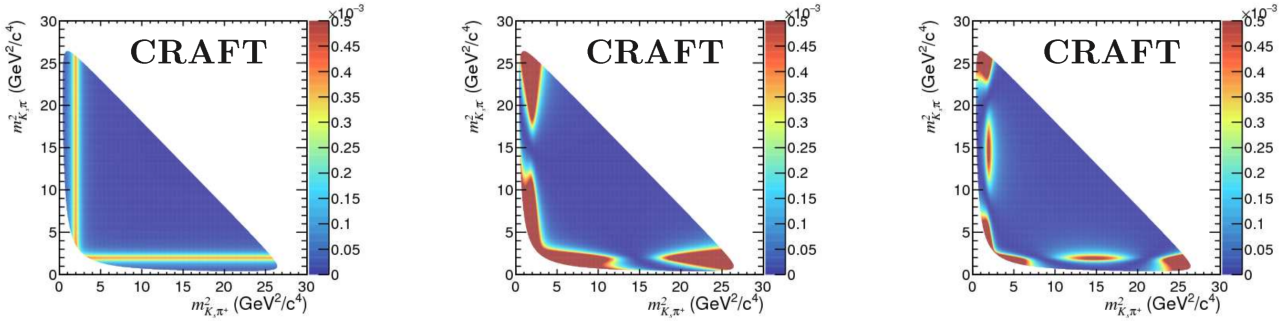

Figure 4.2: Distribution of the $K^{*\pm}(1430)$ resonance in the $B^0 \to K^0_S\pi^+\pi^-$ DP, for different spin values, spin 0 (left), spin 1 (middle) and spin 2 (right).

4.1.3 The Square Dalitz Plot

Usually, most of the interference between the amplitudes implying intermediate resonances are located on the edges of the DP, leading to observe the interesting physics of the decay on a small DP region only. An advantageous transformation can be applied to the standard DP variables to build the square DP (sqDP) variables (m', θ'), to better display the physics of interest. For $B^0_s \to K^0_S\pi^+\pi^-$, the sqDP variables read:

$$m' = \frac{1}{\pi} \arccos\left(2\frac{m_{\pi^+\pi^-} - m^{\min}_{\pi^+\pi^-}}{m^{\max}_{\pi^+\pi^-} - m^{\min}_{\pi^+\pi^-}} - 1\right), \tag{4.1.10}$$

$$\theta' = \frac{(\theta_H)_{\pi^+\pi^-}}{\pi}, \tag{4.1.11}$$

where $m^{(\max,\min)}_{\pi\pi}$ is defined as the square root of the third DP variable (limits) and $(\theta_H)_{\pi^+\pi^-}$ is the helicity angle of the $\pi^+\pi^-$ resonance (CP-eigenstate resonance).

The sqDP differential element can be determined from the DP differential element as:

$$\mathrm{d}m^2_{K^0_S\pi^+}\mathrm{d}m^2_{K^0_S\pi^-} \rightarrow |\det J|\mathrm{d}m'\mathrm{d}\theta', \tag{4.1.12}$$

with J the Jacobian of the transformation. Here $|\det J|$ reads as:

$$|\det J| = 4\sqrt{E^{*,2}_{\pi^+} - m^2_{\pi^+}}\sqrt{E^{*,2}_{K^0_S} - m^2_{K^0_S}}m_{\pi^+\pi^-}\frac{\partial m_{\pi^+\pi^-}}{\partial m'}\frac{\partial \cos(\theta_H)_{\pi^+\pi^-}}{\partial \theta'}, \tag{4.1.13}$$

where the E^*'s are evaluated in the $\pi^+\pi^-$ rest frame and with

$$\frac{\partial m_{\pi^+\pi^-}}{\partial m'} = -\frac{\pi}{2}\sin(\pi m')(m^{max}_{\pi^+\pi^-} - m^{min}_{\pi^+\pi^-}), \tag{4.1.14}$$

$$\frac{\partial \cos(\theta_H)_{\pi^+\pi^-}}{\partial \theta'} = -\pi\sin(\theta'\pi). \tag{4.1.15}$$

The Jacobian definition needs to choose one of the $\pi^+\pi^-$ resonance to be used under the first root squared term, here the π^+ choice is done.

Figure 4.3 displays the DP and the sqDP distribution corresponding to $B^0_s \rightarrow K^0_S\pi^+\pi^-$ 2018 data. The sqDP transformation was first used in 2009 by the BaBar collaboration in the analysis of $B^+ \rightarrow \pi^+\pi^+\pi^-$ [196].

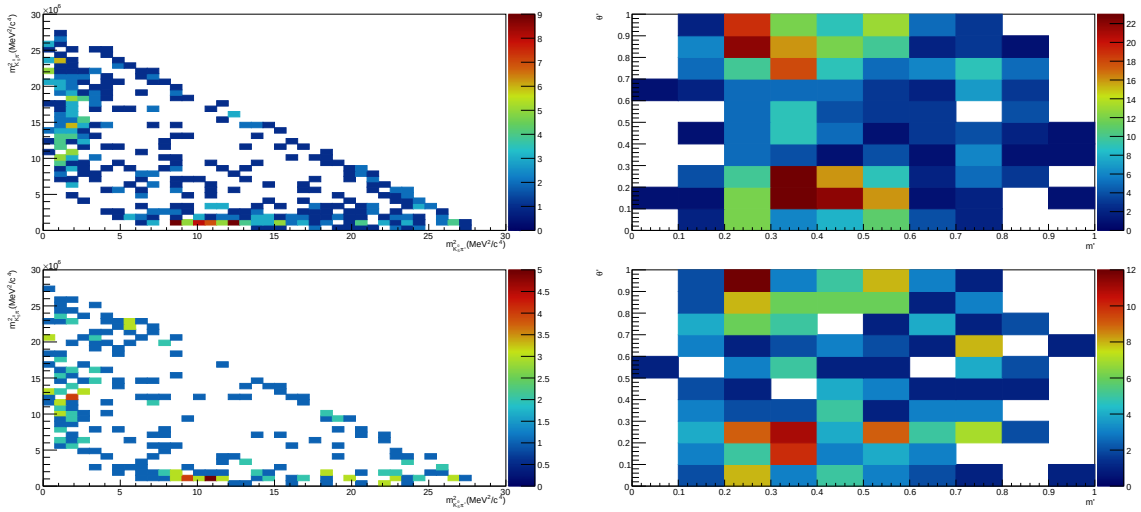

Figure 4.3: $B^0_s \rightarrow K^0_S\pi^+\pi^-$ events distribution in the DP (left) and sqDP (right) for 2018 DD (top) and LL (bottom) samples (unfavoured mode optimisation used to deal with the smaller amount of background). The selected $K^0_S\pi^+\pi^-$ mass ranges are $[5345, 5419]\mathrm{MeV/c^2}$ for DD and $[5345, 5418]\mathrm{MeV/c^2}$ for LL (see Section 4.2.3). The white rectangles denote empty bins. Two very populated areas can be seen on the top and bottom of the sqDP, and on the edges of the DP respectively, they correspond to the $K^{*\pm}$ resonances.

4.1.4 Isobar Model

Equation 4.1.8 indicates that any non-uniformity in the DP event distribution must come from the decay amplitude $\mathcal{A}$ (or the amplitude of the conjugated decay $\bar{\mathcal{A}}$). It is usual to parameterise $\mathcal{A}$ with the isobar model [197]. The isobar model approximates the total amplitude as a coherent sum of terms, each characterised by an individual complex probability amplitude and a corresponding dynamical function. These terms represent either an intermediate resonance

within a specific particle pair, a non-resonant yet strongly interacting particle pair, and/or a non-resonant phase space decay. The decay amplitudes in the Isobar model read:

$$|\mathcal{A}(s_+, s_-)|^2 = |\sum_j c_j F_j(s_+, s_-)|^2 = |\sum_j a_j e^{i\phi_j} F_j(s_+, s_-)|^2, \tag{4.1.16}$$

$$|\bar{\mathcal{A}}(s_+, s_-)|^2 = |\sum_j \bar{c}_j \bar{F}_j(s_+, s_-)|^2 = |\sum_j \bar{a}_j e^{i\bar{\phi}_j} \bar{F}_j(s_+, s_-)|^2, \tag{4.1.17}$$

where j denotes a given amplitude, a_j is its relative magnitude, ϕ_j is its phase and F_j is its spin-dependant dynamical function. The a_j and ϕ_j are named isobar parameters of the amplitude j, they contain both weak and strong phase dependence. F_j contains the strong dynamics only, meaning that:

$$\bar{F}_j(s_+, s_-) = F_j(s_-, s_+). \tag{4.1.18}$$

The spin-dependent dynamical function can be rewritten in terms of resonance mass function, angular distribution probabilities, and corrective factors to conserve the angular momentum due to the spin of the intermediate resonance:

$$\bar{F}_j(s_+, s_-) \to \bar{F}_j(s_+, s_-, L) = \mathcal{R}_j(s) \times X^L((|\vec{p}|r)^2) \times X^L((|\vec{q}|r)^2) \times T_j(L, \vec{p}, \vec{q}), \tag{4.1.19}$$

where s is the invariant mass square of the decay products of the resonance (here it can be s_+, s_- or s_0), $\vec{p}$ and $\vec{q}$ are the momenta in the resonance rest frame of the bachelor particle and one of the $\pi^+\pi^-$ resonance daughters (here π^+), L is the orbital angular momentum between the resonance and the bachelor particle, $\mathcal{R}_j(s)$ is the resonance mass term or lineshape of the j resonance, $T_j(L, \vec{p}, \vec{q})$ is the angular distribution of the j resonance daughters, $X^L((|\vec{p}|r)^2)$ is the barrier factors for the resonance and the bachelor particle production, $X^L((|\vec{q}|r)^2)$ is the barrier factors for the resonance daughter production and r denotes the resonance radius.

The definitions of $X^L((|\vec{p}|r)^2)$, $X^L((|\vec{q}|r)^2)$ and $T_j(L, \vec{p}, \vec{q})$ are given in Section 4.1.5. The lineshape definition is detailed in Section 4.1.6.

4.1.5 Angular distributions

The angular distribution terms $T_j(L, \vec{p}, \vec{q})$ can be written in the Zemach tensor formalism [198] for a given L value as:

$$T_j(0, \vec{p}, \vec{q}) = 1, \tag{4.1.20}$$

$$T_j(1, \vec{p}, \vec{q}) = -2\vec{p}.\vec{q}, \tag{4.1.21}$$

$$T_j(1, \vec{p}, \vec{q}) = \frac{4}{3}[3\vec{p}.\vec{q} - |\vec{p}||\vec{q}|]. \tag{4.1.22}$$

Barrier factors also named Blatt-Weisskopf functions [199], can be written in terms of z with $z = (|\vec{p}|r)^2$ or $z = (|\vec{q}|r)^2$ for a given L, the "primed" form [47] of these functions is given as the Zemach tensor formalism is used above:

$$X_0(z) = 1, \tag{4.1.23}$$

$$X_1(z) = \sqrt{\frac{1 + z_0}{1 + z}}, \tag{4.1.24}$$

$$X_2(z) = \sqrt{\frac{(z_0 - 3)^2 + 9z_0}{(z - 3)^2 + 9z}}, \tag{4.1.25}$$

with z_0, the value of z when the invariant mass is equal to the mass pole of the resonance.

4.1.6 Lineshapes

In an isobar DP analysis, the regular resonances owns specific lineshapes depending on their elastic or inelastic nature as well as on their spin. The lineshapes used in this analysis are reviewed in the following.

Relativistic Breit Wigner

The Relativistic Breit Wigner (RBW) is a common lineshape to model the invariant-mass distribution of an unstable particle travelling at relativistic speed and decaying to a unique final state. The RBW line shape, with $m = \sqrt{s}$, reads:

$$\mathcal{R}(m) = \frac{m_0\Gamma_0}{m^2 - m_0^2 - im_0\Gamma(m)}, \tag{4.1.26}$$

where m_0 is the pole mass of the resonance and Γ_0 is its natural width. $\Gamma(m)$ is given by:

$$\Gamma(m) = \Gamma_0 \frac{m_0}{m} \left(\frac{p(m)}{p(m_0)}\right)^{2J+1} \frac{X^J(z(m))}{X^J(z(m_0))}, \tag{4.1.27}$$

where J is the spin of the resonance, X^J is the barrier factor previously defined, and p is the momentum of one of the resonance daughters. $p(m)$ reads:

$$p(m) = \frac{m}{2}\sqrt{1 - \frac{(m_j + m_k)^2}{m^2}}\sqrt{1 - \frac{(m_j - m_k)^2}{m^2}}, \tag{4.1.28}$$

where j and k denote the resonance daughters.

The RBW line shape is adequate to describe isolated resonance. Figure 4.4 shows an illustration of the RBW probability density function.

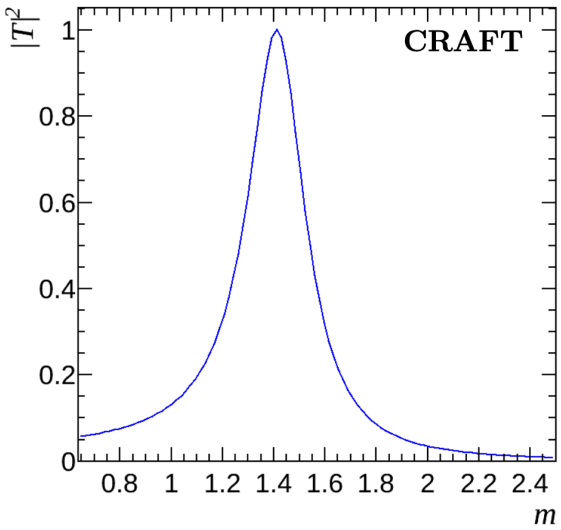

Figure 4.4: Illustration [69] of a RBW probality density function.

Gounaris-Sakurai

The Gounaris-Sakurai (GS) lineshape [200] is a modified RBW. It is an interesting model to describe a broad resonance such as $\rho^0(770)$, because it describes adequately the $\pi^+\pi^-$ P-wave[1]

[1] P-wave means vector resonance (with spin = 1), $\rho^0(770)$ is a vector resonance.

resonance. The GS line shape reads as:

$$\mathcal{R}(m) = \frac{1 + d.\Gamma_0/m_0}{m_0^2 - m^2 + f(m) - im_0\Gamma(m)}, \tag{4.1.29}$$

where:

$$f(m) = \Gamma_0 \frac{m_0^2}{p^3(m_0)} \left[p^2(m)(h(m) - h(m_0)) + (m_0^2 - m^2)p^2(m_0) \left.\frac{\mathrm{d}h}{\mathrm{d}m^2}\right|_{m=m_0} \right], \tag{4.1.30}$$

$$h(m) = \frac{2p(m)}{\pi m} \ln\left(\frac{m + 2p(m)}{2m_\pi}\right), \tag{4.1.31}$$

$$\left.\frac{\mathrm{d}h}{\mathrm{d}m^2}\right|_{m=m_0} = h(m_0)\left(\frac{1}{8p^2(m_0)} - \frac{1}{2\pi m_0^2}\right), \tag{4.1.32}$$

$$d = \frac{3m_\pi^2}{\pi(m_0)^2} \ln\left(\frac{m_0 + 2p(m_0)}{2m_\pi}\right) + \frac{m_0}{2\pi p(m_0)} - \frac{m_\pi^2 m_0}{\pi p(m_0)^3}. \tag{4.1.33}$$

Figure 4.5 displays an illustration of GS probability density function.

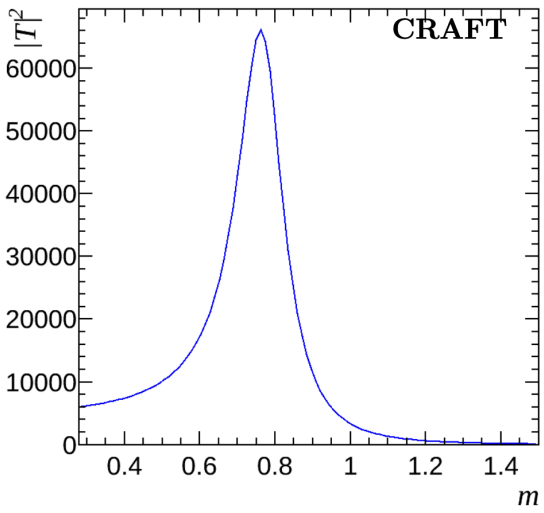

Figure 4.5: Illustration [69] of a GS probality density function.

EFKLLM

The EFKLLM line shape, named after the proponents name initials [201], is suitable to model $K_S^0\pi^\pm$ S-wave[2] resonances such as $K_0^{*\pm}(1430)$. The EFKLLM lineshape reads as:

$$\mathcal{R}(m) = F(m)\left(\frac{c_0}{m^2} + c_1\right), \tag{4.1.34}$$

where $F(m)$ is a form factor tabulated in [201] and $c_{0,1}$ are complex numbers to determine in the fit.

4.1.7 Probability density function

The DP isobar formalism allows to write a signal probability density function (P.D.F.) where the kinematics and the dynamics of the decay are accurately enough for our experimental purpose.

[2] S-wave means scalar resonance (with spin = 0), $K_0^{*\pm}(1430)$ is a scalar resonance.

One needs first to define the $B_s^0 \to f$ time-dependant decay rate (similarly to what was done for B^0 in Section 1.3.2) as [202]:

$$\begin{aligned}\frac{\mathrm{d}\Gamma_{B_s^0\to f}(t)}{\mathrm{d}t} = \frac{e^{-\frac{t}{\tau_s}}}{2\tau_s}\Bigg[&\left(|A_f|^2 + \left|\bar{A}_f\right|^2\right)\cosh\left(\frac{\Delta\Gamma_s t}{2}\right) - 2\,\mathrm{Im}\left(\frac{q}{p}A_f^*\bar{A}_f\right)\sin(\Delta m_s t) + \\ &\left(|A_f|^2 - \left|\bar{A}_f\right|^2\right)\cos(\Delta m_s t) - 2\,\mathrm{Re}\left(\frac{q}{p}A_f^*\bar{A}_f\right)\sinh\left(\frac{\Delta\Gamma_s t}{2}\right)\Bigg],\end{aligned} \tag{4.1.35}$$

where A_f ($\bar{A}_f$) represent the decay amplitude of $B_s^0 \to f$ ($\bar{B_s^0} \to f$), τ_s is the B_s^0 lifetime, $\Delta\Gamma_s$ is the decay rate difference between the two B_s^0 mass eigenstates, Δm_s is the mass difference between the two B_s^0 mass eigenstates, and p and q are the coefficients characterising the $B_s^0 - \bar{B_s^0}$ mixing. Therefore, three equivalent equations can be written for the remaining combinations of $B_s^0/\bar{B_s^0}$ and $f/\bar{f}$.

As an illustration, by integrating the decay rates to a same CP eigenstate, absence of production asymmetry (known as a reasonable approximation [203]), one would obtain :

$$\int_0^\infty \frac{\mathrm{d}\Gamma_{B_s^0/\bar{B_s^0}\to f}(t)}{\mathrm{d}t}\mathrm{d}t = \left(|A_f|^2 + \left|\bar{A}_f\right|^2\right)\left(\frac{1 + yA_f^{\Delta\Gamma_s}}{1-y^2}\right), \tag{4.1.36}$$

with $y = \tau_s\Delta\Gamma_s/2 = 0.065 \pm 0.005$ [67] and $A_f^{\Delta\Gamma_s} = -2\,\mathrm{Re}(\lambda_f)/(1+|\lambda_f|^2)$ using the λ_f definition of Section 1.3.2. The term $A_f^{\Delta\Gamma_s}$ is an additional CP violation parameter to C_f and S_f.

At this stage of the analysis, and for the sake of the installation of the tools, the effect of the B_s^0 nonvanishing lifetime difference is neglected. The DP time-integrated untagged probability density function of $B_s^0/\bar{B_s^0} \to K_S^0\pi^+\pi^-$ therefore simplifies to an incoherent sum of amplitudes where $\mathcal{A}$ and $\bar{\mathcal{A}}$ are defined in Section 4.1.4:

$$\mathcal{P}(s_+, s_-) = |\mathcal{A}(s_+, s_-)|^2 + |\bar{\mathcal{A}}(s_+, s_-)|^2. \tag{4.1.37}$$

4.2 $B_s^0 \to K_S^0\pi^+\pi^-$ time-integrated analysis

In this section a preliminary time-integrated analysis of $B_s^0 \to K_S^0\pi^+\pi^-$ is presented. The analysis was performed using the CRAFT software which is described in Section 4.2.1. To perform the amplitude fit, one needs to define a signal P.D.F. and a likelihood to maximise: those are provided in Section 4.2.2. This analysis is a continuation of the $B_{d,s}^0 \to K_S^0 h^+ h'^-$ branching fraction measurements analysis presented in Chapter 3; in particular, it uses several inputs from the $B_s^0 \to K_S^0\pi^+\pi^-$ BF measurements; Section 4.2.3 provides a description of them. The amplitude fits of the $B_s^0 \to K_S^0\pi^+\pi^-$ spectrum are described in Section 4.2.4. The first preliminary results of the analysis are given in Section 4.2.5.

The work reported here is not the ultimate $B_s^0 \to K_S^0\pi^+\pi^-$ time-integrated amplitude analysis, due to the thesis timescale. It has been decided to focus this preliminary analysis only on one data-taking period, the one with the highest statistics (2018), and to use several simplifications. However, this preliminary analysis will be able to provide the building blocks of the complete analysis and first hints of the results.

4.2.1 CRAFT overview

CRAFT (for Clermont Root-based Amplitude Fitter Tool) is a Root-based package designed for the charmless decays analysis $B_{d,s}^0 \to K_S^0 h^+ h'^-$ [69]. CRAFT involves C++ classes depending on ROOT [130] and RooFit [204] (one of its sub-library). CRAFT is made to perform Dalitz Plot fits to determine the parameters of interest using the isobar model formalism (see Section 4.1.4) to describe the dynamics of the decay. All the lineshapes presented in Section 4.1.6 are implemented in CRAFT together with other models (Gaussian, polynomial, etc.).

CRAFT is a maximum likelihood fitting software which uses the minuit software [205] for the maximisation procedure. CRAFT provides the possibility of performing DP analysis by making use of a simultaneous fit of independent samples to determine a common set of parameters (isobar, lineshapes, ...) by maximising the fit likelihood $\mathcal{L}$:

$$\mathcal{L} = \prod_{i=1}^{n} \mathcal{P}(\{s_+, s_-\}_i), \tag{4.2.1}$$

with $\mathcal{P}$ the P.D.F. used to describe the decay and i denoting one of the n events considered.

To determine the likelihood normalisation and plot drawing, CRAFT performs numerical integration. The type of numerical integration used in CRAFT is the midpoint rule where the integral I of a given P.D.F. $\mathcal{P}$ between two points a and b is given by:

$$I(\mathcal{P}) = (b-a).\mathcal{P}\left(\frac{a+b}{2}\right). \tag{4.2.2}$$

CRAFT is designed to take into account the efficiencies associated with the samples, and also to take into account the background distributions in the phase space. To take advantage of these abilities, inputs from $B_{d,s}^0 \to K_S^0 h^+ h'^-$ branching fraction analysis will be used.

Finally, CRAFT requires the definition of an adequate isobar physics model to fit the data and make the measurements.

4.2.2 $B_s^0 \to K_S^0\pi^+\pi^-$ P.D.F. and likelihood function

The Dalitz time-integrated untagged P.D.F. is given in equation 4.1.37, but it is more usual to use the P.D.F. normalized by itself in order to have an integral equal to one, this new P.D.F. reads:

$$\mathcal{P}(s_+, s_-) = \frac{|\mathcal{A}(s_+, s_-)|^2 + |\bar{\mathcal{A}}(s_+, s_-)|^2}{\iint_{\mathrm{DP}} \left(|\mathcal{A}(s_+, s_-)|^2 + |\bar{\mathcal{A}}(s_+, s_-)|^2\right) \mathrm{d}s_+ \mathrm{d}s_-}. \tag{4.2.3}$$

The events used in this preliminary analysis consist mostly of $B_s^0 \to K_S^0\pi^+\pi^-$ signal and combinatorial background, since the cross-feed background is negligible in the samples used (see Chapter 3 and Section 4.2.3). In order to perform *CP* violation measurements, the CRAFT fit machinery requires a model for the signal with the corresponding efficiency (reconstruction and selection) and a model for the combinatorial background, for each sample (2018 with the DD and LL K_S^0 reconstruction type). The fit maximises, simultaneously for the different samples, a likelihood function by floating the isobar parameters (and resonance parameters if needed) of the signal P.D.F. . Practically CRAFT minimises the negative logarithm likelihood (nll) instead, but this is equivalent. The nll function is:

$$-\ln \mathcal{L}_{tot} = -\sum_{i=1}^{N_{tot}} \ln \mathcal{P}_{tot}, \tag{4.2.4}$$

where $\mathcal{L}_{tot}$ is the total likelihood, i runs over the N_{tot} events and $\mathcal{P}_{tot}$ is the general P.D.F. which reads as:

$$\mathcal{P}_{tot} = f_{\text{sig}} \frac{\epsilon(s_+, s_-)\mathcal{S}(s_+, s_-)}{\iint_{\text{DP}} \epsilon(s_+, s_-)\mathcal{S}(s_+, s_-)\text{ds}_+\text{ds}_-} + (1 - f_{\text{sig}}) \frac{\mathcal{B}(s_+, s_-)}{\iint_{\text{DP}} \mathcal{B}(s_+, s_-)\text{ds}_+\text{ds}_-}, \tag{4.2.5}$$

with $\epsilon(s_+, s_-)$ the signal efficiency across the DP, $\mathcal{B}(s_+, s_-)$ is the distribution of combinatorial background in the DP, f_{sig} is the signal fraction to consider in the fit and $\mathcal{S}(s_+, s_-)$ is the signal P.D.F.. The signal P.D.F. in the isobar model is given by:

$$\mathcal{S}(s_+, s_-) = \sum_{j=1}^{N} \left(\left| \frac{a_j}{a_r} e^{i(\phi_j - \phi_r)} F_j(s_+, s_-) \right|^2 + \left| \frac{\bar{a}_j}{a_r} e^{i(\bar{\phi}_j - \bar{\phi}_r)} \bar{F}_j(s_+, s_-) \right|^2 \right), \tag{4.2.6}$$

where j is the index running on the N resonant and non-resonant signal components in the DP, F_j ($\bar{F}_j(s_+, s_-) = F_j(s_-, s_+)$ see Section 4.1.4) is the spin-dependent dynamical part of the amplitude of the component j, a_j and ϕ_j ($\bar{a}_j$ and $\bar{\phi}_j$) are the magnitude and phase representative of the component j; finally a_r, ϕ_r and $\bar{\phi}_r$ are the isobar parameters of a reference resonance which is needed to introduce to solve the equation.

In the next section, all the inputs needed from the branching fraction analysis in order to write this likelihood are presented.

4.2.3 $B_{d,s}^0 \to K_S^0 h^+ h'^-$ branching fraction measurements inputs

Data used

Namely, in the branching fraction measurement analysis, two different selections have been used in each spectrum ($K_S^0\pi^+\pi^-$ here), to build two working points optimised for the favoured decay ($B^0 \to K_S^0\pi^+\pi^-$ here) or the unfavoured decay ($B_s^0 \to K_S^0\pi^+\pi^-$ here) of the spectrum. So, the data used in this analysis correspond to the unfavoured mode optimisation of the $K_S^0\pi^+\pi^-$ spectrum, as the study is dedicated to $B_s^0 \to K_S^0\pi^+\pi^-$. For simplicity, the data used in this preliminary analysis are restricted to the highest statistic period, which corresponds to 2018. Finally, there are two datasets considered in the preliminary analysis corresponding to the 2018 unfavoured mode optimisation in the $K_S^0\pi^+\pi^-$ spectrum, one made of DD K_S^0 reconstruction type candidates and the other made of LL ones.

By construction, the two datasets used are made up of B_s^0 signal events but also of B^0 signal events and background. As the goal is to study $B_s^0 \to K_S^0\pi^+\pi^-$ an additional cut has been added to select preferentially events compatible with the hypothesis of B_s^0 decay in each dataset. Concretely, a mass window has been set around the B_s^0 mass on the B reconstructed mass with respect to the mass fit performed at the fraction of signal determination level (see below). The DP and sqDP distributions corresponding to the data used are provided in Figure 4.3.

Combinatorial background distributions

From Figure 3.24 and the ones given in Appendix C.2.2, one can see that when the unfavoured mode optimisation is used, the only important background contribution living under the B^0_s signal peak comes from the combinatorial background. The combinatorial background distributions are determined from the upper side band of the reconstructed B-mass in the data, as it is the only remaining contribution here, as explained in Section 3.2.1. Figure 4.6 shows the combinatorial background distributions projected in the DP and in the sqDP, Figure 4.7 displays the Poisson error associated on the sqDP, and Figure 4.8 shows the combinatorial background distributions projected on the individual DP variables, one can see that they are fairly uniformly distributed in the Dalitz Plane, as expected. The deficit of events in central parts of the DP is coming from charmed and charmonia resonances vetoes.

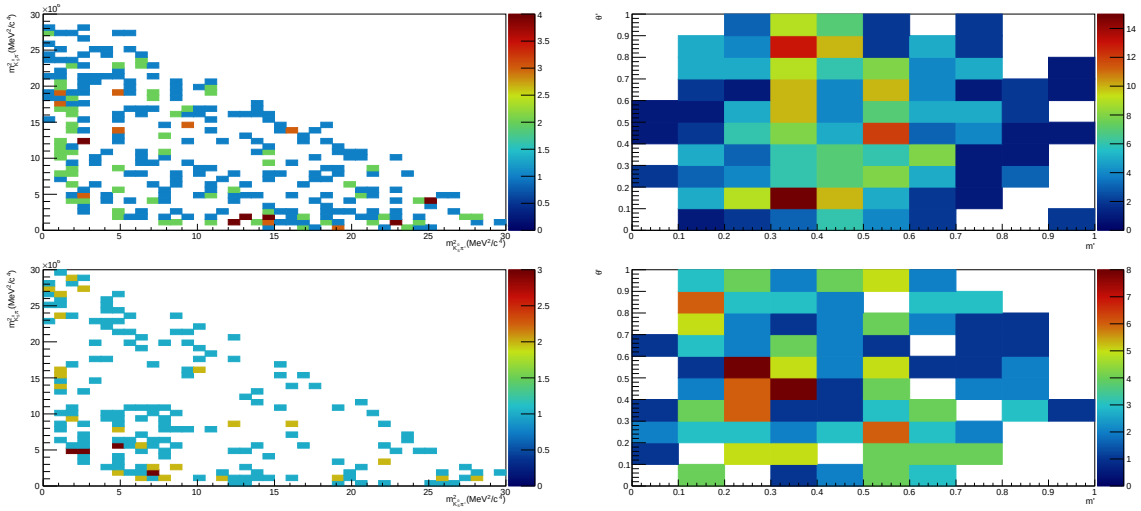

Figure 4.6: Combinatorial background events distribution in the DP (left) and sqDP (right) for 2018 DD (top) and LL (bottom) samples with the unfavoured mode optimisation. A $[5500, 5750]\text{MeV/c}^2$ $K^0_S\pi^+\pi^-$ mass window has been used to isolate the combinatorial background. The white rectangles denote empty bins.

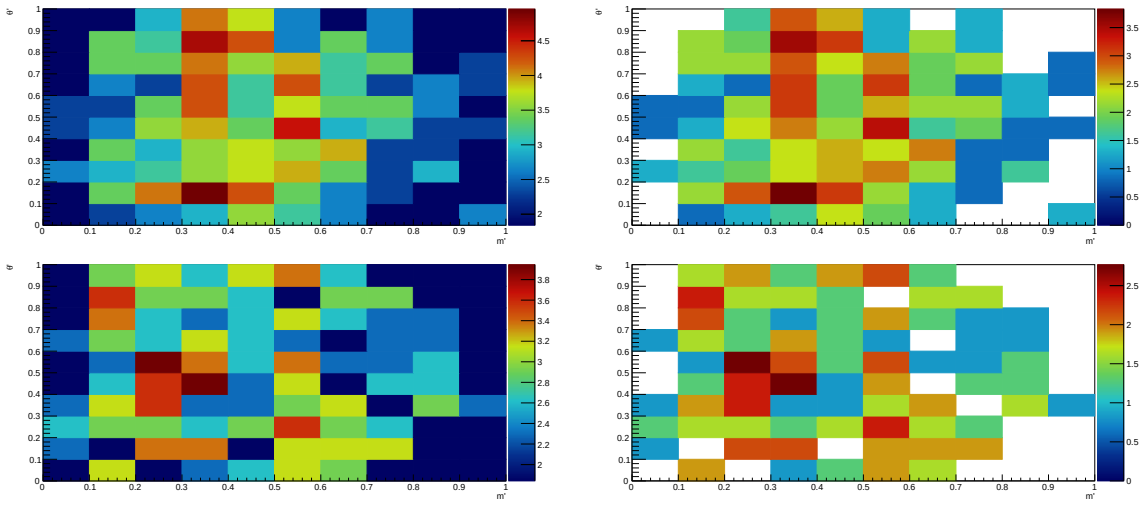

Figure 4.7: Combinatorial background events distribution high error (left) and low error (right) in the sqDP for 2018 DD (top) and LL (bottom) samples with the unfavoured mode optimisation.

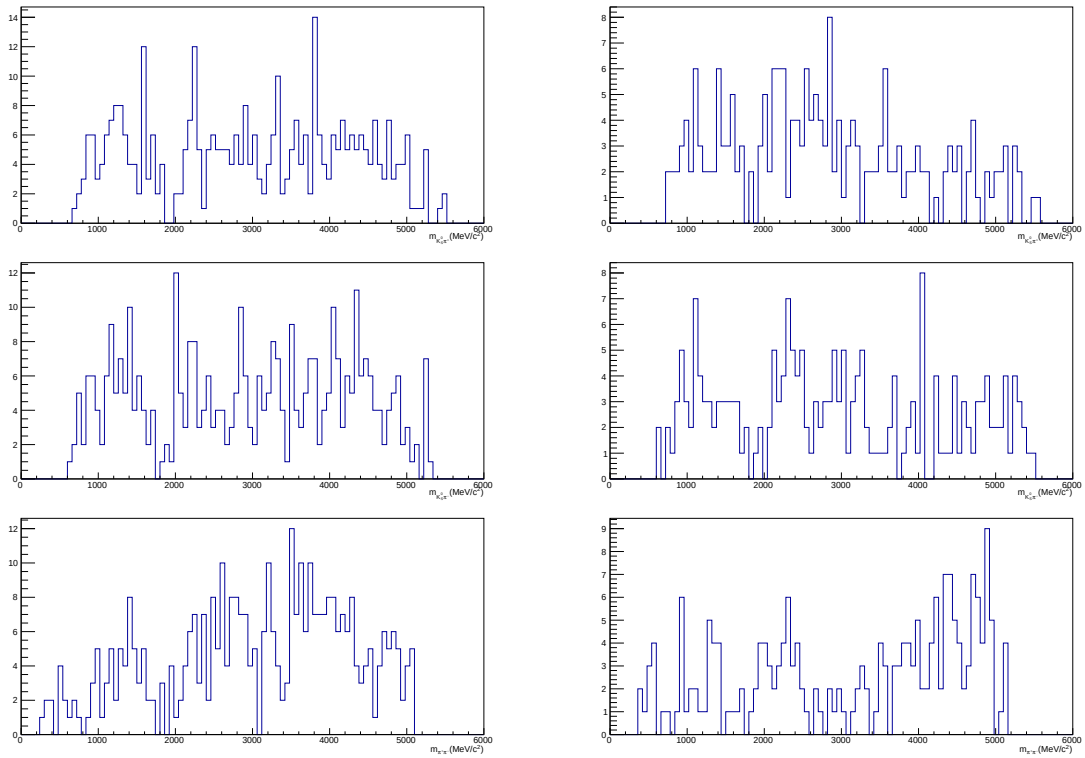

Figure 4.8: Combinatorial background events distribution projected on the three DP variables (from top to bottom: $m_{K^0_S\pi^+}$, $m_{K^0_S\pi^-}$ and $m_{\pi^+\pi^-}$) for 2018 DD (left) and LL (right) samples with the unfavoured mode optimisation.

Fraction of signal

In order to run the amplitude fit in CRAFT, it is needed to know the fraction of signal to consider (and consequently the fraction of combinatorial background) and to set the B mass window of the study (in which the fractions will be determined and the data are taken). For that purpose, the ultimate goal is to reuse the mass fit model defined in Section 3.2.1, but for the preliminary analysis, a simpler mass fitter has been used. The mass fitter used runs on the full B reconstructed mass window (see Section 3.2.2). It features two Double CB [152] models in order to fit the B^0 and the B^0_s signal peaks, a first-order Chebychev [151] to fit the combinatorial background, and it requires adding a Gaussian [150] contribution on the left of the spectrum to tackle the partially reconstructed events.

The Gaussian mean and width are opportunistically fixed to values describing the partially reconstructed bump that lives on the left of the mass spectrum.

The combinatorial background slope and offset are fitted on the right-handed side band of the spectrum. The corresponding fits are given in Figure 4.9.

The double CB shape parameters are fixed from a fit to the 2018 MC samples, which are provided in Figure 4.10.

The same width parameter is taken for the two signal peaks, the B^0 and B^0_s masses difference is constrained to the PDG value, and all these parameters are fitted to the whole data distribution simultaneously with the yield associated to each contribution. In order to work in a window less populated by B^0 and partially reconstructed contributions, it has been decided to set the B mass window of the study as $[m_{B^0_s} - 1.4\sigma_{B^0_s}, m_{B^0_s} + 3\sigma_{B^0_s}]$ (rounded to the integer values in MeV) where $m_{B^0_s}$ and $\sigma_{B^0_s}$ are the fitted mean and width of the B^0_s signal peak. In this window, the B^0_s peak and the combinatorial background are the dominant contributions, other contributions are small. For the purpose of this preliminary analysis, it has been chosen to take

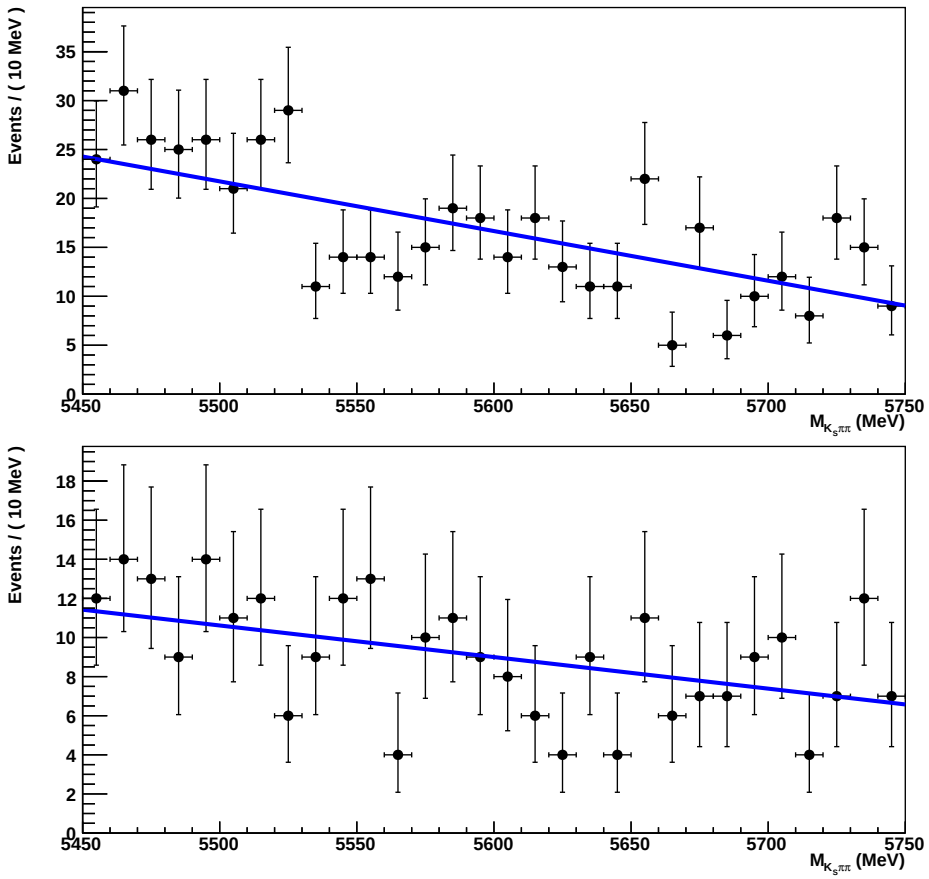

Figure 4.9: Combinatorial fit results for 2018 DD (top) and LL (bottom) K^0_S reconstruction type.

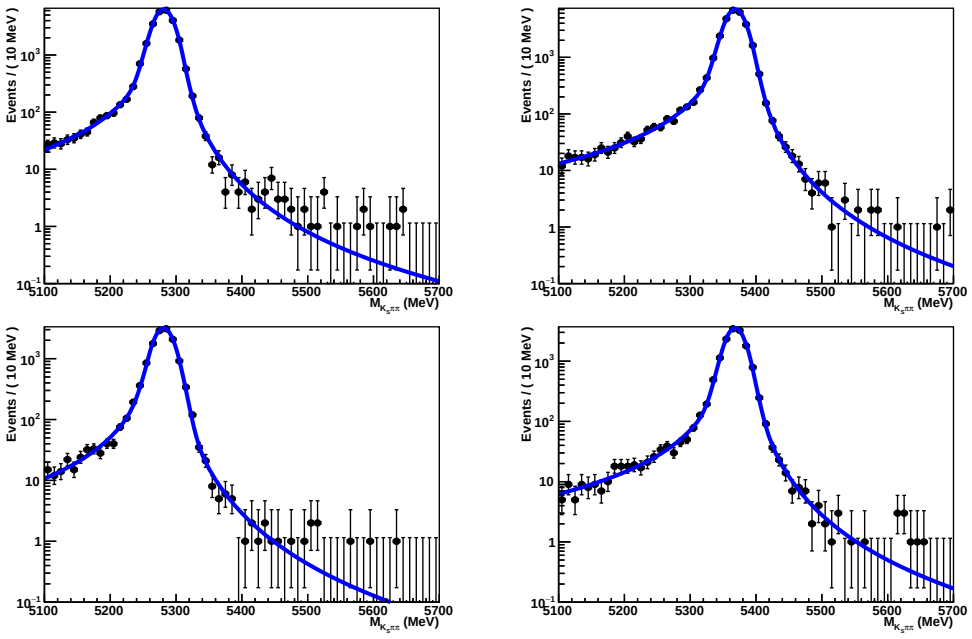

Figure 4.10: B^0 (left) and B^0_s (right) shape parameters MC fit results for 2018 DD (top) and LL (bottom) K^0_S reconstruction type.

the signal fraction as the sum of the one fitted for the B^0_s peak ($\sim$9/10 of the fraction) and the one fitted for the B^0 peak ($\sim$1/10 of the fraction), and the combinatorial fractions from the complement to unity (including the small partially reconstructed part that contributes for $\sim$2% of the fraction). A more elaborated analysis would require to provide a dedicated model

to describe the B^0 candidates. Figure 4.11 displays the mass fit results plots, and Table 4.1 summarises the parameters extracted from it.

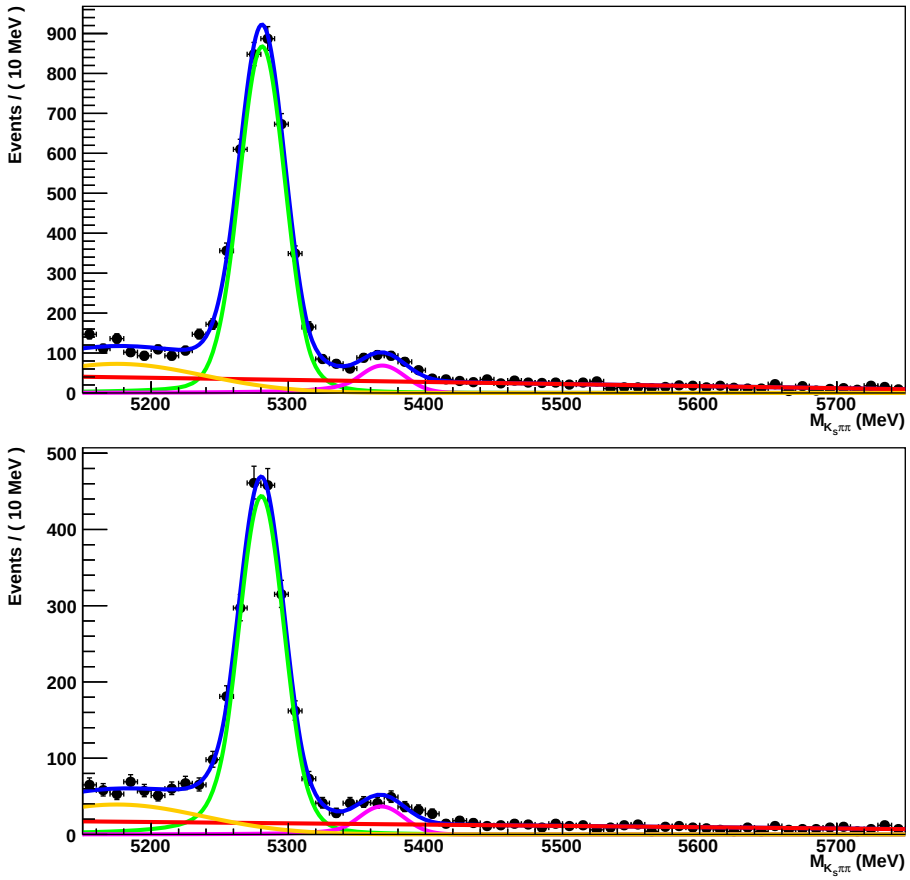

Figure 4.11: Fit results for 2018 DD (top) and LL (bottom) K^0_S reconstruction type. The total fit model is displayed in blue, the B^0 contribution is in green, the B^0_s contribution is in magenta, the combinatorial background contribution is in red and the partially reconstructed background contribution is in orange.

Fit results	2018 DD	2018 LL
$m_{B^0_s}$	5368.49 MeV	5367.91 MeV
$\sigma_{B^0_s}$	16.78 MeV	16.59 MeV
study window	[5345, 5419]MeV	[5345, 5418]MeV
$f_{B^0_s}$	52.7%	56.1%
f_{B^0}	4.6%	4.4%
$f_{\text{combinatorial}}$	41.9%	38.6%
$f_{\text{partially}}$	0.8%	0.9%
$f_{\text{sig}} = f_{B^0_s} + f_{B^0}$	57.3%	60.5%

Table 4.1: Summary of the fitted parameters used as input in CRAFT.

MU-MD combined efficiency maps

In order to correspond to the true number of signal events occurring at LHCb, the signal distributions need to be rescaled by the reconstruction and selection efficiency of the analysis. The total efficiencies associated with $B^0_s \to K^0_S\pi^+\pi^-$ have already been determined in sqDP

for the branching fraction measurements (see Section 3.3.2) via MC events. In principle, it is enough to feed CRAFT with these maps in order to rescale the signal distribution rightly. For now, the efficiency maps feature a 10×10 binning, which is enough for the purpose of this work, but which can cause discontinuities later. In the complete analysis, the maps will be smoothed using a 2D spline method.

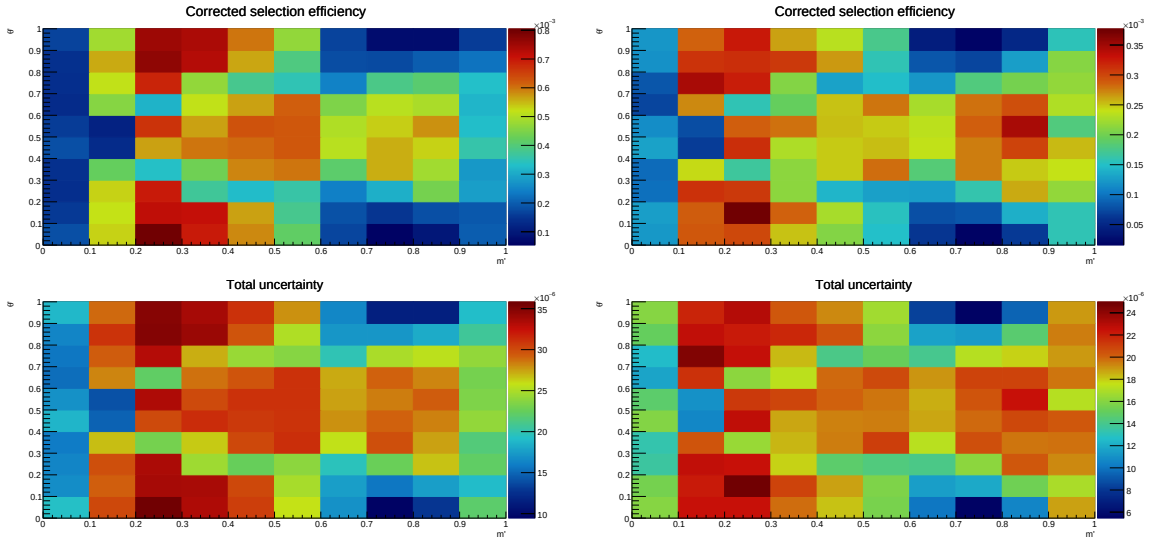

Figure 4.12: Total efficiency map (top) and associated total uncertainty map (bottom) for 2018 DD (left) and LL (right) $B_s^0 \to K_S^0\pi^+\pi^-$ samples with the unfavoured mode optimisation.

4.2.4 DP fit

The amplitude fit of $B_s^0 \to K_S^0\pi^+\pi^-$ is running on the $B_s^0 \to K_S^0\pi^+\pi^-$ data coming from the $B_{d,s}^0 \to K_S^0 h^+ h'^-$ branching fraction analysis measurement (featuring the total selection) restricted to the B invariant mass windows previously determined from the simplify mass fit performed. The selection and reconstruction efficiency of the signal decay is also considered by feeding CRAFT with the sqDP efficiency maps previously determined, including a transformation of the maps from the sqDP to the DP as the fit on the data runs in the DP.

Normally, the isobar model used to fit the signal in an amplitude analysis is the result of a complete process. A way to perform this is to first define a baseline model that includes only the dominant amplitudes, with dedicated lineshapes, of the decay and evaluate its performance through the likelihood maximisation (negative log likelihood minimisation) procedure. An additional (in principle smaller) amplitude is then added in the model and the fit is performed a second time: if the fit performance is improved, the new amplitude is added to the baseline model, if not the baseline model is kept. If relevant and in an iterative way, a set of possible additional amplitudes is tested following the same principle to finally build the best possible model named as nominal model.

For this preliminary analysis, the optimisation step of the fit with the test of additional resonance(s) has not been performed. It has been decided to use a minimal signal model according to the obviously expected SM resonant contributions in the Dalitz projection plans. Namely, the contributions described here by the model are the $K^{*\pm}(892)$, $K_0^{*\pm}(1430)$ and $\rho^0(770)$ resonances, in addition to the combinatorial background contribution.

Table 4.2 summarises the amplitudes considered in the isobar model, together with the associated lineshapes and their parameters. The Feynman diagrams corresponding to these processes were provided in Figures 1.9 to 1.11.

Resonance	Parameters	Lineshape	Value references
$K^{*\pm}(892)$	$m_0 = 891.66 \pm 0.26$ $\Gamma_0 = 50.8 \pm 0.9$	RBW	[47]
$K_0^{*\pm}(1430)$	$\mathcal{R}e(\lambda_0) = 0.204 \pm 0.103$ $\mathcal{I}m(\lambda_0) = 0$ $\mathcal{R}e(\lambda_1) = 1$ $\mathcal{I}m(\lambda_1) = 0$	EFKLLM	[201]
$\rho^0(770)$	$m_0 = 775.26 \pm 0.25$ $\Gamma_0 = 149.8 \pm 0.8$	GS	[47]
Non Resonant (NR)		DP flat	

Table 4.2: Summary of the resonances considered in the nominal fit, together with the lineshape used to model them, the associated parameters and the references from which they come. All the lineshape used are presented in Section 4.1.6 but DP flat, which is a flat lineshape in the DP.

4.2.5 Preliminary results

The previously defined model has been used to fit the $B_s^0 \to K_S^0\pi^+\pi^-$ 2018 data with DD and LL K_S^0 reconstruction types. The projection of the total fit on the DP variables can be seen in Figures 4.13 and 4.14, and projection of the fit on a smaller DP variable window including the main resonances is given in Figures 4.15 and 4.16.

The unzoomed plots display a global good behaviour of the fits performed. However, one has to keep in mind that the analysis presented here is preliminary and the fits are not final. The final analysis will have to optimise the nominal model used and to use smoothed sqDP maps, these will have an impact on the fits. In addition, a complete systematic study will have to be done before diving into quantitative results. For now only the systematic uncertainties coming from the efficiency maps determination are considered, namely the MC statistic, tracking, L0 trigger, and PID MC sampling systematics. In the complete analysis, additional systematics will have to be considered. For example, similarly to the $B^0 \to K_S^0\pi^+\pi^-$ Run I DP analysis [69], uncertainties on the signal/background fraction determination, the efficiency maps binning choice, the choice of the combinatorial background model, and the definition of the nominal signal model; will have to be introduced at least.

In this preliminary analysis, the goal is to draw some perspectives on the upcoming full analysis. Yet, from the zoomed plots of $m^2_{K_S^0\pi^+}$ and $m^2_{K_S^0\pi^-}$, one can see that a noticeable asymmetry of the $K^{*\pm}(892)\pi^{\mp}$ amplitudes is observed, with about twice the yields in the $\bar{B}_s^0 \to K^{*+}(892)\pi^-$ candidates, hinting at a significant direct *CP* violation for those amplitudes, with an opposite sign as its counterpart in the B^0 system. These preliminary findings are calling for the study of the full statistics with an accurate DP analysis and open the way to vibrant measurements!

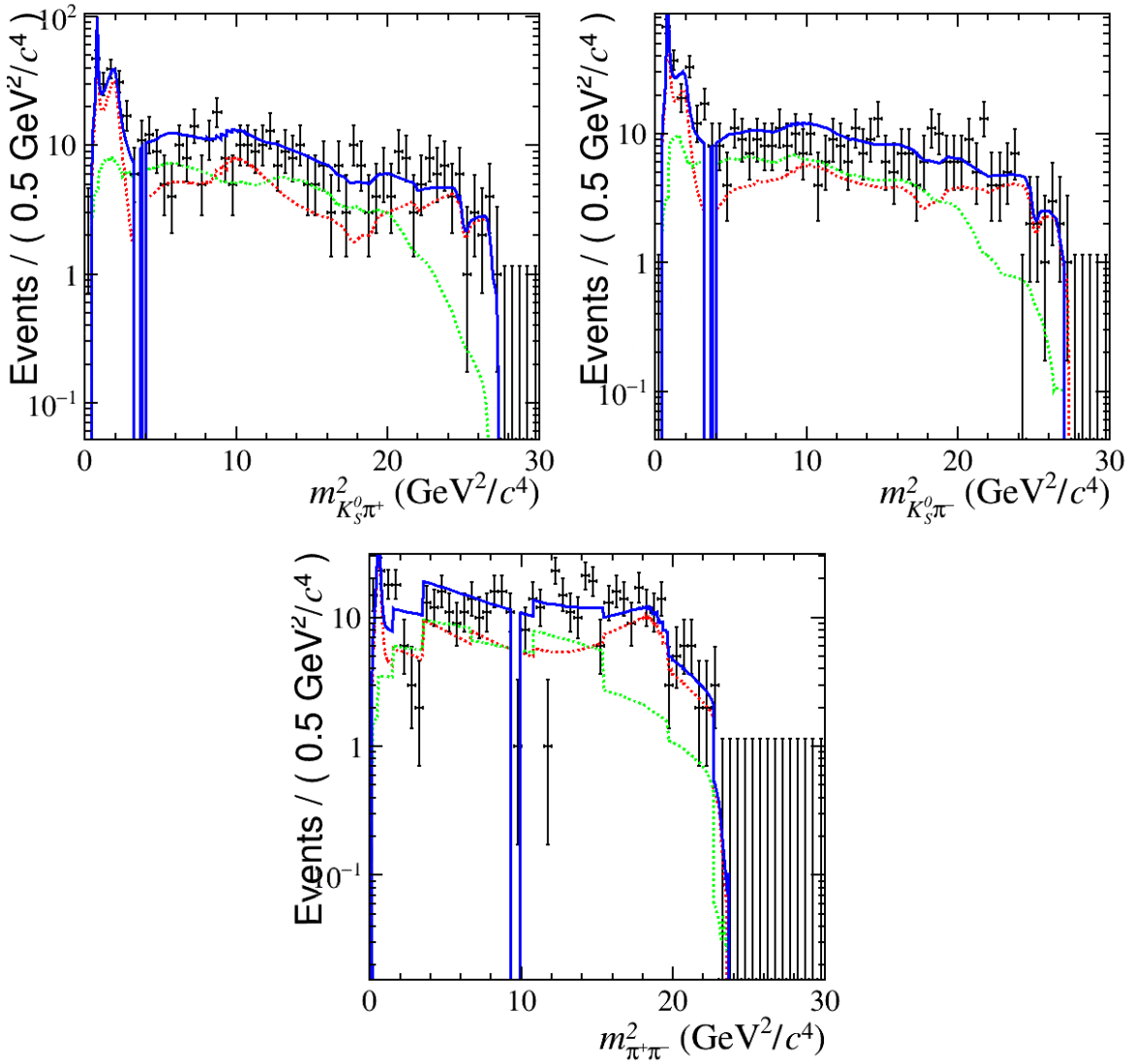

Figure 4.13: Projections of the 2018 data with DD K_S^0 category given in black points, and the nominal fit, onto $m^2_{K^0_S\pi^+}$ (left), $m^2_{K^0_S\pi^-}$ (right) and $m^2_{\pi^+\pi^-}$ (bottom). The full fit is shown in blue, combinatorial background in green and signal model in red. The step effect visible on the bottom plot is caused by the efficiency map binning as explained previously. This effect will be addressed later.

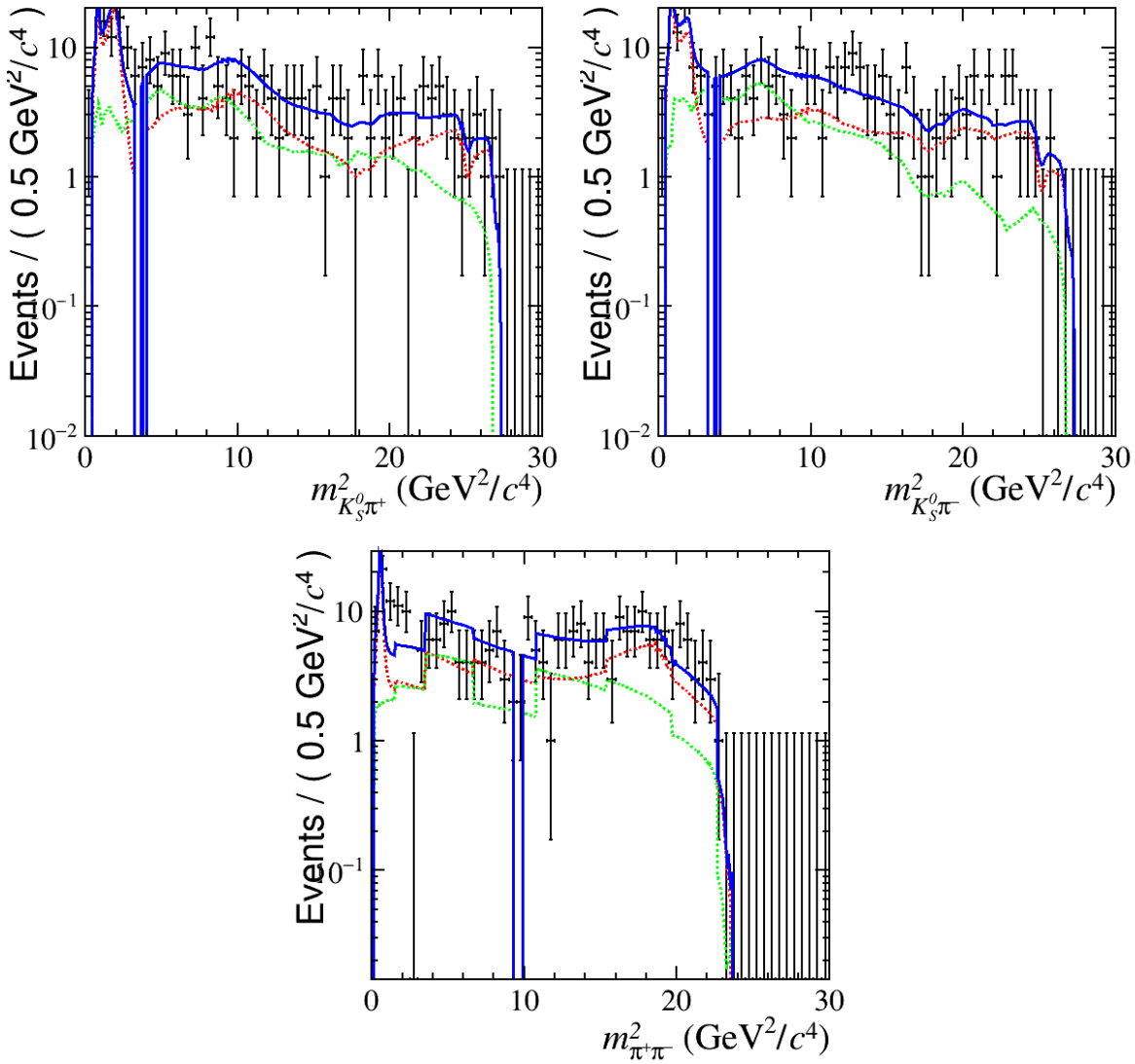

Figure 4.14: Projections of the 2018 data with LL K_S^0 category given in black points, and the nominal fit, onto $m^2_{K^0_S\pi^+}$ (left), $m^2_{K^0_S\pi^-}$ (right) and $m^2_{\pi^+\pi^-}$ (bottom). The full fit is shown in blue, combinatorial background in green and signal model in red. The step effect visible on the bottom plot is caused by the efficiency map binning as explained previously. this effect will be addressed later.

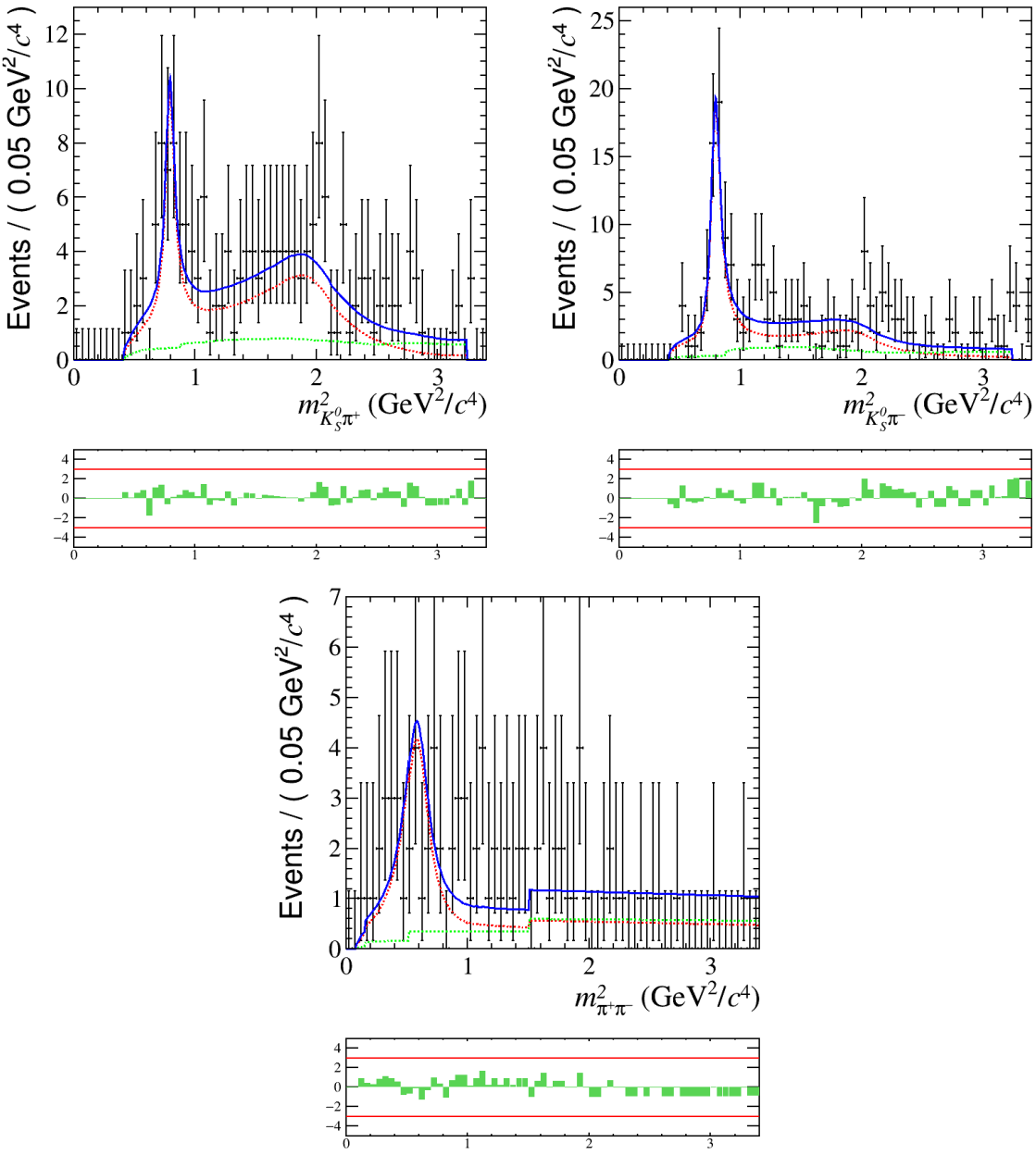

Figure 4.15: Projections of the 2018 data with DD K_S^0 category given in black points, and the nominal fit, with a zoomed view, onto $m^2_{K_S^0\pi^+}$ (left), $m^2_{K_S^0\pi^-}$ (right) and $m^2_{\pi^+\pi^-}$ (bottom). The full fit is shown in blue, combinatorial background in green and signal model in red.

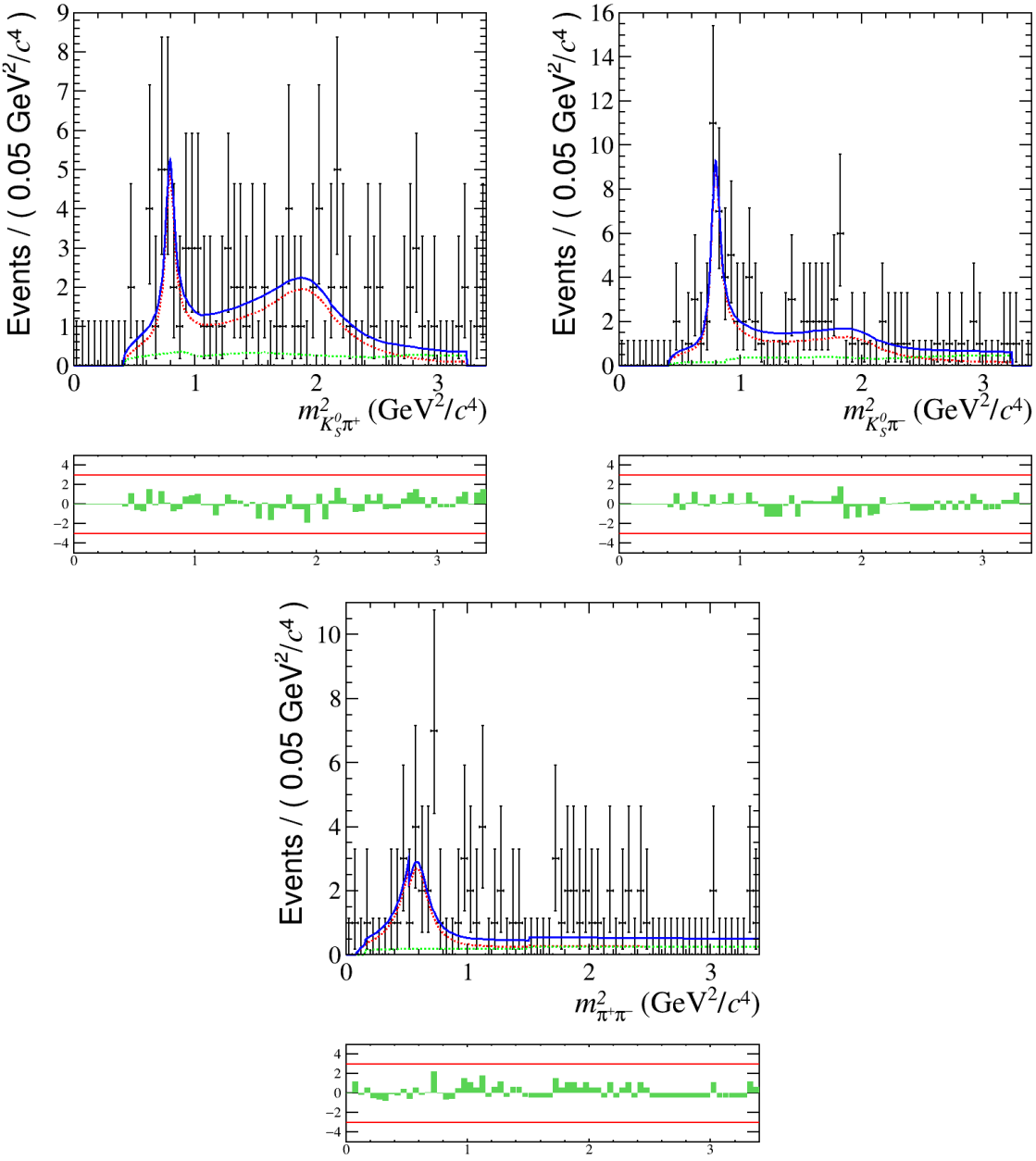

Figure 4.16: Projections of the 2018 data with LL K_S^0 category given in black points, and the nominal fit, with a zoomed view, onto $m^2_{K_S^0\pi^+}$ (left), $m^2_{K_S^0\pi^-}$ (right) and $m^2_{\pi^+\pi^-}$ (bottom). The full fit is shown in blue, combinatorial background in green and signal model in red.

4.3 Chapter conclusion

In this chapter, the Dalitz analysis formalism has been introduced, and the building blocks of the upcoming $B^0_s \to K^0_S\pi^+\pi^-$ Dalitz time-integrated analysis have been presented. This analysis is a follow-up of the branching fraction measurement analysis of Chapter 3 and an emphasis has been placed on the presentation of the necessary inputs.

A preliminary Dalitz analysis of the $B^0_s \to K^0_S\pi^+\pi^-$ spectrum has been performed and the corresponding limitations, related to the assumptions made, have been established. As a reminder, first, the amplitude model used is a simplified but educated baseline model. Second, the mass fit performed to extract the fraction of signal to consider in the fit is a simplified mass fit; it will be needed to use the complete $B^0_{d,s} \to K^0_S h^+ h'^-$ mass fit for the final analysis. Third, the sqDP maps used as inputs in this work are defined with wide binning that causes discontinuities in some fits; smoothed maps are needed to cancel them in the final analysis. Moreover, to produce the results a complete systematic study will have to be performed. Eventually, the B^0 contamination has been opportunistically embodied into the signal but will receive a dedicated modelling in a further stage of the analysis development.

Despite these limitations, the contaminations are modest and the baseline model is likely to describe accurately the subsamples that we are analysing in this preliminary work. A preliminary fit has therefore been performed that allows one to highlight a potential *CP* asymmetry that comes in the $K^{*\pm}(892)\pi^{\mp}$ amplitudes.

Chapter 5

$B^0 \to K^{*0}\tau^+\tau^-$ at FCC-ee

This chapter is dedicated to the feasibility study of $B^0 \to K^{*0}\tau^+\tau^-$ measurements for future experiments at FCC-ee, the scientific motivations of this study were reported in Section 1.5 and details on the FCC-ee project were presented in Section 2.5. The purpose of this study is to determine the detector requirements needed at FCC-ee in order to unravel the $B^0 \to K^{*0}\tau^+\tau^-$ decay. As explained in the following, a specific $\tau^\pm$ decay channel is studied in order to use a method that allows full kinematic reconstruction of the decay and especially the reconstruction of neutrinos in the final state (engendered by the τ decays). Due to that, the key detector parameter of the study is the resolution on the vertices measurements. In this analysis simulation of events at FCC-ee is used with several vertex detector hypotheses to evaluate the precision of the $B^0 \to K^{*0}\tau^+\tau^-$ branching fraction measurement as a function of the vertex detector performances, providing first conclusions on the feasibility of the measurement at FCC-ee and inputs for the FCC-ee detectors designs.

This prospective analysis has been fully conducted by Stéphane Monteil and myself, and it is a part of the analyses done in the FCC LPCA (Clermont) team. For the FCC Collaboration, this work stands as a benchmark for the vertex detectors, and this is why it has been included in the FCC Feasibility Study. The FCC Feasibility Study was launched by the European Strategy for Particle Physics in 2021 and will end in 2025, the goal of this study is to make a complete report of the FCC project (civil engineering, funding, detector concepts, physics opportunities, *etc.*) in order to guide the CERN projects for the next century. This analysis has in particular entered the FCC midterm review report [206], an official document requested by the CERN council (but not public for now) to make a preliminary review of the FCC project. The analysis is documented in an analysis note [207], a CERN internal publication which is a complete summary of the work.

In the first section of this chapter, details on the decay topology are presented together with the development of the mathematical reconstruction method used. In the second section, the $B^0 \to K^{*0}\tau^+\tau^-$ reconstruction in the simulation is presented. The third section contains the exploration of the potential backgrounds to consider as well as the development of a multivariate-based selection to fight against them. The method for assessing the precision of the branching fraction measurement is presented in the fourth section. The feasibility of the measurement and the detector requirements are eventually discussed in the fifth section, where the vertex detector performances are put in perspective with a state-of-the-art vertex detector.

5.1 Topological reconstruction of the decay

5.1.1 The topology of $B^0 \to K^{*0}\tau^+\tau^-$ events

The decay channel $B^0 \to K^{*0}\tau^+\tau^-$ provides a large variety of final states. Since the reconstruction method requires the determination of the secondary vertex, only the charged decay $K^{*0}(892) \to K^-\pi^+$ will be considered. Furthermore, the knowledge of the tertiary vertices (τ decays locations) is as well required by the reconstruction method. This constraint imposes to consider at least the three-prongs decay of the leptons with $\tau^\pm \to \pi^\pm\pi^\pm\pi^\mp\overset{(-)}{\nu_\tau}$[1]. The topology of this process is represented on Figure 5.1: there are three decay vertices, eight charged tracks in the final state, and two undetected neutrinos.

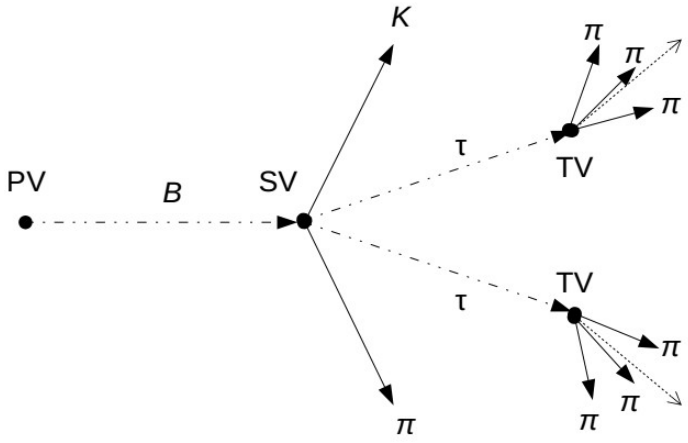

Figure 5.1: $B^0 \to K^{*0}\tau^+\tau^-$ topology with $K^{*0} \to K\pi$ and $\tau \to \pi\pi\pi\nu_\tau$.

5.1.2 Neutrinos reconstruction method

The section 5.1.1 highlighted that 2 out of the 10 final state particles of the decay mode of interest are not detected (and therefore not reconstructed in the data): these are the two neutrinos issued from the tertiary vertices of the τ decays (see figure 5.1). A complete reconstruction of the B^0 candidates requires neutrinos momenta to be inferred from the properties of the reconstructed decays.

It will be shown that the knowledge of the flight vectors of the tau (accessible thanks to the knowledge of the production vertices of the K^{*0} and of the systems of three π) together with the knowledge of the τ mass (measured with high precision at τ factories [47]) can be used to determine the missing coordinates.

The conservation of the energy-momentum at the tertiary vertex (valid for each of the two tertiary vertices) is first required:

$$\begin{cases} E_\tau = E_{\pi_t} + E_{\nu_\tau} \\ \vec{p_\tau} = \vec{p_{\pi_t}} + \vec{p_{\nu_\tau}} \end{cases}, \tag{5.1.1}$$

where π_t denotes the system of the three pions issued from the tau decay. The τ and ν_τ notations designate either the particle or the anti-particle (one equation comes with a single τ).

Introducing, with natural units:

$$E^2 = \vec{p}^2 + m^2$$

[1]For the readability in the following, these notations are simplified as $K^{*0} \to K\pi$ and $\tau \to \pi\pi\pi\nu_{(\tau)}$.

and assuming $E_\nu = p_\nu$ as in Standard Model:

$$\sqrt{m_\tau^2 + p_\tau^2} = \sqrt{m_{\pi_t}^2 + p_{\pi_t}^2} + p_{\nu_\tau}.$$

Squaring the expression

$$m_\tau^2 + p_\tau^2 = E_{\pi_t}^2 + p_{\nu_\tau}^2 + 2p_{\nu_\tau}E_{\pi_t},$$

and projecting the conservation of the momentum onto the tau flight direction:

$$p_\tau = p_{\pi_t}^{\parallel} + p_{\nu_\tau}^{\parallel} \;\&\; 0 = p_{\pi_t}^{\perp} + p_{\nu_\tau}^{\perp},$$

one can find this intermediate equation:

$$p_\tau^2 = p_{\pi_t}^{\parallel,2} + p_{\nu_\tau}^{\parallel,2} + 2p_{\pi_t}^{\parallel} \cdot p_{\nu_\tau}^{\parallel}.$$

Using

$$p^2 = p^{\perp,2} + p^{\parallel,2},$$

one can obtain:

$$m_\tau^2 = E_{\pi_t}^2 + \cancel{p_{\nu_\tau}^{\parallel,2}} + p_{\nu_\tau}^{\perp,2} + 2p_{\nu_\tau}E_{\pi_t} - p_{\pi_t}^{\parallel,2} - \cancel{p_{\nu_\tau}^{\parallel,2}} - 2p_{\pi_t}^{\parallel} \cdot p_{\nu_\tau}^{\parallel}.$$

Developing to determine the neutrino momentum

$$p_{\nu_\tau}^{\perp,2} = p_{\pi_t}^{\perp,2},$$

then:

$$m_\tau^2 - E_{\pi_t}^2 + p_{\pi_t}^{\parallel,2} - p_{\pi_t}^{\perp,2} = 2(p_{\nu_\tau}E_{\pi_t} - p_{\pi_t}^{\parallel} \cdot p_{\nu_\tau}^{\parallel}),$$

let's introduce an intermediary quantity denoted K as:

$$2K = m_\tau^2 - E_{\pi_t}^2 + p_{\pi_t}^{\parallel,2} - p_{\pi_t}^{\perp,2} = m_\tau^2 - m_{\pi_t}^2 - 2p_{\pi_t}^{\perp,2}.$$

One gets the following expressions :

$$K + p_{\pi_t}^{\parallel} \cdot p_{\nu_\tau}^{\parallel} = \sqrt{p_{\nu_\tau}^{\perp,2} + p_{\nu_\tau}^{\parallel,2}}E_{\pi_t}.$$

By squaring the two sides and put all on left, a second degree equation is obtained:

$$p_{\nu_\tau}^{\parallel,2}(p_{\pi_t}^{\parallel,2} - E_{\pi_t}^2) + p_{\nu_\tau}^{\parallel}2Kp_{\pi_t}^{\parallel} + (K^2 - p_{\pi_t}^{\perp,2}E_{\pi_t}^2) = 0,$$

with Δ expressed as

$$\begin{aligned}
&\Delta = 4[K^2 p_{\pi_t}^{\parallel,2} - (p_{\pi_t}^{\parallel,2} - E_{\pi_t}^2)(K^2 - p_{\pi_t}^{\perp,2}E_{\pi_t}^2)] \\
\Leftrightarrow\ &\Delta = 4E_{\pi_t}^2(p_{\pi_t}^{\parallel,2}p_{\pi_t}^{\perp,2} + K^2 - p_{\pi_t}^{\perp,2}E_{\pi_t}^2) \\
\Leftrightarrow\ &\Delta = E_{\pi_t}^2(m_\delta^2 - 4p_{\pi_t}^{\perp,2}m_\tau^2),
\end{aligned}$$

where:

$$m_\delta = m_\tau^2 - m_{\pi_t}^2.$$

The transverse invariant-mass of the three-pions system reads:

$$\begin{aligned} p^{\parallel,2}_{\pi_t} - E^2_{\pi_t} &= -(m^2_{\pi_t} + p^{\perp,2}_{\pi_t}) \\ 2K p^{\parallel}_{\pi_t} &= (m_\delta - p^{\perp,2}_{\pi_t}) p^{\parallel}_{\pi_t}. \end{aligned}$$

One eventually obtains the parallel component of the neutrino momentum:

$$p^{\parallel}_{\nu_\tau} = \frac{((m^2_\tau - m^2_{\pi_t}) - 2p^{\perp,2}_{\pi_t})}{2(p^{\perp,2}_{\pi_t} + m^2_{\pi_t})}.p^{\parallel}_{\pi_t} \pm \frac{\sqrt{(m^2_\tau - m^2_{\pi_t})^2 - 4m^2_\tau p^{\perp,2}_{\pi_t}}}{2(p^{\perp,2}_{\pi_t} + m^2_{\pi_t})}.E_{\pi_t}.$$

To summarise the computation, the reconstructed momentum of the neutrino is given in equation 5.1.2:

$$\begin{cases} p^{\perp}_{\nu_\tau} = -p^{\perp}_{\pi_t} \\ p^{\parallel}_{\nu_\tau} = \dfrac{((m^2_\tau - m^2_{\pi_t}) - 2p^{\perp,2}_{\pi_t})}{2(p^{\perp,2}_{\pi_t} + m^2_{\pi_t})}.p^{\parallel}_{\pi_t} \pm \dfrac{\sqrt{(m^2_\tau - m^2_{\pi_t})^2 - 4m^2_\tau p^{\perp,2}_{\pi_t}}}{2(p^{\perp,2}_{\pi_t} + m^2_{\pi_t})}.E_{\pi_t}. \end{cases} \tag{5.1.2}$$

There is a straightforward result obtained for the transverse momentum of the neutrino since it is the opposite to the transverse momentum of the three-pion system. However, the longitudinal momentum is more involved and reveals a quadratic ambiguity.

The consequence of this quadratic ambiguity is that when reconstructing the neutrinos coming from a B^0 there are four possible solutions per B^0 candidate (namely, there are two solutions per neutrino and two neutrinos per B^0).

5.1.3 Selection rule

It has been proven above that the neutrino reconstruction method leads to four different solutions for the mass of B^0, among which only one is correct ! A selection rule is desirable to choose the "true solution" and the decay properties here are also useful. By using the energy momentum conservation at B^0 decay vertex:

$$\begin{cases} E_{B^0} = E_{\tau^+} + E_{\tau^-} + E_{K^{*0}} \\ \vec{p}_{B^0} = \vec{p}_{\tau^+} + \vec{p}_{\tau^-} + \vec{p}_{K^{*0}}, \end{cases}$$

one obtains:

$$p_{\tau^+}.\vec{e}_{\tau^+} = p_{B^0}.\vec{e}_{B^0} - p_{\tau^-}.\vec{e}_{\tau^-} - p_{K^{*0}}.\vec{e}_{K^{*0}},$$

where $\vec{e}_i$ (unitary flight vectors) denotes the unitary vector of the particle i direction.
It is practical to single out the τ momentum by multiplying each side by $\vec{e}_{\tau^+}$:

$$p_{\tau^+} = p_{B^0}.(\vec{e}_{B^0}.\vec{e}_{\tau^+}) - p_{\tau^-}.(\vec{e}_{\tau^-}.\vec{e}_{\tau^+}) - p_{K^{*0}}.(\vec{e}_{K^{*0}}.\vec{e}_{\tau^+}). \tag{5.1.3}$$

On the other hand, the projection of the momentum equation onto the B^0 direction yields:

$$\begin{cases} 0 = p^{\perp}_{\tau^+} + p^{\perp}_{\tau^-} + p^{\perp}_{K^{*0}} \\ p_{B^0} = p^{\parallel}_{\tau^+} + p^{\parallel}_{\tau^-} + p^{\parallel}_{K^{*0}} \end{cases},$$

that one can rewrite explicitly for the parallel projection with scalar products :

$$p_{B^0} = p_{\tau^+}.(\vec{e}_{B^0}.\vec{e}_{\tau^+}) + p_{\tau^-}.(\vec{e}_{B^0}.\vec{e}_{\tau^-}) + p_{K^{*0}}.(\vec{e}_{B^0}.\vec{e}_{K^{*0}}). \tag{5.1.4}$$

Injecting 5.1.4 in 5.1.3 and isolating p_{τ^+}, one finds:

$$p_{\tau^+} = \frac{\vec{p}_{K^{*0}}.[(\vec{e}_{B^0}.\vec{e}_{K^{*0}}).(\vec{e}_{B^0}.\vec{e}_{\tau^+}) - (\vec{e}_{K^{*0}}.\vec{e}_{\tau^+})]}{1 - (\vec{e}_{\tau^+}.\vec{e}_{B^0})^2} - p_{\tau^-}.\frac{\vec{e}_{\tau^+}.\vec{e}_{\tau^-} - (\vec{e}_{\tau^+}.\vec{e}_{B^0})(\vec{e}_{\tau^-}.\vec{e}_{B^0})}{1 - (\vec{e}_{\tau^+}.\vec{e}_{B^0})^2}.$$

Using the property that three-body decay occurred in a plan, the expression $\vec{p}_{K^{*0}}.[(\vec{e}_{B^0}.\vec{e}_{K^{*0}}).(\vec{e}_{B^0}.\vec{e}_{\tau^+}) - (\vec{e}_{K^{*0}}.\vec{e}_{\tau^+})]$ can simplify to:

$$\vec{p}_{K^{*0}}.[(\vec{e}_{B^0}.\vec{e}_{K^{*0}}).(\vec{e}_{B^0}.\vec{e}_{\tau^+}) - (\vec{e}_{K^{*0}}.\vec{e}_{\tau^+})] = -\vec{p}^{\perp}_{K^{*0}}.\vec{e}_{\tau^+}.$$

An equivalent computation can be performed starting from p_{τ^-}. The energy-momentum conservation applied at the level of the B^0 decay eventually provides a relation between the momentum of the two τ and the K^{*0} as explicitly expressed in equation 5.1.5:

$$p_{\tau^\pm} = -\frac{\vec{p}^{\perp}_{K^{*0}}.\vec{e}_{\tau^\pm}}{1-(\vec{e}_{\tau_\pm}.\vec{e}_{B^0})^2} - p_{\tau^\mp}.\frac{\vec{e}_{\tau^\pm}.\vec{e}_{\tau^\mp} - (\vec{e}_{\tau^\pm}.\vec{e}_{B^0})(\vec{e}_{\tau_\mp}.\vec{e}_{B^0})}{1-(\vec{e}_{\tau^\pm}.\vec{e}_{B^0})^2}. \tag{5.1.5}$$

One τ momentum can be predicted from the other. Therefore, it is possible to choose the reconstructed τ^+/τ^- solution that minimises the deviation between τ momenta predictions and reconstructions.

5.2 Signal reconstruction method

5.2.1 The $B^0 \to K^{*0}\tau^+\tau^-$ signal candidates

The first step of the analysis is to select the $B^0 \to K^{*0}\tau^+\tau^-$ candidates from the final state particles of each event. Pions and kaons are selected from the reconstructed particles (reconstructed through the fast-simulated detector) via their MC-truth PID number (this a number defined in function of the nature of the particle) to limit the multiplicity of the upcoming candidates.

The $K^{*0}(892)$ candidates are made from combinations of opposite charges $\pi - K$. They are selected if their reconstructed invariant-mass is found within $0.1\,\mathrm{GeV/c^2}$ around the K^{*0} PDG [47] mass. Note that the natural width of $K^{*0}(892)$ is about 50 MeV. A perfect seeding of the candidates is performed, ensuring that the daughter candidates occurred from the same vertex, to limit the multiplicity[2]. Its effect will be embodied in the final selection efficiency determination.

The τ candidates are built by combining three charged π which yield to a +1 or -1 electric charge. Candidates are selected when the reconstructed mass falls in the $[3m_\pi, m_\tau]$ range corresponding to the possible mass of the τ built from only 3π due to missing neutrinos. Again, a perfect seeding on the pions is applied to limit combinatorics. The event candidate is retained if two oppositely charged τ candidates are found. Individual τ candidates must not share final state pions.

The B^0 candidates are eventually formed by combining the K^{*0} and the two τ candidates (τ and K^{*0} candidates shall not share final state particles nor a common vertex. The reconstructed mass of the combination must be found below the B^0 PDG [47] mass because of the two undetected neutrinos that take part of the decay kinematics (*e.g.*, it is expected to have a candidate mass that is below the B^0 PDG [47] mass).

In fact, a final particle of the decay can be missed by the simulated detector, or the resolution of the detector on the measured kinematics of the final particles (which are used to build invariant mass) can lead to the cut of an event which was generated at MC-Truth level. These two reasons explain why not all the events have a $B^0 \to K^{*0}\tau^+\tau^-$ candidate. From the simulated signal samples, the efficiency to have $B^0 \to K^{*0}\tau^+\tau^-$ candidate for an event is measured to be 77% for the signal samples (given by the number of candidates obtained divided by the number of generated events). This somehow low reconstruction efficiency can be understood because of the high multiplicity of the decay and the low momenta of the final state particles: the tracking efficiency is worst at low momentum.

The kinematics of the K^{*0} and τ candidates are also computed and saved for the next steps of the analysis.

5.2.2 Neutrino reconstruction and selection rule

To reconstruct the missing neutrinos, the flight vectors of the B^0 and τ's candidates are build (both in a MC-truth version for verification purposes and a reconstructed version for analysis; see below) and used in equation 5.1.2 which yields two solutions of reconstructed neutrinos for each τ. The neutrino reconstructed kinematics is propagated to the τ candidates with the determination of $p_{\tau^+_+}, p_{\tau^+_-}, p_{\tau^-_+}$ and $p_{\tau^-_-}$ where the upper sign denotes the charge of the considered τ and the lower sign denotes the solution taken to reconstruct neutrinos in equation 5.1.2. The τ reconstruction is propagated to B^0 kinematics, which leads to four solutions for each B^0 candidate.

[2]Complementary studies shown that the complete reconstruction from compatibilities of the tracks with the beam spot almost vanish the wrong combinations [208].

The correct B^0 candidate can be identified thanks to the selection rule, described in Section 5.1.3. It provides a prediction for the τ momentum : $p^{pred}_{\tau^+_+}, p^{pred}_{\tau^+_-}, p^{pred}_{\tau^-_+}$ and $p^{pred}_{\tau^-_-}$, where the upper sign denotes the charge of the considered τ and the lower sign denotes the other τ solution that has been used in equation 5.1.5. All the differences between the reconstructed and predicted τ momentum are then built (4 per charge):

- $p_{\tau^+_-} - p^{pred}_{\tau^+_-}$, $p_{\tau^+_-} - p^{pred}_{\tau^+_+}$, $p_{\tau^+_+} - p^{pred}_{\tau^+_-}$, $p_{\tau^+_+} - p^{pred}_{\tau^+_+}$,
- $p_{\tau^-_-} - p^{pred}_{\tau^-_-}$, $p_{\tau^-_-} - p^{pred}_{\tau^-_+}$, $p_{\tau^-_+} - p^{pred}_{\tau^-_-}$, $p_{\tau^-_+} - p^{pred}_{\tau^-_+}$.

The τ reconstruction best solutions (e.g. the lower sign of the two momentum of each difference corresponds to a $\pm$ solution of the two τ reconstruction) are selected by taking the ones that correspond to the smallest difference. It should be noted that the selection efficiency of this rule is 100 % in case of infinite resolution.

Due to the presence of a square root in equation 5.1.2, the neutrino reconstruction could lead to unphysical solutions due to momentum resolutions or due to rounding precision. On the other hand, the selection rule can, for the same reason, lead to consider a wrong solution combination. The neutrino reconstruction method efficiency (an event is lost when at least one neutrino leads to a wrong value) and the purity of the selection rule are evaluated by checking respectively the number of events that pass the neutrino reconstruction and by determining at MC-Truth level the right sign of the τ candidates.

MC reconstruction

For verification purposes, the method explained in this section has been first applied to the $B^0 \to K^{*0}\tau^+\tau^-$ candidates by using the MC-Truth kinematics of the final state particles. The correct solution shall be found for each candidate. Yet, the precision rounding of the flat tuples kinematic variables induced a small inefficiency. The neutrino reconstruction efficiency is about 99% and the selection rule purity is about 98%. These high values, together with the invariant-mass distribution of the B^0 reconstructed in Figure 5.2, are enough to confirm the consistency of the method.

Vertices performance emulation

The main goal of this study is to determine the vertex detector requirements in order to measure $B^0 \to K^{*0}\tau^+\tau^-$ at the SM value. The vertexing performances are varied and therefore emulated for the reconstructed $B^0 \to K^{*0}\tau^+\tau^-$ candidates in this first phase of the study. The primary vertex has been smeared once for all from its MC-Truth position with numbers close to the 3D resolutions determined in the Cartesian coordinates from the determinations done in Section 5.5.1 , *e.g.* 3 µm on the x and z coordinates, 0.0238 µm on y coordinate. This includes the beam spot luminous region constraints. As far as the secondary and tertiary vertices are concerned, regarding the fact that decaying particles are boosted along one direction for each event, it has been decided to perform a 2D ellipsoidal Gaussian smearing with longitudinal directions aligned onto the decaying particle directions and transverse directions picked-up randomly in the corresponding orthogonal plan (via the association of a random angle in the orthogonal plan and a random displacement). Figure 5.3 illustrates the smearing of the vertices.

The SV and TV position reconstruction are the main drivers of the topological reconstruction performances. Several SV and TV smearing configurations are used in term of Longitudinal-Transverse (L-T) Gaussian standard deviation. For SV and TV smearing, three longitudinal resolutions are used: 5 µm, 10 µm, 20 µm, and eight transverse resolutions:1 µm, 2 µm, 3 µm,

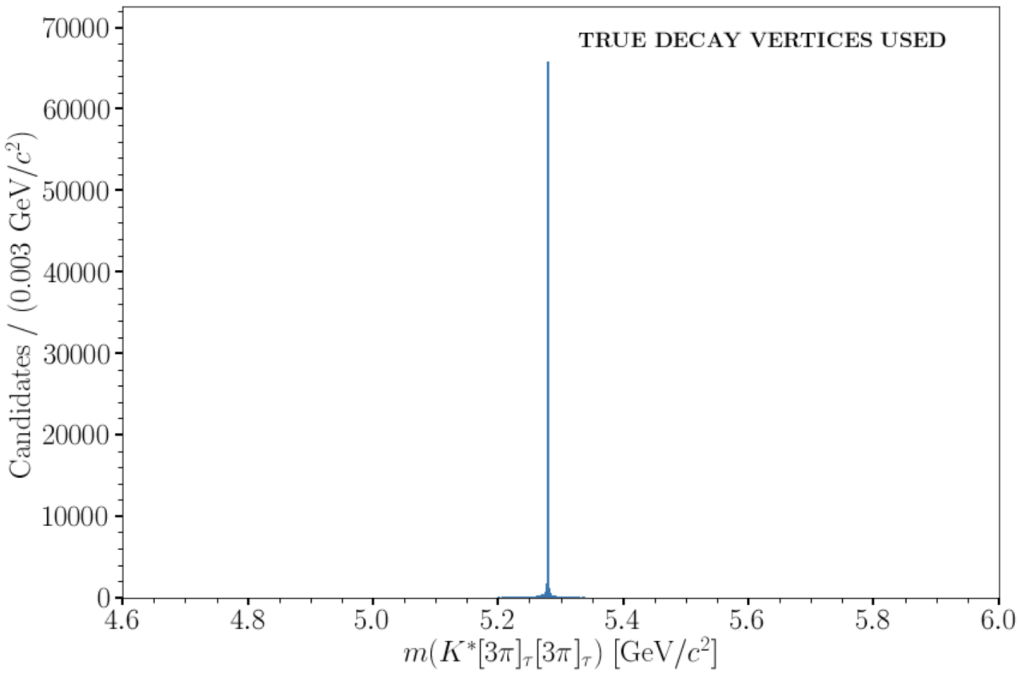

Figure 5.2: The B^0 invariant-mass reconstructed (100000 events file) with the neutrino reconstruction method and the selection rule from the MC-Truth kinematics of the final state particles. A Dirac-like peak is observed at the PDG B^0 invariant mass, validating the method and its implementation.

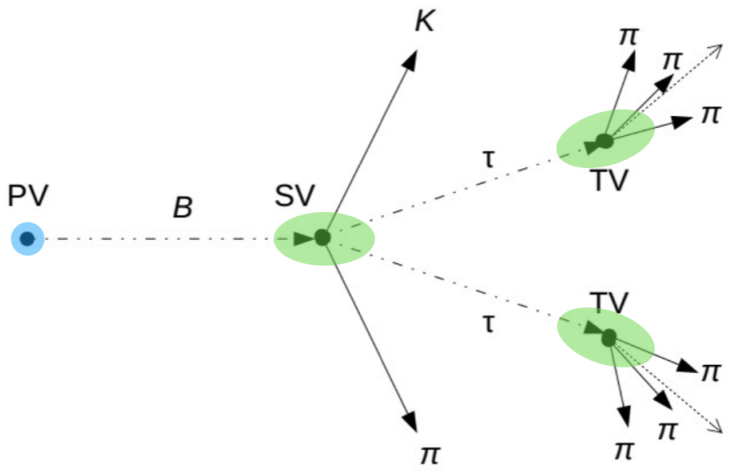

Figure 5.3: Illustration of the smearing applied to the vertices in order to emulate the vertex detector performances, blue circle denotes the 3D smearing of the PV and green ellipses denote the ellipsoidal smearing of SV and TV.

4 µm, 5 µm, 6 µm, 7 µm, 8 µm. Most of the figures in the next sections consider the $20 - 3$µm ellipsoidal smearing for SV and TV as a reference.

This emulation does not take into account any vertexing efficiency. We arbitrarily but conservatively set it to 80% in the derivation of the selection efficiency at the stage of the signal and background yields estimations.

Simulated data reconstruction

The method is finally applied to $B^0 \to K^{*0}\tau^+\tau^-$ candidate by using the reconstructed kinematics of the final state particles for the vertexing working points previously defined. On the reference

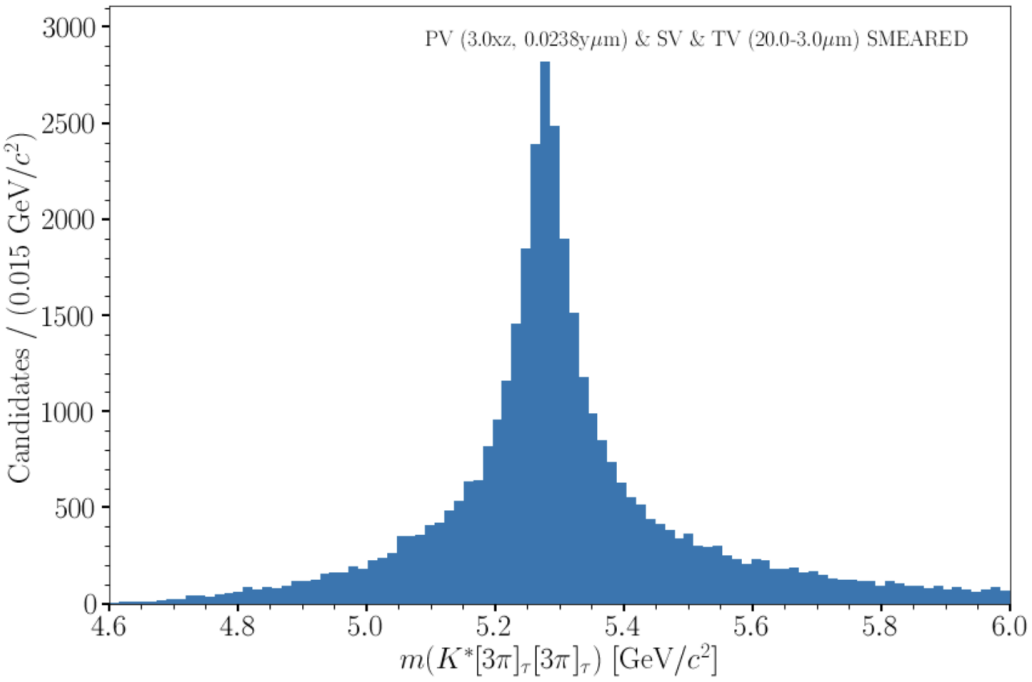

Figure 5.4: Reconstructed B^0 candidate invariant-mass(100000 events file) with the neutrinos reconstruction method and the selection rule from the reconstructed (by the simulated detector) kinematics of the final state particles on the simulated signal samples.

vertexing configuration of $20-3$µm, selection rule purity is about 50% (still better than 25% which corresponds to a random choice) and the total reconstruction efficiency is about 38% (77% of B^0 candidates building and $\sim 50\%$ of neutrinos reconstruction). Figure 5.4 shows the invariant-mass distributions obtained with the reference vertexing working point.

5.2.3 Expected yields of signal at FCC-*ee*

Thanks to the determination of the signal efficiency obtained with the IDEA detector and the vertex detector performance corresponding to the reference working point, it is possible to determine the expected number of selected signal events corresponding to this detector at FCC-*ee*. Equation 5.2.1 shows the formula to determine this number of events:

$$\mathcal{N}_{K^{*0}\tau\tau\to K7\pi2\nu} = \mathcal{N}_Z \cdot BF(Z\to b\bar{b}) \cdot 2f_d \cdot BF(B^0\to K^{*0}\tau\tau) \cdot BF(\tau\to\pi\pi\pi\nu)^2 . BF(K^{*0}\to K\pi) \cdot \epsilon_{\text{reco}} \cdot \epsilon_{\text{vertex}}, \tag{5.2.1}$$

where $\mathcal{N}_Z = 6\times10^{12}$ the expected number of Z produced with respect to FCC-*ee* baseline, $BF(Z\to b\bar{b}) = 0.1512\pm0.0005$ [47], $f_d = 0.407\pm0.007$ is the hadronisation fraction corresponding to $b\to B^0_d$ [161], $BF(K^{*0}\tau\tau) = 1.30\times10^{-7}\pm10\%$ the SM predicted branching fraction [71], $BR(\tau\to\pi\pi\pi\nu) = 0.0931\pm0.0005$ [47], $BR(K^*\to K\pi) = 0.69$ [47] (the PDG $BR(K^{*0}\to K\pi)\simeq 1$ is composed of $0.31(K^0_S\pi^0) + 0.69(K^+\pi^-)$), $\epsilon_{reco} = 0.3840\pm0.0007$ is the total reconstruction efficiency determined for a $3\,\mu\text{m} - 20\,\mu\text{m}$ smearing, and $\epsilon_{vertex} = 0.8$ is the assumed vertex reconstruction efficiency.

Assuming the SM and the baseline FCC-ee luminosity, one would eventually select $\mathcal{N}_{K^{*0}\tau\tau\to K7\pi2\nu} = 176\pm18$. The identification of the background sources and their evaluation will play a major role in the examination of the feasibility of the measurement.

5.3 Backgrounds and selection

5.3.1 Backgrounds

Identification

The potential sources of background to consider are those providing a similar final state as the signal one (one kaon and seven pions); they must be of physical origin and can occur from $b \to c\bar{c}s$ and $b \to c\tau\nu_\tau$ transitions. Among the $b \to c\bar{c}s$ modes, the decays involving a $D_s^{(*)}$ in the final state like $B^0 \to K^{*0} D_s^{(*)} D_s^{(*)}$ are potentially dominant since the D_s decays can provide either a real τ particle or three-prongs mimicking a *tau*: $D_s \to \tau\nu$, $D_s \to 3\pi\pi^0$ and $D_s \to 3\pi 2\pi^0$. For $b \to c\tau\nu_\tau$ modes like $B_s^0 \to K^{*0} D^{(*)} \tau\nu$ with $D \to 3\pi\pi^0$ and/or $D^* \to D\pi^0$ or $D^* \to D^0\pi$ with $D^0 \to 4\pi\pi^0$, and $B^0 \to K^{*0} D_s^{(*)} \tau\nu$ with the aforementioned D_s decays can also mimic the signal. There modes are not measured to date and their branching fractions must be estimated, as detailed in the next Section 5.3.1.

Branching fractions estimation

$B^0 \to K^{*0} D_s^{(*)} D_s^{(*)}$

LHC*b* [10] performed recently the first measurement of the branching fraction of the decay mode $B^+ \to K^+ D_s^+ D_s^-$ [209]:

$$BF(B^+ \to K^+ D_s^+ D_s^-) = (1.15 \pm 0.39) \times 10^{-4}. \tag{5.3.1}$$

This decay proceeds through the same amplitudes as the background source of interest in this work $B^0 \to K^{*0} D_s D_s$. The only difference is carried by the spectator quark (u for B^+ and d for B^0) and this similarity makes this measurement a good proxy for $BF(B^0 \to K^{*0} D_s D_s)$. Yet, a corrective factor that takes into account the difference in the form factors ($B^+ \to K^+$ vs. $B^0 \to K^{*0}$ transitions) and another that accounts for the phase space difference are needed.

The form factor correction is inferred from measured modes with equivalent amplitudes, one with a K, the other with a K^*: it is taken directly as the ratio of their branching fractions. The PDG provides the measurements of $B^+ \to D^0 K^+$ and $B^+ \to D^0 K^{*+}$ branching fractions, which match the aforementioned requirement. The measurements give $BF(B^+ \to D^0 K^+) = (3.64 \pm 0.15) \times 10^{-4}$ and $BF(B^+ \to D^0 K^{*+}) = (5.3 \pm 0.4) \times 10^{-4}$. The form factor correction is determined in equation 5.3.2:

$$\begin{aligned} C_{\mathrm{FF}} =& \frac{\mathrm{FF_{K^*}}}{\mathrm{FF_K}} \\ =& \frac{BF(B^+ \to D^0 K^{*+})}{BF(B^+ \to D^0 K^+)} \\ =& 1.46 \pm 0.13, \end{aligned} \tag{5.3.2}$$

where the uncertainty comes from the standard propagation of the BF uncertainties without correlations .

The phase space correction is accordingly determined by comparing two equivalent modes, one with a K, the other with a K^*, and then building their ratio. Starting from $B^+ \to K^+ D_s^+ D_s^-$, the corresponding mode is $B^+ \to K^{*+} D_s^+ D_s^-$. The phase spaces of the two modes have been computed numerically by 2D integrations in the Dalitz Plane [194] of the decays (the Dalitz Plane is a common representation of the three-body decay phase space) and provides $PS(B^+ \to K^+ D_s^+ D_s^-) = 1.076 \times 10^{-7}$ and $PS(B^+ \to K^{*+} D_s^+ D_s^-) = 3.507 \times 10^{-8}$. The phase

space correction is determined in equation 5.3.3:

$$\begin{aligned} C_{\mathrm{PS}} &= \frac{PS(B^+ \to K^{*+} D_s^+ D_s^-)}{PS(B^+ \to K^+ D_s^+ D_s^-)} \\ &= 0.326, \end{aligned} \tag{5.3.3}$$

where no uncertainty is considered from the computation.

The $B^0 \to K^{*0} D_s D_s$ branching fraction is computed from the $B^+ \to K^+ D_s^+ D_s^-$ measurement and the corrective factors by merging together equations 5.3.1, 5.3.2 and 5.3.3 to obtain the result in equation 5.3.4:

$$\begin{aligned} BF(B^0 \to K^{*0} D_s D_s) &= BF(B^+ \to K^+ D_s^+ D_s^-) \times C_{\mathrm{FF}} \times C_{\mathrm{PS}} \\ &= (5.47 \pm 1.92) \times 10^{-5}, \end{aligned} \tag{5.3.4}$$

where uncertainty comes from the propagation of the previous uncertainties.

To determine $BF(B^0 \to K^{*0} D_s^* D_s)$ and $BF(B^0 \to K^{*0} D_s^* D_s^*)$, the form factor hierarchy between the $D_s D_s$, $D_s^* D_s$ and $D_s^* D_s^*$ final states is needed. One way to determine this hierarchy is to consider the branching fractions of measured modes that involved two $D_s^{(*)}$. The $B_s^0 \to D_s^{(*)} D_s^{(*)}$ [47] match this requirement. The needed branching fractions are given in equations 5.3.5, 5.3.6 and 5.3.7:

$$BF(B_s^0 \to D_s D_s) = (4.4 \pm 0.5) \times 10^{-3}, \tag{5.3.5}$$

$$BF(B_s^0 \to D_s^* D_s) = (1.39 \pm 0.17) \times 10^{-2}, \tag{5.3.6}$$

$$BF(B_s^0 \to D_s^* D_s^*) = (1.44 \pm 0.21) \times 10^{-2}. \tag{5.3.7}$$

The branching fractions given in equations 5.3.5, 5.3.6 and 5.3.7 are added to determine the inclusive $BF(B_s^0 \to D_s^{(*)} D_s^{(*)})$ and with equation 5.3.4 divided by the $B_s^0 \to D_s D_s$ branching fraction it allow the determination of the inclusive $B^0 \to K^{*0} D_s^{(*)} D_s^{(*)}$ branching fraction in equation 5.3.8:

$$\begin{aligned} BF(B^0 \to K^{*0} D_s^{(*)} D_s^{(*)}) =& BF(B^0 \to K^{*0} D_s D_s) \times \frac{BF(B_s^0 \to D_s^{(*)} D_s^{(*)})}{BF(B_s^0 \to D_s D_s)} \\ =& (4.07 \pm 1.54) \times 10^{-4}, \end{aligned} \tag{5.3.8}$$

where the uncertainty is determined by propagating all the intermediate branching fractions uncertainties.

The branching fraction of $B^0 \to K^{*0} D_s^* D_s$ is estimated, by considering the inclusive $BF(B^0 \to K^{*0} D_s^{(*)} D_s^{(*)})$ and following the hierarchy given by $B_s^0 \to D_s^{(*)} D_s^{(*)}$, as written in equation 5.3.9:

$$\begin{aligned} BF(B^0 \to K^{*0} D_s^* D_s) =& BF(B^0 \to K^{*0} D_s^{(*)} D_s^{(*)}) \times \frac{BF(B_s^0 \to D_s^* D_s)}{BF(B_s^0 \to D_s^{(*)} D_s^{(*)})} \\ =& (1.73 \pm 0.70) \times 10^{-4}. \end{aligned} \tag{5.3.9}$$

Similarly the branching fraction of $B^0 \to K^{*0} D_s^* D_s^*$ is estimated by considering the inclusive $BF(B^0 \to K^{*0} D_s^{(*)} D_s^{(*)})$ and following the hierarchy given by $B_s^0 \to D_s^{(*)} D_s^{(*)}$, as written in equation 5.3.10:

$$\begin{aligned} BF(B^0 \to K^{*0} D_s^* D_s^*) =& BF(B^0 \to K^{*0} D_s^{(*)} D_s^{(*)}) \times \frac{BF(B_s^0 \to D_s^* D_s^*)}{BF(B_s^0 \to D_s^{(*)} D_s^{(*)})} \\ =& (1.79 \pm 0.72) \times 10^{-4}. \end{aligned} \tag{5.3.10}$$

$B^0 \to K^{*0} D_s^{(*)} \tau\nu$

To determine the inclusive branching fraction of $B^0 \to K^{*0} D_s^{(*)} \tau\nu$ a strategy of analogy is used [210] considering the mode $B^+ \to K^+ D_s^{(*)} \mu\nu$ as reference with $BF(B^+ \to K^+ D_s^{(*)} \mu\nu) = (6.1 \pm 1.0) \times 10^{-4}$ (PDG). The $BF(B^0 \to K^{*0} D_s^{(*)} \tau\nu)$ can be estimated from $BF(B^+ \to K^+ D_s^{(*)} \mu\nu)$ by correcting for the suppression effects ($s\bar{s}$ and τ) using a phase space ratio. The inclusive branching fraction of $B^0 \to K^{*0} D_s^{(*)} \tau\nu$ is given in equation 5.3.11:

$$\begin{aligned} BF(B^0 \to K^{*0} D_s^{(*)} \tau\nu) =& BF(B^+ \to K^+ D_s^{(*)} \mu\nu) \times \frac{PS(B^0 \to K^{*0} D_s^{(*)} \tau\nu)}{PS(B^+ \to K^+ D_s^{(*)} \mu\nu)} \\ =& (2.95 \pm 0.48) \times 10^{-5}, \end{aligned} \tag{5.3.11}$$

where $PS(B^0 \to K^{*0} D_s^{(*)} \tau\nu) = 3.1 \times 10^{-8}$ and $PS(B^+ \to K^+ D_s^{(*)} \mu\nu) = 6.4 \times 10^{-7}$ are computed via numerical pseudo 3-body phase space integration by considering the dominant $K-D$ hadronic resonances [210]. The uncertainty comes from $BF(B^+ \to K^+ D_s^{(*)} \mu\nu)$.

The $B^0 \to K^{*0} D_s \tau\nu$ and $B^0 \to K^{*0} D_s^* \tau\nu$ branching fraction are then accessed from $BF(B^0 \to K^{*0} D_s^{(*)} \tau\nu)$ following the hierarchy of the $B^0 \to D^* \ell\nu_\ell$ modes, measured to be $BF(B^0 \to D \ell\nu_\ell) = (2.24 \pm 0.09) \times 10^{-2}$ and $BF(B^0 \to D^* \ell\nu_\ell) = (4.97 \pm 0.12) \times 10^{-2}$. The branching fractions $B^0 \to K^{*0} D_s \tau\nu$ and $B^0 \to K^{*0} D_s^* \tau\nu$ are therefore

$$\begin{aligned} BF(B^0 \to K^{*0} D_s \tau\nu) =& BF(B^0 \to K^{*0} D_s^{(*)} \tau\nu) \times \frac{BF(B^0 \to D \ell\nu_\ell)}{BF(B^0 \to D^{(*)} \ell\nu_\ell)} \\ =& (9.17 \pm 1.56) \times 10^{-6}, \end{aligned} \tag{5.3.12}$$

$$\begin{aligned} BF(B^0 \to K^{*0} D_s^* \tau\nu) =& BF(B^0 \to K^{*0} D_s^{(*)} \tau\nu) \times \frac{BF(B^0 \to D^* \ell\nu_\ell)}{BF(B^0 \to D^{(*)} \ell\nu_\ell)} \\ =& (2.03 \pm 0.34) \times 10^{-5}, \end{aligned} \tag{5.3.13}$$

where uncertainties comes from the propagation of the intermediate branching fractions uncertainties.

$B_s^0 \to K^{*0} D^{(*)} \tau\nu$

To determine the inclusive branching fraction of $B_s^0 \to K^{*0} D^{(*)} \tau\nu$ a strategy of analogy is used [210] considering the mode $B_s^0 \to D_{s1}(2536)^- \mu\nu$ as a reference with $BF(B_s^0 \to D_{s1}(2536)^- \mu\nu) = (2.7 \pm 0.7) \times 10^{-3}$ (PDG). The $BF(B_s^0 \to K^{*0} D^{(*)} \tau\nu)$ can be estimated from $BF(B_s^0 \to D_{s1}(2536)^- \mu\nu)$ using the method above. With respect to the method, the inclusive branching fraction of $B_s^0 \to K^{*0} D^{(*)} \tau\nu$ is given in equation 5.3.14:

$$\begin{aligned} BF(B_s^0 \to K^{*0} D^{(*)} \tau\nu) =& BF(B_s^0 \to D_{s1}(2536)^- \mu\nu) \times \frac{PS(B_s^0 \to K^{*0} D^{(*)} \tau\nu)}{PS(B_s^0 \to D_{s1}(2536)^- \mu\nu)} \\ =& (2.34 \pm 0.61) \times 10^{-4}, \end{aligned} \tag{5.3.14}$$

where $PS(B_s^0 \to K^{*0} D^{(*)} \tau\nu) = 5.7 \times 10^{-8}$ and $PS(B_s^0 \to D_{s1}(2536)^- \mu\nu) = 6.6 \times 10^{-7}$ are computed via numerical phase space integration considered as pseudo 3-body [210]. The uncertainty comes from $BF(B_s^0 \to D_{s1}(2536)^- \mu\nu)$.

The $B_s^0 \to K^{*0} D \tau\nu$ and $B_s^0 \to K^{*0} D^* \tau\nu$ branching fractions are accessed following the method developed above. The $B_s^0 \to K^{*0} D \tau\nu$ and $B_s^0 \to K^{*0} D_s^* \tau\nu$ branching fractions are

summarised in equations 5.3.15 and 5.3.16:

$$\begin{aligned} BF(B_s^0 \to K^{*0} D \tau\nu) =& BF(B_s^0 \to K^{*0} D^{(*)} \tau\nu) \times \frac{BF(B^0 \to D \ell\nu_\ell)}{BF(B^0 \to D^{(*)} \ell\nu_\ell)} \\ =& (7.27 \pm 1.92) \times 10^{-5}, \end{aligned} \tag{5.3.15}$$

$$\begin{aligned} BF(B_s^0 \to K^{*0} D^* \tau\nu) =& BF(B_s^0 \to K^{*0} D^{(*)} \tau\nu) \times \frac{BF(B^0 \to D^* \ell\nu_\ell)}{BF(B^0 \to D^{(*)} \ell\nu_\ell)} \\ =& (1.61 \pm 0.42) \times 10^{-4}, \end{aligned} \tag{5.3.16}$$

where uncertainties comes from the propagation of the considered intermediate branching fractions uncertainties.

Visible BF determination

The visible branching fractions of the possible backgrounds are computed following equation 5.3.17:

$$BF(X \to y) = BF(Z^0 \to b\bar{b}) \times 2 \times f_X \times BF(X \to x) \times BF(x \to y), \tag{5.3.17}$$

where $BF(Z^0 \to b\bar{b}) = (15.12 \pm 0.05) \times 10^{-2}$, the factor 2 takes into account the charge conjugated process, X denotes the b-hadron considered, x denotes the decay product of the b-hadron, y denotes the final state, f_X is the hadronisation fraction of the $b \to X$, taken from HFLAV measurements [161], $BF(X \to x)$ comes from Section 5.3.1 and $BF(x \to y)$ is the product of the intermediate BF to obtain the final state.

Here, it is important to notice that the intermediate branching fractions $BF(D_s \to 3\pi\pi^0)$ and $BF(D_s \to 3\pi 2\pi^0)$ require to consider their intermediate η and ω contributions. Equations 5.3.18 and 5.3.19 detail the numbers considered:

$$\begin{aligned} &BF(D_s \to 3\pi\pi^0) = BF(D_s \to \eta\pi) \times BF(\eta \to 2\pi\pi^0) + BF(D_s \to \omega\pi) \times BF(\omega \to 2\pi\pi^0) \\ &BF(D_s \to 3\pi\pi^0) = (5.58 \pm 0.34) \times 10^{-3}, \end{aligned} \tag{5.3.18}$$

$$\begin{aligned} &BF(D_s \to 3\pi 2\pi^0) = BF(D_s \to \eta\pi\pi^0) \times BF(\eta \to 2\pi\pi^0) + BF(D_s \to \omega\pi\pi^0) \times BF(\omega \to 2\pi\pi^0) \\ &BF(D_s \to 3\pi 2\pi^0) = (4.68 \pm 0.64) \times 10^{-2}, \end{aligned} \tag{5.3.19}$$

where the branching fractions values are taken from the PDG.

Table 5.1 summarises the branching fractions of the possible modes and, in addition, provides the list of the additional missing particles for each of them.

Backgrounds to consider

The possible interesting backgrounds have been presented, and their branching fractions are estimated. It is now needed to choose the backgrounds to consider.

Regarding the $b \to c\tau\nu$ backgrounds, they are problematic since the D and most prominently the D_s mesons can decay leptonically to a τ particle or mimic a hadronic final state close to the signal. In terms of lifetime D_s is closer to τ than D, which provides a further advantage to the D_s backgrounds in the reconstruction method. Furthermore, $D_s \to 3\pi 2\pi^0$ is ten times more likely compared to $D \to 3\pi 2\pi^0$. Finally, D_s seems to be a more suitable candidate to mimic a signal τ compared to D, leading to the exclusion of B_s^0 backgrounds for which the simultaneous production of a $D_s K^{*0}(892)$ pair is disfavoured.

Decay	BF (SM/meas.)	Intermediate decay	BF_{had}	Additional missing particles
Signal: $B^0 \to K^{*0}\tau\tau$	1.30×10^{-7}	$\tau \to \pi\pi\pi\nu$, $K^{*0} \to K\pi$	9.57×10^{-11}	
$b \to c\bar{c}s$ bkgs:				
$B^0 \to K^{*0}D_sD_s$	5.47×10^{-5}	$D_s \to \tau\nu$	1.14×10^{-10}	2ν
		$D_s \to \pi\pi\pi\pi^0$	1.45×10^{-10}	$2\pi^0$
		$D_s \to \pi\pi\pi 2\pi^0$	1.02×10^{-8}	$4\pi^0$
		$D_s \to \tau\nu, \pi\pi\pi\pi^0$	1.28×10^{-10}	ν , π^0
		$D_s \to \tau\nu, \pi\pi\pi 2\pi^0$	1.08×10^{-9}	ν , $2\pi^0$
		$D_s \to \pi\pi\pi\pi^0, \pi\pi\pi 2\pi^0$	1.21×10^{-9}	$3\pi^0$
$B^0 \to K^{*0}D_sD_s^*$	1.73×10^{-4}	$D_s \to \tau\nu$	3.60×10^{-10}	2ν, γ/π^0
		$D_s \to \pi\pi\pi\pi^0$	4.57×10^{-10}	$2\pi^0$, γ/π^0
		$D_s \to \pi\pi\pi\pi^0\pi^0$	3.22×10^{-8}	$4\pi^0$, γ/π^0
		$D_s \to \tau\nu, \pi\pi\pi\pi^0$	4.06×10^{-10}	ν , π^0, γ/π^0
		$D_s \to \tau\nu, \pi\pi\pi 2\pi^0$	3.41×10^{-9}	ν , $2\pi^0$, γ/π^0
		$D_s \to \pi\pi\pi\pi^0, \pi\pi\pi 2\pi^0$	3.84×10^{-9}	$3\pi^0$, γ/π^0
$B^0 \to K^{*0}D_s^*D_s^*$	1.79×10^{-4}	$D_s \to \tau\nu$	3.73×10^{-10}	2ν, $2\gamma/\pi^0$
		$D_s \to \pi\pi\pi\pi^0$	4.73×10^{-10}	$2\pi^0$, $2\gamma/\pi^0$
		$D_s \to \pi\pi\pi\pi^0\pi^0$	3.33×10^{-8}	$4\pi^0$, $2\gamma/\pi^0$
		$D_s \to \tau\nu, \pi\pi\pi\pi^0$	4.20×10^{-10}	ν , π^0, $2\gamma/\pi^0$
		$D_s \to \tau\nu, \pi\pi\pi 2\pi^0$	3.52×10^{-9}	ν , $2\pi^0$, $2\gamma/\pi^0$
		$D_s \to \pi\pi\pi\pi^0, \pi\pi\pi 2\pi^0$	3.97×10^{-9}	$3\pi^0$, $2\gamma/\pi^0$
$b \to c\tau\nu$ bkgs:				
$B_s \to K^{*0}D\tau\nu$	7.27×10^{-5}	$D \to \pi\pi\pi\pi^0$	1.65×10^{-9}	ν, π^0
$B_s \to K^{*0}D^*\tau\nu$	1.61×10^{-4}	$D^* \to D^0\pi, D\pi^0$		
		$D \to \pi\pi\pi\pi^0$	1.12×10^{-9}	ν, $2\pi^0$
		$D^0 \to 2\pi 2\pi\pi^0$	8.98×10^{-10}	ν, $2\pi^0$, $\pi^\pm$
$\bar{B}^0 \to \bar{K}^{*0}D_s\tau\nu$	9.17×10^{-6}	$D_s \to \tau\nu$	3.59×10^{-10}	2ν
		$D_s \to \pi\pi\pi\pi^0$	4.05×10^{-10}	ν, π^0
		$D_s \to \pi\pi\pi 2\pi^0$	3.39×10^{-9}	ν, $2\pi^0$
$B^0 \to K^{*0}D_s^*\tau\nu$	2.03×10^{-5}	$D_s \to \tau\nu$	7.95×10^{-10}	2ν, γ/π^0
		$D_s \to \pi\pi\pi\pi^0$	8.96×10^{-10}	ν, π^0, γ/π^0
		$D_s \to \pi\pi\pi\pi^0\pi^0$	7.51×10^{-9}	ν, $\gamma/\pi^0, 2\pi^0$

Table 5.1: Summary table of the possible backgrounds (bkgs), τ decay not specified means $\tau \to \pi\pi\pi\nu$.

In order to choose in an educated way, the backgrounds to consider in the remaining ones, having a look at the branching fractions only, is not enough. The reconstruction efficiency (mostly related to phase space specifics of the background decays) will modulate the toxicity of the backgrounds depending on their abilities to survive the reconstruction method and their abilities to produce invariant masses close to the B^0 invariant mass. To address these effects, simulations of unique background types have been done: $B^0 \to K^{*0}D_s\tau\nu$ with $D_s \to \tau\nu$, $B^0 \to K^{*0}D_sD_s$ with $D_s \to \tau\nu$ and $D_s \to 3\pi\pi^0$ and $D_s \to 3\pi 2\pi^0$ and $D_s \to \tau\nu/3\pi\pi^0$, $B^0 \to K^{*0}D_s^*D_s$ with $D_s \to \tau\nu$. The goal in the following is to build a per-track efficiency to apply to the visible branching fraction to rank and choose the backgrounds to consider.

Each of the background has been used through the reconstruction workflow, with the reference vertexing performances configuration, in order to extract the reconstruction efficiency (which are the product of the efficiency to find a B^0 candidate and the efficiency to pass the neutrinos reconstruction) and the window efficiency which is the efficiency to be in the B^0 mass

Mode	Reconstruction efficiency	Window efficiency	Total efficiency
Signal: $B^0 \to K^{*0}\tau\tau$	0.384	0.810	0.311
$B^0 \to K^{*0}D_sD_s, D_s \to \tau\nu$	0.475	0.213	0.101
$B^0 \to K^{*0}D_sD_s, D_s \to 3\pi\pi^0$	0.022	0.235	0.005
$B^0 \to K^{*0}D_sD_s, D_s \to 3\pi 2\pi^0$	0.563	0.338	0.191
$B^0 \to K^{*0}D_sD_s, D_s \to \tau\nu/3\pi\pi^0$	0.101	0.222	0.023
$B^0 \to K^{*0}D_s^*D_s, D_s \to \tau\nu$	0.483	0.127	0.061
$B^0 \to K^{*0}D_s\tau\nu, D_s \to \tau\nu$	0.428	0.259	0.111

Table 5.2: Efficiency tables of the simulated modes.

window $[5.0, 5.6]$GeV. A total per mode efficiency is then constructed with the product of the two previously defined efficiencies, the results are summarised in table 5.2.

A per track efficiency is then constructed for each D_s taking the square root of the two D_s modes, assuming a uniform repartition of the K^{*0} tracks in the two D_s track efficiencies. The per track efficiencies are written in equations 5.3.20, 5.3.21 and 5.3.22:

$$\epsilon(D_s \to \tau\nu) = \sqrt{\epsilon(B^0 \to K^{*0}D_sD_s, D_s \to \tau\nu)} = \sqrt{0.101}, \tag{5.3.20}$$

$$\epsilon(D_s \to 3\pi\pi^0) = \sqrt{\epsilon(B^0 \to K^{*0}D_sD_s, D_s \to 3\pi\pi^0)} = \sqrt{0.005}, \tag{5.3.21}$$

$$\epsilon(D_s \to 3\pi 2\pi^0) = \sqrt{\epsilon(B^0 \to K^{*0}D_sD_s, D_s \to 3\pi 2\pi^0)} = \sqrt{0.191}. \tag{5.3.22}$$

To check the correctness of the method the agreement of $\epsilon(B^0 \to K^{*0}D_sD_s, D_s \to \tau\nu/3\pi\pi^0)$ with the product of the corresponding per track efficiencies is computed in equation 5.3.23:

$$\epsilon(D_s \to \tau\nu) \times \epsilon(D_s \to 3\pi\pi^0) = 0.022, \tag{5.3.23}$$

which is the same as the efficiency measured with the simulated sample, but the last digit due to rounding done in the computation.

In addition an efficiency to have a D_s^* in place of a D_s is computed thanks to $\epsilon(B^0 \to K^{*0}D_s^*D_s, D_s \to \tau\nu)$ and $\epsilon(D_s \to \tau\nu)$ in equation 5.3.24:

$$\epsilon(*) = \frac{\epsilon(D_s^* \to \tau\nu)}{\epsilon(D_s \to \tau\nu)} = \sqrt{0.365}, \tag{5.3.24}$$

where $\epsilon(D_s^* \to \tau\nu) = \epsilon(B^0 \to K^{*0}D_s^*D_s, D_s \to \tau\nu)/\epsilon(D_s \to \tau\nu)$.

The predicted efficiency is then built for all the modes from these per-track efficiencies. The check about $D_s \to \tau\nu/3\pi\pi^0$ shows that the predicted efficiency seems coherent for the $b \to c\bar{c}s$ backgrounds. On the other hand, the method is less adapted to the $b \to c\tau\nu_\tau$ in B^0 backgrounds, because of the presence of only one D_s, for them only one track efficiency is taken. For $b \to c\tau\nu_\tau$ in B_s backgrounds that have been excluded elsewhere before, the highest predicted efficiency on other $b \to c\tau\nu_\tau$ backgrounds is taken conservatively. The table of the branching fractions times predicted efficiency is displayed in table 5.3 where the modes are ranked thanks to the multiplication of the visible branching fraction by the predicted efficiency.

To keep the bookkeeping of the simulation at a reasonable rate, it has been chosen to simulate the dominant backgrounds in each category to drive the selection ideas. If a non-simulated background is found to be significant after the selection process, it will be re-examined. Namely, $B^0 \to K^{*0}D_s^*D_s$ and $B^0 \to K^{*0}D_sD_s$ with $D_s \to 3\pi 2\pi^0$ have been simulated, considering backgrounds with and without a D_s^* (implying fewer additional missing particles) and having the highest branching fractions (BF). In addition, $B^0 \to K^{*0}D_sD_s$ with $D_s \to 3\pi 2\pi^0/\tau\nu$

Mode	$\mathrm{BF}_{\mathrm{had}}\,(10^{-8})$	$\varepsilon_{\mathrm{pred}}$	$\mathrm{BF}_{\mathrm{had}} \times \varepsilon_{\mathrm{pred}}\,(10^{-9})$
$B_d^0 \to K^{*0} D_s^* D_s (D_s \to 3\pi 2\pi^0)$	3.22	0.115393	3.71
$B_d^0 \to K^{*0} D_s^* D_s^* (D_s \to 3\pi 2\pi^0)$	3.33	0.069715	2.32
$B_d^0 \to K^{*0} D_s^* \tau\nu (D_s \to 3\pi 2\pi^0)$	0.751	0.264036	1.98
$B_d^0 \to K^{*0} D_s D_s (D_s \to 3\pi 2\pi^0)$	1.02	0.191000	1.94
$B_d^0 \to K^{*0} D_s \tau\nu (D_s \to 3\pi 2\pi^0)$	0.339	0.437035	1.48
$B_s^0 \to K^{*0} D \tau\nu (D \to 3\pi\pi^0)$	0.165	0.437035	0.72
$B_s^0 \to K^{*0} D^* \tau\nu (D^* \to D\pi^0, D \to 3\pi\pi^0)$	0.112	0.437035	0.49
$B_s^0 \to K^{*0} D^* \tau\nu (D^* \to D^0\pi, D^0 \to 4\pi\pi^0)$	0.090	0.437035	0.39
$B_d^0 \to K^{*0} D_s^* D_s (D_s \to \tau\nu/3\pi 2\pi^0)$	0.341	0.083912	0.29
$B_d^0 \to K^{*0} D_s^* D_s^* (D_s \to \tau\nu/3\pi 2\pi^0)$	0.352	0.050696	0.18
$B_d^0 \to K^{*0} D_s^* \tau\nu (D_s \to \tau\nu)$	0.080	0.192003	0.15
$B_d^0 \to K^{*0} D_s D_s (D_s \to \tau\nu/3\pi 2\pi^0)$	0.108	0.138892	0.15
$B_d^0 \to K^{*0} D_s \tau\nu (D_s \to \tau\nu)$	0.036	0.317805	0.11
$B_d^0 \to K^{*0} D_s^* D_s (D_s \to 3\pi\pi^0/3\pi 2\pi^0)$	0.384	0.018670	0.07
$B_d^0 \to K^{*0} D_s^* D_s^* (D_s \to 3\pi\pi^0/3\pi 2\pi^0)$	0.397	0.011280	0.04
$B_d^0 \to K^{*0} D_s^* \tau\nu (D_s \to 3\pi\pi^0)$	0.090	0.042720	0.04
$B_d^0 \to K^{*0} D_s D_s (D_s \to 3\pi\pi^0/3\pi 2\pi^0)$	0.121	0.030903	0.04
Signal	0.010	0.313000	0.03
$B_d^0 \to K^{*0} D_s \tau\nu (D_s \to 3\pi\pi^0)$	0.041	0.070711	0.03
$B_d^0 \to K^{*0} D_s^* D_s (D_s \to \tau\nu)$	0.036	0.061019	0.02
$B_d^0 \to K^{*0} D_s^* D_s^* (D_s \to \tau\nu)$	0.037	0.036865	0.01
$B_d^0 \to K^{*0} D_s D_s (D_s \to \tau\nu)$	0.011	0.101000	0.01
$B_d^0 \to K^{*0} D_s^* D_s (D_s \to \tau\nu/3\pi\pi^0)$	0.041	0.013577	0.006
$B_d^0 \to K^{*0} D_s^* D_s^* (D_s \to \tau\nu/3\pi\pi^0)$	0.042	0.008202	0.003
$B_d^0 \to K^{*0} D_s D_s (D_s \to \tau\nu/3\pi\pi^0)$	0.013	0.022472	0.003
$B_d^0 \to K^{*0} D_s^* D_s (D_s \to 3\pi\pi^0)$	0.046	0.003021	0.001
$B_d^0 \to K^{*0} D_s^* D_s^* (D_s \to 3\pi\pi^0)$	0.047	0.001825	0.0009
$B_d^0 \to K^{*0} D_s D_s (D_s \to 3\pi\pi^0)$	0.015	0.005000	0.0007

Table 5.3: Table of the modes ranked as function of the visible branching fraction time predicted efficiency.

represents the dominant crossed mode without D_s^*, while $B^0 \to K^{*0} D_s D_s$ with $D_s \to 3\pi\pi^0/\tau\nu$ is the most irreducible crossed mode, they are both simulated. Moreover, $B^0 \to K^{*0} D_s^* D_s$ and $B^0 \to K^{*0} D_s D_s$ with $D_s \to \tau\nu$ are simulated as the most irreducible $b \to c\bar{c}s$ modes with and without D_s^*. Additionally, $B^0 \to K^{*0} D_s D_s$ with $D_s \to 3\pi\pi^0$ was already simulated. Finally, for the $b \to c\tau\nu$ backgrounds, $B^0 \to K^{*0} D_s^* \tau\nu$ with $D_s \to 3\pi 2\pi^0$ and $B^0 \to K^{*0} D_s \tau\nu$ with $D_s \to \tau\nu$ are simulated as, respectively, the dominant and the most irreducible backgrounds of this category.

Backgrounds generation

The backgrounds defined previously have all been simulated in order to be used in the analysis. The $D_s \to 3\pi n\pi^0$ backgrounds (where $n = 1, 2$) have been generated following the specific intermediate modes by which they are composed, as explained in Section 5.3.1. The next section details the selection criteria used to reduce the background modes.

The decay files used to generate all the modes of the analysis can be found on the winter2023 branch of the official FCC-config github project following the paths (the corresponding generated root files are available following the path in eos:

- FCCee/Generator/EvtGen/Bd2KstarTauTau.dec,
- FCCee/Generator/EvtGen/Bd2DsDsKstarDs2Taunu.dec,

- FCCee/Generator/EvtGen/Bd2DsDsKstarDs2TaunuDs2pipipipi0pi0.dec and FCCee/Generator/EvtGen/Bd2DsDsKstarDs2TaunuDs2pipipipi0pi0ChargeConjugation.dec,
- FCCee/Generator/EvtGen/Bd2DsDsKstarDs2TaunuDs2pipipipi0v2.dec and FCCee/Generator/EvtGen/Bd2DsDsKstarDs2TaunuDs2pipipipi0v2ChargeConjugation.dec,
- FCCee/Generator/EvtGen/Bd2DsDsKstarDs2pipipipi0pi0v2.dec,
- FCCee/Generator/EvtGen/Bd2DsDsKstarDs2pipipipi0v2.dec,
- FCCee/Generator/EvtGen/Bd2DsKstarTauNuDs2TauNu.dec,
- FCCee/Generator/EvtGen/Bd2DsstarDsKstarDs2PiPiPiPi0Pi0Dsstar2Dsgamma.dec,
- FCCee/Generator/EvtGen/Bd2DsstarDsKstarDs2TaunuDsstar2Dsgamma.dec,
- FCCee/Generator/EvtGen/Bd2DsstarKstarTauNuDs2pipipipi0pi0.dec.

5.3.2 Selection

Events weighting

The selection is constructed using datasets of simulated signal and background events, appropriately scaled to reproduce their natural proportion given in the Table of visible branching fractions 5.1. All modes are scaled with respect to their associated BF and reconstruction efficiencies in addition to the expected number of Z produced at FCC-ee $N_Z = 6e^{12}$ in order to consider the natural number of events. Finally, since vertexing is emulated in the analysis, there is no actual vertexing reconstruction efficiency estimation available (ability of the detector to rightly associate tracks). Therefore, a flat vertexing efficiency $\epsilon_{vertexing} = 0.8$ is taken conservatively [3].

Selection rule behavior on the backgrounds

The selection rule developed in Section 5.1.3 is the only educated way available to determine which B^0 signal solution to keep. To evaluate the selection rule behaviour on all the modes considered, the invariant-mass distribution of the reference vertexing configuration has been built for both a case where the four possible B^0 solutions are taken for each event and a case where only the selected solution is taken. The distributions of each mode are displayed in Figure 5.5, with respect to their expected number of events in the $[4.6, 6]$GeV window, their respective branching fractions and the reconstruction efficiencies as determined in the simulation.

The Figure 5.5 shows that the selection rule selects preferentially the low invariant-mass solutions, even for the backgrounds for which the average reconstructed mass are below m_{B^0} due to additional missing particles with respect to the signal. This behavior promotes the selection rule as a prominent tool against the backgrounds. From a quantitative point of view, the signal purity can be used as a figure of merit:

$$P = \frac{S}{S+B}, \tag{5.3.25}$$

where S denotes the signal yield and B denotes the backgrounds yield. The purity observed for the reference vertexing configuration in the $[5.2, 5.6]\text{GeV/c}^2$ reduced window around the B^0 mass is twice larger with the selected solutions. In the following, the solutions selected by the selection rule are therefore always taken.

[3] This is supported by studies conducted after this work and in companion studies [208]

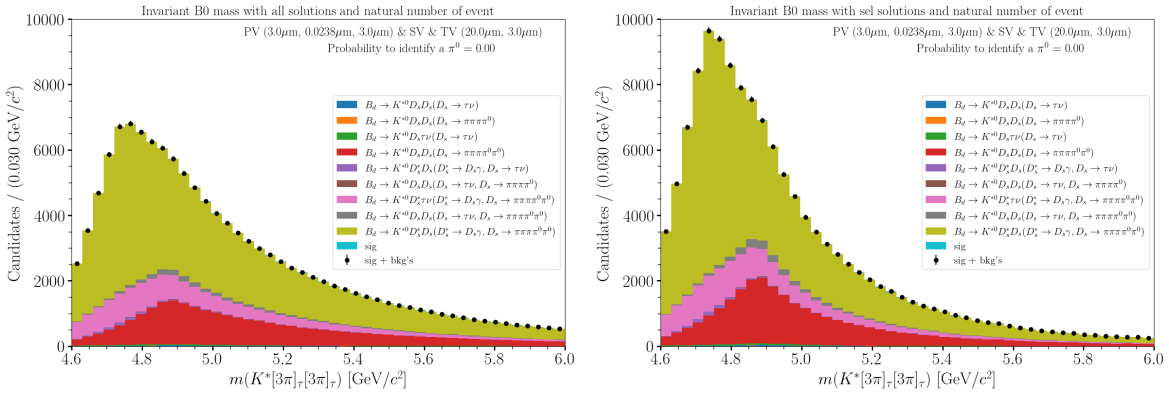

Figure 5.5: Invariant-mass plot of the B^0 candidates with the 20−3µm vertexing resolution configuration for all solutions (left) and selected solutions (right).

Mode	Total reconstruction efficiency (%)
Signal	38.40 ± 0.07
$B^0 \to K^{*0} D_s D_s, D_s \to \tau\nu$	47.49 ± 0.04
$B^0 \to K^{*0} D_s D_s, D_s \to 3\pi\pi^0$	2.190 ± 0.002
$B^0 \to K^{*0} D_s D_s, D_s \to 3\pi 2\pi^0$	56.30 ± 0.05
$B^0 \to K^{*0} D_s D_s, D_s \to \tau\nu/3\pi\pi^0$	10.14 ± 0.01
$B^0 \to K^{*0} D_s D_s, D_s \to \tau\nu/3\pi 2\pi^0$	51.64 ± 0.04
$B^0 \to K^{*0} D_s^* D_s, D_s \to \tau\nu$	48.27 ± 0.04
$B^0 \to K^{*0} D_s^* D_s, D_s \to 3\pi 2\pi^0$	57.30 ± 0.04
$B^0 \to K^{*0} D_s \tau\nu, D_s \to \tau\nu$	42.85 ± 0.04
$B^0 \to K^{*0} D_s^* \tau\nu, D_s \to 3\pi 2\pi^0$	47.26 ± 0.04

Table 5.4: Summary table of the total reconstruction (including the B^0 candidate building and neutrino reconstruction) efficiency as function of the mode for the reference vertexing performances working point.

The total reconstruction efficiencies are summarised, for each mode with the reference vertexing resolution configuration, in Table 5.4. Several of the backgrounds show better reconstruction efficiencies than the signal; this, together with their branching fraction, justify their amplitudes in Figure 5.5.

Calorimeter performance impact

A significant part of the dominant backgrounds comes with an additional π^0 from $D_s \to 3\pi n\pi^0$ ($n = 1, 2$). This type of background is reducible provided that the pi^0 particles can be reconstructed in the calorimeter. Their association with tracks to form a mother particle candidate can be therefore further used to select the signal. The calorimeter performance is parameterised for the sake of simplicity with the sole global π^0 reconstruction efficiency denoted ϵ_{π^0}.

The $D_s \to 3\pi n\pi^0$ decays proceed through the η/ω intermediate state. It is therefore enough to identify only η/ω to reject one of these backgrounds. The surviving probabilities associated to these backgrounds are then:

$$p_{1D_s} = 1 - \epsilon_{\pi^0}, \tag{5.3.26}$$

$$p_{2D_s} = (1 - \epsilon_{\pi^0})^2, \tag{5.3.27}$$

where the surviving probability to the calorimeter is defined for both, backgrounds with one $D_s \to 3\pi n\pi^0$ and backgrounds with two $D_s \to 3\pi n\pi^0$ as function of the calorimeter performances.

The ALEPH calorimeter performance showed a π^0 reconstruction efficiency of about 50 % [211]. It is therefore reasonable to consider that electromagnetic calorimeter designs for FCC-*ee*, especially if they are meeting Flavour Physics and *CP* violation physics requirements would reach 80 %. The application of these calorimeter performances in the analysis clearly improves the picture on the invariant-mass distribution for the reference vertexing configuration as displayed in Figure 5.6. A signal purity in the range $[5.2, 5.6]\text{GeV}/c^2$ of 0.102 is obtained. Yet, a further selection is in order and is described below.

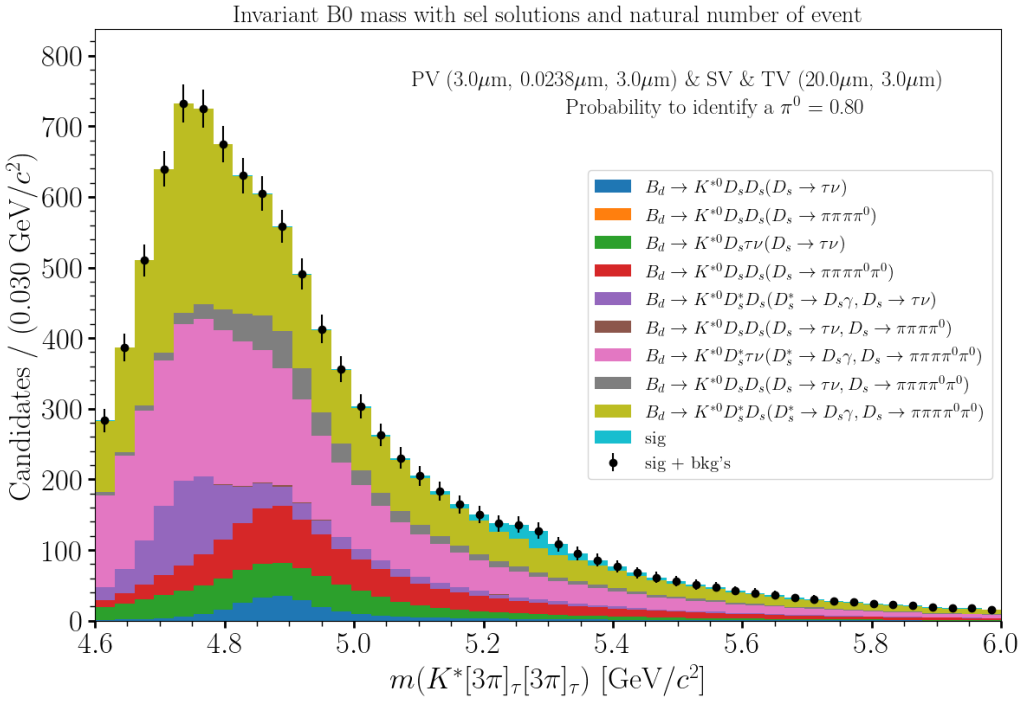

Figure 5.6: Invariant-mass plot of the B^0 candidates with the 20−3µm vertexing resolution configuration after the use of the π^0 reconstruction to reduce the $D_s \to 3\pi n\pi^0$ background.

XGBoost selection

Among the possible selection methods, it has been decided to use an XGBoost [171] algorithm (the same as the one used in the LHCb $B^0_{d,s} \to K^0_S h^+ h'^-$ work), which is a multivariate classifier (MVA). The following will explain the XGBoost selection built for the analyses from, first, the identification of the potential discriminative variables, second, a preselection step, and third, the XGBoost itself.

Discriminative variables

In order to build the selection several quantities have been saved in parallel of the analysis workflow, the most relevant to discriminate background from signal are named discriminative variables, and those are the ones to use in the selection. The discriminative variables are identified from the comparison of their signal and background distributions, the discriminative variables (all displayed in natural units with c=1) found in the analysis are:

- the reconstructed τ candidate momentum that take into account the ν reconstruction displayed in Figure 5.7,

- the reconstructed momentum of the K^{*0} candidate, exhibiting differences because of the phase space of the decay. It is displayed in Appendix D.1,
- the reconstructed momentum combination of the 3π from τ candidates displayed in Appendix D.1,
- the highest measured π momentum from τ candidates, characteristic of the τ decay dynamics, proceeding dominantly from a $a_1(1260)$ intermediate amplitude as displayed in Appendix D.1,
- the lowest measured π momentum from τ candidates based on the properties of the $a_1 \to \rho\pi$ decay (valid for the two latter quantities).It is displayed in Appendix D.1,
- the determined B^0 candidate flight distance displayed in Appendix D.1,
- the determined τ candidate flight distance displayed in Appendix D.1,
- the determined distance between primary and tertiary vertices displayed in Appendix D.1,
- the reconstructed mass of the 3π from τ candidate displayed in Appendix D.1,
- the reconstructed highest 2π combination mass from τ candidate displayed in Appendix D.1,
- the reconstructed lowest 2π combination mass from τ candidate displayed in Appendix D.1.

Finally, the Dalitz plane defined by the reconstructed highest 2π combination squared mass and the reconstructed lowest 2π combination squared mass is a powerful tool to remove the dominant backgrounds as displayed in Figure5.8.

Preselection

The basic discriminative variables identified are first used in a preselection stage in order to reduce, with simple/sanity cuts, the dominant backgrounds. The table 5.5 summarises the cuts used in the preselection. Sanity cuts are applied on $p_{K^{*0}}$, $p_{\pi\,max}$ and $p_{\pi\,min}$. Initial cuts are applied on $p_{3\pi}$ and FD_{B^0} to remove backgrounds without a significant loss of signal events. Cuts are applied on $m_{3\pi}$, $m_{2\pi\,max}$, $m_{2\pi\,min}$ and the Dalitz $m_{2\pi}$ plan to reduce especially the $D_s \to 3\pi n\pi^0$ backgrounds. Eventually, a requirement is applied on FD_τ to reduce specifically the $D_s \to \tau\nu$ backgrounds.

Figure 5.9 shows the invariant-mass distribution of the B^0 candidates after the preselection. By comparing the figures 5.6 and 5.9 one can see a clear improvement of the signal purity by about a factor 3 in the signal region.

Multivariate Analysis

In order to perform the Multivariate Analysis (MVA), it is needed to build a dataset with signal and background events that pass the preselection step, but because of the use of exclusive samples, the available events do not follow the natural proportions of the modes. The strategy to build a coherent dataset is for the signal to take as many events as possible with respect to the statistics available and for the background to take the same number of events by following the natural proportion of each background with respect to the others (taking into account

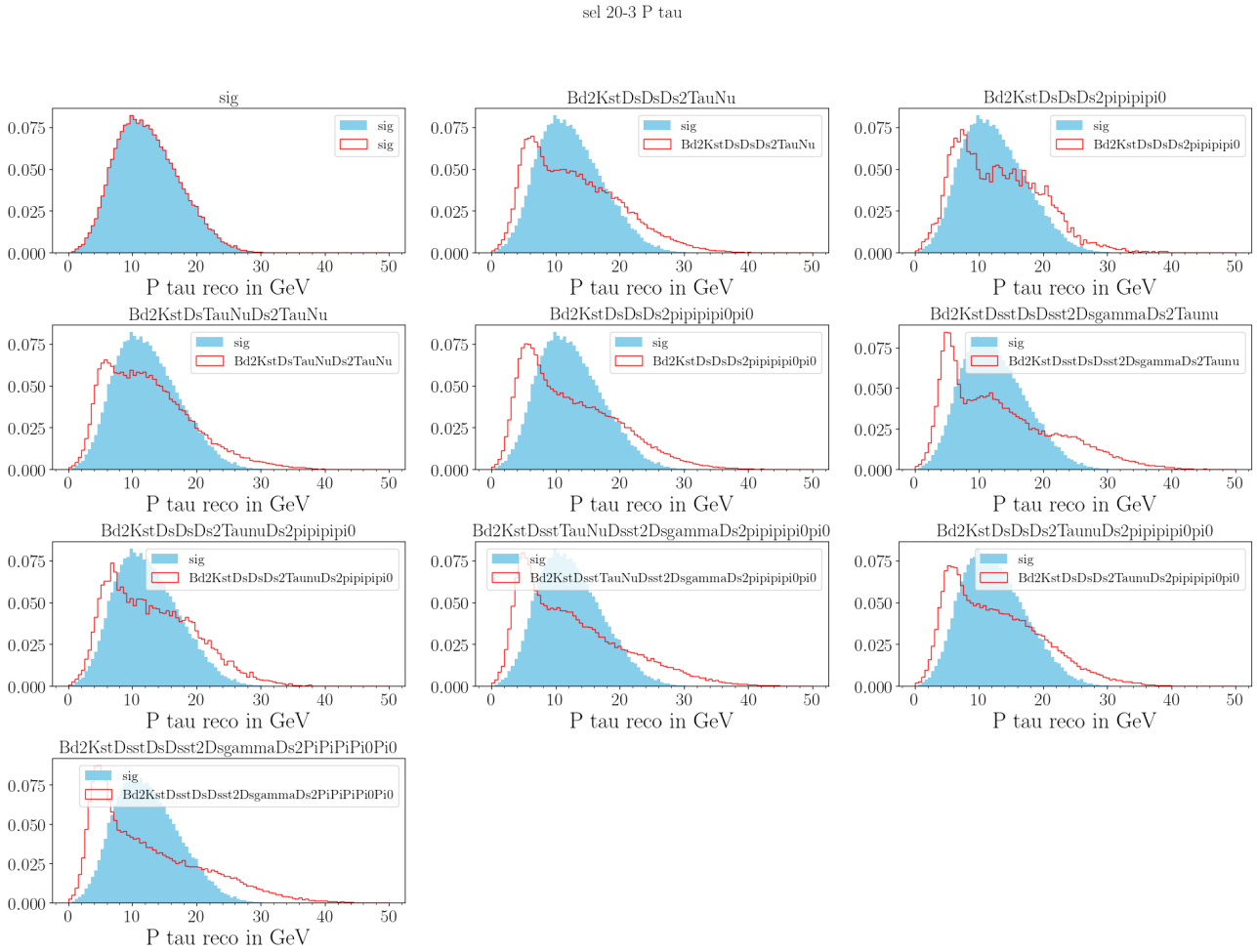

Figure 5.7: p_τ reconstructed with ν from τ candidates distribution as function of the mode.

Variable	Cut
$m^2_{2\pi_{min}}$ & $m^2_{2\pi_{max}}$	< 0.3 & < 0.5 GeV^2/c^4
p_{K^*}	< 1GeV/c
$p_{3\pi}$	< 1GeV/c
$p_{\pi_{max}}$	< 0.25GeV/c
$p_{\pi_{min}}$	< 0.2GeV/c
FD_B	< 0.3mm
FD_τ	> 4mm
$m_{3\pi}$	< 0.750GeV/c^2
$m_{2\pi_{max}}$	< 0.5GeV/c^2
$m_{2\pi_{min}}$	> 1GeV/c^2

Table 5.5: Preselection table

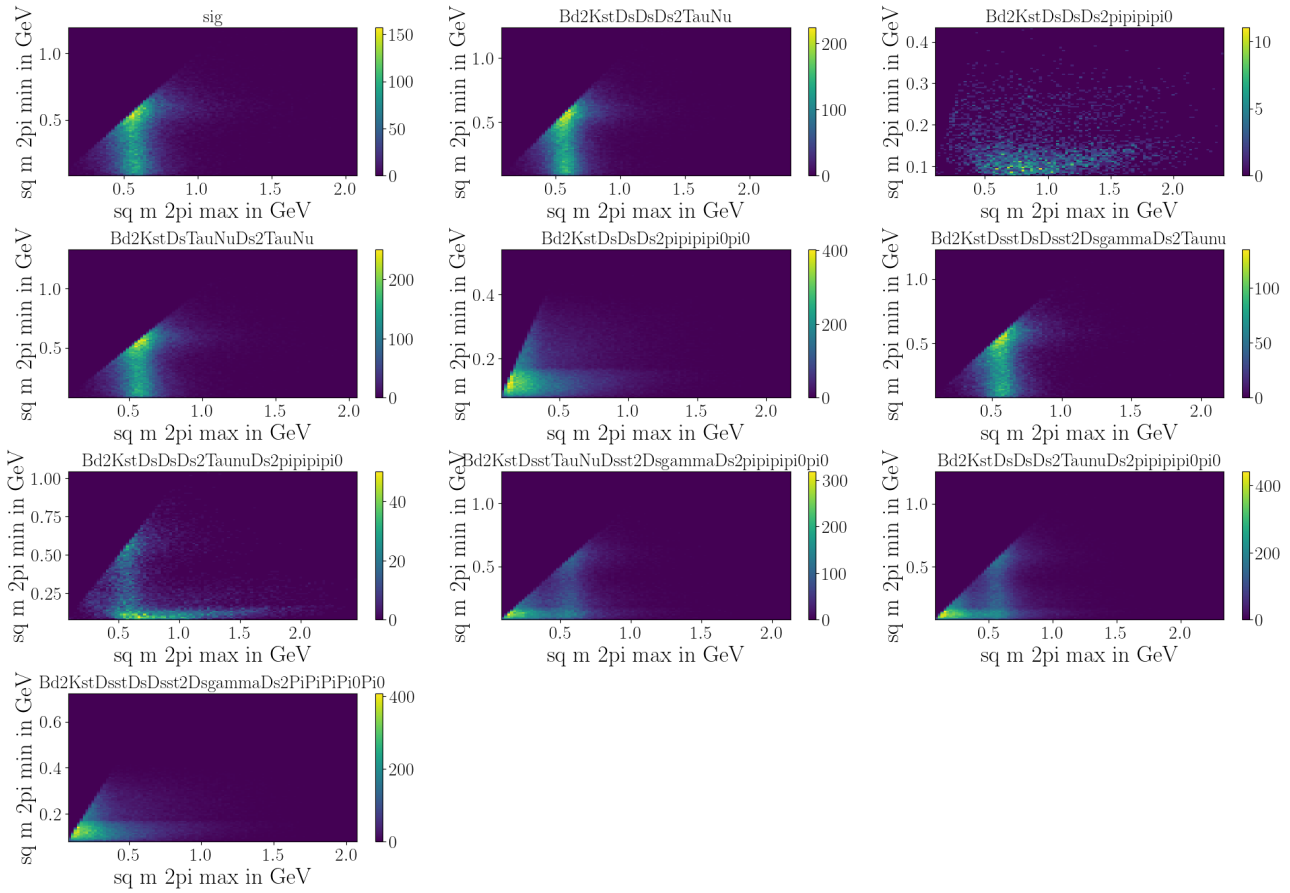

Figure 5.8: Dalitz plan built from $m_{2\pi}$ of τ candidates distribution as function of the mode.

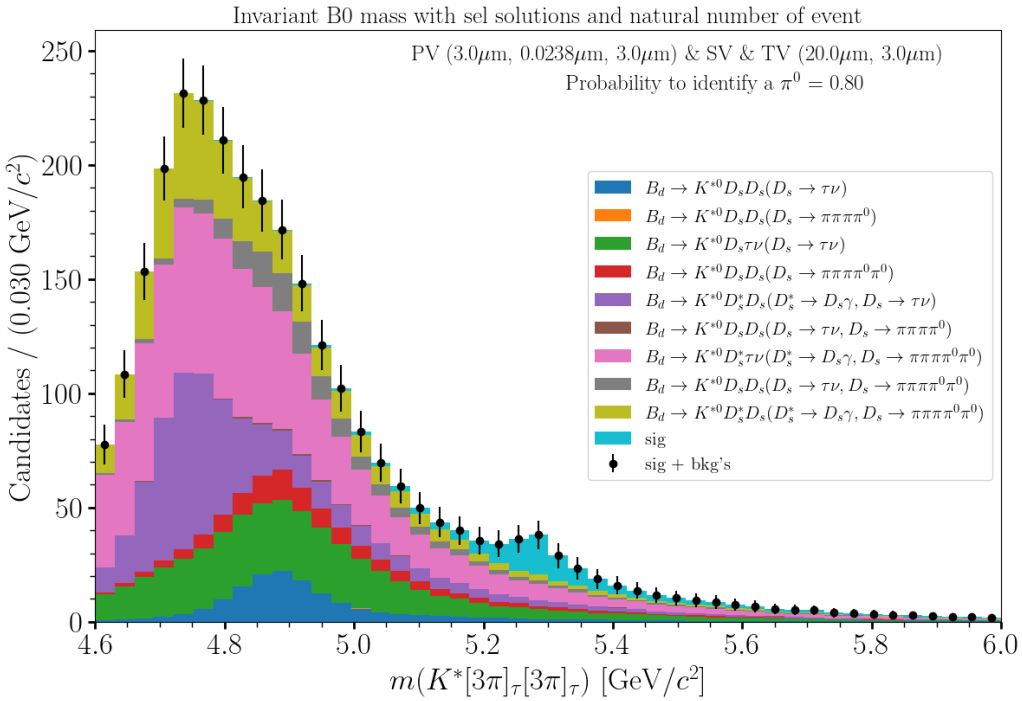

Figure 5.9: Invariant mass distribution for 20 − 3µm working point after the preselection.

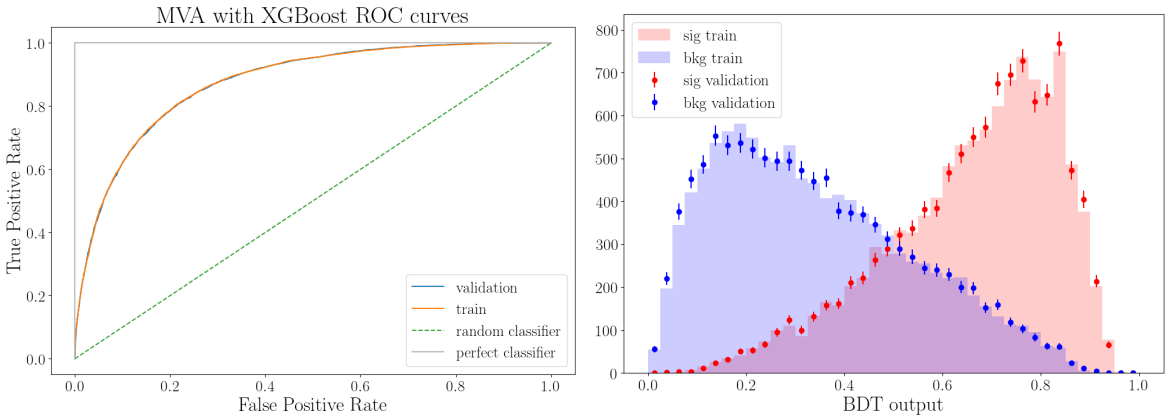

Figure 5.10: ROC curves (left) and overtraining plot (right).

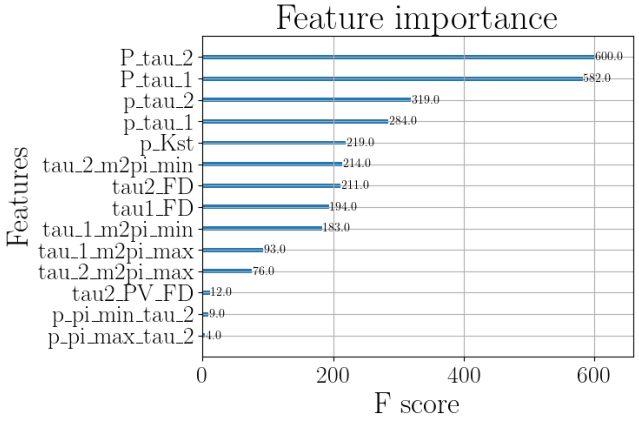

Figure 5.11: Features importance plot.

the branching fractions and efficiencies). The whole dataset is then randomly split into 50/50 train/validation datasets.

The XGBoost algorithm is based on the use of a large number of small decision trees (weak classifier individually) to classify a set of entries by using their characteristics (set of variables available for each entry). The XGBoost model is created using the dedicated Python package and the Scikit-Learn package tools [212], a hyperparameter tuning step is performed to determine the optimal hyperparameter of the model which are a learning rate of 0.01, a maximum depth of 2, 1000 trees, the objective is set at binary logistic (two class classification in order), the evaluating metric is the AUC (Area Under the Curve of the ROC curve) and the early stopping round parameter is set at 10 (in order to avoid overtrain if there is no improvement by adding trees).

The optimal model is trained on the train dataset and the validation dataset is used to control the overtraining. The discriminative variables defined in Section 5.3.2 are given as features in the MVA. The ROC curves shown in Figure 5.10 show that the performance of the model is good with an AUC of 0.8749 on the train dataset and 0.8747 on the validation dataset, and the similarity between the two curves gives a first indication of non-overtraining. The overtraining itself is evaluated through the overtraining plot shown in Figure 5.10 for which the Kolmogorov-Smirnov tests [172] return p-values of 0.98 for the signal and 0.57 for the background train/validation distributions comparison, which are both above the 0.05 threshold over which the hypothesis that the train/validation distributions are compatible has been considered a priori valid. Figure 5.11 shows the importance of the features that entered into the model.

Finally, the MVA selection is applied after the preselection with a cut at 0.5 on the XGB

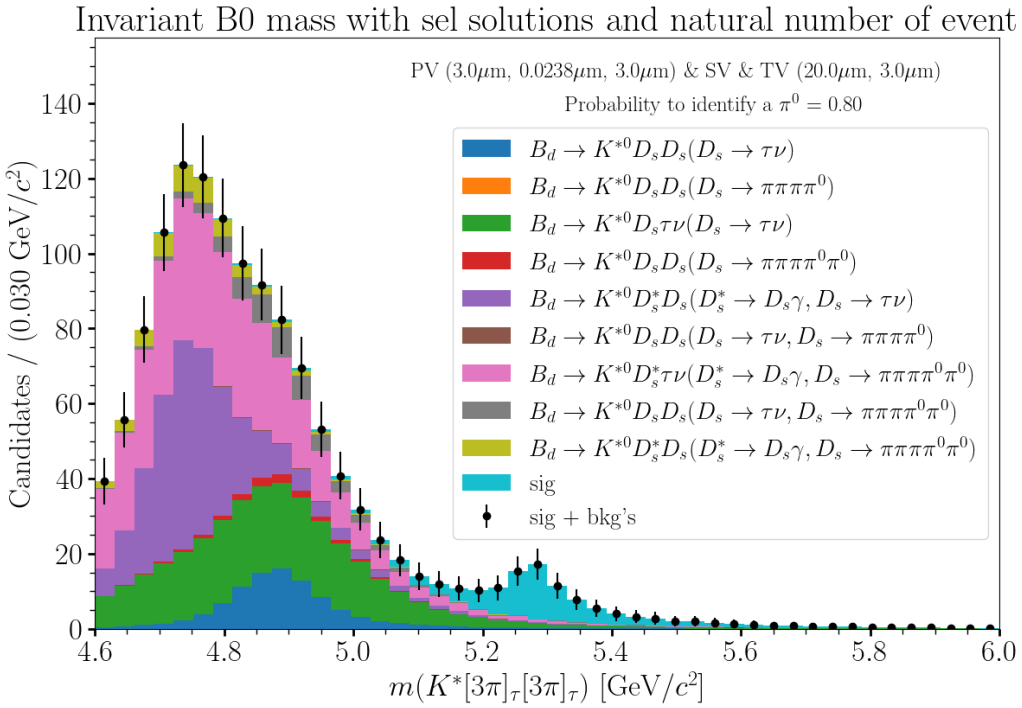

Figure 5.12: Invariant-mass distribution of the B^0 candidates for $20-3$µm working point after the XGBoost selection.

	all solutions	selected solutions	π^0 detection rate	preselection	MVA
purity	0.004	0.008	0.102	0.307	0.753

Table 5.6: Summary table of the purity at each step of the selection, evaluated on the $[5.2, 5.6]$GeV mass window for $20-3$µm working point. All solutions means without using the selection rule. Selected solutions means with the use of the selection rule.

output, Figure 5.12 shows that the picture is improved by this step of the selection, this observation is quantitatively confirmed by the purity on the $[5.2, 5.6]$GeV window which is of 0.753 after the whole selection. To quantitatively summarise the improvements brought about by each step of selection, Table 5.6 displays the purity of the signal evaluated in the $[5.2, 5.6]$GeV/c^2 for each step. None of the backgrounds which have not been generated (see Section 5.3.1) makes it after the selection.

Selection efficiencies

The efficiencies at each step of the selection in the $[5, 5.6]$GeV mass window are summarised in Table 5.7. The numbers indicate that the selection is the most efficient against $D_s \to 3\pi 2\pi^0$ backgrounds, which were the dominant ones. The $D_s \to \tau\nu$ backgrounds, which are the most irreducible ones, are reduced, but the selection is expectedly less efficient on them.

Mode	Preselection efficiency (%)	MVA efficiency (%)	Total selection efficiency (%)
Signal	70.0	78.1	54.7
$B^0 \to K^{*0} D_s D_s, D_s \to \tau\nu$	59.7	60.9	36.4
$B^0 \to K^{*0} D_s D_s, D_s \to 3\pi\pi^0$	60.3	6.5	3.9
$B^0 \to K^{*0} D_s D_s, D_s \to 3\pi 2\pi^0$	10.2	13.1	1.3
$B^0 \to K^{*0} D_s D_s, D_s \to \tau\nu/3\pi\pi^0$	60.8	33.4	20.3
$B^0 \to K^{*0} D_s D_s, D_s \to \tau\nu/3\pi 2\pi^0$	23.7	38.1	9.0
$B^0 \to K^{*0} D_s^* D_s, D_s \to \tau\nu$	58.9	58.7	34.6
$B^0 \to K^{*0} D_s^* D_s, D_s \to 3\pi 2\pi^0$	7.9	11.2	8.1
$B^0 \to K^{*0} D_s \tau\nu, D_s \to \tau\nu$	64.3	65.4	42.1
$B^0 \to K^{*0} D_s^* \tau\nu, D_s \to 3\pi 2\pi^0$	22.9	42.2	9.7

Table 5.7: Summary table of the selection efficiency as function of the mode on the $[5, 5.6]$GeV mass window for $20 - 3$µm working point.

5.4 Precision of the Branching Fraction measurement

5.4.1 Method

The goal of this study is to provide vertex detectors requirements in order to measure $B^0 \to K^{*0}\tau^+\tau^-$ at FCC-*ee*. The quantity chosen to evaluate the feasibility of the measurement is the precision on the branching fraction measurement. The precision on the branching fraction measurement is accessed from a fit to the invariant-mass distributions of the signal and backgrounds that pass the selection (*e.g.* distributions like the one in Figure 5.12) for each vertexing configuration. The precision of the branching fraction measurement is defined as:

$$P = \frac{\sigma_{N_{\text{signal}}}}{N_{\text{signal}}}, \tag{5.4.1}$$

where N_{signal} can be either the fitted or the expected signal yield and $\sigma_{N_{\text{signal}}}$ is the uncertainty associated to the signal fit.

The fit is performed in the invariant mass range of $[5.0, 6.0]$GeV in order to consider the signal and the decreasing part of the backgrounds. The model used to fit the signal part is a double-sided Crystal Ball P.D.F. (Probability Density Function) that describes the tails and the peak, and an additional Gaussian P.D.F. with a shared mean to improve the description of the peak. The background part is described with a double decreasing exponential P.D.F.. The fit is performed with the Maximum Logarithmic Likelihood (MLL) method implemented in RooFit [204] and the convergence is evaluated with error estimates given by Minuit2 minimizer and Hesse.

The fitting scheme is the following :

1. definition of the signal fit model,
2. fit of the signal only on the whole available statistics (no rescale),
3. extraction of the signal fit parameters,
4. set as constant all the signal fit shape parameters,
5. definition of the signal and background fit model (combination of the constrained signal pdf and the free background pdf) by introducing yields parameters,
6. fit of the rescaled signal and background distributions together,
7. extraction of the final fit parameters (yields and background pdf parameters).

As an illustration of the fitting scheme, Figure 5.13 displays the fit of the signal alone and a fit of the background and the signal together for the reference vertexing working point. The uncertainties are given to the readers to judge for the sensitivity of the measurement with the actual statistics.

The precision of the measurement is determined for each vertexing configuration, as explained above. The plots equivalent to Figure 5.13 for other configurations are given in Appendix D.2. The signal yield uncertainty as defined in equation 5.4.1 is measured from the fit, the expected signal yield is used (extracted from the distributions after selection) to minimise the impact of the statistical fit fluctuation from one working point to another and the precision is finally determined.

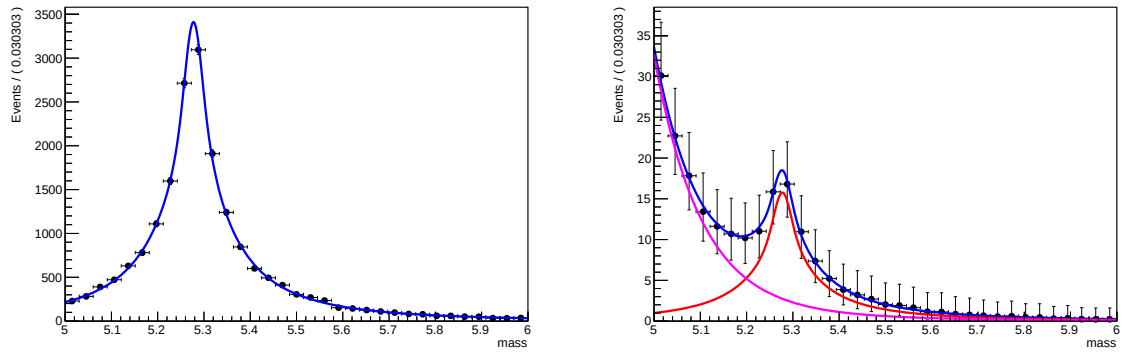

Figure 5.13: Fit of the signal (left) and fit of signal + background (right) in order to determine the precision on the BF measurement for the 20 – 3µm working point.

Results and vertexing requirements

The results of the precision of the BF measurement of $B^0 \to K^{*0}\tau\tau$ with $\tau \to \pi\pi\pi\nu$ are stored in Tables 5.8 to 5.10. In terms of visualisation, the results are shown in Figures 5.14 (only 20 µm longitudinal configuration for readability) and 5.15. The plots show that the main driver of the branching fraction measurement is the transverse resolution on the secondary/tertiary vertices. To be able to observe this mode, even at its SM expectation and regarding the actual baseline luminosity of FCC-*ee*, a very good transverse vertexing resolution is required $\mathcal{O}(1\,\mu m)$.The next step of the analysis is to evaluate the vertexing performances of IDEA, an actual simulation of the detector available for FCC-*ee* to add an IDEA working point in the analysis to determine where the state-of-the-art is.

L-T smearing configuration	20-1µm	20-2µm	20-3µm	20-4µm	20-5µm	20-6µm	20-7µm	20-8µm
N_{signal}	117.79	100.27	86.02	75.70	66.79	59.69	53.62	48.32
$\sigma_{N_{signal}}$	16.55	17.97	20.12	22.09	24.14	24.95	27.76	29.21
Precision	0.14	0.18	0.23	0.29	0.36	0.42	0.52	0.60

Table 5.8: Table of the precision on the branching fraction measurement as function of the transverse emulated smearing on secondary and tertiary vertices, for a longitudinal smearing of 20 µm.

L-T smearing configuration	10-1µm	10-2µm	10-3µm	10-4µm	10-5µm	10-6µm	10-7µm	10-8µm
N_{signal}	125.97	104.07	87.98	76.83	67.86	60.29	54.82	49.10
$\sigma_{N_{signal}}$	15.91	17.09	19.42	21.16	21.98	25.84	26.89	27.94
Precision	0.13	0.16	0.22	0.28	0.32	0.43	0.49	0.57

Table 5.9: Table of the precision on the branching fraction measurement as function of the transverse emulated smearing on secondary and tertiary vertices, for a longitudinal smearing of 10 µm

L-T smearing configuration	5-1µm	5-2µm	5-3µm	5-4µm	5-5µm	5-6µm	5-7µm	5-8µm
N_{sig}	128.09	105.10	89.44	76.00	67.88	61.10	55.01	49.16
$\sigma_{N_{sig}}$	15.68	17.01	18.74	20.48	22.24	24.71	28.11	26.61
Precision	0.12	0.16	0.21	0.27	0.33	0.40	0.51	0.54

Table 5.10: Table of the precision on the branching fraction measurement as function of the transverse emulated smearing on secondary and tertiary vertices, for a longitudinal smearing of 5 µm

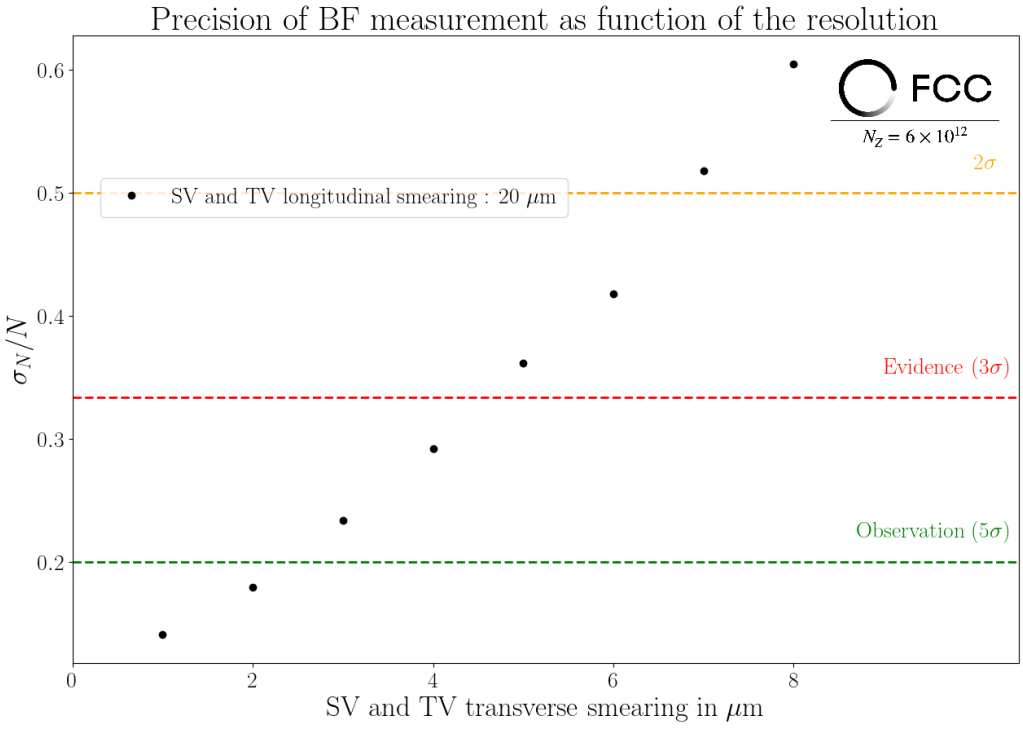

Figure 5.14: Precision of the measurement as function of the transverse vertexing resolution with a longitudinal resolution set at 20 µm.

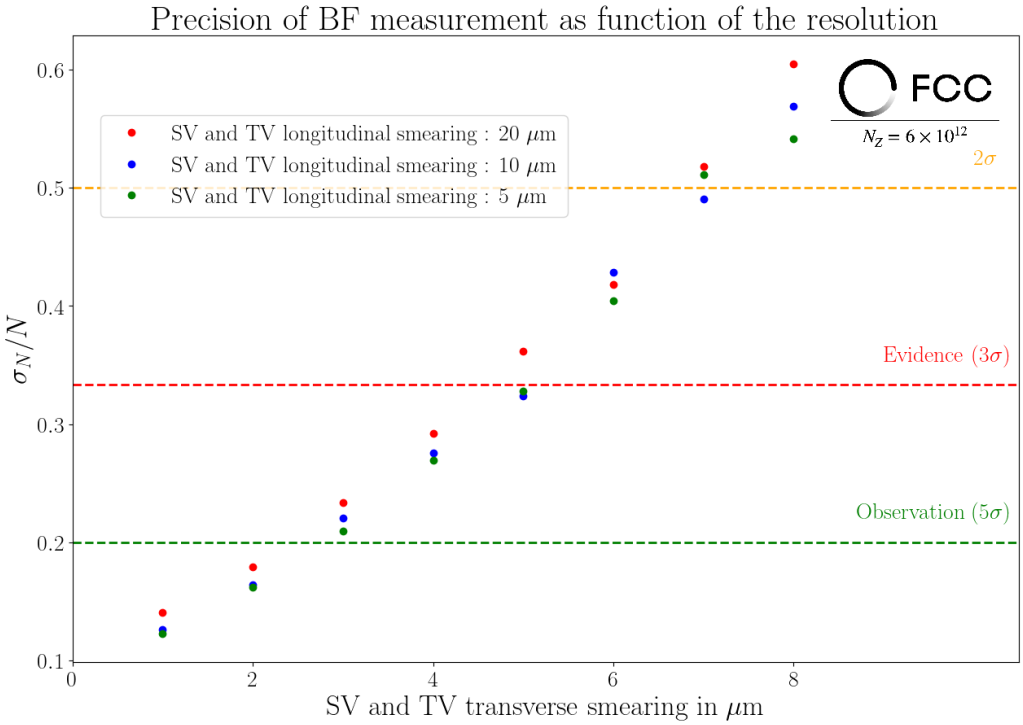

Figure 5.15: Precision of the measurement as function of the transverse vertexing resolution with all longitudinal resolutions. The possible hierarchy issues comes from the interplay between the smearing of the vertexing and the fit model.

5.5 Comparison to state-of-the-art vertex detector

5.5.1 Actual IDEA vertexing performance on $B^0 \to K^{*0}\tau^+\tau^-$

In order to add a state-of-the-art vertex detector working point to the analysis, the FCCAnalyses software VertexFitterSimple tools (allowing to perform vertexing with the IDEA simulated vertex detector) is used. For that purpose another FCCAnalysis analyzer is created to run on the whole available signal statistics and evaluate the primary, secondary, and tertiary vertices reconstruction performances. Given the signal samples generated for the analysis, the analyzer determines the reconstructed vertex position in Cartesian coordinates with respect to the Beam Spot Constraints set to the default FCC$-ee$ Z pole values of $(4.5, 20e^{-3}, 300)$ µm and concurrently saves the MC-Truth vertices information for the upcoming resolution determination.

The primary vertex positions are fitted in the classic way of the vertexing tools implementation; the vertex is first fitted with all the tracks, only the tracks compatible with it are kept and then the vertex is refitted from them. Concerning the secondary and tertiary vertices positions, the algorithm was not adapted to this analysis due to the large soft tracks multiplicity of the signal and was not able to fit their vertices from the secondary tracks alone. To be able to fit the position of the secondary and tertiary vertices in the right way, the tracks have been MC-seeded in the analyzer; this procedure prevents to determine the actual IDEA vertexing efficiency. A conservative vertexing efficiency of $\epsilon_{vertexing} = 0.8$ is therefore used similarly to what was used in the signal selection design. The analyzer outputs are used to construct the distributions of the displacement of the reconstructed vertices with respect to the MC-Truth vertices positions. Concerning the primary vertices, the displacements are built and projected onto the detector Cartesian basis. For the secondary and tertiary vertices, it is more challenging, the displacements are projected onto the particle decaying direction (longitudinal component) and on two orthogonal directions picked up randomly in the transverse plan of the decay (plan orthogonal to the particle decaying direction and that contain the MC-Truth vertex position) by parameterising a unit circle in the transverse plane of each vertex.

Namely, the first step is to use the Cartesian equation of the plane containing the true vertex position and orthogonal to the decaying particle direction. A random vector that belongs to this plane originating at a random (x, y) point can be defined:

$$z = -\frac{a(x - x_0) + b(y - y_0)}{c} + z_0, \tag{5.5.1}$$

where (x_0, y_0, z_0) are the coordinates of the true vertex, $\hat{p} = (a, b, c)$ is the unitary vector corresponding to the decaying particle direction. (x, y) denotes a randomly taken point on a circle in the 2D cartesian xOy basis of the detector and z is determined in order to satisfy that (x, y, z) belongs to the transverse plan. The unitary vector $\vec{Y}$ corresponding to the direction between the true vertex and the (x, y, z) point is then formed. A third unitary vector orthogonal to $\vec{Y}$ and $\vec{Z}$ is subsequently built following $\vec{X} = \vec{Y} \times \vec{Z}$. At this step, $\vec{X}$ and $\vec{Y}$ form an orthonormal basis in the transverse plan of the decay. The last transformation features the parameterisation of a unit circle (with a single parameter θ) in the transverse plane in order to determine an unbiased random vector following equation 5.5.2:

$$\vec{Y'} = \cos\theta\vec{X} + \sin\theta\vec{Y}, \tag{5.5.2}$$

where $\vec{X}$ and $\vec{Y}$ are used as characteristic (unitary and orthogonal) vectors of the transverse plane. $\vec{Y'}$ is therefore the vector between a random point on the circle and the true vertex position. $\vec{X'}$ is then determined from the vectorial product $\vec{X'} = \vec{Y'} \times \vec{Z}$. The basis described by $\vec{X'}$ and $\vec{Y'}$ is now really random and ready for use.

The two transverse directions picked up randomly are by construction equivalent, as can be seen in Figure 5.16 and are combined to determine a signed transverse displacement of the vertices in a single distribution for each vertex. In the following IDEA vertex resolutions are determined on each type of vertex (primary, secondary, and tertiary).

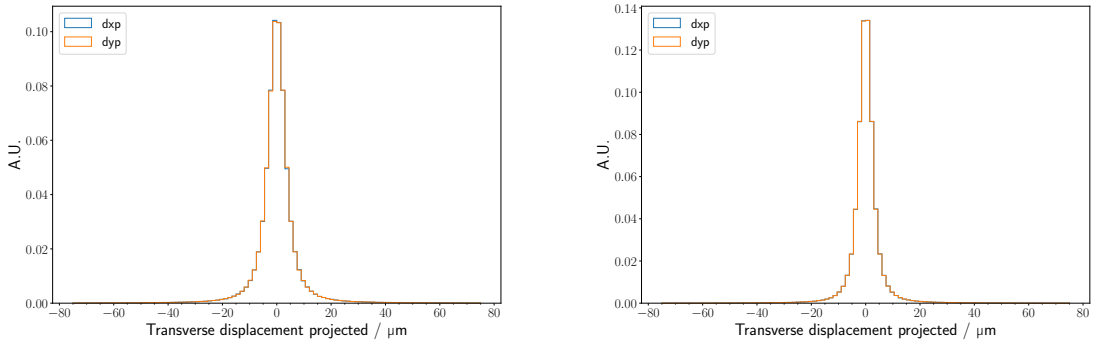

Figure 5.16: Superposition of the displacements along each randomly pick-up transverse direction denoted as *dxp* (along $\vec{X'}$) and *dyp* (along $\vec{Y'}$), for the secondary vertex (left) and tertiary vertex(right).

Resolutions are estimated by fitting the vertices displacement distributions with the zfit tool [213]. The primary vertex resolutions are fitted with double-Gaussian models on the x and z directions and with a simple Gaussian model for the y axis. Regarding Figure 5.17, the combined sigma of the fit provides an estimate of the IDEA primary vertex resolution of $(4.1, 24e^{-3}, 2.9)$µm (the assumptions on the primary vertex fast emulation, in Section 5.2.2, are set close to this measurement). The primary vertex y resolution is dominated by the beam spot constraints. Concerning the secondary and tertiary vertices, the resolutions are fitted with triple-Gaussian models. Figure 5.18 displays the resolutions fitted in the longitudinal direction and Figure 5.19 displays the ones fitted in the transverse direction. There the poor part of the fit taken by the larger Gaussian prevents us from a quick comparison with the fast vertexing emulation shown before, but the core gaussian resolutions seem commensurate with the initial working point assumptions in the emulation study. It is interesting to notice that the vertexing performances on the tertiary vertices are better than the one on the secondary vertices due to the additional track used at the tertiary vertices (3 vs. 2) despite the lower momentum on average of these tracks.

In addition of the actual IDEA vertexing working point, a tool that allows to tune the IDEA vertexing performances themselves is available in the FCCAnalyses software. This can be useful in order to determine which experimental parameters have to be improved in priority for this analysis. The next section will present the use of this tool to build various IDEA vertexing working points.

5.5.2 Vertexing improvement by tuning the tracks performance

To understand how to improve, if possible, the vertex detector design, a first approach can consist in arbitrarily improve the track parameters determinations. A specific FCC-*ee* software has been used to centrally produce four new samples with improved track performance: twice better resolution on the curvature of the track Ω, impact parameters $(z_0; d_0)$ resolutions improved by 17%, 33%, and 50%.

The resolutions from the various IDEA working points are fitted similarly to what has been done for the IDEA baseline working point, all these fits are available in Appendix D.3.

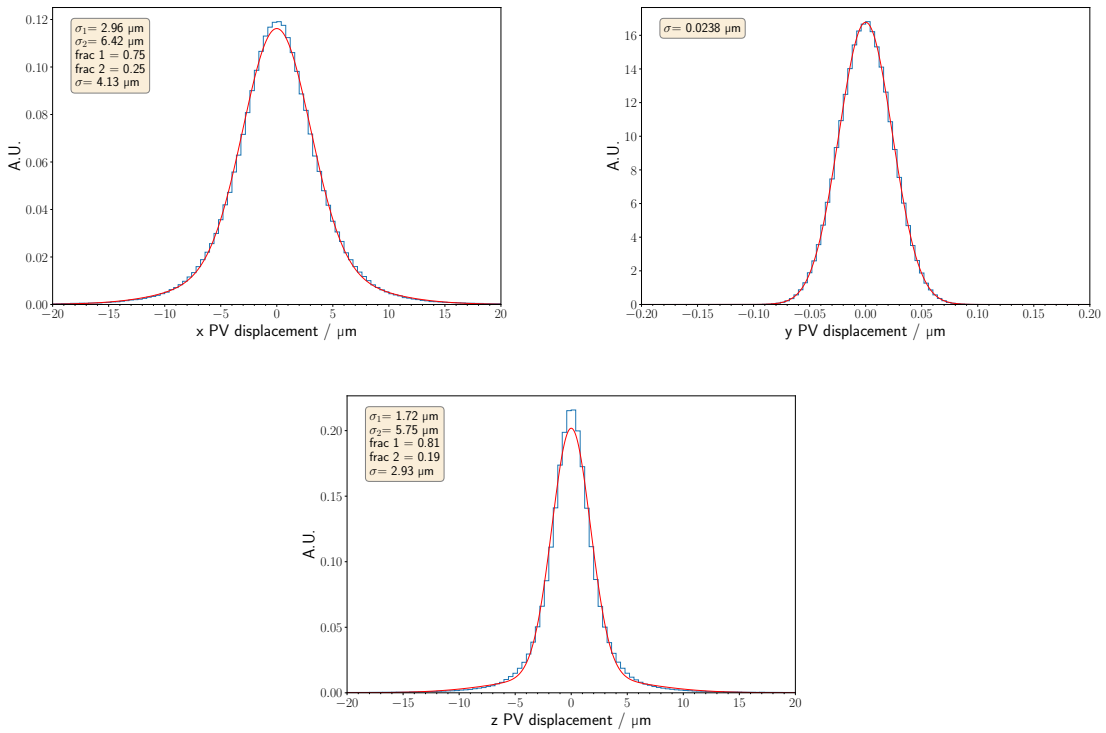

Figure 5.17: Fit of the IDEA primary vertexing resolutions on cartesian coordinates x (upper left), y(upper right) and z (bottom).

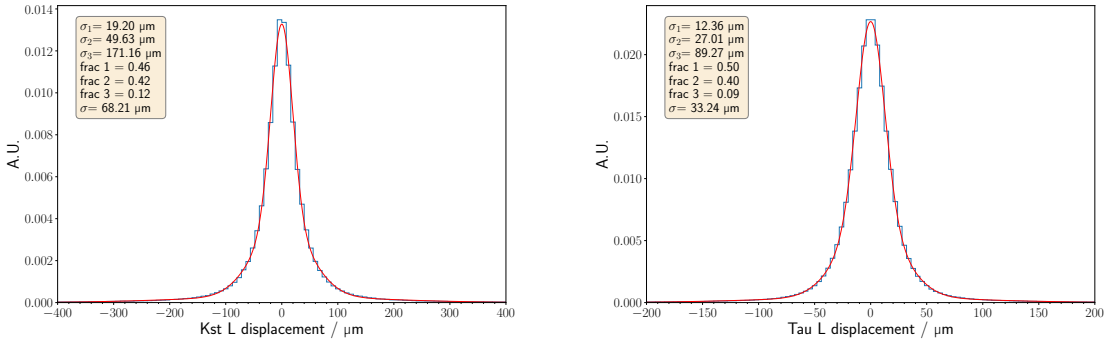

Figure 5.18: Fit of the IDEA secondary (left) and tertiary (right) longitudinal resolutions.

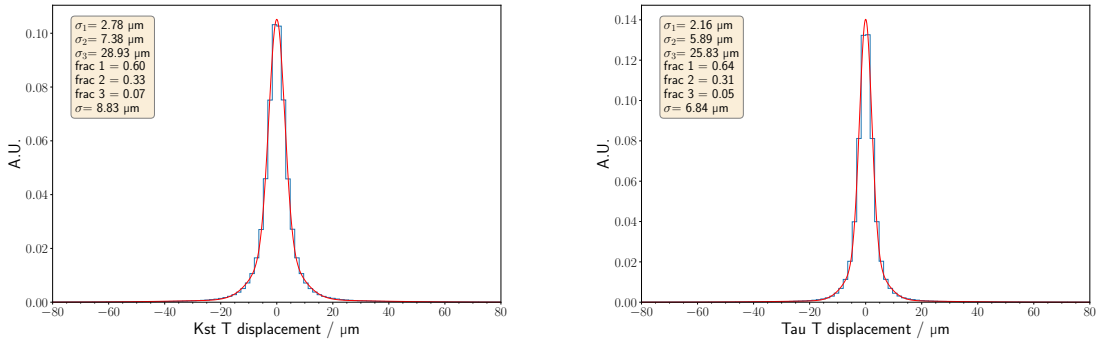

Figure 5.19: Fit of the IDEA secondary (left) and tertiary (right) transverse resolutions.

5.5.3 IDEA emulation

Each IDEA working point is emulated in the analysis following the aforementioned resolutions. Due to the fact that the primary vertex resolution is not the main driver of the performances, the primary vertex position for the IDEA working point is smeared in the analysis by a 3D Gaussian smearing that follows the combined σ given by the fits. Concerning the secondary and tertiary vertices, which are the lever arm of the analysis (the most demanding part in terms of vertexing), the smearing of the longitudinal-transverse direction of these vertices are applied following their fitted P.D.F.s. The model and their parameters used to smear the vertices for the IDEA working points are given in Table 5.11.

Vertex smeared / model	Parameter	IDEA baseline	IDEA $2 \times \Omega$	IDEA $1.2 \times$ IP	IDEA $1.5 \times$ IP	IDEA $2 \times$ IP
PV x / Gauss$(x, 0, \sigma)$	σ(µm)	4.13	4.04	3.67	3.26	2.56
PV y / Gauss$(x, 0, \sigma)$	σ(µm)	2.38e^{-2}	2.38e^{-2}	2.38e^{-2}	2.38e^{-2}	2.38e^{-2}
PV z / Gauss$(x, 0, \sigma)$	σ(µm)	2.93	2.59	2.40	2.09	1.32
SV L / 3-Gauss$(x, 0, \sigma_1, \sigma_2, \sigma_3, f_1, f_2, f_3)$	σ_1(µm)	19.20	18.67	13.57	11.48	8.60
	σ_2(µm)	49.63	47.57	31.86	27.79	20.70
	σ_3(µm)	171.16	163.67	93.19	87.75	66.09
	f_1	0.46	0.46	0.36	0.41	0.43
	f_2	0.42	0.43	0.48	0.45	0.44
	f_3	0.12	0.11	0.16	0.14	0.13
SV T / 3-Gauss$(x, 0, \sigma_1, \sigma_2, \sigma_3, f_1, f_2, f_3)$	σ_1(µm)	2.78	2.69	2.05	1.66	1.14
	σ_2(µm)	7.38	7.21	5.04	4.31	2.75
	σ_3(µm)	28.93	27.82	16.27	15.20	8.55
	f_1	0.60	0.60	0.54	0.58	0.53
	f_2	0.33	0.34	0.37	0.35	0.37
	f_3	0.07	0.06	0.09	0.07	0.10
TV L / 3-Gauss$(x, 0, \sigma_1, \sigma_2, \sigma_3, f_1, f_2, f_3)$	σ_1(µm)	12.36	12.02	9.70	7.45	5.78
	σ_2(µm)	27.01	25.97	20.66	15.46	12.44
	σ_3(µm)	89.27	87.59	67.58	47.49	43.52
	f_1	0.50	0.49	0.48	0.45	0.52
	f_2	0.40	0.42	0.43	0.45	0.40
	f_3	0.09	0.09	0.09	0.10	0.08
TV T / 3-Gauss$(x, 0, \sigma_1, \sigma_2, \sigma_3, f_1, f_2, f_3)$	σ_1(µm)	2.16	2.08	1.62	1.29	0.91
	σ_2(µm)	5.89	5.72	4.17	3.48	2.30
	σ_3(µm)	25.83	25.22	15.29	14.02	8.05
	f_1	0.64	0.64	0.60	0.63	0.62
	f_2	0.31	0.31	0.34	0.31	0.31
	f_3	0.05	0.05	0.06	0.05	0.07

Table 5.11: Summary of the fitted model used to emulate the IDEA working points resolutions in the analysis. Gauss denotes a Gaussian P.D.F. and 3-Gauss denotes a 3 Gaussian P.D.F.s defined as the linear combination of three Gaussian P.D.F.s.,Resolution fits are always centered on 0.

In concrete order to perform the ellipsoidal smearing of the secondary and tertiary vertices, an accept/reject algorithm enhanced in 2D is used to smear each vertex following its associated resolution. As an illustration, a 2D smearing generation is shown in Figure 5.20 for both secondary and tertiary vertices for the IDEA baseline working point. The IDEA working points are used in the analysis in the same way as the fast emulation points: the reconstruction is performed for it; then the same selection is applied; the precision of the branching fraction measurement is accessed. The precision fits of the IDEA baseline working points are shown in Figure 5.21; the ones corresponding to the other configurations are given in Appendix D.4.

5.5.4 IDEA results and vertexing requirements

The detailed results of the IDEA working points are available in Table 5.12. The precision in the measurement of the branching fraction is shown in Figure 5.22 (only the longitudinal configuration 20 µm for readability), where the IDEA working points are displayed on the same plot as the fastly emulated ones. The comparison between the IDEA working points and the emulated ones is not totally fair: the IDEA points are indeed placed at the interpolated position

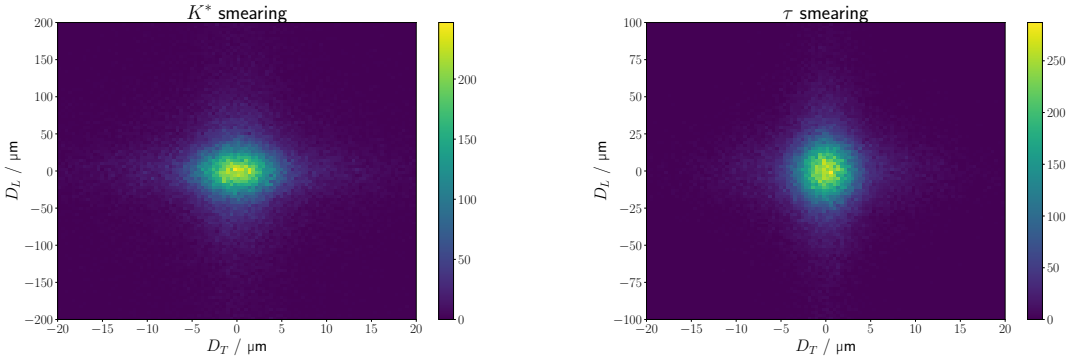

Figure 5.20: Generation of 100000 smearing for the IDEA vertexing working point on secondary (left) and tertiary (right) vertices, D_T denotes the transverse smearing and D_L the longitudinal one.

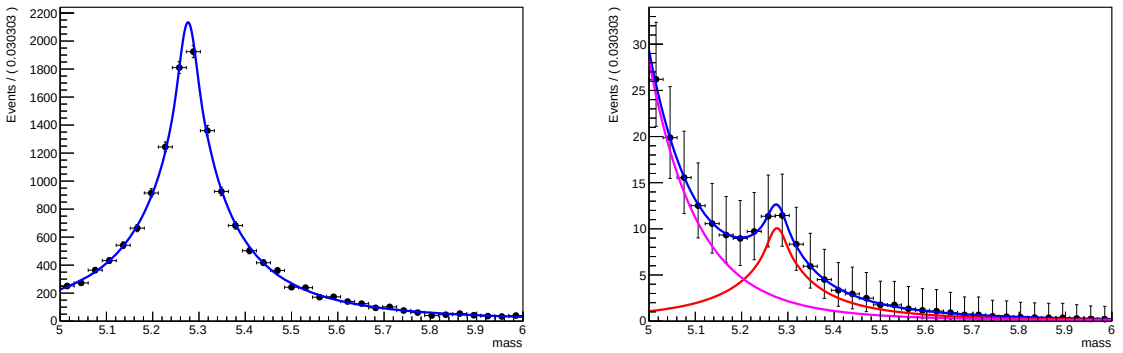

Figure 5.21: Fit of the signal (left) and of signal + background (right) in order to determine the precision on the BF measurement for the IDEA baseline working point.

with respect to the 20 µm longitudinal configuration for a better readability. Both plots confirm that the Ω improvement has a modest impact on precision, while the improvement in IP leads to a far better precision, up to factor 2!

With respect to Figure 5.22, only a hint of $B^0 \to K^{*0}\tau^+\tau^-$ at SM value can be obtained with the baseline state-of-the-art vertex detector. However, improvement of the IP resolutions seems to be the better detector-dependent way to reach at least the evidence of this mode. The twice better IP resolution working point can reach the observation level. The improvements presented in this section are directly applied to the tracks and do not correspond to regular detector improvements, that will be explored in the next section.

It is worth noting that an increase of luminosity by a factor 5 brings this analysis at SM value at the level of observation with a state-of-the-art detector (see Figure 5.23).

IDEA smearing configuration	IDEA baseline	IDEA 2 × Ω	IDEA 1.2 × IP	IDEA 1.5 × IP	IDEA 2 × IP
N_{signal}	66.08	66.76	77.49	85.23	100.06
$\sigma_{N_{signal}}$	23.32	22.98	21.52	19.25	17.44
Precision	0.35	0.34	0.28	0.23	0.17

Table 5.12: Precision on the branching fraction measurement for the various IDEA working points

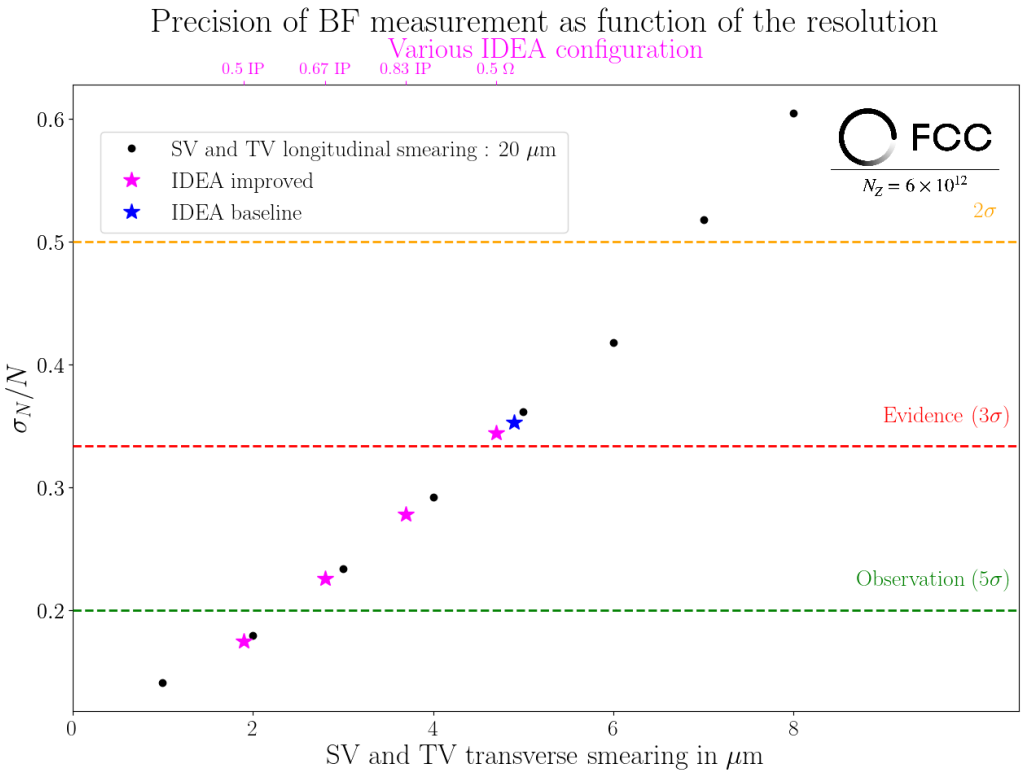

Figure 5.22: Precision of the measurement as function of the transverse vertexing resolution with a longitudinal resolution set at 20 µm for the fast vertexing working point and the addition of the IDEA working points.

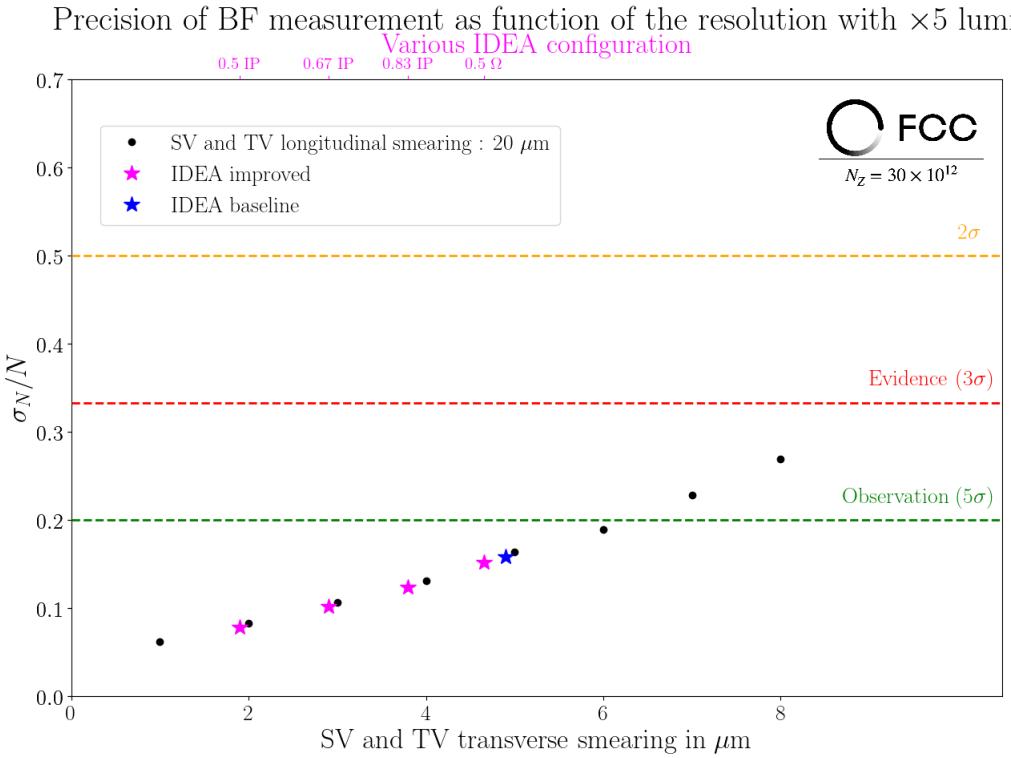

Figure 5.23: Precision of the measurement as function of the transverse vertexing resolution with a longitudinal resolution set at 20 µm for the fast vertexing working point and the additions of the IDEA working points, with in each case a five times higher luminosity.

5.5.5 Regular detector improvements

Motivated by the conclusion of Section 5.5.4, three signal samples with improved vertex detectors have been generated. The first sample features a 30% improvement of the vertex detector single hit resolution, by bringing it from 3 µm to 2 µm for the barrel layers. The second sample involves a 50% reduction of the material budget in the vertex detector layers. The third sample plays a 50% reduction of the material budget in the vertex detector layers and in the beam-pipe.

The generic transverse impact parameter resolution formula, involving the detector characteristics, reads as:

$$\sigma_{\mathrm{d}_0} \simeq \sqrt{\frac{r_2^2\sigma_1^2 + r_1^2\sigma_2^2}{(r_2 - r_1)^2}} \oplus \frac{r}{p_T \sin^{1/2}\theta} 13.6\,\mathrm{MeV}\sqrt{\frac{x}{X_0}}, \tag{5.5.3}$$

where the first term is linked to detector resolution and the second to multiple scattering (depending at first order on p_T^{-1}). The quantity $r_{1(2)}$ is the distance between the first (second) hit of the track and the PV; $\sigma_{1(2)}$ is the resolution on the first (second) hit of the track; r is the distance between the PV and the contact points of the track with the vertex detector layer; p_T is the transverse momentum of the track; θ is the polar angle of the track, x is the thickness and X_0 is the radiation length. Practically, improvements on single hit resolution are expected to decrease linearly the first term, while material budget reductions play linearly with the thickness and so with a square root dependence on the second term.

The first check performed consisted in understanding whether the detector improvements play as expected on the d_0 resolution. For that purpose, the distribution of the differences between the MC truth and the reconstructed d_0 has been determined for the signal tracks on all samples, in several p_T^{-1} bins. Then, resolutions are given in each bin by the sigma fitted with a double crystal ball model (the power law threshold parameter is fixed in all the bins to the one fitted in the higher p_T bin corresponding to the better defined tracks). Finally, the sigma fitted and the associated errors are used to fit the d_0 resolution as a function of p_T^{-1} with a linear function. Figure 5.24 shows that, compared to IDEA, the detector with improved single hit resolution enhanced the offset of the fit linearly, as expected; and detectors with reduced material budget display the expected square root enhancement of the slope only if the beam pipe and the vertex detector layers are both concerned.

This behaviour is expected since the slope is dominated by multiple Coulombian scatterings and is already limited by the beam pipe material. On the other hand, the direct track improvements applied to IDEA simulation are far too optimistic. Actually, they can only be recovered if one reduces the beam pipe material, which dominates the multiple Coulombian scatterings contributions. Any significant further improvement goes therefore via a reduction of the beam pipe material.

In order to look for the impact of regular detector improvements in the analysis, the precision of the branching fraction measurement has been evaluated for three new working points corresponding to their vertexing performance emulations, following all the previously defined methods. Appendix D.5 shows the intermediate plots. Figure 5.25 and Table 5.13 show the precision results. Finally, the regular detector improvements simulated allow one to reach the 3σ threshold but still fail to reach the observation at SM value of the branching fraction. The material budget reduction is as expected the way to reduce the Coulombian scatterings and to improve the measurement status, but the configurations presented here are already very optimistic. In order to make this measurement at SM value level, new vertex detector designs will have to be invented.

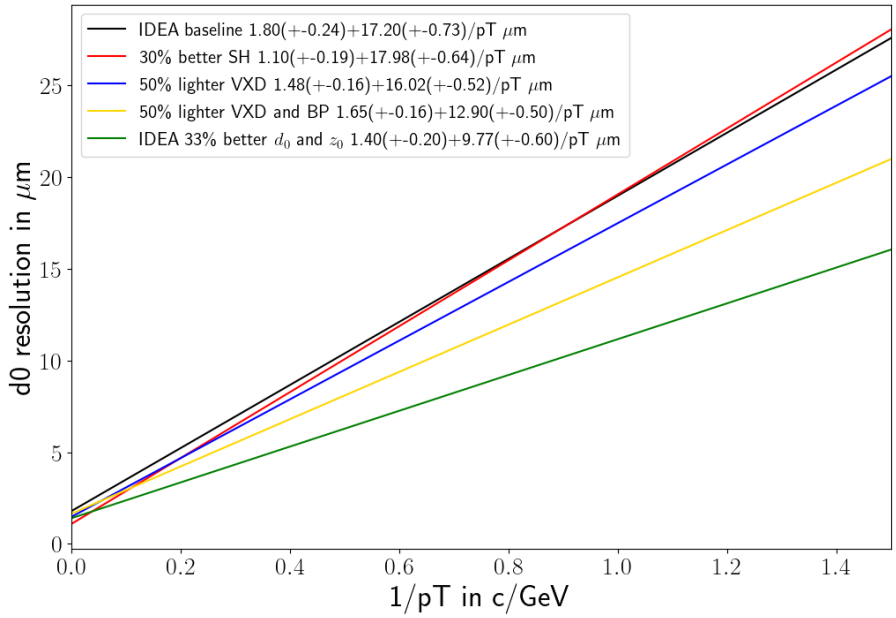

Figure 5.24: d_0 resolution fits corresponding to IDEA baseline, a detector with a 30% better single hit resolution, a detector with 50% lighter VerteX Detector (VXD) layers, a detector with 50% lighter VXD layers and Beam Pipe (BP), and IDEA with 33% better IP.

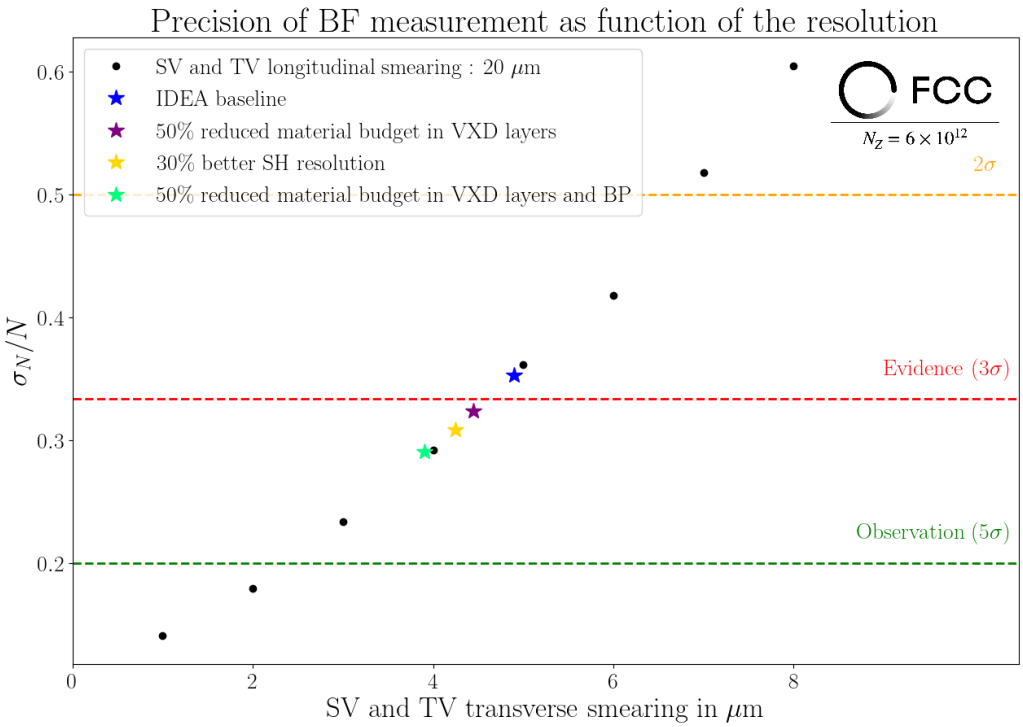

Figure 5.25: Precision of the measurement as function of the transverse vertexing resolution with a longitudinal resolution set at 20 µm for the fast vertexing working points in addition of the IDEA baseline and regular improved detector working points.

Configuration	IDEA baseline	50% lighter VXD layers	30% better SH resolution	50% lighter VXD layers and BP
N_{signal}	66.08	68.47	70.70	74.03
$\sigma_{N_{signal}}$	23.32	22.14	21.83	21.52
Precision	0.35	0.32	0.31	0.29

Table 5.13: Table of the precision on the branching fraction measurement for the IDEA baseline and regular improved detector working points

5.6 Conclusion of the analysis

The scientific context of the study and measurements of the decay mode $B^0 \to K^{*0}\tau^+\tau^-$ is presented. It is used accordingly to provide vertex detector requirements. A method to reconstruct the two undetected neutrinos of $B^0 \to K^{*0}\tau^+\tau^-$ with $\tau \to \pi\pi\pi\nu$ is developed and validated through simulated signal samples. A complete analysis workflow is developed and tested on signal sample with in particular a dedicated emulation of vertexing performances to test several hypotheses. Regarding the small yield of signal expected and for the completeness of the analysis, the possible backgrounds are explored and the dominant ones are considered. Because of the importance of the backgrounds with respect to the signal, an ML based selection is built via the use of the most discriminative variables inside an XGBoost algorithm. After selection, the method to extract the BF($B^0 \to K^{*0}\tau^+\tau^-$) measurement precision as function of the vertex measurement resolution is presented and used on fastly emulated vertexing working points. Finally, thanks to recent improvements in the FCC-*ee* software, several state-of-the-art vertex detector performance working points (baseline + various ones) are added into the analysis.

The main goal of the study is to draw the requirements on vertex detector performances to observe $B^0 \to K^{*0}\tau^+\tau^-$ at FCC-*ee*. It is achieved first by using the emulated vertexing performance working points, which provides the information that the level arm to make the measurement is the vertexing performances on the secondary/tertiary vertices projected in the transverse plan of the decaying particle direction, and gives the target of a 2 µm transverse resolution to reach the observation (5σ threshold) or 4 µm to 5 µm to meet the evidence (at 3σ threshold) at the SM value. In a second step, the use of vertexing configurations based on state-of-the-art simulated vertex detectors show that the baseline detectors only manage to have a hint of the signal at the SM value, and the main area to improve the picture is to enhance the Impact Parameters measurement. In a third stage, vertexing configurations based on regular detector improvements show that the best way to improve the picture is to reduce the material budget in both the vertex detector layers and the beam-pipe. But it seems difficult with actual vertex detector design. Naturally, another way to improve the performance without any change on the detector could be to make an experiment with higher integrated luminosity; several improved instantaneous luminosity designs are being considered [206]. For that, one possibility is tested with a times five hypothesis, and in that case the observation becomes possible with the state-of-the-art performances.

Since this study, developments in the design of the vertex detector have been done [214]; concerning the main way to improve the measurement, these developments lead to a 20% material budget reduction of the beam pipe at best. These developments also bring improvement on the material budget in the vertex detector layers and an alternative design using curved silicon layers. All of these would allow IDEA to reach the 3σ precision threshold, but the performances corresponding to the most optimistic detector working points seem difficult to reach without breakthrough novel designs.

At the moment to conclude on this work, one has to keep in mind that the goal is not to provide the ultimate analysis to make the observation; there will certainly be, at the moment to manipulate real data, room for several improvements. For example, the selection done in this analysis is a first educated one, but it is certainly possible to find other interesting discriminative variables to train the MVA, and even at the MVA place one can imagine that to apply two MVA in place of one, each one trained against one type of background depending on the D_s decay ($\tau\nu$ or $3\pi n\pi^0$). In addition, despite the luminosity or detector improvements assumptions, another way to improve the probability to make this mode could be to consider other τ channels, for example, taking one leptonic τ decay could bring a factor seven for the signal statistic, and considering fully leptonic τ decays could bring a factor fourteen. But in both cases the reconstruction itself becomes more demanding due to the presence of one or two additional

missing neutrinos, and other methods will have to be developed. As a last word, all the work reported here is done under the SM hypothesis, if New Physics plays in $B^0 \to K^{*0}\tau^+\tau^-$ one can imagine its BF to be higher than expected, allowing the state-of-the-art detector to make the measurement and to discover a clear discrepancy with the SM. To draw a perspective on the previous sentence, Figure 5.26 shows that under a three times bigger $B^0 \to K^{*0}\tau^+\tau^-$ branching fraction hypothesis, which is not that far from the New Physics scenarios presented in Figure 1.15, the state-of-the-art vertex detector achieves the observation.

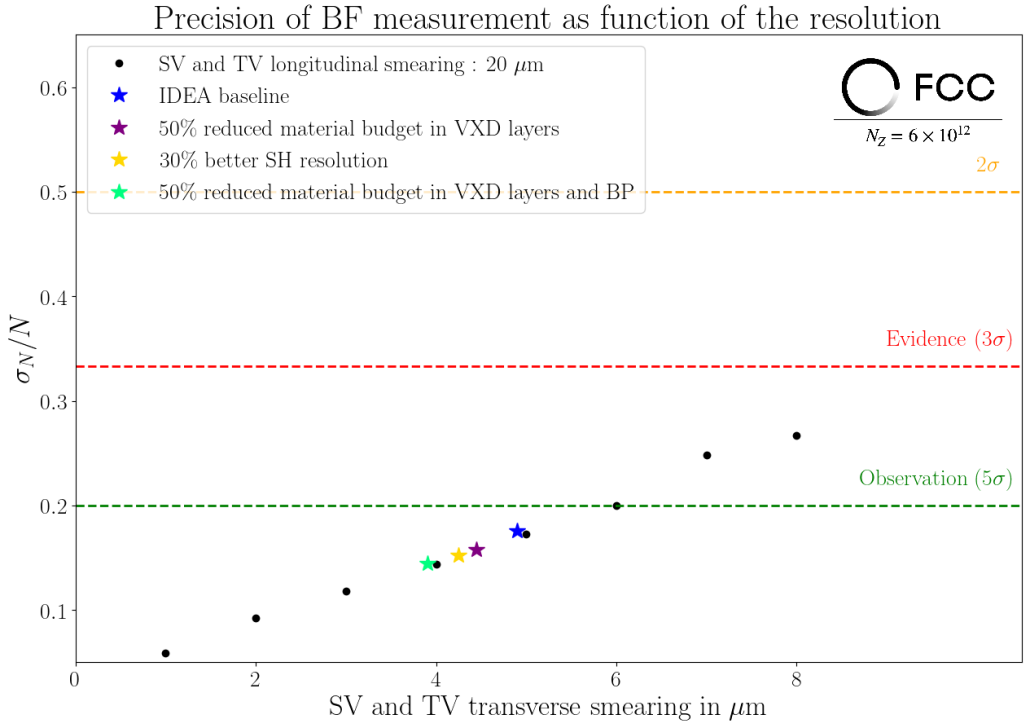

Figure 5.26: Precision of the measurement as function of the transverse vertexing resolution with a longitudinal resolution set at 20 µm for the fast vertexing working points in addition of the IDEA baseline and regular improved detector working points. A three times bigger $BF(B^0 \to K^{*0}\tau^+\tau^-)$ is assumed, with this hypothesis, IDEA baseline reaches the observation.

Conclusion

The goal of this thesis was to present two main studies. The first is the study of charmless three-body neutral B meson decays with K^0_S in the final state, namely $B^0_{d,s} \to K^0_S h^+ h'^-$ decays, using the LHCb spectrometer. The second is a prospective study of the capability of future experiments at FCC-*ee* to unravel $B^0 \to K^{*0}\tau^+\tau^-$.

The theoretical framework of these studies has been introduced with a particular emphasis on *CP* violation and phenomenology of hadronic B-meson decays to motivate the study of the $B^0_{d,s} \to K^0_S h^+ h'^-$ decays, and in addition, the phenomenology of the semileptonic B-mesons has been presented to introduce $B^0 \to K^{*0}\tau^+\tau^-$. The experimental framework has then been explained with a presentation of the LHC and of the LHCb spectrometer. The software tools used at LHCb have been presented with a concrete application for $B^0_{d,s} \to K^0_S h^+ h'^-$ studies. A technical work devoted to the construction of new L0Hadron trigger corrections for LHCb Run I simulations and to improve the ones available for Run II is presented. The experimental framework section is closed with the presentation of the FCC-*ee* project.

The main part of the $B^0_{d,s} \to K^0_S h^+ h'^-$ decay studies consists in the measurements of the corresponding branching fractions through LHCb. The work leading to these measurements has been presented: first, the development of a dedicated selection, featuring in particular two MVA discriminators to reduce the dominant backgrounds; second, the construction of a mass fit in order to determine the number of signal events in the Run I and Run II LHCb dataset; third, the determination of the reconstruction and selection efficiencies attached to all the modes which have to be taken into account at the moment to provide the final physics results, for that purpose an innovative efficiency averaging method has been made; four, a complete systematic study has been conducted to provide results with adequate uncertainties. In the end, all branching fractions relative to $B^0 \to K^0_S \pi^+\pi^-$ have been determined, allowing the improvement of the previously measured modes but also the discovery of $B^0_s \to K^0_S K^+ K^-$, even if the numbers presented in the manuscript will change in the final version of the analysis.

As an outlook to the branching fraction measurements, a preliminary study of the first Dalitz time-integrated analysis of $B^0_s \to K^0_S \pi^+\pi^-$ has been presented. A presentation of the Dalitz formalism has been done, together with the software tools used to do this analysis. The determination of inputs coming from the branching fraction analysis has been done and first preliminary plots have been shown, providing first hints of the possible results to come. In particular, from the asymmetry observed on the plots, the $K^{*+}(892)$ resonance appears as an interesting working point to study *CP* violation. This work is paving the way towards the Dalitz time-dependant analysis of $B^0 \to K^0_S \pi^+\pi^-$ to access $\sin(2\beta)$, an unitary triangle parameter, in order to test the SM.

Concerning the feasibility study of $B^0 \to K^{*0}\tau^+\tau^-$ at FCC-*ee*, the measurement requires to use the full kinematics of the decay, and a dedicated topological reconstruction method has been developed and presented. This method requires precise measurements of all decay vertices. To achieve this, a carefully chosen decay chain is employed, ensuring that all relevant vertices can be accurately measured. Additionally, this approach serves as a benchmark for evaluating the performance of vertex detectors, tested across various hypothetical configurations of the detector. Its implementation on FCC-*ee* simulated signal events has been explained. However,

to be as realistic as possible, a study of the possible background for the measurement has been done, and the dominant ones were simulated in addition to the signal. To fight against them, a selection has been built with the use of an MVA discriminator. The measured branching fractions were determined for each configuration of the vertexing performance. The observation of $B^0 \to K^{*0}\tau^+\tau^-$ with a state-of-the-art vertex detector under the SM hypothesis has been found to be unreachable. Although improvements in vertex detector technologies (especially on the impact parameter measurement) could help to make this mode at the SM value. Before concluding, one has to keep in mind that this feasibility analysis is a first step; for example, there is certainly room to improve the selection, it features no systematic study and another way to make this measurement should be to consider other $\tau^\pm$ decay channels, but this comes at the cost of developing other reconstruction methods. Despite the significant experimental challenges, the study of the quark transitions involving third generation fermions couplings is one of the promising avenues to unravel New Physics indirect effects.

Appendix A

Appendix to Chapter 1

A.1 A demonstration of the neutral meson time dependant decay rates formulae

The demonstration reported here is inspired by the one given in the Marouen Baalouch thesis [69].

A.1.1 The quantum mechanics of neutral B^0 meson mixing

Due to the mixing nature of the $B^0 - \bar{B}^0$ system, it is possible to describe them in another basis. For example the *CP* eigenstate basis could be used with:

$$|B_+\rangle = \frac{|B^0\rangle + |\bar{B}^0\rangle}{\sqrt{2}},$$
$$|B_-\rangle = \frac{|B^0\rangle - |\bar{B}^0\rangle}{\sqrt{2}},$$

this demonstration requires the mass eigenstate basis:

$$|B_L\rangle = p|B^0\rangle + q|\bar{B}^0\rangle,$$
$$|B_H\rangle = p|B^0\rangle - q|\bar{B}^0\rangle,$$

where L and H denotes the lighter and heavier mass eigenstates respectively, p and q are linear complex coefficients satisfying $|p|^2 + |q|^2 = 1$ which describe the $B^0 - \bar{B}^0$ mixing in B_L and B_H. The time-dependent Schrodinger equation for these states is as follows:

$$i\frac{\partial}{\partial t}\begin{pmatrix} p \\ q \end{pmatrix} = \mathcal{H}_{eff}\begin{pmatrix} p \\ q \end{pmatrix}, \tag{A.1.1}$$

where $\mathcal{H}_{eff}$, the effective Hamiltonian describing the neutral mesons mixing, reads:

$$\mathcal{H}_{eff} = \boldsymbol{M} - i\frac{\boldsymbol{\Gamma}}{2},$$

with the 2×2 Hermitian matrices describing the mass and decay rate component of $\mathcal{H}_{eff}$:

$$\boldsymbol{M} = \begin{pmatrix} M_{11} & M_{12} \\ M_{21} & M_{22} \end{pmatrix}, \boldsymbol{\Gamma} = \begin{pmatrix} \Gamma_{11} & \Gamma_{12} \\ \Gamma_{21} & \Gamma_{22} \end{pmatrix},$$

and due to hermicity: $M_{11} = M_{11}^*, M_{22} = M_{22}^*, M_{12} = M_{21}^*, \Gamma_{11} = \Gamma_{11}^*, \Gamma_{22} = \Gamma_{22}^*, \Gamma_{12} = \Gamma_{21}^*$. On the other hand, $\mathcal{H}_{eff}$ is not hermitian due to his definition.

It is possible to rewrite $\mathcal{H}_{eff}$ in the mass eigenstate $\{|B_L\rangle, |B_H\rangle\}$ basis where $\mathcal{H}_{eff}$ is diagonal with the two complex eigenvalues ω_L and ω_H:

$$\omega_{H(L)} = \sqrt{(M_{11} - i\frac{\Gamma_{11}}{2})(M_{22} - i\frac{\Gamma_{22}}{2})} \pm \sqrt{(M_{12} - i\frac{\Gamma_{12}}{2})(M_{12}^* - i\frac{\Gamma_{12}^*}{2})} \equiv m_{H(L)} - i\frac{\Gamma_{H(L)}}{2} \quad \text{(A.1.2)}$$

where m_L and m_H are the mass of the eigenstates $|B_L\rangle$ and $|B_H\rangle$ respectively, and Γ_L and Γ_H their respective decay rates.

The $B^0 - \bar{B^0}$ system is characterised by five physical observables (or mixing observables): the mass average m, the decay rate average Γ, the difference in mass Δm, the difference in decay rate $\Delta\Gamma$ and its composition fraction $|q/p|$. This four firsts observables read:

$$m = \frac{m_H + m_L}{2}, \Gamma = \frac{\Gamma_H + \Gamma_L}{2}, \Delta m = m_H - m_L, \Delta\Gamma = \Gamma_H - \Gamma_L.$$

With this definition Δm is always positive and the sign of $\Delta\Gamma$ depends on which mass eigenstate has the longest lifetime. The sign of $\Delta\Gamma$ is predicted to be negative by the SM, but it has not yet been established. For neutral B mixing systems $B^0, \bar{B^0}$ (denoted by d) and $B_s^0, \bar{B_s^0}$ (denoted by s) the global average measurements [47] give: $\Delta m_d = 0.5065 \pm 0.0019\text{ps}^{-1}$, $\Delta m_s = 17.765 \pm 0.006\text{ps}^{-1}$, $\Delta\Gamma_d/\Gamma_d = 0.001 \pm 0.010$, and $\Delta\Gamma_s = 0.084 \pm 0.005\text{ps}^{-1}$. Regarding the value measured for the ratio $\Delta\Gamma$ associated to B^0, $\Delta\Gamma$ can be neglected in this demonstration.

The last observable, found by solving the eigenvalue equation, are:

$$\left|\frac{q}{p}\right| = \sqrt{\frac{M_{12}^* - i\frac{\Gamma_{12}}{2}}{M_{12}^* - i\frac{\Gamma_{12}}{2}}}. \quad \text{(A.1.3)}$$

If CP is a symmetry of $\mathcal{H}_{eff}$, then Γ_{12} and M_{12} would be real, and leads to:

$$\left(\frac{q}{p}\right) = e^{2i\theta(B^0)} \Rightarrow \left|\frac{q}{p}\right| = 1,$$

where $\theta(B^0)$ is an arbitrary phase occurring in the action of CP operator to switch between the state of the $B^0 - \bar{B^0}$ mixing system:

$$CP|B^0\rangle = e^{2i\theta(B^0)}|\bar{B^0}\rangle, CP|\bar{B^0}\rangle = e^{-2i\theta(B^0)}|B^0\rangle.$$

A.1.2 Time evolution of B^0 meson

The initial flavor states $|B^0(t=0)\rangle \equiv |B^0\rangle$ and $|\bar{B^0}(t=0)\rangle \equiv |\bar{B^0}\rangle$ can be used to write the time evolution of $|B^0(t)\rangle$ and $|\bar{B^0}(t)\rangle$:

$$\begin{aligned} |B^0(t)\rangle &= g_+(t)|B^0\rangle + \frac{q}{p}g_-(t)|\bar{B^0}\rangle, \\ |\bar{B^0}(t)\rangle &= g_+(t)|\bar{B^0}\rangle + \frac{p}{q}g_-(t)|B^0\rangle, \end{aligned} \quad \text{(A.1.4)}$$

where :

$$g_\pm(t) = \frac{1}{2}\left(e^{-i\omega_L t} \pm e^{-i\omega_H t}\right) = \frac{1}{2}\left(e^{\left(-im_L - \frac{\Gamma_L}{2}\right)t} \pm e^{\left(-im_H - \frac{\Gamma_H}{2}\right)t}\right). \quad \text{(A.1.5)}$$

By injecting A.1.5 in A.1.4 the two states can be rewritten as:

$$\begin{aligned}|B^0(t)\rangle &= e^{-imt}e^{-\Gamma t/2}\left[\cos\left(\frac{\Delta mt}{2}\right)|B^0\rangle - i\frac{q}{p}\sin\left(\frac{\Delta mt}{2}\right)|\bar{B^0}\rangle\right],\\ |\bar{B^0}(t)\rangle &= e^{-imt}e^{-\Gamma t/2}\left[\cos\left(\frac{\Delta mt}{2}\right)|\bar{B^0}\rangle - i\frac{p}{q}\sin\left(\frac{\Delta mt}{2}\right)|B^0\rangle\right],\end{aligned} \tag{A.1.6}$$

were $\Delta\Gamma$ is neglected.
The decay rate of a $|B^0\rangle$ or $|\bar{B^0}\rangle$ meson produced at time $t = 0$ to a final state $|f\rangle$ or $|\bar{f}\rangle$ is given by:

$$\frac{\Gamma_{X\to y}(t)}{dt} = |\langle y|\mathcal{T}|X(t)\rangle|^2, \tag{A.1.7}$$

where X ($X(t)$) can be B^0 or $\bar{B^0}$ ($B^0(t)$ or $\bar{B^0}(t)$), y can be f or $\bar{f}$ and $\mathcal{T}$ is the transition matrix. By injecting A.1.6 in A.1.7 the four possible time dependant decay rates of the initially produced $|B^0\rangle$ and $|\bar{B^0}\rangle$, can be written:

$$\begin{aligned}\frac{\Gamma_{B^0\to f}(t)}{dt} &= \frac{e^{-\Gamma t}}{2}|A_f|^2(1+|\lambda_f|^2)[1+C_f\cos(\Delta mt) - S_f\sin(\Delta mt)],\\ \frac{\Gamma_{\bar{B^0}\to f}(t)}{dt} &= \frac{e^{-\Gamma t}}{2}\left|\frac{p}{q}\right|^2|A_f|^2(1+|\lambda_f|^2)[1-C_f\cos(\Delta mt) + S_f\sin(\Delta mt)],\\ \frac{\Gamma_{\bar{B^0}\to \bar{f}}(t)}{dt} &= \frac{e^{-\Gamma t}}{2}|\bar{A}_{\bar{f}}|^2(1+|\bar{\lambda}_{\bar{f}}|^2)[1+\bar{C}_{\bar{f}}\cos(\Delta mt) - \bar{S}_{\bar{f}}\sin(\Delta mt)],\\ \frac{\Gamma_{B^0\to \bar{f}}(t)}{dt} &= \frac{e^{-\Gamma t}}{2}\left|\frac{q}{p}\right|^2|\bar{A}_{\bar{f}}|^2(1+|\bar{\lambda}_{\bar{f}}|^2)[1-\bar{C}_{\bar{f}}\cos(\Delta mt) + \bar{S}_{\bar{f}}\sin(\Delta mt)],\end{aligned} \tag{A.1.8}$$

where $A_f = \langle f|\mathcal{T}|B^0\rangle$ and $\bar{A}_{\bar{f}} = \langle\bar{f}|\mathcal{T}|\bar{B^0}\rangle$ are the decay amplitudes for $|B^0\rangle$ and $|\bar{B^0}\rangle$ decaying to the final state f and $\bar{f}$ respectively, and λ_f and $\bar{\lambda}_{\bar{f}}$ are defined as:

$$\lambda_f = \frac{1}{\bar{\lambda}_f} = \frac{q\bar{A}_f}{pA_f},\ \bar{\lambda}_{\bar{f}} = \frac{1}{\lambda_{\bar{f}}} = \frac{pA_{\bar{f}}}{q\bar{A}_{\bar{f}}}, \tag{A.1.9}$$

with $\bar{A}_f = \langle f|\mathcal{T}|\bar{B^0}\rangle$ and $A_{\bar{f}} = \langle\bar{f}|\mathcal{T}|B^0\rangle$. The CP violation observables $C_f, S_f, \bar{C}_{\bar{f}}$ and $\bar{S}_{\bar{f}}$ introduced in A.1.8 can be defined as:

$$\begin{aligned}C_f &= \frac{1-|\lambda_f|^2}{1+|\lambda_f|^2},\ S_f = \frac{2\,\mathrm{Im}(\lambda_f)}{1+|\lambda_f|^2},\\ \bar{C}_{\bar{f}} &= \frac{1-|\bar{\lambda}_{\bar{f}}|^2}{1+|\bar{\lambda}_{\bar{f}}|^2},\ \bar{S}_{\bar{f}} = \frac{2\,\mathrm{Im}(\bar{\lambda}_{\bar{f}})}{1+|\bar{\lambda}_{\bar{f}}|^2}.\end{aligned} \tag{A.1.10}$$

To evaluate the CP violation parameters, a comparison between the decay rates $\Gamma_{B^0\to f}$ and $\Gamma_{CP(B^0\to f)}$ is made, here $CP(B^0\to f)$ is the transformation of the $B^0\to f$ process under the CP operator. With these notation the corresponding CP asymmetry reads as:

$$\mathcal{A}_{CP} = \frac{\Gamma_{CP(B^0\to f)} - \Gamma_{B^0\to f}}{\Gamma_{CP(B^0\to f)} + \Gamma_{B^0\to f}}. \tag{A.1.11}$$

Appendix B

Appendix to Chapter 2

B.1 Average occupancy maps

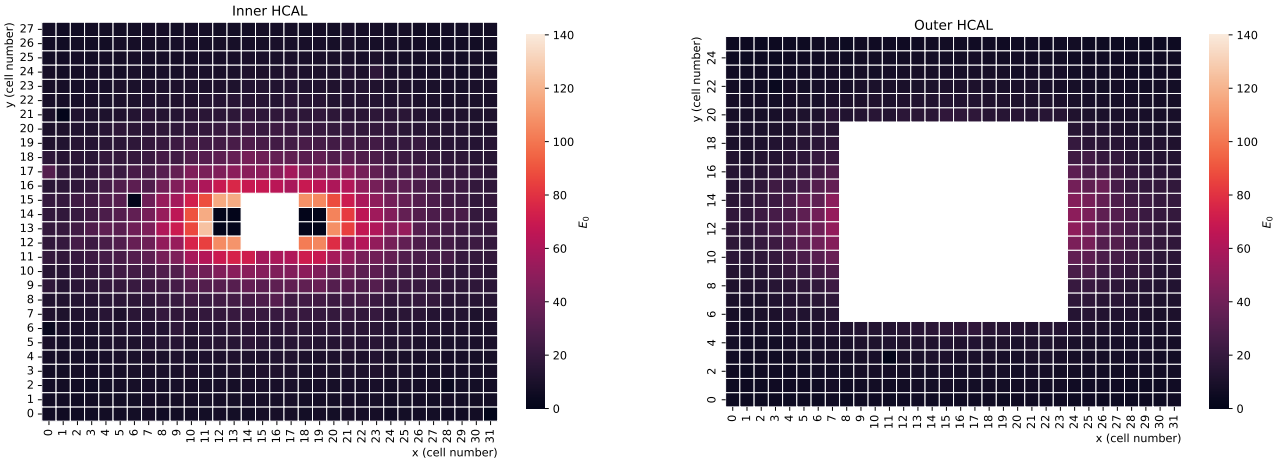

Figure B.1: Average occupancy maps for 2018 MD data with a reconstructed $D^* \to D^0\pi$ candidate.

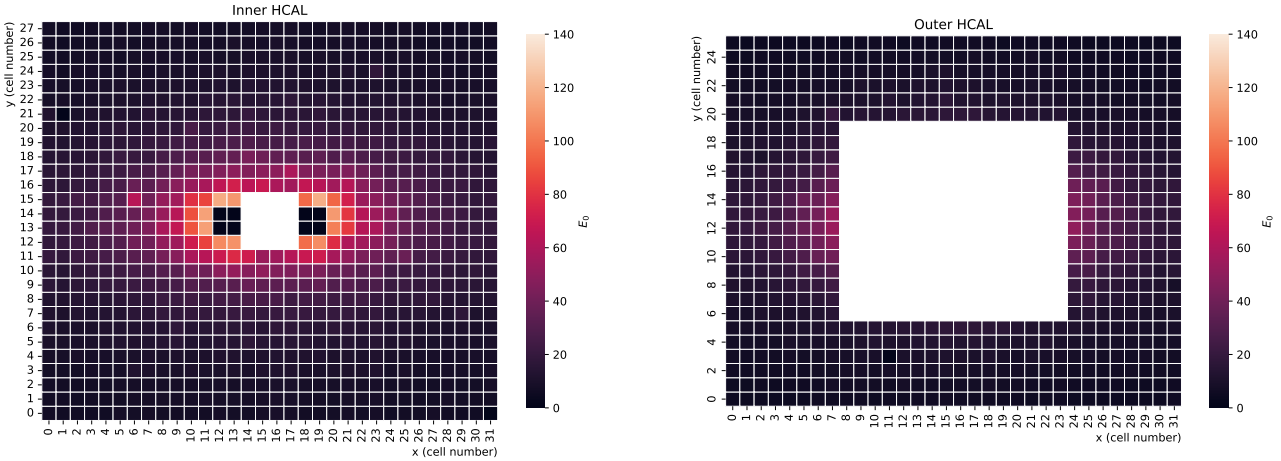

Figure B.2: Average occupancy maps for 2018 MU data with a reconstructed $D^* \to D^0\pi$ candidate.

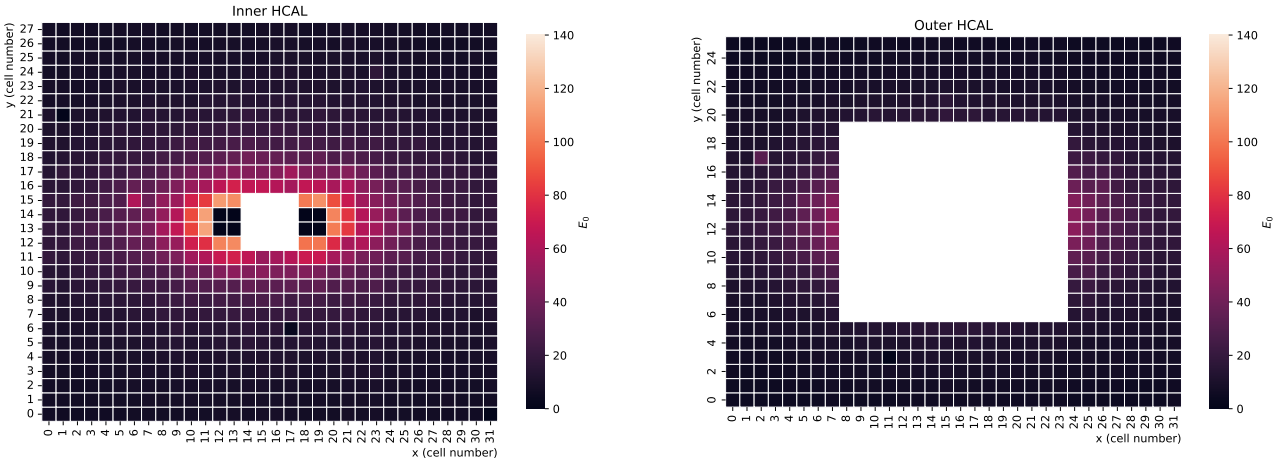

Figure B.3: Average occupancy maps for 2017 MD data with a reconstructed $D^* \to D^0\pi$ candidate.

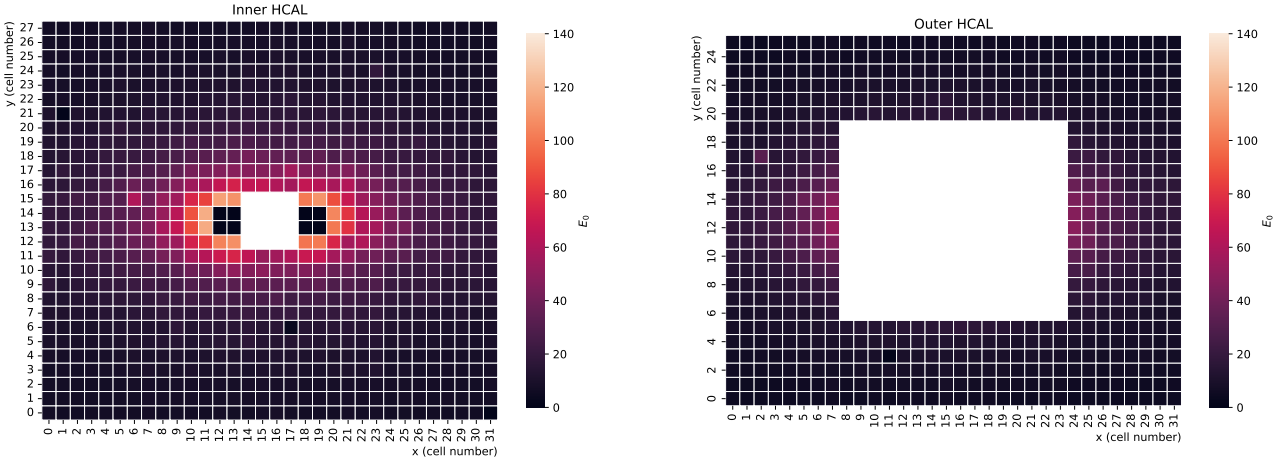

Figure B.4: Average occupancy maps for 2017 MU data with a reconstructed $D^* \to D^0\pi$ candidate.

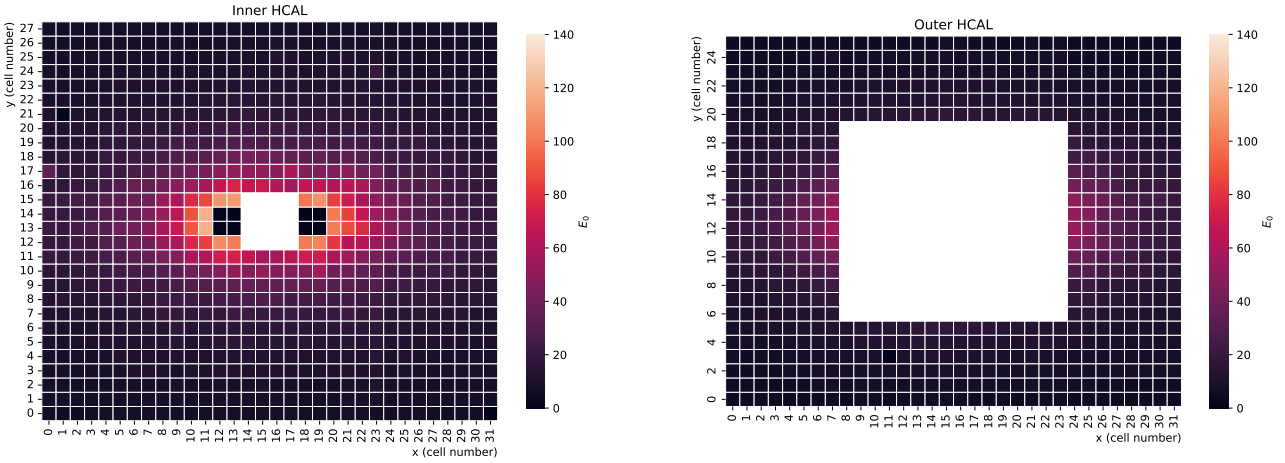

Figure B.5: Average occupancy maps for 2016 MD data with a reconstructed $D^* \to D^0\pi$ candidate.

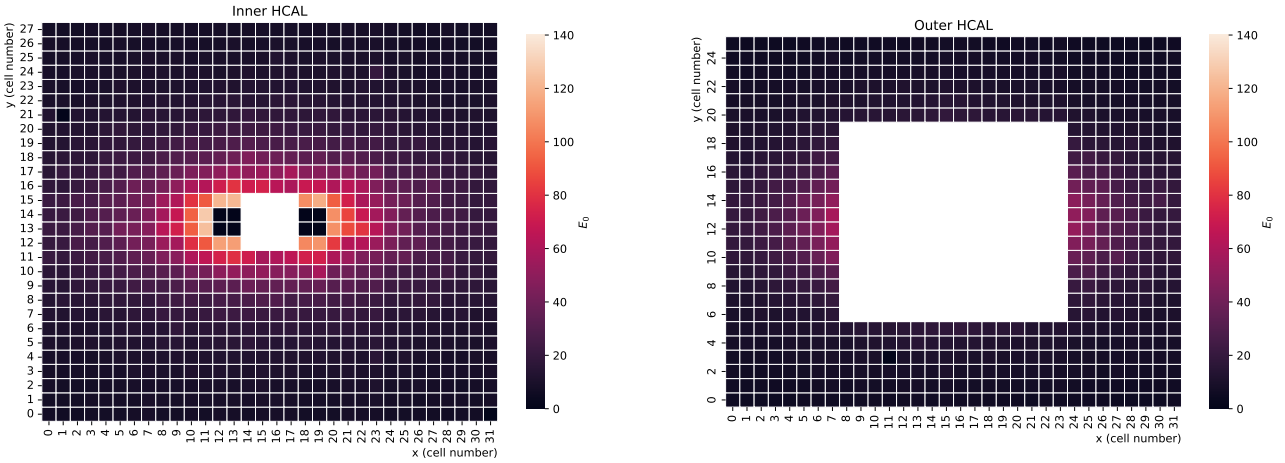

Figure B.6: Average occupancy maps for 2016 MU data with a reconstructed $D^* \to D^0\pi$ candidate.

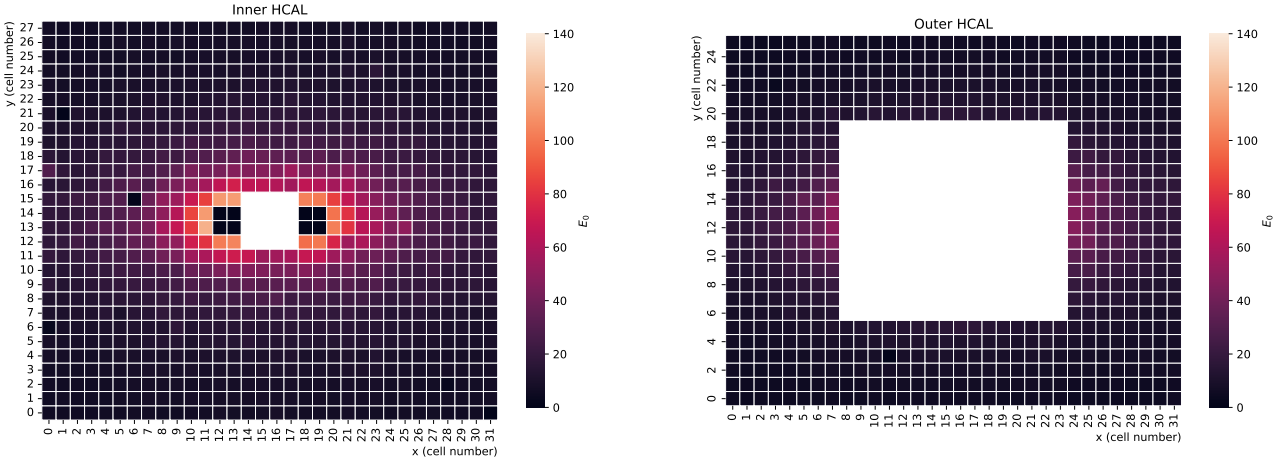

Figure B.7: Average occupancy maps build for 2012 MD.

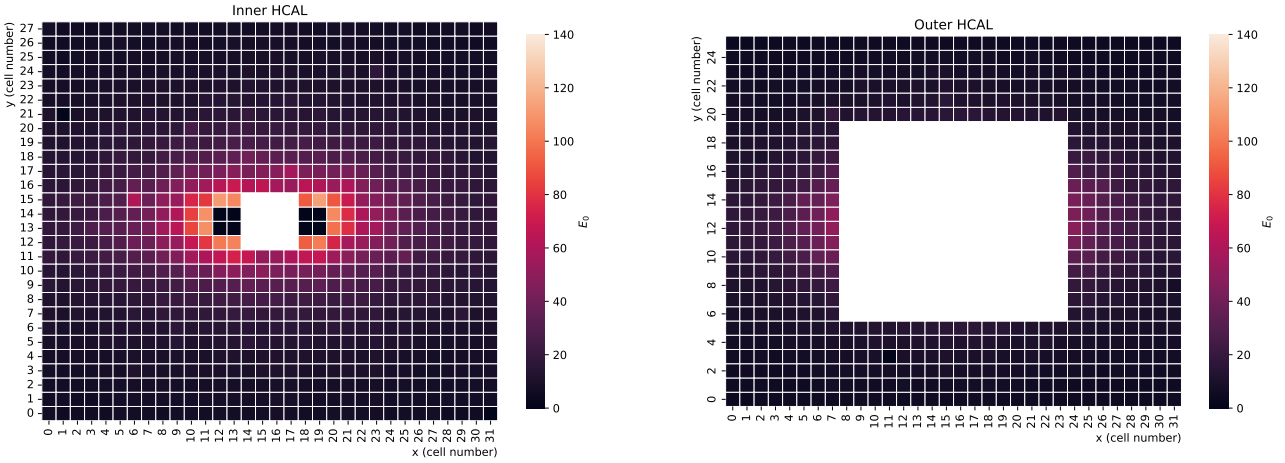

Figure B.8: Average occupancy maps build for 2012 MU.

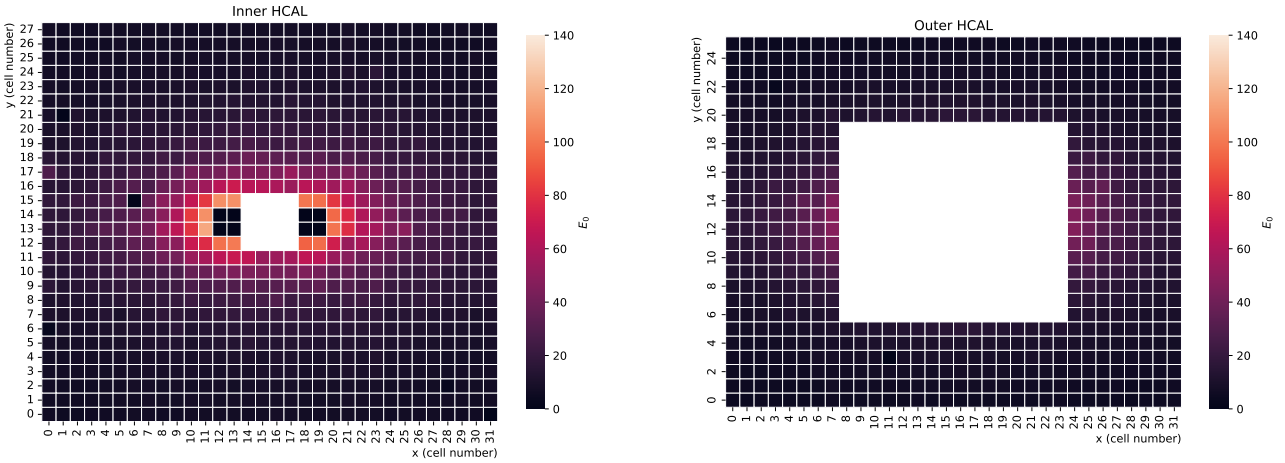

Figure B.9: Average occupancy maps build for 2011 MD.

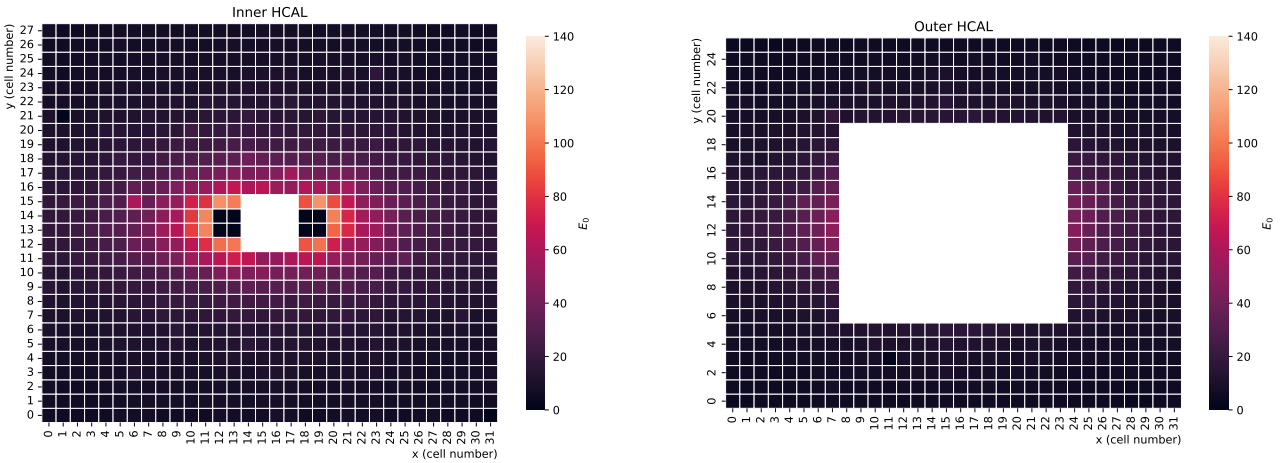

Figure B.10: Average occupancy maps build for 2011 MU.

B.2 π and K trigger efficiency tables

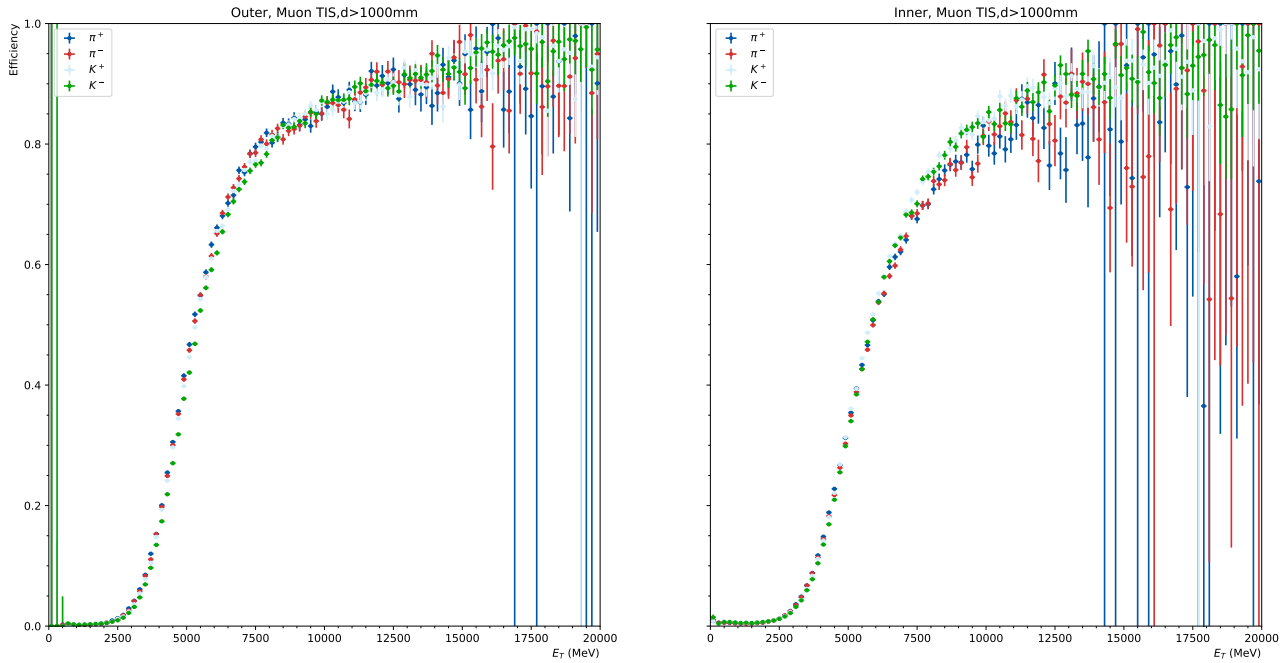

Figure B.11: Efficiency tables for π and K as obtained with the 2018 MD sample.

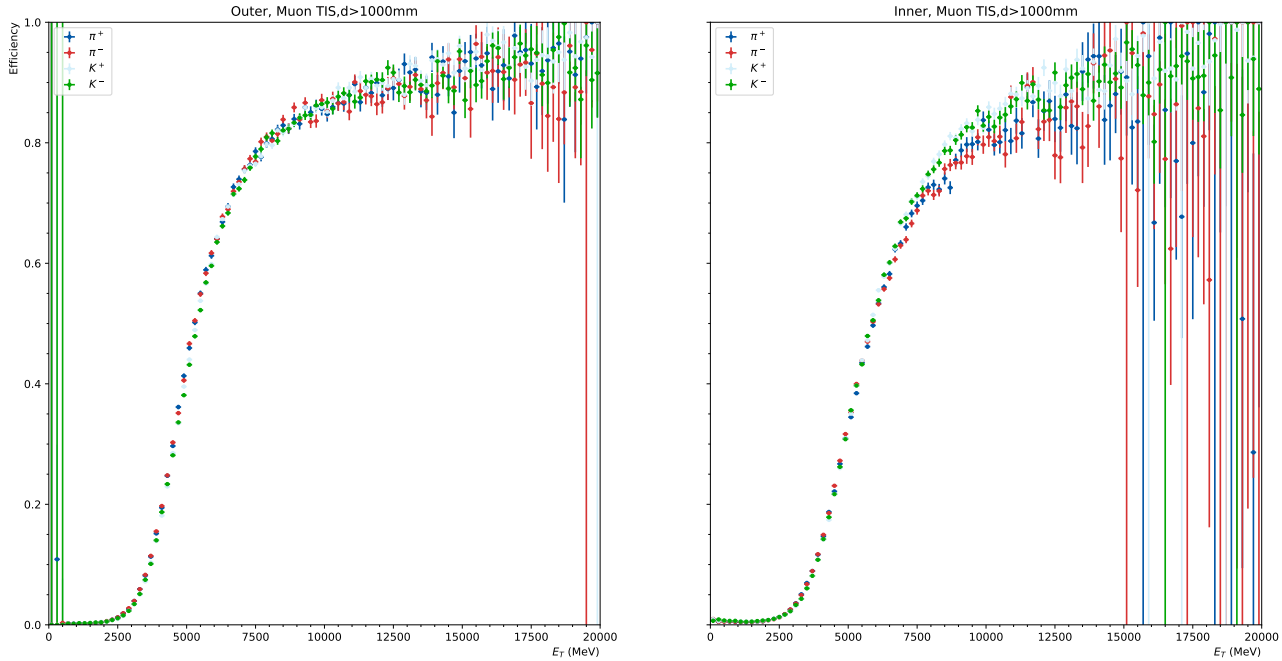

Figure B.12: Efficiency tables for π and K as obtained with the for 2018 MU sample.

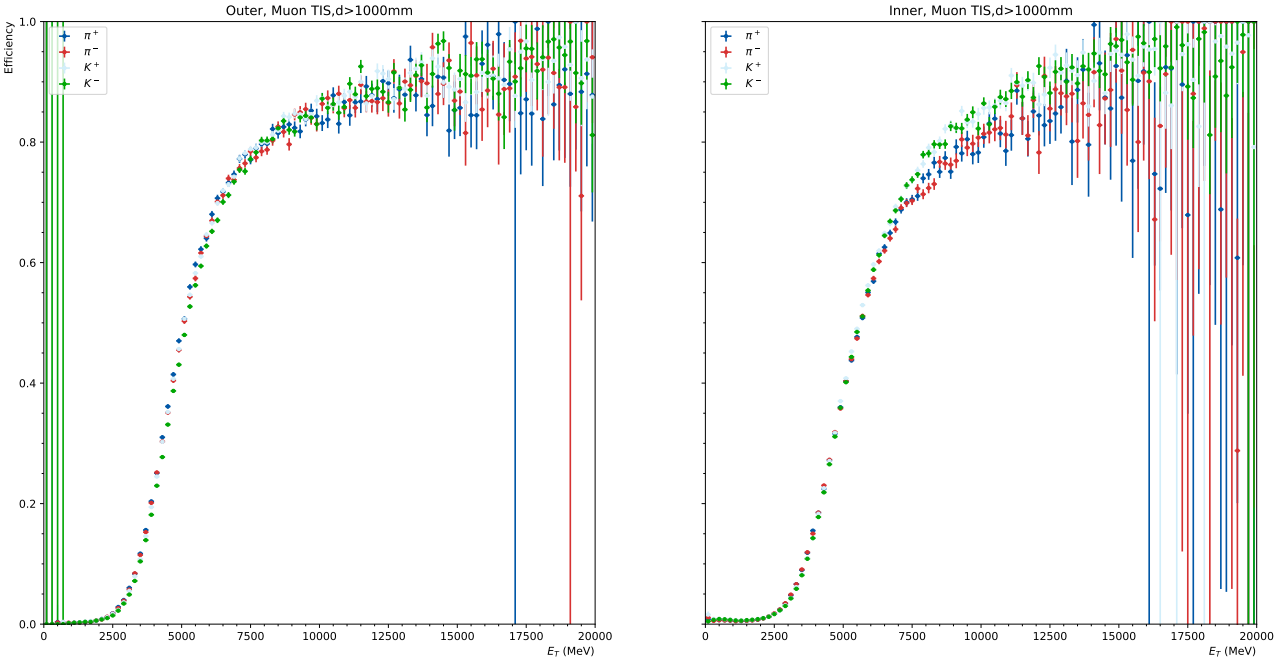

Figure B.13: Efficiency tables for π and K as obtained with the 2017 MD sample.

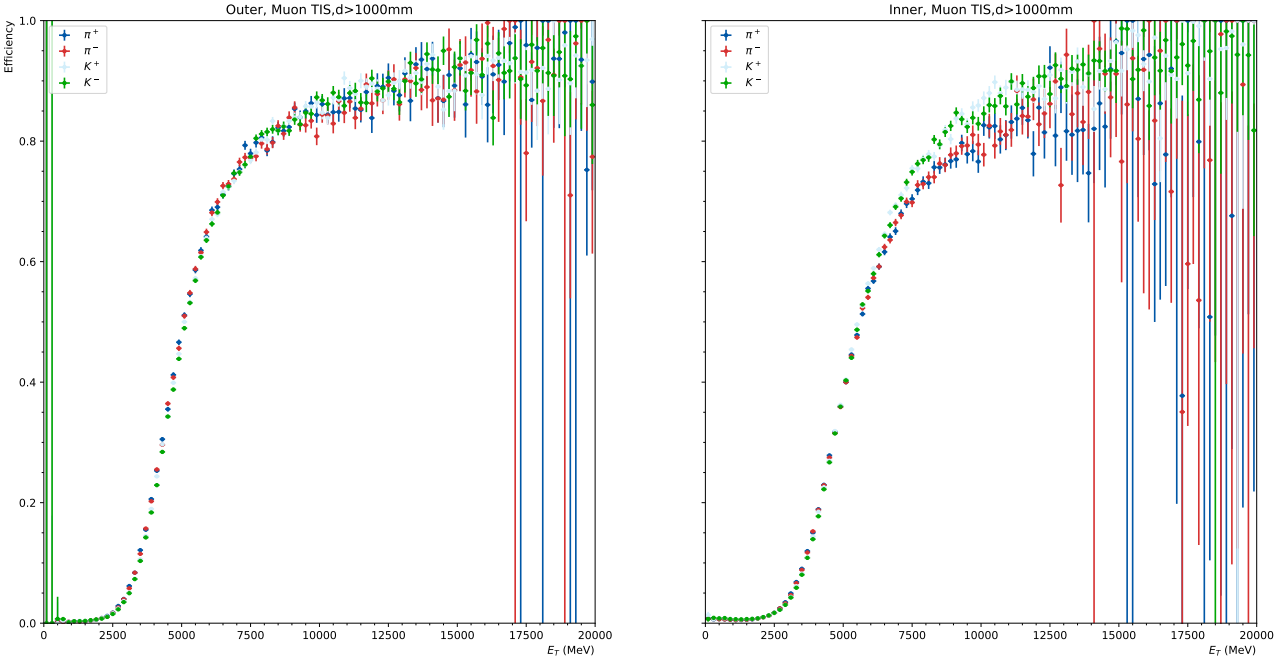

Figure B.14: Efficiency tables for π and K as obtained with the 2017 MU sample.

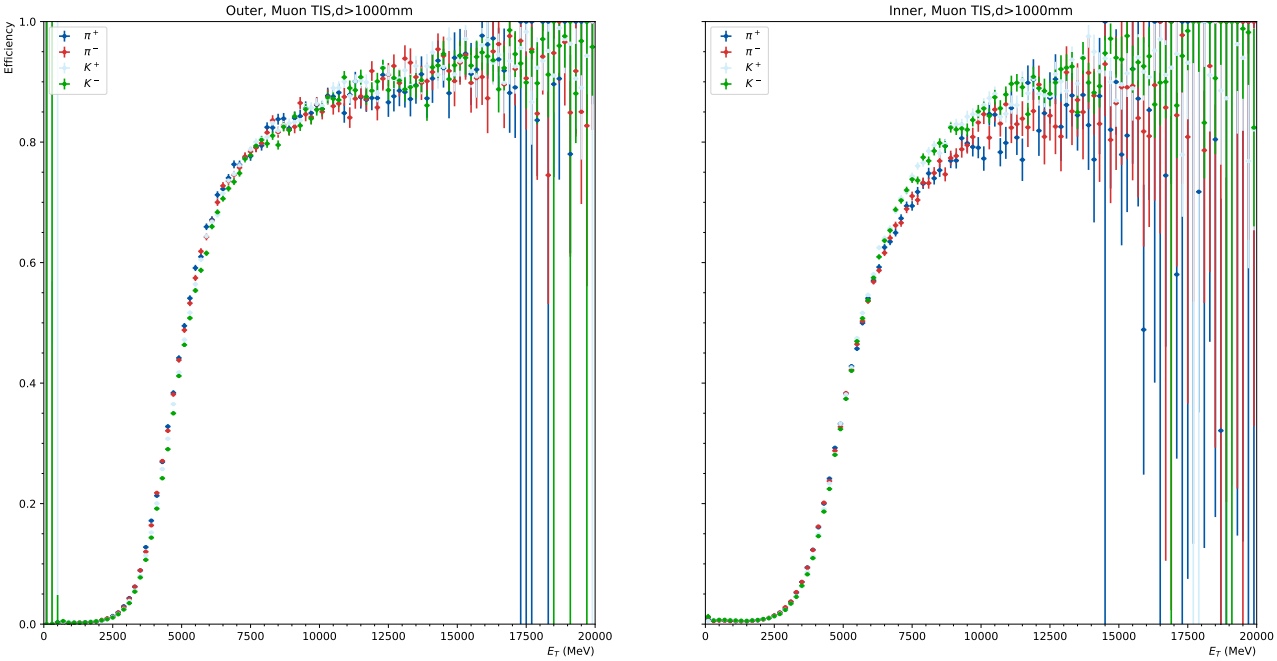

Figure B.15: Efficiency tables for π and K as obtained with the 2016 MD sample.

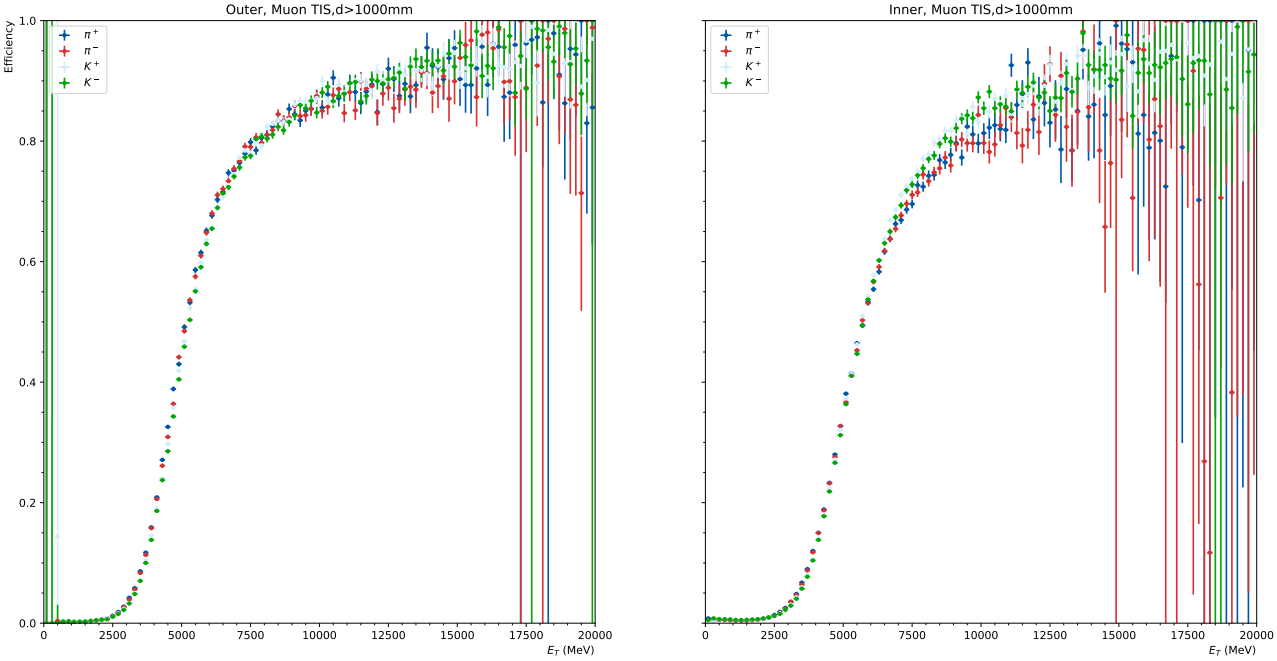

Figure B.16: Efficiency tables for π and K as obtained with the 2016 MU sample.

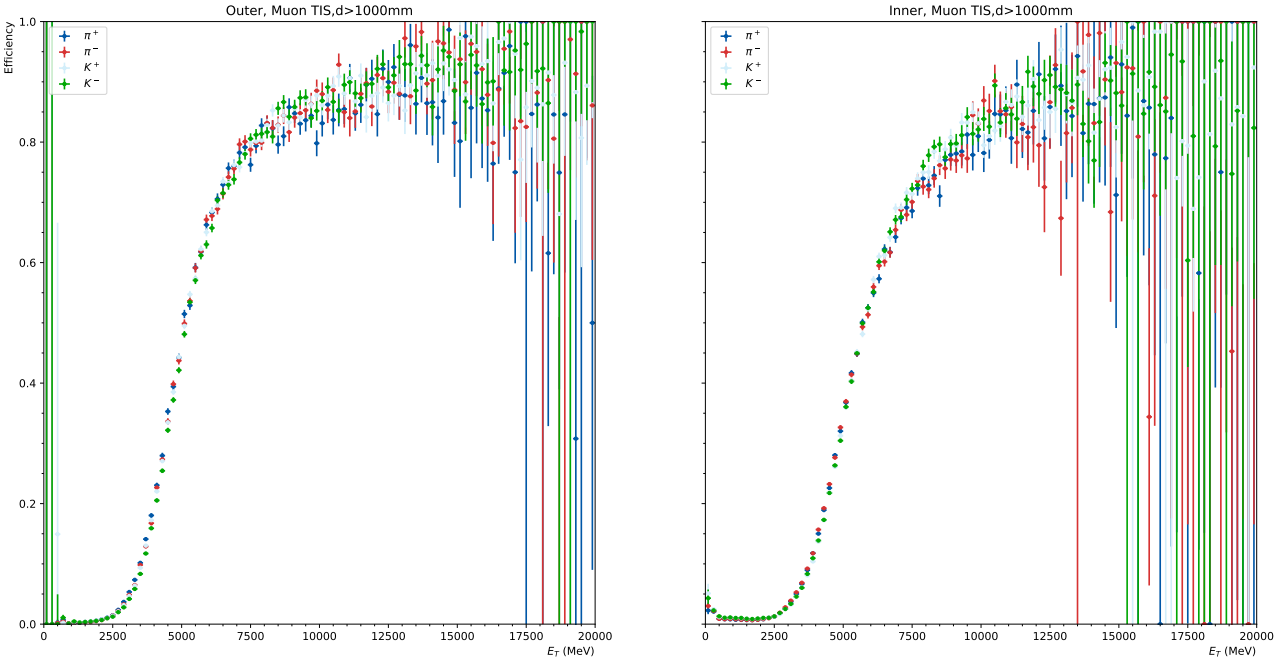

Figure B.17: Efficiency tables for π and K as obtained with the 2012 MD sample.

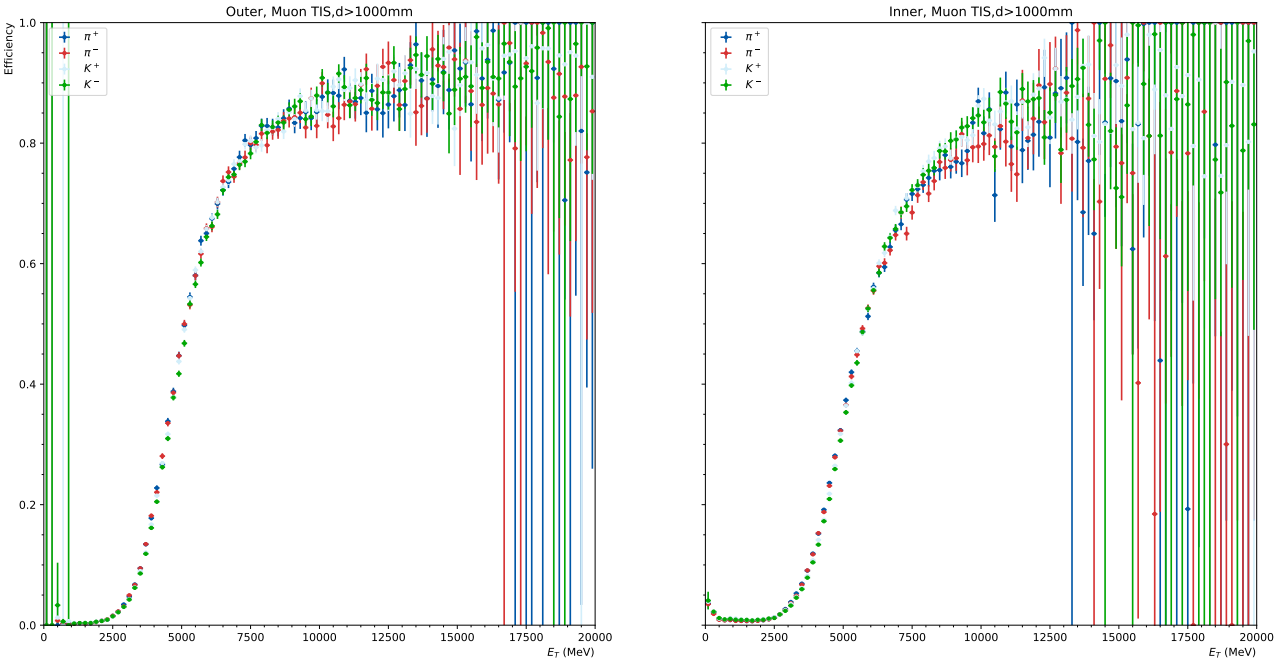

Figure B.18: Efficiency tables for π and K as obtained with the 2012 MU sample.

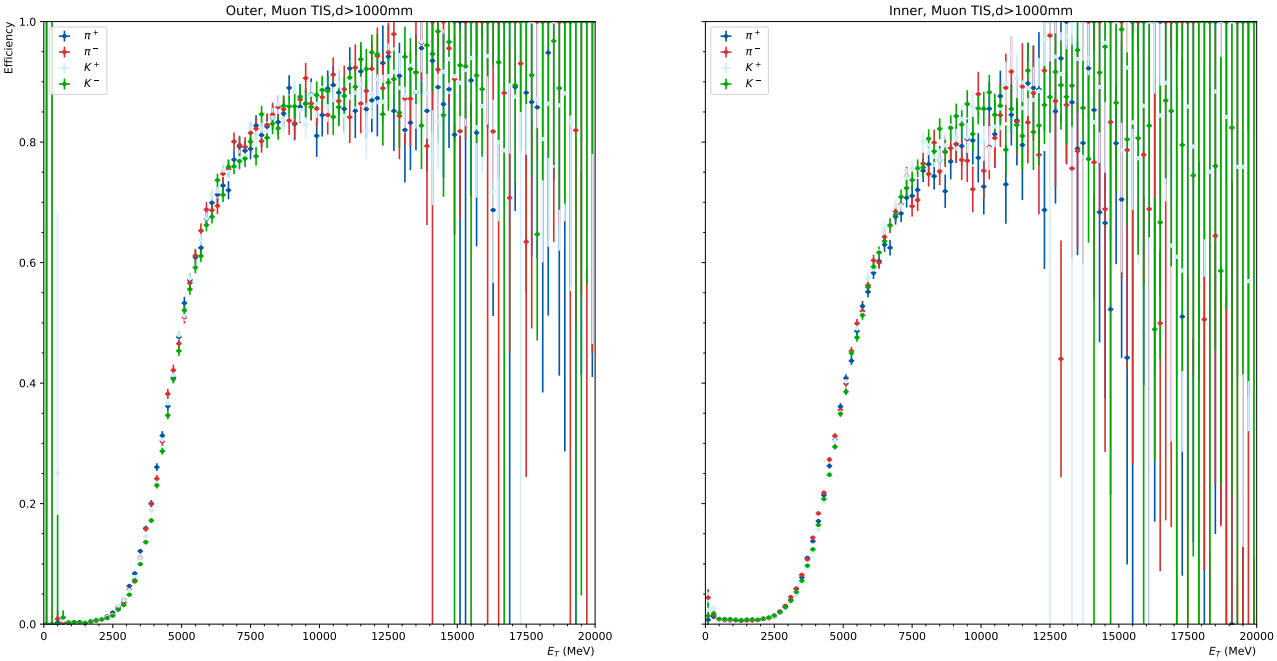

Figure B.19: Efficiency tables for π and K as obtained with the 2011 MD sample.

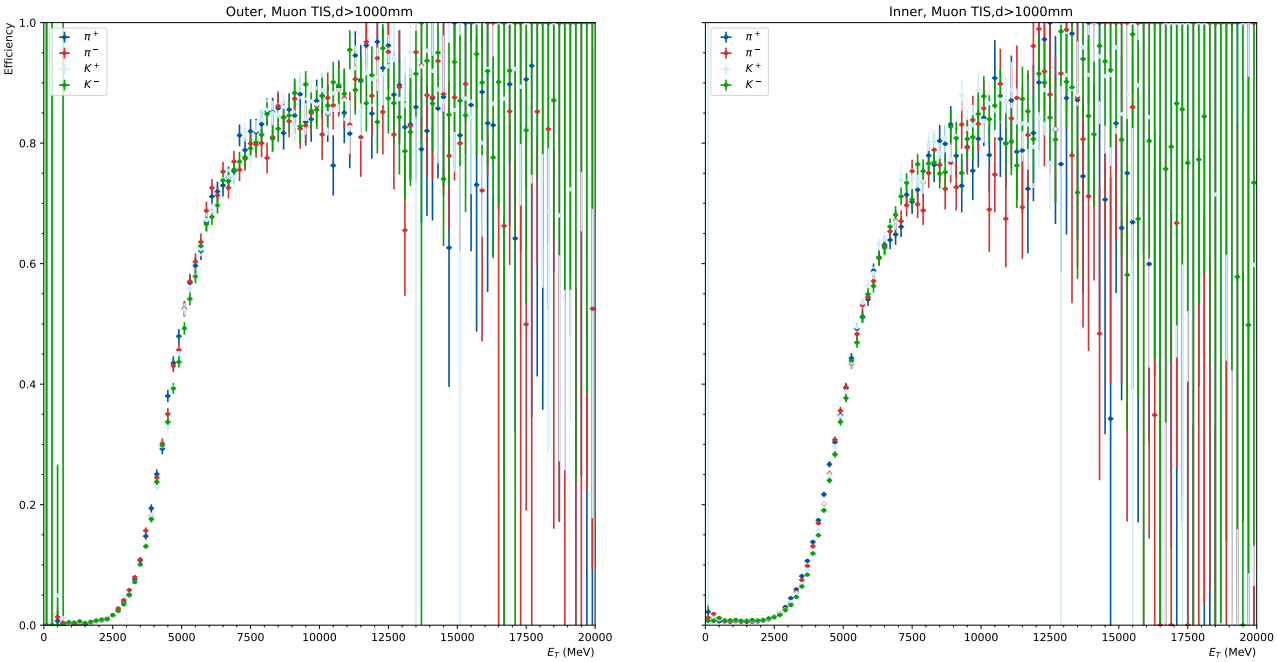

Figure B.20: Efficiency tables for π and K as obtained with the 2011 MU sample.

B.3 Calibration maps

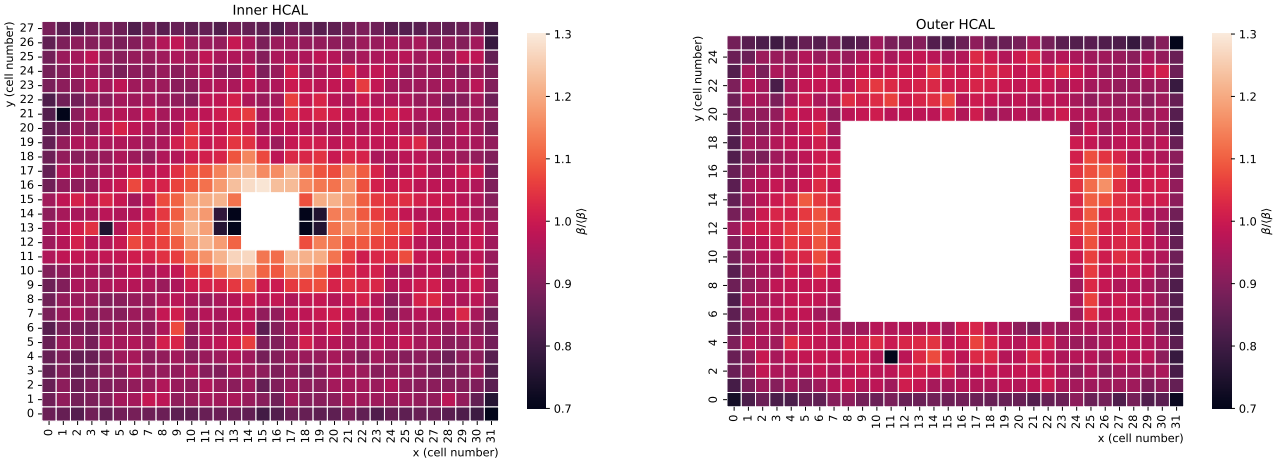

Figure B.21: HCAL cell-by-cell calibration maps obtained for the 2018 MD sample.

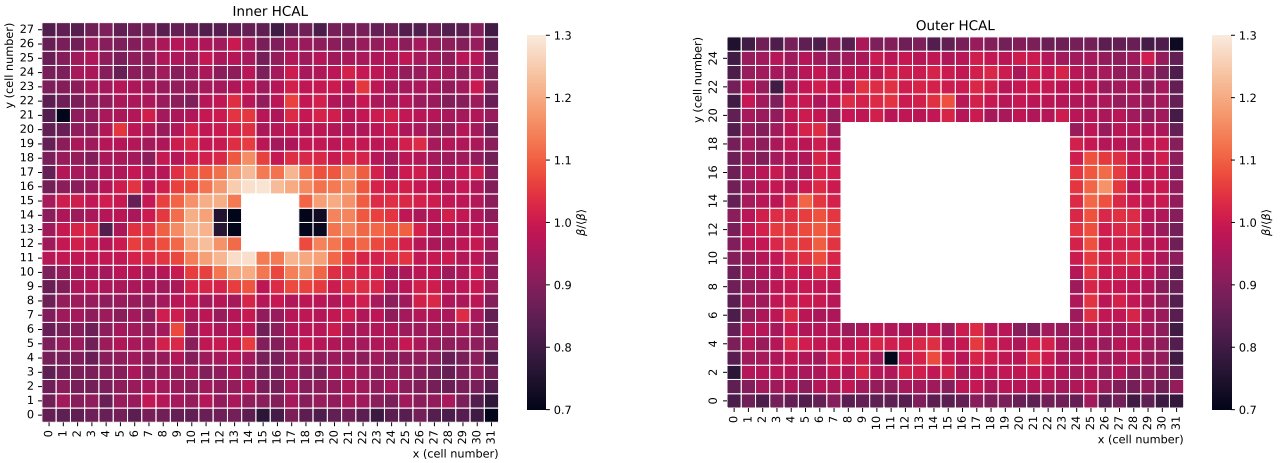

Figure B.22: HCAL cell-by-cell calibration maps obtained for the 2018 MU sample.

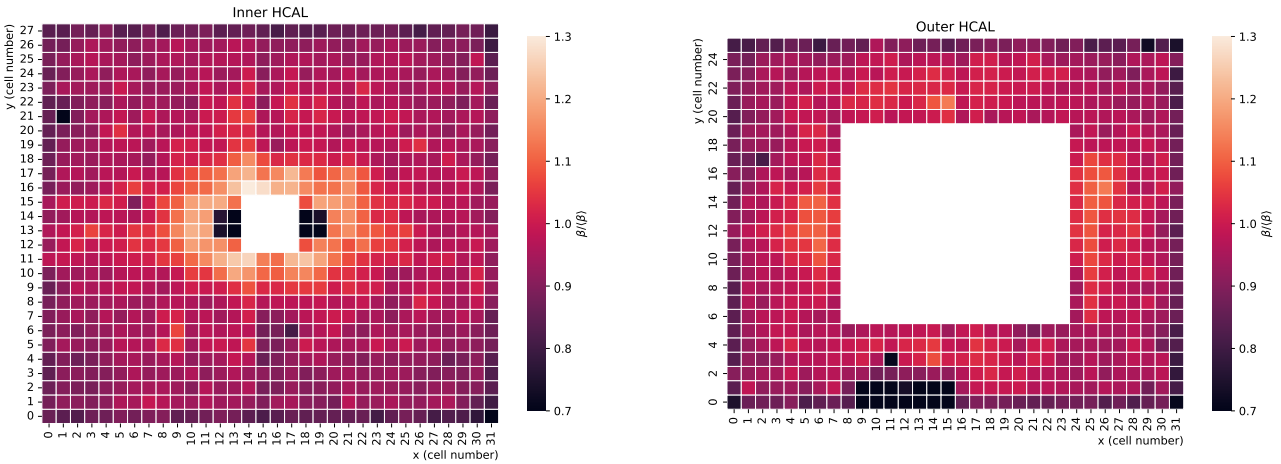

Figure B.23: HCAL cell-by-cell calibration maps obtained for the 2017 MD sample.

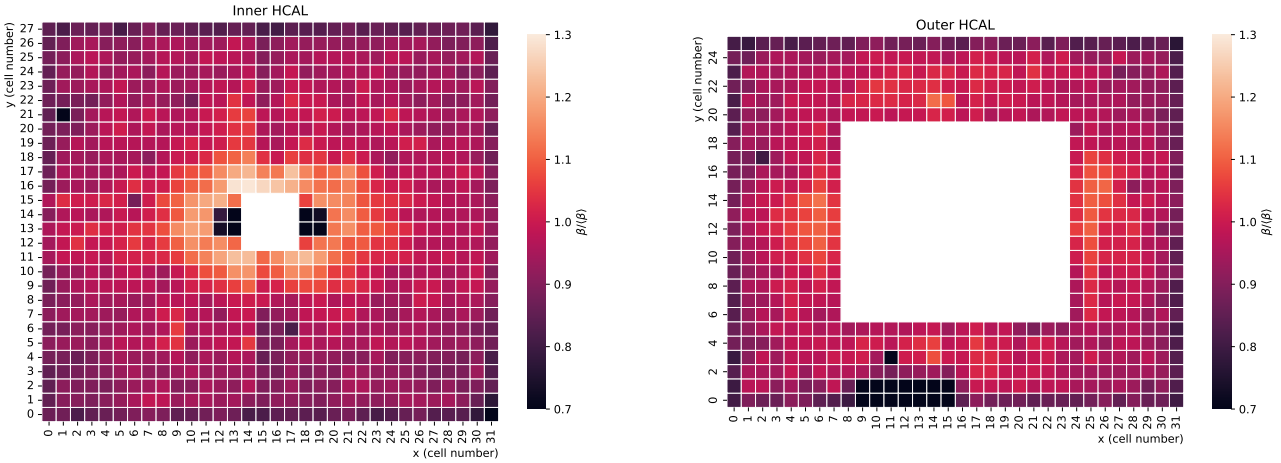

Figure B.24: HCAL cell-by-cell calibration maps obtained for the 2017 MU sample.

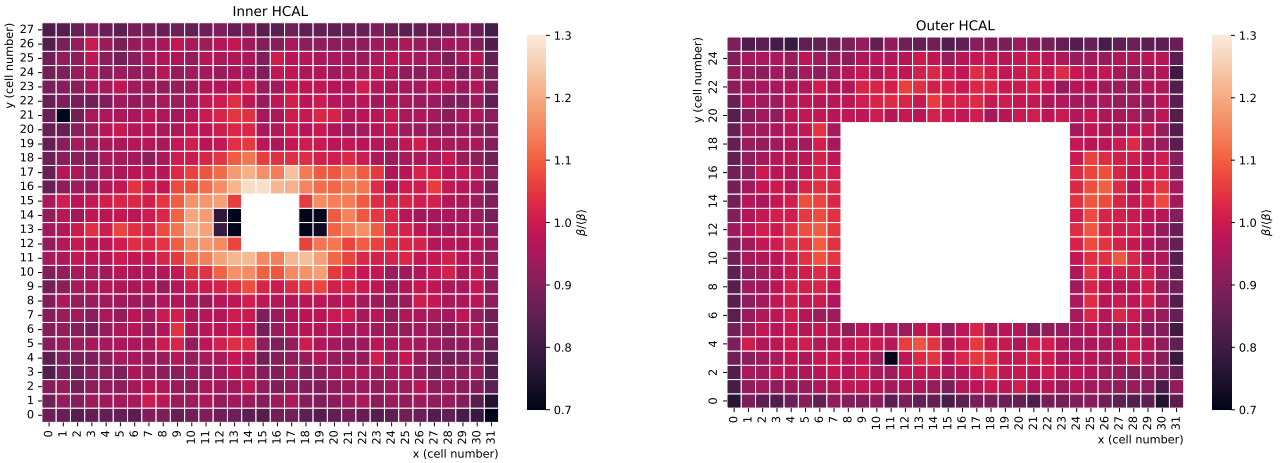

Figure B.25: HCAL cell-by-cell calibration maps obtained for the 2016 MD sample.

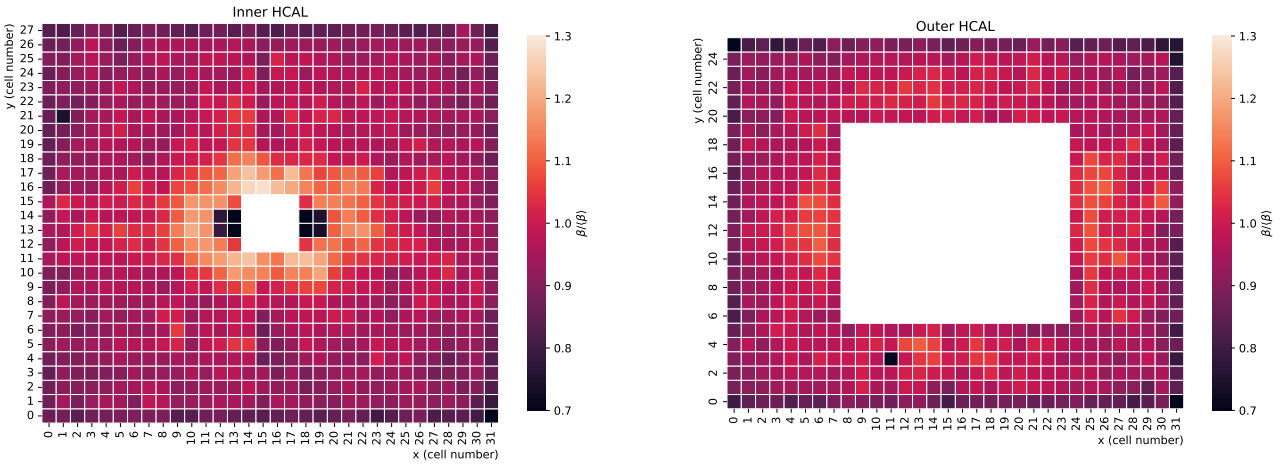

Figure B.26: HCAL cell-by-cell calibration maps obtained for the 2016 MU sample.

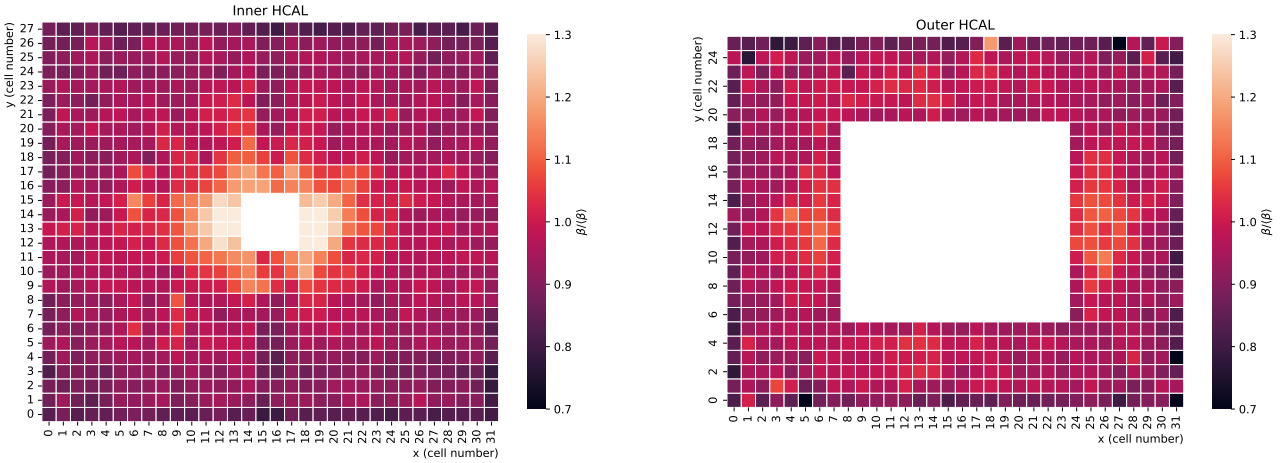

Figure B.27: HCAL cell-by-cell calibration maps obtained for the 2012 MD sample.

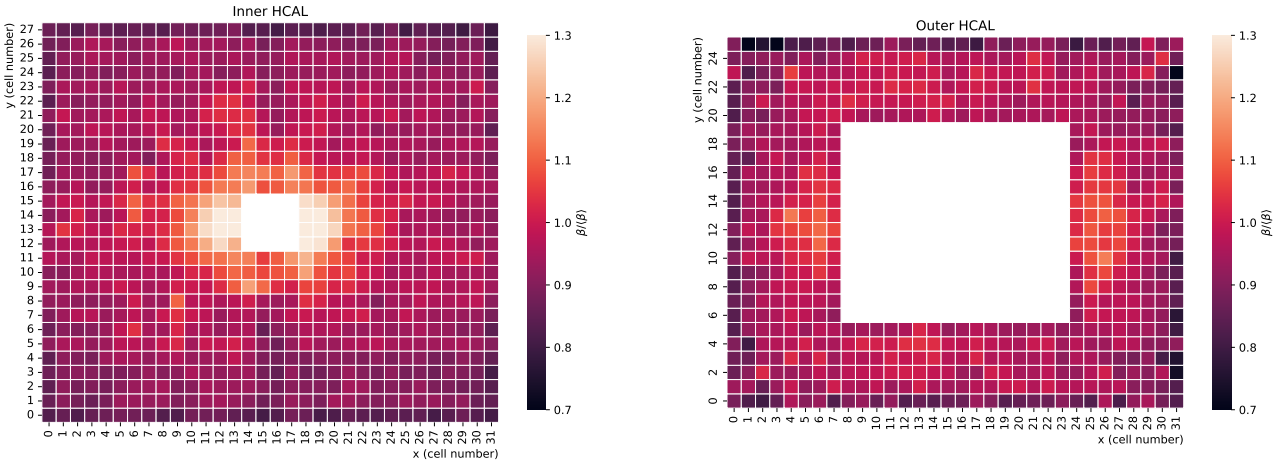

Figure B.28: HCAL cell-by-cell calibration maps obtained for the 2012 MU sample.

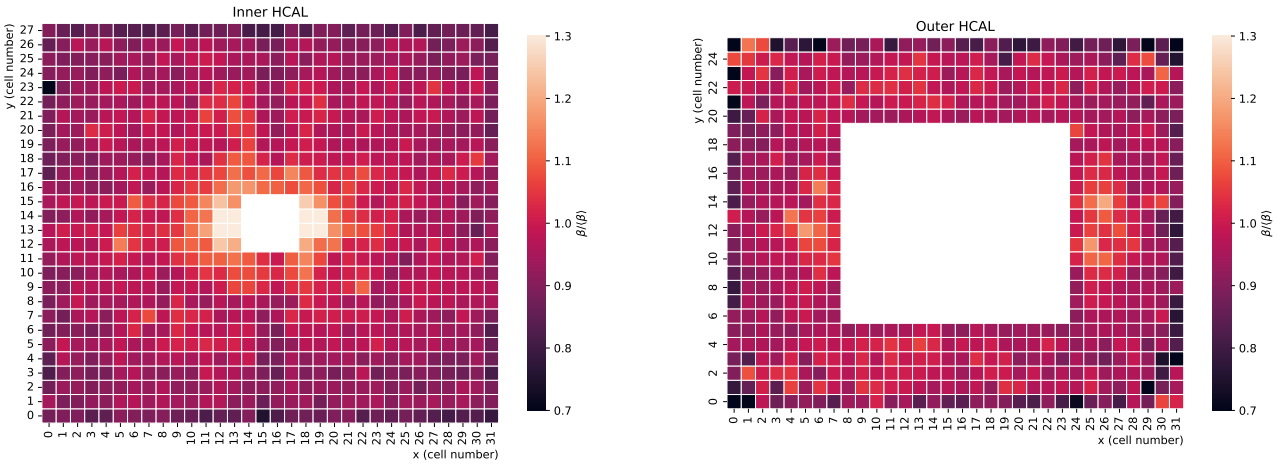

Figure B.29: HCAL cell-by-cell calibration maps obtained for the 2011 MD sample.

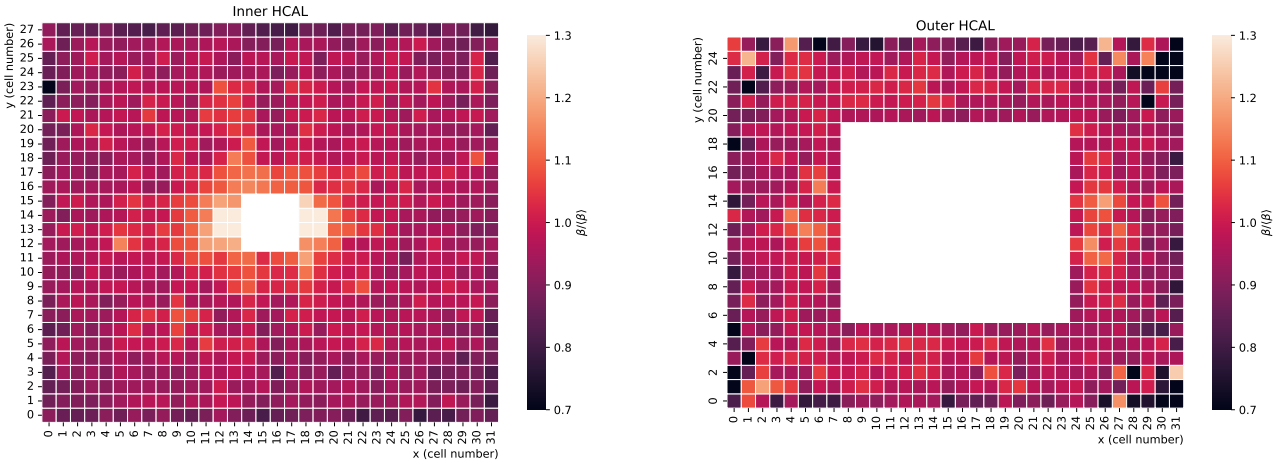

Figure B.30: HCAL cell-by-cell calibration maps obtained for the 2011 MU sample.

B.4 π, K and p trigger efficiency tables

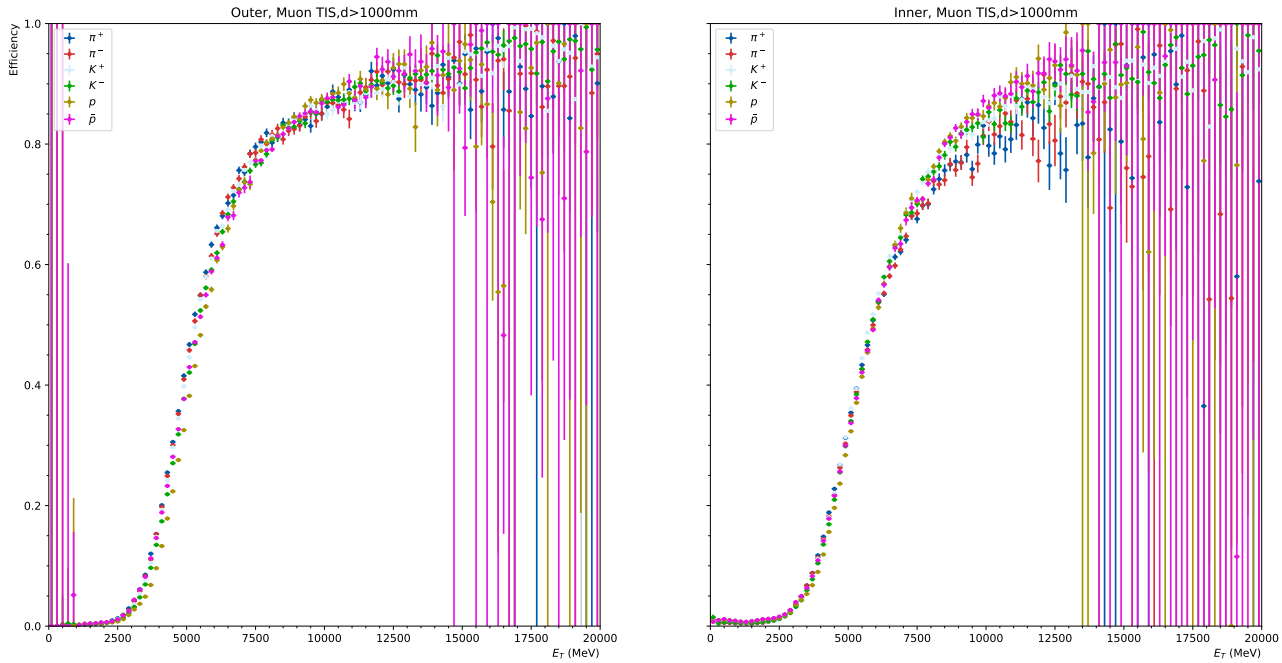

Figure B.31: Efficiency tables for π,K and p build for 2018 MD.

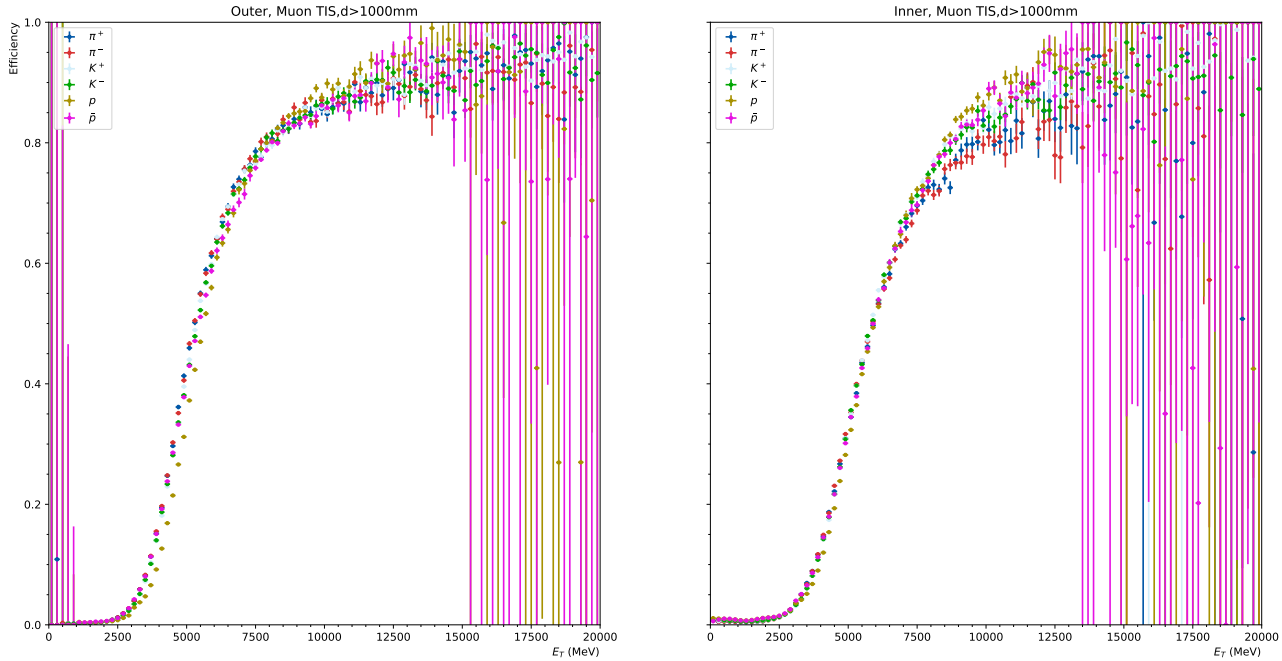

Figure B.32: Efficiency tables for π, K and p build for 2018 MU.

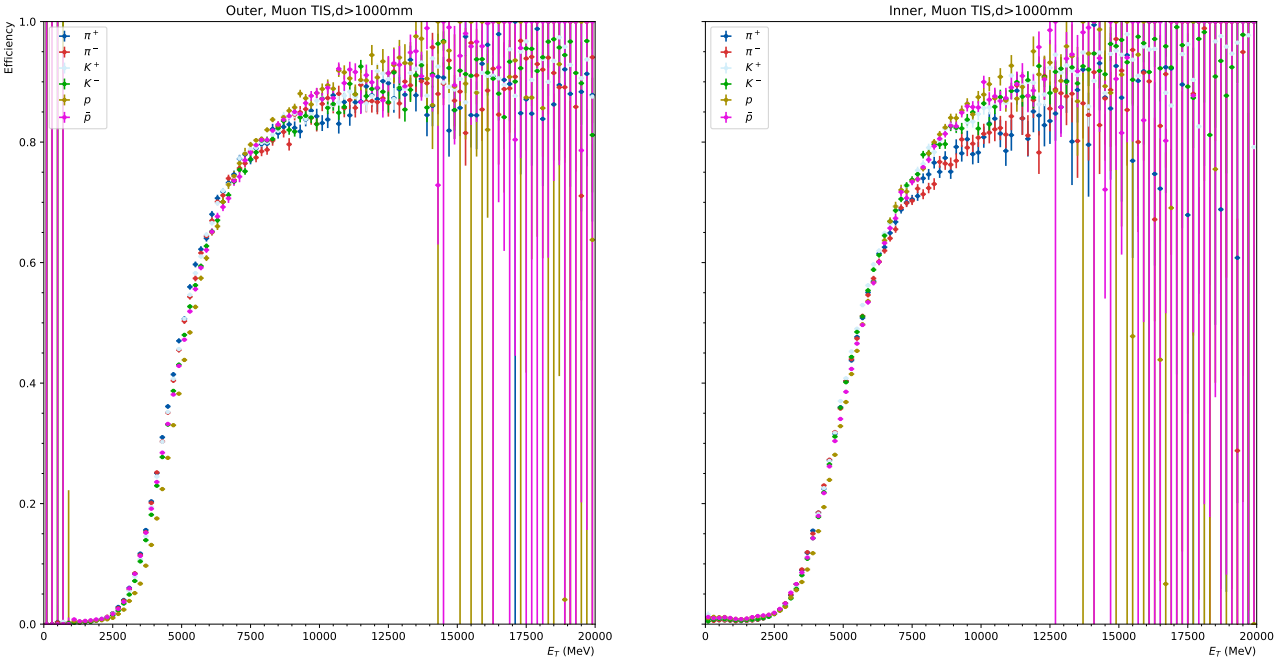

Figure B.33: Efficiency tables for π, K and p build for 2017 MD.

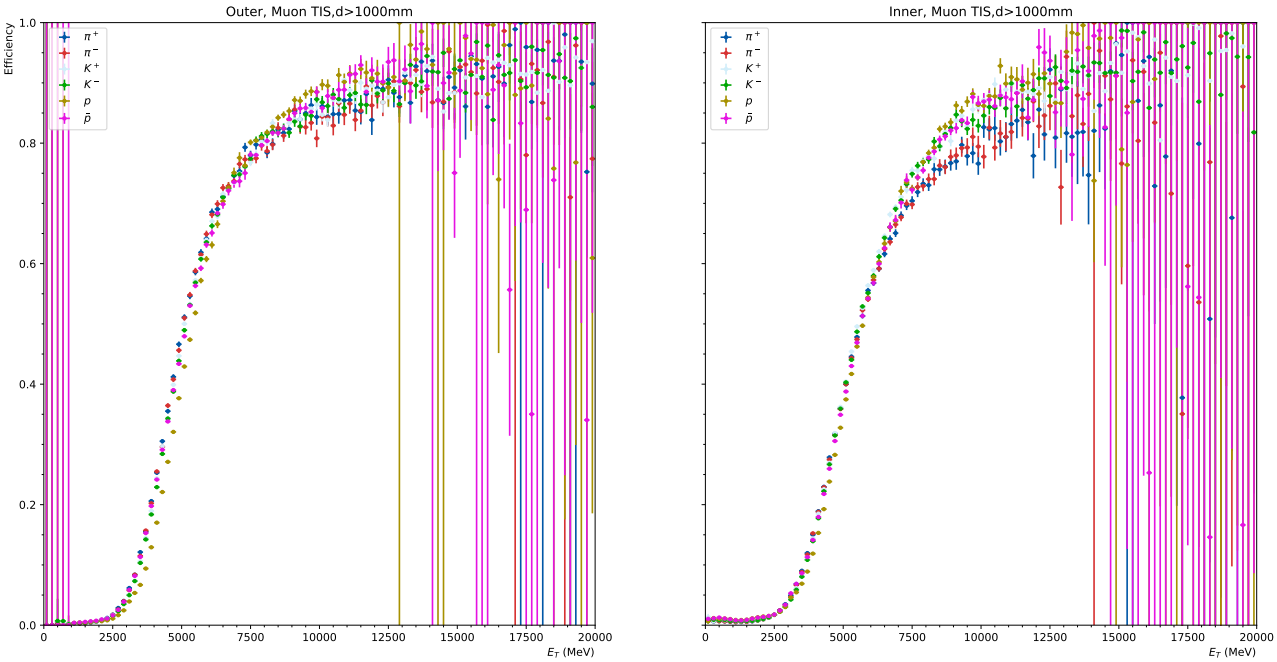

Figure B.34: Efficiency tables for π, K and p build for 2017 MU.

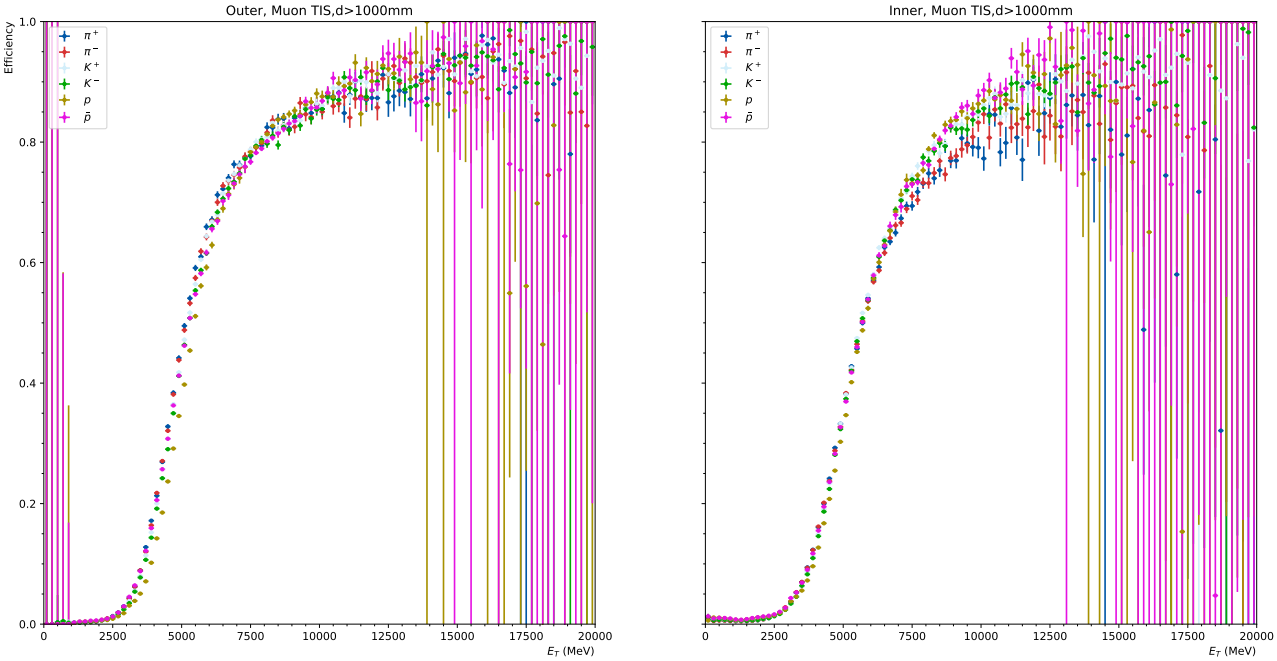

Figure B.35: Efficiency tables for π, K and p build for 2016 MD.

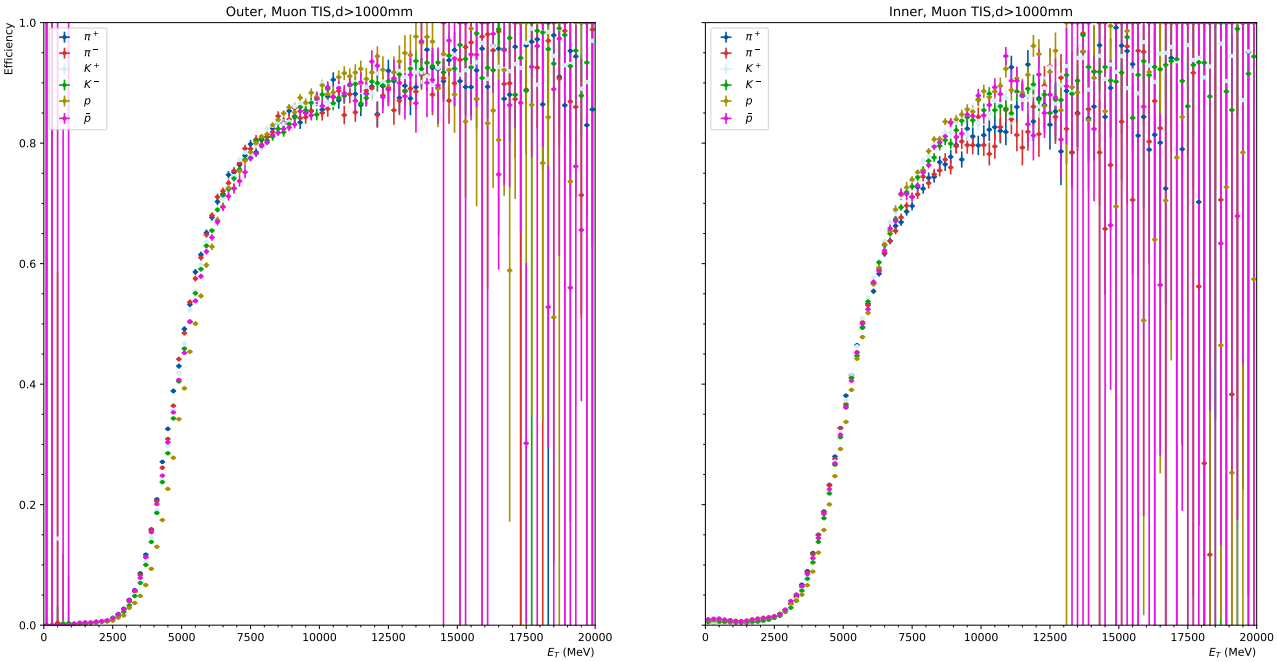

Figure B.36: Efficiency tables for π, K and p build for 2016 MU.

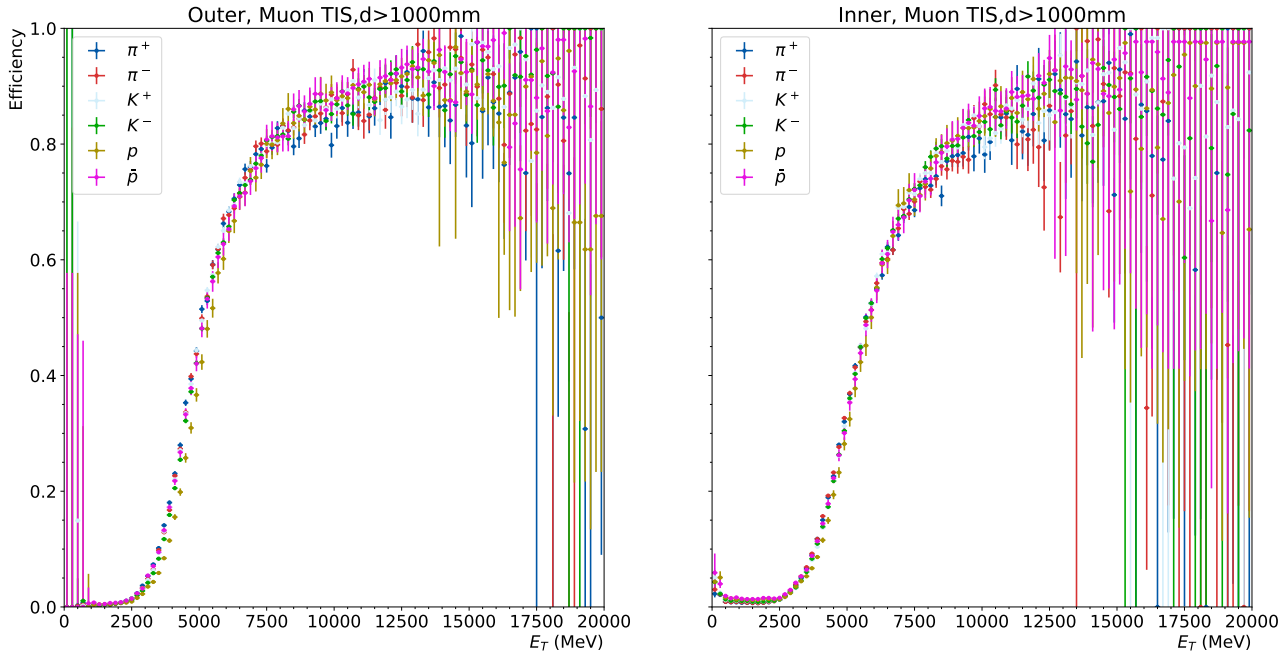

Figure B.37: Efficiency tables for π, K and p build for 2012 MD.

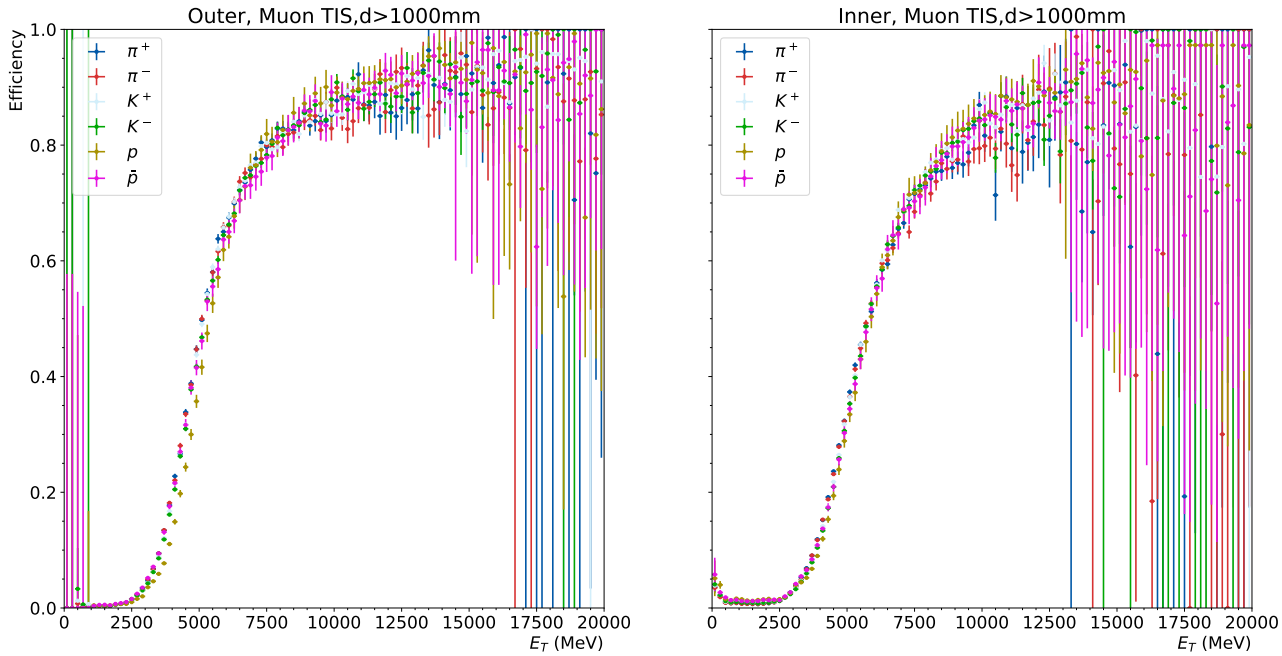

Figure B.38: Efficiency tables for π, K and p build for 2012 MU.

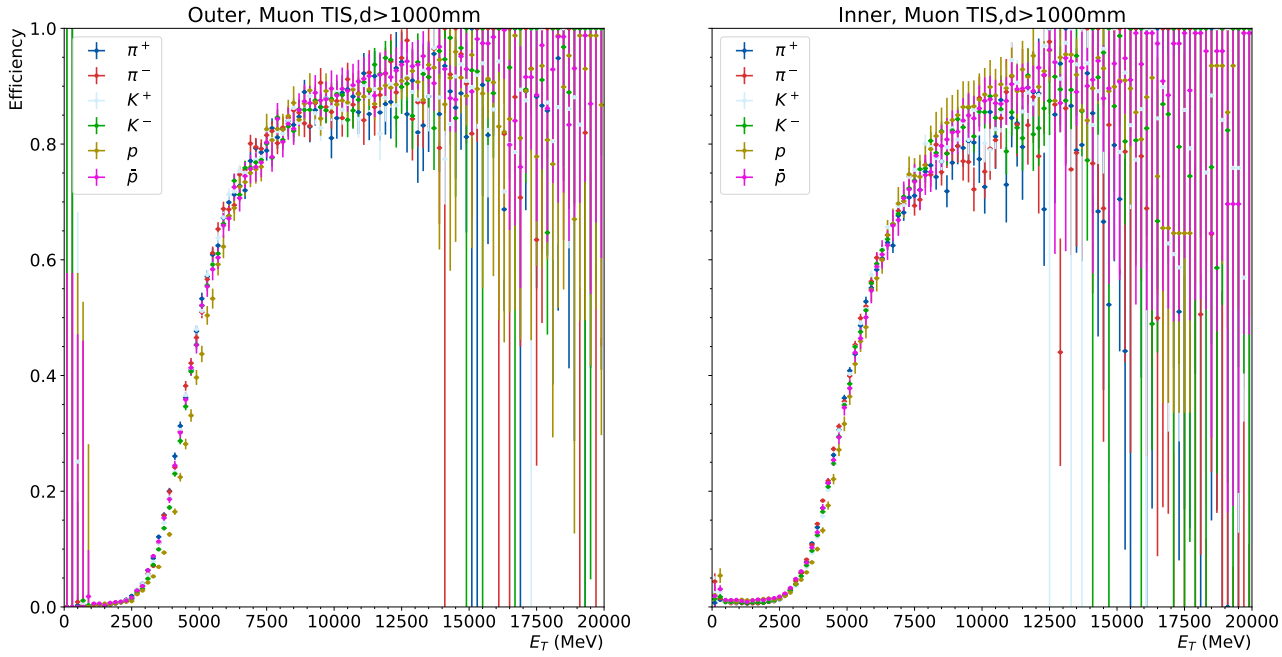

Figure B.39: Efficiency tables for π, K and p build for 2011 MD.

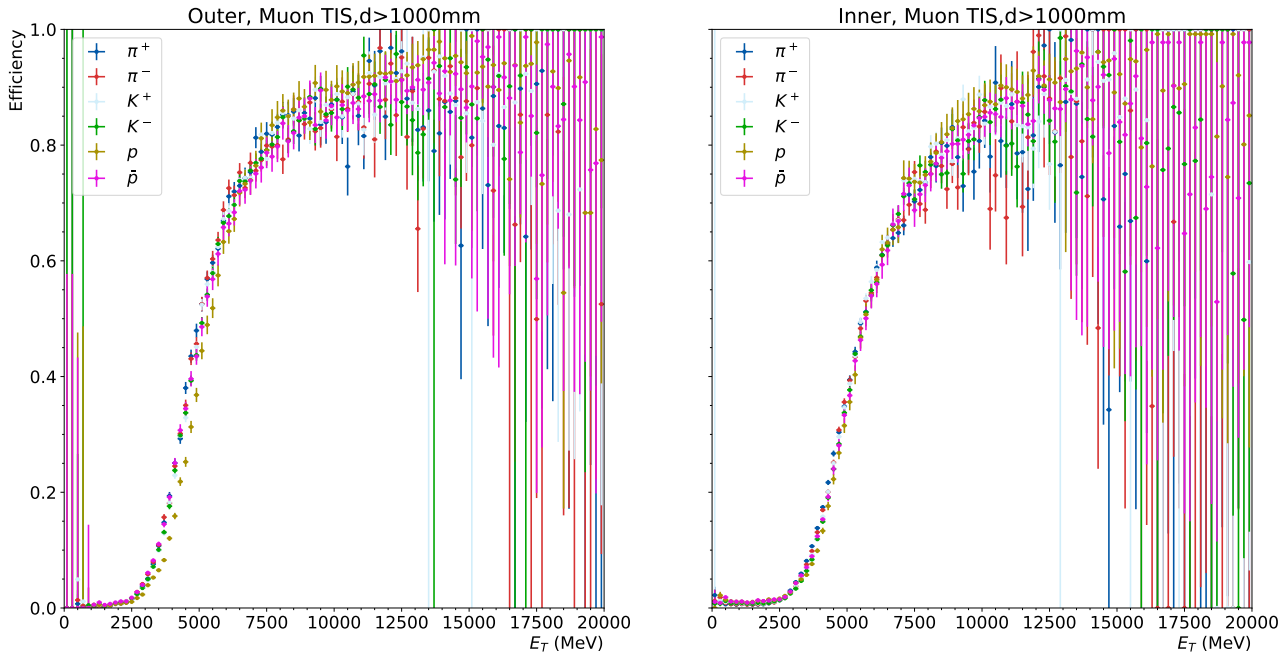

Figure B.40: Efficiency tables for π, K and p build for 2011 MU.

B.5 Proton Run I efficiency tables estimate method

The next paragraphs will describe the estimate method deeper and provide an illustration for the $\bar{p}$ 2012 MU tables determination. The plots for other determinations are available in the dedicated LHCb technical note [147].

The first step of the method is to determine the corrective factors from the hierarchy of kaon efficiency tables between Run I and Run II, which are shown in Figures B.41 and B.42. The corrective factors are projected onto the ratios of the Run I over Run II kaon efficiency table. Taking note of the large uncertainties at high E_T (see Figure B.42) that come from the lack of statistics in this energy regime, it has been decided to provide a unique high E_T corrective factor. The average of the ratios corresponding to the upper range (7500 or 10000 MeV see equation B.5.1) of the efficiency table slopes (different E_T region in inner and outer) is assigned as high E_T corrective factor. In the end, the corrective factors read as written in equation B.5.1:

$$C_{p^x}^{Y1,Y2,MX,area} = \begin{cases} \epsilon_{K^x}^{Y1,MX,inner} / \epsilon_{K^x}^{Y2,MX,inner} & \text{if } E_T < 7500\,\text{MeV and area} = inner \\ M_{p^x}^{Y1,Y2,MX,inner} & \text{if } E_T > 7500\,\text{MeV and area} = inner \\ \epsilon_{K^x}^{Y1,MX,outer} / \epsilon_{K^x}^{Y2,MX,outer} & \text{if } E_T < 10000\,\text{MeVand area} = outer \\ M_{p^x}^{Y1,Y2,MX,outer} & \text{if } E_T > 10000\,\text{MeV and area} = outer \end{cases}, \quad \text{(B.5.1)}$$

where $Y1$ denotes 2011 or 2012, $Y2$ denotes 2016 or 2017 or 2018, MX denotes MU or MD, area denotes *inner* or *outer* HCAL, p^x denotes p or $\bar{p}$ respectively, K^x denotes K^+ or K^- respectively, and $M_{p^x}^{Y1,Y2,MX,area}$ is defined as the average efficiency ratio between [7500,15000] MeV in the inner HCAL or between [10000,15000] MeV in the outer HCAL. The corresponding correction tables are shown in Figure B.43 (in case of bin with a 0 denominator, the correction factor is set to 1 ± 1). It should be noted that the corrections look different depending on the Run II year used.

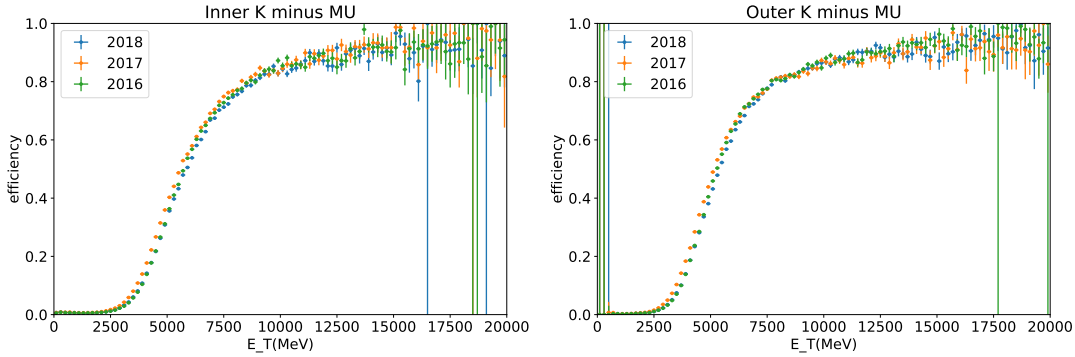

Figure B.41: Efficiency tables for Run II, K^-, MU.

The second step of the method consists in using the previously defined corrections and the protons Run II efficiency tables, shown in Figure B.44. The Run I proton efficiency tables are formed following Equation B.5.2:

$$\epsilon_{p^x}^{Y1,Y2,MX,area} = C_{p^x}^{Y1,Y2,MX,area} \times \epsilon_{p^x}^{Y2,MX,area}, \quad \text{(B.5.2)}$$

where $\epsilon_{p^x}^{Y1,Y2,MX,area}$ denotes the estimated Run I efficiency table and $\epsilon_{p^x}^{Y2,MX,area}$ is the Run II proton efficiency table used in the computation. By construction, the associated statistical uncertainty related to $\epsilon_{p^x}^{Y1,Y2,MX,area}$ can appear to be greater than 1 in some E_T bins with low $K^\pm$ statistics. In these cases the results are replaced by those obtained in a neighbouring bin. The corresponding Run I proton efficiency tables built from each Run II year are displayed

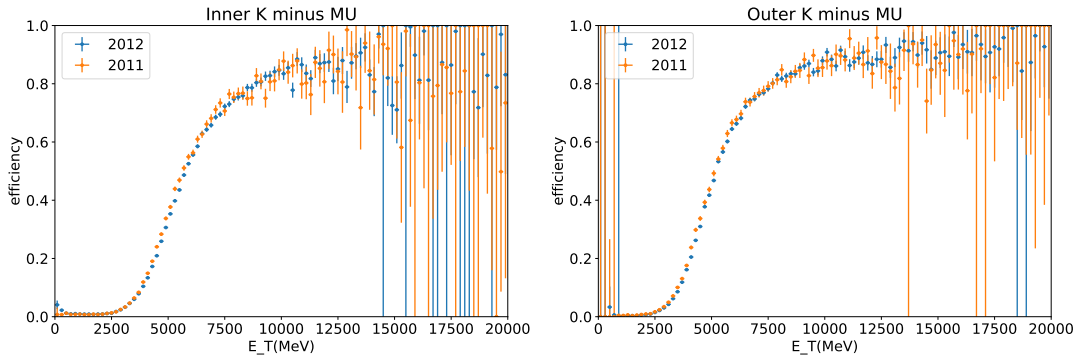

Figure B.42: Efficiency tables for Run I, K^-, MU.

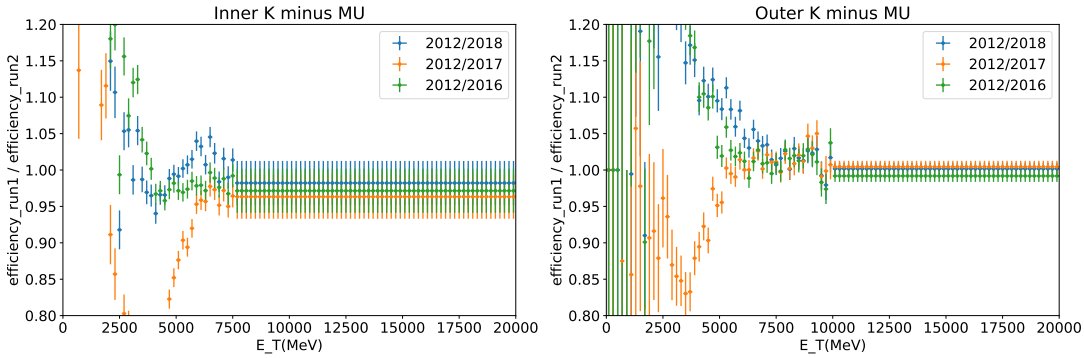

Figure B.43: Correction tables corresponding to $\bar{p}$, 2012, MU.

together on Figure B.45. Here it is important to notice that despite the differences spotted among the different corrections build (depending on the Run II year considered) and others among the protons Run II efficiency tables, the estimated Run I efficiency tables look remarkably close between the Run II years used. To confirm this observation, ratios of estimated efficiency tables are built for each possible Run II year combination as displayed in Figure B.46 and are globally observed close to unity (e.g. compatible estimates). The observed compatibility in the estimated Run I protons tables is a motivation to combine the different estimates performed for each sample. An arithmetic averaging among the guesstimates done with 2016, 2017 and 2018 data is performed to this end, as shown in Figure B.47.

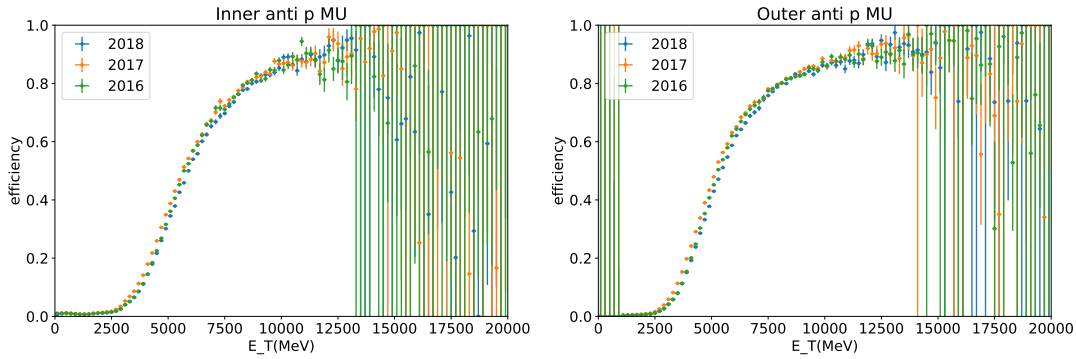

Figure B.44: Efficiency tables for Run II, $\bar{p}$, MU.

A cross-check is performed to verify the self-consistency of the method developed : identically

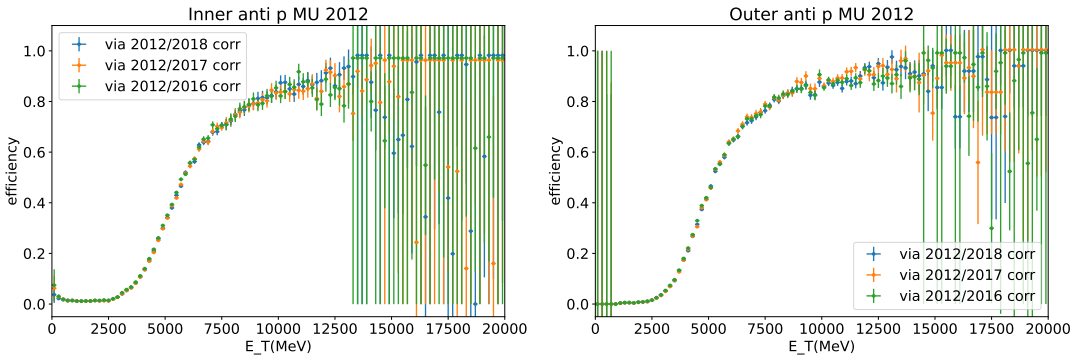

Figure B.45: Estimated efficiency tables for $\bar{p}$, 2012, MU coming from each Run II year.

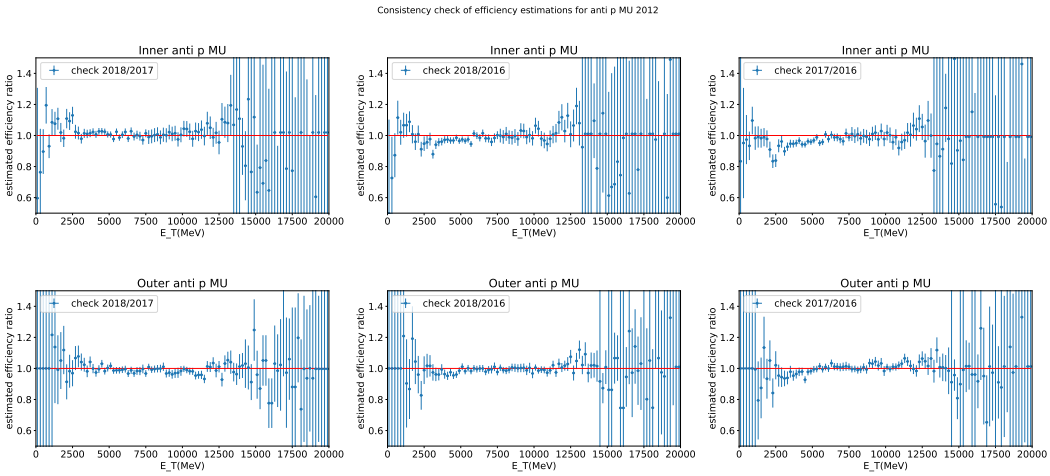

Figure B.46: Ratios of efficiency tables for $\bar{p}$, 2012, MU coming from all the possible Run II years combinations.

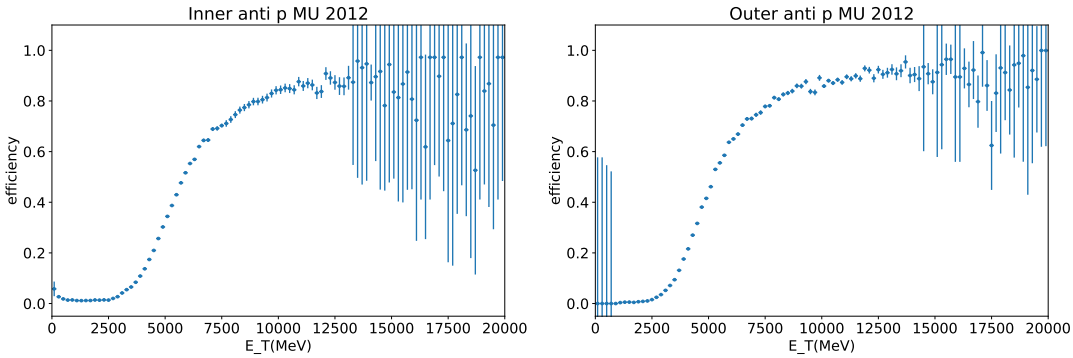

Figure B.47: Combined efficiency tables for $\bar{p}$, 2012, MU.

to what has been done to estimate the Run I protons efficiency tables, one applies the method to determine estimated 2016 and 2017 proton efficiency tables, using the 2018 proton tables, and finally compare these guesstimates to the reference tables. The corresponding 2016 and 2017 estimated efficiency tables are displayed together with the true tables in Figures B.48 and B.49. The ratios of the true and guesstimate efficiency tables are shown in Figures B.50 and B.51. From the previous figures it can be seen that the estimates are coherent with respect to the true tables (the truth over estimated ratios are globally around unity). This allows to check

the global consistency of the method developed. Some slight deviations are also observed, and they can be further used to determine a systematic uncertainty related to the method. The relative differences between the true and estimated 2016 and 2017 efficiency tables are computed following equation B.5.3:

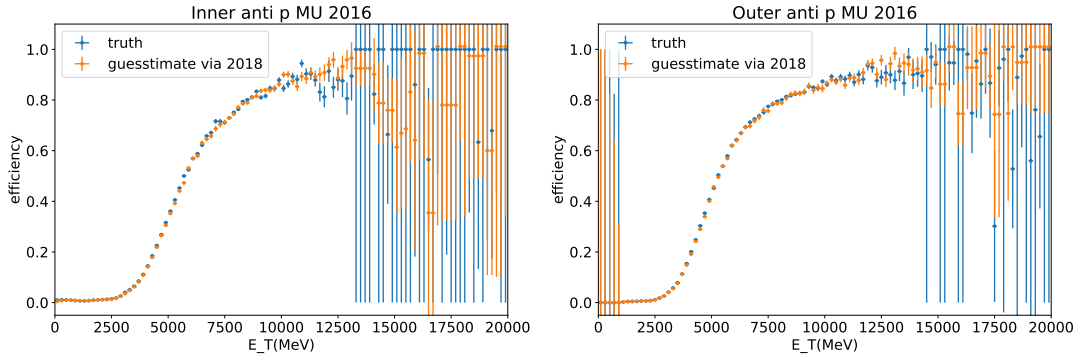

Figure B.48: estimated and true efficiency tables for $\bar{p}$, 2016, MU.

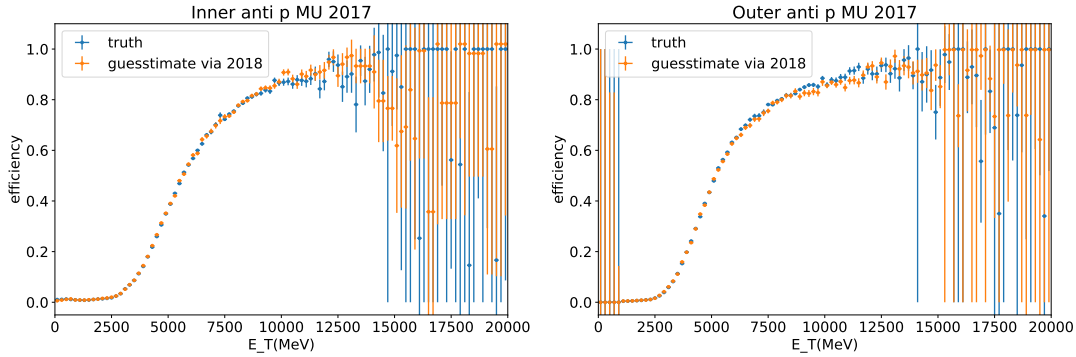

Figure B.49: estimated and true efficiency tables for $\bar{p}$, 2017, MU.

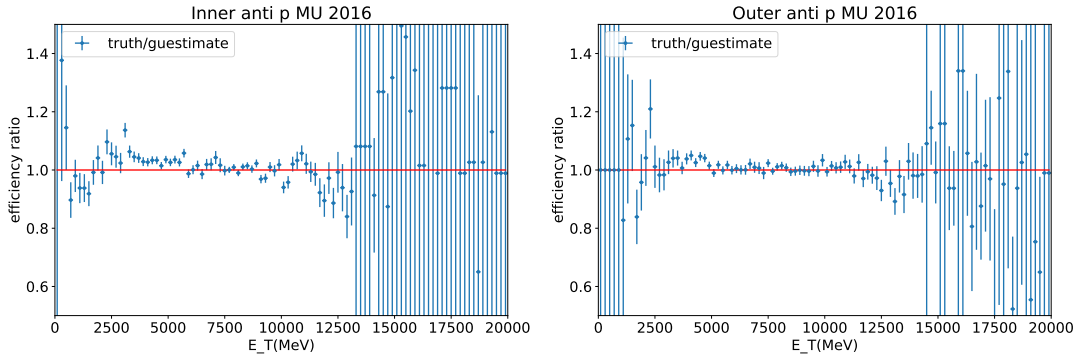

Figure B.50: Ratios of true over estimated efficiency tables for $\bar{p}$, 2016, MU.

$$\Delta_{p^x}^{Y,MX,area} = \frac{\epsilon_{p^x,true}^{Y,MX,area} - \epsilon_{p^x,guest}^{Y,MX,area}}{\epsilon_{p^x,guest}^{Y,MX,area}}, \tag{B.5.3}$$

where $\epsilon_{p^x,true}^{Y,MX,area}$ denotes the true efficiency table and $\epsilon_{p^x,guest}^{Y,MX,area}$ denotes the estimated one. Here, similar patterns are observed on all the ratios built for a given HCAL region, and thus, it has

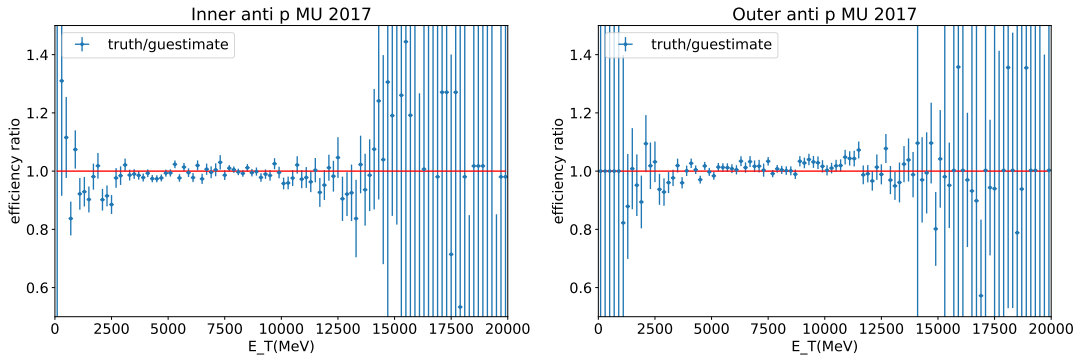

Figure B.51: Ratios of true over estimated efficiency tables for $\bar{p}$, 2017, MU.

been decided to combine the relative differences in order to build a unique distribution for each HCAL region. Furthermore, the points for which the relative statistical uncertainty related to the estimated efficiency is greater than 5% have been excluded from the distributions, in order to not consider points with too low statistics in the systematic uncertainty estimation. Finally, the RMS of the distributions are assigned as relative systematic uncertainty for the inner and outer HCAL separately. As shown in Figure B.52 the relative systematic uncertainty attached to the inner HCAL is 3.9% and the one attached to the outer HCAL is 3.1%. The systematic uncertainty attached to each E_T bin of the Run I protons efficiency tables reads as written in Equation B.5.4:

$$\sigma^{\text{method}}_{\epsilon^{Y1,Y2,MX,area}_{p^x}} = \epsilon^{Y1,Y2,MX,area}_{p^x} \times \text{RMS}_{\text{area}}, \tag{B.5.4}$$

where RMS_{area} denotes the previously defined relative systematic estimator. The final uncertainty attached to the Run I proton efficiency tables reads as written in Equation B.5.5:

$$\sigma^{\text{tot}}_{\epsilon^{Y1,Y2,MX,area}_{p^x}} = \sqrt{\left(\sigma^{\text{stat}}_{\epsilon^{Y1,Y2,MX,area}_{p^x}}\right)^2 + \left(\sigma^{\text{method}}_{\epsilon^{Y1,Y2,MX,area}_{p^x}}\right)^2}, \tag{B.5.5}$$

where $\sigma^{\text{stat}}_{\epsilon^{Y1,Y2,MX,area}_{p^x}}$ denotes the statistical uncertainty attached to proton Run I efficiency tables obtained from the propagation of the statistical uncertainties at each and every step of the method. The final Run I protons efficiency tables including all the uncertainties are given in Figure B.53.

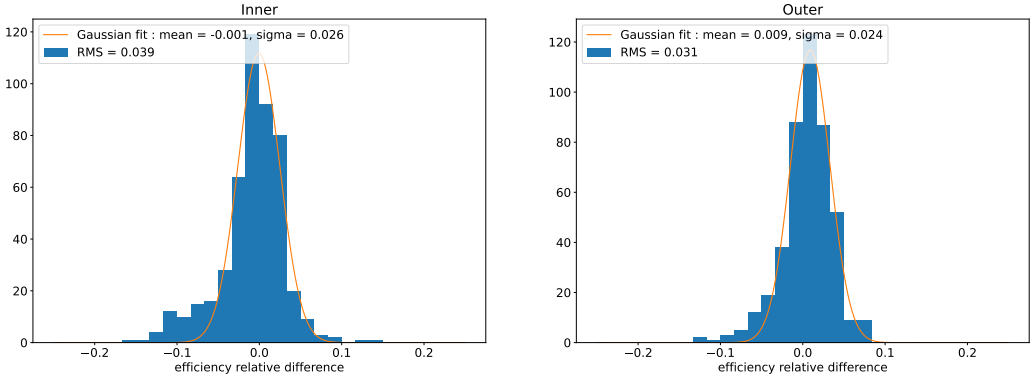

Figure B.52: Distribution of the relative differences between the 2016 and 2017 true and estimated efficiency tables. Two possible systematic estimators are displayed, one from a Gaussian fit (not kept due to the non Gaussian shape) and the global RMS of the distribution (assigned as method systematic in the following).

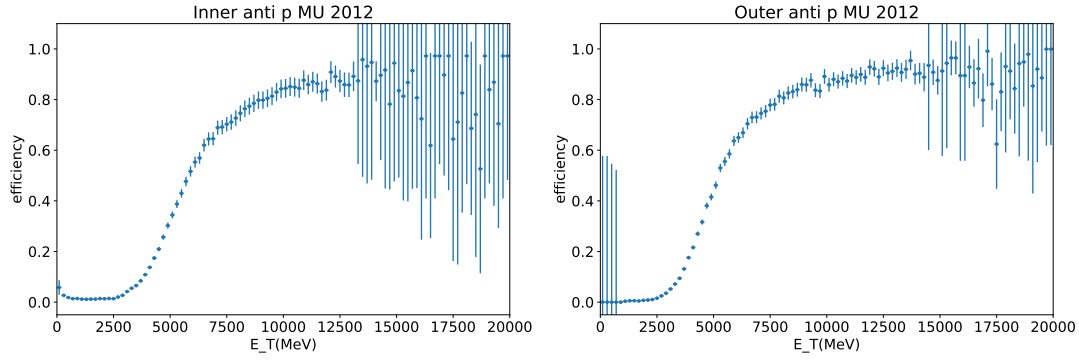

Figure B.53: Final efficiency tables for $\bar{p}$, 2012, MU.

B.6 Comparison of the new and the previous Run I efficiency tables

This work aimed at generalising the L0Hadron correction method developed for Run II to Run I. New efficiency tables, calibration maps and underlying energy maps have been computed for Run I. The previous Run I L0Hadron corrections were made disregarding the calibration and occupancy effects. It is however interesting to compare these two Run I efficiency tables derivations.

Figures B.54 to B.77 display together the new and old efficiency tables for all the particle species, the two polarities, and the two Run I years. Some conclusions can be drawn: the range of the corrections in E_T has improved; the rise of the efficiency is more accurately described; the inner region seems much better understood; proton efficiency tables are behaving reasonably. All in all, the corrective tables determined with the method for Run I are way more educated.

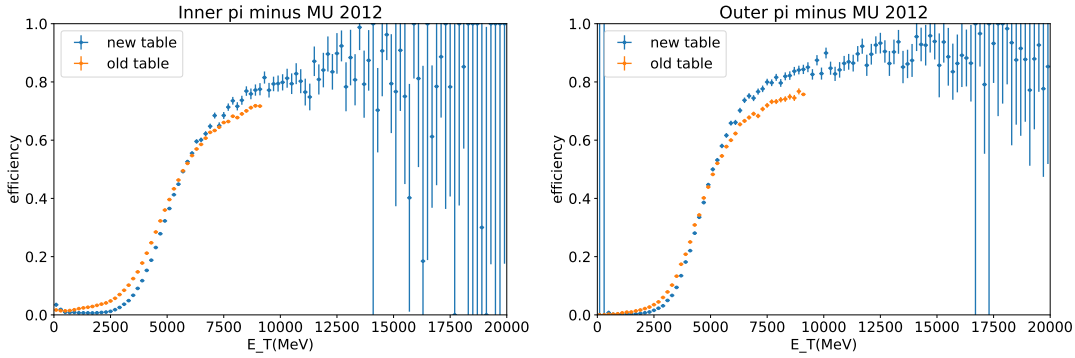

Figure B.54: Plots of the old and new efficiency tables for π^-, 2012, MU.

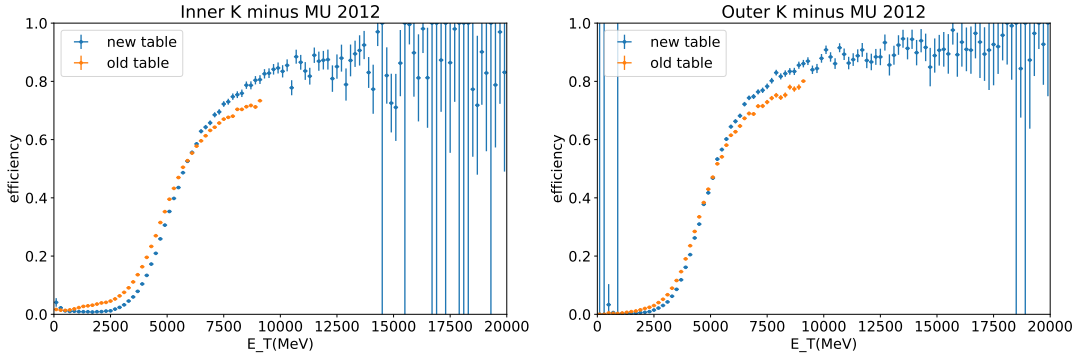

Figure B.55: Plots of the old and new efficiency tables for K^-, 2012, MU.

To close this comparison section: presentations [215, 216] about Run I L0Hadron efficiencies tables reported issues observed in an R_K analysis. The efficiency table given for 2012 K^+ MU in outer HCAL area by the previous L0Hadron correction method was departing a lot from what was given by the measurable TISTOSsed efficiency from data. Figure B.78 displays the efficiency table given by the R_K data together with the corresponding data from the previous and current L0Hadron correction method. The comparison of the different tables given in figure B.78 shows good agreement of the R_K data efficiency with the current efficiency table at low (below 5000 MeV) and high (above 7000 MeV) transverse energy. Some departures can be seen between the R_K data efficiency and the current efficiency table from 5000 MeV to 7000 MeV. A

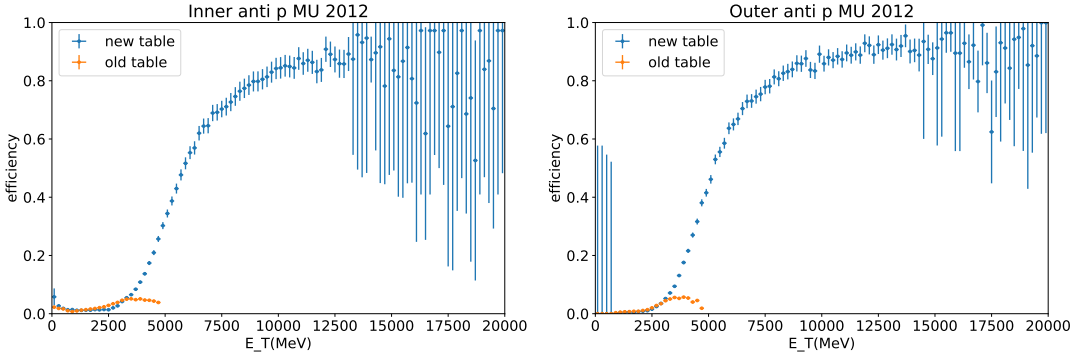

Figure B.56: Plots of the old and new efficiency tables for $\bar{p}$, 2012, MU.

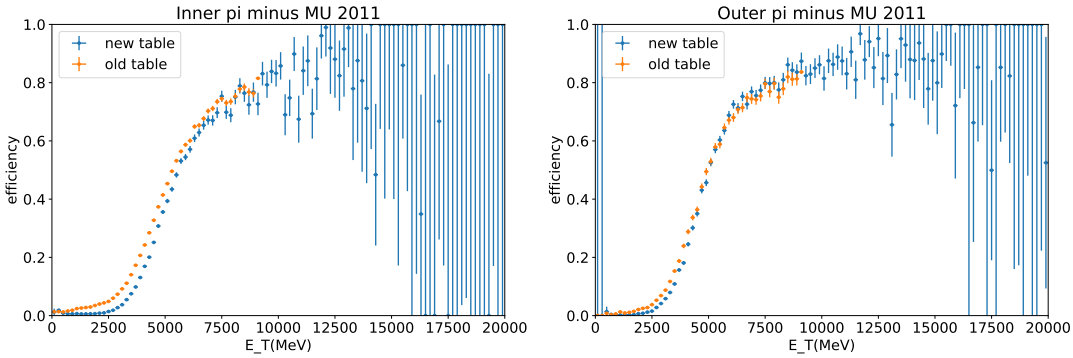

Figure B.57: Plots of the old and new efficiency tables for π^-, 2011, MU.

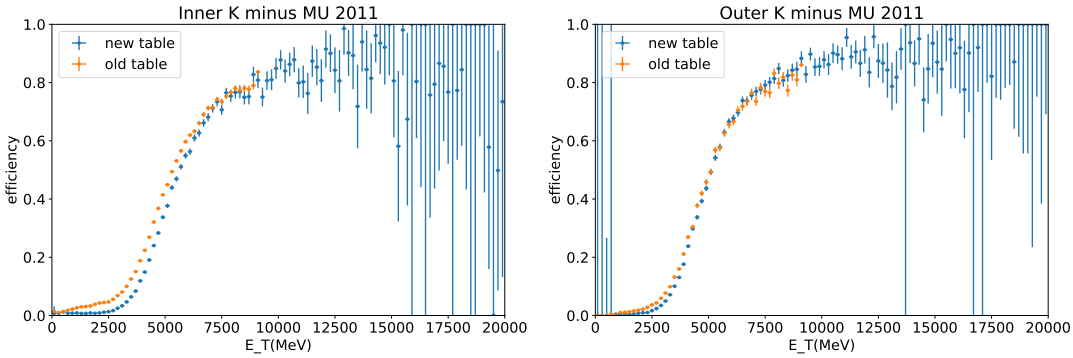

Figure B.58: Plots of the old and new efficiency tables for K^-, 2011, MU.

possible explanation is that the R_K events used ($B^+ \to (J/\psi \to e^\pm e^\mp, \mu^\pm \mu^\mp) K^+$) by including only one signal hadron could be less affected by overlap effects than the calibration events used to build the efficiency tables. In all cases, the efficiency table given by the new L0Hadron correction method is fixing the majority of the previous table issues with respect to the R_K data (the previous table is almost everywhere inconsistent with R_K).

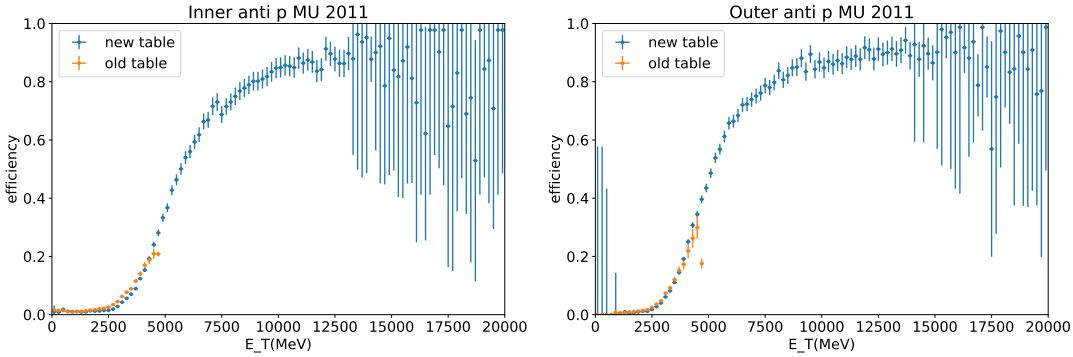

Figure B.59: Plots of the old and new efficiency tables for $\bar{p}$, 2011, MU.

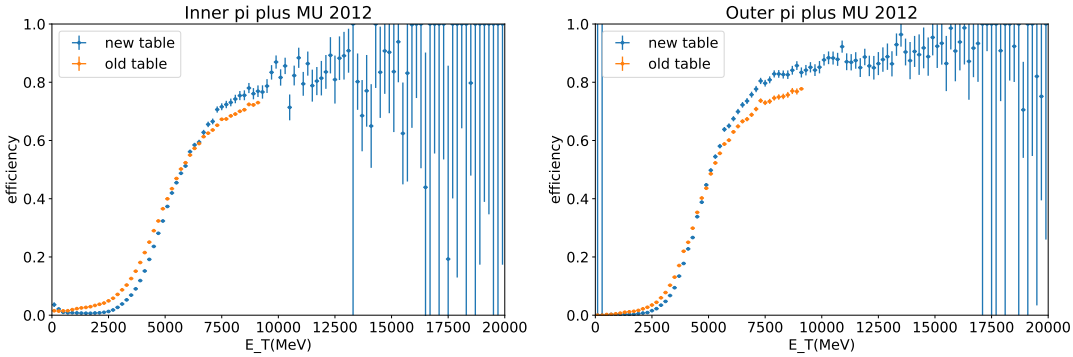

Figure B.60: Plots of the old and new efficiency tables for π^+, 2012, MU.

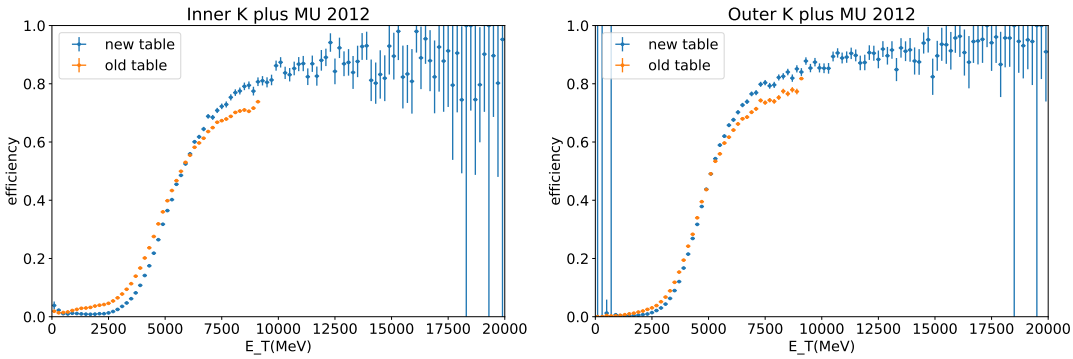

Figure B.61: Plots of the old and new efficiency tables for K^+, 2012, MU.

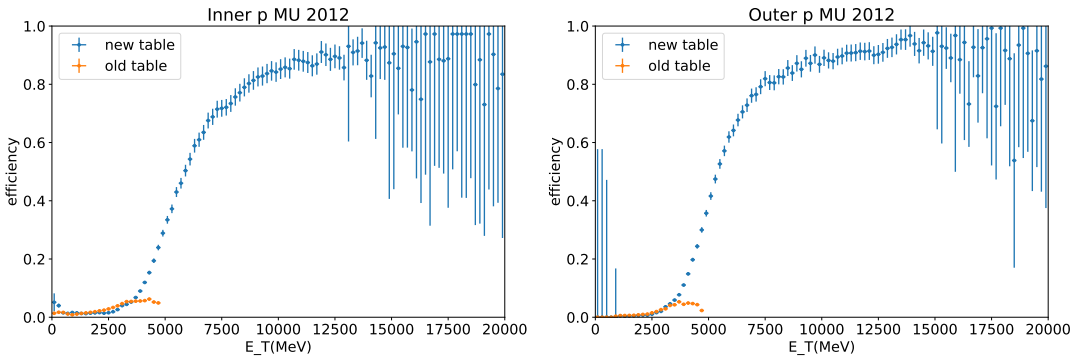

Figure B.62: Plots of the old and new efficiency tables for p, 2012, MU.

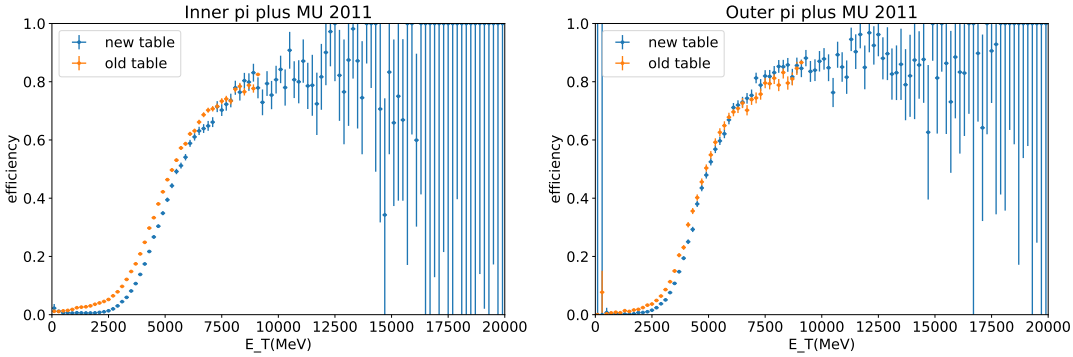

Figure B.63: Plots of the old and new efficiency tables for π^+, 2011, MU.

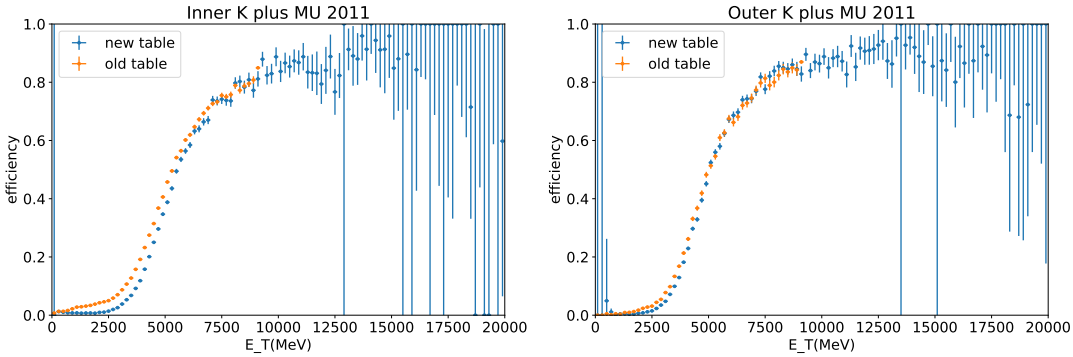

Figure B.64: Plots of the old and new efficiency tables for K^+, 2011, MU.

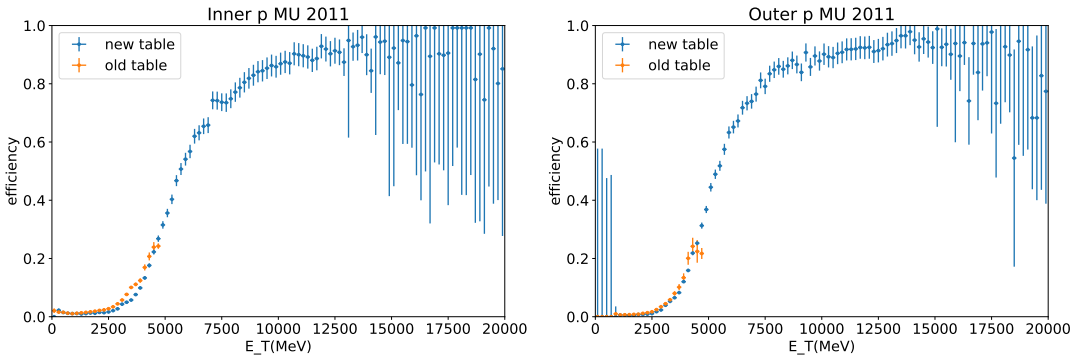

Figure B.65: Plots of the old and new efficiency tables for p, 2011, MU.

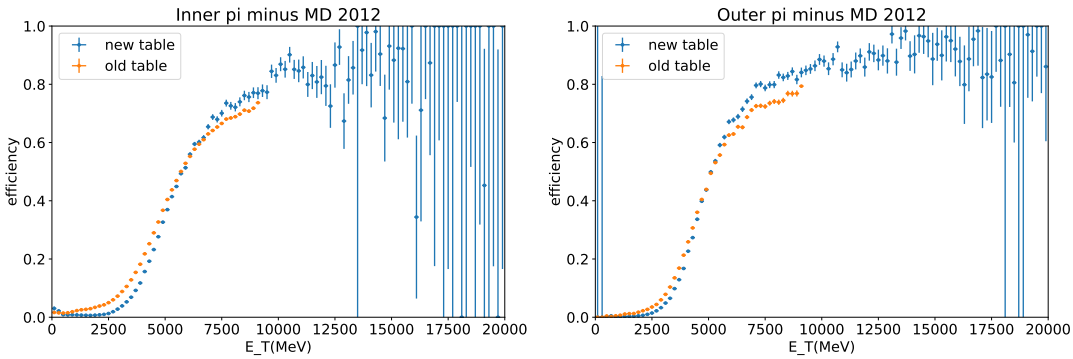

Figure B.66: Plots of the old and new efficiency tables for π^-, 2012, MD.

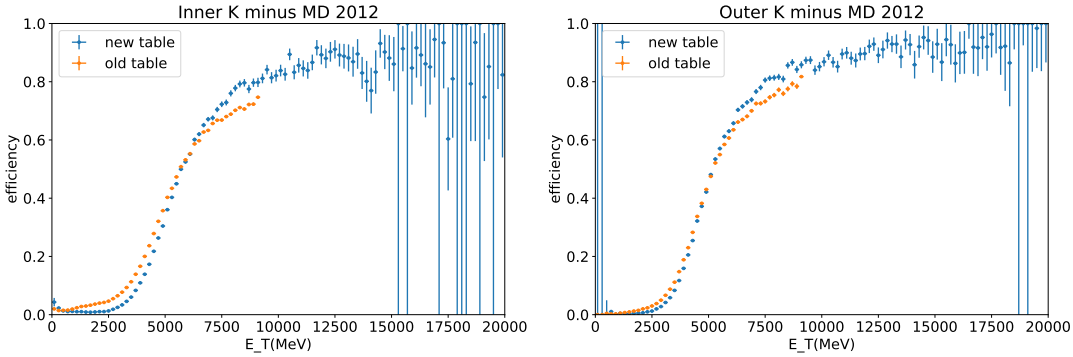

Figure B.67: Plots of the old and new efficiency tables for K^-, 2012, MD.

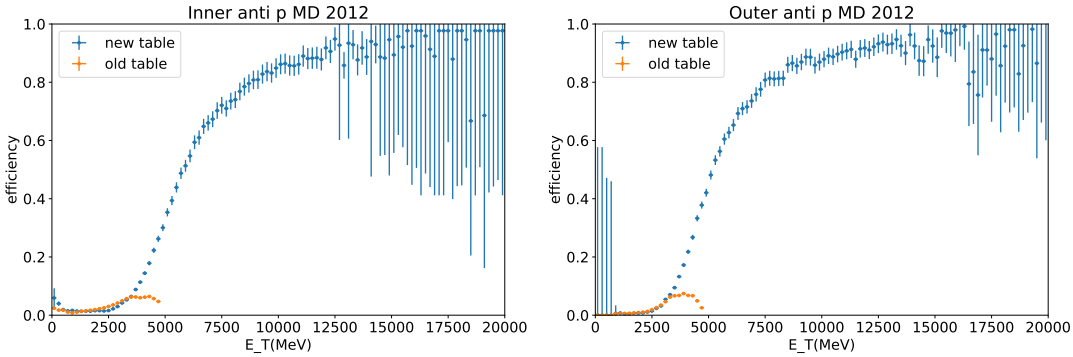

Figure B.68: Plots of the old and new efficiency tables for $\bar{p}$, 2012, MD.

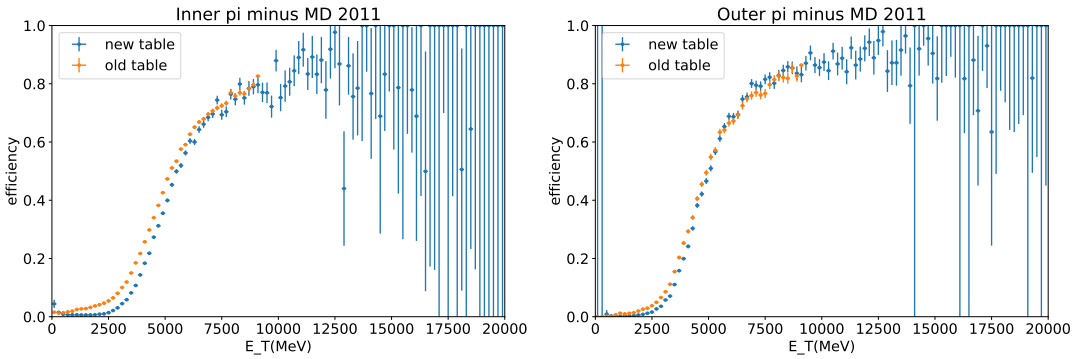

Figure B.69: Plots of the old and new efficiency tables for π^-, 2011, MD.

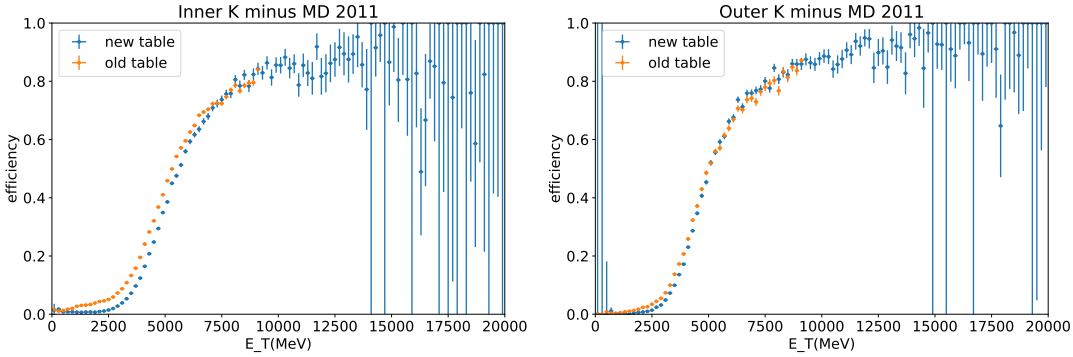

Figure B.70: Plots of the old and new efficiency tables for K^-, 2011, MD.

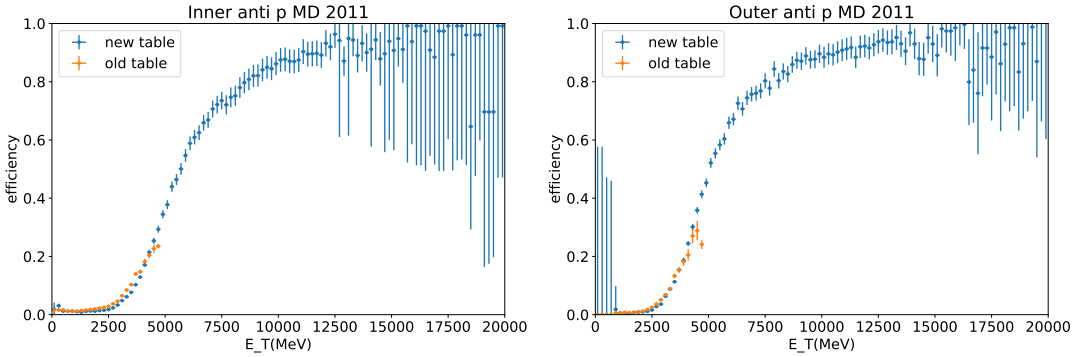

Figure B.71: Plots of the old and new efficiency tables for $\bar{p}$, 2011, MD.

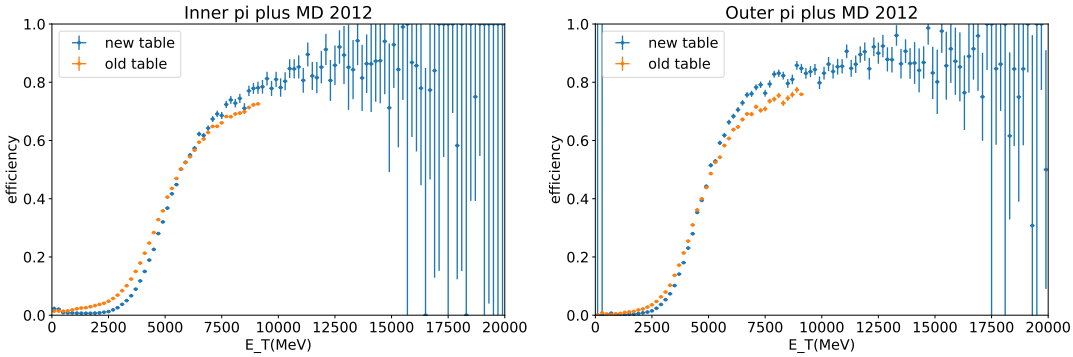

Figure B.72: Plots of the old and new efficiency tables for π^+, 2012, MD.

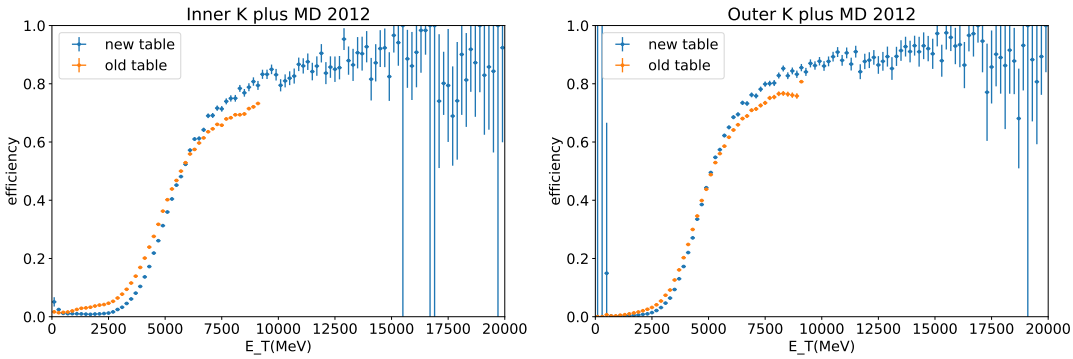

Figure B.73: Plots of the old and new efficiency tables for K^+, 2012, MD.

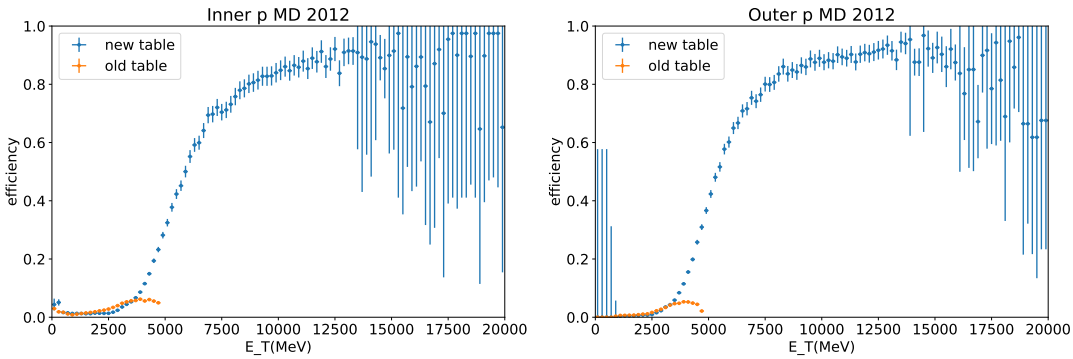

Figure B.74: Plots of the old and new efficiency tables for p, 2012, MD.

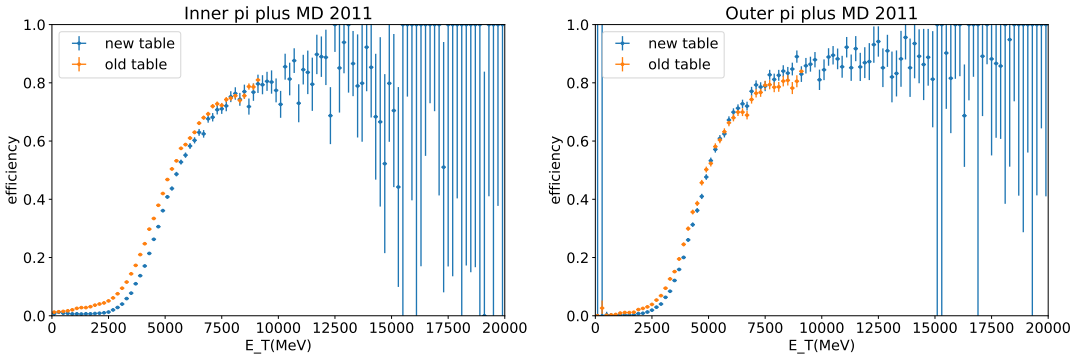

Figure B.75: Plots of the old and new efficiency tables for π^+, 2011, MD.

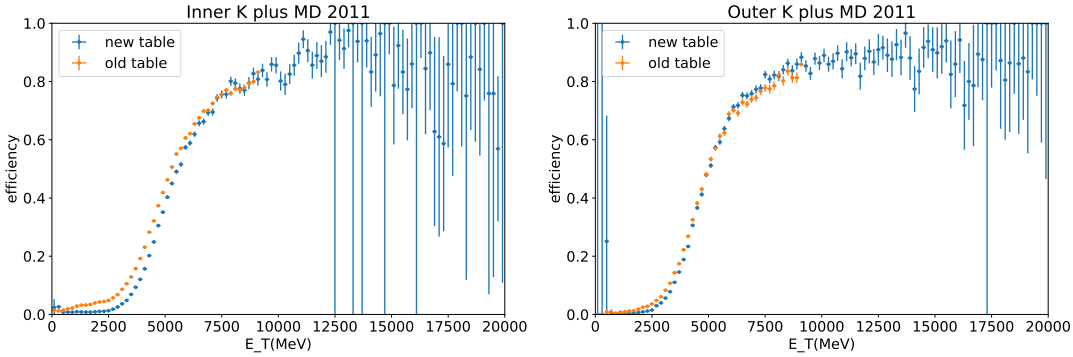

Figure B.76: Plots of the old and new efficiency tables for K^+, 2011, MD.

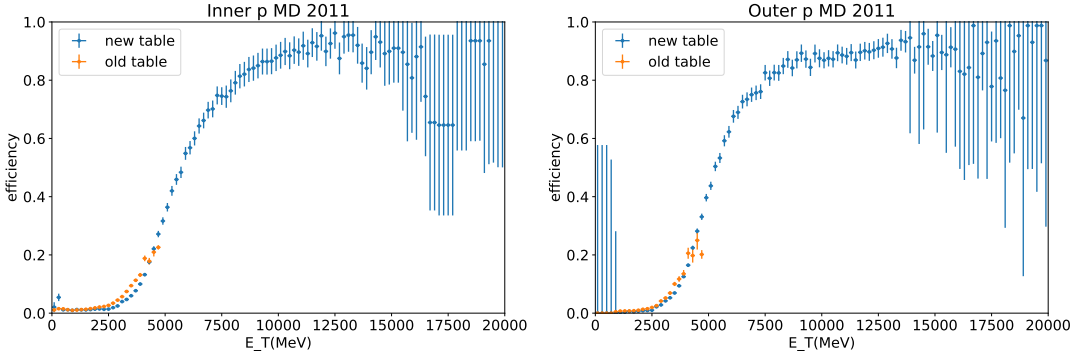

Figure B.77: Plots of the old and new efficiency tables for p, 2011, MD.

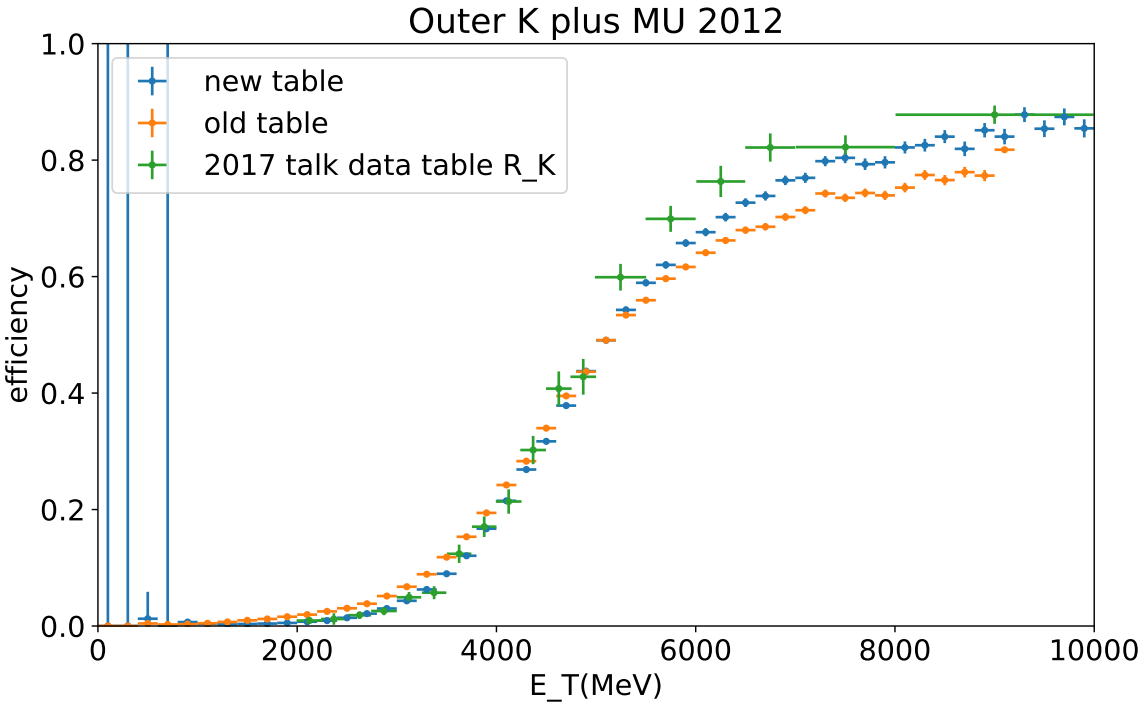

Figure B.78: Plot of the efficiency table given by the R_K data (green) together with the ones from the previous (orange) and the current (blue) L0Hadron correction method.

B.7 $b\bar{b}$ average occupancy maps

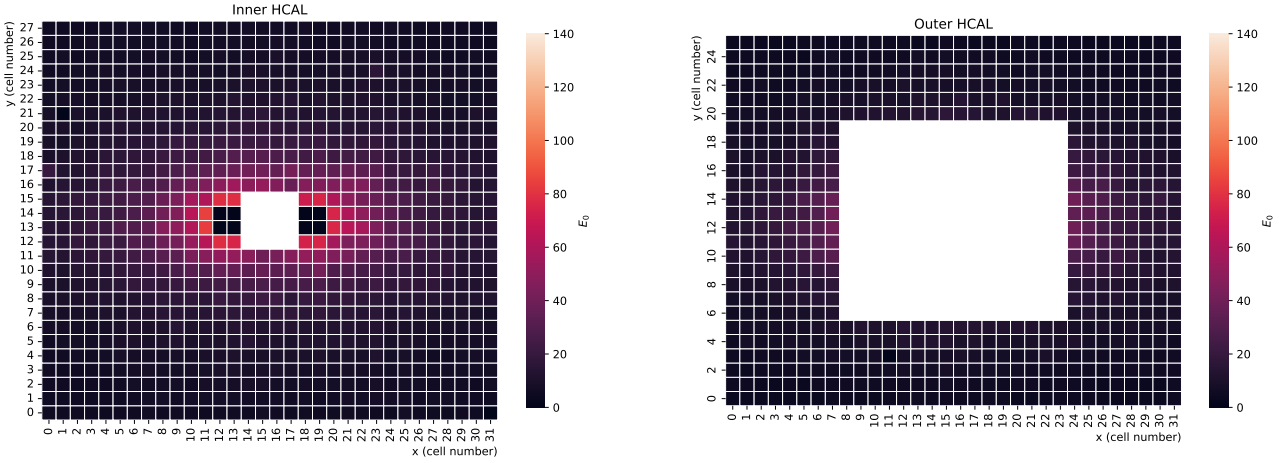

Figure B.79: Average occupancy maps build for Run II MD from $b\bar{b}$ events.

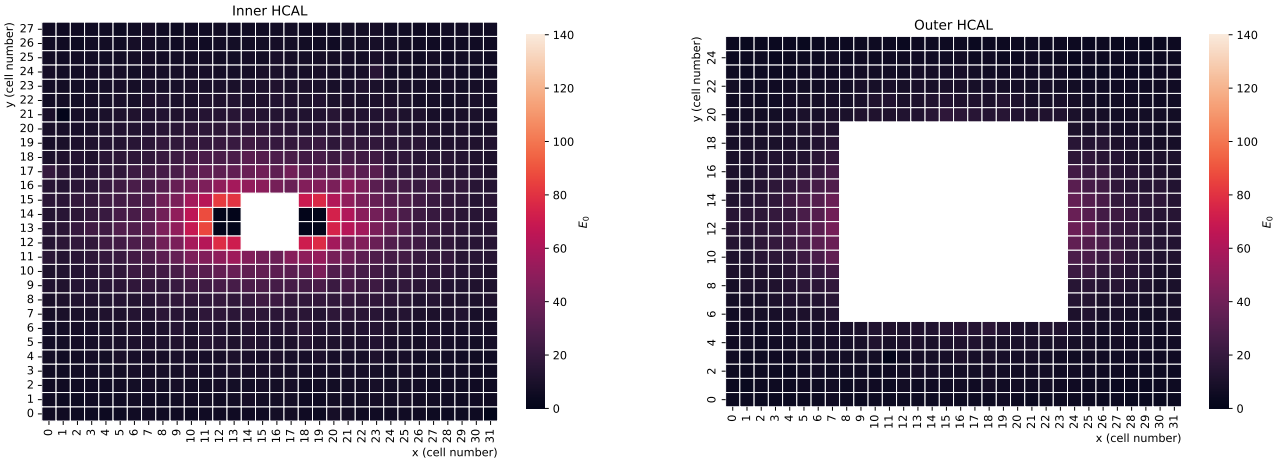

Figure B.80: Average occupancy maps build for Run II MU from $b\bar{b}$ events.

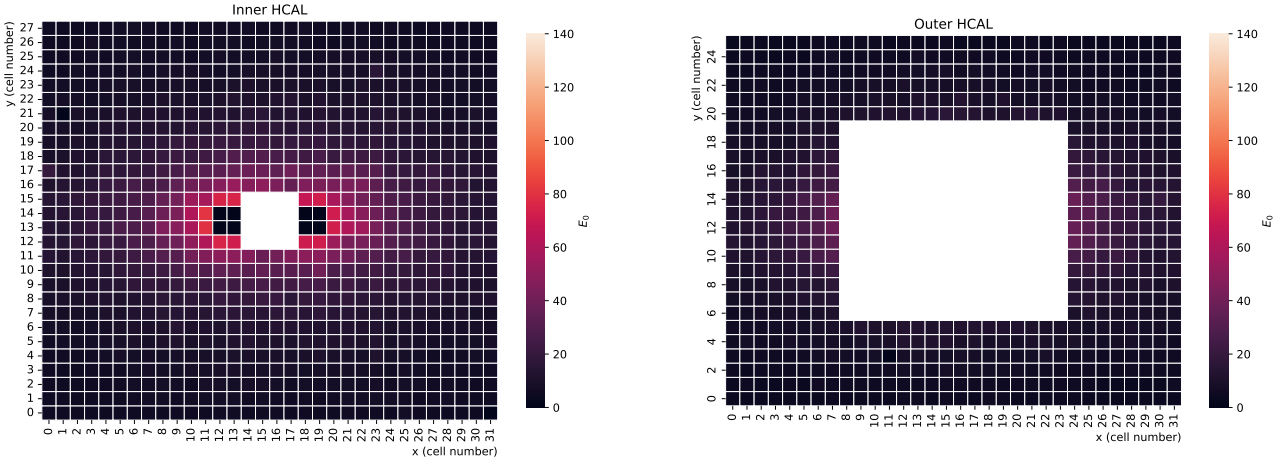

Figure B.81: Average occupancy maps build for 2012 MD from $b\bar{b}$ events.

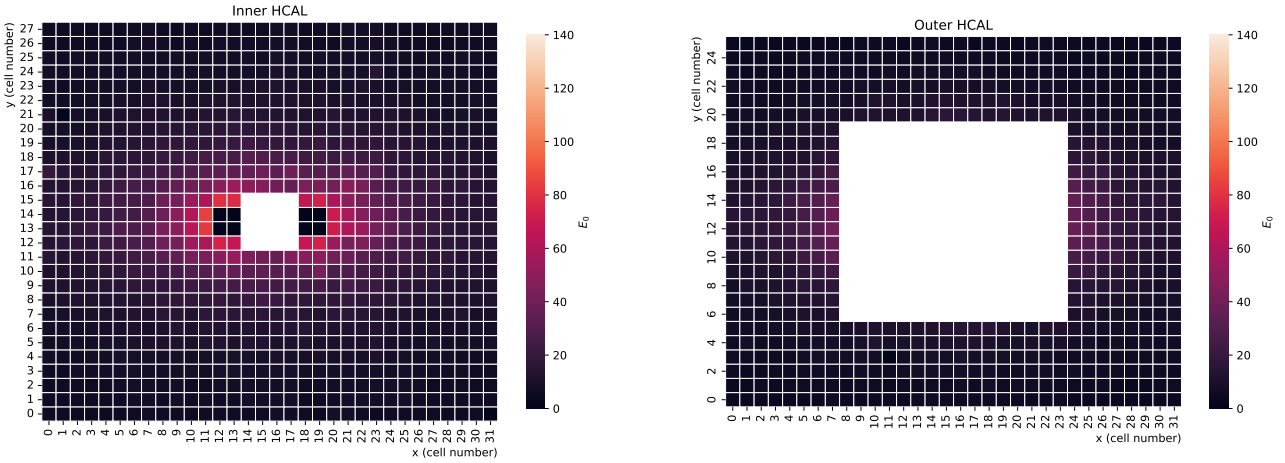

Figure B.82: Average occupancy maps build for 2012 MU from $b\bar{b}$ events.

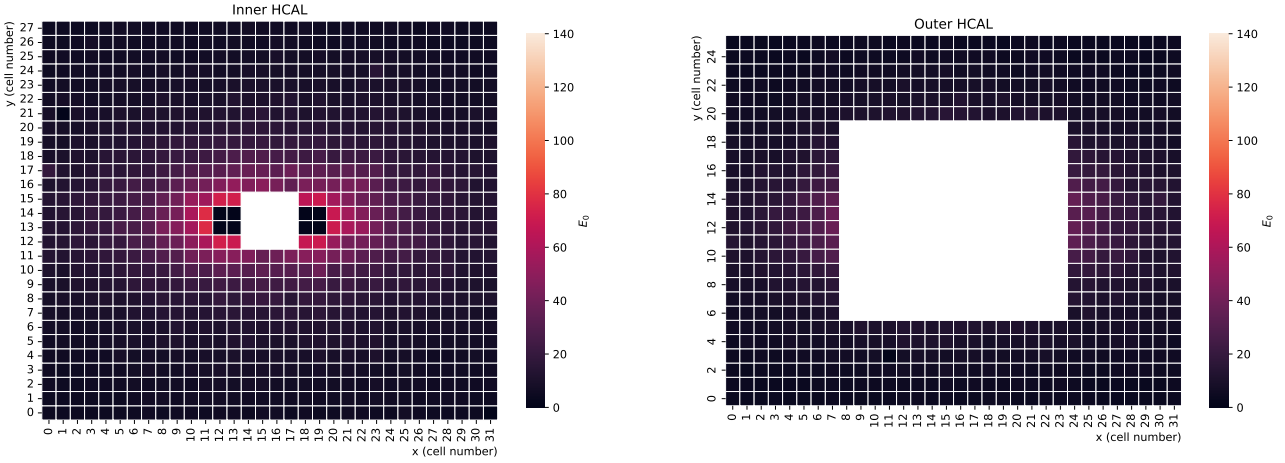

Figure B.83: Average occupancy maps build for 2011 MD from $b\bar{b}$ events.

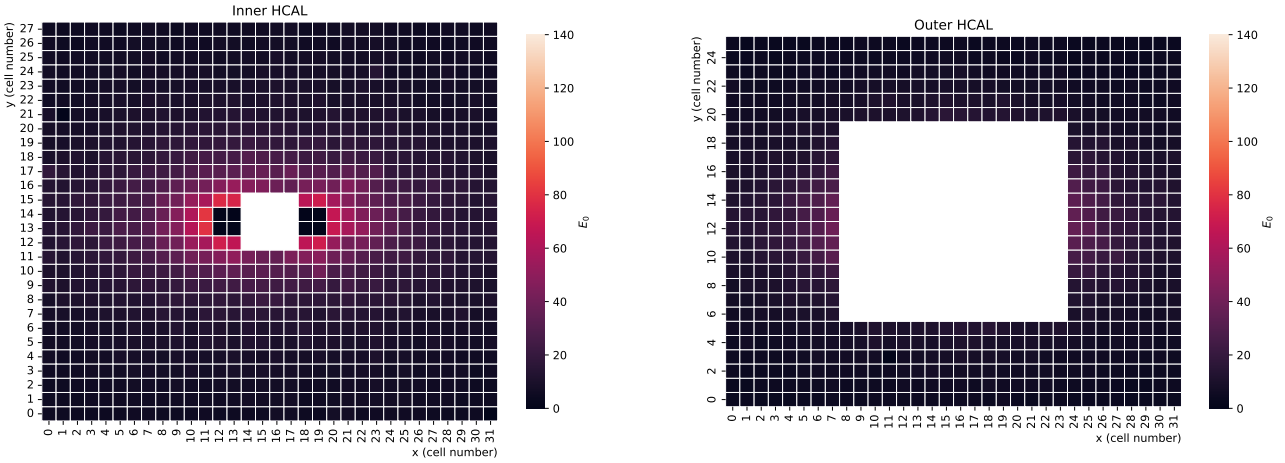

Figure B.84: Average occupancy maps build for 2011 MU.

Appendix C

Appendix to Chapter 3

C.1 MC fit results

C.1.1 Signal

Parameters

Year	2011	2012a	2012b	2015	2016	2017	2018
$f(\pi\pi)$	$0.53_{\pm 0.06}$	$0.50_{\pm 0.07}$	$0.43_{\pm 0.13}$	$0.47_{\pm 0.04}$	$0.529_{\pm 0.024}$	$0.50_{\pm 0.06}$	$0.445_{\pm 0.035}$
$n_0(\pi\pi)$	$1.70_{\pm 0.07}$	$2.01_{\pm 0.11}$	$2.02_{\pm 0.19}$	$1.84_{\pm 0.05}$	$1.81_{\pm 0.04}$	$1.83_{\pm 0.06}$	$1.81_{\pm 0.05}$
$\alpha_0(\pi\pi)$	$1.46_{\pm 0.08}$	$1.30_{\pm 0.10}$	$1.22_{\pm 0.23}$	$1.30_{\pm 0.06}$	$1.377_{\pm 0.033}$	$1.32_{\pm 0.08}$	$1.27_{\pm 0.06}$
$n_1/n_0(\pi\pi)$	$1.95_{\pm 0.15}$	$1.86_{\pm 0.17}$	$1.63_{\pm 0.22}$	$1.46_{\pm 0.06}$	$1.52_{\pm 0.05}$	$1.48_{\pm 0.08}$	$1.40_{\pm 0.06}$
$\alpha_1/\alpha_0(\pi\pi)$	$-1.27_{\pm 0.11}$	$-1.38_{\pm 0.16}$	$-1.6_{\pm 0.4}$	$-1.43_{\pm 0.09}$	$-1.31_{\pm 0.05}$	$-1.38_{\pm 0.13}$	$-1.53_{\pm 0.09}$
$f(KK)$	$0.45_{\pm 0.06}$	$0.59_{\pm 0.12}$	$0.41_{\pm 0.14}$	$0.45_{\pm 0.04}$	$0.53_{\pm 0.08}$	$0.42_{\pm 0.06}$	$0.49_{\pm 0.05}$
$n_0(KK)$	$1.94_{\pm 0.09}$	$1.84_{\pm 0.10}$	$1.94_{\pm 0.13}$	$2.00_{\pm 0.05}$	$1.98_{\pm 0.05}$	$1.95_{\pm 0.06}$	$1.94_{\pm 0.06}$
$\alpha_0(KK)$	$1.52_{\pm 0.09}$	$1.72_{\pm 0.12}$	$1.49_{\pm 0.22}$	$1.47_{\pm 0.05}$	$1.55_{\pm 0.09}$	$1.46_{\pm 0.08}$	$1.55_{\pm 0.06}$
$n_1/n_0(KK)$	$1.17_{\pm 0.08}$	$1.45_{\pm 0.14}$	$1.62_{\pm 0.20}$	$1.54_{\pm 0.07}$	$1.24_{\pm 0.06}$	$1.39_{\pm 0.07}$	$1.32_{\pm 0.06}$
$\alpha_1/\alpha_0(KK)$	$-1.37_{\pm 0.11}$	$-1.15_{\pm 0.16}$	$-1.32_{\pm 0.28}$	$-1.30_{\pm 0.07}$	$-1.24_{\pm 0.12}$	$-1.38_{\pm 0.11}$	$-1.30_{\pm 0.08}$
$f(K\pi)$	$0.47_{\pm 0.05}$	$0.39_{\pm 0.05}$	$0.50_{\pm 0.13}$	$0.45_{\pm 0.04}$	$0.49_{\pm 0.05}$	$0.46_{\pm 0.07}$	$0.48_{\pm 0.04}$
$n_0(K\pi)$	$1.96_{\pm 0.08}$	$2.15_{\pm 0.13}$	$1.86_{\pm 0.11}$	$1.88_{\pm 0.05}$	$1.86_{\pm 0.05}$	$1.75_{\pm 0.06}$	$1.82_{\pm 0.05}$
$\alpha_0(K\pi)$	$1.37_{\pm 0.08}$	$1.26_{\pm 0.10}$	$1.50_{\pm 0.17}$	$1.38_{\pm 0.06}$	$1.43_{\pm 0.07}$	$1.46_{\pm 0.10}$	$1.43_{\pm 0.06}$
$n_1/n_0(K\pi)$	$1.95_{\pm 0.15}$	$1.97_{\pm 0.19}$	$1.88_{\pm 0.22}$	$1.68_{\pm 0.07}$	$1.58_{\pm 0.07}$	$1.66_{\pm 0.10}$	$1.66_{\pm 0.08}$
$\alpha_1/\alpha_0(K\pi)$	$-1.35_{\pm 0.11}$	$-1.47_{\pm 0.15}$	$-1.26_{\pm 0.24}$	$-1.35_{\pm 0.08}$	$-1.31_{\pm 0.10}$	$-1.31_{\pm 0.14}$	$-1.31_{\pm 0.08}$
$\sigma_r(B_s^0)$	$1.008_{\pm 0.004}$	$1.011_{\pm 0.005}$	$1.018_{\pm 0.005}$	$1.0181_{\pm 0.0027}$	$1.0163_{\pm 0.0026}$	$1.0211_{\pm 0.0026}$	$1.0129_{\pm 0.0028}$
$\sigma_r(KK)$	$0.943_{\pm 0.006}$	$0.968_{\pm 0.008}$	$0.948_{\pm 0.007}$	$0.935_{\pm 0.004}$	$0.942_{\pm 0.004}$	$0.949_{\pm 0.004}$	$0.938_{\pm 0.004}$
$\sigma_r(K\pi)$	$0.957_{\pm 0.007}$	$0.974_{\pm 0.008}$	$0.980_{\pm 0.007}$	$0.963_{\pm 0.004}$	$0.965_{\pm 0.004}$	$0.971_{\pm 0.004}$	$0.962_{\pm 0.004}$
$\sigma_r(LL)$	$0.995_{\pm 0.004}$	$0.987_{\pm 0.005}$	$1.017_{\pm 0.005}$	$1.0038_{\pm 0.0029}$	$1.0083_{\pm 0.0028}$	$1.0066_{\pm 0.0028}$	$0.9996_{\pm 0.0031}$

Table C.1: Values of the shape parameters for the signal peaks, extracted from fits to MC samples using the PrincipalPeak optimisation.

Year	2011	2012a	2012b	2015	2016	2017	2018
$f(\pi\pi)$	$0.47_{\pm 0.10}$	$0.49_{\pm 0.10}$	$0.37_{\pm 0.09}$	$0.40_{\pm 0.04}$	$0.52_{\pm 0.05}$	$0.44_{\pm 0.15}$	$0.41_{\pm 0.04}$
$n_0(\pi\pi)$	$1.72_{\pm 0.11}$	$2.19_{\pm 0.17}$	$2.09_{\pm 0.19}$	$2.01_{\pm 0.09}$	$1.88_{\pm 0.06}$	$1.97_{\pm 0.19}$	$1.89_{\pm 0.08}$
$\alpha_0(\pi\pi)$	$1.42_{\pm 0.15}$	$1.24_{\pm 0.14}$	$1.12_{\pm 0.18}$	$1.17_{\pm 0.08}$	$1.36_{\pm 0.06}$	$1.21_{\pm 0.25}$	$1.22_{\pm 0.08}$
$n_1/n_0(\pi\pi)$	$2.19_{\pm 0.30}$	$2.5_{\pm 0.4}$	$1.82_{\pm 0.26}$	$1.59_{\pm 0.11}$	$1.70_{\pm 0.10}$	$1.53_{\pm 0.21}$	$1.46_{\pm 0.09}$
$\alpha_1/\alpha_0(\pi\pi)$	$-1.39_{\pm 0.22}$	$-1.38_{\pm 0.23}$	$-1.69_{\pm 0.35}$	$-1.64_{\pm 0.15}$	$-1.31_{\pm 0.09}$	$-1.5_{\pm 0.4}$	$-1.62_{\pm 0.13}$
$f(KK)$	$0.51_{\pm 0.08}$	$0.54_{\pm 0.11}$	$0.40_{\pm 0.08}$	$0.45_{\pm 0.05}$	$0.49_{\pm 0.05}$	$0.49_{\pm 0.09}$	$0.50_{\pm 0.07}$
$n_0(KK)$	$1.87_{\pm 0.09}$	$1.82_{\pm 0.11}$	$1.92_{\pm 0.11}$	$2.11_{\pm 0.08}$	$2.01_{\pm 0.07}$	$1.91_{\pm 0.07}$	$1.98_{\pm 0.08}$
$\alpha_0(KK)$	$1.62_{\pm 0.10}$	$1.69_{\pm 0.11}$	$1.49_{\pm 0.13}$	$1.48_{\pm 0.06}$	$1.54_{\pm 0.07}$	$1.60_{\pm 0.10}$	$1.58_{\pm 0.08}$
$n_1/n_0(KK)$	$1.17_{\pm 0.10}$	$1.55_{\pm 0.16}$	$1.85_{\pm 0.18}$	$1.54_{\pm 0.09}$	$1.45_{\pm 0.08}$	$1.60_{\pm 0.12}$	$1.48_{\pm 0.10}$
$\alpha_1/\alpha_0(KK)$	$-1.29_{\pm 0.13}$	$-1.18_{\pm 0.14}$	$-1.28_{\pm 0.16}$	$-1.31_{\pm 0.08}$	$-1.25_{\pm 0.08}$	$-1.26_{\pm 0.14}$	$-1.25_{\pm 0.10}$
$f(K\pi)$	$0.44_{\pm 0.05}$	$0.40_{\pm 0.05}$	$0.56_{\pm 0.14}$	$0.44_{\pm 0.04}$	$0.47_{\pm 0.04}$	$0.45_{\pm 0.06}$	$0.48_{\pm 0.05}$
$n_0(K\pi)$	$1.96_{\pm 0.09}$	$2.17_{\pm 0.12}$	$1.80_{\pm 0.10}$	$1.89_{\pm 0.06}$	$1.84_{\pm 0.05}$	$1.82_{\pm 0.06}$	$1.83_{\pm 0.06}$
$\alpha_0(K\pi)$	$1.33_{\pm 0.08}$	$1.28_{\pm 0.09}$	$1.59_{\pm 0.15}$	$1.37_{\pm 0.06}$	$1.44_{\pm 0.06}$	$1.42_{\pm 0.09}$	$1.43_{\pm 0.08}$
$n_1/n_0(K\pi)$	$2.13_{\pm 0.20}$	$1.94_{\pm 0.20}$	$2.13_{\pm 0.28}$	$1.87_{\pm 0.10}$	$1.73_{\pm 0.08}$	$1.73_{\pm 0.10}$	$1.76_{\pm 0.10}$
$\alpha_1/\alpha_0(K\pi)$	$-1.40_{\pm 0.12}$	$-1.47_{\pm 0.13}$	$-1.16_{\pm 0.21}$	$-1.38_{\pm 0.09}$	$-1.30_{\pm 0.08}$	$-1.33_{\pm 0.12}$	$-1.32_{\pm 0.10}$
$\sigma_r(B_s^0)$	$1.004_{\pm 0.005}$	$1.013_{\pm 0.006}$	$1.012_{\pm 0.005}$	$1.0175_{\pm 0.0034}$	$1.0169_{\pm 0.0033}$	$1.0237_{\pm 0.0033}$	$1.0126_{\pm 0.0034}$
$\sigma_r(KK)$	$0.942_{\pm 0.008}$	$0.974_{\pm 0.010}$	$0.954_{\pm 0.009}$	$0.943_{\pm 0.006}$	$0.944_{\pm 0.005}$	$0.933_{\pm 0.006}$	$0.940_{\pm 0.005}$
$\sigma_r(K\pi)$	$0.966_{\pm 0.008}$	$0.987_{\pm 0.010}$	$0.986_{\pm 0.009}$	$0.966_{\pm 0.006}$	$0.979_{\pm 0.005}$	$0.979_{\pm 0.005}$	$0.971_{\pm 0.005}$
$\sigma_r(LL)$	$0.992_{\pm 0.005}$	$0.988_{\pm 0.006}$	$1.009_{\pm 0.006}$	$1.012_{\pm 0.004}$	$1.013_{\pm 0.004}$	$1.009_{\pm 0.004}$	$0.999_{\pm 0.004}$

Table C.2: Values of the shape parameters for the signal peaks, extracted from fits to MC samples using the SecondaryPeak optimisation.

Plots

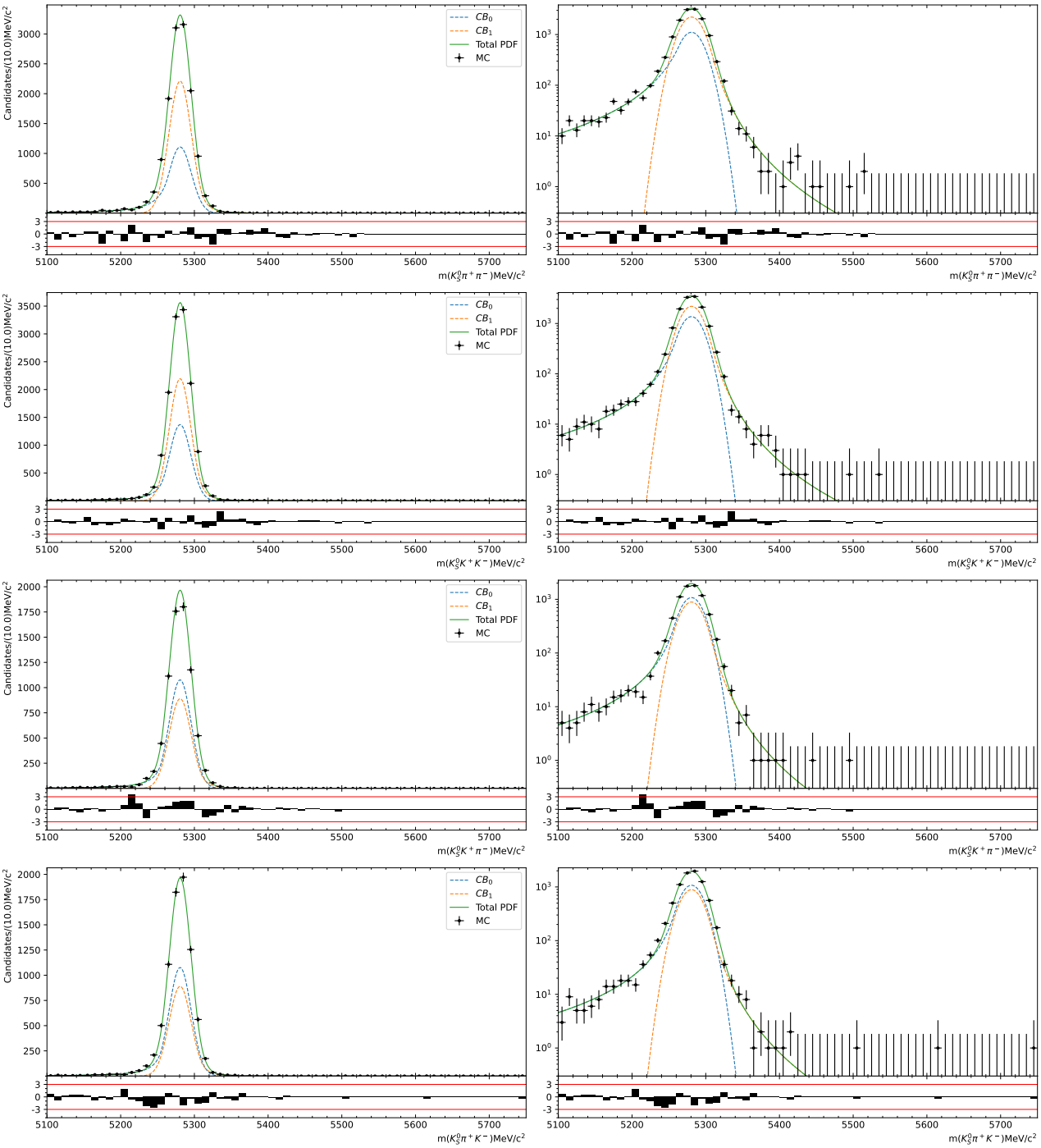

Figure C.1: Results of the fits to B^0 signal MC samples (DD, 2012b) with the SecondaryPeak optimization. The modes $K^0_S\pi^+\pi^-$, $K^0_S K^+K^-$, $K^0_S K^+\pi^-$ and $K^0_S\pi^+K^-$ are shown from top to bottom. The left-hand side plots show the results with a linear scale and the right-hand side with a logarithmic scale.

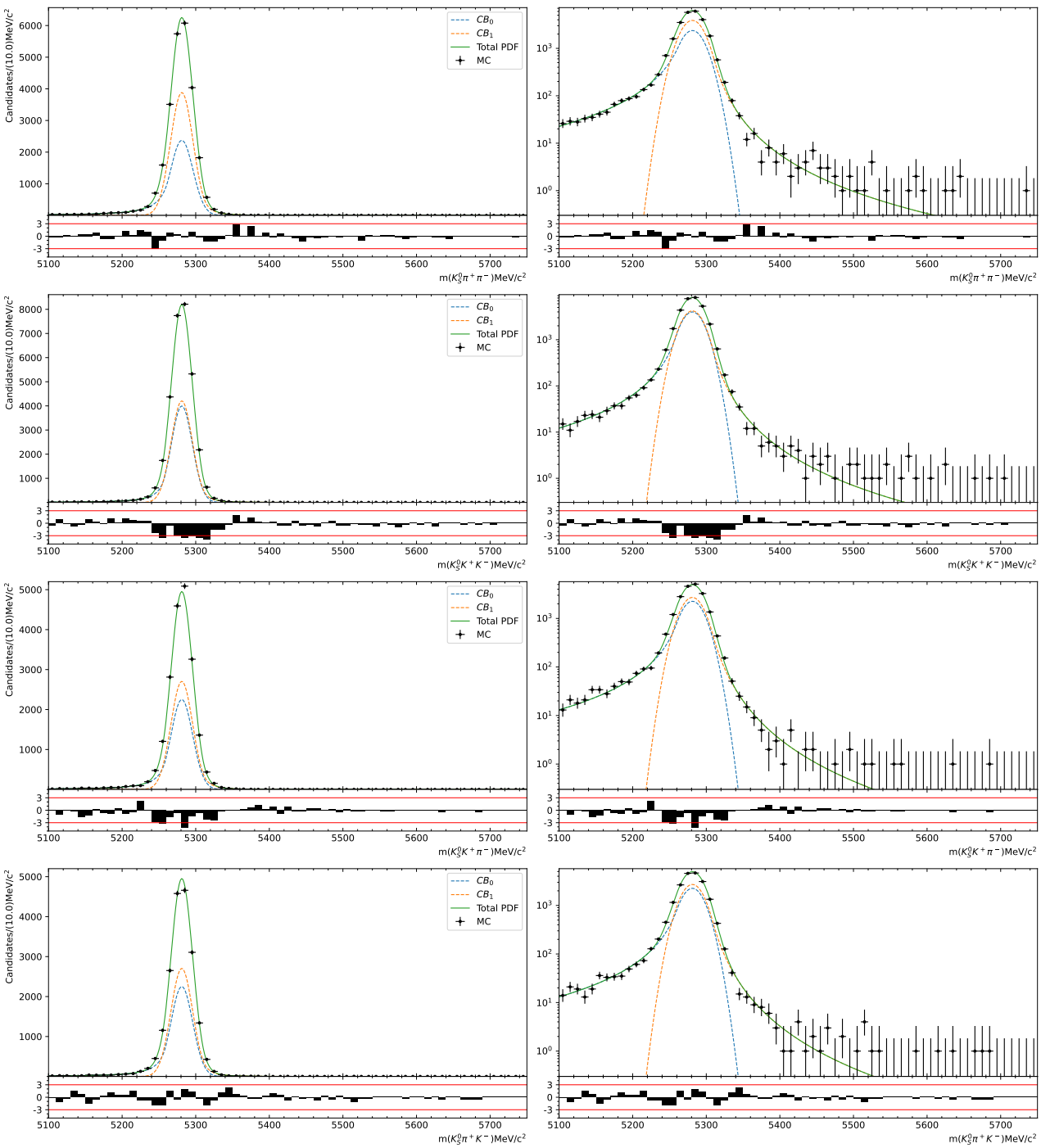

Figure C.2: Results of the fits to B^0 signal MC samples (DD, 2018) with the SecondaryPeak optimization. The modes $K^0_S\pi^+\pi^-$, $K^0_S K^+K^-$, $K^0_S K^+\pi^-$ and $K^0_S\pi^+K^-$ are shown from top to bottom. The left-hand side plots show the results with a linear scale and the right-hand side with a logarithmic scale.

C.1.2 Crossfeed

Plots

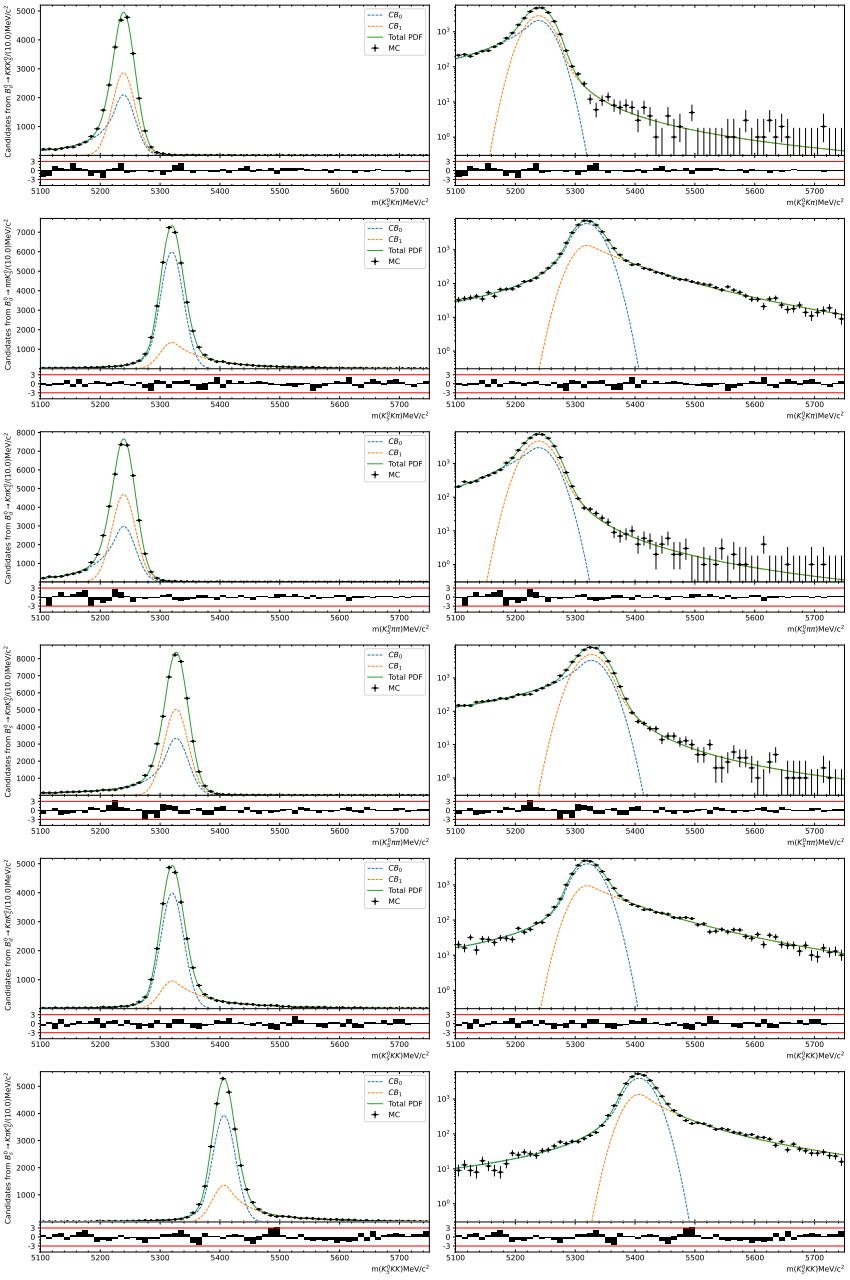

Figure C.3: Results of the fits on crossfeed MC samples with the PrincipalPeak optimization. Events from all data-taking periods and KS reconstructions are combine into one histogram for each type of crossfeed decays. From top to bottom the crossfeeds from $B^0 \to K^0_S K^+ K^-$ and $B^0 \to K^0_S \pi^+ \pi^-$ in the $K^0_S K^\pm \pi^\mp$ spectrum, $B^0 \to K^0_S K^\pm \pi^\mp$ and $B^0_s \to K^0_S K^\pm \pi^\mp$ in the $K^0_S K^\pm \pi^\mp$ spectrum, and $B^0 \to K^0_S K^\pm \pi^\mp$ and $B^0_s \to K^0_S K^\pm \pi^\mp$ in the $K^0_S K^+ K^-$ spectrum,. The left-hand side plots show the results with a linear scale and the right-hand side with a logarithmic scale.

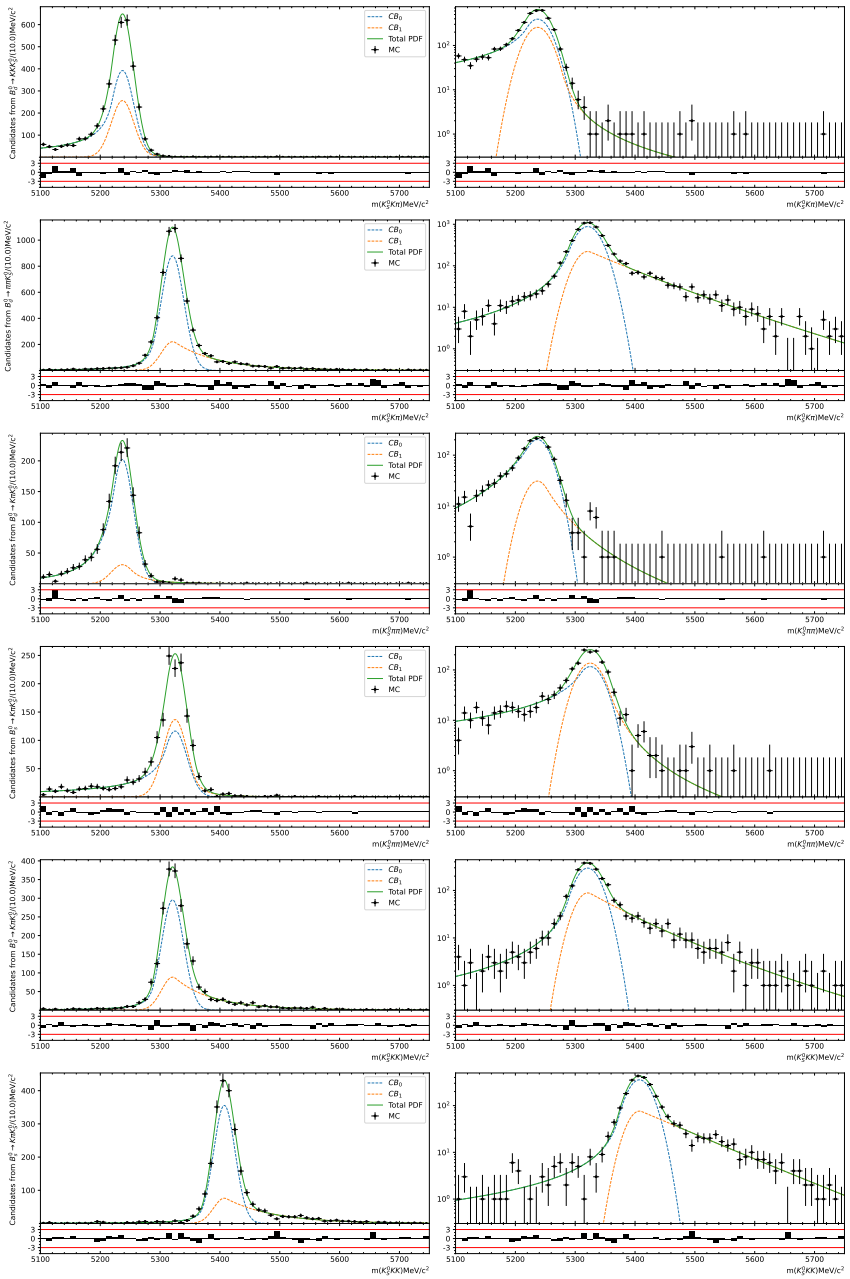

Figure C.4: Results of the fits on crossfeed MC samples with the SecondaryPeak optimization. Events from all data-taking periods and KS reconstructions are combine into one histogram for each type of crossfeed decays. From top to bottom the crossfeeds from $B^0 \to K^0_S K^+ K^-$ and $B^0 \to K^0_S \pi^+ \pi^-$ in the $K^0_S K^\pm \pi^\mp$ spectrum, $B^0 \to K^0_S K^\pm \pi^\mp$ and $B^0_s \to K^0_S K^\pm \pi^\mp$ in the $K^0_S K^\pm \pi^\mp$ spectrum, and $B^0 \to K^0_S K^\pm \pi^\mp$ and $B^0_s \to K^0_S K^\pm \pi^\mp$ in the $K^0_S K^+ K^-$ spectrum,. The left-hand side plots show the results with a linear scale and the right-hand side with a logarithmic scale.

Parameters

CF mode	$B_d^0 \to KKK_S^0 \vert K\pi$	$B_d^0 \to \pi\pi K_S^0 \vert K\pi$	$B_d^0 \to K\pi K_S^0 \vert \pi\pi$	$B_s^0 \to K\pi K_S^0 \vert \pi\pi$	$B_d^0 \to K\pi K_S^0 \vert KK$	$B_s^0 \to K\pi K_S^0 \vert KK$
α_0	$0.70_{\pm 0.17}$	$1.74_{\pm 0.04}$	$0.60_{\pm 0.07}$	$0.83_{\pm 0.08}$	$1.98_{\pm 0.04}$	$1.78_{\pm 0.08}$
α_1/α_0	$-3.2_{\pm 0.9}$	$-0.214_{\pm 0.024}$	$-3.6_{\pm 0.5}$	$-2.59_{\pm 0.31}$	$-0.184_{\pm 0.024}$	$-0.30_{\pm 0.12}$
f	$0.50_{\pm 0.08}$	$0.714_{\pm 0.017}$	$0.46_{\pm 0.04}$	$0.48_{\pm 0.04}$	$0.691_{\pm 0.020}$	$0.65_{\pm 0.07}$
μ	$5238.99_{\pm 0.24}$	$5319.66_{\pm 0.14}$	$5239.17_{\pm 0.17}$	$5326.84_{\pm 0.15}$	$5320.27_{\pm 0.17}$	$5406.84_{\pm 0.16}$
n_0	$1.79_{\pm 0.32}$	$1.57_{\pm 0.08}$	$3.4_{\pm 0.7}$	$1.52_{\pm 0.09}$	$1.30_{\pm 0.08}$	$1.52_{\pm 0.08}$
n_1/n_0	$1.03_{\pm 0.22}$	$3.0_{\pm 0.5}$	$0.68_{\pm 0.15}$	$1.37_{\pm 0.13}$	$3.2_{\pm 0.6}$	$1.6_{\pm 0.5}$
σ	$19.14_{\pm 0.18}$	$19.46_{\pm 0.15}$	$19.84_{\pm 0.14}$	$20.24_{\pm 0.13}$	$19.46_{\pm 0.16}$	$19.32_{\pm 0.19}$

Table C.3: Values of the shape parameters for the crossfeed peaks, extracted from fits to MC samples using the PrincipalPeak optimisation. Note: $A|B$ = Decay A seen as B.

CF mode	$B_d^0 \to KKK_S^0 \vert K\pi$	$B_d^0 \to \pi\pi K_S^0 \vert K\pi$	$B_d^0 \to K\pi K_S^0 \vert \pi\pi$	$B_s^0 \to K\pi K_S^0 \vert \pi\pi$	$B_d^0 \to K\pi K_S^0 \vert KK$	$B_s^0 \to K\pi K_S^0 \vert KK$
α_0	$0.95_{\pm 0.24}$	$1.65_{\pm 0.12}$	$0.78_{\pm 0.23}$	$0.8_{\pm 0.6}$	$1.75_{\pm 0.14}$	$1.97_{\pm 0.16}$
α_1/α_0	$-2.3_{\pm 0.8}$	$-0.162_{\pm 0.030}$	$-1.1_{\pm 1.5}$	$-2.0_{\pm 2.0}$	$-0.17_{\pm 0.05}$	$-0.116_{\pm 0.012}$
f	$0.67_{\pm 0.16}$	$0.668_{\pm 0.027}$	$0.87_{\pm 0.18}$	$0.57_{\pm 0.26}$	$0.64_{\pm 0.05}$	$0.683_{\pm 0.024}$
μ	$5237.3_{\pm 0.6}$	$5320.8_{\pm 0.4}$	$5236.9_{\pm 1.3}$	$5325.1_{\pm 1.0}$	$5320.9_{\pm 0.6}$	$5407.4_{\pm 0.5}$
n_0	$0.89_{\pm 0.18}$	$1.68_{\pm 0.26}$	$2.5_{\pm 1.0}$	$0.95_{\pm 0.27}$	$1.44_{\pm 0.29}$	$1.24_{\pm 0.26}$
n_1/n_0	$1.9_{\pm 0.5}$	$9_{\pm 9}$	$1.2_{\pm 1.1}$	$2.5_{\pm 1.3}$	$6_{\pm 5}$	$50_{\pm 100}$
σ	$18.9_{\pm 0.5}$	$19.0_{\pm 0.5}$	$18.6_{\pm 1.0}$	$19.9_{\pm 0.9}$	$18.6_{\pm 0.7}$	$18.1_{\pm 0.6}$

Table C.4: Values of the shape parameters for the crossfeed peaks, extracted from fits to MC samples using the SecondaryPeak optimisation.

C.2 Data fit results

C.2.1 PrincipalPeak optimisation

Plots

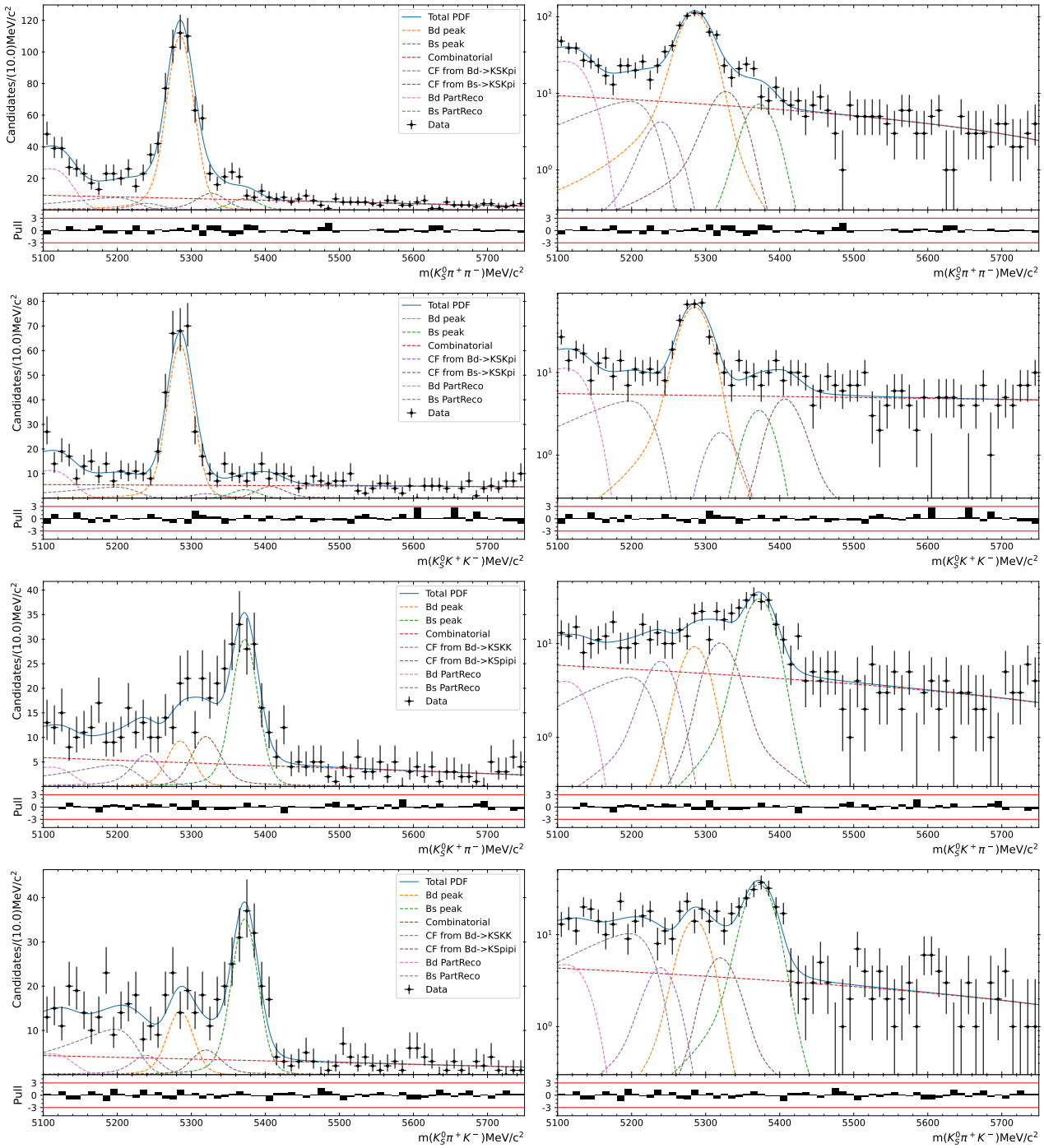

Figure C.5: Results of the simultaneous fit to data (LL, 2011) with the PrincipalPeak optimisation. The modes $K^0_S\pi^+\pi^-$, $K^0_S K^+K^-$, $K^0_S K^+\pi^-$ and $K^0_S\pi^+K^-$ are shown from top to bottom. The left-hand side plots show the results with a linear scale and the right-hand side with a logarithmic scale.

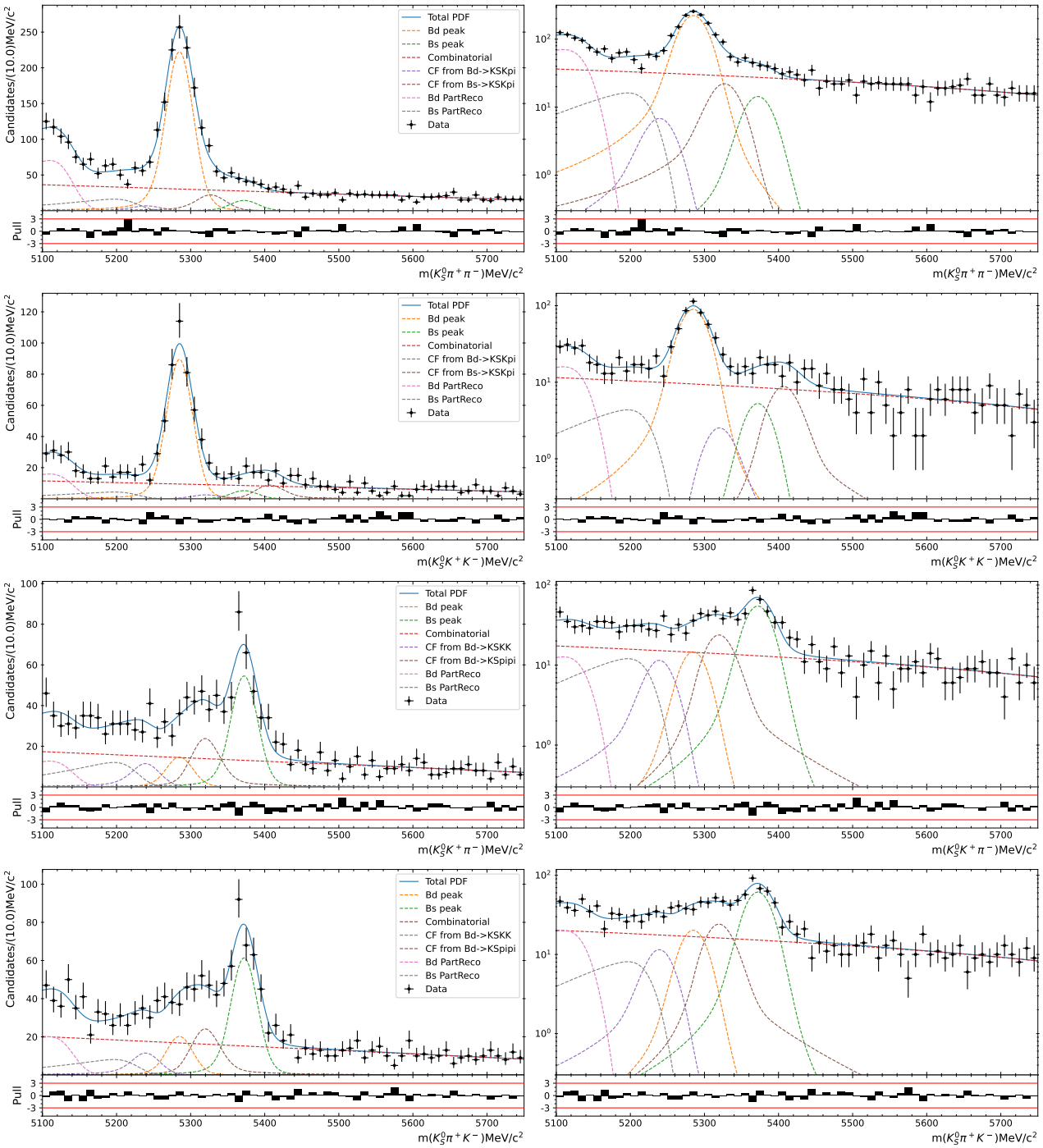

Figure C.6: Results of the simultaneous fit to data (DD, 2011) with the PrincipalPeak optimisation. The modes $K^0_S\pi^+\pi^-$, $K^0_SK^+K^-$, $K^0_SK^+\pi^-$ and $K^0_S\pi^+K^-$ are shown from top to bottom. The left-hand side plots show the results with a linear scale and the right-hand side with a logarithmic scale.

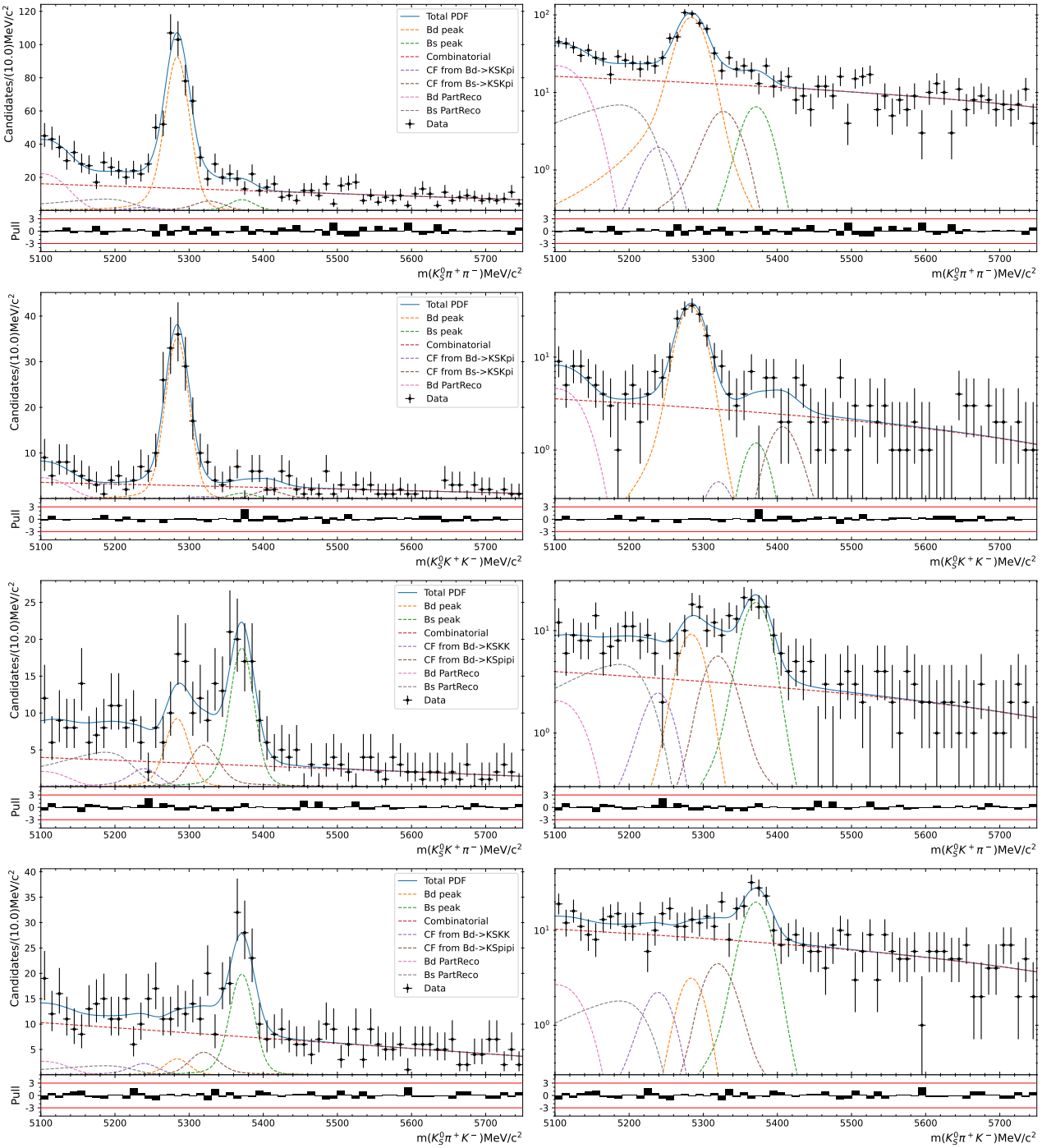

Figure C.7: Results of the simultaneous fit to data (LL, 2012a) with the PrincipalPeak optimisation. The modes $K^0_S\pi^+\pi^-$, $K^0_SK^+K^-$, $K^0_SK^+\pi^-$ and $K^0_S\pi^+K^-$ are shown from top to bottom. The left-hand side plots show the results with a linear scale and the right-hand side with a logarithmic scale.

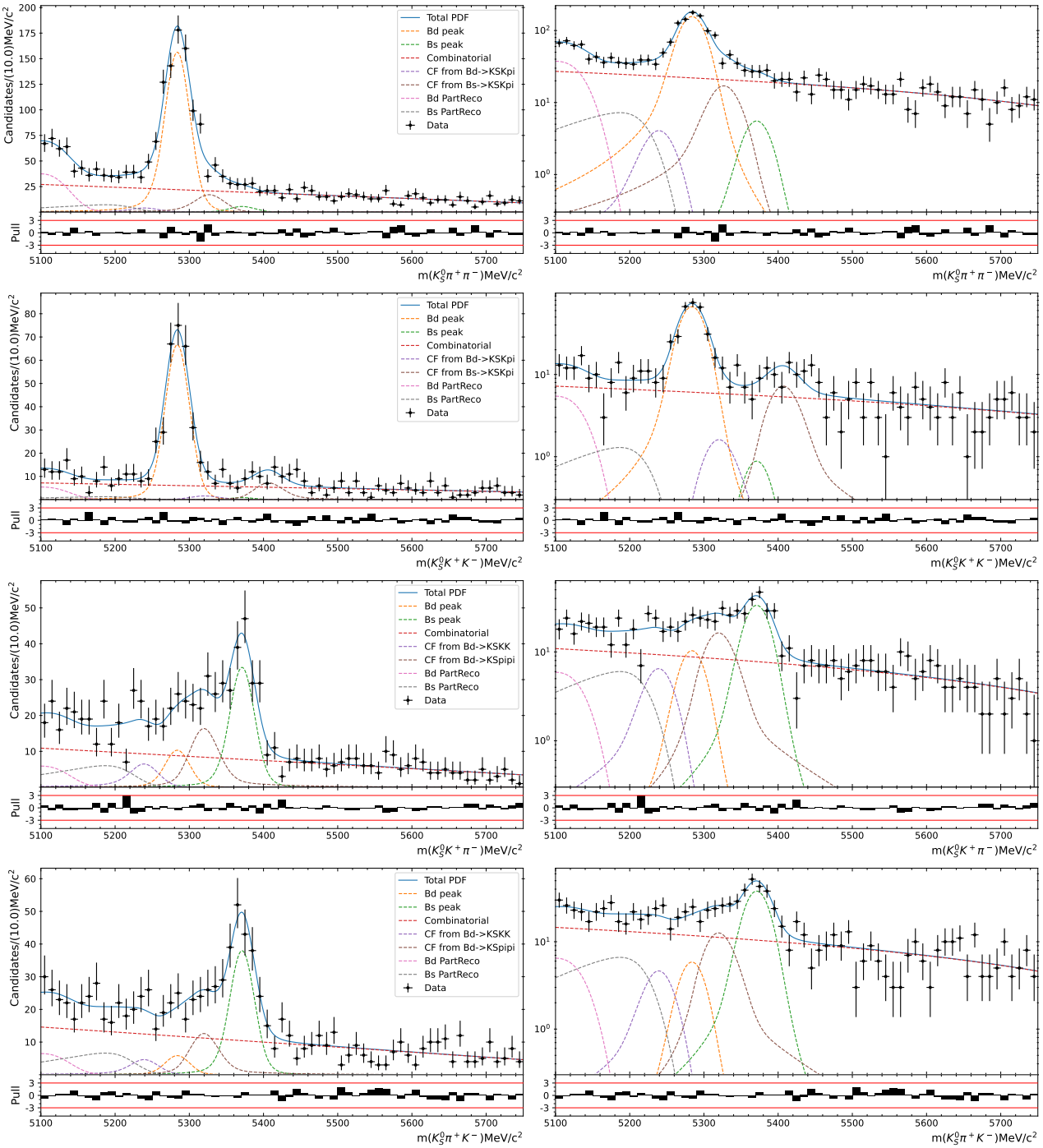

Figure C.8: Results of the simultaneous fit to data (DD, 2012a) with the PrincipalPeak optimisation. The modes $K^0_S\pi^+\pi^-$, $K^0_SK^+K^-$, $K^0_SK^+\pi^-$ and $K^0_S\pi^+K^-$ are shown from top to bottom. The left-hand side plots show the results with a linear scale and the right-hand side with a logarithmic scale.

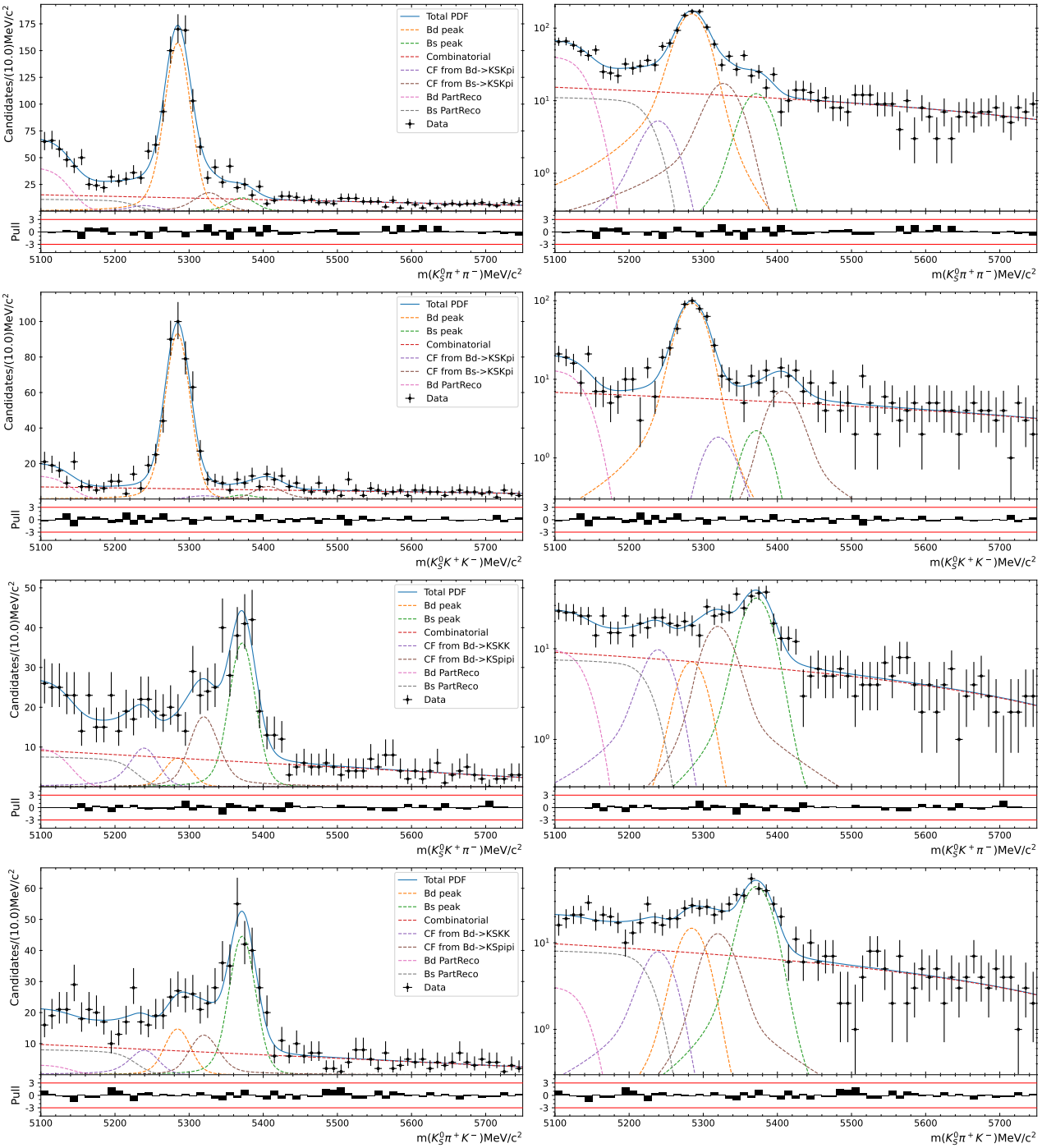

Figure C.9: Results of the simultaneous fit to data (LL, 2012b) with the PrincipalPeak optimisation. The modes $K^0_S\pi^+\pi^-$, $K^0_SK^+K^-$, $K^0_SK^+\pi^-$ and $K^0_S\pi^+K^-$ are shown from top to bottom. The left-hand side plots show the results with a linear scale and the right-hand side with a logarithmic scale.

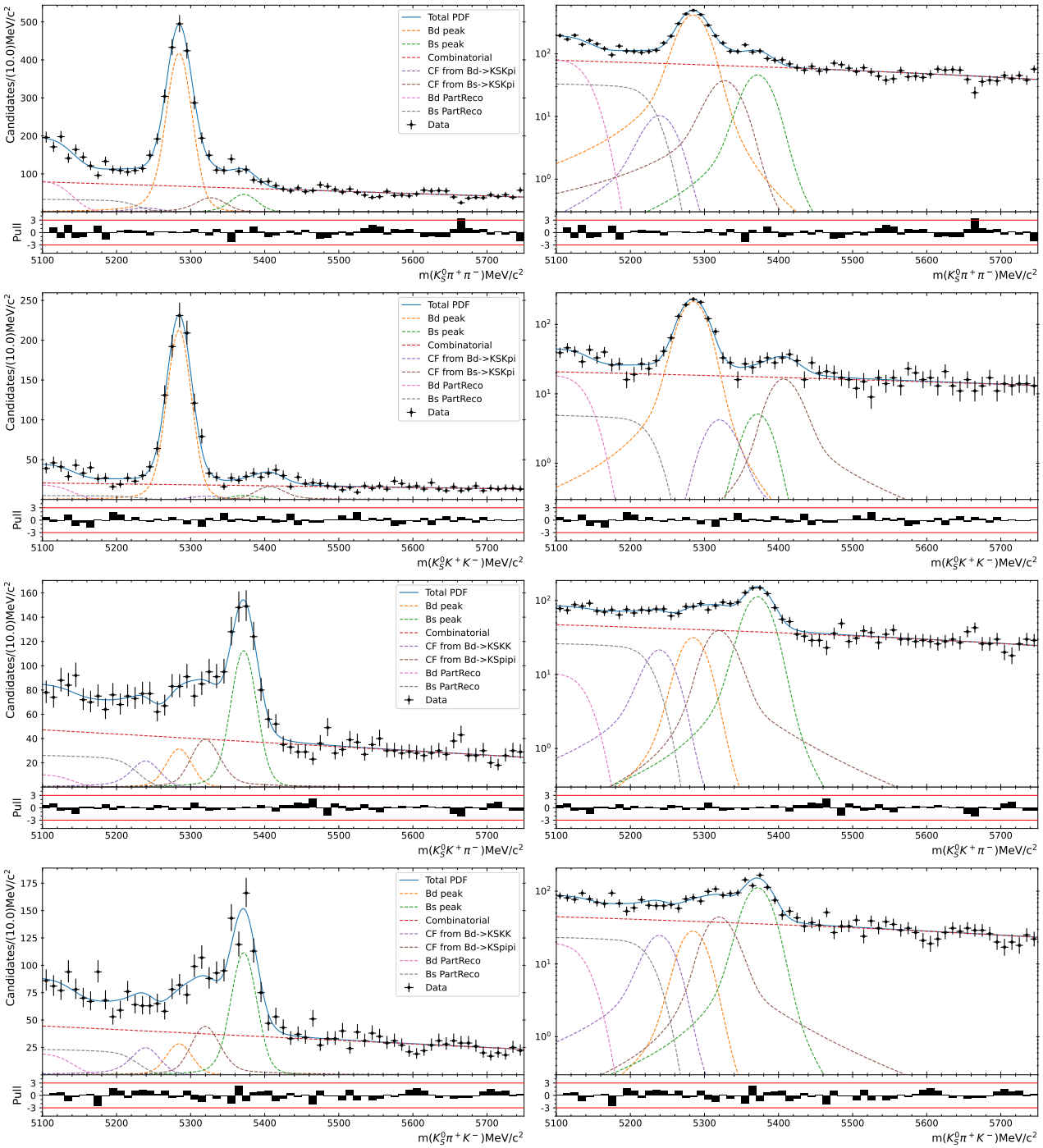

Figure C.10: Results of the simultaneous fit to data (DD, 2012b) with the PrincipalPeak optimisation. The modes $K^0_S\pi^+\pi^-$, $K^0_SK^+K^-$, $K^0_SK^+\pi^-$ and $K^0_S\pi^+K^-$ are shown from top to bottom. The left-hand side plots show the results with a linear scale and the right-hand side with a logarithmic scale.

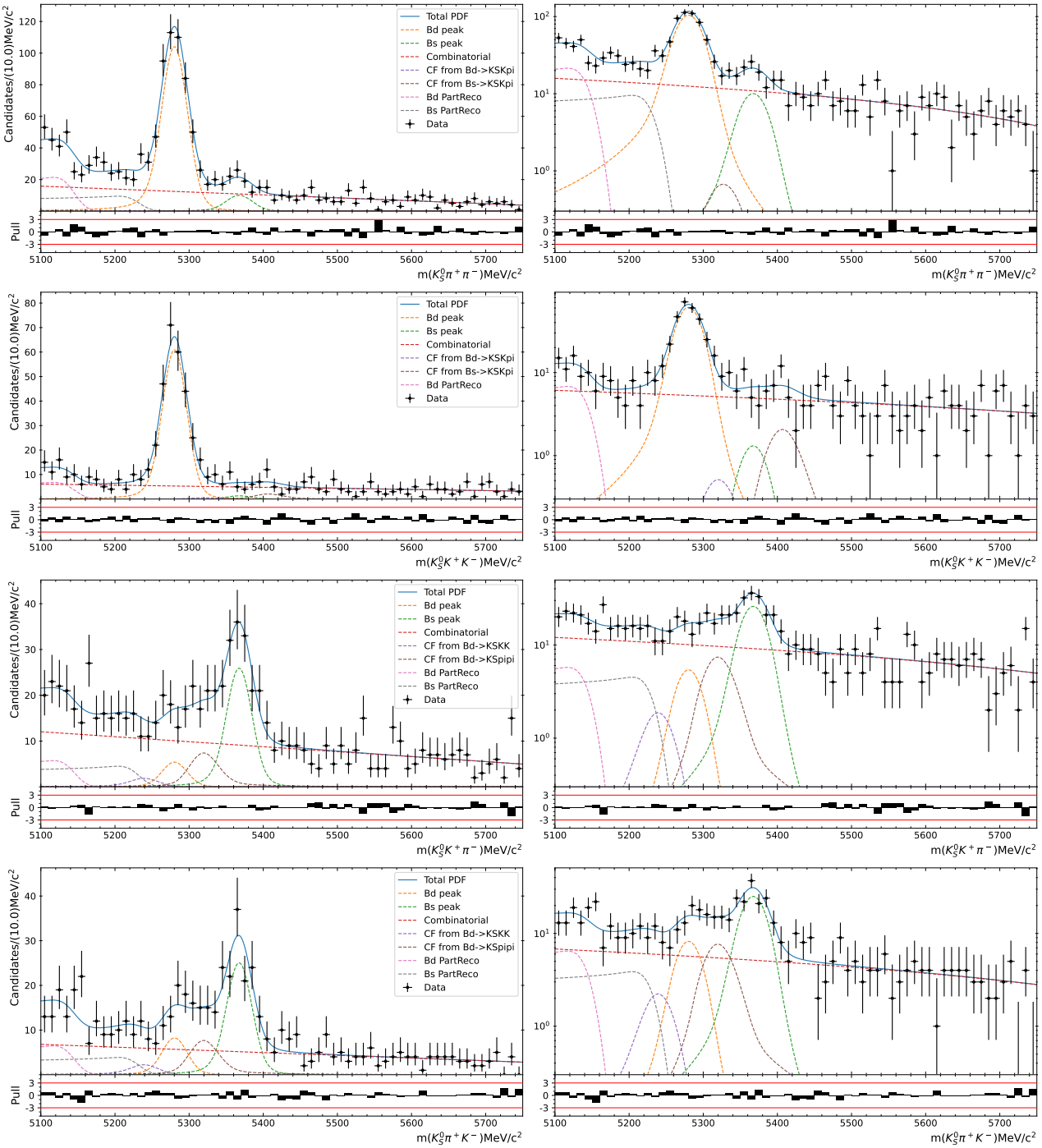

Figure C.11: Results of the simultaneous fit to data (LL, 2015) with the PrincipalPeak optimisation. The modes $K^0_S\pi^+\pi^-$, $K^0_SK^+K^-$, $K^0_SK^+\pi^-$ and $K^0_S\pi^+K^-$ are shown from top to bottom. The left-hand side plots show the results with a linear scale and the right-hand side with a logarithmic scale.

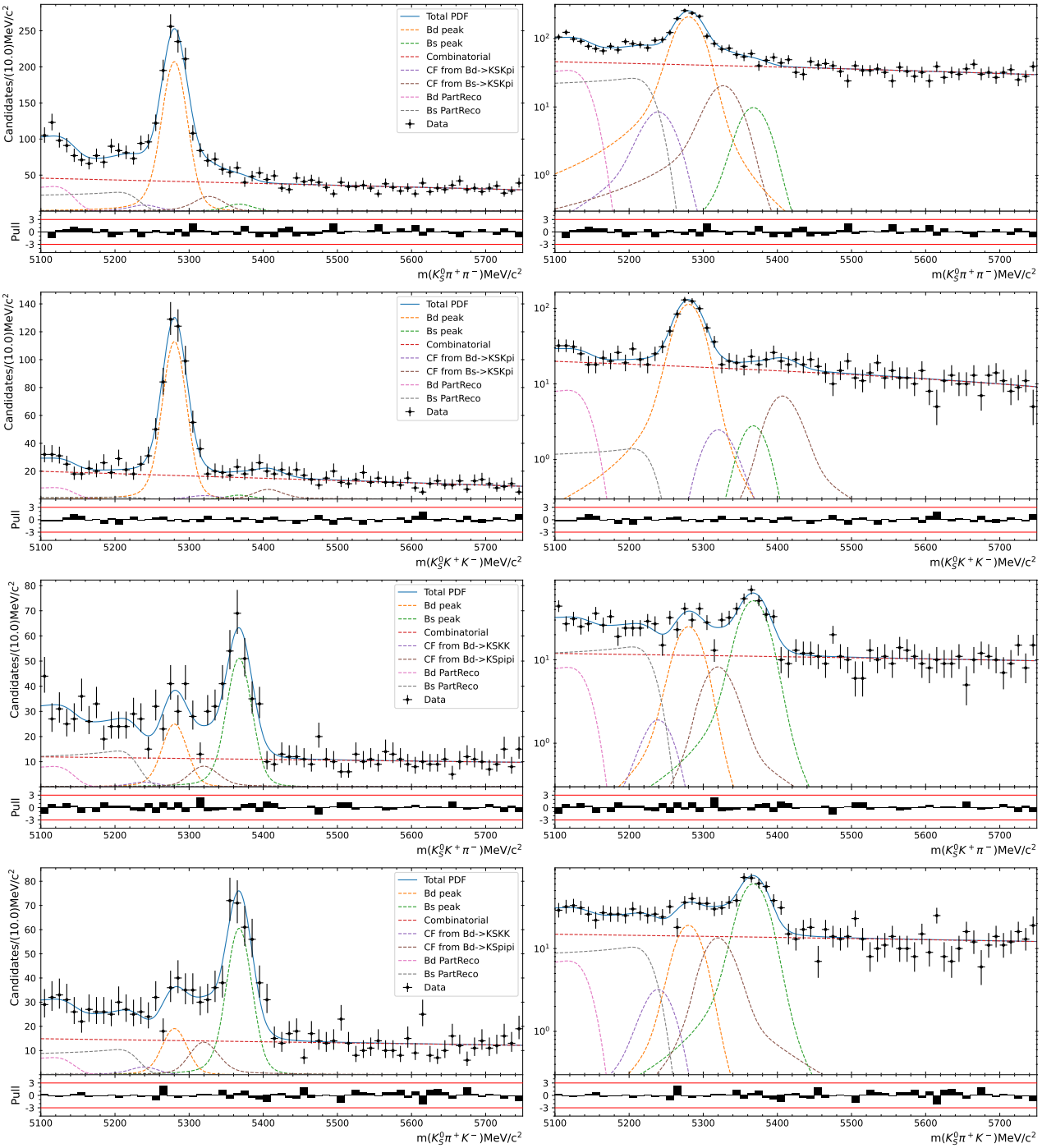

Figure C.12: Results of the simultaneous fit to data (DD, 2015) with the PrincipalPeak optimisation. The modes $K^0_S\pi^+\pi^-$, $K^0_SK^+K^-$, $K^0_SK^+\pi^-$ and $K^0_S\pi^+K^-$ are shown from top to bottom. The left-hand side plots show the results with a linear scale and the right-hand side with a logarithmic scale.

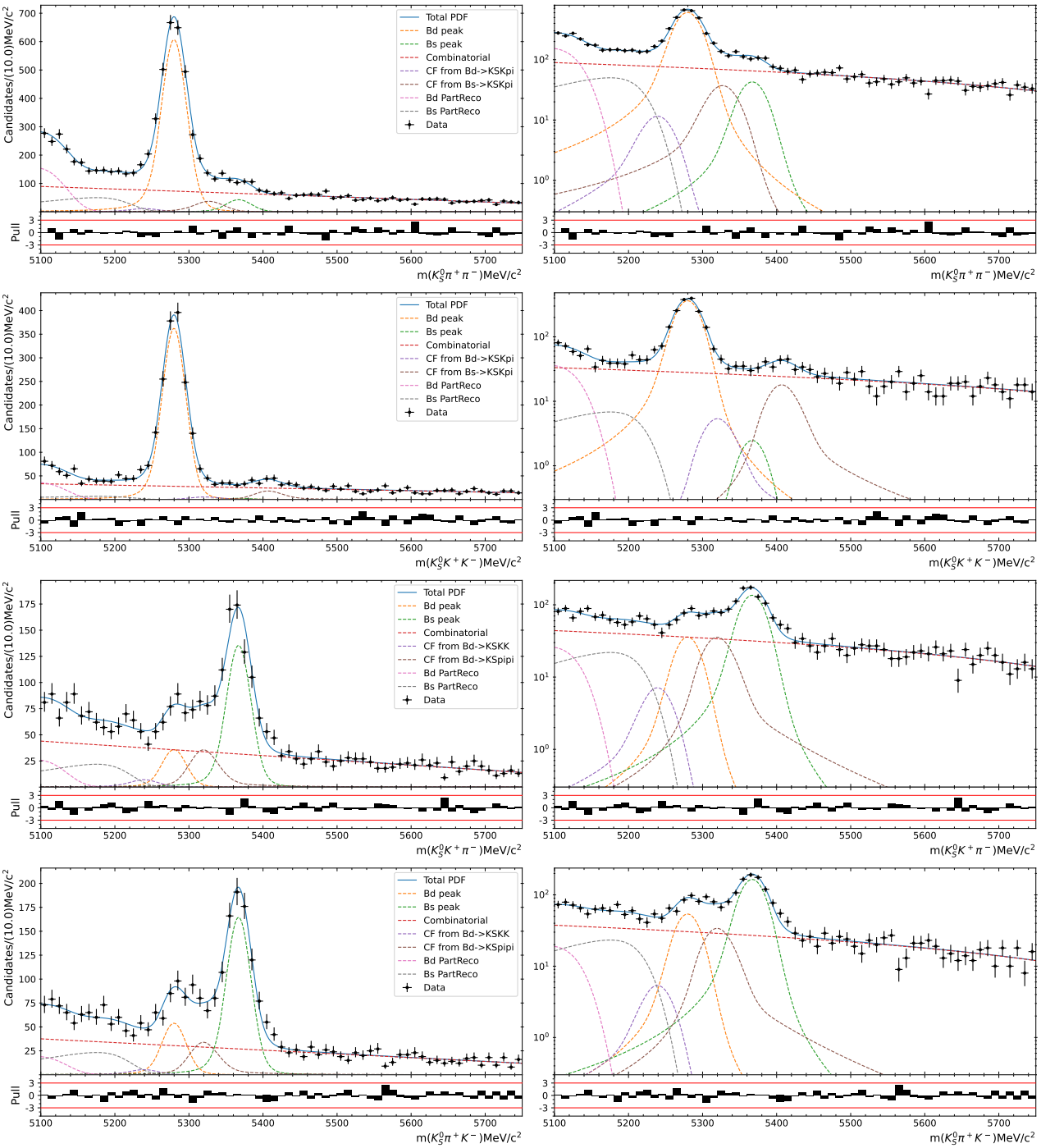

Figure C.13: Results of the simultaneous fit to data (LL, 2016) with the PrincipalPeak optimisation. The modes $K^0_S\pi^+\pi^-$, $K^0_SK^+K^-$, $K^0_SK^+\pi^-$ and $K^0_S\pi^+K^-$ are shown from top to bottom. The left-hand side plots show the results with a linear scale and the right-hand side with a logarithmic scale.

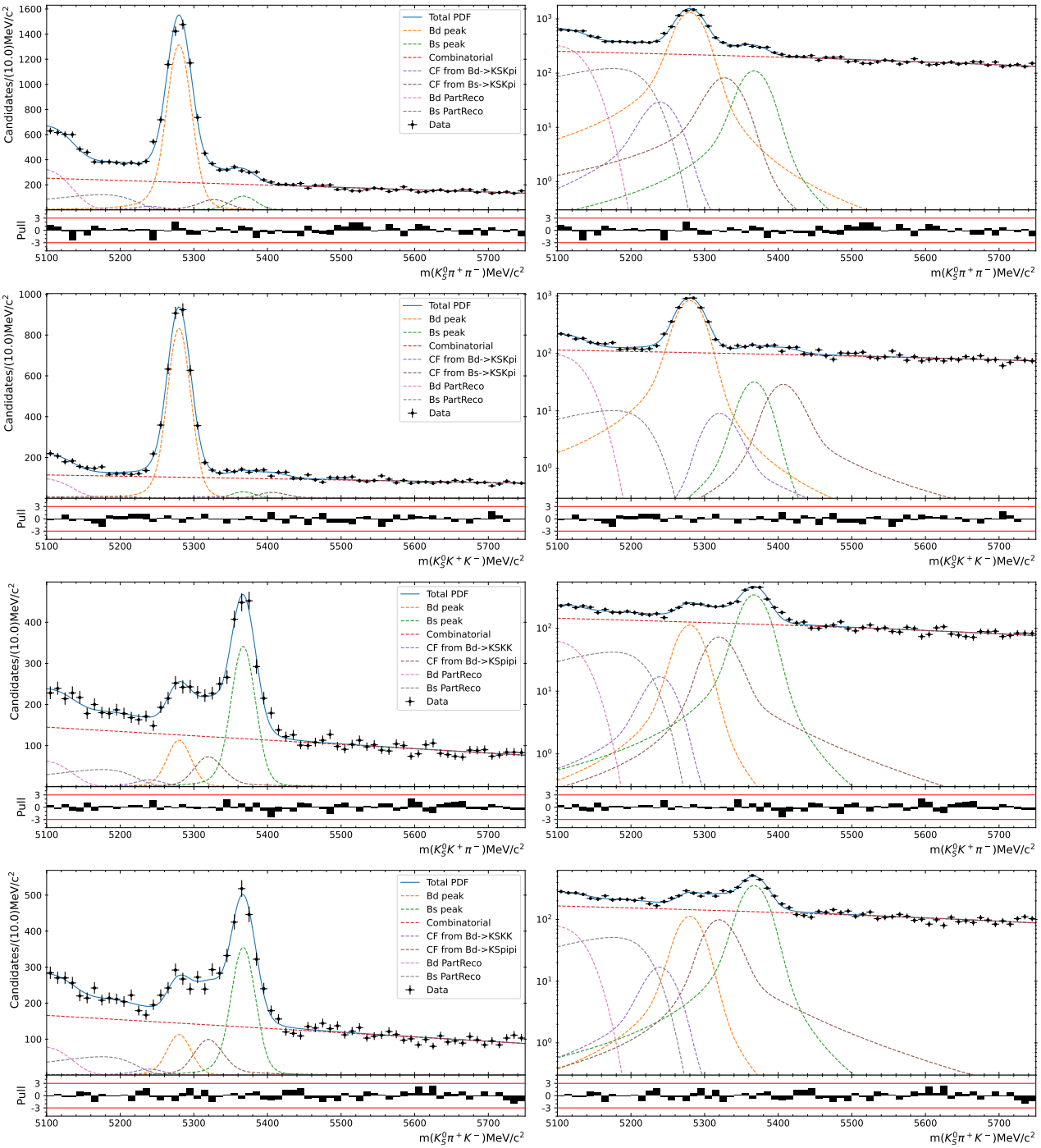

Figure C.14: Results of the simultaneous fit to data (DD, 2016) with the PrincipalPeak optimisation. The modes $K^0_S\pi^+\pi^-$, $K^0_SK^+K^-$, $K^0_SK^+\pi^-$ and $K^0_S\pi^+K^-$ are shown from top to bottom. The left-hand side plots show the results with a linear scale and the right-hand side with a logarithmic scale.

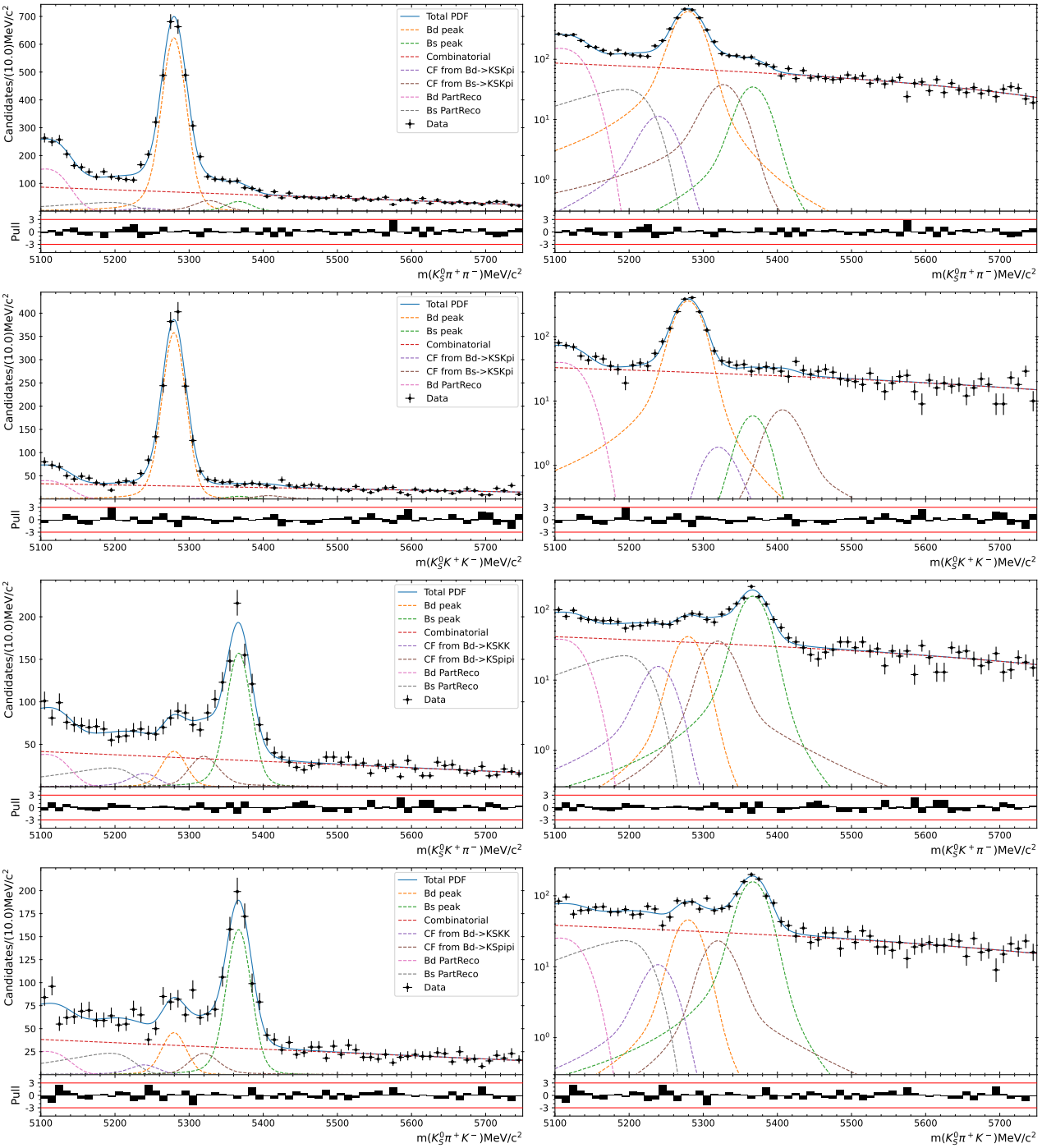

Figure C.15: Results of the simultaneous fit to data (LL, 2017) with the PrincipalPeak optimisation. The modes $K^0_S\pi^+\pi^-$, $K^0_S K^+ K^-$, $K^0_S K^+\pi^-$ and $K^0_S\pi^+ K^-$ are shown from top to bottom. The left-hand side plots show the results with a linear scale and the right-hand side with a logarithmic scale.

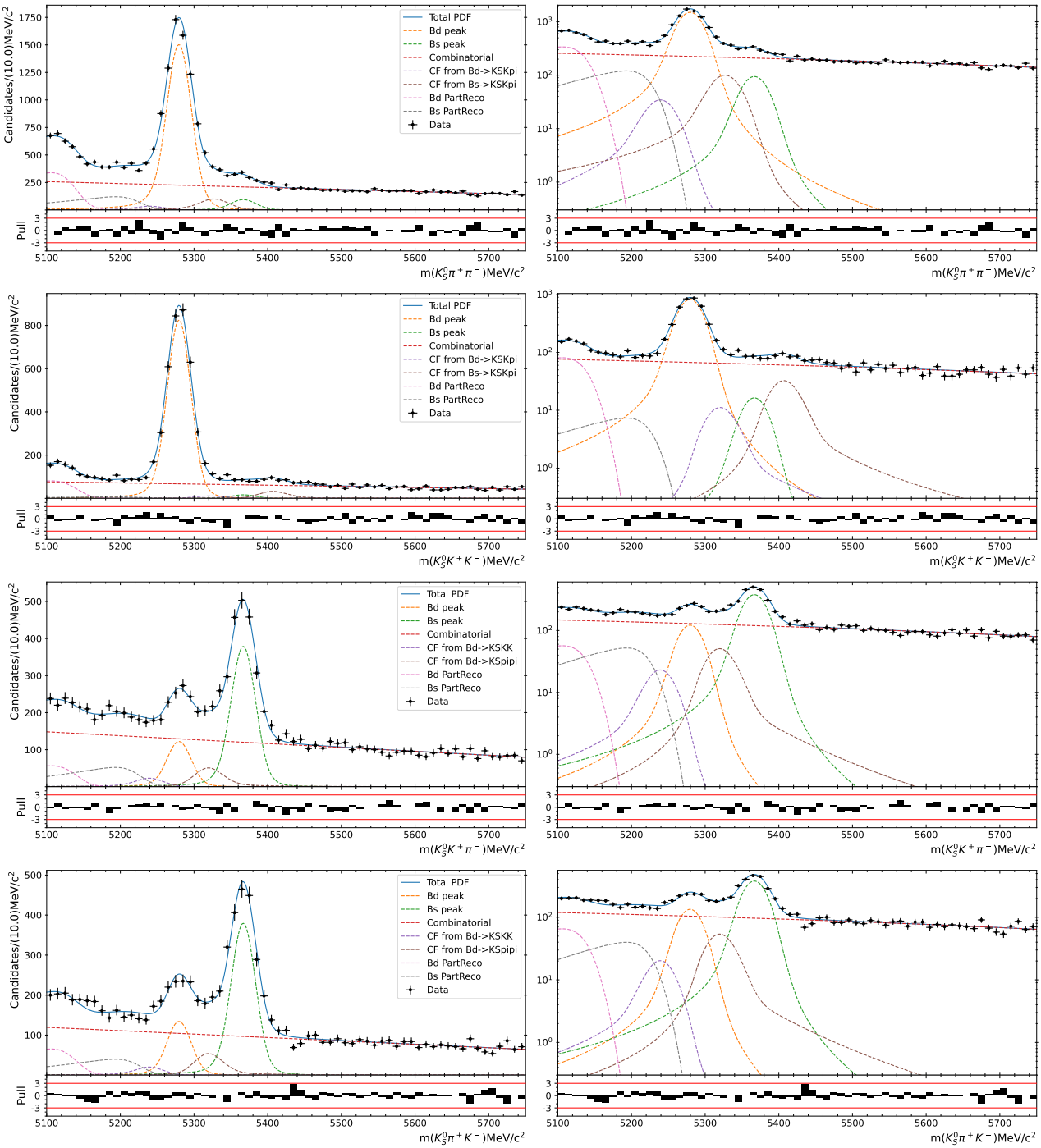

Figure C.16: Results of the simultaneous fit to data (DD, 2017) with the PrincipalPeak optimisation. The modes $K^0_S\pi^+\pi^-$, $K^0_SK^+K^-$, $K^0_SK^+\pi^-$ and $K^0_S\pi^+K^-$ are shown from top to bottom. The left-hand side plots show the results with a linear scale and the right-hand side with a logarithmic scale.

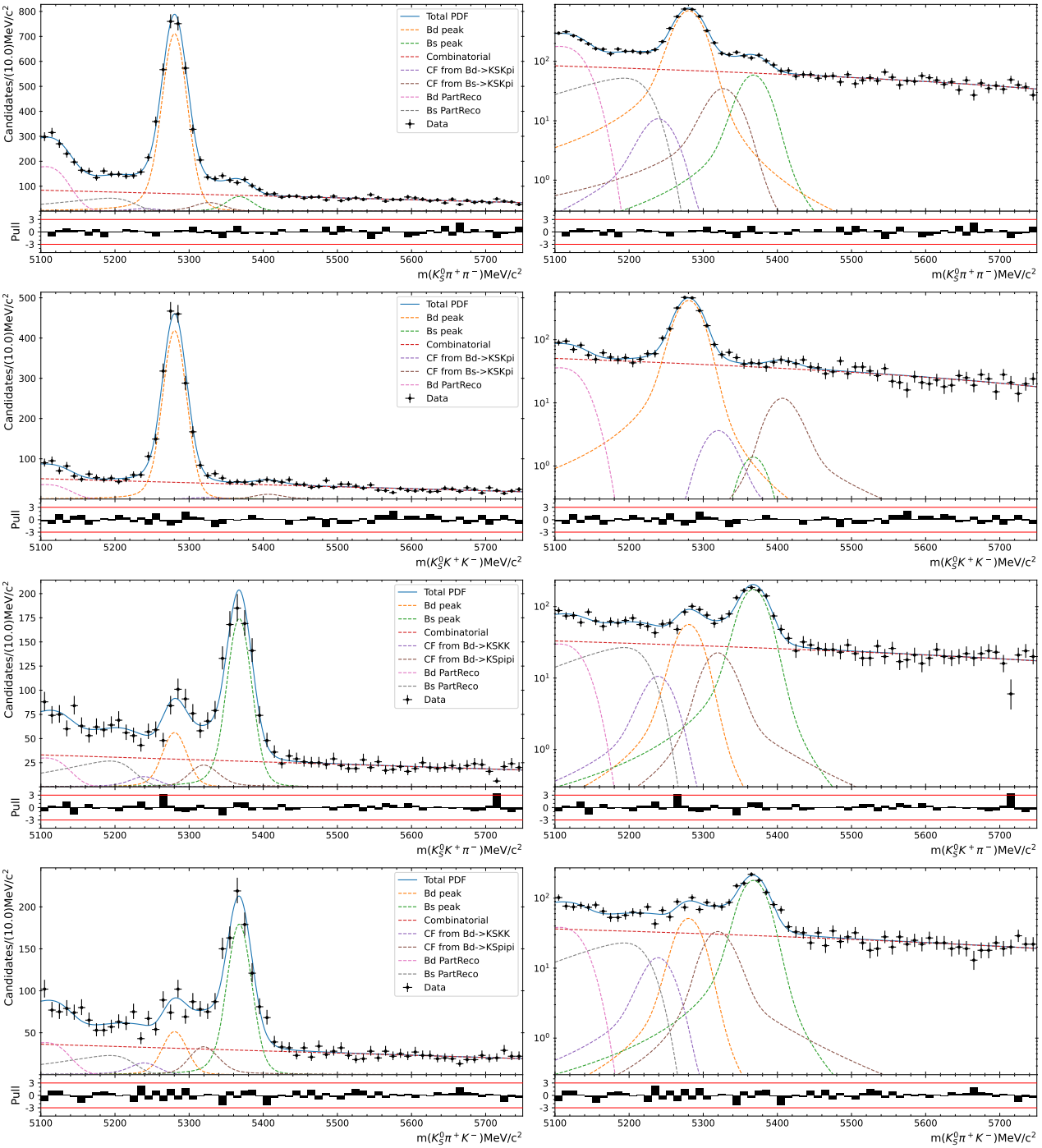

Figure C.17: Results of the simultaneous fit to data (LL, 2018) with the PrincipalPeak optimisation. The modes $K^0_S\pi^+\pi^-$, $K^0_SK^+K^-$, $K^0_SK^+\pi^-$ and $K^0_S\pi^+K^-$ are shown from top to bottom. The left-hand side plots show the results with a linear scale and the right-hand side with a logarithmic scale.

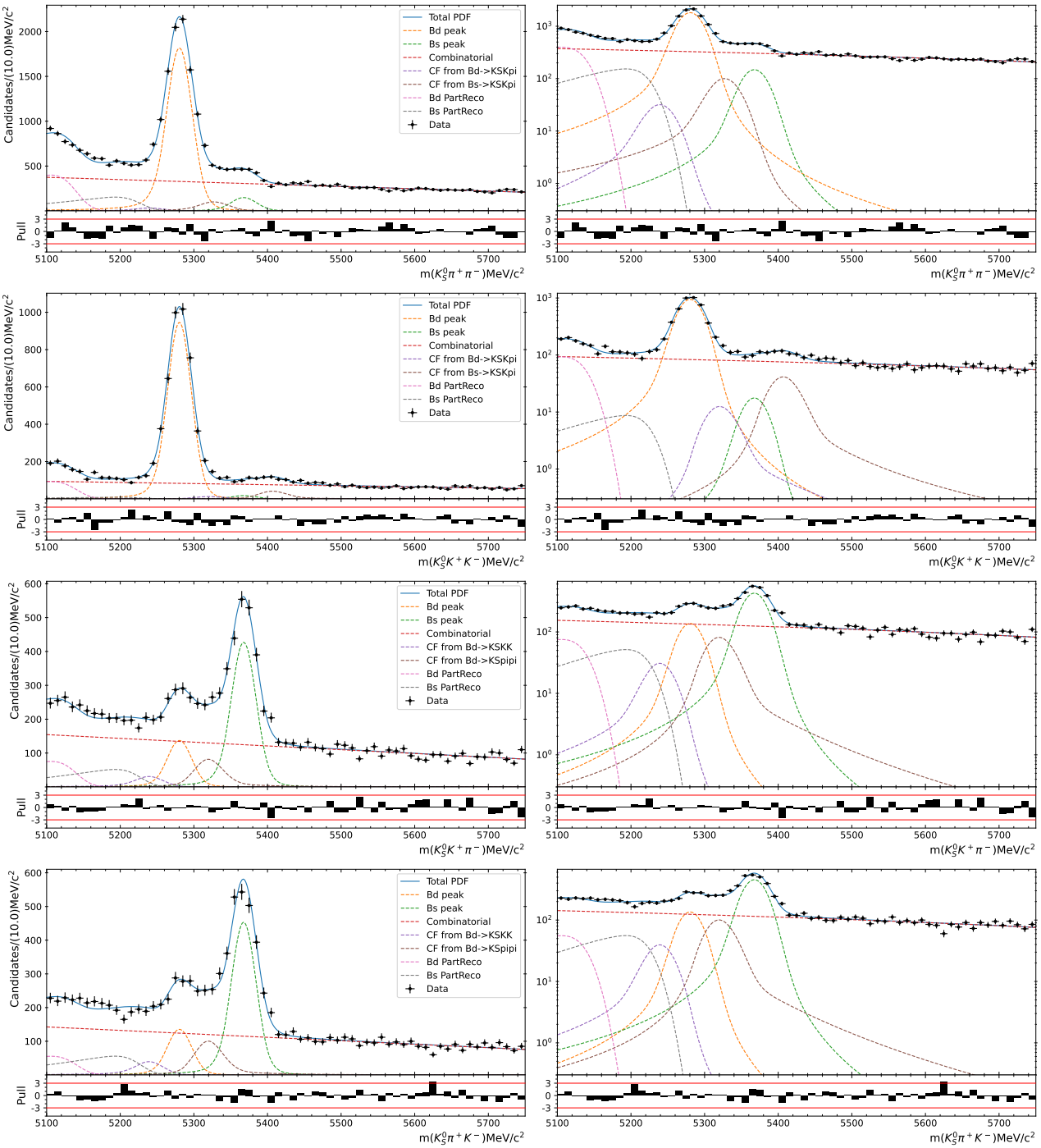

Figure C.18: Results of the simultaneous fit to data (DD, 2018) with the PrincipalPeak optimisation. The modes $K^0_S\pi^+\pi^-$, $K^0_SK^+K^-$, $K^0_SK^+\pi^-$ and $K^0_S\pi^+K^-$ are shown from top to bottom. The left-hand side plots show the results with a linear scale and the right-hand side with a logarithmic scale.

Background yields tables

Crossfeed	2011	2012a	2012b	2015	2016	2017	2018
$B_d^0 \to KKK_S^0(\mathrm{LL})\|K\pi$	$37_{\pm 9}$	$14_{\pm 5}$	$55_{\pm 10}$	$11_{\pm 4}$	$40_{\pm 7}$	$89_{\pm 14}$	$60_{\pm 13}$
$B_d^0 \to KKK_S^0(\mathrm{DD})\|K\pi$	$65_{\pm 11}$	$37_{\pm 8}$	$122_{\pm 18}$	$11_{\pm 5}$	$96_{\pm 13}$	$130_{\pm 24}$	$174_{\pm 22}$
$B_d^0 \to \pi\pi K_S^0(\mathrm{LL})\|K\pi$	$60_{\pm 14}$	$34_{\pm 12}$	$105_{\pm 17}$	$44_{\pm 16}$	$211_{\pm 34}$	$214_{\pm 33}$	$134_{\pm 30}$
$B_d^0 \to \pi\pi K_S^0(\mathrm{DD})\|K\pi$	$141_{\pm 23}$	$97_{\pm 18}$	$234_{\pm 33}$	$49_{\pm 20}$	$430_{\pm 60}$	$300_{\pm 50}$	$480_{\pm 60}$
$B_d^0 \to K\pi K_S^0(\mathrm{LL})\|\pi\pi$	$25_{\pm 9}$	$11_{\pm 7}$	$30.3_{\pm 9}$	$1.1_{\pm 3.1}$	$67_{\pm 15}$	$65_{\pm 14}$	$62_{\pm 15}$
$B_d^0 \to K\pi K_S^0(\mathrm{DD})\|\pi\pi$	$39_{\pm 12}$	$23_{\pm 9}$	$60_{\pm 15}$	$49_{\pm 15}$	$170_{\pm 29}$	$199_{\pm 29}$	$184_{\pm 30}$
$B_s^0 \to K\pi K_S^0(\mathrm{LL})\|\pi\pi$	$63_{\pm 20}$	$34_{\pm 19}$	$103_{\pm 25}$	$4_{\pm 21}$	$220_{\pm 50}$	$230_{\pm 50}$	$210_{\pm 50}$
$B_s^0 \to K\pi K_S^0(\mathrm{DD})\|\pi\pi$	$130_{\pm 40}$	$102_{\pm 27}$	$220_{\pm 50}$	$122_{\pm 34}$	$490_{\pm 80}$	$600_{\pm 80}$	$600_{\pm 90}$
$B_d^0 \to K\pi K_S^0(\mathrm{LL})\|KK$	$11_{\pm 5}$	$2.7_{\pm 2.2}$	$11_{\pm 4}$	$3.1_{\pm 2.5}$	$32_{\pm 8}$	$12_{\pm 6}$	$22_{\pm 8}$
$B_d^0 \to K\pi K_S^0(\mathrm{DD})\|KK$	$15_{\pm 6}$	$10_{\pm 4}$	$25_{\pm 7}$	$15_{\pm 7}$	$54_{\pm 15}$	$67_{\pm 14}$	$74_{\pm 14}$
$B_s^0 \to K\pi K_S^0(\mathrm{LL})\|KK$	$28_{\pm 13}$	$11_{\pm 8}$	$42_{\pm 12}$	$12_{\pm 9}$	$107_{\pm 25}$	$43_{\pm 21}$	$70_{\pm 24}$
$B_s^0 \to K\pi K_S^0(\mathrm{DD})\|KK$	$52_{\pm 17}$	$43_{\pm 14}$	$97_{\pm 23}$	$41_{\pm 19}$	$170_{\pm 50}$	$190_{\pm 40}$	$250_{\pm 40}$

Table C.5: Values and statistical uncertainties on the crossfeeds yields extracted from the fit to data, in the PrincipalPeak optimisation. Note: $A|B$ = Decay A seen as B.

Final State	PartReco	2011	2012a	2012b	2015	2016	2017	2018
$\pi^+\pi^- K_S^0(\mathrm{LL})$	Charmless B^0	$114_{\pm 16}$	$93_{\pm 18}$	$163_{\pm 23}$	$100_{\pm 18}$	$570_{\pm 40}$	$650_{\pm 40}$	$760_{\pm 40}$
	Charmless B_s^0	$84_{\pm 25}$	$78_{\pm 33}$	$130_{\pm 40}$	$119_{\pm 34}$	$570_{\pm 80}$	$350_{\pm 70}$	$570_{\pm 80}$
$\pi^+\pi^- K_S^0(\mathrm{DD})$	Charmless B^0	$307_{\pm 28}$	$158_{\pm 22}$	$330_{\pm 40}$	$159_{\pm 29}$	$1200_{\pm 70}$	$1450_{\pm 70}$	$1690_{\pm 80}$
	Charmless B_s^0	$170_{\pm 50}$	$80_{\pm 40}$	$400_{\pm 90}$	$330_{\pm 60}$	$1390_{\pm 140}$	$1320_{\pm 130}$	$1680_{\pm 160}$
$K^+K^- K_S^0(\mathrm{LL})$	Charmless B^0	$49_{\pm 12}$	$19_{\pm 8}$	$52_{\pm 11}$	$32_{\pm 10}$	$134_{\pm 22}$	$170_{\pm 23}$	$153_{\pm 25}$
	Charmless B_s^0	$48_{\pm 24}$	0	0	0	$80_{\pm 50}$	0	0
$K^+K^- K_S^0(\mathrm{DD})$	Charmless B^0	$69_{\pm 14}$	$23_{\pm 10}$	$75_{\pm 20}$	$38_{\pm 15}$	$360_{\pm 40}$	$345_{\pm 35}$	$390_{\pm 40}$
	Charmless B_s^0	$47_{\pm 29}$	$15_{\pm 24}$	$60_{\pm 50}$	$20_{\pm 40}$	$120_{\pm 100}$	$80_{\pm 80}$	$100_{\pm 90}$
$K^+\pi^- K_S^0(\mathrm{LL})$	Charmless B^0	$17_{\pm 10}$	$9_{\pm 9}$	$39_{\pm 16}$	$27_{\pm 13}$	$96_{\pm 26}$	$163_{\pm 26}$	$127_{\pm 24}$
	Charmless B_s^0	$47_{\pm 19}$	$53_{\pm 15}$	$92_{\pm 28}$	$56_{\pm 27}$	$250_{\pm 50}$	$240_{\pm 50}$	$290_{\pm 40}$
$K^+\pi^- K_S^0(\mathrm{DD})$	Charmless B^0	$55_{\pm 17}$	$25_{\pm 13}$	$42_{\pm 30}$	$38_{\pm 17}$	$230_{\pm 40}$	$240_{\pm 40}$	$320_{\pm 40}$
	Charmless B_s^0	$129_{\pm 30}$	$68_{\pm 24}$	$320_{\pm 60}$	$178_{\pm 32}$	$480_{\pm 90}$	$570_{\pm 90}$	$560_{\pm 90}$
$\pi^+K^- K_S^0(\mathrm{LL})$	Charmless B^0	$21_{\pm 11}$	$11_{\pm 11}$	$13_{\pm 16}$	$30_{\pm 12}$	$71_{\pm 23}$	$108_{\pm 24}$	$163_{\pm 25}$
	Charmless B_s^0	$110_{\pm 19}$	$20_{\pm 22}$	$98_{\pm 29}$	$48_{\pm 20}$	$270_{\pm 50}$	$260_{\pm 40}$	$250_{\pm 50}$
$\pi^+K^- K_S^0(\mathrm{DD})$	Charmless B^0	$88_{\pm 18}$	$27_{\pm 14}$	$78_{\pm 30}$	$33_{\pm 16}$	$290_{\pm 50}$	$280_{\pm 40}$	$240_{\pm 40}$
	Charmless B_s^0	$87_{\pm 32}$	$75_{\pm 28}$	$280_{\pm 60}$	$130_{\pm 34}$	$590_{\pm 90}$	$440_{\pm 70}$	$610_{\pm 80}$

Table C.6: Values and statistical uncertainties on the partially reconstruction decays yields extracted from the fit to data, in the PrincipalPeak optimisation.

Spectrum	2011	2012a	2012b	2015	2016	2017	2018
$\pi^+\pi^-K^0_S$(LL)	380$\pm$50	730$\pm$60	680$\pm$60	640$\pm$60	3900$\pm$140	3570$\pm$140	3850$\pm$150
$\pi^+\pi^-K^0_S$(DD)	1670$\pm$100	1180$\pm$80	3830$\pm$150	2450$\pm$120	12550$\pm$260	12940$\pm$270	18920$\pm$320
$K^+K^-K^0_S$(LL)	330$\pm$50	153$\pm$21	324$\pm$30	303$\pm$28	1540$\pm$110	1560$\pm$60	2230$\pm$70
$K^+K^-K^0_S$(DD)	520$\pm$60	340$\pm$50	1100$\pm$90	940$\pm$90	6140$\pm$210	3880$\pm$180	4850$\pm$200
$K^+\pi^-K^0_S$(LL)	270$\pm$40	175$\pm$25	370$\pm$40	550$\pm$50	1890$\pm$90	1890$\pm$90	1640$\pm$80
$K^+\pi^-K^0_S$(DD)	800$\pm$60	470$\pm$40	2330$\pm$100	710$\pm$50	7200$\pm$160	7410$\pm$180	7690$\pm$180
$\pi^+K^-K^0_S$(LL)	197$\pm$30	450$\pm$50	400$\pm$40	312$\pm$34	1610$\pm$80	1740$\pm$90	1800$\pm$90
$\pi^+K^-K^0_S$(DD)	920$\pm$70	620$\pm$50	2200$\pm$100	880$\pm$60	8250$\pm$180	5970$\pm$150	7100$\pm$170

Table C.7: Values and statistical uncertainties on the combinatorial yields extracted from the fit to data, in the PrincipalPeak optimisation.

C.2.2 Background yields tables of the SecondaryPeak optimisation

Crossfeed	2011	2012a	2012b	2015	2016	2017	2018
$B^0_d \to KKK^0_S(\mathrm{LL})\|K\pi$	1.54±0.12	0.92±0.09	0.336±0.019	0.257±0.018	2.79±0.10	4.81±0.17	6.18±0.19
$B^0_d \to KKK^0_S(\mathrm{DD})\|K\pi$	2.90±0.19	1.13±0.09	3.63±0.15	0.315±0.022	4.24±0.10	11.48±0.30	12.00±0.25
$B^0_d \to \pi\pi K^0_S(\mathrm{LL})\|K\pi$	1.87±0.12	1.35±0.13	0.688±0.034	0.87±0.06	20.0±0.5	13.50±0.33	15.7±0.4
$B^0_d \to \pi\pi K^0_S(\mathrm{DD})\|K\pi$	7.1±0.4	4.10±0.24	5.26±0.18	1.87±0.11	28.7±0.6	30.6±0.6	32.4±0.6
$B^0_d \to K\pi K^0_S(\mathrm{LL})\|\pi\pi$	0.98±0.15	0.023±0.005	1.29±0.23	0.17±0.04	1.85±0.16	3.63±0.30	2.36±0.18
$B^0_d \to K\pi K^0_S(\mathrm{DD})\|\pi\pi$	0.65±0.08	1.27±0.22	2.24±0.29	0.24±0.04	1.04±0.07	3.83±0.22	5.64±0.30
$B^0_s \to K\pi K^0_S(\mathrm{LL})\|\pi\pi$	2.06±0.15	0.044±0.005	3.40±0.31	0.51±0.04	6.97±0.25	13.0±0.5	10.21±0.34
$B^0_s \to K\pi K^0_S(\mathrm{DD})\|\pi\pi$	1.19±0.08	3.23±0.25	10.0±0.5	0.73±0.05	3.89±0.10	11.58±0.28	13.56±0.31
$B^0_d \to K\pi K^0_S(\mathrm{LL})\|KK$	0.47±0.07	0.82±0.16	2.7±0.5	1.7±0.4	1.35±0.11	0.99±0.08	2.67±0.21
$B^0_d \to K\pi K^0_S(\mathrm{DD})\|KK$	1.24±0.16	0.49±0.09	3.2±0.4	0.24±0.04	2.00±0.13	0.77±0.04	5.21±0.27
$B^0_s \to K\pi K^0_S(\mathrm{LL})\|KK$	1.80±0.13	2.24±0.25	8.1±0.7	5.6±0.5	5.40±0.20	2.29±0.08	13.8±0.5
$B^0_s \to K\pi K^0_S(\mathrm{DD})\|KK$	3.34±0.21	2.04±0.16	13.1±0.6	0.85±0.06	6.81±0.18	2.33±0.06	20.4±0.5

Table C.8: Values and statistical uncertainties on the crossfeeds yields extracted from the fit to data, in the SecondaryPeak optimisation. Note: $A|B$ = Decay A seen as B.

Final State	PartReco	2011	2012a	2012b	2015	2016	2017	2018
$\pi^+\pi^- K^0_S(\mathrm{LL})$	Charmless B^0	58±10	18±8	125±14	40±10	320±26	332±30	441±29
	Charmless B^0_s	24±13	29±11	16±17	63±16	300±40	260±50	350±40
$\pi^+\pi^- K^0_S(\mathrm{DD})$	Charmless B^0	95±12	54±12	206±20	77±12	515±34	470±40	640±40
	Charmless B^0_s	17±13	14±21	82±27	92±17	470±50	710±60	590±60
$K^+K^- K^0_S(\mathrm{LL})$	Charmless B^0	24±7	17±7	39±8	22±6	57±9	67±11	105±13
	Charmless B^0_s	21±12	6±10	0	0	0	5±15	0
$K^+K^- K^0_S(\mathrm{DD})$	Charmless B^0	43±8	6±6	40±9	23±6	143±15	104±14	242±20
	Charmless B^0_s	11±11	9±8	0	0	0	0	0
$K^+\pi^- K^0_S(\mathrm{LL})$	Charmless B^0	4±5	2±6	20±6	7±7	48±16	63±20	78±17
	Charmless B^0_s	39±10	27±12	6±9	28±15	137±29	172±34	149±30
$K^+\pi^- K^0_S(\mathrm{DD})$	Charmless B^0	29±11	2±10	44±12	23±10	111±25	40±30	146±27
	Charmless B^0_s	55±20	53±17	66±19	63±17	260±50	480±70	390±50
$\pi^+K^- K^0_S(\mathrm{LL})$	Charmless B^0	14±7	5±6	11±6	15±6	58±16	55±20	82±18
	Charmless B^0_s	56±12	21±10	24±10	28±10	131±29	170±40	161±31
$\pi^+K^- K^0_S(\mathrm{DD})$	Charmless B^0	44±11	6±10	51±16	4±10	148±28	105±30	132±26
	Charmless B^0_s	57±19	41±20	61±32	53±21	320±60	340±50	360±50

Table C.9: Values and statistical uncertainties on the partially reconstruction decays yields extracted from the fit to data, in the SecondaryPeak optimisation.

Spectrum	2011	2012a	2012b	2015	2016	2017	2018
$\pi^+\pi^-K^0_S$(LL)	$121_{\pm 24}$	$26_{\pm 11}$	$216_{\pm 30}$	$114_{\pm 22}$	$630_{\pm 60}$	$760_{\pm 60}$	$840_{\pm 70}$
$\pi^+\pi^-K^0_S$(DD)	$119_{\pm 24}$	$237_{\pm 32}$	$460_{\pm 50}$	$97_{\pm 23}$	$1580_{\pm 90}$	$1310_{\pm 80}$	$1750_{\pm 90}$
$K^+K^-K^0_S$(LL)	$113_{\pm 23}$	$36_{\pm 15}$	$93_{\pm 16}$	$59_{\pm 13}$	$67_{\pm 15}$	$75_{\pm 20}$	$269_{\pm 26}$
$K^+K^-K^0_S$(DD)	$96_{\pm 24}$	$50_{\pm 10}$	$156_{\pm 21}$	$48_{\pm 12}$	$316_{\pm 29}$	$317_{\pm 28}$	$720_{\pm 40}$
$K^+\pi^-K^0_S$(LL)	$64_{\pm 16}$	$61_{\pm 16}$	$80_{\pm 17}$	$168_{\pm 27}$	$590_{\pm 50}$	$600_{\pm 50}$	$870_{\pm 60}$
$K^+\pi^-K^0_S$(DD)	$360_{\pm 40}$	$155_{\pm 24}$	$385_{\pm 34}$	$271_{\pm 29}$	$2350_{\pm 90}$	$3320_{\pm 110}$	$2410_{\pm 90}$
$\pi^+K^-K^0_S$(LL)	$75_{\pm 18}$	$45_{\pm 14}$	$67_{\pm 17}$	$54_{\pm 14}$	$590_{\pm 50}$	$680_{\pm 50}$	$840_{\pm 60}$
$\pi^+K^-K^0_S$(DD)	$310_{\pm 40}$	$256_{\pm 30}$	$1010_{\pm 60}$	$430_{\pm 40}$	$2960_{\pm 100}$	$1680_{\pm 70}$	$2320_{\pm 90}$

Table C.10: Values and statistical uncertainties on the combinatorial yields extracted from the fit to data, in the SecondaryPeak optimisation.

C.3 L0 trigger correction for $B^0_{d,s} \to K^0_S h^+ h'^-$

C.3.1 Context

In this section, an application of the previously determined table efficiencies, average underlying energy maps, calibration maps, and functions on the $B^0_{d,s} \to K^0_S h^+ h'^-$ analysis will be presented. The L0Hadron corrections are needed in the $B^0_{d,s} \to K^0_S h^+ h'^-$ analysis due to the presence of $\pi^\pm$ and $K^\pm$ which are involved in trigger cuts (L0HadronDecision is part of the trigger cut applied), in order to take into account the not/badly MC described calorimeter trigger effects (presented in Section 2.4.

Because of the three-body nature of the studied process, the Dalitz plot formalism (see Section 4.1) has to be used. This requires at the end to provide L0Hadron corrections in the square Dalitz plan (see Section 4.1.3) denoted as sqDP in the following. In the following, the determination of the L0Hadron correction maps onto the sqDP will be described for $B^0_{d,s} \to K^0_S h^+ h'^-$ samples.

C.3.2 Inputs

The two main types of input needed to determine the L0 corrections for the $B^0_{d,s} \to K^0_S h^+ h'^-$ analysis are presented in this section.

MC unfiltered sample

The MC $B^0_{d,s} \to K^0_S h^+ h'^-$ samples used to determine the correction must be unfiltered, which means without any trigger selection applied. These are easy to obtain with the regular stripping line for Run I, but not for the Run II, because in Run II the trigger cuts are parts of the HLT cuts applied in the regular stripping lines. To obtain Run II MC unfiltered samples, various stripping lines that do not contain HLT cuts are used.

The MC unfiltered samples are stored in several ROOT trees depending on the year, B type (d or s), decay mode (hh'), LHCb magnet polarity and K^0_S reconstruction (Down-Down or Long-Long depending on the position of the start of the pions tracks from $K^0_S \to \pi^+\pi^-$).

To determine the corrections, the per-event needed information about the decays generated are:

- for the signal tracks (e.g. h, h', π^- from K^0_S and π^+ from K^0_S):
  - the particle true ID,
  - the recorded hit real transverse energy deposit in the HCAL,
  - the hit position recorded in the HCAL (area, x and y projection).
- for the global variables:
  - the sqDP projection (m', θ'),
  - a boolean to denote if there a signal candidate that is matched to a true candidate in the simulation (B_SIG_mcMatch),
  - the index of signal candidate (iCand).

L0Hadron

From the previously described method and results (see Section 2.4), due to the nature of the $B^0_{d,s} \to K^0_S h^+ h'^-$ decays, the inputs needed to determine correction are the:

- $\pi^\pm$ efficiency tables,

- $K^\pm$ efficiency tables,
- $b\bar{b}$ average underlying energy maps,
- calibration maps,
- function that computes the fraction of tracks that do not reach the HCAL,
- function to determine the overlap between the signal tracks.

C.3.3 Application

In this section, the method used to extract the L0Hadron corrections for $B^0_{d,s} \to K^0_S h^+ h'^-$ is presented. To illustrate the procedure, the results on $B^0_d \to K^0_S \pi^+ \pi^-$ for 2018 and 2012b (in the $B^0_{d,s} \to K^0_S h^+ h'^-$ analysis because of changes in the trigger line, the year 2012 is split into two periods), DD, MD, are displayed.

Event selection

A selection is applied on the events of the MC samples considered in order to determine correction only for events that match the following requirements: having a MC B candidate that matches the signal (e.g. $K^0_S hh'$) to not correct fake events and having a single signal candidate to avoid the correction of the rare multiple signal event. The selection in terms of Tree variables is given in Table C.11.

$B_{d,s} \to K^0_S hh'$	Event selection
	(B_SIG_mcMatch == 1)&(iCand == 0)

Table C.11: Event selection.

Corrected L0Hadron MC efficiency computation

In this section, the per-event computation of the MC efficiency corrected from the L0Hadron tables is explained. Each selected event contains 4 signal tracks $(h, h'\pi^+, \pi^-)$, an efficiency is determined for each of them first and then combined to give the per-event efficiency. In the following an explanation about the efficiency computation for one track is given and then the combination off all the tracks is explained.

Per-track efficiency: A given track, even in MC, could fail to hit the HCAL (absorbed in the material before the HCAL, or because of a decay in flight), if this is the case of the considered track, the associated efficiency in the HCAL is:

$$\epsilon_i = 0, \tag{C.3.1}$$

where i is the index of the track.

If the considered track reaches the HCAL, the hit position of the track projected to the HCAL surface allows to determine which cell of the HCAL is reached, and from this information the average underlying energy and the calibration factor can be taken from the maps previously determined. The probability for this track to reach the HCAL $f_{\text{empty}}(E_T)$ is then computed from the area reached by the track and from its associated real transverse energy from Equation 2.4.5. On the same principle $f_{\text{empty}}(E_T)$ is also computed for the other signal tracks of the event. To take into account the potential overlap in HCAL on the considered signal track and

the others, the overlap energy given from each of them is computed using the Equation 2.4.4 by $f_{\text{overlap}}(E_{T_0}, x_1, x_0, y_1, y_0)$ where 0 denotes the considered signal track and 1 denotes one of the other tracks. Finally, the type of the particle is also taken into account by choosing the corresponding efficiency table.

To determine the efficiency associated to the considered track, it is needed to consider all possible combinations of the other tracks in terms of reaching or not reaching the HCAL (which means 8 combinations of seen/not seen tracks for a given considered track in $B^0_{d,s} \to K^0_S h^+ h'^-$). Finally the efficiency attached to the considered track, denoted i, is written as:

$$\epsilon_i = \sum \left(\left(\prod_{v=0}^{3} F_{\text{empty},v} \right) \times \hat{\epsilon}_i \left[b(i) \times \left(\sum_{v=0}^{3} E(v) \right) + 4E_0(i) \right] \right), \tag{C.3.2}$$

where the sum runs over all the possible combinations of the other tracks in term of reaching or not the HCAL, v denotes one of the signal track, $E_0(i)$ is the average underlying energy attached to i, $b(i)$ is the calibration factor attached to i,

$$F_{\text{empty},v} = \begin{cases} 1 & \text{if } v = i \\ 1 - f_{\text{empty}}(E_{T_v}) & \text{if } v \neq i \,\&\, v \text{ reaches the HCAL} \\ f_{\text{empty}}(E_{T_v}) & \text{if } v \neq i \,\&\, v \text{ does not reach the HCAL} \end{cases},$$

$$E(v) = \begin{cases} E_{T_i} & \text{if } v = i \\ f_{\text{overlap}}(E_{T_i}, x_v, x_i, y_v, y_i) & \text{if } v \neq i \,\&\, v \text{ reaches the HCAL} \\ 0 & \text{if } v \neq i \,\&\, v \text{ not reach the HCAL} \end{cases},$$

and $\hat{\epsilon}_i[E]$ denotes the value given by the efficiency table corresponding to the type of i for a transverse energy E.

From the uncertainty associated to the efficiency into the tables, the efficiency envelop in the bin i is also determined as :

$$\epsilon_{\text{up}_i} = \begin{cases} \epsilon_i + \sigma_{\epsilon_i}[E] & \text{if } i \text{ is in the HCAL} \\ 0 & \text{else} \end{cases}, \tag{C.3.3}$$

$$\epsilon_{\text{down}_\text{i}} = \begin{cases} \epsilon_i - \sigma_{\epsilon_i}[E] & \text{if } i \text{ is in the HCAL} \\ 0 & \text{else} \end{cases}, \tag{C.3.4}$$

where $\sigma_{\epsilon_i}[E]$ is the uncertainty value given by the efficiency table of i for the transverse energy E.

Per-event efficiency: The efficiency attached to a given event to be L0Hadron TOS is computed from the signal per-track efficiencies determined above. An event is TOS if at least one of the tracks is TOS, this is why the event efficiency is computed by using the combination of the tracks. Mathematically, the per-event efficiency is written as:

$$\epsilon^{\text{TOS}} = \sum_{\text{TOS/notTOS},\neq\text{ALLnotTOS}} \left(\prod_{k=0}^{3} \bar{\epsilon}_k \right), \tag{C.3.5}$$

where ϵ^{TOS} denotes the event TOS efficiency, $\sum_{\text{TOS/notTOS},\neq\text{ALLnotTOS}}$ means the sum of all the possible combination of TOS/!TOS tracks by excluding the case where all tracks are !TOS (in that case the event cannot be L0Hadron TOS), k denotes a signal track and

$$\bar{\epsilon}_k = \begin{cases} \epsilon_k & \text{if } k \text{ is TOS} \\ 1 - \epsilon_k & \text{else} \end{cases}.$$

The event efficiency envelop $\bar{\epsilon}_{\text{TOS up,down}}$ are computed on the same principle with the tracks efficiency envelop:

$$\epsilon^{\text{TOS}}_{\text{up,down}} = \sum_{\text{TOS/notTOS},\neq\text{ALLnotTOS}} \left(\prod_{k=0}^{3} \bar{\epsilon}_{\text{up,down}_k} \right), \tag{C.3.6}$$

where:

$$\bar{\epsilon}_{\text{up,down}_k} = \begin{cases} \epsilon_{\text{up,down}_k} & \text{if } k \text{ is TOS} \\ 1 - \epsilon_{\text{up,down}_k} & \text{else} \end{cases}.$$

The upper and lower bound uncertainty can then be defined as:

$$\sigma^{\text{TOS}}_{\text{up,down}} = \left| \epsilon^{\text{TOS}}_{\text{up,down}} - \epsilon^{\text{TOS}} \right|.$$

At the same level, the efficiency for an event to be not TOS and the associated envelop can also be computed (exploratory, not used in $B^0_{d,s} \to K^0_S h^+ h'^-$):

$$\begin{aligned} \epsilon^{\text{!TOS}} &= 1 - \epsilon^{\text{TOS}}, \\ \epsilon^{\text{!TOS}}_{\text{up,down}} &= 1 - \epsilon^{\text{TOS}}_{\text{up,down}}, \\ \sigma^{\text{!TOS}}_{\text{up,down}} &= \left| \epsilon^{\text{!TOS}}_{\text{up,down}} - \epsilon^{\text{!TOS}} \right|. \end{aligned}$$

In addition to TOS events, $B^0_{d,s} \to K^0_S h^+ h'^-$ involves TIS&!TOS events which will also be required to be corrected. Due to the different kinematics between the TIS&!TOS events and the !TOS events, the !TOS efficiency can not be used to correct the $B^0_{d,s} \to K^0_S h^+ h'^-$ TIS&!TOS events. The efficiency of a TIS event not being TOS ($\epsilon^{\text{TIS\&!TOS}}$) and the associated envelope ($\epsilon^{\text{TIS\&!TOS}}_{\text{up,down}}$ and $\sigma^{\text{TIS\&!TOS}}_{\text{up,down}}$), have been determined following the same principle as $\epsilon^{\text{!TOS}}$ but with TIS == 1 added in the event selection. The TIS requirements used for $B^0_{d,s} \to K^0_S h^+ h'^-$ vary among the years and are given in Table 2.7.

Projection in sqDP

The (m', θ') of each event is used to fill efficiency TOS and TIS&!TOS maps onto the sqDP, the same procedure is applied to the associated envelope maps. These maps are normalised by the number of events recorded in each sqDP bin. Upper/lower efficiency error maps for TOS and TIS&!TOS events are built from the difference between upper/lower envelop and the efficiency.

The TOS efficiency and error maps are displayed for the two aforementioned examples in figures C.19 to C.22, the TIS&!TOS efficiency and error maps are displayed for the two aforementioned example in figures C.23 to C.26.

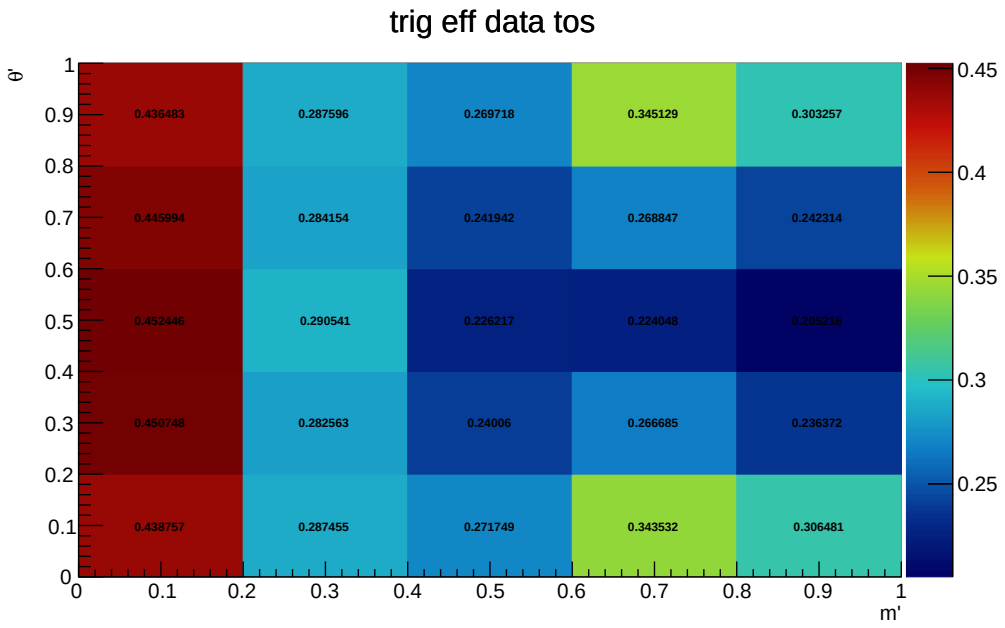

Figure C.19: TOS efficiency map for $B^0_d \to K^0_S \pi\pi$ 2018 MD DD.

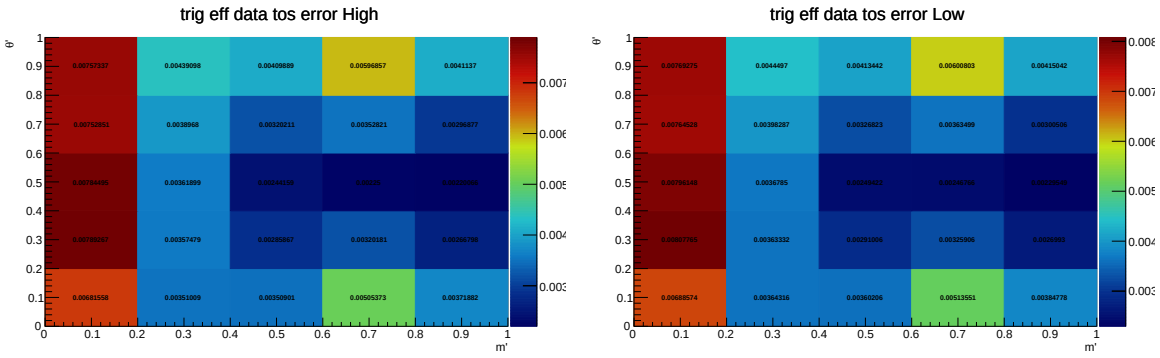

Figure C.20: High (left) and low (right) error on TOS efficiency map for $B^0_d \to K^0_S \pi\pi$ 2018 MD DD.

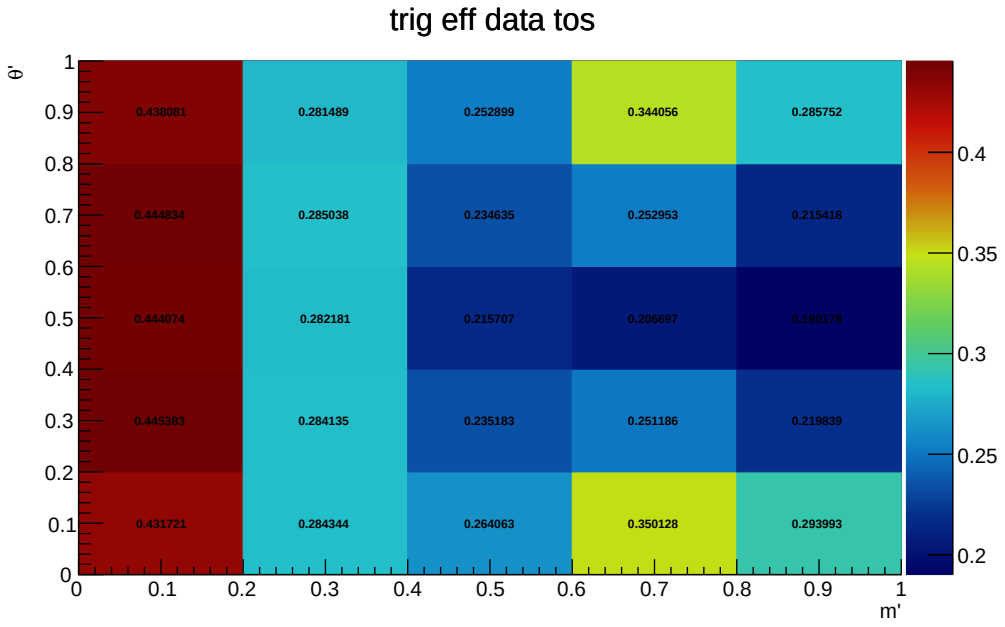

Figure C.21: TOS efficiency map for $B^0_d \to K^0_S \pi\pi$ 2012b MD DD.

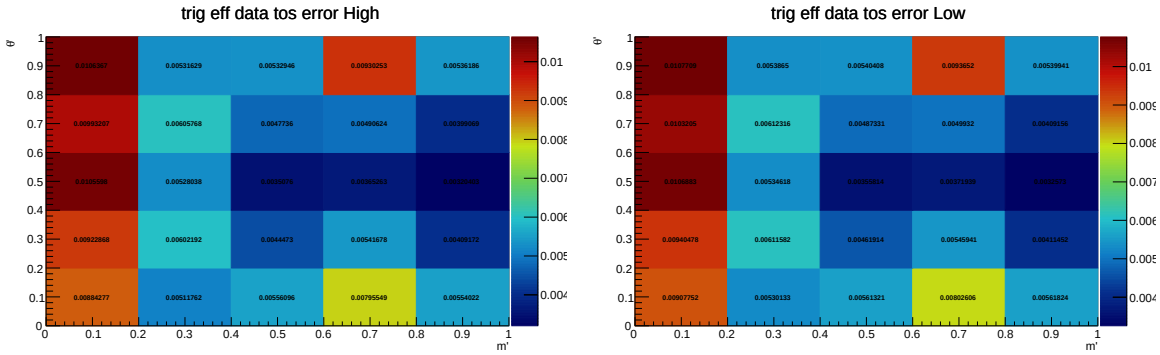

Figure C.22: High (left) and low (right) error on TOS efficiency map for $B^0_d \to K^0_S \pi\pi$ 2012b MD DD.

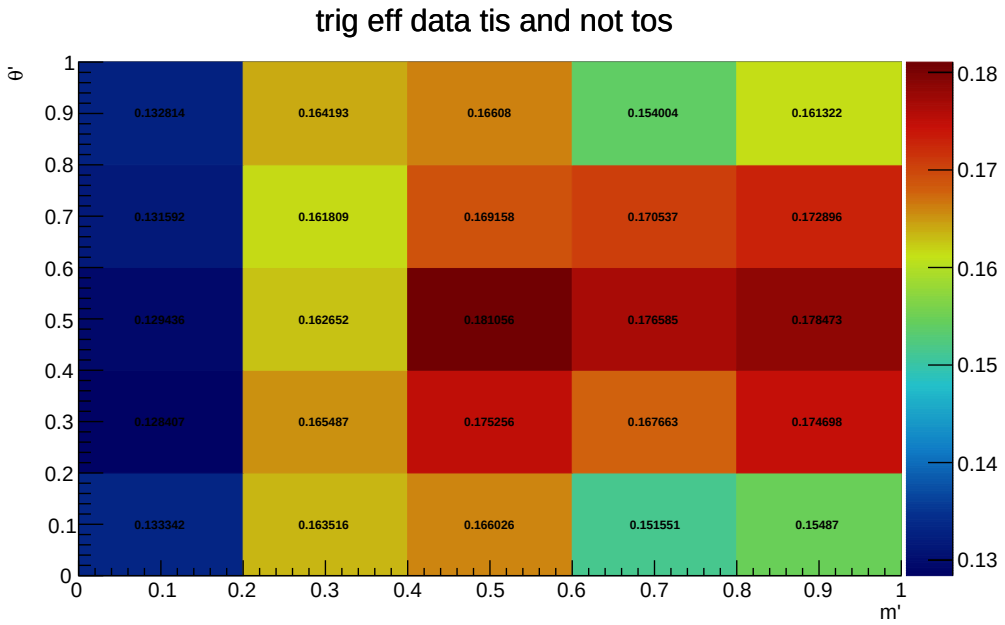

Figure C.23: TIS&!TOS efficiency map for $B^0_d \to K^0_S \pi\pi$ 2018 MD DD.

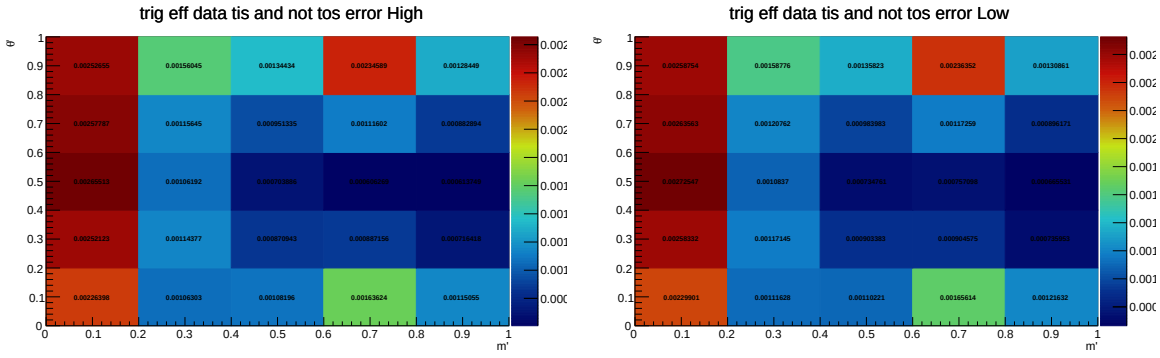

Figure C.24: High (left) and low (right) error on TIS&!TOS efficiency map for $B^0_d \to K^0_S \pi\pi$ 2018 MD DD.

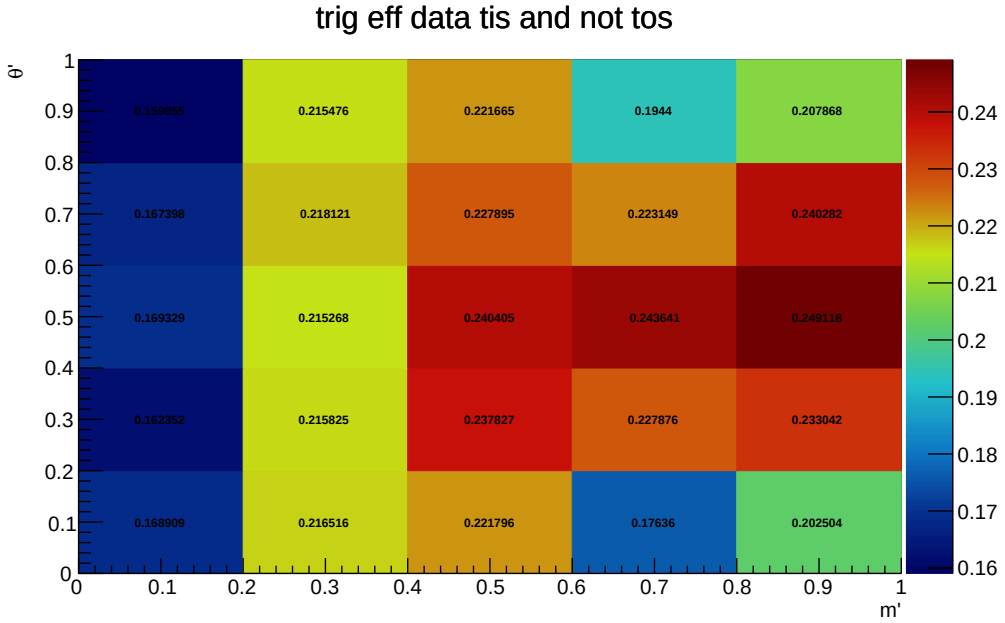

Figure C.25: TIS&!TOS efficiency map for $B^0_d \to K^0_S \pi\pi$ 2012b MD DD.

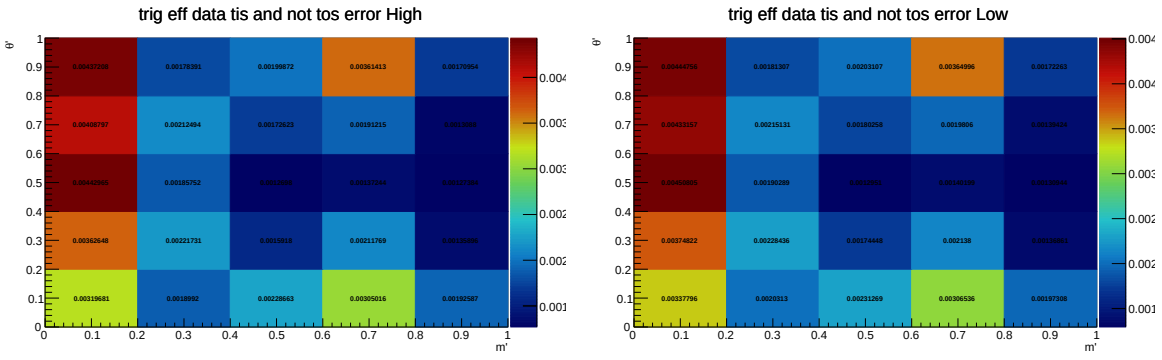

Figure C.26: High (left) and low (right) error on TIS&!TOS efficiency map for $B^0_d \to K^0_S \pi\pi$ 2012b MD DD.

Pure MC efficiency

In order to determine the L0Hadron correction maps, the efficiency maps directly given by the MC samples are needed. To build them, TEfficiency maps onto sqDP are build as:

$$\epsilon^{\text{TOS}}_{\text{MC}} = \frac{\text{evt[iCand==0 and B\_SIG\_mcMatch==1 and B\_L0HadronDecision\_TOS]}}{\text{evt[iCand==0 and B\_SIG\_mcMatch==1]}}, \tag{C.3.7}$$

$$\epsilon^{\text{!TOS}}_{\text{MC}} = \frac{\text{evt[iCand==0 and B\_SIG\_mcMatch==1 and !B\_L0HadronDecision\_TOS]}}{\text{evt[iCand==0 and B\_SIG\_mcMatch==1]}}, \tag{C.3.8}$$

$$\epsilon^{\text{TIS\&!TOS}}_{\text{MC}} = \frac{\text{evt[iCand==0 and B\_SIG\_mcMatch==1 and TIS and !B\_L0HadronDecision\_TOS]}}{\text{evt[iCand==0 and B\_SIG\_mcMatch==1]}}, \tag{C.3.9}$$

where evt denotes sqDP maps of the events with the needed selection applied.

The TOS MC efficiency maps are displayed for the aforementioned examples in Figures C.27 and C.28, and the TIS&!TOS MC efficiency maps are displayed for the aforementioned examples in Figures C.29 and C.30.

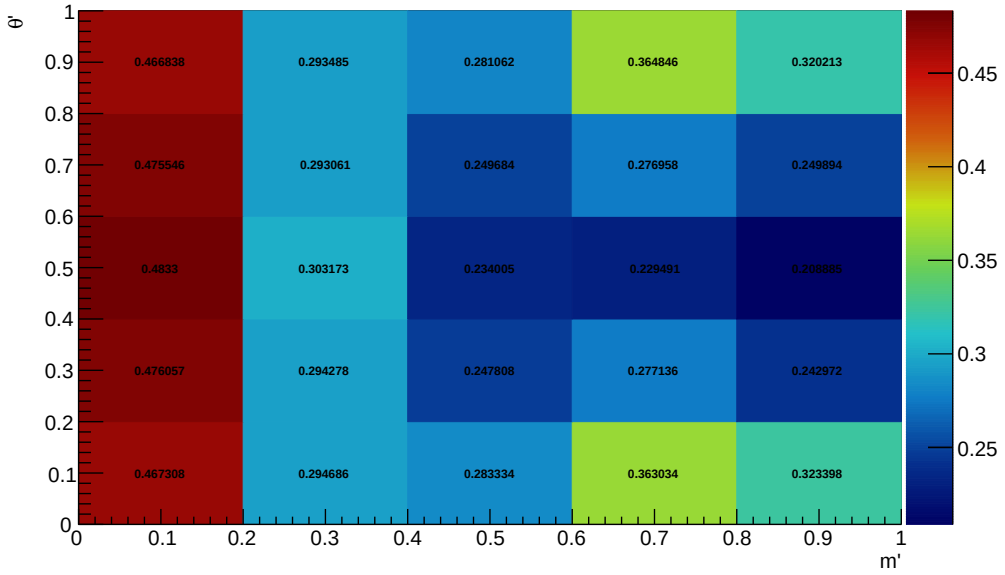

Figure C.27: MC TOS efficiency map for $B^0_d \to K^0_S \pi\pi$ 2018 MD DD.

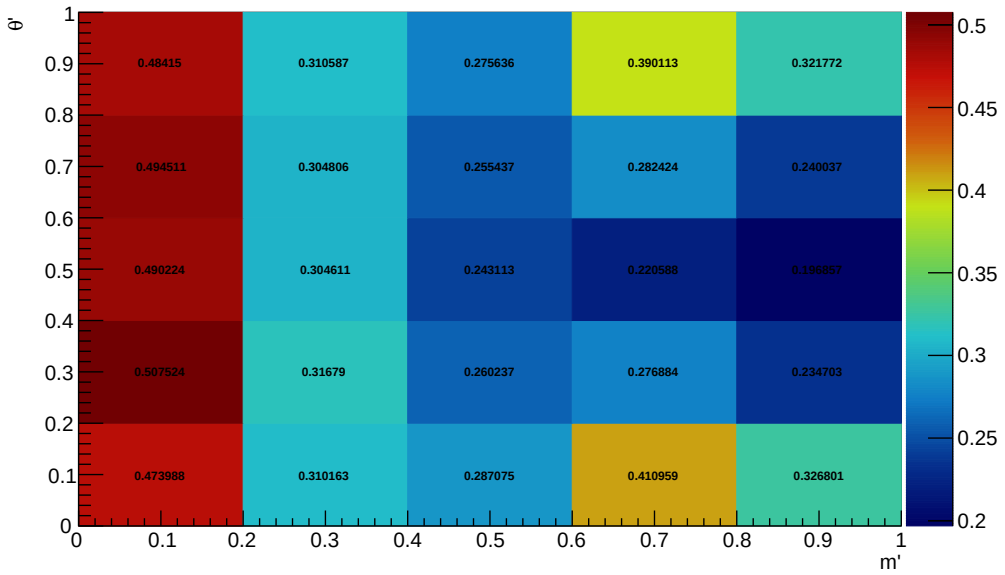

Figure C.28: MC TOS efficiency map for $B^0_d \to K^0_S \pi\pi$ 2012b MD DD.

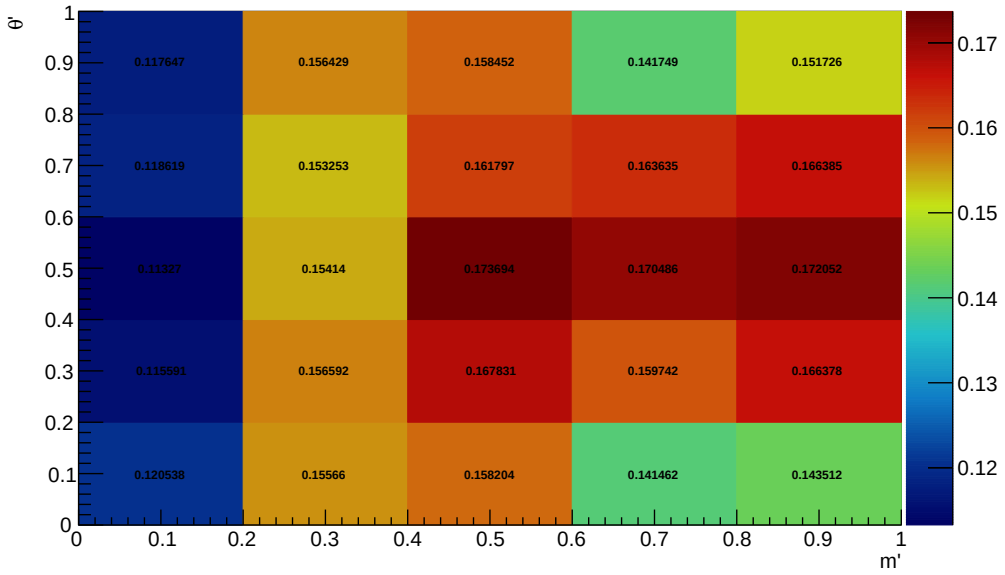

Figure C.29: MC TIS&!TOS efficiency map for $B^0_d \to K^0_S \pi\pi$ 2018 MD DD.

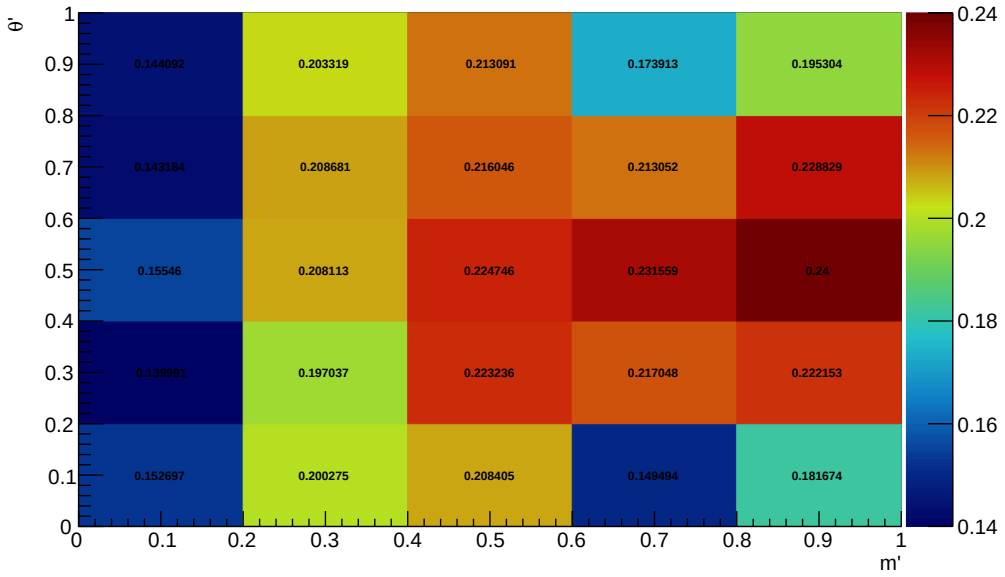

Figure C.30: MC TIS&!TOS efficiency map for $B^0_d \to K^0_S \pi\pi$ 2012b MD DD.

L0Hadron correction determination

The L0Hadron correction maps are built in for the TOS, !TOS and TIS&!TOS cases from the quotient of the efficiency maps computed with the method explained and the MC efficiency maps. Mathematically the correction maps are built bin by bin with:

$$\text{corr}_{\text{TOS}} = \epsilon^{\text{TOS}}/\epsilon^{\text{TOS}}_{\text{MC}}, \tag{C.3.10}$$

$$\text{corr}_{\text{!TOS}} = \epsilon^{\text{!TOS}}/\epsilon^{\text{!TOS}}_{\text{MC}}, \tag{C.3.11}$$

$$\text{corr}_{\text{TIS\&!TOS}} = \epsilon^{\text{TIS\&!TOS}}/\epsilon^{\text{TIS\&!TOS}}_{\text{MC}}. \tag{C.3.12}$$

The TOS L0Hadron correction maps are shown for the aforementioned example in Figures C.31 and C.32 and the TIS&!TOS L0Hadron correction maps are displayed for the aforementioned examples in Figures C.33 and C.34.

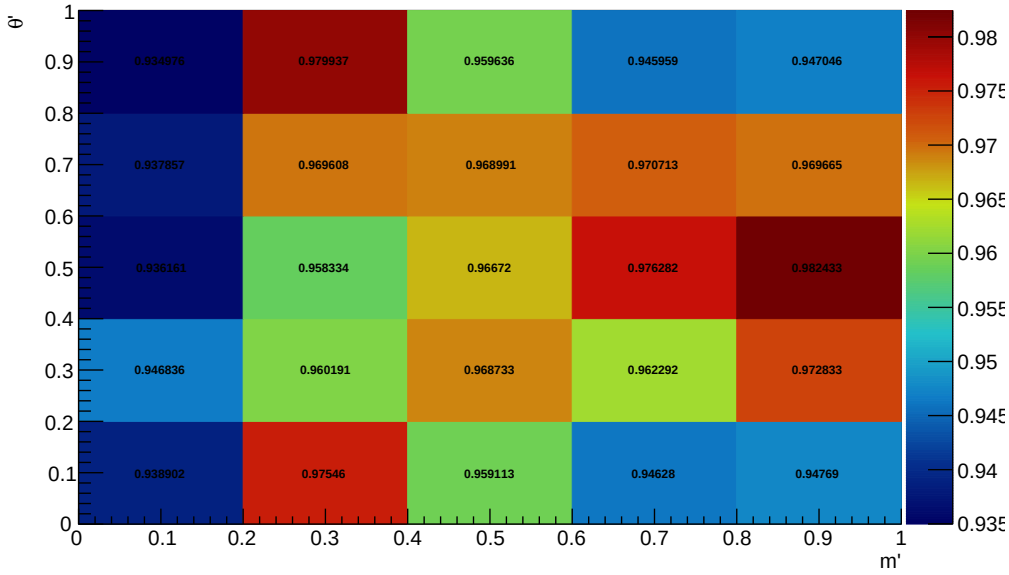

Figure C.31: TOS correction map for $B^0_d \to K^0_S \pi\pi$ 2018 MD DD.

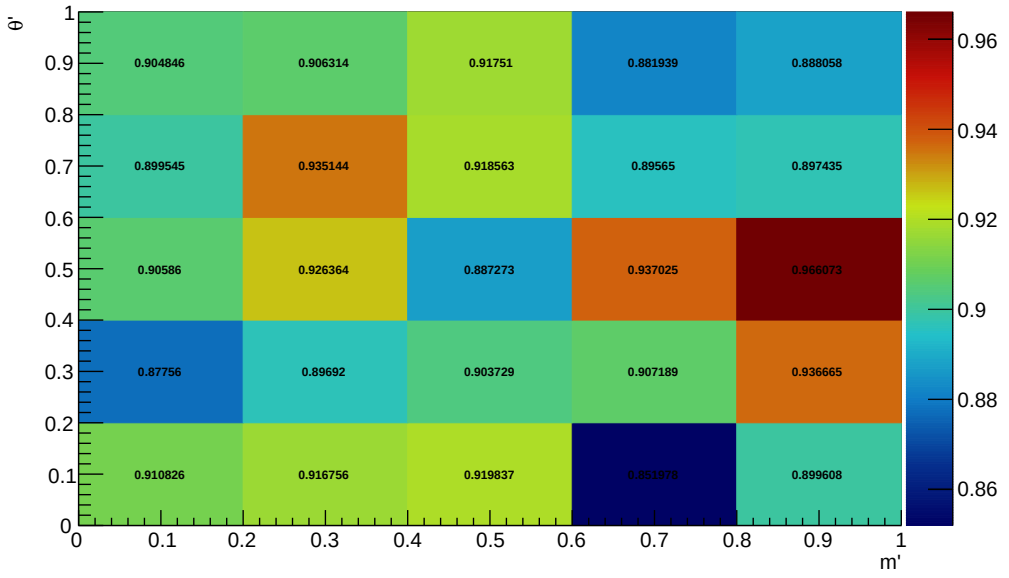

Figure C.32: TOS correction map for $B^0_d \to K^0_S \pi\pi$ 2012b MD DD.

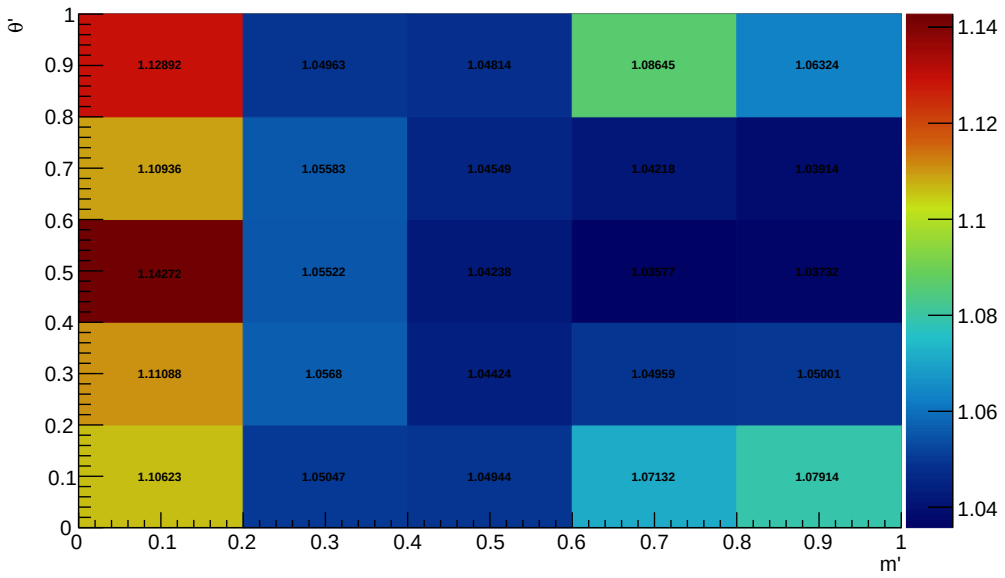

Figure C.33: TIS&!TOS correction map for $B^0_d \to K^0_S \pi\pi$ 2018 MD DD.

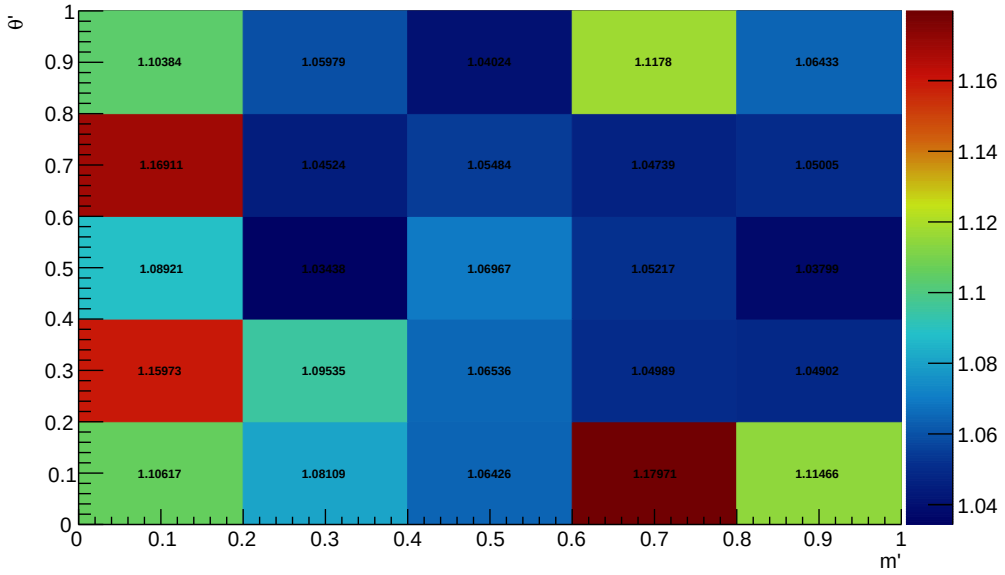

Figure C.34: TIS&!TOS correction map for $B^0_d \to K^0_S \pi\pi$ 2012b MD DD.

At the end, users can apply these corrections to their efficiencies (on the L0Hadron TOS and TIS&!TOS events) in order to take into account the various HCAL effects explained above.

C.3.4 Comparison with former TOS corrections

The purpose of this work was to determine L0Hadron corrections for Run I following the method which was previously only available for Run2 (the update of the Run II corrections was also in order). Previously, another method to correct for L0Hadron efficiency was used for Run I [217], but it neglected effects taken into account by the actual method such as overlap, calibration, and occupancy. Modest changes are expected on the Run II correction such that the method was already used and the updates done are small. For Run I the differences between the former and the actual corrections are expected to be important. The previous TOS correction maps (the TIS&!TOS correction map determination method has been developed later and no former TIS&!TOS maps have been built) corresponding to the examples are displayed in Figures C.35 and C.36.

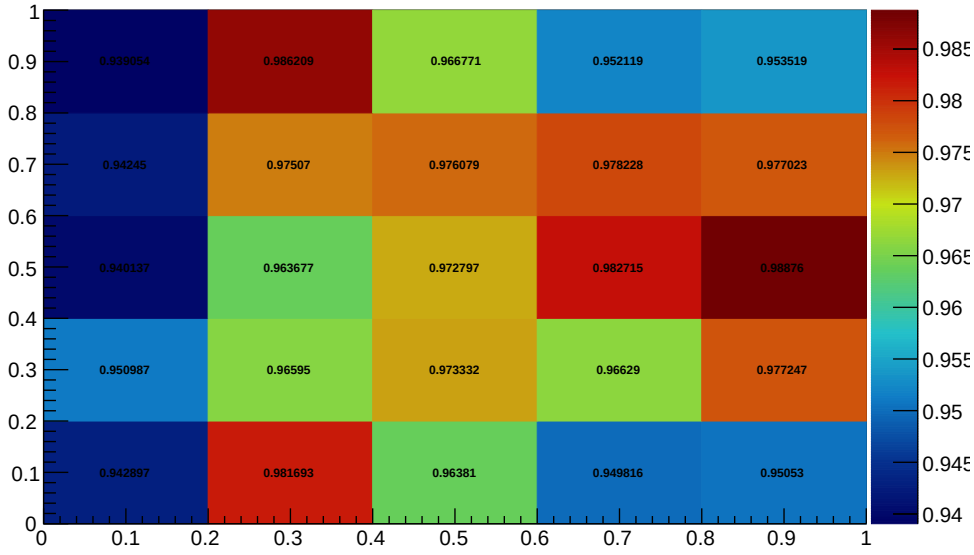

Figure C.35: TOS correction maps for $B^0_d \to K^0_S \pi\pi$ 2018 MD DD with the former corrections determination.

As expected by comparing Figures C.35-C.36 to Figures C.31-C.32, we can see slight changes in the Run II $B^0_{d,s} \to K^0_S h^+ h'^-$ L0Hadron TOS correction maps; the global shapes are conserved. On the other hand, there are important changes on the Run I maps, the shapes are modified.

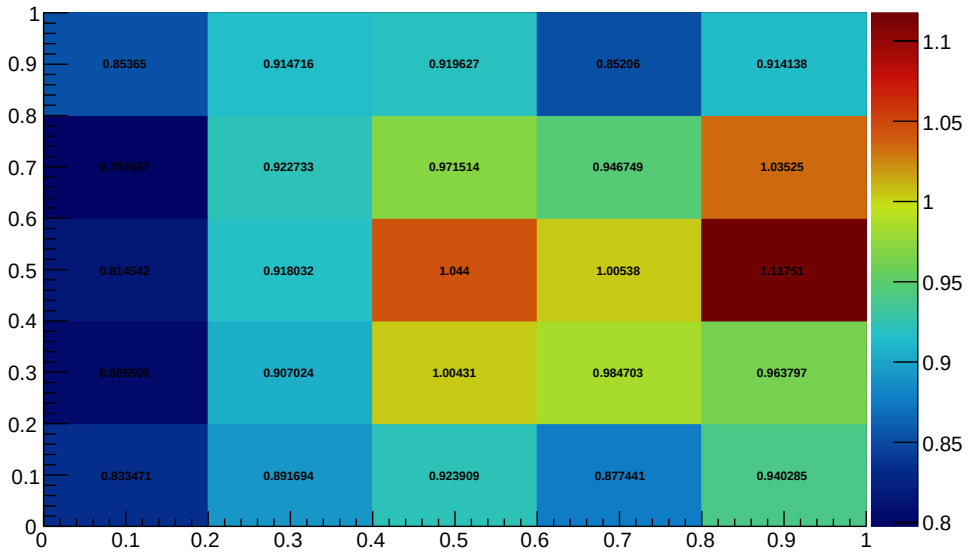

Figure C.36: TOS correction maps for $B^0_d \to K^0_S \pi\pi$ 2012b MD DD with the former corrections determination.

C.3.5 Another correction determination for systematic study

The average occupancy maps built from $b\bar{b}$ events have been taken because it matches the process behind the $B^0_{d,s} \to K^0_S h^+ h'^-$ events. However another possibility can be to consider the regular average occupancy maps built with $c\bar{c}$ events. In order to use this possibility, one can use the building of $c\bar{c}$ correction maps to derive a systematic uncertainty to consider in the efficiency determination. To illustrate this purpose, Figures C.37 and C.38 show the L0Hadron TOS correction maps and Figures C.39 and C.40 display the L0Hadron TIS&!TOS correction maps built with $c\bar{c}$ occupancy for the example of $B^0_{d,s} \to K^0_S h^+ h'^-$.

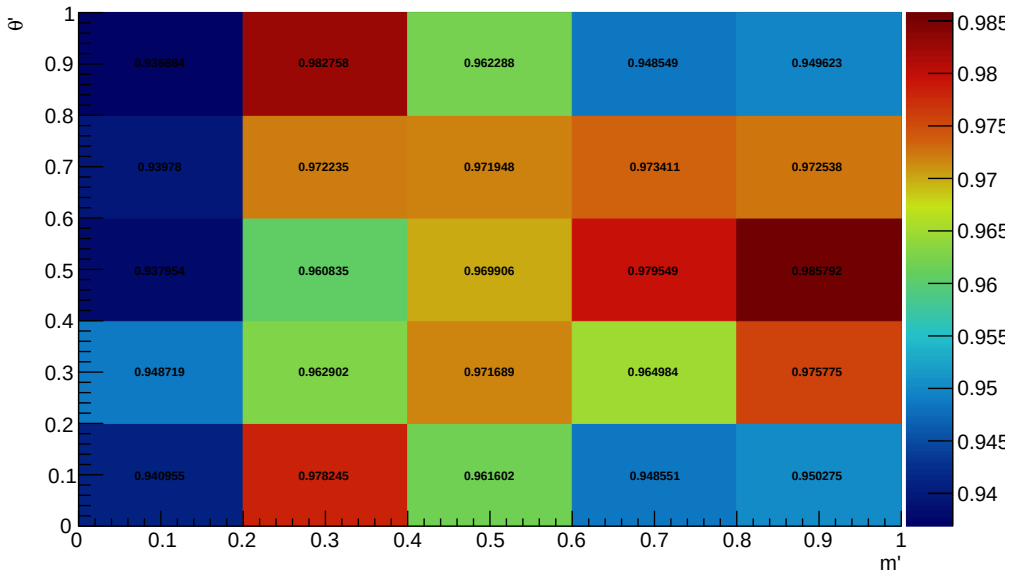

Figure C.37: TOS correction map for $B^0_d \to K^0_S \pi\pi$ 2018 MD DD build with $\bar{c}c$ occupancy maps.

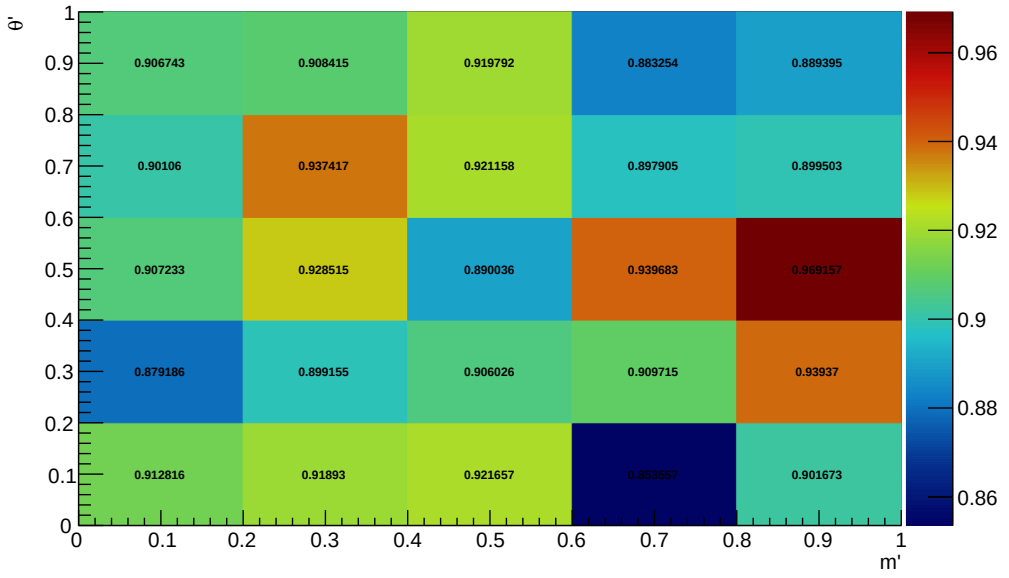

Figure C.38: TOS correction map for $B^0_d \to K^0_S \pi\pi$ 2012b MD DD build with $\bar{c}c$ occupancy maps.

By comparing Figures C.37-C.40 to Figures C.31-C.34, we can see that the choice of occupancy maps considered has only a slight impact on the corrections, the shapes are conserved and the variations are small.

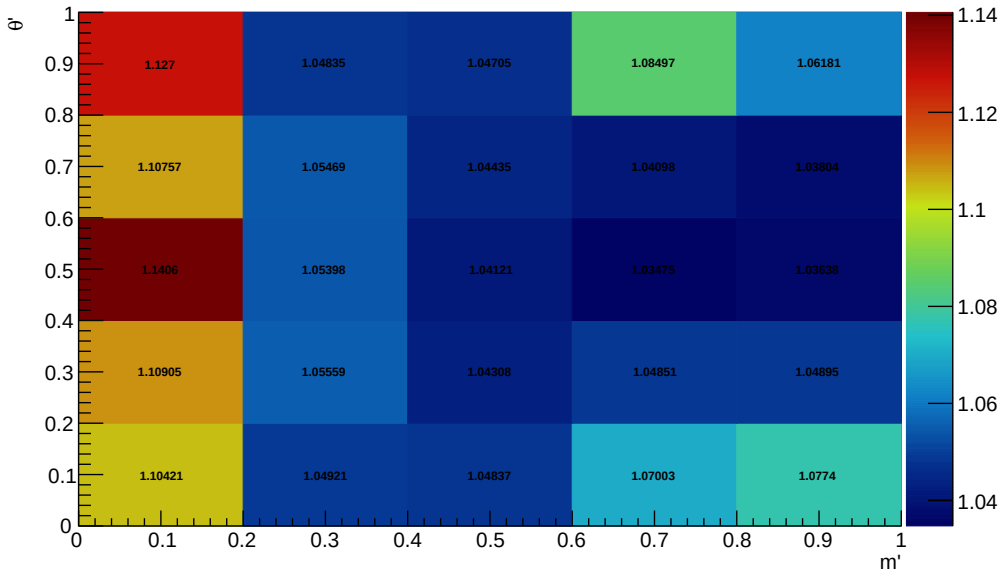

Figure C.39: TIS&!TOS correction map for $B^0_d \to K^0_S \pi\pi$ 2018 MD DD build with $\bar{c}c$ occupancy maps.

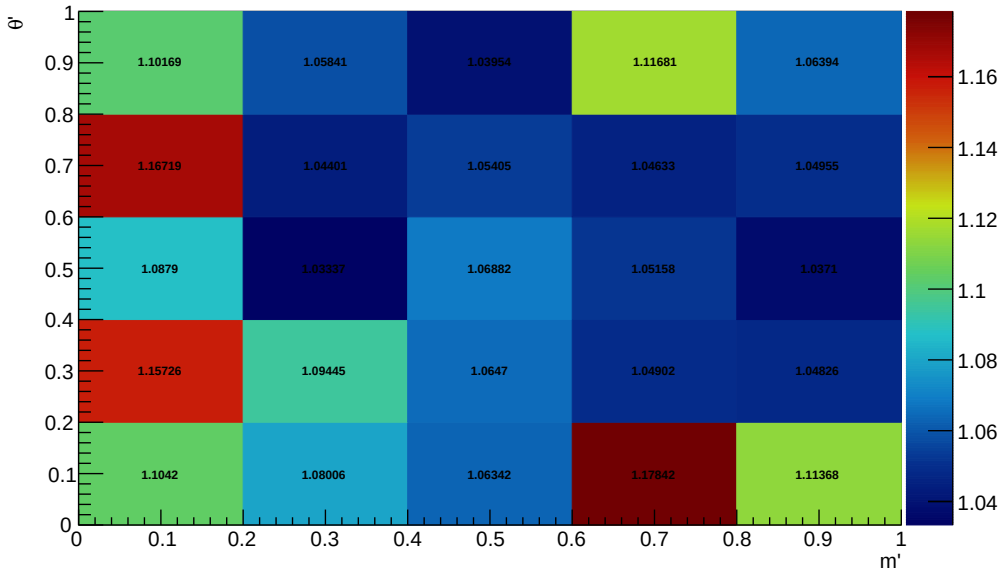

Figure C.40: TIS&!TOS correction map for $B^0_d \to K^0_S \pi\pi$ 2012b MD DD build with $\bar{c}c$ occupancy maps.

C.4 Detailed efficiency tables before magnet combination

Year	Mode	K^0_S	Polarity	Optimisation	$\bar{\varepsilon}$	$\sigma^{\text{cur}}_{\bar{\varepsilon}}$	$\sigma^{\text{ref}}_{\bar{\varepsilon}}$	$\sigma^{\text{RMS}}_{\bar{\varepsilon}}$	$\sigma_{\bar{\varepsilon}}$
2018	$B^0_d \to K^0_S\pi^+\pi^-$	DD	MD	PP	832.5e-6	7.4e-6	4.7e-6	12.2e-6	15.0e-6
2018	$B^0_d \to K^0_S\pi^+\pi^-$	DD	MU	PP	810.3e-6	7.2e-6	5.0e-6	12.2e-6	15.0e-6
2018	$B^0_d \to K^0_S\pi^+\pi^-$	DD	MD	SP	417.1e-6	5.2e-6	2.4e-6	6.3e-6	8.5e-6
2018	$B^0_d \to K^0_S\pi^+\pi^-$	DD	MU	SP	409.8e-6	5.1e-6	2.5e-6	6.3e-6	8.5e-6
2017	$B^0_d \to K^0_S\pi^+\pi^-$	DD	MD	PP	841.8e-6	7.6e-6	4.9e-6	12.2e-6	15.2e-6
2017	$B^0_d \to K^0_S\pi^+\pi^-$	DD	MU	PP	823.4e-6	7.5e-6	5.2e-6	12.2e-6	15.3e-6
2017	$B^0_d \to K^0_S\pi^+\pi^-$	DD	MD	SP	446.4e-6	5.5e-6	2.6e-6	6.3e-6	8.8e-6
2017	$B^0_d \to K^0_S\pi^+\pi^-$	DD	MU	SP	437.5e-6	5.5e-6	2.8e-6	6.3e-6	8.8e-6
2016	$B^0_d \to K^0_S\pi^+\pi^-$	DD	MD	PP	876.9e-6	7.7e-6	5.0e-6	12.2e-6	15.3e-6
2016	$B^0_d \to K^0_S\pi^+\pi^-$	DD	MU	PP	861.1e-6	7.7e-6	5.3e-6	12.2e-6	15.4e-6
2016	$B^0_d \to K^0_S\pi^+\pi^-$	DD	MD	SP	444.0e-6	5.5e-6	2.6e-6	6.3e-6	8.7e-6
2016	$B^0_d \to K^0_S\pi^+\pi^-$	DD	MU	SP	433.3e-6	5.5e-6	2.8e-6	6.3e-6	8.8e-6
2015	$B^0_d \to K^0_S\pi^+\pi^-$	DD	MD	PP	841.0e-6	7.5e-6	5.0e-6	12.2e-6	15.2e-6
2015	$B^0_d \to K^0_S\pi^+\pi^-$	DD	MU	PP	828.6e-6	7.5e-6	5.3e-6	12.2e-6	15.3e-6
2015	$B^0_d \to K^0_S\pi^+\pi^-$	DD	MD	SP	349.0e-6	4.8e-6	2.1e-6	6.3e-6	8.2e-6
2015	$B^0_d \to K^0_S\pi^+\pi^-$	DD	MU	SP	343.1e-6	4.9e-6	2.1e-6	6.3e-6	8.2e-6
2012b	$B^0_d \to K^0_S\pi^+\pi^-$	DD	MD	PP	525.5e-6	7.6e-6	3.6e-6	12.2e-6	14.8e-6
2012b	$B^0_d \to K^0_S\pi^+\pi^-$	DD	MU	PP	513.4e-6	7.1e-6	3.9e-6	12.2e-6	14.6e-6
2012b	$B^0_d \to K^0_S\pi^+\pi^-$	DD	MD	SP	345.9e-6	6.2e-6	2.3e-6	6.3e-6	9.1e-6
2012b	$B^0_d \to K^0_S\pi^+\pi^-$	DD	MU	SP	341.7e-6	5.8e-6	2.5e-6	6.3e-6	8.9e-6
2012a	$B^0_d \to K^0_S\pi^+\pi^-$	DD	MD	PP	401.1e-6	7.1e-6	3.2e-6	12.2e-6	14.5e-6
2012a	$B^0_d \to K^0_S\pi^+\pi^-$	DD	MU	PP	423.6e-6	7.6e-6	2.7e-6	12.2e-6	14.6e-6
2012a	$B^0_d \to K^0_S\pi^+\pi^-$	DD	MD	SP	228.2e-6	5.4e-6	1.8e-6	6.3e-6	8.5e-6
2012a	$B^0_d \to K^0_S\pi^+\pi^-$	DD	MU	SP	238.8e-6	5.7e-6	1.5e-6	6.3e-6	8.6e-6
2011	$B^0_d \to K^0_S\pi^+\pi^-$	DD	MD	PP	485.0e-6	7.4e-6	3.4e-6	12.2e-6	14.6e-6
2011	$B^0_d \to K^0_S\pi^+\pi^-$	DD	MU	PP	500.4e-6	8.1e-6	3.7e-6	12.2e-6	15.1e-6
2011	$B^0_d \to K^0_S\pi^+\pi^-$	DD	MD	SP	230.5e-6	5.1e-6	1.6e-6	6.3e-6	8.3e-6
2011	$B^0_d \to K^0_S\pi^+\pi^-$	DD	MU	SP	248.1e-6	5.8e-6	1.6e-6	6.3e-6	8.7e-6
2018	$B^0_d \to K^0_S\pi^+\pi^-$	LL	MD	PP	296.4e-6	4.4e-6	2.8e-6	6.5e-6	8.4e-6
2018	$B^0_d \to K^0_S\pi^+\pi^-$	LL	MU	PP	297.3e-6	4.5e-6	2.6e-6	6.5e-6	8.3e-6
2018	$B^0_d \to K^0_S\pi^+\pi^-$	LL	MD	SP	193.6e-6	3.6e-6	2.0e-6	4.4e-6	6.0e-6
2018	$B^0_d \to K^0_S\pi^+\pi^-$	LL	MU	SP	188.3e-6	3.6e-6	1.7e-6	4.4e-6	5.9e-6
2017	$B^0_d \to K^0_S\pi^+\pi^-$	LL	MD	PP	318.0e-6	4.7e-6	3.3e-6	6.5e-6	8.7e-6
2017	$B^0_d \to K^0_S\pi^+\pi^-$	LL	MU	PP	315.7e-6	4.8e-6	2.7e-6	6.5e-6	8.5e-6
2017	$B^0_d \to K^0_S\pi^+\pi^-$	LL	MD	SP	216.6e-6	3.9e-6	2.4e-6	4.4e-6	6.3e-6
2017	$B^0_d \to K^0_S\pi^+\pi^-$	LL	MU	SP	213.8e-6	3.9e-6	1.9e-6	4.4e-6	6.2e-6
2016	$B^0_d \to K^0_S\pi^+\pi^-$	LL	MD	PP	359.8e-6	5.0e-6	3.6e-6	6.5e-6	9.0e-6
2016	$B^0_d \to K^0_S\pi^+\pi^-$	LL	MU	PP	352.5e-6	5.0e-6	3.1e-6	6.5e-6	8.8e-6
2016	$B^0_d \to K^0_S\pi^+\pi^-$	LL	MD	SP	222.7e-6	3.9e-6	2.3e-6	4.4e-6	6.3e-6
2016	$B^0_d \to K^0_S\pi^+\pi^-$	LL	MU	SP	219.9e-6	4.0e-6	2.0e-6	4.4e-6	6.2e-6
2015	$B^0_d \to K^0_S\pi^+\pi^-$	LL	MD	PP	328.9e-6	4.8e-6	3.2e-6	6.5e-6	8.7e-6
2015	$B^0_d \to K^0_S\pi^+\pi^-$	LL	MU	PP	325.6e-6	4.9e-6	2.8e-6	6.5e-6	8.6e-6
2015	$B^0_d \to K^0_S\pi^+\pi^-$	LL	MD	SP	197.9e-6	3.7e-6	2.1e-6	4.4e-6	6.1e-6
2015	$B^0_d \to K^0_S\pi^+\pi^-$	LL	MU	SP	201.0e-6	3.9e-6	1.8e-6	4.4e-6	6.1e-6
2012b	$B^0_d \to K^0_S\pi^+\pi^-$	LL	MD	PP	152.2e-6	4.2e-6	1.8e-6	6.5e-6	7.9e-6
2012b	$B^0_d \to K^0_S\pi^+\pi^-$	LL	MU	PP	154.5e-6	4.0e-6	1.6e-6	6.5e-6	7.8e-6
2012b	$B^0_d \to K^0_S\pi^+\pi^-$	LL	MD	SP	108.5e-6	3.5e-6	1.3e-6	4.4e-6	5.8e-6
2012b	$B^0_d \to K^0_S\pi^+\pi^-$	LL	MU	SP	108.4e-6	3.3e-6	1.1e-6	4.4e-6	5.6e-6
2012a	$B^0_d \to K^0_S\pi^+\pi^-$	LL	MD	PP	178.3e-6	5.0e-6	1.9e-6	6.5e-6	8.4e-6
2012a	$B^0_d \to K^0_S\pi^+\pi^-$	LL	MU	PP	175.2e-6	5.0e-6	1.6e-6	6.5e-6	8.4e-6
2012a	$B^0_d \to K^0_S\pi^+\pi^-$	LL	MD	SP	793.0e-7	33.3e-7	9.7e-7	43.8e-7	55.9e-7
2012a	$B^0_d \to K^0_S\pi^+\pi^-$	LL	MU	SP	760.9e-7	33.4e-7	7.0e-7	43.8e-7	55.5e-7
2011	$B^0_d \to K^0_S\pi^+\pi^-$	LL	MD	PP	190.3e-6	4.8e-6	2.1e-6	6.5e-6	8.4e-6
2011	$B^0_d \to K^0_S\pi^+\pi^-$	LL	MU	PP	184.4e-6	5.1e-6	1.7e-6	6.5e-6	8.4e-6
2011	$B^0_d \to K^0_S\pi^+\pi^-$	LL	MD	SP	135.5e-6	4.1e-6	1.5e-6	4.4e-6	6.2e-6
2011	$B^0_d \to K^0_S\pi^+\pi^-$	LL	MU	SP	129.8e-6	4.3e-6	1.2e-6	4.4e-6	6.2e-6

Table C.12: $B^0 \to K^0_S\pi^+\pi^-$ detailed efficiency tables. PP stand for favoured mode optimisation and SP for unfavoured mode optimisation.

Year	Mode	K^0_S	Polarity	Optimisation	$\bar{\varepsilon}$	$\sigma^{\text{cur}}_{\bar{\varepsilon}}$	$\sigma^{\text{ref}}_{\bar{\varepsilon}}$	$\sigma^{\text{RMS}}_{\bar{\varepsilon}}$	$\sigma_{\bar{\varepsilon}}$
2018	$B^0_d \to K^0_S\pi^+K^-$	DD	MD	PP	878.5e-6	13.7e-6	3.9e-6	13.1e-6	19.4e-6
2018	$B^0_d \to K^0_S\pi^+K^-$	DD	MU	PP	891.2e-6	13.4e-6	4.0e-6	13.1e-6	19.2e-6
2018	$B^0_d \to K^0_S\pi^+K^-$	DD	MD	SP	664.9e-6	11.9e-6	2.9e-6	11.4e-6	16.8e-6
2018	$B^0_d \to K^0_S\pi^+K^-$	DD	MU	SP	669.1e-6	11.7e-6	3.1e-6	11.4e-6	16.6e-6
2017	$B^0_d \to K^0_S\pi^+K^-$	DD	MD	PP	940.5e-6	14.5e-6	3.9e-6	13.1e-6	19.9e-6
2017	$B^0_d \to K^0_S\pi^+K^-$	DD	MU	PP	909.0e-6	14.1e-6	4.1e-6	13.1e-6	19.7e-6
2017	$B^0_d \to K^0_S\pi^+K^-$	DD	MD	SP	707.4e-6	12.6e-6	2.9e-6	11.4e-6	17.2e-6
2017	$B^0_d \to K^0_S\pi^+K^-$	DD	MU	SP	685.9e-6	12.3e-6	3.1e-6	11.4e-6	17.1e-6
2016	$B^0_d \to K^0_S\pi^+K^-$	DD	MD	PP	1059.3e-6	15.2e-6	4.7e-6	13.1e-6	20.6e-6
2016	$B^0_d \to K^0_S\pi^+K^-$	DD	MU	PP	1041.8e-6	15.4e-6	4.9e-6	13.1e-6	20.8e-6
2016	$B^0_d \to K^0_S\pi^+K^-$	DD	MD	SP	791.0e-6	13.1e-6	3.5e-6	11.4e-6	17.7e-6
2016	$B^0_d \to K^0_S\pi^+K^-$	DD	MU	SP	786.8e-6	13.4e-6	3.7e-6	11.4e-6	18.0e-6
2015	$B^0_d \to K^0_S\pi^+K^-$	DD	MD	PP	938.8e-6	14.6e-6	4.2e-6	13.1e-6	20.1e-6
2015	$B^0_d \to K^0_S\pi^+K^-$	DD	MU	PP	925.4e-6	14.6e-6	4.2e-6	13.1e-6	20.1e-6
2015	$B^0_d \to K^0_S\pi^+K^-$	DD	MD	SP	688.4e-6	12.6e-6	3.3e-6	11.4e-6	17.3e-6
2015	$B^0_d \to K^0_S\pi^+K^-$	DD	MU	SP	694.4e-6	12.7e-6	3.3e-6	11.4e-6	17.4e-6
2012b	$B^0_d \to K^0_S\pi^+K^-$	DD	MD	PP	660.2e-6	16.5e-6	3.8e-6	13.1e-6	21.4e-6
2012b	$B^0_d \to K^0_S\pi^+K^-$	DD	MU	PP	663.1e-6	15.3e-6	3.9e-6	13.1e-6	20.5e-6
2012b	$B^0_d \to K^0_S\pi^+K^-$	DD	MD	SP	520.0e-6	14.7e-6	3.1e-6	11.4e-6	18.8e-6
2012b	$B^0_d \to K^0_S\pi^+K^-$	DD	MU	SP	512.1e-6	13.4e-6	3.1e-6	11.4e-6	17.9e-6
2012a	$B^0_d \to K^0_S\pi^+K^-$	DD	MD	PP	498.7e-6	15.0e-6	3.1e-6	13.1e-6	20.1e-6
2012a	$B^0_d \to K^0_S\pi^+K^-$	DD	MU	PP	509.1e-6	15.4e-6	3.3e-6	13.1e-6	20.5e-6
2012a	$B^0_d \to K^0_S\pi^+K^-$	DD	MD	SP	418.0e-6	13.8e-6	2.4e-6	11.4e-6	18.1e-6
2012a	$B^0_d \to K^0_S\pi^+K^-$	DD	MU	SP	419.0e-6	14.1e-6	2.8e-6	11.4e-6	18.4e-6
2011	$B^0_d \to K^0_S\pi^+K^-$	DD	MD	PP	611.9e-6	15.8e-6	3.9e-6	13.1e-6	20.9e-6
2011	$B^0_d \to K^0_S\pi^+K^-$	DD	MU	PP	606.7e-6	14.9e-6	3.8e-6	13.1e-6	20.2e-6
2011	$B^0_d \to K^0_S\pi^+K^-$	DD	MD	SP	510.2e-6	14.5e-6	3.3e-6	11.4e-6	18.8e-6
2011	$B^0_d \to K^0_S\pi^+K^-$	DD	MU	SP	492.3e-6	13.5e-6	3.1e-6	11.4e-6	18.0e-6
2018	$B^0_d \to K^0_S\pi^+K^-$	LL	MD	PP	328.0e-6	8.6e-6	5.7e-6	12.0e-6	15.8e-6
2018	$B^0_d \to K^0_S\pi^+K^-$	LL	MU	PP	339.9e-6	8.7e-6	3.8e-6	12.0e-6	15.3e-6
2018	$B^0_d \to K^0_S\pi^+K^-$	LL	MD	SP	271.7e-6	7.8e-6	4.7e-6	8.5e-6	12.5e-6
2018	$B^0_d \to K^0_S\pi^+K^-$	LL	MU	SP	279.5e-6	7.9e-6	3.1e-6	8.5e-6	12.0e-6
2017	$B^0_d \to K^0_S\pi^+K^-$	LL	MD	PP	351.8e-6	9.2e-6	6.2e-6	12.0e-6	16.3e-6
2017	$B^0_d \to K^0_S\pi^+K^-$	LL	MU	PP	392.4e-6	9.9e-6	4.2e-6	12.0e-6	16.1e-6
2017	$B^0_d \to K^0_S\pi^+K^-$	LL	MD	SP	287.3e-6	8.3e-6	5.1e-6	8.5e-6	12.9e-6
2017	$B^0_d \to K^0_S\pi^+K^-$	LL	MU	SP	319.9e-6	8.9e-6	3.5e-6	8.5e-6	12.8e-6
2016	$B^0_d \to K^0_S\pi^+K^-$	LL	MD	PP	387.5e-6	9.7e-6	6.4e-6	12.0e-6	16.7e-6
2016	$B^0_d \to K^0_S\pi^+K^-$	LL	MU	PP	380.8e-6	9.8e-6	4.0e-6	12.0e-6	16.0e-6
2016	$B^0_d \to K^0_S\pi^+K^-$	LL	MD	SP	312.0e-6	8.7e-6	5.1e-6	8.5e-6	13.2e-6
2016	$B^0_d \to K^0_S\pi^+K^-$	LL	MU	SP	311.7e-6	8.8e-6	3.3e-6	8.5e-6	12.7e-6
2015	$B^0_d \to K^0_S\pi^+K^-$	LL	MD	PP	352.5e-6	9.4e-6	5.5e-6	12.0e-6	16.2e-6
2015	$B^0_d \to K^0_S\pi^+K^-$	LL	MU	PP	387.5e-6	10.1e-6	4.1e-6	12.0e-6	16.2e-6
2015	$B^0_d \to K^0_S\pi^+K^-$	LL	MD	SP	235.5e-6	7.6e-6	4.0e-6	8.5e-6	12.1e-6
2015	$B^0_d \to K^0_S\pi^+K^-$	LL	MU	SP	256.0e-6	8.1e-6	2.9e-6	8.5e-6	12.1e-6
2012b	$B^0_d \to K^0_S\pi^+K^-$	LL	MD	PP	179.2e-6	8.8e-6	3.4e-6	12.0e-6	15.3e-6
2012b	$B^0_d \to K^0_S\pi^+K^-$	LL	MU	PP	183.4e-6	8.6e-6	2.2e-6	12.0e-6	14.9e-6
2012b	$B^0_d \to K^0_S\pi^+K^-$	LL	MD	SP	96.2e-6	6.6e-6	1.5e-6	8.5e-6	10.9e-6
2012b	$B^0_d \to K^0_S\pi^+K^-$	LL	MU	SP	92.3e-6	6.0e-6	1.2e-6	8.5e-6	10.5e-6
2012a	$B^0_d \to K^0_S\pi^+K^-$	LL	MD	PP	208.4e-6	10.0e-6	3.6e-6	12.0e-6	16.0e-6
2012a	$B^0_d \to K^0_S\pi^+K^-$	LL	MU	PP	208.4e-6	10.3e-6	1.9e-6	12.0e-6	15.9e-6
2012a	$B^0_d \to K^0_S\pi^+K^-$	LL	MD	SP	155.4e-6	8.7e-6	2.7e-6	8.5e-6	12.5e-6
2012a	$B^0_d \to K^0_S\pi^+K^-$	LL	MU	SP	155.6e-6	8.9e-6	1.6e-6	8.5e-6	12.4e-6
2011	$B^0_d \to K^0_S\pi^+K^-$	LL	MD	PP	232.1e-6	10.3e-6	4.2e-6	12.0e-6	16.3e-6
2011	$B^0_d \to K^0_S\pi^+K^-$	LL	MU	PP	243.5e-6	10.1e-6	3.1e-6	12.0e-6	16.0e-6
2011	$B^0_d \to K^0_S\pi^+K^-$	LL	MD	SP	188.4e-6	9.2e-6	3.4e-6	8.5e-6	13.0e-6
2011	$B^0_d \to K^0_S\pi^+K^-$	LL	MU	SP	200.2e-6	9.2e-6	2.7e-6	8.5e-6	12.8e-6

Table C.13: $B^0 \to K^0_S\pi^+K^-$ detailed efficiency tables. PP stand for favoured mode optimisation and SP for unfavoured mode optimisation.

Year	Mode	K^0_S	Polarity	Optimisation	$\bar{\varepsilon}$	$\sigma^{\text{cur}}_{\bar{\varepsilon}}$	$\sigma^{\text{ref}}_{\bar{\varepsilon}}$	$\sigma^{\text{RMS}}_{\bar{\varepsilon}}$	$\sigma_{\bar{\varepsilon}}$
2018	$B^0_d \to K^0_S K^+\pi^-$	DD	MD	PP	899.2e-6	15.2e-6	4.7e-6	14.7e-6	21.7e-6
2018	$B^0_d \to K^0_S K^+\pi^-$	DD	MU	PP	897.4e-6	14.8e-6	4.1e-6	14.7e-6	21.2e-6
2018	$B^0_d \to K^0_S K^+\pi^-$	DD	MD	SP	678.7e-6	13.2e-6	3.7e-6	11.4e-6	17.8e-6
2018	$B^0_d \to K^0_S K^+\pi^-$	DD	MU	SP	688.6e-6	13.0e-6	3.2e-6	11.4e-6	17.6e-6
2017	$B^0_d \to K^0_S K^+\pi^-$	DD	MD	PP	940.9e-6	16.0e-6	5.3e-6	14.7e-6	22.4e-6
2017	$B^0_d \to K^0_S K^+\pi^-$	DD	MU	PP	972.7e-6	16.3e-6	5.0e-6	14.7e-6	22.5e-6
2017	$B^0_d \to K^0_S K^+\pi^-$	DD	MD	SP	778.0e-6	14.6e-6	4.5e-6	11.4e-6	19.1e-6
2017	$B^0_d \to K^0_S K^+\pi^-$	DD	MU	SP	791.1e-6	14.7e-6	4.1e-6	11.4e-6	19.1e-6
2016	$B^0_d \to K^0_S K^+\pi^-$	DD	MD	PP	1032.0e-6	16.7e-6	5.5e-6	14.7e-6	22.9e-6
2016	$B^0_d \to K^0_S K^+\pi^-$	DD	MU	PP	1009.9e-6	16.7e-6	4.8e-6	14.7e-6	22.8e-6
2016	$B^0_d \to K^0_S K^+\pi^-$	DD	MD	SP	752.2e-6	14.2e-6	4.1e-6	11.4e-6	18.6e-6
2016	$B^0_d \to K^0_S K^+\pi^-$	DD	MU	SP	761.0e-6	14.6e-6	3.7e-6	11.4e-6	18.9e-6
2015	$B^0_d \to K^0_S K^+\pi^-$	DD	MD	PP	944.4e-6	16.2e-6	5.2e-6	14.7e-6	22.5e-6
2015	$B^0_d \to K^0_S K^+\pi^-$	DD	MU	PP	916.8e-6	16.3e-6	4.5e-6	14.7e-6	22.4e-6
2015	$B^0_d \to K^0_S K^+\pi^-$	DD	MD	SP	669.7e-6	13.7e-6	4.0e-6	11.4e-6	18.3e-6
2015	$B^0_d \to K^0_S K^+\pi^-$	DD	MU	SP	647.2e-6	13.8e-6	3.4e-6	11.4e-6	18.2e-6
2012b	$B^0_d \to K^0_S K^+\pi^-$	DD	MD	PP	681.7e-6	18.6e-6	4.4e-6	14.7e-6	24.1e-6
2012b	$B^0_d \to K^0_S K^+\pi^-$	DD	MU	PP	681.4e-6	17.2e-6	4.2e-6	14.7e-6	23.0e-6
2012b	$B^0_d \to K^0_S K^+\pi^-$	DD	MD	SP	494.7e-6	16.1e-6	3.3e-6	11.4e-6	20.0e-6
2012b	$B^0_d \to K^0_S K^+\pi^-$	DD	MU	SP	475.5e-6	14.5e-6	2.9e-6	11.4e-6	18.7e-6
2012a	$B^0_d \to K^0_S K^+\pi^-$	DD	MD	PP	508.3e-6	16.9e-6	3.6e-6	14.7e-6	22.6e-6
2012a	$B^0_d \to K^0_S K^+\pi^-$	DD	MU	PP	531.8e-6	18.0e-6	3.8e-6	14.7e-6	23.5e-6
2012a	$B^0_d \to K^0_S K^+\pi^-$	DD	MD	SP	386.3e-6	14.7e-6	2.8e-6	11.4e-6	18.8e-6
2012a	$B^0_d \to K^0_S K^+\pi^-$	DD	MU	SP	420.1e-6	16.1e-6	3.1e-6	11.4e-6	19.9e-6
2011	$B^0_d \to K^0_S K^+\pi^-$	DD	MD	PP	646.2e-6	18.6e-6	4.7e-6	14.7e-6	24.1e-6
2011	$B^0_d \to K^0_S K^+\pi^-$	DD	MU	PP	623.5e-6	17.4e-6	4.4e-6	14.7e-6	23.2e-6
2011	$B^0_d \to K^0_S K^+\pi^-$	DD	MD	SP	541.8e-6	17.0e-6	3.8e-6	11.4e-6	20.8e-6
2011	$B^0_d \to K^0_S K^+\pi^-$	DD	MU	SP	524.6e-6	16.0e-6	3.9e-6	11.4e-6	20.0e-6
2018	$B^0_d \to K^0_S K^+\pi^-$	LL	MD	PP	328.4e-6	10.1e-6	3.7e-6	13.4e-6	17.2e-6
2018	$B^0_d \to K^0_S K^+\pi^-$	LL	MU	PP	316.9e-6	9.7e-6	3.9e-6	13.4e-6	17.0e-6
2018	$B^0_d \to K^0_S K^+\pi^-$	LL	MD	SP	273.5e-6	9.3e-6	3.2e-6	9.8e-6	13.8e-6
2018	$B^0_d \to K^0_S K^+\pi^-$	LL	MU	SP	261.6e-6	8.8e-6	3.3e-6	9.8e-6	13.6e-6
2017	$B^0_d \to K^0_S K^+\pi^-$	LL	MD	PP	376.6e-6	11.3e-6	4.6e-6	13.4e-6	18.2e-6
2017	$B^0_d \to K^0_S K^+\pi^-$	LL	MU	PP	358.4e-6	11.1e-6	4.2e-6	13.4e-6	17.9e-6
2017	$B^0_d \to K^0_S K^+\pi^-$	LL	MD	SP	291.6e-6	9.9e-6	3.8e-6	9.8e-6	14.4e-6
2017	$B^0_d \to K^0_S K^+\pi^-$	LL	MU	SP	284.6e-6	9.9e-6	3.4e-6	9.8e-6	14.3e-6
2016	$B^0_d \to K^0_S K^+\pi^-$	LL	MD	PP	405.7e-6	11.7e-6	4.4e-6	13.4e-6	18.3e-6
2016	$B^0_d \to K^0_S K^+\pi^-$	LL	MU	PP	395.4e-6	11.7e-6	4.8e-6	13.4e-6	18.4e-6
2016	$B^0_d \to K^0_S K^+\pi^-$	LL	MD	SP	318.5e-6	10.3e-6	3.5e-6	9.8e-6	14.7e-6
2016	$B^0_d \to K^0_S K^+\pi^-$	LL	MU	SP	308.5e-6	10.3e-6	3.7e-6	9.8e-6	14.7e-6
2015	$B^0_d \to K^0_S K^+\pi^-$	LL	MD	PP	382.3e-6	11.5e-6	4.3e-6	13.4e-6	18.2e-6
2015	$B^0_d \to K^0_S K^+\pi^-$	LL	MU	PP	363.6e-6	11.3e-6	4.0e-6	13.4e-6	18.0e-6
2015	$B^0_d \to K^0_S K^+\pi^-$	LL	MD	SP	279.9e-6	9.8e-6	3.3e-6	9.8e-6	14.2e-6
2015	$B^0_d \to K^0_S K^+\pi^-$	LL	MU	SP	262.5e-6	9.5e-6	3.0e-6	9.8e-6	14.0e-6
2012b	$B^0_d \to K^0_S K^+\pi^-$	LL	MD	PP	176.3e-6	10.3e-6	2.3e-6	13.4e-6	17.1e-6
2012b	$B^0_d \to K^0_S K^+\pi^-$	LL	MU	PP	179.6e-6	9.9e-6	3.0e-6	13.4e-6	16.9e-6
2012b	$B^0_d \to K^0_S K^+\pi^-$	LL	MD	SP	87.7e-6	7.2e-6	1.5e-6	9.8e-6	12.2e-6
2012b	$B^0_d \to K^0_S K^+\pi^-$	LL	MU	SP	92.0e-6	7.0e-6	1.5e-6	9.8e-6	12.1e-6
2012a	$B^0_d \to K^0_S K^+\pi^-$	LL	MD	PP	201.8e-6	11.9e-6	2.7e-6	13.4e-6	18.2e-6
2012a	$B^0_d \to K^0_S K^+\pi^-$	LL	MU	PP	173.1e-6	11.1e-6	2.1e-6	13.4e-6	17.6e-6
2012a	$B^0_d \to K^0_S K^+\pi^-$	LL	MD	SP	159.1e-6	10.6e-6	2.2e-6	9.8e-6	14.6e-6
2012a	$B^0_d \to K^0_S K^+\pi^-$	LL	MU	SP	138.0e-6	9.9e-6	1.9e-6	9.8e-6	14.1e-6
2011	$B^0_d \to K^0_S K^+\pi^-$	LL	MD	PP	233.8e-6	12.3e-6	3.5e-6	13.4e-6	18.5e-6
2011	$B^0_d \to K^0_S K^+\pi^-$	LL	MU	PP	224.0e-6	11.5e-6	3.1e-6	13.4e-6	17.9e-6
2011	$B^0_d \to K^0_S K^+\pi^-$	LL	MD	SP	173.3e-6	10.5e-6	2.7e-6	9.8e-6	14.6e-6
2011	$B^0_d \to K^0_S K^+\pi^-$	LL	MU	SP	174.0e-6	10.1e-6	2.5e-6	9.8e-6	14.3e-6

Table C.14: $B^0 \to K^0_S K^+\pi^-$ detailed efficiency tables. PP stand for favoured mode optimisation and SP for unfavoured mode optimisation.

Year	Mode	K^0_S	Polarity	Optimisation	$\bar{\varepsilon}$	$\sigma^{\text{cur}}_{\bar{\varepsilon}}$	$\sigma^{\text{ref}}_{\bar{\varepsilon}}$	$\sigma^{\text{RMS}}_{\bar{\varepsilon}}$	$\sigma_{\bar{\varepsilon}}$
2018	$B^0_d \to K^0_S K^+ K^-$	DD	MD	PP	733.4e-6	7.1e-6	1.5e-6	3.2e-6	7.9e-6
2018	$B^0_d \to K^0_S K^+ K^-$	DD	MU	PP	723.3e-6	7.2e-6	1.5e-6	3.2e-6	8.0e-6
2018	$B^0_d \to K^0_S K^+ K^-$	DD	MD	SP	485.3e-6	5.8e-6	1.0e-6	2.0e-6	6.2e-6
2018	$B^0_d \to K^0_S K^+ K^-$	DD	MU	SP	484.7e-6	5.9e-6	1.0e-6	2.0e-6	6.3e-6
2017	$B^0_d \to K^0_S K^+ K^-$	DD	MD	PP	758.4e-6	7.6e-6	1.7e-6	3.2e-6	8.4e-6
2017	$B^0_d \to K^0_S K^+ K^-$	DD	MU	PP	743.4e-6	7.6e-6	1.6e-6	3.2e-6	8.4e-6
2017	$B^0_d \to K^0_S K^+ K^-$	DD	MD	SP	3788.6e-7	54.4e-7	8.6e-7	20.3e-7	58.7e-7
2017	$B^0_d \to K^0_S K^+ K^-$	DD	MU	SP	3688.1e-7	53.8e-7	8.5e-7	20.3e-7	58.1e-7
2016	$B^0_d \to K^0_S K^+ K^-$	DD	MD	PP	913.1e-6	8.2e-6	2.0e-6	3.2e-6	9.1e-6
2016	$B^0_d \to K^0_S K^+ K^-$	DD	MU	PP	872.0e-6	8.3e-6	1.9e-6	3.2e-6	9.1e-6
2016	$B^0_d \to K^0_S K^+ K^-$	DD	MD	SP	487.9e-6	6.1e-6	1.1e-6	2.0e-6	6.5e-6
2016	$B^0_d \to K^0_S K^+ K^-$	DD	MU	SP	470.0e-6	6.1e-6	1.1e-6	2.0e-6	6.5e-6
2015	$B^0_d \to K^0_S K^+ K^-$	DD	MD	PP	817.1e-6	7.9e-6	1.7e-6	3.2e-6	8.7e-6
2015	$B^0_d \to K^0_S K^+ K^-$	DD	MU	PP	784.8e-6	7.9e-6	1.7e-6	3.2e-6	8.7e-6
2015	$B^0_d \to K^0_S K^+ K^-$	DD	MD	SP	4052.3e-7	56.3e-7	9.2e-7	20.3e-7	60.6e-7
2015	$B^0_d \to K^0_S K^+ K^-$	DD	MU	SP	3930.1e-7	56.2e-7	9.3e-7	20.3e-7	60.5e-7
2012b	$B^0_d \to K^0_S K^+ K^-$	DD	MD	PP	450.4e-6	7.6e-6	1.1e-6	3.2e-6	8.3e-6
2012b	$B^0_d \to K^0_S K^+ K^-$	DD	MU	PP	448.8e-6	7.8e-6	1.2e-6	3.2e-6	8.5e-6
2012b	$B^0_d \to K^0_S K^+ K^-$	DD	MD	SP	3365.3e-7	66.4e-7	9.3e-7	20.3e-7	70.0e-7
2012b	$B^0_d \to K^0_S K^+ K^-$	DD	MU	SP	3320.2e-7	67.4e-7	9.1e-7	20.3e-7	71.0e-7
2012a	$B^0_d \to K^0_S K^+ K^-$	DD	MD	PP	3076.9e-7	68.0e-7	9.2e-7	32.2e-7	75.8e-7
2012a	$B^0_d \to K^0_S K^+ K^-$	DD	MU	PP	3157.8e-7	69.1e-7	9.8e-7	32.2e-7	76.9e-7
2012a	$B^0_d \to K^0_S K^+ K^-$	DD	MD	SP	2073.3e-7	56.3e-7	6.3e-7	20.3e-7	60.2e-7
2012a	$B^0_d \to K^0_S K^+ K^-$	DD	MU	SP	2143.1e-7	57.8e-7	7.0e-7	20.3e-7	61.6e-7
2011	$B^0_d \to K^0_S K^+ K^-$	DD	MD	PP	363.7e-6	7.0e-6	1.1e-6	3.2e-6	7.8e-6
2011	$B^0_d \to K^0_S K^+ K^-$	DD	MU	PP	356.0e-6	6.2e-6	1.1e-6	3.2e-6	7.1e-6
2011	$B^0_d \to K^0_S K^+ K^-$	DD	MD	SP	2747.0e-7	61.1e-7	9.1e-7	20.3e-7	65.0e-7
2011	$B^0_d \to K^0_S K^+ K^-$	DD	MU	SP	2757.5e-7	55.2e-7	8.5e-7	20.3e-7	59.4e-7
2018	$B^0_d \to K^0_S K^+ K^-$	LL	MD	PP	3076.5e-7	45.1e-7	8.4e-7	20.8e-7	50.3e-7
2018	$B^0_d \to K^0_S K^+ K^-$	LL	MU	PP	3022.0e-7	45.6e-7	7.9e-7	20.8e-7	50.7e-7
2018	$B^0_d \to K^0_S K^+ K^-$	LL	MD	SP	2205.6e-7	38.5e-7	6.9e-7	14.8e-7	41.8e-7
2018	$B^0_d \to K^0_S K^+ K^-$	LL	MU	SP	2163.9e-7	38.7e-7	6.5e-7	14.8e-7	42.0e-7
2017	$B^0_d \to K^0_S K^+ K^-$	LL	MD	PP	3303.4e-7	49.4e-7	9.3e-7	20.8e-7	54.4e-7
2017	$B^0_d \to K^0_S K^+ K^-$	LL	MU	PP	3282.8e-7	50.4e-7	9.7e-7	20.8e-7	55.4e-7
2017	$B^0_d \to K^0_S K^+ K^-$	LL	MD	SP	1857.4e-7	37.5e-7	6.2e-7	14.8e-7	40.8e-7
2017	$B^0_d \to K^0_S K^+ K^-$	LL	MU	SP	1813.4e-7	37.8e-7	6.2e-7	14.8e-7	41.1e-7
2016	$B^0_d \to K^0_S K^+ K^-$	LL	MD	PP	376.2e-6	5.3e-6	1.0e-6	2.1e-6	5.8e-6
2016	$B^0_d \to K^0_S K^+ K^-$	LL	MU	PP	3639.4e-7	53.6e-7	9.1e-7	20.8e-7	58.2e-7
2016	$B^0_d \to K^0_S K^+ K^-$	LL	MD	SP	2041.4e-7	39.7e-7	6.5e-7	14.8e-7	42.9e-7
2016	$B^0_d \to K^0_S K^+ K^-$	LL	MU	SP	1948.6e-7	39.5e-7	5.6e-7	14.8e-7	42.5e-7
2015	$B^0_d \to K^0_S K^+ K^-$	LL	MD	PP	3397.5e-7	50.9e-7	9.4e-7	20.8e-7	55.8e-7
2015	$B^0_d \to K^0_S K^+ K^-$	LL	MU	PP	3230.6e-7	51.4e-7	7.9e-7	20.8e-7	56.0e-7
2015	$B^0_d \to K^0_S K^+ K^-$	LL	MD	SP	2859.4e-7	46.4e-7	7.9e-7	14.8e-7	49.4e-7
2015	$B^0_d \to K^0_S K^+ K^-$	LL	MU	SP	2720.3e-7	47.1e-7	6.7e-7	14.8e-7	49.8e-7
2012b	$B^0_d \to K^0_S K^+ K^-$	LL	MD	PP	1470.7e-7	43.6e-7	5.2e-7	20.8e-7	48.6e-7
2012b	$B^0_d \to K^0_S K^+ K^-$	LL	MU	PP	1470.5e-7	45.7e-7	5.5e-7	20.8e-7	50.5e-7
2012b	$B^0_d \to K^0_S K^+ K^-$	LL	MD	SP	1245.2e-7	40.2e-7	4.3e-7	14.8e-7	43.0e-7
2012b	$B^0_d \to K^0_S K^+ K^-$	LL	MU	SP	1234.8e-7	42.2e-7	4.7e-7	14.8e-7	45.0e-7
2012a	$B^0_d \to K^0_S K^+ K^-$	LL	MD	PP	1726.3e-7	51.0e-7	5.5e-7	20.8e-7	55.4e-7
2012a	$B^0_d \to K^0_S K^+ K^-$	LL	MU	PP	1626.7e-7	50.2e-7	6.0e-7	20.8e-7	54.7e-7
2012a	$B^0_d \to K^0_S K^+ K^-$	LL	MD	SP	1421.1e-7	46.3e-7	4.4e-7	14.8e-7	48.8e-7
2012a	$B^0_d \to K^0_S K^+ K^-$	LL	MU	SP	1404.6e-7	47.1e-7	5.6e-7	14.8e-7	49.7e-7
2011	$B^0_d \to K^0_S K^+ K^-$	LL	MD	PP	1916.8e-7	52.1e-7	5.9e-7	20.8e-7	56.4e-7
2011	$B^0_d \to K^0_S K^+ K^-$	LL	MU	PP	1879.3e-7	46.9e-7	6.4e-7	20.8e-7	51.7e-7
2011	$B^0_d \to K^0_S K^+ K^-$	LL	MD	SP	1358.9e-7	44.2e-7	4.8e-7	14.8e-7	46.8e-7
2011	$B^0_d \to K^0_S K^+ K^-$	LL	MU	SP	1402.7e-7	40.9e-7	5.5e-7	14.8e-7	43.9e-7

Table C.15: $B^0 \to K^0_S K^+ K^-$ detailed efficiency tables. PP stand for favoured mode optimisation and SP for unfavoured mode optimisation.

Year	Mode	K^0_S	Polarity	Optimisation	$\bar{\varepsilon}$	$\sigma^{\text{cur}}_{\bar{\varepsilon}}$	$\sigma^{\text{ref}}_{\bar{\varepsilon}}$	$\sigma^{\text{RMS}}_{\bar{\varepsilon}}$	$\sigma_{\bar{\varepsilon}}$
2018	$B^0_s \to K^0_S\pi^+\pi^-$	DD	MD	PP	870.7e-6	9.2e-6	6.9e-6	35.1e-6	36.9e-6
2018	$B^0_s \to K^0_S\pi^+\pi^-$	DD	MU	PP	871.1e-6	9.4e-6	6.6e-6	35.1e-6	36.9e-6
2018	$B^0_s \to K^0_S\pi^+\pi^-$	DD	MD	SP	445.6e-6	6.6e-6	3.5e-6	20.3e-6	21.6e-6
2018	$B^0_s \to K^0_S\pi^+\pi^-$	DD	MU	SP	447.3e-6	6.8e-6	3.4e-6	20.3e-6	21.6e-6
2017	$B^0_s \to K^0_S\pi^+\pi^-$	DD	MD	PP	875.8e-6	9.3e-6	7.1e-6	35.1e-6	37.0e-6
2017	$B^0_s \to K^0_S\pi^+\pi^-$	DD	MU	PP	894.3e-6	9.9e-6	7.0e-6	35.1e-6	37.1e-6
2017	$B^0_s \to K^0_S\pi^+\pi^-$	DD	MD	SP	468.9e-6	6.8e-6	3.8e-6	20.3e-6	21.7e-6
2017	$B^0_s \to K^0_S\pi^+\pi^-$	DD	MU	SP	484.3e-6	7.3e-6	3.8e-6	20.3e-6	21.9e-6
2016	$B^0_s \to K^0_S\pi^+\pi^-$	DD	MD	PP	914.6e-6	10.0e-6	7.5e-6	35.1e-6	37.2e-6
2016	$B^0_s \to K^0_S\pi^+\pi^-$	DD	MU	PP	912.5e-6	10.0e-6	7.2e-6	35.1e-6	37.2e-6
2016	$B^0_s \to K^0_S\pi^+\pi^-$	DD	MD	SP	457.9e-6	7.1e-6	3.8e-6	20.3e-6	21.8e-6
2016	$B^0_s \to K^0_S\pi^+\pi^-$	DD	MU	SP	460.5e-6	7.1e-6	3.7e-6	20.3e-6	21.8e-6
2015	$B^0_s \to K^0_S\pi^+\pi^-$	DD	MD	PP	909.0e-6	9.9e-6	7.5e-6	35.1e-6	37.2e-6
2015	$B^0_s \to K^0_S\pi^+\pi^-$	DD	MU	PP	880.6e-6	10.0e-6	6.8e-6	35.1e-6	37.1e-6
2015	$B^0_s \to K^0_S\pi^+\pi^-$	DD	MD	SP	395.1e-6	6.6e-6	3.2e-6	20.3e-6	21.5e-6
2015	$B^0_s \to K^0_S\pi^+\pi^-$	DD	MU	SP	376.5e-6	6.6e-6	2.9e-6	20.3e-6	21.5e-6
2012b	$B^0_s \to K^0_S\pi^+\pi^-$	DD	MD	PP	562.2e-6	10.0e-6	5.5e-6	35.1e-6	36.9e-6
2012b	$B^0_s \to K^0_S\pi^+\pi^-$	DD	MU	PP	577.6e-6	10.5e-6	5.4e-6	35.1e-6	37.0e-6
2012b	$B^0_s \to K^0_S\pi^+\pi^-$	DD	MD	SP	368.5e-6	8.1e-6	3.6e-6	20.3e-6	22.1e-6
2012b	$B^0_s \to K^0_S\pi^+\pi^-$	DD	MU	SP	365.5e-6	8.3e-6	3.4e-6	20.3e-6	22.2e-6
2012a	$B^0_s \to K^0_S\pi^+\pi^-$	DD	MD	PP	462.3e-6	9.6e-6	4.8e-6	35.1e-6	36.7e-6
2012a	$B^0_s \to K^0_S\pi^+\pi^-$	DD	MU	PP	454.3e-6	9.6e-6	4.6e-6	35.1e-6	36.7e-6
2012a	$B^0_s \to K^0_S\pi^+\pi^-$	DD	MD	SP	268.5e-6	7.3e-6	2.8e-6	20.3e-6	21.7e-6
2012a	$B^0_s \to K^0_S\pi^+\pi^-$	DD	MU	SP	264.6e-6	7.4e-6	2.0e-6	20.3e-6	21.7e-6
2011	$B^0_s \to K^0_S\pi^+\pi^-$	DD	MD	PP	545.6e-6	9.0e-6	5.8e-6	35.1e-6	36.7e-6
2011	$B^0_s \to K^0_S\pi^+\pi^-$	DD	MU	PP	551.8e-6	10.3e-6	4.3e-6	35.1e-6	36.8e-6
2011	$B^0_s \to K^0_S\pi^+\pi^-$	DD	MD	SP	270.6e-6	6.4e-6	2.8e-6	20.3e-6	21.4e-6
2011	$B^0_s \to K^0_S\pi^+\pi^-$	DD	MU	SP	269.9e-6	7.3e-6	2.1e-6	20.3e-6	21.6e-6
2018	$B^0_s \to K^0_S\pi^+\pi^-$	LL	MD	PP	321.2e-6	6.9e-6	4.1e-6	8.2e-6	11.5e-6
2018	$B^0_s \to K^0_S\pi^+\pi^-$	LL	MU	PP	336.8e-6	7.4e-6	5.6e-6	8.2e-6	12.4e-6
2018	$B^0_s \to K^0_S\pi^+\pi^-$	LL	MD	SP	209.8e-6	5.6e-6	2.8e-6	5.7e-6	8.4e-6
2018	$B^0_s \to K^0_S\pi^+\pi^-$	LL	MU	SP	220.4e-6	6.0e-6	3.8e-6	5.7e-6	9.1e-6
2017	$B^0_s \to K^0_S\pi^+\pi^-$	LL	MD	PP	356.9e-6	7.4e-6	4.4e-6	8.2e-6	11.9e-6
2017	$B^0_s \to K^0_S\pi^+\pi^-$	LL	MU	PP	357.2e-6	7.9e-6	5.8e-6	8.2e-6	12.8e-6
2017	$B^0_s \to K^0_S\pi^+\pi^-$	LL	MD	SP	248.8e-6	6.1e-6	3.1e-6	5.7e-6	8.9e-6
2017	$B^0_s \to K^0_S\pi^+\pi^-$	LL	MU	SP	248.8e-6	6.5e-6	4.0e-6	5.7e-6	9.6e-6
2016	$B^0_s \to K^0_S\pi^+\pi^-$	LL	MD	PP	398.4e-6	8.2e-6	5.3e-6	8.2e-6	12.8e-6
2016	$B^0_s \to K^0_S\pi^+\pi^-$	LL	MU	PP	397.1e-6	8.3e-6	6.5e-6	8.2e-6	13.4e-6
2016	$B^0_s \to K^0_S\pi^+\pi^-$	LL	MD	SP	255.1e-6	6.5e-6	3.5e-6	5.7e-6	9.4e-6
2016	$B^0_s \to K^0_S\pi^+\pi^-$	LL	MU	SP	252.2e-6	6.6e-6	4.3e-6	5.7e-6	9.7e-6
2015	$B^0_s \to K^0_S\pi^+\pi^-$	LL	MD	PP	363.5e-6	7.9e-6	4.7e-6	8.2e-6	12.4e-6
2015	$B^0_s \to K^0_S\pi^+\pi^-$	LL	MU	PP	357.1e-6	8.0e-6	5.8e-6	8.2e-6	12.9e-6
2015	$B^0_s \to K^0_S\pi^+\pi^-$	LL	MD	SP	223.2e-6	6.2e-6	3.0e-6	5.7e-6	8.9e-6
2015	$B^0_s \to K^0_S\pi^+\pi^-$	LL	MU	SP	217.7e-6	6.2e-6	3.7e-6	5.7e-6	9.2e-6
2012b	$B^0_s \to K^0_S\pi^+\pi^-$	LL	MD	PP	174.9e-6	6.9e-6	2.6e-6	8.2e-6	11.1e-6
2012b	$B^0_s \to K^0_S\pi^+\pi^-$	LL	MU	PP	174.7e-6	7.5e-6	2.8e-6	8.2e-6	11.5e-6
2012b	$B^0_s \to K^0_S\pi^+\pi^-$	LL	MD	SP	124.4e-6	5.8e-6	1.8e-6	5.7e-6	8.3e-6
2012b	$B^0_s \to K^0_S\pi^+\pi^-$	LL	MU	SP	124.8e-6	6.3e-6	2.0e-6	5.7e-6	8.7e-6
2012a	$B^0_s \to K^0_S\pi^+\pi^-$	LL	MD	PP	201.6e-6	8.2e-6	2.6e-6	8.2e-6	11.9e-6
2012a	$B^0_s \to K^0_S\pi^+\pi^-$	LL	MU	PP	200.4e-6	8.2e-6	3.3e-6	8.2e-6	12.1e-6
2012a	$B^0_s \to K^0_S\pi^+\pi^-$	LL	MD	SP	86.5e-6	5.3e-6	1.2e-6	5.7e-6	7.9e-6
2012a	$B^0_s \to K^0_S\pi^+\pi^-$	LL	MU	SP	86.7e-6	5.3e-6	1.5e-6	5.7e-6	7.9e-6
2011	$B^0_s \to K^0_S\pi^+\pi^-$	LL	MD	PP	223.7e-6	7.5e-6	3.1e-6	8.2e-6	11.5e-6
2011	$B^0_s \to K^0_S\pi^+\pi^-$	LL	MU	PP	204.3e-6	8.2e-6	3.3e-6	8.2e-6	12.1e-6
2011	$B^0_s \to K^0_S\pi^+\pi^-$	LL	MD	SP	159.3e-6	6.3e-6	2.2e-6	5.7e-6	8.7e-6
2011	$B^0_s \to K^0_S\pi^+\pi^-$	LL	MU	SP	143.2e-6	6.9e-6	2.2e-6	5.7e-6	9.2e-6

Table C.16: $B^0_s \to K^0_S\pi^+\pi^-$ detailed efficiency tables. PP stand for favoured mode optimisation and SP for unfavoured mode optimisation.

Year	Mode	K^0_S	Polarity	Optimisation	$\bar{\varepsilon}$	$\sigma^{\text{cur}}_{\bar{\varepsilon}}$	$\sigma^{\text{ref}}_{\bar{\varepsilon}}$	$\sigma^{\text{RMS}}_{\bar{\varepsilon}}$	$\sigma_{\bar{\varepsilon}}$
2018	$B^0_s \to K^0_S\pi^+K^-$	DD	MD	PP	846.4e-6	11.3e-6	4.6e-6	5.7e-6	13.5e-6
2018	$B^0_s \to K^0_S\pi^+K^-$	DD	MU	PP	858.6e-6	11.0e-6	4.9e-6	5.7e-6	13.4e-6
2018	$B^0_s \to K^0_S\pi^+K^-$	DD	MD	SP	641.4e-6	9.8e-6	3.4e-6	5.1e-6	11.6e-6
2018	$B^0_s \to K^0_S\pi^+K^-$	DD	MU	SP	652.8e-6	9.7e-6	3.7e-6	5.1e-6	11.6e-6
2017	$B^0_s \to K^0_S\pi^+K^-$	DD	MD	PP	890.6e-6	11.8e-6	4.8e-6	5.7e-6	14.0e-6
2017	$B^0_s \to K^0_S\pi^+K^-$	DD	MU	PP	880.4e-6	11.5e-6	5.2e-6	5.7e-6	13.8e-6
2017	$B^0_s \to K^0_S\pi^+K^-$	DD	MD	SP	683.6e-6	10.3e-6	3.6e-6	5.1e-6	12.1e-6
2017	$B^0_s \to K^0_S\pi^+K^-$	DD	MU	SP	668.4e-6	10.0e-6	4.0e-6	5.1e-6	11.9e-6
2016	$B^0_s \to K^0_S\pi^+K^-$	DD	MD	PP	1026.3e-6	12.8e-6	5.5e-6	5.7e-6	15.0e-6
2016	$B^0_s \to K^0_S\pi^+K^-$	DD	MU	PP	971.1e-6	12.4e-6	5.9e-6	5.7e-6	14.9e-6
2016	$B^0_s \to K^0_S\pi^+K^-$	DD	MD	SP	780.1e-6	11.1e-6	4.3e-6	5.1e-6	13.0e-6
2016	$B^0_s \to K^0_S\pi^+K^-$	DD	MU	SP	756.8e-6	11.0e-6	4.7e-6	5.1e-6	13.0e-6
2015	$B^0_s \to K^0_S\pi^+K^-$	DD	MD	PP	919.9e-6	12.2e-6	5.0e-6	5.7e-6	14.4e-6
2015	$B^0_s \to K^0_S\pi^+K^-$	DD	MU	PP	880.4e-6	12.1e-6	5.3e-6	5.7e-6	14.4e-6
2015	$B^0_s \to K^0_S\pi^+K^-$	DD	MD	SP	681.1e-6	10.5e-6	3.8e-6	5.1e-6	12.3e-6
2015	$B^0_s \to K^0_S\pi^+K^-$	DD	MU	SP	655.0e-6	10.4e-6	4.1e-6	5.1e-6	12.3e-6
2012b	$B^0_s \to K^0_S\pi^+K^-$	DD	MD	PP	593.7e-6	13.1e-6	3.9e-6	5.7e-6	14.8e-6
2012b	$B^0_s \to K^0_S\pi^+K^-$	DD	MU	PP	580.3e-6	11.9e-6	4.3e-6	5.7e-6	13.9e-6
2012b	$B^0_s \to K^0_S\pi^+K^-$	DD	MD	SP	458.9e-6	11.4e-6	3.1e-6	5.1e-6	12.9e-6
2012b	$B^0_s \to K^0_S\pi^+K^-$	DD	MU	SP	459.0e-6	10.5e-6	3.4e-6	5.1e-6	12.2e-6
2012a	$B^0_s \to K^0_S\pi^+K^-$	DD	MD	PP	470.9e-6	12.0e-6	3.1e-6	5.7e-6	13.7e-6
2012a	$B^0_s \to K^0_S\pi^+K^-$	DD	MU	PP	475.8e-6	12.6e-6	3.2e-6	5.7e-6	14.2e-6
2012a	$B^0_s \to K^0_S\pi^+K^-$	DD	MD	SP	385.5e-6	10.9e-6	2.5e-6	5.1e-6	12.3e-6
2012a	$B^0_s \to K^0_S\pi^+K^-$	DD	MU	SP	392.6e-6	11.3e-6	2.5e-6	5.1e-6	12.7e-6
2011	$B^0_s \to K^0_S\pi^+K^-$	DD	MD	PP	564.3e-6	12.8e-6	3.9e-6	5.7e-6	14.6e-6
2011	$B^0_s \to K^0_S\pi^+K^-$	DD	MU	PP	549.3e-6	12.7e-6	4.8e-6	5.7e-6	14.7e-6
2011	$B^0_s \to K^0_S\pi^+K^-$	DD	MD	SP	458.6e-6	11.6e-6	3.2e-6	5.1e-6	13.1e-6
2011	$B^0_s \to K^0_S\pi^+K^-$	DD	MU	SP	454.2e-6	11.6e-6	3.8e-6	5.1e-6	13.3e-6
2018	$B^0_s \to K^0_S\pi^+K^-$	LL	MD	PP	325.2e-6	7.2e-6	2.7e-6	7.8e-6	11.0e-6
2018	$B^0_s \to K^0_S\pi^+K^-$	LL	MU	PP	317.4e-6	6.7e-6	3.2e-6	7.8e-6	10.8e-6
2018	$B^0_s \to K^0_S\pi^+K^-$	LL	MD	SP	274.4e-6	6.6e-6	2.5e-6	5.9e-6	9.2e-6
2018	$B^0_s \to K^0_S\pi^+K^-$	LL	MU	SP	268.4e-6	6.2e-6	2.8e-6	5.9e-6	9.0e-6
2017	$B^0_s \to K^0_S\pi^+K^-$	LL	MD	PP	370.1e-6	7.9e-6	3.4e-6	7.8e-6	11.6e-6
2017	$B^0_s \to K^0_S\pi^+K^-$	LL	MU	PP	354.9e-6	7.4e-6	3.4e-6	7.8e-6	11.3e-6
2017	$B^0_s \to K^0_S\pi^+K^-$	LL	MD	SP	303.2e-6	7.2e-6	2.8e-6	5.9e-6	9.7e-6
2017	$B^0_s \to K^0_S\pi^+K^-$	LL	MU	SP	293.2e-6	6.7e-6	3.0e-6	5.9e-6	9.4e-6
2016	$B^0_s \to K^0_S\pi^+K^-$	LL	MD	PP	384.6e-6	8.0e-6	3.3e-6	7.8e-6	11.7e-6
2016	$B^0_s \to K^0_S\pi^+K^-$	LL	MU	PP	376.0e-6	8.0e-6	3.6e-6	7.8e-6	11.8e-6
2016	$B^0_s \to K^0_S\pi^+K^-$	LL	MD	SP	320.2e-6	7.4e-6	2.8e-6	5.9e-6	9.8e-6
2016	$B^0_s \to K^0_S\pi^+K^-$	LL	MU	SP	310.9e-6	7.3e-6	3.0e-6	5.9e-6	9.8e-6
2015	$B^0_s \to K^0_S\pi^+K^-$	LL	MD	PP	368.2e-6	7.9e-6	3.1e-6	7.8e-6	11.5e-6
2015	$B^0_s \to K^0_S\pi^+K^-$	LL	MU	PP	352.7e-6	7.8e-6	3.1e-6	7.8e-6	11.4e-6
2015	$B^0_s \to K^0_S\pi^+K^-$	LL	MD	SP	251.1e-6	6.4e-6	2.2e-6	5.9e-6	9.0e-6
2015	$B^0_s \to K^0_S\pi^+K^-$	LL	MU	SP	242.1e-6	6.5e-6	2.2e-6	5.9e-6	9.0e-6
2012b	$B^0_s \to K^0_S\pi^+K^-$	LL	MD	PP	174.4e-6	7.3e-6	1.7e-6	7.8e-6	10.9e-6
2012b	$B^0_s \to K^0_S\pi^+K^-$	LL	MU	PP	177.3e-6	6.8e-6	1.9e-6	7.8e-6	10.5e-6
2012b	$B^0_s \to K^0_S\pi^+K^-$	LL	MD	SP	940.8e-7	55.0e-7	9.9e-7	58.8e-7	81.1e-7
2012b	$B^0_s \to K^0_S\pi^+K^-$	LL	MU	SP	877.1e-7	48.4e-7	9.5e-7	58.8e-7	76.8e-7
2012a	$B^0_s \to K^0_S\pi^+K^-$	LL	MD	PP	209.6e-6	8.3e-6	1.8e-6	7.8e-6	11.5e-6
2012a	$B^0_s \to K^0_S\pi^+K^-$	LL	MU	PP	195.7e-6	7.8e-6	1.9e-6	7.8e-6	11.2e-6
2012a	$B^0_s \to K^0_S\pi^+K^-$	LL	MD	SP	157.2e-6	7.2e-6	1.4e-6	5.9e-6	9.4e-6
2012a	$B^0_s \to K^0_S\pi^+K^-$	LL	MU	SP	144.9e-6	6.6e-6	1.5e-6	5.9e-6	8.9e-6
2011	$B^0_s \to K^0_S\pi^+K^-$	LL	MD	PP	238.0e-6	8.7e-6	2.7e-6	7.8e-6	12.0e-6
2011	$B^0_s \to K^0_S\pi^+K^-$	LL	MU	PP	213.3e-6	8.1e-6	2.1e-6	7.8e-6	11.4e-6
2011	$B^0_s \to K^0_S\pi^+K^-$	LL	MD	SP	192.7e-6	7.8e-6	2.3e-6	5.9e-6	10.1e-6
2011	$B^0_s \to K^0_S\pi^+K^-$	LL	MU	SP	176.7e-6	7.3e-6	1.9e-6	5.9e-6	9.6e-6

Table C.17: $B^0_s \to K^0_S\pi^+K^-$ detailed efficiency tables. PP stand for favoured mode optimisation and SP for unfavoured mode optimisation.

Year	Mode	K^0_S	Polarity	Optimisation	$\bar{\varepsilon}$	$\sigma^{\text{cur}}_{\bar{\varepsilon}}$	$\sigma^{\text{ref}}_{\bar{\varepsilon}}$	$\sigma^{\text{RMS}}_{\bar{\varepsilon}}$	$\sigma_{\bar{\varepsilon}}$
2018	$B^0_s \to K^0_S K^+\pi^-$	DD	MD	PP	872.5e-6	11.0e-6	4.0e-6	4.8e-6	12.7e-6
2018	$B^0_s \to K^0_S K^+\pi^-$	DD	MU	PP	865.9e-6	10.7e-6	3.7e-6	4.8e-6	12.3e-6
2018	$B^0_s \to K^0_S K^+\pi^-$	DD	MD	SP	682.8e-6	9.8e-6	3.2e-6	4.5e-6	11.2e-6
2018	$B^0_s \to K^0_S K^+\pi^-$	DD	MU	SP	673.0e-6	9.4e-6	2.9e-6	4.5e-6	10.8e-6
2017	$B^0_s \to K^0_S K^+\pi^-$	DD	MD	PP	906.8e-6	11.5e-6	4.2e-6	4.8e-6	13.2e-6
2017	$B^0_s \to K^0_S K^+\pi^-$	DD	MU	PP	902.7e-6	11.4e-6	4.3e-6	4.8e-6	13.1e-6
2017	$B^0_s \to K^0_S K^+\pi^-$	DD	MD	SP	749.2e-6	10.5e-6	3.4e-6	4.5e-6	11.9e-6
2017	$B^0_s \to K^0_S K^+\pi^-$	DD	MU	SP	751.3e-6	10.4e-6	3.6e-6	4.5e-6	11.9e-6
2016	$B^0_s \to K^0_S K^+\pi^-$	DD	MD	PP	994.1e-6	12.1e-6	4.7e-6	4.8e-6	13.8e-6
2016	$B^0_s \to K^0_S K^+\pi^-$	DD	MU	PP	951.8e-6	12.0e-6	4.4e-6	4.8e-6	13.6e-6
2016	$B^0_s \to K^0_S K^+\pi^-$	DD	MD	SP	758.6e-6	10.6e-6	3.6e-6	4.5e-6	12.0e-6
2016	$B^0_s \to K^0_S K^+\pi^-$	DD	MU	SP	724.9e-6	10.5e-6	3.5e-6	4.5e-6	11.9e-6
2015	$B^0_s \to K^0_S K^+\pi^-$	DD	MD	PP	887.1e-6	11.6e-6	4.0e-6	4.8e-6	13.2e-6
2015	$B^0_s \to K^0_S K^+\pi^-$	DD	MU	PP	849.0e-6	11.4e-6	4.1e-6	4.8e-6	13.0e-6
2015	$B^0_s \to K^0_S K^+\pi^-$	DD	MD	SP	630.0e-6	9.8e-6	2.9e-6	4.5e-6	11.2e-6
2015	$B^0_s \to K^0_S K^+\pi^-$	DD	MU	SP	595.4e-6	9.5e-6	3.0e-6	4.5e-6	10.9e-6
2012b	$B^0_s \to K^0_S K^+\pi^-$	DD	MD	PP	568.5e-6	12.3e-6	3.6e-6	4.8e-6	13.6e-6
2012b	$B^0_s \to K^0_S K^+\pi^-$	DD	MU	PP	565.5e-6	11.4e-6	3.5e-6	4.8e-6	12.8e-6
2012b	$B^0_s \to K^0_S K^+\pi^-$	DD	MD	SP	419.5e-6	10.7e-6	2.2e-6	4.5e-6	11.8e-6
2012b	$B^0_s \to K^0_S K^+\pi^-$	DD	MU	SP	410.8e-6	9.8e-6	2.5e-6	4.5e-6	11.0e-6
2012a	$B^0_s \to K^0_S K^+\pi^-$	DD	MD	PP	431.4e-6	10.9e-6	2.9e-6	4.8e-6	12.2e-6
2012a	$B^0_s \to K^0_S K^+\pi^-$	DD	MU	PP	444.8e-6	11.2e-6	3.1e-6	4.8e-6	12.6e-6
2012a	$B^0_s \to K^0_S K^+\pi^-$	DD	MD	SP	335.2e-6	9.6e-6	2.2e-6	4.5e-6	10.8e-6
2012a	$B^0_s \to K^0_S K^+\pi^-$	DD	MU	SP	354.2e-6	10.1e-6	2.5e-6	4.5e-6	11.3e-6
2011	$B^0_s \to K^0_S K^+\pi^-$	DD	MD	PP	509.2e-6	11.2e-6	3.7e-6	4.8e-6	12.7e-6
2011	$B^0_s \to K^0_S K^+\pi^-$	DD	MU	PP	503.5e-6	11.3e-6	3.5e-6	4.8e-6	12.8e-6
2011	$B^0_s \to K^0_S K^+\pi^-$	DD	MD	SP	432.6e-6	10.4e-6	3.1e-6	4.5e-6	11.7e-6
2011	$B^0_s \to K^0_S K^+\pi^-$	DD	MU	SP	434.4e-6	10.7e-6	2.8e-6	4.5e-6	12.0e-6
2018	$B^0_s \to K^0_S K^+\pi^-$	LL	MD	PP	325.9e-6	7.1e-6	3.6e-6	12.0e-6	14.4e-6
2018	$B^0_s \to K^0_S K^+\pi^-$	LL	MU	PP	309.0e-6	6.6e-6	4.7e-6	12.0e-6	14.5e-6
2018	$B^0_s \to K^0_S K^+\pi^-$	LL	MD	SP	271.4e-6	6.4e-6	3.1e-6	9.7e-6	12.0e-6
2018	$B^0_s \to K^0_S K^+\pi^-$	LL	MU	SP	257.5e-6	6.0e-6	4.1e-6	9.7e-6	12.1e-6
2017	$B^0_s \to K^0_S K^+\pi^-$	LL	MD	PP	365.7e-6	7.7e-6	3.9e-6	12.0e-6	14.8e-6
2017	$B^0_s \to K^0_S K^+\pi^-$	LL	MU	PP	354.2e-6	7.4e-6	5.9e-6	12.0e-6	15.3e-6
2017	$B^0_s \to K^0_S K^+\pi^-$	LL	MD	SP	291.3e-6	6.9e-6	3.0e-6	9.7e-6	12.3e-6
2017	$B^0_s \to K^0_S K^+\pi^-$	LL	MU	SP	275.8e-6	6.5e-6	4.7e-6	9.7e-6	12.6e-6
2016	$B^0_s \to K^0_S K^+\pi^-$	LL	MD	PP	387.0e-6	8.0e-6	4.1e-6	12.0e-6	15.0e-6
2016	$B^0_s \to K^0_S K^+\pi^-$	LL	MU	PP	410.2e-6	8.3e-6	6.4e-6	12.0e-6	15.9e-6
2016	$B^0_s \to K^0_S K^+\pi^-$	LL	MD	SP	307.8e-6	7.1e-6	3.2e-6	9.7e-6	12.5e-6
2016	$B^0_s \to K^0_S K^+\pi^-$	LL	MU	SP	321.4e-6	7.4e-6	5.2e-6	9.7e-6	13.2e-6
2015	$B^0_s \to K^0_S K^+\pi^-$	LL	MD	PP	370.3e-6	7.9e-6	3.8e-6	12.0e-6	14.9e-6
2015	$B^0_s \to K^0_S K^+\pi^-$	LL	MU	PP	367.8e-6	7.8e-6	6.3e-6	12.0e-6	15.6e-6
2015	$B^0_s \to K^0_S K^+\pi^-$	LL	MD	SP	275.7e-6	6.8e-6	2.9e-6	9.7e-6	12.2e-6
2015	$B^0_s \to K^0_S K^+\pi^-$	LL	MU	SP	274.9e-6	6.7e-6	4.8e-6	9.7e-6	12.7e-6
2012b	$B^0_s \to K^0_S K^+\pi^-$	LL	MD	PP	162.2e-6	6.9e-6	1.9e-6	12.0e-6	14.0e-6
2012b	$B^0_s \to K^0_S K^+\pi^-$	LL	MU	PP	161.6e-6	6.4e-6	2.9e-6	12.0e-6	13.9e-6
2012b	$B^0_s \to K^0_S K^+\pi^-$	LL	MD	SP	832.8e-7	48.7e-7	10.0e-7	96.9e-7	108.9e-7
2012b	$B^0_s \to K^0_S K^+\pi^-$	LL	MU	SP	969.7e-7	51.9e-7	8.3e-7	96.9e-7	110.3e-7
2012a	$B^0_s \to K^0_S K^+\pi^-$	LL	MD	PP	184.4e-6	7.5e-6	2.0e-6	12.0e-6	14.3e-6
2012a	$B^0_s \to K^0_S K^+\pi^-$	LL	MU	PP	191.2e-6	7.7e-6	3.0e-6	12.0e-6	14.5e-6
2012a	$B^0_s \to K^0_S K^+\pi^-$	LL	MD	SP	144.9e-6	6.7e-6	1.6e-6	9.7e-6	11.9e-6
2012a	$B^0_s \to K^0_S K^+\pi^-$	LL	MU	SP	152.5e-6	6.9e-6	2.3e-6	9.7e-6	12.1e-6
2011	$B^0_s \to K^0_S K^+\pi^-$	LL	MD	PP	222.7e-6	8.0e-6	2.6e-6	12.0e-6	14.6e-6
2011	$B^0_s \to K^0_S K^+\pi^-$	LL	MU	PP	209.4e-6	8.0e-6	3.6e-6	12.0e-6	14.9e-6
2011	$B^0_s \to K^0_S K^+\pi^-$	LL	MD	SP	174.4e-6	7.1e-6	2.1e-6	9.7e-6	12.2e-6
2011	$B^0_s \to K^0_S K^+\pi^-$	LL	MU	SP	163.0e-6	7.0e-6	2.7e-6	9.7e-6	12.3e-6

Table C.18: $B^0_s \to K^0_S K^+\pi^-$ detailed efficiency tables. PP stand for favoured mode optimisation and SP for unfavoured mode optimisation.

Year	Mode	K^0_S	Polarity	Optimisation	$\bar{\varepsilon}$	$\sigma^{\text{cur}}_{\bar{\varepsilon}}$	$\sigma^{\text{ref}}_{\bar{\varepsilon}}$	$\sigma^{\text{RMS}}_{\bar{\varepsilon}}$	$\sigma_{\bar{\varepsilon}}$
2018	$B^0_s \to K^0_S K^+ K^-$	DD	MD	PP	851.2e-6	10.8e-6	2.4e-6	63.3e-6	64.2e-6
2018	$B^0_s \to K^0_S K^+ K^-$	DD	MU	PP	820.8e-6	10.2e-6	2.2e-6	63.3e-6	64.1e-6
2018	$B^0_s \to K^0_S K^+ K^-$	DD	MD	SP	562.6e-6	8.8e-6	1.7e-6	37.8e-6	38.8e-6
2018	$B^0_s \to K^0_S K^+ K^-$	DD	MU	SP	534.4e-6	8.2e-6	1.5e-6	37.8e-6	38.7e-6
2017	$B^0_s \to K^0_S K^+ K^-$	DD	MD	PP	896.1e-6	11.4e-6	2.1e-6	63.3e-6	64.3e-6
2017	$B^0_s \to K^0_S K^+ K^-$	DD	MU	PP	860.5e-6	11.0e-6	2.2e-6	63.3e-6	64.3e-6
2017	$B^0_s \to K^0_S K^+ K^-$	DD	MD	SP	432.1e-6	8.0e-6	1.1e-6	37.8e-6	38.6e-6
2017	$B^0_s \to K^0_S K^+ K^-$	DD	MU	SP	418.7e-6	7.7e-6	1.2e-6	37.8e-6	38.6e-6
2016	$B^0_s \to K^0_S K^+ K^-$	DD	MD	PP	1042.4e-6	12.2e-6	2.8e-6	63.3e-6	64.5e-6
2016	$B^0_s \to K^0_S K^+ K^-$	DD	MU	PP	1002.2e-6	11.8e-6	2.6e-6	63.3e-6	64.4e-6
2016	$B^0_s \to K^0_S K^+ K^-$	DD	MD	SP	561.0e-6	9.0e-6	1.6e-6	37.8e-6	38.9e-6
2016	$B^0_s \to K^0_S K^+ K^-$	DD	MU	SP	530.4e-6	8.6e-6	1.5e-6	37.8e-6	38.8e-6
2015	$B^0_s \to K^0_S K^+ K^-$	DD	MD	PP	932.0e-6	11.5e-6	2.4e-6	63.3e-6	64.4e-6
2015	$B^0_s \to K^0_S K^+ K^-$	DD	MU	PP	894.6e-6	10.9e-6	2.4e-6	63.3e-6	64.3e-6
2015	$B^0_s \to K^0_S K^+ K^-$	DD	MD	SP	457.2e-6	8.1e-6	1.2e-6	37.8e-6	38.7e-6
2015	$B^0_s \to K^0_S K^+ K^-$	DD	MU	SP	441.6e-6	7.7e-6	1.3e-6	37.8e-6	38.6e-6
2012b	$B^0_s \to K^0_S K^+ K^-$	DD	MD	PP	576.4e-6	10.9e-6	1.7e-6	63.3e-6	64.2e-6
2012b	$B^0_s \to K^0_S K^+ K^-$	DD	MU	PP	578.0e-6	11.4e-6	1.7e-6	63.3e-6	64.3e-6
2012b	$B^0_s \to K^0_S K^+ K^-$	DD	MD	SP	420.9e-6	9.3e-6	1.3e-6	37.8e-6	38.9e-6
2012b	$B^0_s \to K^0_S K^+ K^-$	DD	MU	SP	424.4e-6	9.7e-6	1.3e-6	37.8e-6	39.0e-6
2012a	$B^0_s \to K^0_S K^+ K^-$	DD	MD	PP	491.5e-6	11.7e-6	1.8e-6	63.3e-6	64.4e-6
2012a	$B^0_s \to K^0_S K^+ K^-$	DD	MU	PP	463.4e-6	10.9e-6	1.6e-6	63.3e-6	64.2e-6
2012a	$B^0_s \to K^0_S K^+ K^-$	DD	MD	SP	317.1e-6	9.4e-6	1.1e-6	37.8e-6	38.9e-6
2012a	$B^0_s \to K^0_S K^+ K^-$	DD	MU	SP	296.6e-6	8.7e-6	1.1e-6	37.8e-6	38.8e-6
2011	$B^0_s \to K^0_S K^+ K^-$	DD	MD	PP	539.2e-6	11.3e-6	1.9e-6	63.3e-6	64.3e-6
2011	$B^0_s \to K^0_S K^+ K^-$	DD	MU	PP	520.9e-6	11.1e-6	1.7e-6	63.3e-6	64.3e-6
2011	$B^0_s \to K^0_S K^+ K^-$	DD	MD	SP	401.7e-6	9.8e-6	1.4e-6	37.8e-6	39.1e-6
2011	$B^0_s \to K^0_S K^+ K^-$	DD	MU	SP	387.7e-6	9.5e-6	1.3e-6	37.8e-6	39.0e-6
2018	$B^0_s \to K^0_S K^+ K^-$	LL	MD	PP	334.4e-6	30.2e-6	1.3e-6	55.6e-6	63.3e-6
2018	$B^0_s \to K^0_S K^+ K^-$	LL	MU	PP	406.5e-6	28.9e-6	1.2e-6	55.6e-6	62.7e-6
2018	$B^0_s \to K^0_S K^+ K^-$	LL	MD	SP	230.3e-6	25.5e-6	1.1e-6	37.2e-6	45.1e-6
2018	$B^0_s \to K^0_S K^+ K^-$	LL	MU	SP	3014.4e-7	244.0e-7	8.7e-7	371.7e-7	444.8e-7
2017	$B^0_s \to K^0_S K^+ K^-$	LL	MD	PP	414.1e-6	33.3e-6	1.5e-6	55.6e-6	64.9e-6
2017	$B^0_s \to K^0_S K^+ K^-$	LL	MU	PP	396.1e-6	31.9e-6	1.3e-6	55.6e-6	64.1e-6
2017	$B^0_s \to K^0_S K^+ K^-$	LL	MD	SP	2349.0e-7	250.9e-7	9.6e-7	371.7e-7	448.6e-7
2017	$B^0_s \to K^0_S K^+ K^-$	LL	MU	SP	2183.0e-7	239.5e-7	8.5e-7	371.7e-7	442.3e-7
2016	$B^0_s \to K^0_S K^+ K^-$	LL	MD	PP	477.0e-6	35.4e-6	1.5e-6	55.6e-6	66.0e-6
2016	$B^0_s \to K^0_S K^+ K^-$	LL	MU	PP	494.2e-6	33.7e-6	1.4e-6	55.6e-6	65.0e-6
2016	$B^0_s \to K^0_S K^+ K^-$	LL	MD	SP	2640.3e-7	260.7e-7	9.7e-7	371.7e-7	454.1e-7
2016	$B^0_s \to K^0_S K^+ K^-$	LL	MU	SP	2479.2e-7	245.7e-7	9.2e-7	371.7e-7	445.7e-7
2015	$B^0_s \to K^0_S K^+ K^-$	LL	MD	PP	410.2e-6	33.1e-6	1.3e-6	55.6e-6	64.7e-6
2015	$B^0_s \to K^0_S K^+ K^-$	LL	MU	PP	431.8e-6	31.4e-6	1.3e-6	55.6e-6	63.9e-6
2015	$B^0_s \to K^0_S K^+ K^-$	LL	MD	SP	337.0e-6	30.4e-6	1.1e-6	37.2e-6	48.0e-6
2015	$B^0_s \to K^0_S K^+ K^-$	LL	MU	SP	369.0e-6	29.0e-6	1.1e-6	37.2e-6	47.1e-6
2012b	$B^0_s \to K^0_S K^+ K^-$	LL	MD	PP	1978.8e-7	275.0e-7	8.9e-7	556.1e-7	620.4e-7
2012b	$B^0_s \to K^0_S K^+ K^-$	LL	MU	PP	1722.8e-7	270.3e-7	8.2e-7	556.1e-7	618.4e-7
2012b	$B^0_s \to K^0_S K^+ K^-$	LL	MD	SP	1674.2e-7	255.0e-7	7.3e-7	371.7e-7	450.8e-7
2012b	$B^0_s \to K^0_S K^+ K^-$	LL	MU	SP	1407.2e-7	253.8e-7	7.4e-7	371.7e-7	450.1e-7
2012a	$B^0_s \to K^0_S K^+ K^-$	LL	MD	PP	1841.8e-7	323.1e-7	9.0e-7	556.1e-7	643.2e-7
2012a	$B^0_s \to K^0_S K^+ K^-$	LL	MU	PP	2211.9e-7	329.3e-7	7.3e-7	556.1e-7	646.3e-7
2012a	$B^0_s \to K^0_S K^+ K^-$	LL	MD	SP	1460.8e-7	298.0e-7	8.3e-7	371.7e-7	476.5e-7
2012a	$B^0_s \to K^0_S K^+ K^-$	LL	MU	SP	1906.5e-7	305.5e-7	7.0e-7	371.7e-7	481.2e-7
2011	$B^0_s \to K^0_S K^+ K^-$	LL	MD	PP	260.8e-6	33.9e-6	1.1e-6	55.6e-6	65.1e-6
2011	$B^0_s \to K^0_S K^+ K^-$	LL	MU	PP	255.4e-6	31.9e-6	1.0e-6	55.6e-6	64.1e-6
2011	$B^0_s \to K^0_S K^+ K^-$	LL	MD	SP	1845.8e-7	289.8e-7	7.9e-7	371.7e-7	471.4e-7
2011	$B^0_s \to K^0_S K^+ K^-$	LL	MU	SP	1655.0e-7	271.3e-7	7.7e-7	371.7e-7	460.2e-7

Table C.19: $B^0_s \to K^0_S K^+ K^-$ detailed efficiency tables. PP stand for favoured mode optimisation and SP for unfavoured mode optimisation.

C.5 Polarity combined efficiency tables

Year	Mode	K_S^0	$\bar{\varepsilon}$	$\sigma_{\bar{\varepsilon}}^{\text{stat}}$	$\sigma_{\bar{\varepsilon}}^{\text{RMS}}$	$\sigma_{\bar{\varepsilon}}$
2018	$B_d^0 \to K_S^0\pi^+\pi^-$	DD	821.0e-6	6.2e-6	12.2e-6	13.7e-6
2017	$B_d^0 \to K_S^0\pi^+\pi^-$	DD	833.3e-6	6.4e-6	12.2e-6	13.8e-6
2016	$B_d^0 \to K_S^0\pi^+\pi^-$	DD	869.3e-6	6.6e-6	12.2e-6	13.9e-6
2015	$B_d^0 \to K_S^0\pi^+\pi^-$	DD	835.9e-6	6.5e-6	12.2e-6	13.8e-6
2012b	$B_d^0 \to K_S^0\pi^+\pi^-$	DD	519.4e-6	5.8e-6	12.2e-6	13.5e-6
2012a	$B_d^0 \to K_S^0\pi^+\pi^-$	DD	411.6e-6	5.6e-6	12.2e-6	13.4e-6
2011	$B_d^0 \to K_S^0\pi^+\pi^-$	DD	492.0e-6	6.0e-6	12.2e-6	13.6e-6
2018	$B_d^0 \to K_S^0\pi^+\pi^-$	LL	296.9e-6	3.7e-6	6.5e-6	7.5e-6
2017	$B_d^0 \to K_S^0\pi^+\pi^-$	LL	316.9e-6	4.0e-6	6.5e-6	7.6e-6
2016	$B_d^0 \to K_S^0\pi^+\pi^-$	LL	356.3e-6	4.3e-6	6.5e-6	7.8e-6
2015	$B_d^0 \to K_S^0\pi^+\pi^-$	LL	327.5e-6	4.1e-6	6.5e-6	7.7e-6
2012b	$B_d^0 \to K_S^0\pi^+\pi^-$	LL	153.3e-6	3.1e-6	6.5e-6	7.2e-6
2012a	$B_d^0 \to K_S^0\pi^+\pi^-$	LL	176.8e-6	3.7e-6	6.5e-6	7.5e-6
2011	$B_d^0 \to K_S^0\pi^+\pi^-$	LL	187.7e-6	3.8e-6	6.5e-6	7.5e-6

Table C.20: $B^0 \to K_S^0\pi^+\pi^-$ efficiency tables with the favoured mode optimisation. For each year and K_S^0 reconstruction type, the average efficiency $\bar{\varepsilon}$, the statistical uncertainty $\sigma_{\bar{\varepsilon}}^{\text{stat}}$, the uncertainty linked to the averaging method $\sigma_{\bar{\varepsilon}}^{\text{RMS}}$ and the total uncertainty $\sigma_{\bar{\varepsilon}}$ are given.

Year	Mode	K_S^0	$\bar{\varepsilon}$	$\sigma_{\bar{\varepsilon}}^{\text{stat}}$	$\sigma_{\bar{\varepsilon}}^{\text{RMS}}$	$\sigma_{\bar{\varepsilon}}$
2018	$B_d^0 \to K_S^0\pi^+\pi^-$	DD	413.3e-6	4.1e-6	6.3e-6	7.5e-6
2017	$B_d^0 \to K_S^0\pi^+\pi^-$	DD	442.3e-6	4.4e-6	6.3e-6	7.6e-6
2016	$B_d^0 \to K_S^0\pi^+\pi^-$	DD	438.9e-6	4.3e-6	6.3e-6	7.6e-6
2015	$B_d^0 \to K_S^0\pi^+\pi^-$	DD	346.6e-6	3.8e-6	6.3e-6	7.3e-6
2012b	$B_d^0 \to K_S^0\pi^+\pi^-$	DD	343.8e-6	4.6e-6	6.3e-6	7.8e-6
2012a	$B_d^0 \to K_S^0\pi^+\pi^-$	DD	233.1e-6	4.1e-6	6.3e-6	7.5e-6
2011	$B_d^0 \to K_S^0\pi^+\pi^-$	DD	238.5e-6	4.0e-6	6.3e-6	7.5e-6
2018	$B_d^0 \to K_S^0\pi^+\pi^-$	LL	190.8e-6	2.8e-6	4.4e-6	5.2e-6
2017	$B_d^0 \to K_S^0\pi^+\pi^-$	LL	215.3e-6	3.2e-6	4.4e-6	5.4e-6
2016	$B_d^0 \to K_S^0\pi^+\pi^-$	LL	221.4e-6	3.2e-6	4.4e-6	5.4e-6
2015	$B_d^0 \to K_S^0\pi^+\pi^-$	LL	199.2e-6	3.1e-6	4.4e-6	5.3e-6
2012b	$B_d^0 \to K_S^0\pi^+\pi^-$	LL	108.5e-6	2.6e-6	4.4e-6	5.1e-6
2012a	$B_d^0 \to K_S^0\pi^+\pi^-$	LL	77.8e-6	2.4e-6	4.4e-6	5.0e-6
2011	$B_d^0 \to K_S^0\pi^+\pi^-$	LL	132.9e-6	3.1e-6	4.4e-6	5.4e-6

Table C.21: $B^0 \to K_S^0\pi^+\pi^-$ efficiency tables with the unfavoured mode optimisation. For each year and K_S^0 reconstruction type, the average efficiency $\bar{\varepsilon}$, the statistical uncertainty $\sigma_{\bar{\varepsilon}}^{\text{stat}}$, the uncertainty linked to the averaging method $\sigma_{\bar{\varepsilon}}^{\text{RMS}}$ and the total uncertainty $\sigma_{\bar{\varepsilon}}$ are given.

Year	Mode	K_S^0	$\bar{\varepsilon}$	$\sigma_{\bar{\varepsilon}}^{\text{stat}}$	$\sigma_{\bar{\varepsilon}}^{\text{RMS}}$	$\sigma_{\bar{\varepsilon}}$
2018	$B_d^0 \to K_S^0\pi^+K^-$	DD	88.5e-5	1.0e-5	1.3e-5	1.6e-5
2017	$B_d^0 \to K_S^0\pi^+K^-$	DD	92.6e-5	1.1e-5	1.3e-5	1.7e-5
2016	$B_d^0 \to K_S^0\pi^+K^-$	DD	105.1e-5	1.1e-5	1.3e-5	1.7e-5
2015	$B_d^0 \to K_S^0\pi^+K^-$	DD	93.3e-5	1.1e-5	1.3e-5	1.7e-5
2012b	$B_d^0 \to K_S^0\pi^+K^-$	DD	66.2e-5	1.2e-5	1.3e-5	1.7e-5
2012a	$B_d^0 \to K_S^0\pi^+K^-$	DD	50.4e-5	1.1e-5	1.3e-5	1.7e-5
2011	$B_d^0 \to K_S^0\pi^+K^-$	DD	61.0e-5	1.1e-5	1.3e-5	1.7e-5
2018	$B_d^0 \to K_S^0\pi^+K^-$	LL	334.2e-6	7.0e-6	12.0e-6	13.9e-6
2017	$B_d^0 \to K_S^0\pi^+K^-$	LL	370.5e-6	7.8e-6	12.0e-6	14.3e-6
2016	$B_d^0 \to K_S^0\pi^+K^-$	LL	384.3e-6	7.9e-6	12.0e-6	14.4e-6
2015	$B_d^0 \to K_S^0\pi^+K^-$	LL	367.0e-6	7.8e-6	12.0e-6	14.3e-6
2012b	$B_d^0 \to K_S^0\pi^+K^-$	LL	181.3e-6	6.5e-6	12.0e-6	13.6e-6
2012a	$B_d^0 \to K_S^0\pi^+K^-$	LL	208.4e-6	7.5e-6	12.0e-6	14.1e-6
2011	$B_d^0 \to K_S^0\pi^+K^-$	LL	237.2e-6	7.7e-6	12.0e-6	14.3e-6

Table C.22: $B^0 \to K_S^0\pi^+K^-$ efficiency tables with the favoured mode optimisation. For each year and K_S^0 reconstruction type, the average efficiency $\bar{\varepsilon}$, the statistical uncertainty $\sigma_{\bar{\varepsilon}}^{\text{stat}}$, the uncertainty linked to the averaging method $\sigma_{\bar{\varepsilon}}^{\text{RMS}}$ and the total uncertainty $\sigma_{\bar{\varepsilon}}$ are given.

Year	Mode	K_S^0	$\bar{\varepsilon}$	$\sigma_{\bar{\varepsilon}}^{\text{stat}}$	$\sigma_{\bar{\varepsilon}}^{\text{RMS}}$	$\sigma_{\bar{\varepsilon}}$
2018	$B_d^0 \to K_S^0\pi^+K^-$	DD	667.1e-6	8.6e-6	11.4e-6	14.3e-6
2017	$B_d^0 \to K_S^0\pi^+K^-$	DD	697.5e-6	9.1e-6	11.4e-6	14.6e-6
2016	$B_d^0 \to K_S^0\pi^+K^-$	DD	789.0e-6	9.7e-6	11.4e-6	15.0e-6
2015	$B_d^0 \to K_S^0\pi^+K^-$	DD	690.9e-6	9.4e-6	11.4e-6	14.8e-6
2012b	$B_d^0 \to K_S^0\pi^+K^-$	DD	51.6e-5	1.0e-5	1.1e-5	1.5e-5
2012a	$B_d^0 \to K_S^0\pi^+K^-$	DD	41.8e-5	1.0e-5	1.1e-5	1.5e-5
2011	$B_d^0 \to K_S^0\pi^+K^-$	DD	50.2e-5	1.0e-5	1.1e-5	1.5e-5
2018	$B_d^0 \to K_S^0\pi^+K^-$	LL	275.8e-6	6.2e-6	8.5e-6	10.6e-6
2017	$B_d^0 \to K_S^0\pi^+K^-$	LL	302.3e-6	6.9e-6	8.5e-6	11.0e-6
2016	$B_d^0 \to K_S^0\pi^+K^-$	LL	311.9e-6	6.9e-6	8.5e-6	11.0e-6
2015	$B_d^0 \to K_S^0\pi^+K^-$	LL	244.0e-6	6.1e-6	8.5e-6	10.5e-6
2012b	$B_d^0 \to K_S^0\pi^+K^-$	LL	94.2e-6	4.6e-6	8.5e-6	9.7e-6
2012a	$B_d^0 \to K_S^0\pi^+K^-$	LL	155.5e-6	6.4e-6	8.5e-6	10.7e-6
2011	$B_d^0 \to K_S^0\pi^+K^-$	LL	193.7e-6	6.9e-6	8.5e-6	11.0e-6

Table C.23: $B^0 \to K_S^0\pi^+K^-$ efficiency tables with the unfavoured mode optimisation. For each year and K_S^0 reconstruction type, the average efficiency $\bar{\varepsilon}$, the statistical uncertainty $\sigma_{\bar{\varepsilon}}^{\text{stat}}$, the uncertainty linked to the averaging method $\sigma_{\bar{\varepsilon}}^{\text{RMS}}$ and the total uncertainty $\sigma_{\bar{\varepsilon}}$ are given.

Year	Mode	K_S^0	$\bar{\varepsilon}$	$\sigma_{\bar{\varepsilon}}^{\text{stat}}$	$\sigma_{\bar{\varepsilon}}^{\text{RMS}}$	$\sigma_{\bar{\varepsilon}}$
2018	$B_d^0 \to K_S^0 K^+\pi^-$	DD	89.8e-5	1.1e-5	1.5e-5	1.8e-5
2017	$B_d^0 \to K_S^0 K^+\pi^-$	DD	95.6e-5	1.2e-5	1.5e-5	1.9e-5
2016	$B_d^0 \to K_S^0 K^+\pi^-$	DD	102.1e-5	1.2e-5	1.5e-5	1.9e-5
2015	$B_d^0 \to K_S^0 K^+\pi^-$	DD	93.3e-5	1.2e-5	1.5e-5	1.9e-5
2012b	$B_d^0 \to K_S^0 K^+\pi^-$	DD	68.2e-5	1.3e-5	1.5e-5	2.0e-5
2012a	$B_d^0 \to K_S^0 K^+\pi^-$	DD	51.9e-5	1.3e-5	1.5e-5	1.9e-5
2011	$B_d^0 \to K_S^0 K^+\pi^-$	DD	63.6e-5	1.3e-5	1.5e-5	2.0e-5
2018	$B_d^0 \to K_S^0 K^+\pi^-$	LL	322.4e-6	7.5e-6	13.4e-6	15.4e-6
2017	$B_d^0 \to K_S^0 K^+\pi^-$	LL	368.2e-6	8.6e-6	13.4e-6	15.9e-6
2016	$B_d^0 \to K_S^0 K^+\pi^-$	LL	400.8e-6	8.9e-6	13.4e-6	16.1e-6
2015	$B_d^0 \to K_S^0 K^+\pi^-$	LL	374.5e-6	8.7e-6	13.4e-6	16.0e-6
2012b	$B_d^0 \to K_S^0 K^+\pi^-$	LL	178.0e-6	7.4e-6	13.4e-6	15.3e-6
2012a	$B_d^0 \to K_S^0 K^+\pi^-$	LL	188.4e-6	8.4e-6	13.4e-6	15.8e-6
2011	$B_d^0 \to K_S^0 K^+\pi^-$	LL	229.4e-6	8.8e-6	13.4e-6	16.1e-6

Table C.24: $B^0 \to K_S^0 K^+\pi^-$ efficiency tables with the favoured mode optimisation. For each year and K_S^0 reconstruction type, the average efficiency $\bar{\varepsilon}$, the statistical uncertainty $\sigma_{\bar{\varepsilon}}^{\text{stat}}$, the uncertainty linked to the averaging method $\sigma_{\bar{\varepsilon}}^{\text{RMS}}$ and the total uncertainty $\sigma_{\bar{\varepsilon}}$ are given.

Year	Mode	K_S^0	$\bar{\varepsilon}$	$\sigma_{\bar{\varepsilon}}^{\text{stat}}$	$\sigma_{\bar{\varepsilon}}^{\text{RMS}}$	$\sigma_{\bar{\varepsilon}}$
2018	$B_d^0 \to K_S^0 K^+\pi^-$	DD	683.8e-6	9.6e-6	11.4e-6	14.9e-6
2017	$B_d^0 \to K_S^0 K^+\pi^-$	DD	78.4e-5	1.1e-5	1.1e-5	1.6e-5
2016	$B_d^0 \to K_S^0 K^+\pi^-$	DD	75.6e-5	1.1e-5	1.1e-5	1.6e-5
2015	$B_d^0 \to K_S^0 K^+\pi^-$	DD	66.0e-5	1.0e-5	1.1e-5	1.5e-5
2012b	$B_d^0 \to K_S^0 K^+\pi^-$	DD	48.5e-5	1.1e-5	1.1e-5	1.6e-5
2012a	$B_d^0 \to K_S^0 K^+\pi^-$	DD	40.2e-5	1.1e-5	1.1e-5	1.6e-5
2011	$B_d^0 \to K_S^0 K^+\pi^-$	DD	53.4e-5	1.2e-5	1.1e-5	1.7e-5
2018	$B_d^0 \to K_S^0 K^+\pi^-$	LL	267.4e-6	6.8e-6	9.8e-6	11.9e-6
2017	$B_d^0 \to K_S^0 K^+\pi^-$	LL	288.4e-6	7.5e-6	9.8e-6	12.3e-6
2016	$B_d^0 \to K_S^0 K^+\pi^-$	LL	313.7e-6	7.7e-6	9.8e-6	12.5e-6
2015	$B_d^0 \to K_S^0 K^+\pi^-$	LL	272.7e-6	7.3e-6	9.8e-6	12.2e-6
2012b	$B_d^0 \to K_S^0 K^+\pi^-$	LL	89.9e-6	5.2e-6	9.8e-6	11.1e-6
2012a	$B_d^0 \to K_S^0 K^+\pi^-$	LL	149.2e-6	7.5e-6	9.8e-6	12.3e-6
2011	$B_d^0 \to K_S^0 K^+\pi^-$	LL	173.6e-6	7.6e-6	9.8e-6	12.4e-6

Table C.25: $B^0 \to K_S^0 K^+\pi^-$ efficiency tables with the unfavoured mode optimisation. For each year and K_S^0 reconstruction type, the average efficiency $\bar{\varepsilon}$, the statistical uncertainty $\sigma_{\bar{\varepsilon}}^{\text{stat}}$, the uncertainty linked to the averaging method $\sigma_{\bar{\varepsilon}}^{\text{RMS}}$ and the total uncertainty $\sigma_{\bar{\varepsilon}}$ are given.

Year	Mode	K_S^0	$\bar{\varepsilon}$	$\sigma_{\bar{\varepsilon}}^{\text{stat}}$	$\sigma_{\bar{\varepsilon}}^{\text{RMS}}$	$\sigma_{\bar{\varepsilon}}$
2018	$B_d^0 \to K_S^0 K^+ K^-$	DD	728.2e-6	5.2e-6	3.2e-6	6.1e-6
2017	$B_d^0 \to K_S^0 K^+ K^-$	DD	751.5e-6	5.5e-6	3.2e-6	6.4e-6
2016	$B_d^0 \to K_S^0 K^+ K^-$	DD	893.4e-6	6.0e-6	3.2e-6	6.8e-6
2015	$B_d^0 \to K_S^0 K^+ K^-$	DD	803.7e-6	5.8e-6	3.2e-6	6.6e-6
2012b	$B_d^0 \to K_S^0 K^+ K^-$	DD	449.6e-6	5.5e-6	3.2e-6	6.4e-6
2012a	$B_d^0 \to K_S^0 K^+ K^-$	DD	311.5e-6	4.9e-6	3.2e-6	5.9e-6
2011	$B_d^0 \to K_S^0 K^+ K^-$	DD	360.3e-6	4.8e-6	3.2e-6	5.8e-6
2018	$B_d^0 \to K_S^0 K^+ K^-$	LL	304.8e-6	3.3e-6	2.1e-6	3.9e-6
2017	$B_d^0 \to K_S^0 K^+ K^-$	LL	329.4e-6	3.6e-6	2.1e-6	4.2e-6
2016	$B_d^0 \to K_S^0 K^+ K^-$	LL	370.3e-6	3.8e-6	2.1e-6	4.4e-6
2015	$B_d^0 \to K_S^0 K^+ K^-$	LL	332.8e-6	3.7e-6	2.1e-6	4.3e-6
2012b	$B_d^0 \to K_S^0 K^+ K^-$	LL	147.1e-6	3.2e-6	2.1e-6	3.8e-6
2012a	$B_d^0 \to K_S^0 K^+ K^-$	LL	168.0e-6	3.6e-6	2.1e-6	4.2e-6
2011	$B_d^0 \to K_S^0 K^+ K^-$	LL	190.0e-6	3.6e-6	2.1e-6	4.1e-6

Table C.26: $B^0 \to K_S^0 K^+ K^-$ efficiency tables with the favoured mode optimisation. For each year and K_S^0 reconstruction type, the average efficiency $\bar{\varepsilon}$, the statistical uncertainty $\sigma_{\bar{\varepsilon}}^{\text{stat}}$, the uncertainty linked to the averaging method $\sigma_{\bar{\varepsilon}}^{\text{RMS}}$ and the total uncertainty $\sigma_{\bar{\varepsilon}}$ are given.

Year	Mode	K_S^0	$\bar{\varepsilon}$	$\sigma_{\bar{\varepsilon}}^{\text{stat}}$	$\sigma_{\bar{\varepsilon}}^{\text{RMS}}$	$\sigma_{\bar{\varepsilon}}$
2018	$B_d^0 \to K_S^0 K^+ K^-$	DD	485.0e-6	4.2e-6	2.0e-6	4.7e-6
2017	$B_d^0 \to K_S^0 K^+ K^-$	DD	374.2e-6	3.9e-6	2.0e-6	4.4e-6
2016	$B_d^0 \to K_S^0 K^+ K^-$	DD	479.3e-6	4.4e-6	2.0e-6	4.8e-6
2015	$B_d^0 \to K_S^0 K^+ K^-$	DD	400.2e-6	4.1e-6	2.0e-6	4.6e-6
2012b	$B_d^0 \to K_S^0 K^+ K^-$	DD	334.3e-6	4.8e-6	2.0e-6	5.2e-6
2012a	$B_d^0 \to K_S^0 K^+ K^-$	DD	210.6e-6	4.1e-6	2.0e-6	4.5e-6
2011	$B_d^0 \to K_S^0 K^+ K^-$	DD	275.2e-6	4.2e-6	2.0e-6	4.7e-6
2018	$B_d^0 \to K_S^0 K^+ K^-$	LL	218.4e-6	2.8e-6	1.5e-6	3.1e-6
2017	$B_d^0 \to K_S^0 K^+ K^-$	LL	183.7e-6	2.7e-6	1.5e-6	3.1e-6
2016	$B_d^0 \to K_S^0 K^+ K^-$	LL	199.7e-6	2.8e-6	1.5e-6	3.2e-6
2015	$B_d^0 \to K_S^0 K^+ K^-$	LL	280.2e-6	3.4e-6	1.5e-6	3.7e-6
2012b	$B_d^0 \to K_S^0 K^+ K^-$	LL	124.0e-6	2.9e-6	1.5e-6	3.3e-6
2012a	$B_d^0 \to K_S^0 K^+ K^-$	LL	141.3e-6	3.3e-6	1.5e-6	3.6e-6
2011	$B_d^0 \to K_S^0 K^+ K^-$	LL	137.9e-6	3.1e-6	1.5e-6	3.4e-6

Table C.27: $B^0 \to K_S^0 K^+ K^-$ efficiency tables with the unfavoured mode optimisation. For each year and K_S^0 reconstruction type, the average efficiency $\bar{\varepsilon}$, the statistical uncertainty $\sigma_{\bar{\varepsilon}}^{\text{stat}}$, the uncertainty linked to the averaging method $\sigma_{\bar{\varepsilon}}^{\text{RMS}}$ and the total uncertainty $\sigma_{\bar{\varepsilon}}$ are given.

Year	Mode	K_S^0	$\bar{\varepsilon}$	$\sigma_{\bar{\varepsilon}}^{\text{stat}}$	$\sigma_{\bar{\varepsilon}}^{\text{RMS}}$	$\sigma_{\bar{\varepsilon}}$
2018	$B_s^0 \to K_S^0\pi^+\pi^-$	DD	870.9e-6	8.1e-6	35.1e-6	36.0e-6
2017	$B_s^0 \to K_S^0\pi^+\pi^-$	DD	884.3e-6	8.4e-6	35.1e-6	36.1e-6
2016	$B_s^0 \to K_S^0\pi^+\pi^-$	DD	913.6e-6	8.8e-6	35.1e-6	36.2e-6
2015	$B_s^0 \to K_S^0\pi^+\pi^-$	DD	897.2e-6	8.8e-6	35.1e-6	36.2e-6
2012b	$B_s^0 \to K_S^0\pi^+\pi^-$	DD	570.0e-6	8.2e-6	35.1e-6	36.0e-6
2012a	$B_s^0 \to K_S^0\pi^+\pi^-$	DD	458.5e-6	7.6e-6	35.1e-6	35.9e-6
2011	$B_s^0 \to K_S^0\pi^+\pi^-$	DD	548.4e-6	7.8e-6	35.1e-6	35.9e-6
2018	$B_s^0 \to K_S^0\pi^+\pi^-$	LL	329.3e-6	6.2e-6	8.2e-6	10.3e-6
2017	$B_s^0 \to K_S^0\pi^+\pi^-$	LL	357.1e-6	6.5e-6	8.2e-6	10.5e-6
2016	$B_s^0 \to K_S^0\pi^+\pi^-$	LL	397.8e-6	7.2e-6	8.2e-6	10.9e-6
2015	$B_s^0 \to K_S^0\pi^+\pi^-$	LL	360.9e-6	6.8e-6	8.2e-6	10.7e-6
2012b	$B_s^0 \to K_S^0\pi^+\pi^-$	LL	174.8e-6	5.4e-6	8.2e-6	9.9e-6
2012a	$B_s^0 \to K_S^0\pi^+\pi^-$	LL	201.1e-6	6.2e-6	8.2e-6	10.3e-6
2011	$B_s^0 \to K_S^0\pi^+\pi^-$	LL	215.0e-6	6.0e-6	8.2e-6	10.2e-6

Table C.28: $B_s^0 \to K_S^0\pi^+\pi^-$ efficiency tables with the favoured mode optimisation. For each year and K_S^0 reconstruction type, the average efficiency $\bar{\varepsilon}$, the statistical uncertainty $\sigma_{\bar{\varepsilon}}^{\text{stat}}$, the uncertainty linked to the averaging method $\sigma_{\bar{\varepsilon}}^{\text{RMS}}$ and the total uncertainty $\sigma_{\bar{\varepsilon}}$ are given.

Year	Mode	K_S^0	$\bar{\varepsilon}$	$\sigma_{\bar{\varepsilon}}^{\text{stat}}$	$\sigma_{\bar{\varepsilon}}^{\text{RMS}}$	$\sigma_{\bar{\varepsilon}}$
2018	$B_s^0 \to K_S^0\pi^+\pi^-$	DD	446.5e-6	5.3e-6	20.3e-6	20.9e-6
2017	$B_s^0 \to K_S^0\pi^+\pi^-$	DD	476.0e-6	5.7e-6	20.3e-6	21.0e-6
2016	$B_s^0 \to K_S^0\pi^+\pi^-$	DD	459.2e-6	5.7e-6	20.3e-6	21.0e-6
2015	$B_s^0 \to K_S^0\pi^+\pi^-$	DD	387.4e-6	5.2e-6	20.3e-6	20.9e-6
2012b	$B_s^0 \to K_S^0\pi^+\pi^-$	DD	367.0e-6	6.3e-6	20.3e-6	21.2e-6
2012a	$B_s^0 \to K_S^0\pi^+\pi^-$	DD	266.7e-6	5.5e-6	20.3e-6	21.0e-6
2011	$B_s^0 \to K_S^0\pi^+\pi^-$	DD	270.3e-6	5.1e-6	20.3e-6	20.9e-6
2018	$B_s^0 \to K_S^0\pi^+\pi^-$	LL	215.3e-6	4.7e-6	5.7e-6	7.4e-6
2017	$B_s^0 \to K_S^0\pi^+\pi^-$	LL	248.8e-6	5.1e-6	5.7e-6	7.7e-6
2016	$B_s^0 \to K_S^0\pi^+\pi^-$	LL	253.7e-6	5.4e-6	5.7e-6	7.9e-6
2015	$B_s^0 \to K_S^0\pi^+\pi^-$	LL	220.9e-6	5.0e-6	5.7e-6	7.6e-6
2012b	$B_s^0 \to K_S^0\pi^+\pi^-$	LL	124.6e-6	4.5e-6	5.7e-6	7.2e-6
2012a	$B_s^0 \to K_S^0\pi^+\pi^-$	LL	86.6e-6	3.9e-6	5.7e-6	6.9e-6
2011	$B_s^0 \to K_S^0\pi^+\pi^-$	LL	152.1e-6	4.9e-6	5.7e-6	7.5e-6

Table C.29: $B_s^0 \to K_S^0\pi^+\pi^-$ efficiency tables with the unfavoured mode optimisation. For each year and K_S^0 reconstruction type, the average efficiency $\bar{\varepsilon}$, the statistical uncertainty $\sigma_{\bar{\varepsilon}}^{\text{stat}}$, the uncertainty linked to the averaging method $\sigma_{\bar{\varepsilon}}^{\text{RMS}}$ and the total uncertainty $\sigma_{\bar{\varepsilon}}$ are given.

Year	Mode	K_S^0	$\bar{\varepsilon}$	$\sigma_{\bar{\varepsilon}}^{\text{stat}}$	$\sigma_{\bar{\varepsilon}}^{\text{RMS}}$	$\sigma_{\bar{\varepsilon}}$
2018	$B_s^0 \to K_S^0\pi^+K^-$	DD	852.7e-6	8.6e-6	5.7e-6	10.3e-6
2017	$B_s^0 \to K_S^0\pi^+K^-$	DD	885.9e-6	9.0e-6	5.7e-6	10.7e-6
2016	$B_s^0 \to K_S^0\pi^+K^-$	DD	999.9e-6	9.8e-6	5.7e-6	11.4e-6
2015	$B_s^0 \to K_S^0\pi^+K^-$	DD	903.5e-6	9.5e-6	5.7e-6	11.1e-6
2012b	$B_s^0 \to K_S^0\pi^+K^-$	DD	586.9e-6	9.3e-6	5.7e-6	10.9e-6
2012a	$B_s^0 \to K_S^0\pi^+K^-$	DD	473.1e-6	9.0e-6	5.7e-6	10.7e-6
2011	$B_s^0 \to K_S^0\pi^+K^-$	DD	557.6e-6	9.6e-6	5.7e-6	11.2e-6
2018	$B_s^0 \to K_S^0\pi^+K^-$	LL	321.2e-6	5.3e-6	7.8e-6	9.5e-6
2017	$B_s^0 \to K_S^0\pi^+K^-$	LL	363.1e-6	6.0e-6	7.8e-6	9.8e-6
2016	$B_s^0 \to K_S^0\pi^+K^-$	LL	380.5e-6	6.2e-6	7.8e-6	10.0e-6
2015	$B_s^0 \to K_S^0\pi^+K^-$	LL	361.8e-6	6.0e-6	7.8e-6	9.9e-6
2012b	$B_s^0 \to K_S^0\pi^+K^-$	LL	175.8e-6	5.2e-6	7.8e-6	9.4e-6
2012a	$B_s^0 \to K_S^0\pi^+K^-$	LL	203.1e-6	5.9e-6	7.8e-6	9.8e-6
2011	$B_s^0 \to K_S^0\pi^+K^-$	LL	226.9e-6	6.3e-6	7.8e-6	10.0e-6

Table C.30: $B_s^0 \to K_S^0\pi^+K^-$ efficiency tables with the favoured mode optimisation. For each year and K_S^0 reconstruction type, the average efficiency $\bar{\varepsilon}$, the statistical uncertainty $\sigma_{\bar{\varepsilon}}^{\text{stat}}$, the uncertainty linked to the averaging method $\sigma_{\bar{\varepsilon}}^{\text{RMS}}$ and the total uncertainty $\sigma_{\bar{\varepsilon}}$ are given.

Year	Mode	K_S^0	$\bar{\varepsilon}$	$\sigma_{\bar{\varepsilon}}^{\text{stat}}$	$\sigma_{\bar{\varepsilon}}^{\text{RMS}}$	$\sigma_{\bar{\varepsilon}}$
2018	$B_s^0 \to K_S^0\pi^+K^-$	DD	647.3e-6	7.3e-6	5.1e-6	9.0e-6
2017	$B_s^0 \to K_S^0\pi^+K^-$	DD	676.6e-6	7.7e-6	5.1e-6	9.3e-6
2016	$B_s^0 \to K_S^0\pi^+K^-$	DD	768.9e-6	8.4e-6	5.1e-6	9.9e-6
2015	$B_s^0 \to K_S^0\pi^+K^-$	DD	670.3e-6	8.0e-6	5.1e-6	9.5e-6
2012b	$B_s^0 \to K_S^0\pi^+K^-$	DD	458.9e-6	8.1e-6	5.1e-6	9.6e-6
2012a	$B_s^0 \to K_S^0\pi^+K^-$	DD	388.8e-6	8.0e-6	5.1e-6	9.5e-6
2011	$B_s^0 \to K_S^0\pi^+K^-$	DD	456.6e-6	8.6e-6	5.1e-6	10.0e-6
2018	$B_s^0 \to K_S^0\pi^+K^-$	LL	271.2e-6	4.9e-6	5.9e-6	7.6e-6
2017	$B_s^0 \to K_S^0\pi^+K^-$	LL	298.6e-6	5.4e-6	5.9e-6	8.0e-6
2016	$B_s^0 \to K_S^0\pi^+K^-$	LL	315.8e-6	5.6e-6	5.9e-6	8.1e-6
2015	$B_s^0 \to K_S^0\pi^+K^-$	LL	247.4e-6	4.9e-6	5.9e-6	7.7e-6
2012b	$B_s^0 \to K_S^0\pi^+K^-$	LL	90.9e-6	3.7e-6	5.9e-6	7.0e-6
2012a	$B_s^0 \to K_S^0\pi^+K^-$	LL	151.5e-6	5.0e-6	5.9e-6	7.7e-6
2011	$B_s^0 \to K_S^0\pi^+K^-$	LL	185.5e-6	5.6e-6	5.9e-6	8.1e-6

Table C.31: $B_s^0 \to K_S^0\pi^+K^-$ efficiency tables with the unfavoured mode optimisation. For each year and K_S^0 reconstruction type, the average efficiency $\bar{\varepsilon}$, the statistical uncertainty $\sigma_{\bar{\varepsilon}}^{\text{stat}}$, the uncertainty linked to the averaging method $\sigma_{\bar{\varepsilon}}^{\text{RMS}}$ and the total uncertainty $\sigma_{\bar{\varepsilon}}$ are given.

Year	Mode	K_S^0	$\bar{\varepsilon}$	$\sigma_{\bar{\varepsilon}}^{\text{stat}}$	$\sigma_{\bar{\varepsilon}}^{\text{RMS}}$	$\sigma_{\bar{\varepsilon}}$
2018	$B_s^0 \to K_S^0 K^+\pi^-$	DD	869.1e-6	8.1e-6	4.8e-6	9.4e-6
2017	$B_s^0 \to K_S^0 K^+\pi^-$	DD	904.9e-6	8.7e-6	4.8e-6	9.9e-6
2016	$B_s^0 \to K_S^0 K^+\pi^-$	DD	973.9e-6	9.1e-6	4.8e-6	10.3e-6
2015	$B_s^0 \to K_S^0 K^+\pi^-$	DD	871.3e-6	8.8e-6	4.8e-6	10.0e-6
2012b	$B_s^0 \to K_S^0 K^+\pi^-$	DD	567.0e-6	8.7e-6	4.8e-6	10.0e-6
2012a	$B_s^0 \to K_S^0 K^+\pi^-$	DD	437.7e-6	8.1e-6	4.8e-6	9.4e-6
2011	$B_s^0 \to K_S^0 K^+\pi^-$	DD	506.6e-6	8.4e-6	4.8e-6	9.7e-6
2018	$B_s^0 \to K_S^0 K^+\pi^-$	LL	317.1e-6	5.7e-6	12.0e-6	13.3e-6
2017	$B_s^0 \to K_S^0 K^+\pi^-$	LL	360.4e-6	6.4e-6	12.0e-6	13.6e-6
2016	$B_s^0 \to K_S^0 K^+\pi^-$	LL	398.1e-6	6.8e-6	12.0e-6	13.8e-6
2015	$B_s^0 \to K_S^0 K^+\pi^-$	LL	369.3e-6	6.6e-6	12.0e-6	13.7e-6
2012b	$B_s^0 \to K_S^0 K^+\pi^-$	LL	161.9e-6	5.0e-6	12.0e-6	13.0e-6
2012a	$B_s^0 \to K_S^0 K^+\pi^-$	LL	187.6e-6	5.7e-6	12.0e-6	13.3e-6
2011	$B_s^0 \to K_S^0 K^+\pi^-$	LL	216.7e-6	6.1e-6	12.0e-6	13.4e-6

Table C.32: $B_s^0 \to K_S^0 K^+\pi^-$ efficiency tables with the favoured mode optimisation. For each year and K_S^0 reconstruction type, the average efficiency $\bar{\varepsilon}$, the statistical uncertainty $\sigma_{\bar{\varepsilon}}^{\text{stat}}$, the uncertainty linked to the averaging method $\sigma_{\bar{\varepsilon}}^{\text{RMS}}$ and the total uncertainty $\sigma_{\bar{\varepsilon}}$ are given.

Year	Mode	K_S^0	$\bar{\varepsilon}$	$\sigma_{\bar{\varepsilon}}^{\text{stat}}$	$\sigma_{\bar{\varepsilon}}^{\text{RMS}}$	$\sigma_{\bar{\varepsilon}}$
2018	$B_s^0 \to K_S^0 K^+\pi^-$	DD	677.8e-6	7.1e-6	4.5e-6	8.4e-6
2017	$B_s^0 \to K_S^0 K^+\pi^-$	DD	750.1e-6	7.8e-6	4.5e-6	9.0e-6
2016	$B_s^0 \to K_S^0 K^+\pi^-$	DD	742.5e-6	7.9e-6	4.5e-6	9.1e-6
2015	$B_s^0 \to K_S^0 K^+\pi^-$	DD	615.6e-6	7.3e-6	4.5e-6	8.5e-6
2012b	$B_s^0 \to K_S^0 K^+\pi^-$	DD	415.1e-6	7.4e-6	4.5e-6	8.7e-6
2012a	$B_s^0 \to K_S^0 K^+\pi^-$	DD	344.1e-6	7.1e-6	4.5e-6	8.4e-6
2011	$B_s^0 \to K_S^0 K^+\pi^-$	DD	433.4e-6	7.8e-6	4.5e-6	9.0e-6
2018	$B_s^0 \to K_S^0 K^+\pi^-$	LL	264.2e-6	5.1e-6	9.7e-6	11.0e-6
2017	$B_s^0 \to K_S^0 K^+\pi^-$	LL	284.2e-6	5.5e-6	9.7e-6	11.1e-6
2016	$B_s^0 \to K_S^0 K^+\pi^-$	LL	314.3e-6	5.9e-6	9.7e-6	11.4e-6
2015	$B_s^0 \to K_S^0 K^+\pi^-$	LL	275.4e-6	5.5e-6	9.7e-6	11.2e-6
2012b	$B_s^0 \to K_S^0 K^+\pi^-$	LL	90.2e-6	3.6e-6	9.7e-6	10.3e-6
2012a	$B_s^0 \to K_S^0 K^+\pi^-$	LL	148.4e-6	5.0e-6	9.7e-6	10.9e-6
2011	$B_s^0 \to K_S^0 K^+\pi^-$	LL	169.3e-6	5.3e-6	9.7e-6	11.0e-6

Table C.33: $B_s^0 \to K_S^0 K^+\pi^-$ efficiency tables with the unfavoured mode optimisation. For each year and K_S^0 reconstruction type, the average efficiency $\bar{\varepsilon}$, the statistical uncertainty $\sigma_{\bar{\varepsilon}}^{\text{stat}}$, the uncertainty linked to the averaging method $\sigma_{\bar{\varepsilon}}^{\text{RMS}}$ and the total uncertainty $\sigma_{\bar{\varepsilon}}$ are given.

Year	Mode	K_S^0	$\bar{\varepsilon}$	$\sigma_{\bar{\varepsilon}}^{\text{stat}}$	$\sigma_{\bar{\varepsilon}}^{\text{RMS}}$	$\sigma_{\bar{\varepsilon}}$
2018	$B_s^0 \to K_S^0 K^+ K^-$	DD	835.4e-6	7.6e-6	63.3e-6	63.7e-6
2017	$B_s^0 \to K_S^0 K^+ K^-$	DD	879.7e-6	8.1e-6	63.3e-6	63.8e-6
2016	$B_s^0 \to K_S^0 K^+ K^-$	DD	1023.2e-6	8.7e-6	63.3e-6	63.9e-6
2015	$B_s^0 \to K_S^0 K^+ K^-$	DD	916.5e-6	8.3e-6	63.3e-6	63.8e-6
2012b	$B_s^0 \to K_S^0 K^+ K^-$	DD	577.2e-6	8.0e-6	63.3e-6	63.8e-6
2012a	$B_s^0 \to K_S^0 K^+ K^-$	DD	478.4e-6	8.2e-6	63.3e-6	63.8e-6
2011	$B_s^0 \to K_S^0 K^+ K^-$	DD	531.0e-6	8.1e-6	63.3e-6	63.8e-6
2018	$B_s^0 \to K_S^0 K^+ K^-$	LL	37.2e-5	2.1e-5	5.6e-5	5.9e-5
2017	$B_s^0 \to K_S^0 K^+ K^-$	LL	40.6e-5	2.3e-5	5.6e-5	6.0e-5
2016	$B_s^0 \to K_S^0 K^+ K^-$	LL	48.5e-5	2.5e-5	5.6e-5	6.1e-5
2015	$B_s^0 \to K_S^0 K^+ K^-$	LL	41.9e-5	2.3e-5	5.6e-5	6.0e-5
2012b	$B_s^0 \to K_S^0 K^+ K^-$	LL	18.5e-5	1.9e-5	5.6e-5	5.9e-5
2012a	$B_s^0 \to K_S^0 K^+ K^-$	LL	20.1e-5	2.3e-5	5.6e-5	6.0e-5
2011	$B_s^0 \to K_S^0 K^+ K^-$	LL	25.8e-5	2.4e-5	5.6e-5	6.0e-5

Table C.34: $B_s^0 \to K_S^0 K^+ K^-$ efficiency tables with the favoured mode optimisation. For each year and K_S^0 reconstruction type, the average efficiency $\bar{\varepsilon}$, the statistical uncertainty $\sigma_{\bar{\varepsilon}}^{\text{stat}}$, the uncertainty linked to the averaging method $\sigma_{\bar{\varepsilon}}^{\text{RMS}}$ and the total uncertainty $\sigma_{\bar{\varepsilon}}$ are given.

Year	Mode	K_S^0	$\bar{\varepsilon}$	$\sigma_{\bar{\varepsilon}}^{\text{stat}}$	$\sigma_{\bar{\varepsilon}}^{\text{RMS}}$	$\sigma_{\bar{\varepsilon}}$
2018	$B_s^0 \to K_S^0 K^+ K^-$	DD	548.0e-6	6.1e-6	37.8e-6	38.3e-6
2017	$B_s^0 \to K_S^0 K^+ K^-$	DD	426.0e-6	5.6e-6	37.8e-6	38.2e-6
2016	$B_s^0 \to K_S^0 K^+ K^-$	DD	546.4e-6	6.3e-6	37.8e-6	38.3e-6
2015	$B_s^0 \to K_S^0 K^+ K^-$	DD	450.7e-6	5.8e-6	37.8e-6	38.2e-6
2012b	$B_s^0 \to K_S^0 K^+ K^-$	DD	422.6e-6	6.8e-6	37.8e-6	38.4e-6
2012a	$B_s^0 \to K_S^0 K^+ K^-$	DD	307.5e-6	6.5e-6	37.8e-6	38.3e-6
2011	$B_s^0 \to K_S^0 K^+ K^-$	DD	395.4e-6	7.0e-6	37.8e-6	38.4e-6
2018	$B_s^0 \to K_S^0 K^+ K^-$	LL	26.7e-5	1.8e-5	3.7e-5	4.1e-5
2017	$B_s^0 \to K_S^0 K^+ K^-$	LL	22.7e-5	1.7e-5	3.7e-5	4.1e-5
2016	$B_s^0 \to K_S^0 K^+ K^-$	LL	25.6e-5	1.8e-5	3.7e-5	4.1e-5
2015	$B_s^0 \to K_S^0 K^+ K^-$	LL	35.0e-5	2.1e-5	3.7e-5	4.3e-5
2012b	$B_s^0 \to K_S^0 K^+ K^-$	LL	15.4e-5	1.8e-5	3.7e-5	4.1e-5
2012a	$B_s^0 \to K_S^0 K^+ K^-$	LL	16.7e-5	2.1e-5	3.7e-5	4.3e-5
2011	$B_s^0 \to K_S^0 K^+ K^-$	LL	17.6e-5	2.0e-5	3.7e-5	4.2e-5

Table C.35: $B_s^0 \to K_S^0 K^+ K^-$ efficiency tables with the unfavoured mode optimisation. For each year and K_S^0 reconstruction type, the average efficiency $\bar{\varepsilon}$, the statistical uncertainty $\sigma_{\bar{\varepsilon}}^{\text{stat}}$, the uncertainty linked to the averaging method $\sigma_{\bar{\varepsilon}}^{\text{RMS}}$ and the total uncertainty $\sigma_{\bar{\varepsilon}}$ are given.

C.6 Mass fit systematics tables

Year	KS	Selection	GlobalAddRadPart	GlobalSmallFixed	GlobalSmallNotFixed	SignalFreeDeltaM	SignalHypatia2	CombExp	CombFit	CombNoKpipiKBinding	CombNoForcePos	PartUseCharm	PartUseAll	CFFreeAll	CFFreeSmall	Total
2011	LL	PP	5.4e-03	0.0e+00	2.0e-05	5.6e-04	2.1e-03	6.9e-03	8.7e-03	7.2e-05	0.0e+00	2.1e-02	4.5e-03	2.9e-02	0.0e+00	6.6e-02
2011	LL	SP	1.3e-02	0.0e+00	6.2e-05	4.6e-04	5.1e-04	1.8e-02	1.8e-02	2.4e-05	0.0e+00	8.7e-03	2.9e-03	6.6e-02	4.3e-02	1.1e-01
2011	DD	PP	6.8e-03	0.0e+00	1.4e-05	3.3e-04	7.1e-04	1.6e-03	5.4e-03	1.4e-04	0.0e+00	7.9e-03	7.1e-03	8.4e-03	0.0e+00	4.6e-02
2011	DD	SP	4.0e-02	0.0e+00	2.5e-05	1.1e-03	1.3e-03	7.8e-03	1.4e-02	4.9e-06	0.0e+00	3.6e-03	2.8e-04	8.3e-03	1.1e-02	7.0e-02
2012a	LL	PP	3.1e-03	1.4e-13	1.1e-05	2.4e-04	5.3e-04	4.8e-03	9.8e-03	4.9e-04	0.0e+00	1.5e-03	1.6e-05	5.4e-03	0.0e+00	5.0e-02
2012a	LL	SP	8.7e-03	0.0e+00	4.3e-06	6.2e-04	1.6e-03	8.6e-03	1.1e-02	2.9e-04	7.9e-05	3.8e-04	8.3e-05	2.8e-03	6.2e-03	9.5e-02
2012a	DD	PP	6.2e-03	1.4e-13	3.7e-06	3.4e-04	8.7e-04	3.4e-04	5.0e-03	5.9e-04	0.0e+00	2.4e-03	6.4e-05	1.4e-02	0.0e+00	5.6e-02
2012a	DD	SP	1.9e-02	0.0e+00	1.6e-05	2.8e-04	3.4e-04	4.0e-03	2.2e-02	2.0e-04	2.2e-03	7.9e-05	1.9e-05	4.8e-03	4.1e-04	5.9e-02
2012b	LL	PP	5.8e-03	7.1e-10	1.0e-05	6.8e-04	1.7e-03	7.0e-03	6.8e-03	5.3e-04	0.0e+00	2.1e-03	8.4e-04	5.2e-03	0.0e+00	5.5e-02
2012b	LL	SP	1.9e-02	6.3e-11	3.5e-05	5.3e-06	8.6e-05	8.1e-03	2.9e-02	2.5e-05	0.0e+00	1.5e-03	7.8e-04	1.4e-02	1.0e-02	7.1e-02
2012b	DD	PP	5.9e-03	1.2e-10	3.7e-05	9.6e-04	1.5e-03	2.9e-03	9.6e-03	1.3e-03	0.0e+00	4.0e-03	2.7e-03	1.7e-02	0.0e+00	4.4e-02
2012b	DD	SP	1.2e-02	3.8e-11	3.8e-05	3.7e-04	1.1e-03	8.5e-03	3.5e-03	2.0e-05	0.0e+00	3.3e-04	4.2e-04	1.5e-02	1.3e-02	5.0e-02
2015	LL	PP	6.3e-03	9.5e-11	3.3e-05	2.1e-04	3.0e-04	1.7e-02	2.8e-03	3.6e-04	0.0e+00	1.9e-03	1.8e-03	5.3e-03	0.0e+00	5.6e-02
2015	LL	SP	6.7e-03	6.9e-10	2.8e-05	5.4e-04	9.3e-04	1.6e-02	1.8e-03	2.1e-04	0.0e+00	4.2e-03	1.7e-03	3.1e-03	9.9e-05	6.9e-02
2015	DD	PP	6.1e-03	5.5e-12	8.0e-06	2.3e-04	3.9e-04	2.2e-04	2.7e-03	6.6e-06	0.0e+00	5.7e-03	4.6e-04	2.2e-03	0.0e+00	4.5e-02
2015	DD	SP	7.1e-03	4.9e-10	1.4e-06	3.4e-04	3.3e-04	7.5e-03	4.2e-03	1.3e-04	0.0e+00	2.8e-03	7.9e-04	1.5e-02	3.0e-02	6.3e-02
2016	LL	PP	6.6e-03	0.0e+00	3.4e-05	1.9e-04	1.5e-03	4.2e-03	4.8e-03	9.3e-07	0.0e+00	2.6e-04	4.8e-04	5.1e-03	0.0e+00	3.1e-02
2016	LL	SP	9.7e-03	1.0e-10	2.6e-05	2.4e-04	1.2e-03	1.1e-02	9.7e-03	3.8e-06	0.0e+00	2.2e-05	3.8e-05	7.2e-03	7.7e-03	3.6e-02
2016	DD	PP	6.1e-03	0.0e+00	1.8e-06	1.3e-04	1.2e-03	4.6e-03	1.4e-02	4.7e-05	0.0e+00	2.0e-03	1.6e-03	2.8e-03	0.0e+00	3.3e-02
2016	DD	SP	1.0e-02	7.1e-11	1.5e-05	6.2e-05	1.3e-03	1.4e-02	1.4e-02	7.0e-06	0.0e+00	1.8e-04	1.9e-04	1.6e-02	1.4e-02	4.3e-02
2017	LL	PP	6.5e-03	2.8e-11	9.3e-06	1.9e-04	2.4e-03	1.3e-02	3.4e-04	8.6e-05	0.0e+00	6.5e-03	6.6e-04	9.6e-04	0.0e+00	3.3e-02
2017	LL	SP	9.7e-03	7.7e-11	6.1e-06	2.8e-04	1.5e-03	1.7e-02	1.2e-02	1.8e-05	0.0e+00	4.0e-04	1.0e-03	1.1e-02	8.5e-03	3.9e-02
2017	DD	PP	6.6e-03	5.8e-11	8.3e-06	2.6e-04	2.8e-03	4.6e-04	4.8e-03	5.9e-05	0.0e+00	1.1e-02	1.7e-03	1.6e-03	0.0e+00	3.0e-02
2017	DD	SP	9.3e-03	4.5e-11	3.4e-06	5.2e-04	1.4e-03	9.2e-03	2.4e-03	3.4e-05	0.0e+00	3.3e-04	1.2e-04	1.3e-02	1.0e-02	3.3e-02
2018	LL	PP	7.1e-03	2.1e-10	7.1e-06	1.3e-04	1.5e-03	5.4e-03	6.1e-03	1.3e-04	0.0e+00	5.2e-03	1.1e-03	4.6e-04	0.0e+00	3.2e-02
2018	LL	SP	8.4e-03	4.3e-13	6.4e-06	4.6e-04	8.5e-04	7.4e-03	5.0e-03	3.7e-06	0.0e+00	2.4e-03	5.3e-04	7.9e-03	3.5e-04	3.5e-02
2018	DD	PP	6.0e-03	1.3e-10	7.6e-06	4.2e-06	2.7e-04	1.1e-03	6.5e-03	9.7e-06	0.0e+00	7.6e-03	5.2e-03	1.1e-03	0.0e+00	2.8e-02
2018	DD	SP	8.8e-03	1.9e-11	1.0e-05	3.8e-04	1.1e-03	1.5e-02	1.1e-02	5.9e-07	0.0e+00	2.8e-03	1.1e-04	2.1e-03	1.3e-03	3.6e-02

Table C.36: Systematics uncertainties from the fit process for decay $B^0 \to K^0_S K^+ K^-$. PP stands for PrincipalPeak optimisation and SP for SecondaryPeak optimisation.

Year	KS	Selection	GlobalAddRadPart	GlobalSmallFixed	GlobalSmallNotFixed	SignalFreeDeltaM	SignalHypatia2	CombExp	CombFit	CombNoKpipiKBinding	CombNoForcePos	PartUseCharm	PartUseAll	CFFreeAll	CFFreeSmall	Total
2011	LL	PP	6.3e-04	0.0e+00	4.6e-06	6.7e-04	9.0e-04	2.4e-03	2.9e-03	3.3e-03	0.0e+00	9.7e-03	1.0e-03	2.4e-03	0.0e+00	2.5e-02
2011	LL	SP	2.1e-03	0.0e+00	3.5e-05	3.3e-04	4.2e-05	1.5e-03	5.6e-04	1.4e-03	0.0e+00	2.7e-03	8.5e-04	4.4e-03	1.2e-02	2.5e-02
2011	DD	PP	1.2e-03	0.0e+00	8.5e-06	5.2e-04	6.9e-04	7.9e-03	1.2e-02	2.3e-03	0.0e+00	8.4e-04	1.7e-03	7.1e-05	0.0e+00	2.2e-02
2011	DD	SP	7.0e-03	0.0e+00	6.1e-06	5.8e-04	1.4e-04	7.0e-03	9.4e-03	3.3e-04	0.0e+00	3.0e-03	2.7e-04	6.5e-03	3.0e-03	2.5e-02
2012a	LL	PP	1.2e-03	2.5e-13	1.9e-06	1.3e-04	6.1e-04	7.1e-03	1.3e-02	1.2e-03	0.0e+00	4.3e-04	3.4e-04	1.6e-03	0.0e+00	2.7e-02
2012a	LL	SP	1.3e-03	0.0e+00	5.2e-06	5.5e-05	2.3e-03	1.1e-02	3.5e-03	5.9e-03	1.0e-04	1.2e-03	1.5e-03	3.3e-02	3.5e-02	6.3e-02
2012a	DD	PP	2.3e-03	3.5e-13	7.3e-06	6.1e-05	5.3e-04	8.6e-03	1.2e-02	7.0e-03	0.0e+00	3.1e-04	1.2e-04	7.7e-04	0.0e+00	2.3e-02
2012a	DD	SP	1.0e-03	0.0e+00	3.5e-06	4.5e-05	4.0e-04	4.1e-03	5.9e-03	5.8e-03	1.5e-05	1.5e-04	6.4e-05	2.4e-04	9.1e-04	1.6e-02
2012b	LL	PP	2.4e-03	7.2e-11	6.4e-05	8.5e-04	4.9e-04	7.3e-03	6.9e-03	2.5e-03	0.0e+00	5.8e-04	1.1e-05	3.3e-03	0.0e+00	2.3e-02
2012b	LL	SP	2.2e-03	8.7e-13	1.4e-06	1.4e-03	3.8e-04	5.8e-03	3.2e-04	5.1e-03	0.0e+00	1.6e-03	2.0e-03	3.2e-03	1.5e-03	2.5e-02
2012b	DD	PP	1.2e-03	5.4e-12	3.5e-06	1.2e-03	6.7e-04	1.5e-03	5.3e-03	5.6e-03	0.0e+00	5.3e-04	5.8e-04	9.2e-04	0.0e+00	1.4e-02
2012b	DD	SP	6.3e-04	3.1e-12	5.6e-06	4.2e-04	1.8e-05	5.2e-03	1.6e-02	2.1e-03	0.0e+00	4.4e-04	5.5e-04	4.4e-03	4.8e-03	2.2e-02
2015	LL	PP	5.8e-04	2.2e-12	9.3e-06	2.1e-04	3.8e-04	1.2e-03	6.9e-03	1.0e-02	0.0e+00	5.9e-05	2.4e-04	1.8e-03	0.0e+00	2.5e-02
2015	LL	SP	7.3e-04	2.2e-12	6.7e-07	2.1e-04	3.5e-04	3.9e-03	2.7e-03	1.6e-02	0.0e+00	9.1e-03	1.4e-03	8.3e-03	1.0e-02	3.1e-02
2015	DD	PP	1.1e-04	1.5e-12	7.2e-06	1.7e-04	2.9e-04	1.0e-03	4.1e-03	1.6e-03	0.0e+00	9.4e-05	3.4e-04	2.0e-03	0.0e+00	1.8e-02
2015	DD	SP	6.5e-04	9.3e-12	1.3e-05	5.0e-05	3.6e-05	5.1e-03	1.2e-02	4.1e-03	0.0e+00	1.9e-02	8.0e-04	9.4e-03	6.1e-03	3.1e-02
2016	LL	PP	5.9e-04	0.0e+00	3.7e-05	1.9e-04	4.4e-04	4.3e-03	9.1e-03	7.0e-04	0.0e+00	2.8e-04	1.9e-05	7.0e-05	0.0e+00	1.4e-02
2016	LL	SP	1.1e-03	7.4e-11	4.2e-05	4.8e-05	3.9e-04	7.6e-03	9.8e-03	2.0e-03	0.0e+00	2.4e-05	2.4e-05	1.8e-03	1.1e-03	1.6e-02
2016	DD	PP	1.1e-03	0.0e+00	3.1e-06	1.2e-05	5.3e-04	3.4e-03	1.4e-02	7.9e-04	0.0e+00	2.1e-04	2.0e-04	7.2e-04	0.0e+00	1.6e-02
2016	DD	SP	6.1e-04	8.3e-12	6.5e-06	2.7e-05	4.7e-04	3.4e-03	1.2e-02	1.4e-03	0.0e+00	6.1e-05	6.0e-05	1.1e-03	1.2e-03	1.4e-02
2017	LL	PP	2.4e-04	7.5e-11	1.6e-05	2.2e-04	2.2e-04	3.0e-03	6.9e-03	1.5e-03	0.0e+00	4.4e-03	1.0e-03	2.1e-04	0.0e+00	1.2e-02
2017	LL	SP	8.1e-04	1.6e-11	1.3e-06	2.0e-04	2.0e-04	2.5e-03	6.2e-03	2.0e-03	0.0e+00	3.0e-03	3.4e-05	1.0e-03	2.0e-03	1.1e-02
2017	DD	PP	2.9e-04	4.6e-12	8.8e-07	2.0e-04	2.1e-04	2.3e-03	8.1e-03	1.0e-03	0.0e+00	1.4e-03	4.3e-06	8.8e-04	0.0e+00	1.1e-02
2017	DD	SP	8.4e-04	2.8e-11	2.0e-06	1.7e-04	2.5e-05	1.5e-03	6.0e-03	3.0e-03	0.0e+00	2.8e-03	8.8e-05	1.3e-04	6.1e-04	9.5e-03
2018	LL	PP	2.1e-04	8.6e-11	4.7e-06	2.3e-04	5.6e-04	1.8e-03	7.1e-03	1.2e-03	0.0e+00	8.9e-04	5.2e-06	4.4e-04	0.0e+00	1.1e-02
2018	LL	SP	7.1e-04	3.3e-12	4.9e-06	1.1e-04	6.0e-04	2.9e-03	8.4e-03	1.4e-03	0.0e+00	9.3e-04	6.3e-05	4.0e-03	4.2e-03	1.4e-02
2018	DD	PP	3.3e-04	4.8e-11	2.7e-06	1.9e-04	2.9e-04	3.1e-03	8.2e-03	8.0e-04	0.0e+00	6.3e-04	9.4e-04	3.1e-04	0.0e+00	1.1e-02
2018	DD	SP	7.1e-04	1.2e-12	2.3e-06	2.6e-05	4.7e-04	2.8e-03	6.0e-03	1.3e-03	0.0e+00	1.4e-03	5.0e-06	3.1e-03	2.6e-03	9.8e-03

Table C.37: Systematics uncertainties from the fit process for decay $B^0 \to K^0_S \pi^+ K^-$. PP stands for PrincipalPeak optimisation and SP for SecondaryPeak optimisation.

Year	KS	Selection	GlobalAddRadPart	GlobalSmallFixed	GlobalSmallNotFixed	SignalFreeDeltaM	SignalHypatia2	CombExp	CombFit	CombNoKpipiKBinding	CombNoForcePos	PartUseCharm	PartUseAll	CFFreeAll	CFFreeSmall	Total
2011	LL	PP	6.0e-04	0.0e+00	5.7e-06	6.3e-04	1.4e-03	3.5e-03	3.6e-03	2.2e-03	0.0e+00	1.6e-03	7.0e-04	1.4e-03	0.0e+00	2.1e-02
2011	LL	SP	1.7e-03	0.0e+00	2.4e-05	2.6e-04	7.5e-04	1.2e-03	5.4e-04	1.0e-03	0.0e+00	2.7e-03	7.1e-04	6.7e-03	9.0e-03	2.3e-02
2011	DD	PP	9.5e-04	0.0e+00	1.1e-05	4.8e-04	2.8e-04	6.2e-03	9.6e-03	2.1e-03	0.0e+00	3.6e-03	1.7e-03	3.9e-05	0.0e+00	1.9e-02
2011	DD	SP	5.2e-03	0.0e+00	2.8e-05	3.2e-04	4.7e-04	7.8e-03	1.1e-02	3.0e-04	0.0e+00	3.5e-03	2.9e-04	1.4e-02	1.2e-02	2.9e-02
2012a	LL	PP	2.1e-04	4.5e-12	2.9e-05	8.0e-04	5.4e-04	1.7e-03	4.9e-03	1.5e-03	0.0e+00	6.2e-04	9.3e-05	8.9e-04	0.0e+00	2.6e-02
2012a	LL	SP	1.1e-03	0.0e+00	4.8e-06	1.4e-04	7.5e-04	8.8e-03	2.1e-03	3.9e-03	5.1e-05	1.1e-03	1.4e-03	4.4e-03	4.9e-03	3.5e-02
2012a	DD	PP	2.1e-03	9.0e-13	6.2e-06	1.6e-04	1.8e-04	5.9e-03	7.8e-03	7.9e-03	0.0e+00	9.5e-05	3.2e-05	3.0e-04	0.0e+00	2.0e-02
2012a	DD	SP	3.1e-03	0.0e+00	4.7e-06	1.6e-04	3.9e-04	3.2e-03	2.8e-03	7.6e-03	3.6e-05	3.1e-05	1.5e-04	1.0e-02	8.2e-03	2.5e-02
2012b	LL	PP	2.4e-03	1.4e-10	8.0e-05	3.0e-04	1.6e-04	7.8e-03	7.5e-03	2.7e-03	0.0e+00	1.4e-04	1.7e-05	3.2e-03	0.0e+00	2.0e-02
2012b	LL	SP	6.9e-04	2.8e-12	7.3e-06	1.0e-03	1.4e-04	5.3e-03	2.2e-03	5.6e-03	0.0e+00	1.5e-03	2.0e-03	8.3e-04	2.3e-03	1.9e-02
2012b	DD	PP	1.3e-03	1.0e-10	3.3e-05	8.0e-04	7.8e-04	1.6e-03	5.5e-03	5.7e-03	0.0e+00	2.1e-04	9.6e-04	7.0e-04	0.0e+00	1.4e-02
2012b	DD	SP	9.3e-04	4.0e-12	8.3e-06	2.0e-04	2.5e-04	1.6e-03	5.7e-03	2.5e-03	0.0e+00	6.0e-05	1.7e-04	2.5e-04	8.5e-04	1.2e-02
2015	LL	PP	4.9e-05	2.2e-12	3.5e-06	6.6e-05	2.0e-04	5.3e-03	1.4e-02	1.0e-02	0.0e+00	5.5e-04	8.9e-04	3.2e-04	0.0e+00	3.0e-02
2015	LL	SP	7.7e-04	5.3e-13	4.2e-06	2.3e-04	3.5e-04	1.1e-02	8.0e-03	9.4e-03	0.0e+00	1.6e-02	2.5e-03	1.2e-03	1.7e-03	3.6e-02
2015	DD	PP	2.0e-04	1.6e-13	1.9e-06	2.7e-04	1.7e-04	6.4e-04	2.1e-03	1.7e-03	0.0e+00	6.9e-05	2.8e-04	1.3e-03	0.0e+00	1.7e-02
2015	DD	SP	1.2e-03	4.1e-12	6.0e-06	2.4e-04	6.5e-05	2.4e-03	7.2e-03	4.4e-03	0.0e+00	1.3e-02	8.3e-04	2.2e-03	4.5e-03	2.4e-02
2016	LL	PP	6.5e-04	0.0e+00	3.4e-05	1.1e-04	4.1e-04	4.8e-03	9.7e-03	6.7e-04	0.0e+00	1.7e-04	1.2e-04	3.8e-04	0.0e+00	1.4e-02
2016	LL	SP	6.5e-04	5.0e-11	3.2e-05	1.0e-05	5.8e-04	7.5e-03	9.8e-03	1.7e-03	0.0e+00	1.3e-05	1.9e-05	3.7e-03	3.7e-03	1.6e-02
2016	DD	PP	8.9e-04	0.0e+00	2.5e-06	9.2e-05	5.3e-04	2.8e-03	1.2e-02	8.6e-04	0.0e+00	2.0e-04	2.6e-04	7.4e-04	0.0e+00	1.4e-02
2016	DD	SP	7.3e-04	1.5e-11	8.8e-06	3.3e-05	3.7e-04	2.4e-03	9.2e-03	1.5e-03	0.0e+00	3.0e-05	3.0e-05	3.7e-04	8.7e-05	1.2e-02
2017	LL	PP	3.4e-04	1.8e-11	3.5e-06	2.2e-04	7.0e-05	3.5e-03	7.6e-03	1.5e-03	0.0e+00	3.5e-03	4.4e-04	7.7e-05	0.0e+00	1.3e-02
2017	LL	SP	7.5e-04	1.9e-11	1.5e-06	1.1e-04	2.6e-04	2.6e-03	6.3e-03	2.1e-03	0.0e+00	2.7e-03	2.8e-05	4.6e-03	4.8e-03	1.3e-02
2017	DD	PP	3.1e-04	3.8e-11	6.0e-06	1.6e-04	2.2e-04	2.7e-03	9.3e-03	9.4e-04	0.0e+00	3.2e-03	3.1e-04	2.1e-04	0.0e+00	1.2e-02
2017	DD	SP	6.2e-04	2.6e-11	1.9e-06	3.7e-05	2.0e-06	3.3e-03	1.1e-02	2.3e-03	0.0e+00	5.9e-03	2.8e-04	2.1e-03	2.4e-03	1.5e-02
2018	LL	PP	9.5e-07	5.5e-11	3.4e-06	3.4e-04	3.8e-04	1.5e-03	6.4e-03	1.2e-03	0.0e+00	1.3e-03	9.6e-05	9.2e-04	0.0e+00	1.1e-02
2018	LL	SP	6.9e-04	2.2e-12	5.1e-06	6.2e-05	5.2e-04	2.7e-03	8.0e-03	1.4e-03	0.0e+00	1.1e-03	1.9e-04	5.9e-04	1.3e-06	1.2e-02
2018	DD	PP	3.5e-04	6.3e-11	3.9e-06	1.1e-04	2.7e-04	3.4e-03	8.9e-03	7.8e-04	0.0e+00	1.1e-03	9.9e-04	4.0e-05	0.0e+00	1.1e-02
2018	DD	SP	7.1e-04	6.2e-13	2.9e-06	2.1e-05	4.8e-04	2.8e-03	6.0e-03	1.3e-03	0.0e+00	1.5e-03	2.4e-05	1.3e-03	2.0e-03	9.2e-03

Table C.38: Systematics uncertainties from the fit process for decay $B^0 \to K^0_S K^+ \pi^-$. PP stands for PrincipalPeak optimisation and SP for SecondaryPeak optimisation.

Year	KS	Selection	GlobalAddRadPart	GlobalSmallFixed	GlobalSmallNotFixed	SignalFreeDeltaM	SignalHypatia2	CombExp	CombFit	CombNoKpipiKBinding	CombNoForcePos	PartUseCharm	PartUseAll	CFFreeAll	CFFreeSmall	Total
2011	LL	PP	5.0e-03	0.0e+00	3.0e-05	5.0e-03	4.7e-03	2.1e-02	5.9e-02	2.4e-04	0.0e+00	4.8e-02	4.9e-04	1.6e-03	0.0e+00	1.2e-01
2011	LL	SP	2.8e-02	0.0e+00	1.9e-05	1.0e-03	7.8e-03	2.2e-02	7.5e-02	3.7e-05	0.0e+00	3.4e-02	6.8e-04	1.0e-02	4.4e-02	1.3e-01
2011	DD	PP	8.8e-03	0.0e+00	1.2e-05	1.2e-03	7.4e-03	2.4e-02	9.9e-02	2.9e-04	0.0e+00	1.3e-02	2.5e-03	2.1e-02	0.0e+00	1.3e-01
2011	DD	SP	7.6e-02	0.0e+00	9.2e-08	4.2e-03	2.1e-04	3.5e-04	6.1e-02	1.3e-05	0.0e+00	7.8e-03	2.8e-04	1.3e-02	4.7e-03	1.3e-01
2012a	LL	PP	6.5e-03	8.4e-12	3.8e-05	2.5e-03	6.7e-03	1.8e-02	6.0e-02	3.8e-04	0.0e+00	6.8e-03	4.0e-04	1.7e-04	0.0e+00	1.4e-01
2012a	LL	SP	9.7e-03	0.0e+00	1.9e-06	4.4e-05	3.0e-03	1.6e-03	7.7e-03	1.6e-04	7.4e-05	9.1e-04	7.7e-04	8.1e-03	1.1e-03	1.6e-01
2012a	DD	PP	3.3e-02	3.2e-12	1.9e-05	1.5e-04	9.3e-03	2.4e-02	9.0e-02	3.2e-04	0.0e+00	4.1e-03	1.9e-04	4.1e-03	0.0e+00	1.3e-01
2012a	DD	SP	7.7e-02	0.0e+00	3.3e-05	1.7e-03	5.2e-03	5.0e-03	7.4e-02	4.5e-04	4.4e-05	5.9e-04	1.3e-04	3.0e-03	1.4e-03	1.3e-01
2012b	LL	PP	1.1e-02	3.4e-10	1.0e-04	1.3e-02	3.6e-03	2.5e-02	5.7e-02	2.2e-04	0.0e+00	4.1e-03	4.7e-04	1.8e-02	0.0e+00	1.1e-01
2012b	LL	SP	5.3e-02	1.7e-11	3.5e-05	7.3e-03	9.6e-05	8.6e-03	8.5e-02	5.6e-05	0.0e+00	1.7e-04	6.8e-04	1.1e-02	1.9e-02	1.3e-01
2012b	DD	PP	1.3e-02	2.4e-10	7.2e-05	1.0e-02	9.3e-03	1.3e-02	9.7e-02	1.4e-04	0.0e+00	1.6e-04	1.1e-03	1.3e-02	0.0e+00	1.2e-01
2012b	DD	SP	4.9e-02	4.1e-11	8.5e-05	4.2e-03	5.1e-03	2.0e-02	3.9e-02	5.4e-05	0.0e+00	5.2e-03	1.5e-03	1.3e-02	1.0e-02	9.1e-02
2015	LL	PP	6.2e-03	1.9e-11	8.3e-05	3.2e-03	1.2e-02	3.0e-02	6.8e-02	2.9e-05	0.0e+00	8.9e-04	2.6e-03	1.7e-03	0.0e+00	1.3e-01
2015	LL	SP	5.3e-03	1.1e-11	1.5e-05	2.5e-03	3.1e-03	2.1e-02	3.8e-02	1.4e-04	0.0e+00	7.6e-02	1.8e-03	1.7e-04	3.2e-05	1.3e-01
2015	DD	PP	5.5e-03	6.3e-12	1.9e-05	2.2e-04	9.8e-03	1.1e-02	9.1e-02	1.6e-04	0.0e+00	1.7e-02	1.4e-03	7.3e-03	0.0e+00	1.3e-01
2015	DD	SP	6.3e-03	3.9e-11	5.7e-05	3.1e-03	3.0e-03	2.4e-02	2.8e-02	1.9e-04	0.0e+00	8.6e-02	1.2e-03	4.7e-02	4.2e-02	1.4e-01
2016	LL	PP	1.2e-02	0.0e+00	1.8e-05	9.2e-04	1.1e-02	2.1e-02	8.6e-02	4.2e-05	0.0e+00	3.4e-03	5.7e-04	9.4e-03	0.0e+00	1.0e-01
2016	LL	SP	7.3e-03	1.7e-11	5.1e-06	1.8e-04	4.6e-03	2.2e-02	5.1e-02	3.4e-05	0.0e+00	3.0e-04	3.5e-04	1.5e-02	1.3e-02	7.1e-02
2016	DD	PP	1.4e-02	0.0e+00	5.3e-05	2.9e-04	1.2e-02	1.4e-02	9.6e-02	5.5e-05	0.0e+00	2.7e-03	2.0e-03	5.1e-03	0.0e+00	1.1e-01
2016	DD	SP	1.0e-02	1.2e-10	4.4e-05	6.1e-04	5.0e-03	2.8e-02	6.8e-02	6.8e-05	0.0e+00	3.8e-04	1.7e-04	1.8e-02	2.1e-02	8.8e-02
2017	LL	PP	6.4e-03	4.0e-11	6.4e-06	2.1e-03	1.2e-02	2.4e-02	6.8e-02	9.1e-05	0.0e+00	8.1e-03	2.4e-03	3.1e-03	0.0e+00	8.4e-02
2017	LL	SP	1.3e-02	8.8e-11	6.2e-06	1.5e-03	5.1e-03	3.2e-02	4.3e-02	6.3e-05	0.0e+00	4.4e-03	1.5e-03	1.7e-02	1.8e-02	6.9e-02
2017	DD	PP	7.8e-03	7.0e-12	1.2e-06	4.7e-04	1.5e-02	1.0e-02	6.9e-02	5.0e-05	0.0e+00	3.5e-02	1.8e-04	4.2e-03	0.0e+00	8.7e-02
2017	DD	SP	7.6e-03	1.1e-11	8.1e-08	2.8e-04	5.7e-03	1.9e-02	4.2e-02	7.6e-05	0.0e+00	1.5e-02	1.7e-04	1.3e-02	1.6e-02	6.2e-02
2018	LL	PP	7.8e-03	3.2e-10	1.8e-05	1.7e-03	1.0e-02	9.2e-03	5.5e-02	1.8e-05	0.0e+00	1.4e-02	3.8e-05	3.1e-03	0.0e+00	7.2e-02
2018	LL	SP	7.3e-03	1.9e-12	8.8e-06	1.3e-03	5.2e-03	1.6e-02	3.5e-02	2.6e-06	0.0e+00	4.3e-03	9.7e-04	6.9e-03	1.3e-04	5.6e-02
2018	DD	PP	9.5e-03	5.6e-10	3.4e-05	9.5e-04	9.0e-03	1.3e-02	8.7e-02	7.3e-06	0.0e+00	1.0e-02	3.6e-03	7.6e-03	0.0e+00	9.6e-02
2018	DD	SP	7.2e-03	5.6e-13	1.3e-05	6.1e-04	3.9e-03	2.7e-02	6.5e-02	5.2e-06	0.0e+00	7.3e-03	7.5e-05	3.4e-03	1.9e-03	7.7e-02

Table C.39: Systematics uncertainties from the fit process for decay $B_s^0 \to K_S^0\pi^+\pi^-$. PP stands for PrincipalPeak optimisation and SP for SecondaryPeak optimisation.

Year	KS	Selection	GlobalAddRadPart	GlobalSmallFixed	GlobalSmallNotFixed	SignalFreeDeltaM	SignalHypatia2	CombExp	CombFit	CombNoKpipiKBinding	CombNoForcePos	PartUseCharm	PartUseAll	CFFreeAll	CFFreeSmall	Total
2011	LL	PP	1.2e-02	0.0e+00	1.0e-05	1.1e-03	2.9e-03	8.6e-03	6.5e-03	1.7e-02	0.0e+00	2.6e-02	1.6e-03	5.3e-03	0.0e+00	1.5e-01
2011	LL	SP	2.4e-02	0.0e+00	2.6e-04	2.5e-03	3.3e-03	3.4e-02	2.9e-02	5.5e-03	0.0e+00	1.5e-02	2.8e-03	9.0e-02	5.9e-02	2.0e-01
2011	DD	PP	1.3e-02	0.0e+00	7.5e-05	8.6e-04	4.5e-04	8.9e-03	2.3e-02	1.1e-02	0.0e+00	1.8e-04	3.0e-03	4.2e-03	0.0e+00	1.1e-01
2011	DD	SP	7.0e-02	0.0e+00	2.1e-05	2.8e-03	2.1e-03	7.9e-03	1.9e-02	1.2e-03	0.0e+00	1.5e-02	1.2e-03	5.7e-03	6.8e-04	1.4e-01
2012a	LL	PP	6.5e-03	5.8e-12	5.1e-05	4.0e-04	2.9e-04	1.5e-03	3.0e-02	5.4e-03	0.0e+00	2.3e-03	1.6e-03	1.3e-02	0.0e+00	1.5e-01
2012a	LL	SP	1.3e-02	0.0e+00	1.5e-05	3.6e-03	3.6e-03	3.0e-02	1.5e-02	1.9e-02	2.4e-04	3.2e-03	5.0e-03	8.5e-02	8.3e-02	2.6e-01
2012a	DD	PP	9.4e-03	1.1e-11	6.2e-05	1.1e-03	2.0e-03	2.4e-03	2.7e-02	2.9e-02	0.0e+00	1.2e-03	8.0e-04	3.3e-03	0.0e+00	1.2e-01
2012a	DD	SP	3.4e-02	0.0e+00	3.4e-05	1.1e-03	4.9e-04	4.4e-03	5.6e-04	2.5e-02	2.7e-04	7.0e-04	3.4e-04	7.7e-03	3.1e-03	1.2e-01
2012b	LL	PP	9.3e-03	1.2e-09	3.1e-04	4.1e-03	4.0e-04	2.1e-03	2.1e-02	1.2e-02	0.0e+00	2.1e-03	4.0e-04	4.2e-03	0.0e+00	1.3e-01
2012b	LL	SP	3.0e-02	1.2e-11	2.0e-05	1.0e-03	3.1e-04	6.5e-03	2.1e-02	2.1e-02	0.0e+00	1.3e-03	5.7e-03	3.1e-02	9.9e-03	1.6e-01
2012b	DD	PP	1.1e-02	1.9e-10	6.9e-05	5.4e-03	1.3e-03	7.2e-03	3.8e-03	2.7e-02	0.0e+00	1.8e-03	9.9e-04	1.9e-02	0.0e+00	9.3e-02
2012b	DD	SP	1.9e-02	2.2e-11	4.0e-05	9.7e-03	1.8e-03	1.8e-03	5.4e-02	8.4e-03	0.0e+00	1.3e-03	1.3e-03	2.5e-02	1.8e-02	1.1e-01
2015	LL	PP	8.7e-03	6.5e-12	2.8e-05	1.0e-03	7.5e-04	2.3e-02	4.8e-03	3.9e-02	0.0e+00	1.5e-03	2.1e-03	6.1e-03	0.0e+00	1.3e-01
2015	LL	SP	1.1e-02	2.4e-11	2.0e-05	2.0e-03	4.1e-04	7.7e-03	3.9e-04	6.2e-02	0.0e+00	4.6e-02	3.3e-03	4.8e-02	4.6e-02	1.9e-01
2015	DD	PP	1.1e-02	6.8e-12	1.5e-05	1.7e-04	1.6e-03	1.5e-03	1.1e-02	5.8e-03	0.0e+00	1.4e-03	5.6e-04	1.3e-02	0.0e+00	1.1e-01
2015	DD	SP	1.2e-02	1.3e-11	2.3e-05	1.1e-03	1.3e-03	4.1e-03	3.9e-02	1.6e-02	0.0e+00	7.8e-02	3.5e-03	1.5e-02	1.1e-02	1.5e-01
2016	LL	PP	1.2e-02	0.0e+00	9.9e-05	1.0e-03	3.0e-03	1.5e-02	1.9e-03	2.3e-03	0.0e+00	2.0e-03	1.9e-04	4.3e-03	0.0e+00	7.3e-02
2016	LL	SP	1.6e-02	1.3e-10	1.2e-04	3.9e-04	1.9e-03	4.2e-03	1.9e-02	6.9e-03	0.0e+00	4.6e-04	5.1e-04	1.5e-03	1.4e-03	7.7e-02
2016	DD	PP	9.0e-03	0.0e+00	9.2e-05	1.3e-03	1.4e-03	3.7e-03	2.0e-02	2.6e-03	0.0e+00	2.5e-03	5.4e-04	9.9e-04	0.0e+00	5.6e-02
2016	DD	SP	1.4e-02	5.6e-11	5.6e-05	4.7e-04	8.3e-04	1.1e-02	2.0e-02	4.9e-03	0.0e+00	6.6e-04	4.0e-04	3.2e-03	5.2e-03	6.1e-02
2017	LL	PP	1.0e-02	2.6e-10	2.7e-05	5.7e-04	2.6e-04	1.4e-02	5.0e-03	5.5e-03	0.0e+00	2.2e-02	1.1e-03	2.3e-03	0.0e+00	6.9e-02
2017	LL	SP	1.4e-02	6.1e-11	4.0e-06	7.7e-04	1.2e-03	1.8e-02	8.5e-03	7.1e-03	0.0e+00	1.5e-02	1.1e-03	2.4e-02	1.5e-02	7.6e-02
2017	DD	PP	9.9e-03	4.8e-11	2.9e-06	1.3e-03	7.9e-04	2.2e-03	9.3e-03	3.7e-03	0.0e+00	8.8e-03	1.4e-03	1.8e-03	0.0e+00	5.2e-02
2017	DD	SP	1.4e-02	2.9e-10	2.2e-05	1.0e-03	9.6e-04	9.3e-03	7.6e-03	1.1e-02	0.0e+00	1.3e-02	1.2e-03	1.5e-02	8.8e-03	6.0e-02
2018	LL	PP	1.0e-02	1.9e-10	1.2e-05	1.3e-03	2.6e-03	2.9e-03	1.1e-02	4.8e-03	0.0e+00	6.3e-03	8.4e-04	1.4e-03	0.0e+00	6.7e-02
2018	LL	SP	1.3e-02	5.7e-13	1.3e-06	6.0e-04	5.2e-03	2.1e-03	2.3e-02	5.2e-03	0.0e+00	4.2e-04	1.9e-03	7.7e-03	1.9e-02	7.9e-02
2018	DD	PP	9.4e-03	2.2e-11	9.7e-07	1.2e-03	7.0e-05	1.3e-03	4.1e-03	3.0e-03	0.0e+00	2.8e-03	8.5e-04	6.5e-03	0.0e+00	5.0e-02
2018	DD	SP	1.3e-02	8.7e-12	1.5e-05	1.2e-03	2.9e-03	1.1e-02	3.6e-03	5.0e-03	0.0e+00	2.1e-03	1.2e-04	1.6e-02	1.6e-02	5.9e-02

Table C.40: Systematics uncertainties from the fit process for decay $B_s^0 \to K_S^0 \pi^+ K^-$. PP stands for PrincipalPeak optimisation and SP for SecondaryPeak optimisation.

Year	KS	Selection	GlobalAddRadPart	GlobalSmallFixed	GlobalSmallNotFixed	SignalFreeDeltaM	SignalHypatia2	CombExp	CombFit	CombNoKpipiKBinding	CombNoForcePos	PartUseCharm	PartUseAll	CFFreeAll	CFFreeSmall	Total
2011	LL	PP	9.0e-03	0.0e+00	1.1e-06	3.4e-03	5.4e-03	2.6e-03	5.1e-03	1.1e-02	0.0e+00	7.2e-03	2.5e-03	1.0e-02	0.0e+00	1.4e-01
2011	LL	SP	2.2e-02	0.0e+00	9.1e-05	2.5e-03	1.1e-03	3.1e-02	2.5e-02	5.0e-03	0.0e+00	1.7e-02	4.0e-03	9.5e-02	5.6e-02	2.1e-01
2011	DD	PP	1.3e-02	0.0e+00	3.8e-05	4.2e-04	1.7e-03	8.8e-03	2.4e-02	1.2e-02	0.0e+00	1.4e-02	5.0e-03	8.5e-03	0.0e+00	1.1e-01
2011	DD	SP	7.7e-02	0.0e+00	1.3e-04	2.6e-03	6.5e-04	1.3e-02	3.0e-02	1.3e-03	0.0e+00	2.0e-02	1.6e-03	2.5e-02	2.8e-02	1.6e-01
2012a	LL	PP	5.2e-03	7.0e-13	3.6e-05	3.9e-03	1.1e-03	4.7e-03	1.1e-02	6.8e-03	0.0e+00	4.8e-03	6.8e-04	1.6e-02	0.0e+00	1.5e-01
2012a	LL	SP	1.2e-02	0.0e+00	2.0e-05	3.0e-03	3.3e-03	3.1e-02	1.4e-02	1.6e-02	3.9e-04	5.8e-03	6.5e-03	6.7e-03	1.3e-02	2.3e-01
2012a	DD	PP	8.9e-03	1.2e-11	8.1e-05	7.4e-04	2.7e-03	7.3e-04	2.1e-02	3.9e-02	0.0e+00	4.0e-04	4.0e-04	4.6e-03	0.0e+00	1.2e-01
2012a	DD	SP	3.7e-02	0.0e+00	3.7e-05	5.9e-04	2.9e-04	2.5e-03	8.6e-03	3.1e-02	2.2e-04	3.5e-05	3.5e-04	2.4e-02	3.1e-02	1.4e-01
2012b	LL	PP	7.8e-03	1.2e-09	3.4e-04	3.3e-03	1.7e-03	3.8e-03	2.4e-02	1.4e-02	0.0e+00	4.8e-04	4.5e-04	1.6e-02	0.0e+00	1.4e-01
2012b	LL	SP	1.9e-02	1.4e-11	3.2e-05	2.1e-04	6.1e-04	3.1e-03	1.0e-02	2.0e-02	0.0e+00	5.7e-03	7.4e-03	3.2e-02	1.9e-02	1.3e-01
2012b	DD	PP	1.1e-02	5.7e-10	2.0e-04	3.4e-03	2.1e-03	7.5e-03	2.7e-03	3.0e-02	0.0e+00	4.5e-05	2.3e-03	2.3e-04	0.0e+00	9.7e-02
2012b	DD	SP	2.1e-02	2.5e-11	5.3e-05	5.3e-03	2.0e-03	1.0e-02	1.4e-02	1.2e-02	0.0e+00	3.9e-03	2.7e-03	8.9e-03	5.6e-03	1.0e-01
2015	LL	PP	8.5e-03	9.7e-12	3.0e-05	1.3e-04	6.1e-04	1.9e-02	2.2e-02	3.5e-02	0.0e+00	3.7e-03	4.9e-03	5.3e-03	0.0e+00	1.4e-01
2015	LL	SP	1.0e-02	2.1e-11	1.7e-05	3.8e-03	8.8e-04	7.4e-03	1.5e-02	3.0e-02	0.0e+00	5.4e-02	6.9e-03	1.1e-02	6.5e-03	1.7e-01
2015	DD	PP	9.3e-03	4.6e-13	9.1e-06	2.3e-03	2.5e-03	1.5e-03	1.2e-02	6.2e-03	0.0e+00	6.0e-04	1.6e-06	9.7e-03	0.0e+00	9.8e-02
2015	DD	SP	1.1e-02	7.9e-12	1.6e-05	2.3e-03	1.6e-03	3.0e-03	1.9e-02	1.6e-02	0.0e+00	5.6e-02	2.6e-03	2.3e-02	2.8e-02	1.3e-01
2016	LL	PP	9.0e-03	0.0e+00	9.1e-05	2.0e-03	2.5e-03	1.0e-02	1.0e-02	2.3e-03	0.0e+00	1.3e-03	7.1e-04	5.9e-04	0.0e+00	6.4e-02
2016	LL	SP	1.3e-02	6.4e-11	7.9e-05	1.3e-03	3.6e-04	2.1e-04	2.3e-02	6.4e-03	0.0e+00	3.0e-04	3.2e-04	2.3e-02	2.2e-02	7.9e-02
2016	DD	PP	9.4e-03	0.0e+00	6.1e-05	5.2e-04	2.1e-03	4.4e-03	1.5e-02	2.8e-03	0.0e+00	2.0e-03	1.4e-03	3.2e-03	0.0e+00	5.4e-02
2016	DD	SP	1.3e-02	3.1e-11	3.7e-05	4.3e-04	6.6e-04	1.2e-02	1.3e-02	5.3e-03	0.0e+00	4.9e-04	2.7e-04	4.3e-03	2.6e-03	5.8e-02
2017	LL	PP	9.7e-03	4.8e-11	2.0e-05	1.0e-03	3.8e-05	1.4e-02	9.0e-03	5.9e-03	0.0e+00	1.8e-02	2.1e-03	2.0e-03	0.0e+00	7.3e-02
2017	LL	SP	1.4e-02	2.5e-10	2.0e-05	1.5e-03	1.3e-03	1.8e-02	1.0e-02	8.0e-03	0.0e+00	1.4e-02	1.1e-03	1.3e-02	1.6e-02	7.9e-02
2017	DD	PP	9.7e-03	2.8e-10	3.5e-05	1.0e-03	6.7e-04	1.4e-03	1.5e-02	3.4e-03	0.0e+00	1.8e-02	9.4e-04	7.2e-03	0.0e+00	5.6e-02
2017	DD	SP	1.2e-02	6.9e-11	4.8e-06	2.0e-03	4.9e-04	4.4e-03	2.7e-02	8.2e-03	0.0e+00	2.6e-02	8.8e-04	4.3e-03	5.7e-03	6.7e-02
2018	LL	PP	1.1e-02	3.7e-11	1.7e-06	1.3e-03	3.1e-04	3.4e-03	8.3e-03	4.8e-03	0.0e+00	8.1e-03	1.8e-04	8.8e-03	0.0e+00	7.1e-02
2018	LL	SP	1.2e-02	8.0e-12	1.9e-08	1.0e-03	3.1e-03	2.3e-03	2.2e-02	5.2e-03	0.0e+00	1.3e-03	1.5e-03	1.0e-03	1.8e-03	7.9e-02
2018	DD	PP	8.7e-03	3.9e-10	2.2e-05	5.8e-04	5.0e-04	3.3e-04	8.0e-03	2.8e-03	0.0e+00	6.5e-04	1.0e-03	5.5e-03	0.0e+00	4.7e-02
2018	DD	SP	1.2e-02	3.2e-12	1.4e-05	1.1e-03	3.0e-03	1.0e-02	5.4e-03	4.7e-03	0.0e+00	2.8e-03	1.5e-04	1.8e-02	1.3e-02	5.7e-02

Table C.41: Systematics uncertainties from the fit process for decay $B_s^0 \to K_S^0 K^+ \pi^-$. PP stands for PrincipalPeak optimisation and SP for SecondaryPeak optimisation.

C.7 Detailed efficiency tables before magnet combination with systematics

Year	Mode	K^0_S	Polarity	Optimisation	$\bar{\varepsilon}$	$\sigma^{\text{stat}}_{\bar{\varepsilon}}$	$\sigma^{\text{tracking}}_{\bar{\varepsilon}}$	$\sigma^{\text{L0corr}}_{\bar{\varepsilon}}$	$\sigma^{\text{PIDMCsampling}}_{\bar{\varepsilon}}$	$\sigma^{\text{PIDkernel}}_{\bar{\varepsilon}}$	$\sigma^{\text{RMS}}_{\bar{\varepsilon}}$	$\sigma_{\bar{\varepsilon}}$
2018	$B^0_d \to K^0_S\pi^+\pi^-$	DD	MD	PP	83247.2e-8	870.8e-8	4.9e-8	128.0e-8	42.9e-8	274.6e-8	1219.8e-8	1529.7e-8
2018	$B^0_d \to K^0_S\pi^+\pi^-$	DD	MU	PP	81034.7e-8	878.5e-8	4.9e-8	110.4e-8	42.8e-8	267.3e-8	1219.8e-8	1531.4e-8
2018	$B^0_d \to K^0_S\pi^+\pi^-$	DD	MD	SP	41708.3e-8	574.7e-8	2.5e-8	67.5e-8	21.7e-8	137.6e-8	628.5e-8	865.6e-8
2018	$B^0_d \to K^0_S\pi^+\pi^-$	DD	MU	SP	40980.3e-8	572.5e-8	2.5e-8	58.2e-8	21.3e-8	135.2e-8	628.5e-8	863.1e-8
2017	$B^0_d \to K^0_S\pi^+\pi^-$	DD	MD	PP	84175.2e-8	899.5e-8	4.8e-8	115.9e-8	43.2e-8	190.7e-8	1219.8e-8	1532.6e-8
2017	$B^0_d \to K^0_S\pi^+\pi^-$	DD	MU	PP	82335.2e-8	917.1e-8	4.7e-8	127.4e-8	41.5e-8	186.5e-8	1219.8e-8	1543.3e-8
2017	$B^0_d \to K^0_S\pi^+\pi^-$	DD	MD	SP	44640.9e-8	610.0e-8	2.6e-8	62.9e-8	22.8e-8	101.1e-8	628.5e-8	884.2e-8
2017	$B^0_d \to K^0_S\pi^+\pi^-$	DD	MU	SP	43746.0e-8	619.7e-8	2.5e-8	69.9e-8	22.1e-8	99.1e-8	628.5e-8	891.2e-8
2016	$B^0_d \to K^0_S\pi^+\pi^-$	DD	MD	PP	87690.4e-8	919.5e-8	4.9e-8	131.0e-8	38.8e-8	231.4e-8	1219.8e-8	1551.0e-8
2016	$B^0_d \to K^0_S\pi^+\pi^-$	DD	MU	PP	86109.8e-8	937.0e-8	4.8e-8	121.4e-8	38.5e-8	227.2e-8	1219.8e-8	1560.1e-8
2016	$B^0_d \to K^0_S\pi^+\pi^-$	DD	MD	SP	44395.2e-8	605.7e-8	2.5e-8	67.2e-8	19.5e-8	117.2e-8	628.5e-8	883.5e-8
2016	$B^0_d \to K^0_S\pi^+\pi^-$	DD	MU	SP	43333.5e-8	615.0e-8	2.5e-8	62.8e-8	19.2e-8	114.3e-8	628.5e-8	889.2e-8
2015	$B^0_d \to K^0_S\pi^+\pi^-$	DD	MD	PP	84102.3e-8	903.3e-8	4.7e-8	134.9e-8	70.8e-8	303.1e-8	1219.8e-8	1555.3e-8
2015	$B^0_d \to K^0_S\pi^+\pi^-$	DD	MU	PP	82862.0e-8	919.4e-8	4.7e-8	123.8e-8	69.5e-8	298.6e-8	1219.8e-8	1562.9e-8
2015	$B^0_d \to K^0_S\pi^+\pi^-$	DD	MD	SP	34903.5e-8	527.1e-8	2.0e-8	58.7e-8	29.1e-8	125.8e-8	628.5e-8	832.4e-8
2015	$B^0_d \to K^0_S\pi^+\pi^-$	DD	MU	SP	34306.8e-8	530.6e-8	1.9e-8	54.4e-8	29.2e-8	123.6e-8	628.5e-8	834.0e-8
2012b	$B^0_d \to K^0_S\pi^+\pi^-$	DD	MD	PP	52553.7e-8	844.0e-8	2.7e-8	120.1e-8	38.6e-8	720.2e-8	1219.8e-8	1653.8e-8
2012b	$B^0_d \to K^0_S\pi^+\pi^-$	DD	MU	PP	51339.2e-8	806.8e-8	2.5e-8	122.4e-8	39.3e-8	703.6e-8	1219.8e-8	1628.0e-8
2012b	$B^0_d \to K^0_S\pi^+\pi^-$	DD	MD	SP	34585.9e-8	663.9e-8	1.8e-8	82.2e-8	24.9e-8	474.0e-8	628.5e-8	1033.3e-8
2012b	$B^0_d \to K^0_S\pi^+\pi^-$	DD	MU	SP	34168.4e-8	635.0e-8	1.7e-8	84.0e-8	26.1e-8	468.3e-8	628.5e-8	1012.5e-8
2012a	$B^0_d \to K^0_S\pi^+\pi^-$	DD	MD	PP	40111.6e-8	781.6e-8	2.4e-8	107.2e-8	35.1e-8	528.4e-8	1219.8e-8	1546.2e-8
2012a	$B^0_d \to K^0_S\pi^+\pi^-$	DD	MU	PP	42357.0e-8	806.6e-8	2.5e-8	113.3e-8	36.9e-8	557.9e-8	1219.8e-8	1569.7e-8
2012a	$B^0_d \to K^0_S\pi^+\pi^-$	DD	MD	SP	22816.5e-8	569.8e-8	1.4e-8	59.0e-8	21.1e-8	300.5e-8	628.5e-8	902.2e-8
2012a	$B^0_d \to K^0_S\pi^+\pi^-$	DD	MU	SP	23876.8e-8	593.3e-8	1.4e-8	63.4e-8	20.7e-8	314.5e-8	628.5e-8	922.1e-8
2011	$B^0_d \to K^0_S\pi^+\pi^-$	DD	MD	PP	48503.2e-8	810.8e-8	2.5e-8	179.1e-8	43.4e-8	656.8e-8	1219.8e-8	1615.8e-8
2011	$B^0_d \to K^0_S\pi^+\pi^-$	DD	MU	PP	50044.0e-8	885.1e-8	2.7e-8	237.6e-8	44.2e-8	677.6e-8	1219.8e-8	1670.0e-8
2011	$B^0_d \to K^0_S\pi^+\pi^-$	DD	MD	SP	23053.7e-8	536.6e-8	1.2e-8	87.5e-8	20.3e-8	312.2e-8	628.5e-8	888.0e-8
2011	$B^0_d \to K^0_S\pi^+\pi^-$	DD	MU	SP	24813.3e-8	600.2e-8	1.4e-8	120.1e-8	21.8e-8	336.0e-8	628.5e-8	939.7e-8
2018	$B^0_d \to K^0_S\pi^+\pi^-$	LL	MD	PP	29638.3e-8	524.9e-8	2.8e-8	37.9e-8	20.7e-8	66.0e-8	649.9e-8	839.1e-8
2018	$B^0_d \to K^0_S\pi^+\pi^-$	LL	MU	PP	29729.0e-8	517.5e-8	2.9e-8	35.8e-8	20.1e-8	66.2e-8	649.9e-8	834.4e-8
2018	$B^0_d \to K^0_S\pi^+\pi^-$	LL	MD	SP	19359.3e-8	408.1e-8	1.9e-8	24.8e-8	13.7e-8	43.1e-8	437.9e-8	600.9e-8
2018	$B^0_d \to K^0_S\pi^+\pi^-$	LL	MU	SP	18829.8e-8	395.8e-8	1.9e-8	22.6e-8	12.7e-8	41.9e-8	437.9e-8	592.4e-8
2017	$B^0_d \to K^0_S\pi^+\pi^-$	LL	MD	PP	31797.5e-8	573.5e-8	2.8e-8	38.8e-8	24.3e-8	67.7e-8	649.9e-8	870.6e-8
2017	$B^0_d \to K^0_S\pi^+\pi^-$	LL	MU	PP	31573.2e-8	551.1e-8	2.8e-8	42.8e-8	23.6e-8	67.2e-8	649.9e-8	856.1e-8
2017	$B^0_d \to K^0_S\pi^+\pi^-$	LL	MD	SP	21657.4e-8	453.5e-8	1.9e-8	26.4e-8	16.7e-8	46.1e-8	437.9e-8	632.9e-8
2017	$B^0_d \to K^0_S\pi^+\pi^-$	LL	MU	SP	21384.6e-8	437.6e-8	1.9e-8	29.3e-8	16.0e-8	45.5e-8	437.9e-8	621.7e-8
2016	$B^0_d \to K^0_S\pi^+\pi^-$	LL	MD	PP	35981.4e-8	618.2e-8	3.0e-8	46.7e-8	23.6e-8	104.2e-8	649.9e-8	904.5e-8
2016	$B^0_d \to K^0_S\pi^+\pi^-$	LL	MU	PP	35246.8e-8	590.6e-8	3.0e-8	44.3e-8	21.6e-8	102.0e-8	649.9e-8	885.4e-8
2016	$B^0_d \to K^0_S\pi^+\pi^-$	LL	MD	SP	22273.3e-8	457.2e-8	1.9e-8	28.5e-8	14.5e-8	64.5e-8	437.9e-8	637.2e-8
2016	$B^0_d \to K^0_S\pi^+\pi^-$	LL	MU	SP	21988.3e-8	445.2e-8	1.9e-8	27.5e-8	13.5e-8	63.7e-8	437.9e-8	628.5e-8
2015	$B^0_d \to K^0_S\pi^+\pi^-$	LL	MD	PP	32887.3e-8	575.1e-8	2.8e-8	44.0e-8	26.2e-8	99.2e-8	649.9e-8	875.0e-8
2015	$B^0_d \to K^0_S\pi^+\pi^-$	LL	MU	PP	32563.1e-8	563.5e-8	2.9e-8	40.1e-8	25.7e-8	98.2e-8	649.9e-8	867.1e-8
2015	$B^0_d \to K^0_S\pi^+\pi^-$	LL	MD	SP	19792.6e-8	425.3e-8	1.7e-8	26.3e-8	15.8e-8	59.7e-8	437.9e-8	614.2e-8
2015	$B^0_d \to K^0_S\pi^+\pi^-$	LL	MU	SP	20103.3e-8	428.2e-8	1.8e-8	24.7e-8	16.3e-8	60.6e-8	437.9e-8	616.2e-8
2012b	$B^0_d \to K^0_S\pi^+\pi^-$	LL	MD	PP	15215.6e-8	453.1e-8	1.3e-8	30.4e-8	21.6e-8	178.3e-8	649.9e-8	812.9e-8
2012b	$B^0_d \to K^0_S\pi^+\pi^-$	LL	MU	PP	15450.3e-8	427.1e-8	1.3e-8	33.4e-8	30.0e-8	181.0e-8	649.9e-8	799.7e-8
2012b	$B^0_d \to K^0_S\pi^+\pi^-$	LL	MD	SP	108531.0e-9	3765.0e-9	9.8e-9	215.2e-9	145.9e-9	1271.7e-9	4379.5e-9	5919.5e-9
2012b	$B^0_d \to K^0_S\pi^+\pi^-$	LL	MU	SP	108385.3e-9	3513.0e-9	9.2e-9	233.1e-9	219.9e-9	1270.0e-9	4379.5e-9	5765.1e-9
2012a	$B^0_d \to K^0_S\pi^+\pi^-$	LL	MD	PP	17829.9e-8	531.1e-8	1.4e-8	33.0e-8	19.4e-8	265.0e-8	649.9e-8	881.0e-8
2012a	$B^0_d \to K^0_S\pi^+\pi^-$	LL	MU	PP	17519.4e-8	524.9e-8	1.4e-8	33.6e-8	19.0e-8	260.4e-8	649.9e-8	875.9e-8
2012a	$B^0_d \to K^0_S\pi^+\pi^-$	LL	MD	SP	79296.5e-9	3466.7e-9	6.7e-9	179.2e-9	90.2e-9	1178.5e-9	4379.5e-9	5712.0e-9
2012a	$B^0_d \to K^0_S\pi^+\pi^-$	LL	MU	SP	76093.2e-9	3415.9e-9	6.5e-9	175.9e-9	90.3e-9	1130.9e-9	4379.5e-9	5671.5e-9
2011	$B^0_d \to K^0_S\pi^+\pi^-$	LL	MD	PP	19028.7e-8	525.4e-8	1.4e-8	58.0e-8	21.4e-8	275.2e-8	649.9e-8	882.0e-8
2011	$B^0_d \to K^0_S\pi^+\pi^-$	LL	MU	PP	18444.1e-8	536.5e-8	1.5e-8	72.4e-8	20.1e-8	266.7e-8	649.9e-8	887.1e-8
2011	$B^0_d \to K^0_S\pi^+\pi^-$	LL	MD	SP	13551.6e-8	435.9e-8	1.0e-8	39.2e-8	15.5e-8	196.0e-8	437.9e-8	649.6e-8
2011	$B^0_d \to K^0_S\pi^+\pi^-$	LL	MU	SP	12977.0e-8	443.9e-8	1.0e-8	48.2e-8	14.2e-8	187.7e-8	437.9e-8	653.1e-8

Table C.42: $B^0 \to K^0_S\pi^+\pi^-$ detailed efficiency tables with systematics. PP stands for favoured mode optimisation and SP for unfavoured mode optimisation.

Year	Mode	K^0_S	Polarity	Optimisation	$\bar{\varepsilon}$	$\sigma^{\text{stat}}_{\bar{\varepsilon}}$	$\sigma^{\text{tracking}}_{\bar{\varepsilon}}$	$\sigma^{\text{L0corr}}_{\bar{\varepsilon}}$	$\sigma^{\text{PIDMCsampling}}_{\bar{\varepsilon}}$	$\sigma^{\text{PIDkernel}}_{\bar{\varepsilon}}$	$\sigma^{\text{RMS}}_{\bar{\varepsilon}}$	$\sigma_{\bar{\varepsilon}}$
2018	$B^0_d \to K^0_S\pi^+K^-$	DD	MD	PP	87845.1e-8	1426.4e-8	9.4e-8	139.8e-8	147.5e-8	350.1e-8	1311.5e-8	1979.6e-8
2018	$B^0_d \to K^0_S\pi^+K^-$	DD	MU	PP	89121.4e-8	1402.8e-8	9.1e-8	157.7e-8	159.2e-8	355.2e-8	1311.5e-8	1965.8e-8
2018	$B^0_d \to K^0_S\pi^+K^-$	DD	MD	SP	66490.1e-8	1228.2e-8	7.1e-8	107.5e-8	111.2e-8	265.0e-8	1143.8e-8	1706.1e-8
2018	$B^0_d \to K^0_S\pi^+K^-$	DD	MU	SP	66913.1e-8	1208.0e-8	6.9e-8	122.4e-8	120.5e-8	266.7e-8	1143.8e-8	1693.6e-8
2017	$B^0_d \to K^0_S\pi^+K^-$	DD	MD	PP	94045.1e-8	1498.1e-8	9.3e-8	164.6e-8	167.6e-8	353.6e-8	1311.5e-8	2035.9e-8
2017	$B^0_d \to K^0_S\pi^+K^-$	DD	MU	PP	90901.1e-8	1468.3e-8	9.0e-8	134.9e-8	160.2e-8	341.8e-8	1311.5e-8	2009.2e-8
2017	$B^0_d \to K^0_S\pi^+K^-$	DD	MD	SP	70737.9e-8	1288.9e-8	6.9e-8	129.3e-8	124.3e-8	266.0e-8	1143.8e-8	1752.8e-8
2017	$B^0_d \to K^0_S\pi^+K^-$	DD	MU	SP	68593.6e-8	1267.6e-8	6.8e-8	105.6e-8	123.3e-8	257.9e-8	1143.8e-8	1734.4e-8
2016	$B^0_d \to K^0_S\pi^+K^-$	DD	MD	PP	105931.3e-8	1587.3e-8	9.5e-8	176.4e-8	134.0e-8	317.2e-8	1311.5e-8	2095.1e-8
2016	$B^0_d \to K^0_S\pi^+K^-$	DD	MU	PP	104176.3e-8	1613.5e-8	9.5e-8	156.2e-8	131.0e-8	312.0e-8	1311.5e-8	2112.5e-8
2016	$B^0_d \to K^0_S\pi^+K^-$	DD	MD	SP	79098.9e-8	1356.2e-8	7.1e-8	131.5e-8	99.4e-8	236.9e-8	1143.8e-8	1797.4e-8
2016	$B^0_d \to K^0_S\pi^+K^-$	DD	MU	SP	78676.6e-8	1387.5e-8	7.2e-8	117.8e-8	98.5e-8	235.6e-8	1143.8e-8	1820.0e-8
2015	$B^0_d \to K^0_S\pi^+K^-$	DD	MD	PP	93881.3e-8	1521.7e-8	8.7e-8	167.2e-8	205.9e-8	673.9e-8	1311.5e-8	2135.4e-8
2015	$B^0_d \to K^0_S\pi^+K^-$	DD	MU	PP	92538.3e-8	1521.6e-8	8.6e-8	145.1e-8	198.2e-8	664.2e-8	1311.5e-8	2130.0e-8
2015	$B^0_d \to K^0_S\pi^+K^-$	DD	MD	SP	68842.8e-8	1296.8e-8	6.5e-8	120.5e-8	147.2e-8	494.1e-8	1143.8e-8	1808.4e-8
2015	$B^0_d \to K^0_S\pi^+K^-$	DD	MU	SP	69441.2e-8	1317.7e-8	6.6e-8	107.6e-8	148.2e-8	498.4e-8	1143.8e-8	1823.9e-8
2012b	$B^0_d \to K^0_S\pi^+K^-$	DD	MD	PP	66016.2e-8	1693.0e-8	5.5e-8	161.0e-8	149.9e-8	4486.1e-8	1311.5e-8	4975.9e-8
2012b	$B^0_d \to K^0_S\pi^+K^-$	DD	MU	PP	66311.1e-8	1573.2e-8	5.1e-8	237.5e-8	152.5e-8	4506.1e-8	1311.5e-8	4957.8e-8
2012b	$B^0_d \to K^0_S\pi^+K^-$	DD	MD	SP	51999.1e-8	1497.2e-8	4.4e-8	120.3e-8	118.9e-8	3533.6e-8	1143.8e-8	4008.0e-8
2012b	$B^0_d \to K^0_S\pi^+K^-$	DD	MU	SP	51208.4e-8	1371.7e-8	4.0e-8	169.4e-8	115.3e-8	3479.8e-8	1143.8e-8	3916.8e-8
2012a	$B^0_d \to K^0_S\pi^+K^-$	DD	MD	PP	49869.4e-8	1527.7e-8	4.6e-8	150.5e-8	142.9e-8	4020.8e-8	1311.5e-8	4501.5e-8
2012a	$B^0_d \to K^0_S\pi^+K^-$	DD	MU	PP	50907.2e-8	1576.6e-8	4.7e-8	271.0e-8	150.3e-8	4104.5e-8	1311.5e-8	4598.7e-8
2012a	$B^0_d \to K^0_S\pi^+K^-$	DD	MD	SP	41799.9e-8	1398.0e-8	3.9e-8	120.1e-8	119.0e-8	3370.2e-8	1143.8e-8	3827.4e-8
2012a	$B^0_d \to K^0_S\pi^+K^-$	DD	MU	SP	41898.5e-8	1437.6e-8	4.0e-8	220.6e-8	122.5e-8	3378.1e-8	1143.8e-8	3853.6e-8
2011	$B^0_d \to K^0_S\pi^+K^-$	DD	MD	PP	61193.2e-8	1624.5e-8	5.0e-8	267.6e-8	212.2e-8	4569.0e-8	1311.5e-8	5035.1e-8
2011	$B^0_d \to K^0_S\pi^+K^-$	DD	MU	PP	60669.1e-8	1540.8e-8	4.8e-8	336.8e-8	199.7e-8	4529.9e-8	1311.5e-8	4976.7e-8
2011	$B^0_d \to K^0_S\pi^+K^-$	DD	MD	SP	51018.2e-8	1489.9e-8	4.2e-8	223.8e-8	178.2e-8	3809.3e-8	1143.8e-8	4256.9e-8
2011	$B^0_d \to K^0_S\pi^+K^-$	DD	MU	SP	49231.8e-8	1383.9e-8	3.9e-8	270.6e-8	158.1e-8	3675.9e-8	1143.8e-8	4102.9e-8
2018	$B^0_d \to K^0_S\pi^+K^-$	LL	MD	PP	32800.1e-8	1031.2e-8	5.5e-8	44.3e-8	97.7e-8	168.9e-8	1199.5e-8	1594.4e-8
2018	$B^0_d \to K^0_S\pi^+K^-$	LL	MU	PP	33994.0e-8	947.2e-8	5.6e-8	45.8e-8	110.4e-8	175.0e-8	1199.5e-8	1543.0e-8
2018	$B^0_d \to K^0_S\pi^+K^-$	LL	MD	SP	27167.9e-8	912.1e-8	4.6e-8	36.3e-8	78.5e-8	139.9e-8	853.2e-8	1259.8e-8
2018	$B^0_d \to K^0_S\pi^+K^-$	LL	MU	SP	27953.9e-8	846.1e-8	4.5e-8	38.3e-8	87.1e-8	143.9e-8	853.2e-8	1213.9e-8
2017	$B^0_d \to K^0_S\pi^+K^-$	LL	MD	PP	35179.1e-8	1108.1e-8	5.6e-8	59.4e-8	115.5e-8	112.9e-8	1199.5e-8	1642.0e-8
2017	$B^0_d \to K^0_S\pi^+K^-$	LL	MU	PP	39236.9e-8	1079.1e-8	5.8e-8	53.5e-8	117.4e-8	125.9e-8	1199.5e-8	1623.5e-8
2017	$B^0_d \to K^0_S\pi^+K^-$	LL	MD	SP	28729.3e-8	973.6e-8	4.6e-8	48.3e-8	99.3e-8	92.2e-8	853.2e-8	1302.5e-8
2017	$B^0_d \to K^0_S\pi^+K^-$	LL	MU	SP	31992.1e-8	959.4e-8	4.7e-8	43.1e-8	97.6e-8	102.7e-8	853.2e-8	1292.4e-8
2016	$B^0_d \to K^0_S\pi^+K^-$	LL	MD	PP	38753.2e-8	1163.7e-8	6.0e-8	62.9e-8	76.2e-8	129.6e-8	1199.5e-8	1679.1e-8
2016	$B^0_d \to K^0_S\pi^+K^-$	LL	MU	PP	38075.9e-8	1057.7e-8	5.7e-8	50.7e-8	70.6e-8	127.3e-8	1199.5e-8	1606.6e-8
2016	$B^0_d \to K^0_S\pi^+K^-$	LL	MD	SP	31201.4e-8	1008.3e-8	4.8e-8	49.0e-8	61.4e-8	104.3e-8	853.2e-8	1327.3e-8
2016	$B^0_d \to K^0_S\pi^+K^-$	LL	MU	SP	31170.9e-8	944.0e-8	4.7e-8	40.8e-8	58.3e-8	104.2e-8	853.2e-8	1278.7e-8
2015	$B^0_d \to K^0_S\pi^+K^-$	LL	MD	PP	35248.3e-8	1084.5e-8	5.7e-8	51.4e-8	147.8e-8	253.3e-8	1199.5e-8	1644.2e-8
2015	$B^0_d \to K^0_S\pi^+K^-$	LL	MU	PP	38750.7e-8	1087.9e-8	6.2e-8	53.9e-8	174.6e-8	278.5e-8	1199.5e-8	1653.2e-8
2015	$B^0_d \to K^0_S\pi^+K^-$	LL	MD	SP	23546.0e-8	854.0e-8	3.8e-8	33.5e-8	92.3e-8	169.2e-8	853.2e-8	1222.9e-8
2015	$B^0_d \to K^0_S\pi^+K^-$	LL	MU	SP	25604.2e-8	863.8e-8	4.1e-8	35.1e-8	115.7e-8	184.0e-8	853.2e-8	1234.0e-8
2012b	$B^0_d \to K^0_S\pi^+K^-$	LL	MD	PP	17917.3e-8	946.8e-8	2.9e-8	46.7e-8	156.4e-8	1450.0e-8	1199.5e-8	2112.9e-8
2012b	$B^0_d \to K^0_S\pi^+K^-$	LL	MU	PP	18338.2e-8	888.8e-8	2.7e-8	53.6e-8	150.8e-8	1484.1e-8	1199.5e-8	2111.1e-8
2012b	$B^0_d \to K^0_S\pi^+K^-$	LL	MD	SP	9616.8e-8	680.3e-8	1.6e-8	28.5e-8	90.7e-8	778.3e-8	853.2e-8	1343.7e-8
2012b	$B^0_d \to K^0_S\pi^+K^-$	LL	MU	SP	9227.0e-8	616.8e-8	1.4e-8	28.2e-8	69.2e-8	746.7e-8	853.2e-8	1292.9e-8
2012a	$B^0_d \to K^0_S\pi^+K^-$	LL	MD	PP	20839.5e-8	1061.9e-8	3.2e-8	44.4e-8	153.6e-8	1504.2e-8	1199.5e-8	2203.3e-8
2012a	$B^0_d \to K^0_S\pi^+K^-$	LL	MU	PP	20836.0e-8	1044.2e-8	2.9e-8	88.7e-8	160.9e-8	1503.9e-8	1199.5e-8	2196.5e-8
2012a	$B^0_d \to K^0_S\pi^+K^-$	LL	MD	SP	15539.4e-8	908.6e-8	2.4e-8	34.8e-8	102.2e-8	1121.6e-8	853.2e-8	1680.2e-8
2012a	$B^0_d \to K^0_S\pi^+K^-$	LL	MU	SP	15557.0e-8	901.0e-8	2.2e-8	70.8e-8	113.5e-8	1122.9e-8	853.2e-8	1678.9e-8
2011	$B^0_d \to K^0_S\pi^+K^-$	LL	MD	PP	23210.4e-8	1108.5e-8	3.2e-8	79.2e-8	110.8e-8	1336.5e-8	1199.5e-8	2114.8e-8
2011	$B^0_d \to K^0_S\pi^+K^-$	LL	MU	PP	24349.4e-8	1057.6e-8	3.0e-8	107.6e-8	122.6e-8	1402.1e-8	1199.5e-8	2133.0e-8
2011	$B^0_d \to K^0_S\pi^+K^-$	LL	MD	SP	18844.2e-8	982.0e-8	2.6e-8	61.8e-8	91.5e-8	1085.1e-8	853.2e-8	1697.6e-8
2011	$B^0_d \to K^0_S\pi^+K^-$	LL	MU	SP	20016.1e-8	960.3e-8	2.5e-8	84.9e-8	103.8e-8	1152.6e-8	853.2e-8	1731.0e-8

Table C.43: $B^0 \to K^0_S\pi^+K^-$ detailed efficiency tables with systematics. PP stands for favoured mode optimisation and SP for unfavoured mode optimisation.

Year	Mode	K^0_S	Polarity	Optimisation	$\bar{\varepsilon}$	$\sigma^{\text{stat}}_{\bar{\varepsilon}}$	$\sigma^{\text{tracking}}_{\bar{\varepsilon}}$	$\sigma^{\text{L0corr}}_{\bar{\varepsilon}}$	$\sigma^{\text{PIDMCsampling}}_{\bar{\varepsilon}}$	$\sigma^{\text{PIDkernel}}_{\bar{\varepsilon}}$	$\sigma^{\text{RMS}}_{\bar{\varepsilon}}$	$\sigma_{\bar{\varepsilon}}$
2018	$B^0_d \to K^0_S K^+\pi^-$	DD	MD	PP	89924.9e-8	1592.4e-8	9.9e-8	150.3e-8	133.4e-8	341.1e-8	1468.9e-8	2202.3e-8
2018	$B^0_d \to K^0_S K^+\pi^-$	DD	MU	PP	89740.8e-8	1534.5e-8	9.8e-8	150.4e-8	131.4e-8	340.4e-8	1468.9e-8	2160.6e-8
2018	$B^0_d \to K^0_S K^+\pi^-$	DD	MD	SP	67869.5e-8	1372.4e-8	7.5e-8	117.3e-8	98.9e-8	257.4e-8	1136.8e-8	1807.1e-8
2018	$B^0_d \to K^0_S K^+\pi^-$	DD	MU	SP	68860.1e-8	1337.5e-8	7.5e-8	119.6e-8	100.0e-8	261.2e-8	1136.8e-8	1781.5e-8
2017	$B^0_d \to K^0_S K^+\pi^-$	DD	MD	PP	94090.5e-8	1685.8e-8	9.5e-8	178.1e-8	130.4e-8	367.1e-8	1468.9e-8	2276.7e-8
2017	$B^0_d \to K^0_S K^+\pi^-$	DD	MU	PP	97274.0e-8	1707.1e-8	9.8e-8	173.2e-8	137.1e-8	379.6e-8	1468.9e-8	2294.5e-8
2017	$B^0_d \to K^0_S K^+\pi^-$	DD	MD	SP	77803.3e-8	1529.7e-8	7.9e-8	151.0e-8	107.8e-8	303.6e-8	1136.8e-8	1938.8e-8
2017	$B^0_d \to K^0_S K^+\pi^-$	DD	MU	SP	79114.9e-8	1528.9e-8	8.0e-8	142.5e-8	111.8e-8	308.7e-8	1136.8e-8	1938.6e-8
2016	$B^0_d \to K^0_S K^+\pi^-$	DD	MD	PP	10320.4e-7	175.3e-7	1.0e-7	18.3e-7	12.6e-7	29.7e-7	146.9e-7	231.7e-7
2016	$B^0_d \to K^0_S K^+\pi^-$	DD	MU	PP	10099.3e-7	173.8e-7	1.0e-7	19.7e-7	12.2e-7	29.0e-7	146.9e-7	230.6e-7
2016	$B^0_d \to K^0_S K^+\pi^-$	DD	MD	SP	75219.7e-8	1476.4e-8	7.5e-8	133.3e-8	91.2e-8	216.1e-8	1136.8e-8	1882.8e-8
2016	$B^0_d \to K^0_S K^+\pi^-$	DD	MU	SP	76100.3e-8	1504.9e-8	7.8e-8	150.8e-8	93.1e-8	218.6e-8	1136.8e-8	1907.0e-8
2015	$B^0_d \to K^0_S K^+\pi^-$	DD	MD	PP	94442.7e-8	1706.3e-8	9.8e-8	194.3e-8	337.7e-8	793.5e-8	1468.9e-8	2418.8e-8
2015	$B^0_d \to K^0_S K^+\pi^-$	DD	MU	PP	91683.9e-8	1693.3e-8	9.8e-8	187.3e-8	297.4e-8	770.3e-8	1468.9e-8	2396.3e-8
2015	$B^0_d \to K^0_S K^+\pi^-$	DD	MD	SP	66971.8e-8	1428.2e-8	7.0e-8	143.0e-8	263.2e-8	562.7e-8	1136.8e-8	1933.5e-8
2015	$B^0_d \to K^0_S K^+\pi^-$	DD	MU	SP	64715.6e-8	1420.3e-8	6.9e-8	133.9e-8	216.1e-8	543.7e-8	1136.8e-8	1915.7e-8
2012b	$B^0_d \to K^0_S K^+\pi^-$	DD	MD	PP	68174.0e-8	1914.1e-8	6.4e-8	195.8e-8	352.6e-8	5532.5e-8	1468.9e-8	6049.2e-8
2012b	$B^0_d \to K^0_S K^+\pi^-$	DD	MU	PP	68137.2e-8	1773.7e-8	6.1e-8	276.9e-8	397.4e-8	5529.5e-8	1468.9e-8	6009.4e-8
2012b	$B^0_d \to K^0_S K^+\pi^-$	DD	MD	SP	49469.8e-8	1643.5e-8	4.7e-8	153.3e-8	241.4e-8	4014.6e-8	1136.8e-8	4493.6e-8
2012b	$B^0_d \to K^0_S K^+\pi^-$	DD	MU	SP	47546.1e-8	1483.6e-8	4.3e-8	215.7e-8	296.6e-8	3858.5e-8	1136.8e-8	4303.0e-8
2012a	$B^0_d \to K^0_S K^+\pi^-$	DD	MD	PP	50826.5e-8	1723.2e-8	5.4e-8	149.4e-8	193.1e-8	4332.0e-8	1468.9e-8	4894.2e-8
2012a	$B^0_d \to K^0_S K^+\pi^-$	DD	MU	PP	53181.9e-8	1840.7e-8	5.6e-8	229.1e-8	207.6e-8	4532.8e-8	1468.9e-8	5117.4e-8
2012a	$B^0_d \to K^0_S K^+\pi^-$	DD	MD	SP	38629.7e-8	1495.7e-8	4.1e-8	112.6e-8	150.5e-8	3292.5e-8	1136.8e-8	3795.4e-8
2012a	$B^0_d \to K^0_S K^+\pi^-$	DD	MU	SP	42011.2e-8	1635.7e-8	4.5e-8	180.6e-8	164.3e-8	3580.7e-8	1136.8e-8	4104.7e-8
2011	$B^0_d \to K^0_S K^+\pi^-$	DD	MD	PP	64618.3e-8	1915.5e-8	5.9e-8	320.9e-8	203.8e-8	4965.8e-8	1468.9e-8	5534.5e-8
2011	$B^0_d \to K^0_S K^+\pi^-$	DD	MU	PP	62346.9e-8	1791.7e-8	5.4e-8	422.0e-8	197.0e-8	4791.3e-8	1468.9e-8	5342.4e-8
2011	$B^0_d \to K^0_S K^+\pi^-$	DD	MD	SP	54181.4e-8	1741.2e-8	5.0e-8	260.8e-8	171.5e-8	4163.8e-8	1136.8e-8	4664.6e-8
2011	$B^0_d \to K^0_S K^+\pi^-$	DD	MU	SP	52459.6e-8	1642.6e-8	4.6e-8	348.5e-8	165.7e-8	4031.5e-8	1136.8e-8	4515.7e-8
2018	$B^0_d \to K^0_S K^+\pi^-$	LL	MD	PP	32839.9e-8	1077.6e-8	6.4e-8	48.6e-8	95.5e-8	159.8e-8	1344.2e-8	1733.5e-8
2018	$B^0_d \to K^0_S K^+\pi^-$	LL	MU	PP	31689.0e-8	1042.2e-8	6.2e-8	48.4e-8	89.4e-8	154.2e-8	1344.2e-8	1710.9e-8
2018	$B^0_d \to K^0_S K^+\pi^-$	LL	MD	SP	27352.8e-8	979.1e-8	5.3e-8	40.9e-8	79.7e-8	133.1e-8	977.7e-8	1393.0e-8
2018	$B^0_d \to K^0_S K^+\pi^-$	LL	MU	SP	26164.1e-8	938.2e-8	5.1e-8	39.0e-8	76.3e-8	127.3e-8	977.7e-8	1363.7e-8
2017	$B^0_d \to K^0_S K^+\pi^-$	LL	MD	PP	37662.0e-8	1224.8e-8	6.8e-8	66.3e-8	285.0e-8	213.5e-8	1344.2e-8	1854.2e-8
2017	$B^0_d \to K^0_S K^+\pi^-$	LL	MU	PP	35837.8e-8	1183.6e-8	6.5e-8	60.8e-8	334.5e-8	203.2e-8	1344.2e-8	1834.3e-8
2017	$B^0_d \to K^0_S K^+\pi^-$	LL	MD	SP	29162.8e-8	1060.4e-8	5.3e-8	51.4e-8	238.8e-8	165.3e-8	977.7e-8	1472.2e-8
2017	$B^0_d \to K^0_S K^+\pi^-$	LL	MU	SP	28460.5e-8	1046.6e-8	5.2e-8	49.0e-8	228.3e-8	161.3e-8	977.7e-8	1460.1e-8
2016	$B^0_d \to K^0_S K^+\pi^-$	LL	MD	PP	40569.1e-8	1247.3e-8	7.1e-8	66.7e-8	650.3e-8	174.1e-8	1344.2e-8	1954.5e-8
2016	$B^0_d \to K^0_S K^+\pi^-$	LL	MU	PP	39542.8e-8	1260.7e-8	7.0e-8	68.4e-8	841.6e-8	169.7e-8	1344.2e-8	2034.2e-8
2016	$B^0_d \to K^0_S K^+\pi^-$	LL	MD	SP	31846.6e-8	1091.8e-8	5.6e-8	53.6e-8	510.2e-8	136.7e-8	977.7e-8	1558.7e-8
2016	$B^0_d \to K^0_S K^+\pi^-$	LL	MU	SP	30849.2e-8	1098.1e-8	5.4e-8	54.3e-8	696.2e-8	132.4e-8	977.7e-8	1633.1e-8
2015	$B^0_d \to K^0_S K^+\pi^-$	LL	MD	PP	38225.6e-8	1224.8e-8	6.7e-8	68.0e-8	207.8e-8	451.2e-8	1344.2e-8	1886.4e-8
2015	$B^0_d \to K^0_S K^+\pi^-$	LL	MU	PP	36360.6e-8	1200.1e-8	6.4e-8	69.5e-8	216.8e-8	429.2e-8	1344.2e-8	1866.3e-8
2015	$B^0_d \to K^0_S K^+\pi^-$	LL	MD	SP	27994.5e-8	1032.5e-8	4.9e-8	49.9e-8	148.4e-8	330.4e-8	977.7e-8	1468.2e-8
2015	$B^0_d \to K^0_S K^+\pi^-$	LL	MU	SP	26245.3e-8	999.8e-8	4.6e-8	50.4e-8	148.7e-8	309.8e-8	977.7e-8	1440.9e-8
2012b	$B^0_d \to K^0_S K^+\pi^-$	LL	MD	PP	17628.9e-8	1057.8e-8	3.2e-8	59.6e-8	276.2e-8	1330.6e-8	1344.2e-8	2185.4e-8
2012b	$B^0_d \to K^0_S K^+\pi^-$	LL	MU	PP	17962.6e-8	1030.0e-8	3.3e-8	70.2e-8	269.5e-8	1355.8e-8	1344.2e-8	2187.1e-8
2012b	$B^0_d \to K^0_S K^+\pi^-$	LL	MD	SP	8770.4e-8	736.7e-8	1.9e-8	25.0e-8	112.0e-8	662.0e-8	977.7e-8	1396.4e-8
2012b	$B^0_d \to K^0_S K^+\pi^-$	LL	MU	SP	9199.3e-8	720.3e-8	1.7e-8	28.8e-8	141.7e-8	694.3e-8	977.7e-8	1406.3e-8
2012a	$B^0_d \to K^0_S K^+\pi^-$	LL	MD	PP	20175.4e-8	1220.7e-8	3.6e-8	50.3e-8	145.4e-8	1009.1e-8	1344.2e-8	2083.0e-8
2012a	$B^0_d \to K^0_S K^+\pi^-$	LL	MU	PP	17305.4e-8	1132.6e-8	3.0e-8	70.5e-8	130.7e-8	865.6e-8	1344.2e-8	1964.9e-8
2012a	$B^0_d \to K^0_S K^+\pi^-$	LL	MD	SP	15912.9e-8	1081.1e-8	2.8e-8	40.4e-8	117.2e-8	795.9e-8	977.7e-8	1665.4e-8
2012a	$B^0_d \to K^0_S K^+\pi^-$	LL	MU	SP	13796.9e-8	1012.0e-8	2.4e-8	56.1e-8	108.0e-8	690.1e-8	977.7e-8	1572.0e-8
2011	$B^0_d \to K^0_S K^+\pi^-$	LL	MD	PP	23384.1e-8	1278.2e-8	3.8e-8	109.2e-8	128.5e-8	1376.5e-8	1344.2e-8	2316.0e-8
2011	$B^0_d \to K^0_S K^+\pi^-$	LL	MU	PP	22401.9e-8	1186.3e-8	3.4e-8	133.4e-8	122.2e-8	1318.7e-8	1344.2e-8	2232.9e-8
2011	$B^0_d \to K^0_S K^+\pi^-$	LL	MD	SP	17331.6e-8	1088.7e-8	2.9e-8	75.1e-8	89.6e-8	1020.3e-8	977.7e-8	1787.6e-8
2011	$B^0_d \to K^0_S K^+\pi^-$	LL	MU	SP	17398.6e-8	1042.9e-8	2.6e-8	99.8e-8	96.1e-8	1024.2e-8	977.7e-8	1764.0e-8

Table C.44: $B^0 \to K^0_S K^+\pi^-$ detailed efficiency tables with systematics. PP stands for favoured mode optimisation and SP for unfavoured mode optimisation.

Year	Mode	K^0_S	Polarity	Optimisation	$\bar{\varepsilon}$	$\sigma^{\text{stat}}_{\bar{\varepsilon}}$	$\sigma^{\text{tracking}}_{\bar{\varepsilon}}$	$\sigma^{\text{L0corr}}_{\bar{\varepsilon}}$	$\sigma^{\text{PIDMCsampling}}_{\bar{\varepsilon}}$	$\sigma^{\text{PIDkernel}}_{\bar{\varepsilon}}$	$\sigma^{\text{RMS}}_{\bar{\varepsilon}}$	$\sigma_{\bar{\varepsilon}}$
2018	$B^0_d \to K^0_S K^+ K^-$	DD	MD	PP	73336.9e-8	723.5e-8	4.7e-8	72.9e-8	72.1e-8	154.5e-8	322.3e-8	813.5e-8
2018	$B^0_d \to K^0_S K^+ K^-$	DD	MU	PP	72334.1e-8	734.9e-8	4.7e-8	84.2e-8	73.5e-8	152.4e-8	322.3e-8	824.4e-8
2018	$B^0_d \to K^0_S K^+ K^-$	DD	MD	SP	48525.4e-8	587.5e-8	3.1e-8	51.0e-8	48.4e-8	102.2e-8	202.8e-8	633.8e-8
2018	$B^0_d \to K^0_S K^+ K^-$	DD	MU	SP	48473.8e-8	601.3e-8	3.2e-8	59.5e-8	48.1e-8	102.1e-8	202.8e-8	647.3e-8
2017	$B^0_d \to K^0_S K^+ K^-$	DD	MD	PP	75839.8e-8	778.4e-8	4.6e-8	196.4e-8	56.8e-8	174.6e-8	322.3e-8	884.3e-8
2017	$B^0_d \to K^0_S K^+ K^-$	DD	MU	PP	74337.8e-8	773.8e-8	4.5e-8	76.2e-8	56.3e-8	171.1e-8	322.3e-8	860.8e-8
2017	$B^0_d \to K^0_S K^+ K^-$	DD	MD	SP	37886.2e-8	550.6e-8	2.3e-8	103.3e-8	27.7e-8	87.2e-8	202.8e-8	602.7e-8
2017	$B^0_d \to K^0_S K^+ K^-$	DD	MU	SP	36881.3e-8	544.8e-8	2.2e-8	40.8e-8	27.3e-8	84.9e-8	202.8e-8	589.6e-8
2016	$B^0_d \to K^0_S K^+ K^-$	DD	MD	PP	91311.2e-8	847.3e-8	5.2e-8	103.7e-8	64.0e-8	262.5e-8	322.3e-8	951.6e-8
2016	$B^0_d \to K^0_S K^+ K^-$	DD	MU	PP	87198.9e-8	848.0e-8	5.0e-8	95.4e-8	59.8e-8	250.6e-8	322.3e-8	947.9e-8
2016	$B^0_d \to K^0_S K^+ K^-$	DD	MD	SP	48790.7e-8	615.7e-8	2.8e-8	61.1e-8	34.2e-8	140.2e-8	202.8e-8	666.9e-8
2016	$B^0_d \to K^0_S K^+ K^-$	DD	MU	SP	46997.4e-8	620.2e-8	2.7e-8	56.7e-8	32.2e-8	135.1e-8	202.8e-8	669.5e-8
2015	$B^0_d \to K^0_S K^+ K^-$	DD	MD	PP	81713.7e-8	809.3e-8	4.8e-8	97.6e-8	86.6e-8	212.4e-8	322.3e-8	906.1e-8
2015	$B^0_d \to K^0_S K^+ K^-$	DD	MU	PP	78482.5e-8	807.5e-8	4.8e-8	87.3e-8	82.5e-8	204.0e-8	322.3e-8	901.1e-8
2015	$B^0_d \to K^0_S K^+ K^-$	DD	MD	SP	40522.7e-8	570.6e-8	2.4e-8	54.3e-8	40.9e-8	105.4e-8	202.8e-8	618.4e-8
2015	$B^0_d \to K^0_S K^+ K^-$	DD	MU	SP	39301.0e-8	570.0e-8	2.4e-8	48.3e-8	39.6e-8	102.2e-8	202.8e-8	616.7e-8
2012b	$B^0_d \to K^0_S K^+ K^-$	DD	MD	PP	45044.1e-8	769.0e-8	2.4e-8	72.8e-8	323.0e-8	1026.4e-8	322.3e-8	1363.2e-8
2012b	$B^0_d \to K^0_S K^+ K^-$	DD	MU	PP	44883.8e-8	788.7e-8	2.5e-8	268.5e-8	330.8e-8	1022.7e-8	322.3e-8	1397.6e-8
2012b	$B^0_d \to K^0_S K^+ K^-$	DD	MD	SP	33652.7e-8	670.2e-8	1.9e-8	58.5e-8	240.8e-8	766.8e-8	202.8e-8	1067.6e-8
2012b	$B^0_d \to K^0_S K^+ K^-$	DD	MU	SP	33202.2e-8	680.3e-8	1.9e-8	216.6e-8	252.8e-8	756.5e-8	202.8e-8	1089.6e-8
2012a	$B^0_d \to K^0_S K^+ K^-$	DD	MD	PP	30768.9e-8	685.8e-8	2.1e-8	69.1e-8	45.2e-8	625.9e-8	322.3e-8	986.2e-8
2012a	$B^0_d \to K^0_S K^+ K^-$	DD	MU	PP	31578.1e-8	698.2e-8	2.1e-8	241.2e-8	47.9e-8	642.3e-8	322.3e-8	1031.7e-8
2012a	$B^0_d \to K^0_S K^+ K^-$	DD	MD	SP	20733.1e-8	566.9e-8	1.4e-8	44.4e-8	30.5e-8	421.7e-8	202.8e-8	737.1e-8
2012a	$B^0_d \to K^0_S K^+ K^-$	DD	MU	SP	21431.2e-8	581.9e-8	1.5e-8	154.8e-8	30.9e-8	435.9e-8	202.8e-8	771.1e-8
2011	$B^0_d \to K^0_S K^+ K^-$	DD	MD	PP	36371.5e-8	706.3e-8	2.1e-8	110.6e-8	33.5e-8	301.8e-8	322.3e-8	840.9e-8
2011	$B^0_d \to K^0_S K^+ K^-$	DD	MU	PP	35604.6e-8	631.4e-8	1.8e-8	202.1e-8	32.7e-8	295.4e-8	322.3e-8	794.8e-8
2011	$B^0_d \to K^0_S K^+ K^-$	DD	MD	SP	27469.9e-8	617.7e-8	1.7e-8	83.6e-8	25.8e-8	227.9e-8	202.8e-8	694.5e-8
2011	$B^0_d \to K^0_S K^+ K^-$	DD	MU	SP	27575.1e-8	558.3e-8	1.4e-8	154.7e-8	26.1e-8	228.8e-8	202.8e-8	655.5e-8
2018	$B^0_d \to K^0_S K^+ K^-$	LL	MD	PP	30764.6e-8	458.5e-8	3.0e-8	22.3e-8	46.7e-8	61.7e-8	208.1e-8	509.9e-8
2018	$B^0_d \to K^0_S K^+ K^-$	LL	MU	PP	30220.0e-8	462.5e-8	3.0e-8	25.1e-8	43.4e-8	60.6e-8	208.1e-8	513.3e-8
2018	$B^0_d \to K^0_S K^+ K^-$	LL	MD	SP	22056.5e-8	391.0e-8	2.2e-8	16.7e-8	33.1e-8	44.2e-8	148.4e-8	422.2e-8
2018	$B^0_d \to K^0_S K^+ K^-$	LL	MU	SP	21638.9e-8	392.6e-8	2.2e-8	18.3e-8	29.4e-8	43.4e-8	148.4e-8	423.4e-8
2017	$B^0_d \to K^0_S K^+ K^-$	LL	MD	PP	33033.6e-8	502.7e-8	2.9e-8	61.0e-8	35.5e-8	98.7e-8	208.1e-8	557.4e-8
2017	$B^0_d \to K^0_S K^+ K^-$	LL	MU	PP	32828.1e-8	513.3e-8	3.0e-8	25.9e-8	39.2e-8	98.0e-8	208.1e-8	564.5e-8
2017	$B^0_d \to K^0_S K^+ K^-$	LL	MD	SP	18573.8e-8	379.6e-8	1.7e-8	36.0e-8	19.8e-8	55.5e-8	148.4e-8	413.3e-8
2017	$B^0_d \to K^0_S K^+ K^-$	LL	MU	SP	18134.3e-8	382.9e-8	1.7e-8	15.1e-8	20.2e-8	54.2e-8	148.4e-8	415.0e-8
2016	$B^0_d \to K^0_S K^+ K^-$	LL	MD	PP	37615.8e-8	543.7e-8	3.2e-8	33.3e-8	31.2e-8	91.8e-8	208.1e-8	591.1e-8
2016	$B^0_d \to K^0_S K^+ K^-$	LL	MU	PP	36394.5e-8	543.5e-8	3.1e-8	32.0e-8	32.5e-8	88.8e-8	208.1e-8	590.4e-8
2016	$B^0_d \to K^0_S K^+ K^-$	LL	MD	SP	20413.7e-8	402.3e-8	1.8e-8	19.5e-8	17.6e-8	49.8e-8	148.4e-8	432.5e-8
2016	$B^0_d \to K^0_S K^+ K^-$	LL	MU	SP	19485.6e-8	398.6e-8	1.7e-8	18.5e-8	17.0e-8	47.6e-8	148.4e-8	428.7e-8
2015	$B^0_d \to K^0_S K^+ K^-$	LL	MD	PP	33974.5e-8	517.7e-8	3.0e-8	32.3e-8	73.8e-8	220.9e-8	208.1e-8	605.5e-8
2015	$B^0_d \to K^0_S K^+ K^-$	LL	MU	PP	32306.4e-8	520.4e-8	2.8e-8	31.0e-8	75.1e-8	210.0e-8	208.1e-8	604.0e-8
2015	$B^0_d \to K^0_S K^+ K^-$	LL	MD	SP	28594.2e-8	471.2e-8	2.5e-8	26.9e-8	63.6e-8	185.9e-8	148.4e-8	532.3e-8
2015	$B^0_d \to K^0_S K^+ K^-$	LL	MU	SP	27203.0e-8	475.6e-8	2.4e-8	26.1e-8	61.7e-8	176.8e-8	148.4e-8	532.9e-8
2012b	$B^0_d \to K^0_S K^+ K^-$	LL	MD	PP	14706.8e-8	439.1e-8	1.4e-8	23.4e-8	31.2e-8	207.8e-8	208.1e-8	529.9e-8
2012b	$B^0_d \to K^0_S K^+ K^-$	LL	MU	PP	14705.5e-8	460.4e-8	1.4e-8	85.8e-8	28.6e-8	207.7e-8	208.1e-8	553.8e-8
2012b	$B^0_d \to K^0_S K^+ K^-$	LL	MD	SP	12452.3e-8	403.9e-8	1.2e-8	20.8e-8	25.7e-8	175.9e-8	148.4e-8	466.1e-8
2012b	$B^0_d \to K^0_S K^+ K^-$	LL	MU	SP	12347.7e-8	424.9e-8	1.2e-8	75.7e-8	24.2e-8	174.4e-8	148.4e-8	489.2e-8
2012a	$B^0_d \to K^0_S K^+ K^-$	LL	MD	PP	17262.5e-8	513.0e-8	1.4e-8	26.4e-8	56.5e-8	317.6e-8	208.1e-8	641.3e-8
2012a	$B^0_d \to K^0_S K^+ K^-$	LL	MU	PP	16267.2e-8	506.0e-8	1.4e-8	66.3e-8	50.2e-8	299.3e-8	208.1e-8	629.2e-8
2012a	$B^0_d \to K^0_S K^+ K^-$	LL	MD	SP	14211.3e-8	464.8e-8	1.2e-8	21.7e-8	45.2e-8	261.5e-8	148.4e-8	555.8e-8
2012a	$B^0_d \to K^0_S K^+ K^-$	LL	MU	SP	14046.3e-8	473.9e-8	1.2e-8	58.7e-8	44.3e-8	258.4e-8	148.4e-8	564.6e-8
2011	$B^0_d \to K^0_S K^+ K^-$	LL	MD	PP	19168.4e-8	524.5e-8	1.4e-8	44.4e-8	43.0e-8	224.5e-8	208.1e-8	610.5e-8
2011	$B^0_d \to K^0_S K^+ K^-$	LL	MU	PP	18793.1e-8	473.4e-8	1.3e-8	79.0e-8	44.4e-8	220.1e-8	208.1e-8	569.3e-8
2011	$B^0_d \to K^0_S K^+ K^-$	LL	MD	SP	13589.0e-8	444.3e-8	1.0e-8	30.1e-8	31.3e-8	159.2e-8	148.4e-8	496.6e-8
2011	$B^0_d \to K^0_S K^+ K^-$	LL	MU	SP	140267.3e-9	4127.0e-9	9.9e-9	583.2e-9	362.3e-9	1642.8e-9	1483.6e-9	4733.3e-9

Table C.45: $B^0 \to K^0_S K^+ K^-$ detailed efficiency tables with systematics. PP stands for favoured mode optimisation and SP for unfavoured mode optimisation.

Year	Mode	K^0_S	Polarity	Optimisation	$\bar{\varepsilon}$	$\sigma^{\text{stat}}_{\bar{\varepsilon}}$	$\sigma^{\text{tracking}}_{\bar{\varepsilon}}$	$\sigma^{\text{L0corr}}_{\bar{\varepsilon}}$	$\sigma^{\text{PIDMCsampling}}_{\bar{\varepsilon}}$	$\sigma^{\text{PIDkernel}}_{\bar{\varepsilon}}$	$\sigma^{\text{RMS}}_{\bar{\varepsilon}}$	$\sigma_{\bar{\varepsilon}}$
2018	$B^0_s \to K^0_S\pi^+\pi^-$	DD	MD	PP	87067.9e-8	1149.7e-8	7.2e-8	172.8e-8	130.7e-8	381.5e-8	3509.2e-8	3718.7e-8
2018	$B^0_s \to K^0_S\pi^+\pi^-$	DD	MU	PP	87109.7e-8	1152.4e-8	7.3e-8	155.0e-8	127.7e-8	381.7e-8	3509.2e-8	3718.7e-8
2018	$B^0_s \to K^0_S\pi^+\pi^-$	DD	MD	SP	44559.6e-8	746.3e-8	3.7e-8	91.4e-8	66.9e-8	195.3e-8	2025.9e-8	2170.8e-8
2018	$B^0_s \to K^0_S\pi^+\pi^-$	DD	MU	SP	44727.7e-8	757.7e-8	3.8e-8	82.6e-8	65.7e-8	196.0e-8	2025.9e-8	2174.4e-8
2017	$B^0_s \to K^0_S\pi^+\pi^-$	DD	MD	PP	87577.8e-8	1171.4e-8	6.7e-8	158.9e-8	105.4e-8	366.8e-8	3509.2e-8	3722.6e-8
2017	$B^0_s \to K^0_S\pi^+\pi^-$	DD	MU	PP	89429.2e-8	1217.8e-8	7.1e-8	181.3e-8	106.0e-8	374.5e-8	3509.2e-8	3739.2e-8
2017	$B^0_s \to K^0_S\pi^+\pi^-$	DD	MD	SP	46891.0e-8	779.6e-8	3.6e-8	86.7e-8	55.9e-8	196.4e-8	2025.9e-8	2182.1e-8
2017	$B^0_s \to K^0_S\pi^+\pi^-$	DD	MU	SP	48427.6e-8	827.1e-8	3.9e-8	99.9e-8	57.5e-8	202.8e-8	2025.9e-8	2200.7e-8
2016	$B^0_s \to K^0_S\pi^+\pi^-$	DD	MD	PP	91464.2e-8	1247.2e-8	7.1e-8	181.4e-8	123.6e-8	445.2e-8	3509.2e-8	3757.2e-8
2016	$B^0_s \to K^0_S\pi^+\pi^-$	DD	MU	PP	91254.1e-8	1230.4e-8	7.0e-8	171.9e-8	122.1e-8	444.1e-8	3509.2e-8	3751.0e-8
2016	$B^0_s \to K^0_S\pi^+\pi^-$	DD	MD	SP	45793.7e-8	804.7e-8	3.6e-8	92.4e-8	61.8e-8	222.9e-8	2025.9e-8	2194.1e-8
2016	$B^0_s \to K^0_S\pi^+\pi^-$	DD	MU	SP	46050.5e-8	802.8e-8	3.6e-8	87.9e-8	61.5e-8	224.1e-8	2025.9e-8	2193.3e-8
2015	$B^0_s \to K^0_S\pi^+\pi^-$	DD	MD	PP	90896.5e-8	1240.8e-8	7.8e-8	189.0e-8	198.8e-8	748.7e-8	3509.2e-8	3806.6e-8
2015	$B^0_s \to K^0_S\pi^+\pi^-$	DD	MU	PP	88059.7e-8	1209.8e-8	7.6e-8	174.3e-8	186.8e-8	725.3e-8	3509.2e-8	3790.7e-8
2015	$B^0_s \to K^0_S\pi^+\pi^-$	DD	MD	SP	39508.2e-8	731.1e-8	3.4e-8	87.1e-8	85.8e-8	325.4e-8	2025.9e-8	2181.7e-8
2015	$B^0_s \to K^0_S\pi^+\pi^-$	DD	MU	SP	37651.2e-8	716.3e-8	3.3e-8	79.0e-8	78.9e-8	310.1e-8	2025.9e-8	2174.0e-8
2012b	$B^0_s \to K^0_S\pi^+\pi^-$	DD	MD	PP	56215.1e-8	1136.5e-8	3.9e-8	176.0e-8	152.0e-8	3762.8e-8	3509.2e-8	5274.3e-8
2012b	$B^0_s \to K^0_S\pi^+\pi^-$	DD	MU	PP	57764.5e-8	1174.9e-8	4.1e-8	176.0e-8	159.9e-8	3866.5e-8	3509.2e-8	5357.3e-8
2012b	$B^0_s \to K^0_S\pi^+\pi^-$	DD	MD	SP	36849.8e-8	884.2e-8	2.6e-8	118.0e-8	97.9e-8	2466.5e-8	2025.9e-8	3315.7e-8
2012b	$B^0_s \to K^0_S\pi^+\pi^-$	DD	MU	SP	36551.9e-8	898.8e-8	2.6e-8	115.9e-8	97.1e-8	2446.6e-8	2025.9e-8	3304.7e-8
2012a	$B^0_s \to K^0_S\pi^+\pi^-$	DD	MD	PP	46226.3e-8	1072.4e-8	3.6e-8	161.7e-8	123.0e-8	3367.3e-8	3509.2e-8	4984.4e-8
2012a	$B^0_s \to K^0_S\pi^+\pi^-$	DD	MU	PP	45429.5e-8	1066.3e-8	3.6e-8	155.4e-8	115.7e-8	3309.3e-8	3509.2e-8	4943.7e-8
2012a	$B^0_s \to K^0_S\pi^+\pi^-$	DD	MD	SP	26851.5e-8	783.1e-8	2.1e-8	90.2e-8	71.9e-8	1956.0e-8	2025.9e-8	2925.2e-8
2012a	$B^0_s \to K^0_S\pi^+\pi^-$	DD	MU	SP	26460.2e-8	771.2e-8	2.0e-8	87.2e-8	68.0e-8	1927.5e-8	2025.9e-8	2902.9e-8
2011	$B^0_s \to K^0_S\pi^+\pi^-$	DD	MD	PP	54563.0e-8	1072.3e-8	3.7e-8	262.7e-8	287.1e-8	5376.0e-8	3509.2e-8	6520.5e-8
2011	$B^0_s \to K^0_S\pi^+\pi^-$	DD	MU	PP	55175.3e-8	1121.7e-8	4.0e-8	315.3e-8	276.6e-8	5436.3e-8	3509.2e-8	6580.4e-8
2011	$B^0_s \to K^0_S\pi^+\pi^-$	DD	MD	SP	27060.4e-8	700.3e-8	1.9e-8	132.8e-8	137.6e-8	2666.2e-8	2025.9e-8	3426.4e-8
2011	$B^0_s \to K^0_S\pi^+\pi^-$	DD	MU	SP	26986.0e-8	758.2e-8	1.9e-8	158.4e-8	130.8e-8	2658.9e-8	2025.9e-8	3433.8e-8
2018	$B^0_s \to K^0_S\pi^+\pi^-$	LL	MD	PP	32123.3e-8	806.0e-8	4.6e-8	65.0e-8	73.4e-8	169.3e-8	824.4e-8	1169.4e-8
2018	$B^0_s \to K^0_S\pi^+\pi^-$	LL	MU	PP	33679.5e-8	926.9e-8	4.9e-8	61.6e-8	76.6e-8	177.5e-8	824.4e-8	1257.0e-8
2018	$B^0_s \to K^0_S\pi^+\pi^-$	LL	MD	SP	20984.7e-8	624.2e-8	3.0e-8	41.7e-8	47.2e-8	110.6e-8	568.6e-8	853.9e-8
2018	$B^0_s \to K^0_S\pi^+\pi^-$	LL	MU	SP	22036.3e-8	707.7e-8	3.2e-8	39.8e-8	49.7e-8	116.2e-8	568.6e-8	917.4e-8
2017	$B^0_s \to K^0_S\pi^+\pi^-$	LL	MD	PP	35690.0e-8	861.1e-8	4.6e-8	64.8e-8	64.6e-8	195.1e-8	824.4e-8	1211.4e-8
2017	$B^0_s \to K^0_S\pi^+\pi^-$	LL	MU	PP	35723.1e-8	979.4e-8	4.9e-8	72.2e-8	63.9e-8	195.3e-8	824.4e-8	1298.6e-8
2017	$B^0_s \to K^0_S\pi^+\pi^-$	LL	MD	SP	24878.9e-8	688.8e-8	3.2e-8	45.1e-8	44.1e-8	136.0e-8	568.6e-8	905.7e-8
2017	$B^0_s \to K^0_S\pi^+\pi^-$	LL	MU	SP	24881.2e-8	768.5e-8	3.4e-8	49.6e-8	44.1e-8	136.0e-8	568.6e-8	967.9e-8
2016	$B^0_s \to K^0_S\pi^+\pi^-$	LL	MD	PP	39844.9e-8	978.5e-8	5.4e-8	80.6e-8	57.2e-8	208.6e-8	824.4e-8	1300.2e-8
2016	$B^0_s \to K^0_S\pi^+\pi^-$	LL	MU	PP	39710.7e-8	1056.7e-8	5.3e-8	74.6e-8	57.6e-8	207.9e-8	824.4e-8	1359.6e-8
2016	$B^0_s \to K^0_S\pi^+\pi^-$	LL	MD	SP	25513.6e-8	743.9e-8	3.4e-8	51.1e-8	36.4e-8	133.6e-8	568.6e-8	947.9e-8
2016	$B^0_s \to K^0_S\pi^+\pi^-$	LL	MU	SP	25217.0e-8	788.7e-8	3.4e-8	46.7e-8	36.6e-8	132.0e-8	568.6e-8	983.0e-8
2015	$B^0_s \to K^0_S\pi^+\pi^-$	LL	MD	PP	36351.7e-8	919.7e-8	4.9e-8	77.5e-8	122.4e-8	333.3e-8	824.4e-8	1287.5e-8
2015	$B^0_s \to K^0_S\pi^+\pi^-$	LL	MU	PP	35710.1e-8	986.7e-8	4.9e-8	68.9e-8	122.4e-8	327.4e-8	824.4e-8	1334.3e-8
2015	$B^0_s \to K^0_S\pi^+\pi^-$	LL	MD	SP	22316.0e-8	686.7e-8	3.0e-8	46.2e-8	72.8e-8	204.6e-8	568.6e-8	918.8e-8
2015	$B^0_s \to K^0_S\pi^+\pi^-$	LL	MU	SP	21768.1e-8	719.5e-8	2.9e-8	41.5e-8	72.6e-8	199.6e-8	568.6e-8	942.3e-8
2012b	$B^0_s \to K^0_S\pi^+\pi^-$	LL	MD	PP	17494.9e-8	740.7e-8	2.4e-8	54.4e-8	90.2e-8	1363.8e-8	824.4e-8	1760.5e-8
2012b	$B^0_s \to K^0_S\pi^+\pi^-$	LL	MU	PP	17467.7e-8	797.1e-8	2.4e-8	58.1e-8	91.9e-8	1361.6e-8	824.4e-8	1783.5e-8
2012b	$B^0_s \to K^0_S\pi^+\pi^-$	LL	MD	SP	12442.1e-8	605.8e-8	1.7e-8	37.0e-8	59.3e-8	969.9e-8	568.6e-8	1279.0e-8
2012b	$B^0_s \to K^0_S\pi^+\pi^-$	LL	MU	SP	12478.6e-8	658.6e-8	1.7e-8	40.0e-8	58.5e-8	972.7e-8	568.6e-8	1307.0e-8
2012a	$B^0_s \to K^0_S\pi^+\pi^-$	LL	MD	PP	20160.2e-8	857.4e-8	2.5e-8	51.2e-8	139.0e-8	2099.4e-8	824.4e-8	2417.4e-8
2012a	$B^0_s \to K^0_S\pi^+\pi^-$	LL	MU	PP	20044.2e-8	883.4e-8	2.6e-8	64.3e-8	134.1e-8	2087.3e-8	824.4e-8	2416.4e-8
2012a	$B^0_s \to K^0_S\pi^+\pi^-$	LL	MD	SP	8649.7e-8	545.0e-8	1.1e-8	24.5e-8	55.9e-8	900.7e-8	568.6e-8	1198.1e-8
2012a	$B^0_s \to K^0_S\pi^+\pi^-$	LL	MU	SP	8669.0e-8	552.1e-8	1.1e-8	31.0e-8	56.0e-8	902.7e-8	568.6e-8	1203.0e-8
2011	$B^0_s \to K^0_S\pi^+\pi^-$	LL	MD	PP	22373.9e-8	806.9e-8	2.3e-8	108.7e-8	100.3e-8	1665.8e-8	824.4e-8	2031.6e-8
2011	$B^0_s \to K^0_S\pi^+\pi^-$	LL	MU	PP	20429.2e-8	886.5e-8	2.4e-8	112.7e-8	93.5e-8	1521.0e-8	824.4e-8	1949.5e-8
2011	$B^0_s \to K^0_S\pi^+\pi^-$	LL	MD	SP	15930.2e-8	664.9e-8	1.6e-8	73.2e-8	69.6e-8	1186.0e-8	568.6e-8	1477.3e-8
2011	$B^0_s \to K^0_S\pi^+\pi^-$	LL	MU	SP	14323.1e-8	722.5e-8	1.7e-8	76.6e-8	64.2e-8	1066.4e-8	568.6e-8	1411.6e-8

Table C.46: $B^0_s \to K^0_S\pi^+\pi^-$ detailed efficiency tables with systematics. PP stands for favoured mode optimisation and SP for unfavoured mode optimisation.

Year	Mode	K^0_S	Polarity	Optimisation	$\bar{\varepsilon}$	$\sigma^{\text{stat}}_{\bar{\varepsilon}}$	$\sigma^{\text{tracking}}_{\bar{\varepsilon}}$	$\sigma^{\text{L0corr}}_{\bar{\varepsilon}}$	$\sigma^{\text{PIDMCsampling}}_{\bar{\varepsilon}}$	$\sigma^{\text{PIDkernel}}_{\bar{\varepsilon}}$	$\sigma^{\text{RMS}}_{\bar{\varepsilon}}$	$\sigma_{\bar{\varepsilon}}$
2018	$B^0_s \to K^0_S\pi^+K^-$	DD	MD	PP	84638.3e-8	1219.6e-8	7.6e-8	112.9e-8	116.1e-8	321.8e-8	574.8e-8	1395.6e-8
2018	$B^0_s \to K^0_S\pi^+K^-$	DD	MU	PP	85856.1e-8	1207.3e-8	7.4e-8	116.9e-8	117.9e-8	326.4e-8	574.8e-8	1386.4e-8
2018	$B^0_s \to K^0_S\pi^+K^-$	DD	MD	SP	64139.8e-8	1034.3e-8	5.7e-8	85.6e-8	84.2e-8	243.8e-8	514.9e-8	1186.9e-8
2018	$B^0_s \to K^0_S\pi^+K^-$	DD	MU	SP	65282.1e-8	1035.3e-8	5.7e-8	91.1e-8	91.0e-8	248.2e-8	514.9e-8	1189.6e-8
2017	$B^0_s \to K^0_S\pi^+K^-$	DD	MD	PP	89059.4e-8	1272.1e-8	7.2e-8	140.7e-8	79.3e-8	181.1e-8	574.8e-8	1416.9e-8
2017	$B^0_s \to K^0_S\pi^+K^-$	DD	MU	PP	88044.1e-8	1258.0e-8	7.1e-8	115.9e-8	80.8e-8	179.0e-8	574.8e-8	1401.8e-8
2017	$B^0_s \to K^0_S\pi^+K^-$	DD	MD	SP	68361.2e-8	1094.6e-8	5.5e-8	112.8e-8	61.3e-8	139.0e-8	514.9e-8	1224.4e-8
2017	$B^0_s \to K^0_S\pi^+K^-$	DD	MU	SP	66837.4e-8	1076.6e-8	5.4e-8	90.8e-8	62.0e-8	135.9e-8	514.9e-8	1206.2e-8
2016	$B^0_s \to K^0_S\pi^+K^-$	DD	MD	PP	102634.3e-8	1390.7e-8	8.2e-8	139.9e-8	89.0e-8	217.2e-8	574.8e-8	1529.4e-8
2016	$B^0_s \to K^0_S\pi^+K^-$	DD	MU	PP	97106.8e-8	1374.2e-8	7.8e-8	133.1e-8	84.7e-8	205.5e-8	574.8e-8	1511.9e-8
2016	$B^0_s \to K^0_S\pi^+K^-$	DD	MD	SP	78014.6e-8	1191.1e-8	6.3e-8	107.1e-8	67.7e-8	165.1e-8	514.9e-8	1314.2e-8
2016	$B^0_s \to K^0_S\pi^+K^-$	DD	MU	SP	75677.0e-8	1192.4e-8	6.1e-8	103.7e-8	65.7e-8	160.2e-8	514.9e-8	1314.4e-8
2015	$B^0_s \to K^0_S\pi^+K^-$	DD	MD	PP	91987.1e-8	1324.2e-8	7.7e-8	141.0e-8	173.3e-8	394.2e-8	574.8e-8	1513.1e-8
2015	$B^0_s \to K^0_S\pi^+K^-$	DD	MU	PP	88040.7e-8	1315.7e-8	7.5e-8	139.7e-8	166.2e-8	377.3e-8	574.8e-8	1500.3e-8
2015	$B^0_s \to K^0_S\pi^+K^-$	DD	MD	SP	68110.3e-8	1113.1e-8	5.7e-8	100.1e-8	134.9e-8	291.9e-8	514.9e-8	1271.8e-8
2015	$B^0_s \to K^0_S\pi^+K^-$	DD	MU	SP	65499.9e-8	1115.3e-8	5.6e-8	99.4e-8	135.6e-8	280.7e-8	514.9e-8	1271.3e-8
2012b	$B^0_s \to K^0_S\pi^+K^-$	DD	MD	PP	59368.3e-8	1365.0e-8	4.5e-8	128.9e-8	95.2e-8	1224.1e-8	574.8e-8	1928.1e-8
2012b	$B^0_s \to K^0_S\pi^+K^-$	DD	MU	PP	58031.9e-8	1267.0e-8	4.2e-8	195.7e-8	101.1e-8	1196.5e-8	574.8e-8	1848.3e-8
2012b	$B^0_s \to K^0_S\pi^+K^-$	DD	MD	SP	45893.8e-8	1182.1e-8	3.5e-8	92.0e-8	72.3e-8	946.3e-8	514.9e-8	1603.6e-8
2012b	$B^0_s \to K^0_S\pi^+K^-$	DD	MU	SP	45895.9e-8	1103.7e-8	3.3e-8	143.7e-8	77.3e-8	946.3e-8	514.9e-8	1551.0e-8
2012a	$B^0_s \to K^0_S\pi^+K^-$	DD	MD	PP	47086.2e-8	1244.4e-8	4.1e-8	123.3e-8	73.8e-8	993.1e-8	574.8e-8	1698.8e-8
2012a	$B^0_s \to K^0_S\pi^+K^-$	DD	MU	PP	47575.2e-8	1297.3e-8	4.3e-8	186.8e-8	77.6e-8	1003.4e-8	574.8e-8	1749.6e-8
2012a	$B^0_s \to K^0_S\pi^+K^-$	DD	MD	SP	38545.6e-8	1114.8e-8	3.3e-8	96.0e-8	61.9e-8	812.9e-8	514.9e-8	1477.1e-8
2012a	$B^0_s \to K^0_S\pi^+K^-$	DD	MU	SP	39258.3e-8	1156.6e-8	3.5e-8	147.4e-8	67.5e-8	828.0e-8	514.9e-8	1521.4e-8
2011	$B^0_s \to K^0_S\pi^+K^-$	DD	MD	PP	56430.0e-8	1340.7e-8	4.3e-8	229.3e-8	125.0e-8	2118.5e-8	574.8e-8	2585.4e-8
2011	$B^0_s \to K^0_S\pi^+K^-$	DD	MU	PP	54933.4e-8	1351.6e-8	4.5e-8	277.5e-8	122.5e-8	2062.4e-8	574.8e-8	2550.0e-8
2011	$B^0_s \to K^0_S\pi^+K^-$	DD	MD	SP	45860.8e-8	1199.7e-8	3.5e-8	184.8e-8	102.2e-8	1721.7e-8	514.9e-8	2171.0e-8
2011	$B^0_s \to K^0_S\pi^+K^-$	DD	MU	SP	45419.9e-8	1224.2e-8	3.7e-8	230.1e-8	104.8e-8	1705.2e-8	514.9e-8	2176.1e-8
2018	$B^0_s \to K^0_S\pi^+K^-$	LL	MD	PP	32520.7e-8	766.3e-8	4.5e-8	36.1e-8	49.7e-8	76.5e-8	782.6e-8	1099.7e-8
2018	$B^0_s \to K^0_S\pi^+K^-$	LL	MU	PP	31740.5e-8	744.5e-8	4.4e-8	34.4e-8	51.2e-8	74.7e-8	782.6e-8	1084.5e-8
2018	$B^0_s \to K^0_S\pi^+K^-$	LL	MD	SP	27436.5e-8	703.4e-8	3.9e-8	30.4e-8	42.9e-8	64.6e-8	588.1e-8	920.6e-8
2018	$B^0_s \to K^0_S\pi^+K^-$	LL	MU	SP	26835.3e-8	680.9e-8	3.7e-8	29.0e-8	44.1e-8	63.1e-8	588.1e-8	903.5e-8
2017	$B^0_s \to K^0_S\pi^+K^-$	LL	MD	PP	37014.3e-8	858.8e-8	4.7e-8	51.9e-8	104.4e-8	100.2e-8	782.6e-8	1172.0e-8
2017	$B^0_s \to K^0_S\pi^+K^-$	LL	MU	PP	35490.0e-8	815.1e-8	4.4e-8	40.7e-8	81.2e-8	96.0e-8	782.6e-8	1137.7e-8
2017	$B^0_s \to K^0_S\pi^+K^-$	LL	MD	SP	30323.7e-8	767.8e-8	3.9e-8	42.6e-8	82.6e-8	82.1e-8	588.1e-8	975.1e-8
2017	$B^0_s \to K^0_S\pi^+K^-$	LL	MU	SP	29323.5e-8	737.8e-8	3.7e-8	34.2e-8	65.9e-8	79.3e-8	588.1e-8	949.8e-8
2016	$B^0_s \to K^0_S\pi^+K^-$	LL	MD	PP	38464.1e-8	868.4e-8	4.8e-8	46.5e-8	42.9e-8	103.9e-8	782.6e-8	1175.4e-8
2016	$B^0_s \to K^0_S\pi^+K^-$	LL	MU	PP	37596.6e-8	877.1e-8	4.8e-8	44.4e-8	43.0e-8	101.6e-8	782.6e-8	1181.5e-8
2016	$B^0_s \to K^0_S\pi^+K^-$	LL	MD	SP	32022.3e-8	787.3e-8	4.0e-8	38.7e-8	35.6e-8	86.5e-8	588.1e-8	987.9e-8
2016	$B^0_s \to K^0_S\pi^+K^-$	LL	MU	SP	31092.1e-8	784.9e-8	3.9e-8	35.8e-8	35.3e-8	84.0e-8	588.1e-8	985.6e-8
2015	$B^0_s \to K^0_S\pi^+K^-$	LL	MD	PP	36821.2e-8	845.5e-8	4.7e-8	44.3e-8	96.8e-8	177.1e-8	782.6e-8	1170.5e-8
2015	$B^0_s \to K^0_S\pi^+K^-$	LL	MU	PP	35265.9e-8	834.2e-8	4.6e-8	42.8e-8	111.2e-8	169.6e-8	782.6e-8	1162.5e-8
2015	$B^0_s \to K^0_S\pi^+K^-$	LL	MD	SP	25111.4e-8	682.4e-8	3.2e-8	30.1e-8	68.6e-8	120.8e-8	588.1e-8	912.0e-8
2015	$B^0_s \to K^0_S\pi^+K^-$	LL	MU	SP	24209.9e-8	684.8e-8	3.2e-8	30.0e-8	76.3e-8	116.5e-8	588.1e-8	913.8e-8
2012b	$B^0_s \to K^0_S\pi^+K^-$	LL	MD	PP	17437.9e-8	754.5e-8	2.4e-8	36.1e-8	50.9e-8	361.3e-8	782.6e-8	1147.2e-8
2012b	$B^0_s \to K^0_S\pi^+K^-$	LL	MU	PP	17727.8e-8	705.0e-8	2.3e-8	46.6e-8	65.0e-8	367.3e-8	782.6e-8	1118.4e-8
2012b	$B^0_s \to K^0_S\pi^+K^-$	LL	MD	SP	9408.0e-8	558.6e-8	1.4e-8	20.1e-8	30.1e-8	194.9e-8	588.1e-8	835.0e-8
2012b	$B^0_s \to K^0_S\pi^+K^-$	LL	MU	SP	8770.9e-8	493.3e-8	1.2e-8	22.3e-8	32.0e-8	181.7e-8	588.1e-8	789.8e-8
2012a	$B^0_s \to K^0_S\pi^+K^-$	LL	MD	PP	20964.4e-8	848.4e-8	2.4e-8	36.4e-8	49.5e-8	697.5e-8	782.6e-8	1350.0e-8
2012a	$B^0_s \to K^0_S\pi^+K^-$	LL	MU	PP	19568.7e-8	799.3e-8	2.2e-8	54.9e-8	47.9e-8	651.1e-8	782.6e-8	1296.4e-8
2012a	$B^0_s \to K^0_S\pi^+K^-$	LL	MD	SP	15719.2e-8	731.7e-8	1.8e-8	29.4e-8	37.5e-8	523.0e-8	588.1e-8	1075.6e-8
2012a	$B^0_s \to K^0_S\pi^+K^-$	LL	MU	SP	14491.5e-8	671.3e-8	1.6e-8	42.4e-8	35.7e-8	482.1e-8	588.1e-8	1015.9e-8
2011	$B^0_s \to K^0_S\pi^+K^-$	LL	MD	PP	23797.8e-8	913.6e-8	2.9e-8	73.8e-8	67.6e-8	699.3e-8	782.6e-8	1395.1e-8
2011	$B^0_s \to K^0_S\pi^+K^-$	LL	MU	PP	21333.2e-8	832.9e-8	2.4e-8	73.7e-8	48.7e-8	626.9e-8	782.6e-8	1306.5e-8
2011	$B^0_s \to K^0_S\pi^+K^-$	LL	MD	SP	19270.9e-8	816.9e-8	2.3e-8	58.2e-8	52.0e-8	566.3e-8	588.1e-8	1157.6e-8
2011	$B^0_s \to K^0_S\pi^+K^-$	LL	MU	SP	17671.8e-8	755.7e-8	2.0e-8	59.8e-8	38.3e-8	519.3e-8	588.1e-8	1091.6e-8

Table C.47: $B^0_s \to K^0_S\pi^+K^-$ detailed efficiency tables with systematics. PP stands for favoured mode optimisation and SP for unfavoured mode optimisation.

Year	Mode	K^0_S	Polarity	Optimisation	$\bar{\varepsilon}$	$\sigma^{\text{stat}}_{\bar{\varepsilon}}$	$\sigma^{\text{tracking}}_{\bar{\varepsilon}}$	$\sigma^{\text{L0corr}}_{\bar{\varepsilon}}$	$\sigma^{\text{PIDMCsampling}}_{\bar{\varepsilon}}$	$\sigma^{\text{PIDkernel}}_{\bar{\varepsilon}}$	$\sigma^{\text{RMS}}_{\bar{\varepsilon}}$	$\sigma_{\bar{\varepsilon}}$
2018	$B^0_s \to K^0_S K^+\pi^-$	DD	MD	PP	87245.8e-8	1172.0e-8	7.5e-8	114.4e-8	95.7e-8	248.4e-8	477.2e-8	1298.2e-8
2018	$B^0_s \to K^0_S K^+\pi^-$	DD	MU	PP	86594.0e-8	1129.3e-8	7.2e-8	110.8e-8	97.9e-8	246.6e-8	477.2e-8	1259.3e-8
2018	$B^0_s \to K^0_S K^+\pi^-$	DD	MD	SP	68282.8e-8	1028.1e-8	5.9e-8	92.0e-8	74.0e-8	194.4e-8	447.6e-8	1144.2e-8
2018	$B^0_s \to K^0_S K^+\pi^-$	DD	MU	SP	67304.8e-8	985.9e-8	5.6e-8	88.2e-8	75.4e-8	191.6e-8	447.6e-8	1105.7e-8
2017	$B^0_s \to K^0_S K^+\pi^-$	DD	MD	PP	90676.9e-8	1225.7e-8	7.2e-8	142.8e-8	102.9e-8	290.5e-8	477.2e-8	1358.5e-8
2017	$B^0_s \to K^0_S K^+\pi^-$	DD	MU	PP	90265.9e-8	1215.4e-8	7.0e-8	113.8e-8	101.2e-8	289.2e-8	477.2e-8	1346.0e-8
2017	$B^0_s \to K^0_S K^+\pi^-$	DD	MD	SP	74917.0e-8	1103.7e-8	5.9e-8	119.4e-8	84.5e-8	240.0e-8	447.6e-8	1223.7e-8
2017	$B^0_s \to K^0_S K^+\pi^-$	DD	MU	SP	75128.6e-8	1097.8e-8	5.8e-8	95.4e-8	82.9e-8	240.7e-8	447.6e-8	1216.3e-8
2016	$B^0_s \to K^0_S K^+\pi^-$	DD	MD	PP	99411.6e-8	1294.4e-8	7.8e-8	140.5e-8	63.5e-8	225.8e-8	477.2e-8	1406.4e-8
2016	$B^0_s \to K^0_S K^+\pi^-$	DD	MU	PP	95182.8e-8	1276.0e-8	7.6e-8	119.1e-8	60.4e-8	216.2e-8	477.2e-8	1385.9e-8
2016	$B^0_s \to K^0_S K^+\pi^-$	DD	MD	SP	75856.1e-8	1118.4e-8	6.0e-8	108.8e-8	48.7e-8	172.3e-8	447.6e-8	1222.8e-8
2016	$B^0_s \to K^0_S K^+\pi^-$	DD	MU	SP	72493.4e-8	1103.6e-8	5.8e-8	93.1e-8	45.8e-8	164.6e-8	447.6e-8	1206.8e-8
2015	$B^0_s \to K^0_S K^+\pi^-$	DD	MD	PP	88707.8e-8	1228.9e-8	7.4e-8	133.6e-8	131.7e-8	332.1e-8	477.2e-8	1372.4e-8
2015	$B^0_s \to K^0_S K^+\pi^-$	DD	MU	PP	84899.2e-8	1209.5e-8	7.1e-8	110.1e-8	123.0e-8	317.9e-8	477.2e-8	1348.6e-8
2015	$B^0_s \to K^0_S K^+\pi^-$	DD	MD	SP	63000.0e-8	1021.4e-8	5.3e-8	94.8e-8	94.9e-8	235.9e-8	447.6e-8	1147.7e-8
2015	$B^0_s \to K^0_S K^+\pi^-$	DD	MU	SP	59536.7e-8	999.1e-8	5.0e-8	77.4e-8	87.0e-8	222.9e-8	447.6e-8	1123.3e-8
2012b	$B^0_s \to K^0_S K^+\pi^-$	DD	MD	PP	56849.0e-8	1278.0e-8	4.4e-8	117.4e-8	66.9e-8	1500.9e-8	477.2e-8	2032.7e-8
2012b	$B^0_s \to K^0_S K^+\pi^-$	DD	MU	PP	56546.7e-8	1191.7e-8	4.2e-8	183.1e-8	64.4e-8	1493.0e-8	477.2e-8	1978.5e-8
2012b	$B^0_s \to K^0_S K^+\pi^-$	DD	MD	SP	41948.0e-8	1093.0e-8	3.2e-8	90.9e-8	49.1e-8	1107.5e-8	447.6e-8	1622.5e-8
2012b	$B^0_s \to K^0_S K^+\pi^-$	DD	MU	SP	41083.0e-8	1008.1e-8	3.0e-8	142.3e-8	46.2e-8	1084.7e-8	447.6e-8	1554.2e-8
2012a	$B^0_s \to K^0_S K^+\pi^-$	DD	MD	PP	43138.9e-8	1124.0e-8	3.8e-8	104.5e-8	65.9e-8	1749.4e-8	477.2e-8	2137.0e-8
2012a	$B^0_s \to K^0_S K^+\pi^-$	DD	MU	PP	44484.6e-8	1161.5e-8	3.9e-8	173.2e-8	70.5e-8	1804.0e-8	477.2e-8	2206.0e-8
2012a	$B^0_s \to K^0_S K^+\pi^-$	DD	MD	SP	33519.7e-8	982.2e-8	2.9e-8	80.9e-8	51.9e-8	1359.3e-8	447.6e-8	1738.5e-8
2012a	$B^0_s \to K^0_S K^+\pi^-$	DD	MU	SP	35425.0e-8	1036.4e-8	3.2e-8	142.1e-8	56.7e-8	1436.6e-8	447.6e-8	1833.5e-8
2011	$B^0_s \to K^0_S K^+\pi^-$	DD	MD	PP	50917.3e-8	1181.2e-8	4.0e-8	195.3e-8	74.6e-8	1730.3e-8	477.2e-8	2158.8e-8
2011	$B^0_s \to K^0_S K^+\pi^-$	DD	MU	PP	50350.3e-8	1188.4e-8	3.9e-8	242.6e-8	79.8e-8	1711.0e-8	477.2e-8	2152.4e-8
2011	$B^0_s \to K^0_S K^+\pi^-$	DD	MD	SP	43263.1e-8	1082.2e-8	3.4e-8	160.7e-8	64.8e-8	1470.2e-8	447.6e-8	1887.6e-8
2011	$B^0_s \to K^0_S K^+\pi^-$	DD	MU	SP	43442.7e-8	1108.2e-8	3.3e-8	204.6e-8	71.2e-8	1476.3e-8	447.6e-8	1911.8e-8
2018	$B^0_s \to K^0_S K^+\pi^-$	LL	MD	PP	32586.9e-8	794.5e-8	4.7e-8	36.7e-8	76.1e-8	207.5e-8	1198.8e-8	1455.5e-8
2018	$B^0_s \to K^0_S K^+\pi^-$	LL	MU	PP	30897.2e-8	809.8e-8	4.4e-8	34.0e-8	77.9e-8	196.7e-8	1198.8e-8	1462.4e-8
2018	$B^0_s \to K^0_S K^+\pi^-$	LL	MD	SP	27138.0e-8	714.3e-8	4.0e-8	29.9e-8	63.8e-8	172.8e-8	969.3e-8	1218.4e-8
2018	$B^0_s \to K^0_S K^+\pi^-$	LL	MU	SP	25746.6e-8	726.0e-8	3.7e-8	27.5e-8	66.7e-8	163.9e-8	969.3e-8	1224.2e-8
2017	$B^0_s \to K^0_S K^+\pi^-$	LL	MD	PP	36566.9e-8	862.2e-8	4.8e-8	51.4e-8	50.4e-8	117.4e-8	1198.8e-8	1483.1e-8
2017	$B^0_s \to K^0_S K^+\pi^-$	LL	MU	PP	35424.2e-8	945.1e-8	4.6e-8	40.0e-8	47.1e-8	113.7e-8	1198.8e-8	1532.0e-8
2017	$B^0_s \to K^0_S K^+\pi^-$	LL	MD	SP	29133.2e-8	756.2e-8	3.9e-8	41.5e-8	39.8e-8	93.5e-8	969.3e-8	1234.2e-8
2017	$B^0_s \to K^0_S K^+\pi^-$	LL	MU	SP	27576.1e-8	801.4e-8	3.6e-8	31.4e-8	36.8e-8	88.5e-8	969.3e-8	1261.7e-8
2016	$B^0_s \to K^0_S K^+\pi^-$	LL	MD	PP	38698.2e-8	894.8e-8	4.9e-8	47.6e-8	38.9e-8	143.0e-8	1198.8e-8	1504.0e-8
2016	$B^0_s \to K^0_S K^+\pi^-$	LL	MU	PP	41017.9e-8	1045.6e-8	5.3e-8	45.0e-8	43.2e-8	151.6e-8	1198.8e-8	1599.2e-8
2016	$B^0_s \to K^0_S K^+\pi^-$	LL	MD	SP	30782.2e-8	782.5e-8	3.9e-8	38.9e-8	31.1e-8	113.8e-8	969.3e-8	1251.9e-8
2016	$B^0_s \to K^0_S K^+\pi^-$	LL	MU	SP	32142.3e-8	901.2e-8	4.2e-8	37.2e-8	34.2e-8	118.8e-8	969.3e-8	1329.8e-8
2015	$B^0_s \to K^0_S K^+\pi^-$	LL	MD	PP	37032.7e-8	877.0e-8	4.8e-8	51.6e-8	88.1e-8	204.5e-8	1198.8e-8	1502.8e-8
2015	$B^0_s \to K^0_S K^+\pi^-$	LL	MU	PP	36776.3e-8	999.1e-8	4.9e-8	43.8e-8	89.6e-8	203.1e-8	1198.8e-8	1576.8e-8
2015	$B^0_s \to K^0_S K^+\pi^-$	LL	MD	SP	27569.1e-8	742.3e-8	3.6e-8	38.1e-8	67.8e-8	152.3e-8	969.3e-8	1232.8e-8
2015	$B^0_s \to K^0_S K^+\pi^-$	LL	MU	SP	27489.4e-8	827.5e-8	3.7e-8	33.7e-8	67.5e-8	151.8e-8	969.3e-8	1285.7e-8
2012b	$B^0_s \to K^0_S K^+\pi^-$	LL	MD	PP	16224.2e-8	713.6e-8	2.3e-8	31.8e-8	62.8e-8	388.6e-8	1198.8e-8	1449.9e-8
2012b	$B^0_s \to K^0_S K^+\pi^-$	LL	MU	PP	16160.2e-8	703.3e-8	2.3e-8	50.6e-8	80.3e-8	387.1e-8	1198.8e-8	1445.9e-8
2012b	$B^0_s \to K^0_S K^+\pi^-$	LL	MD	SP	8328.4e-8	496.8e-8	1.2e-8	12.8e-8	32.8e-8	199.5e-8	969.3e-8	1107.8e-8
2012b	$B^0_s \to K^0_S K^+\pi^-$	LL	MU	SP	9697.3e-8	525.7e-8	1.4e-8	25.9e-8	59.7e-8	232.3e-8	969.3e-8	1128.7e-8
2012a	$B^0_s \to K^0_S K^+\pi^-$	LL	MD	PP	18444.6e-8	776.3e-8	2.2e-8	32.4e-8	78.8e-8	646.2e-8	1198.8e-8	1569.9e-8
2012a	$B^0_s \to K^0_S K^+\pi^-$	LL	MU	PP	19115.9e-8	824.0e-8	2.4e-8	60.1e-8	77.5e-8	669.7e-8	1198.8e-8	1604.4e-8
2012a	$B^0_s \to K^0_S K^+\pi^-$	LL	MD	SP	14489.5e-8	687.4e-8	1.8e-8	26.2e-8	63.5e-8	507.6e-8	969.3e-8	1294.0e-8
2012a	$B^0_s \to K^0_S K^+\pi^-$	LL	MU	SP	15246.0e-8	725.7e-8	1.9e-8	48.2e-8	62.2e-8	534.1e-8	969.3e-8	1325.8e-8
2011	$B^0_s \to K^0_S K^+\pi^-$	LL	MD	PP	22270.4e-8	838.7e-8	2.5e-8	68.7e-8	56.4e-8	558.4e-8	1198.8e-8	1568.5e-8
2011	$B^0_s \to K^0_S K^+\pi^-$	LL	MU	PP	20937.2e-8	876.8e-8	2.4e-8	91.2e-8	63.3e-8	525.0e-8	1198.8e-8	1579.2e-8
2011	$B^0_s \to K^0_S K^+\pi^-$	LL	MD	SP	17436.4e-8	734.8e-8	2.0e-8	51.2e-8	45.6e-8	437.2e-8	969.3e-8	1294.3e-8
2011	$B^0_s \to K^0_S K^+\pi^-$	LL	MU	SP	16302.4e-8	753.9e-8	1.9e-8	67.1e-8	48.7e-8	408.8e-8	969.3e-8	1296.8e-8

Table C.48: $B^0_s \to K^0_S K^+\pi^-$ detailed efficiency tables with systematics. PP stands for favoured mode optimisation and SP for unfavoured mode optimisation.

Year	Mode	K^0_S	Polarity	Optimisation	$\bar{\varepsilon}$	$\sigma^{\text{stat}}_{\bar{\varepsilon}}$	$\sigma^{\text{tracking}}_{\bar{\varepsilon}}$	$\sigma^{\text{L0corr}}_{\bar{\varepsilon}}$	$\sigma^{\text{PIDMCsampling}}_{\bar{\varepsilon}}$	$\sigma^{\text{PIDkernel}}_{\bar{\varepsilon}}$	$\sigma^{\text{RMS}}_{\bar{\varepsilon}}$	$\sigma_{\bar{\varepsilon}}$
2018	$B^0_s \to K^0_S K^+ K^-$	DD	MD	PP	85119.3e-8	1102.2e-8	7.4e-8	119.7e-8	158.6e-8	354.4e-8	6328.2e-8	6436.3e-8
2018	$B^0_s \to K^0_S K^+ K^-$	DD	MU	PP	82078.7e-8	1045.0e-8	6.9e-8	131.8e-8	152.8e-8	341.8e-8	6328.2e-8	6426.2e-8
2018	$B^0_s \to K^0_S K^+ K^-$	DD	MD	SP	56258.4e-8	894.0e-8	5.0e-8	82.1e-8	105.8e-8	234.3e-8	3777.9e-8	3891.6e-8
2018	$B^0_s \to K^0_S K^+ K^-$	DD	MU	SP	53443.6e-8	837.1e-8	4.5e-8	88.8e-8	99.3e-8	222.5e-8	3777.9e-8	3878.2e-8
2017	$B^0_s \to K^0_S K^+ K^-$	DD	MD	PP	89607.3e-8	1161.8e-8	7.5e-8	264.0e-8	187.6e-8	464.1e-8	6328.2e-8	6458.8e-8
2017	$B^0_s \to K^0_S K^+ K^-$	DD	MU	PP	86047.7e-8	1123.5e-8	7.1e-8	123.9e-8	177.5e-8	445.7e-8	6328.2e-8	6446.2e-8
2017	$B^0_s \to K^0_S K^+ K^-$	DD	MD	SP	43214.9e-8	802.6e-8	3.7e-8	132.6e-8	87.8e-8	223.8e-8	3777.9e-8	3872.0e-8
2017	$B^0_s \to K^0_S K^+ K^-$	DD	MU	SP	41871.1e-8	776.1e-8	3.5e-8	62.3e-8	83.2e-8	216.9e-8	3777.9e-8	3864.3e-8
2016	$B^0_s \to K^0_S K^+ K^-$	DD	MD	PP	104239.8e-8	1251.9e-8	8.7e-8	166.9e-8	192.5e-8	360.4e-8	6328.2e-8	6465.9e-8
2016	$B^0_s \to K^0_S K^+ K^-$	DD	MU	PP	100224.3e-8	1212.8e-8	8.2e-8	159.5e-8	195.2e-8	346.5e-8	6328.2e-8	6457.6e-8
2016	$B^0_s \to K^0_S K^+ K^-$	DD	MD	SP	56104.7e-8	911.3e-8	4.7e-8	95.5e-8	105.1e-8	194.0e-8	3777.9e-8	3893.7e-8
2016	$B^0_s \to K^0_S K^+ K^-$	DD	MU	SP	53040.6e-8	877.0e-8	4.4e-8	90.3e-8	102.3e-8	183.4e-8	3777.9e-8	3885.1e-8
2015	$B^0_s \to K^0_S K^+ K^-$	DD	MD	PP	93200.5e-8	1178.7e-8	8.3e-8	151.0e-8	251.6e-8	496.8e-8	6328.2e-8	6462.8e-8
2015	$B^0_s \to K^0_S K^+ K^-$	DD	MU	PP	89459.1e-8	1118.0e-8	7.6e-8	151.1e-8	233.7e-8	476.9e-8	6328.2e-8	6449.9e-8
2015	$B^0_s \to K^0_S K^+ K^-$	DD	MD	SP	45722.4e-8	817.8e-8	4.1e-8	78.4e-8	122.6e-8	243.7e-8	3777.9e-8	3875.8e-8
2015	$B^0_s \to K^0_S K^+ K^-$	DD	MU	SP	44161.3e-8	778.1e-8	3.8e-8	79.4e-8	111.2e-8	235.4e-8	3777.9e-8	3866.8e-8
2012b	$B^0_s \to K^0_S K^+ K^-$	DD	MD	PP	57639.5e-8	1105.8e-8	3.8e-8	143.9e-8	142.5e-8	4128.3e-8	6328.2e-8	7638.9e-8
2012b	$B^0_s \to K^0_S K^+ K^-$	DD	MU	PP	57801.8e-8	1148.5e-8	3.9e-8	336.5e-8	142.5e-8	4139.9e-8	6328.2e-8	7657.5e-8
2012b	$B^0_s \to K^0_S K^+ K^-$	DD	MD	SP	42085.3e-8	943.4e-8	2.8e-8	109.4e-8	102.5e-8	3014.3e-8	3777.9e-8	4926.5e-8
2012b	$B^0_s \to K^0_S K^+ K^-$	DD	MU	SP	42440.0e-8	981.7e-8	2.9e-8	262.8e-8	103.1e-8	3039.7e-8	3777.9e-8	4955.4e-8
2012a	$B^0_s \to K^0_S K^+ K^-$	DD	MD	PP	49150.9e-8	1184.5e-8	3.9e-8	144.7e-8	144.5e-8	3254.0e-8	6328.2e-8	7216.6e-8
2012a	$B^0_s \to K^0_S K^+ K^-$	DD	MU	PP	46342.6e-8	1104.4e-8	3.4e-8	291.6e-8	134.1e-8	3068.1e-8	6328.2e-8	7126.1e-8
2012a	$B^0_s \to K^0_S K^+ K^-$	DD	MD	SP	31713.5e-8	942.7e-8	2.5e-8	86.9e-8	93.3e-8	2099.6e-8	3777.9e-8	4425.6e-8
2012a	$B^0_s \to K^0_S K^+ K^-$	DD	MU	SP	29660.7e-8	874.5e-8	2.2e-8	174.8e-8	86.1e-8	1963.7e-8	3777.9e-8	4351.0e-8
2011	$B^0_s \to K^0_S K^+ K^-$	DD	MD	PP	53924.5e-8	1150.2e-8	3.5e-8	238.4e-8	258.0e-8	4685.6e-8	6328.2e-8	7965.4e-8
2011	$B^0_s \to K^0_S K^+ K^-$	DD	MU	PP	52085.8e-8	1121.8e-8	3.3e-8	346.0e-8	245.7e-8	4525.8e-8	6328.2e-8	7871.9e-8
2011	$B^0_s \to K^0_S K^+ K^-$	DD	MD	SP	40166.5e-8	993.0e-8	2.6e-8	175.9e-8	191.6e-8	3490.1e-8	3777.9e-8	5244.7e-8
2011	$B^0_s \to K^0_S K^+ K^-$	DD	MU	SP	38767.2e-8	959.3e-8	2.5e-8	249.6e-8	182.4e-8	3368.5e-8	3777.9e-8	5161.0e-8
2018	$B^0_s \to K^0_S K^+ K^-$	LL	MD	PP	3343.6e-7	302.0e-7	2.1e-7	15.8e-7	49.2e-7	21.9e-7	556.1e-7	635.3e-7
2018	$B^0_s \to K^0_S K^+ K^-$	LL	MU	PP	4065.3e-7	289.3e-7	2.0e-7	17.9e-7	44.8e-7	26.6e-7	556.1e-7	629.3e-7
2018	$B^0_s \to K^0_S K^+ K^-$	LL	MD	SP	2303.2e-7	255.4e-7	1.5e-7	11.5e-7	35.4e-7	15.1e-7	371.7e-7	452.8e-7
2018	$B^0_s \to K^0_S K^+ K^-$	LL	MU	SP	3014.4e-7	244.2e-7	1.4e-7	12.8e-7	32.9e-7	19.8e-7	371.7e-7	446.6e-7
2017	$B^0_s \to K^0_S K^+ K^-$	LL	MD	PP	4141.0e-7	333.7e-7	2.3e-7	36.5e-7	60.4e-7	17.2e-7	556.1e-7	652.6e-7
2017	$B^0_s \to K^0_S K^+ K^-$	LL	MU	PP	3960.6e-7	319.1e-7	2.2e-7	17.2e-7	61.0e-7	16.5e-7	556.1e-7	644.5e-7
2017	$B^0_s \to K^0_S K^+ K^-$	LL	MD	SP	2349.0e-7	251.1e-7	1.3e-7	21.6e-7	33.0e-7	9.8e-7	371.7e-7	450.4e-7
2017	$B^0_s \to K^0_S K^+ K^-$	LL	MU	SP	2183.0e-7	239.7e-7	1.2e-7	10.0e-7	34.9e-7	9.1e-7	371.7e-7	443.9e-7
2016	$B^0_s \to K^0_S K^+ K^-$	LL	MD	PP	4769.6e-7	354.6e-7	2.6e-7	24.1e-7	57.2e-7	24.6e-7	556.1e-7	662.9e-7
2016	$B^0_s \to K^0_S K^+ K^-$	LL	MU	PP	4941.7e-7	336.9e-7	2.4e-7	21.7e-7	48.2e-7	25.5e-7	556.1e-7	652.8e-7
2016	$B^0_s \to K^0_S K^+ K^-$	LL	MD	SP	2640.3e-7	260.9e-7	1.4e-7	13.7e-7	28.2e-7	13.6e-7	371.7e-7	455.4e-7
2016	$B^0_s \to K^0_S K^+ K^-$	LL	MU	SP	2479.2e-7	245.8e-7	1.3e-7	12.0e-7	26.1e-7	12.8e-7	371.7e-7	446.8e-7
2015	$B^0_s \to K^0_S K^+ K^-$	LL	MD	PP	4101.9e-7	330.8e-7	2.0e-7	21.1e-7	40.2e-7	23.7e-7	556.1e-7	649.0e-7
2015	$B^0_s \to K^0_S K^+ K^-$	LL	MU	PP	4318.5e-7	314.5e-7	1.9e-7	20.6e-7	37.5e-7	24.9e-7	556.1e-7	640.8e-7
2015	$B^0_s \to K^0_S K^+ K^-$	LL	MD	SP	3369.7e-7	304.4e-7	1.7e-7	17.7e-7	33.5e-7	19.4e-7	371.7e-7	482.3e-7
2015	$B^0_s \to K^0_S K^+ K^-$	LL	MU	SP	3690.4e-7	290.0e-7	1.6e-7	17.4e-7	32.2e-7	21.3e-7	371.7e-7	473.4e-7
2012b	$B^0_s \to K^0_S K^+ K^-$	LL	MD	PP	19787.7e-8	2751.8e-8	8.8e-8	168.4e-8	412.0e-8	1470.2e-8	5560.9e-8	6391.8e-8
2012b	$B^0_s \to K^0_S K^+ K^-$	LL	MU	PP	17228.0e-8	2704.4e-8	8.4e-8	474.4e-8	402.8e-8	1280.0e-8	5560.9e-8	6345.3e-8
2012b	$B^0_s \to K^0_S K^+ K^-$	LL	MD	SP	16741.6e-8	2551.2e-8	7.5e-8	149.8e-8	359.1e-8	1243.9e-8	3717.1e-8	4693.0e-8
2012b	$B^0_s \to K^0_S K^+ K^-$	LL	MU	SP	14071.8e-8	2538.6e-8	7.4e-8	431.6e-8	368.1e-8	1045.5e-8	3717.1e-8	4655.8e-8
2012a	$B^0_s \to K^0_S K^+ K^-$	LL	MD	PP	18417.8e-8	3231.9e-8	9.2e-8	157.7e-8	238.6e-8	1252.5e-8	5560.9e-8	6558.9e-8
2012a	$B^0_s \to K^0_S K^+ K^-$	LL	MU	PP	22118.6e-8	3294.0e-8	9.7e-8	506.3e-8	251.5e-8	1504.1e-8	5560.9e-8	6660.0e-8
2012a	$B^0_s \to K^0_S K^+ K^-$	LL	MD	SP	14607.7e-8	2980.8e-8	7.9e-8	134.8e-8	201.7e-8	993.4e-8	3717.1e-8	4873.2e-8
2012a	$B^0_s \to K^0_S K^+ K^-$	LL	MU	SP	19065.3e-8	3055.4e-8	8.3e-8	438.7e-8	213.2e-8	1296.5e-8	3717.1e-8	5007.1e-8
2011	$B^0_s \to K^0_S K^+ K^-$	LL	MD	PP	26078.4e-8	3392.3e-8	9.6e-8	360.1e-8	586.1e-8	1490.6e-8	5560.9e-8	6717.6e-8
2011	$B^0_s \to K^0_S K^+ K^-$	LL	MU	PP	25542.5e-8	3189.9e-8	8.8e-8	482.1e-8	604.4e-8	1460.0e-8	5560.9e-8	6620.3e-8
2011	$B^0_s \to K^0_S K^+ K^-$	LL	MD	SP	18458.2e-8	2898.8e-8	7.0e-8	243.0e-8	432.2e-8	1055.1e-8	3717.1e-8	4855.9e-8
2011	$B^0_s \to K^0_S K^+ K^-$	LL	MU	SP	16550.2e-8	2713.7e-8	6.3e-8	333.1e-8	480.0e-8	946.0e-8	3717.1e-8	4734.7e-8

Table C.49: $B^0_s \to K^0_S K^+ K^-$ detailed efficiency tables with systematics. PP stands for favoured mode optimisation and SP for unfavoured mode optimisation.

C.8 Polarity combined efficiency tables with systematics

Year	Mode	K^0_S	$\bar{\varepsilon}$	$\sigma^{\text{stat}}_{\bar{\varepsilon}}$	$\sigma^{\text{tracking}}_{\bar{\varepsilon}}$	$\sigma^{\text{L0corr}}_{\bar{\varepsilon}}$	$\sigma^{\text{PIDMCsampling}}_{\bar{\varepsilon}}$	$\sigma^{\text{PIDkernel}}_{\bar{\varepsilon}}$	$\sigma^{\text{RMS}}_{\bar{\varepsilon}}$	$\sigma_{\bar{\varepsilon}}$
2018	$B^0_d \to K^0_S\pi^+\pi^-$	DD	82098.9e-8	619.1e-8	3.5e-8	84.1e-8	42.9e-8	270.8e-8	1219.8e-8	1397.7e-8
2017	$B^0_d \to K^0_S\pi^+\pi^-$	DD	83328.8e-8	643.4e-8	3.4e-8	85.7e-8	42.4e-8	188.8e-8	1219.8e-8	1395.2e-8
2016	$B^0_d \to K^0_S\pi^+\pi^-$	DD	86933.3e-8	656.5e-8	3.4e-8	89.7e-8	38.6e-8	229.4e-8	1219.8e-8	1407.5e-8
2015	$B^0_d \to K^0_S\pi^+\pi^-$	DD	83587.6e-8	651.8e-8	3.4e-8	94.2e-8	70.3e-8	301.2e-8	1219.8e-8	1420.3e-8
2012b	$B^0_d \to K^0_S\pi^+\pi^-$	DD	51940.4e-8	583.6e-8	1.8e-8	85.8e-8	38.9e-8	711.8e-8	1219.8e-8	1531.0e-8
2012a	$B^0_d \to K^0_S\pi^+\pi^-$	DD	41160.2e-8	561.6e-8	1.7e-8	77.9e-8	36.0e-8	542.2e-8	1219.8e-8	1450.7e-8
2011	$B^0_d \to K^0_S\pi^+\pi^-$	DD	49196.5e-8	597.9e-8	1.8e-8	145.4e-8	43.8e-8	666.1e-8	1219.8e-8	1520.6e-8
2018	$B^0_d \to K^0_S\pi^+\pi^-$	LL	29685.4e-8	368.6e-8	2.0e-8	26.0e-8	20.4e-8	66.1e-8	649.9e-8	750.8e-8
2017	$B^0_d \to K^0_S\pi^+\pi^-$	LL	31694.3e-8	400.2e-8	2.0e-8	28.7e-8	24.0e-8	67.5e-8	649.9e-8	767.1e-8
2016	$B^0_d \to K^0_S\pi^+\pi^-$	LL	35629.5e-8	428.7e-8	2.1e-8	32.3e-8	22.7e-8	103.1e-8	649.9e-8	786.3e-8
2015	$B^0_d \to K^0_S\pi^+\pi^-$	LL	32752.8e-8	409.7e-8	2.0e-8	30.7e-8	26.0e-8	98.8e-8	649.9e-8	775.6e-8
2012b	$B^0_d \to K^0_S\pi^+\pi^-$	LL	153341.4e-9	3111.4e-9	9.3e-9	225.9e-9	258.1e-9	1796.8e-9	6498.7e-9	7433.8e-9
2012a	$B^0_d \to K^0_S\pi^+\pi^-$	LL	17684.9e-8	374.5e-8	1.0e-8	23.6e-8	19.3e-8	262.8e-8	649.9e-8	795.3e-8
2011	$B^0_d \to K^0_S\pi^+\pi^-$	LL	18765.6e-8	376.6e-8	1.0e-8	45.6e-8	20.8e-8	271.4e-8	649.9e-8	800.2e-8

Table C.50: $B^0 \to K^0_S\pi^+\pi^-$ efficiency table with the favoured mode optimisation. For each year and K^0_S reconstruction type, the average efficiency $\bar{\varepsilon}$, the statistical uncertainty $\sigma^{\text{stat}}_{\bar{\varepsilon}}$, the uncertainty linked to the tracking correction $\sigma^{\text{tracking}}_{\bar{\varepsilon}}$, the uncertainty linked to the L0Hadron trigger correction $\sigma^{\text{L0corr}}_{\bar{\varepsilon}}$, the uncertainty related to the PID MC sampling effect $\sigma^{\text{PIDMCsampling}}_{\bar{\varepsilon}}$, the uncertainty linked to the PID kernel variation $\sigma^{\text{PIDkernel}}_{\bar{\varepsilon}}$, the uncertainty linked to the averaging method $\sigma^{\text{RMS}}_{\bar{\varepsilon}}$ and the total uncertainty $\sigma_{\bar{\varepsilon}}$ are given.

Year	Mode	K^0_S	$\bar{\varepsilon}$	$\sigma^{\text{stat}}_{\bar{\varepsilon}}$	$\sigma^{\text{tracking}}_{\bar{\varepsilon}}$	$\sigma^{\text{L0corr}}_{\bar{\varepsilon}}$	$\sigma^{\text{PIDMCsampling}}_{\bar{\varepsilon}}$	$\sigma^{\text{PIDkernel}}_{\bar{\varepsilon}}$	$\sigma^{\text{RMS}}_{\bar{\varepsilon}}$	$\sigma_{\bar{\varepsilon}}$
2018	$B^0_d \to K^0_S\pi^+K^-$	DD	88507.5e-8	1000.4e-8	6.5e-8	105.9e-8	153.6e-8	352.7e-8	1311.5e-8	1697.1e-8
2017	$B^0_d \to K^0_S\pi^+K^-$	DD	92598.9e-8	1053.9e-8	6.5e-8	108.4e-8	164.2e-8	348.2e-8	1311.5e-8	1729.4e-8
2016	$B^0_d \to K^0_S\pi^+K^-$	DD	105090.7e-8	1131.9e-8	6.7e-8	118.5e-8	132.6e-8	314.7e-8	1311.5e-8	1769.8e-8
2015	$B^0_d \to K^0_S\pi^+K^-$	DD	93324.0e-8	1091.4e-8	6.2e-8	114.8e-8	202.7e-8	669.9e-8	1311.5e-8	1847.8e-8
2012b	$B^0_d \to K^0_S\pi^+K^-$	DD	66165.1e-8	1154.7e-8	3.8e-8	144.0e-8	151.2e-8	4496.2e-8	1311.5e-8	4828.4e-8
2012a	$B^0_d \to K^0_S\pi^+K^-$	DD	50354.0e-8	1097.8e-8	3.3e-8	149.8e-8	146.4e-8	4059.9e-8	1311.5e-8	4410.4e-8
2011	$B^0_d \to K^0_S\pi^+K^-$	DD	60957.4e-8	1131.0e-8	3.5e-8	211.3e-8	206.6e-8	4551.4e-8	1311.5e-8	4878.7e-8
2018	$B^0_d \to K^0_S\pi^+K^-$	LL	33419.7e-8	698.3e-8	3.9e-8	31.9e-8	104.3e-8	172.1e-8	1199.5e-8	1402.8e-8
2017	$B^0_d \to K^0_S\pi^+K^-$	LL	37045.7e-8	777.5e-8	4.0e-8	40.4e-8	116.4e-8	118.9e-8	1199.5e-8	1439.6e-8
2016	$B^0_d \to K^0_S\pi^+K^-$	LL	38428.8e-8	790.1e-8	4.1e-8	40.8e-8	73.5e-8	128.5e-8	1199.5e-8	1444.5e-8
2015	$B^0_d \to K^0_S\pi^+K^-$	LL	36701.8e-8	778.7e-8	4.2e-8	37.5e-8	158.9e-8	263.7e-8	1199.5e-8	1463.3e-8
2012b	$B^0_d \to K^0_S\pi^+K^-$	LL	18129.8e-8	648.9e-8	2.0e-8	35.6e-8	153.5e-8	1467.2e-8	1199.5e-8	2009.3e-8
2012a	$B^0_d \to K^0_S\pi^+K^-$	LL	20837.8e-8	747.1e-8	2.2e-8	47.7e-8	157.0e-8	1504.0e-8	1199.5e-8	2070.3e-8
2011	$B^0_d \to K^0_S\pi^+K^-$	LL	23722.9e-8	773.4e-8	2.2e-8	65.1e-8	116.1e-8	1366.0e-8	1199.5e-8	1980.1e-8

Table C.51: $B^0 \to K^0_S\pi^+K^-$ efficiency table with the favoured mode optimisation. For each year and K^0_S reconstruction type, the average efficiency $\bar{\varepsilon}$, the statistical uncertainty $\sigma^{\text{stat}}_{\bar{\varepsilon}}$, the uncertainty linked to the tracking correction $\sigma^{\text{tracking}}_{\bar{\varepsilon}}$, the uncertainty linked to the L0Hadron trigger correction $\sigma^{\text{L0corr}}_{\bar{\varepsilon}}$, the uncertainty related to the PID MC sampling effect $\sigma^{\text{PIDMCsampling}}_{\bar{\varepsilon}}$, the uncertainty linked to the PID kernel variation $\sigma^{\text{PIDkernel}}_{\bar{\varepsilon}}$, the uncertainty linked to the averaging method $\sigma^{\text{RMS}}_{\bar{\varepsilon}}$ and the total uncertainty $\sigma_{\bar{\varepsilon}}$ are given.

Year	Mode	K^0_S	$\bar{\varepsilon}$	$\sigma^{\text{stat}}_{\bar{\varepsilon}}$	$\sigma^{\text{tracking}}_{\bar{\varepsilon}}$	$\sigma^{\text{L0corr}}_{\bar{\varepsilon}}$	$\sigma^{\text{PIDMCsampling}}_{\bar{\varepsilon}}$	$\sigma^{\text{PIDkernel}}_{\bar{\varepsilon}}$	$\sigma^{\text{RMS}}_{\bar{\varepsilon}}$	$\sigma_{\bar{\varepsilon}}$
2018	$B^0_d \to K^0_S K^+\pi^-$	DD	89829.4e-8	1105.0e-8	7.0e-8	106.4e-8	132.4e-8	340.7e-8	1468.9e-8	1877.1e-8
2017	$B^0_d \to K^0_S K^+\pi^-$	DD	95554.9e-8	1202.2e-8	6.9e-8	124.9e-8	133.5e-8	372.9e-8	1468.9e-8	1943.1e-8
2016	$B^0_d \to K^0_S K^+\pi^-$	DD	102144.9e-8	1235.7e-8	7.3e-8	134.3e-8	124.3e-8	293.5e-8	1468.9e-8	1950.4e-8
2015	$B^0_d \to K^0_S K^+\pi^-$	DD	93297.8e-8	1220.7e-8	7.0e-8	137.7e-8	321.0e-8	783.9e-8	1468.9e-8	2093.9e-8
2012b	$B^0_d \to K^0_S K^+\pi^-$	DD	68155.4e-8	1303.8e-8	4.4e-8	170.1e-8	375.2e-8	5531.0e-8	1468.9e-8	5883.8e-8
2012a	$B^0_d \to K^0_S K^+\pi^-$	DD	51926.5e-8	1258.0e-8	3.9e-8	133.4e-8	199.9e-8	4425.7e-8	1468.9e-8	4835.8e-8
2011	$B^0_d \to K^0_S K^+\pi^-$	DD	63596.2e-8	1326.6e-8	4.0e-8	259.3e-8	200.7e-8	4887.3e-8	1468.9e-8	5283.1e-8
2018	$B^0_d \to K^0_S K^+\pi^-$	LL	32242.5e-8	749.1e-8	4.5e-8	34.3e-8	92.3e-8	156.9e-8	1344.2e-8	1550.0e-8
2017	$B^0_d \to K^0_S K^+\pi^-$	LL	36822.9e-8	856.7e-8	4.8e-8	45.4e-8	307.8e-8	208.7e-8	1344.2e-8	1637.4e-8
2016	$B^0_d \to K^0_S K^+\pi^-$	LL	40077.5e-8	887.1e-8	5.0e-8	47.8e-8	741.9e-8	172.0e-8	1344.2e-8	1782.1e-8
2015	$B^0_d \to K^0_S K^+\pi^-$	LL	37451.6e-8	872.6e-8	4.7e-8	49.1e-8	211.5e-8	442.1e-8	1344.2e-8	1676.6e-8
2012b	$B^0_d \to K^0_S K^+\pi^-$	LL	17797.4e-8	738.0e-8	2.3e-8	46.1e-8	272.8e-8	1343.3e-8	1344.2e-8	2057.3e-8
2012a	$B^0_d \to K^0_S K^+\pi^-$	LL	18835.1e-8	838.5e-8	2.4e-8	42.5e-8	138.5e-8	942.1e-8	1344.2e-8	1848.9e-8
2011	$B^0_d \to K^0_S K^+\pi^-$	LL	22942.1e-8	882.7e-8	2.6e-8	84.9e-8	125.7e-8	1350.5e-8	1344.2e-8	2105.4e-8

Table C.52: $B^0 \to K^0_S K^+\pi^-$ efficiency table with the favoured mode optimisation. For each year and K^0_S reconstruction type, the average efficiency $\bar{\varepsilon}$, the statistical uncertainty $\sigma^{\text{stat}}_{\bar{\varepsilon}}$, the uncertainty linked to the tracking correction $\sigma^{\text{tracking}}_{\bar{\varepsilon}}$, the uncertainty linked to the L0Hadron trigger correction $\sigma^{\text{L0corr}}_{\bar{\varepsilon}}$, the uncertainty related to the PID MC sampling effect $\sigma^{\text{PIDMCsampling}}_{\bar{\varepsilon}}$, the uncertainty linked to the PID kernel variation $\sigma^{\text{PIDkernel}}_{\bar{\varepsilon}}$, the uncertainty linked to the averaging method $\sigma^{\text{RMS}}_{\bar{\varepsilon}}$ and the total uncertainty $\sigma_{\bar{\varepsilon}}$ are given.

Year	Mode	K^0_S	$\bar{\varepsilon}$	$\sigma^{\text{stat}}_{\bar{\varepsilon}}$	$\sigma^{\text{tracking}}_{\bar{\varepsilon}}$	$\sigma^{\text{L0corr}}_{\bar{\varepsilon}}$	$\sigma^{\text{PIDMCsampling}}_{\bar{\varepsilon}}$	$\sigma^{\text{PIDkernel}}_{\bar{\varepsilon}}$	$\sigma^{\text{RMS}}_{\bar{\varepsilon}}$	$\sigma_{\bar{\varepsilon}}$
2018	$B^0_d \to K^0_S K^+K^-$	DD	72816.4e-8	516.3e-8	3.3e-8	56.0e-8	72.8e-8	153.4e-8	322.3e-8	634.4e-8
2017	$B^0_d \to K^0_S K^+K^-$	DD	75148.9e-8	550.8e-8	3.2e-8	111.7e-8	56.6e-8	173.0e-8	322.3e-8	672.9e-8
2016	$B^0_d \to K^0_S K^+K^-$	DD	89341.4e-8	599.9e-8	3.6e-8	70.8e-8	62.0e-8	256.8e-8	322.3e-8	733.8e-8
2015	$B^0_d \to K^0_S K^+K^-$	DD	80372.8e-8	580.0e-8	3.4e-8	67.6e-8	84.9e-8	209.0e-8	322.3e-8	704.1e-8
2012b	$B^0_d \to K^0_S K^+K^-$	DD	44963.1e-8	550.9e-8	1.7e-8	140.3e-8	326.9e-8	1024.5e-8	322.3e-8	1258.4e-8
2012a	$B^0_d \to K^0_S K^+K^-$	DD	31146.8e-8	489.8e-8	1.5e-8	118.5e-8	46.5e-8	633.5e-8	322.3e-8	872.5e-8
2011	$B^0_d \to K^0_S K^+K^-$	DD	36026.4e-8	481.3e-8	1.4e-8	109.4e-8	33.2e-8	298.9e-8	322.3e-8	661.7e-8
2018	$B^0_d \to K^0_S K^+K^-$	LL	30481.9e-8	326.0e-8	2.1e-8	16.8e-8	45.0e-8	61.1e-8	208.1e-8	394.5e-8
2017	$B^0_d \to K^0_S K^+K^-$	LL	32939.1e-8	359.8e-8	2.1e-8	35.0e-8	37.2e-8	98.4e-8	208.1e-8	430.2e-8
2016	$B^0_d \to K^0_S K^+K^-$	LL	37030.8e-8	384.7e-8	2.3e-8	23.1e-8	31.8e-8	90.4e-8	208.1e-8	448.4e-8
2015	$B^0_d \to K^0_S K^+K^-$	LL	33282.3e-8	372.0e-8	2.1e-8	22.8e-8	74.4e-8	216.4e-8	208.1e-8	484.3e-8
2012b	$B^0_d \to K^0_S K^+K^-$	LL	14706.1e-8	318.3e-8	1.0e-8	44.9e-8	29.9e-8	207.8e-8	208.1e-8	436.7e-8
2012a	$B^0_d \to K^0_S K^+K^-$	LL	16797.7e-8	361.4e-8	1.0e-8	34.0e-8	53.6e-8	309.1e-8	208.1e-8	522.9e-8
2011	$B^0_d \to K^0_S K^+K^-$	LL	189995.0e-9	3586.2e-9	9.8e-9	431.4e-9	436.4e-9	2225.2e-9	2081.1e-9	4745.5e-9

Table C.53: $B^0 \to K^0_S K^+K^-$ efficiency table with the favoured mode optimisation. For each year and K^0_S reconstruction type, the average efficiency $\bar{\varepsilon}$, the statistical uncertainty $\sigma^{\text{stat}}_{\bar{\varepsilon}}$, the uncertainty linked to the tracking correction $\sigma^{\text{tracking}}_{\bar{\varepsilon}}$, the uncertainty linked to the L0Hadron trigger correction $\sigma^{\text{L0corr}}_{\bar{\varepsilon}}$, the uncertainty related to the PID MC sampling effect $\sigma^{\text{PIDMCsampling}}_{\bar{\varepsilon}}$, the uncertainty linked to the PID kernel variation $\sigma^{\text{PIDkernel}}_{\bar{\varepsilon}}$, the uncertainty linked to the averaging method $\sigma^{\text{RMS}}_{\bar{\varepsilon}}$ and the total uncertainty $\sigma_{\bar{\varepsilon}}$ are given.

Year	Mode	K^0_S	$\bar{\varepsilon}$	$\sigma^{\text{stat}}_{\bar{\varepsilon}}$	$\sigma^{\text{tracking}}_{\bar{\varepsilon}}$	$\sigma^{\text{L0corr}}_{\bar{\varepsilon}}$	$\sigma^{\text{PIDMCsampling}}_{\bar{\varepsilon}}$	$\sigma^{\text{PIDkernel}}_{\bar{\varepsilon}}$	$\sigma^{\text{RMS}}_{\bar{\varepsilon}}$	$\sigma_{\bar{\varepsilon}}$
2018	$B^0_s \to K^0_S\pi^+\pi^-$	DD	87089.6e-8	814.6e-8	5.1e-8	115.7e-8	129.1e-8	381.6e-8	3509.2e-8	3626.8e-8
2017	$B^0_s \to K^0_S\pi^+\pi^-$	DD	88429.5e-8	844.9e-8	4.9e-8	119.6e-8	105.6e-8	370.3e-8	3509.2e-8	3632.0e-8
2016	$B^0_s \to K^0_S\pi^+\pi^-$	DD	91363.6e-8	877.2e-8	5.0e-8	125.3e-8	122.9e-8	444.7e-8	3509.2e-8	3648.6e-8
2015	$B^0_s \to K^0_S\pi^+\pi^-$	DD	89719.2e-8	882.6e-8	5.5e-8	132.1e-8	193.8e-8	739.0e-8	3509.2e-8	3700.6e-8
2012b	$B^0_s \to K^0_S\pi^+\pi^-$	DD	56997.6e-8	817.6e-8	2.9e-8	124.5e-8	156.0e-8	3815.1e-8	3509.2e-8	5251.5e-8
2012a	$B^0_s \to K^0_S\pi^+\pi^-$	DD	45854.2e-8	758.1e-8	2.5e-8	112.6e-8	119.6e-8	3340.2e-8	3509.2e-8	4906.4e-8
2011	$B^0_s \to K^0_S\pi^+\pi^-$	DD	54838.5e-8	776.3e-8	2.7e-8	202.5e-8	282.4e-8	5403.1e-8	3509.2e-8	6498.6e-8
2018	$B^0_s \to K^0_S\pi^+\pi^-$	LL	32931.0e-8	617.8e-8	3.4e-8	44.7e-8	75.1e-8	173.6e-8	824.4e-8	1048.4e-8
2017	$B^0_s \to K^0_S\pi^+\pi^-$	LL	35705.2e-8	647.4e-8	3.4e-8	48.2e-8	64.3e-8	195.2e-8	824.4e-8	1069.3e-8
2016	$B^0_s \to K^0_S\pi^+\pi^-$	LL	39780.6e-8	718.4e-8	3.8e-8	55.2e-8	57.4e-8	208.2e-8	824.4e-8	1116.0e-8
2015	$B^0_s \to K^0_S\pi^+\pi^-$	LL	36085.5e-8	676.1e-8	3.5e-8	53.6e-8	122.4e-8	330.9e-8	824.4e-8	1124.3e-8
2012b	$B^0_s \to K^0_S\pi^+\pi^-$	LL	17481.2e-8	544.5e-8	1.7e-8	39.8e-8	91.0e-8	1362.7e-8	824.4e-8	1686.1e-8
2012a	$B^0_s \to K^0_S\pi^+\pi^-$	LL	20106.0e-8	615.6e-8	1.8e-8	40.5e-8	136.7e-8	2093.7e-8	824.4e-8	2337.2e-8
2011	$B^0_s \to K^0_S\pi^+\pi^-$	LL	21498.8e-8	596.8e-8	1.7e-8	78.4e-8	97.2e-8	1600.6e-8	824.4e-8	1900.9e-8

Table C.54: $B^0_s \to K^0_S\pi^+\pi^-$ efficiency table with the favoured mode optimisation. For each year and K^0_S reconstruction type, the average efficiency $\bar{\varepsilon}$, the statistical uncertainty $\sigma^{\text{stat}}_{\bar{\varepsilon}}$, the uncertainty linked to the tracking correction $\sigma^{\text{tracking}}_{\bar{\varepsilon}}$, the uncertainty linked to the L0Hadron trigger correction $\sigma^{\text{L0corr}}_{\bar{\varepsilon}}$, the uncertainty related to the PID MC sampling effect $\sigma^{\text{PIDMCsampling}}_{\bar{\varepsilon}}$, the uncertainty linked to the PID kernel variation $\sigma^{\text{PIDkernel}}_{\bar{\varepsilon}}$, the uncertainty linked to the averaging method $\sigma^{\text{RMS}}_{\bar{\varepsilon}}$ and the total uncertainty $\sigma_{\bar{\varepsilon}}$ are given.

Year	Mode	K^0_S	$\bar{\varepsilon}$	$\sigma^{\text{stat}}_{\bar{\varepsilon}}$	$\sigma^{\text{tracking}}_{\bar{\varepsilon}}$	$\sigma^{\text{L0corr}}_{\bar{\varepsilon}}$	$\sigma^{\text{PIDMCsampling}}_{\bar{\varepsilon}}$	$\sigma^{\text{PIDkernel}}_{\bar{\varepsilon}}$	$\sigma^{\text{RMS}}_{\bar{\varepsilon}}$	$\sigma_{\bar{\varepsilon}}$
2018	$B^0_s \to K^0_S\pi^+K^-$	DD	85270.4e-8	858.3e-8	5.3e-8	81.4e-8	117.1e-8	324.2e-8	574.8e-8	1092.1e-8
2017	$B^0_s \to K^0_S\pi^+K^-$	DD	88592.4e-8	898.2e-8	5.1e-8	92.8e-8	80.0e-8	180.1e-8	574.8e-8	1088.4e-8
2016	$B^0_s \to K^0_S\pi^+K^-$	DD	99986.7e-8	978.9e-8	5.7e-8	96.9e-8	86.9e-8	211.6e-8	574.8e-8	1162.1e-8
2015	$B^0_s \to K^0_S\pi^+K^-$	DD	90349.3e-8	947.8e-8	5.5e-8	100.8e-8	170.4e-8	387.2e-8	574.8e-8	1190.7e-8
2012b	$B^0_s \to K^0_S\pi^+K^-$	DD	58693.4e-8	930.5e-8	3.1e-8	117.7e-8	98.2e-8	1210.2e-8	574.8e-8	1638.4e-8
2012a	$B^0_s \to K^0_S\pi^+K^-$	DD	47314.6e-8	898.3e-8	3.0e-8	109.2e-8	75.6e-8	997.9e-8	574.8e-8	1466.6e-8
2011	$B^0_s \to K^0_S\pi^+K^-$	DD	55756.5e-8	955.8e-8	3.1e-8	177.5e-8	123.9e-8	2093.3e-8	574.8e-8	2381.7e-8
2018	$B^0_s \to K^0_S\pi^+K^-$	LL	32115.8e-8	534.0e-8	3.1e-8	24.9e-8	50.5e-8	75.6e-8	782.6e-8	952.1e-8
2017	$B^0_s \to K^0_S\pi^+K^-$	LL	36313.1e-8	596.4e-8	3.3e-8	33.7e-8	93.7e-8	98.3e-8	782.6e-8	993.8e-8
2016	$B^0_s \to K^0_S\pi^+K^-$	LL	38048.6e-8	617.4e-8	3.4e-8	32.2e-8	43.0e-8	102.8e-8	782.6e-8	1003.6e-8
2015	$B^0_s \to K^0_S\pi^+K^-$	LL	36175.8e-8	603.7e-8	3.4e-8	31.4e-8	102.8e-8	174.0e-8	782.6e-8	1009.4e-8
2012b	$B^0_s \to K^0_S\pi^+K^-$	LL	17584.3e-8	516.0e-8	1.7e-8	29.5e-8	58.0e-8	364.3e-8	782.6e-8	1007.8e-8
2012a	$B^0_s \to K^0_S\pi^+K^-$	LL	20312.6e-8	586.4e-8	1.7e-8	32.2e-8	48.7e-8	675.8e-8	782.6e-8	1190.1e-8
2011	$B^0_s \to K^0_S\pi^+K^-$	LL	22688.7e-8	626.9e-8	1.9e-8	52.4e-8	59.1e-8	666.7e-8	782.6e-8	1206.7e-8

Table C.55: $B^0_s \to K^0_S\pi^+K^-$ efficiency table with the favoured mode optimisation. For each year and K^0_S reconstruction type, the average efficiency $\bar{\varepsilon}$, the statistical uncertainty $\sigma^{\text{stat}}_{\bar{\varepsilon}}$, the uncertainty linked to the tracking correction $\sigma^{\text{tracking}}_{\bar{\varepsilon}}$, the uncertainty linked to the L0Hadron trigger correction $\sigma^{\text{L0corr}}_{\bar{\varepsilon}}$, the uncertainty related to the PID MC sampling effect $\sigma^{\text{PIDMCsampling}}_{\bar{\varepsilon}}$, the uncertainty linked to the PID kernel variation $\sigma^{\text{PIDkernel}}_{\bar{\varepsilon}}$, the uncertainty linked to the averaging method $\sigma^{\text{RMS}}_{\bar{\varepsilon}}$ and the total uncertainty $\sigma_{\bar{\varepsilon}}$ are given.

Year	Mode	K^0_S	$\bar{\varepsilon}$	$\sigma^{\text{stat}}_{\bar{\varepsilon}}$	$\sigma^{\text{tracking}}_{\bar{\varepsilon}}$	$\sigma^{\text{L0corr}}_{\bar{\varepsilon}}$	$\sigma^{\text{PIDMCsampling}}_{\bar{\varepsilon}}$	$\sigma^{\text{PIDkernel}}_{\bar{\varepsilon}}$	$\sigma^{\text{RMS}}_{\bar{\varepsilon}}$	$\sigma_{\bar{\varepsilon}}$
2018	$B^0_s \to K^0_S K^+\pi^-$	DD	86907.5e-8	813.2e-8	5.2e-8	79.6e-8	96.9e-8	247.5e-8	477.2e-8	982.9e-8
2017	$B^0_s \to K^0_S K^+\pi^-$	DD	90487.8e-8	866.4e-8	5.0e-8	93.2e-8	102.1e-8	289.9e-8	477.2e-8	1040.0e-8
2016	$B^0_s \to K^0_S K^+\pi^-$	DD	97386.0e-8	910.1e-8	5.5e-8	92.8e-8	62.0e-8	221.2e-8	477.2e-8	1057.1e-8
2015	$B^0_s \to K^0_S K^+\pi^-$	DD	87127.2e-8	876.8e-8	5.2e-8	90.6e-8	128.1e-8	326.2e-8	477.2e-8	1061.8e-8
2012b	$B^0_s \to K^0_S K^+\pi^-$	DD	56696.3e-8	873.1e-8	3.0e-8	109.2e-8	65.6e-8	1496.9e-8	477.2e-8	1801.9e-8
2012a	$B^0_s \to K^0_S K^+\pi^-$	DD	43767.3e-8	808.2e-8	2.7e-8	98.2e-8	68.1e-8	1774.9e-8	477.2e-8	2011.3e-8
2011	$B^0_s \to K^0_S K^+\pi^-$	DD	50662.2e-8	841.4e-8	2.8e-8	153.2e-8	76.9e-8	1721.6e-8	477.2e-8	1982.2e-8
2018	$B^0_s \to K^0_S K^+\pi^-$	LL	31710.0e-8	568.0e-8	3.2e-8	25.0e-8	77.0e-8	201.9e-8	1198.8e-8	1344.3e-8
2017	$B^0_s \to K^0_S K^+\pi^-$	LL	36041.3e-8	637.0e-8	3.4e-8	33.3e-8	48.9e-8	115.7e-8	1198.8e-8	1363.7e-8
2016	$B^0_s \to K^0_S K^+\pi^-$	LL	39809.3e-8	684.2e-8	3.6e-8	32.9e-8	41.0e-8	147.1e-8	1198.8e-8	1389.1e-8
2015	$B^0_s \to K^0_S K^+\pi^-$	LL	36926.3e-8	659.6e-8	3.5e-8	35.2e-8	88.7e-8	204.0e-8	1198.8e-8	1386.7e-8
2012b	$B^0_s \to K^0_S K^+\pi^-$	LL	16191.9e-8	500.9e-8	1.6e-8	30.0e-8	71.6e-8	387.8e-8	1198.8e-8	1358.1e-8
2012a	$B^0_s \to K^0_S K^+\pi^-$	LL	18758.1e-8	565.1e-8	1.6e-8	33.0e-8	78.2e-8	657.2e-8	1198.8e-8	1481.7e-8
2011	$B^0_s \to K^0_S K^+\pi^-$	LL	21670.5e-8	607.0e-8	1.8e-8	55.8e-8	59.5e-8	543.4e-8	1198.8e-8	1451.7e-8

Table C.56: $B^0_s \to K^0_S K^+\pi^-$ efficiency table with the favoured mode optimisation. For each year and K^0_S reconstruction type, the average efficiency $\bar{\varepsilon}$, the statistical uncertainty $\sigma^{\text{stat}}_{\bar{\varepsilon}}$, the uncertainty linked to the tracking correction $\sigma^{\text{tracking}}_{\bar{\varepsilon}}$, the uncertainty linked to the L0Hadron trigger correction $\sigma^{\text{L0corr}}_{\bar{\varepsilon}}$, the uncertainty related to the PID MC sampling effect $\sigma^{\text{PIDMCsampling}}_{\bar{\varepsilon}}$, the uncertainty linked to the PID kernel variation $\sigma^{\text{PIDkernel}}_{\bar{\varepsilon}}$, the uncertainty linked to the averaging method $\sigma^{\text{RMS}}_{\bar{\varepsilon}}$ and the total uncertainty $\sigma_{\bar{\varepsilon}}$ are given.

Year	Mode	K^0_S	$\bar{\varepsilon}$	$\sigma^{\text{stat}}_{\bar{\varepsilon}}$	$\sigma^{\text{tracking}}_{\bar{\varepsilon}}$	$\sigma^{\text{L0corr}}_{\bar{\varepsilon}}$	$\sigma^{\text{PIDMCsampling}}_{\bar{\varepsilon}}$	$\sigma^{\text{PIDkernel}}_{\bar{\varepsilon}}$	$\sigma^{\text{RMS}}_{\bar{\varepsilon}}$	$\sigma_{\bar{\varepsilon}}$
2018	$B^0_s \to K^0_S K^+K^-$	DD	83541.2e-8	758.5e-8	5.1e-8	89.4e-8	155.6e-8	347.9e-8	6328.2e-8	6385.5e-8
2017	$B^0_s \to K^0_S K^+K^-$	DD	87969.9e-8	812.8e-8	5.2e-8	153.5e-8	183.0e-8	455.6e-8	6328.2e-8	6400.9e-8
2016	$B^0_s \to K^0_S K^+K^-$	DD	102316.3e-8	873.5e-8	6.0e-8	115.7e-8	193.8e-8	353.8e-8	6328.2e-8	6401.9e-8
2015	$B^0_s \to K^0_S K^+K^-$	DD	91647.8e-8	831.1e-8	5.8e-8	108.3e-8	244.2e-8	488.6e-8	6328.2e-8	6406.8e-8
2012b	$B^0_s \to K^0_S K^+K^-$	DD	57721.5e-8	797.5e-8	2.7e-8	184.3e-8	142.5e-8	4134.2e-8	6328.2e-8	7604.5e-8
2012a	$B^0_s \to K^0_S K^+K^-$	DD	47839.4e-8	815.2e-8	2.6e-8	156.5e-8	139.7e-8	3167.2e-8	6328.2e-8	7126.4e-8
2011	$B^0_s \to K^0_S K^+K^-$	DD	53097.1e-8	809.4e-8	2.4e-8	203.5e-8	252.4e-8	4613.7e-8	6328.2e-8	7879.9e-8
2018	$B^0_s \to K^0_S K^+K^-$	LL	3718.2e-7	208.9e-7	1.5e-7	12.0e-7	46.9e-7	24.4e-7	556.1e-7	596.5e-7
2017	$B^0_s \to K^0_S K^+K^-$	LL	4058.0e-7	232.4e-7	1.6e-7	21.2e-7	60.6e-7	16.9e-7	556.1e-7	606.3e-7
2016	$B^0_s \to K^0_S K^+K^-$	LL	4852.0e-7	245.3e-7	1.8e-7	16.3e-7	52.9e-7	25.0e-7	556.1e-7	610.8e-7
2015	$B^0_s \to K^0_S K^+K^-$	LL	4191.7e-7	233.4e-7	1.4e-7	15.0e-7	39.1e-7	24.2e-7	556.1e-7	605.0e-7
2012b	$B^0_s \to K^0_S K^+K^-$	LL	18495.1e-8	1928.9e-8	6.1e-8	253.7e-8	407.4e-8	1374.2e-8	5560.9e-8	6063.2e-8
2012a	$B^0_s \to K^0_S K^+K^-$	LL	20146.1e-8	2309.5e-8	6.7e-8	250.9e-8	244.6e-8	1370.0e-8	5560.9e-8	6185.2e-8
2011	$B^0_s \to K^0_S K^+K^-$	LL	25837.3e-8	2354.1e-8	6.6e-8	293.8e-8	594.3e-8	1476.8e-8	5560.9e-8	6251.8e-8

Table C.57: $B^0_s \to K^0_S K^+K^-$ efficiency table with the favoured mode optimisation. For each year and K^0_S reconstruction type, the average efficiency $\bar{\varepsilon}$, the statistical uncertainty $\sigma^{\text{stat}}_{\bar{\varepsilon}}$, the uncertainty linked to the tracking correction $\sigma^{\text{tracking}}_{\bar{\varepsilon}}$, the uncertainty linked to the L0Hadron trigger correction $\sigma^{\text{L0corr}}_{\bar{\varepsilon}}$, the uncertainty related to the PID MC sampling effect $\sigma^{\text{PIDMCsampling}}_{\bar{\varepsilon}}$, the uncertainty linked to the PID kernel variation $\sigma^{\text{PIDkernel}}_{\bar{\varepsilon}}$, the uncertainty linked to the averaging method $\sigma^{\text{RMS}}_{\bar{\varepsilon}}$ and the total uncertainty $\sigma_{\bar{\varepsilon}}$ are given.

Year	Mode	K^0_S	$\bar{\varepsilon}$	$\sigma^{\text{stat}}_{\bar{\varepsilon}}$	$\sigma^{\text{tracking}}_{\bar{\varepsilon}}$	$\sigma^{\text{L0corr}}_{\bar{\varepsilon}}$	$\sigma^{\text{PIDMCsampling}}_{\bar{\varepsilon}}$	$\sigma^{\text{PIDkernel}}_{\bar{\varepsilon}}$	$\sigma^{\text{RMS}}_{\bar{\varepsilon}}$	$\sigma_{\bar{\varepsilon}}$
2018	$B^0_d \to K^0_S\pi^+\pi^-$	DD	41330.5e-8	405.8e-8	1.8e-8	44.3e-8	21.5e-8	136.3e-8	628.5e-8	762.1e-8
2017	$B^0_d \to K^0_S\pi^+\pi^-$	DD	44229.2e-8	435.6e-8	1.8e-8	46.8e-8	22.5e-8	100.2e-8	628.5e-8	773.0e-8
2016	$B^0_d \to K^0_S\pi^+\pi^-$	DD	43886.7e-8	431.7e-8	1.8e-8	46.2e-8	19.4e-8	115.8e-8	628.5e-8	772.9e-8
2015	$B^0_d \to K^0_S\pi^+\pi^-$	DD	34655.9e-8	378.9e-8	1.4e-8	41.1e-8	29.2e-8	124.9e-8	628.5e-8	746.1e-8
2012b	$B^0_d \to K^0_S\pi^+\pi^-$	DD	34375.0e-8	459.1e-8	1.2e-8	58.8e-8	25.5e-8	471.1e-8	628.5e-8	912.1e-8
2012a	$B^0_d \to K^0_S\pi^+\pi^-$	DD	23311.6e-8	411.1e-8	1.0e-8	43.2e-8	20.9e-8	307.1e-8	628.5e-8	812.8e-8
2011	$B^0_d \to K^0_S\pi^+\pi^-$	DD	238455.0e-9	4000.9e-9	9.0e-9	723.7e-9	210.1e-9	3228.8e-9	6285.0e-9	8154.8e-9
2018	$B^0_d \to K^0_S\pi^+\pi^-$	LL	19084.5e-8	284.1e-8	1.3e-8	16.7e-8	13.2e-8	42.5e-8	437.9e-8	524.2e-8
2017	$B^0_d \to K^0_S\pi^+\pi^-$	LL	21531.9e-8	317.0e-8	1.4e-8	19.6e-8	16.4e-8	45.8e-8	437.9e-8	543.2e-8
2016	$B^0_d \to K^0_S\pi^+\pi^-$	LL	22136.8e-8	319.7e-8	1.3e-8	19.9e-8	14.0e-8	64.1e-8	437.9e-8	546.5e-8
2015	$B^0_d \to K^0_S\pi^+\pi^-$	LL	19921.6e-8	305.7e-8	1.3e-8	18.5e-8	16.0e-8	60.1e-8	437.9e-8	538.0e-8
2012b	$B^0_d \to K^0_S\pi^+\pi^-$	LL	108457.4e-9	2573.1e-9	6.7e-9	158.8e-9	183.3e-9	1270.9e-9	4379.5e-9	5241.6e-9
2012a	$B^0_d \to K^0_S\pi^+\pi^-$	LL	77800.5e-9	2441.1e-9	4.7e-9	126.0e-9	90.2e-9	1156.3e-9	4379.5e-9	5147.8e-9
2011	$B^0_d \to K^0_S\pi^+\pi^-$	LL	132930.2e-9	3120.4e-9	7.3e-9	305.7e-9	149.2e-9	1922.4e-9	4379.5e-9	5720.8e-9

Table C.58: $B^0 \to K^0_S\pi^+\pi^-$ efficiency table with the unfavoured mode optimisation. For each year and K^0_S reconstruction type, the average efficiency $\bar{\varepsilon}$, the statistical uncertainty $\sigma^{\text{stat}}_{\bar{\varepsilon}}$, the uncertainty linked to the tracking correction $\sigma^{\text{tracking}}_{\bar{\varepsilon}}$, the uncertainty linked to the L0Hadron trigger correction $\sigma^{\text{L0corr}}_{\bar{\varepsilon}}$, the uncertainty related to the PID MC sampling effect $\sigma^{\text{PIDMCsampling}}_{\bar{\varepsilon}}$, the uncertainty linked to the PID kernel variation $\sigma^{\text{PIDkernel}}_{\bar{\varepsilon}}$, the uncertainty linked to the averaging method $\sigma^{\text{RMS}}_{\bar{\varepsilon}}$ and the total uncertainty $\sigma_{\bar{\varepsilon}}$ are given.

Year	Mode	K^0_S	$\bar{\varepsilon}$	$\sigma^{\text{stat}}_{\bar{\varepsilon}}$	$\sigma^{\text{tracking}}_{\bar{\varepsilon}}$	$\sigma^{\text{L0corr}}_{\bar{\varepsilon}}$	$\sigma^{\text{PIDMCsampling}}_{\bar{\varepsilon}}$	$\sigma^{\text{PIDkernel}}_{\bar{\varepsilon}}$	$\sigma^{\text{RMS}}_{\bar{\varepsilon}}$	$\sigma_{\bar{\varepsilon}}$
2018	$B^0_d \to K^0_S\pi^+K^-$	DD	66709.6e-8	861.4e-8	4.9e-8	81.9e-8	116.0e-8	265.9e-8	1143.8e-8	1463.3e-8
2017	$B^0_d \to K^0_S\pi^+K^-$	DD	69751.5e-8	908.0e-8	4.9e-8	85.1e-8	123.8e-8	262.3e-8	1143.8e-8	1491.3e-8
2016	$B^0_d \to K^0_S\pi^+K^-$	DD	78896.6e-8	970.0e-8	5.1e-8	88.7e-8	99.0e-8	236.3e-8	1143.8e-8	1524.0e-8
2015	$B^0_d \to K^0_S\pi^+K^-$	DD	69091.1e-8	935.2e-8	4.7e-8	83.5e-8	147.6e-8	495.9e-8	1143.8e-8	1567.6e-8
2012b	$B^0_d \to K^0_S\pi^+K^-$	DD	51599.8e-8	1014.4e-8	3.0e-8	104.2e-8	117.1e-8	3506.4e-8	1143.8e-8	3828.4e-8
2012a	$B^0_d \to K^0_S\pi^+K^-$	DD	41845.9e-8	1003.0e-8	2.8e-8	121.3e-8	120.6e-8	3373.9e-8	1143.8e-8	3704.9e-8
2011	$B^0_d \to K^0_S\pi^+K^-$	DD	50214.3e-8	1029.3e-8	2.9e-8	173.2e-8	169.1e-8	3749.3e-8	1143.8e-8	4060.0e-8
2018	$B^0_d \to K^0_S\pi^+K^-$	LL	27575.9e-8	620.7e-8	3.2e-8	26.5e-8	83.0e-8	142.0e-8	853.2e-8	1068.2e-8
2017	$B^0_d \to K^0_S\pi^+K^-$	LL	30230.2e-8	686.4e-8	3.3e-8	32.8e-8	98.5e-8	97.0e-8	853.2e-8	1104.2e-8
2016	$B^0_d \to K^0_S\pi^+K^-$	LL	31186.8e-8	693.1e-8	3.4e-8	32.1e-8	59.9e-8	104.3e-8	853.2e-8	1106.3e-8
2015	$B^0_d \to K^0_S\pi^+K^-$	LL	24400.2e-8	614.9e-8	2.8e-8	24.4e-8	102.0e-8	175.3e-8	853.2e-8	1071.4e-8
2012b	$B^0_d \to K^0_S\pi^+K^-$	LL	9419.9e-8	458.7e-8	1.1e-8	20.1e-8	79.9e-8	762.3e-8	853.2e-8	1235.5e-8
2012a	$B^0_d \to K^0_S\pi^+K^-$	LL	15547.7e-8	641.5e-8	1.6e-8	37.9e-8	107.4e-8	1122.2e-8	853.2e-8	1553.0e-8
2011	$B^0_d \to K^0_S\pi^+K^-$	LL	19371.5e-8	691.7e-8	1.8e-8	51.1e-8	97.0e-8	1115.5e-8	853.2e-8	1569.3e-8

Table C.59: $B^0 \to K^0_S\pi^+K^-$ efficiency table with the unfavoured mode optimisation. For each year and K^0_S reconstruction type, the average efficiency $\bar{\varepsilon}$, the statistical uncertainty $\sigma^{\text{stat}}_{\bar{\varepsilon}}$, the uncertainty linked to the tracking correction $\sigma^{\text{tracking}}_{\bar{\varepsilon}}$, the uncertainty linked to the L0Hadron trigger correction $\sigma^{\text{L0corr}}_{\bar{\varepsilon}}$, the uncertainty related to the PID MC sampling effect $\sigma^{\text{PIDMCsampling}}_{\bar{\varepsilon}}$, the uncertainty linked to the PID kernel variation $\sigma^{\text{PIDkernel}}_{\bar{\varepsilon}}$, the uncertainty linked to the averaging method $\sigma^{\text{RMS}}_{\bar{\varepsilon}}$ and the total uncertainty $\sigma_{\bar{\varepsilon}}$ are given.

Year	Mode	K^0_S	$\bar{\varepsilon}$	$\sigma^{\text{stat}}_{\bar{\varepsilon}}$	$\sigma^{\text{tracking}}_{\bar{\varepsilon}}$	$\sigma^{\text{L0corr}}_{\bar{\varepsilon}}$	$\sigma^{\text{PIDMCsampling}}_{\bar{\varepsilon}}$	$\sigma^{\text{PIDkernel}}_{\bar{\varepsilon}}$	$\sigma^{\text{RMS}}_{\bar{\varepsilon}}$	$\sigma_{\bar{\varepsilon}}$
2018	$B^0_d \to K^0_S K^+\pi^-$	DD	68383.6e-8	957.9e-8	5.3e-8	83.9e-8	99.5e-8	259.4e-8	1136.8e-8	1514.7e-8
2017	$B^0_d \to K^0_S K^+\pi^-$	DD	78406.6e-8	1084.9e-8	5.6e-8	104.6e-8	109.6e-8	305.9e-8	1136.8e-8	1608.1e-8
2016	$B^0_d \to K^0_S K^+\pi^-$	DD	75641.5e-8	1054.2e-8	5.4e-8	100.2e-8	92.1e-8	217.3e-8	1136.8e-8	1571.5e-8
2015	$B^0_d \to K^0_S K^+\pi^-$	DD	66035.5e-8	1022.5e-8	5.0e-8	100.4e-8	243.7e-8	554.8e-8	1136.8e-8	1647.8e-8
2012b	$B^0_d \to K^0_S K^+\pi^-$	DD	48498.4e-8	1105.9e-8	3.2e-8	132.7e-8	269.3e-8	3935.8e-8	1136.8e-8	4253.9e-8
2012a	$B^0_d \to K^0_S K^+\pi^-$	DD	40208.9e-8	1104.1e-8	3.0e-8	103.5e-8	157.0e-8	3427.0e-8	1136.8e-8	3780.4e-8
2011	$B^0_d \to K^0_S K^+\pi^-$	DD	53406.6e-8	1209.7e-8	3.4e-8	212.5e-8	168.9e-8	4104.2e-8	1136.8e-8	4435.6e-8
2018	$B^0_d \to K^0_S K^+\pi^-$	LL	26735.8e-8	677.4e-8	3.7e-8	28.2e-8	77.9e-8	130.1e-8	977.7e-8	1199.4e-8
2017	$B^0_d \to K^0_S K^+\pi^-$	LL	28839.7e-8	748.1e-8	3.7e-8	35.7e-8	233.9e-8	163.5e-8	977.7e-8	1264.2e-8
2016	$B^0_d \to K^0_S K^+\pi^-$	LL	31368.8e-8	774.7e-8	3.9e-8	38.2e-8	599.3e-8	134.6e-8	977.7e-8	1391.0e-8
2015	$B^0_d \to K^0_S K^+\pi^-$	LL	27268.6e-8	732.8e-8	3.4e-8	35.9e-8	148.5e-8	321.9e-8	977.7e-8	1272.7e-8
2012b	$B^0_d \to K^0_S K^+\pi^-$	LL	8987.0e-8	515.1e-8	1.3e-8	19.1e-8	127.0e-8	678.3e-8	977.7e-8	1303.0e-8
2012a	$B^0_d \to K^0_S K^+\pi^-$	LL	14924.7e-8	745.2e-8	1.9e-8	33.9e-8	112.9e-8	746.5e-8	977.7e-8	1443.1e-8
2011	$B^0_d \to K^0_S K^+\pi^-$	LL	17361.8e-8	760.8e-8	2.0e-8	61.0e-8	92.5e-8	1022.0e-8	977.7e-8	1609.8e-8

Table C.60: $B^0 \to K^0_S K^+\pi^-$ efficiency table with the unfavoured mode optimisation. For each year and K^0_S reconstruction type, the average efficiency $\bar{\varepsilon}$, the statistical uncertainty $\sigma^{\text{stat}}_{\bar{\varepsilon}}$, the uncertainty linked to the tracking correction $\sigma^{\text{tracking}}_{\bar{\varepsilon}}$, the uncertainty linked to the L0Hadron trigger correction $\sigma^{\text{L0corr}}_{\bar{\varepsilon}}$, the uncertainty related to the PID MC sampling effect $\sigma^{\text{PIDMCsampling}}_{\bar{\varepsilon}}$, the uncertainty linked to the PID kernel variation $\sigma^{\text{PIDkernel}}_{\bar{\varepsilon}}$, the uncertainty linked to the averaging method $\sigma^{\text{RMS}}_{\bar{\varepsilon}}$ and the total uncertainty $\sigma_{\bar{\varepsilon}}$ are given.

Year	Mode	K^0_S	$\bar{\varepsilon}$	$\sigma^{\text{stat}}_{\bar{\varepsilon}}$	$\sigma^{\text{tracking}}_{\bar{\varepsilon}}$	$\sigma^{\text{L0corr}}_{\bar{\varepsilon}}$	$\sigma^{\text{PIDMCsampling}}_{\bar{\varepsilon}}$	$\sigma^{\text{PIDkernel}}_{\bar{\varepsilon}}$	$\sigma^{\text{RMS}}_{\bar{\varepsilon}}$	$\sigma_{\bar{\varepsilon}}$
2018	$B^0_d \to K^0_S K^+K^-$	DD	48498.6e-8	421.0e-8	2.2e-8	39.5e-8	48.2e-8	102.2e-8	202.8e-8	482.4e-8
2017	$B^0_d \to K^0_S K^+K^-$	DD	37423.9e-8	388.9e-8	1.6e-8	58.8e-8	27.5e-8	86.1e-8	202.8e-8	451.6e-8
2016	$B^0_d \to K^0_S K^+K^-$	DD	47931.7e-8	437.2e-8	1.9e-8	41.8e-8	33.2e-8	137.8e-8	202.8e-8	504.1e-8
2015	$B^0_d \to K^0_S K^+K^-$	DD	40015.7e-8	409.1e-8	1.7e-8	37.6e-8	40.4e-8	104.0e-8	202.8e-8	471.5e-8
2012b	$B^0_d \to K^0_S K^+K^-$	DD	33425.2e-8	477.6e-8	1.3e-8	113.1e-8	246.9e-8	761.6e-8	202.8e-8	960.7e-8
2012a	$B^0_d \to K^0_S K^+K^-$	DD	21059.1e-8	406.4e-8	1.0e-8	76.1e-8	30.7e-8	428.4e-8	202.8e-8	629.7e-8
2011	$B^0_d \to K^0_S K^+K^-$	DD	27517.3e-8	422.5e-8	1.1e-8	83.4e-8	25.9e-8	228.3e-8	202.8e-8	528.6e-8
2018	$B^0_d \to K^0_S K^+K^-$	LL	21839.8e-8	277.3e-8	1.5e-8	12.4e-8	31.2e-8	43.8e-8	148.4e-8	319.3e-8
2017	$B^0_d \to K^0_S K^+K^-$	LL	18371.6e-8	270.2e-8	1.2e-8	20.7e-8	20.0e-8	54.9e-8	148.4e-8	314.5e-8
2016	$B^0_d \to K^0_S K^+K^-$	LL	19969.2e-8	283.5e-8	1.2e-8	13.5e-8	17.3e-8	48.7e-8	148.4e-8	324.4e-8
2015	$B^0_d \to K^0_S K^+K^-$	LL	28016.8e-8	339.0e-8	1.8e-8	19.1e-8	62.8e-8	182.1e-8	148.4e-8	417.7e-8
2012b	$B^0_d \to K^0_S K^+K^-$	LL	123994.6e-9	2933.0e-9	8.5e-9	395.8e-9	249.3e-9	1751.7e-9	1483.6e-9	3753.8e-9
2012a	$B^0_d \to K^0_S K^+K^-$	LL	141342.3e-9	3322.1e-9	8.5e-9	297.6e-9	447.5e-9	2600.5e-9	1483.6e-9	4504.3e-9
2011	$B^0_d \to K^0_S K^+K^-$	LL	137859.8e-9	3069.1e-9	7.3e-9	310.4e-9	335.1e-9	1614.6e-9	1483.6e-9	3799.5e-9

Table C.61: $B^0 \to K^0_S K^+K^-$ efficiency table with the unfavoured mode optimisation. For each year and K^0_S reconstruction type, the average efficiency $\bar{\varepsilon}$, the statistical uncertainty $\sigma^{\text{stat}}_{\bar{\varepsilon}}$, the uncertainty linked to the tracking correction $\sigma^{\text{tracking}}_{\bar{\varepsilon}}$, the uncertainty linked to the L0Hadron trigger correction $\sigma^{\text{L0corr}}_{\bar{\varepsilon}}$, the uncertainty related to the PID MC sampling effect $\sigma^{\text{PIDMCsampling}}_{\bar{\varepsilon}}$, the uncertainty linked to the PID kernel variation $\sigma^{\text{PIDkernel}}_{\bar{\varepsilon}}$, the uncertainty linked to the averaging method $\sigma^{\text{RMS}}_{\bar{\varepsilon}}$ and the total uncertainty $\sigma_{\bar{\varepsilon}}$ are given.

Year	Mode	K^0_S	$\bar{\varepsilon}$	$\sigma^{\text{stat}}_{\bar{\varepsilon}}$	$\sigma^{\text{tracking}}_{\bar{\varepsilon}}$	$\sigma^{\text{L0corr}}_{\bar{\varepsilon}}$	$\sigma^{\text{PIDMCsampling}}_{\bar{\varepsilon}}$	$\sigma^{\text{PIDkernel}}_{\bar{\varepsilon}}$	$\sigma^{\text{RMS}}_{\bar{\varepsilon}}$	$\sigma_{\bar{\varepsilon}}$
2018	$B^0_s \to K^0_S\pi^+\pi^-$	DD	44646.8e-8	532.4e-8	2.7e-8	61.4e-8	66.3e-8	195.7e-8	2025.9e-8	2105.8e-8
2017	$B^0_s \to K^0_S\pi^+\pi^-$	DD	47597.8e-8	567.4e-8	2.7e-8	65.6e-8	56.7e-8	199.3e-8	2025.9e-8	2115.1e-8
2016	$B^0_s \to K^0_S\pi^+\pi^-$	DD	45916.7e-8	568.9e-8	2.5e-8	64.0e-8	61.7e-8	223.5e-8	2025.9e-8	2118.0e-8
2015	$B^0_s \to K^0_S\pi^+\pi^-$	DD	38737.5e-8	520.9e-8	2.4e-8	60.6e-8	82.9e-8	319.1e-8	2025.9e-8	2118.5e-8
2012b	$B^0_s \to K^0_S\pi^+\pi^-$	DD	36699.4e-8	630.5e-8	1.8e-8	82.7e-8	97.5e-8	2456.5e-8	2025.9e-8	3248.5e-8
2012a	$B^0_s \to K^0_S\pi^+\pi^-$	DD	26668.8e-8	551.3e-8	1.5e-8	63.0e-8	70.1e-8	1942.7e-8	2025.9e-8	2862.0e-8
2011	$B^0_s \to K^0_S\pi^+\pi^-$	DD	27026.9e-8	514.6e-8	1.3e-8	102.0e-8	134.5e-8	2662.9e-8	2025.9e-8	3389.5e-8
2018	$B^0_s \to K^0_S\pi^+\pi^-$	LL	21530.5e-8	474.4e-8	2.2e-8	28.8e-8	48.5e-8	113.5e-8	568.6e-8	751.3e-8
2017	$B^0_s \to K^0_S\pi^+\pi^-$	LL	24880.0e-8	513.1e-8	2.3e-8	33.4e-8	44.1e-8	136.0e-8	568.6e-8	779.9e-8
2016	$B^0_s \to K^0_S\pi^+\pi^-$	LL	25371.5e-8	541.2e-8	2.4e-8	34.8e-8	36.5e-8	132.8e-8	568.6e-8	797.8e-8
2015	$B^0_s \to K^0_S\pi^+\pi^-$	LL	22088.6e-8	500.5e-8	2.1e-8	32.0e-8	72.7e-8	202.5e-8	568.6e-8	788.2e-8
2012b	$B^0_s \to K^0_S\pi^+\pi^-$	LL	12460.5e-8	447.8e-8	1.2e-8	27.3e-8	58.9e-8	971.3e-8	568.6e-8	1213.1e-8
2012a	$B^0_s \to K^0_S\pi^+\pi^-$	LL	86587.3e-9	3884.1e-9	7.7e-9	194.9e-9	559.8e-9	9016.7e-9	5686.2e-9	11360.9e-9
2011	$B^0_s \to K^0_S\pi^+\pi^-$	LL	15207.0e-8	489.3e-8	1.2e-8	53.0e-8	67.2e-8	1132.2e-8	568.6e-8	1360.9e-8

Table C.62: $B^0_s \to K^0_S\pi^+\pi^-$ efficiency table with the unfavoured mode optimisation. For each year and K^0_S reconstruction type, the average efficiency $\bar{\varepsilon}$, the statistical uncertainty $\sigma^{\text{stat}}_{\bar{\varepsilon}}$, the uncertainty linked to the tracking correction $\sigma^{\text{tracking}}_{\bar{\varepsilon}}$, the uncertainty linked to the L0Hadron trigger correction $\sigma^{\text{L0corr}}_{\bar{\varepsilon}}$, the uncertainty related to the PID MC sampling effect $\sigma^{\text{PIDMCsampling}}_{\bar{\varepsilon}}$, the uncertainty linked to the PID kernel variation $\sigma^{\text{PIDkernel}}_{\bar{\varepsilon}}$, the uncertainty linked to the averaging method $\sigma^{\text{RMS}}_{\bar{\varepsilon}}$ and the total uncertainty $\sigma_{\bar{\varepsilon}}$ are given.

Year	Mode	K^0_S	$\bar{\varepsilon}$	$\sigma^{\text{stat}}_{\bar{\varepsilon}}$	$\sigma^{\text{tracking}}_{\bar{\varepsilon}}$	$\sigma^{\text{L0corr}}_{\bar{\varepsilon}}$	$\sigma^{\text{PIDMCsampling}}_{\bar{\varepsilon}}$	$\sigma^{\text{PIDkernel}}_{\bar{\varepsilon}}$	$\sigma^{\text{RMS}}_{\bar{\varepsilon}}$	$\sigma_{\bar{\varepsilon}}$
2018	$B^0_s \to K^0_S\pi^+K^-$	DD	64732.7e-8	732.3e-8	4.0e-8	62.7e-8	87.7e-8	246.1e-8	514.9e-8	934.6e-8
2017	$B^0_s \to K^0_S\pi^+K^-$	DD	67660.2e-8	771.2e-8	3.9e-8	73.9e-8	61.6e-8	137.6e-8	514.9e-8	942.4e-8
2016	$B^0_s \to K^0_S\pi^+K^-$	DD	76894.9e-8	843.4e-8	4.4e-8	74.7e-8	66.7e-8	162.7e-8	514.9e-8	1006.5e-8
2015	$B^0_s \to K^0_S\pi^+K^-$	DD	67027.0e-8	798.9e-8	4.1e-8	71.6e-8	135.2e-8	287.3e-8	514.9e-8	1004.7e-8
2012b	$B^0_s \to K^0_S\pi^+K^-$	DD	45894.8e-8	808.1e-8	2.4e-8	85.7e-8	74.8e-8	946.3e-8	514.9e-8	1351.5e-8
2012a	$B^0_s \to K^0_S\pi^+K^-$	DD	38878.4e-8	803.0e-8	2.4e-8	85.8e-8	64.5e-8	820.0e-8	514.9e-8	1262.5e-8
2011	$B^0_s \to K^0_S\pi^+K^-$	DD	45662.4e-8	859.6e-8	2.6e-8	145.1e-8	103.4e-8	1714.3e-8	514.9e-8	1993.6e-8
2018	$B^0_s \to K^0_S\pi^+K^-$	LL	27124.4e-8	489.2e-8	2.7e-8	21.0e-8	43.5e-8	63.8e-8	588.1e-8	769.2e-8
2017	$B^0_s \to K^0_S\pi^+K^-$	LL	29863.6e-8	535.8e-8	2.7e-8	27.9e-8	74.9e-8	80.8e-8	588.1e-8	803.7e-8
2016	$B^0_s \to K^0_S\pi^+K^-$	LL	31576.7e-8	556.4e-8	2.8e-8	26.5e-8	35.5e-8	85.3e-8	588.1e-8	815.3e-8
2015	$B^0_s \to K^0_S\pi^+K^-$	LL	24737.3e-8	490.0e-8	2.3e-8	21.6e-8	71.8e-8	119.0e-8	588.1e-8	778.3e-8
2012b	$B^0_s \to K^0_S\pi^+K^-$	LL	90862.7e-9	3721.8e-9	9.0e-9	150.2e-9	310.8e-9	1882.6e-9	5881.0e-9	7218.1e-9
2012a	$B^0_s \to K^0_S\pi^+K^-$	LL	15145.9e-8	500.4e-8	1.2e-8	25.3e-8	36.7e-8	503.9e-8	588.1e-8	923.1e-8
2011	$B^0_s \to K^0_S\pi^+K^-$	LL	18551.3e-8	563.5e-8	1.6e-8	41.8e-8	45.8e-8	545.1e-8	588.1e-8	982.0e-8

Table C.63: $B^0_s \to K^0_S\pi^+K^-$ efficiency table with the unfavoured mode optimisation. For each year and K^0_S reconstruction type, the average efficiency $\bar{\varepsilon}$, the statistical uncertainty $\sigma^{\text{stat}}_{\bar{\varepsilon}}$, the uncertainty linked to the tracking correction $\sigma^{\text{tracking}}_{\bar{\varepsilon}}$, the uncertainty linked to the L0Hadron trigger correction $\sigma^{\text{L0corr}}_{\bar{\varepsilon}}$, the uncertainty related to the PID MC sampling effect $\sigma^{\text{PIDMCsampling}}_{\bar{\varepsilon}}$, the uncertainty linked to the PID kernel variation $\sigma^{\text{PIDkernel}}_{\bar{\varepsilon}}$, the uncertainty linked to the averaging method $\sigma^{\text{RMS}}_{\bar{\varepsilon}}$ and the total uncertainty $\sigma_{\bar{\varepsilon}}$ are given.

Year	Mode	K_S^0	$\bar{\varepsilon}$	$\sigma_{\bar{\varepsilon}}^{\text{stat}}$	$\sigma_{\bar{\varepsilon}}^{\text{tracking}}$	$\sigma_{\bar{\varepsilon}}^{\text{L0corr}}$	$\sigma_{\bar{\varepsilon}}^{\text{PIDMCsampling}}$	$\sigma_{\bar{\varepsilon}}^{\text{PIDkernel}}$	$\sigma_{\bar{\varepsilon}}^{\text{RMS}}$	$\sigma_{\bar{\varepsilon}}$
2018	$B_s^0 \to K_S^0 K^+ \pi^-$	DD	67775.2e-8	711.6e-8	4.1e-8	63.7e-8	74.7e-8	193.0e-8	447.6e-8	868.1e-8
2017	$B_s^0 \to K_S^0 K^+ \pi^-$	DD	75014.3e-8	781.2e-8	4.2e-8	78.0e-8	83.8e-8	240.3e-8	447.6e-8	938.9e-8
2016	$B_s^0 \to K_S^0 K^+ \pi^-$	DD	74245.4e-8	786.8e-8	4.2e-8	72.1e-8	47.3e-8	168.6e-8	447.6e-8	924.8e-8
2015	$B_s^0 \to K_S^0 K^+ \pi^-$	DD	61562.7e-8	727.3e-8	3.7e-8	64.1e-8	91.6e-8	230.5e-8	447.6e-8	891.6e-8
2012b	$B_s^0 \to K_S^0 K^+ \pi^-$	DD	41511.2e-8	742.9e-8	2.2e-8	84.8e-8	47.6e-8	1096.0e-8	447.6e-8	1401.0e-8
2012a	$B_s^0 \to K_S^0 K^+ \pi^-$	DD	34409.5e-8	713.0e-8	2.2e-8	79.1e-8	54.1e-8	1395.4e-8	447.6e-8	1632.5e-8
2011	$B_s^0 \to K_S^0 K^+ \pi^-$	DD	43343.9e-8	776.5e-8	2.4e-8	127.6e-8	67.7e-8	1472.9e-8	447.6e-8	1730.3e-8
2018	$B_s^0 \to K_S^0 K^+ \pi^-$	LL	26415.9e-8	509.9e-8	2.7e-8	20.3e-8	65.3e-8	168.2e-8	969.3e-8	1110.2e-8
2017	$B_s^0 \to K_S^0 K^+ \pi^-$	LL	28416.9e-8	550.1e-8	2.7e-8	26.7e-8	38.4e-8	91.2e-8	969.3e-8	1119.2e-8
2016	$B_s^0 \to K_S^0 K^+ \pi^-$	LL	31433.7e-8	593.7e-8	2.9e-8	27.0e-8	32.6e-8	116.2e-8	969.3e-8	1143.4e-8
2015	$B_s^0 \to K_S^0 K^+ \pi^-$	LL	27536.0e-8	553.6e-8	2.6e-8	26.3e-8	67.6e-8	152.1e-8	969.3e-8	1128.9e-8
2012b	$B_s^0 \to K_S^0 K^+ \pi^-$	LL	90197.1e-9	3618.9e-9	9.2e-9	145.1e-9	463.9e-9	2160.3e-9	9692.6e-9	10580.5e-9
2012a	$B_s^0 \to K_S^0 K^+ \pi^-$	LL	14842.8e-8	499.1e-8	1.3e-8	26.5e-8	62.9e-8	520.0e-8	969.3e-8	1209.8e-8
2011	$B_s^0 \to K_S^0 K^+ \pi^-$	LL	16926.1e-8	527.7e-8	1.4e-8	41.3e-8	47.0e-8	424.4e-8	969.3e-8	1184.0e-8

Table C.64: $B_s^0 \to K_S^0 K^+ \pi^-$ efficiency table with the unfavoured mode optimisation. For each year and K_S^0 reconstruction type, the average efficiency $\bar{\varepsilon}$, the statistical uncertainty $\sigma_{\bar{\varepsilon}}^{\text{stat}}$, the uncertainty linked to the tracking correction $\sigma_{\bar{\varepsilon}}^{\text{tracking}}$, the uncertainty linked to the L0Hadron trigger correction $\sigma_{\bar{\varepsilon}}^{\text{L0corr}}$, the uncertainty related to the PID MC sampling effect $\sigma_{\bar{\varepsilon}}^{\text{PIDMCsampling}}$, the uncertainty linked to the PID kernel variation $\sigma_{\bar{\varepsilon}}^{\text{PIDkernel}}$, the uncertainty linked to the averaging method $\sigma_{\bar{\varepsilon}}^{\text{RMS}}$ and the total uncertainty $\sigma_{\bar{\varepsilon}}$ are given.

Year	Mode	K_S^0	$\bar{\varepsilon}$	$\sigma_{\bar{\varepsilon}}^{\text{stat}}$	$\sigma_{\bar{\varepsilon}}^{\text{tracking}}$	$\sigma_{\bar{\varepsilon}}^{\text{L0corr}}$	$\sigma_{\bar{\varepsilon}}^{\text{PIDMCsampling}}$	$\sigma_{\bar{\varepsilon}}^{\text{PIDkernel}}$	$\sigma_{\bar{\varepsilon}}^{\text{RMS}}$	$\sigma_{\bar{\varepsilon}}$
2018	$B_s^0 \to K_S^0 K^+ K^-$	DD	54797.5e-8	611.3e-8	3.4e-8	60.7e-8	102.4e-8	228.2e-8	3777.9e-8	3835.7e-8
2017	$B_s^0 \to K_S^0 K^+ K^-$	DD	42596.8e-8	561.5e-8	2.6e-8	77.1e-8	85.7e-8	220.6e-8	3777.9e-8	3827.5e-8
2016	$B_s^0 \to K_S^0 K^+ K^-$	DD	54637.0e-8	634.0e-8	3.2e-8	65.9e-8	103.7e-8	188.9e-8	3777.9e-8	3837.4e-8
2015	$B_s^0 \to K_S^0 K^+ K^-$	DD	45074.6e-8	577.2e-8	2.9e-8	56.5e-8	117.9e-8	240.3e-8	3777.9e-8	3831.5e-8
2012b	$B_s^0 \to K_S^0 K^+ K^-$	DD	42264.4e-8	681.1e-8	2.0e-8	143.4e-8	102.8e-8	3027.1e-8	3777.9e-8	4891.9e-8
2012a	$B_s^0 \to K_S^0 K^+ K^-$	DD	30754.9e-8	647.5e-8	1.7e-8	93.9e-8	89.9e-8	2036.1e-8	3777.9e-8	4342.2e-8
2011	$B_s^0 \to K_S^0 K^+ K^-$	DD	39536.8e-8	696.2e-8	1.8e-8	148.3e-8	187.4e-8	3435.4e-8	3777.9e-8	5159.1e-8
2018	$B_s^0 \to K_S^0 K^+ K^-$	LL	2672.3e-7	176.5e-7	1.1e-7	8.6e-7	34.1e-7	17.5e-7	371.7e-7	413.4e-7
2017	$B_s^0 \to K_S^0 K^+ K^-$	LL	22726.5e-8	1747.5e-8	9.0e-8	125.4e-8	338.9e-8	94.6e-8	3717.1e-8	4124.4e-8
2016	$B_s^0 \to K_S^0 K^+ K^-$	LL	25631.5e-8	1798.3e-8	9.6e-8	91.8e-8	272.0e-8	132.2e-8	3717.1e-8	4141.4e-8
2015	$B_s^0 \to K_S^0 K^+ K^-$	LL	3502.8e-7	214.9e-7	1.2e-7	12.6e-7	33.0e-7	20.2e-7	371.7e-7	431.3e-7
2012b	$B_s^0 \to K_S^0 K^+ K^-$	LL	15393.4e-8	1799.5e-8	5.3e-8	230.2e-8	363.6e-8	1143.7e-8	3717.1e-8	4306.8e-8
2012a	$B_s^0 \to K_S^0 K^+ K^-$	LL	16689.4e-8	2135.4e-8	5.7e-8	217.1e-8	207.0e-8	1134.9e-8	3717.1e-8	4444.7e-8
2011	$B_s^0 \to K_S^0 K^+ K^-$	LL	17599.6e-8	2008.3e-8	4.8e-8	200.8e-8	453.7e-8	1006.0e-8	3717.1e-8	4371.3e-8

Table C.65: $B_s^0 \to K_S^0 K^+ K^-$ efficiency table with the unfavoured mode optimisation. For each year and K_S^0 reconstruction type, the average efficiency $\bar{\varepsilon}$, the statistical uncertainty $\sigma_{\bar{\varepsilon}}^{\text{stat}}$, the uncertainty linked to the tracking correction $\sigma_{\bar{\varepsilon}}^{\text{tracking}}$, the uncertainty linked to the L0Hadron trigger correction $\sigma_{\bar{\varepsilon}}^{\text{L0corr}}$, the uncertainty related to the PID MC sampling effect $\sigma_{\bar{\varepsilon}}^{\text{PIDMCsampling}}$, the uncertainty linked to the PID kernel variation $\sigma_{\bar{\varepsilon}}^{\text{PIDkernel}}$, the uncertainty linked to the averaging method $\sigma_{\bar{\varepsilon}}^{\text{RMS}}$ and the total uncertainty $\sigma_{\bar{\varepsilon}}$ are given.

C.9 Relative efficiency tables

Tables C.66 to C.79 display the relative efficiency tables with the associated absolute uncertainties. Tables C.80 to C.93 display the relative efficiency tables with the associated relative uncertainties.

Year	Mode	K^0_S	$\varepsilon_{B\to K^0_S hh'}$	$\varepsilon_{B^0_d\to K^0_S\pi^+\pi^-}$	$\frac{\varepsilon_{B^0_d\to K^0_S\pi^+\pi^-}}{\varepsilon_{B\to K^0_S hh'}}$	$\sigma^{\text{stat}}_{\frac{\varepsilon_{B^0_d\to K^0_S\pi^+\pi^-}}{\varepsilon_{B\to K^0_S hh'}}}$	$\sigma^{\text{tracking}}_{\frac{\varepsilon_{B^0_d\to K^0_S\pi^+\pi^-}}{\varepsilon_{B\to K^0_S hh'}}}$	$\sigma^{\text{L0corr}}_{\frac{\varepsilon_{B^0_d\to K^0_S\pi^+\pi^-}}{\varepsilon_{B\to K^0_S hh'}}}$	$\sigma^{\text{PIDMCsampling}}_{\frac{\varepsilon_{B^0_d\to K^0_S\pi^+\pi^-}}{\varepsilon_{B\to K^0_S hh'}}}$	$\sigma^{\text{PIDkernel}}_{\frac{\varepsilon_{B^0_d\to K^0_S\pi^+\pi^-}}{\varepsilon_{B\to K^0_S hh'}}}$	$\sigma^{\text{RMS}}_{\frac{\varepsilon_{B^0_d\to K^0_S\pi^+\pi^-}}{\varepsilon_{B\to K^0_S hh'}}}$	$\sigma^{\text{binning}}_{\frac{\varepsilon_{B^0_d\to K^0_S\pi^+\pi^-}}{\varepsilon_{B\to K^0_S hh'}}}$	$\sigma^{\text{L0Echoice}}_{\frac{\varepsilon_{B^0_d\to K^0_S\pi^+\pi^-}}{\varepsilon_{B\to K^0_S hh'}}}$	$\sigma^{\text{FTrigger}}_{\frac{\varepsilon_{B^0_d\to K^0_S\pi^+\pi^-}}{\varepsilon_{B\to K^0_S hh'}}}$	$\sigma^{\text{MCreweighting}}_{\frac{\varepsilon_{B^0_d\to K^0_S\pi^+\pi^-}}{\varepsilon_{B\to K^0_S hh'}}}$	$\sigma^{\text{K}^0_S\text{tracking}}_{\frac{\varepsilon_{B^0_d\to K^0_S\pi^+\pi^-}}{\varepsilon_{B\to K^0_S hh'}}}$	$\sigma^{\text{tot}}_{\frac{\varepsilon_{B^0_d\to K^0_S\pi^+\pi^-}}{\varepsilon_{B\to K^0_S hh'}}}$
2018	$B^0_d\to K^0_S\pi^+K^-$	DD	8.85e-04	8.21e-04	0.92759	0.01260	0.00008	0.00146	0.00168	0.00480	0.01946	0.01357	0.00004	0.00082	0.00616	0.00008	0.02808
2017	$B^0_d\to K^0_S\pi^+K^-$	DD	9.26e-04	8.33e-04	0.89989	0.01238	0.00007	0.00140	0.00166	0.00395	0.01833	0.01357	0.00004	0.00604	0.00598	0.00007	0.02767
2016	$B^0_d\to K^0_S\pi^+K^-$	DD	1.05e-03	8.69e-04	0.82722	0.01088	0.00006	0.00126	0.00111	0.00330	0.01553	0.01357	0.00004	0.00198	0.00549	0.00006	0.02432
2015	$B^0_d\to K^0_S\pi^+K^-$	DD	9.33e-04	8.36e-04	0.89567	0.01259	0.00007	0.00149	0.00209	0.00719	0.01815	0.01357	0.00004	0.00081	0.00595	0.00007	0.02768
2012b	$B^0_d\to K^0_S\pi^+K^-$	DD	6.62e-04	5.19e-04	0.78501	0.01629	0.00005	0.00214	0.00189	0.05442	0.02412	0.01357	0.00007	0.00508	0.00521	0.00005	0.06367
2012a	$B^0_d\to K^0_S\pi^+K^-$	DD	5.04e-04	4.12e-04	0.81742	0.02102	0.00006	0.00288	0.00248	0.06678	0.03225	0.01357	0.00002	0.00061	0.00543	0.00006	0.07855
2011	$B^0_d\to K^0_S\pi^+K^-$	DD	6.10e-04	4.92e-04	0.80706	0.01790	0.00006	0.00368	0.00283	0.06124	0.02649	0.01357	0.00009	0.00029	0.00536	0.00006	0.07076
2018	$B^0_d\to K^0_S\pi^+K^-$	LL	3.34e-04	2.97e-04	0.88826	0.02159	0.00012	0.00115	0.00284	0.00498	0.03734	0.01743	0.00025	0.00371	0.00590	0.00012	0.04741
2017	$B^0_d\to K^0_S\pi^+K^-$	LL	3.70e-04	3.17e-04	0.85555	0.02095	0.00011	0.00121	0.00276	0.00329	0.03279	0.01743	0.00025	0.00235	0.00568	0.00011	0.04331
2016	$B^0_d\to K^0_S\pi^+K^-$	LL	3.84e-04	3.56e-04	0.92716	0.02209	0.00011	0.00129	0.00187	0.00410	0.03352	0.01743	0.00025	0.00120	0.00616	0.00011	0.04446
2015	$B^0_d\to K^0_S\pi^+K^-$	LL	3.67e-04	3.28e-04	0.89240	0.02198	0.00012	0.00124	0.00393	0.00695	0.03412	0.01743	0.00025	0.00281	0.00593	0.00012	0.04538
2012b	$B^0_d\to K^0_S\pi^+K^-$	LL	1.81e-04	1.53e-04	0.84580	0.03480	0.00011	0.00208	0.00730	0.06916	0.06645	0.01743	0.00040	0.00004	0.00562	0.00011	0.10394
2012a	$B^0_d\to K^0_S\pi^+K^-$	LL	2.08e-04	1.77e-04	0.84869	0.03534	0.00010	0.00225	0.00646	0.06254	0.05796	0.01743	0.00018	0.00489	0.00564	0.00010	0.09448
2011	$B^0_d\to K^0_S\pi^+K^-$	LL	2.37e-04	1.88e-04	0.79103	0.03028	0.00008	0.00290	0.00397	0.04696	0.04848	0.01743	0.00024	0.00619	0.00525	0.00008	0.07659

Table C.66: $B^0\to K^0_S\pi^+\pi^-$ over $B^0\to K^0_S\pi^+K^-$ efficiency table for the favoured mode optimisation. For each year and K^0_S reconstruction type, the average efficiency of the considered mode, the average efficiency of $B^0\to K^0_S\pi^+\pi^-$, the ratio of average efficiencies, the related uncertainties split by sources and the final uncertainty are given.

Year	Mode	K^0_S	$\varepsilon_{B\to K^0_S hh'}$	$\varepsilon_{B^0_d\to K^0_S\pi^+\pi^-}$	$\frac{\varepsilon_{B^0_d\to K^0_S\pi^+\pi^-}}{\varepsilon_{B\to K^0_S hh'}}$	$\sigma^{\text{stat}}_{\frac{\varepsilon_{B^0_d\to K^0_S\pi^+\pi^-}}{\varepsilon_{B\to K^0_S hh'}}}$	$\sigma^{\text{tracking}}_{\frac{\varepsilon_{B^0_d\to K^0_S\pi^+\pi^-}}{\varepsilon_{B\to K^0_S hh'}}}$	$\sigma^{\text{L0corr}}_{\frac{\varepsilon_{B^0_d\to K^0_S\pi^+\pi^-}}{\varepsilon_{B\to K^0_S hh'}}}$	$\sigma^{\text{PIDMCsampling}}_{\frac{\varepsilon_{B^0_d\to K^0_S\pi^+\pi^-}}{\varepsilon_{B\to K^0_S hh'}}}$	$\sigma^{\text{PIDkernel}}_{\frac{\varepsilon_{B^0_d\to K^0_S\pi^+\pi^-}}{\varepsilon_{B\to K^0_S hh'}}}$	$\sigma^{\text{RMS}}_{\frac{\varepsilon_{B^0_d\to K^0_S\pi^+\pi^-}}{\varepsilon_{B\to K^0_S hh'}}}$	$\sigma^{\text{binning}}_{\frac{\varepsilon_{B^0_d\to K^0_S\pi^+\pi^-}}{\varepsilon_{B\to K^0_S hh'}}}$	$\sigma^{\text{L0Echoice}}_{\frac{\varepsilon_{B^0_d\to K^0_S\pi^+\pi^-}}{\varepsilon_{B\to K^0_S hh'}}}$	$\sigma^{\text{FTrigger}}_{\frac{\varepsilon_{B^0_d\to K^0_S\pi^+\pi^-}}{\varepsilon_{B\to K^0_S hh'}}}$	$\sigma^{\text{MCreweighting}}_{\frac{\varepsilon_{B^0_d\to K^0_S\pi^+\pi^-}}{\varepsilon_{B\to K^0_S hh'}}}$	$\sigma^{\text{K}^0_S\text{tracking}}_{\frac{\varepsilon_{B^0_d\to K^0_S\pi^+\pi^-}}{\varepsilon_{B\to K^0_S hh'}}}$	$\sigma^{\text{tot}}_{\frac{\varepsilon_{B^0_d\to K^0_S\pi^+\pi^-}}{\varepsilon_{B\to K^0_S hh'}}}$
2018	$B^0_d\to K^0_S K^+\pi^-$	DD	8.98e-04	8.21e-04	0.91394	0.01319	0.00008	0.00143	0.00143	0.00459	0.02019	0.01062	0.00003	0.00304	0.00607	0.00008	0.02767
2017	$B^0_d\to K^0_S K^+\pi^-$	DD	9.56e-04	8.33e-04	0.87205	0.01287	0.00007	0.00145	0.00130	0.00393	0.01851	0.01062	0.00003	0.00324	0.00579	0.00007	0.02616
2016	$B^0_d\to K^0_S K^+\pi^-$	DD	1.02e-03	8.69e-04	0.85108	0.01214	0.00007	0.00142	0.00110	0.00332	0.01710	0.01062	0.00003	0.00198	0.00565	0.00007	0.02455
2015	$B^0_d\to K^0_S K^+\pi^-$	DD	9.33e-04	8.36e-04	0.89592	0.01365	0.00008	0.00166	0.00317	0.00819	0.01923	0.01062	0.00003	0.00068	0.00595	0.00008	0.02801
2012b	$B^0_d\to K^0_S K^+\pi^-$	DD	6.82e-04	5.19e-04	0.76209	0.01691	0.00006	0.00228	0.00423	0.06272	0.02429	0.01062	0.00009	0.00562	0.00506	0.00006	0.07073
2012a	$B^0_d\to K^0_S K^+\pi^-$	DD	5.19e-04	4.12e-04	0.79266	0.02204	0.00007	0.00253	0.00313	0.06836	0.03248	0.01062	0.00010	0.00572	0.00526	0.00007	0.08002
2011	$B^0_d\to K^0_S K^+\pi^-$	DD	6.36e-04	4.92e-04	0.77358	0.01868	0.00006	0.00390	0.00254	0.06036	0.02621	0.01062	0.00010	0.00080	0.00514	0.00006	0.06958
2018	$B^0_d\to K^0_S K^+\pi^-$	LL	3.22e-04	2.97e-04	0.92069	0.02426	0.00014	0.00127	0.00271	0.00493	0.04335	0.03237	0.00016	0.00899	0.00611	0.00014	0.06056
2017	$B^0_d\to K^0_S K^+\pi^-$	LL	3.68e-04	3.17e-04	0.86072	0.02278	0.00012	0.00132	0.00722	0.00521	0.03604	0.03237	0.00016	0.00424	0.00572	0.00012	0.05475
2016	$B^0_d\to K^0_S K^+\pi^-$	LL	4.01e-04	3.56e-04	0.88901	0.02240	0.00012	0.00133	0.01647	0.00460	0.03394	0.03237	0.00016	0.00358	0.00590	0.00012	0.05517
2015	$B^0_d\to K^0_S K^+\pi^-$	LL	3.75e-04	3.28e-04	0.87453	0.02313	0.00012	0.00141	0.00499	0.01065	0.03586	0.03237	0.00016	0.00011	0.00581	0.00012	0.05516
2012b	$B^0_d\to K^0_S K^+\pi^-$	LL	1.78e-04	1.53e-04	0.86159	0.03978	0.00012	0.00257	0.01329	0.06581	0.07462	0.03237	0.00038	0.00107	0.00572	0.00012	0.11290
2012a	$B^0_d\to K^0_S K^+\pi^-$	LL	1.88e-04	1.77e-04	0.93893	0.04629	0.00013	0.00246	0.00698	0.04899	0.07537	0.03237	0.00004	0.00009	0.00623	0.00013	0.10660
2011	$B^0_d\to K^0_S K^+\pi^-$	LL	2.29e-04	1.88e-04	0.81795	0.03549	0.00010	0.00362	0.00457	0.04958	0.05567	0.03237	0.00019	0.00096	0.00543	0.00010	0.08905

Table C.67: $B^0\to K^0_S\pi^+\pi^-$ over $B^0\to K^0_S K^+\pi^-$ efficiency table for the favoured mode optimisation. For each year and K^0_S reconstruction type, the average efficiency of the considered mode, the average efficiency of $B^0\to K^0_S\pi^+\pi^-$, the ratio of average efficiencies, the related uncertainties split by sources and the final uncertainty are given.

Year	Mode	K^0_S	$\varepsilon_{B\to K^0_S hh'}$	$\varepsilon_{B^0_d\to K^0_S\pi^+\pi^-}$	$\frac{\varepsilon_{B^0_d\to K^0_S\pi^+\pi^-}}{\varepsilon_{B\to K^0_S hh'}}$	$\sigma^{\text{stat}}_{\frac{\varepsilon_{B^0_d\to K^0_S\pi^+\pi^-}}{\varepsilon_{B\to K^0_S hh'}}}$	$\sigma^{\text{tracking}}_{\frac{\varepsilon_{B^0_d\to K^0_S\pi^+\pi^-}}{\varepsilon_{B\to K^0_S hh'}}}$	$\sigma^{\text{L0corr}}_{\frac{\varepsilon_{B^0_d\to K^0_S\pi^+\pi^-}}{\varepsilon_{B\to K^0_S hh'}}}$	$\sigma^{\text{PIDMCsampling}}_{\frac{\varepsilon_{B^0_d\to K^0_S\pi^+\pi^-}}{\varepsilon_{B\to K^0_S hh'}}}$	$\sigma^{\text{PIDkernel}}_{\frac{\varepsilon_{B^0_d\to K^0_S\pi^+\pi^-}}{\varepsilon_{B\to K^0_S hh'}}}$	$\sigma^{\text{RMS}}_{\frac{\varepsilon_{B^0_d\to K^0_S\pi^+\pi^-}}{\varepsilon_{B\to K^0_S hh'}}}$	$\sigma^{\text{binning}}_{\frac{\varepsilon_{B^0_d\to K^0_S\pi^+\pi^-}}{\varepsilon_{B\to K^0_S hh'}}}$	$\sigma^{\text{L0Echoice}}_{\frac{\varepsilon_{B^0_d\to K^0_S\pi^+\pi^-}}{\varepsilon_{B\to K^0_S hh'}}}$	$\sigma^{\text{FTrigger}}_{\frac{\varepsilon_{B^0_d\to K^0_S\pi^+\pi^-}}{\varepsilon_{B\to K^0_S hh'}}}$	$\sigma^{\text{MCreweighting}}_{\frac{\varepsilon_{B^0_d\to K^0_S\pi^+\pi^-}}{\varepsilon_{B\to K^0_S hh'}}}$	$\sigma^{\text{K}^0_S\text{tracking}}_{\frac{\varepsilon_{B^0_d\to K^0_S\pi^+\pi^-}}{\varepsilon_{B\to K^0_S hh'}}}$	$\sigma^{\text{tot}}_{\frac{\varepsilon_{B^0_d\to K^0_S\pi^+\pi^-}}{\varepsilon_{B\to K^0_S hh'}}}$
2018	$B^0_d\to K^0_S K^+K^-$	DD	7.28e-04	8.21e-04	1.12748	0.01167	0.00007	0.00144	0.00127	0.00441	0.01748	0.03701	0.00057	0.00696	0.00749	0.00007	0.04404
2017	$B^0_d\to K^0_S K^+K^-$	DD	7.51e-04	8.33e-04	1.10885	0.01180	0.00007	0.00200	0.00101	0.00358	0.01691	0.03701	0.00057	0.00623	0.00736	0.00007	0.04366
2016	$B^0_d\to K^0_S K^+K^-$	DD	8.93e-04	8.69e-04	0.97305	0.00983	0.00005	0.00127	0.00080	0.00380	0.01410	0.03701	0.00057	0.00431	0.00646	0.00005	0.04174
2015	$B^0_d\to K^0_S K^+K^-$	DD	8.04e-04	8.36e-04	1.04000	0.01105	0.00006	0.00146	0.00140	0.00462	0.01574	0.03701	0.00057	0.00638	0.00691	0.00006	0.04305
2012b	$B^0_d\to K^0_S K^+K^-$	DD	4.50e-04	5.19e-04	1.15518	0.01920	0.00006	0.00408	0.00844	0.03072	0.02836	0.03701	0.00018	0.00392	0.00767	0.00006	0.06040
2012a	$B^0_d\to K^0_S K^+K^-$	DD	3.11e-04	4.12e-04	1.32149	0.02751	0.00008	0.00561	0.00228	0.03202	0.04148	0.03701	0.00028	0.00023	0.00877	0.00008	0.07062
2011	$B^0_d\to K^0_S K^+K^-$	DD	3.60e-04	4.92e-04	1.36557	0.02466	0.00007	0.00579	0.00175	0.02169	0.03599	0.03701	0.00023	0.00050	0.00907	0.00007	0.06215
2018	$B^0_d\to K^0_S K^+K^-$	LL	3.05e-04	2.97e-04	0.97387	0.01596	0.00009	0.00101	0.00159	0.00292	0.02233	0.02898	0.00065	0.01729	0.00647	0.00009	0.04412
2017	$B^0_d\to K^0_S K^+K^-$	LL	3.29e-04	3.17e-04	0.96221	0.01606	0.00009	0.00134	0.00131	0.00353	0.02064	0.02898	0.00065	0.01569	0.00639	0.00009	0.04275
2016	$B^0_d\to K^0_S K^+K^-$	LL	3.70e-04	3.56e-04	0.96216	0.01529	0.00008	0.00106	0.00103	0.00364	0.01836	0.02898	0.00065	0.00670	0.00639	0.00008	0.03889
2015	$B^0_d\to K^0_S K^+K^-$	LL	3.33e-04	3.28e-04	0.98409	0.01651	0.00009	0.00114	0.00233	0.00705	0.02047	0.02898	0.00065	0.00656	0.00653	0.00009	0.04092
2012b	$B^0_d\to K^0_S K^+K^-$	LL	1.47e-04	1.53e-04	1.04271	0.03093	0.00010	0.00353	0.00275	0.01914	0.04659	0.02898	0.00047	0.00326	0.00692	0.00010	0.06643
2012a	$B^0_d\to K^0_S K^+K^-$	LL	1.68e-04	1.77e-04	1.05282	0.03178	0.00009	0.00255	0.00355	0.02490	0.04083	0.02898	0.00030	0.00833	0.00699	0.00009	0.06538
2011	$B^0_d\to K^0_S K^+K^-$	LL	1.90e-04	1.88e-04	0.98769	0.02721	0.00007	0.00328	0.00252	0.01838	0.03587	0.02898	0.00036	0.00345	0.00656	0.00007	0.05725

Table C.68: $B^0\to K^0_S\pi^+\pi^-$ over $B^0\to K^0_S K^+K^-$ efficiency table for the favoured mode optimisation. For each year and K^0_S reconstruction type, the average efficiency of the considered mode, the average efficiency of $B^0\to K^0_S\pi^+\pi^-$, the ratio of average efficiencies, the related uncertainties split by sources and the final uncertainty are given.

Year	Mode	K^0_S	$\bar{\varepsilon}_{B\to K^0_S hh'}$	$\bar{\varepsilon}_{B^0_s\to K^0_S\pi^+\pi^-}$	$\frac{\bar{\varepsilon}_{B^0_s\to K^0_S\pi^+\pi^-}}{\bar{\varepsilon}_{B\to K^0_S hh'}}$	$\sigma^{\text{stat}}_{\frac{\bar{\varepsilon}_{B^0_s\to K^0_S\pi^+\pi^-}}{\bar{\varepsilon}_{B\to K^0_S hh'}}}$	$\sigma^{\text{tracking}}_{\frac{\bar{\varepsilon}_{B^0_s\to K^0_S\pi^+\pi^-}}{\bar{\varepsilon}_{B\to K^0_S hh'}}}$	$\sigma^{\text{L0corr}}_{\frac{\bar{\varepsilon}_{B^0_s\to K^0_S\pi^+\pi^-}}{\bar{\varepsilon}_{B\to K^0_S hh'}}}$	$\sigma^{\text{PIDMCsampling}}_{\frac{\bar{\varepsilon}_{B^0_s\to K^0_S\pi^+\pi^-}}{\bar{\varepsilon}_{B\to K^0_S hh'}}}$	$\sigma^{\text{PIDkernel}}_{\frac{\bar{\varepsilon}_{B^0_s\to K^0_S\pi^+\pi^-}}{\bar{\varepsilon}_{B\to K^0_S hh'}}}$	$\sigma^{\text{RMS}}_{\frac{\bar{\varepsilon}_{B^0_s\to K^0_S\pi^+\pi^-}}{\bar{\varepsilon}_{B\to K^0_S hh'}}}$	$\sigma^{\text{binning}}_{\frac{\bar{\varepsilon}_{B^0_s\to K^0_S\pi^+\pi^-}}{\bar{\varepsilon}_{B\to K^0_S hh'}}}$	$\sigma^{\text{L0E0choice}}_{\frac{\bar{\varepsilon}_{B^0_s\to K^0_S\pi^+\pi^-}}{\bar{\varepsilon}_{B\to K^0_S hh'}}}$	$\sigma^{\text{FTrigger}}_{\frac{\bar{\varepsilon}_{B^0_s\to K^0_S\pi^+\pi^-}}{\bar{\varepsilon}_{B\to K^0_S hh'}}}$	$\sigma^{\text{MCreweighting}}_{\frac{\bar{\varepsilon}_{B^0_s\to K^0_S\pi^+\pi^-}}{\bar{\varepsilon}_{B\to K^0_S hh'}}}$	$\sigma^{\text{K}^0_S\text{tracking}}_{\frac{\bar{\varepsilon}_{B^0_s\to K^0_S\pi^+\pi^-}}{\bar{\varepsilon}_{B\to K^0_S hh'}}}$	$\sigma^{\text{tot}}_{\frac{\bar{\varepsilon}_{B^0_s\to K^0_S\pi^+\pi^-}}{\bar{\varepsilon}_{B\to K^0_S hh'}}}$
2018	$B^0_s\to K^0_S\pi^+\pi^-$	DD	8.71e-04	8.21e-04	0.942695	0.011326	N/A	N/A	N/A	N/A	0.040485	0.016535	7.582000e-05	0.001743	0.006259	N/A	0.045640
2017	$B^0_s\to K^0_S\pi^+\pi^-$	DD	8.84e-04	8.33e-04	0.942319	0.011576	N/A	N/A	N/A	N/A	0.039858	0.016535	7.582000e-05	0.002949	0.006257	N/A	0.045210
2016	$B^0_s\to K^0_S\pi^+\pi^-$	DD	9.14e-04	8.69e-04	0.951509	0.011623	N/A	N/A	N/A	N/A	0.038909	0.016535	7.582000e-05	0.000830	0.006318	N/A	0.044306
2015	$B^0_s\to K^0_S\pi^+\pi^-$	DD	8.97e-04	8.36e-04	0.931657	0.011695	N/A	N/A	N/A	N/A	0.038894	0.016535	7.582000e-05	0.001304	0.006186	N/A	0.044304
2012b	$B^0_s\to K^0_S\pi^+\pi^-$	DD	5.70e-04	5.19e-04	0.911273	0.016604	N/A	N/A	N/A	N/A	0.060048	0.016535	6.234000e-05	0.000600	0.006051	N/A	0.064745
2012a	$B^0_s\to K^0_S\pi^+\pi^-$	DD	4.59e-04	4.12e-04	0.897631	0.019241	N/A	N/A	N/A	N/A	0.073666	0.016535	4.188000e-05	0.000531	0.005960	N/A	0.078142
2011	$B^0_s\to K^0_S\pi^+\pi^-$	DD	5.48e-04	4.92e-04	0.897117	0.016738	N/A	N/A	N/A	N/A	0.061567	0.016535	3.000000e-06	0.000433	0.005957	N/A	0.066179
2018	$B^0_s\to K^0_S\pi^+\pi^-$	LL	3.29e-04	2.97e-04	0.901442	0.020282	N/A	N/A	N/A	N/A	0.029979	0.024603	1.839600e-04	0.000167	0.005986	N/A	0.044173
2017	$B^0_s\to K^0_S\pi^+\pi^-$	LL	3.57e-04	3.17e-04	0.887666	0.019614	N/A	N/A	N/A	N/A	0.027411	0.024603	1.839600e-04	0.002213	0.005894	N/A	0.042202
2016	$B^0_s\to K^0_S\pi^+\pi^-$	LL	3.98e-04	3.56e-04	0.895650	0.019435	N/A	N/A	N/A	N/A	0.024727	0.024603	1.839600e-04	0.000887	0.005947	N/A	0.040381
2015	$B^0_s\to K^0_S\pi^+\pi^-$	LL	3.61e-04	3.28e-04	0.907644	0.020448	N/A	N/A	N/A	N/A	0.027465	0.024603	1.839600e-04	0.001385	0.006027	N/A	0.042615
2012b	$B^0_s\to K^0_S\pi^+\pi^-$	LL	1.75e-04	1.53e-04	0.877179	0.032607	N/A	N/A	N/A	N/A	0.055617	0.024603	7.000000e-08	0.001253	0.005824	N/A	0.069263
2012a	$B^0_s\to K^0_S\pi^+\pi^-$	LL	2.01e-04	1.77e-04	0.879581	0.032745	N/A	N/A	N/A	N/A	0.048430	0.024603	1.672300e-04	0.001568	0.005840	N/A	0.063715
2011	$B^0_s\to K^0_S\pi^+\pi^-$	LL	2.15e-04	1.88e-04	0.872869	0.029897	N/A	N/A	N/A	N/A	0.045101	0.024603	1.197300e-04	0.000186	0.005796	N/A	0.059723

Table C.69: $B^0\to K^0_S\pi^+\pi^-$ over $B^0_s\to K^0_S\pi^+\pi^-$ efficiency table for the favoured mode optimisation. For each year and K^0_S reconstruction type, the average efficiency of the considered mode, the average efficiency of $B^0\to K^0_S\pi^+\pi^-$, the ratio of average efficiencies, the related uncertainties split by sources and the final uncertainty are given. An uncertainty at N/A means maximally correlated (same final state) uncertainty which are cancelled in the ratio.

Year	Mode	K^0_S	$\bar{\varepsilon}_{B\to K^0_S hh'}$	$\bar{\varepsilon}_{B^0_s\to K^0_S\pi^+\pi^-}$	$\frac{\bar{\varepsilon}_{B^0_s\to K^0_S\pi^+\pi^-}}{\bar{\varepsilon}_{B\to K^0_S hh'}}$	$\sigma^{\text{stat}}_{\frac{\bar{\varepsilon}_{B^0_s\to K^0_S\pi^+\pi^-}}{\bar{\varepsilon}_{B\to K^0_S hh'}}}$	$\sigma^{\text{tracking}}_{\frac{\bar{\varepsilon}_{B^0_s\to K^0_S\pi^+\pi^-}}{\bar{\varepsilon}_{B\to K^0_S hh'}}}$	$\sigma^{\text{L0corr}}_{\frac{\bar{\varepsilon}_{B^0_s\to K^0_S\pi^+\pi^-}}{\bar{\varepsilon}_{B\to K^0_S hh'}}}$	$\sigma^{\text{PIDMCsampling}}_{\frac{\bar{\varepsilon}_{B^0_s\to K^0_S\pi^+\pi^-}}{\bar{\varepsilon}_{B\to K^0_S hh'}}}$	$\sigma^{\text{PIDkernel}}_{\frac{\bar{\varepsilon}_{B^0_s\to K^0_S\pi^+\pi^-}}{\bar{\varepsilon}_{B\to K^0_S hh'}}}$	$\sigma^{\text{RMS}}_{\frac{\bar{\varepsilon}_{B^0_s\to K^0_S\pi^+\pi^-}}{\bar{\varepsilon}_{B\to K^0_S hh'}}}$	$\sigma^{\text{binning}}_{\frac{\bar{\varepsilon}_{B^0_s\to K^0_S\pi^+\pi^-}}{\bar{\varepsilon}_{B\to K^0_S hh'}}}$	$\sigma^{\text{L0E0choice}}_{\frac{\bar{\varepsilon}_{B^0_s\to K^0_S\pi^+\pi^-}}{\bar{\varepsilon}_{B\to K^0_S hh'}}}$	$\sigma^{\text{FTrigger}}_{\frac{\bar{\varepsilon}_{B^0_s\to K^0_S\pi^+\pi^-}}{\bar{\varepsilon}_{B\to K^0_S hh'}}}$	$\sigma^{\text{MCreweighting}}_{\frac{\bar{\varepsilon}_{B^0_s\to K^0_S\pi^+\pi^-}}{\bar{\varepsilon}_{B\to K^0_S hh'}}}$	$\sigma^{\text{K}^0_S\text{tracking}}_{\frac{\bar{\varepsilon}_{B^0_s\to K^0_S\pi^+\pi^-}}{\bar{\varepsilon}_{B\to K^0_S hh'}}}$	$\sigma^{\text{tot}}_{\frac{\bar{\varepsilon}_{B^0_s\to K^0_S\pi^+\pi^-}}{\bar{\varepsilon}_{B\to K^0_S hh'}}}$
2018	$B^0_s\to K^0_S\pi^+K^-$	DD	8.53e-04	8.21e-04	0.96281	0.01211	0.00007	0.00135	0.00141	0.00485	0.01571	0.01344	0.00007	0.00024	0.00639	0.00007	0.02534
2017	$B^0_s\to K^0_S\pi^+K^-$	DD	8.86e-04	8.33e-04	0.94059	0.01199	0.00007	0.00138	0.00097	0.00286	0.01506	0.01344	0.00007	0.00172	0.00625	0.00007	0.02458
2016	$B^0_s\to K^0_S\pi^+K^-$	DD	1.00e-03	8.69e-04	0.86945	0.01075	0.00006	0.00123	0.00085	0.00294	0.01318	0.01344	0.00007	0.00079	0.00577	0.00006	0.02269
2015	$B^0_s\to K^0_S\pi^+K^-$	DD	9.03e-04	8.36e-04	0.92516	0.01209	0.00007	0.00147	0.00191	0.00518	0.01473	0.01344	0.00007	0.00018	0.00614	0.00007	0.02478
2012b	$B^0_s\to K^0_S\pi^+K^-$	DD	5.87e-04	5.19e-04	0.88494	0.01720	0.00006	0.00230	0.00162	0.02191	0.02252	0.01344	0.00008	0.00174	0.00588	0.00006	0.03884
2012a	$B^0_s\to K^0_S\pi^+K^-$	DD	4.73e-04	4.12e-04	0.86993	0.02034	0.00007	0.00260	0.00158	0.02163	0.02786	0.01344	0.00006	0.00078	0.00578	0.00007	0.04338
2011	$B^0_s\to K^0_S\pi^+K^-$	DD	5.58e-04	4.92e-04	0.88235	0.01854	0.00006	0.00383	0.00211	0.03521	0.02369	0.01344	0.00002	0.00002	0.00586	0.00006	0.04878
2018	$B^0_s\to K^0_S\pi^+K^-$	LL	3.21e-04	2.97e-04	0.92432	0.01918	0.00011	0.00108	0.00159	0.00299	0.03028	0.01385	0.00024	0.00466	0.00614	0.00011	0.03936
2017	$B^0_s\to K^0_S\pi^+K^-$	LL	3.63e-04	3.17e-04	0.87281	0.01808	0.00010	0.00113	0.00235	0.00300	0.02596	0.01385	0.00024	0.00500	0.00580	0.00010	0.03560
2016	$B^0_s\to K^0_S\pi^+K^-$	LL	3.80e-04	3.56e-04	0.93642	0.01892	0.00010	0.00116	0.00121	0.00371	0.02574	0.01385	0.00024	0.00152	0.00622	0.00010	0.03564
2015	$B^0_s\to K^0_S\pi^+K^-$	LL	3.62e-04	3.28e-04	0.90538	0.01888	0.00010	0.00116	0.00267	0.00514	0.02658	0.01385	0.00024	0.00370	0.00601	0.00010	0.03660
2012b	$B^0_s\to K^0_S\pi^+K^-$	LL	1.76e-04	1.53e-04	0.87204	0.03111	0.00010	0.00195	0.00323	0.02076	0.05359	0.01385	0.00031	0.00067	0.00579	0.00010	0.06717
2012a	$B^0_s\to K^0_S\pi^+K^-$	LL	2.03e-04	1.77e-04	0.87064	0.03117	0.00009	0.00180	0.00229	0.03173	0.04636	0.01385	0.00005	0.00085	0.00578	0.00009	0.06604
2011	$B^0_s\to K^0_S\pi^+K^-$	LL	2.27e-04	1.88e-04	0.82709	0.02824	0.00008	0.00277	0.00234	0.02709	0.04043	0.01385	0.00005	0.00610	0.00549	0.00008	0.05864

Table C.70: $B^0\to K^0_S\pi^+\pi^-$ over $B^0_s\to K^0_S\pi^+K^-$ efficiency table for the favoured mode optimisation. For each year and K^0_S reconstruction type, the average efficiency of the considered mode, the average efficiency of $B^0\to K^0_S\pi^+\pi^-$, the ratio of average efficiencies, the related uncertainties split by sources and the final uncertainty are given.

Year	Mode	K^0_S	$\bar{\varepsilon}_{B\to K^0_S hh'}$	$\bar{\varepsilon}_{B^0_s\to K^0_S\pi^+\pi^-}$	$\frac{\bar{\varepsilon}_{B^0_s\to K^0_S\pi^+\pi^-}}{\bar{\varepsilon}_{B\to K^0_S hh'}}$	$\sigma^{\text{stat}}_{\frac{\bar{\varepsilon}_{B^0_s\to K^0_S\pi^+\pi^-}}{\bar{\varepsilon}_{B\to K^0_S hh'}}}$	$\sigma^{\text{tracking}}_{\frac{\bar{\varepsilon}_{B^0_s\to K^0_S\pi^+\pi^-}}{\bar{\varepsilon}_{B\to K^0_S hh'}}}$	$\sigma^{\text{L0corr}}_{\frac{\bar{\varepsilon}_{B^0_s\to K^0_S\pi^+\pi^-}}{\bar{\varepsilon}_{B\to K^0_S hh'}}}$	$\sigma^{\text{PIDMCsampling}}_{\frac{\bar{\varepsilon}_{B^0_s\to K^0_S\pi^+\pi^-}}{\bar{\varepsilon}_{B\to K^0_S hh'}}}$	$\sigma^{\text{PIDkernel}}_{\frac{\bar{\varepsilon}_{B^0_s\to K^0_S\pi^+\pi^-}}{\bar{\varepsilon}_{B\to K^0_S hh'}}}$	$\sigma^{\text{RMS}}_{\frac{\bar{\varepsilon}_{B^0_s\to K^0_S\pi^+\pi^-}}{\bar{\varepsilon}_{B\to K^0_S hh'}}}$	$\sigma^{\text{binning}}_{\frac{\bar{\varepsilon}_{B^0_s\to K^0_S\pi^+\pi^-}}{\bar{\varepsilon}_{B\to K^0_S hh'}}}$	$\sigma^{\text{L0E0choice}}_{\frac{\bar{\varepsilon}_{B^0_s\to K^0_S\pi^+\pi^-}}{\bar{\varepsilon}_{B\to K^0_S hh'}}}$	$\sigma^{\text{FTrigger}}_{\frac{\bar{\varepsilon}_{B^0_s\to K^0_S\pi^+\pi^-}}{\bar{\varepsilon}_{B\to K^0_S hh'}}}$	$\sigma^{\text{MCreweighting}}_{\frac{\bar{\varepsilon}_{B^0_s\to K^0_S\pi^+\pi^-}}{\bar{\varepsilon}_{B\to K^0_S hh'}}}$	$\sigma^{\text{K}^0_S\text{tracking}}_{\frac{\bar{\varepsilon}_{B^0_s\to K^0_S\pi^+\pi^-}}{\bar{\varepsilon}_{B\to K^0_S hh'}}}$	$\sigma^{\text{tot}}_{\frac{\bar{\varepsilon}_{B^0_s\to K^0_S\pi^+\pi^-}}{\bar{\varepsilon}_{B\to K^0_S hh'}}}$
2018	$B^0_s\to K^0_S K^+\pi^-$	DD	8.69e-04	8.21e-04	0.94467	0.01135	0.00007	0.00130	0.00116	0.00412	0.01496	0.01290	0.00010	0.00153	0.00627	0.00007	0.02410
2017	$B^0_s\to K^0_S K^+\pi^-$	DD	9.05e-04	8.33e-04	0.92088	0.01133	0.00006	0.00134	0.00114	0.00361	0.01433	0.01290	0.00010	0.00146	0.00611	0.00006	0.02357
2016	$B^0_s\to K^0_S K^+\pi^-$	DD	9.74e-04	8.69e-04	0.89267	0.01073	0.00006	0.00125	0.00069	0.00311	0.01327	0.01290	0.00010	0.00017	0.00593	0.00006	0.02246
2015	$B^0_s\to K^0_S K^+\pi^-$	DD	8.71e-04	8.36e-04	0.95937	0.01221	0.00007	0.00147	0.00162	0.00499	0.01495	0.01290	0.00010	0.00026	0.00637	0.00007	0.02469
2012b	$B^0_s\to K^0_S K^+\pi^-$	DD	5.67e-04	5.19e-04	0.91611	0.01746	0.00006	0.00232	0.00126	0.02725	0.02285	0.01290	0.00008	0.00215	0.00608	0.00006	0.04225
2012a	$B^0_s\to K^0_S K^+\pi^-$	DD	4.38e-04	4.12e-04	0.94043	0.02159	0.00007	0.00276	0.00168	0.04010	0.02970	0.01290	0.00007	0.00105	0.00624	0.00007	0.05633
2011	$B^0_s\to K^0_S K^+\pi^-$	DD	5.07e-04	4.92e-04	0.97107	0.01999	0.00007	0.00411	0.00171	0.03552	0.02576	0.01290	0.00001	0.00074	0.00645	0.00007	0.05053
2018	$B^0_s\to K^0_S K^+\pi^-$	LL	3.17e-04	2.97e-04	0.93615	0.02041	0.00011	0.00110	0.00236	0.00631	0.04090	0.01369	0.00019	0.00377	0.00622	0.00011	0.04874
2017	$B^0_s\to K^0_S K^+\pi^-$	LL	3.60e-04	3.17e-04	0.87939	0.01910	0.00010	0.00114	0.00137	0.00339	0.03436	0.01369	0.00019	0.00490	0.00584	0.00010	0.04249
2016	$B^0_s\to K^0_S K^+\pi^-$	LL	3.98e-04	3.56e-04	0.89500	0.01878	0.00010	0.00110	0.00108	0.00420	0.03151	0.01369	0.00019	0.00137	0.00594	0.00010	0.03988
2015	$B^0_s\to K^0_S K^+\pi^-$	LL	3.69e-04	3.28e-04	0.88698	0.01934	0.00010	0.00119	0.00224	0.00558	0.03375	0.01369	0.00019	0.00145	0.00589	0.00010	0.04213
2012b	$B^0_s\to K^0_S K^+\pi^-$	LL	1.62e-04	1.53e-04	0.94702	0.03504	0.00011	0.00224	0.00448	0.02525	0.08079	0.01369	0.00011	0.00253	0.00629	0.00011	0.09301
2012a	$B^0_s\to K^0_S K^+\pi^-$	LL	1.88e-04	1.77e-04	0.94279	0.03471	0.00010	0.00208	0.00406	0.03588	0.06950	0.01369	0.00008	0.00012	0.00626	0.00010	0.08701
2011	$B^0_s\to K^0_S K^+\pi^-$	LL	2.17e-04	1.88e-04	0.86595	0.02984	0.00008	0.00307	0.00257	0.02507	0.05652	0.01369	0.00013	0.00315	0.00575	0.00008	0.07042

Table C.71: $B^0\to K^0_S\pi^+\pi^-$ over $B^0_s\to K^0_S K^+\pi^-$ efficiency table for the favoured mode optimisation. For each year and K^0_S reconstruction type, the average efficiency of the considered mode, the average efficiency of $B^0\to K^0_S\pi^+\pi^-$, the ratio of average efficiencies, the related uncertainties split by sources and the final uncertainty are given.

Year	Mode	K^0_S	$\bar{\varepsilon}_{B\to K^0_S hh'}$	$\bar{\varepsilon}_{B^0_s\to K^0_S\pi^+\pi^-}$	$\frac{\bar{\varepsilon}_{B^0_s\to K^0_S\pi^+\pi^-}}{\bar{\varepsilon}_{B\to K^0_S hh'}}$	$\sigma^{\text{stat}}_{\frac{\bar{\varepsilon}_{B^0_s\to K^0_S\pi^+\pi^-}}{\bar{\varepsilon}_{B\to K^0_S hh'}}}$	$\sigma^{\text{tracking}}_{\frac{\bar{\varepsilon}_{B^0_s\to K^0_S\pi^+\pi^-}}{\bar{\varepsilon}_{B\to K^0_S hh'}}}$	$\sigma^{\text{L0corr}}_{\frac{\bar{\varepsilon}_{B^0_s\to K^0_S\pi^+\pi^-}}{\bar{\varepsilon}_{B\to K^0_S hh'}}}$	$\sigma^{\text{PIDMCsampling}}_{\frac{\bar{\varepsilon}_{B^0_s\to K^0_S\pi^+\pi^-}}{\bar{\varepsilon}_{B\to K^0_S hh'}}}$	$\sigma^{\text{PIDkernel}}_{\frac{\bar{\varepsilon}_{B^0_s\to K^0_S\pi^+\pi^-}}{\bar{\varepsilon}_{B\to K^0_S hh'}}}$	$\sigma^{\text{RMS}}_{\frac{\bar{\varepsilon}_{B^0_s\to K^0_S\pi^+\pi^-}}{\bar{\varepsilon}_{B\to K^0_S hh'}}}$	$\sigma^{\text{binning}}_{\frac{\bar{\varepsilon}_{B^0_s\to K^0_S\pi^+\pi^-}}{\bar{\varepsilon}_{B\to K^0_S hh'}}}$	$\sigma^{\text{L0E0choice}}_{\frac{\bar{\varepsilon}_{B^0_s\to K^0_S\pi^+\pi^-}}{\bar{\varepsilon}_{B\to K^0_S hh'}}}$	$\sigma^{\text{FTrigger}}_{\frac{\bar{\varepsilon}_{B^0_s\to K^0_S\pi^+\pi^-}}{\bar{\varepsilon}_{B\to K^0_S hh'}}}$	$\sigma^{\text{MCreweighting}}_{\frac{\bar{\varepsilon}_{B^0_s\to K^0_S\pi^+\pi^-}}{\bar{\varepsilon}_{B\to K^0_S hh'}}}$	$\sigma^{\text{K}^0_S\text{tracking}}_{\frac{\bar{\varepsilon}_{B^0_s\to K^0_S\pi^+\pi^-}}{\bar{\varepsilon}_{B\to K^0_S hh'}}}$	$\sigma^{\text{tot}}_{\frac{\bar{\varepsilon}_{B^0_s\to K^0_S\pi^+\pi^-}}{\bar{\varepsilon}_{B\to K^0_S hh'}}}$
2018	$B^0_s\to K^0_S K^+K^-$	DD	8.35e-04	8.21e-04	0.98274	0.01160	0.00007	0.00146	0.00190	0.00522	0.07586	0.03929	0.00051	0.00229	0.00653	0.00007	0.08668
2017	$B^0_s\to K^0_S K^+K^-$	DD	8.80e-04	8.33e-04	0.94724	0.01141	0.00007	0.00192	0.00203	0.00535	0.06954	0.03929	0.00051	0.00184	0.00629	0.00007	0.08117
2016	$B^0_s\to K^0_S K^+K^-$	DD	1.02e-03	8.69e-04	0.84965	0.00968	0.00006	0.00130	0.00165	0.00370	0.05389	0.03929	0.00051	0.00199	0.00564	0.00006	0.06779
2015	$B^0_s\to K^0_S K^+K^-$	DD	9.16e-04	8.36e-04	0.91205	0.01091	0.00007	0.00149	0.00255	0.00587	0.06437	0.03929	0.00051	0.00201	0.00606	0.00007	0.07675
2012b	$B^0_s\to K^0_S K^+K^-$	DD	5.77e-04	5.19e-04	0.89984	0.01602	0.00005	0.00323	0.00232	0.06562	0.10089	0.03929	0.00025	0.00169	0.00597	0.00005	0.12783
2012a	$B^0_s\to K^0_S K^+K^-$	DD	4.78e-04	4.12e-04	0.86038	0.01878	0.00006	0.00325	0.00262	0.05808	0.11663	0.03929	0.00025	0.00097	0.00571	0.00006	0.13756
2011	$B^0_s\to K^0_S K^+K^-$	DD	5.31e-04	4.92e-04	0.92654	0.01806	0.00005	0.00448	0.00448	0.08148	0.11279	0.03929	0.00034	0.00058	0.00615	0.00005	0.14598
2018	$B^0_s\to K^0_S K^+K^-$	LL	3.72e-04	2.97e-04	0.79838	0.04594	0.00032	0.00267	0.01009	0.00552	0.12068	0.12936	0.00137	0.00554	0.00530	0.00032	0.18332
2017	$B^0_s\to K^0_S K^+K^-$	LL	4.06e-04	3.17e-04	0.78103	0.04580	0.00031	0.00415	0.01169	0.00365	0.10822	0.12936	0.00137	0.00847	0.00519	0.00031	0.17553
2016	$B^0_s\to K^0_S K^+K^-$	LL	4.85e-04	3.56e-04	0.73432	0.03816	0.00027	0.00256	0.00801	0.00434	0.08522	0.12936	0.00137	0.00455	0.00488	0.00027	0.15996
2015	$B^0_s\to K^0_S K^+K^-$	LL	4.19e-04	3.28e-04	0.78136	0.04459	0.00027	0.00290	0.00731	0.00509	0.10481	0.12936	0.00137	0.00494	0.00519	0.00027	0.17277
2012b	$B^0_s\to K^0_S K^+K^-$	LL	1.85e-04	1.53e-04	0.82909	0.08809	0.00028	0.01144	0.01831	0.06236	0.25175	0.12936	0.00039	0.00173	0.00551	0.00028	0.30374
2012a	$B^0_s\to K^0_S K^+K^-$	LL	2.01e-04	1.77e-04	0.87783	0.10233	0.00030	0.01100	0.01070	0.06110	0.24444	0.12936	0.00041	0.00160	0.00583	0.00030	0.30160
2011	$B^0_s\to K^0_S K^+K^-$	LL	2.58e-04	1.88e-04	0.72630	0.06776	0.00019	0.00844	0.01673	0.04282	0.15833	0.12936	0.00055	0.00526	0.00482	0.00019	0.22052

Table C.72: $B^0\to K^0_S\pi^+\pi^-$ over $B^0_s\to K^0_S K^+K^-$ efficiency table for the favoured mode optimisation. For each year and K^0_S reconstruction type, the average efficiency of the considered mode, the average efficiency of $B^0\to K^0_S\pi^+\pi^-$, the ratio of average efficiencies, the related uncertainties split by sources and the final uncertainty are given.

Year	Mode	K_S^0	$\bar{\varepsilon}_{B\to K_S^0hh'}$	$\bar{\varepsilon}_{B^0_{(s)}\to K_S^0\pi^+\pi^-}$	$\frac{\bar{\varepsilon}_{B^0_{(s)}\to K_S^0\pi^+\pi^-}}{\bar{\varepsilon}_{B\to K_S^0hh'}}$	$\sigma^{\text{stat}}_{\frac{\bar{\varepsilon}_{B^0_{(s)}\to K_S^0\pi^+\pi^-}}{\bar{\varepsilon}_{B\to K_S^0hh'}}}$	$\sigma^{\text{tracking}}_{\frac{\bar{\varepsilon}_{B^0_{(s)}\to K_S^0\pi^+\pi^-}}{\bar{\varepsilon}_{B\to K_S^0hh'}}}$	$\sigma^{\text{L0corr}}_{\frac{\bar{\varepsilon}_{B^0_{(s)}\to K_S^0\pi^+\pi^-}}{\bar{\varepsilon}_{B\to K_S^0hh'}}}$	$\sigma^{\text{PIDMCsampling}}_{\frac{\bar{\varepsilon}_{B^0_{(s)}\to K_S^0\pi^+\pi^-}}{\bar{\varepsilon}_{B\to K_S^0hh'}}}$	$\sigma^{\text{PIDkernel}}_{\frac{\bar{\varepsilon}_{B^0_{(s)}\to K_S^0\pi^+\pi^-}}{\bar{\varepsilon}_{B\to K_S^0hh'}}}$	$\sigma^{\text{RMS}}_{\frac{\bar{\varepsilon}_{B^0_{(s)}\to K_S^0\pi^+\pi^-}}{\bar{\varepsilon}_{B\to K_S^0hh'}}}$	$\sigma^{\text{binning}}_{\frac{\bar{\varepsilon}_{B^0_{(s)}\to K_S^0\pi^+\pi^-}}{\bar{\varepsilon}_{B\to K_S^0hh'}}}$	$\sigma^{\text{L0E0choice}}_{\frac{\bar{\varepsilon}_{B^0_{(s)}\to K_S^0\pi^+\pi^-}}{\bar{\varepsilon}_{B\to K_S^0hh'}}}$	$\sigma^{\text{FTrigger}}_{\frac{\bar{\varepsilon}_{B^0_{(s)}\to K_S^0\pi^+\pi^-}}{\bar{\varepsilon}_{B\to K_S^0hh'}}}$	$\sigma^{\text{MCreweighting}}_{\frac{\bar{\varepsilon}_{B^0_{(s)}\to K_S^0\pi^+\pi^-}}{\bar{\varepsilon}_{B\to K_S^0hh'}}}$	$\sigma^{\text{K}^0_S\text{tracking}}_{\frac{\bar{\varepsilon}_{B^0_{(s)}\to K_S^0\pi^+\pi^-}}{\bar{\varepsilon}_{B\to K_S^0hh'}}}$	$\sigma^{\text{tot}}_{\frac{\bar{\varepsilon}_{B^0_{(s)}\to K_S^0\pi^+\pi^-}}{\bar{\varepsilon}_{B\to K_S^0hh'}}}$
2018	$B^0_d\to K^0_S\pi^+K^-$	DD	6.67e-04	4.13e-04	0.61956	0.01005	0.00005	0.00101	0.00112	0.00321	0.01420	0.00937	0.00002	0.00010	0.00411	0.00005	0.02049
2017	$B^0_d\to K^0_S\pi^+K^-$	DD	6.98e-04	4.42e-04	0.63410	0.01035	0.00005	0.00102	0.00117	0.00278	0.01376	0.00937	0.00002	0.00307	0.00421	0.00005	0.02053
2016	$B^0_d\to K^0_S\pi^+K^-$	DD	7.89e-04	4.39e-04	0.55626	0.00876	0.00004	0.00086	0.00074	0.00222	0.01134	0.00937	0.00002	0.00110	0.00369	0.00004	0.01772
2015	$B^0_d\to K^0_S\pi^+K^-$	DD	6.91e-04	3.47e-04	0.50160	0.00873	0.00004	0.00085	0.00115	0.00403	0.01232	0.00937	0.00002	0.00031	0.00333	0.00004	0.01858
2012b	$B^0_d\to K^0_S\pi^+K^-$	DD	5.16e-04	3.44e-04	0.66619	0.01583	0.00005	0.00176	0.00159	0.04618	0.01914	0.00937	0.00006	0.00662	0.00442	0.00005	0.05391
2012a	$B^0_d\to K^0_S\pi^+K^-$	DD	4.18e-04	2.33e-04	0.55708	0.01658	0.00004	0.00192	0.00168	0.04551	0.02139	0.00937	0.00002	0.00101	0.00370	0.00004	0.05397
2011	$B^0_d\to K^0_S\pi^+K^-$	DD	5.02e-04	2.38e-04	0.47487	0.01258	0.00003	0.00218	0.00165	0.03604	0.01654	0.00937	0.00005	0.00031	0.00315	0.00003	0.04285
2018	$B^0_d\to K^0_S\pi^+K^-$	LL	2.76e-04	1.91e-04	0.69207	0.01868	0.00009	0.00090	0.00214	0.00388	0.02666	0.02253	0.00023	0.00271	0.00460	0.00009	0.04020
2017	$B^0_d\to K^0_S\pi^+K^-$	LL	3.02e-04	2.15e-04	0.71227	0.01928	0.00009	0.00101	0.00238	0.00274	0.02478	0.02253	0.00023	0.00221	0.00473	0.00009	0.03918
2016	$B^0_d\to K^0_S\pi^+K^-$	LL	3.12e-04	2.21e-04	0.70981	0.01881	0.00009	0.00097	0.00144	0.00314	0.02396	0.02253	0.00023	0.00145	0.00471	0.00009	0.03838
2015	$B^0_d\to K^0_S\pi^+K^-$	LL	2.44e-04	1.99e-04	0.81645	0.02409	0.00011	0.00111	0.00348	0.00636	0.03372	0.02253	0.00023	0.00292	0.00542	0.00011	0.04814
2012b	$B^0_d\to K^0_S\pi^+K^-$	LL	9.42e-05	1.08e-04	1.15136	0.06237	0.00015	0.00297	0.00995	0.09415	0.11418	0.02253	0.00056	0.00075	0.00765	0.00015	0.16268
2012a	$B^0_d\to K^0_S\pi^+K^-$	LL	1.55e-04	7.78e-05	0.50040	0.02594	0.00006	0.00146	0.00351	0.03688	0.03934	0.02253	0.00012	0.00022	0.00332	0.00006	0.06414
2011	$B^0_d\to K^0_S\pi^+K^-$	LL	1.94e-04	1.33e-04	0.68621	0.02932	0.00007	0.00240	0.00352	0.04074	0.03774	0.02253	0.00020	0.00754	0.00456	0.00007	0.06744

Table C.73: $B^0\to K^0_S\pi^+\pi^-$ over $B^0\to K^0_S\pi^+K^-$ efficiency table for the unfavoured mode optimisation. For each year and K^0_S reconstruction type, the average efficiency of the considered mode, the average efficiency of $B^0\to K^0_S\pi^+\pi^-$, the ratio of average efficiencies, the related uncertainties split by sources and the final uncertainty are given.

Year	Mode	K_S^0	$\bar{\varepsilon}_{B\to K_S^0hh'}$	$\bar{\varepsilon}_{B^0_{(s)}\to K_S^0\pi^+\pi^-}$	$\frac{\bar{\varepsilon}_{B^0_{(s)}\to K_S^0\pi^+\pi^-}}{\bar{\varepsilon}_{B\to K_S^0hh'}}$	$\sigma^{\text{stat}}_{\frac{\bar{\varepsilon}_{B^0_{(s)}\to K_S^0\pi^+\pi^-}}{\bar{\varepsilon}_{B\to K_S^0hh'}}}$	$\sigma^{\text{tracking}}_{\frac{\bar{\varepsilon}_{B^0_{(s)}\to K_S^0\pi^+\pi^-}}{\bar{\varepsilon}_{B\to K_S^0hh'}}}$	$\sigma^{\text{L0corr}}_{\frac{\bar{\varepsilon}_{B^0_{(s)}\to K_S^0\pi^+\pi^-}}{\bar{\varepsilon}_{B\to K_S^0hh'}}}$	$\sigma^{\text{PIDMCsampling}}_{\frac{\bar{\varepsilon}_{B^0_{(s)}\to K_S^0\pi^+\pi^-}}{\bar{\varepsilon}_{B\to K_S^0hh'}}}$	$\sigma^{\text{PIDkernel}}_{\frac{\bar{\varepsilon}_{B^0_{(s)}\to K_S^0\pi^+\pi^-}}{\bar{\varepsilon}_{B\to K_S^0hh'}}}$	$\sigma^{\text{RMS}}_{\frac{\bar{\varepsilon}_{B^0_{(s)}\to K_S^0\pi^+\pi^-}}{\bar{\varepsilon}_{B\to K_S^0hh'}}}$	$\sigma^{\text{binning}}_{\frac{\bar{\varepsilon}_{B^0_{(s)}\to K_S^0\pi^+\pi^-}}{\bar{\varepsilon}_{B\to K_S^0hh'}}}$	$\sigma^{\text{L0E0choice}}_{\frac{\bar{\varepsilon}_{B^0_{(s)}\to K_S^0\pi^+\pi^-}}{\bar{\varepsilon}_{B\to K_S^0hh'}}}$	$\sigma^{\text{FTrigger}}_{\frac{\bar{\varepsilon}_{B^0_{(s)}\to K_S^0\pi^+\pi^-}}{\bar{\varepsilon}_{B\to K_S^0hh'}}}$	$\sigma^{\text{MCreweighting}}_{\frac{\bar{\varepsilon}_{B^0_{(s)}\to K_S^0\pi^+\pi^-}}{\bar{\varepsilon}_{B\to K_S^0hh'}}}$	$\sigma^{\text{K}^0_S\text{tracking}}_{\frac{\bar{\varepsilon}_{B^0_{(s)}\to K_S^0\pi^+\pi^-}}{\bar{\varepsilon}_{B\to K_S^0hh'}}}$	$\sigma^{\text{tot}}_{\frac{\bar{\varepsilon}_{B^0_{(s)}\to K_S^0\pi^+\pi^-}}{\bar{\varepsilon}_{B\to K_S^0hh'}}}$
2018	$B^0_d\to K^0_S K^+\pi^-$	DD	6.84e-04	4.13e-04	0.60439	0.01034	0.00005	0.00098	0.00093	0.00304	0.01362	0.00959	0.00002	0.00132	0.00401	0.00005	0.02033
2017	$B^0_d\to K^0_S K^+\pi^-$	DD	7.84e-04	4.42e-04	0.56410	0.00958	0.00005	0.00096	0.00084	0.00255	0.01145	0.00959	0.00002	0.00135	0.00375	0.00005	0.01841
2016	$B^0_d\to K^0_S K^+\pi^-$	DD	7.56e-04	4.39e-04	0.58019	0.00990	0.00005	0.00098	0.00075	0.00226	0.01204	0.00959	0.00002	0.00119	0.00385	0.00005	0.01892
2015	$B^0_d\to K^0_S K^+\pi^-$	DD	6.60e-04	3.47e-04	0.52481	0.00995	0.00005	0.00101	0.00199	0.00480	0.01312	0.00959	0.00002	0.00041	0.00348	0.00005	0.02009
2012b	$B^0_d\to K^0_S K^+\pi^-$	DD	4.85e-04	3.44e-04	0.70879	0.01873	0.00005	0.00229	0.00397	0.05833	0.02107	0.00959	0.00008	0.00103	0.00471	0.00005	0.06583
2012a	$B^0_d\to K^0_S K^+\pi^-$	DD	4.02e-04	2.33e-04	0.57976	0.01892	0.00005	0.00184	0.00232	0.05000	0.02265	0.00959	0.00007	0.00334	0.00385	0.00005	0.05914
2011	$B^0_d\to K^0_S K^+\pi^-$	DD	5.34e-04	2.38e-04	0.44649	0.01259	0.00003	0.00223	0.00147	0.03484	0.01513	0.00959	0.00006	0.00086	0.00296	0.00003	0.04135
2018	$B^0_d\to K^0_S K^+\pi^-$	LL	2.67e-04	1.91e-04	0.71382	0.02098	0.00011	0.00098	0.00214	0.00382	0.03082	0.03155	0.00014	0.00722	0.00474	0.00011	0.04980
2017	$B^0_d\to K^0_S K^+\pi^-$	LL	2.88e-04	2.15e-04	0.74661	0.02227	0.00011	0.00115	0.00608	0.00452	0.02952	0.03155	0.00014	0.00304	0.00496	0.00011	0.04955
2016	$B^0_d\to K^0_S K^+\pi^-$	LL	3.14e-04	2.21e-04	0.70569	0.02019	0.00010	0.00107	0.01349	0.00365	0.02605	0.03155	0.00014	0.00108	0.00469	0.00010	0.04797
2015	$B^0_d\to K^0_S K^+\pi^-$	LL	2.73e-04	1.99e-04	0.73057	0.02261	0.00010	0.00118	0.00402	0.00890	0.03073	0.03155	0.00014	0.00135	0.00485	0.00010	0.05072
2012b	$B^0_d\to K^0_S K^+\pi^-$	LL	8.99e-05	1.08e-04	1.20683	0.07486	0.00019	0.00311	0.01718	0.09218	0.14004	0.03155	0.00056	0.00007	0.00801	0.00019	0.18729
2012a	$B^0_d\to K^0_S K^+\pi^-$	LL	1.49e-04	7.78e-05	0.52129	0.03074	0.00007	0.00145	0.00399	0.02720	0.04502	0.03155	0.00002	0.00030	0.00346	0.00007	0.06883
2011	$B^0_d\to K^0_S K^+\pi^-$	LL	1.74e-04	1.33e-04	0.76565	0.03806	0.00010	0.00322	0.00417	0.04641	0.04995	0.03155	0.00017	0.00060	0.00508	0.00010	0.08454

Table C.74: $B^0\to K^0_S\pi^+\pi^-$ over $B^0\to K^0_S K^+\pi^-$ efficiency table for the unfavoured mode optimisation. For each year and K^0_S reconstruction type, the average efficiency of the considered mode, the average efficiency of $B^0\to K^0_S\pi^+\pi^-$, the ratio of average efficiencies, the related uncertainties split by sources and the final uncertainty are given.

Year	Mode	K_S^0	$\bar{\varepsilon}_{B\to K_S^0hh'}$	$\bar{\varepsilon}_{B^0_{(s)}\to K_S^0\pi^+\pi^-}$	$\frac{\bar{\varepsilon}_{B^0_{(s)}\to K_S^0\pi^+\pi^-}}{\bar{\varepsilon}_{B\to K_S^0hh'}}$	$\sigma^{\text{stat}}_{\frac{\bar{\varepsilon}_{B^0_{(s)}\to K_S^0\pi^+\pi^-}}{\bar{\varepsilon}_{B\to K_S^0hh'}}}$	$\sigma^{\text{tracking}}_{\frac{\bar{\varepsilon}_{B^0_{(s)}\to K_S^0\pi^+\pi^-}}{\bar{\varepsilon}_{B\to K_S^0hh'}}}$	$\sigma^{\text{L0corr}}_{\frac{\bar{\varepsilon}_{B^0_{(s)}\to K_S^0\pi^+\pi^-}}{\bar{\varepsilon}_{B\to K_S^0hh'}}}$	$\sigma^{\text{PIDMCsampling}}_{\frac{\bar{\varepsilon}_{B^0_{(s)}\to K_S^0\pi^+\pi^-}}{\bar{\varepsilon}_{B\to K_S^0hh'}}}$	$\sigma^{\text{PIDkernel}}_{\frac{\bar{\varepsilon}_{B^0_{(s)}\to K_S^0\pi^+\pi^-}}{\bar{\varepsilon}_{B\to K_S^0hh'}}}$	$\sigma^{\text{RMS}}_{\frac{\bar{\varepsilon}_{B^0_{(s)}\to K_S^0\pi^+\pi^-}}{\bar{\varepsilon}_{B\to K_S^0hh'}}}$	$\sigma^{\text{binning}}_{\frac{\bar{\varepsilon}_{B^0_{(s)}\to K_S^0\pi^+\pi^-}}{\bar{\varepsilon}_{B\to K_S^0hh'}}}$	$\sigma^{\text{L0E0choice}}_{\frac{\bar{\varepsilon}_{B^0_{(s)}\to K_S^0\pi^+\pi^-}}{\bar{\varepsilon}_{B\to K_S^0hh'}}}$	$\sigma^{\text{FTrigger}}_{\frac{\bar{\varepsilon}_{B^0_{(s)}\to K_S^0\pi^+\pi^-}}{\bar{\varepsilon}_{B\to K_S^0hh'}}}$	$\sigma^{\text{MCreweighting}}_{\frac{\bar{\varepsilon}_{B^0_{(s)}\to K_S^0\pi^+\pi^-}}{\bar{\varepsilon}_{B\to K_S^0hh'}}}$	$\sigma^{\text{K}^0_S\text{tracking}}_{\frac{\bar{\varepsilon}_{B^0_{(s)}\to K_S^0\pi^+\pi^-}}{\bar{\varepsilon}_{B\to K_S^0hh'}}}$	$\sigma^{\text{tot}}_{\frac{\bar{\varepsilon}_{B^0_{(s)}\to K_S^0\pi^+\pi^-}}{\bar{\varepsilon}_{B\to K_S^0hh'}}}$
2018	$B^0_d\to K^0_S K^+K^-$	DD	4.85e-04	4.13e-04	0.85220	0.01117	0.00005	0.00115	0.00096	0.00334	0.01344	0.03448	0.00049	0.00293	0.00566	0.00005	0.03935
2017	$B^0_d\to K^0_S K^+K^-$	DD	3.74e-04	4.42e-04	1.18184	0.01692	0.00007	0.00224	0.00106	0.00382	0.01797	0.03448	0.00049	0.00214	0.00785	0.00007	0.04342
2016	$B^0_d\to K^0_S K^+K^-$	DD	4.79e-04	4.39e-04	0.91561	0.01228	0.00005	0.00125	0.00075	0.00357	0.01367	0.03448	0.00049	0.00198	0.00608	0.00005	0.03978
2015	$B^0_d\to K^0_S K^+K^-$	DD	4.00e-04	3.47e-04	0.86606	0.01296	0.00005	0.00131	0.00114	0.00385	0.01631	0.03448	0.00049	0.00181	0.00575	0.00005	0.04095
2012b	$B^0_d\to K^0_S K^+K^-$	DD	3.34e-04	3.44e-04	1.02842	0.02012	0.00005	0.00390	0.00763	0.02735	0.01981	0.03448	0.00016	0.00145	0.00683	0.00005	0.05344
2012a	$B^0_d\to K^0_S K^+K^-$	DD	2.11e-04	2.33e-04	1.10696	0.02894	0.00007	0.00449	0.00190	0.02682	0.03169	0.03448	0.00024	0.00052	0.00735	0.00007	0.06187
2011	$B^0_d\to K^0_S K^+K^-$	DD	2.75e-04	2.38e-04	0.86657	0.01971	0.00005	0.00372	0.00112	0.01376	0.02372	0.03448	0.00013	0.00065	0.00575	0.00005	0.04876
2018	$B^0_d\to K^0_S K^+K^-$	LL	2.18e-04	1.91e-04	0.87384	0.01710	0.00009	0.00091	0.00139	0.00262	0.02091	0.02784	0.00071	0.01573	0.00580	0.00009	0.04238
2017	$B^0_d\to K^0_S K^+K^-$	LL	1.84e-04	2.15e-04	1.17202	0.02439	0.00011	0.00170	0.00156	0.00430	0.02565	0.02784	0.00071	0.01233	0.00778	0.00011	0.04759
2016	$B^0_d\to K^0_S K^+K^-$	LL	2.00e-04	2.21e-04	1.10855	0.02245	0.00010	0.00124	0.00119	0.00420	0.02343	0.02784	0.00071	0.00436	0.00736	0.00010	0.04385
2015	$B^0_d\to K^0_S K^+K^-$	LL	2.80e-04	1.99e-04	0.71106	0.01390	0.00006	0.00082	0.00169	0.00510	0.01608	0.02784	0.00071	0.00752	0.00472	0.00006	0.03655
2012b	$B^0_d\to K^0_S K^+K^-$	LL	1.24e-04	1.08e-04	0.87469	0.02930	0.00008	0.00307	0.00230	0.01605	0.03684	0.02784	0.00039	0.00069	0.00581	0.00008	0.05743
2012a	$B^0_d\to K^0_S K^+K^-$	LL	1.41e-04	7.78e-05	0.55044	0.02158	0.00005	0.00146	0.00186	0.01302	0.03152	0.02784	0.00015	0.00380	0.00365	0.00005	0.04937
2011	$B^0_d\to K^0_S K^+K^-$	LL	1.38e-04	1.33e-04	0.96424	0.03120	0.00007	0.00310	0.00258	0.01794	0.03342	0.02784	0.00033	0.00166	0.00640	0.00007	0.05699

Table C.75: $B^0\to K^0_S\pi^+\pi^-$ over $B^0\to K^0_S K^+K^-$ efficiency table for the unfavoured mode optimisation. For each year and K^0_S reconstruction type, the average efficiency of the considered mode, the average efficiency of $B^0\to K^0_S\pi^+\pi^-$, the ratio of average efficiencies, the related uncertainties split by sources and the final uncertainty are given.

Year	Mode	K_S^0	$\bar{\varepsilon}_{B\to K_S^0hh'}$	$\bar{\varepsilon}_{B^0_{(s)}\to K_S^0\pi^+\pi^-}$	$\frac{\bar{\varepsilon}_{B^0_{(s)}\to K_S^0\pi^+\pi^-}}{\bar{\varepsilon}_{B\to K_S^0hh'}}$	$\sigma^{\text{stat}}_{\frac{\bar{\varepsilon}_{B^0_{(s)}\to K_S^0\pi^+\pi^-}}{\bar{\varepsilon}_{B\to K_S^0hh'}}}$	$\sigma^{\text{tracking}}_{\frac{\bar{\varepsilon}_{B^0_{(s)}\to K_S^0\pi^+\pi^-}}{\bar{\varepsilon}_{B\to K_S^0hh'}}}$	$\sigma^{\text{L0corr}}_{\frac{\bar{\varepsilon}_{B^0_{(s)}\to K_S^0\pi^+\pi^-}}{\bar{\varepsilon}_{B\to K_S^0hh'}}}$	$\sigma^{\text{PIDMCsampling}}_{\frac{\bar{\varepsilon}_{B^0_{(s)}\to K_S^0\pi^+\pi^-}}{\bar{\varepsilon}_{B\to K_S^0hh'}}}$	$\sigma^{\text{PIDkernel}}_{\frac{\bar{\varepsilon}_{B^0_{(s)}\to K_S^0\pi^+\pi^-}}{\bar{\varepsilon}_{B\to K_S^0hh'}}}$	$\sigma^{\text{RMS}}_{\frac{\bar{\varepsilon}_{B^0_{(s)}\to K_S^0\pi^+\pi^-}}{\bar{\varepsilon}_{B\to K_S^0hh'}}}$	$\sigma^{\text{binning}}_{\frac{\bar{\varepsilon}_{B^0_{(s)}\to K_S^0\pi^+\pi^-}}{\bar{\varepsilon}_{B\to K_S^0hh'}}}$	$\sigma^{\text{L0E0choice}}_{\frac{\bar{\varepsilon}_{B^0_{(s)}\to K_S^0\pi^+\pi^-}}{\bar{\varepsilon}_{B\to K_S^0hh'}}}$	$\sigma^{\text{FTrigger}}_{\frac{\bar{\varepsilon}_{B^0_{(s)}\to K_S^0\pi^+\pi^-}}{\bar{\varepsilon}_{B\to K_S^0hh'}}}$	$\sigma^{\text{MCreweighting}}_{\frac{\bar{\varepsilon}_{B^0_{(s)}\to K_S^0\pi^+\pi^-}}{\bar{\varepsilon}_{B\to K_S^0hh'}}}$	$\sigma^{\text{K}^0_S\text{tracking}}_{\frac{\bar{\varepsilon}_{B^0_{(s)}\to K_S^0\pi^+\pi^-}}{\bar{\varepsilon}_{B\to K_S^0hh'}}}$	$\sigma^{\text{tot}}_{\frac{\bar{\varepsilon}_{B^0_{(s)}\to K_S^0\pi^+\pi^-}}{\bar{\varepsilon}_{B\to K_S^0hh'}}}$
2018	$B^0_s\to K^0_S\pi^+\pi^-$	DD	4.46e-04	4.13e-04	0.925720	0.014300	N/A	N/A	N/A	N/A	0.044302	0.016149	0.000076	0.000669	0.006147	N/A	0.049661
2017	$B^0_s\to K^0_S\pi^+\pi^-$	DD	4.76e-04	4.42e-04	0.929228	0.014369	N/A	N/A	N/A	N/A	0.041697	0.016149	0.000076	0.002202	0.006170	N/A	0.047422
2016	$B^0_s\to K^0_S\pi^+\pi^-$	DD	4.59e-04	4.39e-04	0.955789	0.015121	N/A	N/A	N/A	N/A	0.044337	0.016149	0.000076	0.000185	0.006346	N/A	0.049955
2015	$B^0_s\to K^0_S\pi^+\pi^-$	DD	3.87e-04	3.47e-04	0.894633	0.015503	N/A	N/A	N/A	N/A	0.049522	0.016149	0.000076	0.000431	0.005940	N/A	0.054672
2012b	$B^0_s\to K^0_S\pi^+\pi^-$	DD	3.67e-04	3.44e-04	0.936666	0.020384	N/A	N/A	N/A	N/A	0.054470	0.016149	0.000065	0.000133	0.006219	N/A	0.060679
2012a	$B^0_s\to K^0_S\pi^+\pi^-$	DD	2.67e-04	2.33e-04	0.874118	0.023751	N/A	N/A	N/A	N/A	0.070462	0.016149	0.000036	0.001025	0.005804	N/A	0.076319
2011	$B^0_s\to K^0_S\pi^+\pi^-$	DD	2.70e-04	2.38e-04	0.882287	0.022390	N/A	N/A	N/A	N/A	0.070105	0.016149	0.000017	0.000898	0.005858	N/A	0.075578
2018	$B^0_s\to K^0_S\pi^+\pi^-$	LL	2.15e-04	1.91e-04	0.886392	0.023571	N/A	N/A	N/A	N/A	0.031012	0.030852	0.000185	0.001815	0.005886	N/A	0.050071
2017	$B^0_s\to K^0_S\pi^+\pi^-$	LL	2.49e-04	2.15e-04	0.865431	0.021931	N/A	N/A	N/A	N/A	0.026477	0.030852	0.000185	0.003341	0.005746	N/A	0.046669
2016	$B^0_s\to K^0_S\pi^+\pi^-$	LL	2.54e-04	2.21e-04	0.872506	0.022477	N/A	N/A	N/A	N/A	0.026083	0.030852	0.000185	0.000833	0.005793	N/A	0.046601
2015	$B^0_s\to K^0_S\pi^+\pi^-$	LL	2.21e-04	1.99e-04	0.901892	0.024684	N/A	N/A	N/A	N/A	0.030531	0.030852	0.000185	0.001302	0.005989	N/A	0.050307
2012b	$B^0_s\to K^0_S\pi^+\pi^-$	LL	1.25e-04	1.08e-04	0.870408	0.037483	N/A	N/A	N/A	N/A	0.053037	0.030852	0.000001	0.002075	0.005780	N/A	0.072163
2012a	$B^0_s\to K^0_S\pi^+\pi^-$	LL	8.66e-05	7.78e-05	0.898522	0.049187	N/A	N/A	N/A	N/A	0.077717	0.030852	0.000179	0.000766	0.005966	N/A	0.097197
2011	$B^0_s\to K^0_S\pi^+\pi^-$	LL	1.52e-04	1.33e-04	0.874139	0.034817	N/A	N/A	N/A	N/A	0.043563	0.030852	0.000101	0.001105	0.005804	N/A	0.064006

Table C.76: $B^0\to K^0_S\pi^+\pi^-$ over $B^0_s\to K^0_S\pi^+\pi^-$ efficiency table for the unfavoured mode optimisation. For each year and K^0_S reconstruction type, the average efficiency of the considered mode, the average efficiency of $B^0\to K^0_S\pi^+\pi^-$, the ratio of average efficiencies, the related uncertainties split by sources and the final uncertainty are given. An uncertainty at N/A means maximally correlated (same final state) uncertainty which are cancelled in the ratio.

Year	Mode	K^0_S	$\bar{\varepsilon}_{B\to K^0_S hh'}$	$\bar{\varepsilon}_{B^0_s\to K^0_S\pi^+\pi^-}$	$\frac{\bar{\varepsilon}_{B^0_s\to K^0_S\pi^+\pi^-}}{\bar{\varepsilon}_{B\to K^0_S hh'}}$	$\sigma^{\rm stat}_{\frac{\bar{\varepsilon}_{B^0_s\to K^0_S\pi^+\pi^-}}{\bar{\varepsilon}_{B\to K^0_S hh'}}}$	$\sigma^{\rm tracking}_{\frac{\bar{\varepsilon}_{B^0_s\to K^0_S\pi^+\pi^-}}{\bar{\varepsilon}_{B\to K^0_S hh'}}}$	$\sigma^{\rm L0corr}_{\frac{\bar{\varepsilon}_{B^0_s\to K^0_S\pi^+\pi^-}}{\bar{\varepsilon}_{B\to K^0_S hh'}}}$	$\sigma^{\rm PIDMCsampling}_{\frac{\bar{\varepsilon}_{B^0_s\to K^0_S\pi^+\pi^-}}{\bar{\varepsilon}_{B\to K^0_S hh'}}}$	$\sigma^{\rm PIDkernel}_{\frac{\bar{\varepsilon}_{B^0_s\to K^0_S\pi^+\pi^-}}{\bar{\varepsilon}_{B\to K^0_S hh'}}}$	$\sigma^{\rm RMS}_{\frac{\bar{\varepsilon}_{B^0_s\to K^0_S\pi^+\pi^-}}{\bar{\varepsilon}_{B\to K^0_S hh'}}}$	$\sigma^{\rm binning}_{\frac{\bar{\varepsilon}_{B^0_s\to K^0_S\pi^+\pi^-}}{\bar{\varepsilon}_{B\to K^0_S hh'}}}$	$\sigma^{\rm L0E0choice}_{\frac{\bar{\varepsilon}_{B^0_s\to K^0_S\pi^+\pi^-}}{\bar{\varepsilon}_{B\to K^0_S hh'}}}$	$\sigma^{\rm FTrigger}_{\frac{\bar{\varepsilon}_{B^0_s\to K^0_S\pi^+\pi^-}}{\bar{\varepsilon}_{B\to K^0_S hh'}}}$	$\sigma^{\rm MCreweighting}_{\frac{\bar{\varepsilon}_{B^0_s\to K^0_S\pi^+\pi^-}}{\bar{\varepsilon}_{B\to K^0_S hh'}}}$	$\sigma^{\rm K^0_S tracking}_{\frac{\bar{\varepsilon}_{B^0_s\to K^0_S\pi^+\pi^-}}{\bar{\varepsilon}_{B\to K^0_S hh'}}}$	$\sigma^{\rm tot}_{\frac{\bar{\varepsilon}_{B^0_s\to K^0_S\pi^+\pi^-}}{\bar{\varepsilon}_{B\to K^0_S hh'}}}$
2018	$B^0_s\to K^0_S\pi^+K^-$	DD	6.47e-04	4.13e-04	0.63848	0.00956	0.00005	0.00092	0.00093	0.00321	0.01096	0.01036	0.00005	0.00051	0.00424	0.00005	0.01869
2017	$B^0_s\to K^0_S\pi^+K^-$	DD	6.77e-04	4.42e-04	0.65370	0.00985	0.00005	0.00099	0.00068	0.00199	0.01054	0.01036	0.00005	0.00054	0.00434	0.00005	0.01844
2016	$B^0_s\to K^0_S\pi^+K^-$	DD	7.69e-04	4.39e-04	0.57074	0.00841	0.00004	0.00082	0.00056	0.00193	0.00902	0.01036	0.00005	0.00023	0.00379	0.00004	0.01669
2015	$B^0_s\to K^0_S\pi^+K^-$	DD	6.70e-04	3.47e-04	0.51704	0.00836	0.00004	0.00083	0.00113	0.00290	0.01018	0.01036	0.00005	0.00019	0.00343	0.00004	0.01741
2012b	$B^0_s\to K^0_S\pi^+K^-$	DD	4.59e-04	3.44e-04	0.74900	0.01655	0.00005	0.00190	0.00134	0.01854	0.01607	0.01036	0.00007	0.00310	0.00497	0.00005	0.03199
2012a	$B^0_s\to K^0_S\pi^+K^-$	DD	3.89e-04	2.33e-04	0.59960	0.01628	0.00005	0.00173	0.00113	0.01491	0.01801	0.01036	0.00005	0.00119	0.00398	0.00005	0.03067
2011	$B^0_s\to K^0_S\pi^+K^-$	DD	4.57e-04	2.38e-04	0.52221	0.01317	0.00004	0.00229	0.00127	0.02084	0.01497	0.01036	0.00002	0.00007	0.00347	0.00004	0.03095
2018	$B^0_s\to K^0_S\pi^+K^-$	LL	2.71e-04	1.91e-04	0.70359	0.01646	0.00008	0.00082	0.00123	0.00228	0.02221	0.02108	0.00021	0.00414	0.00467	0.00008	0.03542
2017	$B^0_s\to K^0_S\pi^+K^-$	LL	2.99e-04	2.15e-04	0.72101	0.01673	0.00008	0.00094	0.00189	0.00248	0.02041	0.02108	0.00021	0.00322	0.00479	0.00008	0.03442
2016	$B^0_s\to K^0_S\pi^+K^-$	LL	3.16e-04	2.21e-04	0.70105	0.01597	0.00008	0.00086	0.00090	0.00278	0.01905	0.02108	0.00021	0.00129	0.00465	0.00008	0.03309
2015	$B^0_s\to K^0_S\pi^+K^-$	LL	2.47e-04	1.99e-04	0.80532	0.02018	0.00009	0.00103	0.00243	0.00457	0.02608	0.02108	0.00021	0.00223	0.00535	0.00009	0.03991
2012b	$B^0_s\to K^0_S\pi^+K^-$	LL	9.09e-05	1.08e-04	1.19364	0.05650	0.00014	0.00264	0.00455	0.02841	0.09106	0.02108	0.00045	0.00238	0.00793	0.00014	0.11328
2012a	$B^0_s\to K^0_S\pi^+K^-$	LL	1.51e-04	7.78e-05	0.51367	0.02340	0.00005	0.00119	0.00138	0.01872	0.03513	0.02108	0.00003	0.00014	0.00341	0.00005	0.05090
2011	$B^0_s\to K^0_S\pi^+K^-$	LL	1.86e-04	1.33e-04	0.71655	0.02751	0.00007	0.00231	0.00194	0.02347	0.03276	0.02108	0.00003	0.00659	0.00476	0.00007	0.05385

Table C.77: $B^0\to K^0_S\pi^+\pi^-$ over $B^0_s\to K^0_S\pi^+K^-$ efficiency table for the unfavoured mode optimisation. For each year and K^0_S reconstruction type, the average efficiency of the considered mode, the average efficiency of $B^0\to K^0_S\pi^+\pi^-$, the ratio of average efficiencies, the related uncertainties split by sources and the final uncertainty are given.

Year	Mode	K^0_S	$\bar{\varepsilon}_{B\to K^0_S hh'}$	$\bar{\varepsilon}_{B^0_s\to K^0_S\pi^+\pi^-}$	$\frac{\bar{\varepsilon}_{B^0_s\to K^0_S\pi^+\pi^-}}{\bar{\varepsilon}_{B\to K^0_S hh'}}$	$\sigma^{\rm stat}_{\frac{\bar{\varepsilon}_{B^0_s\to K^0_S\pi^+\pi^-}}{\bar{\varepsilon}_{B\to K^0_S hh'}}}$	$\sigma^{\rm tracking}_{\frac{\bar{\varepsilon}_{B^0_s\to K^0_S\pi^+\pi^-}}{\bar{\varepsilon}_{B\to K^0_S hh'}}}$	$\sigma^{\rm L0corr}_{\frac{\bar{\varepsilon}_{B^0_s\to K^0_S\pi^+\pi^-}}{\bar{\varepsilon}_{B\to K^0_S hh'}}}$	$\sigma^{\rm PIDMCsampling}_{\frac{\bar{\varepsilon}_{B^0_s\to K^0_S\pi^+\pi^-}}{\bar{\varepsilon}_{B\to K^0_S hh'}}}$	$\sigma^{\rm PIDkernel}_{\frac{\bar{\varepsilon}_{B^0_s\to K^0_S\pi^+\pi^-}}{\bar{\varepsilon}_{B\to K^0_S hh'}}}$	$\sigma^{\rm RMS}_{\frac{\bar{\varepsilon}_{B^0_s\to K^0_S\pi^+\pi^-}}{\bar{\varepsilon}_{B\to K^0_S hh'}}}$	$\sigma^{\rm binning}_{\frac{\bar{\varepsilon}_{B^0_s\to K^0_S\pi^+\pi^-}}{\bar{\varepsilon}_{B\to K^0_S hh'}}}$	$\sigma^{\rm L0E0choice}_{\frac{\bar{\varepsilon}_{B^0_s\to K^0_S\pi^+\pi^-}}{\bar{\varepsilon}_{B\to K^0_S hh'}}}$	$\sigma^{\rm FTrigger}_{\frac{\bar{\varepsilon}_{B^0_s\to K^0_S\pi^+\pi^-}}{\bar{\varepsilon}_{B\to K^0_S hh'}}}$	$\sigma^{\rm MCreweighting}_{\frac{\bar{\varepsilon}_{B^0_s\to K^0_S\pi^+\pi^-}}{\bar{\varepsilon}_{B\to K^0_S hh'}}}$	$\sigma^{\rm K^0_S tracking}_{\frac{\bar{\varepsilon}_{B^0_s\to K^0_S\pi^+\pi^-}}{\bar{\varepsilon}_{B\to K^0_S hh'}}}$	$\sigma^{\rm tot}_{\frac{\bar{\varepsilon}_{B^0_s\to K^0_S\pi^+\pi^-}}{\bar{\varepsilon}_{B\to K^0_S hh'}}}$
2018	$B^0_s\to K^0_S K^+\pi^-$	DD	6.78e-04	4.13e-04	0.60982	0.00877	0.00004	0.00087	0.00074	0.00266	0.01011	0.01200	0.00006	0.00050	0.00405	0.00004	0.01866
2017	$B^0_s\to K^0_S K^+\pi^-$	DD	7.50e-04	4.42e-04	0.58961	0.00845	0.00004	0.00087	0.00072	0.00231	0.00909	0.01200	0.00006	0.00045	0.00392	0.00004	0.01789
2016	$B^0_s\to K^0_S K^+\pi^-$	DD	7.42e-04	4.39e-04	0.59110	0.00855	0.00004	0.00085	0.00046	0.00206	0.00918	0.01200	0.00006	0.00009	0.00392	0.00004	0.01794
2015	$B^0_s\to K^0_S K^+\pi^-$	DD	6.16e-04	3.47e-04	0.56294	0.00906	0.00004	0.00089	0.00096	0.00293	0.01100	0.01200	0.00006	0.00066	0.00374	0.00004	0.01928
2012b	$B^0_s\to K^0_S K^+\pi^-$	DD	4.15e-04	3.44e-04	0.82809	0.01849	0.00005	0.00221	0.00113	0.02463	0.01758	0.01200	0.00008	0.00007	0.00550	0.00005	0.03792
2012a	$B^0_s\to K^0_S K^+\pi^-$	DD	3.44e-04	2.33e-04	0.67748	0.01843	0.00005	0.00200	0.00123	0.02889	0.02028	0.01200	0.00005	0.00080	0.00450	0.00005	0.04190
2011	$B^0_s\to K^0_S K^+\pi^-$	DD	4.33e-04	2.38e-04	0.55015	0.01350	0.00004	0.00233	0.00099	0.02012	0.01557	0.01200	0.00001	0.00023	0.00365	0.00004	0.03152
2018	$B^0_s\to K^0_S K^+\pi^-$	LL	2.64e-04	1.91e-04	0.72246	0.01761	0.00009	0.00084	0.00185	0.00487	0.03127	0.02211	0.00015	0.00465	0.00480	0.00009	0.04300
2017	$B^0_s\to K^0_S K^+\pi^-$	LL	2.84e-04	2.15e-04	0.75771	0.01843	0.00009	0.00099	0.00118	0.00292	0.03009	0.02211	0.00015	0.00319	0.00503	0.00009	0.04220
2016	$B^0_s\to K^0_S K^+\pi^-$	LL	3.14e-04	2.21e-04	0.70424	0.01674	0.00008	0.00088	0.00085	0.00331	0.02580	0.02211	0.00015	0.00021	0.00468	0.00008	0.03833
2015	$B^0_s\to K^0_S K^+\pi^-$	LL	2.75e-04	1.99e-04	0.72347	0.01830	0.00008	0.00096	0.00187	0.00455	0.03002	0.02211	0.00015	0.00234	0.00480	0.00008	0.04218
2012b	$B^0_s\to K^0_S K^+\pi^-$	LL	9.02e-05	1.08e-04	1.20245	0.05605	0.00014	0.00262	0.00651	0.03206	0.13804	0.02211	0.00016	0.00351	0.00798	0.00014	0.15440
2012a	$B^0_s\to K^0_S K^+\pi^-$	LL	1.48e-04	7.78e-05	0.52416	0.02411	0.00006	0.00126	0.00230	0.01995	0.04519	0.02211	0.00005	0.00082	0.00348	0.00006	0.05941
2011	$B^0_s\to K^0_S K^+\pi^-$	LL	1.69e-04	1.33e-04	0.78536	0.03065	0.00008	0.00263	0.00235	0.02273	0.05188	0.02211	0.00011	0.00152	0.00521	0.00008	0.06840

Table C.78: $B^0\to K^0_S\pi^+\pi^-$ over $B^0_s\to K^0_S K^+\pi^-$ efficiency table for the unfavoured mode optimisation. For each year and K^0_S reconstruction type, the average efficiency of the considered mode, the average efficiency of $B^0\to K^0_S\pi^+\pi^-$, the ratio of average efficiencies, the related uncertainties split by sources and the final uncertainty are given.

Year	Mode	K^0_S	$\bar{\varepsilon}_{B\to K^0_S hh'}$	$\bar{\varepsilon}_{B^0_s\to K^0_S\pi^+\pi^-}$	$\frac{\bar{\varepsilon}_{B^0_s\to K^0_S\pi^+\pi^-}}{\bar{\varepsilon}_{B\to K^0_S hh'}}$	$\sigma^{\rm stat}_{\frac{\bar{\varepsilon}_{B^0_s\to K^0_S\pi^+\pi^-}}{\bar{\varepsilon}_{B\to K^0_S hh'}}}$	$\sigma^{\rm tracking}_{\frac{\bar{\varepsilon}_{B^0_s\to K^0_S\pi^+\pi^-}}{\bar{\varepsilon}_{B\to K^0_S hh'}}}$	$\sigma^{\rm L0corr}_{\frac{\bar{\varepsilon}_{B^0_s\to K^0_S\pi^+\pi^-}}{\bar{\varepsilon}_{B\to K^0_S hh'}}}$	$\sigma^{\rm PIDMCsampling}_{\frac{\bar{\varepsilon}_{B^0_s\to K^0_S\pi^+\pi^-}}{\bar{\varepsilon}_{B\to K^0_S hh'}}}$	$\sigma^{\rm PIDkernel}_{\frac{\bar{\varepsilon}_{B^0_s\to K^0_S\pi^+\pi^-}}{\bar{\varepsilon}_{B\to K^0_S hh'}}}$	$\sigma^{\rm RMS}_{\frac{\bar{\varepsilon}_{B^0_s\to K^0_S\pi^+\pi^-}}{\bar{\varepsilon}_{B\to K^0_S hh'}}}$	$\sigma^{\rm binning}_{\frac{\bar{\varepsilon}_{B^0_s\to K^0_S\pi^+\pi^-}}{\bar{\varepsilon}_{B\to K^0_S hh'}}}$	$\sigma^{\rm L0E0choice}_{\frac{\bar{\varepsilon}_{B^0_s\to K^0_S\pi^+\pi^-}}{\bar{\varepsilon}_{B\to K^0_S hh'}}}$	$\sigma^{\rm FTrigger}_{\frac{\bar{\varepsilon}_{B^0_s\to K^0_S\pi^+\pi^-}}{\bar{\varepsilon}_{B\to K^0_S hh'}}}$	$\sigma^{\rm MCreweighting}_{\frac{\bar{\varepsilon}_{B^0_s\to K^0_S\pi^+\pi^-}}{\bar{\varepsilon}_{B\to K^0_S hh'}}}$	$\sigma^{\rm K^0_S tracking}_{\frac{\bar{\varepsilon}_{B^0_s\to K^0_S\pi^+\pi^-}}{\bar{\varepsilon}_{B\to K^0_S hh'}}}$	$\sigma^{\rm tot}_{\frac{\bar{\varepsilon}_{B^0_s\to K^0_S\pi^+\pi^-}}{\bar{\varepsilon}_{B\to K^0_S hh'}}}$
2018	$B^0_s\to K^0_S K^+K^-$	DD	5.48e-04	4.13e-04	0.75424	0.01121	0.00006	0.00116	0.00146	0.00401	0.05325	0.03539	0.00133	0.00123	0.00501	0.00006	0.06528
2017	$B^0_s\to K^0_S K^+K^-$	DD	4.26e-04	4.42e-04	1.03832	0.01709	0.00008	0.00218	0.00215	0.00587	0.09326	0.03539	0.00133	0.00128	0.00689	0.00008	0.10167
2016	$B^0_s\to K^0_S K^+K^-$	DD	5.46e-04	4.39e-04	0.80324	0.01222	0.00006	0.00129	0.00157	0.00349	0.05672	0.03539	0.00133	0.00124	0.00533	0.00006	0.06832
2015	$B^0_s\to K^0_S K^+K^-$	DD	4.51e-04	3.47e-04	0.76886	0.01295	0.00006	0.00133	0.00211	0.00495	0.06593	0.03539	0.00133	0.00129	0.00511	0.00006	0.07634
2012b	$B^0_s\to K^0_S K^+K^-$	DD	4.23e-04	3.44e-04	0.81333	0.01702	0.00005	0.00309	0.00207	0.05931	0.07421	0.03539	0.00027	0.00105	0.00540	0.00005	0.10301
2012a	$B^0_s\to K^0_S K^+K^-$	DD	3.08e-04	2.33e-04	0.75798	0.02082	0.00005	0.00271	0.00232	0.05117	0.09533	0.03539	0.00030	0.00017	0.00503	0.00005	0.11588
2011	$B^0_s\to K^0_S K^+K^-$	DD	3.95e-04	2.38e-04	0.60312	0.01467	0.00004	0.00291	0.00291	0.05304	0.05978	0.03539	0.00027	0.00061	0.00400	0.00004	0.08882
2018	$B^0_s\to K^0_S K^+K^-$	LL	2.67e-04	1.91e-04	0.71415	0.04836	0.00029	0.00239	0.00912	0.00494	0.10068	0.13006	0.00165	0.00384	0.00474	0.00029	0.17189
2017	$B^0_s\to K^0_S K^+K^-$	LL	2.27e-04	2.15e-04	0.94744	0.07417	0.00038	0.00530	0.01415	0.00443	0.15616	0.13006	0.00165	0.00728	0.00629	0.00038	0.21713
2016	$B^0_s\to K^0_S K^+K^-$	LL	2.56e-04	2.21e-04	0.86366	0.06187	0.00033	0.00319	0.00918	0.00511	0.12641	0.13006	0.00165	0.00312	0.00573	0.00033	0.19207
2015	$B^0_s\to K^0_S K^+K^-$	LL	3.50e-04	1.99e-04	0.56874	0.03597	0.00020	0.00212	0.00537	0.00370	0.06164	0.13006	0.00165	0.00548	0.00378	0.00020	0.14867
2012b	$B^0_s\to K^0_S K^+K^-$	LL	1.54e-04	1.08e-04	0.70457	0.08405	0.00024	0.01059	0.01669	0.05300	0.17250	0.13006	0.00039	0.00305	0.00468	0.00024	0.23868
2012a	$B^0_s\to K^0_S K^+K^-$	LL	1.67e-04	7.78e-05	0.46617	0.06141	0.00016	0.00611	0.00581	0.03245	0.10709	0.13006	0.00023	0.00048	0.00310	0.00016	0.18246
2011	$B^0_s\to K^0_S K^+K^-$	LL	1.76e-04	1.33e-04	0.75530	0.08799	0.00021	0.00879	0.01949	0.04453	0.16145	0.13006	0.00099	0.00376	0.00502	0.00021	0.23067

Table C.79: $B^0\to K^0_S\pi^+\pi^-$ over $B^0_s\to K^0_S K^+K^-$ efficiency table for the unfavoured mode optimisation. For each year and K^0_S reconstruction type, the average efficiency of the considered mode, the average efficiency of $B^0\to K^0_S\pi^+\pi^-$, the ratio of average efficiencies, the related uncertainties split by sources and the final uncertainty are given.

Year	Mode	K^0_S	$\bar{\varepsilon}_{B\to K^0_S hh'}$	$\bar{\varepsilon}_{B^0_s\to K^0_S\pi^+\pi^-}$	$\frac{\bar{\varepsilon}_{B^0_s\to K^0_S\pi^+\pi^-}}{\bar{\varepsilon}_{B\to K^0_S hh'}}$	$\sigma^{\rm stat}_{\frac{\bar{\varepsilon}_{B^0_s\to K^0_S\pi^+\pi^-}}{\bar{\varepsilon}_{B\to K^0_S hh'}}}$	$\sigma^{\rm tracking}_{\frac{\bar{\varepsilon}_{B^0_s\to K^0_S\pi^+\pi^-}}{\bar{\varepsilon}_{B\to K^0_S hh'}}}$	$\sigma^{\rm L0corr}_{\frac{\bar{\varepsilon}_{B^0_s\to K^0_S\pi^+\pi^-}}{\bar{\varepsilon}_{B\to K^0_S hh'}}}$	$\sigma^{\rm PIDMCsampling}_{\frac{\bar{\varepsilon}_{B^0_s\to K^0_S\pi^+\pi^-}}{\bar{\varepsilon}_{B\to K^0_S hh'}}}$	$\sigma^{\rm PIDkernel}_{\frac{\bar{\varepsilon}_{B^0_s\to K^0_S\pi^+\pi^-}}{\bar{\varepsilon}_{B\to K^0_S hh'}}}$	$\sigma^{\rm RMS}_{\frac{\bar{\varepsilon}_{B^0_s\to K^0_S\pi^+\pi^-}}{\bar{\varepsilon}_{B\to K^0_S hh'}}}$	$\sigma^{\rm binning}_{\frac{\bar{\varepsilon}_{B^0_s\to K^0_S\pi^+\pi^-}}{\bar{\varepsilon}_{B\to K^0_S hh'}}}$	$\sigma^{\rm L0E0choice}_{\frac{\bar{\varepsilon}_{B^0_s\to K^0_S\pi^+\pi^-}}{\bar{\varepsilon}_{B\to K^0_S hh'}}}$	$\sigma^{\rm FTrigger}_{\frac{\bar{\varepsilon}_{B^0_s\to K^0_S\pi^+\pi^-}}{\bar{\varepsilon}_{B\to K^0_S hh'}}}$	$\sigma^{\rm MCreweighting}_{\frac{\bar{\varepsilon}_{B^0_s\to K^0_S\pi^+\pi^-}}{\bar{\varepsilon}_{B\to K^0_S hh'}}}$	$\sigma^{\rm K^0_S tracking}_{\frac{\bar{\varepsilon}_{B^0_s\to K^0_S\pi^+\pi^-}}{\bar{\varepsilon}_{B\to K^0_S hh'}}}$	$\sigma^{\rm tot}_{\frac{\bar{\varepsilon}_{B^0_s\to K^0_S\pi^+\pi^-}}{\bar{\varepsilon}_{B\to K^0_S hh'}}}$
2018	$B^0_d\to K^0_S\pi^+K^-$	DD	8.85e-04	8.21e-04	0.92759	0.01359	0.00008	0.00158	0.00181	0.00517	0.02098	0.01463	0.00004	0.00088	0.00664	0.00008	0.03027
2017	$B^0_d\to K^0_S\pi^+K^-$	DD	9.26e-04	8.33e-04	0.89989	0.01375	0.00008	0.00156	0.00184	0.00439	0.02037	0.01508	0.00004	0.00672	0.00664	0.00008	0.03075
2016	$B^0_d\to K^0_S\pi^+K^-$	DD	1.05e-03	8.69e-04	0.82722	0.01315	0.00008	0.00153	0.00134	0.00399	0.01878	0.01640	0.00004	0.00239	0.00664	0.00008	0.02940
2015	$B^0_d\to K^0_S\pi^+K^-$	DD	9.33e-04	8.36e-04	0.89567	0.01406	0.00008	0.00167	0.00233	0.00803	0.02026	0.01515	0.00004	0.00090	0.00664	0.00008	0.03091
2012b	$B^0_d\to K^0_S\pi^+K^-$	DD	6.62e-04	5.19e-04	0.78501	0.02076	0.00007	0.00273	0.00241	0.06932	0.03073	0.01728	0.00009	0.00648	0.00664	0.00007	0.08111
2012a	$B^0_d\to K^0_S\pi^+K^-$	DD	5.04e-04	4.12e-04	0.81742	0.02572	0.00008	0.00353	0.00304	0.08170	0.03945	0.01660	0.00003	0.00075	0.00664	0.00008	0.09609
2011	$B^0_d\to K^0_S\pi^+K^-$	DD	6.10e-04	4.92e-04	0.80706	0.02218	0.00007	0.00455	0.00350	0.07588	0.03283	0.01681	0.00011	0.00036	0.00664	0.00007	0.08768
2018	$B^0_d\to K^0_S\pi^+K^-$	LL	3.34e-04	2.97e-04	0.88826	0.02431	0.00014	0.00130	0.00320	0.00561	0.04204	0.01962	0.00028	0.00418	0.00664	0.00014	0.05337
2017	$B^0_d\to K^0_S\pi^+K^-$	LL	3.70e-04	3.17e-04	0.85555	0.02449	0.00013	0.00142	0.00323	0.00385	0.03832	0.02037	0.00029	0.00274	0.00664	0.00013	0.05062
2016	$B^0_d\to K^0_S\pi^+K^-$	LL	3.84e-04	3.56e-04	0.92716	0.02382	0.00012	0.00140	0.00202	0.00442	0.03615	0.01880	0.00027	0.00130	0.00664	0.00012	0.04795
2015	$B^0_d\to K^0_S\pi^+K^-$	LL	3.67e-04	3.28e-04	0.89240	0.02463	0.00013	0.00139	0.00440	0.00779	0.03823	0.01953	0.00028	0.00315	0.00664	0.00013	0.05085
2012b	$B^0_d\to K^0_S\pi^+K^-$	LL	1.81e-04	1.53e-04	0.84580	0.04114	0.00012	0.00245	0.00863	0.08177	0.07857	0.02061	0.00047	0.00005	0.00664	0.00012	0.12289
2012a	$B^0_d\to K^0_S\pi^+K^-$	LL	2.08e-04	1.77e-04	0.84869	0.04164	0.00012	0.00265	0.00761	0.07369	0.06829	0.02054	0.00021	0.00576	0.00664	0.00012	0.11132
2011	$B^0_d\to K^0_S\pi^+K^-$	LL	2.37e-04	1.88e-04	0.79103	0.03828	0.00011	0.00367	0.00502	0.05937	0.06128	0.02203	0.00030	0.00783	0.00664	0.00011	0.09683

Table C.80: $B^0\to K^0_S\pi^+\pi^-$ over $B^0\to K^0_S\pi^+K^-$ efficiency table for the favoured mode optimisation. For each year and K^0_S reconstruction type, the average efficiency of the considered mode, the average efficiency of $B^0\to K^0_S\pi^+\pi^-$, the ratio of average efficiencies, the related relative uncertainties split by sources and the final relative uncertainty are given.

Year	Mode	K^0_S	$\bar{\varepsilon}_{B\to K^0_S hh'}$	$\bar{\varepsilon}_{B^0_s\to K^0_S\pi^+\pi^-}$	$\frac{\bar{\varepsilon}_{B^0_s\to K^0_S\pi^+\pi^-}}{\bar{\varepsilon}_{B\to K^0_S hh'}}$	$\sigma^{\rm stat}_{\frac{\bar{\varepsilon}_{B^0_s\to K^0_S\pi^+\pi^-}}{\bar{\varepsilon}_{B\to K^0_S hh'}}}$	$\sigma^{\rm tracking}_{\frac{\bar{\varepsilon}_{B^0_s\to K^0_S\pi^+\pi^-}}{\bar{\varepsilon}_{B\to K^0_S hh'}}}$	$\sigma^{\rm L0corr}_{\frac{\bar{\varepsilon}_{B^0_s\to K^0_S\pi^+\pi^-}}{\bar{\varepsilon}_{B\to K^0_S hh'}}}$	$\sigma^{\rm PIDMCsampling}_{\frac{\bar{\varepsilon}_{B^0_s\to K^0_S\pi^+\pi^-}}{\bar{\varepsilon}_{B\to K^0_S hh'}}}$	$\sigma^{\rm PIDkernel}_{\frac{\bar{\varepsilon}_{B^0_s\to K^0_S\pi^+\pi^-}}{\bar{\varepsilon}_{B\to K^0_S hh'}}}$	$\sigma^{\rm RMS}_{\frac{\bar{\varepsilon}_{B^0_s\to K^0_S\pi^+\pi^-}}{\bar{\varepsilon}_{B\to K^0_S hh'}}}$	$\sigma^{\rm binning}_{\frac{\bar{\varepsilon}_{B^0_s\to K^0_S\pi^+\pi^-}}{\bar{\varepsilon}_{B\to K^0_S hh'}}}$	$\sigma^{\rm L0E0choice}_{\frac{\bar{\varepsilon}_{B^0_s\to K^0_S\pi^+\pi^-}}{\bar{\varepsilon}_{B\to K^0_S hh'}}}$	$\sigma^{\rm FTrigger}_{\frac{\bar{\varepsilon}_{B^0_s\to K^0_S\pi^+\pi^-}}{\bar{\varepsilon}_{B\to K^0_S hh'}}}$	$\sigma^{\rm MCreweighting}_{\frac{\bar{\varepsilon}_{B^0_s\to K^0_S\pi^+\pi^-}}{\bar{\varepsilon}_{B\to K^0_S hh'}}}$	$\sigma^{\rm K^0_S tracking}_{\frac{\bar{\varepsilon}_{B^0_s\to K^0_S\pi^+\pi^-}}{\bar{\varepsilon}_{B\to K^0_S hh'}}}$	$\sigma^{\rm tot}_{\frac{\bar{\varepsilon}_{B^0_s\to K^0_S\pi^+\pi^-}}{\bar{\varepsilon}_{B\to K^0_S hh'}}}$
2018	$B^0_d\to K^0_S K^+\pi^-$	DD	8.98e-04	8.21e-04	0.91394	0.01443	0.00009	0.00157	0.00156	0.00503	0.02209	0.01162	0.00003	0.00333	0.00664	0.00009	0.03028
2017	$B^0_d\to K^0_S K^+\pi^-$	DD	9.56e-04	8.33e-04	0.87205	0.01476	0.00008	0.00166	0.00149	0.00451	0.02123	0.01218	0.00003	0.00371	0.00664	0.00008	0.03000
2016	$B^0_d\to K^0_S K^+\pi^-$	DD	1.02e-03	8.69e-04	0.85108	0.01426	0.00008	0.00167	0.00130	0.00390	0.02009	0.01248	0.00003	0.00233	0.00664	0.00008	0.02884
2015	$B^0_d\to K^0_S K^+\pi^-$	DD	9.33e-04	8.36e-04	0.89592	0.01523	0.00009	0.00186	0.00354	0.00914	0.02147	0.01185	0.00003	0.00075	0.00664	0.00009	0.03127
2012b	$B^0_d\to K^0_S K^+\pi^-$	DD	6.82e-04	5.19e-04	0.76209	0.02219	0.00007	0.00299	0.00556	0.08230	0.03188	0.01393	0.00011	0.00737	0.00664	0.00007	0.09281
2012a	$B^0_d\to K^0_S K^+\pi^-$	DD	5.19e-04	4.12e-04	0.79266	0.02780	0.00009	0.00319	0.00395	0.08624	0.04097	0.01340	0.00012	0.00722	0.00664	0.00009	0.10095
2011	$B^0_d\to K^0_S K^+\pi^-$	DD	6.36e-04	4.92e-04	0.77358	0.02414	0.00007	0.00504	0.00328	0.07803	0.03389	0.01373	0.00013	0.00104	0.00664	0.00007	0.08994
2018	$B^0_d\to K^0_S K^+\pi^-$	LL	3.22e-04	2.97e-04	0.92069	0.02635	0.00015	0.00138	0.00295	0.00535	0.04709	0.03516	0.00018	0.00977	0.00664	0.00015	0.06577
2017	$B^0_d\to K^0_S K^+\pi^-$	LL	3.68e-04	3.17e-04	0.86072	0.02647	0.00014	0.00153	0.00839	0.00606	0.04187	0.03761	0.00019	0.00492	0.00664	0.00014	0.06361
2016	$B^0_d\to K^0_S K^+\pi^-$	LL	4.01e-04	3.56e-04	0.88901	0.02519	0.00014	0.00150	0.01852	0.00518	0.03818	0.03641	0.00018	0.00403	0.00664	0.00014	0.06205
2015	$B^0_d\to K^0_S K^+\pi^-$	LL	3.75e-04	3.28e-04	0.87453	0.02645	0.00014	0.00161	0.00570	0.01218	0.04101	0.03701	0.00019	0.00013	0.00664	0.00014	0.06308
2012b	$B^0_d\to K^0_S K^+\pi^-$	LL	1.78e-04	1.53e-04	0.86159	0.04617	0.00014	0.00298	0.01542	0.07638	0.08660	0.03757	0.00044	0.00124	0.00664	0.00014	0.13103
2012a	$B^0_d\to K^0_S K^+\pi^-$	LL	1.88e-04	1.77e-04	0.93893	0.04930	0.00014	0.00262	0.00744	0.05218	0.08027	0.03448	0.00004	0.00010	0.00664	0.00014	0.11354
2011	$B^0_d\to K^0_S K^+\pi^-$	LL	2.29e-04	1.88e-04	0.81795	0.04339	0.00013	0.00443	0.00559	0.06062	0.06806	0.03957	0.00024	0.00117	0.00664	0.00013	0.10887

Table C.81: $B^0\to K^0_S\pi^+\pi^-$ over $B^0\to K^0_S K^+\pi^-$ efficiency table for the favoured mode optimisation. For each year and K^0_S reconstruction type, the average efficiency of the considered mode, the average efficiency of $B^0\to K^0_S\pi^+\pi^-$, the ratio of average efficiencies, the related relative uncertainties split by sources and the final relative uncertainty are given.

Year	Mode	K^0_S	$\bar{\varepsilon}_{B\to K^0_S hh'}$	$\bar{\varepsilon}_{B^0_s\to K^0_S\pi^+\pi^-}$	$\frac{\bar{\varepsilon}_{B^0_s\to K^0_S\pi^+\pi^-}}{\bar{\varepsilon}_{B\to K^0_S hh'}}$	$\sigma^{\rm stat}_{\frac{\bar{\varepsilon}_{B^0_s\to K^0_S\pi^+\pi^-}}{\bar{\varepsilon}_{B\to K^0_S hh'}}}$	$\sigma^{\rm tracking}_{\frac{\bar{\varepsilon}_{B^0_s\to K^0_S\pi^+\pi^-}}{\bar{\varepsilon}_{B\to K^0_S hh'}}}$	$\sigma^{\rm L0corr}_{\frac{\bar{\varepsilon}_{B^0_s\to K^0_S\pi^+\pi^-}}{\bar{\varepsilon}_{B\to K^0_S hh'}}}$	$\sigma^{\rm PIDMCsampling}_{\frac{\bar{\varepsilon}_{B^0_s\to K^0_S\pi^+\pi^-}}{\bar{\varepsilon}_{B\to K^0_S hh'}}}$	$\sigma^{\rm PIDkernel}_{\frac{\bar{\varepsilon}_{B^0_s\to K^0_S\pi^+\pi^-}}{\bar{\varepsilon}_{B\to K^0_S hh'}}}$	$\sigma^{\rm RMS}_{\frac{\bar{\varepsilon}_{B^0_s\to K^0_S\pi^+\pi^-}}{\bar{\varepsilon}_{B\to K^0_S hh'}}}$	$\sigma^{\rm binning}_{\frac{\bar{\varepsilon}_{B^0_s\to K^0_S\pi^+\pi^-}}{\bar{\varepsilon}_{B\to K^0_S hh'}}}$	$\sigma^{\rm L0E0choice}_{\frac{\bar{\varepsilon}_{B^0_s\to K^0_S\pi^+\pi^-}}{\bar{\varepsilon}_{B\to K^0_S hh'}}}$	$\sigma^{\rm FTrigger}_{\frac{\bar{\varepsilon}_{B^0_s\to K^0_S\pi^+\pi^-}}{\bar{\varepsilon}_{B\to K^0_S hh'}}}$	$\sigma^{\rm MCreweighting}_{\frac{\bar{\varepsilon}_{B^0_s\to K^0_S\pi^+\pi^-}}{\bar{\varepsilon}_{B\to K^0_S hh'}}}$	$\sigma^{\rm K^0_S tracking}_{\frac{\bar{\varepsilon}_{B^0_s\to K^0_S\pi^+\pi^-}}{\bar{\varepsilon}_{B\to K^0_S hh'}}}$	$\sigma^{\rm tot}_{\frac{\bar{\varepsilon}_{B^0_s\to K^0_S\pi^+\pi^-}}{\bar{\varepsilon}_{B\to K^0_S hh'}}}$
2018	$B^0_d\to K^0_S K^+K^-$	DD	7.28e-04	8.21e-04	1.12748	0.01035	0.00006	0.00128	0.00113	0.00391	0.01550	0.03282	0.00051	0.00617	0.00664	0.00006	0.03906
2017	$B^0_d\to K^0_S K^+K^-$	DD	7.51e-04	8.33e-04	1.10885	0.01065	0.00006	0.00181	0.00091	0.00323	0.01525	0.03338	0.00052	0.00562	0.00664	0.00006	0.03938
2016	$B^0_d\to K^0_S K^+K^-$	DD	8.93e-04	8.69e-04	0.97305	0.01011	0.00006	0.00130	0.00082	0.00390	0.01449	0.03803	0.00059	0.00443	0.00664	0.00006	0.04290
2015	$B^0_d\to K^0_S K^+K^-$	DD	8.04e-04	8.36e-04	1.04000	0.01062	0.00006	0.00141	0.00135	0.00444	0.01513	0.03559	0.00055	0.00613	0.00664	0.00006	0.04140
2012b	$B^0_d\to K^0_S K^+K^-$	DD	4.50e-04	5.19e-04	1.15518	0.01662	0.00005	0.00353	0.00731	0.02659	0.02455	0.03204	0.00016	0.00339	0.00664	0.00005	0.05229
2012a	$B^0_d\to K^0_S K^+K^-$	DD	3.11e-04	4.12e-04	1.32149	0.02082	0.00006	0.00425	0.00173	0.02423	0.03139	0.02801	0.00021	0.00017	0.00664	0.00006	0.05344
2011	$B^0_d\to K^0_S K^+K^-$	DD	3.60e-04	4.92e-04	1.36557	0.01806	0.00005	0.00424	0.00128	0.01588	0.02636	0.02710	0.00017	0.00036	0.00664	0.00005	0.04551
2018	$B^0_d\to K^0_S K^+K^-$	LL	3.05e-04	2.97e-04	0.97387	0.01639	0.00010	0.00104	0.00163	0.00300	0.02293	0.02976	0.00067	0.01775	0.00664	0.00010	0.04530
2017	$B^0_d\to K^0_S K^+K^-$	LL	3.29e-04	3.17e-04	0.96221	0.01670	0.00009	0.00140	0.00136	0.00367	0.02146	0.03012	0.00068	0.01631	0.00664	0.00009	0.04443
2016	$B^0_d\to K^0_S K^+K^-$	LL	3.70e-04	3.56e-04	0.96216	0.01590	0.00009	0.00110	0.00107	0.00379	0.01909	0.03012	0.00068	0.00697	0.00664	0.00009	0.04042
2015	$B^0_d\to K^0_S K^+K^-$	LL	3.33e-04	3.28e-04	0.98409	0.01678	0.00009	0.00116	0.00237	0.00717	0.02080	0.02945	0.00066	0.00667	0.00664	0.00009	0.04158
2012b	$B^0_d\to K^0_S K^+K^-$	LL	1.47e-04	1.53e-04	1.04271	0.02967	0.00009	0.00339	0.00264	0.01835	0.04468	0.02779	0.00045	0.00313	0.00664	0.00009	0.06370
2012a	$B^0_d\to K^0_S K^+K^-$	LL	1.68e-04	1.77e-04	1.05282	0.03019	0.00008	0.00242	0.00337	0.02365	0.03878	0.02752	0.00029	0.00791	0.00664	0.00008	0.06210
2011	$B^0_d\to K^0_S K^+K^-$	LL	1.90e-04	1.88e-04	0.98769	0.02755	0.00008	0.00333	0.00255	0.01861	0.03632	0.02934	0.00036	0.00349	0.00664	0.00008	0.05796

Table C.82: $B^0\to K^0_S\pi^+\pi^-$ over $B^0\to K^0_S K^+K^-$ efficiency table for the favoured mode optimisation. For each year and K^0_S reconstruction type, the average efficiency of the considered mode, the average efficiency of $B^0\to K^0_S\pi^+\pi^-$, the ratio of average efficiencies, the related relative uncertainties split by sources and the final relative uncertainty are given.

Year	Mode	K^0_S	$\bar{\varepsilon}_{B\to K^0_S hh'}$	$\bar{\varepsilon}_{B^0_s\to K^0_S\pi^+\pi^-}$	$\frac{\bar{\varepsilon}_{B^0_s\to K^0_S\pi^+\pi^-}}{\bar{\varepsilon}_{B\to K^0_S hh'}}$	$\sigma^{\rm stat}_{\frac{\bar{\varepsilon}_{B^0_s\to K^0_S\pi^+\pi^-}}{\bar{\varepsilon}_{B\to K^0_S hh'}}}$	$\sigma^{\rm tracking}_{\frac{\bar{\varepsilon}_{B^0_s\to K^0_S\pi^+\pi^-}}{\bar{\varepsilon}_{B\to K^0_S hh'}}}$	$\sigma^{\rm L0corr}_{\frac{\bar{\varepsilon}_{B^0_s\to K^0_S\pi^+\pi^-}}{\bar{\varepsilon}_{B\to K^0_S hh'}}}$	$\sigma^{\rm PIDMCsampling}_{\frac{\bar{\varepsilon}_{B^0_s\to K^0_S\pi^+\pi^-}}{\bar{\varepsilon}_{B\to K^0_S hh'}}}$	$\sigma^{\rm PIDkernel}_{\frac{\bar{\varepsilon}_{B^0_s\to K^0_S\pi^+\pi^-}}{\bar{\varepsilon}_{B\to K^0_S hh'}}}$	$\sigma^{\rm RMS}_{\frac{\bar{\varepsilon}_{B^0_s\to K^0_S\pi^+\pi^-}}{\bar{\varepsilon}_{B\to K^0_S hh'}}}$	$\sigma^{\rm binning}_{\frac{\bar{\varepsilon}_{B^0_s\to K^0_S\pi^+\pi^-}}{\bar{\varepsilon}_{B\to K^0_S hh'}}}$	$\sigma^{\rm L0E0choice}_{\frac{\bar{\varepsilon}_{B^0_s\to K^0_S\pi^+\pi^-}}{\bar{\varepsilon}_{B\to K^0_S hh'}}}$	$\sigma^{\rm FTrigger}_{\frac{\bar{\varepsilon}_{B^0_s\to K^0_S\pi^+\pi^-}}{\bar{\varepsilon}_{B\to K^0_S hh'}}}$	$\sigma^{\rm MCreweighting}_{\frac{\bar{\varepsilon}_{B^0_s\to K^0_S\pi^+\pi^-}}{\bar{\varepsilon}_{B\to K^0_S hh'}}}$	$\sigma^{\rm K^0_S tracking}_{\frac{\bar{\varepsilon}_{B^0_s\to K^0_S\pi^+\pi^-}}{\bar{\varepsilon}_{B\to K^0_S hh'}}}$	$\sigma^{\rm tot}_{\frac{\bar{\varepsilon}_{B^0_s\to K^0_S\pi^+\pi^-}}{\bar{\varepsilon}_{B\to K^0_S hh'}}}$
2018	$B^0_s\to K^0_S\pi^+\pi^-$	DD	8.71e-04	8.21e-04	0.942695	0.012015	N/A	N/A	N/A	N/A	0.042946	0.017541	8.043000e-05	0.001849	0.00664	N/A	0.048414
2017	$B^0_s\to K^0_S\pi^+\pi^-$	DD	8.84e-04	8.33e-04	0.942319	0.012285	N/A	N/A	N/A	N/A	0.042297	0.017548	8.046000e-05	0.003130	0.00664	N/A	0.047977
2016	$B^0_s\to K^0_S\pi^+\pi^-$	DD	9.14e-04	8.69e-04	0.951509	0.012216	N/A	N/A	N/A	N/A	0.040892	0.017378	7.969000e-05	0.000872	0.00664	N/A	0.046564
2015	$B^0_s\to K^0_S\pi^+\pi^-$	DD	8.97e-04	8.36e-04	0.931657	0.012553	N/A	N/A	N/A	N/A	0.041747	0.017748	8.139000e-05	0.001400	0.00664	N/A	0.047554
2012b	$B^0_s\to K^0_S\pi^+\pi^-$	DD	5.70e-04	5.19e-04	0.911273	0.018221	N/A	N/A	N/A	N/A	0.065895	0.018145	6.841000e-05	0.000659	0.00664	N/A	0.071048
2012a	$B^0_s\to K^0_S\pi^+\pi^-$	DD	4.59e-04	4.12e-04	0.897631	0.021436	N/A	N/A	N/A	N/A	0.082067	0.018421	4.666000e-05	0.000592	0.00664	N/A	0.087053
2011	$B^0_s\to K^0_S\pi^+\pi^-$	DD	5.48e-04	4.92e-04	0.897117	0.018657	N/A	N/A	N/A	N/A	0.068627	0.018432	3.350000e-06	0.000483	0.00664	N/A	0.073769
2018	$B^0_s\to K^0_S\pi^+\pi^-$	LL	3.29e-04	2.97e-04	0.901442	0.022499	N/A	N/A	N/A	N/A	0.033256	0.027293	2.040700e-04	0.000185	0.00664	N/A	0.049003
2017	$B^0_s\to K^0_S\pi^+\pi^-$	LL	3.57e-04	3.17e-04	0.887666	0.022096	N/A	N/A	N/A	N/A	0.030880	0.027717	2.072400e-04	0.002494	0.00664	N/A	0.047543
2016	$B^0_s\to K^0_S\pi^+\pi^-$	LL	3.98e-04	3.56e-04	0.895650	0.021700	N/A	N/A	N/A	N/A	0.027607	0.027470	2.053900e-04	0.000990	0.00664	N/A	0.045086
2015	$B^0_s\to K^0_S\pi^+\pi^-$	LL	3.61e-04	3.28e-04	0.907644	0.022529	N/A	N/A	N/A	N/A	0.030259	0.027107	2.026800e-04	0.001526	0.00664	N/A	0.046951
2012b	$B^0_s\to K^0_S\pi^+\pi^-$	LL	1.75e-04	1.53e-04	0.877179	0.037173	N/A	N/A	N/A	N/A	0.063405	0.028048	8.000000e-08	0.001428	0.00664	N/A	0.078961
2012a	$B^0_s\to K^0_S\pi^+\pi^-$	LL	2.01e-04	1.77e-04	0.879581	0.037228	N/A	N/A	N/A	N/A	0.055060	0.027971	1.901200e-04	0.001783	0.00664	N/A	0.072438
2011	$B^0_s\to K^0_S\pi^+\pi^-$	LL	2.15e-04	1.88e-04	0.872869	0.034251	N/A	N/A	N/A	N/A	0.051670	0.028187	1.371700e-04	0.000213	0.00664	N/A	0.068422

Table C.83: $B^0\to K^0_S\pi^+\pi^-$ over $B^0_s\to K^0_S\pi^+\pi^-$ efficiency table for the favoured mode optimisation. For each year and K^0_S reconstruction type, the average efficiency of the considered mode, the average efficiency of $B^0\to K^0_S\pi^+\pi^-$, the ratio of average efficiencies, the related relative uncertainties split by sources and the final relative uncertainty are given. An uncertainty at N/A means maximally correlated (same final state) uncertainty which are cancelled in the ratio.

Year	Mode	K^0_S	$\bar{\varepsilon}_{B\to K^0_S hh'}$	$\bar{\varepsilon}_{B^0_s\to K^0_S\pi^+\pi^-}$	$\frac{\bar{\varepsilon}_{B^0_s\to K^0_S\pi^+\pi^-}}{\bar{\varepsilon}_{B\to K^0_S hh'}}$	$\sigma^{\rm stat}_{\frac{\bar{\varepsilon}_{B^0_s\to K^0_S\pi^+\pi^-}}{\bar{\varepsilon}_{B\to K^0_S hh'}}}$	$\sigma^{\rm tracking}_{\frac{\bar{\varepsilon}_{B^0_s\to K^0_S\pi^+\pi^-}}{\bar{\varepsilon}_{B\to K^0_S hh'}}}$	$\sigma^{\rm L0corr}_{\frac{\bar{\varepsilon}_{B^0_s\to K^0_S\pi^+\pi^-}}{\bar{\varepsilon}_{B\to K^0_S hh'}}}$	$\sigma^{\rm PIDMCsampling}_{\frac{\bar{\varepsilon}_{B^0_s\to K^0_S\pi^+\pi^-}}{\bar{\varepsilon}_{B\to K^0_S hh'}}}$	$\sigma^{\rm PIDkernel}_{\frac{\bar{\varepsilon}_{B^0_s\to K^0_S\pi^+\pi^-}}{\bar{\varepsilon}_{B\to K^0_S hh'}}}$	$\sigma^{\rm RMS}_{\frac{\bar{\varepsilon}_{B^0_s\to K^0_S\pi^+\pi^-}}{\bar{\varepsilon}_{B\to K^0_S hh'}}}$	$\sigma^{\rm binning}_{\frac{\bar{\varepsilon}_{B^0_s\to K^0_S\pi^+\pi^-}}{\bar{\varepsilon}_{B\to K^0_S hh'}}}$	$\sigma^{\rm L0E0choice}_{\frac{\bar{\varepsilon}_{B^0_s\to K^0_S\pi^+\pi^-}}{\bar{\varepsilon}_{B\to K^0_S hh'}}}$	$\sigma^{\rm FTrigger}_{\frac{\bar{\varepsilon}_{B^0_s\to K^0_S\pi^+\pi^-}}{\bar{\varepsilon}_{B\to K^0_S hh'}}}$	$\sigma^{\rm MCreweighting}_{\frac{\bar{\varepsilon}_{B^0_s\to K^0_S\pi^+\pi^-}}{\bar{\varepsilon}_{B\to K^0_S hh'}}}$	$\sigma^{\rm K^0_S tracking}_{\frac{\bar{\varepsilon}_{B^0_s\to K^0_S\pi^+\pi^-}}{\bar{\varepsilon}_{B\to K^0_S hh'}}}$	$\sigma^{\rm tot}_{\frac{\bar{\varepsilon}_{B^0_s\to K^0_S\pi^+\pi^-}}{\bar{\varepsilon}_{B\to K^0_S hh'}}}$
2018	$B^0_s\to K^0_S K^+K^-$	DD	8.53e-04	8.21e-04	0.96281	0.01258	0.00008	0.00140	0.00147	0.00503	0.01632	0.01396	0.00007	0.00025	0.00664	0.00008	0.02632
2017	$B^0_s\to K^0_S K^+K^-$	DD	8.86e-04	8.33e-04	0.94059	0.01274	0.00007	0.00147	0.00104	0.00304	0.01601	0.01429	0.00007	0.00183	0.00664	0.00007	0.02613
2016	$B^0_s\to K^0_S K^+K^-$	DD	1.00e-03	8.69e-04	0.86945	0.01236	0.00007	0.00142	0.00098	0.00338	0.01516	0.01546	0.00008	0.00091	0.00664	0.00007	0.02610
2015	$B^0_s\to K^0_S K^+K^-$	DD	9.03e-04	8.36e-04	0.92516	0.01307	0.00007	0.00159	0.00206	0.00560	0.01592	0.01453	0.00008	0.00019	0.00664	0.00007	0.02679
2012b	$B^0_s\to K^0_S K^+K^-$	DD	5.87e-04	5.19e-04	0.88494	0.01943	0.00006	0.00260	0.00183	0.02476	0.02545	0.01519	0.00009	0.00196	0.00664	0.00006	0.04389
2012a	$B^0_s\to K^0_S K^+K^-$	DD	4.73e-04	4.12e-04	0.86993	0.02338	0.00008	0.00299	0.00182	0.02487	0.02203	0.01545	0.00007	0.00090	0.00664	0.00008	0.04987
2011	$B^0_s\to K^0_S K^+K^-$	DD	5.58e-04	4.92e-04	0.88235	0.02101	0.00007	0.00434	0.00239	0.03991	0.02685	0.01523	0.00002	0.00002	0.00664	0.00007	0.05528
2018	$B^0_s\to K^0_S K^+K^-$	LL	3.21e-04	2.97e-04	0.92432	0.02075	0.00012	0.00117	0.00171	0.00324	0.03276	0.01499	0.00026	0.00504	0.00664	0.00012	0.04258
2017	$B^0_s\to K^0_S K^+K^-$	LL	3.63e-04	3.17e-04	0.87281	0.02072	0.00011	0.00130	0.00269	0.00344	0.02975	0.01587	0.00028	0.00573	0.00664	0.00011	0.04079
2016	$B^0_s\to K^0_S K^+K^-$	LL	3.80e-04	3.56e-04	0.93642	0.02020	0.00011	0.00124	0.00130	0.00396	0.02749	0.01479	0.00026	0.00162	0.00664	0.00011	0.03806
2015	$B^0_s\to K^0_S K^+K^-$	LL	3.62e-04	3.28e-04	0.90538	0.02086	0.00011	0.00128	0.00295	0.00568	0.02935	0.01530	0.00027	0.00409	0.00664	0.00011	0.04043
2012b	$B^0_s\to K^0_S K^+K^-$	LL	1.76e-04	1.53e-04	0.87204	0.03568	0.00011	0.00223	0.00370	0.02380	0.06146	0.01589	0.00036	0.00077	0.00664	0.00011	0.07702
2012a	$B^0_s\to K^0_S K^+K^-$	LL	2.03e-04	1.77e-04	0.87064	0.03580	0.00010	0.00207	0.00264	0.03644	0.05324	0.01591	0.00005	0.00097	0.00664	0.00010	0.07585
2011	$B^0_s\to K^0_S K^+K^-$	LL	2.27e-04	1.88e-04	0.82709	0.03415	0.00010	0.00335	0.00283	0.03275	0.04888	0.01675	0.00006	0.00738	0.00664	0.00010	0.07090

Table C.84: $B^0\to K^0_S\pi^+\pi^-$ over $B^0_s\to K^0_S\pi^+K^-$ efficiency table for the favoured mode optimisation. For each year and K^0_S reconstruction type, the average efficiency of the considered mode, the average efficiency of $B^0\to K^0_S\pi^+\pi^-$, the ratio of average efficiencies, the related relative uncertainties split by sources and the final relative uncertainty are given.

Year	Mode	K^0_S	$\bar{\varepsilon}_{B\to K^0_S hh'}$	$\bar{\varepsilon}_{B^0_s\to K^0_S\pi^+\pi^-}$	$\frac{\bar{\varepsilon}_{B^0_s\to K^0_S\pi^+\pi^-}}{\bar{\varepsilon}_{B\to K^0_S hh'}}$	$\sigma^{\rm stat}_{\frac{\bar{\varepsilon}_{B^0_s\to K^0_S\pi^+\pi^-}}{\bar{\varepsilon}_{B\to K^0_S hh'}}}$	$\sigma^{\rm tracking}_{\frac{\bar{\varepsilon}_{B^0_s\to K^0_S\pi^+\pi^-}}{\bar{\varepsilon}_{B\to K^0_S hh'}}}$	$\sigma^{\rm L0corr}_{\frac{\bar{\varepsilon}_{B^0_s\to K^0_S\pi^+\pi^-}}{\bar{\varepsilon}_{B\to K^0_S hh'}}}$	$\sigma^{\rm PIDMCsampling}_{\frac{\bar{\varepsilon}_{B^0_s\to K^0_S\pi^+\pi^-}}{\bar{\varepsilon}_{B\to K^0_S hh'}}}$	$\sigma^{\rm PIDkernel}_{\frac{\bar{\varepsilon}_{B^0_s\to K^0_S\pi^+\pi^-}}{\bar{\varepsilon}_{B\to K^0_S hh'}}}$	$\sigma^{\rm RMS}_{\frac{\bar{\varepsilon}_{B^0_s\to K^0_S\pi^+\pi^-}}{\bar{\varepsilon}_{B\to K^0_S hh'}}}$	$\sigma^{\rm binning}_{\frac{\bar{\varepsilon}_{B^0_s\to K^0_S\pi^+\pi^-}}{\bar{\varepsilon}_{B\to K^0_S hh'}}}$	$\sigma^{\rm L0Echoice}_{\frac{\bar{\varepsilon}_{B^0_s\to K^0_S\pi^+\pi^-}}{\bar{\varepsilon}_{B\to K^0_S hh'}}}$	$\sigma^{\rm FTrigger}_{\frac{\bar{\varepsilon}_{B^0_s\to K^0_S\pi^+\pi^-}}{\bar{\varepsilon}_{B\to K^0_S hh'}}}$	$\sigma^{\rm MCreweighting}_{\frac{\bar{\varepsilon}_{B^0_s\to K^0_S\pi^+\pi^-}}{\bar{\varepsilon}_{B\to K^0_S hh'}}}$	$\sigma^{\rm K^0_S tracking}_{\frac{\bar{\varepsilon}_{B^0_s\to K^0_S\pi^+\pi^-}}{\bar{\varepsilon}_{B\to K^0_S hh'}}}$	$\sigma^{\rm tot}_{\frac{\bar{\varepsilon}_{B^0_s\to K^0_S\pi^+\pi^-}}{\bar{\varepsilon}_{B\to K^0_S hh'}}}$
2018	$B^0_s\to K^0_S K^+\pi^-$	DD	8.69e-04	8.21e-04	0.94467	0.01202	0.00007	0.00137	0.00123	0.00436	0.01584	0.01366	0.00011	0.00162	0.00664	0.00007	0.02551
2017	$B^0_s\to K^0_S K^+\pi^-$	DD	9.05e-04	8.33e-04	0.92088	0.01230	0.00007	0.00146	0.00124	0.00392	0.01556	0.01401	0.00011	0.00159	0.00664	0.00007	0.02560
2016	$B^0_s\to K^0_S K^+\pi^-$	DD	9.74e-04	8.69e-04	0.89267	0.01202	0.00007	0.00140	0.00078	0.00348	0.01486	0.01445	0.00011	0.00019	0.00664	0.00007	0.02516
2015	$B^0_s\to K^0_S K^+\pi^-$	DD	8.71e-04	8.36e-04	0.95937	0.01273	0.00007	0.00153	0.00169	0.00520	0.01559	0.01345	0.00011	0.00027	0.00664	0.00007	0.02573
2012b	$B^0_s\to K^0_S K^+\pi^-$	DD	5.67e-04	5.19e-04	0.91611	0.01906	0.00006	0.00254	0.00138	0.02975	0.02495	0.01408	0.00009	0.00235	0.00664	0.00006	0.04612
2012a	$B^0_s\to K^0_S K^+\pi^-$	DD	4.38e-04	4.12e-04	0.94043	0.02296	0.00008	0.00294	0.00178	0.04264	0.03158	0.01372	0.00007	0.00112	0.00664	0.00008	0.05990
2011	$B^0_s\to K^0_S K^+\pi^-$	DD	5.07e-04	4.92e-04	0.97107	0.02058	0.00007	0.00423	0.00176	0.03658	0.02652	0.01328	0.00001	0.00076	0.00664	0.00007	0.05203
2018	$B^0_s\to K^0_S K^+\pi^-$	LL	3.17e-04	2.97e-04	0.93615	0.02180	0.00012	0.00118	0.00252	0.00674	0.04369	0.01462	0.00020	0.00403	0.00664	0.00012	0.05207
2017	$B^0_s\to K^0_S K^+\pi^-$	LL	3.60e-04	3.17e-04	0.87939	0.02172	0.00011	0.00129	0.00155	0.00385	0.03907	0.01557	0.00021	0.00557	0.00664	0.00011	0.04832
2016	$B^0_s\to K^0_S K^+\pi^-$	LL	3.98e-04	3.56e-04	0.89500	0.02098	0.00011	0.00123	0.00121	0.00469	0.03521	0.01530	0.00021	0.00153	0.00664	0.00011	0.04455
2015	$B^0_s\to K^0_S K^+\pi^-$	LL	3.69e-04	3.28e-04	0.88698	0.02181	0.00011	0.00134	0.00253	0.00629	0.03805	0.01543	0.00021	0.00164	0.00664	0.00011	0.04750
2012b	$B^0_s\to K^0_S K^+\pi^-$	LL	1.62e-04	1.53e-04	0.94702	0.03700	0.00012	0.00237	0.00473	0.02666	0.08531	0.01446	0.00011	0.00267	0.00664	0.00012	0.09821
2012a	$B^0_s\to K^0_S K^+\pi^-$	LL	1.88e-04	1.77e-04	0.94279	0.03682	0.00010	0.00221	0.00431	0.03806	0.07372	0.01452	0.00008	0.00012	0.00664	0.00010	0.09229
2011	$B^0_s\to K^0_S K^+\pi^-$	LL	2.17e-04	1.88e-04	0.86595	0.03446	0.00010	0.00354	0.00296	0.02895	0.06526	0.01581	0.00016	0.00364	0.00664	0.00010	0.08132

Table C.85: $B^0\to K^0_S\pi^+\pi^-$ over $B^0_s\to K^0_S K^+\pi^-$ efficiency table for the favoured mode optimisation. For each year and K^0_S reconstruction type, the average efficiency of the considered mode, the average efficiency of $B^0\to K^0_S\pi^+\pi^-$, the ratio of average efficiencies, the related relative uncertainties split by sources and the final relative uncertainty are given.

Year	Mode	K^0_S	$\bar{\varepsilon}_{B\to K^0_S hh'}$	$\bar{\varepsilon}_{B^0_s\to K^0_S\pi^+\pi^-}$	$\frac{\bar{\varepsilon}_{B^0_s\to K^0_S\pi^+\pi^-}}{\bar{\varepsilon}_{B\to K^0_S hh'}}$	$\sigma^{\rm stat}_{\frac{\bar{\varepsilon}_{B^0_s\to K^0_S\pi^+\pi^-}}{\bar{\varepsilon}_{B\to K^0_S hh'}}}$	$\sigma^{\rm tracking}_{\frac{\bar{\varepsilon}_{B^0_s\to K^0_S\pi^+\pi^-}}{\bar{\varepsilon}_{B\to K^0_S hh'}}}$	$\sigma^{\rm L0corr}_{\frac{\bar{\varepsilon}_{B^0_s\to K^0_S\pi^+\pi^-}}{\bar{\varepsilon}_{B\to K^0_S hh'}}}$	$\sigma^{\rm PIDMCsampling}_{\frac{\bar{\varepsilon}_{B^0_s\to K^0_S\pi^+\pi^-}}{\bar{\varepsilon}_{B\to K^0_S hh'}}}$	$\sigma^{\rm PIDkernel}_{\frac{\bar{\varepsilon}_{B^0_s\to K^0_S\pi^+\pi^-}}{\bar{\varepsilon}_{B\to K^0_S hh'}}}$	$\sigma^{\rm RMS}_{\frac{\bar{\varepsilon}_{B^0_s\to K^0_S\pi^+\pi^-}}{\bar{\varepsilon}_{B\to K^0_S hh'}}}$	$\sigma^{\rm binning}_{\frac{\bar{\varepsilon}_{B^0_s\to K^0_S\pi^+\pi^-}}{\bar{\varepsilon}_{B\to K^0_S hh'}}}$	$\sigma^{\rm L0Echoice}_{\frac{\bar{\varepsilon}_{B^0_s\to K^0_S\pi^+\pi^-}}{\bar{\varepsilon}_{B\to K^0_S hh'}}}$	$\sigma^{\rm FTrigger}_{\frac{\bar{\varepsilon}_{B^0_s\to K^0_S\pi^+\pi^-}}{\bar{\varepsilon}_{B\to K^0_S hh'}}}$	$\sigma^{\rm MCreweighting}_{\frac{\bar{\varepsilon}_{B^0_s\to K^0_S\pi^+\pi^-}}{\bar{\varepsilon}_{B\to K^0_S hh'}}}$	$\sigma^{\rm K^0_S tracking}_{\frac{\bar{\varepsilon}_{B^0_s\to K^0_S\pi^+\pi^-}}{\bar{\varepsilon}_{B\to K^0_S hh'}}}$	$\sigma^{\rm tot}_{\frac{\bar{\varepsilon}_{B^0_s\to K^0_S\pi^+\pi^-}}{\bar{\varepsilon}_{B\to K^0_S hh'}}}$
2018	$B^0_s\to K^0_S K^+K^-$	DD	8.35e-04	8.21e-04	0.98274	0.01180	0.00007	0.00148	0.00193	0.00531	0.07719	0.03998	0.00052	0.00233	0.00664	0.00007	0.08821
2017	$B^0_s\to K^0_S K^+K^-$	DD	8.80e-04	8.33e-04	0.94724	0.01204	0.00007	0.00203	0.00214	0.00565	0.07341	0.04148	0.00054	0.00194	0.00664	0.00007	0.08569
2016	$B^0_s\to K^0_S K^+K^-$	DD	1.02e-03	8.69e-04	0.84965	0.01140	0.00007	0.00153	0.00195	0.00435	0.06342	0.04624	0.00060	0.00234	0.00664	0.00007	0.07978
2015	$B^0_s\to K^0_S K^+K^-$	DD	9.16e-04	8.36e-04	0.91205	0.01196	0.00008	0.00163	0.00279	0.00643	0.07057	0.04308	0.00056	0.00221	0.00664	0.00008	0.08415
2012b	$B^0_s\to K^0_S K^+K^-$	DD	5.77e-04	5.19e-04	0.89984	0.01781	0.00006	0.00359	0.00258	0.07292	0.11212	0.04366	0.00028	0.00187	0.00664	0.00006	0.14205
2012a	$B^0_s\to K^0_S K^+K^-$	DD	4.78e-04	4.12e-04	0.86038	0.02183	0.00007	0.00378	0.00305	0.06750	0.13556	0.04566	0.00029	0.00113	0.00664	0.00007	0.15989
2011	$B^0_s\to K^0_S K^+K^-$	DD	5.31e-04	4.92e-04	0.92654	0.01950	0.00006	0.00484	0.00484	0.08794	0.12173	0.04240	0.00037	0.00062	0.00664	0.00006	0.15755
2018	$B^0_s\to K^0_S K^+K^-$	LL	3.72e-04	2.97e-04	0.79838	0.05754	0.00040	0.00335	0.01263	0.00692	0.15115	0.16203	0.00172	0.00694	0.00664	0.00040	0.22962
2017	$B^0_s\to K^0_S K^+K^-$	LL	4.06e-04	3.17e-04	0.78103	0.05864	0.00040	0.00531	0.01496	0.00467	0.13856	0.16563	0.00175	0.01085	0.00664	0.00040	0.22474
2016	$B^0_s\to K^0_S K^+K^-$	LL	4.85e-04	3.56e-04	0.73432	0.05197	0.00037	0.00348	0.01091	0.00591	0.11605	0.17616	0.00187	0.00619	0.00664	0.00037	0.21784
2015	$B^0_s\to K^0_S K^+K^-$	LL	4.19e-04	3.28e-04	0.78136	0.05707	0.00035	0.00371	0.00935	0.00651	0.13414	0.16555	0.00175	0.00633	0.00664	0.00035	0.22111
2012b	$B^0_s\to K^0_S K^+K^-$	LL	1.85e-04	1.53e-04	0.82909	0.10625	0.00033	0.01379	0.02209	0.07522	0.30364	0.15602	0.00047	0.00208	0.00664	0.00033	0.36635
2012a	$B^0_s\to K^0_S K^+K^-$	LL	2.01e-04	1.77e-04	0.87783	0.11658	0.00034	0.01253	0.01219	0.06961	0.27846	0.14736	0.00047	0.00182	0.00664	0.00034	0.34358
2011	$B^0_s\to K^0_S K^+K^-$	LL	2.58e-04	1.88e-04	0.72630	0.09329	0.00026	0.01163	0.02303	0.05896	0.21799	0.17811	0.00076	0.00724	0.00664	0.00026	0.30362

Table C.86: $B^0\to K^0_S\pi^+\pi^-$ over $B^0_s\to K^0_S K^+K^-$ efficiency table for the favoured mode optimisation. For each year and K^0_S reconstruction type, the average efficiency of the considered mode, the average efficiency of $B^0\to K^0_S\pi^+\pi^-$, the ratio of average efficiencies, the related relative uncertainties split by sources and the final relative uncertainty are given.

Year	Mode	K^0_S	$\bar{\varepsilon}_{B\to K^0_S hh'}$	$\bar{\varepsilon}_{B^0_s\to K^0_S\pi^+\pi^-}$	$\frac{\bar{\varepsilon}_{B^0_s\to K^0_S\pi^+\pi^-}}{\bar{\varepsilon}_{B\to K^0_S hh'}}$	$\sigma^{\rm stat}_{\frac{\bar{\varepsilon}_{B^0_s\to K^0_S\pi^+\pi^-}}{\bar{\varepsilon}_{B\to K^0_S hh'}}}$	$\sigma^{\rm tracking}_{\frac{\bar{\varepsilon}_{B^0_s\to K^0_S\pi^+\pi^-}}{\bar{\varepsilon}_{B\to K^0_S hh'}}}$	$\sigma^{\rm L0corr}_{\frac{\bar{\varepsilon}_{B^0_s\to K^0_S\pi^+\pi^-}}{\bar{\varepsilon}_{B\to K^0_S hh'}}}$	$\sigma^{\rm PIDMCsampling}_{\frac{\bar{\varepsilon}_{B^0_s\to K^0_S\pi^+\pi^-}}{\bar{\varepsilon}_{B\to K^0_S hh'}}}$	$\sigma^{\rm PIDkernel}_{\frac{\bar{\varepsilon}_{B^0_s\to K^0_S\pi^+\pi^-}}{\bar{\varepsilon}_{B\to K^0_S hh'}}}$	$\sigma^{\rm RMS}_{\frac{\bar{\varepsilon}_{B^0_s\to K^0_S\pi^+\pi^-}}{\bar{\varepsilon}_{B\to K^0_S hh'}}}$	$\sigma^{\rm binning}_{\frac{\bar{\varepsilon}_{B^0_s\to K^0_S\pi^+\pi^-}}{\bar{\varepsilon}_{B\to K^0_S hh'}}}$	$\sigma^{\rm L0Echoice}_{\frac{\bar{\varepsilon}_{B^0_s\to K^0_S\pi^+\pi^-}}{\bar{\varepsilon}_{B\to K^0_S hh'}}}$	$\sigma^{\rm FTrigger}_{\frac{\bar{\varepsilon}_{B^0_s\to K^0_S\pi^+\pi^-}}{\bar{\varepsilon}_{B\to K^0_S hh'}}}$	$\sigma^{\rm MCreweighting}_{\frac{\bar{\varepsilon}_{B^0_s\to K^0_S\pi^+\pi^-}}{\bar{\varepsilon}_{B\to K^0_S hh'}}}$	$\sigma^{\rm K^0_S tracking}_{\frac{\bar{\varepsilon}_{B^0_s\to K^0_S\pi^+\pi^-}}{\bar{\varepsilon}_{B\to K^0_S hh'}}}$	$\sigma^{\rm tot}_{\frac{\bar{\varepsilon}_{B^0_s\to K^0_S\pi^+\pi^-}}{\bar{\varepsilon}_{B\to K^0_S hh'}}}$
2018	$B^0_s\to K^0_S\pi^+K^-$	DD	6.67e-04	4.13e-04	0.61956	0.01622	0.00009	0.00163	0.00182	0.00517	0.02292	0.01513	0.00004	0.00017	0.00664	0.00009	0.03308
2017	$B^0_s\to K^0_S\pi^+K^-$	DD	6.98e-04	4.42e-04	0.63410	0.01632	0.00008	0.00161	0.00185	0.00439	0.02170	0.01478	0.00004	0.00484	0.00664	0.00008	0.03238
2016	$B^0_s\to K^0_S\pi^+K^-$	DD	7.89e-04	4.39e-04	0.55626	0.01575	0.00008	0.00154	0.00133	0.00399	0.02038	0.01685	0.00004	0.00197	0.00664	0.00008	0.03186
2015	$B^0_s\to K^0_S\pi^+K^-$	DD	6.91e-04	3.47e-04	0.50160	0.01740	0.00008	0.00169	0.00230	0.00803	0.02456	0.01869	0.00005	0.00063	0.00664	0.00008	0.03704
2012b	$B^0_s\to K^0_S\pi^+K^-$	DD	5.16e-04	3.44e-04	0.66619	0.02377	0.00007	0.00265	0.00239	0.06932	0.02873	0.01407	0.00009	0.00993	0.00664	0.00007	0.08093
2012a	$B^0_s\to K^0_S\pi^+K^-$	DD	4.18e-04	2.33e-04	0.55708	0.02976	0.00008	0.00344	0.00302	0.08170	0.03839	0.01683	0.00003	0.00181	0.00664	0.00008	0.09688
2011	$B^0_s\to K^0_S\pi^+K^-$	DD	5.02e-04	2.38e-04	0.47487	0.02649	0.00007	0.00459	0.00348	0.07588	0.03484	0.01974	0.00010	0.00065	0.00664	0.00007	0.09023
2018	$B^0_s\to K^0_S\pi^+K^-$	LL	2.76e-04	1.91e-04	0.69207	0.02699	0.00014	0.00130	0.00309	0.00561	0.03852	0.03256	0.00033	0.00392	0.00664	0.00014	0.05809
2017	$B^0_s\to K^0_S\pi^+K^-$	LL	3.02e-04	2.15e-04	0.71227	0.02706	0.00013	0.00142	0.00335	0.00385	0.03479	0.03163	0.00032	0.00310	0.00664	0.00013	0.05500
2016	$B^0_s\to K^0_S\pi^+K^-$	LL	3.12e-04	2.21e-04	0.70981	0.02651	0.00012	0.00137	0.00202	0.00442	0.03376	0.03174	0.00032	0.00205	0.00664	0.00012	0.05407
2015	$B^0_s\to K^0_S\pi^+K^-$	LL	2.44e-04	1.99e-04	0.81645	0.02951	0.00013	0.00136	0.00426	0.00779	0.04130	0.02760	0.00028	0.00358	0.00664	0.00013	0.05896
2012b	$B^0_s\to K^0_S\pi^+K^-$	LL	9.42e-05	1.08e-04	1.15136	0.05417	0.00013	0.00258	0.00864	0.08177	0.09917	0.01957	0.00048	0.00065	0.00664	0.00013	0.14130
2012a	$B^0_s\to K^0_S\pi^+K^-$	LL	1.55e-04	7.78e-05	0.50040	0.05184	0.00012	0.00293	0.00701	0.07369	0.07861	0.04503	0.00023	0.00043	0.00664	0.00012	0.12817
2011	$B^0_s\to K^0_S\pi^+K^-$	LL	1.94e-04	1.33e-04	0.68621	0.04273	0.00011	0.00350	0.00513	0.05937	0.05500	0.03284	0.00030	0.01099	0.00664	0.00011	0.09828

Table C.87: $B^0\to K^0_S\pi^+\pi^-$ over $B^0\to K^0_S\pi^+K^-$ efficiency table for the unfavoured mode optimisation. For each year and K^0_S reconstruction type, the average efficiency of the considered mode, the average efficiency of $B^0\to K^0_S\pi^+\pi^-$, the ratio of average efficiencies, the related relative uncertainties split by sources and the final relative uncertainty are given.

Year	Mode	K^0_S	$\bar{\varepsilon}_{B\to K^0_S hh'}$	$\bar{\varepsilon}_{B^0_s\to K^0_S\pi^+\pi^-}$	$\frac{\bar{\varepsilon}_{B^0_s\to K^0_S\pi^+\pi^-}}{\bar{\varepsilon}_{B\to K^0_S hh'}}$	$\sigma^{\rm stat}_{\frac{\bar{\varepsilon}_{B^0_s\to K^0_S\pi^+\pi^-}}{\bar{\varepsilon}_{B\to K^0_S hh'}}}$	$\sigma^{\rm tracking}_{\frac{\bar{\varepsilon}_{B^0_s\to K^0_S\pi^+\pi^-}}{\bar{\varepsilon}_{B\to K^0_S hh'}}}$	$\sigma^{\rm L0corr}_{\frac{\bar{\varepsilon}_{B^0_s\to K^0_S\pi^+\pi^-}}{\bar{\varepsilon}_{B\to K^0_S hh'}}}$	$\sigma^{\rm PIDMCsampling}_{\frac{\bar{\varepsilon}_{B^0_s\to K^0_S\pi^+\pi^-}}{\bar{\varepsilon}_{B\to K^0_S hh'}}}$	$\sigma^{\rm PIDkernel}_{\frac{\bar{\varepsilon}_{B^0_s\to K^0_S\pi^+\pi^-}}{\bar{\varepsilon}_{B\to K^0_S hh'}}}$	$\sigma^{\rm RMS}_{\frac{\bar{\varepsilon}_{B^0_s\to K^0_S\pi^+\pi^-}}{\bar{\varepsilon}_{B\to K^0_S hh'}}}$	$\sigma^{\rm binning}_{\frac{\bar{\varepsilon}_{B^0_s\to K^0_S\pi^+\pi^-}}{\bar{\varepsilon}_{B\to K^0_S hh'}}}$	$\sigma^{\rm L0Echoice}_{\frac{\bar{\varepsilon}_{B^0_s\to K^0_S\pi^+\pi^-}}{\bar{\varepsilon}_{B\to K^0_S hh'}}}$	$\sigma^{\rm FTrigger}_{\frac{\bar{\varepsilon}_{B^0_s\to K^0_S\pi^+\pi^-}}{\bar{\varepsilon}_{B\to K^0_S hh'}}}$	$\sigma^{\rm MCreweighting}_{\frac{\bar{\varepsilon}_{B^0_s\to K^0_S\pi^+\pi^-}}{\bar{\varepsilon}_{B\to K^0_S hh'}}}$	$\sigma^{\rm K^0_S tracking}_{\frac{\bar{\varepsilon}_{B^0_s\to K^0_S\pi^+\pi^-}}{\bar{\varepsilon}_{B\to K^0_S hh'}}}$	$\sigma^{\rm tot}_{\frac{\bar{\varepsilon}_{B^0_s\to K^0_S\pi^+\pi^-}}{\bar{\varepsilon}_{B\to K^0_S hh'}}}$
2018	$B^0_s\to K^0_S K^+\pi^-$	DD	6.84e-04	4.13e-04	0.60439	0.01711	0.00009	0.00163	0.00154	0.00503	0.02253	0.01587	0.00003	0.00218	0.00664	0.00009	0.03364
2017	$B^0_s\to K^0_S K^+\pi^-$	DD	7.84e-04	4.42e-04	0.56410	0.01698	0.00008	0.00170	0.00149	0.00451	0.02030	0.01701	0.00003	0.00239	0.00664	0.00008	0.03264
2016	$B^0_s\to K^0_S K^+\pi^-$	DD	7.56e-04	4.39e-04	0.58019	0.01706	0.00008	0.00169	0.00130	0.00390	0.02076	0.01654	0.00003	0.00204	0.00664	0.00008	0.03261
2015	$B^0_s\to K^0_S K^+\pi^-$	DD	6.60e-04	3.47e-04	0.52481	0.01895	0.00009	0.00193	0.00378	0.00914	0.02501	0.01828	0.00003	0.00078	0.00664	0.00009	0.03828
2012b	$B^0_s\to K^0_S K^+\pi^-$	DD	4.85e-04	3.44e-04	0.70879	0.02643	0.00007	0.00323	0.00560	0.08230	0.02973	0.01354	0.00012	0.00146	0.00664	0.00007	0.09288
2012a	$B^0_s\to K^0_S K^+\pi^-$	DD	4.02e-04	2.33e-04	0.57976	0.03263	0.00009	0.00317	0.00401	0.08624	0.03907	0.01655	0.00012	0.00575	0.00664	0.00009	0.10201
2011	$B^0_s\to K^0_S K^+\pi^-$	DD	5.34e-04	2.38e-04	0.44649	0.02819	0.00007	0.00500	0.00328	0.07803	0.03388	0.02149	0.00014	0.00193	0.00664	0.00007	0.09261
2018	$B^0_s\to K^0_S K^+\pi^-$	LL	2.67e-04	1.91e-04	0.71382	0.02939	0.00015	0.00137	0.00300	0.00535	0.04317	0.04420	0.00019	0.01012	0.00664	0.00015	0.06977
2017	$B^0_s\to K^0_S K^+\pi^-$	LL	2.88e-04	2.15e-04	0.74661	0.02983	0.00014	0.00154	0.00815	0.00606	0.03953	0.04226	0.00018	0.00407	0.00664	0.00014	0.06637
2016	$B^0_s\to K^0_S K^+\pi^-$	LL	3.14e-04	2.21e-04	0.70569	0.02861	0.00014	0.00151	0.01911	0.00518	0.03692	0.04471	0.00019	0.00154	0.00664	0.00014	0.06798
2015	$B^0_s\to K^0_S K^+\pi^-$	LL	2.73e-04	1.99e-04	0.73057	0.03095	0.00014	0.00161	0.00550	0.01218	0.04206	0.04319	0.00019	0.00185	0.00664	0.00014	0.06943
2012b	$B^0_s\to K^0_S K^+\pi^-$	LL	8.99e-05	1.08e-04	1.20683	0.06203	0.00015	0.00258	0.01423	0.07638	0.11604	0.02614	0.00046	0.00006	0.00664	0.00015	0.15519
2012a	$B^0_s\to K^0_S K^+\pi^-$	LL	1.49e-04	7.78e-05	0.52129	0.05897	0.00014	0.00279	0.00765	0.05218	0.08637	0.06052	0.00003	0.00058	0.00664	0.00014	0.13204
2011	$B^0_s\to K^0_S K^+\pi^-$	LL	1.74e-04	1.33e-04	0.76565	0.04971	0.00013	0.00420	0.00544	0.06062	0.06524	0.04121	0.00022	0.00078	0.00664	0.00013	0.11042

Table C.88: $B^0\to K^0_S\pi^+\pi^-$ over $B^0\to K^0_S K^+\pi^-$ efficiency table for the unfavoured mode optimisation. For each year and K^0_S reconstruction type, the average efficiency of the considered mode, the average efficiency of $B^0\to K^0_S\pi^+\pi^-$, the ratio of average efficiencies, the related relative uncertainties split by sources and the final relative uncertainty are given.

Year	Mode	K^0_S	$\bar{\varepsilon}_{B\to K^0_S hh'}$	$\bar{\varepsilon}_{B^0_d\to K^0_S\pi^+\pi^-}$	$\frac{\bar{\varepsilon}_{B^0_d\to K^0_S\pi^+\pi^-}}{\bar{\varepsilon}_{B\to K^0_S hh'}}$	$\sigma^{\text{stat}}_{\frac{\bar{\varepsilon}_{B^0_d\to K^0_S\pi^+\pi^-}}{\bar{\varepsilon}_{B\to K^0_S hh'}}}$	$\sigma^{\text{tracking}}_{\frac{\bar{\varepsilon}_{B^0_d\to K^0_S\pi^+\pi^-}}{\bar{\varepsilon}_{B\to K^0_S hh'}}}$	$\sigma^{\text{L0corr}}_{\frac{\bar{\varepsilon}_{B^0_d\to K^0_S\pi^+\pi^-}}{\bar{\varepsilon}_{B\to K^0_S hh'}}}$	$\sigma^{\text{PIDMCsampling}}_{\frac{\bar{\varepsilon}_{B^0_d\to K^0_S\pi^+\pi^-}}{\bar{\varepsilon}_{B\to K^0_S hh'}}}$	$\sigma^{\text{PIDkernel}}_{\frac{\bar{\varepsilon}_{B^0_d\to K^0_S\pi^+\pi^-}}{\bar{\varepsilon}_{B\to K^0_S hh'}}}$	$\sigma^{\text{RMS}}_{\frac{\bar{\varepsilon}_{B^0_d\to K^0_S\pi^+\pi^-}}{\bar{\varepsilon}_{B\to K^0_S hh'}}}$	$\sigma^{\text{binning}}_{\frac{\bar{\varepsilon}_{B^0_d\to K^0_S\pi^+\pi^-}}{\bar{\varepsilon}_{B\to K^0_S hh'}}}$	$\sigma^{\text{L0E0choice}}_{\frac{\bar{\varepsilon}_{B^0_d\to K^0_S\pi^+\pi^-}}{\bar{\varepsilon}_{B\to K^0_S hh'}}}$	$\sigma^{\text{FTrigger}}_{\frac{\bar{\varepsilon}_{B^0_d\to K^0_S\pi^+\pi^-}}{\bar{\varepsilon}_{B\to K^0_S hh'}}}$	$\sigma^{\text{MCreweighting}}_{\frac{\bar{\varepsilon}_{B^0_d\to K^0_S\pi^+\pi^-}}{\bar{\varepsilon}_{B\to K^0_S hh'}}}$	$\sigma^{\text{K}^0_S\text{tracking}}_{\frac{\bar{\varepsilon}_{B^0_d\to K^0_S\pi^+\pi^-}}{\bar{\varepsilon}_{B\to K^0_S hh'}}}$	$\sigma^{\text{tot}}_{\frac{\bar{\varepsilon}_{B^0_d\to K^0_S\pi^+\pi^-}}{\bar{\varepsilon}_{B\to K^0_S hh'}}}$
2018	$B^0_d\to K^0_S K^+K^-$	DD	4.85e-04	4.13e-04	0.85220	0.01311	0.00006	0.00135	0.00112	0.00391	0.01577	0.04046	0.00058	0.00344	0.00664	0.00006	0.04617
2017	$B^0_d\to K^0_S K^+K^-$	DD	3.74e-04	4.42e-04	1.18184	0.01432	0.00006	0.00189	0.00089	0.00323	0.01521	0.02917	0.00042	0.00181	0.00664	0.00006	0.03674
2016	$B^0_d\to K^0_S K^+K^-$	DD	4.79e-04	4.39e-04	0.91561	0.01342	0.00006	0.00137	0.00082	0.00390	0.01493	0.03765	0.00054	0.00216	0.00664	0.00006	0.04345
2015	$B^0_d\to K^0_S K^+K^-$	DD	4.00e-04	3.47e-04	0.86606	0.01497	0.00006	0.00151	0.00131	0.00444	0.01883	0.03981	0.00057	0.00209	0.00664	0.00006	0.04729
2012b	$B^0_d\to K^0_S K^+K^-$	DD	3.34e-04	3.44e-04	1.02842	0.01956	0.00005	0.00379	0.00742	0.02659	0.01926	0.03352	0.00016	0.00141	0.00664	0.00005	0.05196
2012a	$B^0_d\to K^0_S K^+K^-$	DD	2.11e-04	2.33e-04	1.10696	0.02614	0.00006	0.00406	0.00171	0.02423	0.02863	0.03114	0.00021	0.00047	0.00664	0.00006	0.05589
2011	$B^0_d\to K^0_S K^+K^-$	DD	2.75e-04	2.38e-04	0.86657	0.02274	0.00006	0.00429	0.00129	0.01588	0.02737	0.03979	0.00015	0.00076	0.00664	0.00006	0.05627
2018	$B^0_d\to K^0_S K^+K^-$	LL	2.18e-04	1.91e-04	0.87384	0.01957	0.00010	0.00105	0.00159	0.00300	0.02393	0.03186	0.00081	0.01801	0.00664	0.00010	0.04850
2017	$B^0_d\to K^0_S K^+K^-$	LL	1.84e-04	2.15e-04	1.17202	0.02081	0.00009	0.00145	0.00133	0.00367	0.02188	0.02376	0.00060	0.01052	0.00664	0.00009	0.04061
2016	$B^0_d\to K^0_S K^+K^-$	LL	2.00e-04	2.21e-04	1.10855	0.02025	0.00009	0.00112	0.00107	0.00379	0.02113	0.02512	0.00064	0.00394	0.00664	0.00009	0.03955
2015	$B^0_d\to K^0_S K^+K^-$	LL	2.80e-04	1.99e-04	0.71106	0.01954	0.00009	0.00115	0.00238	0.00717	0.02261	0.03916	0.00099	0.01058	0.00664	0.00009	0.05140
2012b	$B^0_d\to K^0_S K^+K^-$	LL	1.24e-04	1.08e-04	0.87469	0.03350	0.00009	0.00351	0.00263	0.01835	0.04212	0.03183	0.00045	0.00079	0.00664	0.00009	0.06565
2012a	$B^0_d\to K^0_S K^+K^-$	LL	1.41e-04	7.78e-05	0.55044	0.03920	0.00009	0.00266	0.00337	0.02365	0.05726	0.05059	0.00028	0.00691	0.00664	0.00009	0.08969
2011	$B^0_d\to K^0_S K^+K^-$	LL	1.38e-04	1.33e-04	0.96424	0.03235	0.00008	0.00322	0.00268	0.01861	0.03466	0.02888	0.00034	0.00173	0.00664	0.00008	0.05910

Table C.89: $B^0\to K^0_S\pi^+\pi^-$ over $B^0\to K^0_S K^+K^-$ efficiency table for the unfavoured mode optimisation. For each year and K^0_S reconstruction type, the average efficiency of the considered mode, the average efficiency of $B^0\to K^0_S\pi^+\pi^-$, the ratio of average efficiencies, the related relative uncertainties split by sources and the final relative uncertainty are given.

Year	Mode	K^0_S	$\bar{\varepsilon}_{B\to K^0_S hh'}$	$\bar{\varepsilon}_{B^0_s\to K^0_S\pi^+\pi^-}$	$\frac{\bar{\varepsilon}_{B^0_s\to K^0_S\pi^+\pi^-}}{\bar{\varepsilon}_{B\to K^0_S hh'}}$	$\sigma^{\text{stat}}_{\frac{\bar{\varepsilon}_{B^0_s\to K^0_S\pi^+\pi^-}}{\bar{\varepsilon}_{B\to K^0_S hh'}}}$	$\sigma^{\text{tracking}}_{\frac{\bar{\varepsilon}_{B^0_s\to K^0_S\pi^+\pi^-}}{\bar{\varepsilon}_{B\to K^0_S hh'}}}$	$\sigma^{\text{L0corr}}_{\frac{\bar{\varepsilon}_{B^0_s\to K^0_S\pi^+\pi^-}}{\bar{\varepsilon}_{B\to K^0_S hh'}}}$	$\sigma^{\text{PIDMCsampling}}_{\frac{\bar{\varepsilon}_{B^0_s\to K^0_S\pi^+\pi^-}}{\bar{\varepsilon}_{B\to K^0_S hh'}}}$	$\sigma^{\text{PIDkernel}}_{\frac{\bar{\varepsilon}_{B^0_s\to K^0_S\pi^+\pi^-}}{\bar{\varepsilon}_{B\to K^0_S hh'}}}$	$\sigma^{\text{RMS}}_{\frac{\bar{\varepsilon}_{B^0_s\to K^0_S\pi^+\pi^-}}{\bar{\varepsilon}_{B\to K^0_S hh'}}}$	$\sigma^{\text{binning}}_{\frac{\bar{\varepsilon}_{B^0_s\to K^0_S\pi^+\pi^-}}{\bar{\varepsilon}_{B\to K^0_S hh'}}}$	$\sigma^{\text{L0E0choice}}_{\frac{\bar{\varepsilon}_{B^0_s\to K^0_S\pi^+\pi^-}}{\bar{\varepsilon}_{B\to K^0_S hh'}}}$	$\sigma^{\text{FTrigger}}_{\frac{\bar{\varepsilon}_{B^0_s\to K^0_S\pi^+\pi^-}}{\bar{\varepsilon}_{B\to K^0_S hh'}}}$	$\sigma^{\text{MCreweighting}}_{\frac{\bar{\varepsilon}_{B^0_s\to K^0_S\pi^+\pi^-}}{\bar{\varepsilon}_{B\to K^0_S hh'}}}$	$\sigma^{\text{K}^0_S\text{tracking}}_{\frac{\bar{\varepsilon}_{B^0_s\to K^0_S\pi^+\pi^-}}{\bar{\varepsilon}_{B\to K^0_S hh'}}}$	$\sigma^{\text{tot}}_{\frac{\bar{\varepsilon}_{B^0_s\to K^0_S\pi^+\pi^-}}{\bar{\varepsilon}_{B\to K^0_S hh'}}}$
2018	$B^0_s\to K^0_S\pi^+\pi^-$	DD	4.46e-04	4.13e-04	0.925720	0.015448	N/A	N/A	N/A	N/A	0.047857	0.017444	0.000082	0.000723	0.00664	N/A	0.053646
2017	$B^0_s\to K^0_S\pi^+\pi^-$	DD	4.76e-04	4.42e-04	0.929228	0.015464	N/A	N/A	N/A	N/A	0.044873	0.017379	0.000082	0.002370	0.00664	N/A	0.051034
2016	$B^0_s\to K^0_S\pi^+\pi^-$	DD	4.59e-04	4.39e-04	0.955789	0.015820	N/A	N/A	N/A	N/A	0.046388	0.016896	0.000080	0.000194	0.00664	N/A	0.052266
2015	$B^0_s\to K^0_S\pi^+\pi^-$	DD	3.87e-04	3.47e-04	0.894633	0.017329	N/A	N/A	N/A	N/A	0.055354	0.018051	0.000085	0.000481	0.00664	N/A	0.061111
2012b	$B^0_s\to K^0_S\pi^+\pi^-$	DD	3.67e-04	3.44e-04	0.936666	0.021763	N/A	N/A	N/A	N/A	0.058153	0.017241	0.000069	0.000142	0.00664	N/A	0.064782
2012a	$B^0_s\to K^0_S\pi^+\pi^-$	DD	2.67e-04	2.33e-04	0.874118	0.027172	N/A	N/A	N/A	N/A	0.080609	0.018474	0.000041	0.001173	0.00664	N/A	0.087309
2011	$B^0_s\to K^0_S\pi^+\pi^-$	DD	2.70e-04	2.38e-04	0.882287	0.025377	N/A	N/A	N/A	N/A	0.079459	0.018303	0.000020	0.001018	0.00664	N/A	0.085661
2018	$B^0_s\to K^0_S\pi^+\pi^-$	LL	2.15e-04	1.91e-04	0.886392	0.026592	N/A	N/A	N/A	N/A	0.034987	0.034806	0.000209	0.002047	0.00664	N/A	0.056489
2017	$B^0_s\to K^0_S\pi^+\pi^-$	LL	2.49e-04	2.15e-04	0.865431	0.025341	N/A	N/A	N/A	N/A	0.030594	0.035649	0.000214	0.003860	0.00664	N/A	0.053926
2016	$B^0_s\to K^0_S\pi^+\pi^-$	LL	2.54e-04	2.21e-04	0.872506	0.025761	N/A	N/A	N/A	N/A	0.029894	0.035360	0.000212	0.000955	0.00664	N/A	0.053411
2015	$B^0_s\to K^0_S\pi^+\pi^-$	LL	2.21e-04	1.99e-04	0.901892	0.027369	N/A	N/A	N/A	N/A	0.033852	0.034208	0.000205	0.001443	0.00664	N/A	0.055780
2012b	$B^0_s\to K^0_S\pi^+\pi^-$	LL	1.25e-04	1.08e-04	0.870408	0.043063	N/A	N/A	N/A	N/A	0.060934	0.035445	0.000002	0.002384	0.00664	N/A	0.082907
2012a	$B^0_s\to K^0_S\pi^+\pi^-$	LL	8.66e-05	7.78e-05	0.898522	0.054742	N/A	N/A	N/A	N/A	0.086494	0.034336	0.000199	0.000853	0.00664	N/A	0.108174
2011	$B^0_s\to K^0_S\pi^+\pi^-$	LL	1.52e-04	1.33e-04	0.874139	0.039830	N/A	N/A	N/A	N/A	0.049835	0.035294	0.000116	0.001264	0.00664	N/A	0.073221

Table C.90: $B^0\to K^0_S\pi^+\pi^-$ over $B^0_s\to K^0_S\pi^+\pi^-$ efficiency table for the unfavoured mode optimisation. For each year and K^0_S reconstruction type, the average efficiency of the considered mode, the average efficiency of $B^0\to K^0_S\pi^+\pi^-$, the ratio of average efficiencies, the related relative uncertainties split by sources and the final relative uncertainty are given. An uncertainty at N/A means maximally correlated (same final state) uncertainty which are cancelled in the ratio.

Year	Mode	K^0_S	$\bar{\varepsilon}_{B\to K^0_S hh'}$	$\bar{\varepsilon}_{B^0_d\to K^0_S\pi^+\pi^-}$	$\frac{\bar{\varepsilon}_{B^0_d\to K^0_S\pi^+\pi^-}}{\bar{\varepsilon}_{B\to K^0_S hh'}}$	$\sigma^{\text{stat}}_{\frac{\bar{\varepsilon}_{B^0_d\to K^0_S\pi^+\pi^-}}{\bar{\varepsilon}_{B\to K^0_S hh'}}}$	$\sigma^{\text{tracking}}_{\frac{\bar{\varepsilon}_{B^0_d\to K^0_S\pi^+\pi^-}}{\bar{\varepsilon}_{B\to K^0_S hh'}}}$	$\sigma^{\text{L0corr}}_{\frac{\bar{\varepsilon}_{B^0_d\to K^0_S\pi^+\pi^-}}{\bar{\varepsilon}_{B\to K^0_S hh'}}}$	$\sigma^{\text{PIDMCsampling}}_{\frac{\bar{\varepsilon}_{B^0_d\to K^0_S\pi^+\pi^-}}{\bar{\varepsilon}_{B\to K^0_S hh'}}}$	$\sigma^{\text{PIDkernel}}_{\frac{\bar{\varepsilon}_{B^0_d\to K^0_S\pi^+\pi^-}}{\bar{\varepsilon}_{B\to K^0_S hh'}}}$	$\sigma^{\text{RMS}}_{\frac{\bar{\varepsilon}_{B^0_d\to K^0_S\pi^+\pi^-}}{\bar{\varepsilon}_{B\to K^0_S hh'}}}$	$\sigma^{\text{binning}}_{\frac{\bar{\varepsilon}_{B^0_d\to K^0_S\pi^+\pi^-}}{\bar{\varepsilon}_{B\to K^0_S hh'}}}$	$\sigma^{\text{L0E0choice}}_{\frac{\bar{\varepsilon}_{B^0_d\to K^0_S\pi^+\pi^-}}{\bar{\varepsilon}_{B\to K^0_S hh'}}}$	$\sigma^{\text{FTrigger}}_{\frac{\bar{\varepsilon}_{B^0_d\to K^0_S\pi^+\pi^-}}{\bar{\varepsilon}_{B\to K^0_S hh'}}}$	$\sigma^{\text{MCreweighting}}_{\frac{\bar{\varepsilon}_{B^0_d\to K^0_S\pi^+\pi^-}}{\bar{\varepsilon}_{B\to K^0_S hh'}}}$	$\sigma^{\text{K}^0_S\text{tracking}}_{\frac{\bar{\varepsilon}_{B^0_d\to K^0_S\pi^+\pi^-}}{\bar{\varepsilon}_{B\to K^0_S hh'}}}$	$\sigma^{\text{tot}}_{\frac{\bar{\varepsilon}_{B^0_d\to K^0_S\pi^+\pi^-}}{\bar{\varepsilon}_{B\to K^0_S hh'}}}$
2018	$B^0_d\to K^0_S K^+K^-$	DD	6.47e-04	4.13e-04	0.63848	0.01498	0.00008	0.00144	0.00145	0.00503	0.01716	0.01623	0.00007	0.00080	0.00664	0.00008	0.02927
2017	$B^0_d\to K^0_S K^+K^-$	DD	6.77e-04	4.42e-04	0.65370	0.01506	0.00007	0.00152	0.00104	0.00304	0.01612	0.01585	0.00007	0.00083	0.00664	0.00007	0.02820
2016	$B^0_d\to K^0_S K^+K^-$	DD	7.69e-04	4.39e-04	0.57074	0.01473	0.00007	0.00143	0.00097	0.00338	0.01581	0.01815	0.00008	0.00040	0.00664	0.00007	0.02925
2015	$B^0_d\to K^0_S K^+K^-$	DD	6.70e-04	3.47e-04	0.51704	0.01617	0.00007	0.00160	0.00219	0.00560	0.01970	0.02004	0.00009	0.00037	0.00664	0.00007	0.03368
2012b	$B^0_d\to K^0_S K^+K^-$	DD	4.59e-04	3.44e-04	0.74900	0.02210	0.00006	0.00253	0.00179	0.02476	0.02145	0.01383	0.00009	0.00414	0.00664	0.00006	0.04271
2012a	$B^0_d\to K^0_S K^+K^-$	DD	3.89e-04	2.33e-04	0.59960	0.02716	0.00008	0.00288	0.00189	0.02487	0.03004	0.01728	0.00008	0.00198	0.00664	0.00008	0.05115
2011	$B^0_d\to K^0_S K^+K^-$	DD	4.57e-04	2.38e-04	0.52221	0.02522	0.00007	0.00439	0.00243	0.03991	0.02867	0.01984	0.00004	0.00013	0.00664	0.00007	0.05928
2018	$B^0_d\to K^0_S K^+K^-$	LL	2.71e-04	1.91e-04	0.70359	0.02339	0.00012	0.00117	0.00175	0.00324	0.03157	0.02996	0.00030	0.00588	0.00664	0.00012	0.05035
2017	$B^0_d\to K^0_S K^+K^-$	LL	2.99e-04	2.15e-04	0.72101	0.02321	0.00011	0.00130	0.00262	0.00344	0.02831	0.02923	0.00030	0.00446	0.00664	0.00011	0.04774
2016	$B^0_d\to K^0_S K^+K^-$	LL	3.16e-04	2.21e-04	0.70105	0.02278	0.00011	0.00123	0.00129	0.00396	0.02717	0.03007	0.00030	0.00183	0.00664	0.00011	0.04720
2015	$B^0_d\to K^0_S K^+K^-$	LL	2.47e-04	1.99e-04	0.80532	0.02506	0.00011	0.00127	0.00301	0.00568	0.03238	0.02617	0.00026	0.00277	0.00664	0.00011	0.04956
2012b	$B^0_d\to K^0_S K^+K^-$	LL	9.09e-05	1.08e-04	1.19364	0.04734	0.00012	0.00221	0.00382	0.02380	0.07629	0.01766	0.00038	0.00199	0.00664	0.00012	0.09490
2012a	$B^0_d\to K^0_S K^+K^-$	LL	1.51e-04	7.78e-05	0.51367	0.04556	0.00010	0.00232	0.00268	0.03644	0.06838	0.04103	0.00005	0.00028	0.00664	0.00010	0.09910
2011	$B^0_d\to K^0_S K^+K^-$	LL	1.86e-04	1.33e-04	0.71655	0.03839	0.00010	0.00322	0.00271	0.03275	0.04572	0.02942	0.00004	0.00920	0.00664	0.00010	0.07516

Table C.91: $B^0\to K^0_S\pi^+\pi^-$ over $B^0_s\to K^0_S\pi^+K^-$ efficiency table for the unfavoured mode optimisation. For each year and K^0_S reconstruction type, the average efficiency of the considered mode, the average efficiency of $B^0\to K^0_S\pi^+\pi^-$, the ratio of average efficiencies, the related relative uncertainties split by sources and the final relative uncertainty are given.

Year	Mode	K^0_S	$\bar{\varepsilon}_{B\to K^0_S hh'}$	$\bar{\varepsilon}_{B^0_d\to K^0_S\pi^+\pi^-}$	$\frac{\bar{\varepsilon}_{B^0_d\to K^0_S\pi^+\pi^-}}{\bar{\varepsilon}_{B\to K^0_S hh'}}$	$\sigma^{\text{stat}}_{\frac{\bar{\varepsilon}_{B^0_d\to K^0_S\pi^+\pi^-}}{\bar{\varepsilon}_{B\to K^0_S hh'}}}$	$\sigma^{\text{tracking}}_{\frac{\bar{\varepsilon}_{B^0_d\to K^0_S\pi^+\pi^-}}{\bar{\varepsilon}_{B\to K^0_S hh'}}}$	$\sigma^{\text{L0corr}}_{\frac{\bar{\varepsilon}_{B^0_d\to K^0_S\pi^+\pi^-}}{\bar{\varepsilon}_{B\to K^0_S hh'}}}$	$\sigma^{\text{PIDMCsampling}}_{\frac{\bar{\varepsilon}_{B^0_d\to K^0_S\pi^+\pi^-}}{\bar{\varepsilon}_{B\to K^0_S hh'}}}$	$\sigma^{\text{PIDkernel}}_{\frac{\bar{\varepsilon}_{B^0_d\to K^0_S\pi^+\pi^-}}{\bar{\varepsilon}_{B\to K^0_S hh'}}}$	$\sigma^{\text{RMS}}_{\frac{\bar{\varepsilon}_{B^0_d\to K^0_S\pi^+\pi^-}}{\bar{\varepsilon}_{B\to K^0_S hh'}}}$	$\sigma^{\text{binning}}_{\frac{\bar{\varepsilon}_{B^0_d\to K^0_S\pi^+\pi^-}}{\bar{\varepsilon}_{B\to K^0_S hh'}}}$	$\sigma^{\text{L0E0choice}}_{\frac{\bar{\varepsilon}_{B^0_d\to K^0_S\pi^+\pi^-}}{\bar{\varepsilon}_{B\to K^0_S hh'}}}$	$\sigma^{\text{FTrigger}}_{\frac{\bar{\varepsilon}_{B^0_d\to K^0_S\pi^+\pi^-}}{\bar{\varepsilon}_{B\to K^0_S hh'}}}$	$\sigma^{\text{MCreweighting}}_{\frac{\bar{\varepsilon}_{B^0_d\to K^0_S\pi^+\pi^-}}{\bar{\varepsilon}_{B\to K^0_S hh'}}}$	$\sigma^{\text{K}^0_S\text{tracking}}_{\frac{\bar{\varepsilon}_{B^0_d\to K^0_S\pi^+\pi^-}}{\bar{\varepsilon}_{B\to K^0_S hh'}}}$	$\sigma^{\text{tot}}_{\frac{\bar{\varepsilon}_{B^0_d\to K^0_S\pi^+\pi^-}}{\bar{\varepsilon}_{B\to K^0_S hh'}}}$
2018	$B^0_s\to K^0_S K^+\pi^-$	DD	6.78e-04	4.13e-04	0.60982	0.01438	0.00007	0.00143	0.00122	0.00436	0.01658	0.01968	0.00010	0.00081	0.00664	0.00007	0.03060
2017	$B^0_s\to K^0_S K^+\pi^-$	DD	7.50e-04	4.42e-04	0.58961	0.01433	0.00007	0.00148	0.00123	0.00392	0.01541	0.02035	0.00010	0.00077	0.00664	0.00007	0.03035
2016	$B^0_s\to K^0_S K^+\pi^-$	DD	7.42e-04	4.39e-04	0.59110	0.01446	0.00007	0.00143	0.00078	0.00348	0.01554	0.02030	0.00010	0.00015	0.00664	0.00007	0.03036
2015	$B^0_s\to K^0_S K^+\pi^-$	DD	6.16e-04	3.47e-04	0.56294	0.01610	0.00007	0.00158	0.00171	0.00520	0.01954	0.02132	0.00011	0.00118	0.00664	0.00007	0.03425
2012b	$B^0_s\to K^0_S K^+\pi^-$	DD	4.15e-04	3.44e-04	0.82809	0.02233	0.00006	0.00266	0.00137	0.02975	0.02123	0.01449	0.00009	0.00008	0.00664	0.00006	0.04580
2012a	$B^0_s\to K^0_S K^+\pi^-$	DD	3.44e-04	2.33e-04	0.67748	0.02721	0.00008	0.00295	0.00181	0.04264	0.02994	0.01771	0.00008	0.00119	0.00664	0.00008	0.06185
2011	$B^0_s\to K^0_S K^+\pi^-$	DD	4.33e-04	2.38e-04	0.55015	0.02455	0.00007	0.00423	0.00179	0.03658	0.02831	0.02181	0.00002	0.00042	0.00664	0.00007	0.05730
2018	$B^0_s\to K^0_S K^+\pi^-$	LL	2.64e-04	1.91e-04	0.72246	0.02438	0.00012	0.00117	0.00257	0.00674	0.04328	0.03061	0.00020	0.00644	0.00664	0.00012	0.05952
2017	$B^0_s\to K^0_S K^+\pi^-$	LL	2.84e-04	2.15e-04	0.75771	0.02432	0.00011	0.00131	0.00155	0.00385	0.03971	0.02918	0.00020	0.00422	0.00664	0.00011	0.05569
2016	$B^0_s\to K^0_S K^+\pi^-$	LL	3.14e-04	2.21e-04	0.70424	0.02378	0.00011	0.00124	0.00121	0.00469	0.03664	0.03140	0.00021	0.00030	0.00664	0.00011	0.05443
2015	$B^0_s\to K^0_S K^+\pi^-$	LL	2.75e-04	1.99e-04	0.72347	0.02529	0.00011	0.00133	0.00258	0.00629	0.04150	0.03057	0.00020	0.00323	0.00664	0.00011	0.05830
2012b	$B^0_s\to K^0_S K^+\pi^-$	LL	9.02e-05	1.08e-04	1.20245	0.04661	0.00012	0.00218	0.00541	0.02666	0.11480	0.01839	0.00013	0.00292	0.00664	0.00012	0.12840
2012a	$B^0_s\to K^0_S K^+\pi^-$	LL	1.48e-04	7.78e-05	0.52416	0.04599	0.00011	0.00241	0.00439	0.03806	0.08621	0.04219	0.00010	0.00157	0.00664	0.00011	0.11335
2011	$B^0_s\to K^0_S K^+\pi^-$	LL	1.69e-04	1.33e-04	0.78536	0.03902	0.00010	0.00335	0.00299	0.02895	0.06607	0.02816	0.00014	0.00194	0.00664	0.00010	0.08710

Table C.92: $B^0\to K^0_S\pi^+\pi^-$ over $B^0_s\to K^0_S K^+\pi^-$ efficiency table for the unfavoured mode optimisation. For each year and K^0_S reconstruction type, the average efficiency of the considered mode, the average efficiency of $B^0\to K^0_S\pi^+\pi^-$, the ratio of average efficiencies, the related relative uncertainties split by sources and the final relative uncertainty are given.

Year	Mode	K^0_S	$\bar{\varepsilon}_{B\to K^0_S hh'}$	$\bar{\varepsilon}_{B^0_s\to K^0_S\pi^+\pi^-}$	$\frac{\bar{\varepsilon}_{B^0_d\to K^0_S\pi^+\pi^-}}{\bar{\varepsilon}_{B\to K^0_S hh'}}$	$\sigma^{\text{stat}}_{\frac{\bar{\varepsilon}_{B^0_d\to K^0_S\pi^+\pi^-}}{\bar{\varepsilon}_{B\to K^0_S hh'}}}$	$\sigma^{\text{tracking}}_{\frac{\bar{\varepsilon}_{B^0_d\to K^0_S\pi^+\pi^-}}{\bar{\varepsilon}_{B\to K^0_S hh'}}}$	$\sigma^{\text{L0corr}}_{\frac{\bar{\varepsilon}_{B^0_d\to K^0_S\pi^+\pi^-}}{\bar{\varepsilon}_{B\to K^0_S hh'}}}$	$\sigma^{\text{PIDMCsampling}}_{\frac{\bar{\varepsilon}_{B^0_d\to K^0_S\pi^+\pi^-}}{\bar{\varepsilon}_{B\to K^0_S hh'}}}$	$\sigma^{\text{PIDkernel}}_{\frac{\bar{\varepsilon}_{B^0_d\to K^0_S\pi^+\pi^-}}{\bar{\varepsilon}_{B\to K^0_S hh'}}}$	$\sigma^{\text{BMS}}_{\frac{\bar{\varepsilon}_{B^0_d\to K^0_S\pi^+\pi^-}}{\bar{\varepsilon}_{B\to K^0_S hh'}}}$	$\sigma^{\text{binning}}_{\frac{\bar{\varepsilon}_{B^0_d\to K^0_S\pi^+\pi^-}}{\bar{\varepsilon}_{B\to K^0_S hh'}}}$	$\sigma^{\text{L0E2choice}}_{\frac{\bar{\varepsilon}_{B^0_d\to K^0_S\pi^+\pi^-}}{\bar{\varepsilon}_{B\to K^0_S hh'}}}$	$\sigma^{\text{F'Trigger}}_{\frac{\bar{\varepsilon}_{B^0_d\to K^0_S\pi^+\pi^-}}{\bar{\varepsilon}_{B\to K^0_S hh'}}}$	$\sigma^{\text{MCreweighting}}_{\frac{\bar{\varepsilon}_{B^0_d\to K^0_S\pi^+\pi^-}}{\bar{\varepsilon}_{B\to K^0_S hh'}}}$	$\sigma^{\text{K}^0_S\text{tracking}}_{\frac{\bar{\varepsilon}_{B^0_d\to K^0_S\pi^+\pi^-}}{\bar{\varepsilon}_{B\to K^0_S hh'}}}$	$\sigma^{\text{tot}}_{\frac{\bar{\varepsilon}_{B^0_d\to K^0_S\pi^+\pi^-}}{\bar{\varepsilon}_{B\to K^0_S hh'}}}$
2018	$B^0_s\to K^0_S K^+K^-$	DD	5.48e-04	4.13e-04	0.75424	0.01486	0.00007	0.00154	0.00194	0.00531	0.07060	0.04692	0.00177	0.00164	0.00664	0.00007	0.08655
2017	$B^0_s\to K^0_S K^+K^-$	DD	4.26e-04	4.42e-04	1.03832	0.01645	0.00007	0.00210	0.00208	0.00565	0.08982	0.03409	0.00129	0.00123	0.00664	0.00007	0.09792
2016	$B^0_s\to K^0_S K^+K^-$	DD	5.46e-04	4.39e-04	0.80324	0.01521	0.00007	0.00160	0.00195	0.00435	0.07061	0.04406	0.00166	0.00155	0.00664	0.00007	0.08505
2015	$B^0_s\to K^0_S K^+K^-$	DD	4.51e-04	3.47e-04	0.76886	0.01684	0.00008	0.00173	0.00275	0.00643	0.08575	0.04603	0.00174	0.00167	0.00664	0.00008	0.09929
2012b	$B^0_s\to K^0_S K^+K^-$	DD	4.23e-04	3.44e-04	0.81333	0.02093	0.00006	0.00380	0.00254	0.07292	0.09124	0.04352	0.00033	0.00129	0.00664	0.00006	0.12665
2012a	$B^0_s\to K^0_S K^+K^-$	DD	3.08e-04	2.33e-04	0.75798	0.02746	0.00007	0.00357	0.00306	0.06750	0.12576	0.04669	0.00040	0.00023	0.00664	0.00007	0.15288
2011	$B^0_s\to K^0_S K^+K^-$	DD	3.95e-04	2.38e-04	0.60312	0.02432	0.00006	0.00482	0.00482	0.08794	0.09912	0.05868	0.00045	0.00101	0.00664	0.00006	0.14726
2018	$B^0_s\to K^0_S K^+K^-$	LL	2.67e-04	1.91e-04	0.71415	0.06771	0.00040	0.00335	0.01277	0.00692	0.14098	0.18213	0.00231	0.00537	0.00664	0.00040	0.24069
2017	$B^0_s\to K^0_S K^+K^-$	LL	2.27e-04	2.15e-04	0.94744	0.07829	0.00040	0.00559	0.01493	0.00467	0.16482	0.13728	0.00174	0.00769	0.00664	0.00040	0.22918
2016	$B^0_s\to K^0_S K^+K^-$	LL	2.56e-04	2.21e-04	0.86366	0.07163	0.00038	0.00369	0.01063	0.00591	0.14637	0.15060	0.00191	0.00361	0.00664	0.00038	0.22239
2015	$B^0_s\to K^0_S K^+K^-$	LL	3.50e-04	1.99e-04	0.56874	0.06324	0.00035	0.00372	0.00945	0.00651	0.10837	0.22869	0.00290	0.00964	0.00664	0.00035	0.26141
2012b	$B^0_s\to K^0_S K^+K^-$	LL	1.54e-04	1.08e-04	0.70457	0.11929	0.00035	0.01503	0.02368	0.07522	0.24483	0.18460	0.00055	0.00432	0.00664	0.00035	0.33876
2012a	$B^0_s\to K^0_S K^+K^-$	LL	1.67e-04	7.78e-05	0.46617	0.13174	0.00035	0.01311	0.01246	0.06961	0.22973	0.27901	0.00049	0.00103	0.00664	0.00035	0.39140
2011	$B^0_s\to K^0_S K^+K^-$	LL	1.76e-04	1.33e-04	0.75530	0.11650	0.00028	0.01164	0.02581	0.05896	0.21376	0.17220	0.00131	0.00498	0.00664	0.00028	0.30540

Table C.93: $B^0\to K^0_S\pi^+\pi^-$ over $B^0_s\to K^0_S K^+K^-$ efficiency table for the unfavoured mode optimisation. For each year and K^0_S reconstruction type, the average efficiency of the considered mode, the average efficiency of $B^0\to K^0_S\pi^+\pi^-$, the ratio of average efficiencies, the related relative uncertainties split by sources and the final relative uncertainty are given.

C.10 Self concistency test results

Mode	$\frac{\varepsilon_{\bar{\mathrm{DD}}}}{\varepsilon_{\bar{\mathrm{LL}}}}$	$\frac{\mathrm{Y_{DD}}}{\mathrm{Y_{LL}}}$	$\sigma_{\frac{\varepsilon_{\bar{\mathrm{DD}}}}{\varepsilon_{\bar{\mathrm{LL}}}}}$	$\sigma_{\frac{\mathrm{Y_{DD}}}{\mathrm{Y_{LL}}}}$	distance
$B^0_d \to K^0_S\pi^+\pi^-$	2.17	1.97	0.08	0.14	-1.23
$B^0_d \to K^0_S K^+\pi^-$	2.56	2.50	0.17	0.64	-0.09
$B^0_d \to K^0_S\pi^+ K^-$	2.42	2.21	0.16	0.60	-0.34
$B^0_d \to K^0_S K^+ K^-$	2.22	2.13	0.04	0.09	-0.90
$B^0_s \to K^0_S\pi^+\pi^-$	2.07	1.95	0.15	0.74	-0.16
$B^0_s \to K^0_S K^+\pi^-$	2.57	2.32	0.14	0.23	-0.90
$B^0_s \to K^0_S\pi^+ K^-$	2.39	2.22	0.13	0.22	-0.65
$B^0_s \to K^0_S K^+ K^-$	2.05	2.31	0.54	1.66	0.15

Table C.94: 2018 self consistency test table with systematics propagated. For each mode, the ratio of average efficiencies, the ratio of yields, the associated uncertainties and the distance are given.

Mode	$\frac{\varepsilon_{\bar{\mathrm{DD}}}}{\varepsilon_{\bar{\mathrm{LL}}}}$	$\frac{\mathrm{Y_{DD}}}{\mathrm{Y_{LL}}}$	$\sigma_{\frac{\varepsilon_{\bar{\mathrm{DD}}}}{\varepsilon_{\bar{\mathrm{LL}}}}}$	$\sigma_{\frac{\mathrm{Y_{DD}}}{\mathrm{Y_{LL}}}}$	distance
$B^0_d \to K^0_S\pi^+\pi^-$	2.05	1.77	0.07	0.15	-1.67
$B^0_d \to K^0_S K^+\pi^-$	2.72	2.87	0.17	1.01	0.15
$B^0_d \to K^0_S\pi^+ K^-$	2.31	2.31	0.15	0.57	0.00
$B^0_d \to K^0_S K^+ K^-$	2.04	1.93	0.05	0.10	-0.95
$B^0_s \to K^0_S\pi^+\pi^-$	1.91	2.70	0.13	1.34	0.59
$B^0_s \to K^0_S K^+\pi^-$	2.64	2.47	0.13	0.31	-0.49
$B^0_s \to K^0_S\pi^+ K^-$	2.27	2.26	0.12	0.20	-0.02
$B^0_s \to K^0_S K^+ K^-$	1.87	2.10	0.56	1.27	0.17

Table C.95: 2017 self consistency test table with systematics propagated. For each mode, the ratio of average efficiencies, the ratio of yields, the associated uncertainties and the distance are given.

Mode	$\frac{\varepsilon_{\bar{\mathrm{DD}}}}{\varepsilon_{\bar{\mathrm{LL}}}}$	$\frac{\mathrm{Y_{DD}}}{\mathrm{Y_{LL}}}$	$\sigma_{\frac{\varepsilon_{\bar{\mathrm{DD}}}}{\varepsilon_{\bar{\mathrm{LL}}}}}$	$\sigma_{\frac{\mathrm{Y_{DD}}}{\mathrm{Y_{LL}}}}$	distance
$B^0_d \to K^0_S\pi^+\pi^-$	1.98	1.70	0.07	0.15	-1.70
$B^0_d \to K^0_S K^+\pi^-$	2.41	2.66	0.16	1.07	0.23
$B^0_d \to K^0_S\pi^+ K^-$	2.53	1.89	0.15	0.66	-0.95
$B^0_d \to K^0_S K^+ K^-$	2.40	2.35	0.05	0.12	-0.40
$B^0_s \to K^0_S\pi^+\pi^-$	1.81	2.07	0.13	0.93	0.28
$B^0_s \to K^0_S K^+\pi^-$	2.36	2.28	0.12	0.30	-0.26
$B^0_s \to K^0_S\pi^+ K^-$	2.44	2.10	0.12	0.25	-1.21
$B^0_s \to K^0_S K^+ K^-$	2.13	41.59	0.56	141.42	0.28

Table C.96: 2016 self consistency test table with systematics propagated. For each mode, the ratio of average efficiencies, the ratio of yields, the associated uncertainties and the distance are given. The pathological values for $B^0_s \to K^0_S K^+ K^-$ reflects the absence of signal in 2016 data for the Long-Long category. They are kept since the uncertainties do cover as they should.

Mode	$\frac{\varepsilon_{\bar{DD}}}{\varepsilon_{\bar{LL}}}$	$\frac{Y_{DD}}{Y_{LL}}$	$\sigma_{\frac{\varepsilon_{\bar{DD}}}{\varepsilon_{\bar{LL}}}}$	$\sigma_{\frac{Y_{DD}}{Y_{LL}}}$	distance
$B^0_d \to K^0_S\pi^+\pi^-$	1.74	1.46	0.07	0.17	-1.50
$B^0_d \to K^0_S K^+\pi^-$	2.42	2.12	0.17	0.97	-0.30
$B^0_d \to K^0_S\pi^+ K^-$	2.83	1.99	0.18	1.41	-0.59
$B^0_d \to K^0_S K^+ K^-$	1.43	1.05	0.03	0.11	-3.26
$B^0_s \to K^0_S\pi^+\pi^-$	1.75	1.75	0.14	1.09	0.00
$B^0_s \to K^0_S K^+\pi^-$	2.24	1.67	0.12	0.33	-1.58
$B^0_s \to K^0_S\pi^+ K^-$	2.71	2.08	0.14	0.48	-1.27
$B^0_s \to K^0_S K^+ K^-$	1.29	1.07	0.46	0.97	-0.20

Table C.97: 2015 self consistency test table with systematics propagated. For each mode, the ratio of average efficiencies, the ratio of yields, the associated uncertainties and the distance are given.

Mode	$\frac{\varepsilon_{\bar{DD}}}{\varepsilon_{\bar{LL}}}$	$\frac{Y_{DD}}{Y_{LL}}$	$\sigma_{\frac{\varepsilon_{\bar{DD}}}{\varepsilon_{\bar{LL}}}}$	$\sigma_{\frac{Y_{DD}}{Y_{LL}}}$	distance
$B^0_d \to K^0_S\pi^+\pi^-$	3.17	2.17	0.17	0.22	-3.58
$B^0_d \to K^0_S K^+\pi^-$	5.40	4.89	0.70	2.25	-0.22
$B^0_d \to K^0_S\pi^+ K^-$	5.48	2.37	0.60	1.10	-2.48
$B^0_d \to K^0_S K^+ K^-$	2.70	1.81	0.09	0.14	-5.43
$B^0_s \to K^0_S\pi^+\pi^-$	2.95	2.64	0.26	1.42	-0.21
$B^0_s \to K^0_S K^+\pi^-$	4.60	5.52	0.54	0.97	0.82
$B^0_s \to K^0_S\pi^+ K^-$	5.05	3.63	0.41	0.61	-1.92
$B^0_s \to K^0_S K^+ K^-$	2.75	0.99	0.88	0.80	-1.47

Table C.98: 2012b self consistency test table with systematics propagated. For each mode, the ratio of average efficiencies, the ratio of yields, the associated uncertainties and the distance are given.

Mode	$\frac{\varepsilon_{\bar{DD}}}{\varepsilon_{\bar{LL}}}$	$\frac{Y_{DD}}{Y_{LL}}$	$\sigma_{\frac{\varepsilon_{\bar{DD}}}{\varepsilon_{\bar{LL}}}}$	$\sigma_{\frac{Y_{DD}}{Y_{LL}}}$	distance
$B^0_d \to K^0_S\pi^+\pi^-$	3.00	3.37	0.22	0.44	0.75
$B^0_d \to K^0_S K^+\pi^-$	2.69	2.76	0.27	1.15	0.06
$B^0_d \to K^0_S\pi^+ K^-$	2.69	0.79	0.24	0.53	-3.26
$B^0_d \to K^0_S K^+ K^-$	1.49	1.32	0.05	0.18	-0.88
$B^0_s \to K^0_S\pi^+\pi^-$	3.08	0.84	0.36	1.09	-1.95
$B^0_s \to K^0_S K^+\pi^-$	2.32	2.38	0.20	0.50	0.12
$B^0_s \to K^0_S\pi^+ K^-$	2.57	2.23	0.18	0.51	-0.63
$B^0_s \to K^0_S K^+ K^-$	1.84	1.06	0.67	0.87	-0.71

Table C.99: 2012a self consistency test table with systematics propagated. For each mode, the ratio of average efficiencies, the ratio of yields, the associated uncertainties and the distance are given.

Mode	$\frac{\bar{\varepsilon_{\mathrm{DD}}}}{\varepsilon_{\mathrm{LL}}}$	$\frac{\mathrm{Y_{DD}}}{\mathrm{Y_{LL}}}$	$\sigma_{\frac{\bar{\varepsilon_{\mathrm{DD}}}}{\varepsilon_{\mathrm{LL}}}}$	$\sigma_{\frac{\mathrm{Y_{DD}}}{\mathrm{Y_{LL}}}}$	distance
$B^0_d \to K^0_S\pi^+\pi^-$	1.79	1.36	0.10	0.25	-1.62
$B^0_d \to K^0_S K^+\pi^-$	3.08	2.32	0.27	1.07	-0.69
$B^0_d \to K^0_S\pi^+ K^-$	2.59	2.10	0.20	0.67	-0.71
$B^0_d \to K^0_S K^+ K^-$	2.00	1.37	0.06	0.16	-3.68
$B^0_s \to K^0_S\pi^+\pi^-$	1.78	2.20	0.18	1.79	0.24
$B^0_s \to K^0_S K^+\pi^-$	2.56	1.97	0.19	0.35	-1.49
$B^0_s \to K^0_S\pi^+ K^-$	2.46	1.61	0.16	0.25	-2.87
$B^0_s \to K^0_S K^+ K^-$	2.25	1.69	0.72	1.13	-0.41

Table C.100: 2011 self consistency test table with systematics propagated. For each mode, the ratio of average efficiencies, the ratio of yields, the associated uncertainties and the distance are given.

C.11 Individual relative branching fractions

In this appendix, the averaged ratios of branching fractions are given with the systematic uncertainties split into uncorrelated and correlated categories.

C.11.1 $B^0 \to K^0_S K^\pm \pi^\pm$

The final state $K^0_S K^+ \pi^-$ is first considered, then the final state $K^0_S K^- \pi^+$, and finally the sum of the two. Note that, because this is an untagged analysis, there is no distinction between B^0 and $\overline{B}^0$.

B^0 or $\overline{B}^0 \to K^0_S K^+ \pi^-$:

$$\frac{BF(B^0 \to K^0_S K^+ \pi^-)}{BF(B^0 \to K^0_S \pi^+ \pi^-)}_{\text{LL,2011}} = 0.077 \pm 0.018\,(\text{stat.}) \pm 0.015\,(\text{syst.})$$

$$\frac{BF(B^0 \to K^0_S K^+ \pi^-)}{BF(B^0 \to K^0_S \pi^+ \pi^-)}_{\text{DD,2011}} = 0.076 \pm 0.015\,(\text{stat.}) \pm 0.025\,(\text{syst.})$$

$$\frac{BF(B^0 \to K^0_S K^+ \pi^-)}{BF(B^0 \to K^0_S \pi^+ \pi^-)}_{\text{LL,2012a}} = 0.097 \pm 0.030\,(\text{stat.}) \pm 0.018\,(\text{syst.})$$

$$\frac{BF(B^0 \to K^0_S K^+ \pi^-)}{BF(B^0 \to K^0_S \pi^+ \pi^-)}_{\text{DD,2012a}} = 0.088 \pm 0.016\,(\text{stat.}) \pm 0.018\,(\text{syst.})$$

$$\frac{BF(B^0 \to K^0_S K^+ \pi^-)}{BF(B^0 \to K^0_S \pi^+ \pi^-)}_{\text{LL,2012b}} = 0.043 \pm 0.015\,(\text{stat.}) \pm 0.011\,(\text{syst.})$$

$$\frac{BF(B^0 \to K^0_S K^+ \pi^-)}{BF(B^0 \to K^0_S \pi^+ \pi^-)}_{\text{DD,2012b}} = 0.057 \pm 0.009\,(\text{stat.}) \pm 0.008\,(\text{syst.})$$

$$\frac{BF(B^0 \to K^0_S K^+ \pi^-)}{BF(B^0 \to K^0_S \pi^+ \pi^-)}_{\text{LL,2015}} = 0.093 \pm 0.026\,(\text{stat.}) \pm 0.024\,(\text{syst.})$$

$$\frac{BF(B^0 \to K^0_S K^+ \pi^-)}{BF(B^0 \to K^0_S \pi^+ \pi^-)}_{\text{DD,2015}} = 0.097 \pm 0.017\,(\text{stat.}) \pm 0.017\,(\text{syst.})$$

$$\frac{BF(B^0 \to K^0_S K^+ \pi^-)}{BF(B^0 \to K^0_S \pi^+ \pi^-)}_{\text{LL,2016}} = 0.052 \pm 0.007\,(\text{stat.}) \pm 0.014\,(\text{syst.})$$

$$\frac{BF(B^0 \to K^0_S K^+ \pi^-)}{BF(B^0 \to K^0_S \pi^+ \pi^-)}_{\text{DD,2016}} = 0.068 \pm 0.006\,(\text{stat.}) \pm 0.010\,(\text{syst.})$$

$$\frac{BF(B^0 \to K^0_S K^+ \pi^-)}{BF(B^0 \to K^0_S \pi^+ \pi^-)}_{\text{LL,2017}} = 0.058 \pm 0.007\,(\text{stat.}) \pm 0.011\,(\text{syst.})$$

$$\frac{BF(B^0 \to K^0_S K^+ \pi^-)}{BF(B^0 \to K^0_S \pi^+ \pi^-)}_{\text{DD,2017}} = 0.071 \pm 0.006\,(\text{stat.}) \pm 0.014\,(\text{syst.})$$

$$\frac{BF(B^0 \to K^0_S K^+ \pi^-)}{BF(B^0 \to K^0_S \pi^+ \pi^-)}_{\text{LL,2018}} = 0.065 \pm 0.007\,(\text{stat.}) \pm 0.010\,(\text{syst.})$$

$$\frac{BF(B^0 \to K^0_S K^+ \pi^-)}{BF(B^0 \to K^0_S \pi^+ \pi^-)}_{\text{DD,2018}} = 0.070 \pm 0.005\,(\text{stat.}) \pm 0.008\,(\text{syst.})$$

$$\frac{BF(B^0 \to K^0_S K^+ \pi^-)}{BF(B^0 \to K^0_S \pi^+ \pi^-)}_{\text{Averaged}} = 0.0662 \pm 0.0025\,(\text{stat.}) \pm 0.0032\,(\text{syst.uncorr}) \pm 0.0019\,(\text{syst.corr})$$

B^0 or $\overline{B}^0 \to K^0_S K^-\pi^+$:

$$\frac{BF(B^0 \to K^0_S\pi^+K^-)}{BF(B^0 \to K^0_S\pi^+\pi^-)}_{\text{LL,2011}} = 0.098 \pm 0.020\,(\text{stat.}) \pm 0.016\,(\text{syst.})$$

$$\frac{BF(B^0 \to K^0_S\pi^+K^-)}{BF(B^0 \to K^0_S\pi^+\pi^-)}_{\text{DD,2011}} = 0.104 \pm 0.016\,(\text{stat.}) \pm 0.018\,(\text{syst.})$$

$$\frac{BF(B^0 \to K^0_S\pi^+K^-)}{BF(B^0 \to K^0_S\pi^+\pi^-)}_{\text{LL,2012a}} = 0.130 \pm 0.034\,(\text{stat.}) \pm 0.052\,(\text{syst.})$$

$$\frac{BF(B^0 \to K^0_S\pi^+K^-)}{BF(B^0 \to K^0_S\pi^+\pi^-)}_{\text{DD,2012a}} = 0.034 \pm 0.013\,(\text{stat.}) \pm 0.010\,(\text{syst.})$$

$$\frac{BF(B^0 \to K^0_S\pi^+K^-)}{BF(B^0 \to K^0_S\pi^+\pi^-)}_{\text{LL,2012b}} = 0.093 \pm 0.019\,(\text{stat.}) \pm 0.016\,(\text{syst.})$$

$$\frac{BF(B^0 \to K^0_S\pi^+K^-)}{BF(B^0 \to K^0_S\pi^+\pi^-)}_{\text{DD,2012b}} = 0.059 \pm 0.012\,(\text{stat.}) \pm 0.019\,(\text{syst.})$$

$$\frac{BF(B^0 \to K^0_S\pi^+K^-)}{BF(B^0 \to K^0_S\pi^+\pi^-)}_{\text{LL,2015}} = 0.071 \pm 0.021\,(\text{stat.}) \pm 0.024\,(\text{syst.})$$

$$\frac{BF(B^0 \to K^0_S\pi^+K^-)}{BF(B^0 \to K^0_S\pi^+\pi^-)}_{\text{DD,2015}} = 0.059 \pm 0.017\,(\text{stat.}) \pm 0.026\,(\text{syst.})$$

$$\frac{BF(B^0 \to K^0_S\pi^+K^-)}{BF(B^0 \to K^0_S\pi^+\pi^-)}_{\text{LL,2016}} = 0.079 \pm 0.008\,(\text{stat.}) \pm 0.014\,(\text{syst.})$$

$$\frac{BF(B^0 \to K^0_S\pi^+K^-)}{BF(B^0 \to K^0_S\pi^+\pi^-)}_{\text{DD,2016}} = 0.069 \pm 0.006\,(\text{stat.}) \pm 0.013\,(\text{syst.})$$

$$\frac{BF(B^0 \to K^0_S\pi^+K^-)}{BF(B^0 \to K^0_S\pi^+\pi^-)}_{\text{LL,2017}} = 0.063 \pm 0.007\,(\text{stat.}) \pm 0.009\,(\text{syst.})$$

$$\frac{BF(B^0 \to K^0_S\pi^+K^-)}{BF(B^0 \to K^0_S\pi^+\pi^-)}_{\text{DD,2017}} = 0.073 \pm 0.005\,(\text{stat.}) \pm 0.008\,(\text{syst.})$$

$$\frac{BF(B^0 \to K^0_S\pi^+K^-)}{BF(B^0 \to K^0_S\pi^+\pi^-)}_{\text{LL,2018}} = 0.071 \pm 0.007\,(\text{stat.}) \pm 0.012\,(\text{syst.})$$

$$\frac{BF(B^0 \to K^0_S\pi^+K^-)}{BF(B^0 \to K^0_S\pi^+\pi^-)}_{\text{DD,2018}} = 0.072 \pm 0.005\,(\text{stat.}) \pm 0.008\,(\text{syst.})$$

$$\frac{BF(B^0 \to K^0_S\pi^+K^-)}{BF(B^0 \to K^0_S\pi^+\pi^-)}_{\text{Averaged}} = 0.0704 \pm 0.0025\,(\text{stat.}) \pm 0.0033\,(\text{syst.uncorr}) \pm 0.0017\,(\text{syst.corr})$$

B^0 or $\overline{B}^0 \to K^0_S K^\pm \pi^\pm$: The combination the two final states $K^0_S K^+\pi^-$ and $K^0_S K^-\pi^+$ is now realised. Again, there is no distinction between B^0 and $\overline{B}^0$, so what is measured is the sum of the two ratios of branching fractions, *i.e.*

$$\frac{BF(B^0 \to K^0_S K^\pm \pi^\mp)}{BF(B^0 \to K^0_S \pi^+\pi^-)} = \frac{BF(B^0 \to K^0_S K^+\pi^-) + BF(B^0 \to K^0_S K^-\pi^+)}{BF(B^0 \to K^0_S \pi^+\pi^-)} \tag{C.11.1}$$

$$\frac{BF(B^0 \to K^0_S K^\pm \pi^\mp)}{BF(B^0 \to K^0_S \pi^+\pi^-)}_{\text{LL,2011}} = 0.175 \pm 0.026\,(\text{stat.}) \pm 0.016\,(\text{syst.})$$

$$\frac{BF(B^0 \to K^0_S K^\pm \pi^\mp)}{BF(B^0 \to K^0_S \pi^+\pi^-)}_{\text{DD,2011}} = 0.181 \pm 0.022\,(\text{stat.}) \pm 0.018\,(\text{syst.})$$

$$\frac{BF(B^0 \to K^0_S K^\pm \pi^\mp)}{BF(B^0 \to K^0_S \pi^+\pi^-)}_{\text{LL,2012a}} = 0.23 \pm 0.05\,(\text{stat.}) \pm 0.05\,(\text{syst.})$$

$$\frac{BF(B^0 \to K^0_S K^\pm \pi^\mp)}{BF(B^0 \to K^0_S \pi^+\pi^-)}_{\text{DD,2012a}} = 0.122 \pm 0.021\,(\text{stat.}) \pm 0.010\,(\text{syst.})$$

$$\frac{BF(B^0 \to K^0_S K^\pm \pi^\mp)}{BF(B^0 \to K^0_S \pi^+\pi^-)}_{\text{LL,2012b}} = 0.136 \pm 0.024\,(\text{stat.}) \pm 0.016\,(\text{syst.})$$

$$\frac{BF(B^0 \to K^0_S K^\pm \pi^\mp)}{BF(B^0 \to K^0_S \pi^+\pi^-)}_{\text{DD,2012b}} = 0.116 \pm 0.014\,(\text{stat.}) \pm 0.019\,(\text{syst.})$$

$$\frac{BF(B^0 \to K^0_S K^\pm \pi^\mp)}{BF(B^0 \to K^0_S \pi^+\pi^-)}_{\text{LL,2015}} = 0.164 \pm 0.033\,(\text{stat.}) \pm 0.024\,(\text{syst.})$$

$$\frac{BF(B^0 \to K^0_S K^\pm \pi^\mp)}{BF(B^0 \to K^0_S \pi^+\pi^-)}_{\text{DD,2015}} = 0.156 \pm 0.024\,(\text{stat.}) \pm 0.026\,(\text{syst.})$$

$$\frac{BF(B^0 \to K^0_S K^\pm \pi^\mp)}{BF(B^0 \to K^0_S \pi^+\pi^-)}_{\text{LL,2016}} = 0.131 \pm 0.011\,(\text{stat.}) \pm 0.014\,(\text{syst.})$$

$$\frac{BF(B^0 \to K^0_S K^\pm \pi^\mp)}{BF(B^0 \to K^0_S \pi^+\pi^-)}_{\text{DD,2016}} = 0.136 \pm 0.009\,(\text{stat.}) \pm 0.013\,(\text{syst.})$$

$$\frac{BF(B^0 \to K^0_S K^\pm \pi^\mp)}{BF(B^0 \to K^0_S \pi^+\pi^-)}_{\text{LL,2017}} = 0.121 \pm 0.010\,(\text{stat.}) \pm 0.009\,(\text{syst.})$$

$$\frac{BF(B^0 \to K^0_S K^\pm \pi^\mp)}{BF(B^0 \to K^0_S \pi^+\pi^-)}_{\text{DD,2017}} = 0.144 \pm 0.008\,(\text{stat.}) \pm 0.008\,(\text{syst.})$$

$$\frac{BF(B^0 \to K^0_S K^\pm \pi^\mp)}{BF(B^0 \to K^0_S \pi^+\pi^-)}_{\text{LL,2018}} = 0.136 \pm 0.010\,(\text{stat.}) \pm 0.012\,(\text{syst.})$$

$$\frac{BF(B^0 \to K^0_S K^\pm \pi^\mp)}{BF(B^0 \to K^0_S \pi^+\pi^-)}_{\text{DD,2018}} = 0.142 \pm 0.007\,(\text{stat.}) \pm 0.008\,(\text{syst.})$$

$$\frac{BF(B^0 \to K^0_S K^\pm \pi^\mp)}{BF(B^0 \to K^0_S \pi^+\pi^-)}_{\text{Averaged}} = 0.1366 \pm 0.0035\,(\text{stat.}) \pm 0.0046\,(\text{syst.uncorr}) \pm 0.0025\,(\text{syst.corr})$$

C.11.2 $B^0 \to K^0_S K^+ K^-$

$$\frac{BF(B^0 \to K^0_S K^+ K^-)}{BF(B^0 \to K^0_S \pi^+ \pi^-)}_{\text{LL,2011}} = 0.52 \pm 0.05\,(\text{stat.}) \pm 0.05\,(\text{syst.})$$

$$\frac{BF(B^0 \to K^0_S K^+ K^-)}{BF(B^0 \to K^0_S \pi^+ \pi^-)}_{\text{DD,2011}} = 0.510 \pm 0.036\,(\text{stat.}) \pm 0.028\,(\text{syst.})$$

$$\frac{BF(B^0 \to K^0_S K^+ K^-)}{BF(B^0 \to K^0_S \pi^+ \pi^-)}_{\text{LL,2012a}} = 0.375 \pm 0.042\,(\text{stat.}) \pm 0.027\,(\text{syst.})$$

$$\frac{BF(B^0 \to K^0_S K^+ K^-)}{BF(B^0 \to K^0_S \pi^+ \pi^-)}_{\text{DD,2012a}} = 0.529 \pm 0.045\,(\text{stat.}) \pm 0.033\,(\text{syst.})$$

$$\frac{BF(B^0 \to K^0_S K^+ K^-)}{BF(B^0 \to K^0_S \pi^+ \pi^-)}_{\text{LL,2012b}} = 0.57 \pm 0.04\,(\text{stat.}) \pm 0.04\,(\text{syst.})$$

$$\frac{BF(B^0 \to K^0_S K^+ K^-)}{BF(B^0 \to K^0_S \pi^+ \pi^-)}_{\text{DD,2012b}} = 0.544 \pm 0.027\,(\text{stat.}) \pm 0.036\,(\text{syst.})$$

$$\frac{BF(B^0 \to K^0_S K^+ K^-)}{BF(B^0 \to K^0_S \pi^+ \pi^-)}_{\text{LL,2015}} = 0.525 \pm 0.047\,(\text{stat.}) \pm 0.029\,(\text{syst.})$$

$$\frac{BF(B^0 \to K^0_S K^+ K^-)}{BF(B^0 \to K^0_S \pi^+ \pi^-)}_{\text{DD,2015}} = 0.517 \pm 0.039\,(\text{stat.}) \pm 0.023\,(\text{syst.})$$

$$\frac{BF(B^0 \to K^0_S K^+ K^-)}{BF(B^0 \to K^0_S \pi^+ \pi^-)}_{\text{LL,2016}} = 0.529 \pm 0.021\,(\text{stat.}) \pm 0.024\,(\text{syst.})$$

$$\frac{BF(B^0 \to K^0_S K^+ K^-)}{BF(B^0 \to K^0_S \pi^+ \pi^-)}_{\text{DD,2016}} = 0.568 \pm 0.016\,(\text{stat.}) \pm 0.029\,(\text{syst.})$$

$$\frac{BF(B^0 \to K^0_S K^+ K^-)}{BF(B^0 \to K^0_S \pi^+ \pi^-)}_{\text{LL,2017}} = 0.510 \pm 0.019\,(\text{stat.}) \pm 0.028\,(\text{syst.})$$

$$\frac{BF(B^0 \to K^0_S K^+ K^-)}{BF(B^0 \to K^0_S \pi^+ \pi^-)}_{\text{DD,2017}} = 0.561 \pm 0.015\,(\text{stat.}) \pm 0.026\,(\text{syst.})$$

$$\frac{BF(B^0 \to K^0_S K^+ K^-)}{BF(B^0 \to K^0_S \pi^+ \pi^-)}_{\text{LL,2018}} = 0.523 \pm 0.018\,(\text{stat.}) \pm 0.027\,(\text{syst.})$$

$$\frac{BF(B^0 \to K^0_S K^+ K^-)}{BF(B^0 \to K^0_S \pi^+ \pi^-)}_{\text{DD,2018}} = 0.536 \pm 0.013\,(\text{stat.}) \pm 0.025\,(\text{syst.})$$

$$\frac{BF(B^0 \to K^0_S K^+ K^-)}{BF(B^0 \to K^0_S \pi^+ \pi^-)}_{\text{Averaged}} = 0.533 \pm 0.006\,(\text{stat.}) \pm 0.006\,(\text{syst.uncorr}) \pm 0.013\,(\text{syst.corr})$$

C.11.3 $B^0_s \to K^0_S\pi^+\pi^-$

$\frac{BF(B^0_s \to K^0_S\pi^+\pi^-)}{BF(B^0 \to K^0_S\pi^+\pi^-)}_{\text{LL,2011}}$	$= 0.199$	$\pm 0.085\,(\text{stat.})$	$\pm 0.101\,(\text{syst.})$	$\pm 0.006\,(f_s/f_d)$
$\frac{BF(B^0_s \to K^0_S\pi^+\pi^-)}{BF(B^0 \to K^0_S\pi^+\pi^-)}_{\text{DD,2011}}$	$= 0.324$	$\pm 0.074\,(\text{stat.})$	$\pm 0.103\,(\text{syst.})$	$\pm 0.010\,(f_s/f_d)$
$\frac{BF(B^0_s \to K^0_S\pi^+\pi^-)}{BF(B^0 \to K^0_S\pi^+\pi^-)}_{\text{LL,2012a}}$	$= 0.429$	$\pm 0.147\,(\text{stat.})$	$\pm 0.049\,(\text{syst.})$	$\pm 0.014\,(f_s/f_d)$
$\frac{BF(B^0_s \to K^0_S\pi^+\pi^-)}{BF(B^0 \to K^0_S\pi^+\pi^-)}_{\text{DD,2012a}}$	$= 0.1041$	$\pm 0.0735\,(\text{stat.})$	$\pm 0.1075\,(\text{syst.})$	$\pm 0.0033\,(f_s/f_d)$
$\frac{BF(B^0_s \to K^0_S\pi^+\pi^-)}{BF(B^0 \to K^0_S\pi^+\pi^-)}_{\text{LL,2012b}}$	$= 0.283$	$\pm 0.071\,(\text{stat.})$	$\pm 0.106\,(\text{syst.})$	$\pm 0.009\,(f_s/f_d)$
$\frac{BF(B^0_s \to K^0_S\pi^+\pi^-)}{BF(B^0 \to K^0_S\pi^+\pi^-)}_{\text{DD,2012b}}$	$= 0.370$	$\pm 0.054\,(\text{stat.})$	$\pm 0.073\,(\text{syst.})$	$\pm 0.012\,(f_s/f_d)$
$\frac{BF(B^0_s \to K^0_S\pi^+\pi^-)}{BF(B^0 \to K^0_S\pi^+\pi^-)}_{\text{LL,2015}}$	$= 0.298$	$\pm 0.098\,(\text{stat.})$	$\pm 0.089\,(\text{syst.})$	$\pm 0.009\,(f_s/f_d)$
$\frac{BF(B^0_s \to K^0_S\pi^+\pi^-)}{BF(B^0 \to K^0_S\pi^+\pi^-)}_{\text{DD,2015}}$	$= 0.355$	$\pm 0.080\,(\text{stat.})$	$\pm 0.115\,(\text{syst.})$	$\pm 0.011\,(f_s/f_d)$
$\frac{BF(B^0_s \to K^0_S\pi^+\pi^-)}{BF(B^0 \to K^0_S\pi^+\pi^-)}_{\text{LL,2016}}$	$= 0.250$	$\pm 0.035\,(\text{stat.})$	$\pm 0.061\,(\text{syst.})$	$\pm 0.008\,(f_s/f_d)$
$\frac{BF(B^0_s \to K^0_S\pi^+\pi^-)}{BF(B^0 \to K^0_S\pi^+\pi^-)}_{\text{DD,2016}}$	$= 0.334$	$\pm 0.033\,(\text{stat.})$	$\pm 0.081\,(\text{syst.})$	$\pm 0.010\,(f_s/f_d)$
$\frac{BF(B^0_s \to K^0_S\pi^+\pi^-)}{BF(B^0 \to K^0_S\pi^+\pi^-)}_{\text{LL,2017}}$	$= 0.177$	$\pm 0.030\,(\text{stat.})$	$\pm 0.062\,(\text{syst.})$	$\pm 0.006\,(f_s/f_d)$
$\frac{BF(B^0_s \to K^0_S\pi^+\pi^-)}{BF(B^0 \to K^0_S\pi^+\pi^-)}_{\text{DD,2017}}$	$= 0.290$	$\pm 0.027\,(\text{stat.})$	$\pm 0.056\,(\text{syst.})$	$\pm 0.009\,(f_s/f_d)$
$\frac{BF(B^0_s \to K^0_S\pi^+\pi^-)}{BF(B^0 \to K^0_S\pi^+\pi^-)}_{\text{LL,2018}}$	$= 0.277$	$\pm 0.034\,(\text{stat.})$	$\pm 0.043\,(\text{syst.})$	$\pm 0.009\,(f_s/f_d)$
$\frac{BF(B^0_s \to K^0_S\pi^+\pi^-)}{BF(B^0 \to K^0_S\pi^+\pi^-)}_{\text{DD,2018}}$	$= 0.287$	$\pm 0.025\,(\text{stat.})$	$\pm 0.073\,(\text{syst.})$	$\pm 0.009\,(f_s/f_d)$
$\frac{BF(B^0_s \to K^0_S\pi^+\pi^-)}{BF(B^0 \to K^0_S\pi^+\pi^-)}_{\text{Averaged}}$	$= 0.276$	$\pm 0.013\,(\text{stat.})$	$\pm 0.019\,(\text{syst.uncorr})$	$\pm 0.010\,(\text{syst.corr}) \pm 0.005\,(f_s/f_d)$

C.11.4 $B^0_s \to K^0_S K^\pm \pi^\pm$

As for $B^0 \to K^0_S K^\pm \pi^\mp$, the final state $K^0_S K^+ \pi^-$ is first considered, then the final state $K^0_S K^- \pi^+$, and finally the sum of the two. Again, there is no distinction between B^0_s and $\overline{B}^0_s$.

B^0_s or $\overline{B}^0_s \to K^0_S K^+ \pi^-$:

$\frac{BF(B^0_s \to K^0_S K^+ \pi^-)}{BF(B^0 \to K^0_S \pi^+ \pi^-)}_{\text{LL,2011}}$	$= 0.951 \pm 0.116\,(\text{stat.}) \pm 0.080\,(\text{syst.})$	$\pm 0.030\,(f_s/f_d)$
$\frac{BF(B^0_s \to K^0_S K^+ \pi^-)}{BF(B^0 \to K^0_S \pi^+ \pi^-)}_{\text{DD,2011}}$	$= 0.962 \pm 0.091\,(\text{stat.}) \pm 0.061\,(\text{syst.})$	$\pm 0.031\,(f_s/f_d)$
$\frac{BF(B^0_s \to K^0_S K^+ \pi^-)}{BF(B^0 \to K^0_S \pi^+ \pi^-)}_{\text{LL,2012a}}$	$= 0.784 \pm 0.122\,(\text{stat.}) \pm 0.076\,(\text{syst.})$	$\pm 0.025\,(f_s/f_d)$
$\frac{BF(B^0_s \to K^0_S K^+ \pi^-)}{BF(B^0 \to K^0_S \pi^+ \pi^-)}_{\text{DD,2012a}}$	$= 0.822 \pm 0.101\,(\text{stat.}) \pm 0.067\,(\text{syst.})$	$\pm 0.026\,(f_s/f_d)$
$\frac{BF(B^0_s \to K^0_S K^+ \pi^-)}{BF(B^0 \to K^0_S \pi^+ \pi^-)}_{\text{LL,2012b}}$	$= 0.899 \pm 0.100\,(\text{stat.}) \pm 0.094\,(\text{syst.})$	$\pm 0.028\,(f_s/f_d)$
$\frac{BF(B^0_s \to K^0_S K^+ \pi^-)}{BF(B^0 \to K^0_S \pi^+ \pi^-)}_{\text{DD,2012b}}$	$= 1.018 \pm 0.071\,(\text{stat.}) \pm 0.058\,(\text{syst.})$	$\pm 0.032\,(f_s/f_d)$
$\frac{BF(B^0_s \to K^0_S K^+ \pi^-)}{BF(B^0 \to K^0_S \pi^+ \pi^-)}_{\text{LL,2015}}$	$= 0.845 \pm 0.123\,(\text{stat.}) \pm 0.062\,(\text{syst.})$	$\pm 0.026\,(f_s/f_d)$
$\frac{BF(B^0_s \to K^0_S K^+ \pi^-)}{BF(B^0 \to K^0_S \pi^+ \pi^-)}_{\text{DD,2015}}$	$= 0.905 \pm 0.089\,(\text{stat.}) \pm 0.030\,(\text{syst.})$	$\pm 0.028\,(f_s/f_d)$
$\frac{BF(B^0_s \to K^0_S K^+ \pi^-)}{BF(B^0 \to K^0_S \pi^+ \pi^-)}_{\text{LL,2016}}$	$= 0.766 \pm 0.046\,(\text{stat.}) \pm 0.038\,(\text{syst.})$	$\pm 0.024\,(f_s/f_d)$
$\frac{BF(B^0_s \to K^0_S K^+ \pi^-)}{BF(B^0 \to K^0_S \pi^+ \pi^-)}_{\text{DD,2016}}$	$= 0.887 \pm 0.036\,(\text{stat.}) \pm 0.029\,(\text{syst.})$	$\pm 0.028\,(f_s/f_d)$
$\frac{BF(B^0_s \to K^0_S K^+ \pi^-)}{BF(B^0 \to K^0_S \pi^+ \pi^-)}_{\text{LL,2017}}$	$= 0.853 \pm 0.047\,(\text{stat.}) \pm 0.049\,(\text{syst.})$	$\pm 0.027\,(f_s/f_d)$
$\frac{BF(B^0_s \to K^0_S K^+ \pi^-)}{BF(B^0 \to K^0_S \pi^+ \pi^-)}_{\text{DD,2017}}$	$= 0.892 \pm 0.034\,(\text{stat.}) \pm 0.035\,(\text{syst.})$	$\pm 0.028\,(f_s/f_d)$
$\frac{BF(B^0_s \to K^0_S K^+ \pi^-)}{BF(B^0 \to K^0_S \pi^+ \pi^-)}_{\text{LL,2018}}$	$= 0.872 \pm 0.044\,(\text{stat.}) \pm 0.049\,(\text{syst.})$	$\pm 0.027\,(f_s/f_d)$
$\frac{BF(B^0_s \to K^0_S K^+ \pi^-)}{BF(B^0 \to K^0_S \pi^+ \pi^-)}_{\text{DD,2018}}$	$= 0.844 \pm 0.030\,(\text{stat.}) \pm 0.025\,(\text{syst.})$	$\pm 0.026\,(f_s/f_d)$
$\frac{BF(B^0_s \to K^0_S K^+ \pi^-)}{BF(B^0 \to K^0_S \pi^+ \pi^-)}_{\text{Averaged}}$	$= 0.866 \pm 0.014\,(\text{stat.}) \pm 0.009\,(\text{syst.uncorr}) \pm 0.015\,(\text{syst.corr})$	$\pm 0.017\,(f_s/f_d)$

B_s^0 or $\overline{B}_s^0 \to K_S^0 K^- \pi^+$:

$$\frac{BF(B_s^0 \to K_S^0\pi^+K^-)}{BF(B^0 \to K_S^0\pi^+\pi^-)}_{\text{LL,2011}} = 1.067 \pm 0.115\,(\text{stat.}) \pm 0.084\,(\text{syst.}) \pm 0.034\,(f_s/f_d)$$

$$\frac{BF(B_s^0 \to K_S^0\pi^+K^-)}{BF(B^0 \to K_S^0\pi^+\pi^-)}_{\text{DD,2011}} = 0.983 \pm 0.089\,(\text{stat.}) \pm 0.062\,(\text{syst.}) \pm 0.031\,(f_s/f_d)$$

$$\frac{BF(B_s^0 \to K_S^0\pi^+K^-)}{BF(B^0 \to K_S^0\pi^+\pi^-)}_{\text{LL,2012a}} = 0.764 \pm 0.127\,(\text{stat.}) \pm 0.067\,(\text{syst.}) \pm 0.024\,(f_s/f_d)$$

$$\frac{BF(B_s^0 \to K_S^0\pi^+K^-)}{BF(B^0 \to K_S^0\pi^+\pi^-)}_{\text{DD,2012a}} = 0.864 \pm 0.101\,(\text{stat.}) \pm 0.060\,(\text{syst.}) \pm 0.027\,(f_s/f_d)$$

$$\frac{BF(B_s^0 \to K_S^0\pi^+K^-)}{BF(B^0 \to K_S^0\pi^+\pi^-)}_{\text{LL,2012b}} = 1.021 \pm 0.102\,(\text{stat.}) \pm 0.083\,(\text{syst.}) \pm 0.032\,(f_s/f_d)$$

$$\frac{BF(B_s^0 \to K_S^0\pi^+K^-)}{BF(B^0 \to K_S^0\pi^+\pi^-)}_{\text{DD,2012b}} = 0.975 \pm 0.068\,(\text{stat.}) \pm 0.056\,(\text{syst.}) \pm 0.031\,(f_s/f_d)$$

$$\frac{BF(B_s^0 \to K_S^0\pi^+K^-)}{BF(B^0 \to K_S^0\pi^+\pi^-)}_{\text{LL,2015}} = 0.834 \pm 0.114\,(\text{stat.}) \pm 0.057\,(\text{syst.}) \pm 0.026\,(f_s/f_d)$$

$$\frac{BF(B_s^0 \to K_S^0\pi^+K^-)}{BF(B^0 \to K_S^0\pi^+\pi^-)}_{\text{DD,2015}} = 1.034 \pm 0.096\,(\text{stat.}) \pm 0.035\,(\text{syst.}) \pm 0.032\,(f_s/f_d)$$

$$\frac{BF(B_s^0 \to K_S^0\pi^+K^-)}{BF(B^0 \to K_S^0\pi^+\pi^-)}_{\text{LL,2016}} = 0.973 \pm 0.052\,(\text{stat.}) \pm 0.042\,(\text{syst.}) \pm 0.030\,(f_s/f_d)$$

$$\frac{BF(B_s^0 \to K_S^0\pi^+K^-)}{BF(B^0 \to K_S^0\pi^+\pi^-)}_{\text{DD,2016}} = 0.899 \pm 0.037\,(\text{stat.}) \pm 0.032\,(\text{syst.}) \pm 0.028\,(f_s/f_d)$$

$$\frac{BF(B_s^0 \to K_S^0\pi^+K^-)}{BF(B^0 \to K_S^0\pi^+\pi^-)}_{\text{LL,2017}} = 0.849 \pm 0.046\,(\text{stat.}) \pm 0.045\,(\text{syst.}) \pm 0.026\,(f_s/f_d)$$

$$\frac{BF(B_s^0 \to K_S^0\pi^+K^-)}{BF(B^0 \to K_S^0\pi^+\pi^-)}_{\text{DD,2017}} = 0.913 \pm 0.033\,(\text{stat.}) \pm 0.029\,(\text{syst.}) \pm 0.028\,(f_s/f_d)$$

$$\frac{BF(B_s^0 \to K_S^0\pi^+K^-)}{BF(B^0 \to K_S^0\pi^+\pi^-)}_{\text{LL,2018}} = 0.887 \pm 0.045\,(\text{stat.}) \pm 0.042\,(\text{syst.}) \pm 0.028\,(f_s/f_d)$$

$$\frac{BF(B_s^0 \to K_S^0\pi^+K^-)}{BF(B^0 \to K_S^0\pi^+\pi^-)}_{\text{DD,2018}} = 0.914 \pm 0.031\,(\text{stat.}) \pm 0.027\,(\text{syst.}) \pm 0.028\,(f_s/f_d)$$

$$\frac{BF(B_s^0 \to K_S^0\pi^+K^-)}{BF(B^0 \to K_S^0\pi^+\pi^-)}_{\text{Averaged}} = 0.916 \pm 0.014\,(\text{stat.}) \pm 0.009\,(\text{syst.uncorr}) \pm 0.013\,(\text{syst.corr}) \pm 0.018\,(f_s/f_d)$$

B_s^0 or $\overline{B}_s^0 \to K_S^0 K^\pm \pi^\pm$: The combination the two final states $K_S^0 K^+\pi^-$ and $K_S^0 K^-\pi^+$ is now realised. Again, there is no distinction between B_s^0 and $\overline{B}_s^0$, so what is measured is the sum of the two ratios of branching fractions, *i.e.*

$$\frac{BF(B_s^0 \to K_S^0 K^\pm \pi^\mp)}{BF(B^0 \to K_S^0 \pi^+\pi^-)} = \frac{BF(B_s^0 \to K_S^0 K^+ \pi^-) + BF(B_s^0 \to K_S^0 K^- \pi^+)}{BF(B^0 \to K_S^0 \pi^+\pi^-)} \tag{C.11.2}$$

$$\frac{BF(B_s^0 \to K_S^0 K^\pm \pi^\mp)}{BF(B^0 \to K_S^0 \pi^+\pi^-)}_{\text{LL,2011}} = 2.02 \pm 0.16\,(\text{stat.}) \pm 0.08\,(\text{syst.}) \pm 0.05\,(f_s/f_d)$$

$$\frac{BF(B_s^0 \to K_S^0 K^\pm \pi^\mp)}{BF(B^0 \to K_S^0 \pi^+\pi^-)}_{\text{DD,2011}} = 1.95 \pm 0.13\,(\text{stat.}) \pm 0.06\,(\text{syst.}) \pm 0.04\,(f_s/f_d)$$

$$\frac{BF(B_s^0 \to K_S^0 K^\pm \pi^\mp)}{BF(B^0 \to K_S^0 \pi^+\pi^-)}_{\text{LL,2012a}} = 1.547 \pm 0.176\,(\text{stat.}) \pm 0.067\,(\text{syst.}) \pm 0.034\,(f_s/f_d)$$

$$\frac{BF(B_s^0 \to K_S^0 K^\pm \pi^\mp)}{BF(B^0 \to K_S^0 \pi^+\pi^-)}_{\text{DD,2012a}} = 1.69 \pm 0.14\,(\text{stat.}) \pm 0.06\,(\text{syst.}) \pm 0.04\,(f_s/f_d)$$

$$\frac{BF(B_s^0 \to K_S^0 K^\pm \pi^\mp)}{BF(B^0 \to K_S^0 \pi^+\pi^-)}_{\text{LL,2012b}} = 1.92 \pm 0.14\,(\text{stat.}) \pm 0.08\,(\text{syst.}) \pm 0.04\,(f_s/f_d)$$

$$\frac{BF(B_s^0 \to K_S^0 K^\pm \pi^\mp)}{BF(B^0 \to K_S^0 \pi^+\pi^-)}_{\text{DD,2012b}} = 1.99 \pm 0.10\,(\text{stat.}) \pm 0.06\,(\text{syst.}) \pm 0.04\,(f_s/f_d)$$

$$\frac{BF(B_s^0 \to K_S^0 K^\pm \pi^\mp)}{BF(B^0 \to K_S^0 \pi^+\pi^-)}_{\text{LL,2015}} = 1.68 \pm 0.17\,(\text{stat.}) \pm 0.06\,(\text{syst.}) \pm 0.04\,(f_s/f_d)$$

$$\frac{BF(B_s^0 \to K_S^0 K^\pm \pi^\mp)}{BF(B^0 \to K_S^0 \pi^+\pi^-)}_{\text{DD,2015}} = 1.94 \pm 0.13\,(\text{stat.}) \pm 0.04\,(\text{syst.}) \pm 0.04\,(f_s/f_d)$$

$$\frac{BF(B_s^0 \to K_S^0 K^\pm \pi^\mp)}{BF(B^0 \to K_S^0 \pi^+\pi^-)}_{\text{LL,2016}} = 1.74 \pm 0.07\,(\text{stat.}) \pm 0.04\,(\text{syst.}) \pm 0.04\,(f_s/f_d)$$

$$\frac{BF(B_s^0 \to K_S^0 K^\pm \pi^\mp)}{BF(B^0 \to K_S^0 \pi^+\pi^-)}_{\text{DD,2016}} = 1.785 \pm 0.051\,(\text{stat.}) \pm 0.032\,(\text{syst.}) \pm 0.039\,(f_s/f_d)$$

$$\frac{BF(B_s^0 \to K_S^0 K^\pm \pi^\mp)}{BF(B^0 \to K_S^0 \pi^+\pi^-)}_{\text{LL,2017}} = 1.70 \pm 0.07\,(\text{stat.}) \pm 0.05\,(\text{syst.}) \pm 0.04\,(f_s/f_d)$$

$$\frac{BF(B_s^0 \to K_S^0 K^\pm \pi^\mp)}{BF(B^0 \to K_S^0 \pi^+\pi^-)}_{\text{DD,2017}} = 1.805 \pm 0.047\,(\text{stat.}) \pm 0.029\,(\text{syst.}) \pm 0.040\,(f_s/f_d)$$

$$\frac{BF(B_s^0 \to K_S^0 K^\pm \pi^\mp)}{BF(B^0 \to K_S^0 \pi^+\pi^-)}_{\text{LL,2018}} = 1.76 \pm 0.06\,(\text{stat.}) \pm 0.04\,(\text{syst.}) \pm 0.04\,(f_s/f_d)$$

$$\frac{BF(B_s^0 \to K_S^0 K^\pm \pi^\mp)}{BF(B^0 \to K_S^0 \pi^+\pi^-)}_{\text{DD,2018}} = 1.758 \pm 0.043\,(\text{stat.}) \pm 0.027\,(\text{syst.}) \pm 0.039\,(f_s/f_d)$$

$$\frac{BF(B_s^0 \to K_S^0 K^\pm \pi^\mp)}{BF(B^0 \to K_S^0 \pi^+\pi^-)}_{\text{Averaged}} = 1.782 \pm 0.020\,(\text{stat.}) \pm 0.013\,(\text{syst.uncorr}) \pm 0.020\,(\text{syst.corr}) \pm 0.025\,(f_s/f_d)$$

C.11.5 $B^0_s \to K^0_S K^+ K^-$

$\frac{BF(B^0_s \to K^0_S K^+ K^-)}{BF(B^0 \to K^0_S \pi^+ \pi^-)}_{\text{LL,2011}}$	$= 0.129$	$\pm 0.062\,(\text{stat.})$	$\pm 0.040\,(\text{syst.})$	$\pm 0.004\,(f_s/f_d)$
$\frac{BF(B^0_s \to K^0_S K^+ K^-)}{BF(B^0 \to K^0_S \pi^+ \pi^-)}_{\text{DD,2011}}$	$= 0.128$	$\pm 0.043\,(\text{stat.})$	$\pm 0.041\,(\text{syst.})$	$\pm 0.004\,(f_s/f_d)$
$\frac{BF(B^0_s \to K^0_S K^+ K^-)}{BF(B^0 \to K^0_S \pi^+ \pi^-)}_{\text{LL,2012a}}$	$= 0.123$	$\pm 0.073\,(\text{stat.})$	$\pm 0.053\,(\text{syst.})$	$\pm 0.004\,(f_s/f_d)$
$\frac{BF(B^0_s \to K^0_S K^+ K^-)}{BF(B^0 \to K^0_S \pi^+ \pi^-)}_{\text{DD,2012a}}$	$= 0.0630$	$\pm 0.0328\,(\text{stat.})$	$\pm 0.0148\,(\text{syst.})$	$\pm 0.0020\,(f_s/f_d)$
$\frac{BF(B^0_s \to K^0_S K^+ K^-)}{BF(B^0 \to K^0_S \pi^+ \pi^-)}_{\text{LL,2012b}}$	$= 0.0845$	$\pm 0.0331\,(\text{stat.})$	$\pm 0.0351\,(\text{syst.})$	$\pm 0.0027\,(f_s/f_d)$
$\frac{BF(B^0_s \to K^0_S K^+ K^-)}{BF(B^0 \to K^0_S \pi^+ \pi^-)}_{\text{DD,2012b}}$	$= 0.0447$	$\pm 0.0214\,(\text{stat.})$	$\pm 0.0210\,(\text{syst.})$	$\pm 0.0014\,(f_s/f_d)$
$\frac{BF(B^0_s \to K^0_S K^+ K^-)}{BF(B^0 \to K^0_S \pi^+ \pi^-)}_{\text{LL,2015}}$	$= 0.0749$	$\pm 0.0403\,(\text{stat.})$	$\pm 0.0283\,(\text{syst.})$	$\pm 0.0023\,(f_s/f_d)$
$\frac{BF(B^0_s \to K^0_S K^+ K^-)}{BF(B^0 \to K^0_S \pi^+ \pi^-)}_{\text{DD,2015}}$	$= 0.0745$	$\pm 0.0374\,(\text{stat.})$	$\pm 0.0307\,(\text{syst.})$	$\pm 0.0023\,(f_s/f_d)$
$\frac{BF(B^0_s \to K^0_S K^+ K^-)}{BF(B^0 \to K^0_S \pi^+ \pi^-)}_{\text{LL,2016}}$	$= 0.00302$	$\pm 0.00829\,(\text{stat.})$	$\pm 0.00577\,(\text{syst.})$	$\pm 0.00009\,(f_s/f_d)$
$\frac{BF(B^0_s \to K^0_S K^+ K^-)}{BF(B^0 \to K^0_S \pi^+ \pi^-)}_{\text{DD,2016}}$	$= 0.0689$	$\pm 0.0124\,(\text{stat.})$	$\pm 0.0133\,(\text{syst.})$	$\pm 0.0021\,(f_s/f_d)$
$\frac{BF(B^0_s \to K^0_S K^+ K^-)}{BF(B^0 \to K^0_S \pi^+ \pi^-)}_{\text{LL,2017}}$	$= 0.0381$	$\pm 0.0121\,(\text{stat.})$	$\pm 0.0088\,(\text{syst.})$	$\pm 0.0012\,(f_s/f_d)$
$\frac{BF(B^0_s \to K^0_S K^+ K^-)}{BF(B^0 \to K^0_S \pi^+ \pi^-)}_{\text{DD,2017}}$	$= 0.0496$	$\pm 0.0118\,(\text{stat.})$	$\pm 0.0207\,(\text{syst.})$	$\pm 0.0015\,(f_s/f_d)$
$\frac{BF(B^0_s \to K^0_S K^+ K^-)}{BF(B^0 \to K^0_S \pi^+ \pi^-)}_{\text{LL,2018}}$	$= 0.0287$	$\pm 0.0115\,(\text{stat.})$	$\pm 0.0092\,(\text{syst.})$	$\pm 0.0009\,(f_s/f_d)$
$\frac{BF(B^0_s \to K^0_S K^+ K^-)}{BF(B^0 \to K^0_S \pi^+ \pi^-)}_{\text{DD,2018}}$	$= 0.0355$	$\pm 0.0099\,(\text{stat.})$	$\pm 0.0156\,(\text{syst.})$	$\pm 0.0011\,(f_s/f_d)$
$\frac{BF(B^0_s \to K^0_S K^+ K^-)}{BF(B^0 \to K^0_S \pi^+ \pi^-)}_{\text{Averaged}}$	$= 0.0343$	$\pm 0.0044\,(\text{stat.})$	$\pm 0.0031\,(\text{syst.uncorr}) \pm 0.0042\,(\text{syst.corr})$	$\pm 0.0006\,(f_s/f_d)$

Appendix D

Appendix to Chapter 5

D.1 Discriminative variables distributions

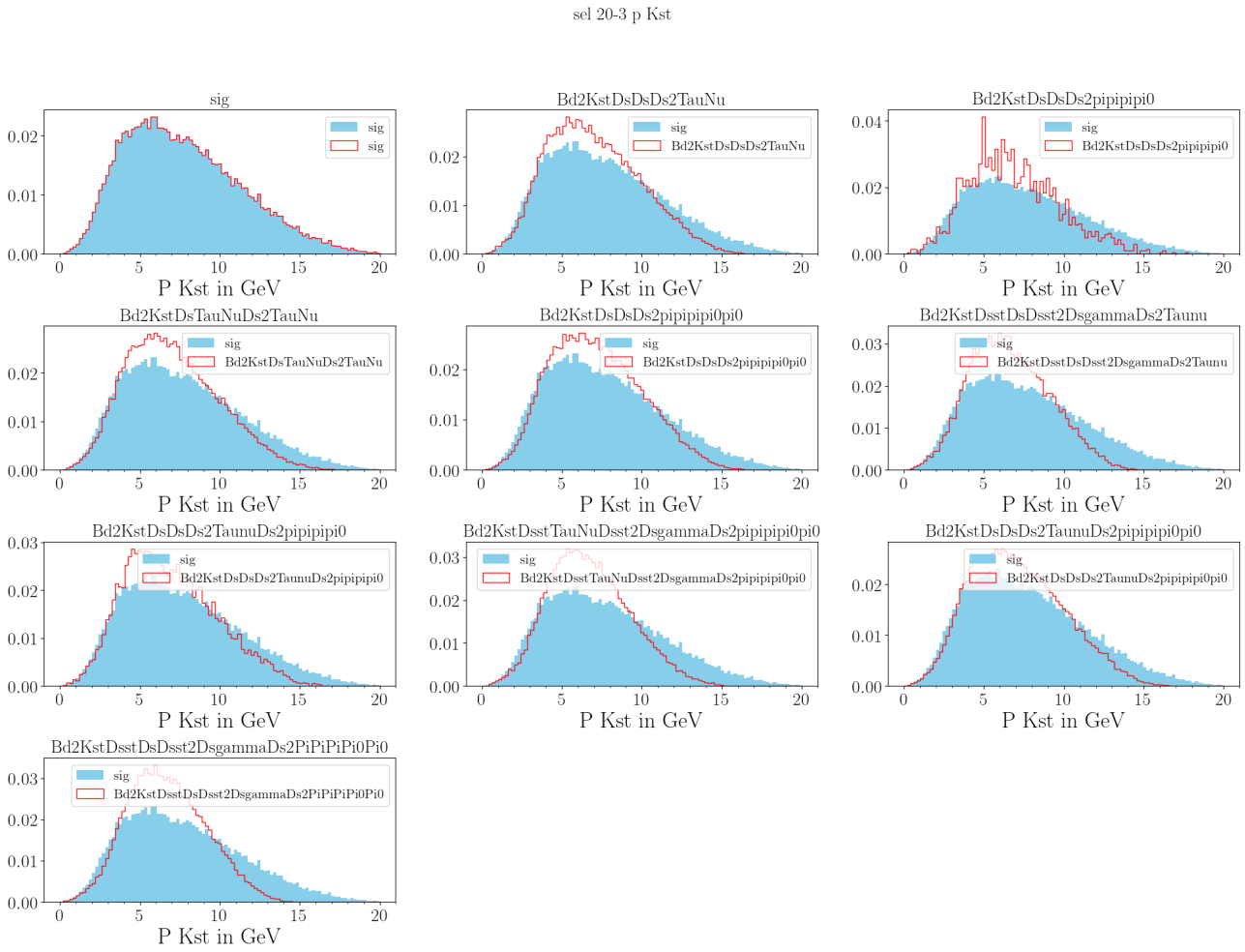

Figure D.1: $p_{K^{*0}}$ candidates distribution as function of the mode.

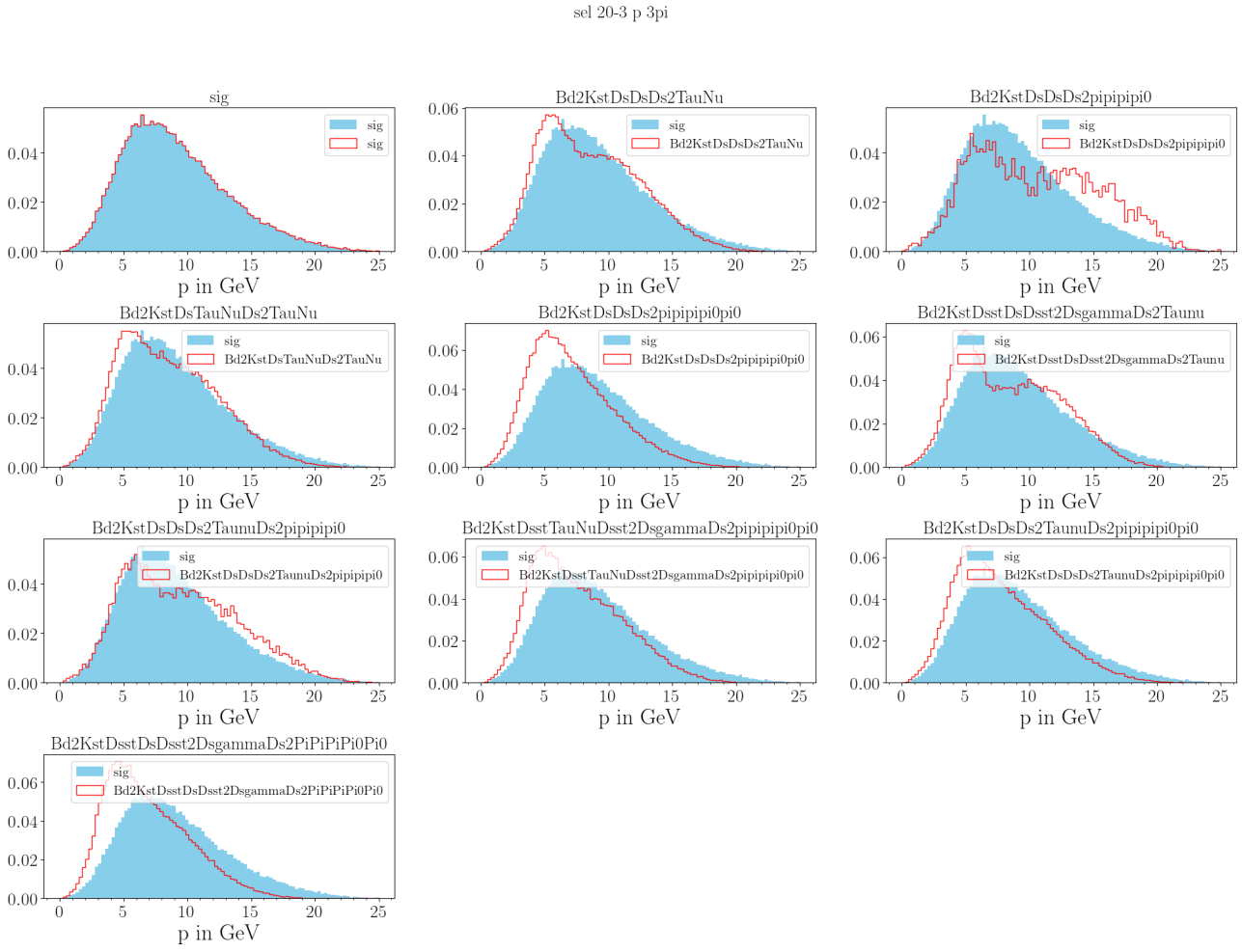

Figure D.2: $p_{3\pi}$ from τ candidates distribution as function of the mode.

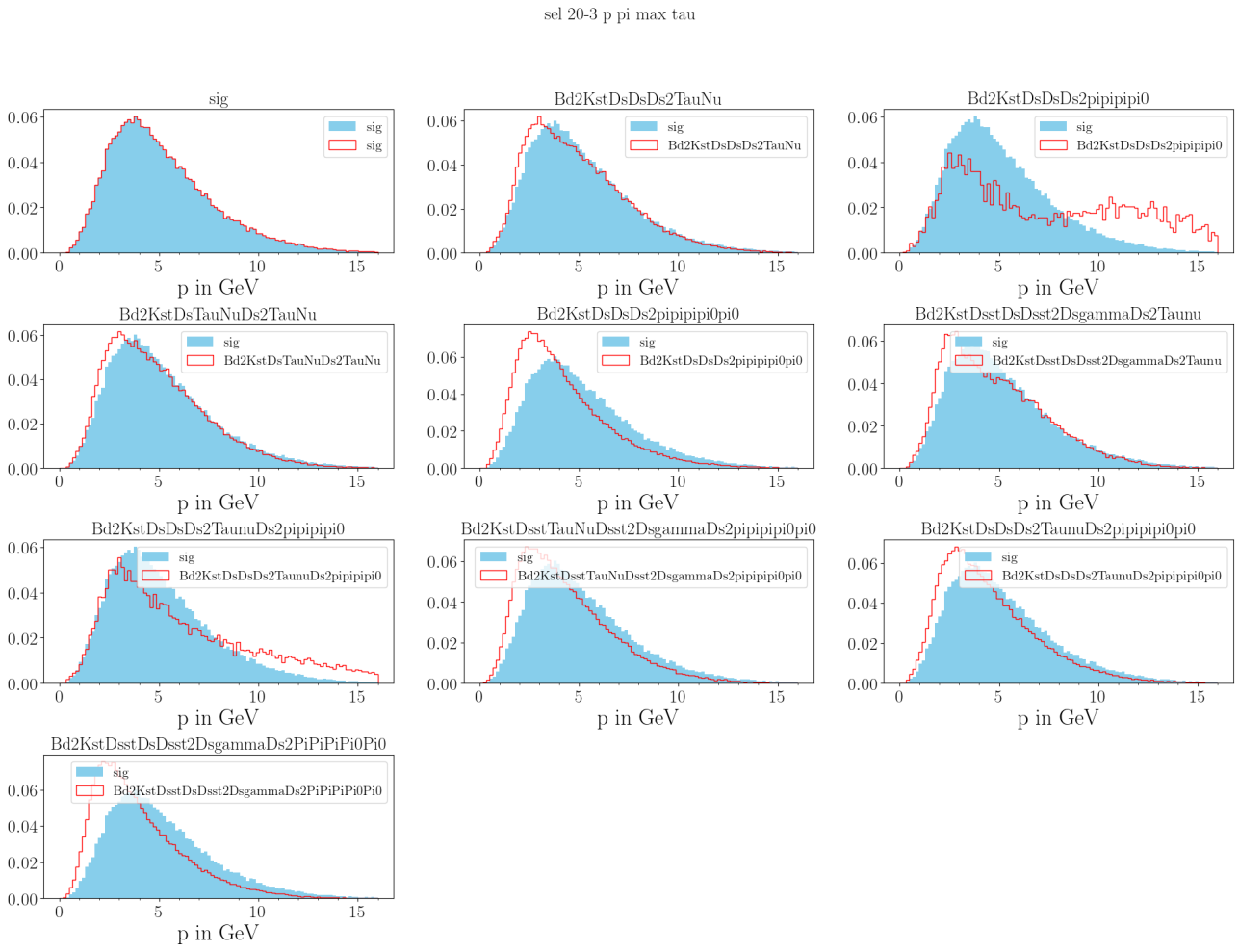

Figure D.3: $p_{\pi_{max}}$ from τ candidates distribution as function of the mode.

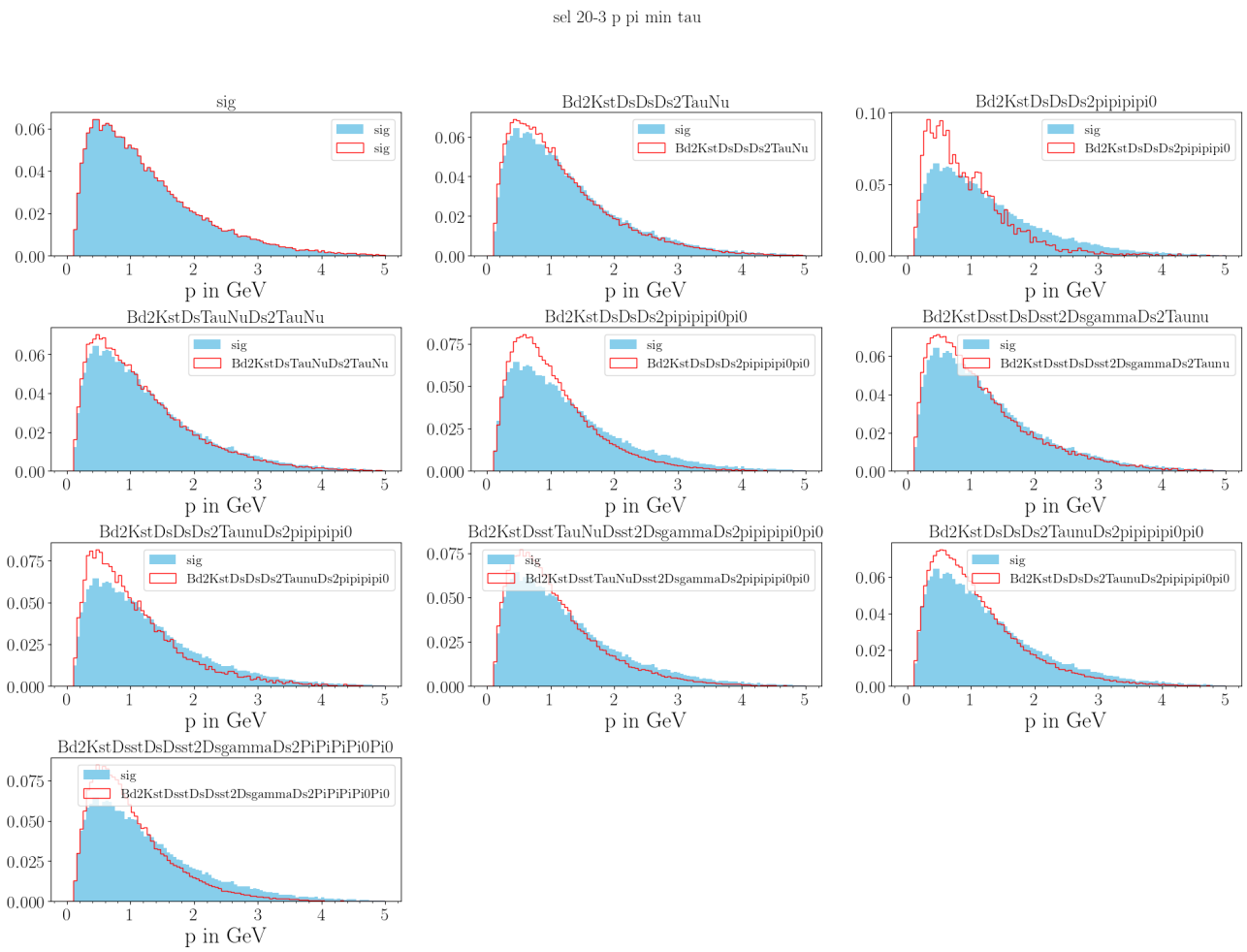

Figure D.4: $p_{\pi_{min}}$ from τ candidates distribution as function of the mode.

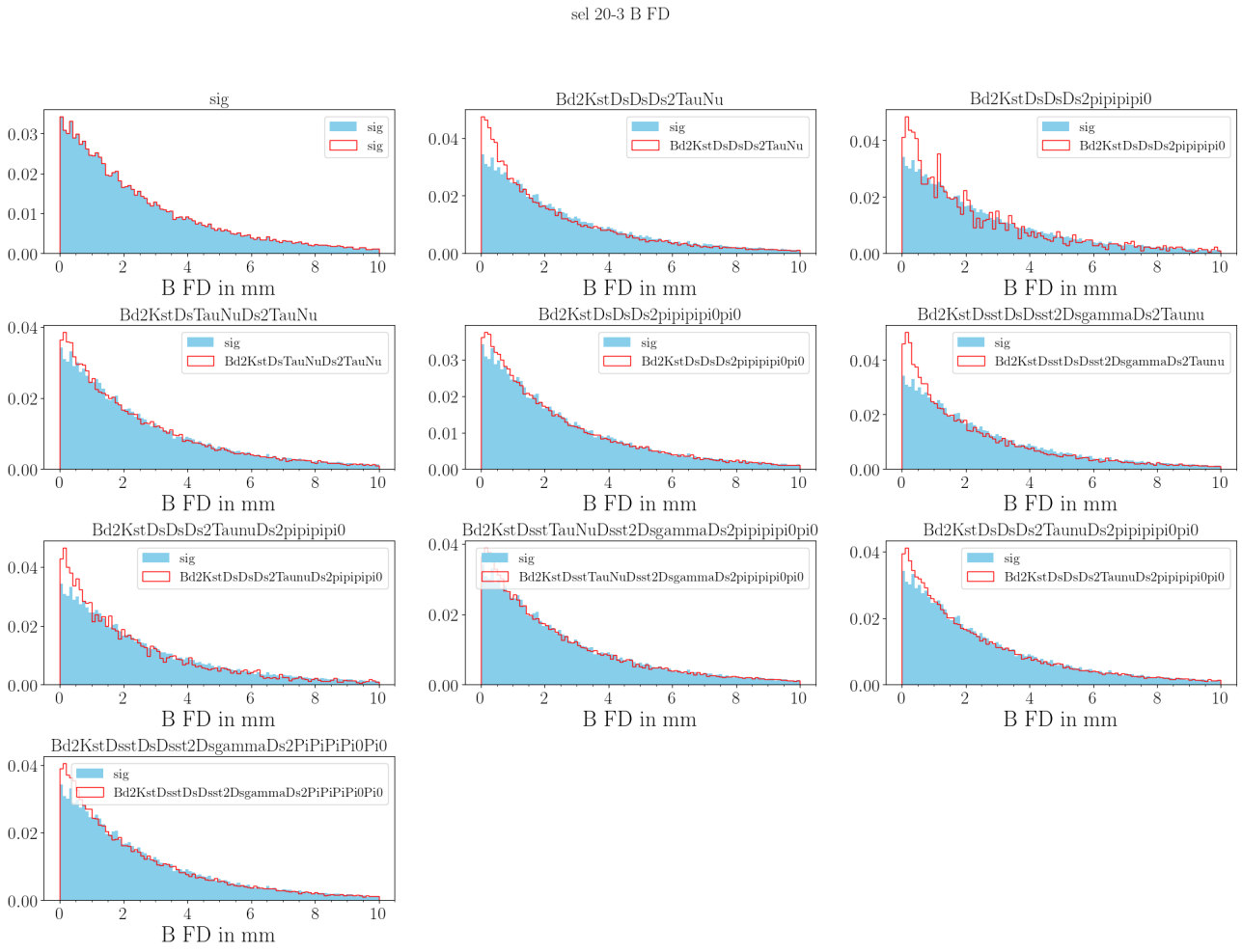

Figure D.5: FD_{B^0} candidates distribution as function of the mode.

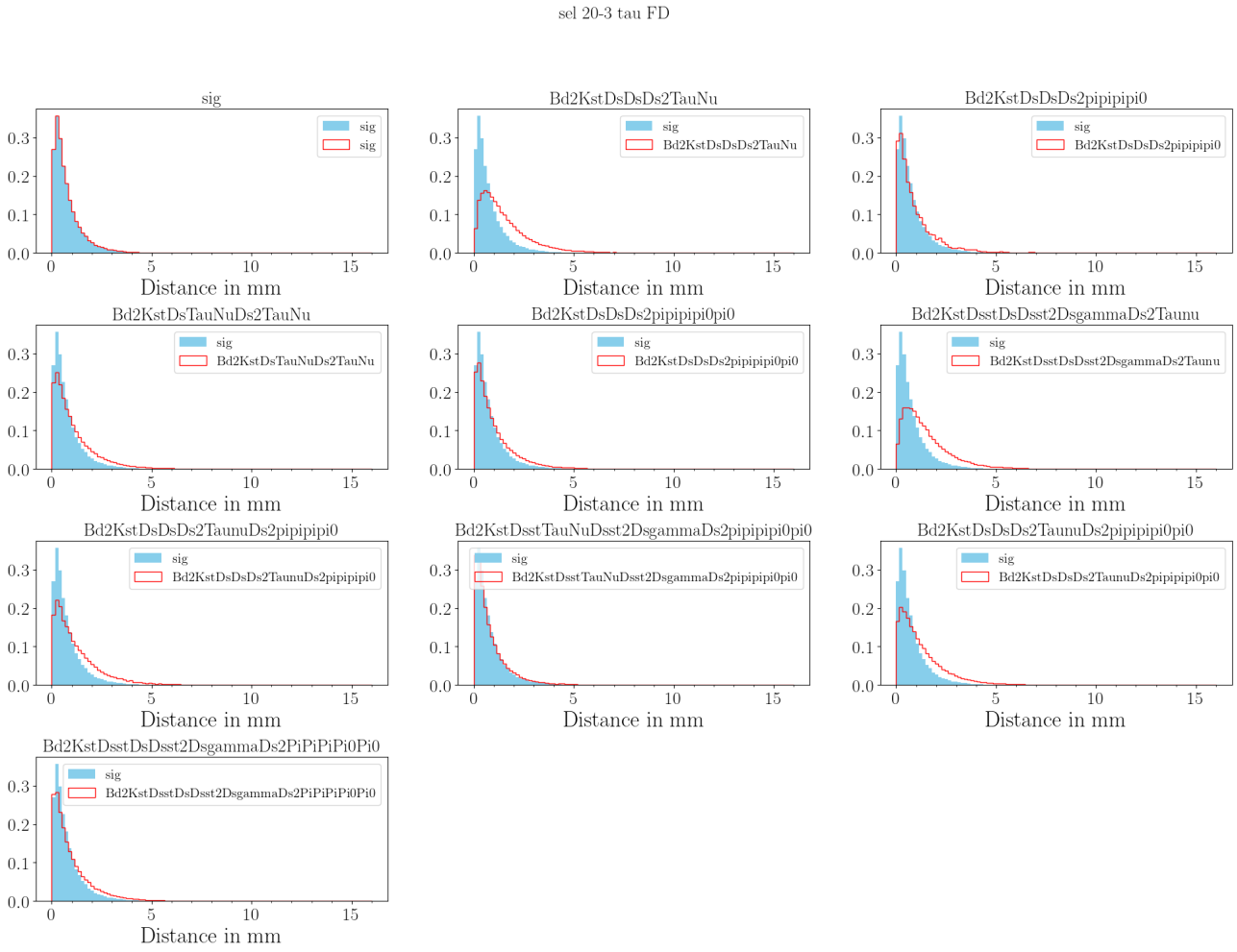

Figure D.6: FD_τ candidates distribution as function of the mode.

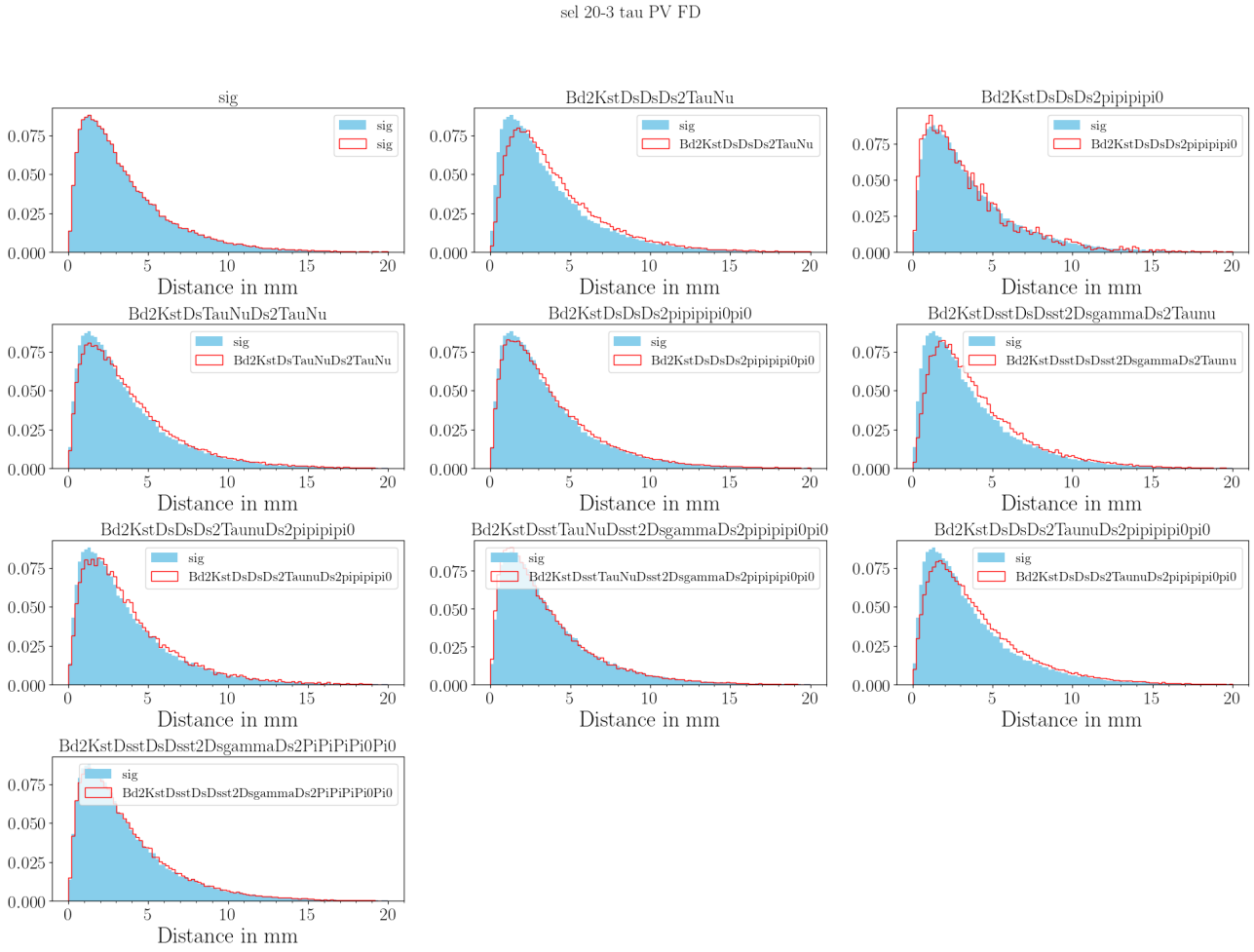

Figure D.7: PV to TV distance distribution as function of the mode.

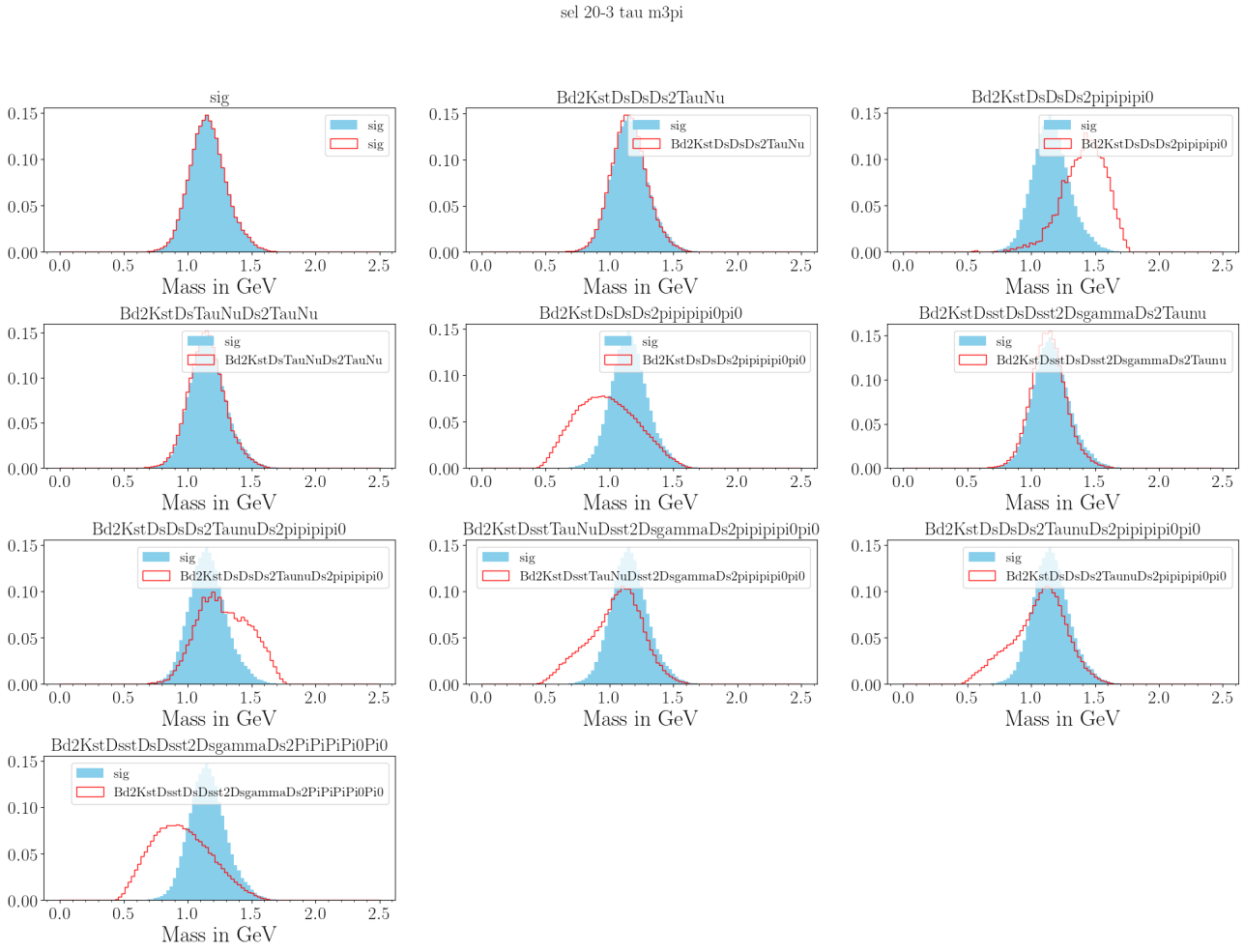

Figure D.8: $m_{3\pi}$ from τ candidates distribution as function of the mode.

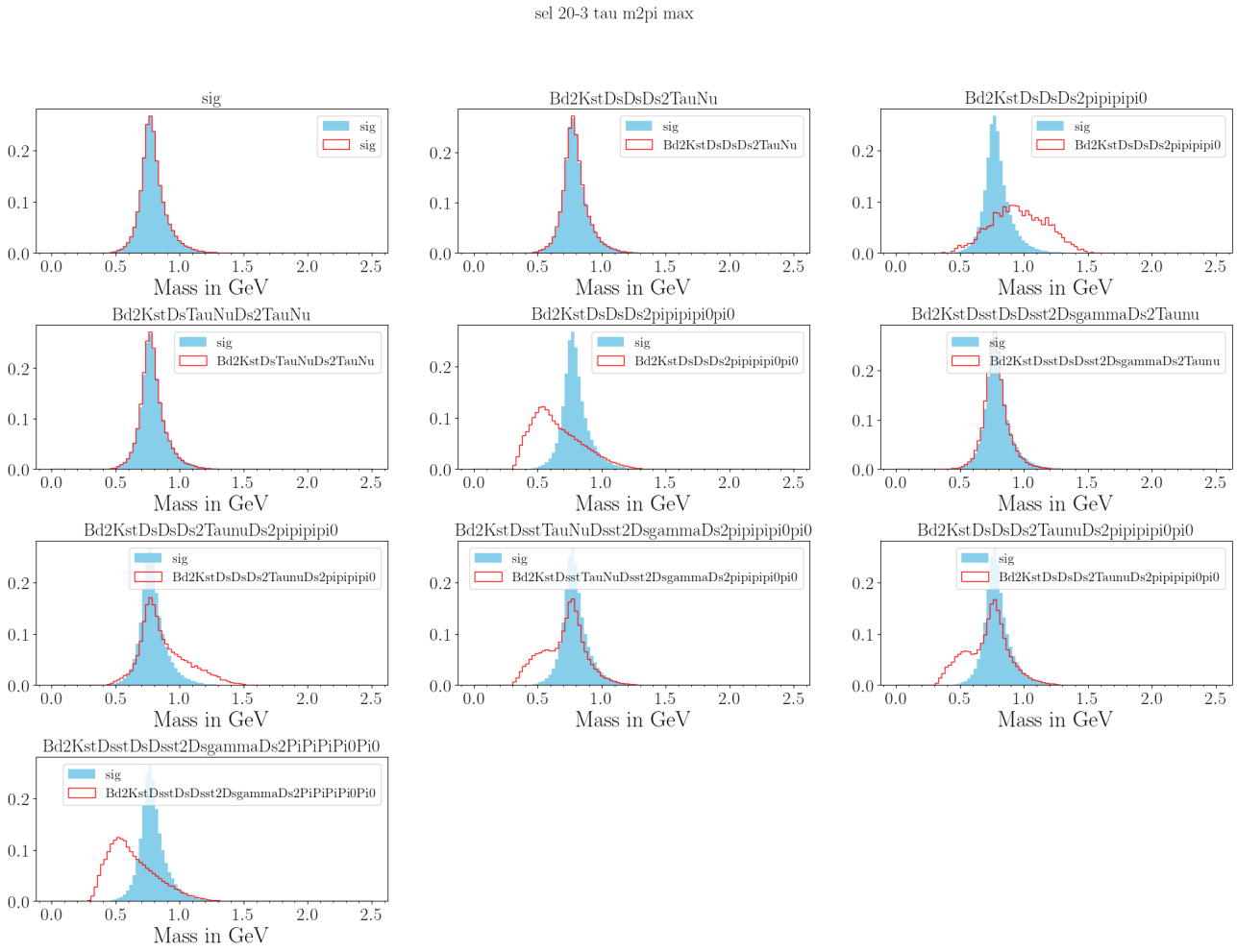

Figure D.9: $m_{2\pi\,max}$ from τ candidates distribution as function of the mode.

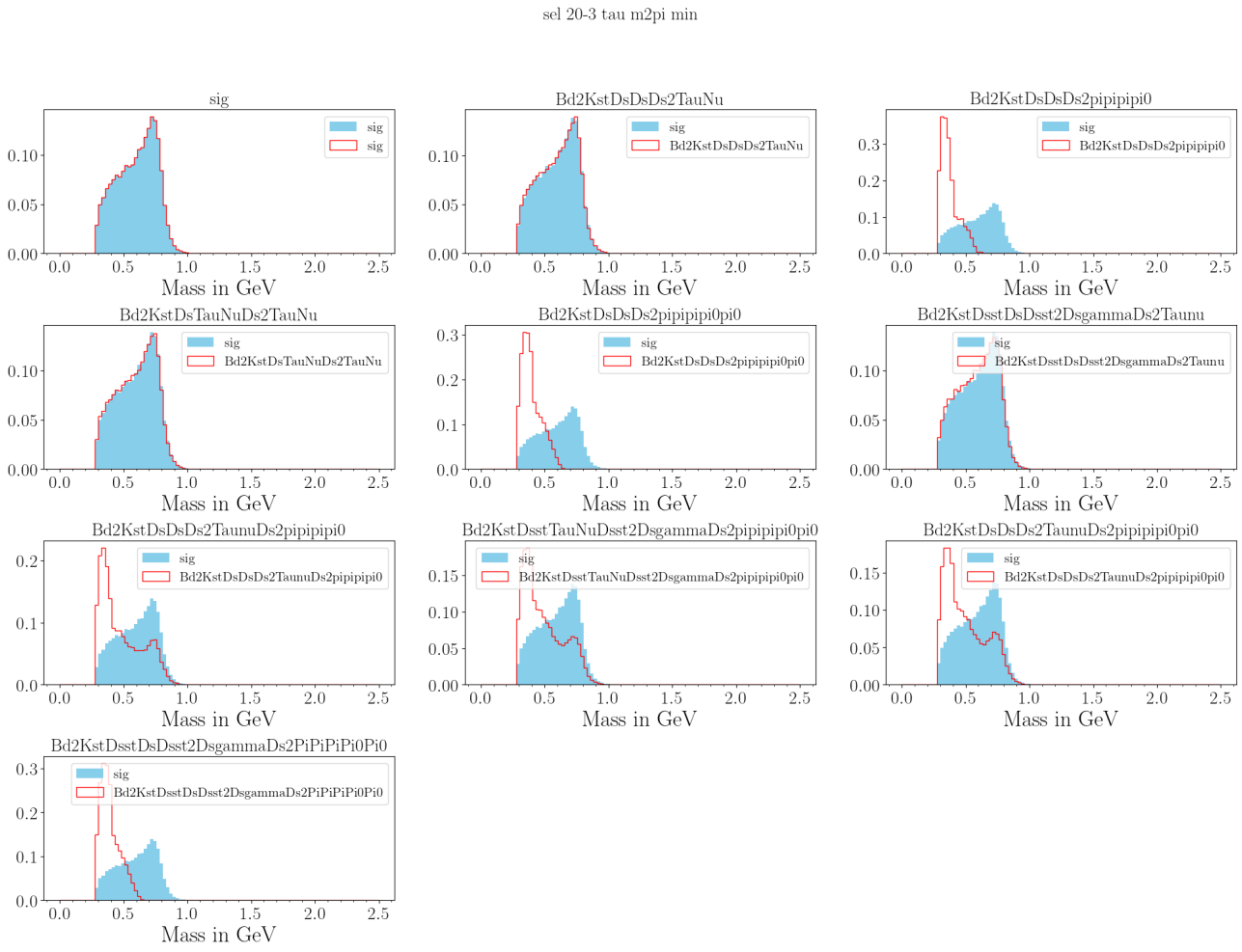

Figure D.10: $m_{2\pi\,min}$ from τ candidates distribution as function of the mode.

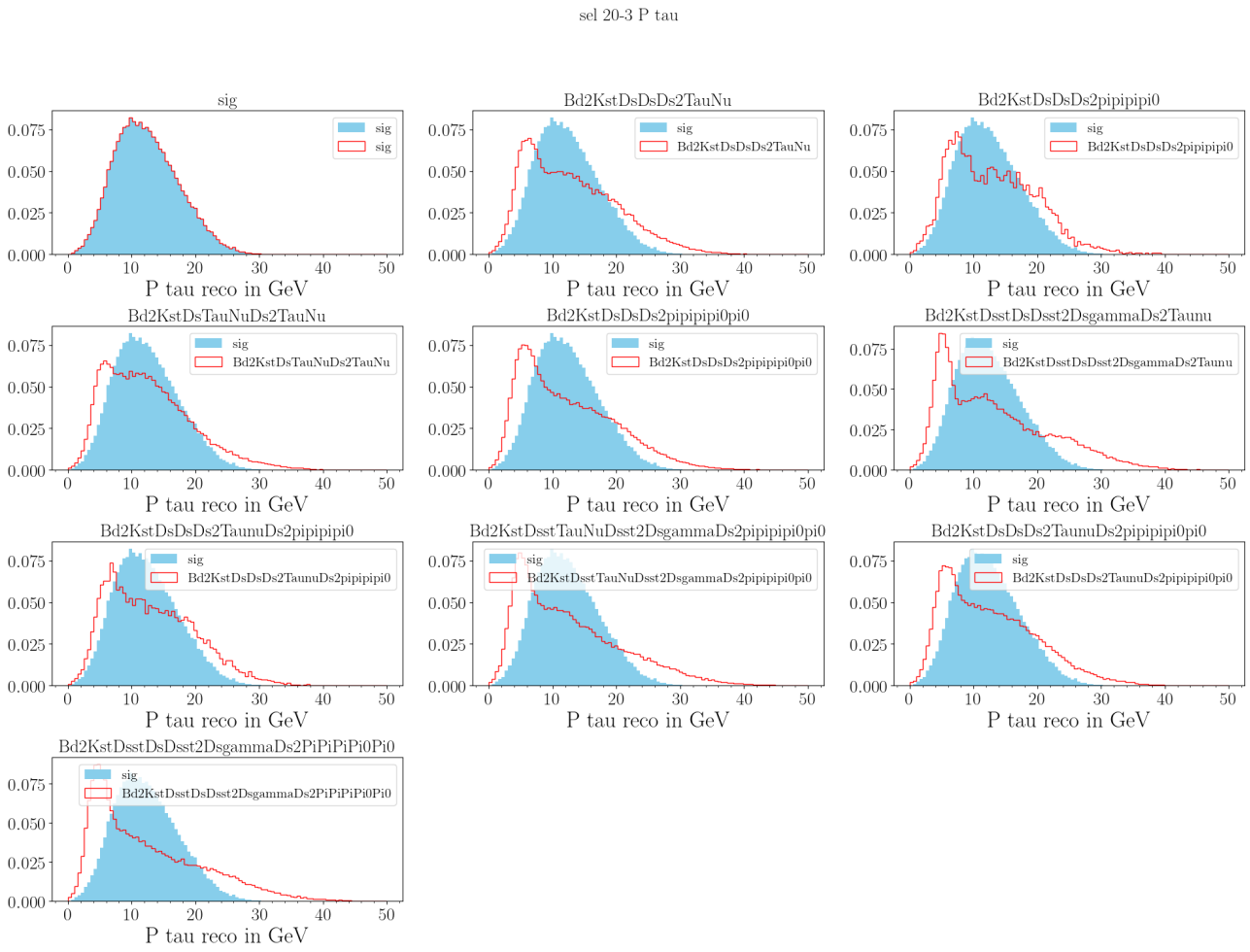

Figure D.11: p_τ reconstructed with ν from τ candidates distribution as function of the mode.

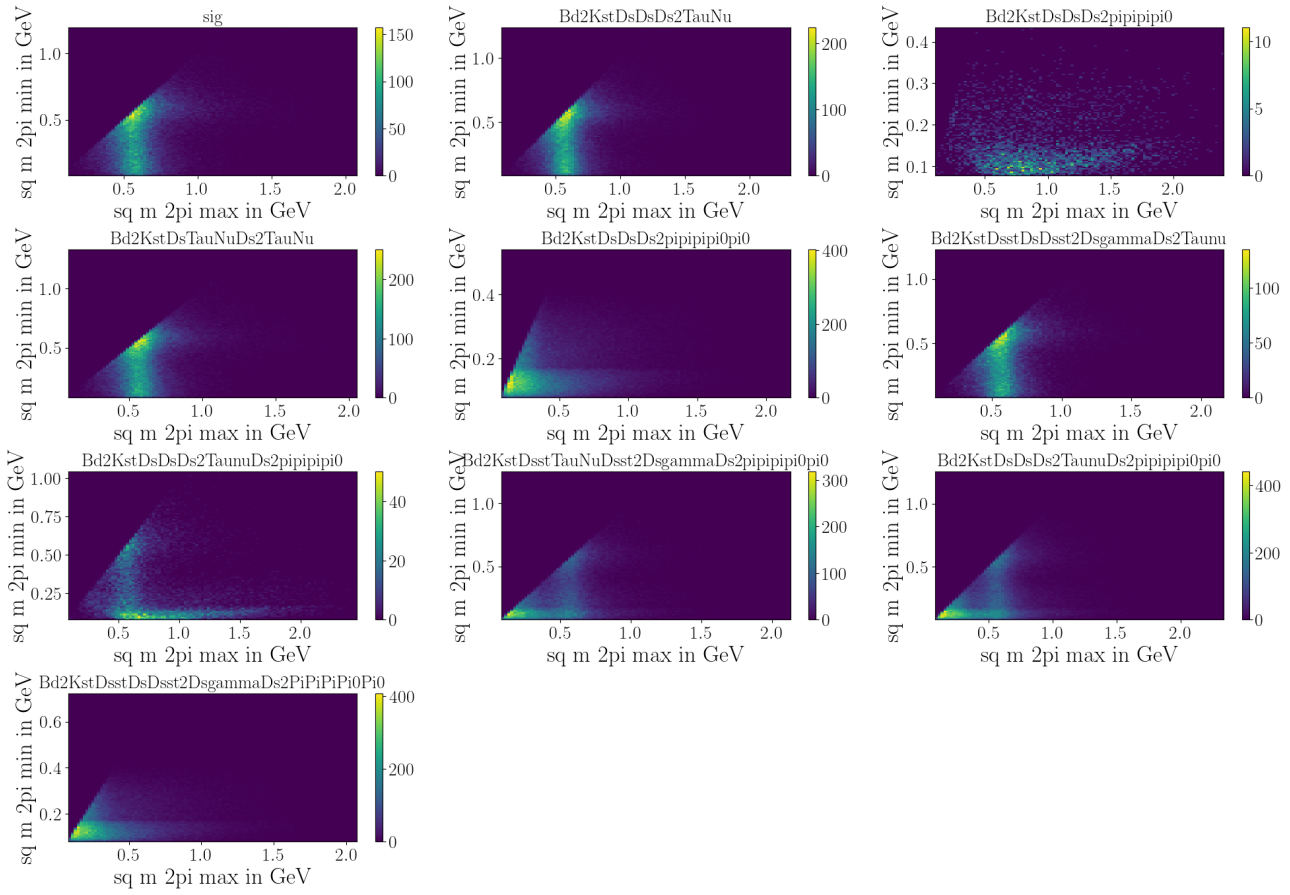

Figure D.12: Dalitz plan built from $m_{2\pi}$ of τ candidates distribution as function of the mode.

D.2 Precision of the BF measurement extra-plots

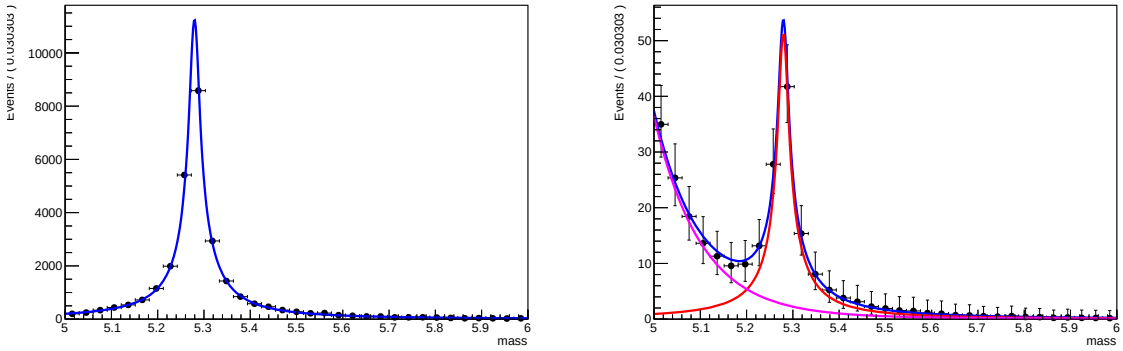

Figure D.13: Fit of the signal (left) and fit of signal + background (right) in order to determine the precision on the BF measurement for the $5-1\mu m$ working point.

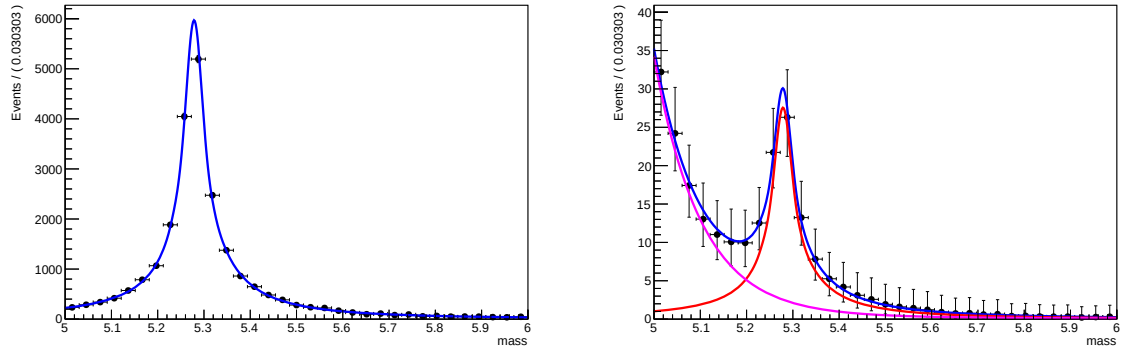

Figure D.14: Fit of the signal (left) and fit of signal + background (right) in order to determine the precision on the BF measurement for the $5-2\mu m$ working point.

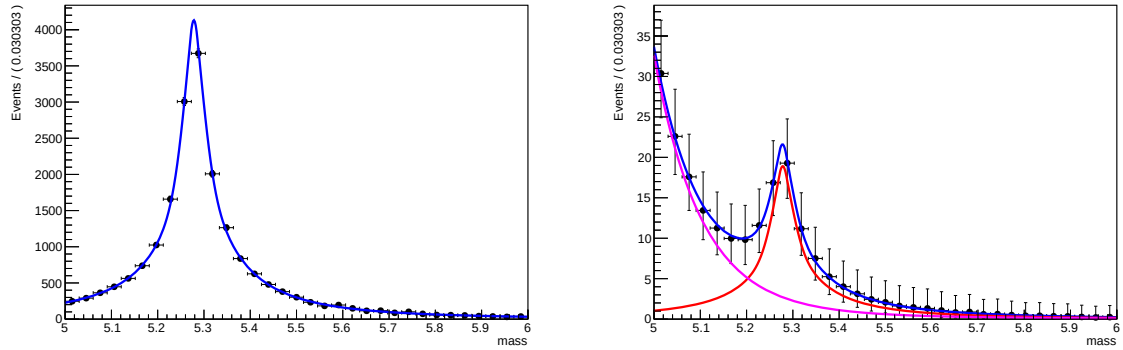

Figure D.15: Fit of the signal (left) and fit of signal + background (right) in order to determine the precision on the BF measurement for the $5-3\mu m$ working point.

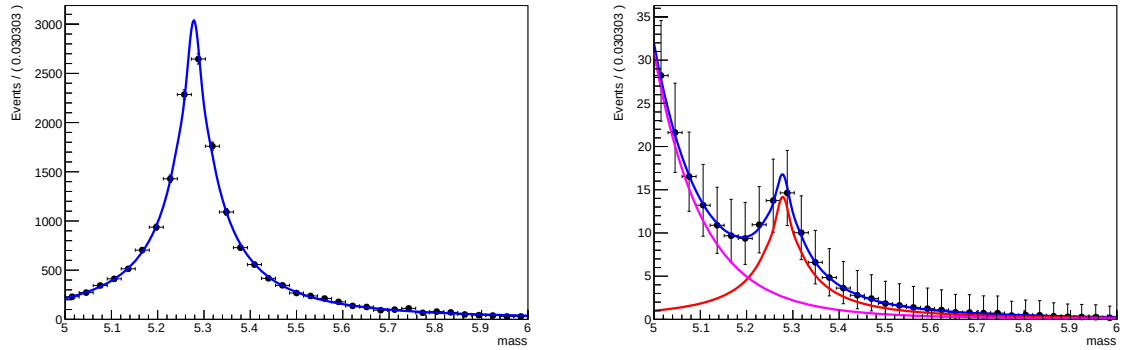

Figure D.16: Fit of the signal (left) and fit of signal + background (right) in order to determine the precision on the BF measurement for the $5-4\mu$m working point.

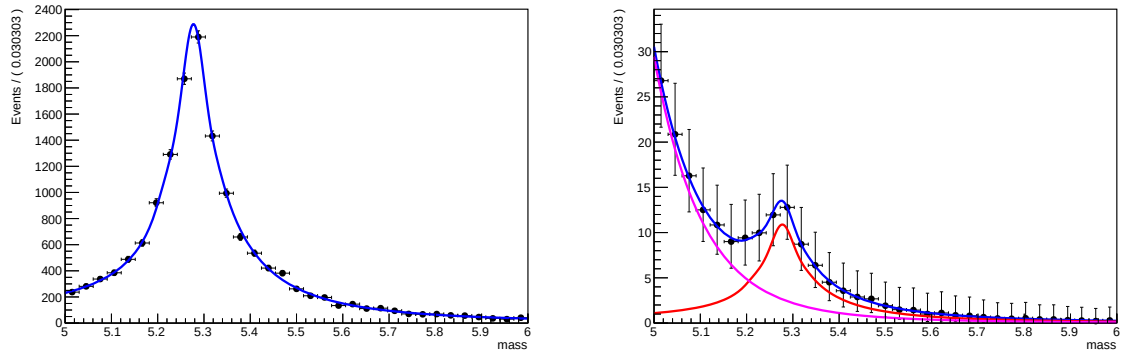

Figure D.17: Fit of the signal (left) and fit of signal + background (right) in order to determine the precision on the BF measurement for the $5-5\mu$m working point.

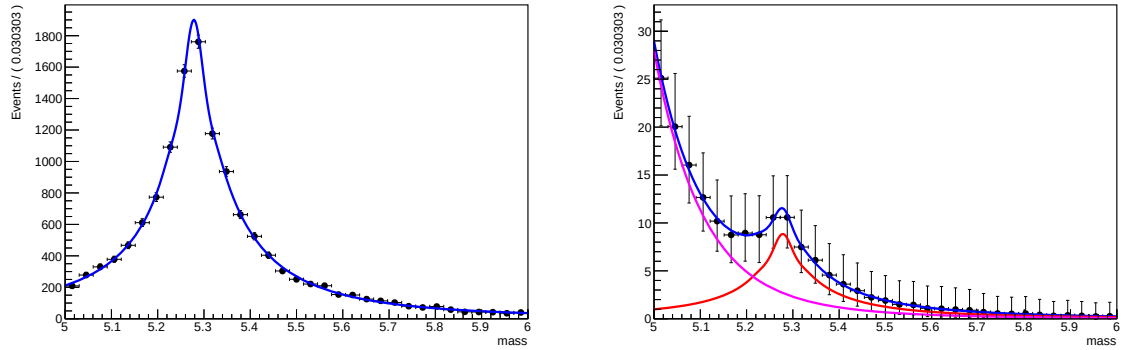

Figure D.18: Fit of the signal (left) and fit of signal + background (right) in order to determine the precision on the BF measurement for the $5-6\mu$m working point.

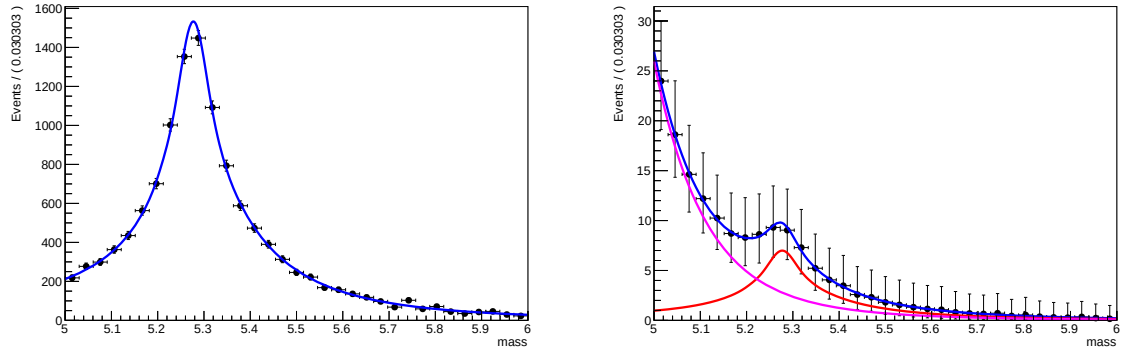

Figure D.19: Fit of the signal (left) and fit of signal + background (right) in order to determine the precision on the BF measurement for the $5-7\mu$m working point.

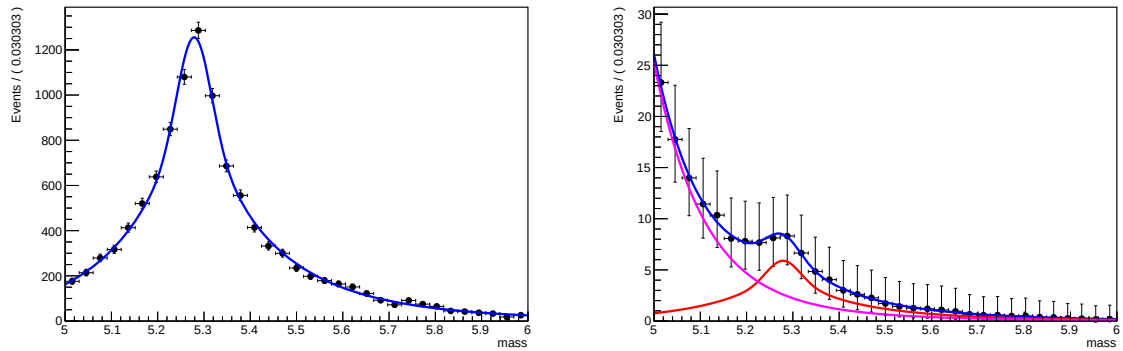

Figure D.20: Fit of the signal (left) and fit of signal + background (right) in order to determine the precision on the BF measurement for the $5-8\mu$m working point.

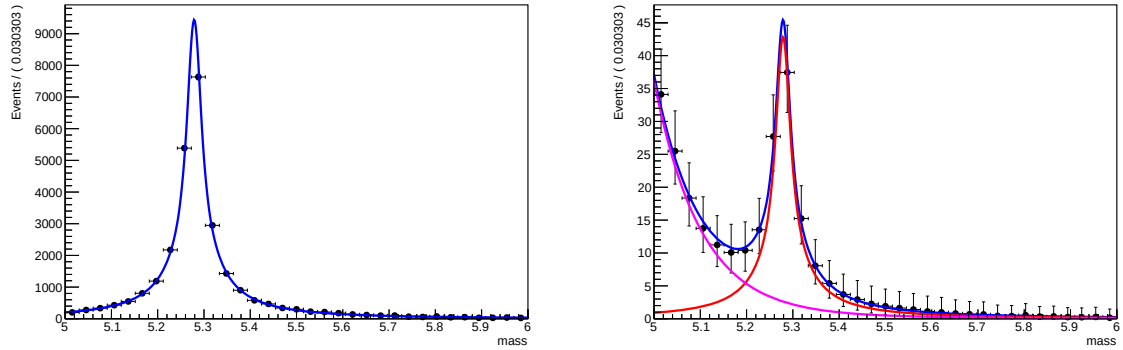

Figure D.21: Fit of the signal (left) and fit of signal + background (right) in order to determine the precision on the BF measurement for the $10-1\mu$m working point.

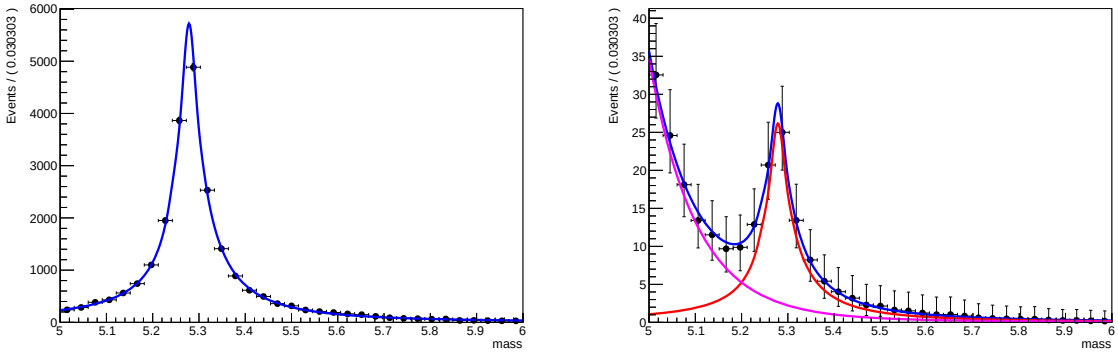

Figure D.22: Fit of the signal (left) and fit of signal + background (right) in order to determine the precision on the BF measurement for the $10-2\mu$m working point.

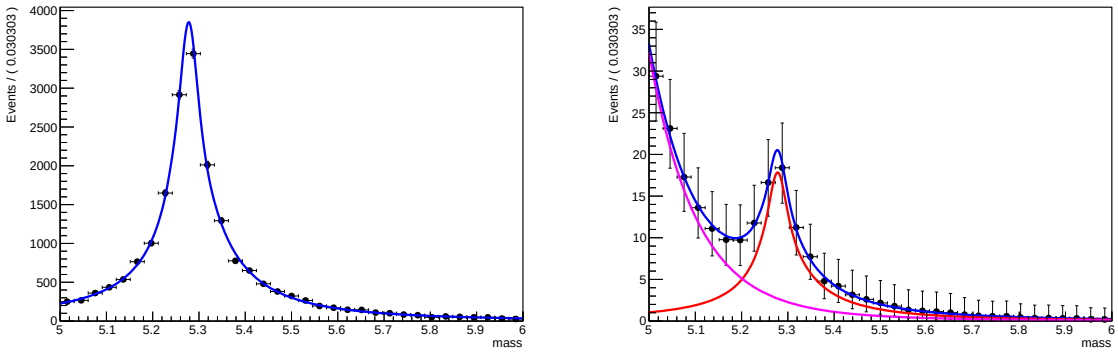

Figure D.23: Fit of the signal (left) and fit of signal + background (right) in order to determine the precision on the BF measurement for the $10-3\mu$m working point.

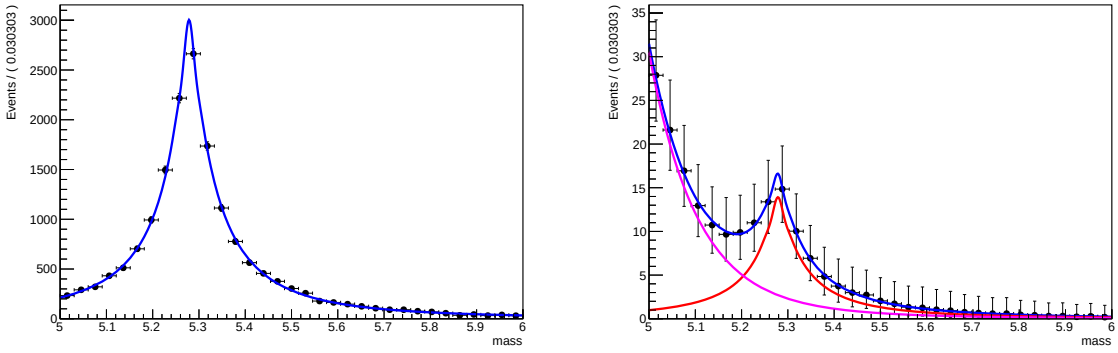

Figure D.24: Fit of the signal (left) and fit of signal + background (right) in order to determine the precision on the BF measurement for the $10-4\mu$m working point.

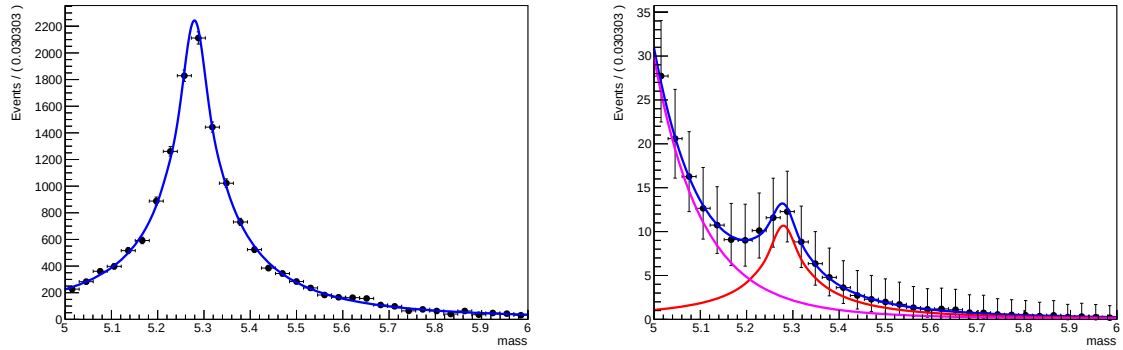

Figure D.25: Fit of the signal (left) and fit of signal + background (right) in order to determine the precision on the BF measurement for the $10-5\mu$m working point.

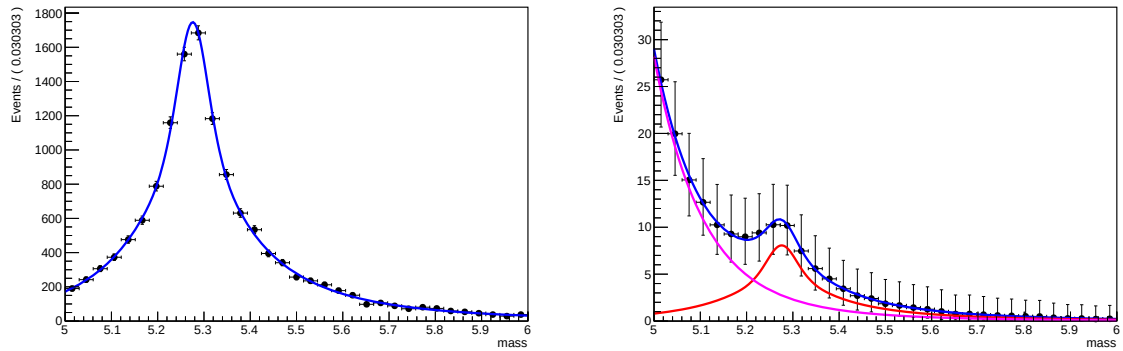

Figure D.26: Fit of the signal (left) and fit of signal + background (right) in order to determine the precision on the BF measurement for the $10-6\mu$m working point.

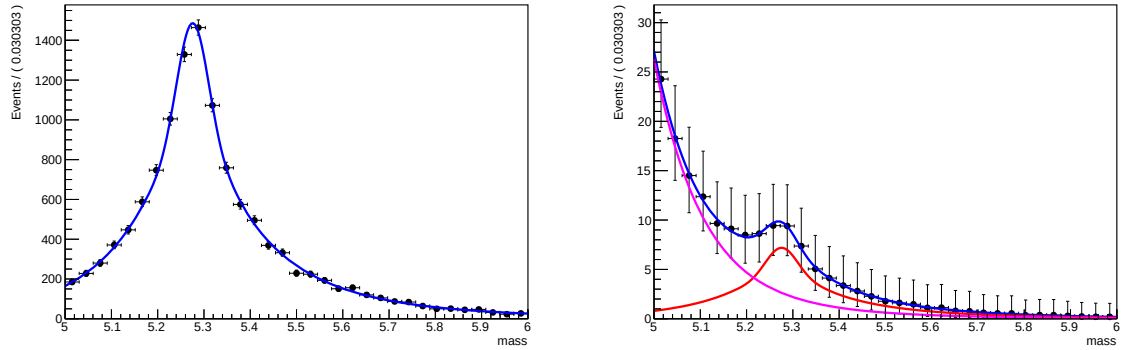

Figure D.27: Fit of the signal (left) and fit of signal + background (right) in order to determine the precision on the BF measurement for the $10-7\mu$m working point.

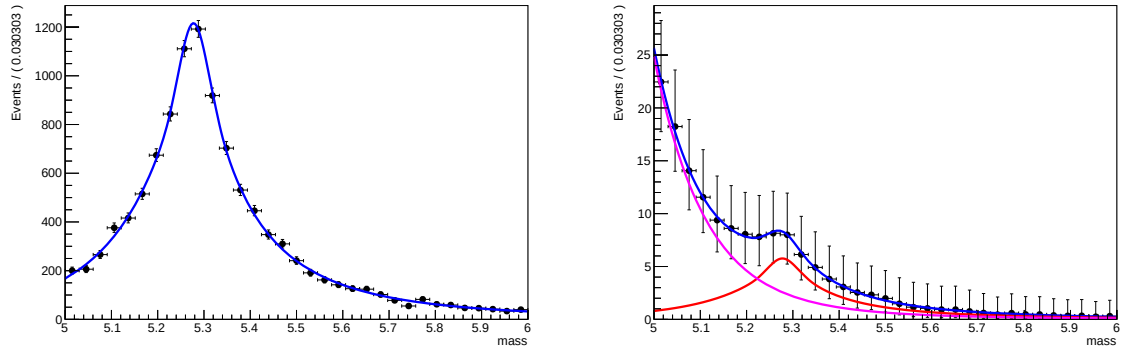

Figure D.28: Fit of the signal (left) and fit of signal + background (right) in order to determine the precision on the BF measurement for the $10-8\mu$m working point.

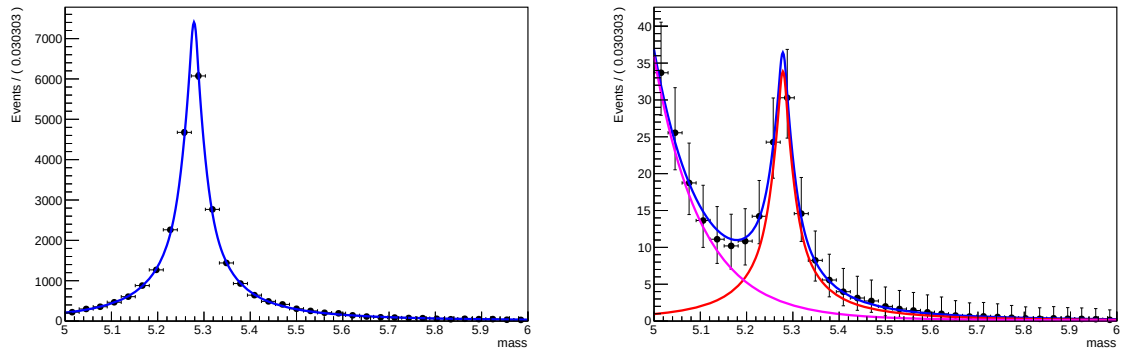

Figure D.29: Fit of the signal (left) and fit of signal + background (right) in order to determine the precision on the BF measurement for the $20-1\mu$m working point.

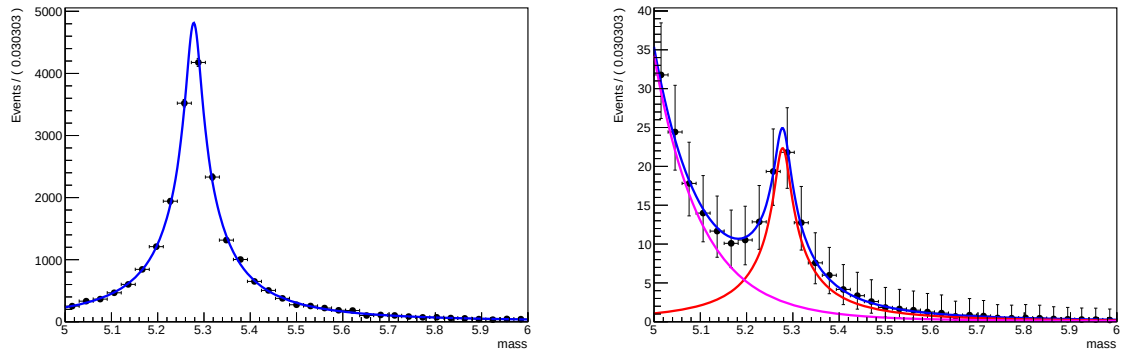

Figure D.30: Fit of the signal (left) and fit of signal + background (right) in order to determine the precision on the BF measurement for the $20-2\mu$m working point.

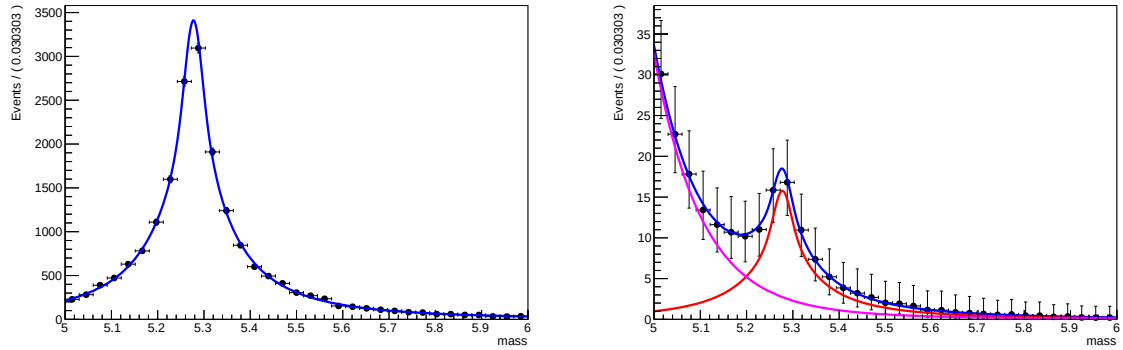

Figure D.31: Fit of the signal (left) and fit of signal + background (right) in order to determine the precision on the BF measurement for the $20-3\mu$m working point.

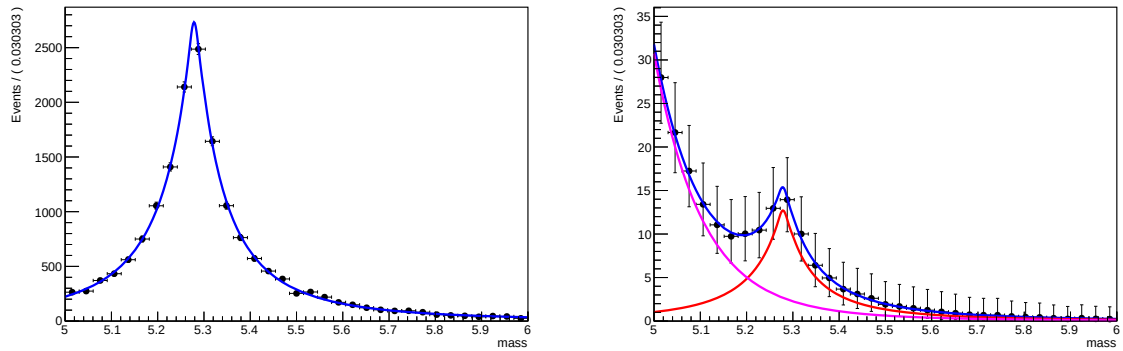

Figure D.32: Fit of the signal (left) and fit of signal + background (right) in order to determine the precision on the BF measurement for the $20-4\mu$m working point.

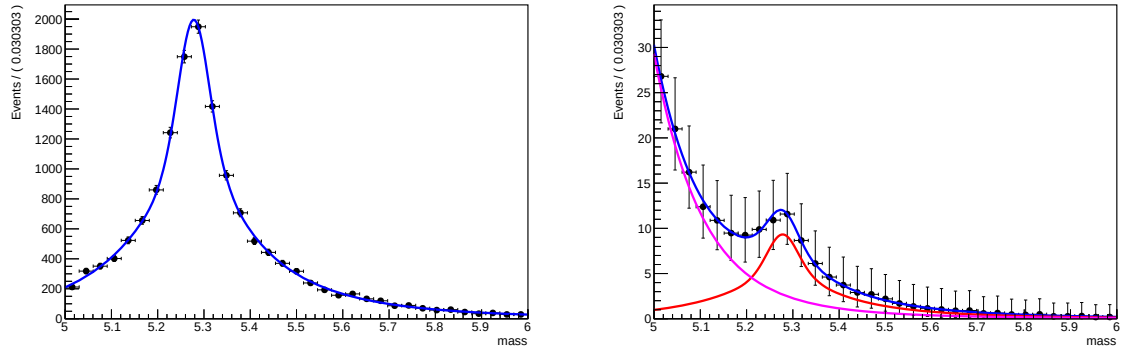

Figure D.33: Fit of the signal (left) and fit of signal + background (right) in order to determine the precision on the BF measurement for the $20-5\mu$m working point.

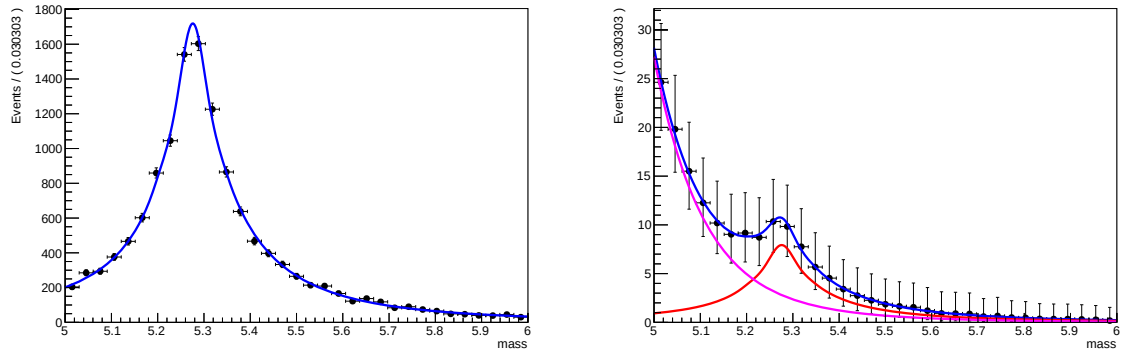

Figure D.34: Fit of the signal (left) and fit of signal + background (right) in order to determine the precision on the BF measurement for the $20-6\mu$m working point.

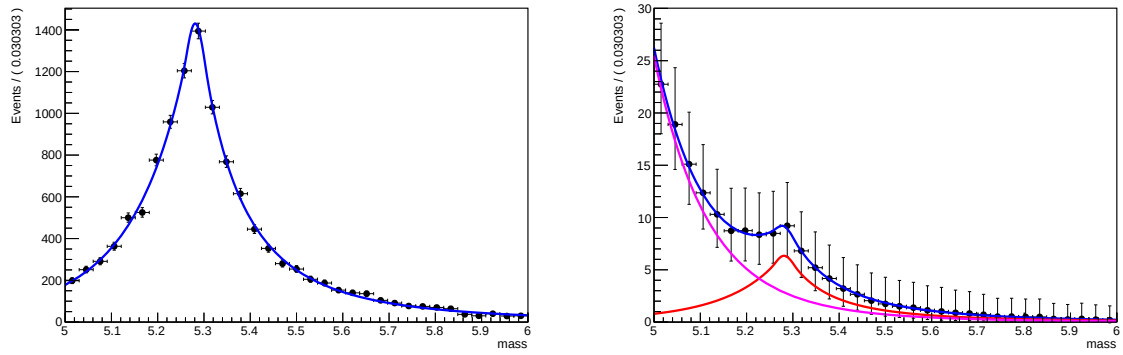

Figure D.35: Fit of the signal (left) and fit of signal + background (right) in order to determine the precision on the BF measurement for the $20-7\mu$m working point.

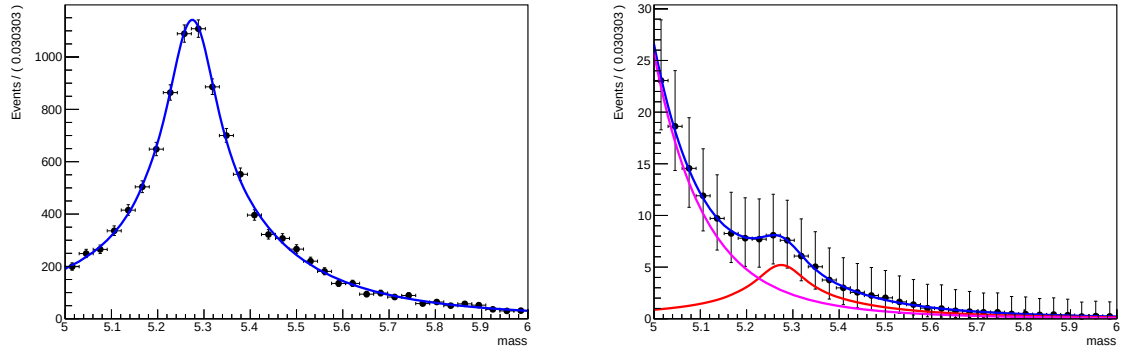

Figure D.36: Fit of the signal (left) and fit of signal + background (right) in order to determine the precision on the BF measurement for the $20-8\mu$m working point.

D.3 IDEA resolution extra plots

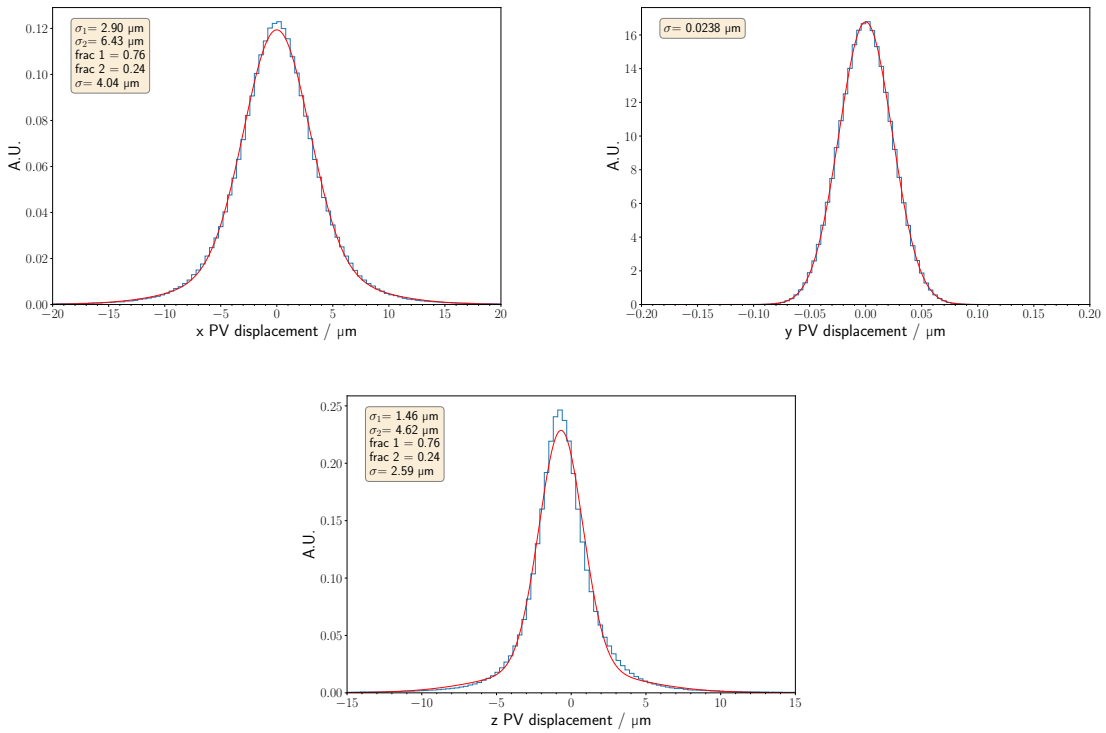

Figure D.37: Fit of the various IDEA, with two times better Ω measurement, primary vertexing resolutions on cartesian coordinates x (upper left), y(upper right) and z (bottom).

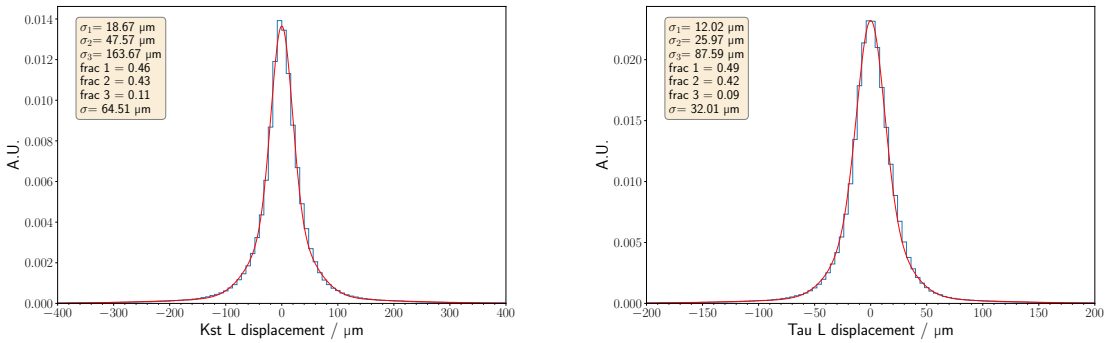

Figure D.38: Fit of the various IDEA, with two times better Ω measurement, secondary (left) and tertiary (right) longitudinal resolutions.

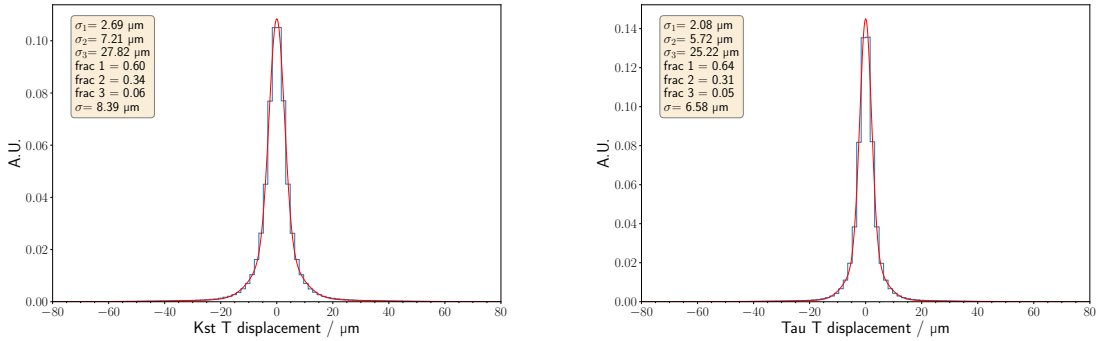

Figure D.39: Fit of the various IDEA, with two times better Ω measurement, secondary (left) and tertiary (right) transverse resolutions.

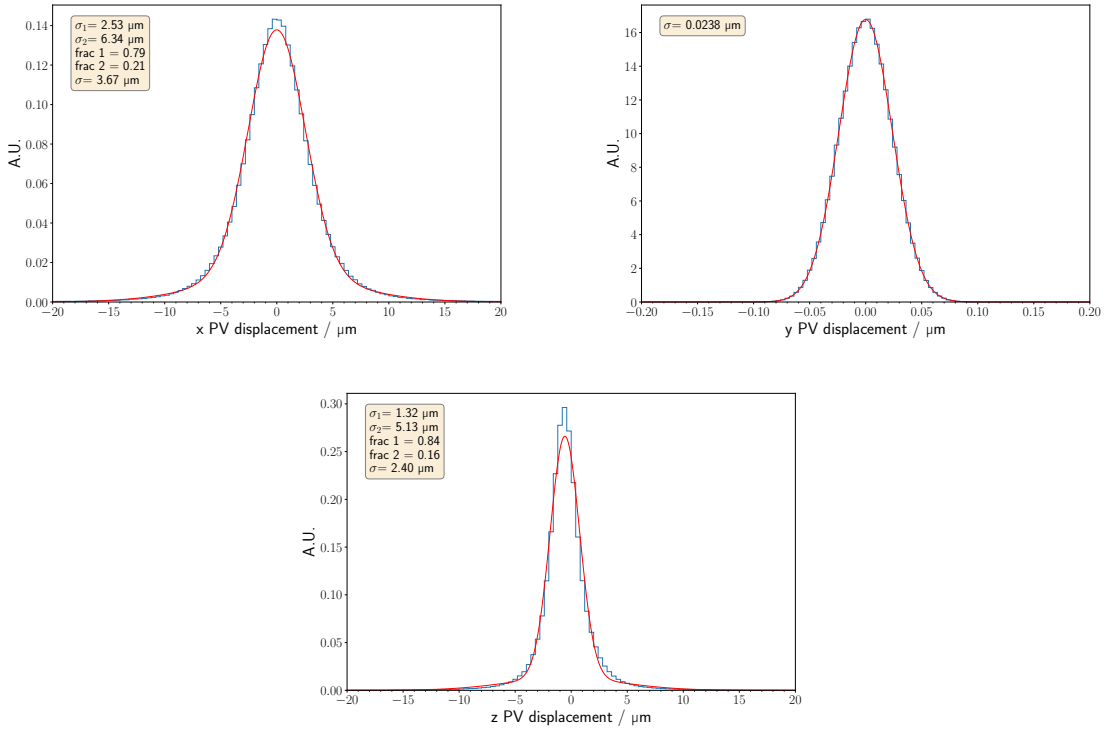

Figure D.40: Fit of the various IDEA, with 1.2 times better IP measurement, primary vertexing resolutions on cartesian coordinates x (upper left), y(upper right) and z (bottom).

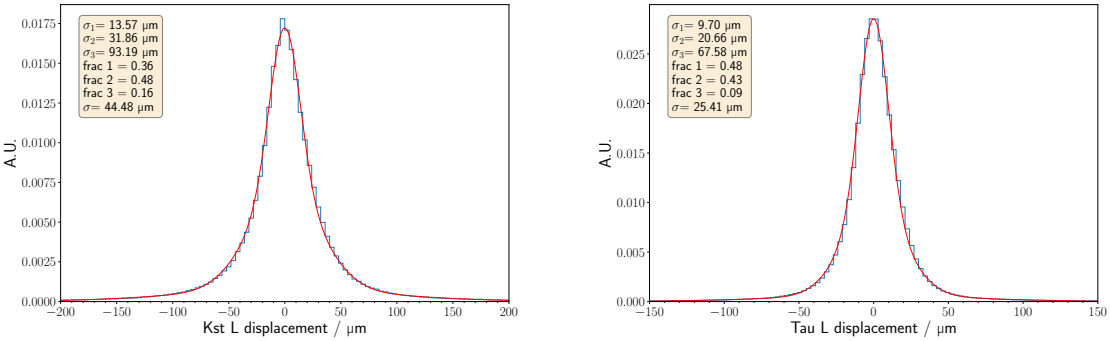

Figure D.41: Fit of the various IDEA, with 1.2 times better IP measurement, secondary (left) and tertiary (right) longitudinal resolutions.

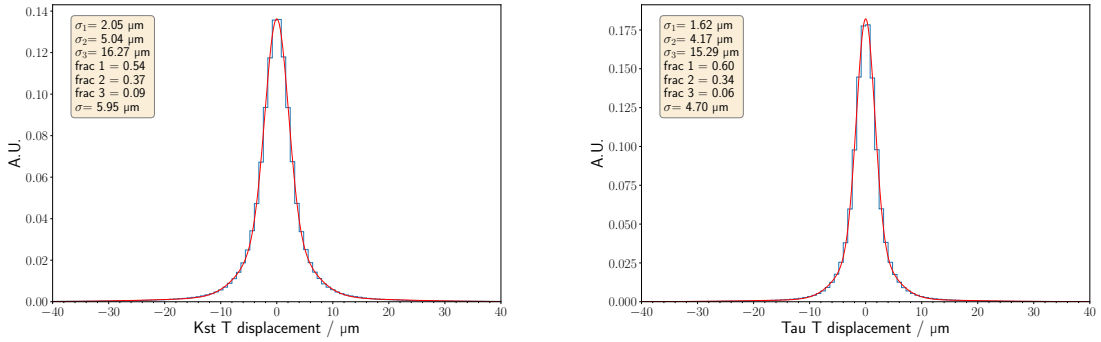

Figure D.42: Fit of the various IDEA, with 1.2 times better IP measurement, secondary (left) and tertiary (right) transverse resolutions.

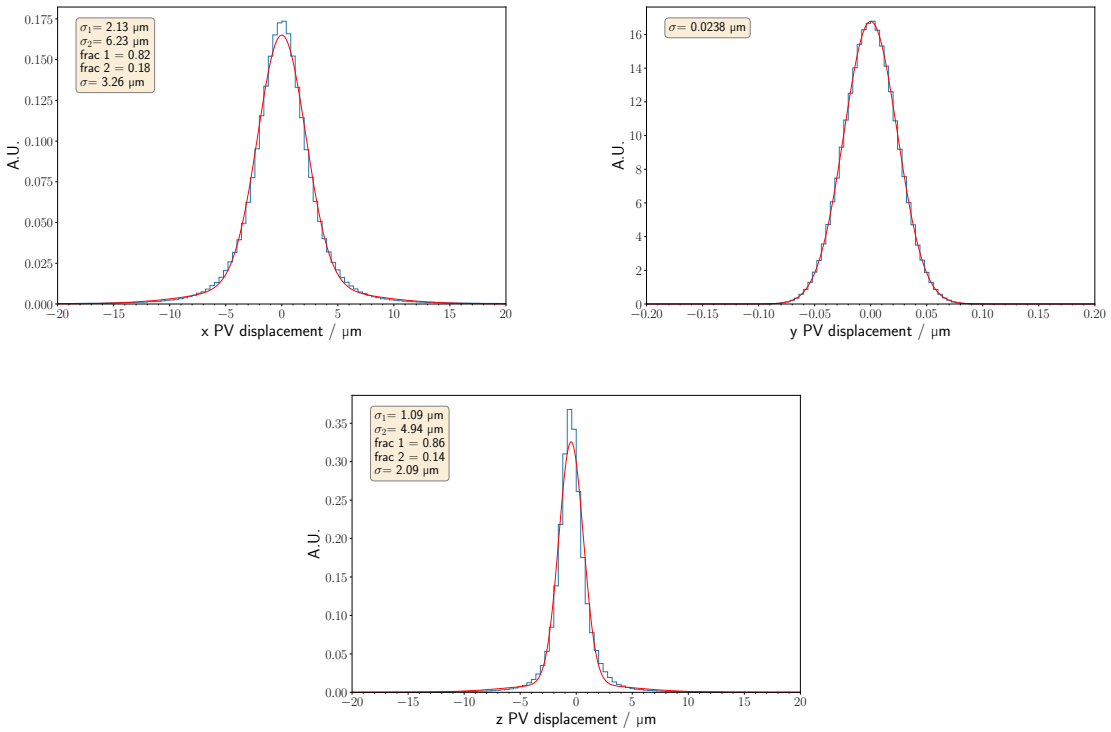

Figure D.43: Fit of the various IDEA, with 1.5 times better IP measurement, primary vertexing resolutions on cartesian coordinates x (upper left), y(upper right) and z (bottom).

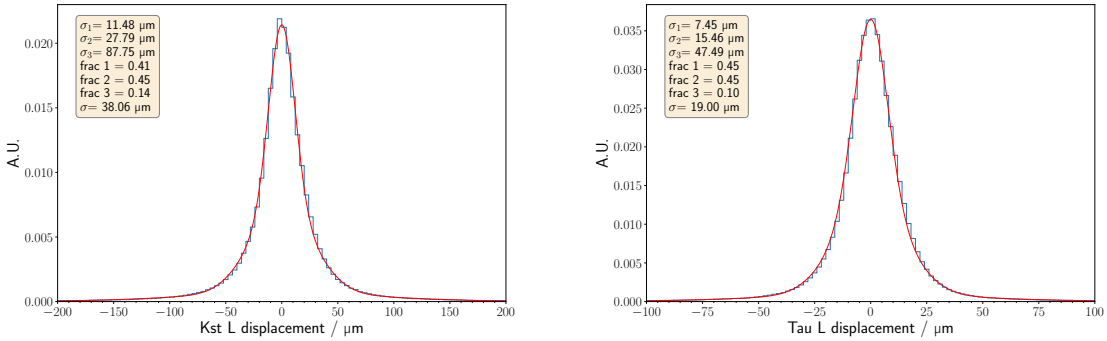

Figure D.44: Fit of the various IDEA, with 1.5 times better IP measurement, secondary (left) and tertiary (right) longitudinal resolutions.

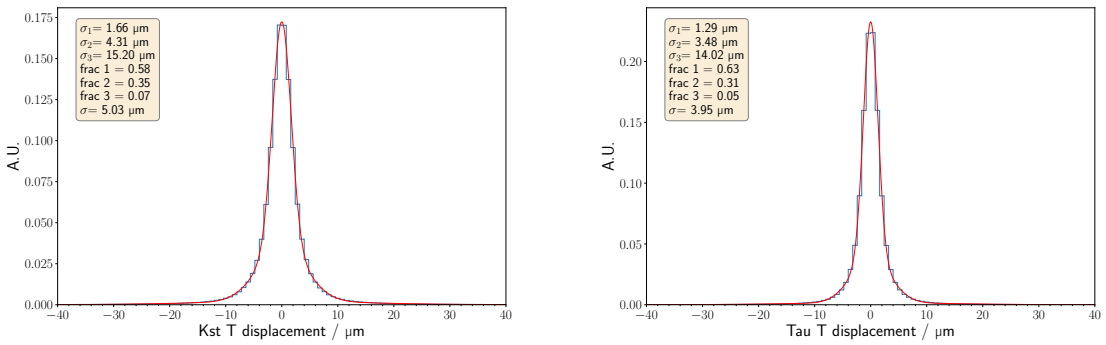

Figure D.45: Fit of the various IDEA, with 1.5 times better IP measurement, secondary (left) and tertiary (right) transverse resolutions.

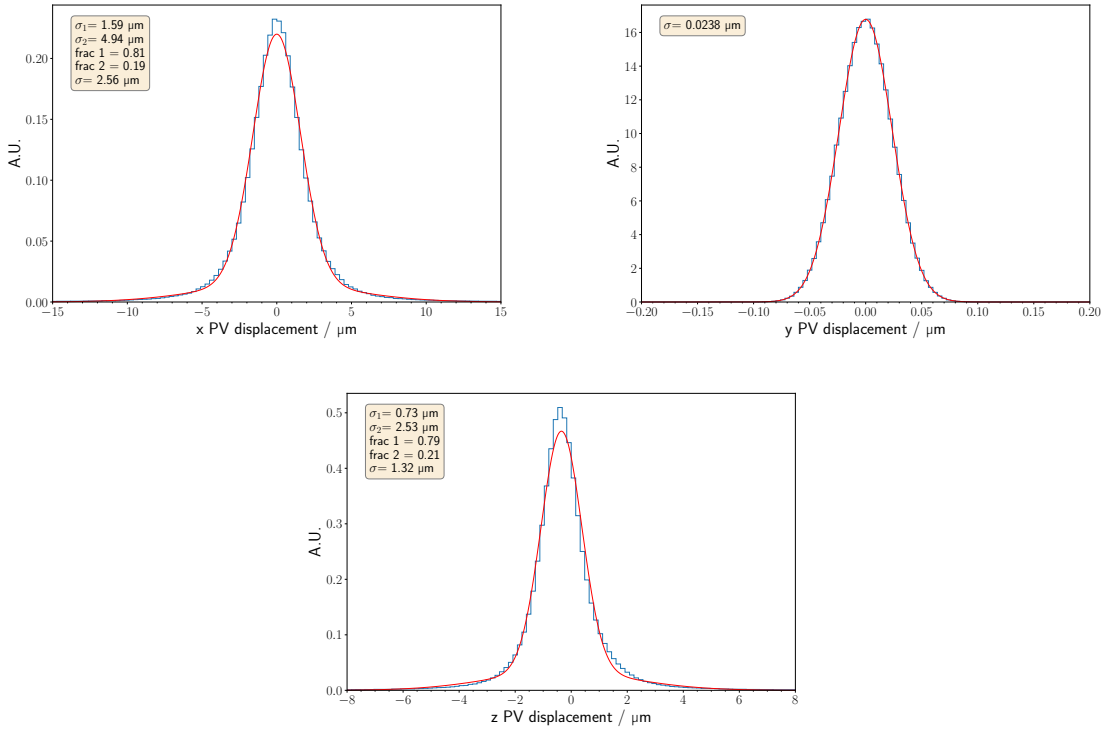

Figure D.46: Fit of the various IDEA, with two times better IP measurement, primary vertexing resolutions on cartesian coordinates x (upper left), y(upper right) and z (bottom).

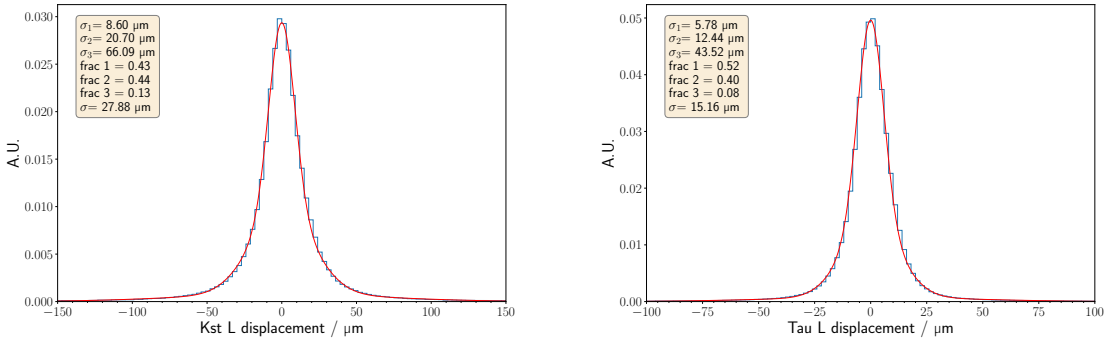

Figure D.47: Fit of the various IDEA, with two times better IP measurement, secondary (left) and tertiary (right) longitudinal resolutions.

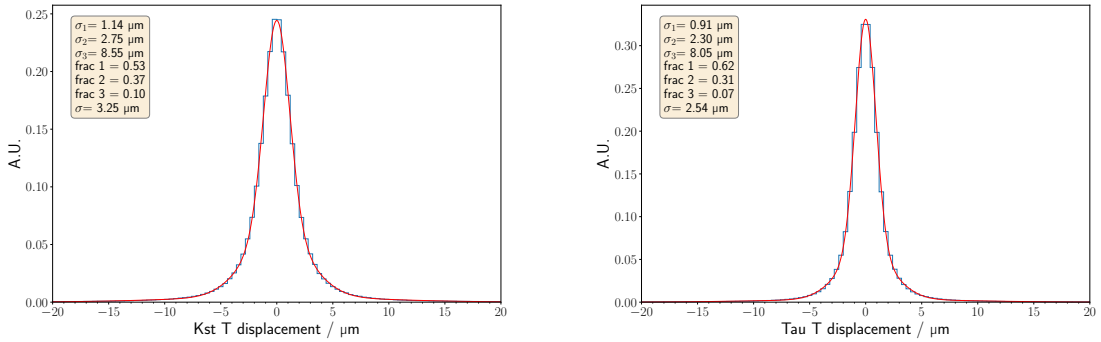

Figure D.48: Fit of the various IDEA, with two times better IP measurement, secondary (left) and tertiary (right) transverse resolutions.

D.4 IDEA fitted precision extra-plots

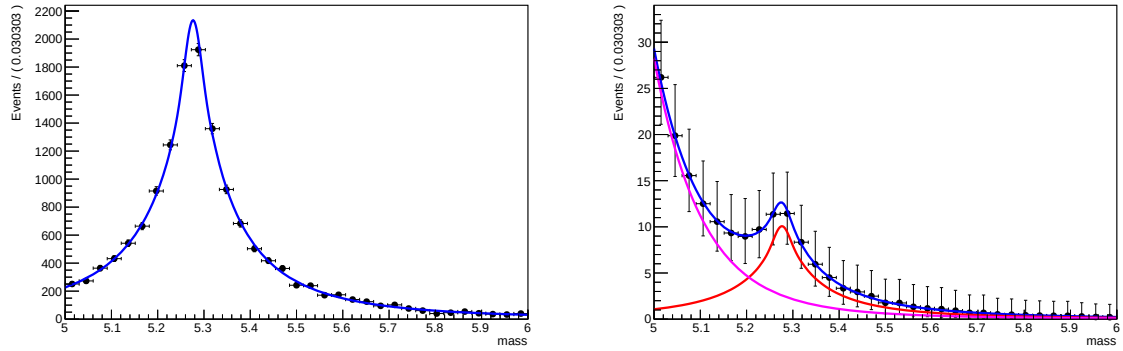

Figure D.49: Fit of the signal (left) and fit of signal + background (right) in order to determine the precision on the BF measurement for the IDEA baseline working point.

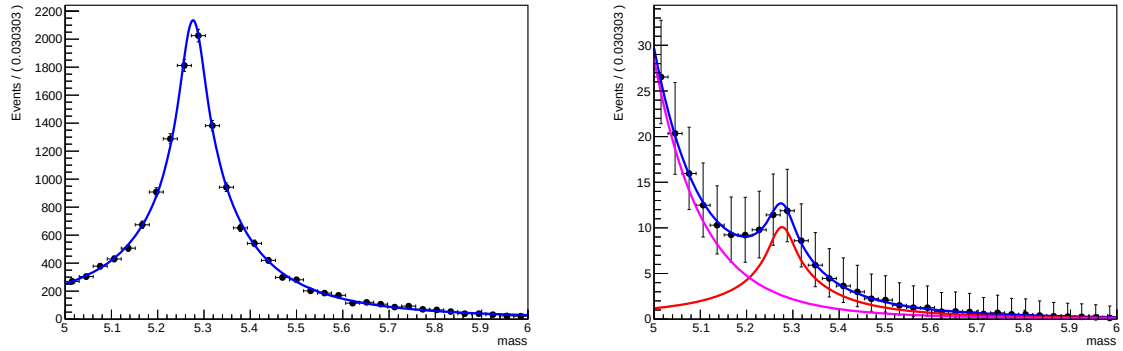

Figure D.50: Fit of the signal (left) and fit of signal + background (right) in order to determine the precision on the BF measurement for the IDEA $\Omega \times 2$ working point.

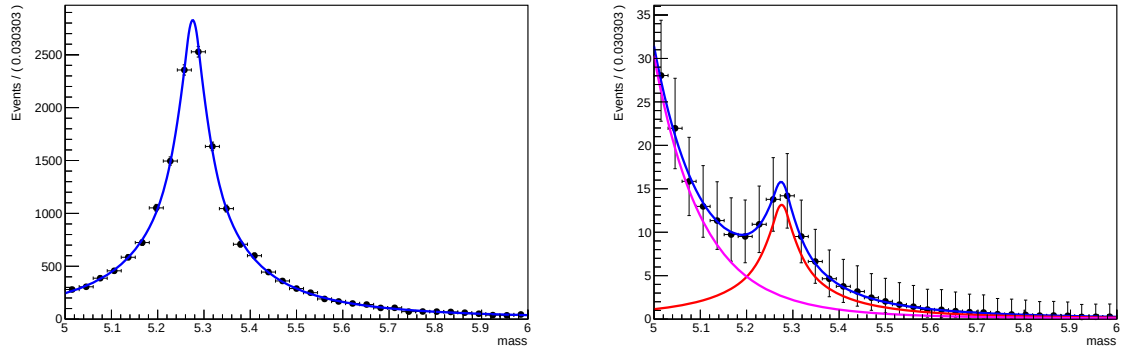

Figure D.51: Fit of the signal (left) and fit of signal + background (right) in order to determine the precision on the BF measurement for the IDEA $IP \times 1.2$ working point.

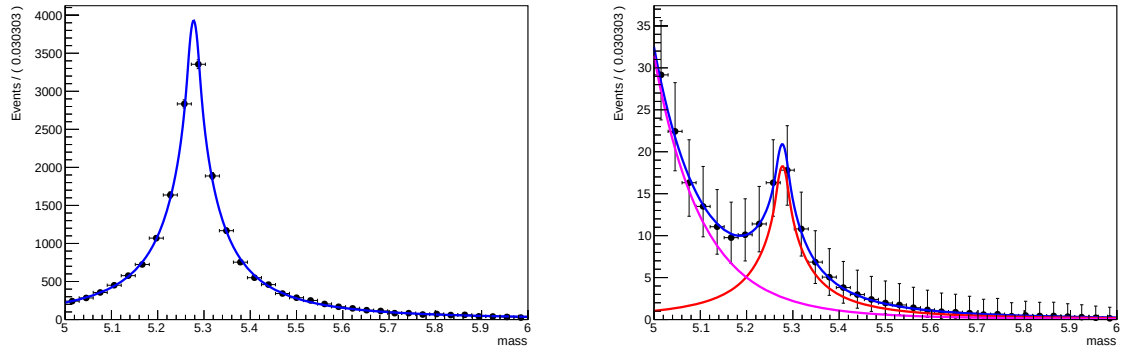

Figure D.52: Fit of the signal (left) and fit of signal + background (right) in order to determine the precision on the BF measurement for the IDEA $IP \times 1.5$ working point.

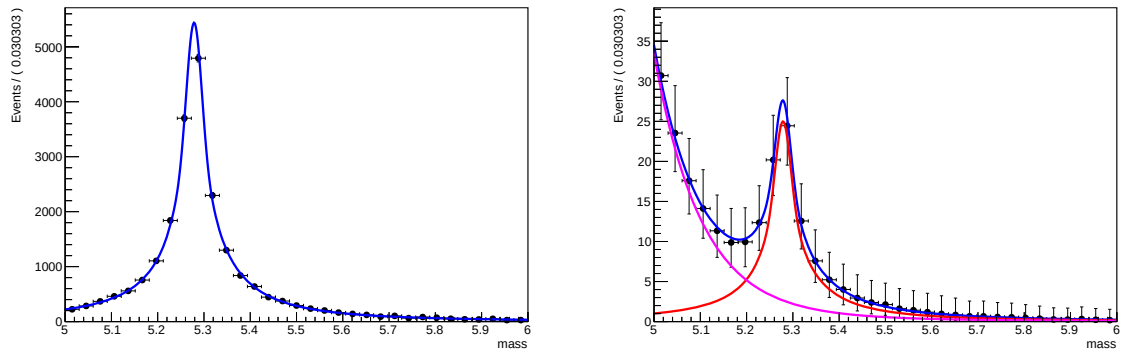

Figure D.53: Fit of the signal (left) and fit of signal + background (right) in order to determine the precision on the BF measurement for the IDEA $IP \times 2$ working point.

D.5 Improved detectors extra-plots

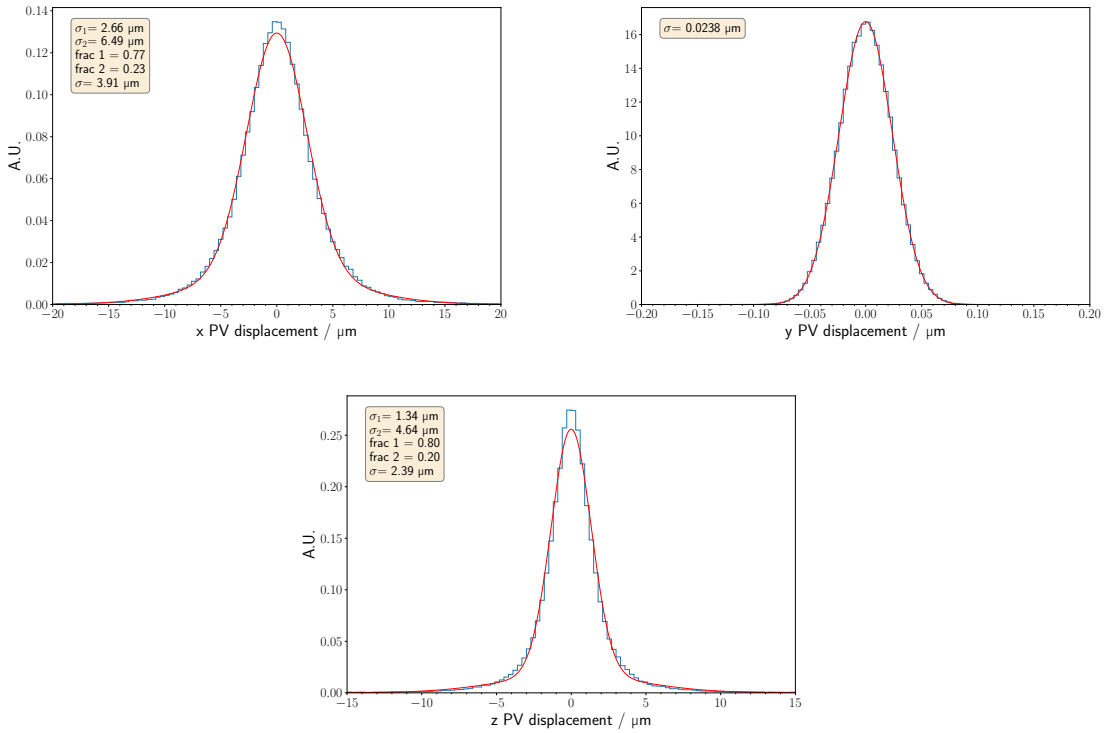

Figure D.54: Fit of the 30% better single hit resolution detector primary vertexing resolutions on cartesian coordinates x (upper left), y(upper right) and z (bottom).

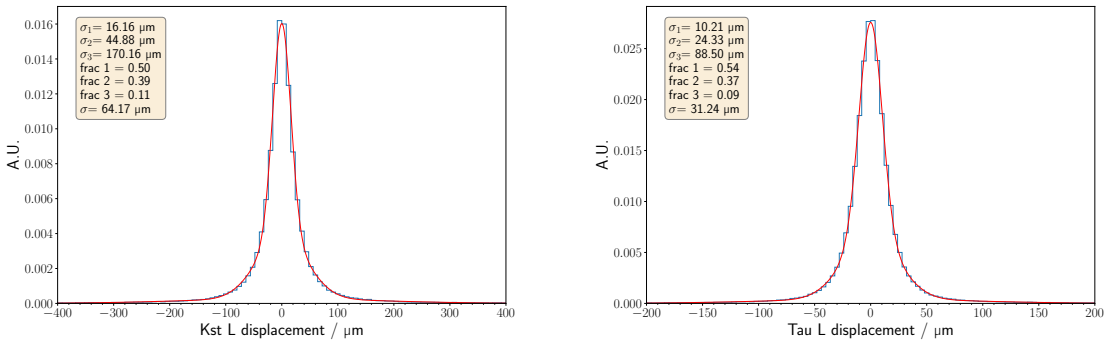

Figure D.55: Fit of the 30% better single hit resolution detector secondary (left) and tertiary (right) longitudinal resolutions.

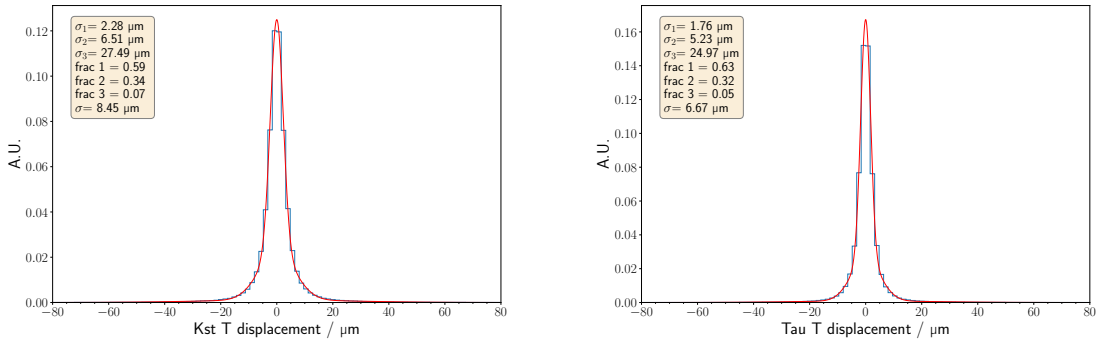

Figure D.56: Fit of the 30% better single hit resolution detector secondary (left) and tertiary (right) transverse resolutions.

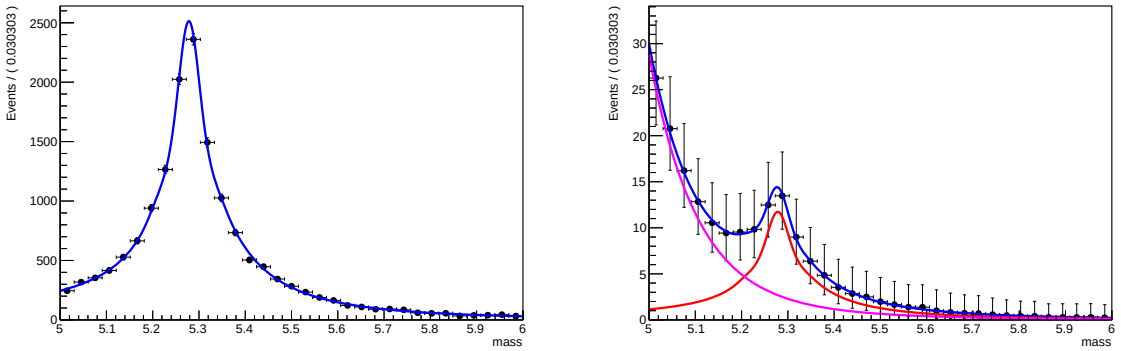

Figure D.57: Fit of the signal (left) and fit of signal + background (right) in order to determine the precision on the BF measurement for the 30% better single hit resolution detector working point.

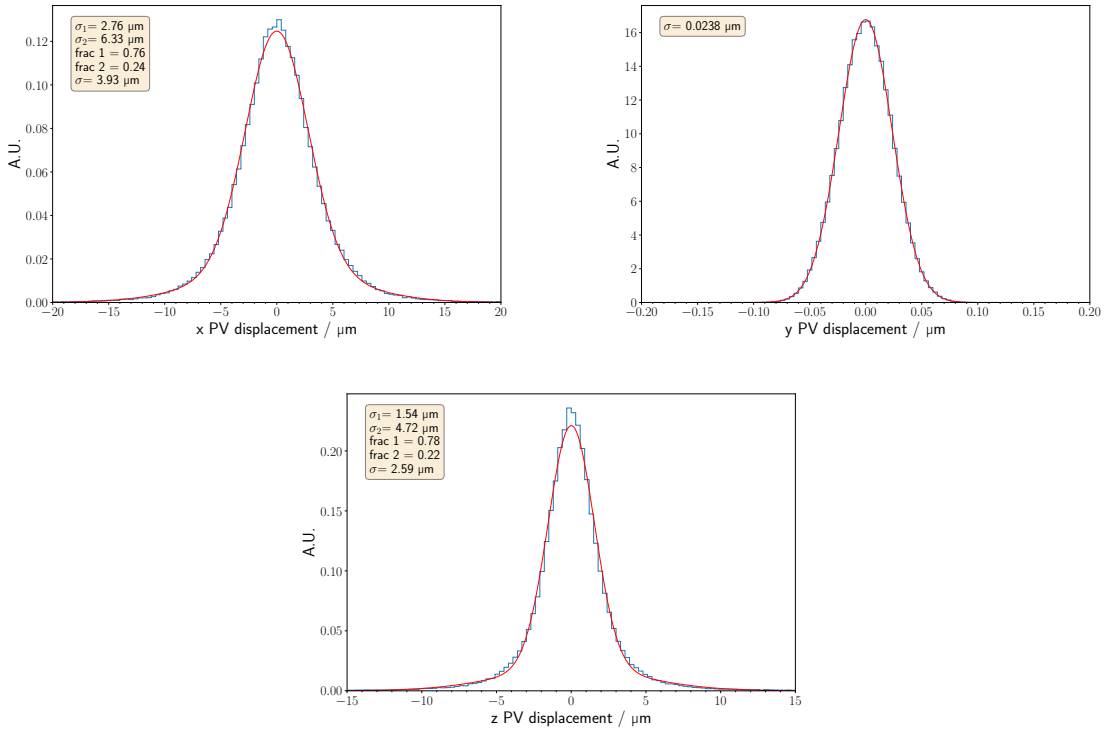

Figure D.58: Fit of the 50% lighter VXD layers detector primary vertexing resolutions on cartesian coordinates x (upper left), y(upper right) and z (bottom).

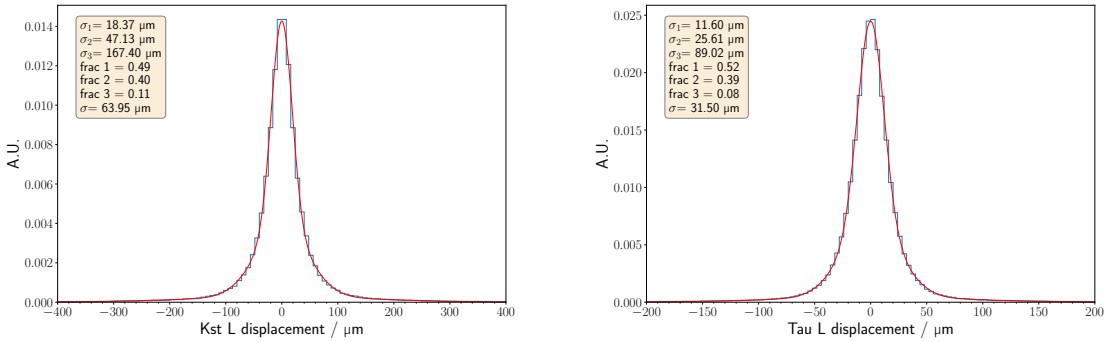

Figure D.59: Fit of the 50% lighter VXD layers detector secondary (left) and tertiary (right) longitudinal resolutions.

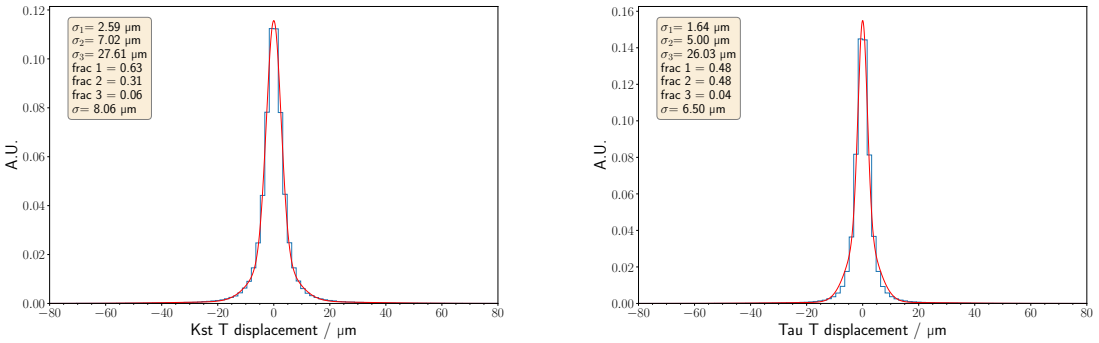

Figure D.60: Fit of the 50% lighter VXD layers detector secondary (left) and tertiary (right) transverse resolutions.

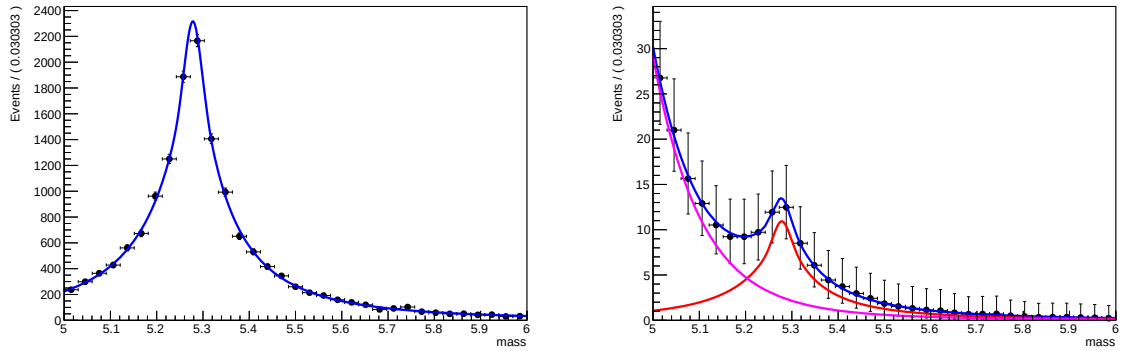

Figure D.61: Fit of the signal (left) and fit of signal + background (right) in order to determine the precision on the BF measurement for the 50% lighter VXD layers detector working point.

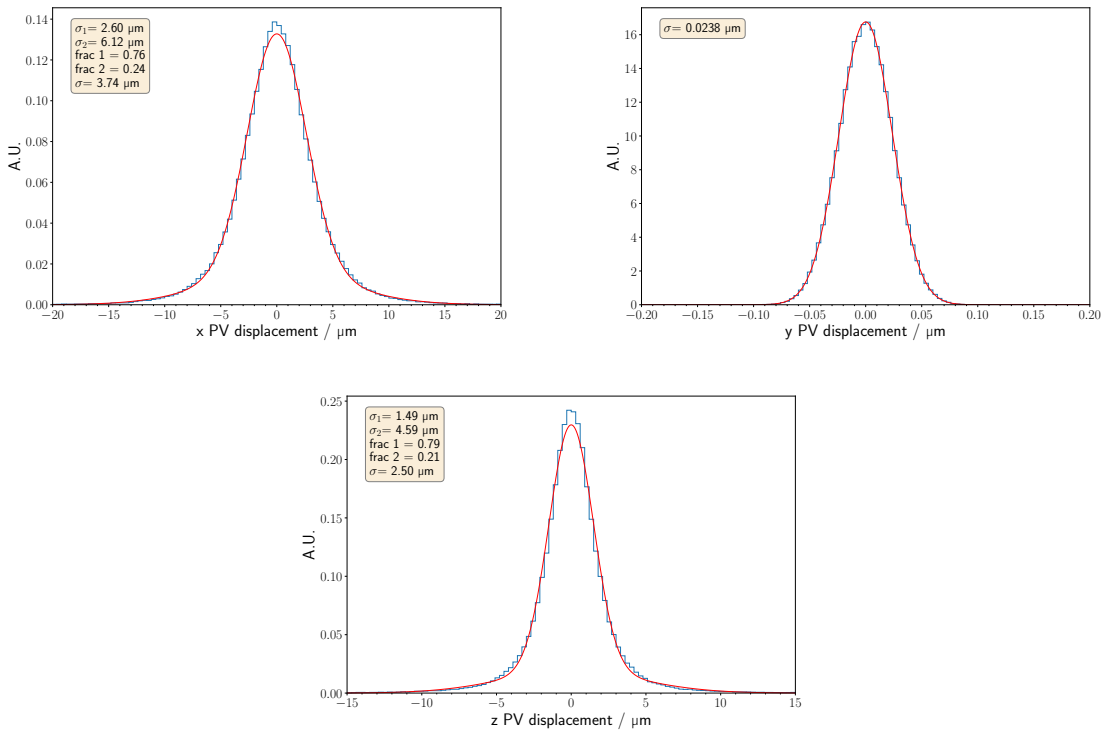

Figure D.62: Fit of the 50% lighter VXD layers and beam-pipe detector primary vertexing resolutions on cartesian coordinates x (upper left), y(upper right) and z (bottom).

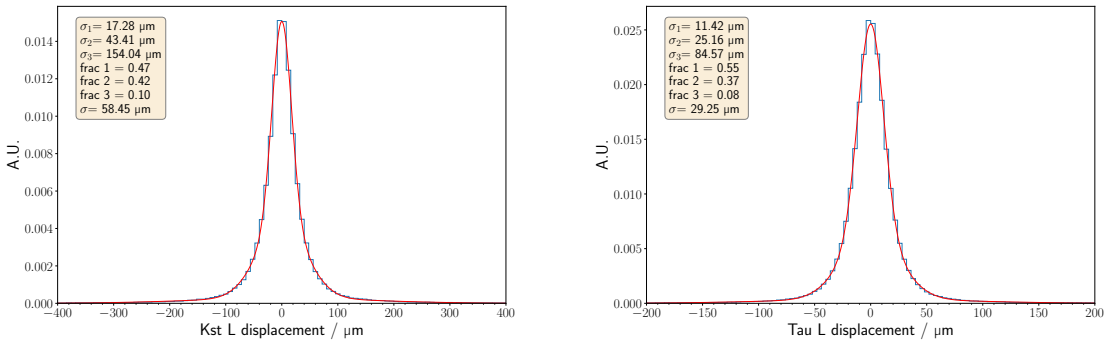

Figure D.63: Fit of the 50% lighter VXD layers and beam-pipe detector secondary (left) and tertiary (right) longitudinal resolutions.

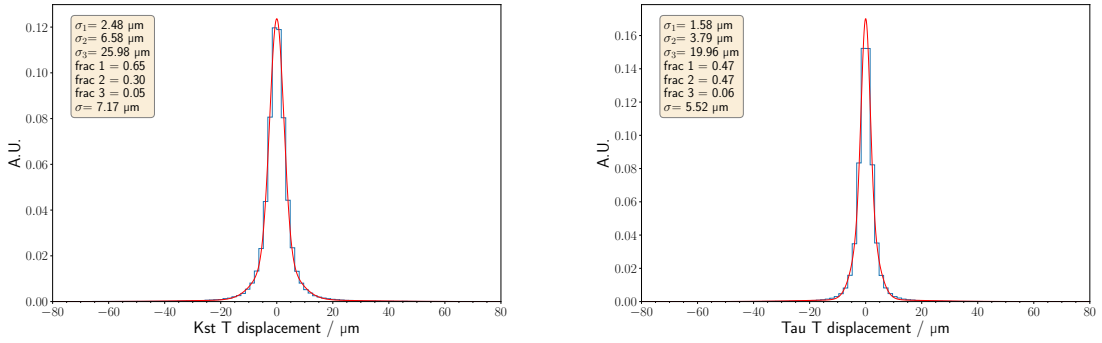

Figure D.64: Fit of the 50% lighter VXD layers and beam-pipe detector secondary (left) and tertiary (right) transverse resolutions.

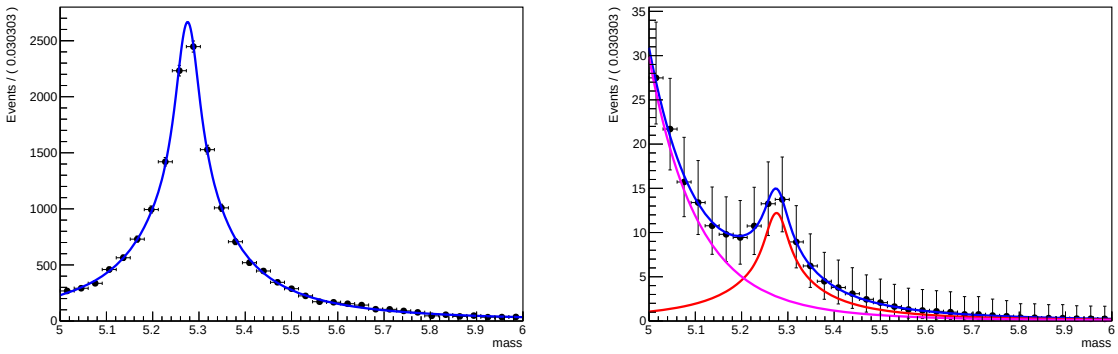

Figure D.65: Fit of the signal (left) and fit of signal + background (right) in order to determine the precision on the BF measurement for the 50% lighter VXD layers and beam-pipe detector working point.

Appendix E

Résumé français

Ce résumé en français a été rédigé à partir de la thèse en anglais et avec l'aide d'un assistant conversationnel pour la traduction.

E.1 Introduction

Depuis Newton, les physiciens ont cherché à élaborer des modèles mathématiques pour décrire les phénomènes naturels. Au début du XXe siècle, la physique quantique a été développée pour expliquer des observations inattendues, telles que l'effet photoélectrique [218].

Le Modèle Standard (SM) de la physique des particules décrit avec succès trois des quatre forces fondamentales et les phénomènes naturels à des échelles de l'ordre de 10^{-18} m. Par exemple, le moment magnétique anormal de l'électron est prédit avec une précision remarquable [219, 220]. Cependant, le SM ne parvient pas à expliquer certaines observations, comme l'asymétrie baryonique de l'Univers [4] et l'origine de la masse des neutrinos [5]. Pour remédier à ces lacunes, des modèles au-delà du SM (BSM) ont été proposés, incluant par exemple de nouveaux bosons de jauge comme le Z' [6] ou de nouvelles particules comme les leptoquarks [7, 8].

Pour tester ces théories, des collisionneurs de particules de plus en plus puissants et complexes ont été construits, jusqu'au LHC [9].

Cette thèse se concentre sur deux études des désintégrations de mésons B neutres. La première analyse les désintégrations hadroniques à trois corps et sans charme des mésons B neutres avec un K^0_S dans l'état final, utilisant les données enregistrées par LHCb (Large Hadron Collider beauty) de 2011 à 2018 [10]. L'objectif principal est de mesurer les rapports d'embranchement des modes $B^0_{d,s} \to K^0_S h^+ h'^-$ et de rechercher $B^0_s \to K^0_S K^+ K^-$, non observés à ce jour. La deuxième étude explore le potentiel des futures expériences au FCC-*ee* [11] pour observer la transition de quark rare $b \to s\tau^+\tau^-$, testant ainsi les limites du SM et des modèles BSM.

La première section présente le contexte scientifique global, en introduisant le SM et en explorant la phénoménologie des désintégrations de mésons B. La deuxième section décrit le cadre expérimental, du LHC (Large Hadron Collider) au spectromètre LHCb jusqu'au projet FCC-*ee* (Future Circular Collider). La troisième section détaille l'analyse des modes $B^0_{d,s} \to K^0_S h^+ h'^-$ et la recherche de $B^0_s \to K^0_S K^+ K^-$. La quatrième section présente une analyse d'amplitude préliminaire de $B^0_s \to K^0_S \pi^+ \pi^-$, visant à fournir les éléments de base de l'analyse complète et les premières indications d'une éventuelle observation de violation de *CP* (la symétrie conjugaison de charge - parité). Enfin, la cinquième section est dédiée à l'étude prospective de la transition $b \to s\tau^+\tau^-$ au FCC-*ee*, utilisant la transition $B^0 \to K^{*0}\tau^+\tau^-$. Une méthode de reconstruction spécifique a été développée pour résoudre complètement la cinématique de la désintégration, permettant de dessiner des perspectives d'observation en fonction des performances du détecteur de vertex.

E.2 Contexte des études

E.2.1 Modèle Standard et Physique des saveurs

Le SM [12] décrit trois des quatre interactions fondamentales: électromagnétique, faible et forte. Il implique des particules élémentaires : les fermions (quarks et leptons) et les bosons de jauge. L'interaction électromagnétique est portée par les photons, l'interaction faible par les bosons W et Z, et l'interaction forte par les gluons.

Le SM est une théorie quantique des champs renormalisable basée sur le groupe de symétrie $SU(3)_C \otimes SU(2)_L \otimes U(1)_Y$. Le mécanisme de BEH (Brout-Englert-Higgs) [13, 14] introduit un doublet de champs scalaires qui brise la symétrie spontanément, donnant de la masse aux bosons W et Z tout en gardant le photon sans masse. La découverte du boson de BEH (boson de Higgs) en 2012 au LHC [15, 16] a confirmé ce mécanisme. Les masses des fermions proviennent des couplages de Yukawa avec le boson de BEH.

Dans le SM, la matrice de Cabibbo-Kobayashi-Maskawa (CKM) [3] décrit le mélange entre les saveurs de quarks dans les interactions faibles. Elle est cruciale pour comprendre la violation CP, un phénomène où les lois de la physique changent lorsque les particules sont remplacées par leurs antiparticules et que leurs coordonnées spatiales sont inversées.

La physique des saveurs étudie les particules lourdes en saveur dans le SM. Les saveurs lourdes incluent les quarks strange, charm, bottom et top, ainsi que les muons, les taus et leurs neutrinos parmi les leptons. Ce sont des particules supplémentaires aux quarks de saveur up et down et à l'électron et son neutrino (qui composent la matière ordinaire). Les découvertes de ces particules ont façonné le SM, fournissant des informations sur les durées de vie des particules, l'unification électrofaible et la violation CP. La figure E.1 résume les particules élémentaires du SM.

Malgré son succès, le SM a des limites. Par exemple, il ne peut pas expliquer l'asymétrie matière-antimatière [46] dans l'univers, car l'ampleur prédite de la violation CP est insuffisante pour expliquer la dominance observée de la matière sur l'antimatière. Ou encore, le SM ne tient pas compte de la matière noire [38] et de l'énergie noire [39], qui sont des composantes essentielles du contenu en masse-énergie de l'univers. Ces limitations suggèrent la nécessité de théories au-delà du SM (BSM).

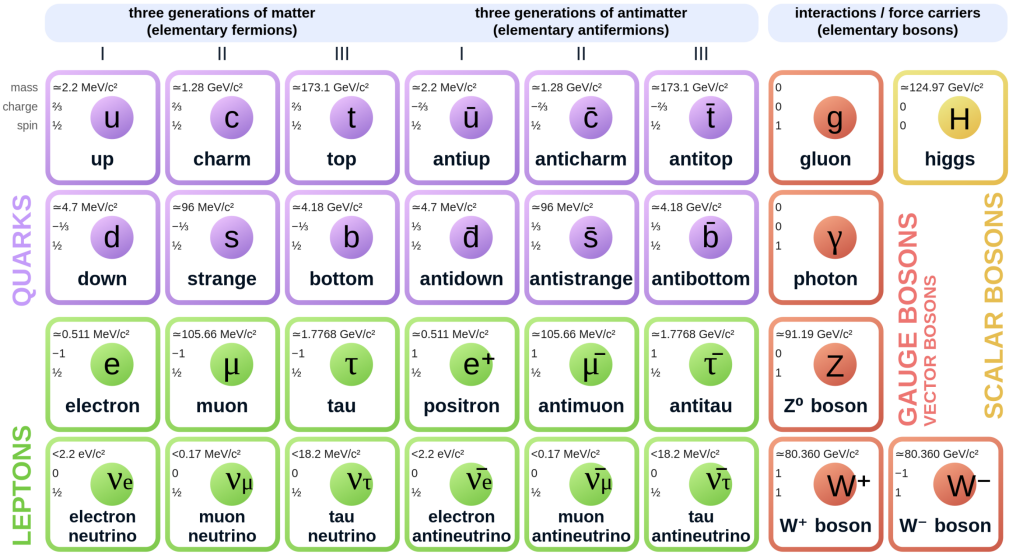

Figure E.1: Résumé des particules élémentaires du SM.

E.2.2 Motivation pour l'étude de $B^0_{d,s} \to K^0_S h^+ h'^-$

Le travail réalisé au sein de la collaboration LHCb rapporté dans cette thèse est dédié à l'étude des modes de désintégration $B^0_{(s)} \to K^0_S hh'$, où $h^{(\prime)}$ peut être $\pi^\pm$ ou $K^\pm$. Le premier objectif de cette étude est de réaliser les mesures des rapports d'embranchement de ces modes avec l'ensemble des données de LHCb disponibles à ce jour.

Une analyse précédente de LHCb, effectuée avec les données disponibles en 2012, a mesuré les rapports d'embranchement pour les modes $B^0_{(s)} \to K^0_S hh'$ relativement au mode $B^0 \to K^0_S \pi^+\pi^-$ (le mode le plus probable, afin de neutraliser les effets de détecteur). Les résultats obtenus étaient les suivants [68] :

$$\frac{BF(B^0 \to K^0_S K^+ K^-)}{BF(B^0 \to K^0_S \pi^+\pi^-)} = 0.549 \pm 0.018, (\text{stat.}) \pm 0.033, (\text{syst.}), \tag{E.2.1}$$

$$\frac{BF(B^0 \to K^0_S K^\pm \pi^\mp)}{BF(B^0 \to K^0_S \pi^+\pi^-)} = 0.123 \pm 0.009, (\text{stat.}) \pm 0.015, (\text{syst.}), \tag{E.2.2}$$

$$\frac{BF(B^0_s \to K^0_S \pi^+\pi^-)}{BF(B^0 \to K^0_S \pi^+\pi^-)} = 0.191 \pm 0.027, (\text{stat.}) \pm 0.031, (\text{syst.}) \pm 0.011, (f_s/f_d), \tag{E.2.3}$$

$$\frac{BF(B^0_s \to K^0_S K^\pm \pi^\mp)}{BF(B^0 \to K^0_S \pi^+\pi^-)} = 1.70 \pm 0.07, (\text{stat.}) \pm 0.11, (\text{syst.}) \pm 0.10, (f_s/f_d), \tag{E.2.4}$$

et

$$\frac{BF(B^0_s \to K^0_S K^+ K^-)}{BF(B^0 \to K^0_S \pi^+\pi^-)} \in [0.008, 0.051], \text{ au niveau de confiance de } 90\%, \tag{E.2.5}$$

ce qui n'était pas suffisant pour valider la découverte de $B^0_s \to K^0_S K^+ K^-$. L'objectif de l'analyse actuelle pour les rapports d'embranchement est de mettre à jour ces résultats et de découvrir $B^0_s \to K^0_S K^+ K^-$ avec l'ensemble des données de LHCb disponibles en 2018, ce travail est décrit dans la Section E.4.

En plus de la mise à jour des rapports d'embranchement, l'étude de la violation de *CP* dans ces désintégrations est un objectif crucial. En particulier, les observables de violation de *CP* dans les désintégrations $B^0_{(s)} \to K^0_S hh'$ peuvent fournir des informations uniques sur les mécanismes de la violation de *CP* au-delà du SM. Par exemple, l'interférence entre les différentes amplitudes de désintégration et le mélange des états B^0 et $\bar{B}^0$ peut révéler des écarts par rapport aux prédictions du SM. En analysant l'asymétrie de *CP* dans ces désintégrations, on peut sonder la présence d'effets de nouvelle physique (NP) qui pourraient ne pas être visibles dans d'autres canaux. Concrètement, une version préliminaire de l'analyse en amplitude intégrée dans le temps de $B^0_s \to K^0_S \pi^+\pi^-$ est présentée en Section E.5. Ainsi, l'analyse des rapports d'embranchement servira de point de départ pour ces études plus détaillées de la violation de *CP*, qui pourraient finalement révéler des effets de NP si des écarts par rapport au SM sont détectés.

E.2.3 Motivation pour l'étude de $B^0 \to K^{*0}\tau^+\tau^-$

Le travail réalisé dans le cadre du projet FCC-*ee* rapporté dans cette thèse est consacré à l'étude du mode de désintégration $B^0 \to K^{*0}\tau^+\tau^-$. Le mode de désintégration $B^0 \to K^{*0}\tau^+\tau^-$ revêt un intérêt significatif dans l'étude des désintégrations rares des mésons B. Ce processus implique une transition d'un quark b en un quark s et une paire de leptons $\tau^+\tau^-$.

La désintégration $B^0 \to K^{*0}\tau^+\tau^-$ est un processus rare en raison de la suppression des courants neutres à changement de saveur (FCNC). Cette rareté en fait une sonde sensible aux sources de NP. Dans le SM, ce mode de désintégration est prédit pour se produire avec un rapport d'embranchement d'environ $\mathcal{O}(10^{-7})$, une valeur difficile à mesurer mais qui constitue un critère crucial pour tester les prédictions théoriques. Concrètement, ce mode n'a pas encore été observé à ce jour.

La principale motivation pour étudier ce mode de désintégration est la possibilité de découvrir des écarts par rapport aux prédictions du SM qui pourraient indiquer la présence de NP. Plus précisément, la transition $b \to s\tau^+\tau^-$ est sensible aux effets de particules lourdes qui pourraient ne pas être présentes dans le SM, telles que de nouveaux bosons de jauge (par exemple, Z' [6]) ou des leptoquarks [7, 8]. Ces nouvelles particules pourraient altérer de manière significatif le processus de désintégration, entraînant des écarts observables dans le rapport d'embranchement et les distributions angulaires des particules finales par exemple.

Plusieurs observables peuvent être définies en relation avec la désintégration $B^0 \to K^{*0}\tau^+\tau^-$, telles que le rapport d'embranchement, les asymétries de polarisation des τ, et les asymétries avant-arrière. Leur mesure peut être utilisée pour tester la validité du SM et potentiellement découvrir des signes de NP. L'étude de telles désintégrations rares ne sert donc pas seulement à sonder le SM, mais aussi à offrir une fenêtre sur la physique au-delà. Par exemple, la Figure E.2 affiche une comparaison entre le rapport d'embranchement prédit par le SM et celui prédit dans un scénario de NP.

Le FCC-*ee* offre des avantages uniques pour cette investigation. L'environnement propre qui sera disponible à FCC-*ee* est particulièrement adapté pour détecter les signaux faibles associés aux désintégrations rares telles que $B^0 \to K^{*0}\tau^+\tau^-$. Contrairement aux expériences au LHC, où le fort niveau de bruit de fond associé à l'environnement hadronique posent des défis pour isoler de telles désintégrations. Tout cela fait de $B^0 \to K^{*0}\tau^+\tau^-$ un étalon intéressant pour évaluer les capacités de FCC-*ee* et déterminer les exigences associées à ces détecteurs. La Section E.6 présente l'étude de la faisabilité de la mesure du rapport d'embranchement de $B^0 \to K^{*0}\tau^+\tau^-$ à FCC-*ee*.

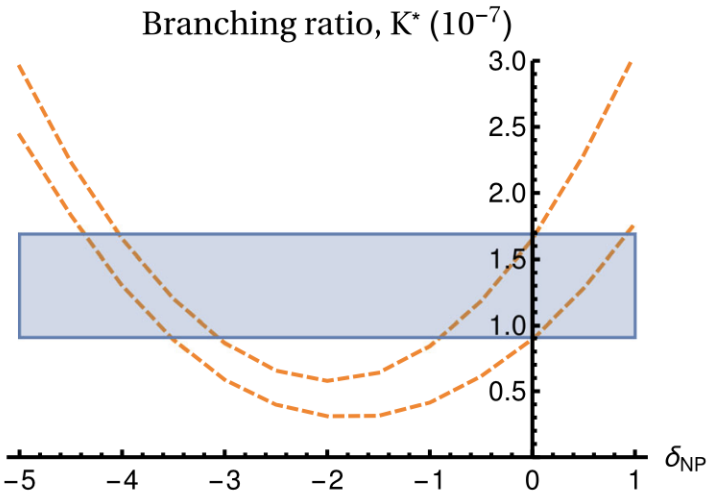

Figure E.2: $BF(B^0 \to K^{*0}\tau^+\tau^-) \pm 1\sigma$ prédit par le SM (rectangle bleu) et predit par un scenario avec NP en fonction de δ_{NP}, un paramètre réel modélisant une deviation par rapport au SM (délimité par les lignes pointillés orange) [71].

E.3 Les instruments

Les travaux présentés dans cette thèse prennent place au sein de la collaboration LHCb et du projet FCC-*ee*. Dans cette section l'accélérateur de particules LHC est présenté ainsi que le spectromètre LHCb et le projet FCC-*ee*.

E.3.1 Le LHC

Le Grand collisionneur de hadrons (LHC) [9] du CERN (l'organisation européenne pour la recherche nucléaire), situé à la frontière franco-suisse, est la plus grande installation scientifique dédiée à la physique des hautes énergies (HEP). Il comporte un accélérateur de particules à double anneaux, où des faisceaux de protons ou d'ions circulent dans des directions opposées à l'intérieur d'un tunnel souterrain de 27 kilomètres. Le LHC, successeur du Grand collisionneur électron-positron (LEP) [80], peut accélérer les protons jusqu'à 6,5 TeV par faisceau, atteignant une énergie de collision dans le centre de masse de 13 TeV.

Depuis ses premières collisions de protons en 2008, le LHC a connu plusieurs périodes de collecte de données appelées Runs. Le Run I (2011-2012) a fonctionné avec une énergie dans le centre de masse de 7 TeV (2011) et 8 TeV (2012), tandis que le Run II (2015-2018) a fonctionné à 13 TeV. L'utilisation de protons au lieu d'électrons, comme au LEP, permet d'éviter la perte d'énergie due au rayonnement synchrotron [81], mais cela vient en contre partie avec des événements (collisions) plus peuplés et compliqués à analyser (le proton n'étant pas une particule élémentaire).

Comme le travail présenté dans cette thèse est axé sur l'étude des désintégrations des hadrons b, il est important d'expliquer leur production au LHC. La production des hadrons b commence par la production de quarks b, dominée par la création de paires $b\bar{b}$. Dans les collisions pp, les contributions à la production des paires $b\bar{b}$ proviennent de l'interaction gluon-gluon $gg \to b\bar{b}$, dominante au LHC, et de l'annihilation quark-antiquark $q\bar{q} \to b\bar{b}$.

En raison des énormes asymétries d'impulsions entre les partons (gluons ou quarks) impliqués dans la collision et du fait que l'énergie de collision au LHC est supérieure à la masse du b, la paire $b\bar{b}$ produite au LHC est généralement boostée le long de la direction avant ou arrière de l'axe du faisceau. Ce comportement permet de construire des détecteurs focalisés sur des plages spécifiques d'angle polaire et/ou de pseudorapidité pour étudier les événements $b\bar{b}$.

Lorsqu'un quark b ($\bar{b}$) est créé, il doit s'hadroniser avec un ou deux autres quarks pour former un hadron. La proportion des différents hadrons b générés est dominée par les fractions d'hadronisation qui ont été mesurées dans les collisions pp par LHCb [93, 94].

Quatre expériences principales sont associées au LHC : ALICE, ATLAS, CMS et LHCb. ALICE [88] étudie la physique des ions lourds et le plasma quark-gluon, tandis qu'ATLAS [89] et CMS [90] sont des détecteurs polyvalents qui ont conjointement découvert le boson de Higgs en 2012. LHCb [10] se concentre sur l'étude des particules lourdes et des différences entre la matière et l'antimatière. La figure E.3 montre l'empreinte du LHC et la localisation des quatre expériences.

E.3.2 Le spéctromètre LHCb

Le détecteur LHCb, dédié à l'étude des quarks lourds, en particulier des paires $b\bar{b}$, est un spectromètre à dipôle à un seul bras qui est placé en avant du point de collision des protons, en raison des attributs de la production des paires $b\bar{b}$. Situé à 100 m sous terre près de Ferney-Voltaire en France, il pèse 5600 t et mesure 21 m de long, 10 m de haut et 13 m de large. La Figure E.4 illustre la disposition du détecteur pendant les Run I et Run II du LHC.

La couverture spatiale du détecteur varie de 10 mrad à 250 mrad horizontalement et de 10 mrad à 300 mrad verticalement, couvrant environ 4% de l'angle solide. Cette conception

Figure E.3: Empreinte du LHC, les quatre expériences sont également indiquées.

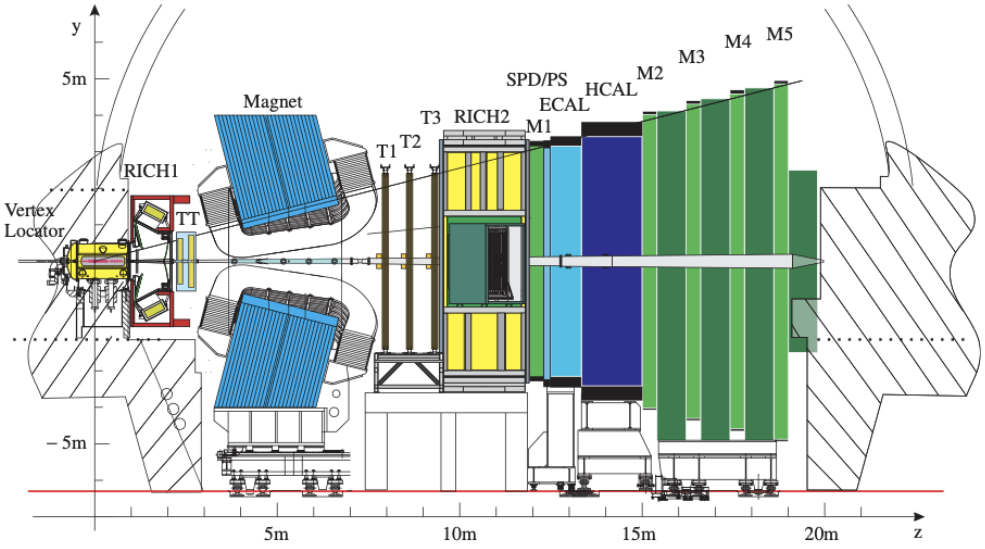

Figure E.4: Vue schématique latérale de LHCb [95] pendant les Run I et Run II du LHC.

facilite l'analyse des hadrons beaux volants le plus, améliorant les mesures de déplacement de vertex.

À 14 TeV, LHCb capture 24% des paires $b\bar{b}$ dans son acceptance, comparé à 41% pour les détecteurs polyvalents comme ATLAS ou CMS. La section efficace inélastique des collisions pp de LHCb et la section efficace de production des paires $b\bar{b}$ sont plus faibles que celles des autres expériences du LHC. Le bruit de fond important provenant des événements pp nécessite un taux de collision plus faible pour LHCb par rapport aux autres détecteurs, le rendant moins compétitif en termes de statistiques pures mais spécialisé pour l'étude des hadrons beaux.

LHCb a enregistré $3\,\text{fb}^{-1}$ de données pendant Run I et $6\,\text{fb}^{-1}$ pendant Run II. Les composants du détecteur sont divisés en deux parties: le système de suivi (detecteur de vertex ou VELO, aimant, Tracker Turicencis, et stations T), pour mesurer l'impulsion des particules, et le système d'identification des particules (détecteurs Cherenkov à image annulaire ou RICH, système de calorimétrie, et chambres à muons), pour identifier leurs natures.

Une autre partie très importante de LHCb est son logiciel. Des outils ont été développés

pour effectuer une reconstruction simple des événements enregistrés afin de faire une première sélection des événements intéressants (trigger [120] et stripping). De plus, une chaîne complète de génération d'événements Monte Carlo a été développée pour utiliser la simulation d'événements à LHCb afin de déterminer des quantités inaccessibles avec les données seules (comme l'efficacité de reconstruction ou de sélection, par exemple).

E.3.3 Le projet FCC-*ee*

Le Future Circular Collider (FCC) [11, 157, 158] est un projet de collisionneur de particules en cours de développement au CERN, actuellement en phase d'étude de faisabilité. Prévu pour potentiellement succéder à la phase haute luminosité du LHC (HL-LHC) [159] d'ici 2040, le FCC vise à faire avancer la recherche en physique des particules avec deux phases. La première phase consiste en un collisionneur e^+e^- avec une énergie dans le centre de masse variant de 90 GeV à 360 GeV, suivi d'un collisionneur pp avec une énergie dans le centre de masse égale ou supérieure à 100 TeV. L'infrastructure du collisionneur comporterait un anneau circulaire d'environ 91 km de circonférence, situé à 300 m sous terre entre la France et la Suisse, comme illustré dans la Figure E.5.

La phase FCC-*ee* est conçue pour atteindre une haute luminosité et réaliser des mesures de précision grâce à la propreté des collisions e^+e^-. Le collisionneur fonctionnera avec quatre points d'interaction et effectuera en particulier, quatre années de prises de données au pôle du Z (environ 90 GeV) pour recueillir environ 6×10^{12} désintégrations de Z. Le processus de production des hadrons b à FCC-*ee* au pôle du Z résulte de la transition $e^+e^- \to b\bar{b}$. Concrètement, les quatre années de prises de données au pôle du Z à FCC-*ee* aboutiront à environ 740×10^9 mesons $B^0/\bar{B}^0$. L'environnement propre des collisions e^+e^-, combiné à leur énergie et à leur grande statistique, offre un avantage significatif pour l'étude de la physique des hadrons b à FCC-*ee* par rapport aux expériences actuelles telles que Belle II [99] et LHCb.

En termes de détecteur, le concept IDEA (Innovative Detector for Electron-positron Accelerators) [163–165] est envisagé dans l'étude de faisabilité de la mesure de $B^0 \to K^{*0}\tau^+\tau^-$. Ce détecteur est doté d'un détecteur de vertex à haute granularité, d'une chambre à dérive ultralégère, et d'un calorimètre à double lecture. Une représentation artistique du détecteur IDEA est montrée dans la Figure E.5. La version d'IDEA utilisée est limitée au système de suivi. L'objectif de la Section E.6 est d'évaluer les performances du détecteur de vertex nécessaires pour observer $B^0 \to K^{*0}\tau^+\tau^-$ à la valeur du SM (voir Section E.6). La résolution sur la mesure de la position des vertex de désintégration sera donc simulée (plusieurs performances étant alors testées) et comparée au point de fonctionnement actuel d'IDEA.

Les événements de FCC-*ee* utilisés dans cette thèse sont simulés avec Pythia [98] et EvtGen [133] fournissant des échantillons de signal et de bruit de fond. La reconstruction de ces événements est effectuée en utilisant le logiciel FCCAnalyses [167] intégrant le modèle de détecteur IDEA mentionné ci-dessus.

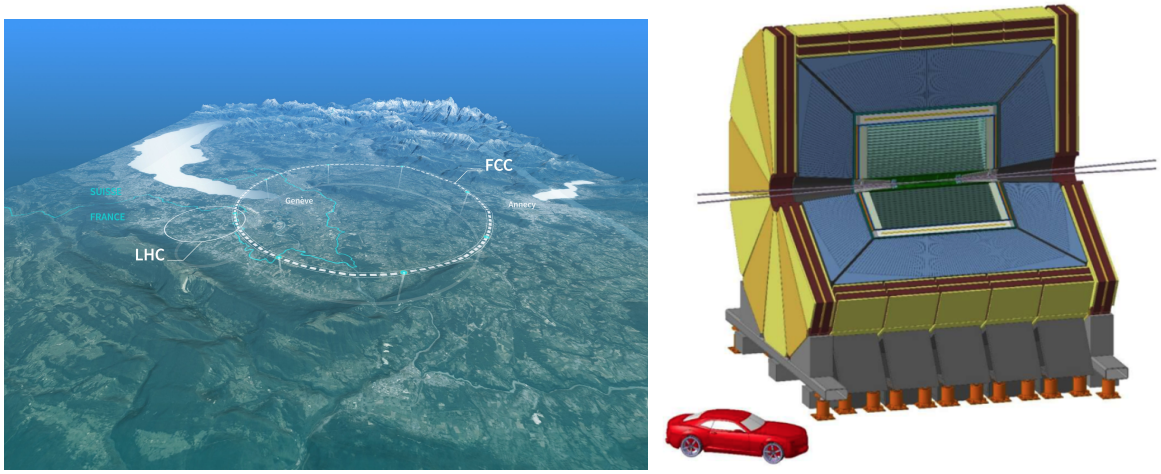

Figure E.5: Left: empreinte du FCC, un collisionneur circulaire de 91 km. Right: représentation artistique de IDEA.

E.4 Recherche de $B_s^0 \to K_S^0 K^+ K^-$

Cette section est dédiée à l'analyse qui a permis la mesure des rapports d'embranchement $B_{d,s}^0 \to K_S^0 h^+ h'^-$ (avec $h' = \pi^\pm, K^\pm$) avec les données de LHCb colléctées lors du Run I et du Run II du LHC. Dans cette analyse, les rapports d'embranchement sont mesurés relativement à $B^0 \to K_S^0 \pi^+ \pi^-$ dans le but de factoriser et supprimer les possibles effets (biais) du détecteur LHCb. La formule permettant de déterminer ces rapports d'embranchement est :

$$\frac{BF(B_{d,s}^0 \to K_S^0 h^+ h'^-)}{BF(B^0 \to K_S^0 \pi^+ \pi^-)} = \frac{N_{B_{d,s}^0 \to K_S^0 h^+ h'^-}}{N_{B^0 \to K_S^0 \pi^+ \pi^-}} \frac{\epsilon_{B^0 \to K_S^0 \pi^+ \pi^-}}{\epsilon_{B_{d,s}^0 \to K_S^0 h^+ h'^-}} \frac{f_d}{f_{d,s}} \tag{E.4.1}$$

où BF veut dire rapport d'embranchement, N signifie nombre d'événements mesurés dans les données, ϵ symbolise l'éfficacité (selection + reconstruction) déterminée à partir de simulations et $f_{d(s)}$ est le facteur d'hadronisation du quark b en $B^0(B_s^0)$ qui est mesuré par LHCb.

Dans cette section, les grands principes de la sélection construite pour les différents modes vont être introduits. Après, le mass fit permettant l'extraction des nombres d'événements sera rapidement présenté. Ensuite, la méthode de détermination des efficacités sera succinctement décrite. Puis, la question des systématiques sera évoquée et enfin, les résultats seront présentés.

E.4.1 Sélection

Tous les événements (collisions) enregistrés par LHCb ne contiennent pas $B_{d,s}^0 \to K_S^0 h^+ h'^-$, c'est pourquoi une sélection des événements d'intérêt a été développée. De plus, là où le nombre d'événements est extrait des données, les efficacités sont extraites de simulations, la sélection construite (pour chaque mode) doit donc être appliquée simultanément aux données et à ces simulations.

Le processus de sélection commence avec l'utilisation de triggers et de lignes de stripping dédiés. Il s'agit de prérequis basiques sur les informations brutes issues des événements (dont des informations provenant de reconstructions automatisées simples), afin de faire un premier tri important des événements. Ensuite, une étape appelée présélection est réalisée afin de ne garder que les événements les mieux définis (les plus intéressants pour la mesure), c'est-à-dire ceux avec un vertex de B isolé, ceux avec un vertex $K_S^0 \to \pi^+ \pi^-$ suffisamment séparé (30 mm en avant) du vertex du B, et ceux où l'impulsion des particules $h^{(\prime)}$ permet une identification optimale des $\pi^\pm$ et $K^\pm$ par LHCb.

Après ces étapes, le cœur de la sélection est l'utilisation de deux outils d'analyse multivariés qui permettent la discrimination des deux types de bruits de fond restants les plus toxiques pour la mesure. Le premier type de bruit de fond à discriminer est le bruit de fond combinatoire. Il s'agit d'événements reconstruits à partir d'une mauvaise association des particules (ne correspondant donc pas au signal $B_{d,s}^0 \to K_S^0 h^+ h'^-$) et qui peuplent tout le spectre de masse. Le second type de bruit de fond à traiter sont les cross-feeds. Ce sont des événements de signal, mais où $h^{(\prime)}$ est mal identifié (par exemple $B^0 \to K_S^0 \pi^+ K^-$ dans $B^0 \to K_S^0 \pi^+ \pi^-$ à cause d'une erreur d'identification de K^- en π^-), ils peuplent les régions autour des événements de signal. Pour combattre ces deux types de bruits de fond, deux sélections de machine learning basées sur l'algorithme XGBoost [171] sont développées. L'algorithme XGBoost réalise la classification des événements en tant que signal et bruit de fond en utilisant un grand nombre de petits arbres de décision (faibles individuellement) via une optimisation en descente de gradient. En nourrissant l'algorithme avec un groupe de variables appelées variables discriminatives pour chaque événement, celui-ci donne en sortie un nombre symbolisant la probabilité pour chaque événement d'être un signal ou non. À la fin, il suffit de placer une coupure sur cette variable pour sélectionner les événements d'intérêt. L'analyse multivariée est un puissant outil de sélection car elle permet la prise en compte des corrélations entre les variables discriminatives. La sélection

dédiée à la discrimination des bruits de fond combinatoires utilise les variables topologiques des événements en entrée (par exemple, l'impulsion transverse du B reconstruit, la distance de vol du K_S^0, etc.) et celle dédiée à la discrimination des cross-feeds utilise un ensemble de variables d'identification de particules déterminées à partir de réseaux de neurones.

Un processus d'optimisation à deux dimensions des coupures à appliquer sur les variables de sortie des deux outils est réalisé afin de déterminer un point de fonctionnement (combinaison des deux coupures) optimal pour chaque mode. Concrètement, étant donné qu'il y a du signal B^0 et B_s^0 dans les données de chaque état final ($K_S^0 hh'$), un point de fonctionnement est déterminé pour chacun d'eux. Dans chaque spectre (état final), un des deux types de B est favorisé (c'est-à-dire plus présent) que l'autre, on parle alors de sélection du mode favorisé et du mode supprimé. Par construction, les bruits de fonds sont plus toxiques pour le mode supprimé et donc, la selection du mode supprimé utilise des coupures plus sévéres (rejetant plus d'événements, et donc plus de signal) que la selection du mode favorisé. Pour simplifier ici, seule une séparation des données/simulations par mode est évoquée, mais en réalité il y a aussi séparation par période de prise de données et type de reconstruction du K_S^0 (dépendant de l'endroit où $K_S^0 \to \pi^+\pi^-$ est mesuré dans le détecteur). La reconstruction du K_S^0 est alors dénotée DD pour Down-Down ou LL pour Long-Long.

E.4.2 Nombre d'événements

Le nombre d'événements de signal dans les données est mesuré pour chaque mode via l'utilisation d'un mass fit sur chaque spectre de données après sélection. Le mass fit est réalisé sur la distribution en masse invariante de B reconstruite des événements mesurés dans la fenêtre $[5100, 5750]$ MeV afin de pouvoir en modéliser toutes les composantes. Les composantes du fit sont les contributions considérées dans la modélisation par les analystes. Ici, dans chaque spectre, il s'agit des pics de signal (B^0 et B_s^0), du bruit de fond combinatoire et des cross-feeds ayant survécu à la sélection totale, ainsi que d'un autre bruit de fond appelé les partiellement reconstruits. Les partiellement reconstruits sont des événements qui ne sont pas des événements de signal car avec une (des) particule(s) additionnelle(s) (π^0 par exemple) mais où seules les particules de signal ont été reconstruites par le détecteur. Ils peuplent les régions avant les pics de signal. La Figure E.6 illustre la forme d'un spectre $B^0 \to K_S^0\pi^+\pi^-$ typique avec les différents types d'événements.

Chaque composante du mass fit doit être modélisée dans le fit total, afin d'extraire les nombres d'événements de signal. Ici, les pics de signal sont chacun modélisés par une double Crystal Ball [152], le bruit de fond combinatoire par une fonction linéaire [151], chaque cross-feed (B^0 et B_s^0) par une double Crystal Ball et chaque partiellement reconstruit (B^0 et B_s^0) par la convolution d'une ARGUS [180] et d'une Gaussienne [150]. Afin de simplifier le fit, certains paramètres sont d'abord déterminés à partir de fits sur simulations avant d'être fixés dans le fit final (paramètres de forme des pics de signal par exemple). De plus, certains paramètres sont partagés entre les spectres (moyenne/masse des pics de signal par exemple). Le mass fit final est réalisé en trouvant le modèle total minimisant l'écart avec les données. Le nombre d'événements associé à un pic de signal donné est alors déterminé par l'intégrale du modèle associé obtenu. La Figure E.7 montre les résultats du mass fit réalisé sur un spectre $K_S^0\pi^+\pi^-$. Le Tableau E.1 résume les nombres d'événements mesurés par le mass fit sur les données avec l'optimisation du mode favorisé.

E.4.3 Efficacités

Les efficacités totales (reconstruction et sélection) associées à chaque mode sont nécessaires afin de renormaliser les nombres d'événements mesurés aux nombres réels d'événements qui ont eu

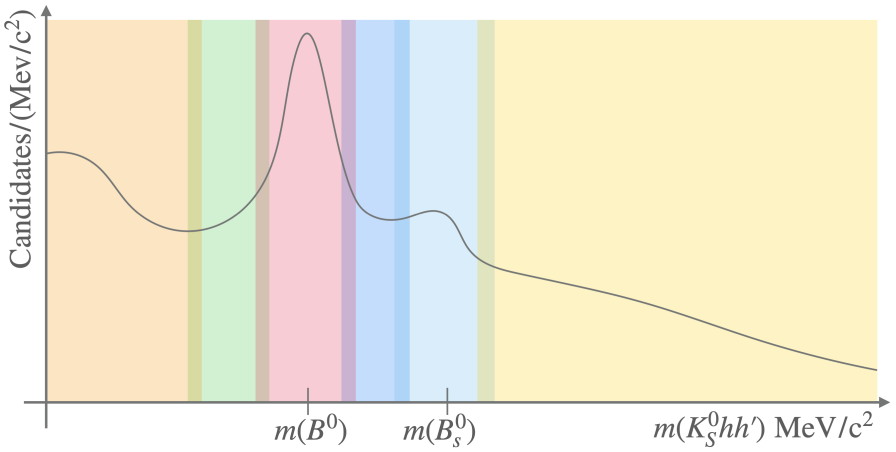

Figure E.6: Illustration d'un spectre de masse $B^0 \to K_S^0 \pi^+ \pi^-$ typique, avec les zones d'influence de chaque composante et où les données sont représentées par la ligne. Les pics de signal se trouvent dans les zones rouge (B^0) et bleu clair (B_s^0), le bruit de fond combinatoire est partout mais seulement seul dans la région jaune à droite, les cross-feeds dans les queues des pics de signal en vert et bleu foncé, et les partiellement reconstruits sont regroupés à gauche dans la zone orange.

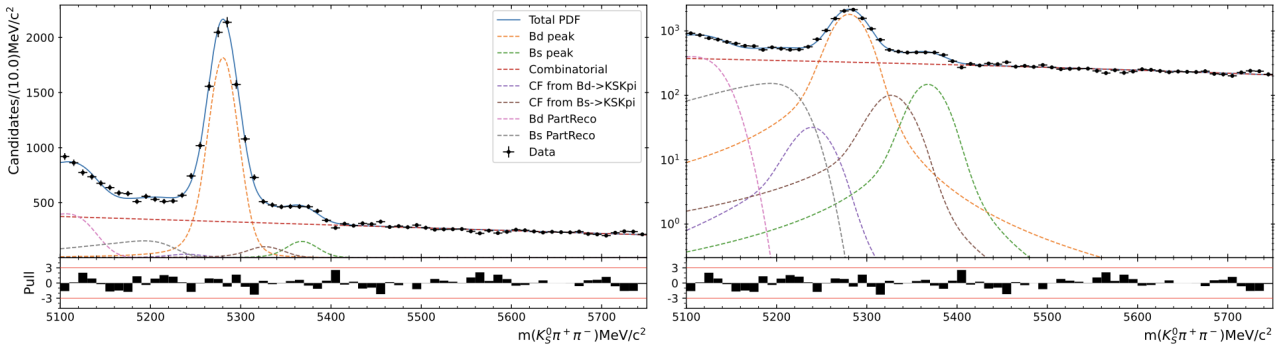

Figure E.7: Résultat d'un mass fit avec l'optimisation du mode favorisé en 2018 pour le spectre $K_S^0 \pi^+ \pi^-$ avec la reconstruction de K_S^0 DD (Down-Down). Le résultat est montré en échelle linéaire sur la gauche et en échelle logarithmique sur la droite.

lieu. Cela est nécessaire pour factoriser les effets de détecteur et les choix d'analyse de la mesure et donc ici déterminer des rapports d'embranchement généraux. Pour déterminer les efficacités, des événements simulés sont utilisés afin d'estimer la proportion d'événements de signal qui survivent à l'analyse (sélection et reconstruction).

La mesure des rapports d'embranchement étant le point de départ d'analyses en amplitudes visant à comprendre les états intermédiaires (quasi deux corps) des désintégrations, les efficacités sont déterminées projetées dans le plan du square Dalitz (sqDP) [196]. L'utilisation du sqDP permet la mise en évidence de la cinématique des résonances intermédiaires à l'œuvre dans le processus. Le sqDP est un plan 2D défini par deux variables (m', θ') qui sont définies de 0 à 1.

Certains effets de détecteurs dans les simulations d'événements expérimentaux en physique des particules peuvent souffrir de mauvaises modélisations (réponse des détecteurs responsables de l'identification, efficacité de certains triggers, ...). Des corrections aux simulations doivent donc être considérées pour améliorer l'accord entre celles-ci et les données. Or l'amplitude de ces effets varie souvent avec la cinématique de la désintégration. C'est pourquoi l'utilisation de corrections définies dans le sqDP est intéressante pour corriger l'efficacité des événements en fonction de leur cinématique. Donc, au-delà de la réutilisation des efficacités pour de futures analyses, l'utilisation du sqDP est aussi motivée par le fait de corriger les efficacités de la

Decays	2011	2012a	2012b	2015	2016	2017	2018	Sum
$B_d^0 \to K_S^0(\mathrm{LL})\pi^+\pi^-$	550±31	421±28	760±40	501±29	2820±70	2900±70	3350±70	11300±140
$B_d^0 \to K_S^0(\mathrm{DD})\pi^+\pi^-$	1120±50	720±40	1990±60	990±50	6070±110	6940±120	8550±130	26380±230
$B_d^0 \to K_S^0(\mathrm{LL})K^+K^-$	288±21	150±14	418±23	267±19	1550±50	1530±40	1800±50	6010±90
$B_d^0 \to K_S^0(\mathrm{DD})K^+K^-$	417±26	288±21	940±40	494±30	3540±80	3510±70	4060±80	13250±150
$B_d^0 \to K_S^0(\mathrm{LL})K^+\pi^-$	44±13	40±10	34±14	25±13	159±25	185±27	251±27	740±50
$B_d^0 \to K_S^0(\mathrm{DD})K^+\pi^-$	70±19	46±14	144±28	114±18	500±50	540±50	610±50	2020±90
$B_d^0 \to K_S^0(\mathrm{LL})\pi^+K^-$	69±13	14±11	69±15	38±12	239±27	202±26	229±28	860±50
$B_d^0 \to K_S^0(\mathrm{DD})\pi^+K^-$	97±21	26±13	130±27	87±18	500±50	590±50	610±50	2030±90
$B_s^0 \to K_S^0(\mathrm{LL})\pi^+\pi^-$	37±13	30±14	62±16	49±15	204±34	166±33	280±40	830±70
$B_s^0 \to K_S^0(\mathrm{DD})\pi^+\pi^-$	73±23	26±17	225±35	48±25	520±60	450±60	710±70	2050±120
$B_s^0 \to K_S^0(\mathrm{LL})K^+K^-$	16±10	5±6	10±9	6±8	11±18	26±17	6±19	80±30
$B_s^0 \to K_S^0(\mathrm{DD})K^+K^-$	25±13	4±9	23±16	13±14	140±40	71±29	77±32	350±60
$B_s^0 \to K_S^0(\mathrm{LL})K^+\pi^-$	145±16	83±12	172±18	121±16	613±34	710±40	790±40	2640±70
$B_s^0 \to K_S^0(\mathrm{DD})K^+\pi^-$	264±23	150±17	527±34	238±21	1530±60	1710±60	1940±60	6360±110
$B_s^0 \to K_S^0(\mathrm{LL})\pi^+K^-$	170±16	88±14	213±19	117±15	750±40	715±35	820±40	2860±70
$B_s^0 \to K_S^0(\mathrm{DD})\pi^+K^-$	297±24	171±18	523±33	282±24	1590±60	1710±60	2060±60	6640±120

Table E.1: Nombres d'événements de signal et incertitudes statistiques associées retournés par le mass fit sur les données avec l'optimisation du mode favorisé.

meilleure façon possible. La Figure E.8 montre la distribution de l'efficacité totale dans le sqDP pour les deux optimisations de $B^0 \to K_S^0\pi^+\pi^-$ 2018 avec la reconstruction DD de K_S^0.

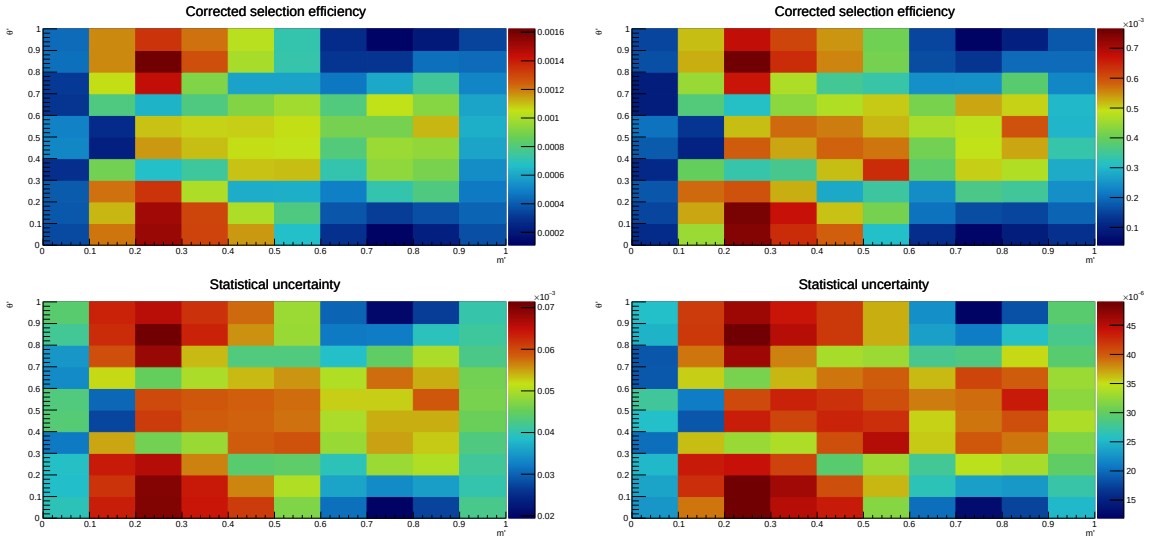

Figure E.8: La colonne de gauche (droite) représente l'éfficacité totale à travers le sqDP pour la sélection du mode favorisé (supprimé) des échantillons simulés de 2018 $B^0 \to K_S^0\pi^+\pi^-$ pour la reconstruction DD de K_S^0 et la direction magnétique vers le bas. La première ligne indique l'efficacité totale et la deuxième ligne indique l'incertitude statistique.

La distribution de l'efficacité dans le sqDP est donc déterminée pour tous les échantillons disponibles. Cependant, pour la mesure des rapports d'embranchement, une seule efficacité par échantillon est nécessaire (la combinaison des échantillons d'un même mode pour obtenir un seul rapport d'embranchement par mode se fait plus tard), c'est pourquoi il est nécessaire de réaliser une moyenne de la distribution de chaque échantillon. Pour cette analyse, une méthode dédiée a

été développée et le moyennage se fait en prenant en compte la distribution des événements de données dans le sqDP. Cette information est modélisée par des poids statistiques symbolisant la probabilité qu'un événement soit de signal, les sWeights [182]. Ces poids sont déterminés pour chaque événement de données en réalisant un nouveau mass fit après la détermination des nombres d'événements. Afin qu'ils soient utilisables avec les efficacités précédemment déterminées, eux aussi sont projetés dans le sqDP. La Figure E.9 montre une distribution de sWeights associée à $B^0 \to K_S^0 \pi^+ \pi^-$ 2018.

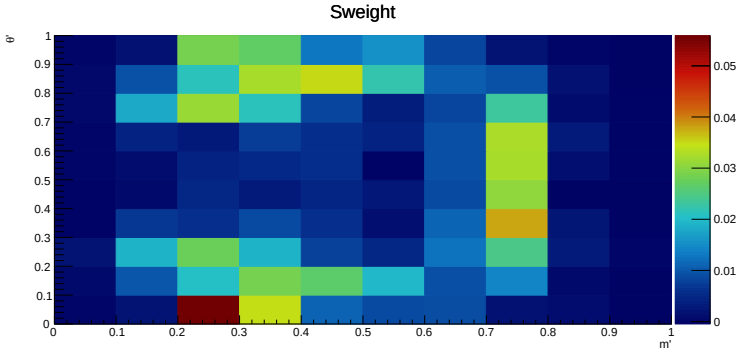

Figure E.9: Distrubution des sWeights B^0 déterminée sur le spectre $K_S^0 \pi^+ \pi^-$ pour la reconstruction DD de K_S^0 en 2018.

Un des problème possible de l'utilisation des sWeights dans le moyennage pourrait venir du fait que certains échantillons de données ont une faible statistique, conduisant donc à des poids faiblement définis. La méthode de moyennage développée adresse ce problème en utilisant seulement les sWeights des périodes avec le plus de données (e.g. ceux de 2018, 2017 et 2016) et aussi en utilisant les poids provenant des échantillons les moins pollués par les bruits de fond (e.g. avec la sélection sur le mode supprimé). Ainsi, la formule de détermination des efficacités moyennes par échantillon est :

$$\bar{\varepsilon}_k = \frac{\sum_{k'} \bar{\varepsilon}_{k,k'}}{3}, \tag{E.4.2}$$

où $\bar{\varepsilon}_k$ est l'efficacité moyenne associée à un échantillon k (n'importe quel mode, période, ...), k' est un indice courant sur l'échantillon à haute statistique (2018, 2017 et 2016 avec la sélection du mode supprimé, correspondant à k) de référence utilisé dans le moyennage et $\bar{\varepsilon}_{k,k'}$ est l'efficacité moyenne déterminée pour l'échantillon k avec la période de référence k'. Cette moyenne est définie comme :

$$\bar{\varepsilon}_{k,k'} = \frac{\sum_j sW_{j,k'} \varepsilon_{j,k'}^{-1} \varepsilon_{j,k}}{\sum_j sW_{j,k'} \varepsilon_{j,k'}^{-1}}, \tag{E.4.3}$$

où j est l'indice des bins du sqDP, $sW_{j,k'}$ symbolise la valeur de sWeight du bin j et de l'échantillon k', $\varepsilon_{j,X}$ signifie la valeur de l'efficacité totale dans le bin j pour l'échantillon X.

Ainsi, une valeur d'efficacité moyenne par échantillon est déterminée. Cette détermination est naturellement dépendante de la statistique des événements simulés utilisés dans le calcul (e.g. provenant de k et k'), c'est pourquoi une incertitude sur la statistique Monte Carlo (MC) est associée à chaque moyenne. De plus, l'utilisation de la méthode de moyennage décrite est un choix possible parmi d'autres et une incertitude supplémentaire lui est associée, celle-ci est construite à partir de la dispersion des $\bar{\varepsilon}_{k,k'}$ autour de $\bar{\varepsilon}_k$. Dans le but de mesurer cette dispersion avec le maximum de points possible, la distribution utilisée combine les différentes périodes de prise de données. Le Tableau E.2 montre les efficacités moyennes obtenues et les incertitudes associées pour $B^0 \to K_S^0 \pi^+ \pi^-$ avec la sélection du mode favorisé. On peut remarquer que par construction, l'incertitude associée à la méthode de moyennage est constante entre les périodes.

Year	Mode	K_S^0	$\bar{\varepsilon}$	$\sigma_{\bar{\varepsilon}}^{\text{stat}}$	$\sigma_{\bar{\varepsilon}}^{\text{RMS}}$	$\sigma_{\bar{\varepsilon}}$
2018	$B_d^0 \to K_S^0\pi^+\pi^-$	DD	821.0e-6	6.2e-6	12.2e-6	13.7e-6
2017	$B_d^0 \to K_S^0\pi^+\pi^-$	DD	833.3e-6	6.4e-6	12.2e-6	13.8e-6
2016	$B_d^0 \to K_S^0\pi^+\pi^-$	DD	869.3e-6	6.6e-6	12.2e-6	13.9e-6
2015	$B_d^0 \to K_S^0\pi^+\pi^-$	DD	835.9e-6	6.5e-6	12.2e-6	13.8e-6
2012b	$B_d^0 \to K_S^0\pi^+\pi^-$	DD	519.4e-6	5.8e-6	12.2e-6	13.5e-6
2012a	$B_d^0 \to K_S^0\pi^+\pi^-$	DD	411.6e-6	5.6e-6	12.2e-6	13.4e-6
2011	$B_d^0 \to K_S^0\pi^+\pi^-$	DD	492.0e-6	6.0e-6	12.2e-6	13.6e-6
2018	$B_d^0 \to K_S^0\pi^+\pi^-$	LL	296.9e-6	3.7e-6	6.5e-6	7.5e-6
2017	$B_d^0 \to K_S^0\pi^+\pi^-$	LL	316.9e-6	4.0e-6	6.5e-6	7.6e-6
2016	$B_d^0 \to K_S^0\pi^+\pi^-$	LL	356.3e-6	4.3e-6	6.5e-6	7.8e-6
2015	$B_d^0 \to K_S^0\pi^+\pi^-$	LL	327.5e-6	4.1e-6	6.5e-6	7.7e-6
2012b	$B_d^0 \to K_S^0\pi^+\pi^-$	LL	153.3e-6	3.1e-6	6.5e-6	7.2e-6
2012a	$B_d^0 \to K_S^0\pi^+\pi^-$	LL	176.8e-6	3.7e-6	6.5e-6	7.5e-6
2011	$B_d^0 \to K_S^0\pi^+\pi^-$	LL	187.7e-6	3.8e-6	6.5e-6	7.5e-6

Table E.2: Table d'efficacité pour $B^0 \to K_S^0\pi^+\pi^-$ avec la selection du mode favorisé. Pour chaque année et chaque type de reconstruction de K_S^0, l'efficacité moyenne $\bar{\varepsilon}$, l'incertitude statistique $\sigma_{\bar{\varepsilon}}^{\text{stat}}$, l'incertitude liée à la méthode de moyennage $\sigma_{\bar{\varepsilon}}^{\text{RMS}}$ et l'incertitude totale $\sigma_{\bar{\varepsilon}}$ sont données.

E.4.4 Systématiques

Toute mesure expérimentale vient avec des incertitudes, et donc la mesure des rapports d'embranchement décrite ici également. Une incertitude statistique a déjà été déterminée au niveau de la détermination des nombres d'événements. Les mesures à venir étant issues de données expérimentales, ce n'est cependant pas suffisant et d'autres sources d'incertitudes doivent être considérées, liées à la fois aux spécificités de LHCb et aux choix faits lors de l'analyse. Ce sont les incertitudes systématiques.

Concernant les incertitudes systématiques liées au nombre d'événements mesurés, celles-ci sont déterminées en utilisant des versions alternatives du mass fit. Dans ces versions alternatives, le mass fit est identique à un changement près qui peut être : l'ajout d'une composante, le retrait d'une composante, un changement de modèle, etc. Une systématique est associée à chacun de ces changements à partir de l'écart entre les résultats du mass fit de base et celui du mass fit variant. Ici, il a été observé que la plus grande source d'incertitude systématique venait de la modélisation des bruits de fond combinatoires.

Pour ce qui est des efficacités, deux incertitudes systématiques ont déjà été introduites : celle liée à la statistique des événements simulés et celle liée à la méthode de moyennage. En plus de celles-ci, neuf autres incertitudes systématiques ont été déterminées. Huit de ces incertitudes concernent les corrections considérées dans la détermination des efficacités pour prendre en compte les effets mal simulés. La dernière incertitude est issue du choix du nombre de bins utilisé pour construire les efficacités dans le sqDP. Les deux systématiques précédemment introduites et la majorité de celles provenant des corrections sont propagées classiquement jusqu'aux résultats finaux. Pour les autres, dont celle associée au nombre de bins, les résultats ont été déterminés à partir d'écarts entre des configurations de calcul différentes et la configuration de base. Parmi toutes ces incertitudes, trois sont dominantes : celle associée à la statistique des événements simulés, celle associée à la méthode de moyennage et celle associée au choix du nombre de bins dans le sqDP.

Une dernière source d'incertitude systématique à considérer dans la mesure des rapports d'embranchement provient de la mesure des fractions d'hadronisation du quark b. Ici, les

incertitudes associées aux mesures de LHCb sont considérées.

E.4.5 Résultats

Une valeur de rapport d'embranchement relative à $B^0 \to K_S^0 \pi^+ \pi^-$ est déterminée pour chaque échantillon à partir du nombre d'événements mesurés, des efficacités déterminées, et des fractions d'hadronisation mesurées par LHCb si nécessaire. Dans ce calcul, pour un échantillon donné, seuls les résultats correspondant à la sélection optimisant le mode de cet échantillon sont utilisés.

À partir de ces valeurs par échantillon, les rapports d'embranchement finaux par mode sont obtenus en combinant tous les échantillons d'un même mode via la détermination d'une valeur moyenne par mode. Cette moyenne est la valeur permettant la minimisation d'un χ^2 défini par mode. Les rapports d'embranchement finaux sont :

$$\begin{aligned}
\frac{BF(B^0 \to K_S^0 K^+ K^-)}{BF(B^0 \to K_S^0 \pi^+ \pi^-)}_{\text{Combined}} &= 0.533 \pm 0.015\,(\text{tot.}) \\
\frac{BF(B^0 \to K_S^0 K^\pm \pi^\mp)}{BF(B^0 \to K_S^0 \pi^+ \pi^-)}_{\text{Combined}} &= 0.137 \pm 0.006\,(\text{tot.}) \\
\frac{BF(B_s^0 \to K_S^0 \pi^+ \pi^-)}{BF(B^0 \to K_S^0 \pi^+ \pi^-)}_{\text{Combined}} &= 0.276 \pm 0.025\,(\text{tot.}) \\
\frac{BF(B_s^0 \to K_S^0 K^+ K^-)}{BF(B^0 \to K_S^0 \pi^+ \pi^-)}_{\text{Combined}} &= 0.034 \pm 0.007\,(\text{tot.}) \\
\frac{BF(B_s^0 \to K_S^0 K^\pm \pi^\mp)}{BF(B^0 \to K_S^0 \pi^+ \pi^-)}_{\text{Combined}} &= 1.78 \quad \pm 0.04\,(\text{tot.})
\end{aligned}$$

où tot. correspond à l'incertitude totale.

Comparée à l'analyse précédente de LHCb, celle-ci fournit des résultats compatibles, sauf pour $B_s^0 \to K_S^0 \pi^+ \pi^-$, avec une précision améliorée. L'écart observé sur le mode mentionné provient du fait que les techniques d'analyse utilisées sont améliorées. Les nouveaux résultats sont beaucoup plus fiables. Enfin, cette analyse permet la découverte de $B_s^0 \to K_S^0 K^+ K^-$.

L'analyse est proche de sa version publiée mais est encore en cours de révision par la collaboration. Cela signifie que les résultats présentés ici peuvent évoluer d'ici à la publication si des modifications sont nécessaires. Au vu de la découverte d'une contribution de bruit de fond manquante dans le mass fit $K_S^0 K^+ K^-$, qui devra être adressée dans la version finale de l'analyse, les rapports d'embranchement correspondants seront nécessairement affectés. Néanmoins, la découverte de $B_s^0 \to K_S^0 K^+ K^-$ est déjà garantie grâce au nombre d'événements mesurés.

Cette analyse des rapports d'embranchement est la première étape vers des analyses d'amplitude qui aborderont la riche phénoménologie des transitions $B_{d,s}^0 \to K_S^0 h^+ h'^-$. La Section E.5 présente une analyse préliminaire des amplitudes de $B_s^0 \to K_S^0 \pi^+ \pi^-$.

E.5 Analyse en amplitude intégrée dans le temps de $B_s^0 \to K_S^0\pi^+\pi^-$

Dans cette section, une exploration préliminaire de l'analyse en amplitude intégrée dans le temps de $B_s^0 \to K_S^0\pi^+\pi^-$ à venir est réalisée. Plusieurs amplitudes intermédiaires (quasi deux corps) contribuent à $B_s^0 \to K_S^0\pi^+\pi^-$, ce qui en fait un laboratoire intéressant pour étudier la violation de *CP* et pourrait permettre la mise en évidence de désaccord avec le modèle standard (SM). Une analyse intégrée dans le temps permet l'étude de la violation de *CP* entre les désintégrations directes $B_s^0 \to K_S^0\pi^+\pi^-$ et $\bar{B}_s^0 \to K_S^0\pi^+\pi^-$. En raison de la nature quasi deux corps de $B_s^0 \to K_S^0\pi^+\pi^-$, le formalisme du plan de Dalitz (DP) [194, 195] est utilisé dans cette analyse. L'analyse présentée ici est préliminaire ; il s'agit de dessiner les grandes lignes de la méthode, aucun résultat quantitatif n'est encore obtenu.

Tout d'abord, le logiciel utilisé pour cette analyse est rapidement présenté. Dans un second temps, les informations nécessaires provenant de la mesure des rapports d'embranchement de $B_{d,s}^0 \to K_S^0 h^+ h'^-$ sont listées. Enfin, une première version du fit réalisé pour mesurer la violation de *CP* est montrée.

E.5.1 CRAFT

CRAFT (pour Clermont Root-based Amplitude Fitter Tool) est un package basé sur ROOT conçu pour l'analyse des désintégrations sans charme $B_{d,s}^0 \to K_S^0 h^+ h'^-$. Il a été développé par Marouen Baalouch, Stéphane Monteil et Stéphane Pruvot [69]. CRAFT utilise des classes C++ dépendantes de ROOT [130] et RooFit [204]. CRAFT est conçu pour réaliser des ajustements de plans de Dalitz afin de déterminer les paramètres d'intérêt en utilisant le formalisme du modèle isobare [197] pour décrire la dynamique de la désintégration. Plusieurs profils de résonance sont implémentés dans CRAFT, ainsi que d'autres modèles (gaussien, polynomial, etc.).

CRAFT est un logiciel de fit par maximum de vraisemblance (ou likelihood) qui utilise le logiciel minuit [205] pour la procédure de maximisation. CRAFT permet de réaliser une analyse du plan de Dalitz en effectuant un fit simultané de plusieurs échantillons indépendants pour déterminer un ensemble commun de paramètres (isobare, profils de résonance, ...) en maximisant la likelihood du fit.

E.5.2 Apport de la mesure des rapports d'embranchement

Cette analyse est la suite directe de la mesure des rapports d'embranchement de $B_{d,s}^0 \to K_S^0 h^+ h^-$. Un certain nombre de variables / informations de $B_{d,s}^0 \to K_S^0 h^+ h^-$ sont réutilisées ici. Ces quantités vont être présentées dans la suite.

Les données utilisées dans cette analyse préliminaire sont celles de l'échantillon $K_S^0\pi^+\pi^-$ de 2018 avec la sélection sur le mode supprimé qui est $B_s^0 \to K_S^0\pi^+\pi^-$ (deux échantillons : K_S^0 DD et K_S^0 LL). Ce travail utilise seulement les données de 2018 dans le but d'arriver plus vite à des plots illustratifs tout en utilisant les échantillons de plus grande statistique. L'étude étant concentrée sur B_s^0, une coupure autour de la masse de B_s^0 est utilisée. La Figure E.10 montre la distribution des événements de données $B_s^0 \to K_S^0\pi^+\pi^-$ utilisés dans le DP et le sqDP.

Assumant en première approximation que les données utilisées ne contiennent que des événements $B_s^0 \to K_S^0\pi^+\pi^-$ et du bruit de fond combinatoire, ce dernier doit être considéré dans ce travail. La distribution dans le DP et le sqDP du bruit de fond combinatoire associé à ces échantillons est déterminée à partir des événements avec une masse de B reconstruite supérieure à 5500 MeV (là où seul le bruit de fond combinatoire se trouve). Ces distributions permettent la modélisation d'une composante dédiée dans le fit final.

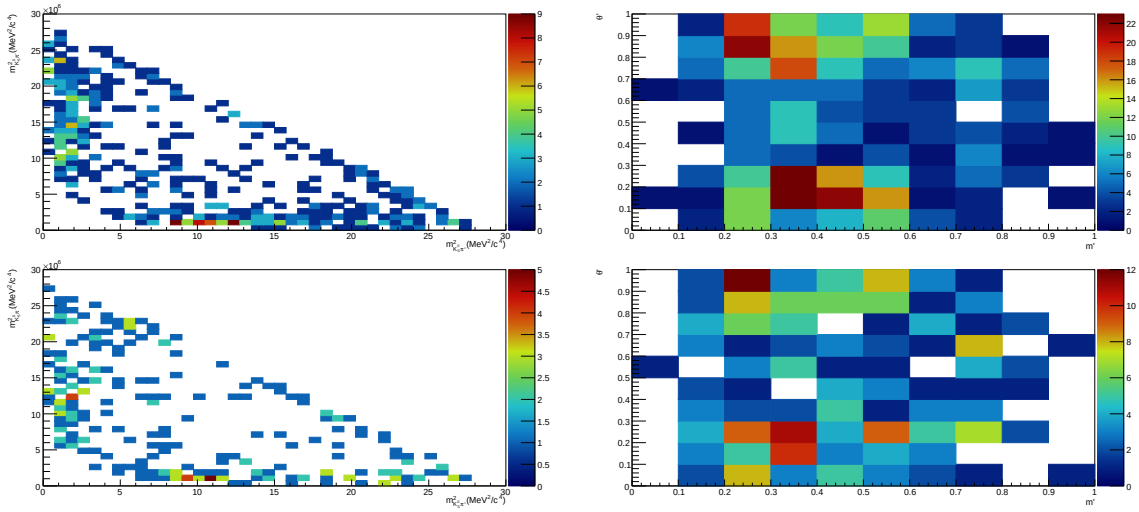

Figure E.10: Distribution des événements $B_s^0 \to K_S^0\pi^+\pi^-$ dans le DP (à gauche) et le sqDP (à droite) pour les échantillons 2018 DD (en haut) et LL (en bas). Les rectangles blancs dénotent les bins vides. Deux zones très peuplées peuvent être vues en haut et en bas du sqDP, et sur les bords du DP respectivement, correspondant aux résonances $K^{*\pm}(K_S^0\pi^\pm)$.

Le pattern de l'efficacité totale associée aux échantillons utilisés doit aussi être pris en compte pour avoir la meilleure description possible des données. Les distributions dans le sqDP des efficacités correspondantes aux échantillons utilisés sont reprises de la mesure des rapports d'embranchement.

Enfin, pour fonctionner, CRAFT a besoin des fractions de signal et de bruits de fond combinatoires à considérer dans le fit. Ces fractions sont déterminées à partir d'un fit de masse simplifié par rapport à celui de la mesure des rapports d'embranchement pour l'instant.

E.5.3 DP fit

Une première version du fit dans le DP a été réalisée pour cette analyse préliminaire. Le signal est modélisé en utilisant le modèle isobar [197], qui prend en compte une fonction de densité de probabilité (p.d.f.) pour chaque composante issue des états intermédiaires constituant le signal. Le Tableau E.3 présente les résonances considérées dans ce fit (par exemple, la particule à quasi deux corps qui se désintègre) avec les modèles utilisés pour les décrire ainsi que leurs paramètres.

Resonance	Parameters	Lineshape	Value references
$K^{*\pm}(892)$	$m_0 = 891.66 \pm 0.26$ $\Gamma_0 = 50.8 \pm 0.9$	RBW	[47]
$K_0^{*\pm}(1430)$	$\mathcal{R}e(\lambda_0) = 0.204 \pm 0.103$ $\mathcal{I}m(\lambda_0) = 0$ $\mathcal{R}e(\lambda_1) = 1$ $\mathcal{I}m(\lambda_1) = 0$	EFKLLM	[201]
$\rho^0(770)$	$m_0 = 775.26 \pm 0.25$ $\Gamma_0 = 149.8 \pm 0.8$	GS	[47]
Non Resonant (NR)		DP flat	

Table E.3: Résumé des résonances considérées dans le fit, ainsi que des modèles utilisés pour les décrire, des paramètres associés et des références d'où ils proviennent.

La Figure E.11 affiche le résultat du fit réalisé sur le sqDP pour 2018 avec la reconstruction DD de K_S^0 via CRAFT. La projection sur chacune des variables de Dalitz est présentée. La version du fit correspondant au K_S^0 LL est similaire, avec moins d'événements. Pour les besoins de cette analyse préliminaire, il est intéressant de noter qu'une asymétrie visuelle est déjà observée pour la résonance $K^{*\pm}(892)$ entre $m^2_{K_S^0\pi^+}$ et $m^2_{K_S^0\pi^-}$, avec environ deux fois plus de $K^{*-}(892)$ que de $K^{*+}(892)$. Pour aller plus loin, la détermination d'observables pour quantifier l'asymétrie sera nécessaire. Le but final de cette analyse sera de comparer les observables expérimentales déterminées pour chaque résonance aux prédictions du SM afin de vérifier s'il y aurait une nouvelle source de violation de *CP*.

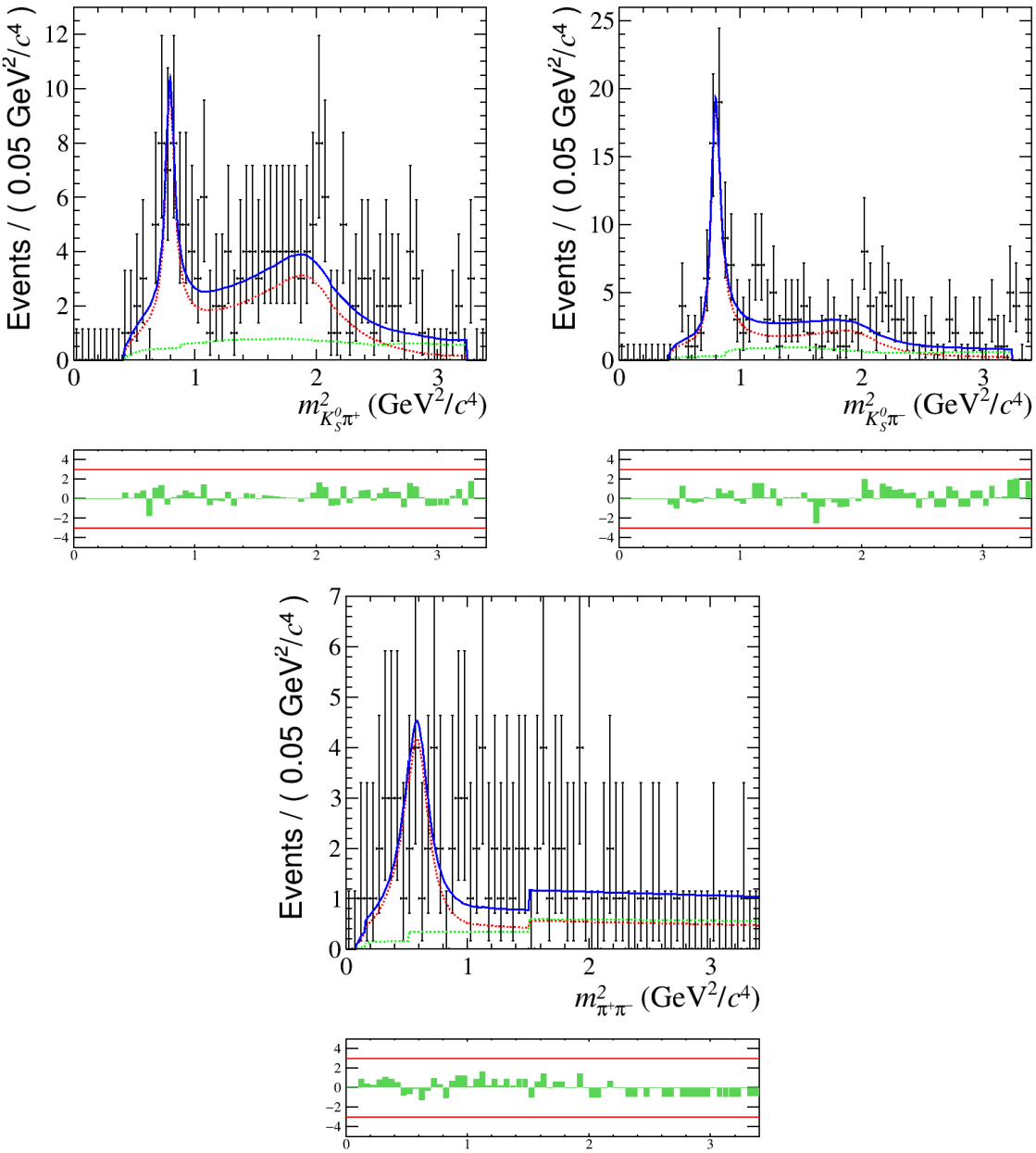

Figure E.11: Projections des données de 2018 avec la reconstruction de K_S^0 DD, présentées en points noirs, pour le fit sur $m^2_{K_S^0\pi^+}$ (à gauche), $m^2_{K_S^0\pi^-}$ (à droite) et $m^2_{\pi^+\pi^-}$ (en bas). Le fit complet est montré en bleu, le bruit de fond combinatoire en vert et le modèle du signal en rouge.

E.6 $B^0 \to K^{*0}\tau^+\tau^-$ à FCC-*ee*

Ce chapitre est dédié à l'étude de faisabilité de la mesure de $B^0 \to K^{*0}\tau^+\tau^-$ pour de futures expériences à FCC-*ee*. Le but de cette étude est de déterminer les prérequis des détecteurs nécessaires à FCC-*ee* afin de découvrir la désintégration $B^0 \to K^{*0}\tau^+\tau^-$ sous l'hypothèse du SM. Comme expliqué ci-après, un canal de désintégration spécifique de $\tau^\pm$ est étudié afin d'utiliser une méthode permettant la reconstruction cinématique complète de la désintégration, en particulier la reconstruction des neutrinos dans l'état final. Pour cette raison, le paramètre clé du détecteur dans cette étude est la résolution sur la position des vertex. Dans cette analyse, une simulation d'événements au FCC-*ee* est utilisée avec plusieurs hypothèses de détecteur de vertex pour évaluer la précision de la mesure du rapport d'embranchement de $B^0 \to K^{*0}\tau^+\tau^-$ en fonction des performances du détecteur de vertex, fournissant ainsi de premières conclusions sur la faisabilité de la mesure à FCC-*ee* et des éléments pour la conception des détecteurs.

La méthode de reconstruction topologique de la désintégration est d'abord introduite. Ensuite, les bruits de fond dominants et la sélection construite pour les combattre sont décrits. Puis, la façon d'accéder à la précision sur la mesure du rapport d'embranchement est présentée. Enfin, les résultats de l'analyse sont montrés.

E.6.1 Reconstruction topologique de la désintégration

Le canal de désintégration $B^0 \to K^{*0}\tau^+\tau^-$ fournit une grande variété d'états finaux. Comme la méthode de reconstruction nécessite la détermination du vertex secondaire, seule la désintégration chargée $K^{*0}(892) \to K^-\pi^+$ sera considérée. De plus, la connaissance des vertex tertiaires (lieux de désintégration des taus) est également requise par la méthode de reconstruction. Cette contrainte impose de considérer au moins $\tau \to \pi\pi\pi\nu_\tau$.

La topologie de ce processus est représentée sur la Figure E.12 : il y a trois vertex de désintégration, huit traces chargées dans l'état final et deux neutrinos non détectés.

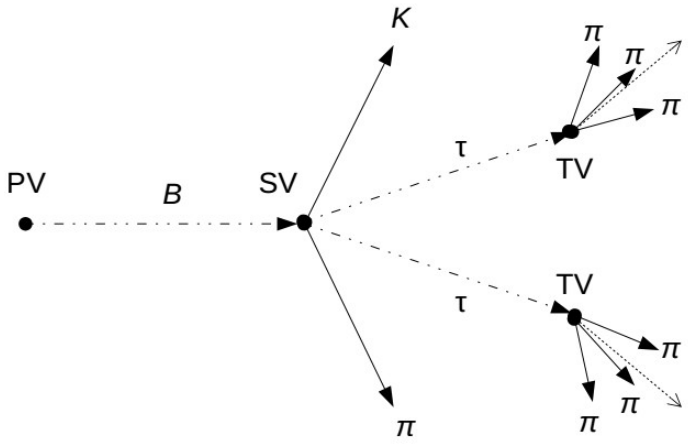

Figure E.12: Topologie de $B^0 \to K^{*0}\tau^+\tau^-$ avec $K^{*0} \to K\pi$ et $\tau \to \pi\pi\pi\nu_\tau$.

Avec cette topologie, deux des dix particules de l'état final du mode de désintégration d'intérêt ne sont pas détectées (et donc non reconstruites dans les données) : ce sont les deux neutrinos issus des vertex tertiaires. Une reconstruction complète des candidats B^0 nécessite les impulsions de neutrinos.

La connaissance des vecteurs de vol de τ (accessibles grâce à la connaissance des vertex secondaire et tertiaires) ainsi que la connaissance de la masse des τ [47] peuvent être utilisées pour déterminer les coordonnées manquantes. En effet, il est possible de déterminer l'impulsion

des neutrinos en partant de la conservation de l'énergie-impulsion de chaque vertex tertiaire :

$$\begin{cases} p^{\perp}_{\nu_\tau} = -p^{\perp}_{\pi_t}, \\ p^{\parallel}_{\nu_\tau} = \dfrac{((m^2_\tau - m^2_{\pi_t}) - 2p^{\perp,2}_{\pi_t})}{2(p^{\perp,2}_{\pi_t} + m^2_{\pi_t})} \cdot p^{\parallel}_{\pi_t} \pm \dfrac{\sqrt{(m^2_\tau - m^2_{\pi_t})^2 - 4m^2_\tau p^{\perp,2}_{\pi_t}}}{2(p^{\perp,2}_{\pi_t} + m^2_{\pi_t})} \cdot E_{\pi_t}, \end{cases} \tag{E.6.1}$$

avec $p^{\perp(\parallel)}_{\nu_\tau}$ l'impulsion transverse (longitudinale) du neutrino selon la direction du τ, $p^{\perp}_{\pi_t}$ l'impulsion transverse associée au système des trois pions, m_τ la masse du τ, m_{π_t} la masse reconstruite associée au système des trois pions et E_{π_t} l'énergie associée au système des trois pions.

Le résultat obtenu pour l'impulsion transverse du neutrino est simple. En revanche, l'impulsion longitudinale est plus complexe et révèle une ambiguïté quadratique. En conséquence, il y a quatre reconstructions de neutrinos possibles pour chaque candidat B^0 et donc quatre reconstructions de B^0, pourtant une seule peut être correcte.

Une règle de sélection est souhaitable pour choisir la "vraie solution". Or, il est possible d'en déterminer une en utilisant la conservation de l'énergie-impulsion au vertex de désintégration du B^0 (vertex secondaire). Cette règle de sélection est :

$$p_{\tau^\pm} = -\frac{\vec{p}^{\perp}_{K^{*0}} \cdot \vec{e}_{\tau^\pm}}{1 - (\vec{e}_{\tau^\pm} \cdot \vec{e}_{B^0})^2} - p_{\tau^\mp} \cdot \frac{\vec{e}_{\tau^\pm} \cdot \vec{e}_{\tau^\mp} - (\vec{e}_{\tau^\pm} \cdot \vec{e}_{B^0})(\vec{e}_{\tau^\mp} \cdot \vec{e}_{B^0})}{1 - (\vec{e}_{\tau^\pm} \cdot \vec{e}_{B^0})^2}. \tag{E.6.2}$$

où $p_{\tau^\pm}$ symbolise l'impulsion de $\tau^\pm$, $\vec{p}^{\perp}_{K^{*0}}$ est l'impulsion transverse de K^{*0} selon la direction du B^0 (définie par les vertex primaire et secondaire), $\vec{e}_{\tau^\pm}$ est le vecteur unitaire de $\tau^\pm$ et $\vec{e}_{B^0}$ est le vecteur unitaire du B^0.

Cette relation permet de prédire l'impulsion d'un τ en fonction des propriétés restantes de la désintégration au vertex secondaire. Il est donc possible de choisir la solution reconstruite τ^+/τ^- qui minimise l'écart entre les prédictions et les reconstructions d'impulsion des τ pour sélectionner la vraie solution.

E.6.2 Bruit de fond et sélection

Dans cette analyse, des événements de signal simulés à FCC-*ee* avec IDEA et différentes hypothèses de résolution sur la mesure des vertex sont utilisés. La configuration correspondant à une résolution longitudinale-transverse de $20 - 3$µm sur les vertex secondaire et tertiaire est utilisée comme référence.

Le signal recherché ayant un faible rapport d'embranchement prédit, il est important de déterminer les bruits de fond pouvant impacter (voire empêcher) la mesure afin de les prendre en compte dans l'analyse. À cet effet, une étude des bruits de fond potentiels a été réalisée. Elle a montré que les bruits de fond les plus préoccupants devraient provenir des processus $b \to c\bar{c}s$ et $b \to c\tau\nu$. Après évaluation de la toxicité potentielle de plusieurs bruits de fond, il a été décidé de considérer neuf bruits de fond, dont les plus toxiques ont un rapport d'embranchement jusqu'à 100 fois plus grand que celui du signal. Le Tableau E.4 présente ces neuf bruits de fond avec le signal, ainsi que, pour chaque mode, le rapport d'embranchement correspondant et les particules additionnelles qui ne sont pas présentes dans le signal.

Les bruits de fond considérés ont été simulés en plus du signal, ce qui a permis d'appliquer la méthode de reconstruction topologique à tous ces modes afin de reconstruire la masse invariante des candidats B^0 correspondants. Cependant, il a été constaté que, même en supposant des performances optimistes pour l'identification des π^0 (80%), lorsque les nombres naturels d'événements de chaque mode sont considérés, la distribution en masse invariante de B^0, donnée en Figure E.13, est dominée par les bruits de fond.

Decay	BF (SM/meas.)	Intermediate decay	BF_had	Additional missing particles
Signal: $B^0 \to K^*\tau\tau$	1.30×10^{-7}	$\tau \to \pi\pi\pi\nu$, $K^* \to K\pi$	9.57×10^{-11}	
Backgrounds $b \to c\bar{c}s$:				
$B^0 \to K^{*0} D_s D_s$	5.47×10^{-5}	$D_s \to \tau\nu$	1.14×10^{-10}	2ν
		$D_s \to \tau\nu, \pi\pi\pi\pi^0$	1.28×10^{-10}	ν , π^0
		$D_s \to \pi\pi\pi\pi^0$	1.45×10^{-10}	$2\pi^0$
		$D_s \to \tau\nu, \pi\pi\pi\pi^0\pi^0$	1.08×10^{-9}	ν , $2\pi^0$
		$D_s \to \pi\pi\pi 2\pi^0$	1.02×10^{-8}	$4\pi^0$
$B^0 \to K^{*0} D_s D_s^*$	1.73×10^{-4}	$D_s \to \tau\nu$	3.60×10^{-10}	2ν, γ/π^0
		$D_s \to \pi\pi\pi\pi^0\pi^0$	3.22×10^{-8}	$4\pi^0$, γ/π^0
Backgrounds $b \to c\tau\nu$:				
$B^0 \to K^{*0} D_s \tau\nu$	9.17×10^{-6}	$D_s \to \tau\nu$	3.59×10^{-10}	2ν
$B^0 \to K^{*0} D_s^* \tau\nu$	2.03×10^{-5}	$D_s \to \pi\pi\pi\pi^0\pi^0$	7.51×10^{-9}	ν, γ, $2\pi^0$

Table E.4: Tableau récapitulatif des bruits de fond possibles. Lorsque la désintégration de τ n'est pas spécifiée, cela signifie $\tau \to \pi\pi\pi\nu$.

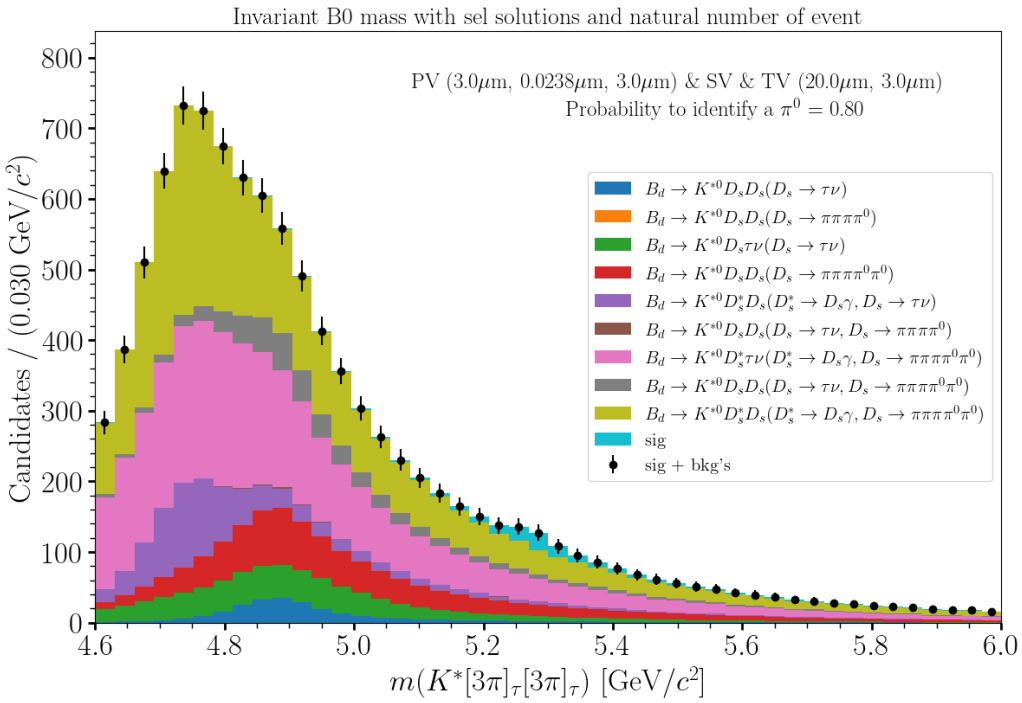

Figure E.13: Distribution en masse invariante des candidats B^0 avec la configuration de résolution des vertex de référence après utilisation de l'identification des π^0.

Pour combattre la toxicité des bruits de fond, une sélection a été développée. Cette sélection se base sur l'utilisation d'un outil d'analyse multivarié, l'algorithme de machine learning XGBoost [171]. Afin de se servir de cet algorithme, plusieurs quantités ont été déterminées au cours de l'analyse, certaines ayant a priori un bon pouvoir discriminant. C'est par exemple le cas de l'impulsion de τ reconstruite avec la méthode de reconstruction topologique, comme le montre la Figure E.14.

L'algorithme XGBoost a été entraîné avec toutes les variables déterminées pour chaque mode, en fournissant un échantillon de signal et un échantillon des bruits de fond combinés en proportion naturelle (afin de mieux combattre les bruits de fond les plus toxiques). En sortie, l'algorithme donne une variable unique par événement, caractérisant la probabilité que l'événement soit un signal ou non. La dernière étape de la sélection consiste à appliquer une coupure sur cette variable. La Figure E.15 montre la distribution en masse invariante des candidats B^0 après sélection ; cette sélection permet une bien meilleure visibilité du pic de signal. L'algorithme XGBoost a été développé avec les performances de mesure de vertex de

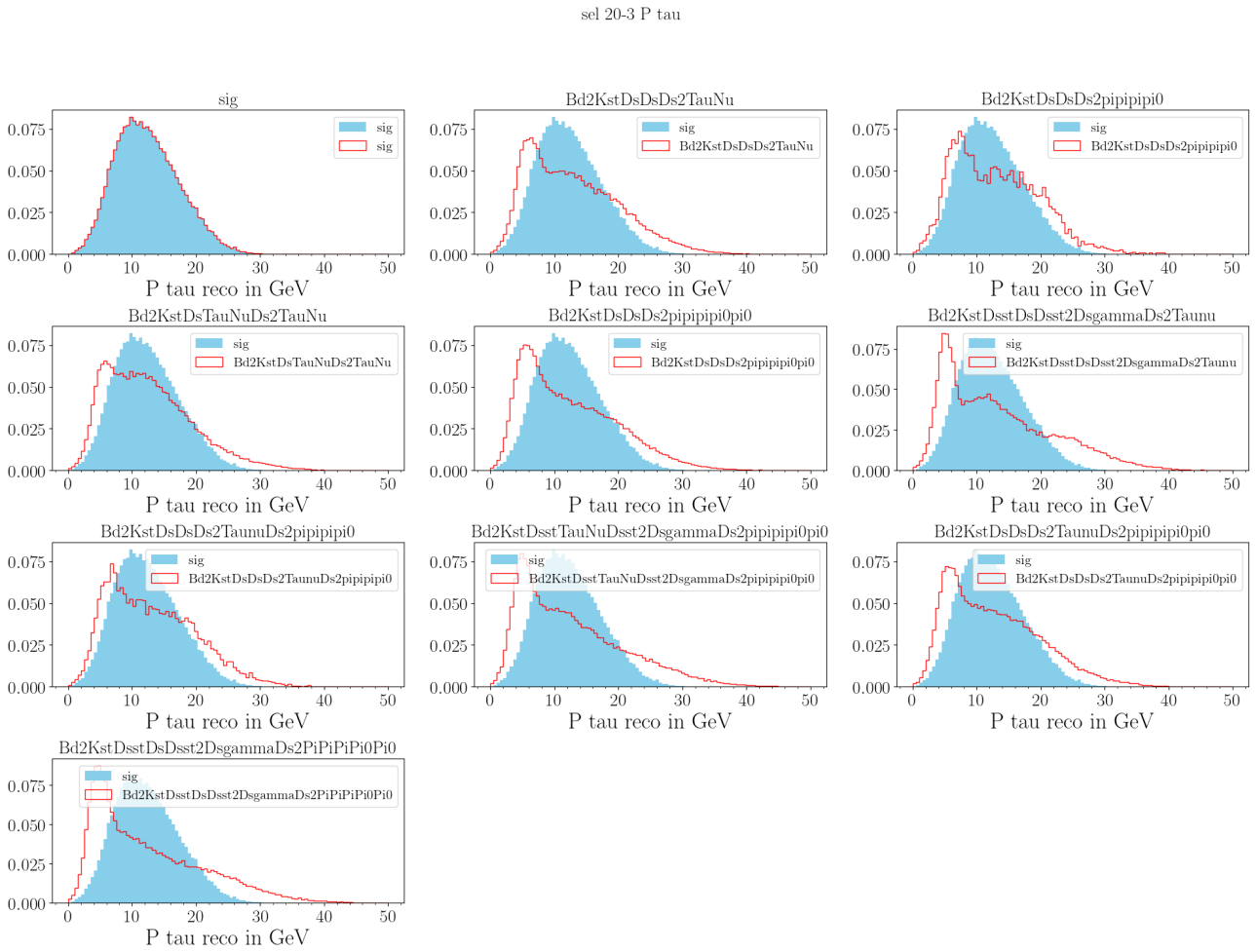

Figure E.14: Distribution de p_τ reconstruit avec ν en fonction du mode de désintégration. La distribution du signal apparaît en bleu sur chacun des graphiques et montre que cette variable a un pouvoir discriminant sur tous les bruits de fond.

référence, mais il est appliqué à toutes les configurations.

E.6.3 Détermination de la précision sur le rapport d'embranchement

Le but de cette analyse est de déterminer les caractéristiques du détecteur de vertex permettant l'observation du signal à FCC-*ee*. À cette fin, il est nécessaire de déterminer la précision de la mesure du rapport d'embranchement du signal pour chaque hypothèse de résolution des vertex.

La précision de la mesure du rapport d'embranchement du signal est déterminée en fittant la distribution en masse invariante des candidats B^0. Pour simplifier ce fit, une fenêtre de masse invariante autour du signal a été définie, permettant d'utiliser seulement un modèle de signal et un modèle simple de bruit de fond. Le modèle de signal utilisé est la combinaison d'une double Crystal Ball [152] et d'une Gaussienne [150] de cœur partageant la même moyenne. Le modèle de bruit de fond est la combinaison de deux exponentielles décroissantes.

Le principe de fonctionnement du fit est d'abord de fitter les paramètres de forme du modèle de signal sur toute la statistique disponible. Ensuite, de fitter la distribution de masse invariante de B^0 totale en fixant les paramètres précédemment déterminés et en introduisant le modèle de bruit de fond. La Figure E.16 montre les deux fits réalisés pour la configuration de référence. En fin de compte, la précision sur le rapport d'embranchement est définie comme le rapport entre l'incertitude sur le nombre d'événements de signal mesuré par le fit et le nombre d'événements de signal.

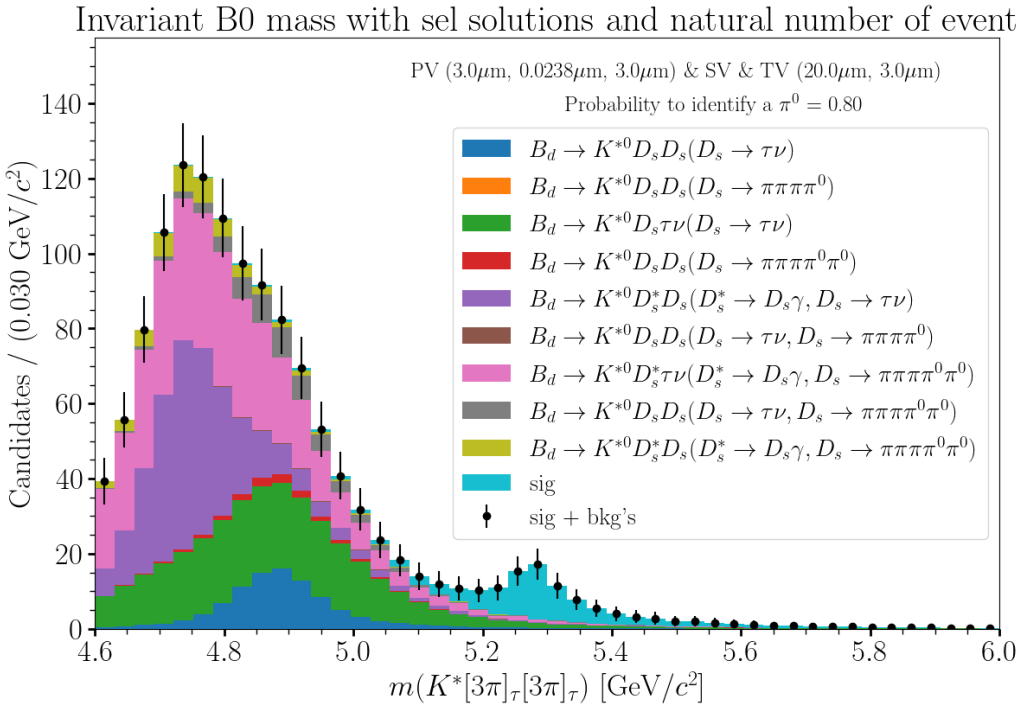

Figure E.15: Distribution en masse invariante des candidats B^0 avec la configuration de résolution des vertex de référence après utilisation de la sélection.

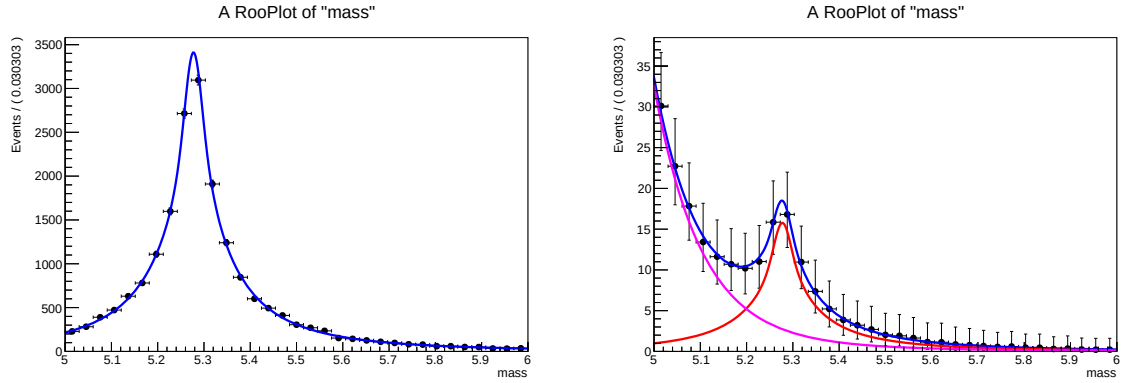

Figure E.16: Fit du signal seul (à gauche) et fit signal + bruit de fond (à droite) pour déterminer la précision de la mesure du rapport d'embranchement pour la configuration de référence. Les distributions de masse invariante de B^0 sont représentées par les points noirs. À droite, le modèle de bruit de fond est en rose, celui du signal en rouge, et le modèle total est en bleu.

La précision de la mesure du rapport d'embranchement de $B^0 \to K^{*0}\tau^+\tau^-$ a été déterminée de la même manière pour plusieurs hypothèses de résolution des vertex. En particulier, des configurations de performance de mesure des vertex correspondant à IDEA dans sa version actuelle, ainsi qu'à des versions améliorées, ont été utilisées. Cela permet de définir des configurations réalistes pour tirer les conclusions de ce travail.

E.6.4 Résultats

Le résultat de ce travail est présenté dans la Figure E.17, qui montre la précision de la mesure du rapport d'embranchement de $B^0 \to K^{*0}\tau^+\tau^-$ en fonction des performances de détecteur de vertex. Sur cette figure, des lignes de niveau correspondant aux seuils d'évidence (3σ) et de découverte (5σ) sont affichées. Il est intéressant de noter que la version actuelle de

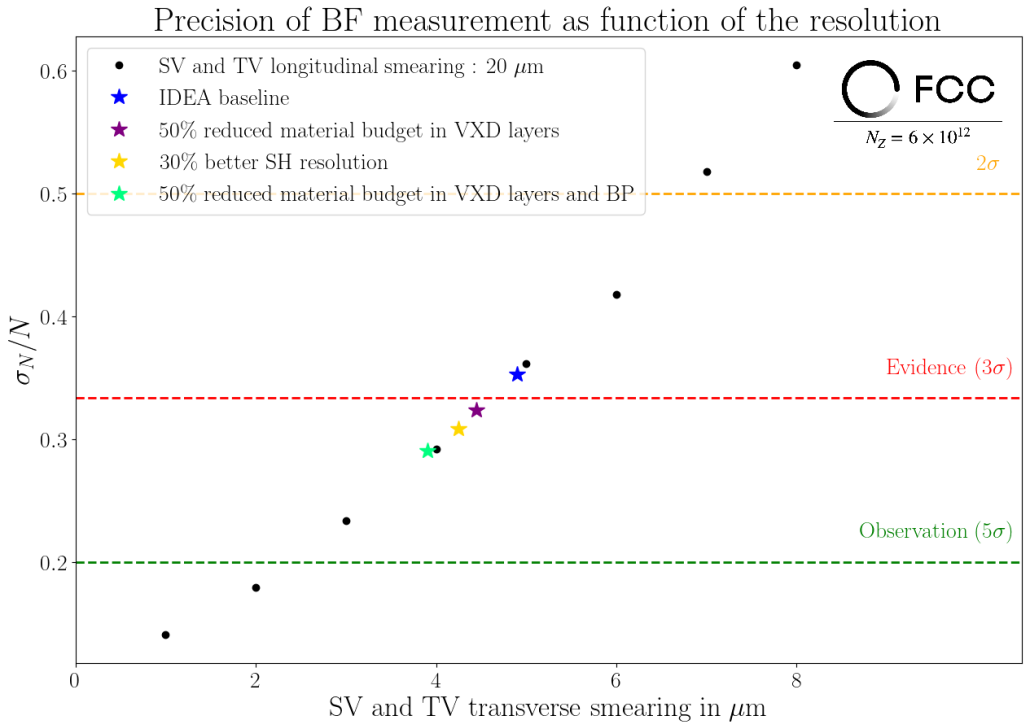

Figure E.17: Précision de la mesure du rapport d'embranchement de $B^0 \to K^{*0}\tau^+\tau^-$ en fonction de la résolution transversale des vertex, avec une résolution longitudinale fixée à 20 µm, en comparaison avec des points représentant des détecteurs de vertex réels.

IDEA ne permet pas d'atteindre le seuil d'évidence, et même des améliorations optimistes ne permettent pas d'atteindre le seuil de découverte. Cela signifie que, même à FCC-*ee*, la mesure de $B^0 \to K^{*0}\tau^+\tau^-$ s'annonce complexe.

Ce travail est un premier pas et ne prend pas en compte, par exemple, les incertitudes systémiques, la prise en compte de l'incertitude statistique étant considérée comme suffisante pour une étude portant sur une machine qui n'existe pas encore. La conclusion de ce travail souligne le défi que représentera la mesure de $B^0 \to K^{*0}\tau^+\tau^-$ à FCC-*ee*, cependant plusieurs pistes peuvent être envisagées pour améliorer les résultats obtenus. Par exemple, en considérant des modes de désintégration leptoniques des τ en plus du modes étudiés, il serait possible d'augmenter la statistique ; néanmoins, cela nécessiterait le développement de nouvelles méthodes de reconstruction. De plus, de nouveaux concepts de détecteurs de vertex utilisant des technologies innovantes pourraient émerger. Il est également envisageable d'améliorer la sélection développée en prenant en compte de nouvelles variables et/ou en utilisant un autre algorithme. Enfin, il est important de garder à l'esprit que cette analyse a été effectuée sous l'hypothèse du Modèle Standard, et que des effets de NP pourraient augmenter le rapport d'embranchement et permettre aux détecteurs testés ici de réaliser la mesure. Il semble donc crucial de poursuivre les efforts pour réaliser cette mesure, car une découverte inattendue signifierait également un désaccord avec le Modèle Standard.

E.7 Conclusion

Dans cette thèse, l'objectif était de présenter deux études clés. La première porte sur les désintégrations sans charme à trois corps des mésons B neutres avec un K^0_S dans l'état final, en particulier les désintégrations $B^0_{d,s} \to K^0_S h^+ h'^-$, en utilisant le spectromètre LHCb. La deuxième est une étude prospective sur la capacité des futures expériences au FCC-*ee* à mesurer la transition $B^0 \to K^{*0}\tau^+\tau^-$.

Le cadre théorique de ces études a été introduit en mettant l'accent sur la violation de *CP* et la phénoménologie des désintégrations hadroniques des mésons B pour justifier l'étude des désintégrations $B^0_{d,s} \to K^0_S h^+ h'^-$. De plus, la phénoménologie des desintégrations semi-leptoniques des mésons B a été présentée pour introduire $B^0 \to K^{*0}\tau^+\tau^-$. Le cadre expérimental a été détaillé, incluant une présentation du LHC, du spectromètre LHCb, et du projet FCC-*ee*.

La partie principale des études sur les désintégrations $B^0_{d,s} \to K^0_S h^+ h'^-$ a porté sur la mesure des rapports d'embranchement correspondants à l'aide des données de LHCb. Les étapes clés comprenaient la création d'une sélection dédiée avec deux MVAs, la construction d'un fit de masse complexe pour déterminer le nombre d'événements de signal, la détermination des efficacités de reconstruction et de sélection avec une méthode innovante de moyennage, et la réalisation d'une étude des systématiques pour fournir les résultats avec les incertitudes appropriées. Cela a conduit à l'amélioration des mesures pour les modes déjà observés et à la découverte de $B^0_s \to K^0_S K^+ K^-$, même si les chiffres présentés dans le manuscrit changeront dans la version finale de l'analyse.

Une version préliminaire de la première analyse Dalitz intégrée dans le temps de $B^0_s \to K^0_S \pi^+\pi^-$ a également été présentée, montrant des premiers graphiques et asymétries, notamment autour de la résonance $K^{*+}(892)$, indiquant une éventuelle violation de *CP*. L'objectif final est de réaliser une analyse de Dalitz dépendante du temps de $B^0 \to K^0_S \pi^+\pi^-$ pour accéder à $\sin(2\beta)$ et tester le SM.

Concernant l'étude de la faisabilité de la mesure de $B^0 \to K^{*0}\tau^+\tau^-$ au FCC-*ee*, une méthode de reconstruction dédiée a été développée, nécessitant la mesure précise des vertex de désintégration. Cette étude, en utilisant plusieurs hypothèses de détecteur de vertex et en considérant les bruits de fond dominants en plus du signal, a été un banc d'essai pour le projet FCC-*ee*. Au final, il semble que la mesure de cette désintégration, sous l'hypothèse du SM, reste inateignable à FCC-*ee*. Néanmoins, des améliorations futures dans la technologie des détecteurs de vertex et/ou l'ajout de canaux de désintégration $\tau^\pm$ alternatifs pourraient permettre l'observation. Dans tous les cas, cette mesure est une étape essentielle pour tester les limites du SM et explorer la NP, il sera donc important d'essayer de la réaliser.

Bibliography

[1] S. Schael et al. Precision electroweak measurements on the Z resonance. *Phys. Rept.*, 427:257–454, 2006.

[2] Nicola Cabibbo. Unitary symmetry and leptonic decays. *Physical Review Letters*, 10(12):531, 1963.

[3] Makoto Kobayashi and Toshihide Maskawa. CP-violation in the renormalizable theory of weak interaction. *Progress of theoretical physics*, 49(2):652–657, 1973.

[4] Patrick Huet and Eric Sather. Electroweak baryogenesis and standard model *CP* violation. *Phys. Rev.*, D51:379–394, 1995.

[5] Tzee-Ke Kuo and James Pantaleone. Neutrino oscillations in matter. *Reviews of Modern Physics*, 61(4):937, 1989.

[6] Paul Langacker. The physics of heavy z' gauge bosons. *Reviews of Modern Physics*, 81(3):1199, 2009.

[7] I Dorsner, S Fajfer, A Greljo, JF Kamenik, and N Kosnik. Physics of leptoquarks in precision experiments and at particle colliders. *Physics Reports*, 641:1–68, 2016.

[8] Marzia Bordone, Claudia Cornella, Javier Fuentes-Martin, and Gino Isidori. A three-site gauge model for flavor hierarchies and flavor anomalies. *Phys. Lett. B*, 779:317–323, 2018.

[9] Lyndon Evans and Philip Bryant. LHC machine. *Journal of instrumentation*, 3(08):S08001, 2008.

[10] A Augusto Alves Jr, LM Andrade Filho, AF Barbosa, I Bediaga, G Cernicchiaro, G Guerrer, HP Lima Jr, AA Machado, J Magnin, F Marujo, et al. The LHCb detector at the LHC. *Journal of instrumentation*, 3(08):S08005, 2008.

[11] FCC collaboration et al. Fcc-ee: The lepton collider: Future circular collider conceptual design report volume 2. *European Physical Journal: Special Topics*, 228(2):261–623, 2019.

[12] Mary K Gaillard, Paul D Grannis, and Frank J Sciulli. The standard model of particle physics. *Reviews of Modern Physics*, 71(2):S96, 1999.

[13] Peter W Higgs. Broken symmetries and the masses of gauge bosons. *Physical review letters*, 13(16):508, 1964.

[14] François Englert and Robert Brout. Broken symmetry and the mass of gauge vector mesons. *Physical review letters*, 13(9):321, 1964.

[15] Georges Aad, Tatevik Abajyan, Brad Abbott, Jalal Abdallah, S Abdel Khalek, Ahmed Ali Abdelalim, R Aben, B Abi, M Abolins, OS AbouZeid, et al. Observation of a new particle in the search for the Standard Model Higgs boson with the ATLAS detector at the LHC. *Physics Letters B*, 716(1):1–29, 2012.

[16] Serguei Chatrchyan, Vardan Khachatryan, Albert M Sirunyan, Armen Tumasyan, Wolfgang Adam, Ernest Aguilo, Thomas Bergauer, Marko Dragicevic, Janos Erö, Christian Fabjan, et al. Observation of a new boson at a mass of 125 GeV with the CMS experiment at the LHC. *Physics Letters B*, 716(1):30–61, 2012.

[17] Julia Woithe, Gerfried J Wiener, and Frederik F Van der Veken. Let's have a coffee with the Standard Model of particle physics! *Physics Education*, 52(3):034001, mar 2017.

[18] Joseph John Thomson. XL. Cathode rays. *The London, Edinburgh, and Dublin Philosophical Magazine and Journal of Science*, 44(269):293–316, 1897.

[19] W. Pauli. Dear radioactive ladies and gentlemen. *Phys. Today*, 31N9:27, 1978.

[20] Clyde L Cowan Jr, Frederick Reines, FB Harrison, HW Kruse, and AD McGuire. Detection of the free neutrino: a confirmation. *Science*, 124(3212):103–104, 1956.

[21] Murray Gell-Mann. A Schematic Model of Baryons and Mesons. *Phys. Lett.*, 8:214–215, 1964.

[22] Martin Breidenbach, Jerome I. Friedman, Henry W. Kendall, Elliott D. Bloom, D. H. Coward, H. C. DeStaebler, J. Drees, Luke W. Mo, and Richard E. Taylor. Observed behavior of highly inelastic electron-proton scattering. *Phys. Rev. Lett.*, 23:935–939, 1969.

[23] S. H. Neddermeyer and C. D. Anderson. Note on the Nature of Cosmic Ray Particles. *Phys. Rev.*, 51:884–886, 1937.

[24] J. C. Street and E. C. Stevenson. New Evidence for the Existence of a Particle of Mass Intermediate Between the Proton and Electron. *Phys. Rev.*, 52:1003–1004, 1937.

[25] G. Danby, J. M. Gaillard, Konstantin A. Goulianos, L. M. Lederman, Nari B. Mistry, M. Schwartz, and J. Steinberger. Observation of High-Energy Neutrino Reactions and the Existence of Two Kinds of Neutrinos. *Phys. Rev. Lett.*, 9:36–44, 1962.

[26] S. L. Glashow, J. Iliopoulos, and L. Maiani. Weak Interactions with Lepton-Hadron Symmetry. *Phys. Rev. D*, 2:1285–1292, 1970.

[27] J. E. Augustin et al. Discovery of a Narrow Resonance in e^+e^- Annihilation. *Phys. Rev. Lett.*, 33:1406–1408, 1974.

[28] Jean-Jacques Aubert, U Becker, PJ Biggs, J Burger, M Chen, G Everhart, P Goldhagen, J Leong, T McCorriston, TG Rhoades, et al. Experimental observation of a heavy particle J. *Physical Review Letters*, 33(23):1404, 1974.

[29] Antonino Zichichi. Foundations of Sequential Heavy Lepton Searches. *History of Original Ideas and Basic Discoveries in Particle Physics*, pages 227–275, 1996.

[30] Yung-Su Tsai. Decay Correlations of Heavy Leptons in $e^+ + e^- \to l^+ + l^-$. *Phys. Rev. D*, 4:2821–2837, Nov 1971.

[31] Martin L. Perl et al. Evidence for Anomalous Lepton Production in e+ - e- Annihilation. *Phys. Rev. Lett.*, 35:1489–1492, 1975.

[32] K. Kodama et al. Observation of tau neutrino interactions. *Phys. Lett. B*, 504:218–224, 2001.

[33] Makoto Kobayashi and Toshihide Maskawa. *CP*-violation in the renormalizable theory of weak interaction. *Prog. Theor. Phys.*, 49:652–657, 1973.

[34] S. W. Herb et al. Observation of a Dimuon Resonance at 9.5-GeV in 400-GeV Proton-Nucleus Collisions. *Phys. Rev. Lett.*, 39:252–255, 1977.

[35] W. G. Cobau. The observation of the top quark at D0. In *International Europhysics Conference on High-energy Physics (HEP 95)*, pages 651–654, 1995.

[36] A. Caner. Observation of top quark production in $\bar{p}p$ collisions with the Collider Detector at Fermilab. In *23rd International Meeting on Fundamental Physics: The Top Quark, Heavy Flavor Physics and Symmetry Breaking*, pages 188–197, 5 1995.

[37] Albert Einstein. Die feldgleichungen der gravitation. *Sitzungsberichte der Königlich Preußischen Akademie der Wissenschaften*, pages 844–847, 1915.

[38] Katherine Garrett and Gintaras Duda. Dark matter: A primer. *Advances in Astronomy*, 2011:1–22, 2011.

[39] Edmund J Copeland, Mohammad Sami, and Shinji Tsujikawa. Dynamics of dark energy. *International Journal of Modern Physics D*, 15(11):1753–1935, 2006.

[40] Andrei D Linde. A new inflationary universe scenario: a possible solution of the horizon, flatness, homogeneity, isotropy and primordial monopole problems. *Physics Letters B*, 108(6):389–393, 1982.

[41] Yoshiyuki Fukuda, T Hayakawa, E Ichihara, K Inoue, K Ishihara, Hirokazu Ishino, Y Itow, T Kajita, J Kameda, S Kasuga, et al. Evidence for oscillation of atmospheric neutrinos. *Physical review letters*, 81(8):1562, 1998.

[42] Y. Fukuda, T. Hayakawa, E. Ichihara, K. Inoue, K. Ishihara, H. Ishino, Y. Itow, T. Kajita, J. Kameda, S. Kasuga, K. Kobayashi, Y. Kobayashi, Y. Koshio, M. Miura, M. Nakahata, S. Nakayama, A. Okada, K. Okumura, N. Sakurai, M. Shiozawa, Y. Suzuki, Y. Takeuchi, Y. Totsuka, S. Yamada, M. Earl, A. Habig, E. Kearns, M. D. Messier, K. Scholberg, J. L. Stone, L. R. Sulak, C. W. Walter, M. Goldhaber, T. Barszczak, D. Casper, W. Gajewski, W. R. Kropp, L. R. Price, F. Reines, M. Smy, H. W. Sobel, M. R. Vagins, K. S. Ganezer, W. E. Keig, R. W. Ellsworth, S. Tasaka, J. W. Flanagan, A. Kibayashi, J. G. Learned, S. Matsuno, V. J. Stenger, D. Takemori, T. Ishii, J. Kanzaki, T. Kobayashi, S. Mine, K. Nakamura, K. Nishikawa, Y. Oyama, A. Sakai, M. Sakuda, O. Sasaki, S. Echigo, M. Kohama, A. T. Suzuki, T. J. Haines, E. Blaufuss, B. K. Kim, R. Sanford, R. Svoboda, M. L. Chen, J. A. Goodman, G. W. Sullivan, J. Hill, C. K. Jung, K. Martens, C. Mauger, C. McGrew, E. Sharkey, B. Viren, C. Yanagisawa, W. Doki, K. Miyano, H. Okazawa, C. Saji, M. Takahata, Y. Nagashima, M. Takita, T. Yamaguchi, M. Yoshida, S. B. Kim, M. Etoh, K. Fujita, A. Hasegawa, T. Hasegawa, S. Hatakeyama, T. Iwamoto, M. Koga, T. Maruyama, H. Ogawa, J. Shirai, A. Suzuki, F. Tsushima, M. Koshiba, M. Nemoto, K. Nishijima, T. Futagami, Y. Hayato, Y. Kanaya, K. Kaneyuki, Y. Watanabe, D. Kielczewska, R. A. Doyle, J. S. George, A. L. Stachyra, L. L. Wai, R. J. Wilkes, and K. K. Young. Measurement of the Flux and Zenith-Angle Distribution of Upward Throughgoing Muons by Super-Kamiokande. *Phys. Rev. Lett.*, 82:2644–2648, Mar 1999.

[43] A. D. Sakharov. Violation of CP Invariance, C asymmetry, and baryon asymmetry of the universe. *Pisma Zh. Eksp. Teor. Fiz.*, 5:32–35, 1967.

[44] M. E. Shaposhnikov. Baryon Asymmetry of the Universe in Standard Electroweak Theory. *Nucl. Phys. B*, 287:757–775, 1987.

[45] Gerard 't Hooft. Symmetry Breaking Through Bell-Jackiw Anomalies. *Phys. Rev. Lett.*, 37:8–11, 1976.

[46] María Belén Gavela, P Hernandez, Jean Orloff, and Olivier Pène. Standard model CP-violation and baryon asymmetry. *Modern Physics Letters A*, 9(09):795–809, 1994.

[47] Particle Data Group, RL Workman, VD Burkert, V Crede, E Klempt, U Thoma, L Tiator, K Agashe, G Aielli, BC Allanach, et al. Review of particle physics. *Progress of theoretical and experimental physics*, 2022(8):083C01, 2022.

[48] Ling-Lie Chau and Wai-Yee Keung. Comments on the parametrization of the Kobayashi-Maskawa matrix. *Physical Review Letters*, 53(19):1802, 1984.

[49] T Altomari and Lincoln Wolfenstein. Calculation of the rates for semileptonic B decays, 1986.

[50] Timothy Altomari and Lincoln Wolfenstein. Constraints on semileptonic B decays from the measurement of the D' polarization in $B \to D'\bar{\nu}$. *Phys. Rev. D*, 37:681–687, 1988.

[51] Jérôme Charles, A Höcker, Heiko Lacker, Sandrine Laplace, François R Le Diberder, Julie Malclès, José Ocariz, Muriel Pivk, and Lydia Roos. CP violation and the CKM matrix: Assessing the impact of the asymmetric B factories. *The European Physical Journal C-Particles and Fields*, 41(1):1–131, 2005. Updated results and plots available at: http://ckmfitter.in2p3.fr.

[52] Chien-Shiung Wu, Ernest Ambler, Raymond W Hayward, Dale D Hoppes, and Ralph Percy Hudson. Experimental test of parity conservation in beta decay. *Physical review*, 105(4):1413, 1957.

[53] Maurice Goldhaber, Lee Grodzins, and Andrew W Sunyar. Helicity of neutrinos. *Physical review*, 109(3):1015, 1958.

[54] M Gormley, E Hyman, W Lee, T Nash, J Peoples, C Schultz, and S Stein. Experimental test of C invariance in $\eta \to \pi+ \pi- \pi\ 0$. *Physical Review Letters*, 21(6):402, 1968.

[55] James H Christenson, Jeremiah W Cronin, Val L Fitch, and René Turlay. Evidence for the 2 π Decay of the K 2 0 Meson. *Physical Review Letters*, 13(4):138, 1964.

[56] J Richard Batley, RS Dosanjh, TJ Gershon, GE Kalmus, C Lazzeroni, DJ Munday, E Olaiya, M Patel, Michael Andrew Parker, TO White, et al. A precision measurement of direct CP violation in the decay of neutral kaons into two pions. *Physics Letters B*, 544(1-2):97–112, 2002.

[57] A Alavi-Harati, T Alexopoulos, M Arenton, K Arisaka, S Averitte, RF Barbosa, AR Barker, M Barrio, Leo Bellantoni, A Bellavance, et al. Measurements of direct CP violation, CPT symmetry, and other parameters in the neutral kaon system. *Physical Review D*, 67(1):012005, 2003.

[58] BaBar Collaboration et al. Direct CP violating asymmetry in B-0-¿ K+ pi (-) decays. *Physical Review Letters*, 93(13), 2004.

[59] Y Chao, P Chang, K Abe, K Abe, N Abe, I Adachi, H Aihara, K Akai, M Akatsu, M Akemoto, et al. Evidence for direct CP violation in B 0→ K+ π-decays. *Physical review letters*, 93(19):191802, 2004.

[60] Roel Aaij, C Abellan Beteta, B Adeva, M Adinolfi, C Adrover, A Affolder, Z Ajaltouni, J Albrecht, F Alessio, M Alexander, et al. First Observation of C P Violation in the Decays of B s 0 Mesons. *Physical review letters*, 110(22):221601, 2013.

[61] Roel Aaij et al. Observation of CP Violation in Charm Decays. *Phys. Rev. Lett.*, 122(21):211803, 2019.

[62] A Apostolakis, E Aslanides, G Backenstoss, P Bargassa, O Behnke, A Benelli, V Bertin, F Blanc, P Bloch, P Carlson, et al. A determination of the CP violation parameter η+- from the decay of strangeness-tagged neutral kaons. *Physics Letters B*, 458(4):545–552, 1999.

[63] Kazuo Abe, R Abe, I Adachi, Byoung Sup Ahn, H Aihara, M Akatsu, G Alimonti, K Asai, M Asai, Y Asano, et al. Observation of large CP violation in the neutral B meson system. *Physical review letters*, 87(9):091802, 2001.

[64] Bernard Aubert, D Boutigny, J-M Gaillard, A Hicheur, Y Karyotakis, JP Lees, P Robbe, V Tisserand, Antimo Palano, GP Chen, et al. Observation of CP violation in the B 0 meson system. *Physical review letters*, 87(9):091801, 2001.

[65] MATTHIAS NEUBERT. *B DECAYS AND THE HEAVY-QUARK EXPANSION*, page 239–293. WORLD SCIENTIFIC, June 1998.

[66] Luis Alejandro Pérez Pérez. *Time-Dependent Amplitude Analysis of B^ 0-¿ Kspi+ pi- decays with the BaBar Experiment and constraints on the CKM matrix using the B-¿ K* pi and B-¿ rho K modes*. PhD thesis, Université Paris-Diderot-Paris VII, 2008.

[67] Yasmine Sara Amhis et al. Averages of b-hadron, c-hadron, and τ-lepton properties as of 2021. *Phys. Rev. D*, 107(5):052008, 2023.

[68] Roel Aaij et al. Updated branching fraction measurements of $B^0_{(s)} \to K^0_S h^+ h'^-$ decays. *JHEP*, 11:027, 2017.

[69] Marouen Baalouch. *Dalitz analysis of the three-body charmless decay $B^0 \to K^0_S \pi^+ \pi^-$ with the LHCb spectrometer*. PhD thesis, Clermont-Ferrand U., 2015.

[70] R. Aaij et al. Amplitude analysis of the decay $\overline{B}^0 \to K^0_S \pi^+ \pi^-$ and first observation of the CP asymmetry in $\overline{B}^0 \to K^*(892)^- \pi^+$. *Phys. Rev. Lett.*, 120(26):261801, 2018.

[71] JF Kamenik, S Monteil, A Semkiv, and L Vale Silva. Lepton polarization asymmetries in rare semi-tauonic $b \to s$ exclusive decays at fcc-ee. *The European Physical Journal C*, 77(10):1–19, 2017.

[72] Paolo Branchini. The belle ii experiment: Status and prospects. *Universe*, 4(10):101, 2018.

[73] BABAR Collaboration et al. Search for B+-¿ K+ tau (+) tau (-) at the BABAR Experiment. *Physical Review Letters, 2017, vol. 118, num. 3, p. 031802*, 2017.

[74] Roel Aaij, B Adeva, M Adinolfi, A Affolder, Z Ajaltouni, S Akar, J Albrecht, F Alessio, M Alexander, S Ali, et al. Test of lepton universality using $b^+ \to k^+ \ell^+ \ell^-$ decays. *Physical Review Letters*, 113(15):151601, 2014.

[75] LHCb Collaboration et al. Measurement of lepton universality parameters in $b^+ \to k^+\ell^+\ell^-$ and $b^0 \to k^{*0}\ell^+\ell^-$ decays. *Physical Review D-Particles, Fields, Gravitation and Cosmology*, 2023.

[76] Roel Aaij, B Adeva, M Adinolfi, A Affolder, Z Ajaltouni, S Akar, J Albrecht, F Alessio, M Alexander, S Ali, et al. Measurement of the ratio of branching fractions b ($b^0 \to d^{*+}\tau^-\nu_\tau$)/ b ($b^0 \to d^{*+}\mu^-\nu_\mu$). *Physical review letters*, 115(11):111803, 2015.

[77] Alejandro Alfonso Albero, Alexey Badalov, Miriam Calvo Gomez, Alessandro Camboni, Samuel Coquereau, G Fernandez, Lluis Garrido Beltran, David Gascon Fora, Ricardo Graciani Diaz, Carla Marin Benito, et al. Measurement of the ratio of the $b^0 \to d^{*+}\tau^-\nu_\tau$ and $b^0 \to d^{*+}\mu^-\nu_\mu$ branching fractions using three-prong τ-lepton decays. *Physical Review Letters, 2018, vol. 120, num. 17, p. 171802*, 2018.

[78] LHCb Collaboration et al. Angular analysis of the b^0ß$k^{*0}\mu^+\mu^-$ decay using 3 fb- 1 of integrated luminosity. *Journal of High Energy Physics*, 2016(2):1–79, 2016.

[79] S Wehle, C Niebuhr, S Yashchenko, I Adachi, H Aihara, S Al Said, DM Asner, V Aulchenko, T Aushev, R Ayad, et al. Lepton-flavor-dependent angular analysis of $b \to k^*\ell\ell$. *Physical review letters*, 118(11):111801, 2017.

[80] S Myers and Emilio Picasso. The design, construction and commissioning of the cern large electron–positron collider. *Contemporary Physics*, 31(6):387–403, 1990.

[81] Antonella Balerna and Settimio Mobilio. Introduction to synchrotron radiation. In *Synchrotron Radiation: Basics, Methods and Applications*, pages 3–28. Springer, 2014.

[82] LHCb Collaboration et al. Measurement of the inelastic pp cross-section at a centre-of-mass energy of 7 TeV. *Journal of High Energy Physics*, 2015(2), 2015.

[83] CJG Onderwater, LHCb Collaboration, et al. Measurement of the inelastic pp cross-section at a centre-of-mass energy of 13 TeV. *Journal of High Energy Physics*, 2018(6):100, 2018.

[84] Edouard Regenstreif. The CERN proton synchrotron. Technical report, CERN, 1959.

[85] G. Arnison et al. Experimental Observation of Isolated Large Transverse Energy Electrons with Associated Missing Energy at $\sqrt{s} = 540$ GeV. *Phys. Lett. B*, 122:103–116, 1983.

[86] G. Arnison et al. Experimental Observation of Lepton Pairs of Invariant Mass Around 95-GeV/c**2 at the CERN SPS Collider. *Phys. Lett. B*, 126:398–410, 1983.

[87] JT Boyd. LHC Run-2 and future prospects. *arXiv preprint arXiv:2001.04370*, 2020.

[88] Kenneth Aamodt, A Abrahantes Quintana, R Achenbach, S Acounis, D Adamová, C Adler, M Aggarwal, F Agnese, G Aglieri Rinella, Z Ahammed, et al. The ALICE experiment at the CERN LHC. *Journal of Instrumentation*, 3(08):S08002, 2008.

[89] Georges Aad, Xabier Sebastian Anduaga, S Antonelli, M Bendel, B Breiler, F Castrovillari, JV Civera, T Del Prete, Maria Teresa Dova, S Duffin, et al. The ATLAS experiment at the CERN large hadron collider. *JInst*, 2008.

[90] CMS Collaboration, S Chatrchyan, G Hmayakyan, V Khachatryan, AM Sirunyan, W Adam, T Bauer, T Bergauer, H Bergauer, M Dragicevic, et al. The CMS experiment at the CERN LHC. *JInst*, 3:S08004, 2008.

[91] Roel Aaij, Bernardo Adeva, Marco Adinolfi, Ziad Ajaltouni, Simon Akar, Johannes Albrecht, Federico Alessio, Michael Alexander, Suvayu Ali, Georgy Alkhazov, et al. Measurement of the b-Quark Production Cross Section in 7 and 13 TeV p p Collisions. *Physical review letters*, 118(5):052002, 2017.

[92] Javier Mazzitelli, Alessandro Ratti, Marius Wiesemann, and Giulia Zanderighi. B-hadron production at the LHC from bottom-quark pair production at NNLO+ PS. *Physics Letters B*, 843:137991, 2023.

[93] R Aaji, C Abellan Beteta, B Adeva, M Adinolfi, C Adrover, A Affolder, Ziad Ajaltouni, J Albrecht, F Alessio, M Alexander, et al. Measurement of b hadron production fractions in 7 TeV p p collisions. *Physical Review D*, 85(3):032008, 2012.

[94] Roel Aaij, C Abellan Beteta, Bernardo Adeva, Marco Adinolfi, Christine Angela Aidala, Ziad Ajaltouni, Simon Akar, Pietro Albicocco, Johannes Albrecht, Federico Alessio, et al. Measurement of b hadron fractions in 13 TeV p p collisions. *Physical Review D*, 100(3):031102, 2019.

[95] ATLAS Inner Detector. Technical design report. *CERN= LHCC*, pages 98–13, 1997.

[96] S Amato, D Carvalho, T Da Silva, JRT De Mello, L De Paula, F Galvez-Durand, M Gandelman, J Helder Lopes, B Marechal, L Martinelli, et al. LHCb magnet: Technical design report. *LHCb TDR 4*, 2000.

[97] Christian Elsasser. $\bar{b}b$ production angle plots. link.

[98] Torbjörn Sjöstrand. The PYTHIA event generator: past, present and future. *Computer Physics Communications*, 246:106910, 2020.

[99] Belle-II Collaboration, II Belle, et al. Technical design report. *arXiv preprint arXiv:1011.0352*, 2010.

[100] Evgenii Kurbatov. LHCb results on rare leptonic decays of B-mesons. *EPJ Web of Conferences*, 222:02008, 01 2019.

[101] Ya V Pavlenko, O Omelaenko, P Dalpiaz, Z Guzik, VK Semenov, J Ocariz, A Khan, P Perret, S Laptek, O Schneider, et al. LHCb VELO (VErtex LOcator): Technical Design Report. Technical report, LHCb-TDR-005, 2001.

[102] Roel Aaij, A Affolder, K Akiba, M Alexander, S Ali, RB Appleby, M Artuso, A Bates, A Bay, O Behrendt, et al. Performance of the LHCb vertex locator. *Journal of Instrumentation*, 9(09):P09007, 2014.

[103] J Gassner, M Needham, and O Steinkamp. Layout and expected performance of the LHCb TT station. Technical report, CERN-LHCb-2003-140, 2004.

[104] Roel Aaij, S Akar, J Albrecht, M Alexander, A Alfonso Albero, S Amerio, L Anderlini, P d'Argent, A Baranov, W Barter, et al. Design and performance of the LHCb trigger and full real-time reconstruction in Run 2 of the LHC. *Journal of instrumentation*, 14(04):P04013, 2019.

[105] Daniel Esperante. The LHCb Silicon Tracker, first operational results. In *2010 IEEE Instrumentation & Measurement Technology Conference Proceedings*, pages 1057–1062. IEEE, 2010.

[106] J Andre, P Charra, W Flegel, PA Giudici, O Jamet, P Lancon, M Losasso, F Rohner, and C Rosset. Status of the LHCb magnet system. *IEEE transactions on applied superconductivity*, 12(1):366–371, 2002.

[107] Jeroen J van Hunen. The LHCb tracking system. *Nuclear Instruments and Methods in Physics Research Section A: Accelerators, Spectrometers, Detectors and Associated Equipment*, 572(1):149–153, 2007.

[108] Roel Aaij, Bernardo Adeva, Marco Adinolfi, Anthony Affolder, Ziad Ajaltouni, Simon Akar, Johannes Albrecht, Federico Alessio, Michael Alexander, Suvayu Ali, et al. Measurement of the track reconstruction efficiency at LHCb. *arXiv preprint arXiv:1408.1251*, 2014.

[109] PA Cerenkov et al. Visible emission of clean liquids by action of γ radiation. In *Dokl. Akad. Nauk SSSR*, volume 2, pages 451–454, 1934.

[110] R Calabrese, M Fiorini, E Luppi, L Minzoni, I Slazyk, L Tomassetti, M Bartolini, R Cardinale, F Fontanelli, A Petrolini, et al. Performance of the LHCb RICH detectors during LHC Run 2. *Journal of Instrumentation*, 17(07):P07013, 2022.

[111] O Omelaenko, P Dalpiaz, Z Guzik, E Spiridenkov, P Jarron, VK Semenov, J Ocariz, A Khan, P Perret, O Schneider, et al. LHCb Calorimeters: Technical Design Report. Technical report, LHCb-TDR-002, 2000.

[112] Patrick Robbe. *Generators, Calorimeter Trigger and J/ψ production at LHCb*. PhD thesis, Orsay, LAL, 2012.

[113] LHCb Collaboration et al. Search for Hidden-Sector Bosons in $B^0 \to K^{*0}\mu^+\mu^-$ Decays. *Physical Review Letters*, 115(16):161802, 2015.

[114] LHCb Collaboration et al. First Evidence for the Decay $B_s^0 \to \mu^+\mu^-$. *Physical Review Letters*, 110(2):021801, 2013.

[115] LHCb Collaboration et al. Measurement of the CP-Violating Phase ϕ_s in the Decay $B_s^0 \to J/\psi\phi$. *Phys. Rev. Lett.*, 108:101803, 2012.

[116] RICH LHCb. Muon System Technical Design Report. *CERN/LHCC*, 11:2001, 2001.

[117] LHCb Collaboration. Addendum to the muon system technical design report. *CERN/LHCC*, 2:2003, 2003.

[118] Giovanni Passaleva. A recurrent neural network for track reconstruction in the LHCb muon system. In *2008 IEEE Nuclear Science Symposium Conference Record*, pages 867–872. IEEE, 2008.

[119] A Dziurda et al. The LHCb trigger and its upgrade. *Nuclear Instruments and Methods in Physics Research Section A: Accelerators, Spectrometers, Detectors and Associated Equipment*, 824:277–279, 2016.

[120] T Head. The LHCb trigger system. *Journal of Instrumentation*, 9(09):C09015, 2014.

[121] Trigger schemes. link.

[122] Remi Cornat, Jacques Lecoq, and Pascal Perret. Level-0 decision unit for LHCb. Technical report, CERN-LHCb-2003-065, 2003.

[123] R Antunes Nobrega, A Franca Barbosa, I Bediaga, G Cernicchiaro, E Correa De Oliveira, J Magnin, L Manhaes de Andrade Filho, J Marques de Miranda, H Pessoa Lima Junior, A Reis, et al. LHCb computing technical design report, 2005.

[124] Marco Clemencic, Hubert Degaudenzi, Pere Mato, Sebastien Binet, Wim Lavrijsen, Charles Leggett, and Ivan Belyaev. Recent developments in the LHCb software framework Gaudi. In *Journal of Physics: Conference Series*, volume 219, page 042006. IOP Publishing, 2010.

[125] GAUDI& Barrand, I Belyaev, P Binko, M Cattaneo, R Chytracek, G Corti, M Frank, G Gracia, J Harvey, Eric Van Herwijnen, et al. GAUDI—A software architecture and framework for building HEP data processing applications. *Computer physics communications*, 140(1-2):45–55, 2001.

[126] LHCb. Moore Gitlab page, 2024. Link.

[127] Massimo Lamanna. The LHC computing grid project at CERN. *Nuclear Instruments and Methods in Physics Research Section A: Accelerators, Spectrometers, Detectors and Associated Equipment*, 534(1-2):1–6, 2004.

[128] LHCb. Brunel Gitlab page, 2024. Link.

[129] LHCb. DaVinci Gitlab page, 2024. Link.

[130] Rene Brun and Fons Rademakers. ROOT—An object oriented data analysis framework. *Nuclear instruments and methods in physics research section A: accelerators, spectrometers, detectors and associated equipment*, 389(1-2):81–86, 1997.

[131] LHCb. Gauss Gitlab page, 2024. Link.

[132] Torbjörn Sjöstrand, Stefan Ask, Jesper R Christiansen, Richard Corke, Nishita Desai, Philip Ilten, Stephen Mrenna, Stefan Prestel, Christine O Rasmussen, and Peter Z Skands. An introduction to PYTHIA 8.2. *Computer physics communications*, 191:159–177, 2015.

[133] Anders Ryd, David Lange, Natalia Kuznetsova, Sophie Versille, Marcello Rotondo, DP Kirkby, FK Wuerthwein, and A Ishikawa. Evtgen: a monte carlo generator for b-physics. *BAD*, 522:v6, 2005.

[134] Piotr Golonka and Zbigniew Was. PHOTOS Monte Carlo: a precision tool for QED correctionsin Z and W decays. *The European Physical Journal C-Particles and Fields*, 45(1):97–107, 2006.

[135] GEANT Collaboration, S Agostinelli, et al. GEANT4–a simulation toolkit. *Nucl. Instrum. Meth. A*, 506(25):0, 2003.

[136] LHCb. LHCb Gitlab page, 2024. Link.

[137] Mark Lutz. *Programming python*. " O'Reilly Media, Inc.", 2001.

[138] Jim Pivarski, Henry Schreiner, Angus Hollands, Pratyush Das, Kush Kothari, Aryan Roy, Jerry Ling, Nicholas Smith, Chris Burr, and Giordon Stark. Uproot. *Zenodo*, 2017.

[139] Jim Pivarski, Pratyush Das, Matthew Feickert, Henry Schreiner, Daniel Marley, Ruggero Turra, Chris Burr, Chao Gu, et al. Scikit-hep/uproot: 3.2. 2. *Zenodo*, 2019.

[140] Jim Pivarski, Peter Elmer, and David Lange. Awkward arrays in python, c++, and numba. In *EPJ Web of Conferences*, volume 245, page 05023. EDP Sciences, 2020.

[141] Stefan Van Der Walt, S Chris Colbert, and Gael Varoquaux. The NumPy array: a structure for efficient numerical computation. *Computing in science & engineering*, 13(2):22–30, 2011.

[142] Wes McKinney et al. Pandas: a foundational Python library for data analysis and statistics. *Python for high performance and scientific computing*, 14(9):1–9, 2011.

[143] John D Hunter. Matplotlib: A 2D graphics environment. *Computing in science & engineering*, 9(03):90–95, 2007.

[144] R. Aaij et al. Updated branching fraction measurements of $B^0_{(s)} \to K^0_S h^+ h'^-$ decays. *JHEP*, 11:027, 2017.

[145] LHCb. Bender Gitlab page, 2024. Link.

[146] Wouter D. Hulsbergen. Decay chain fitting with a Kalman filter. *Nucl. Instrum. Meth.*, A552:566–575, 2005.

[147] Stephane Monteil, Patrick Robbe, and Tristan Miralles. Determination of the L0Hadron trigger efficiency corrections. Technical report, CERN, Geneva, 2024. Link.

[148] Alexandra Martin Sanchez. *CP violation studies on the $B^0 \to DK^{*0}$ decays and hadronic trigger performance with the LHCb detector at CERN*. PhD thesis, Université Paris Sud-Paris XI, 2013.

[149] Muriel Pivk and Francois R Le Diberder. sPlots: A statistical tool to unfold data distributions. *Nuclear Instruments and Methods in Physics Research Section A: Accelerators, Spectrometers, Detectors and Associated Equipment*, 555(1-2):356–369, 2005.

[150] RooGaussian Class Reference. https://root.cern.ch/doc/master/classRooGaussian.html.

[151] RooChebychev Class Reference. https://root.cern.ch/doc/master/classRooChebychev.html.

[152] RooCBShape Class Reference. https://root.cern.ch/doc/master/classRooCBShape.html.

[153] Patrick Robbe. Run 1-2 performance meeting, May 2020. Available at `https://indico.cern.ch/event/917857/#39-update-on-l0hadron-efficien`.

[154] Olli Lupton, Vladimir Gligorov, Lucio Anderlini, and Barbara Sciascia. Calibration samples for particle identification at LHCb in Run 2. Technical report, CERN, 2016.

[155] Ilka Antcheva, Maarten Ballintijn, Bertrand Bellenot, Marek Biskup, Rene Brun, Nenad Buncic, Ph Canal, Diego Casadei, Olivier Couet, Valery Fine, et al. ROOT—A C++ framework for petabyte data storage, statistical analysis and visualization. *Computer Physics Communications*, 180(12):2499–2512, 2009.

[156] Karl Harrison, Wim TLP Lavrijsen, P Mato, A Soroko, CL Tan, Craig E. Tull, N Brook, and RWL Jones. GANGA: a user-Grid interface for Atlas and LHCb. *arXiv preprint cs/0306085*, 2003.

[157] Asmaa Abada, Marcello Abbrescia, Shehu S AbdusSalam, I Abdyukhanov, J Abelleira Fernandez, A Abramov, Mohamed Aburaia, AO Acar, PR Adzic, Prateek Agrawal, et al. Fcc physics opportunities. *The European Physical Journal C*, 79(6):1–161, 2019.

[158] FCC collaboration et al. Fcc-hh: The hadron collider: Future circular collider conceptual design report volume 3. *European Physical Journal: Special Topics*, 228(4):755–1107, 2019.

[159] Giorgio Apollinari, O Brüning, Tatsushi Nakamoto, and Lucio Rossi. High luminosity large hadron collider HL-LHC. *arXiv preprint arXiv:1705.08830*, 2017.

[160] R. L. Workman et al. Review of particle physics. *Prog. Theor. Exp. Phys.*, 2022(8):083C01, 2022.

[161] Yasmine Amhis, Sw Banerjee, Eli Ben-Haim, Florian Urs Bernlochner, Marcella Bona, Andrzej Bozek, Concezio Bozzi, Jolanta Brodzicka, M Chrzaszcz, J Dingfelder, et al. Averages of b-hadron, c-hadron, and τ τ-lepton properties as of 2018: Heavy flavor averaging group (hflav). *The European Physical Journal C*, 81:1–326, 2021.

[162] Kazunori Akai, Kazuro Furukawa, Haruyo Koiso, et al. SuperKEKB collider. *Nuclear Instruments and Methods in Physics Research Section A: Accelerators, Spectrometers, Detectors and Associated Equipment*, 907:188–199, 2018.

[163] R Aly, M Antonello, P Azzi, F Bedeschi, G Bencivenni, L Borgonovi, MLM Caccia, X Chu, G Cibinetto, T Coates, et al. First test-beam results obtained with idea, a detector concept designed for future lepton colliders. *Nuclear Instruments and Methods in Physics Research Section A: Accelerators, Spectrometers, Detectors and Associated Equipment*, 958:162088, 2020.

[164] G Chiarello, A Corvaglia, F Grancagnolo, A Miccoli, M Panareo, and GF Tassielli. The tracking system for the idea detector at future lepton colliders. *Nuclear Instruments and Methods in Physics Research Section A: Accelerators, Spectrometers, Detectors and Associated Equipment*, 936:503–504, 2019.

[165] M Antonello. Italian Physical Society: IDEA: A detector concept for future leptonic colliders. *Nuovo Cimento C*, 43:27, 2020.

[166] W Snoeys, M Campbell, E Cantatore, V Cencelli, R Dinapoli, E Heijne, P Jarron, P Lamanna, D Minervini, V O'Shea, et al. Pixel readout electronics development for the alice pixel vertex and lhcb rich detector. *Nuclear Instruments and Methods in Physics Research Section A: Accelerators, Spectrometers, Detectors and Associated Equipment*, 465(1):176–189, 2001.

[167] FCCAnalyses github repository. Link.

[168] J De Favereau, Christophe Delaere, Pavel Demin, Andrea Giammanco, Vincent Lemaitre, Alexandre Mertens, Michele Selvaggi, Delphes 3 Collaboration, et al. Delphes 3: a modular framework for fast simulation of a generic collider experiment. *Journal of High Energy Physics*, 2014(2):57, 2014.

[169] LHCb collaboration. Search for Bs→KSKK and updated branching fraction measurements of B(d,s)→KShh using Run 1+2 data. Link.

[170] Émilie Bertholet. *Search for new physics in charmless three-body B-meson decays*. PhD thesis, UPMC, 2019. Available as HAL:tel-02932152.

[171] Tianqi Chen and Carlos Guestrin. Xgboost: A scalable tree boosting system. In *Proceedings of the 22nd acm sigkdd international conference on knowledge discovery and data mining*, pages 785–794, 2016.

[172] Vance W Berger and YanYan Zhou. Kolmogorov–smirnov test: Overview. *Wiley statsref: Statistics reference online*, 2014.

[173] Thomas Grammatico. *Measurement of the branching fractions of B0s → KShh decays in LHCb, insights on the CKM angle gamma and monitoring of the Scintillating Fibre Tracker for the LHCb upgrade*. PhD thesis, Laboratoire de Physique Nucléaire et de Hautes Énergies, France, Paris U., VI-VII, 2022.

[174] Lucio Anderlini, Andrea Contu, Christopher Rob Jones, Sneha Sirirshkumar Malde, Dominik Muller, Stephen Ogilvy, Juan Martin Otalora Goicochea, Alex Pearce, Ivan Polyakov, Wenbin Qian, Barbara Sciascia, Ricardo Vazquez Gomez, and Yanxi Zhang. The PIDCalib package. Technical report, CERN, Geneva, Jul 2016.

[175] Hossein Afsharnia. *Study of the Charmless b-hadron decay using the LHCb spectrometer*. PhD thesis, Clermont-Ferrand U., 2022.

[176] Fabian Pedregosa et al. Scikit-learn: Machine learning in Python. *J. Machine Learning Res.*, 12:2825, 2011. and online at `http://scikit-learn.org/stable/`.

[177] Giovanni Punzi. Sensitivity of searches for new signals and its optimization. *eConf*, C030908:MODT002, 2003.

[178] F and James. MINUIT: Function Minimization and Error Analysis Reference Manual, 1998. CERN Program Library Long Writeups.

[179] R. L. Workman and Others. Review of Particle Physics. *PTEP*, 2022:083C01, 2022.

[180] RooArgusBG Class Reference. https://root.cern.ch/doc/master/classRooArgusBG.html.

[181] RooFFTConvPdf Class Reference. https://root.cern.ch/doc/master/classRooFFTConvPdf.html.

[182] M. Pivk and F.R. Le Diberder. : A statistical tool to unfold data distributions. *Nuclear Instruments and Methods in Physics Research Section A: Accelerators, Spectrometers, Detectors and Associated Equipment*, 555(1-2):356–369, dec 2005.

[183] sweights package. https://sweights.readthedocs.io/en/latest/index.html.

[184] Hans Dembinski, Matthew Kenzie, Christoph Langenbruch, and Michael Schmelling. Custom orthogonal weight functions (COWs) for event classification. *Nuclear Instruments and Methods in Physics Research Section A: Accelerators, Spectrometers, Detectors and Associated Equipment*, 1040:167270, oct 2022.

[185] John Back, Tim Gershon, Paul Harrison, Thomas Latham, Daniel O'Hanlon, Wenbin Qian, Pablo del Amo Sanchez, Daniel Craik, Jelena Ilic, Juan Martin Otalora Goicochea, Eugenia Puccio, Rafael Silva Coutinho, and Mark Whitehead. Laura ++: A dalitz plot fitter. *Computer Physics Communications*, 231:198–242, 2018.

[186] Michel De Cian, Stephanie Hansmann-Menzemer, Andreas Jaeger, Paul Seyfert, Jeroen van Tilburg, and Sebastian Wandernoth. Measurement of the track finding efficiency. Technical report, CERN, Geneva, Apr 2012.

[187] Vitalii Lisovskyi. The Calorimeter Objects Tools Group : Documentation page, 2021. Link.

[188] RooHypatia2 Class Reference. https://root.cern.ch/doc/master/classRooHypatia2.html.

[189] Michel De Cian. *Track Reconstruction Efficiency and Analysis of $B^0 \to K^{*0}\mu^+\mu^-$ at the LHCb Experiment*. PhD thesis, Universität Zürich, Sep 2013. Presented 14 Mar 2013.

[190] P Owen and T Blake. Reconstruction efficiency of DD K^0_s mesons using $D^0 \to \phi K^0_s$ decays. Technical report, CERN, Geneva, 2013.

[191] Marouen Baalouch, Eli Ben Haim, Timothy Gershon, Marc Grabalosa Gandara, Louis Henry, Thomas Edward Latham, James Mccarthy, Jan Mickelle Maratas, Diego Milanes Carreno, Stephane Monteil, Rafael Silva Coutinho, and Nigel Watson. Dalitz-plot analyses of the decays $B^0_s \to K^0_S K^\pm \pi^\mp$. *Phys. Rev. D*, 104, 2014.

[192] Roger W Johnson. An introduction to the bootstrap. *Teaching statistics*, 23(2):49–54, 2001.

[193] Roel Aaij et al. Precise measurement of the f_s/f_d ratio of fragmentation fractions and of B^0_s decay branching fractions. *Phys. Rev. D*, 104(3):032005, 2021. All figures and tables, along with any supplementary material and additional information, are available at https://cern.ch/lhcbproject/Publications/p/LHCb-PAPER-2020-046.html (LHCb public pages).

[194] RH Dalitz. Cxii. on the analysis of τ-meson data and the nature of the τ-meson. *The London, Edinburgh, and Dublin Philosophical Magazine and Journal of Science*, 44(357):1068–1080, 1953.

[195] RH Dalitz. Decay of τ mesons of known charge. *Physical review*, 94(4):1046, 1954.

[196] Bernard Aubert et al. Dalitz Plot Analysis of B+- —> pi+-pi+-pi-+ Decays. *Phys. Rev. D*, 79:072006, 2009.

[197] Gordon N. Fleming. Recoupling Effects in the Isobar Model. 1. General Formalism for Three-Pion Scattering. *Phys. Rev.*, 135:B551–B560, 1964.

[198] Charles Zemach. Determination of the Spins and Parities of Resonances. *Phys. Rev.*, 140:B109–B124, 1965.

[199] John Markus Blatt and Victor Frederick Weisskopf. *Theoretical nuclear physics*. Springer, New York, 1952.

[200] G. J. Gounaris and J. J. Sakurai. Finite width corrections to the vector meson dominance prediction for $\rho \to e^+e^-$. *Phys. Rev. Lett.*, 21:244–247, 1968.

[201] B. El-Bennich, A. Furman, R. Kaminski, L. Lesniak, B. Loiseau, and B. Moussallam. CP violation and kaon-pion interactions in B —> K pi+ pi- decays. *Phys. Rev. D*, 79:094005, 2009. [Erratum: Phys.Rev.D 83, 039903 (2011)].

[202] Roel Aaij et al. Amplitude analysis of $B^0_s \to K^0_S K^\pm \pi^\mp$ decays. *JHEP*, 06:114, 2019.

[203] LHCb collaboration. Measurement of b^0, b^0_s, b^+ and λ^0_b production asymmetries in 7 and 8 tev proton–proton collisions. *Physics Letters B*, 774:139–158, 2017.

[204] Wouter Verkerke and David Kirkby. The roofit toolkit for data modeling. In *Statistical Problems in Particle Physics, Astrophysics and Cosmology*, pages 186–189. World Scientific, 2006.

[205] Fred James, Matthias Winkler, et al. Minuit user's guide. *CERN, Geneva*, 23:94, 2004.

[206] FCC Collaboration. Future Circular Collider (FCC) Feasibility Study Midterm Report.

[207] Tristan Miralles and Stéphane Monteil. Study of the feasibility of the observation of $B^0 \to K^*(892)\tau^+\tau^-$ at FCC-*ee* and related vertex detector performance requirements, September 2024. Link.

[208] Kevin Kroeninger, Romain Madar, Stéphane Monteil, Fabrizio Palla, and Lars Roehrig. Reconstructed exclusive *b*-hadron decays as hemisphere jet charge tagger and its application for the measurement of R_b and A_{FB}^b, September 2023.

[209] LHCb collaboration. First observation of the $b^+ \to d_s^+ d_s^- k^+$ decay, 2022.

[210] Lingfeng Li and Tao Liu. b→ sτ+ τ- physics at future z factories. *Journal of High Energy Physics*, 2021(6):1–31, 2021.

[211] Damir Buskulic, D Casper, I De Bonis, D Decamp, P Ghez, C Goy, J-P Lees, M-N Minard, P Odier, B Pietrzyk, et al. Performance of the aleph detector at lep. *Nuclear Instruments and Methods in Physics Research Section A: Accelerators, Spectrometers, Detectors and Associated Equipment*, 360(3):481–506, 1995.

[212] Oliver Kramer and Oliver Kramer. Scikit-learn. *Machine learning for evolution strategies*, pages 45–53, 2016.

[213] Jonas Eschle, Albert Puig Navarro, Rafael Silva Coutinho, and Nicola Serra. zfit: Scalable pythonic fitting. *SoftwareX*, 11:100508, 2020.

[214] Fabrizio Palla. Vertex detector design and integration. Link.

[215] Greg Ciezarek, Mika Vesterinen. 67th Analysis and Software Week, April 2017. Available at `https://indico.cern.ch/event/603961/#23-limits-of-l0hadron-efficien`.

[216] Thibaud Humair. Rare Electroweak Penguins, July 2016. Available at `https://indico.cern.ch/event/557249/#10-r_k-status-update`.

[217] Alexandra Martin Sanchez, Patrick Robbe, and Marie-Hélène Schune. Performances of the LHCb L0 Calorimeter Trigger. Technical report, CERN, 2012.

[218] Albert Einstein. On a heuristic point of view concerning the production and transformation of light. *Annalen der Physik*, 17(1905):199–206, 1905.

[219] Tatsumi Aoyama, M. Hayakawa, Toichiro Kinoshita, and Makiko Nio. Tenth-Order Electron Anomalous Magnetic Moment — Contribution of Diagrams without Closed Lepton Loops. *Phys. Rev. D*, 91(3):033006, 2015. [Erratum: Phys.Rev.D 96, 019901 (2017)].

[220] X. Fan, T. G. Myers, B. A. D. Sukra, and G. Gabrielse. Measurement of the Electron Magnetic Moment. *Phys. Rev. Lett.*, 130(7):071801, 2023.